Microstrip Lines and Slotlines

THIRD EDITION

Ramesh Garg
Inder Bahl
Maurizio Bozzi

Microstrip Lines and Slotlines

Third Edition

For a listing of recent titles in the/
Artech House Microwave Library,
turn to the back of this book.

Microstrip Lines and Slotlines

Third Edition

Ramesh Garg
Inder Bahl
Maurizio Bozzi

ARTECH
HOUSE
BOSTON | LONDON
artechhouse.com

Library of Congress Cataloging-in-Publication Data
A catalog record for this book is available from the U.S. Library of Congress.

British Library Cataloguing in Publication Data
A catalog record for this book is available from the British Library.

ISBN-13: 978-1-60807-535-5

Cover design by Vicki Kane

10 9 8 7 6 5 4 3 2 1

Contents

CHAPTER 9

Preface to the Third Edition

Planar transmission line technology has progressed considerably since the second edition of this book was published in 1996. The impetus for this advancement has been provided principally by the UWB communications, imaging at THz frequencies, RFID, and so forth. It is imperative in such a scenario to revise this text to meet current needs. In this context, two new chapters—one on substrate integrated waveguide (SIW), and another on defected ground structures (DGSs)—have been added. The other chapters have been revised to include the recent developments in those areas. Due to the emphasis on compactness of device, use of UWB technology, and improved performance requirements, the use of computer-aided analysis and design is necessary. However, the efficient use of computer-aided techniques depends on the insight gained from the analytical techniques. This book elaborates on both types of techniques that have been successfully presented in its last two editions. The applications of computational techniques to planar lines are the highlight of the book. The details include the development of governing equations, basis functions, Green's function, and typical results. Realizing the increasing importance of simulation software in the design of complex devices, the chapters on SIW and DGS emphasize the connection between the data obtained from simulation software and the design.

Like its previous editions, this book is primarily intended for design engineers and research and development specialists who need to employ planar transmission lines in realizing distributed circuits and antenna systems. This book may also be helpful for advanced undergraduate and graduate courses in electronics and telecommunication engineering.

The extensive revisions included in this edition are based on the authors' own research and the extensive research material reported by others in journals and conferences throughout the world since 1996. It is sad to say that Professor K. C. Gupta is no longer leading the revision of the book. To augment the expertise, we have invited Professor M. Bozzi from the Department of Electronics, University of Pavia, Italy. Chapters on SIW and DGS are contributed by him.

Revisions to Chapter 1 include a section on fabrication. Sections on the lumped element model of the microstrip interconnect and buried microstrip line have been included in Chapter 2.

Chapters 3 and 4 elaborate on the characterization of microstrip discontinuities. RF short and via hole discontinuity characterization has been added in Chapter 3. Chapter 4 includes curved microstrip bend analysis based on planar waveguide model.

Chapter 5 discusses slotlines and has been largely revised with the addition of slotline variants, such as the sandwich slotline. The ultrawideband directional coupler realized using slotline-coupled microstrip lines is another useful addition in this chapter.

Chapter 6 is about defect ground structures and is a new addition to this book. A large number of research articles have been published since DGS was first introduced in 2001. This chapter includes topics such as the bandstop filter characteristics of DGS, equivalent circuit modeling, and applications of DGS to circuits and antennas. A typical application of DGS is the out-of-band performance improvement of devices.

Keeping in mind the importance of coplanar lines in compact planar circuits, antennas, and VLSI technology as an interconnect, Chapter 7 on coplanar lines has been revised extensively. The major changes in this chapter include new variants of CPW and CPS, the effect of thick metallization on line characteristics, broadband determination of conductor loss for application to digital signals, UWB transitions, and CAD models for discontinuities in CPW and CPS. The number of references has increased from 122 to 145.

Chapter 8 discusses coupled microstrip lines and has been revised by introducing a new section on the analysis of slot-coupled microstrip lines. In addition, the following changes have been introduced: new directivity improvement techniques for coupled microstrip line directional couplers, and ever-elusive accurate conformal mapping analysis of coupled microstrip lines.

The substrate integrated waveguide is a printed version of a rectangular waveguide, thus making these printed waveguide circuits light, compact, and cheaper. SIW technology was first proposed in 1994 although it was noticed in 2001. Substrate integrated waveguide forms the last chapter (Chapter 9) of the book. The topics discussed in this chapter include analysis and design of SIW, equivalent circuit modeling of SIW interconnect, and discontinuities. A number of variants of SIW are discussed, including substrate integrated folded waveguide. Transitions of SIW to microstrip and CPW are included. Typical applications of SIW include passive components, active circuits, antennas, and feed networks for array antennas. SIW technology promises possible integration of waveguide and planar transmission line-based components utilizing the positive features of each technology. This integrated system is called the system-on-substrate (SoS) concept and its realizations are the highlight of this chapter.

We believe that this thoroughly revised third edition contains the most up-to-date body of knowledge on this topic. We hope that the concepts included in *Microstrip Lines and Slotlines* will be helpful to the design and research engineers in continued development and applications of planar transmission line techniques.

The authors express their appreciation to colleagues in several organizations and a number of publishing houses for copyright permissions for figures and other material from their works. These items are duly acknowledged in the text. Thanks are also due to our colleagues in the authors' respective organizations. Finally, we would like to record the support and cooperation of the staff at Artech House, including Mark Walsh, Lindsay Moore, and Samantha Ronan.

CHAPTER 1

Microstrip Lines I: Quasi-Static Analyses, Dispersion Models, and Measurements

1.1 Introduction

1.1.1 Planar Transmission Structures

One of the principal requirements for a transmission structure to be suitable as a circuit element in *microwave integrated circuits* (MICs) is that the structure should be "planar" in configuration. A planar configuration implies that the characteristics of the element can be determined by the dimensions in a single plane. For example, the width of a microstrip line on a dielectric substrate can be adjusted to control its impedance. When the impedance can be controlled by dimensions in a single plane, the circuit fabrication can be conveniently carried out by techniques of photolithography and photoetching of thin films. Use of these techniques at microwave and millimeter wave frequencies has led to the development of hybrid and monolithic MICs. Microwave integrated circuits have been widely discussed in the literature [1-6].

There are several transmission structures that satisfy the requirement of being planar. The most common of these are: (i) microstrip, (ii) coplanar waveguide,

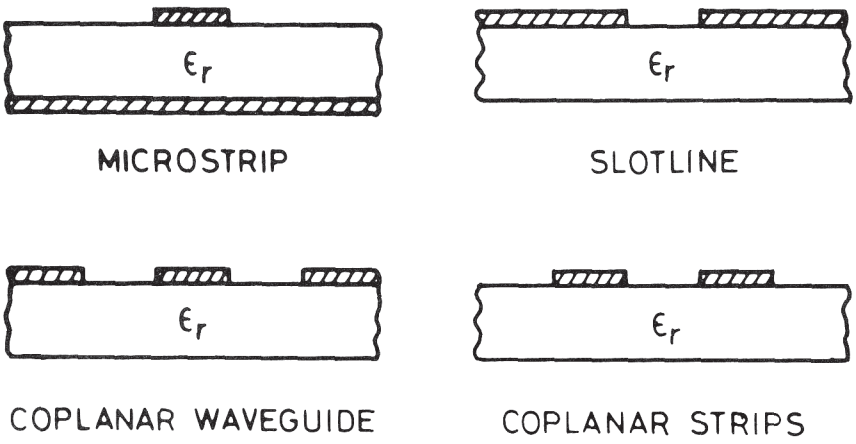

Figure 1.1 Planar transmission lines used in microwave integrated circuits.

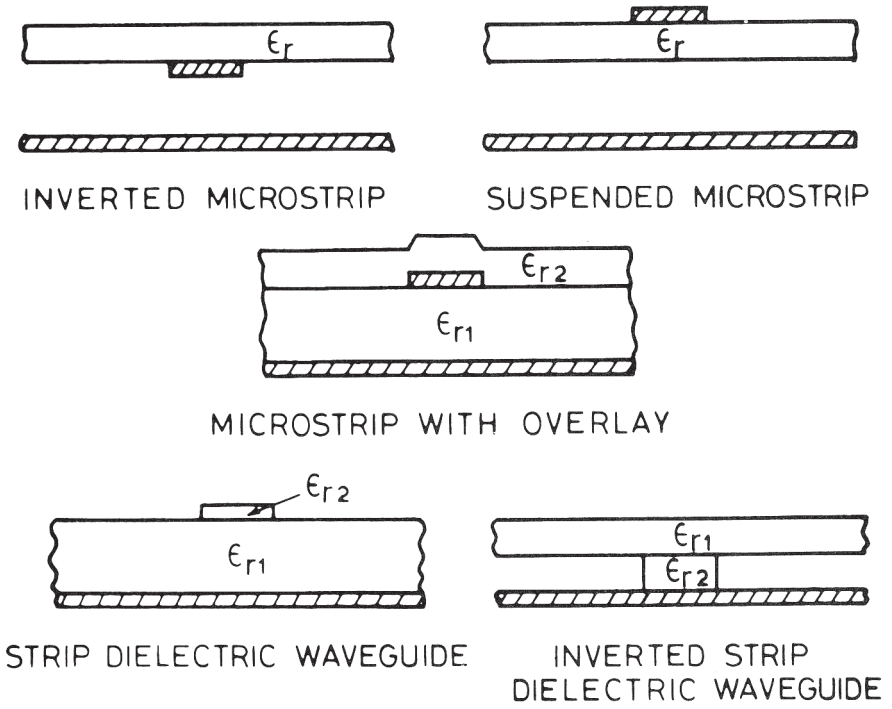

Figure 1.2 Various transmission lines derived from a microstrip.

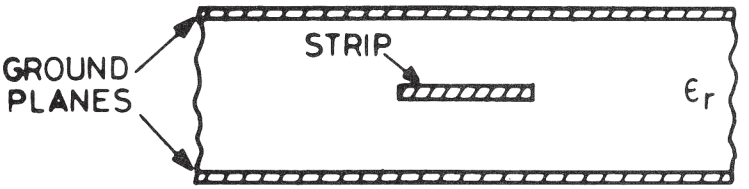

Figure 1.3 Stripline configuration.

(iii) slotline, and (iv) coplanar strips. Cross-sectional views of these lines are shown in Figure 1.1. A microstrip line is the most popular of these transmission structures, mainly due to the fact that the mode of propagation in a microstrip is almost transverse electro magnetic (TEM). This allows an easy approximate analysis and yields wide band circuits. Also simple transitions to coaxial circuits are feasible. Chapters 1 and 2 present various aspects of microstrip analysis and design. Slotline, coplanar strips, and coplanar waveguide are discussed in later chapters. A comparison of the characteristics of these lines is given in Section 7.6.

There are several variations of the microstrip configuration that have also been suggested for use in MICs. These include the inverted microstrip, suspended microstrip, microstrip with overlay, strip dielectric waveguide, and inverted strip dielectric waveguide. Cross-sectional views of these structures are given in Figure 1.2, and their analysis is available in references [7-10].

Another very commonly used transmission line that resembles a microstrip line is the stripline [11, 12], shown in Figure 1.3. This is also called a triplate line. Most of the basic circuit design ideas implemented in a stripline are also applicable to microstrip line circuits.

1.1.2 Microstrip Field Configuration

A microstrip is a two-conductor transmission line that can be considered to have evolved conceptually from a two-wire line as shown in Figure 1.4. Transformation from (a) to (b) is essentially a change in the shape of the conductors, whereas that from (b) to (c) involves placing a conducting sheet at the plane of symmetry. The final configuration (d) is obtained by inserting a thin dielectric slab between the two conductors. As a consequence of the last step, the dielectric medium of the transmission line becomes inhomogeneous.

Microstrip lines differ considerably from other transmission lines. For example, comparing a microstrip line with a stripline, one observes that the microstrip structure is open at the top. This open configuration makes a microstrip very convenient for use in MICs where discrete lumped devices (active or passive) must be mounted in the circuit. Also, small adjustments or tuning can possibly be incorporated after the circuit has been fabricated. However, along with these advantages, the open structure of a microstrip causes some complications in microstrip analysis and design. This is due to the fact that the presence of the dielectric-air interface modifies the mode of propagation in a microstrip to a non-TEM hybrid mode (as compared to a pure TEM-mode in a stripline).

Simple arguments based on the known quasi-static field distribution of the microstrip and Maxwell's equations can be presented to show that a microstrip stucture cannot support a pure TEM wave. Continuity of the tangential component of the electric field along a dielectric-air interface (see Figure 1.5) yields

$$E_x\big|_d = E_x\big|_a \tag{1.1}$$

where subscripts d and a refer to the dielectric and the air side of the interface, respectively. Using Maxwell's equations, one may thus write

$$(\nabla \times \mathbf{H})_x\big|_d = \varepsilon_r (\nabla \times \mathbf{H})_x\big|_a \tag{1.2}$$

Expanding (1.2) and using the continuity of the normal component of the magnetic flux, we obtain (for the case when $\mu_r = 1$)

$$\varepsilon_r \, \partial H_z / \partial y\big|_a - \partial H_z / \partial y\big|_d = \left(\varepsilon_r - 1\right) \partial H_y / \partial z \tag{1.3}$$

As ε_r is not equal to unity and $H_y \neq 0$, (1.3) implies that the expression on the left-hand side should be a nonzero quantity, which can only be true if H_z is nonzero. Thus we note that for Maxwell's equations to hold good for the configuration of Figure 1.5, the longitudinal component of **H** must exist.

Similar arguments can be advanced to show that E_z, the longitudinal component of the electric field, is also a nonzero quantity. It may be pointed out that it is only the fringing components E_x and H_x at the dielectric-air interface that lead to

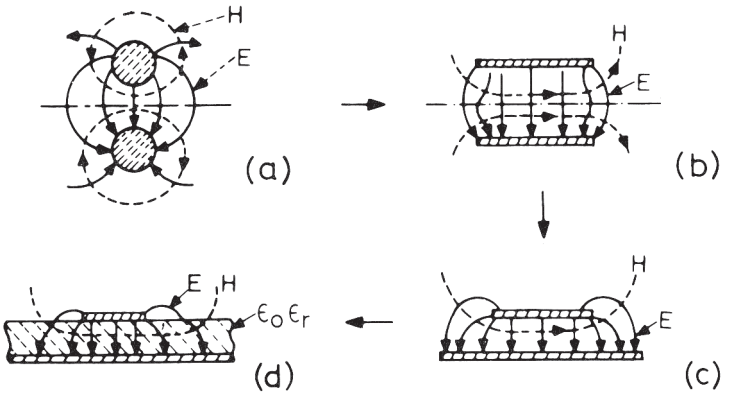

Figure 1.4 Conceptual evolution of a microstrip from a two-wire line.

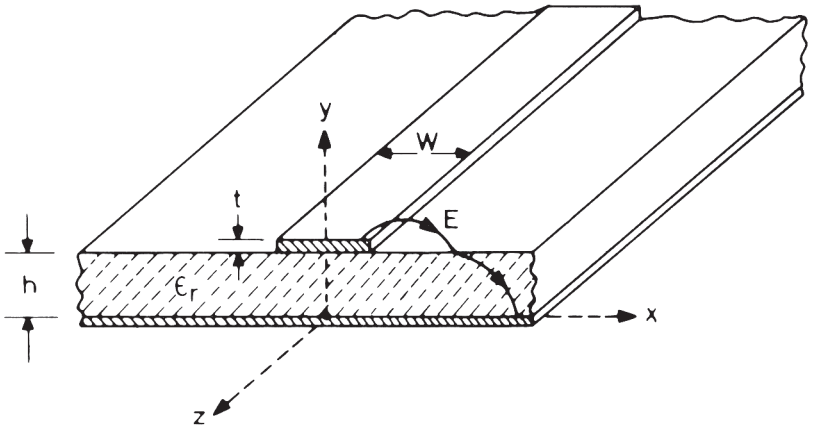

Figure 1.5 Microstrip configuration.

the non-TEM nature of the microstrip mode. Since these fringing field components are much smaller than the main field (within the substrate below the strip), the departure from the TEM behavior should be small. This conjecture is supported by the results based on a rigorous fullwave analysis of the microstrip, which will be discussed later in the book.

1.1.3 Methods of Microstrip Analysis

As with any other transmission line structure, the analysis methods for a microstrip line are aimed at determining the characteristic impedance and propagation constant (phase velocity and attenuation constant). The various methods of microstrip analysis may be divided into two main groups as shown in Figure 1.6. In the first group, which comprises quasi-static methods, the nature of the mode of propagation is considered to be pure TEM and the microstrip characteristics are calculated from the electrostatic capacitance of the structure. It is found that this analysis

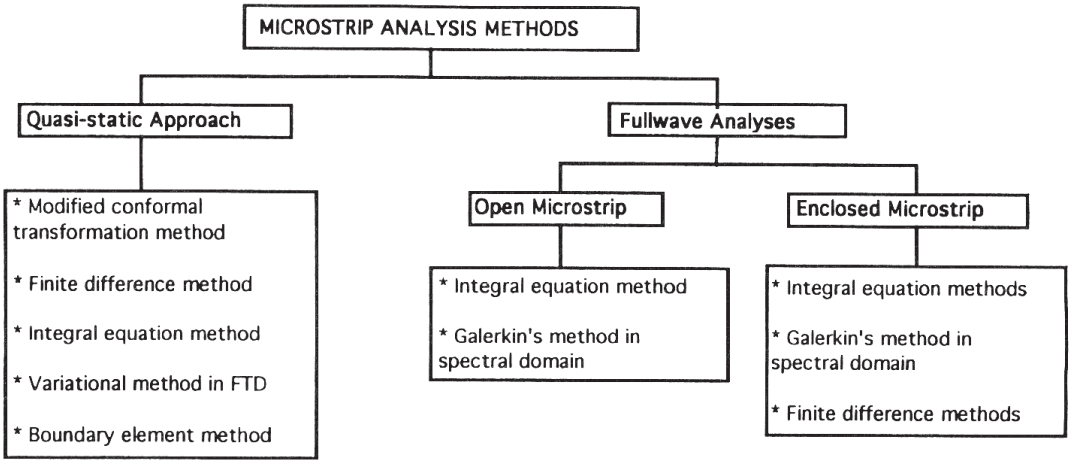

Figure 1.6 Various methods of microstrip analysis.

is adequate for designing circuits at lower frequencies (below X-band) where the strip width and the substrate thickness are much smaller than the wavelength in the dielectric material. The methods in the second group take into account the hybrid nature of the mode of propagation. The techniques followed for fullwave analysis are more rigorous and analytically complex. An important outcome of the fullwave analysis is information about the dispersive nature of the microstrip line. This includes variation of characteristic impedance, Z_0, and phase velocity (or effective dielectric constant, ε_{re}) with frequency. As a fullwave analysis becomes fairly complicated, several quasi-empirical methods known as "dispersion models" have been developed for finding variations of Z_0 and ε_{re} with frequency.

The methods of quasi-static analysis are discussed in this chapter. Microstrip dispersion models, transitions, and measurement techniques are also included. Techniques of fullwave analysis are described in the next chapter.

1.2 Quasi-Static Analyses of a Microstrip

In quasi-static analyses, the mode of wave propagation in a microstrip is assumed to be pure TEM. Transmission characteristics are then calculated from the values of two capacitances, one (C_a) for a unit length of the microstrip configuration with the dielectric substrate replaced by air, and the other (C) for a unit length of the microstrip with the dielectric substrate present. Values of characteristic impedance Z_{0m} and the phase constant β can be written in terms of these capacitances as

$$Z_{0m} = Z_{0m}^{a}(C_a/C)^{1/2} \tag{1.4}$$

and

$$\beta = \beta_0 (C/C_a)^{1/2} \tag{1.5}$$

where $Z_{0m}^{a} = l/(cC_a)$ and $\beta_0 = \omega/c$, where c is the velocity of electromagnetic waves in free space. There are various methods available for calculating the electrostatic capacitances C_a and C. Five of these are listed in Figure 1.6 and will be discussed in the following subsections.

1.2.1 Modified Conformal Transformation Method

An exact conformal transformation for the impedance of a zero-thickness, homogeneous dielectric microstrip has been given by Schneider [9]. The transformation from the microstrip (z-plane) to a parallel plate capacitor (z'-plane) is expressed in terms of the logarithmic derivative of the theta function θ_4 and a parameter $\kappa = K'/K$ as

$$z = -\frac{2hK}{\pi}\frac{\partial}{\partial z'}\ell n[\theta_4(z',\kappa)] \tag{1.6}$$

where $K = K(m)$ and $K' = K'(m)$ are complete elliptic integrals of the first kind with modulus m. The characteristic impedance Z_{0m} of the microstrip of width W and height h (and $t = 0$) is obtained by solving the equations

$$\frac{W}{h} = \frac{2}{\pi}\frac{\partial}{\partial \zeta}\ell n[\theta_4(\zeta,\kappa)] \tag{1.7}$$

$$dn^2(2K\zeta) = E/K \tag{1.8}$$

$$Z_{0m}^{a} = \frac{1}{2}(\mu_0/\varepsilon_0)^{1/2}K'/K \tag{1.9}$$

where μ_0 and ε_0 are the free-space permeability and permittivity constants, respectively, and Z_{0m}^{a} is the characteristic impedance of the microstrip with the dielectric substrate replaced by air. The function $E = E(m)$ is the complete elliptic integral of the second kind and dn is the Jacobian elliptic function. The logarithmic derivative of the theta function is given by the (rapidly converging) series expansion

$$\frac{\partial}{\partial \zeta}\ell n[\theta_4(\zeta,\kappa)] = 4\pi\sum_{n=1}^{\infty}\frac{\sin(2n\pi\zeta)}{\exp(n\pi\kappa) - \exp(-n\pi\kappa)} \tag{1.10}$$

Equations (1.7) to (1.9) can be used for the design of microstrip lines as follows. For a given characteristic impedance Z_{0m}^{a}, K'/K is calculated from (1.9). The modulus m for the elliptic functions is found by looking up tables for K'/K. Also E and K are determined using this value of m. The solution of (1.8) now gives the value of ζ. For known ζ and κ (= K'/K), W/h for the microstrip is calculated from (1.7) and (1.10). A practical solution to this set of equations is obtained with the help of a computer or with numerical tables. The conformal transformation given by Schneider yields Z_{0m}^{a}, the characteristic impedance for a homogeneously filled microstrip line. It is perhaps because of this limitation that the above method is not used very frequently.

The most widely used technique for microstrip analysis was introduced by Wheeler [13, 14] in 1964-65. The method uses a conformal transformation for the

evaluation of C_a and introduces a concept of effective dielectric constant for the evaluation of C. The conformal transformation selected is such that the resulting expressions are explicit and can be written in terms of simple functions. The transformation used for the wide strip ($W/h > 2$) is

$$z = j\pi + d\tanh(z'/2) - z' \tag{1.11}$$

The variable z refers to the microstrip plane (see Figure 1.7) and z' is the plane in which the microstrip configuration transforms into a parallel plate capacitor configuration. The parameter d is approximately equal to g' of Figure 1.7(b). The dielectric-air boundary of the microstrip substrate is transformed into an elliptical-looking curve bd' as shown in Figure 1.7(b). To evaluate the capacitance C, it is necessary to introduce approximations in order to modify the dielectric-air boundary. The curved dielectric-air boundary of Figure 1.7(b) is approximated by a rectangular boundary as shown in Figure 1.7(c). The area ($\pi s'$) over the curve is written in terms of a "parallel area" $\pi s''$ and a "series area" $\pi(s' - s'')$. These series and parallel areas can be expressed in terms of an equivalent parallel area s given by (Figure 1.7(d))

$$s = s'' + (s' - s'')/\varepsilon_r \tag{1.12}$$

The effective filling fraction can then be written as

$$q = (g' - a' + s)/g' \tag{1.13}$$

The effective dielectric constant is related to the effective filling fraction as

$$\varepsilon_{re} = (1 - q) + q\,\varepsilon_r \tag{1.14}$$

Different expressions for ε_{re} are derived for a wide microstrip ($W/h > 2$) and for a narrow microstrip ($W/h < 2$) because of the different approximations used in the two cases. For wide strips [15]

$$q = 1 - \frac{1}{d}\ell n\frac{d+c}{d-c} + \frac{0.732}{d\varepsilon_r}\left[\ell n\frac{d+c}{d-c} - \cosh^{-1}(0.358d + 0.595)\right] + \frac{\varepsilon_r - 1}{d\varepsilon_r}\left[0.386 - \frac{1}{2(d-1)}\right] \tag{1.15}$$

where $d = 1 + \sqrt{1 + c^2}$ and c are found implicitly from

$$\frac{\pi}{2}\frac{W}{h} = c - \sinh^{-1} c \tag{1.16}$$

and for narrow strips

$$\varepsilon_{re} = \frac{\varepsilon_r + 1}{2} + \frac{\varepsilon_r - 1}{2}\,\frac{\ell n(\pi/2) + (1/\varepsilon_r)\,\ell n(4/\pi)}{\ell n(8h/W)} \tag{1.17}$$

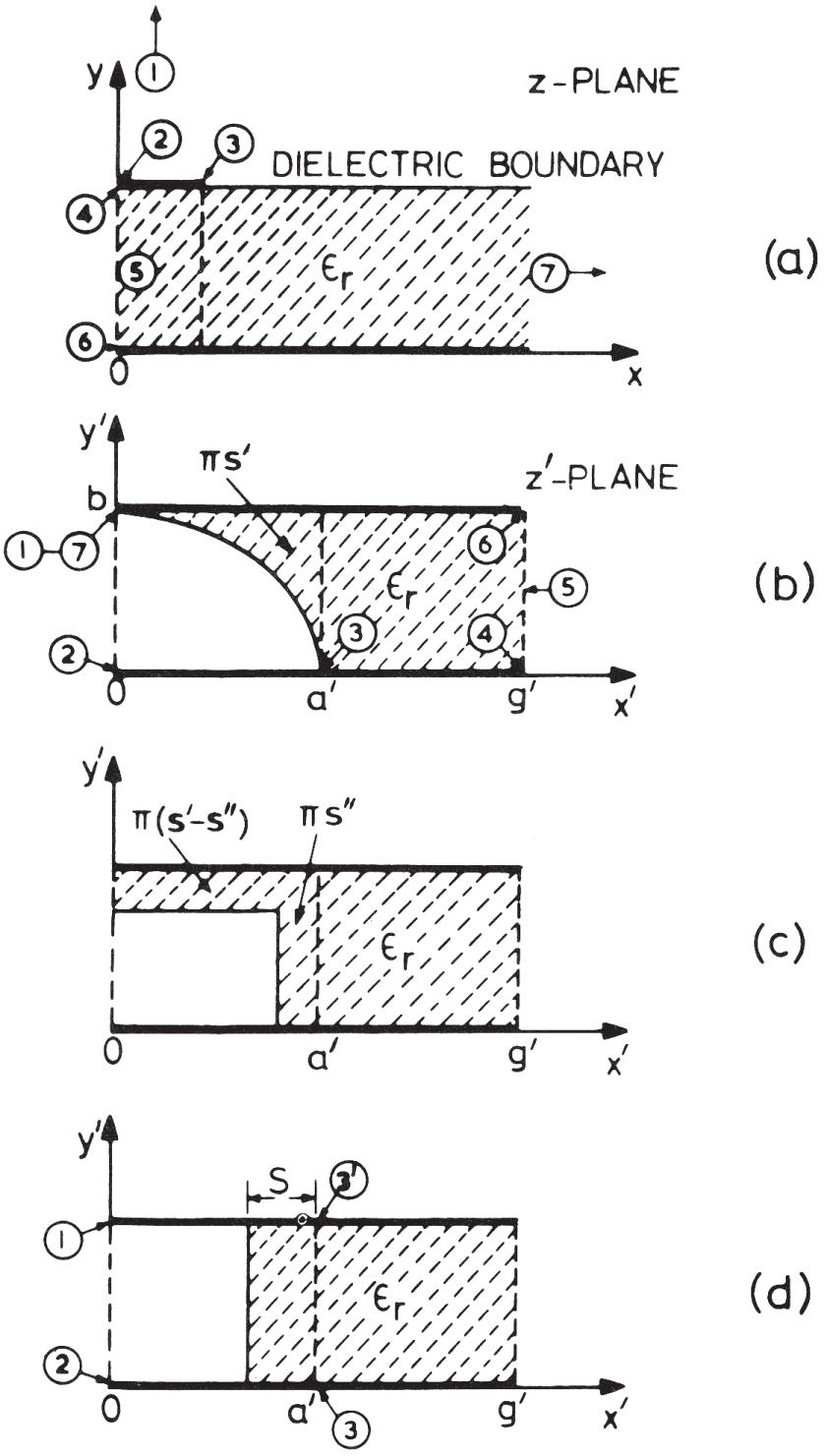

Figure 1.7 Conformal transformation and evaluation of the effective dielectric constant (from [14], © 1965 IEEE. Reprinted with permission.).

Formulas for the impedance of microstrip lines can be derived from these results. It is an advantage of the transformation selected by Wheeler that the impedance formulas can be written explicitly both for analysis (Z_{0m} in terms of W/h and ε_r) and for synthesvis (W/h in terms of Z_{0m} and ε_r). These relations are listed below. For wide strips ($W/h > 2$)

$$Z_{0m} = \frac{377}{(\varepsilon_r)^{1/2}}\left[\frac{W}{h} + 0.883 + \frac{\varepsilon_r + 1}{\pi\varepsilon_r}\left\{\ell n\left(\frac{W}{2h} + 0.94\right) + 1.451\right\} + 0.165\frac{\varepsilon_r - 1}{\varepsilon_r^2}\right]^{-1} \tag{1.18}$$

and for narrow strips ($W/h < 2$)

$$Z_{0m} = \frac{377}{2\pi\{(\varepsilon_r + 1)/2\}^{1/2}}\left[\ell n\left(\frac{8h}{W}\right) + \frac{1}{8}\left(\frac{W}{2h}\right)^2 - \frac{1}{2}\frac{\varepsilon_r - 1}{\varepsilon_r + 1}\left\{\ell n\frac{\pi}{2} + \frac{1}{\varepsilon_r}\ell n\frac{4}{\pi}\right\}\right] \tag{1.19}$$

where W is the strip width and h is the thickness of the substrate. Expressions giving the strip width for a desired impedance may be written [2] for wide strips ($W/h > 2$) as

$$\frac{W}{2h}\pi = \frac{377\pi}{2(\varepsilon_r)^{1/2}Z_{0m}} - 1 - \ell_n\left\{\frac{377\pi}{(\varepsilon_r)^{1/2}Z_{0m}} - 1\right\} + \frac{\varepsilon_r - 1}{2\varepsilon_r}\left[\ell n\left\{\frac{377\pi}{2(\varepsilon_r)^{1/2}Z_{0m}} - 1\right\} + 0.293 - \frac{0517}{\varepsilon_r}\right] \tag{1.20}$$

and for narrow strips ($W/h < 2$) as

$$2h/W = \frac{1}{4}e^{h'} - \frac{1}{2}e^{-h'}$$

where

$$h' = \left(\frac{\varepsilon_r + 1}{2}\right)^{1/2}\frac{Z_{0m}}{60} + \frac{\varepsilon_r - 1}{\varepsilon_r + 1}\left(0.226 + \frac{0.120}{\varepsilon_r}\right) \tag{1.21}$$

However, Wheeler's analysis does not lead to closed form expressions for the effective dielectric constant when $W/h \geq 2$. Such expressions have been derived empirically by curve fitting the numerical data and will be discussed in Section 2.4.

Values of the characteristic impedance and effective dielectric constant of a microstrip, based on the method discussed above, may be obtained from Figure 1.8. In this figure, the value of $\sqrt{\varepsilon_{re}}$ is plotted as a function of W/h for various values of the substrate dielectric constant ε_r. The variation of the characteristic impedance for air microstrip (Z_{0m}^a for $\varepsilon_r = 1$) is also shown by a dotted curve. The impedance for any value of ε_r can be obtained by dividing Z_{0m}^a by the corresponding value of $\sqrt{\varepsilon_{re}}$. It may be seen from Figure 1.8 that the impedance value decreases when the strip width-to-height ratio (W/h) of the substrate is increased because an increase in W (or decrease in h) increases the line capacitance.

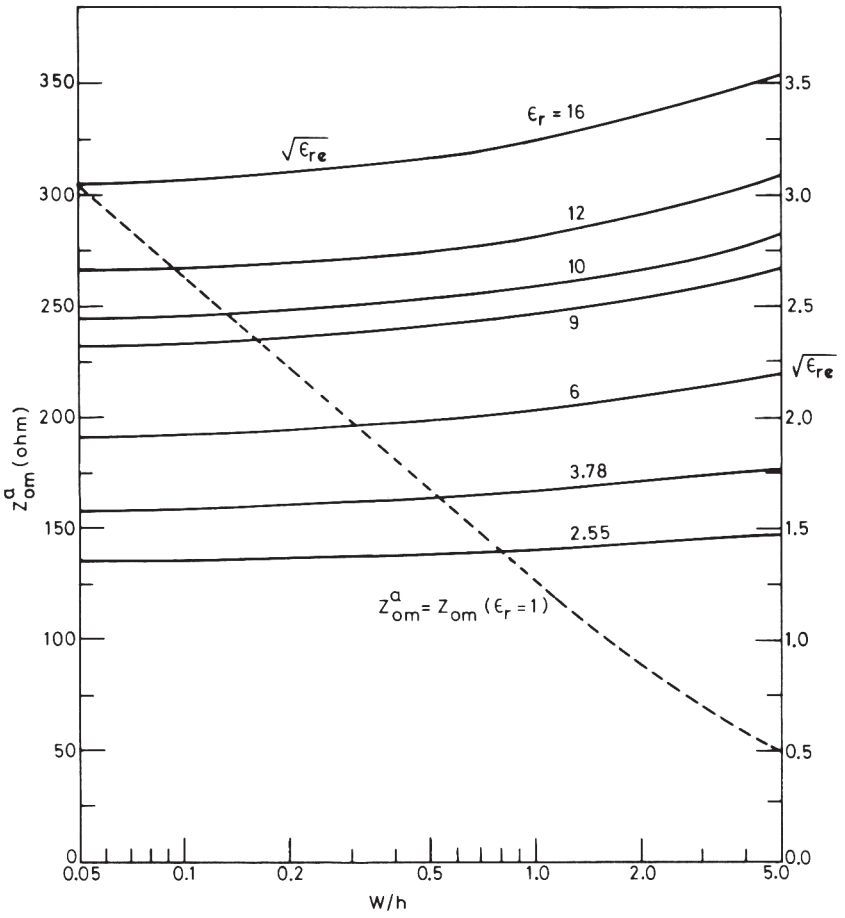

Figure 1.8 Characteristic impedance and effective dielectric constant of microstrip lines calculated using Wheeler's method.

Since the wavelength in microstrip λ_m is related to ε_{re} by the expression

$$\lambda_m = \frac{\lambda_0}{\sqrt{\varepsilon_{re}}} \tag{1.22}$$

we notice from Figure 1.8 that λ_m is a function of W/h and hence of Z_{0m}. This implies that, for example, the length for a quarter wave section of 25-Ω impedance would be different from that of a section of 100-Ω impedance (at the same frequency!). This factor must be kept in mind while designing microstrip circuits.

It may be pointed out that in the modified conformal transformation method discussed above, the thickness of the microstrip conductor is ignored and the analysis is restricted to an open microstrip without any enclosure.

The conformal mapping approach for calculating the capacitance has also been extended to the analysis of multilayer microstrip lines [16]. Two types of three-layered structures have been considered: a substrate consisting of two layers of dif-

ferent dielectric constants and a single-layered substrate microstrip structure with a dielectric cover layer. Expressions for filling factors and for effective permittivity for these two cases are available in [16].

1.2.2 Finite Difference Method

Another method for quasi-static analysis of microstrip lines is based on the numerical solution of Laplace's equation in the finite difference form [17]. This method is more suitable for enclosed microstrip lines, and the finite thickness of the microstrip conductor can easily be incorporated into the analysis. Laplace's equation may be written in finite difference form by considering the configuration shown in Figure 1.9. Potentials at the points A, B, C, D in the immediate vicinity of a point P may be written as

$$\phi_A = \phi_p - \frac{\Delta\,\partial\phi}{\partial x} + \frac{\Delta^2}{2!}\frac{\partial^2\phi}{\partial x^2} - \frac{\Delta^3}{3!}\frac{\partial^3\phi}{\partial x^3} + \cdots \tag{1.23}$$

$$\phi_{\mathrm{B}} = \phi_{\mathrm{p}} + \frac{\Delta\,\partial\phi}{\partial x} + \frac{\Delta^2}{2!}\frac{\partial^2\phi}{\partial x^2} + \frac{\Delta^3}{3!}\frac{\partial^3\phi}{\partial x^3} + \cdots \tag{1.24}$$

$$\phi_{\mathrm{C}} = \phi_{\mathrm{p}} - \frac{\Delta\,\partial\phi}{\partial y} + \frac{\Delta^2}{2!}\frac{\partial^2\phi}{\partial y^2} - \frac{\Delta^3}{3!}\frac{\partial^3\phi}{\partial y^3} + \cdots \tag{1.25}$$

$$\phi_{\mathrm{D}} = \phi_{\mathrm{P}} + \frac{\Delta\,\partial\phi}{\partial y} + \frac{\Delta^2}{2!}\frac{\partial^2\phi}{\partial y^2} + \frac{\Delta^3}{3!}\frac{\partial^3\phi}{\partial y^3} + \cdots \tag{1.26}$$

When we ignore the fourth- and higher order terms and use $(\partial^2\phi/\partial x^2 + \partial^2\phi/\partial y^2) = 0$, the above relations yield

$$\phi_A + \phi_B + \phi_{\mathrm{C}} + \phi_D \simeq 4\,\phi_P \tag{1.27a}$$

For nodes on the interface, (1.27a) should be modified as

$$\frac{\varepsilon + \varepsilon_0}{2}\phi_{\mathrm{A}} + \frac{\varepsilon + \varepsilon_0}{2}\phi_{\mathrm{B}} + \phi_{\mathrm{C}} + \phi_{\mathrm{D}} \cong 4\,\frac{\varepsilon + \varepsilon_0}{2}\phi_{\mathrm{P}} \tag{1.27b}$$

where ε is the permittivity of the substrate and ε_0 is the permittivity of air above the substrate.

The most common method of solving the finite difference equation (1.27) is the "relaxation method." In this method one starts with assumed values of ϕ at all the grid points. These values are modified successively as follows:

$$\text{New}\,\phi_P = \text{old}\,\phi_P - \alpha\,R_P \tag{1.28}$$

where the "residuals" R_{p} are given by

$$R_P = \phi_P - (\phi_A + \phi_B + \phi_{\mathrm{C}} + \phi_D)/4 \tag{1.29}$$

This successive "relaxation" is carried out until the differences between the old and new values become less than the allowed error. The speed of convergence of

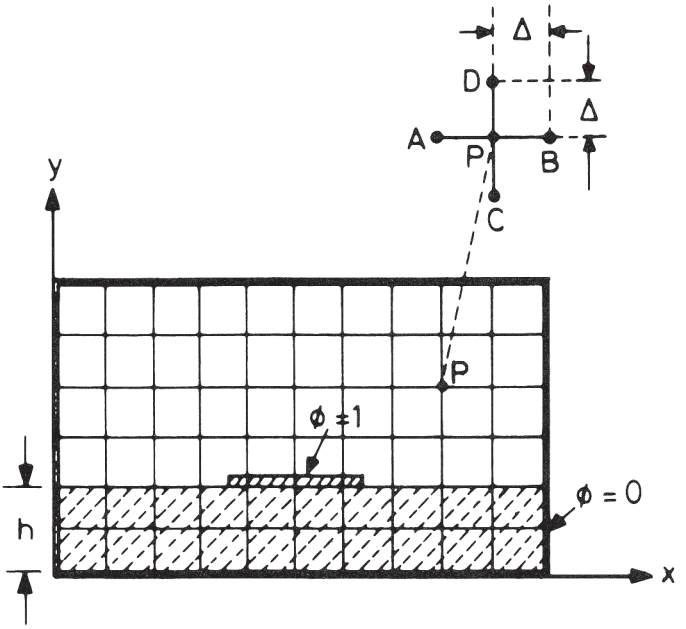

Figure 1.9 Enclosed microstrip configuration for analysis by the finite difference method.

the "relaxation" process is determined by the constant α. Relation (1.29) needs to be modified for points near the dielectric-air boundary and corners. A detailed discussion of the method is given by Green [18]. The solution of Laplace's equation by the method discussed above yields information about the potential distribution in the microstrip cross-section, from which the field distributions and the charge on the strip can be calculated. We have

$$Q = \oint \varepsilon \, E_n \cdot ds \tag{1.30}$$

where the integral is taken over a surface that encloses the strip conductor and ε represents the permittivity of the respective region about the strip. The capacitance is obtained as the ratio of charge to voltage. Again two capacitances C and C_a are evaluated and the microstrip parameters Z_{0m} and β calculated using (1.4) and (1.5), respectively.

1.2.3 Integral Equation Method

The quasi-static analysis of a microstrip may also be formulated in the form of an integral equation rather than a differential equation. We consider the Poisson equation in terms of a line charge distribution and define a Green's function G as

$$\nabla_t^2 G(x, y; x_0, y_0) = -\frac{1}{\varepsilon_0 \varepsilon_r} \delta(y - y_0)\delta(x - x_0) \tag{1.31}$$

where subscript t refers to transverse coordinates (x and y) and coordinates x_0, y_0 refer to the source location and x, y to the field point. Thus $G(x, y; x_0, y_0)$ is the potential at (x, y) produced by a line charge of unit magnitude located at (x_0, y_0).

The function G satisfies the boundary and the interface conditions of the microstrip configuration but not the source condition. Using Green's function, an integral equation of the following form can be formulated and solved to determine the charge distribution:

$$\phi(x,y) = \int G(x,\, y;\, x_0,\, y_0)\rho(x_0,y_0)\,dx_0 \tag{1.32}$$

where ϕ and ρ are the potential and the charge distributions, respectively, and the integration is carried out over the surface of the microstrip conductor at $y_0 = h$. The analysis can be divided into two parts: first, the formulation of a suitable Green's function G, and second, the solution of the integral equation (1.32) by writing it in the form of a matrix equation and carrying out the matrix inversion numerically. The matrix equation corresponding to (1.32) may be written as

$$[\mathbf{v}] = [\mathbf{p}] \cdot [\mathbf{q}] \tag{1.33}$$

where [**v**] and [**q**] are column matrices representing the potential ϕ and the charge q, respectively, and the matrix [**p**] can be recognized as the matrix of Maxwell's potential coefficients. Since the conductors may be presumed to be at known potentials, the matrix [**v**] is known and (1.33) may be solved for [**q**] by inversion of the matrix [**p**]. Total charge Q and capacitance C for the microstrip can then be calculated as

$$C = Q/v = \sum_{\mathrm{j}} \sum_{\mathrm{k}} (\mathbf{p}^{-1})_{jk} \tag{1.34}$$

where $(\mathbf{p}^{-1})_{jk}$ is the jkth term of the inverse of the [**p**] matrix. Green's function G for the microstrip configuration is obtained from the theory of images for a charge placed in front of a dielectric-air interface and has been described by Silvester [19]. The method of images is illustrated in Figure 1.10. In this figure, the partial image coefficient K is given by

$$K = (1 - \varepsilon_{\mathrm{r}})/(1 + \varepsilon_{\mathrm{r}}) \tag{1.35}$$

The Green's function G for the configuration as shown in Figure 1.10 may be written as [19]

$$\begin{aligned} G(h,x) = {} & \frac{1}{2\pi(\varepsilon_{\mathrm{r}}+1)\varepsilon_0} \\ & \cdot \left\{ \sum_{n=1}^{\infty} K^{n-1} \right. \\ & \cdot \ell n \left[\left\{ \left(4n^2 + \left(\frac{x-x_0}{h} \right)^2 \right) \left(4n^2 + \left(\frac{x+x_0}{h} \right)^2 \right) \right\} \Big/ \right. \\ & \left. \left. \cdot \left\{ \left(4(n-1)^2 + \left(\frac{x-x_0}{h} \right)^2 \right) \left(4(n-1)^2 + \left(\frac{x+x_0}{h} \right)^2 \right) \right\} \right] \right\} \end{aligned} \tag{1.36}$$

Since K is negative, (1.36) becomes an alternating series that is convergent and lends itself to the simple estimation of the truncation error. It has been found that for a value of ε_r between 2 and 20, the number of terms of (1.36) sufficient to ensure convergence to seven significant figures lies between 15 to 150. Green's function for thick conductor microstrip lines has also been reported [19].

1.2.4 Variational Method in the Fourier Transform Domain

The search for microstrip analysis techniques that are computationally more efficient has led to the variational method in the *Fourier transform domain* (FTD). There are two significant features of this method [20]. First, a variational method for calculating the capacitance C from the charge density ρ is used. This avoids the need for an accurate knowledge of the charge density distribution. Second, a major portion of analysis is carried out in FTD with the result that the integral equation for the potential gets replaced by an algebraic product of an approximate $\tilde{\rho}$ and a factor $\tilde{g}$ derived in FTD (see (1.41)).

The variational expression for the capacitance (upper bound) may be written as [20]

$$\frac{1}{C} = \frac{1}{Q^2}\int_s \rho(x)\,\phi(x,h)\,dx \tag{1.37}$$

where

$$Q = \int_s \rho(x)\,dx \tag{1.38}$$

Here s indicates that the integral is over the strip conductor. Taking the Fourier transform of (1.37) along the x-axis and using Parseval's formula, one gets

$$\frac{1}{C} = \frac{1}{2\pi Q^2}\int_{-\infty}^{\infty} \tilde{\rho}(\alpha)\,\tilde{\phi}(\alpha,h)\,d\alpha \tag{1.39}$$

where the superscript ~ indicates a transformed function obtained from the transformation:

$$\tilde{f}(\alpha) = \int_{-\infty}^{\infty} f(x)e^{j\alpha x}\,dx \tag{1.40}$$

It may be pointed out that it is simpler to evaluate $\tilde{\phi}(\alpha, h)$ than to evaluate $\phi(x, h)$ since

$$\tilde{\phi}(\alpha,h) = \frac{1}{\varepsilon_0}\,\tilde{\rho}(\alpha)\tilde{g}(\alpha) \tag{1.41}$$

whereas $\phi(x, h)$ is an integral given by

$$\phi(x,h) = \frac{1}{\varepsilon_0}\int_{-W/2}^{W/2} \rho(x')g(x,h;\,x',h)\,dx' \tag{1.42}$$

The potential function in the transform domain, $\tilde{\phi}(\alpha)$ is evaluated as follows. Except for $y = h$, the transform of potential $\phi(\alpha, y)$ satisfies the Laplace equation in the (α, y)-plane, namely;

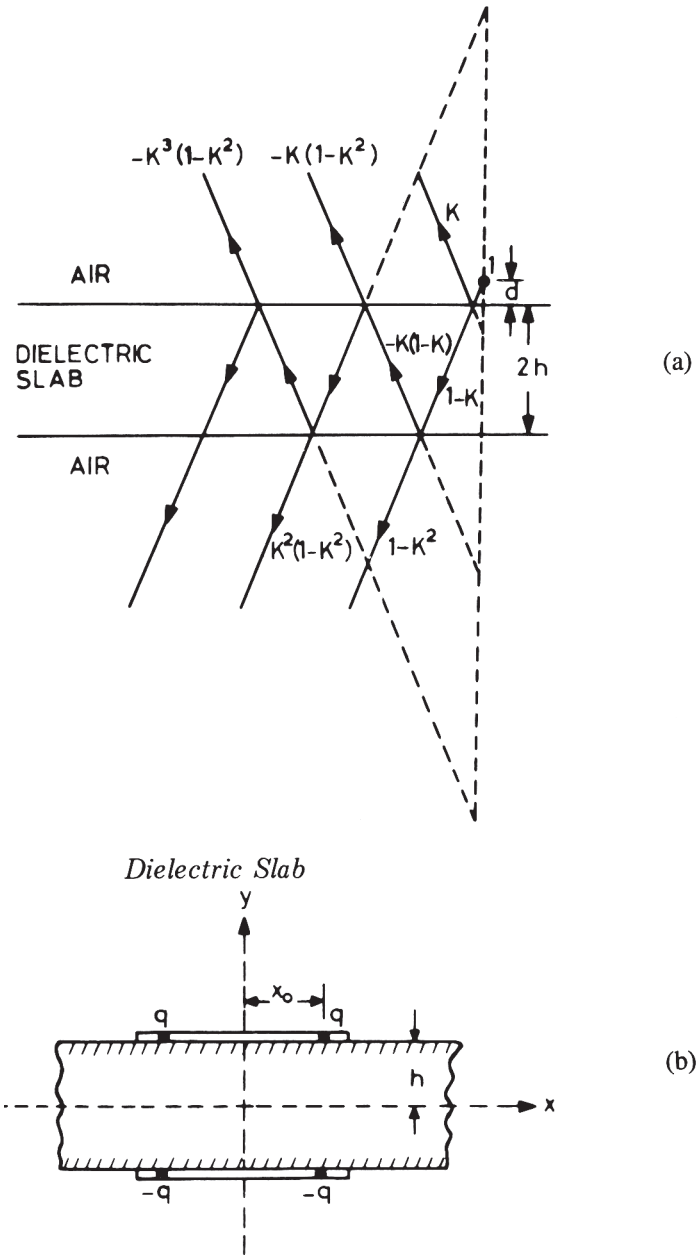

Figure 1.10 (a) Multiple images of a line charge in front of a dielectric slab and (b) microstrip configuration used in the integral equation method.

$$\left(-\alpha^2 + \frac{d^2}{dy^2}\right)\tilde{\phi}(\alpha, y) = 0 \tag{1.43}$$

Boundary conditions to be satisfied by $\tilde{\phi}(\alpha, y)$ may be listed as:

$$\text{at } y = 0 \qquad \tilde{\phi}(\alpha, 0) = 0 \tag{1.44a}$$

$$\text{across } y = h \qquad \tilde{\phi}(\alpha, h+0) = \tilde{\phi}(\alpha, h-0) \tag{1.44b}$$

$$\text{at } y = \infty \qquad \tilde{\phi}(\alpha, \infty) = 0 \tag{1.44c}$$

and for $\frac{d}{dy}\tilde{\phi}$ at $y = h$, we have

$$\frac{d}{dy}\tilde{\phi}(\alpha, h+0) = \varepsilon_r \frac{d}{dy}\tilde{\phi}(\alpha, h-0) - \frac{1}{\varepsilon_0}\tilde{\rho}(\alpha) \tag{1.44d}$$

In the region $0 \le y \le h$, the general solution satisfying (1.44) is a linear combination of $\exp(-\alpha y)$ and $\exp(\alpha y)$; whereas for $y \ge h$, the solution is of the form $\exp(-|\alpha| y)$ alone. Using the boundary conditions given in (1.44), the solution for $\tilde{\phi}(\alpha, y)$ at $y = h$ is given by

$$\tilde{\phi}(\alpha, h) = \frac{1}{\varepsilon_0}\tilde{\rho}(\alpha)\tilde{g}(\alpha) = \frac{\tilde{\rho}(\alpha)}{\varepsilon_0 |\alpha| [1 + \varepsilon_r \coth(|\alpha| h)]} \tag{1.45}$$

$\tilde{\phi}(\alpha, h)$ given by (1.45) is used in (1.39) to evaluate the capacitance C.

We still must find $\rho(\alpha)$ before C can be computed. However, since (1.37) is variational, one may use an approximate trial function for $\rho(x)$ and incur only a second-order error in the value of capacitance. A trial function that maximizes the value of C gives the closest value to the exact result for the capacitance. Variation of the charge proportional to $|x|$ yields the following expression for $\tilde{\rho}(\alpha)$ [20]:

$$\frac{\tilde{\rho}(\alpha)}{Q} = \frac{2\sin(\alpha W/2)}{\alpha W/2} - \left\{\frac{\sin(\alpha W/4)}{\alpha W/4}\right\}^2 \tag{1.46}$$

Results obtained by this method agree well with those of the modified conformal transformation method discussed earlier. This method can also be used to take into account the effect of finite strip thickness and enclosure. It can easily be extended for a microstrip on composite substrates or where a dielectric overlay exists over the microstrip [21]. In these situations one simply has to find an appropriate expression for $\tilde{g}(\alpha)$ and use the above procedure. For a microstrip with a composite substrate (the lower layer with dielectric constant ε_{r1} and height h and the upper layer with dielectric constant ε_{r2} and height s) and shielded by a top metallic wall at a distance d from the strip, the value of $\tilde{g}(\alpha)$ is given as

$$\tilde{g}(\alpha) = \frac{\varepsilon_{r1}\coth(|\alpha| h) + \varepsilon_{r2}\coth(|\alpha| s)}{|\alpha|\{\varepsilon_{r1}\coth(|\alpha| h)[\varepsilon_{r3}\coth(|\alpha| d) + \varepsilon_{r2}\coth(|\alpha| s)] + \varepsilon_{r2}[\varepsilon_{r2} + \varepsilon_{r3}\coth(|\alpha| d)\coth(|\alpha| s)\}} \tag{1.47}$$

1.2.5 Segmentation and Boundary Element Method (SBEM)

Another microstrip developed analysis method [22] is based on a combination of the segmentation method [23, 24] and the boundary element method [24, 25]. This

method is well suited for multiconductor microstrip-like transmission structures with multilayered dielectric substrates. The cross-section of the microstrip configuration is first separated into several homogeneous regions and analyzed separately by the boundary element method. The results are then combined to yield the final result by using the segmentation method. This strategy makes it possible to take into account local modifications of the transmission line configuration by conducting new analyses only at those regions nearby the modification.

The boundary element method is widely used in structural analysis and acoustics [25, 26]. Some applications in electromagnetics have also been reported [27, 28]. For the quasi-TEM mode microstrip line analysis, we solve the Laplace equation in the cross-sectional plane of the transmission structure. Instead of dealing with the differential equation directly, we use the integral equation form of the Poisson equation (which is derived using Green's third identity [29, 30]):

$$\frac{1}{2}\Phi(r)=\oint_s\left(\Phi(r')\frac{\partial G(r,r')}{\partial n(r')}-G(r,r')\frac{\partial \Phi(r')}{\partial n(r')}\right)dr'+\int_D \rho(r')\,G(r',r')\,dv(r') \tag{1.48}$$

where $\Phi(r)$ is the potential at any point on the contour S, $G(r, r')$ is the Green's function that satisfies Poisson's equation for a point charge at r' in the homogeneous domain D bounded by the contour S, $n(r')$ is the normal vector at r' on the contour S pointing toward the domain, and $\rho(r')$ is the charge density function (see Figure 1.11).

The method described in [22] is based on the solution for the "basic capacitance matrix" (the relation between the boundary voltages and boundary electric flux) for each homogeneous region first (see Figure 1.12). Then the segmentation method [31] is used to connect all of these basic capacitance matrices into one matrix, which is the relation between potential and charges on all the conductor surfaces. By using the segmentation method, those fields (Φ and $\partial\Phi/\partial n$) on the dielectric interfaces are treated as dummy variables and need not be really evaluated. This saves time in comparison to the traditional boundary element method. As a last step, the condition of equal potential on each conductor surface is applied to this matrix, and this yields the final capacitance matrix **C** or, in the case of a single microstrip line, capacitance per unit length.

For each of these homogeneous regions, the equation

$$\frac{1}{2}\Phi(r)=\oint_s\left(\Phi(r')\frac{\partial G(r,r')}{\partial n(r')}-G(r,r')\frac{\partial \Phi(r')}{\partial n(r')}\right)dr' \tag{1.49}$$

is solved by using the weighted residual method [25]. Here the pulse function is used as the basis function and the delta function is used as the testing function. The free space Green's function for a line charge is used as $G(r,r')$, that is,

$$G(r,r')=-\frac{\ell n|r-r'|}{2\pi\varepsilon} \tag{1.50}$$

where ε is the permittivity for that homogeneous region. This results in a system of linear equations or in the matrix form

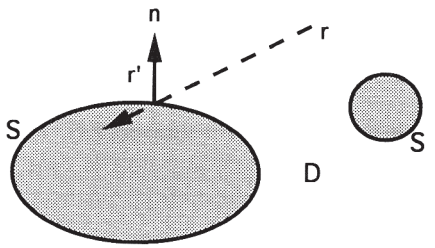

Figure 1.11 Definitions of the notation used in (1.48).

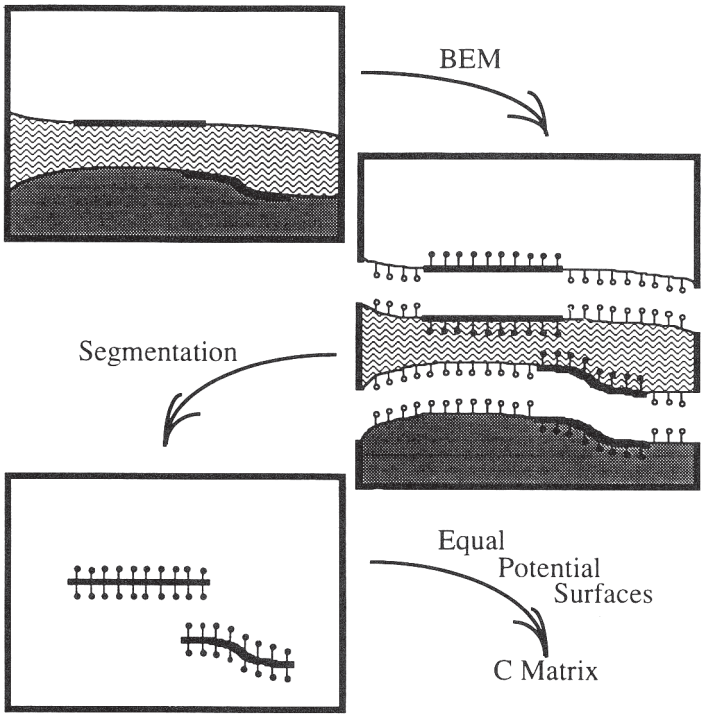

Figure 1.12 Calculation of capacitance matrices by using segmentation and the boundary element method.

$$\overline{\overline{\mathbf{H}}}\overline{\Phi} = \overline{\overline{\mathbf{U}}}\overline{Q} \tag{1.51}$$

where

$$\overline{\Phi} = [\Phi_1 \Phi_2 \ldots \Phi_N]^T \tag{1.52}$$

$$\overline{\mathbf{Q}} = [(-\varepsilon)\,\partial\Phi/\partial n_1\,(-\varepsilon)\,\partial\Phi/\partial n_2 \ldots (-\varepsilon)\,\partial\Phi/\partial n_N]^{\mathrm{T}} \tag{1.53}$$

$$H_{ij} = 1/2 \qquad \text{for } i = j \tag{1.54}$$

$$= \frac{-1}{2\pi} \int_{1j} \vec{n_j} \cdot \vec{r_{ij}} / |\vec{r_{ij}}|^2 dl' \qquad \text{for } i \neq j \tag{1.55}$$

$$U_{ij} = \frac{W_i}{2\pi\varepsilon} \left[\ell n \frac{2}{W_i} + 1 \right] \qquad \text{for } i = j \tag{1.56}$$

$$= -\frac{1}{2\pi\varepsilon} \int_{lj} \ell n \, |\vec{r_{lj}}| \, dl' \qquad \text{for } i \neq j \tag{1.57}$$

The integrals in (1.55) and (1.57) are carried out numerically by the Gaussian quadrature formula [24]. It also should be noted that the $\overline{\overline{U}}$ matrix is not symmetrical because of (1.55). The basic capacitance matrix $\overline{\overline{C}}_B$ for this region is then defined as

$$\overline{\overline{C}}_B = [\overline{\overline{U}}]^{-1} \, \overline{\overline{H}} \tag{1.58}$$

where $\overline{\overline{C}}_B$ has units of Farads/meter. However, because the definition of $\overline{Q}$ in (1.53), $\overline{\overline{C}}_B$ is not a real capacitance matrix unless all this region's boundary is conductor. It also should be noted that each element of $\overline{\overline{C}}_B$ is proportional to ε, the permittivity for that homogeneous region. If the geometry of this region is kept unchanged and the permittivity is changed to a new value, the basic capacitance matrix does not need to be calculated using (1.58) again; instead, each element of the original $\overline{\overline{C}}_B$ needs only to be scaled to the new permittivity value. (This makes the calculation of inductance matrix **L** for this transmission-line system much easier when the capacitance matrix **C** has been calculated using SBEM.) Once the basic capacitance matrices have been calculated for all the homogeneous regions, they are connected to each other using the boundary condition on dielectric interfaces. This is done by the segmentation method.

Suppose we have two basic capacitance matrices $\mathbf{C}_{B1}$ and $\mathbf{C}_{B2}$ (Figure 1.13), for homogeneous region 1 and region 2, respectively, given by

$$\begin{bmatrix} Q_{p1} \\ Q_q \end{bmatrix} = \overline{\overline{\mathbf{C}}}_{B1} \begin{bmatrix} \Phi_{p1} \\ \Phi_q \end{bmatrix} = \begin{bmatrix} C_{p1p1} & C_{p1q} \\ C_{qp1} & C_{qq} \end{bmatrix} \begin{bmatrix} \Phi_{p1} \\ \Phi_q \end{bmatrix} \tag{1.59}$$

and

$$\begin{bmatrix} Q_{p2} \\ Q_r \end{bmatrix} = \overline{\overline{\mathbf{C}}}_{B2} \begin{bmatrix} \Phi_{p2} \\ \Phi_r \end{bmatrix} = \begin{bmatrix} C_{p2p2} & C_{p2r} \\ C_{rp2} & C_{rr} \end{bmatrix} \begin{bmatrix} \Phi_{p2} \\ \Phi_r \end{bmatrix} \tag{1.60}$$

The ports q in region 1 need to be connected to the ports r in region 2 using the boundary condition on dielectric interfaces; that is, the electric flux should be continuous ($Q_q = -Q_r$) and the voltage should be continuous ($\Phi_q = \Phi_r$). Equations (1.59) and (1.60) are combined to form the new equation

$$\begin{bmatrix} Q_p \\ Q_q \\ Q_r \end{bmatrix} \equiv \begin{bmatrix} Q_{p1} \\ Q_{p2} \\ \hline Q_q \\ \hline Q_r \end{bmatrix} = \left[\begin{array}{cc:c:c} C_{p1p1} & 0 & C_{p1q} & 0 \\ 0 & C_{p2p2} & 0 & C_{p2r} \\ \hdashline C_{qp1} & 0 & C_{qq} & 0 \\ \hdashline 0 & C_{rp2} & 0 & C_{rr} \end{array}\right] \left[\begin{array}{c} \Phi_{p1} \\ \Phi_{p2} \\ \hdashline \Phi_q \\ \hdashline \Phi_r \end{array}\right] \equiv \begin{bmatrix} C_{pp} & C_{pq} & C_{pr} \\ C_{qp} & C_{qq} & 0 \\ C_{rp} & 0 & C_{\mathrm{rr}} \end{bmatrix} \begin{bmatrix} \Phi_p \\ \Phi_q \\ \Phi_r \end{bmatrix} \tag{1.61}$$

This equation contains all the information about these two regions. Using the boundary conditions and the second and third rows of equation (1.61), it can be shown that

$$\Phi_q = -\left[C_{qq} + C_{rr}\right]^{-1}\left[C_{qp} + C_{rp}\right]\Phi_p \tag{1.62}$$

which relates the voltages at the interconnected ports to the voltages at the unconnected ports. So, the basic capacitance matrix $\overline{\overline{C}}_B$ for the combination of these two regions is given from the first row of (1.61) as

$$\overline{\overline{\mathbf{C}}}_{\mathrm{B}} = C_{pp} - \left[C_{pq} + C_{pr}\right]\left[C_{qq} + C_{rr}\right]^{-1}\left[C_{qp} + C_{rp}\right] \tag{1.63}$$

which gives the relation between the voltage and electric flux at unconnected ports only.

The segmentation method is applied to connect all the basic capacitance matrices and to eliminate all the ports on the dielectric interfaces. This results in a matrix that relates the potential and charges on all conductor surfaces. The last condition that needs to be applied is that all the ports on the same conductor should have the same potential. This condition can easily be applied by simply summing the related elements in the matrix. All the elements that relate the charges on conductor i due to the voltage on conductor j should be added to become the element C_{ij} of the final capacitance matrix **C**. It should be noted that, in the whole process of this capacitance matrix calculation, we try to avoid calculating the fields we do not need so that the process can be as efficient as possible. The boundary element method helps us to concentrate only on the boundary fields, and the segmentation method helps us to eliminate the unknown fields at the dielectric interfaces. In cases where the fields on the dielectric interfaces or the fields in the domain are needed, (1.62) can be used to recover all the details.

In addition to the five methods for quasi-static analysis of microstrip lines discussed in this chapter, several other numerical electromagnetic analysis techniques are applicable to microstrip line. An overview of these methods is available in [32]. The finite element method [33] has been used for quasi-static analysis of microstrip lines, and a computer program based on this method is available in [33].

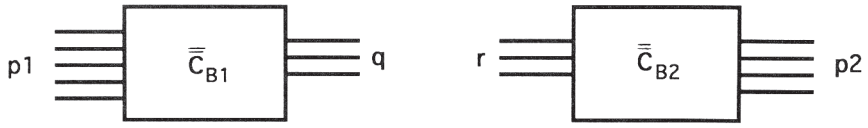

Figure 1.13 Definition of the notation used in the segmentation method.

1.3 Microstrip Dispersion Models

The quasi-static methods of microstrip analysis do not take into account the non-TEM nature of the microstrip mode. The non-TEM behavior causes the effective dielectric constant (ε_{re}) and impedance Z_{0m} of the microstrip to be functions of frequency. Of these two, the variation of the effective dielectric constant is more significant. An exact evaluation of these variations involves a fullwave analysis of the microstrip configuration, which will be discussed in Chapter 2. However, there are several semi-empirical techniques [34–50] available that lead to a closed-form solution for the dependence of ε_{re} and Z_{0m} on frequency. These dispersion models may be listed as follows:

- Model based on coupling between TEM and TM_0 surface wave modes [34];
- An empirical relation for frequency-dependent phase velocity [35];
- Model based on LSE mode using a dielectric loaded ridged waveguide and its modifications [36, 39, 43];
- Model based on coupling between a TEM mode and a TE mode transmission line [37];
- Model based on coupling between the LSE mode and surface-wave mode [47];
- Empirical formulae based on fullwave numerical data [41, 44, 49];
- Planar waveguide model [38].

Some of these dispersion models are discussed briefly in this section.

1.3.1 Coupled TEM Mode and TM Mode Model

In this model [34] the deviation from the TEM behavior or the dispersion is considered to be caused by the coupling between the fundamental TEM mode and the lowest order surface wave TM_0 mode. Using the theory of coupled modes, the frequency-dependent effective dielectric constant may be written as

$$\varepsilon_{re}(f) = \left[0.5(\sqrt{\varepsilon_{re}(0)} + \sqrt{\varepsilon_{eTM}}) + \left\{ \varepsilon_{12}^2 + 0.25(\sqrt{\varepsilon_{re}(0)} - \sqrt{\varepsilon_{eTM}})^2 \right\}^{1/2} \right]^2 \quad (1.64)$$

where $\varepsilon_{re}(0)$ is the quasi-static value of the effective dielectric constant and ε_{eTM} is the effective dielectric constant for the TM_0 mode. An expression for the coupling parameter ε_{12}, obtained by a series of qualitative arguments, may be written as

$$\varepsilon_{12}^2 = k(\sqrt{\varepsilon_r} - 1)^2 (W/h)^{n_3} (f/f_e)^{n_2} \quad (1.65)$$

where f_e is the frequency at which the phase velocity of the TEM mode equals the phase velocity of the TM_0 mode and k, n_2, n_3 are three constants found empirically for the best fit between the behavior of the coupled line model and the experimental results. The values of n_2, n_3, and k are 4/3, 3/4, and 0.22, respectively; and the range of validity for the model is stated as $2 \le \varepsilon_r \le 104$, 0.025 in $\le h \le$ 0.125 in, $0.9 \le W/h \le 6$, and $f < 0.5 f_e$.

1.3.2 An Empirical Relation [35]

Based on the results of various theoretical and experimental studies of dispersion, it may be noted that:

1. The normalized phase velocity v_p is a monotonically decreasing function of frequency f.
2. v_p and its first-order derivative at $f = 0$ are given by

$$v_p|_{f=0} = 1/\sqrt{\varepsilon_{re}(0)} \quad \text{and} \quad \left.\frac{\partial v_p}{\partial f}\right|_{f=0} = 0 \tag{1.66}$$

3. v_p and its derivative at $f \to \infty$ are given by

$$v_p|_{f\to\infty} = 1/\sqrt{\varepsilon_r} \quad \text{and} \quad \left.\frac{\partial v_p}{\partial f}\right|_{f\to\infty} = 0 \tag{1.67}$$

4. The second derivative of v_p is zero in the vicinity of the cutoff frequency (f_c) of the lowest order transverse electric surface wave mode; that is,

$$\left.\frac{\partial^2 v_p}{\partial f^2}\right|_{f=f_c} = 0 \tag{1.68}$$

The above conditions are fulfilled by the relation [35]

$$v_p = \frac{1}{\sqrt{\varepsilon_r \varepsilon_{re}(0)}} \frac{\sqrt{\varepsilon_{re}(0)}\, f_n^2 + \sqrt{\varepsilon_r}}{f_n^2 + 1} \tag{1.69}$$

where $\varepsilon_{re}(0)$ is the quasi-static value of ε_{re} and f_n is defined by

$$f_n = \frac{f}{f_c} = \frac{4h\sqrt{\varepsilon_r - 1}}{\lambda_0} \tag{1.70}$$

where h is the substrate thickness.

Comparison with experimental results shows that the error in (1.69) is less than 3 percent.

1.3.3 Dielectric-Loaded Ridged Waveguide Model [36]

This model for the microstrip dispersion is based on the study of another structure that resembles a microstrip as far as inhomogeneity of the dielectric medium is

concerned but has a shape that can be analyzed mathematically. This structure is shown in Figure 1.14. The configuration shown in Figure 1.14(b) corresponds to the microstrip cross section shown in Figure 1.14(a). The dimensions of the structure are chosen such that it has the same electrical characteristics at zero frequency as the microstrip. The structure is analyzed for dispersion, and the results are compared with measured microstrip dispersion values to determine the unknown parameter H'/h. The comparison shows that H'/h and related parameters are nearly constant or vary linearly with characteristic impedance. This feature is used to derive a simple formula that can be used to predict the dispersion of a microstrip transmission line. The resulting dispersion formula may be written as

$$\varepsilon_{re}(f) = \varepsilon_r - \frac{\varepsilon_r - \varepsilon_{re}(0)}{1 + \left(f^2/f_p^2 \right) G} \tag{1.71}$$

where

$$f_p = Z_{0m}/(2\mu_0 h) \tag{1.72}$$

or

$$f_p(GHz) = 0.398\ Z_{0m}/h(\text{mm})$$

and

$$G = 0.6 + 0.009\ Z_{0m} \qquad (Z_{0m} \text{ in ohms}) \tag{1.73}$$

In (1.71), $\varepsilon_{re}(f)$ is the frequency-dependent effective dielectric constant and $\varepsilon_{re}(0)$ is the zero-frequency (quasi-static) value of ε_{re}.

Modification of Getsinger's Formula

Edwards and Owens [39] have reported extensive measurement results of dispersion in microstrip lines of characteristic impedance ranging from 10 Ω to 100 Ω over the frequency range of 2 GHz to 18 GHz. They have pointed out that measured results show better agreement with Getsinger's formula when G of (1.73) is modified as

$$G = \left\{ \frac{Z_{0m} - 5}{60} \right\}^{1/2} + 0.004\ Z_{0m} \tag{1.74}$$

The experiments of Edwards and Owens [39] were carried out on sapphire substrates (ε_r = 10.73 to 11.50), and their results were found to be in good agreement with the fullwave analysis using Galerkin's method in the spectral domain (discussed later in Section 2.2.2). Modification of (1.71), which results in a more accurate formula, has also been suggested. This may be written as

$$\varepsilon_{re}(f) = \varepsilon_r - \frac{\varepsilon_r - \varepsilon_{re}(0)}{1 + P} \tag{1.75}$$

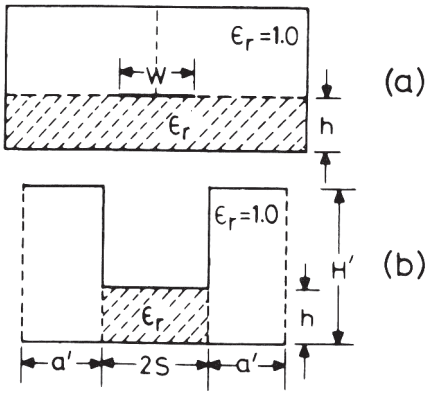

Figure 1.14 Ridged waveguide model for a microstrip line (from [36], © 1973 IEEE. Reprinted with permission.).

where

$$P = (h/Z_{0\mathrm{m}})^{1.33}\left[0.43f^2 - 0.009f^3\right] \tag{1.76}$$

with h in millimeters and f in gigahertz.

1.3.4 Empirical Formulae for Broad Frequency Range

The aforementioned dispersion models have been tested by comparison with experimental results up to 18 GHz and, in general, found to be in good agreement. However, they have limited range in terms of frequency, dielectric constant values, and W/h ratios. Several dispersion formulae have been developed by fitting full-wave numerical data in order to extend the validity range of the above-described dispersion model expressions.

Yamashita et al. [41] published a dispersion model that is valid up to 100 GHz. The following expressions describe the dispersion in $\varepsilon_{\mathrm{re}}$:

$$\varepsilon_{\mathrm{re}}(f) = \left(\frac{\sqrt{\varepsilon_{\mathrm{r}}} - \sqrt{\varepsilon_{\mathrm{re}}(0)}}{1 + 4F^{-1.5}} + \sqrt{\varepsilon_{\mathrm{re}}(0)}\right)^2 \tag{1.77}$$

where

$$F = \frac{4h\sqrt{\varepsilon_{\mathrm{r}} - 1}}{\lambda_0}\left\{0.5 + \left[1 + 2\log_{10}\left(1 + \frac{W}{h}\right)\right]^2\right\} \tag{1.78}$$

and $\varepsilon_{\mathrm{re}}(0)$ is the quasi-static value obtained earlier. The model is applicable in the range $2 \le \varepsilon_{\mathrm{r}} \le 16$, $0.06 \le W/h \le 16$, and $f \le 100$ GHz.

In 1982, Kirschning and Jansen improved the accuracy of dispersion characteristics and claimed accuracy better than 0.6 percent up to 60 GHz. The following

expressions are valid over the range $1 \le \varepsilon_r \le 20$, $0.1 \le W/h \le 100$, and $0 \le h/\lambda_0 \le 0.13$ [44]:

$$\varepsilon_{re}(f) = \varepsilon_r - \frac{\varepsilon_r - \varepsilon_{re}(0)}{1 + P(f)} \tag{1.79}$$

where

$$P(f) = P_1 P_2 \left\{(0.1844 + P_3 P_4)\, 10fh\right\}^{1.5763} \tag{1.80}$$

and

$$\begin{aligned}
P_1 &= 0.27488 + \{0.6315 + 0.525/(1 + 0.157\, fh)^{20}\}(W/h) \\
&\quad - 0.065683 \exp(-8.7513\, W/h) \\
P_2 &= 0.33622\{1 - \exp(-0.03442\, \varepsilon_r)\} \\
P_3 &= 0.0363 \exp(-4.6\, W/h)[1 - \exp\{-fh/3.87)^{4.97}\}] \\
P_4 &= 1 + 2.751[1 - \exp\{\varepsilon_r/15.916)^8\}]
\end{aligned}$$

The frequency f is in gigahertz and the thickness h is in centimeters.

Kobayashi [49] further improved the accuracy of the dispersion model in terms of dielectric constant and frequency range. Since his formula has no restriction on the h/λ_0 ratio, it will predict more accurately the distortion in pulse propagation along a microstrip line. The proposed model uses normalizing frequency f_{50} at which the dispersion is 50 percent and the expressions for f_{50} is derived using extensive fullwave numerical data. The Kobayashi's dispersion formula for the effective relative dielectric constant is given by

$$\varepsilon_{re}(f) = \varepsilon_r - \frac{\varepsilon_r - \varepsilon_{re}(0)}{1 + (f/f_{50})^m} \tag{1.81}$$

where

$$\begin{aligned}
f_{50} &= \frac{f_{k,TM_0}}{0.75 + \left\{0.75 - (0.332/\varepsilon_r^{1.73})\right\} W/h} \\
f_{k,TM_0} &= \frac{c \tan^{-1}\left\{\varepsilon_r \sqrt{(\varepsilon_{re}(0) - 1)/(\varepsilon_r - \varepsilon_{re}(0))}\right\}}{2\pi h \sqrt{\varepsilon_r - \varepsilon_{re}(0)}} \\
m &= m_0 m_c \\
m_0 &= 1 + \frac{1}{1 + \sqrt{W/h}} + 0.32\left(\frac{1}{1 + \sqrt{W/h}}\right)^3 \\
m_c &= \begin{cases} 1 + \dfrac{1.4}{1 + W/h}\left\{0.15 - 0.235 \exp\left(\dfrac{-0.45f}{f_{50}}\right)\right\} & \text{where } W/h \le 0.7 \\ 1 & \text{where } W/h > 0.7 \end{cases}
\end{aligned} \tag{1.82}$$

and c is the velocity of light. The above equations are claimed to predict dispersion better than 0.6 percent in the range $1 \le \varepsilon_r \le 128$ and $0.1 \le W/h \le 10$.

The closed-form expression describing the effect of frequency on Z_{0m} has also been reported and is given below [42]

$$Z_{0m}(f) = Z_{0m} \frac{\varepsilon_{re}(f) - 1}{\varepsilon_{re}(0) - 1} \sqrt{\frac{\varepsilon_{re}(0)}{\varepsilon_{re}(f)}} \tag{1.83}$$

where Z_{0m} is the quasi-static value.

1.3.5 Planar Waveguide Model

It has been shown [38] that the dynamic properties of a microstrip (including higher order modes) can be approximated by a planar waveguide model. In this model, the microstrip is represented by a parallel plate waveguide of width W_{eff} and height h as shown in Figure 1.15a. The top and bottom plates are of infinite conductivity, and there are magnetic walls at the sides. It is filled with a medium of dielectric constant ε_{re}. The value of ε_{re} at zero frequency is determined from a quasi-static analysis. The effective width W_{eff} and the effective dielectric constant ε_{re} are frequency dependent. The frequency dependence of the effective dielectric constant describes the influence of the dispersion on the phase velocity, whereas the frequency dependence of the effective width describes the influence of the dispersion on the characteristic impedance. It is found, from the results of the fullwave analysis discussed later in Chapter 2, that the phase velocity of the waves in a microstrip decreases with increasing frequency. Thus the value of ε_{re} increases with frequency. Also, the characteristic impedance of a microstrip increases with frequency (Section 2.4). This increase in impedance can be explained only by a hypothetical decrease in the effective strip width caused by the concentration of electric field lines below the strip at higher frequency. The decrease of the effective strip width with frequency is described by the empirical relation [38]

$$W_{eff}(f) = W + \frac{W_{eff}(0) - W}{1 + f/f_g} \tag{1.84a}$$

where

$$f_g = c/\left(2W\sqrt{\varepsilon_r}\right)$$

$W_{eff}(0)$ = effective width calculated from quasi-static analysis

$$= 120\pi h/\left(Z_{0m}\sqrt{\varepsilon_{re}(0)}\right)$$

Frequency-dependent impedance is given by

$$Z_{0m}(f) = 120\pi h \,/\left(W_{eff}(f)\sqrt{\varepsilon_{re}(f)}\right) \tag{1.84b}$$

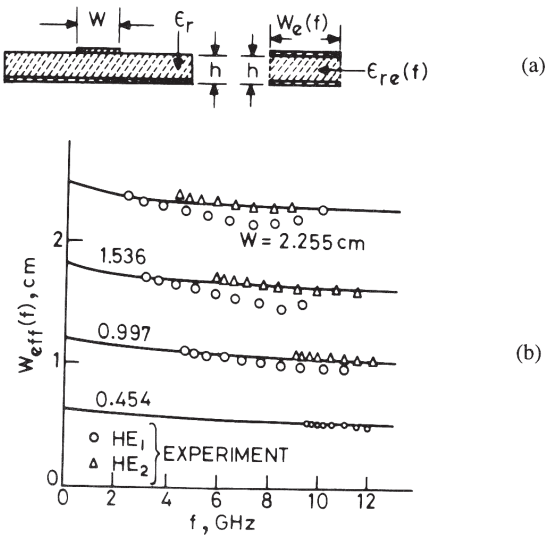

Figure 1.15 (a) Planar waveguide model for a microstrip line and (b) variation of the effective width with frequency $\varepsilon_r = 9.7$, $h = 0.0635$ cm (from [38], © 1975 IEE (U.K.). Reprinted with permission.).

A comparison of the experimental results with the values calculated using (1.84) is shown in Figure 1.15(b). Further, knowing $W_{\text{eff}}(f)$ one can calculate the cut-off frequencies for higher order modes from the relation [38]

$$f_c(m,0) = \frac{mc}{2\sqrt{\varepsilon_{\text{re}}(f)}W_{\text{eff}}(f)} \tag{1.85}$$

The guide wavelength for hybrid modes in terms of $f_c(m, 0)$ is given by

$$\lambda_{\text{HE}_m} = \frac{\lambda_0}{\sqrt{\varepsilon_{\text{re}}(f)}\sqrt{1-\left[f_c(m,0)/f\right]^2}} \tag{1.86}$$

Measured and calculated cut-off frequencies of the first two higher order modes are shown in Figure 1.16 [38]. The two modes indicated as $m = 1$ and $m = 2$ in this figure are the HE_1 and HE_2 modes, respectively. There is a fairly good agreement between the measured results and theoretical values.

1.3.6 Some Comments

The aforementioned models assume an open microstrip line on a nonmagnetic substrate ($\mu_r = 1$) and that the thickness effect is included in the quasi-static value $\varepsilon_{re}(0)$. Atwater [48] and Edwards [6] reported dispersion data comparison for several microstrip lines using many dispersion models. York and Compton [51] provided a comparison between the measured data and the several above-described dispersion models up to 18 GHz for several substrate thicknesses. Microstrip lines used

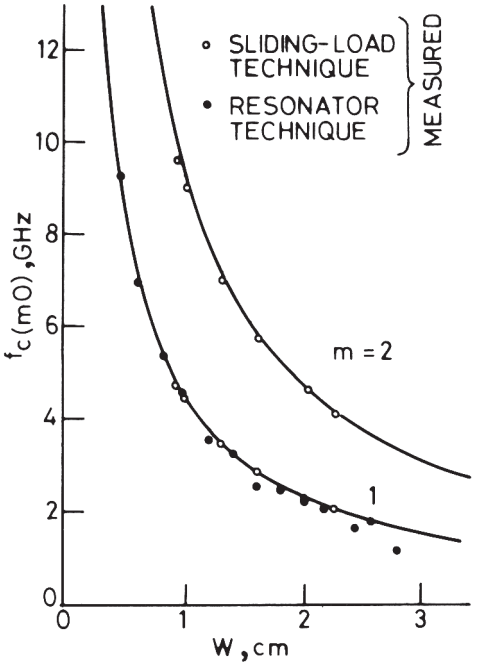

Figure 1.16 Cut-off frequencies for higher order modes in a microstrip computed from the planar waveguide model: $\varepsilon_r = 9.7$, $h = 0.0635$ cm (from [38], © 1975 IEE (U.K.). Reprinted with permission.).

for comparison were fabricated on alumina and plastic substrates having an impedance range from 35 Ω to 70 Ω. A summary of their comparison is given in Table 1.1, which shows that the models of Edwards and Owens [39], Kirschning and Jansen [44] and Kobayashi [49] gave the most consistent results when compared with measured data. Figure 1.17 compares measured and simulated [52] $\sqrt{\varepsilon_{re}(f)}$ as a function of frequency for a microstrip on 0.97-mm alumina substrate ($\varepsilon_r = 9$) with $W/h = 0.867$.

The frequency dependence of the effective dielectric constant describes the influence of dispersion on the phase velocity, whereas the frequency dependence of the effective width describes the influence of the dispersion on the characteristic impedance. Fortunately for high-impedance lines and thin substrates, the changes in ε_{re} and Z_{0m} with frequency are very small. The frequency below which dispersion effects may be neglected is given by the relation

$$f_d = 0.3\sqrt{\frac{Z_{0m}}{h\sqrt{\varepsilon_r - 1}}} \tag{1.87}$$

where f_d is in gigahertz and h is in centimeters. Equation (1.87) shows that f_d is higher for high-impedance lines on thin substrates. For example, a 50-Ω line on a 100-μm-thick GaAs substrate has negligible dispersion below 11 GHz.

Table 1.1 Average Percent Deviation Between the Measured Dispersion and the Models Listed in [51] (© 1990 IEEE. Reprinted with permission.)

ε_r	*Thickness (mm)*	Z_{0m} (Ω)	*[44]*	*[49]*	*[41]*	*[42]*	*[47]*	*[36]*	*[39]*	*[37]*	*[35]*
9.80	0.655	50	0.51	0.37	1.56	3.14	1.27	0.70	**0.34**	1.41	1.91
9.80	0.655	50	**0.47**	0.55	1.38	2.95	1.69	0.76	0.62	1.83	2.32
9.80	0.648	35	0.38	**0.28**	1.46	3.07	0.94	1.06	0.69	1.85	3.80
9.80	0.648	50	0.39	**0.32**	1.39	2.92	1.50	0.77	0.43	1.69	2.23
9.80	0.648	70	0.56	**0.55**	1.35	3.00	1.89	0.95	0.65	1.44	0.84
9.80	0.668	50	**0.58**	0.84	1.13	2.71	1.99	0.69	0.95	2.16	2.69
9.80	0.668	50	0.54	0.67	1.04	2.54	1.84	**0.51**	0.74	1.95	2.45
9.80	0.635	50	**0.31**	0.32	1.31	2.95	1.60	0.78	0.47	1.80	2.24
9.80	0.635	70	**0.32**	0.32	1.17	2.80	1.81	0.69	0.41	1.50	1.10
2.20	1.605	50	0.56	**0.51**	0.65	1.18	1.99	2.57	0.78	1.87	2.67
2.20	1.605	70	0.52	0.54	0.41	0.88	1.24	2.49	**0.45**	1.61	2.50
2.20	0.780	50	0.56	0.58	0.54	0.48	0.68	1.01	0.53	**0.39**	1.67
2.20	0.780	70	0.53	0.53	0.56	**0.50**	0.56	1.01	0.76	0.51	0.98
2.33	1.524	50	0.48	0.46	0.50	**0.45**	0.81	1.28	0.61	0.99	1.51
2.33	1.524	35	0.46	**0.43**	0.59	0.51	0.77	1.12	0.86	1.17	1.21
2.17	0.686	50	**0.41**	0.42	0.52	0.41	0.80	1.02	0.75	0.50	1.14
2.33	0.787	50	0.53	0.55	0.57	0.45	0.78	1.10	0.71	**0.44**	1.59
2.50	0.762	50	**0.23**	0.27	0.47	0.41	0.71	1.14	0.63	0.37	1.50

Note: The results for 18 different resonators are given, and the smallest deviation for each case is shown in bold print.

1.4 Microstrip Transitions

A microwave transition is an interface used to launch microwave power from one transmission line to another with the minimum possible reflective and dissipative losses. This structure is also called a *launcher.* The desirable features of a microstrip transition are:

1. Low transmission and reflection losses over the operating bandwidth;
2. Easily connectable and disconnectable to a microstrip with reproducible results;
3. In-line design and simple fabrication;
4. Adaptability to different substrate thicknesses.

The design of these transitions consists of two parts: mechanical design to match physically both electrical and magnetic field distributions between the two media as close as possible in order to keep the discontinuity reactances small, and the electrical design to match the impedances and any other interface discontinuity reactances over the operating frequency range to minimize losses. Generally, fields are matched by shaping the structure, and the impedance matching and discontinuity reactance compensation are realized by using $\lambda/4$ transformers or tapered sections. Various microstrip transitions used in practice are, for example, coaxial-to-microstrip, waveguide-to-microstrip, microstrip-to-coplanar waveguide, and microstrip-to-slotline. Microstrip-to-slotline and microstrip-to-coplanar line transitions will be treated in Chapters 5 and 7, respectively. Coaxial-to-microstrip and waveguide-to-microstrip transitions are briefly described in this section.

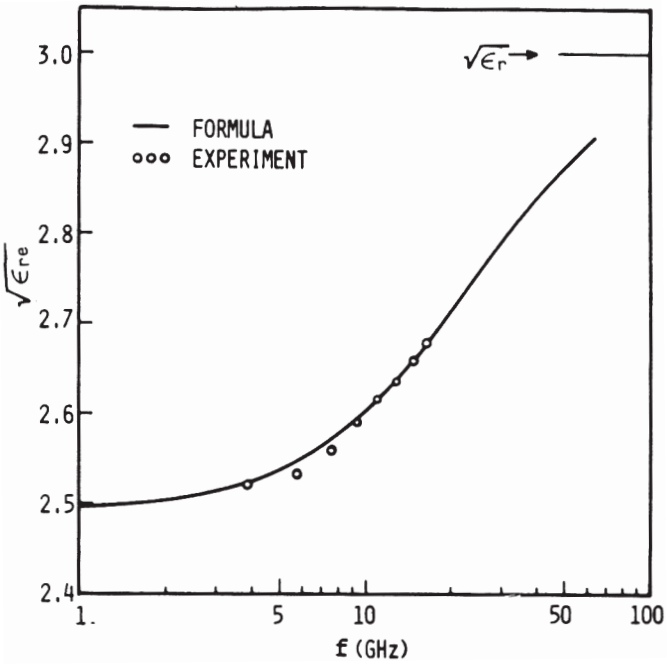

Figure 1.17 The measured dispersion of a microstrip line on an Alumina substrate: ε_r = 9.0, W/h = 0.867, h = 0.97 mm (from [52], © 1981 IEEE. Reprinted with permission.).

1.4.1 Coaxial-to-Microstrip Transition

A coaxial-to-microstrip transition is the simplest and in general is broadband because both media support TEM mode. This transition is generally realized by shaping the coaxial connector's structure and has been well treated in the literature [4, 6, 53-56].

Figure 1.18 shows typical in-plane and right-angle coaxial-to-microstrip transitions. The center conductor pin in these connectors is generally soldered to the microstrip for high reliability. In an in-plane transition, there should be no gap between the microstrip ground plane and the fixture's top surface and between the connector's flange and the fixture front side. Any such gap, as shown in Figure 1.19, will result in an additional discontinuity reactance due to long ground plane current flow.

In general, the coaxial-to-microstrip transition can be represented by a simple equivalent circuit as shown in Figure 1.20, where L_s and C_s are the series inductance and shunt capacitance, respectively. The design of such a transition consists of either minimizing these reactances or compensating for them by making $\sqrt{L_s/C_s}$ = 50 Ω or any other characteristic impedance value used.

An accurate characterization of packaged microwave circuits such as broadband MMIC power amplifiers require coaxial-to-microstrip transitions with VSWR lower than 1.2. In such cases, minimizing the interface discontinuity reactances is desired rather than compensating for the discontinuities, which limits the

frequency range. This is accomplished by matching both the electric and magnetic field patterns of the two media at the interface using an off-centered inner conductor as shown in Figure 1.21 [54]. In this case the center conductor of the coaxial connector is gradually shifted down so that its end touches the microstrip conductor. Throughout the connector length, the characteristic impedance of 50 Ω is maintained.

Figure 1.22(a) shows the Eisenhart transition with APC 7 connector that uses 7-mm of outer diameter coaxial line. The transition was tested by connecting back-to-back using a 5.1-cm-long 50-Ω microstrip line on 25-mil alumina substrate. The measured VSWR shown in Figure 1.22(b) was less than 1.12 up to 18 GHz, implying that each transition's VSWR is less than 1.06. A similar transition is also available with SMA connectors. These transitions are called Eisenhart connectors. The Eisenhart connectors were characterized using 50-Ω microstrip lines printed on 10-, 15-, 20-, and 25-mil-thick alumina substrates (ε_r = 9.9). For Eisenhart connector evaluation and consequently coaxial-to-microstrip transition model development, microstrip lines were 243-mil long. Figure 1.23 shows measured and modeled responses for a 15-mil-thick microstrip line. Two different line lengths were used (printed in 15-mil-thick substrate) to extract connector losses from total measured losses. Figure 1.24 shows the transition model values as a function of substrate thickness. In general, Eisenhart connectors work very well up to 18 GHz.

Several other coaxial-to-microstrip interface discontinuity minimization techniques have also been used in practice. One of them uses a metal screw in order to reduce the transition capacitance [53]. This transition uses a hole in the fixture for the screw and a circular hole in the ground plane of the microstrip near the transition. The coaxial connector is of the SMA type, and the microstrip uses 0.5-mm-thick sapphire substrate. Measured VSWR was less than 1.01 over the 1-GHz to 18-GHz frequency range [6].

1.4.2 Waveguide-to-Microstrip Transition

The use of microstrip in millimeter-wave ICs up to 110 GHz has generated a requirement for broadband waveguide-to-microstrip transitions, as nearly all laboratory equipment is fitted with rectangular waveguide RF connectors. Since the maximum operating bandwidth of a millimeter-wave waveguide is about 50%, the waveguide-to-microstrip transition bandwidth is limited to the waveguide operating bandwidth. Several different techniques [57-66] have been used to design a waveguide-to-microstrip transition; however, the commonly used method employs a ridged waveguide as an intermediate step because of broad bandwidth, better field match, and wider range of available impedances. Electric field matching from a rectangular waveguide to a microstrip through a ridged waveguide is shown in Figure 1.25. The waveguide wave impedance is transformed to a microstrip characteristic impedance by using a broadband stepped ridged waveguide transformer [57]. It is found that four- or five-step $\lambda/4$ transformers occupy a very small space and provide satisfactory performance. A four-step ridged waveguide transformer operating over the 27.5-GHz to 31.3-GHz band was designed connected to the

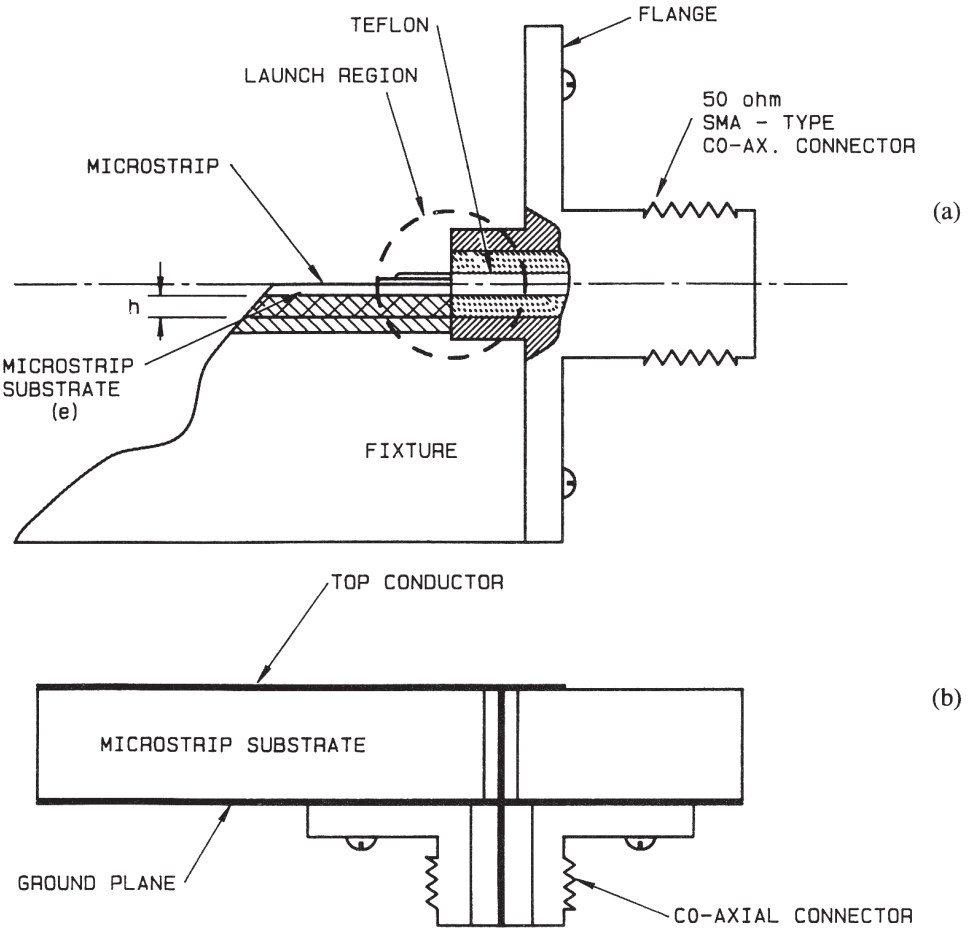

Figure 1.18 Typical coaxial-to-microstrip transitions: (a) in-plane and (b) right-angle.

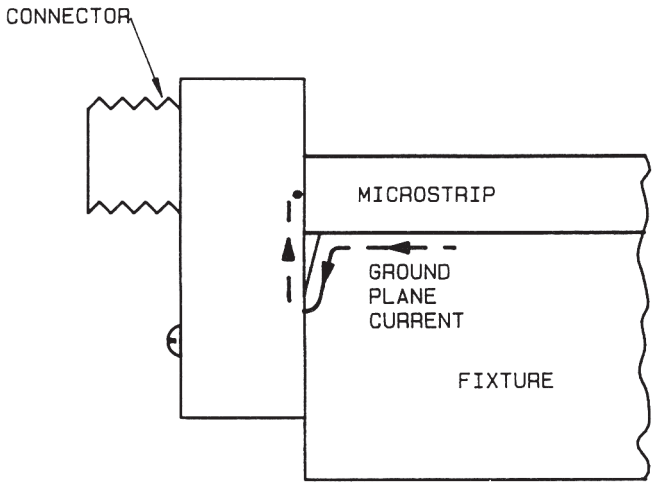

Figure 1.19 Effect of the gap between the connector flange and the front-side wall of the fixture on the ground plane current.

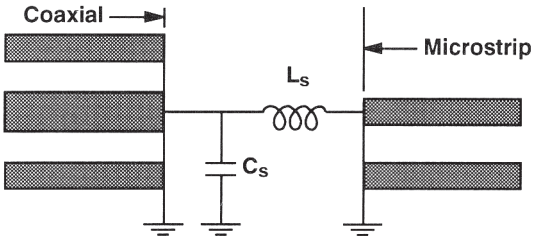

Figure 1.20 Equivalent circuit representation of a coaxial-to-microstrip transition.

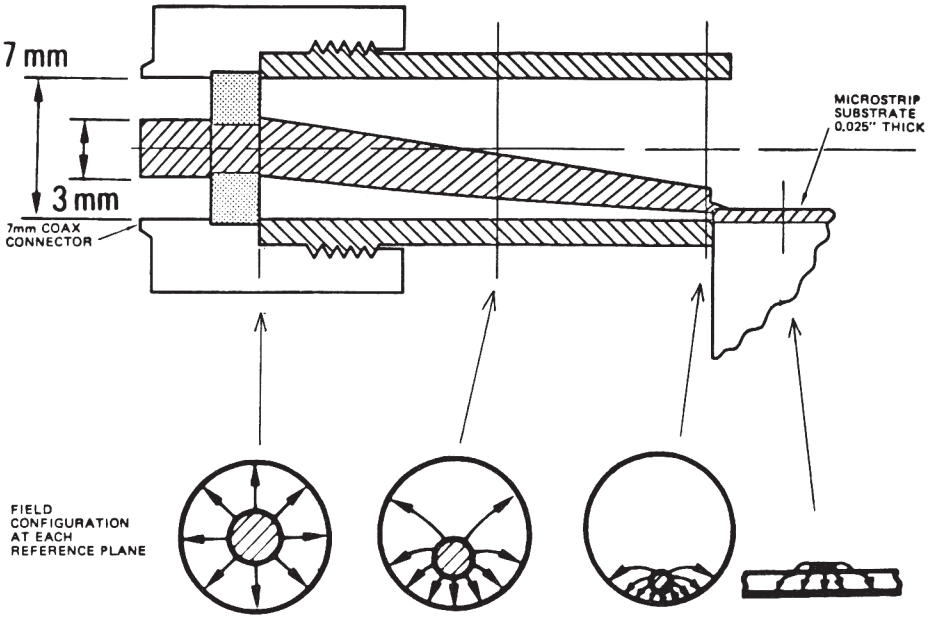

Figure 1.21 High-performance coaxial-to-microstrip transition.

microstrip by a tab as shown in Figure 1.26. The microstrip used was fabricated on a 0.76-mm-thick quartz substrate. The transition measured greater than a 30-dB return loss and less than a 0.1-dB insertion loss over the band. A similar transition was also analyzed using the mode matching method and the cascading procedure using generalized scattering matrices [66].

However, at higher frequencies, the accuracy limitations of achieving the small dimensions required dictates the performance possible, and the fabrication of such a transition poses serious problems. Tapered ridged waveguide transformers, as shown in Figure 1.27, were also investigated. It was found that a cosine-shaped taper over about three-guide wavelengths long at midband resulted in excellent performance and was considerably less critical in terms of mechanical problems.

Several other waveguide-to-microstrip transitions have been described in the literature [58-60, 62-65]. The simple probe-type waveguide-to-microstrip transition [63] shown in Figure l.28 is very suitable for combining MIC/MMIC components with waveguide components. As shown in Figure 1.28, the transition con-

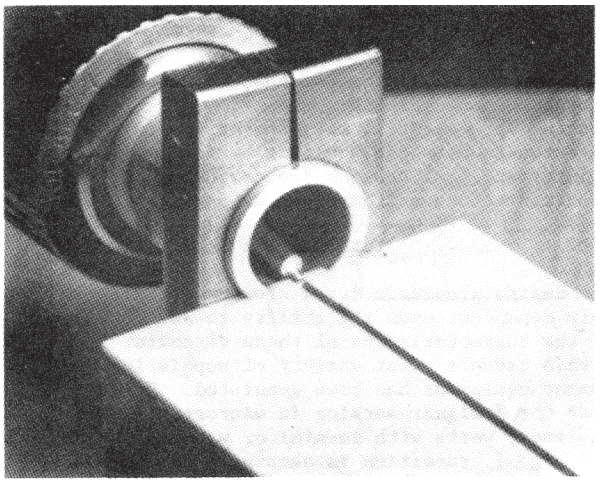

(a)

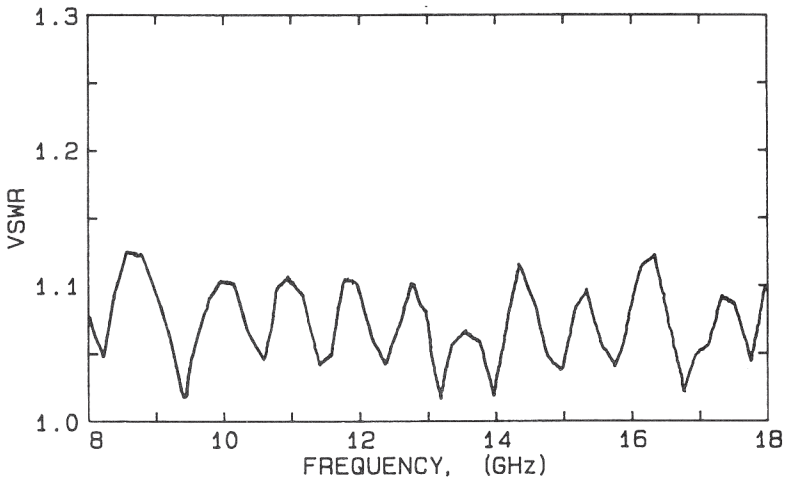

(b)

Figure 1.22 (a) Eisenhart transition's side view and (b) measured performance by connecting two transitions back-to-back (from [54], © 1978 IEEE. Reprinted with permission.).

sists of a microstrip integrated circuit that is partially extended into the waveguide through an aperture in the broad wall. The substrate fits the full height to facilitate precise alignment. The probe conductor couples the energy from the waveguide; and its input impedance, which is about 75 Ω, is matched to 50 Ω by using a $\lambda/4$ transformer.

The critical dimensions shown in Figure 1.28 fare optimized and summarized in Table 1.2 [63]. An RT5880/Duroid ($\varepsilon_r = 2.2$) substrate was used for microstrip lines. The transition was characterized by connecting two transitions back-to-back by a 1.524-cm-long microstrip line. The measured performance for several transitions is also given in Table 1.2.

Microstrip-to-substrate integrated waveguide and coplanar waveguide-to-substrate integrated waveguide transitions are described in Chapter 9.

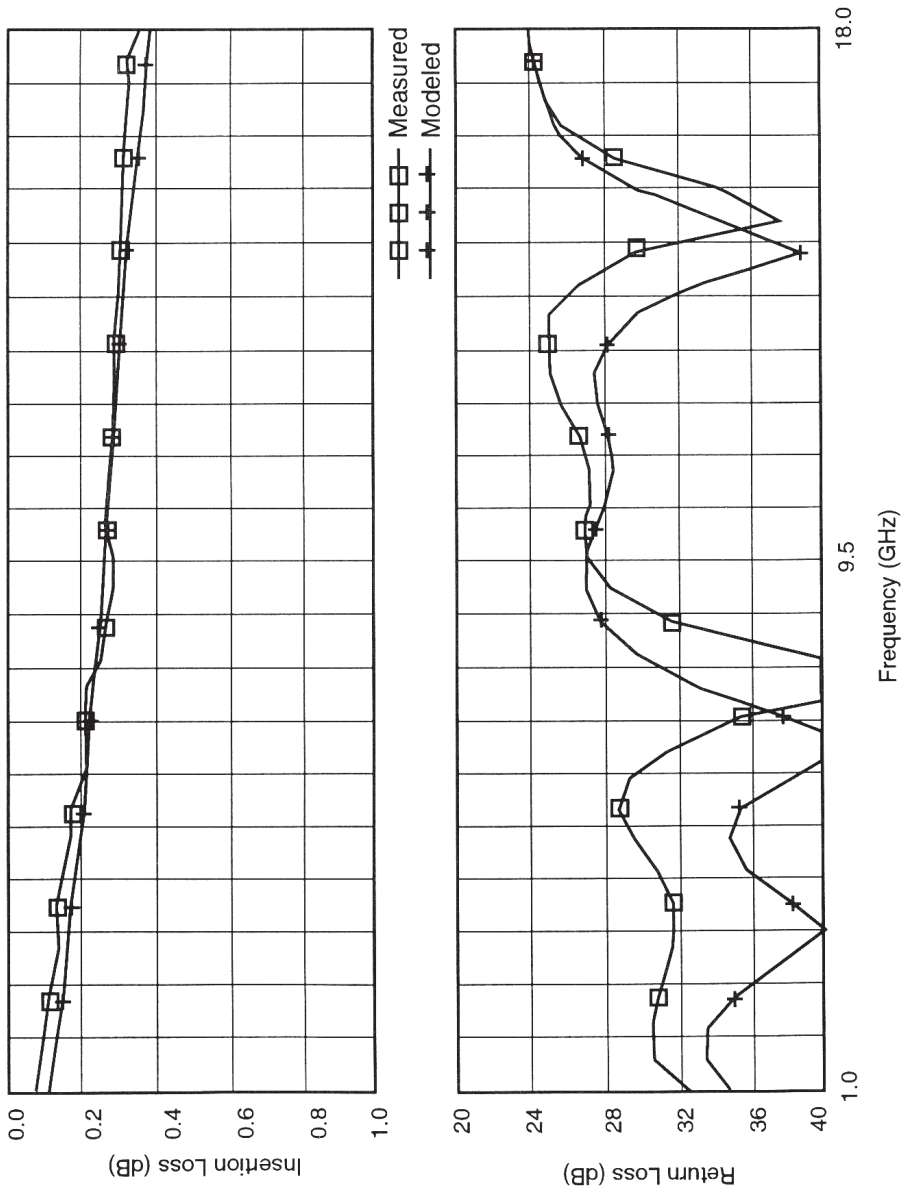

Figure 1.23 A comparison between the modeled and measured insertion loss and return loss of a microstrip line using Eisenhart connectors.

1.5 Microstrip Measurements

As in the case of other transmission structures the important characteristics that need be measured for a microstrip are: (i) characteristic impedance, (ii) phase velocity, and (iii) attenuation constant. Also, in several cases, the dielectric constant of the substrate material is not known accurately. Since this information is required for microstrip circuit design, methods have been devised for quick determination of the dielectric constant of metallized substrates [67–69].

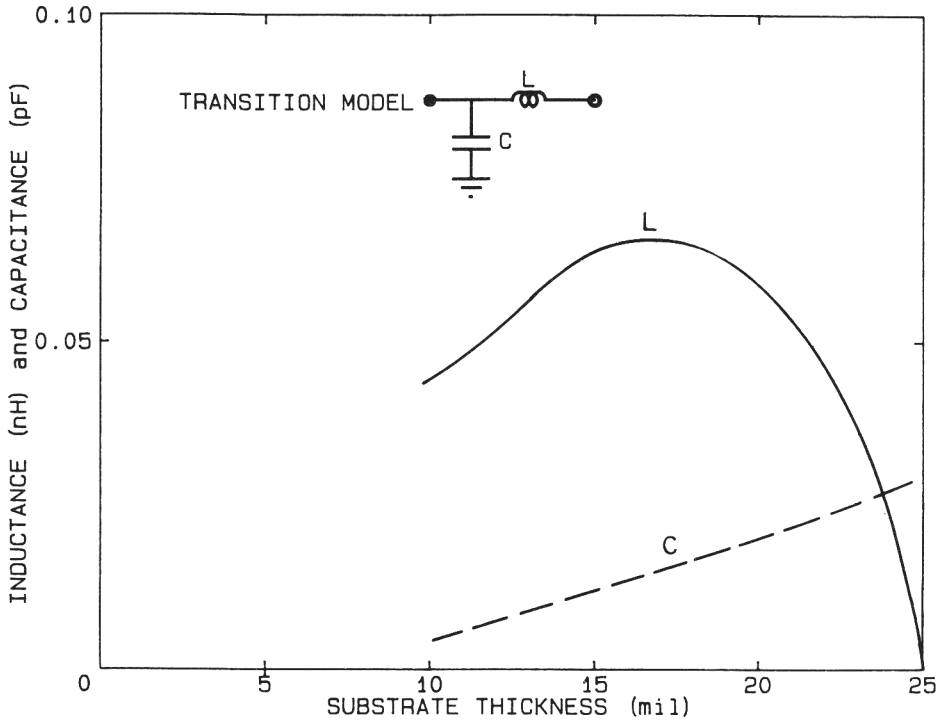

Figure 1.24 Eisenhart connector-to-microstrip transition model values.

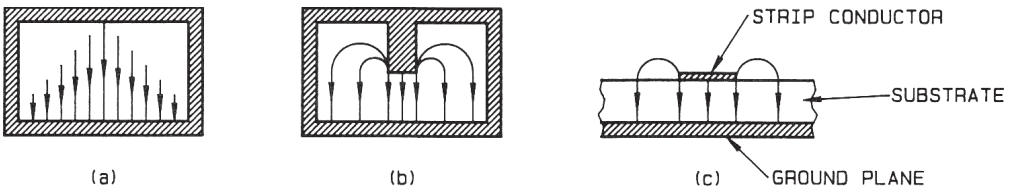

Figure 1.25 Electric field configurations in (a) a waveguide, (b) a ridged waveguide, and (c) an open microstrip.

In this section we will briefly outline the methods for measuring the substrate dielectric constant and microstrip line characteristics.

1.5.1 Substrate Dielectric Constant

An accurate knowledge of the relative dielectric constant value of substrates is very important for circuit design because this value is used to determine the characteristic impedance and phase velocity. Dielectric constant values for monocrystalline materials such as quartz, sapphire, and GaAs, are fixed. However, for plastic substrates, amorphous materials such as glass, and polycrystalline materials such as ceramics, the dielectric constant value depends upon the manufacturing process and the composition of the final material. In order to control the process, an accurate and automatic ε_r measurement technique is necessary.

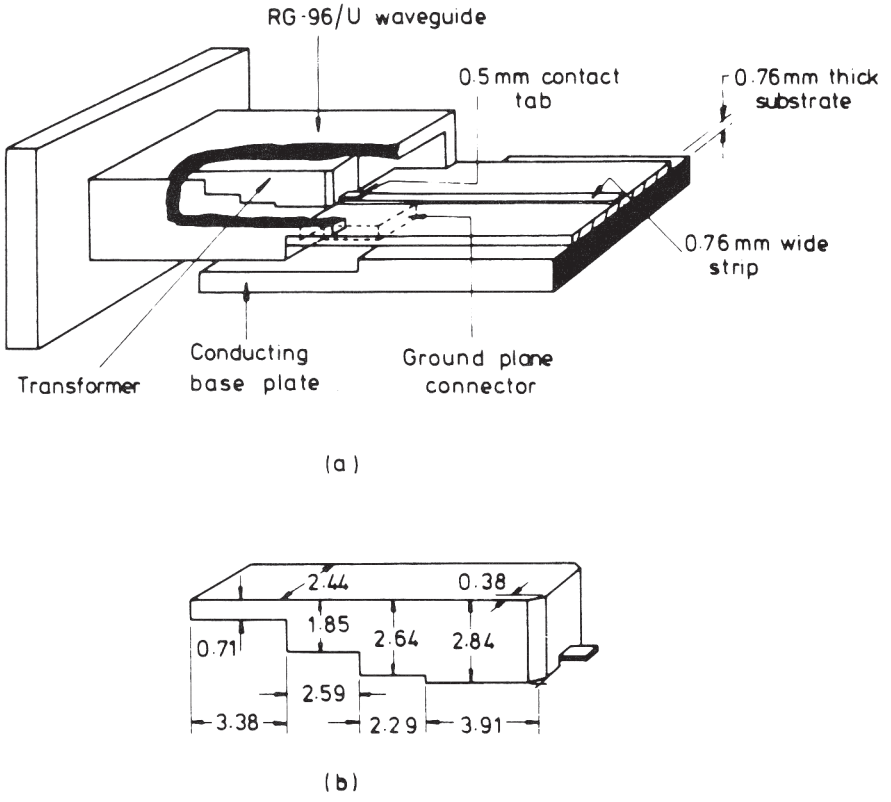

Figure 1.26 Rectangular waveguide-to-microstrip transition using a ridgeline transformer for the 27.5 GHz to 31.3-GHz Band: (a) complete mechanical structure and (b) ridge line transformer dimensions (all in millimeters) (from [57], © 1969 *The Bell System Technical Journal*, the American Telephone and Telegraph Company. Reprinted with permission.).

Table 1.2 Critical Dimensions for Waveguide-to-Microstrip Transitions and Measured Data for Two Transitions Connected Back-to-Back by 1.524-cm-long Microstrip Line

Waveguide						*Measured Performance (dB)*	
Type	*Band*	*Inside Dimensions (a × b) mm*	*Substrate Thickness (mm)*	*D (mm)*	*L (mm)*	*Return Loss*	*Insertion Loss*
WR28	Ka	7.112 × 3.556	0.254	2.032	2.032	15	0.4
WR22	Q	5.69 × 2.845	0.254	1.524	1.524	10	1.0
WR15	V	3.759 × 1.88	0.127	1.143	1.270	10	2.0
WR10	W	2.54 × 1.27	0.127	0.711	0.762	14	2.0

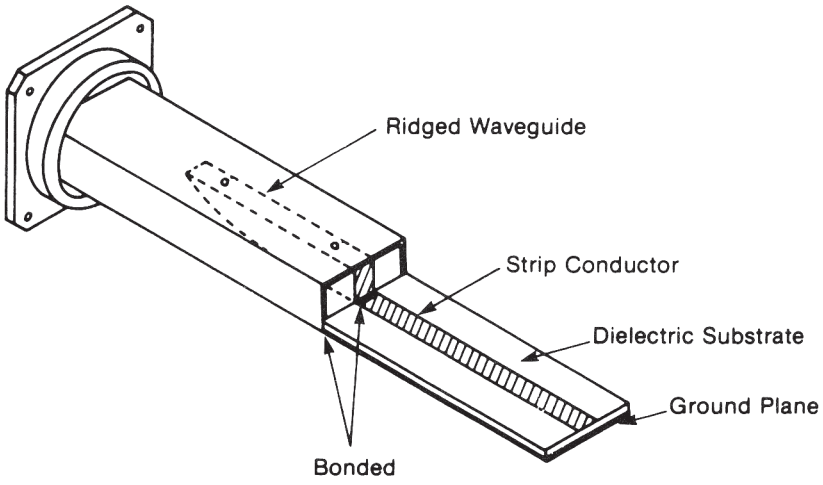

Figure 1.27 Waveguide-to-microstrip transition.

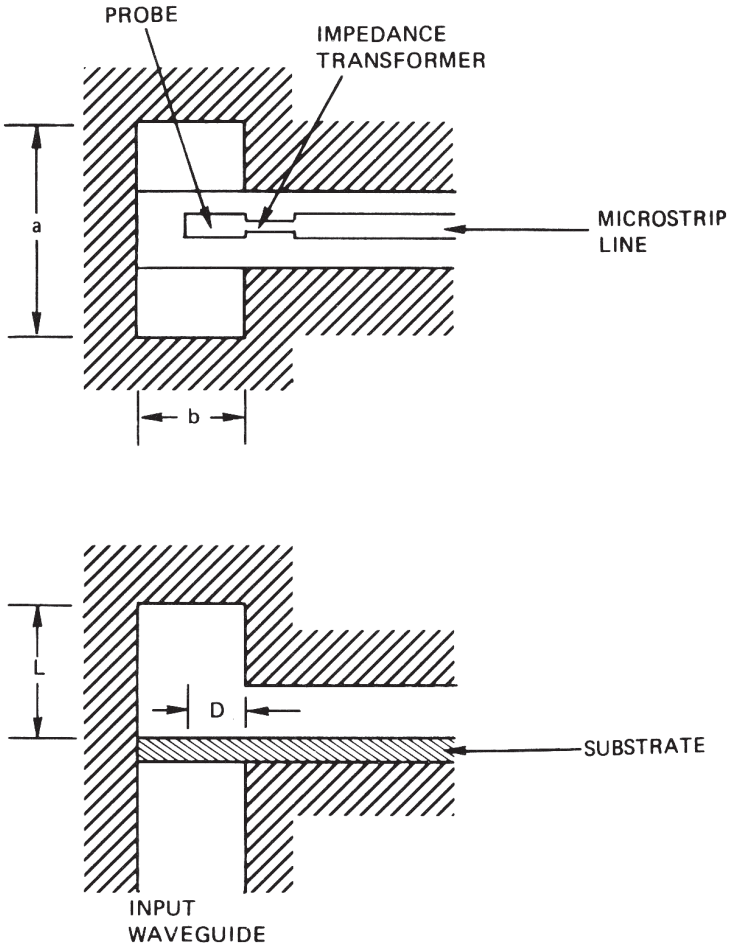

Figure 1.28 Cross-sectional view of a waveguide-to-microstrip transition (from [63], © 1988 IEEE. Reprinted with permission.).

Basic requirements of an accurate method of measuring ε_r include rapid and nondestructive testing, no machining or metallization of the sample (accept substrate as is), real-time measurement, error less than 1 percent, frequency range of 1 GHz to 20 GHz, and handling capability for substrates 0.2-mm to 2-mm thick and 2.5-cm to 10.0-cm long. Several simple techniques for the dielectric constant measurement of microwave substrates have been reported in the literature and are in common use [67–72]. These techniques incorporate the dielectric specimen in a resonant structure, and the permittivity is calculated from a measurement of the resonant frequencies.

In the normal course of fabricating dielectric substrates for MICs, a dielectric-filled resonator cavity is automatically constructed. The rectangular substrate with its top- and bottom-surface metallization (sides not metallized) becomes a parallel plate dielectric-loaded waveguide resonator. This structure is shown in Figure l.29(a). For high dielectric constant substrates the fringing field is very small, and the sides of the resonator are good approximations to open circuits. The resonant frequency f_{mn} for this type of resonator is given by

$$f_{mn}^2 = \frac{c^2}{\varepsilon_r}\left\{\left(\frac{m}{2W}\right)^2 + \left(\frac{n}{2\ell}\right)^2\right\} \tag{1.88}$$

where m and n represent the mode of resonance and correspond to the number of half cycle variations along W and ℓ, respectively. Values of f_{mn} are shown in Figure 1.29(b) as dots superimposed on the dispersion curves.

To measure the substrate dielectric constant, the parallel plate resonator is coupled to the measurement system by placing it between two APC-7 type coaxial connectors [67] as shown in Figure 1.30(a). Details of the coupling are shown in Figure 1.30(b). Transmission measurements may be carried out by using a network analyzer or any other suitable system. The modes are identified by referring to Figure 1.29(b).

The accuracy of the above method is limited because of the fringing field and radiation from the open sides of the resonator. A modification has been suggested [68] wherein the substrate is metallized on all sides so that a small microwave cavity is formed. Equation (1.88) for the various resonant frequencies is still valid. Resonant frequencies are measured by clearing metallization from the corners of the cavity and positioning the center conductor in APC-7 connectors as shown in Figure 1.30.

Coupling errors in cavity resonance measurements on MIC dielectric substrates are discussed by Ladbrooke et al. [69]. An alternative coupling scheme wherein a coupling aperture is photolithographically cut in the top plane has been suggested. Details of this scheme are shown in Figure 1.31. The broadwall hole with an overlaid strip provides the required coupling, and the energy transfer into and out of the cavity is adequate without having to make the aperture unacceptably large. This type of coupling scheme has been used with substrates that are metallized on the sides also.

Errors because of coupling are analyzed by considering the perturbation of fields. It has been pointed out [69] that the two methods of coupling, namely, corner coupling for resonators with open sides and aperture coupling for resonators

with metallized sides, are complementary. As shown in Figures 1.30(b) and 1.31(b) respectively, corner coupling involves the perturbation of electric field lines whereas in the aperture coupling the magnetic field of the resonator is distributed. Errors in the two cases are of opposite natures, and an improved accuracy ($\simeq 0.5$ percent) can be obtained by averaging the results obtained by the two methods.

Although cavity methods are straightforward, they do not lend themselves readily to automated measurements. On the other hand, transmission line methods [73,74] are particularly well suited to automated measurements. In these methods, the sample is placed in a waveguide and the dielectric constant value is extracted from the two-port scattering parameter measurement using an automatic vector network analyzer. The unmetallized sample is centered between the sidewalls of the waveguide as shown in Figure 1.32 and is easily inserted or extracted via a slot. The widespread availability of accurate computer-eontrolled network analyzers makes this technique attractive. This method of measurement has been described by York and Compton [74].

The dielectric constant can also be determined by measuring the reflection coefficient using an open-ended coaxial line [75] in contact with the unmetallized dielectric substrate. This method has been commercialized by Hewlett-Packard by developing an HP 85070B dielectric probe kit that includes a coaxial probe and the software. The probe is placed in contact with the dielectric substrate and the reflection coefficient is measured using a vector network analyzer. Since the coaxial's open-end fringing fields interact with the dielectric material, ε_r and tan δ are derived from the reflected signal by solving the boundary value problem. The frequency range of the measurement is from 0.2 GHz to 20 GHz and the accuracy of measurement is about 5 percent. This probe can only be used with thick substrates.

All the above-described transmission and reflection measurement methods require special tools and software to determine the dielectric constant value. The dielectric constant value can also easily be determined by making transmission measurements on a 50-Ω microstrip line using RF probes [76] or using microstrip transitions as described in the previous section. The effective dielectric constant may be written as

$$\varepsilon_{re} = \frac{\varepsilon_r + 1}{2} + \frac{\varepsilon_r - 1}{2} F$$

or

$$\varepsilon_r = [2\varepsilon_{re} + F - 1]/(F + 1) \tag{1.89}$$

where F is obtained from (1.17). For a given 50-Ω microstrip line length ℓ, if the measured transmission phase ($\angle S_{21}$) in degrees is ϕ, then

$$\varepsilon_r = \left[\frac{1}{72}\left(\frac{\phi}{f\ell}\right)^2 + F - 1\right]/(F + 1) \tag{1.90}$$

where f is in gigahertz and ℓ is in centimeters. Thus, by calculating F as described in Chapter 2, the ε_r value can easily be determined. In these measurements, either dispersion effects are kept at a minimum or taken into account in the calculations.

Precise characterization of MIC, MMIC, and plastic substrates for dielectric properties have been reported recently. Many methods are suggested to measure

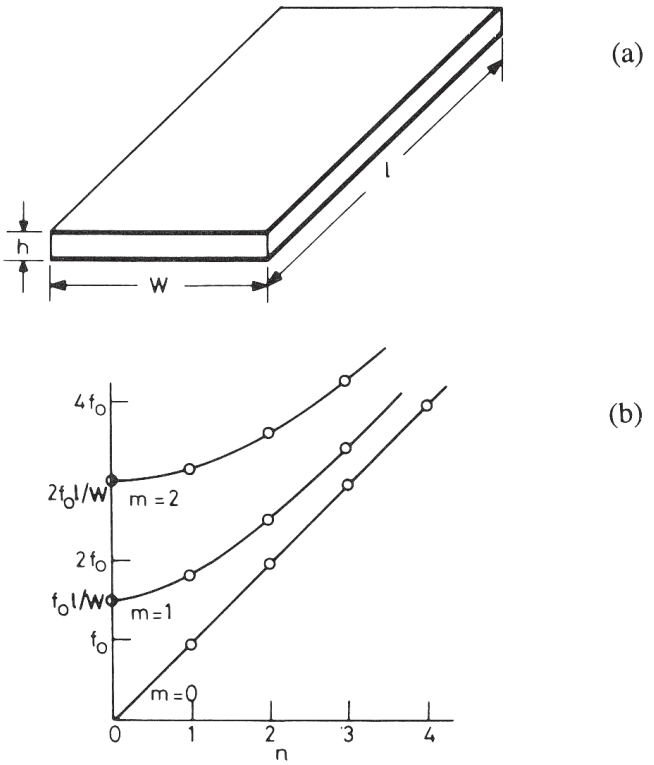

Figure 1.29 (a) Metallized substrate as a parallel plate resonator and (b) resonance frequencies for various modes of a metallized substrate resonator (from [67], © 1971 IEEE. Reprinted with permission.).

the dielectric constant, loss tangent, and anisotropy of these substrates. Some of these methods are modified versions of aforementioned techniques, and others are based on the measurement of various resonant frequencies. Because it is not in the scope of this book to discuss these methods further, the readers are referred to numerous published papers [120–126] on this topic. Anistropy in the substrates is covered in Section 2.4.4.

1.5.2 Characteristic Impendance

Since fairly good coaxial-to-microstrip transitions are available, impedance measurement methods are identical to those employed for other transmission lines.

The characteristic impedance can be measured by terminating the microstrip in a matched load and measuring the maximum and minimum VSWR values as functions of frequency. If the impedance to be measured is Z_{0m} Ω using a 50-Ω reference line, then

$$\left(\frac{Z_{0m}}{50}\right)^{\pm 1} = \sqrt{\mathrm{VSWR}_{max}.\mathrm{VSWR}_{min}} \tag{1.91}$$

where the exponent +1 is associated with high impedance lines and –1 with low impedance lines. An approximate value of Z_{0m} can be obtained from time domain

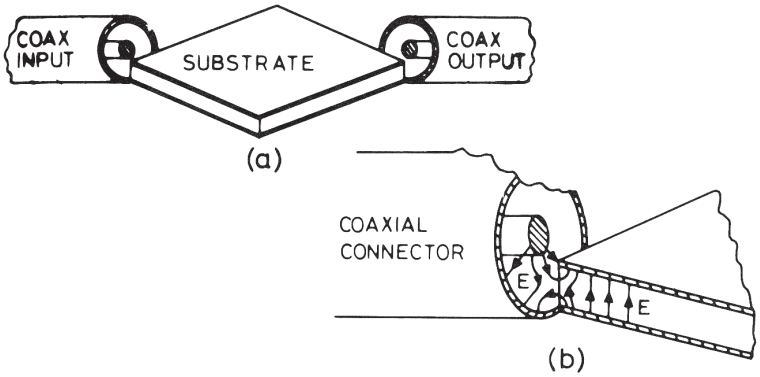

Figure 1.30 Coupling to metallized substrate resonators through coaxial connectors.

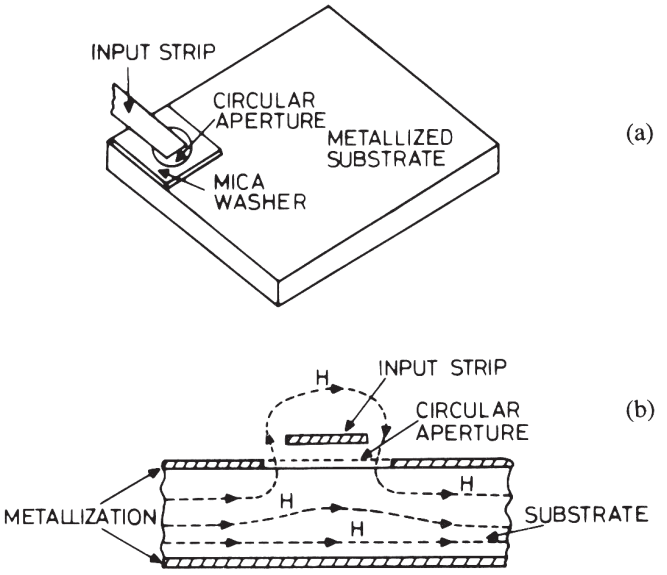

Figure 1.31 Aperture coupling to a substrate resonator metallized on all the sides: (a) configuration and (b) magnetic field distribution (from [69]).

reflectometry (TDR), and thus the ambiguity between the exponents +1 and –1 can be resolved very easily. It may be noted that this method assumes the frequency insensivity of Z_{0m}, which is a good approximation for the frequency range of interest.

The above method of measurement has been described by Caulton et al. [77] and by Seckelmann [78]. Several other methods of measuring the characteristic impedance of microstrip lines have been discussed by Getsinger [79].

1.5.3 Phase Velocity or Effective Dielectric Constant

The effective dielectric constant of a microstrip can be measured quite accurately by using resonance techniques. Both the ring and the linear type resonators have been used.

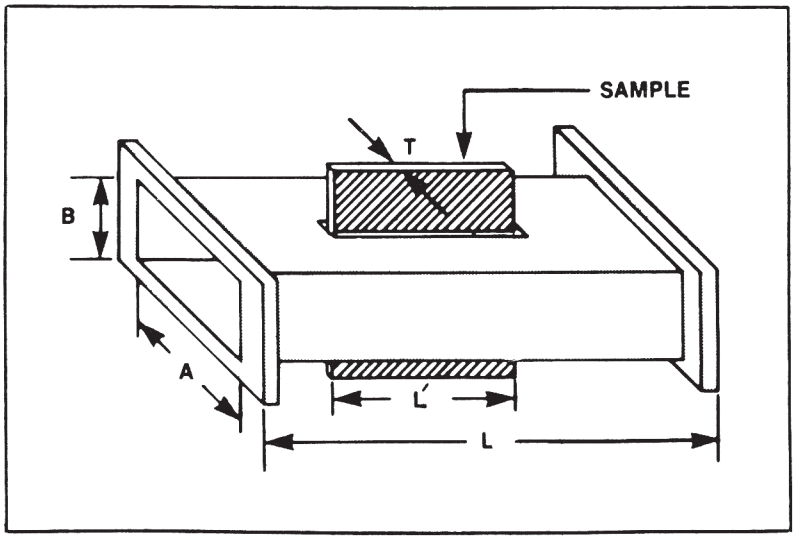

Figure 1.32 A waveguide holder for measuring 2-port S-parameters of a microwave substrate for dielectric constant evaluation (from [74]).

Use of Ring Resonators

A microstrip ring resonator is a microstrip line bent in a circular shape to close in upon itself (Figure 1.33(a)). The main advantage of using ring resonators for dispersion measurements [80] is that, in contrast to the linear resonators, no end effects need to be considered. The resonant frequencies of this type of resonator could be calculated assuming that the mean length of the strip forming the resonator is a multiple of the guide wavelength on the microstrip.

For ring resonators, the curvature of the ring influences the resonance frequencies, so only large resonators can be used. The influence of the curvature becomes large if substrate materials with small relative permittivities and lines with small impedances are used. Under these conditions, the width of the lines becomes large and a mean radius cannot be well defined. When short resonators are used, an accurate analysis of ring resonators is needed. A magnetic wall model of microstrip ring resonators has been discussed by Wolff and Knoppik [81].

The eigenvalue equation resulting from the boundary conditions of a magnetic wall ring resonator model may be written as

$$\frac{J_n'(kr_a)}{J_n'(kr_i)} - \frac{N_n'(kr_a)}{N_n'(kr_i)} = 0 \tag{1.92}$$

where k is the wave number in unbounded dielectric and r_a and r_i represent outer and inner radii, respectively. $J_n'(x)$ and $N_n'(x)$ represent derivatives of Bessel functions of the first and the second kind, respectively. Some results based on the solution of (1.92) are described in [81]. It is shown that curvature effects are more pronounced for wider lines (impedances smaller than 50 Ω).

More accurate calculations for curvature effect in microstrip ring resonators are presented by Owens [82]. In this method a planar waveguide model is used

for the microstrip. Equation (1.92) still holds provided the width of the strip is replaced by the effective width given by this model. Since the effective width is frequency dependent, the frequency variation of the fringing field at the edges of the microstrip is also taken into account.

Extensive measurements were made using ring resonators realized with characteristic impedances in the range of 20 Ω to 86 Ω on 200-μm-thick GaAs substrate ($\varepsilon_r = 12.9$). In these measurements the microstrip configuration uses the composite dielectric structure shown in Figure 1.33 [83]. Here the thicknesses of silicon nitride and dielectric composite layers are very small compared to the substrate thickness. Simulated and measured effective dielectric constant versus frequency are shown in Figure 1.33(b). Note that dispersion effects are negligible up to 18 GHz for microstrip lines of $Z_{0m} \geq 50$ Ω on 200-μm-thick substrate.

Linear Resonator Method

The main difficulty with the use of a linear resonator is caused by the end effects. When a linear resonator is coupled to the measurement system at one end, as shown in Figure 1.34(a), the reactances at the two ends are different. The open end can be represented either by a shunt capacitance or by an incremental line length $\Delta\ell_{0c}$. On the other hand, the gap between the input line and the resonator is represented by a π-network of capacitances, and the incremental length $\Delta\ell_g$ shown in the figure is different from $\Delta\ell_{0c}$. Measurement of the discontinuity reactances will be discussed in detail in Chapter 4. For the purposes of the present discussion, one requires incorporating the effect of these reactances for the accurate measurement of resonant frequencies. A method suitable for this purpose has been described by Richings [84] and by Easter [85]. This method suggests the use of a modified resonator set up as shown in Figure 1.34(b). A $\lambda_m/4$ section at the other end of the resonator ensures that the reactances at two ends of the resonator are identical. Thus, there are only two unknowns now, and these (ε_{re} and $\Delta\ell_g$) can be evaluated if measurements are carried out for two different lengths of the resonator.

Alternatively, the effective dielectric constant can be measured by the substitution method using two resonators [6, 51]. Here it is assumed that the two resonant frequencies f_1 and f_2 are very close and that the two structures as shown in Figure 1.35 are identical except for the physical lengths L_1 and L_2 of the resonators. In this configuration, the resonators are loosely coupled, and from the nth-order $\lambda/2$ resonance frequency

$$\varepsilon_{re} = \left[\frac{nc}{2f_{1,2}(L_{1,2} + \ell_e)}\right]^2 \tag{1.93}$$

where subscripts 1 and 2 denote resonators 1 and 2, respectively, and c is the velocity of light. The term ℓ_e represents the sum of the coupling-gap end effect $\Delta\ell_g$ and the open-end effect $\Delta\ell_{oc}$. When ε_{re} and ℓ_e are constant over the $f_2 - f_1$ range, (1.93) becomes

$$\varepsilon_{re} = \left[\frac{nc(f_1 - f_2)}{2f_1 f_2(L_2 - L_1)}\right]^2 \tag{1.94}$$

where

$$\ell_e = \frac{f_2 L_2 - f_1 L_1}{f_1 - f_2} \tag{1.95}$$

This method provides ε_{re} as a function of frequency and can also be used to calculate ε_r from ε_{re} as described previously in Section 1.5.1.

1.5.4 Attenuation Constant

The most satisfactory method for measuring the attenuation constant for low-loss substrates is from the Q-factor of a resonant section of the line. The attenuation constant and the unloaded quality factor Q_0 are related by the expression

$$\alpha = \frac{27.3n}{Q_0 \lambda_m}(\text{dB/cm}) \tag{1.96}$$

where n is the number of half wavelengths and λ_m is the guide wavelength in centimeters.

It has been pointed out that the ring resonator technique is less suitable for the accurate measurement of microstrip losses because of increased surface wave radiation loss [86]. On the other hand, the shielded open-ended linear resonator in a waveguide below cut-off gives a reliable value of the attenuation constant.

More accurate methods for measuring microstrip line losses have also been described in the literature [87, 88]. Extensive measured data for microstrip loss on GaAs substrates as shown in Figure 1.36 have been given by Goldfarb and Platzker [87]. The results given are for an impedance range of 20 Ω to 90 Ω and for frequencies up to 40 GHz. Figure 1.37 shows a 50-Ω microstrip line loss as a function of frequency. Measured data was also compared with Touchstone (TS1.7), Super Compact (SC2.0), and MDS (HP85150B). The microstrip parameters used for comparison were: unit line length = 1 mm, $\varepsilon_r = 12.9$, $h = 100$ μm, $t = 3$ μm, conductor resistivity = 2.44 μΩ.cm, tan δ = 0, and roughness factor = 0. Figure 1.38 shows measured loss versus line width at several frequencies [87].

An approximate but very simple method for measuring the attenuation constant is based on the comparison technique. In this method two microstrip lines with identical electrical characteristics but different lengths are used. Their insertion losses are measured. The difference between the two values of insertion loss is used to evaluate the attenuation constant. This procedure avoids the systematic errors caused by radiation, coaxial-to-microstrip transition, and so forth. With recent advancements in the de-embedding techniques and RF probes, the attenuation constant of a microstrip line can also be measured accurately using two-port scattering parameter measurements.

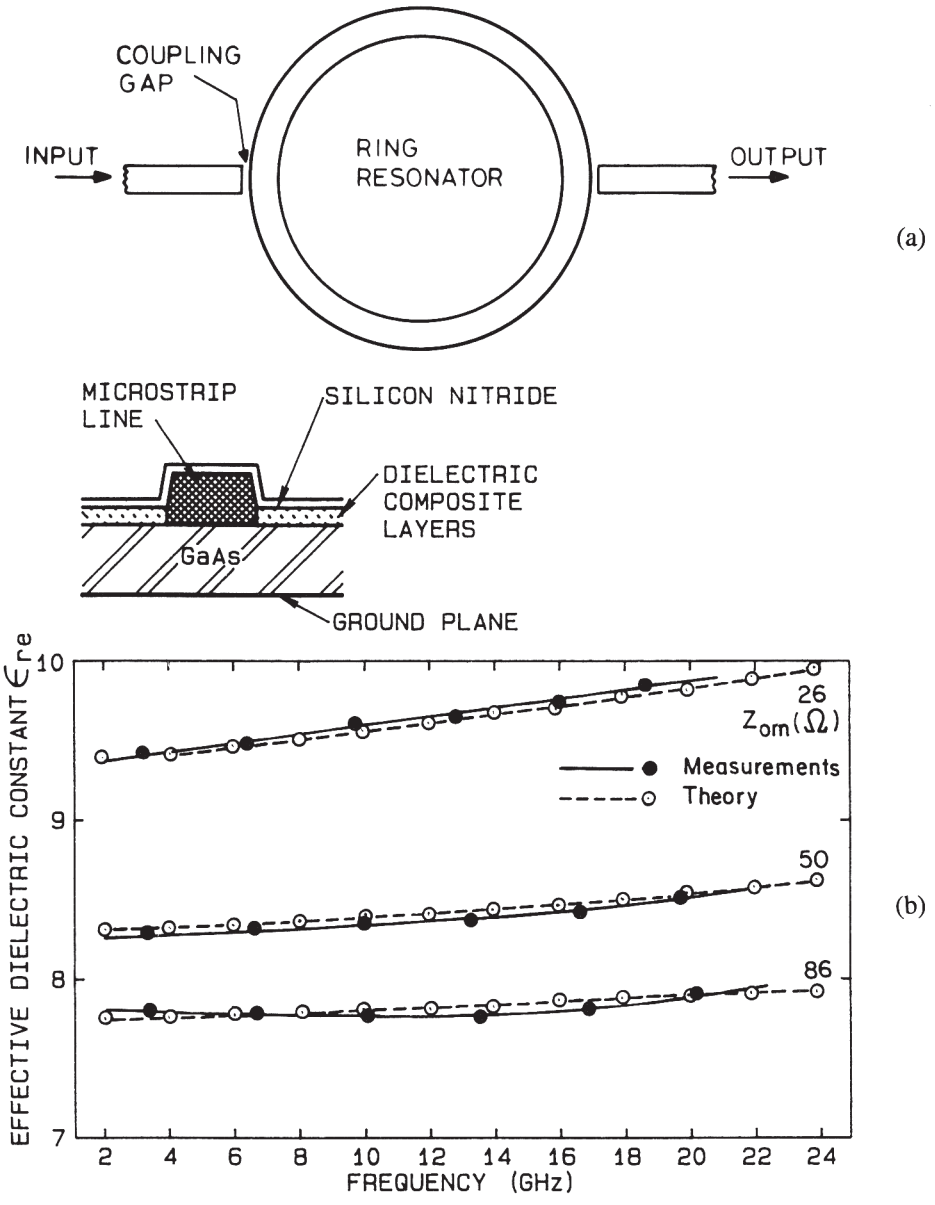

Figure 1.33 (a) A ring resonator set-up for microstrip dispersion measurements and (b) simulated and measured effective dielectric constant versus frequency for a line on 200-μm-thick GaAs substrate (from [83], © 1988 IEEE. Reprinted with permission.).

1.6 Fabrication

Since the early 1950s, after the invention of planar transmission lines, such as striplines and microstrip lines, work on microwave planar printed circuits, as well as the usage of lumped elements at microwave frequencies, began. The miniaturization and batch fabrication of several microwave functions for large volume production brought about a revolution in the microwave industry. Early work on planar print-

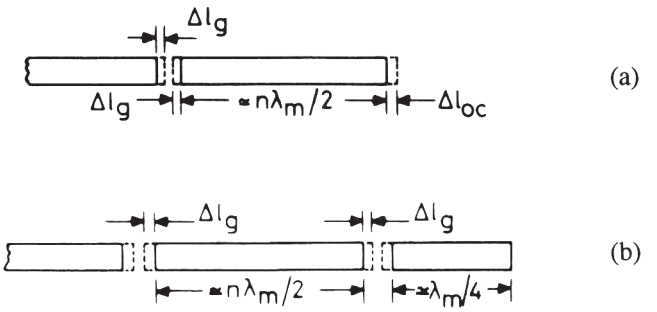

Figure 1.34 A linear microstrip resonator and (b) a modified linear resonator configuration.

ed circuits served as the seed for the successful introduction of radio frequency (RF) and microwave integrated circuits (MICs), including microwave printed circuits, printed circuit boards [89, 90], thin and thick film MICs, low-temperature cofired ceramic (LTCC) [91–107], and monolithic integrated circuits [108–119]. Various integrated fabrication techniques based on the substrate used can be grouped into three categories: plastic substrates, glass and ceramic substrates, and semiconductor substrates. Salient features of fabrication steps are described in this section.

1.6.1 Printed Circuit Technologies

Microwave Printed Circuits

Microwave printed circuit (MPC) technology is widely used for microwave passive circuits and printed antennas. The first step is to generate the artwork from design. The enlarged artwork is then photo reduced using a high-precision camera to produce a high-resolution negative (also known as a mask), which is used for exposing the photoresist that is spun over the substrate. The mask is placed on the substrate and held using a vacuum frame or other technique in order to assure the fine-line resolution that is required. With exposure to the proper wavelength light, a polymerization of the exposed photoresist occurs, making it insoluble in the developer solution. The backside of the substrate is exposed completely without a mask, since the copper foil is retained to act as a ground plane. The substrate is developed in a developer that removes the soluble photoresist material. When these steps have been completed, the substrate is now ready for etching. This is a critical step and requires considerable care so that proper etch rates are achieved. After etching, the excess photoresist is removed using a stripping solution. The substrate is then rinsed in water and dried. Finally, the substrate is cut into the required small sizes. MPCs use a large range of plastic type substrates.

Printed Circuit Board

Printed circuit boards are fabricated like conventional MPCs using photo-etching process. In a basic multilayer printed circuit board fabrication process, first a copper foil is laminated to the dielectric sheets. The required interconnect and component patterns are then etched on all substrates by using a photolithography

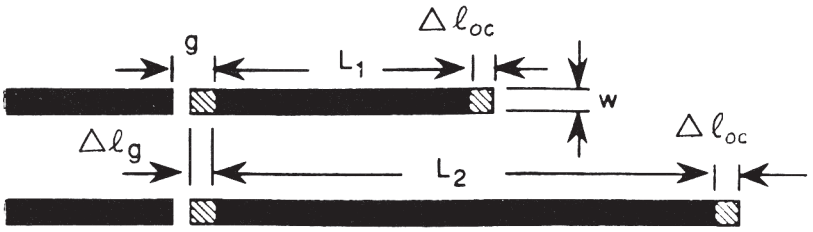

Figure 1.35 Linear resonator pair for dispersion measurements. By measuring the resonant frequency of the two resonators, end effects can be canceled.

technique. The substrates are stacked and laminated under heat and pressure to make a monolithic board. Next, via holes are drilled in the board to make interlayer metallic connections and are catalyzed; the whole board is plated with electroless copper. This increases the thickness of the surface conductor pattern and provides the copper layer in the via holes. The board is then tinned for soldering, or nickel or gold plated for gold wire bonding. These circuits are generally made from multilayer FR-4 substrate material.

1.6.2 Hybrid Microwave Integrated Circuits

Thin-Film MIC Technology

The first step in the fabrication process of thin-film MIC is the deposition of a first layer (seed layer) of metal film on a commonly used alumina substrate. The selection of the film is made based on the criterion of good adhesion to the substrate and is one of the most important factors in selecting a conductor material for the first layer of metal film. At radio frequencies, the electromagnetic fields are confined to several skin depths of the conductors. In order to achieve low loss, the layer of high-resistivity material, such as chromium used for adhesion, must be extremely thin. Metal films are deposited on substrates by three methods: vacuum evaporation, electron-beam evaporation, and sputtering. A typical metal combination for alumina substrate is Cr/Cu/Au or NiCr/Ni/Au. A very thin seed layer of suitable metal is deposited on the substrate by one of the preceding techniques, and then the bulk conductor metal is deposited by electroplating techniques. The seed layers of metal provide mechanical and electrical foundation layers on which to electroplate a good-quality bulk conductor metal. The circuit definition can be accomplished by a plate-through technique or by an etchback technique. The plate-through technique begins with a substrate coated with a thin layer of evaporated metal, followed by an application of a thick photoresist. The thickness of this photoresist is similar to the thickness of the final metal film required. After defining a pattern in the photoresist, the second metal layer is plated up to the desired thickness with precise definition, only in the areas where metal is required. The photoresist layer is then washed away and the thick seed-metal is etched with very little undercut from the undesired areas. This technique is also suitable for fabricating lines that are 25–50 μm wide and/or when the separation between them is 25–50 μm.

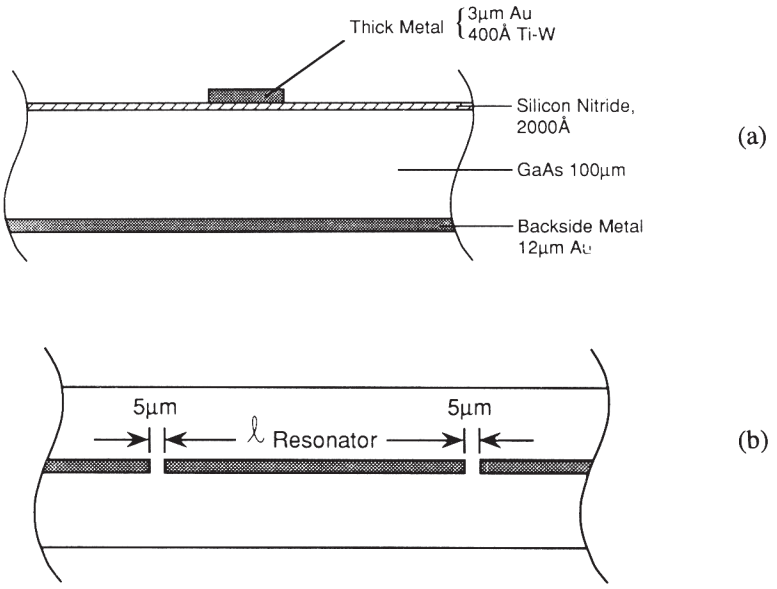

Figure 1.36 Microstrip resonator on GaAs substrate: (a) cross-section view and (b) top view.

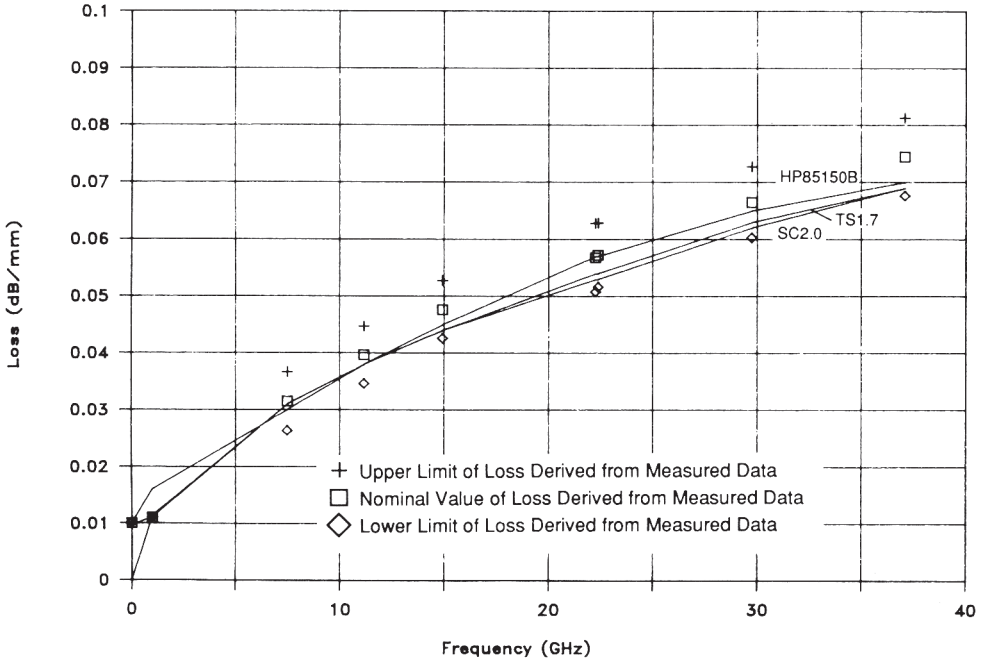

Figure 1.37 Losses in GaAs microstrip for 70-μm width on 100-μm GaAs (from [87],© 1990 IEEE. Reprinted with permission.).

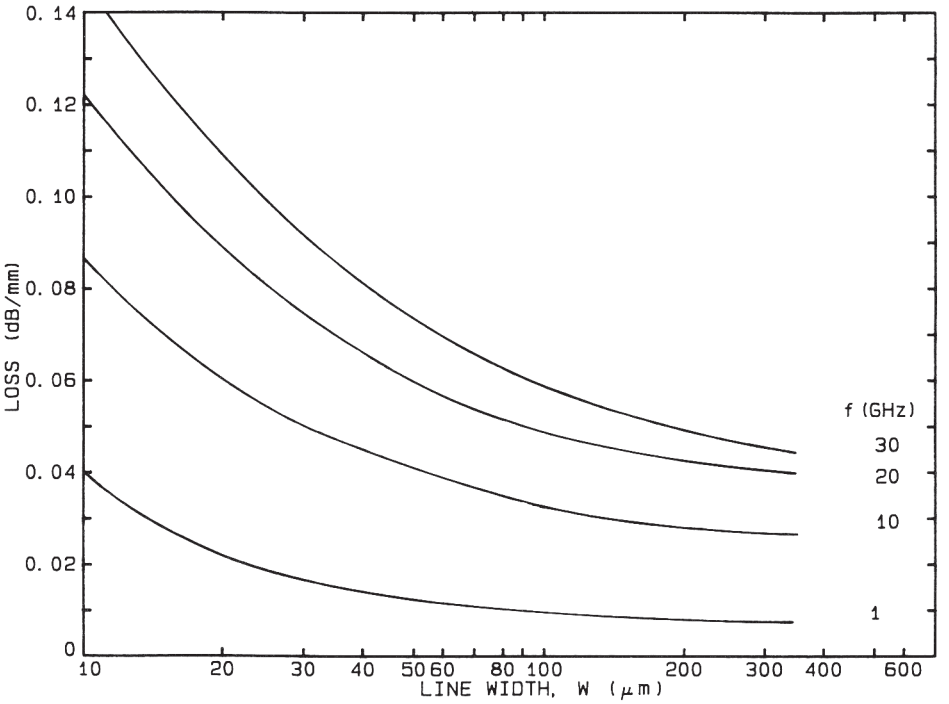

Figure 1.38 Measured microstrip loss versus line width at 1 GHz, 10 GHz, 20 GHz, and 30 GHz; substrate thickness of GaAs: 100 μm.

The second technique is the etchback technique that utilizes a thick metal layer defined either completely by evaporation or by a combination of a thin evaporated layer and a thicker plated layer. A thin photoresist layer is used as a mask to define the circuit pattern. The undesired areas of metal are then removed by etching. This technique results in undercutting the metal film by about twice the line conductor thickness. The plate-through technique not only permits better definition for thick conductors, but also saves on cost in that only the required material (gold in this case) is deposited.

Thick-Film MIC Technology

Thick-film MICs are fabricated using various inks pressed through patterned silk screens. Thick-film MICs are inexpensive and are generally limited to the lower end of the microwave spectrum. In a conventional thick-film technology, the multilayer interconnects are formed by successive screen printing of conductors, dielectric layers, and resistor patterns on a base substrate. The materials are in the form of inks or pastes. After screen printing, each layer is dried at about 150°C for 15 minutes and fired at about 850°C for 30–60 minutes. The printing, drying, and firing steps are repeated to fabricate the multilayer circuitry in a fully automated way to produce high-volume, cost-effective components.

Low-Temperature Cofired Ceramic

The low-temperature cofired ceramic (LTCC) manufacturing process is similar to the thick-film process, except that it does not use a base substrate. Dielectric layers are in the form of unfired ceramic tapes (also called green tapes) instead of paste. This technology also enables the printing of reliable capacitors and resistors. The process consists of blanking, punching vias, conductor screen printing, collating, laminating, and firing. The vias are punched in the green tape and filled with conducting paste. At the same time, conductor patterns are screen printed. This process is carried over for each dielectric layer, and finally the composite structure is fired to obtain a monolithic substrate. The firing temperature for glass–ceramic substrates is 850–900°C; this technology is known as LTCC technology. Because of the low-temperature firing, LTCC allows one to use high-conductivity metals such as Ag, Cu, and Au. The dielectric tapes use a glass–ceramic composite optimized for a better CTE match with base metal and the semiconductor chips. As many as 50 layers can be combined in a single LTCC substrate measuring 6 × 6 inches. When ceramic tapes are used, they are fired at 1500–1600°C, and the technology is known as high-temperature cofired ceramic (HTCC) technology. Commonly used conductors in this case are tungsten (W) and molybdenum (Mo).

1.6.3 Monolithic Integrated Circuit Technologies

In fabricating monolithic integrated circuit technologies, all active and passive circuit elements and interconnections are formed together on the surface of a semiconductor substrate. There are many ways to fabricate radio frequency (RF) and microwave monolithic integrated circuits. Various substrate materials used include GaAs, InP, GaN/silicon carbide, and bulk silicon. GaAs, InP, and GaN/silicon carbide-based technology is known as monolithic microwave integrated circuit (MMIC). while Si-based technology is referred to as RF integrated circuit (RFIC). Both technologies basically consist of fabrication of active devices, interconnects and passive circuits, and back side processes. Fabrication of interconnects and passive circuits and back side processes involve a relatively larger number of process steps of deposition/sputtering, evaporation, and etching, as compared to hybrid MICs. In MMICs, microstrip interconnections, crossovers, inductors, and capacitors are formed by using two levels of metal layer system. Backside processing consists of thinning by grinding or lapping via hole etching and ground contact metallization and plating. In RFICs, inductors, passive circuits, and interconnects are realized by using many available thin deposited metal layers to reduce the circuit loss due to high dielectric loss in Si substrates because of poor semi-insulating property. Micromachining is commonly used to enhance the quality factor of inductors and passive circuits.

Table 1.3 compares the advantages and disadvantages of various microstrip fabrication technologies. Monolithic technology is particularly suited for millimeter-wave applications through the elimination of the parasitic effects of bond wires, which connect discrete components in conventional hybrid microwave integrated circuits.

Table 1.3 Advantage and Disadvantage of Various Microstrip Fabrication Technologies

	Microwave Printed Circuit/PCB	Thin film MIC	Thick film MIC	LTCC	MMIC/RFIC
Major Advantages	High volume capability Primary support for electronic packaging Good substrate conformability Supports large size circuit/antenna Low cost Short fabrication time	High Q passives Good circuit tweaking Short fabrication time Suitable for passives and active circuits	High volume capability Low cost in high volume	High volume capability Medium cost Substrate supports large multilayers Suitable for vertical integration Supports integration of different transmission lines	High level of integration and reproducibility Solid state devices integrated Low cost in high volume Compact size and light weight High-volume production Broadband performance Suitable up to THz High reliability
Major disadvantages	High component loss for PCB Limited to low microwave frequencies Limited to passives	Single layer substrate Limited batch production High production cost Limited reproducibility Labor intensive Limited to microwave frequency range	Large dimensional tolerances Limited to low microwave frequencies	High thermal resistance substrate	High equipment cost High initial design cost Difficult debugging Impossible post tuning Long fabrication time

References

[1] Gupta, K. C., and A. Singh (Eds.), *Microwave Integrated Circuits*, New York: Halsted Press (John Wiley and Sons), 1974.

[2] Young, L., and H. Sobol (Eds.), *Advances in Microwaves*, Vol. 8, New York: Academic Press, 1974.

[3] Frey J., (Ed.), *Microwave Integrated Circuits*, Dedham, MA: Artech House, 1975. (a reprint volume).

[4] Hoffman, *R.K. Handbook of Microwave Integrated Circuits*, Norwood, MA: Artech House, 1987.

[5] Sweet, A. A., *MIC & MMIC Amplifier and Oscillator Circuit Design*, Norwood, MA: Artech House, 1990.

[6] Edwards, Terry, Foundations for Microstrip Circuit Design, 2nd ed., Chichester, U.K.: John Wiley & Sons, 1992.

[7] Buntschuh, C., "A Study of the Transmission Line Properties of Trapped Inverted Microstrip Line," *Rome Air Development Center-Technical* Report-74–311, AD# A-003633, December 1974.

[8] Yamashita, E., and K. Atsuki, "Analysis of Microstrip-like Transmission Lines by Non-Uniform Discretization of Integral Equations," *IEEE Trans.*, Vol. MTT-24, 1976, pp. 195–200.

[9] Schneider, M. V., "Microstrip Lines for Microwave Integrated Circuits," Bell System Technical Journal, Vol. 48, 1969, pp. 1421–1444.

[10] McLevige, W. V., et al., "New Waveguide Structures for Millimeter Wave and Optical Integrated Circuits," *IEEE Trans.*, Vol. MTT-23, 1975, pp. 788–794.

[11] Howe, H., Stripline Circuit Design, Dedham, MA: Artech House, 1974.

[12] Bahl. I.J., and Ramesh Garg, "A Designer's Guide to Stripline Circuits," *Microwaves*, Vol. 17, 1978, pp. 90–96.

[13] Wheeler, H. A., "Transmission Line Properties of Parallel Wide Strips by Conformal Mapping Approximation," *IEEE Trans.*, Vol. MTT-12, 1964, pp. 280–289.

[14] Wheeler, H. A., "Transmission Line Properties of Parallel Strips Separated by a Dielectric Sheet," *IEEE Trans.*, Vol. MTT-13, 1965, pp. 172–185.

[15] Sobol, H., "Application of Integrated Circuit Technology to Microwave Frequencies," *Proc. IEEE*, Vol. 59, 1971, pp. 1200–1211.

[16] Svacina, J., "Analysis of Multilayer Microstrip Lines by a Conformal Mapping," *IEEE Trans.*, Vol. MTT-40, No.4, 1992, pp. 769–782.

[17] Stinehelfer, H. E., "An Accurate Calculation of Uniform Microstrip Transmission Lines," *IEEE Trans.*, Vol. MTT-16, 1968, pp. 439–444.

[18] Green, H. E., "The Numerical Solution of Some Important Transmission Line Problems," *IEEE Trans.*, Vol. MTT-13, 1965, pp. 676–692.

[19] Silvester, P., "TEM Properties of Microstrip Transmission Lines," Proc. IEE, Vol. 115, 1968, pp. 42–49.

[20] Yamashita, E., and R. Mittra, "Variational Method for the Analysis of Microstrip Lines," *IEEE Trans.*, Vol. MTT-16, 1968, pp. 251–256.

[21] Yamashita, E., "Variational Method for the Analysis of Microstrip-like Transmission Lines," *IEEE Trans.*, Vol. MTT-16, 1968, pp. 529–535.

[22] Tsai, C.-M., "Field Analysis, Network Modeling and Circuit Applications of Inhomogeneous MultiConductor Transmission Lines," Ph.D. Thesis, Dept. of Electrical and Computer Engineering, University of Colorado, Boulder, CO, June 1993.

[23] Gupta, K. C., and M. D. Abouzahra, "Planar Circuit Analysis," *Numerical Techniques for Microwave and Millimeter-Wave Passive Structures* (ed. T. Itoh), New York: John Wiley & Sons, 1989, pp. 256–260.

[24] Gupta, K. C., and M. D. Abouzahra, "Segmentation and Desegmentation Techniques," *Analysis and Design of Planar Microwave Components*, Piscataway, NJ: IEEE Press, 1994, pp. 75–86.

[25] Brebbia, C. A., *The Boundary Element Method for Engineers*, New York: John Wiley & Sons, 1978.
[26] Banerjee, P. K., and R. Butterfield, *Boundary Element Methods in Engineering Science*, New York: McGraw-Hill, 1981.
[27] Sano, H., and K. Sadao, "Analysis of Dielectric Waveguide Problem by Boundary Element Method," *Electronics and Communications in Japan*, Part 1, Vol. 70, No.1, 1987.
[28] Peaiyoung, S., and S. J. Salon, "Some Technical Aspects of Implementing Boundary Element Equations," *IEEE Trans. on Magnetics*, Vol. 25, No. 4, July 1989.
[29] Fairweather, G. F., J. Rizzo, D. J. Shippy, and Y. S. Wu, "On the Numerical Solution of Two Dimensional Potential Problems by an Improved Boundary Integral Equation Method,"*J. Computational Physics*, Vol. 31, 1979, pp. 96–112.
[30] Kellogg, O. D., *Foundations of Potential Theory*, Berlin: Springer, 1929.
[31] Gupta, K. C., Ramesh Garg, and Rakesh Chadha, *Computer-Aided Design of Microwave Circuits*, Norwood, MA: Artech House, 1981.
[32] Itoh, T. (Ed.), *Numerical Techniques for Microwave and Millimeter-Wave Passive Structures*, New York: John Wiley & Sons, 1989.
[33] Davies, J. B., "The Finite Element Method," *Numerical Techniques for Microwave and Millimeter-Wave Passive Structures* (ed. T. Itoh), New York: John Wiley & Sons, 1989.
[34] Jain, O. P. et al., "Coupled Mode Model of Dispersion in Microstrip," *Electron. Lett.*, Vol. 7, 1971, pp. 405–407.
[35] Schneider, M. V., "Microstrip Dispersion," *Proc. IEEE*, Vol. 60, 1972, pp. 144–146.
[36] Getsinger, W. J., "Microstrip Dispersion Model," *IEEE Trans.*, Vol. MTT-21, 1973, pp. 34–39.
[37] Carlin, H. J., "A Simplified Circuit Model for Microstrip," *IEEE Trans.*, Vol. MTT-21, 1973, pp. 589–591.
[38] Kompa, G., and R. Mehran, "Planar Waveguide Model for Calculating Microstrip Components," *Electron. Lett.*, Vol. 11, 1975, pp. 459–460.
[39] Edwards, T. C., and R. R. Owens, "2–18 GHz Dispersion Measurements on 10–100 ohm Microstrip Lines on Sapphire," *IEEE Trans.*, Vol. MTT-24, 1976, pp. 506–513.
[40] Noble, D. F., and H. J. Carlin, "Circuit Properties of Coupled Dispersive Transmission Lines," *IEEE Trans. on Circuit Theory*, Vol. CT-20, 1973, pp. 56–65.
[41] Yamashita, E., K. Atsuki, and T. Ueda, "An Approximate Dispersion Formula of Microstrip Lines for Computer-Aided Design of Microwave Integrated Circuits,"*IEEE Trans.*, Vol. MTT-27, December 1979, pp. 1036–1038.
[42] Hammerstad, E., and O. Jensen, "Accurate Models for Microstrip Computer-Aided Design," *IEEE MTT-S Int. Microwave Symp. Digest*, 1980, pp. 407–409.
[43] Pues, H. F., and A. R. van de Capelle, "Approximate Formulas for Frequency Dependence of Microstrip Parameters," *Electron Lett.*, Vol. 16, No. 23, 1980, pp. 870–872.
[44] Kirschning, M., and R. H. Jansen, "Accurate Model for Effective Dielectric Constant of Microstrip and Validity up to Millimeter-wave Frequencies," *Electron. Lett.*, Vol. 18, March 18, 1982, pp. 272–273.
[45] Kobayashi, M., "Frequency Dependent Characteristics of Microstrips on Anisotropic Substrates," *IEEE Trans.*, Vol. MTT-30, November 1982, pp. 2054–2057.
[46] Kobayashi, M., "Important Role of Inflection Frequency in the Dispersive Property of Microstrip Lines," *IEEE Trans.*, Vol. MTT-30, November 1982, pp. 2057–2059.
[47] Pramanick, P. and P. Bhartia, "An Accurate Description of Dispersion in Microstrip Lines," *Microwave J.*, Vol. 26, December 1983, pp. 89–92.
[48] Atwater, H. A., "Tests of Microstrip Dispersion Formulas," *IEEE Trans.*, Vol. MTT-36, March 1988, pp. 619–621.
[49] Kobayashi, M., "A Dispersion Formula Satisfying Recent Requirements in Microstrip CAD," *IEEE Trans.*, Vol. MTT-36, August 1988, pp. 1246–1250.
[50] Roy, J. S., et. al., "Dispersion Characteristics of Curved Microstrip Transmission Lines," *IEEE Trans.*, Vol. MTT-38, August 1990, pp. 1366–1370.

[51] York, R. A., and Compton, R. C., "Experimental Evaluation of Existing CAD Models for Microstrip Dispersion," *IEEE Trans.*, Vol. MTT-38, No. 3, March 1990, pp. 327–328.
[52] Yamashita, E., K. Atsuki, and T. Hirahata, Microstrip Dispersion in a Wide Frequency Range," *IEEE Trans.*, Vol. MTT-29, June 1981, pp. 610–611.
[53] England, E. H., "A Coaxial to Microstrip Transition," *IEEE Trans.*, Vol. MTT-26, January 1976, pp. 47–48.
[54] Eisenhart, E. L., "A Better Microstrip Connector," *IEEE MTT-S Int. Microwave Symp. Digest*, 1978, pp. 318–320.
[55] Majewski, M. L., R. W. Rose, and J. R. Scott, "Modeling and Characterization of Microstrip-to Coaxial Transitions," *IEEE Trans.*, Vol. MTT-29, August 1981, pp. 799–805.
[56] Izadian, J. S., and S. M. Izadian, *Microwave Transition Design*, Norwood, MA: Artech House, 1988.
[57] Schneider, M. V., B. Glance, and W. F. Bodtmann, "Microwave and Millimeter Wave Integrated Circuits for Radio Systems," *Bell Syst. Tech. J.*, Vol. 48, July–Aug. 1969, pp. 1703–1726.
[58] Van Heuven, J. H. C., "A New Integrated Waveguide-Microstrip Transition," *IEEE Trans.*, Vol. MTT-26, March 1976, pp. 144–147.
[59] Lavedan, L. J., "Design of Waveguide-to-Microstrip Transitions Specially Suited to Millimeter-wave Applications," *Electron. Lett.*, Vol. 13, September 1977, pp. 81–82.
[60] Bharj, S. S., and S. Mak, "Waveguide-to-Microstrip Transition Uses Evanescent Mode," *Microwave & RF*, Vol. 23, January 1984, pp. 99–100, 134.
[61] Moochalla, S. S., and C. An, "Ridge Waveguide Used in Microstrip Transition, *Microwaves & RF*, Vol. 23, March 1984, pp. 149–152.
[62] Ponchak, G. E., and A. N. Downey, "A New Model for Broadband Waveguide-to-Microstrip Transition Design," *Microwave J.*, Vol. 31, May 1988, pp. 333–343.
[63] Shih, Y. C., T. N. Ton, and L. Q. Bui, "Waveguide-to-Microstrip Transitions for Millimeter-Wave Applications," *IEEE MTT-S Int. Microwave Symp. Digest*, 1988, pp. 473–475.
[64] Beaudette, R. G., and L. J. Kushner, "Waveguide-to-Microstrip Transitions," *Microwave J.*, Vol. 32, September 1989, pp. 211–216.
[65] Huang, X., and K.-L. Wu, "A Broadband U-Slot Coupled Microstrip-to-Waveguide Transition," *IEEE Trans. Microwave Theory Tech.*, Vol. 60, May 2012, pp. 1210–1217.
[66] Yao, H. W., et al., "Analysis and Design of Microstrip-to-Waveguide Transitions," *IEEE Trans.*, Vol. MTT-42, December 1994, pp. 2371–2380.
[67] Napoli, L. S., and J. J. Hughes, "A Simple Technique for the Accurate Determination of the Microwave Dielectric Constant for Microwave Integrated Circuits," *IEEE Trans.*, Vol. MTT-19, 1971, pp. 664–665.
[68] Howell, J. Q., "A Quick, Accurate Method to Measure the Dielectric Constant of Microwave Integrated Circuit Substrates," *IEEE Trans.*, Vol. MTT-21, 1973, pp. 142–143.
[69] Ladbrooke, P. H., et al., "Coupling Errors in Cavity Resonance Measurements on MIC Dielectrics," *IEEE Trans.*, Vol. MTT-21, 1973, pp. 560–562.
[70] Traut, G. R., "Electrical Test Methods for Microwave PCBs," *Microwave J.*, Vol. 24, December 1981, pp. 73–79.
[71] Kent, G., "Dielectric Resonances for Measuring Dielectric Properties," *Microwave J.*, Vol. 31, October 1988, pp. 99–114.
[72] Kent, G., "An Evanescent-Mode Tester for Ceramic Dielectric Substrates," *IEEE Trans.*, Vol. MTT-31, October 1988, pp. 1452–1454.
[73] Kent, G., "A New Method for Measuring the Properties of Dielectric Substrates," *IEEE MTT-Symp. Digest*, 1988, pp. 751–754.

[74] York, R. A., and R. C. Compton, "An Automated Method for Dielectric Constant Measurements of Microwave Substrates," *Microwave J.*, Vol. 33, March 1990, pp. 115–12l.
[75] Athey, T. W., M. A. Stuchly, and S. S. Stuchly, "Measurement of Radio Frequency Permittivity of Biological Tissues with an Open-Ended Coaxial Line: Part I," *IEEE Trans.*, Vol. MTT-30, January 1982, pp. 82–86.
[76] Bahl, I., G. Lewis, and J. Jorgenson, "Automatic Testing of MMIC Wafers," *Int. J. Microwave and Millimeter-Wave Computer-Aided Engineering*, Vol. 1, January 1991, pp. 77–89.
[77] Caulton, M., et al., "Measurements on the Properties of Microstrip Transmission Lines for Microwave Integrated Circuits," *RCA Review*, Vol. 27, 1966, pp. 377–391.
[78] Seckelmann, R., "On the Measurement of Microstrip Properties," *Microwave J.*, Vol. 11, January 1968, pp. 61–64.
[79] Getsinger, W. J., "Measurement and Modeling of the Apparent Characteristic Impedance of Microstrip," *IEEE Trans.*, Vol. MTT-31, August 1983, pp. 624–632.
[80] Troughton, P., "Measurement Technique in Microstrip," *Electron. Lett.*, Vol. 5, 1969, pp. 25–26.
[81] Wolff, I., and N. Knoppik, "Microstrip Ring Resonator and Dispersion Measurement on Microstrip Lines," *Electron. Lett.*, Vol. 7, 1971, pp. 779–78l.
[82] Owens, R. P., "Curvature Effect in Microstrip Ring Resonators," *Electron. Lett.*, Vol. 12, 1976, pp. 356–357.
[83] Finlay, H., et al., "Accurate Characterization and Modeling of Transmission Lines for GaAs MMICs," *IEEE Trans.*, Vol. MTT-36, June 1988, pp. 961–967.
[84] Richings, J. G., "An Accurate Experimental Method for Determining the Important Properties of Microstrip Transmission Lines," *Marconi Review*, 1974, pp. 210–216.
[85] Easter, B., "The Equivalent Circuit of Some Microstrip Discontinuities," *IEEE Trans.*, Vol. MTT-23, 1975, pp. 655–660.
[86] Van Heuven, J. H. C., "Conduction and Radiation Losses in Microstrip," *IEEE Trans.*, Vol. MTT-22, 1974, pp. 841–844.
[87] Goldfarb, M., and A. Platzker, "Losses in GaAs Microstrip," *IEEE Trans. on Microwave Theory Tech.*, Vol. MTT-38, December 1990, pp. 1957–1963.
[88] Carroll, J., M. Li, and K. Chang, "New Technique to Measure Transmission Line Attenuation," *IEEE Trans. on Microwave Theory Tech.*, Vol. MTT-43, January 1995, pp. 219–222.
[89] Tummala, R. R., and E. J. Rayaszewski (eds.), *Microelectronic Packaging Handbook*, New York: Van Nostrand Reinhold, 1989.
[90] Manzione, L. T., *Plastic Packing of Microelectronic Devices*, New York: Van Nostrand Reinhold, 1990.
[91] Sergent, J. E., and C. A. Harper (eds.), *Hybrid Microelectronic Handbook*, *Second Edition*, New York: McGraw-Hill, 1995.
[92] Garrou, P. E., and I. Turlik, *Multichip Module Technology Handbook*, New York: McGraw-Hill, 1998.
[93] Kesiter, F. Z., "An Evaluation of Materials and Processes for Integrated Microwave Circuits," *IEEE Trans. Microwave Theory Tech.*, Vol. MTT-16, July 1978, pp. 469–475.
[94] Caulton, M., and H. Sobol, "Microwave Integrated Circuit Technology—A Survey," *IEEE J. Solid-State Circuits*, Vol. SC-5, 1970, pp. 292–303.
[95] Sobol, H., "Applications of Integrated Circuit Technology to Microwave Frequencies," *Proc. IEEE*, Vol. 59, 1971, pp. 1200–1211.
[96] Sobol, H., "Technology and Design of Hybrid Integrated Circuits," *Solid State Technol.*, Vol. 13, 1970, pp. 49–57.
[97] Laverghetta, T. S., *Microwave Materials and Fabrication Techniques*, Norwood, MA: Artech House, 1984.
[98] Jones, R. D., *Hybrid Circuit Design and Manufacture*, New York: Dekker, 1982.
[99] Elliott, D. J., *Integrated Circuit Mask Technology*, New York: McGraw-Hill, 1985.

[100] Farquhar, D. S., A. M. Seman, and M. D. Paliks, "Manufacturing Experience with High Performance Mixed Dielectric Circuit Board," *IEEE Trans. Advanced Packaging*, Vol. 22, 1999, pp. 153–159.
[101] Hoffmann, R. K., *Handbook of Microwave Integrated Circuits*, Norwood, MA: Artech House, 1987.
[102] Walpita, L. M., et al., "Temperature-Compensated Thermoplastic High Dielectric-Constant Microwave Laminates," *IEEE Trans. Microwave Theory Tech.*, Vol. 47, 1999, pp. 1577–1583.
[103] Sechi, F., et al., "Miniature Beryllia Circuits—A New Technology for Microwave Power Circuits," *RCA Rev.*, Vol. 43, 1982, p. 363.
[104] Devoe, L., and A. Devoe, "Technology and Innovation in Single Layer Capacitors," *Microwave J.*, Vol. 37, 2002, pp. 144–152.
[105] Barnwell, P., and J. Wood, "A Novel Thick Film on Ceramic MCM Technology Offering MCM-D Performance," *Presented at the 6th Int. Conf. Multichip Modules*, Denver, CO, April 1997.
[106] Brown, R. L., P. W. Polinski, and A. S. Shaikh, "Manufacturing of Microwave Modules Using Low-Temperature Cofired Ceramics," *IEEE MTT-S Int. Microwave Symp. Dig.*, 1994, pp. 1727–1730.
[107] Mohammed, A. A., "LTCC for High-Power RF Applications," *Advanced Packaging*, 1999, pp. 46–50.
[108] Williams, R. E., *Gallium Arsenide Processing Techniques*, Norwood, MA: Artech House, 1984.
[109] Pucel, R. A., (ed.), *Monolithic Microwave Integrated Circuits (A Reprint Volume)*, Piscataway, NJ: IEEE Press, 1985.
[110] Ferry, D. K., (ed.), *Gallium Arsenide Technology*, Indianapolis, IN: Howards, Sams, 1985.
[111] Einspruch, N. G., and W. R. Wisseman, *GaAs Microelectronics*, New York: Academic Press, 1985.
[112] Mun, J., (ed.), *GaAs Integrated Circuits: Design and Technology*, New York: Macmillan Publishing Company, 1988.
[113] Goyal, R., (ed.), *Monolithic Microwave Integrated Circuits: Technology and Design*, Norwood, MA: Artech House, 1989.
[114] Fisher, D., and I. Bahl, *Gallium Arsenide IC Applications Handbook,* San Diego, CA: Academic Press, 1995.
[115] Bahl, I. J., "Monolithic Microwave Integrated Circuits," *Wiley Encyclopedia of Electrical and Electronics*, Vol. 13, Hoboken, NJ: John Wiley, 1999, pp. 490–513.
[116] Baker, R. J., H. W. Li, and D. E. Boyce, *CMOS Circuit Design, Layout, and Simulation,* Piscataway, NJ: IEEE Press, 1997.
[117] Bahl, I. J., and P. Bhartia, *Microwave Solid State Circuit Design*, *Second Edition*, Hoboken, NJ: John Wiley, 2003, Chapter 15.
[118] Bahl, I., *Lumped Elements for RF and Microwave Circuits*, Norwood, MA: Artech House, 2003, Chapter 13.
[119] Bahl, I. J., *Fundamental of RF and Microwave Transistor Amplifiers,* Hoboken, NJ: John Wiley, 2009, Chapters 4, 15 and 20.
[120] Das, N. K., S. M. Voda, and D. M. Pozar, "Two Methods for the Measurement of Substrate Dielectric Constant," *IEEE Trans. Microwave Theory and Tech.*, Vol. MTT-35, 1987, pp. 636–642.
[121] *IPC-TM-650 Standard Test Methods Manual*, Mar. 1998, www.ipc.org.
[122] Baker-Jarvis, J., B. Riddle, and M. D. Janezic, "Dielectric and Magnetic Properties of Printed Wiring Boards and Other Substrate Materials," *National Institute of Standards and Technology, Technical Note 1512, Boulder*, CO, 1999.
[123] Chen, L. F., C. K. Ong, C. P. Neo, V. V. Varadan, and V. K. Varadan, *Microwave Electronics, Measurement and Materials Characterization,* Hoboken, NJ: John Wiley, 2004.

[124] Dankov, P. I., "Two-Resonator Method for Measurement of Dielectric Anisotropy in Multi-layer Samples," *IEEE Trans. Microwave Theory and Tech.*, Vol. 54, 2006, pp. 1534–1544.

[125] Rautio, J. C., "Measurement of Planar Substrate Uniaxial Anisotropy," *IEEE Trans. Microwave Theory and Tech., Vol. 57, October 2009*, pp. 2456–2463.

[126] Coonrod, J., "Methods for Characterizing the Dielectric Constant of Microwave PCB Laminates," *Microwave Journal*, 2011, pp. 132–145.

CHAPTER 2

Microstrip Lines II: Fullwave Analyses, Design Considerations, and Applications

2.1 Methods of Fullwave Analysis

As pointed out in Chapter 1, the microstrip configuration is not capable of supporting a pure TEM mode, and small longitudinal components of both the electric and magnetic fields need to be present to satisfy boundary conditions at the dielectric-air interface. These hybrid modes supported by the microstrip cannot be fully described in terms of static capacitances and inductances only. Therefore, one has to consider time-varying electric and magnetic fields and solve the wave equation subject to appropriate boundary conditions. Field analysis of the microstrip (or any other structure, for that matter) without invoking any quasi-static approximations is known as fullwave analysis. Fullwave analysis is carried out to determine the propagation constant instead of the capacitance evaluated in quasi-static analysis.

Methods of studying wave propagation along a microstrip line without making any quasi-static assumption will now be discussed. These methods may be divided into two groups. In one group, the microstrip is considered with a rectangular enclosure, and the other group deals with open microstrip lines. This grouping becomes convenient since different types of mathematical tools are needed to handle closed and open geometries. For example, a Fourier series representation can be used to express the fields in a closed rectangular structure whereas a Fourier integral representation is suited for an open structure.

From the arguments given in Section 1.1.2, it can be seen that the microstrip modes cannot be pure TM or TE waves either. Longitudinal components of both the electric and the magnetic fields are needed. These hybrid modes may be considered as superposition of TE and TM fields that may, in turn, be expressed in terms of two scalar potentials ψ^{h} and ψ^{e}, respectively. Referring to the microstrip configuration of Figure 2.1, the longitudinal and transverse components of the electric and magnetic fields may be written as

$$E_z = j\left[(k^2 - \beta^2)/\beta\right]\psi^{e}(x,y)\exp(-j\beta z) \tag{2.1}$$

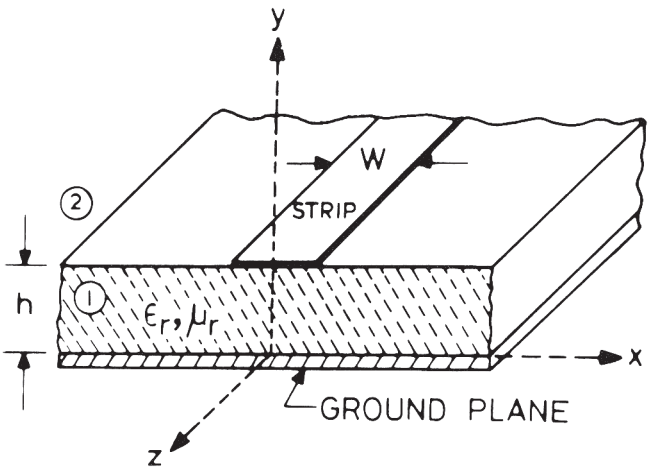

Figure 2.1 Open microstrip configuration.

$$H_z = j[(k^2 - \beta^2)/\beta]\psi^{\mathrm{h}}(x,y)\exp(-j\beta z) \tag{2.2}$$

$$E_{\mathrm{t}} = \left[\nabla_{\mathrm{t}}\psi^{e}(x,y) - (\omega\mu/\beta)(\hat{z}\times\nabla_{\mathrm{t}})\psi^{\mathrm{h}}(x,y)\right]\exp(-j\beta z) \tag{2.3}$$

$$H_{\mathrm{t}} = \left[(\omega\varepsilon/\beta)(\hat{z}\times\nabla_{\mathrm{t}})\psi^{\mathrm{e}}(x,y) + \nabla_{\mathrm{t}}\psi^{\mathrm{h}}(x,y)\right]\exp(-j\beta z) \tag{2.4}$$

where β is the unknown propagation constant along the z-direction and $k = \omega(\varepsilon_0 \varepsilon_{\mathrm{r}} \mu_0)^{1/2}$. Subscript t refers to transverse coordinates (x, y), and $\hat{\mathbf{z}}$ is a unit vector in the z-direction. These relations hold good for both regions 1 and 2, shown in Figure 2.1, when a suitable value of ε_{r} is used in the wavenumber k. Appropriate expressions for ψ^{e} and ψ^{h} are chosen for regions 1 and 2. It has been assumed that the structure is lossless and the substrate is nonmagnetic. The field representation of (2.1) to (2.4) is also valid for an enclosed microstrip structure.

The modes of propagation can be divided into two orthogonal sets of modes because the structure is symmetrical about the y-z-plane. One of these sets has a symmetric E_z component and an antisymmetric H_z component (E_z even – H_z odd), while the other set is designated as E_z odd – H_z even. The dominant mode is the lowest order E_z even – H_z odd mode and approaches the quasi-TEM solution at low frequencies.

2.2 Analysis of an Open Microstrip

Fullwave analysis of an open microstrip may be carried out by using a Fourier transformation along the x-direction (parallel to the substrate and perpendicular to the strip). The two methods for analysis described in this section employ such a

transformation and, to that extent, resemble the variational method in the Fourier transform domain used for quasi-static analysis of microstrip lines in Chapter 1.

As illustrated in the previous section, various components of the **E** and **H** fields are expressed in terms of two potentials ψ^{h} and ψ^{e}. Fourier transformation is taken along the x-direction. Solutions for the transforms of ψ^{e} and ψ^{h} are obtained by matching the boundary conditions in the transform domain. The interface condition in the $y = h$ plane is written in terms of longitudinal and transverse electric currents on the strip conductor. The two methods described in this section differ mainly with regard to the manner in which the boundary conditions at the dielectric-air interface ($y = h$) are applied.

In the Fourier transform domain, potentials ψ^{e} and ψ^{h} may be written as

$$\tilde{\psi}_{\mathrm{i}}^{\mathrm{e}}(\alpha, y) = \int_{-\infty}^{\infty} \psi_{\mathrm{i}}^{\mathrm{e}}(x, y) e^{j\alpha x} dx \tag{2.5}$$

and a similar relation holds for $\psi_{\mathrm{i}}^{\mathrm{h}}$. The subscript $i = 1, 2$ designates the regions 1 (substrate) and 2 (air), respectively. $\tilde{\psi}_i$'s satisfy the transformed wave equation, which may be written as

$$(d^2/dy^2 - \gamma_i^2)\,\tilde{\psi}_i(\alpha, y) = 0 \tag{2.6}$$

where

$$\gamma_{\mathrm{i}}^2 = \alpha^2 + \beta^2 - k_i^2 \qquad i = 1, 2$$
$$k_{\mathrm{i}}^2 = \omega^2 \varepsilon_{\mathrm{r}} \mu_{\mathrm{r}} \varepsilon_0 \mu_0 \qquad k_2^2 = \omega^2 \varepsilon_0 \mu_0$$

The next step is to write expressions for $\tilde{\psi}_i$ in the two regions such that boundary conditions at $y = 0$ and at $y \to \infty$ are satisfied. These may be written as

$$\tilde{\psi}_1^{\mathrm{e}}(\alpha, y) = A(\alpha)\,\sinh(\gamma_1 y) \tag{2.7}$$

$$\tilde{\psi}_2^{\mathrm{e}}(\alpha, y) = B(\alpha)\,\exp[-\gamma_2(y - h)] \tag{2.8}$$

$$\tilde{\psi}_1^{\mathrm{h}}(\alpha, y) = C(\alpha)\,\cosh(\gamma_1 y) \tag{2.9}$$

$$\tilde{\psi}_2^{\mathrm{h}}(\alpha, y) = D(\alpha)\,\exp\left[-\gamma_2(y - h)\right] \tag{2.10}$$

The coefficients A, B, C, and D are determined by applying continuity conditions across the interface $y = h$. These conditions are

$$\tilde{E}_{z1}(\alpha, h) = \tilde{E}_{z2}(\alpha, h) \tag{2.11}$$

$$\tilde{E}_{x1}(\alpha, h) = \tilde{E}_{x2}(\alpha, h) \tag{2.12}$$

$$\tilde{H}_{z1}(\alpha,h) - \tilde{H}_{z2}(\alpha,h) = -\tilde{J}_x(\alpha) \tag{2.13}$$

$$\tilde{H}_{x1}(\alpha,h) - \tilde{H}_{x2}(\alpha,h) = \tilde{J}_z(\alpha) \tag{2.14}$$

where $\tilde{J}_x(\alpha)$ and $\tilde{J}_z(\alpha)$ are the Fourier transforms of the unknown current components on the strip and the second subscript (l or 2) indicates the region 1 or 2. In addition, the boundary condition that must be satisfied on the strip may be written as

$$E_{z2}(x,h) = 0 \qquad |x| < W/2 \tag{2.15a}$$

$$(d/dy)H_{z2}(x,h) = 0 \qquad |x| < W/2 \tag{2.15b}$$

We now describe two methods of analyzing open microstrip lines by using the aforementioned formulation. These methods differ because of the manner in which the boundary conditions (2.15) are applied. In one of the methods, called the integral equation method by Denlinger [1], boundary conditions (2.15) are applied in the space domain ($(x$-$y)$-plane). In the other method, called Galerkin's method in FTD [2, 3], the boundary conditions (2.15) are applied in the Fourier transform domain ($(\alpha$-$y)$-plane).

2.2.1 Integral Equation Method in the Space Domain

Equation (2.7) to (2.15) lead to a set of coupled integral equations for the currents $\tilde{J}_x(\alpha)$ and $\tilde{J}_z(\alpha)$. These integral equations are derived to be [1]

$$I_{x0}\int_{-\infty}^{\infty} G_{11}(\alpha,\beta)\tilde{I}_x(\alpha)e^{-j\alpha x}\,d\alpha + I_{z0}\int_{-\infty}^{\infty} G_{12}(\alpha,\beta)\tilde{I}_z(\alpha)e^{-j\alpha x}\,d\alpha = 0 \tag{2.16a}$$

and

$$I_{x0}\int_{-\infty}^{\infty} G_{21}(\alpha,\beta)\tilde{I}_x(\alpha)e^{-j\alpha x}\,d\alpha + I_{z0}\int_{-\infty}^{\infty} G_{22}(\alpha,\beta)\tilde{I}_z(\alpha)e^{-j\alpha x}\,d\alpha = 0 \tag{2.16b}$$

where $-W/2 < x < W/2$, $\mu_r = 1$, $k_0 = k_2$,

$$G_{11}(\alpha,\beta) = \frac{1}{\det}\left[F_1 b_{22} + \frac{\alpha\beta}{k_1^2 - \beta^2} b_{12}\right] \tag{2.17}$$

$$G_{12}(\alpha,\beta) = b_{12}/\det \tag{2.18}$$

$$G_{21}(\alpha,\beta) = \frac{\gamma_2}{\det}\left[F_1 b_{21} + \frac{\alpha\beta}{k_1^2 - \beta^2} b_{11}\right] \tag{2.19}$$

$$G_{22}(\alpha,\beta) = \gamma_2 b_{11}/\det \tag{2.20}$$

$$b_{11} = -b_{22} = j\alpha\left\{\frac{k_0^2-\beta^2}{k_1^2-\beta^2}-1\right\} \tag{2.21}$$

$$b_{12} = \frac{\omega\mu_0\gamma_1}{\beta}\left[\frac{\gamma_2}{\gamma_1}+\frac{k_0^2-\beta^2}{k_1^2-\beta^2}\tanh\gamma_1 h\right] \tag{2.22}$$

$$b_{21} = \frac{\omega\varepsilon_0\gamma_1}{\beta}\left[\frac{\gamma_2}{\gamma_1}+\varepsilon_r\frac{k_2^2-\beta^2}{k_1^2-\beta^2}\coth\gamma_1 h\right] \tag{2.23}$$

$$\det = b_{11}b_{22} - b_{12}b_{21} \tag{2.24}$$

$$F_1 = \omega\mu_0\gamma_1 \tanh(\gamma_1 h)/[j(k_0^2-\beta^2)] \tag{2.25}$$

In deriving (2.16), a one-term approximation has been used for the unknown current distributions. $\tilde{J}_x(\alpha)$ and $\tilde{J}_z(\alpha)$. These approximations are given as

$$\tilde{J}_x(\alpha) = I_{x0}\tilde{I}_x(\alpha) \tag{2.26a}$$

$$\tilde{J}_z(\alpha) = I_{z0}\tilde{I}_z(\alpha) \tag{2.26b}$$

It has been assumed that $\tilde{J}_x$ and $\tilde{J}_z$ have known forms, and the only unknowns in their representation are the amplitude coefficients I_{x0} and I_{z0}.

The unknown propagation constant β can now be solved by equating the determinant of the coefficient matrix for the unknowns I_{x0} and I_{z0} to zero.

The current distributions I_x and I_z, chosen by Denlinger [1], are

$$I_z(x) = \begin{cases} 1+|2x/W|^3 & |x| \le W/2 \\ 0 & \text{otherwise} \end{cases} \tag{2.27a}$$

$$I_x(x) = \begin{cases} \sin(\pi x/0.7W) & |x| \le 0.8W/2 \\ \cos(\pi x/0.2W) & 0.8W/2 < |x| \le W/2 \\ 0 & \text{otherwise} \end{cases} \tag{2.27b}$$

It may be pointed out that because of the one-term approximation used here, the results are critically dependent on the choice of the form of the current distribution. This is a disadvantage of this method.

A considerable simplification in the above analysis results from neglecting the transverse current component $\tilde{J}_x$. This is a good approximation when the strip

width is small as compared to the wavelength (i.e., $W/\lambda_0 < 0.1$) and when the lowest order mode is being considered. This approximation reduces the coupled pair of integral equations to a single integral equation containing β as a parameter. The computer time requirement is therefore considerably reduced.

The dispersion curves based on this method will be discussed along with the results of the second method described next.

2.2.2 Galerkin's Method in the Spectral Domain [2, 3]

In this method, the formulation of the problem is similar to that in the above method, but the boundary conditions on the strip, given by Equations (2.15), are now applied in the spectral domain (or Fourier Transform Domain, FTD) rather than in the space domain. In place of integral equations (2.16), one now obtains

$$G_{11}(\alpha,\beta)\tilde{J}_x(\alpha) + G_{12}(\alpha,\beta)\tilde{J}_z(\alpha) = \tilde{U}_1(\alpha) + \tilde{U}_2(\alpha) \tag{2.28a}$$

$$G_{21}(\alpha,\beta)\tilde{J}_x(\alpha) + G_{22}(\alpha,\beta)\tilde{J}_z(\alpha) = \tilde{V}_1(\alpha) + \tilde{V}_2(\alpha) \tag{2.28b}$$

where

$$\tilde{U}_1(\alpha) = \int_{-\infty}^{-W/2} u(x)e^{j\alpha x}\,dx \qquad \tilde{U}_2(\alpha) = \int_{W/2}^{\infty} u(x)e^{j\alpha x}\,dx \tag{2.29}$$

$$\tilde{V}_1(\alpha) = \int_{-\infty}^{-W/2} v(x)e^{j\alpha x}\,dx \qquad \tilde{V}_2(\alpha) = \int_{W/2}^{\infty} v(x)e^{j\alpha x}\,dx \tag{2.30}$$

Functions such as G_{11} are defined in (2.17) to (2.20) and $u(x)$, $v(x)$ are defined by

$$E_{z2}(x,h) = \begin{cases} 0 & -W/2 < x < W/2 \\ j[(k_2^2-\beta^2)/\beta]u(x) & \text{otherwise} \end{cases} \tag{2.31}$$

$$\frac{d}{dy}H_{z2}(x,h) = \begin{cases} 0 & -W/2 < x < W/2 \\ j[(k_2^2-\beta^2)/\beta^2)/\beta]v(x) & \text{otherwise} \end{cases} \tag{2.32}$$

Equations (2.28) are solved by the method of moments using Galerkin's approach. As a first step $\tilde{J}_x$ and $\tilde{J}_z$ are expanded in terms of known basis functions $\tilde{J}_{xn}$ and $\tilde{J}_{zn}$ as follows:

$$\tilde{J}_x(\alpha) = \sum_{n=1}^{M} c_n\tilde{J}_{xn}(\alpha) \qquad \tilde{J}_z(\alpha) = \sum_{n=1}^{N} d_n\tilde{J}_{zn}(\alpha) \tag{2.33}$$

The basis functions $\tilde{J}_{xn}(\alpha)$ and $\tilde{J}_{zn}(\alpha)$ are chosen such that their inverse Fourier transforms are nonzero only on the strip $-W/2 < x < W/2$. After substituting (2.33) into (2.28) and taking the inner product with the basis functions $\tilde{J}_{xn}$ and $\tilde{J}_{zn}$ for different values of n, we obtain the matrix equation

$$\sum_{n=1}^{M} K_{m,n}^{1,1} c_n + \sum_{n=1}^{N} K_{m,n}^{1,2} d_n = 0 \quad m = 1,2\cdots,N \tag{2.34a}$$

$$\sum_{n=1}^{M} K_{m,n}^{2,1} c_n + \sum_{n=1}^{M} K_{m,n}^{2,2} d_n = 0 \quad m = 1,2\ldots,M \tag{2.34b}$$

where

$$K_{m,n}^{1,1} = \int_{-\infty}^{\infty} \tilde{J}_{zm}(\alpha) G_{11}(\alpha,\beta) \tilde{J}_{xn}(\alpha)\, d\alpha \tag{2.35}$$

and similar relations hold for other $K_{m,n}$'s. The simultaneous equations (2.34a) and (2.34b) are solved for the propagation constant β by setting the determinant of this set of equations equal to zero. In this method also, the results depend on the choice of basis functions and the values of M and N selected, and the accuracy of the results can be increased by selecting higher values of M and N.

Galerkin's method in FTD has several advantages as compared with the space domain integral equation method discussed in the previous subsection.

1. The method is simpler since the solution is extracted from algebraic equations and not from the coupled integral equations.
2. The physical nature of the mode for each solution can easily be recognized via the corresponding selection made for the basis functions.

Galerkin's method in the spectral domain as discussed earlier for an open microstrip line is also applicable to a shielded microstrip line (with a metallic cover shield but no side walls), to a line with two layers of dielectric substrates, to a microstrip line with a dielectric layer on the strip and substrate, and to similar generalized printed transmission lines that contain several dielectric layers and conductors appearing at several dielectric interfaces. This generalized method is known as the spectral domain immittance approach [4, 5]. A solution of the equations for the transforms of currents in the spectral domain (such as (2.28a, b)) are solved by deriving the dyadic Green's functions (for example, G_{11}, G_{12}, in (2.28))based on the transverse equivalent circuit concept applied in the spectral domain in conjunction with a simple coordinate transformation rule.

2.2.3 Discussion of Results

The results for the effective dielectric constant found from Galerkin's method in the spectral domain by considering two different sets of M and N are shown in Figure 2.2. The basis functions chosen are also shown in this figure. The results (effective dielectric constant versus frequency) are compared with Denlinger's results [1] based on the method described in Section 2.2.1. It may be noted that the first-order solution ($N = M = 1$) does not give satisfactory values since J_{x1} shown in Figure 2.2(a) is not a good choice for J_x.

Fullwave analysis of an open microstrip has been extended for the calculation of characteristic impedance by Knorr and Tufekcioglu [3]. Galerkin's approach in the spectral domain, as discussed in Section 2.2.2, is used for this computation.

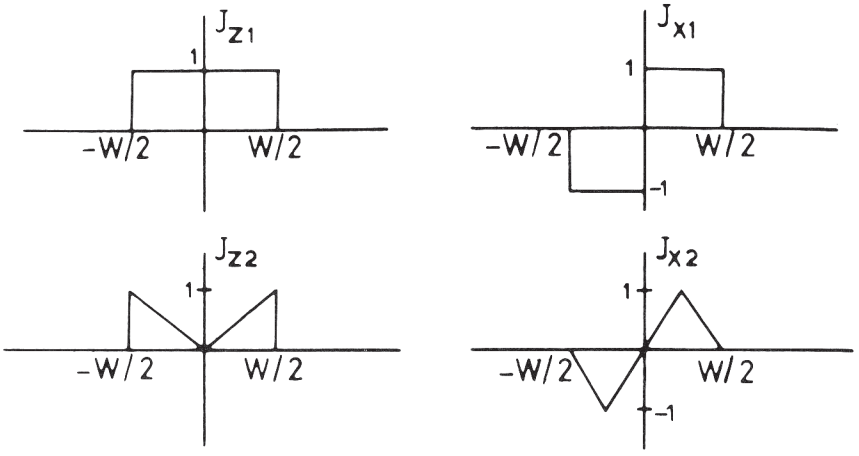

(a)

Analysis by using Galerkin's Method in FTD)

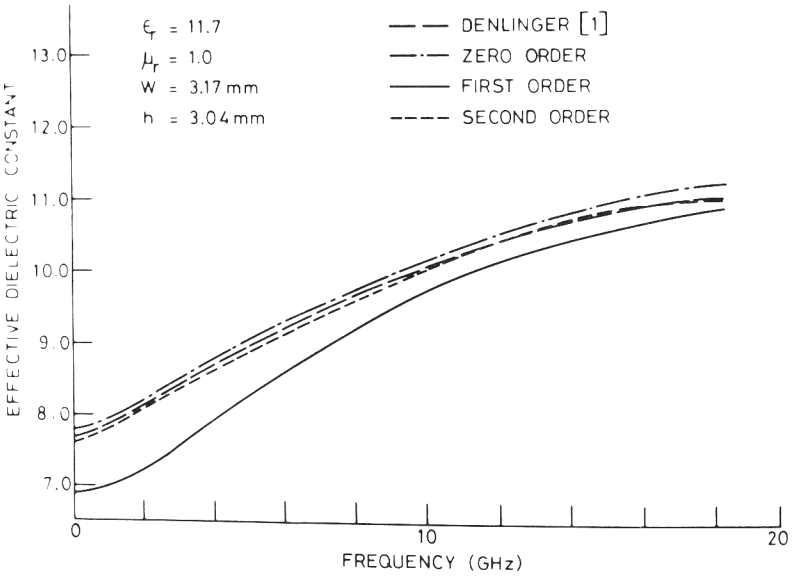

(b)

Figure 2.2 (a) Basis functions for currents in a microstrip (used for analysis by using Galerkin's method in FTD) and (b) variation of effective dielectric constant with frequency for an open microstrip (from [2], © 1973 IEEE. Reprinted with permission.).

When the transverse component of the current is ignored, we can define the characteristic impedance Z_{0i} as

$$Z_{0\mathrm{i}} = 2P_{\mathrm{avg}}/I_z^2 \tag{2.36}$$

where I_z is the total z-directed strip current. The average power is calculated as

$$P_{\mathrm{avg}} = \frac{1}{2}\mathrm{Re}\iint \left(E_x H_y^* - E_y H_x^*\right) dx\, dy \tag{2.37}$$

This relation can be written in the spectral domain, using Parseval's theorem, as

$$P_{\mathrm{avg}} = \frac{1}{4\pi}\mathrm{Re}\int_{-\infty}^{\infty}\int_{-\infty}^{\infty}[\tilde{E}_x(\alpha,y)\tilde{H}_y^*(\alpha,y) - \tilde{E}_y(\alpha,y)\tilde{H}_x^*(\alpha,y)]\, dy\, d\alpha \tag{2.38}$$

Integration with respect to y can be carried out analytically. This yields an equation of the form

$$P_{\mathrm{avg}} = \frac{1}{4\pi}\int_{-\infty}^{\infty} g(\alpha)\, d\alpha \tag{2.39}$$

which is evaluated numerically in each of the two regions.

As in the case of waveguides, alternative definitions of characteristic impedance are possible. One can write

$$Z_{0\mathrm{v}} = \frac{V^2(0)}{2P_{\mathrm{avg}}} \tag{2.40}$$

where $V(0)$ is given by

$$V(0) = -\int_0^h E_y(0,y)\, dy \tag{2.41}$$

and denotes the voltage between the center of the strip and the ground plane.

Results based on these two definitions are shown in Figure 2.3(a). The quasi-static value of the impedance is also shown. We note that the impedance based on current (i.e., Z_{0i}) converges to the quasi-static value whereas $Z_{0\mathrm{v}}$ does not. This is perhaps due to the fact that $V(0)$ is a sensitive function of the assumed current distribution whereas the total current used in (2.36) is not.

The results in Figure 2.3(b) show that the characteristic impedance increases with frequency. It may be added that for a 1-mm-thick substrate $h/\lambda_0 = 0.4$ corresponds to 120 GHz, and at this frequency the impedance increases by about 16 percent above the quasi-static value.

The increase in the characteristic impedance with frequency can be interpreted qualitatively as follows. When the frequency increases, the effective dielectric constant for the microstrip increases. This has been observed from the results based on

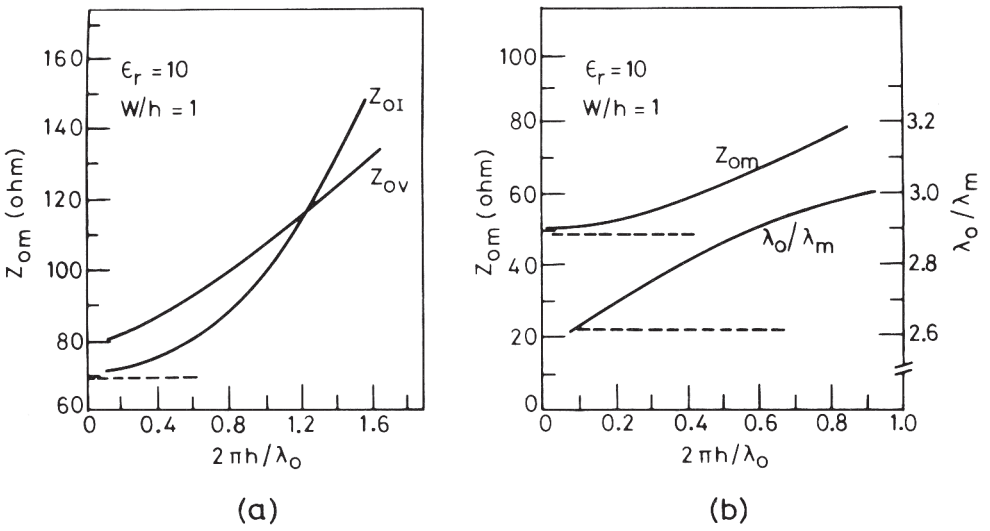

Figure 2.3 Variation of microstrip impedance and wavelength with frequency: (- - - -) quasi-static values (from [3], © 1975 IEEE. Reprinted with permission.).

fullwave analysis. An increase in the effective dielectric constant implies that the fields are getting concentrated below the strip, which also amounts to a decrease in the effective width of the microstrip. The characteristic impedance of a microstrip should decrease with the increase of ε_{re}. On the other hand, a decrease in the effective strip width should increase the characteristic impedance. The fullwave analysis described above shows that the latter effect is more pronounced. The results based on the planar waveguide model discussed in Chapter 1 agree with this interpretation.

The results for the characteristic impedance and effective dielectric constant for the dominant mode of propagation in open microstrip lines may also be obtained from the results for enclosed microstrips discussed in Section 2.3. The simplest approach for this purpose is to make the enclosure dimensions much larger (typically 10 times) than strip width and substrate height so that the presence of walls do not affect the microstrip line characteristics.

2.3 Analysis of an Enclosed Microstrip

Three different methods of fullwave analysis for an enclosed microstrip structure were illustrated in Figure 1.6. Of these, the finite difference method is conceptually the simplest. The other methods involved forming and solving integral equations. Since the integral equation methods are used most frequently, we discuss them first in Section 2.3.1. The configuration of the enclosed microstrip is shown in Figure 2.4.

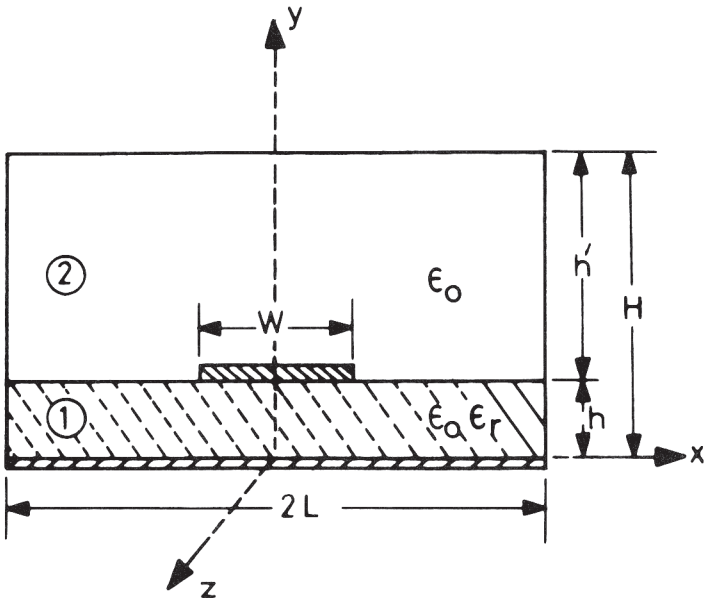

FIgure 2.4 Enclosed microstrip configuration.

2.3.1 Integral Equation Methods [6–10]

The most commonly used methods for the fullwave analysis of enclosed microstrip lines use integral equation formulation. The features of these methods are as follows: Expressions for potentials ψ^{e} and ψ^{h}, in regions 1 and 2, are written in the form of series expansions such that the boundary conditions on the metallic periphery of the enclosure are satisfied. Also, since the main interest lies in the dominant mode, which is E_z even – H_z odd, the total magnetic field is made to vanish at the plane of symmetry $x = 0$. The appropriate expressions are

$$\psi_1^{\mathrm{e}} = \sum_{n=1}^{\infty} A_n^{\mathrm{e}} \sinh \alpha_n^{(1)} y \cos k_n x \tag{2.42}$$

$$\psi_2^{\mathrm{e}} = \sum_{n=1}^{\infty} B_n^{\mathrm{e}} \sinh \alpha_n^{(2)} (H - y) \cos k_n x \tag{2.43}$$

$$\psi_1^{\mathrm{h}} = \sum_{n=1}^{\infty} A_n^{h} \cosh \alpha_n^{(1)} y \sin k_n x \tag{2.44}$$

$$\psi_2^{\mathrm{h}} = \sum_{n=1}^{\infty} B_n^{\mathrm{h}} \cosh \alpha_n^{(2)} (H - y) \sin k_n x \tag{2.45}$$

where

$$k_n = [n - (1/2)]\pi / L \tag{2.46}$$

$$\alpha_n^{(1)} = (k_n^2 + \beta^2 - \varepsilon_r k_0^2)^{1/2} \tag{2.47}$$

$$\alpha_n^{(2)} = (k_n^2 + \beta^2 - k_0^2)^{1/2} \tag{2.48}$$

where k_0 is the free-space wavenumber and the coefficients A_n and B_n are yet unknown. L is the width and H is the height of the enclosure as shown in Figure 2.4.

Interface conditions in the plane $y = h$ are applied to the field components derived from (2.42) to (2.45). This results in relations that equate the series of infinite terms. These equations are converted to an infinite set of homogeneous simultaneous equations for coefficients A_n and B_n by taking scalar products with a complete set of functions appropriate to the various ranges of x. The resulting equations may be written either in terms of integral equations or in terms of a matrix equation and solved for β. The various methods differ in the manner in which the interface conditions are applied and in the method of solving the resulting equations. As for open microstrip lines, both space domain and spectral domain formulations have been developed, and the spectral domain approach is used more frequently.

Space Domain Approach [6]

This method by Zysman and Varon [6] is a straightforward implementation of the steps outlined above. Four mutually independent interface conditions at $y = h$ are written as (Figure 2.4)

$$E_{x1} = E_{x2}, \qquad 0 < |x| < L \tag{2.49}$$

$$E_{z1} = E_{z2}, \qquad 0 < |x| < L \tag{2.50}$$

$$\begin{aligned} E_{x1} &= 0, & 0 < |x| < W/2 \\ H_{x1} &= H_{x2} & W/2 < |x| < L \end{aligned} \tag{2.51}$$

$$\begin{aligned} E_{z1} &= 0, & 0 < |x| < W/2 \\ H_{z1} &= H_{z2} & W/2 < |x| < L \end{aligned} \tag{2.52}$$

These conditions are now imposed on the field components derivable from (2.42) to (2.45). One obtains a pair of coupled homogeneous Fredholm integral equations of the first kind [6] as

$$\sum_{n=1}^{\infty}\left[G_n^{(1)}\int_0^{W/2} h_1(\xi)\cos k_n\xi\, d\xi + G_n^{(2)}\int_{W/2}^{L} h_2(\xi)\sin k_n\xi\, d\xi\right]\sin k_n x = 0 \tag{2.53}$$

$$\sum_{n=1}^{\infty}\left[G_n^{(3)}\int_0^{W/2} h_1(\xi)\cos k_n\xi\, d\xi + G_n^{(4)}\int_{W/2}^{L} h_2(\xi)\sin k_n\xi\, d\xi\right]\cos k_n x = 0 \tag{2.54}$$

Here the G_n's are known functions of β and $h_1(\zeta)$, $h_2(\zeta)$ are unknown functions of ζ. These equations may be transformed into a matrix equation algorithm. The

roots of the determinantal equation of the resulting matrix can be obtained numerically and yield the phase constant values for propagating waves.

Other variations of the space domain integral equation formulations are discussed in [7–9].

Galerkin's Method in FTD [10]

This method is similar to Galerkin's method in FTD used for open microstrip lines in Section 2.2.2. The bounded nature of the geometry (Figure 2.4) requires the use of the finite Fourier transform instead of the conventional Fourier transform over an infinite range. The latter type of transform was used for open microstrip analysis in Section 2.2.2. The transform used in the present analysis is defined as

$$\tilde{\psi}_i(\alpha_n, y) = \int_{-L}^{L} \psi_i(x, y) \exp(j\alpha_n x)\, dx \tag{2.55}$$

where $\alpha_n = (n - 1/2)\,\pi/L$ for E_z even – H_z odd modes and $\alpha_n = (n\pi/L)$ for E_z odd – H_z even modes ($n = 1, 2, \ldots$). The next step is to transform all the field components and to apply boundary and interface conditions in the transform domain. This leads to [10]

$$G_{11}(\alpha_n, \beta)\tilde{J}_x(\alpha_n) + G_{12}(\alpha_n, \beta)\tilde{J}_z(\alpha_n) = K_z\tilde{E}_z(\alpha_n) \tag{2.56a}$$

$$G_{21}(\alpha_n, \beta)\tilde{J}_x(\alpha_n) + G_{22}(\alpha_n, \beta)\tilde{J}_z(\alpha_n) = K_x\tilde{E}_x(\alpha_n) \tag{2.56b}$$

where

$$G_{11} = G_{22} = \alpha_n\beta(\gamma_{n,2}\tanh\gamma_{n,2}h' + \gamma_{n,1}\tanh\gamma_{n,1}h)/\det \tag{2.57a}$$

$$G_{12} = \left[\left(\varepsilon_r k_0^2 - \beta^2\right)\gamma_{n,2}\tanh\gamma_{n,2}h' + \left(k_0^2 - \beta^2\right)\gamma_{n,1}\tanh\gamma_{n,1}h\right]/\det \tag{2.57b}$$

$$G_{21} = \left[\left(\varepsilon_r k_0^2 - \alpha_n^2\right)\gamma_{n,2}\tanh\gamma_{n,2}h' + \left(k_0^2 - \alpha_n^2\right)\gamma_{n,1}\tanh\gamma_{n,1}h\right]/\det \tag{2.57c}$$

$$\det = \left(\gamma_{n,1}\tanh\gamma_{n,1}h + \varepsilon_r\gamma_{n,2}\tanh\gamma_{n,2}h'\right)\left(\gamma_{n,1}\coth\gamma_{n,1}h + \gamma_{n,2}\coth\gamma_{n,2}h'\right) \tag{2.57d}$$

and K_z and K_x are known constants. Also

$$\gamma_{n,1}^2 = \alpha_n^2 + \beta^2 - k_0^2\varepsilon_r \qquad \gamma_{n,2}^2 = \alpha_n^2 + \beta^2 - k_0^2 \qquad h' = H - h$$

$\tilde{J}_x(\alpha_n)$ and $\tilde{J}_z(\alpha_n)$ represent transforms of strip currents $J_x(x)$ and $J_z(x)$, respectively, and $\tilde{E}_z(\alpha_n)$ and $\tilde{E}_x(\alpha_n)$ are transforms of electric field components in the plane $y = h$. The electric field components are unknown for $W/2 < |x| < L$, though they are zero on the strip. These two unknowns are eliminated by applying Galerkin's

method. For this purpose, the currents are written in terms of known basis functions $\tilde{J}_{xm}$ and $\tilde{J}_{zm}$ as

$$\tilde{J}_x(\alpha_n) = \sum_{m=1}^{M} c_m \tilde{J}_{xm}(\alpha_n) \tag{2.58a}$$

$$\tilde{J}_z(\alpha_n) = \sum_{m=1}^{M} d_m \tilde{J}_{zm}(\alpha_n) \tag{2.58b}$$

where c_m and d_m are unknown coefficients. These expressions for the currents are substituted into (2.56). Taking inner products of both sides of (2.56) with the basis functions $\tilde{J}_{zi}$ and $\tilde{J}_{xi}$ for different values of i, one obtains

$$\sum_{m=1}^{M} K_{im}^{1,1} c_m + \sum_{m=1}^{N} K_{im}^{1,2} d_m = 0 \qquad \text{i} = 1,2,\ldots, N \tag{2.59a}$$

$$\sum_{m=1}^{M} K_{im}^{2,1} c_m + \sum_{m=1}^{N} K_{im}^{2,2} d_m = 0 \qquad \text{i} = 1,2,\ldots, M \tag{2.59b}$$

The coefficients K_{im}^{pq}, obtained by the inner products, are written as

$$K_{im}^{1,1} = \sum_{n=1}^{\infty} \tilde{J}_{zi}(\alpha_n) G(\alpha_n, \beta) \tilde{J}_{xm}(\alpha_n) \tag{2.60}$$

It is seen that the right-hand sides of (2.56) are eliminated through the use of Parseval's theorem, because the currents $J_{zi}(x)$, $J_{xi}(x)$ and the field components $E_z(x, h)$, $E_x(x, h)$ are zero in the complementary regions of x.

The simultaneous equations (2.59) are solved for the propagation constant β at each frequency ω by setting the determinant of the coefficient matrix equal to zero and by seeking the root of the resulting equation. The dispersion characteristics of microstrip are derived from the values of β.

The choice of the basis functions is important for the numerical efficiency of the method. The accuracy can be improved systematically by increasing the number of basis functions M or N. However, if the first few basis functions approximate the actual unknown current reasonably well, the necessary size of the matrix can be held small for a given accurancy of the solution. For the dominant mode, the following forms for J_{z1} and J_{x1} are suitable:

$$J_{z1}(x) = \begin{cases} \dfrac{1}{W}\left[1 + \left|\dfrac{2x}{W}\right|^3\right] & |x| \le W/2 \\ 0 & W/2 < |x| < L \end{cases} \tag{2.61}$$

$$J_{x1}(x) = \begin{cases} \dfrac{2}{W}\sin\dfrac{2\pi x}{W} & |x| \le W/2 \\ 0 & W/2 < |x| < L \end{cases} \tag{2.62}$$

The Fourier transforms of the above current distributions are given by

$$\tilde{J}_{z1}(\alpha_n) = \frac{2\sin(\alpha_n W/2)}{\alpha_n W/2} + \frac{3}{(\alpha_n W/2)^3} \left\{ \cos(k_n W/2) - \frac{2\sin(\alpha_n W/2)}{\alpha_n W/2} + \frac{2[1-\cos(\alpha_n W/2)]}{(\alpha_n W/2)^2} \right\} \tag{2.63}$$

and

$$\tilde{J}_{x1}(\alpha_n) = \frac{2\pi \sin(\alpha_n W/2)}{(\alpha_n W/2)^2 - \pi^2} \tag{2.64}$$

Results based on this analysis [10] have been compared with the results of the space domain integral equation method discussed earlier, and the agreement is good.

2.3.2 Finite Difference Method

In this method the microstrip cross section is divided into small rectangles by means of a rectangular net. Wave equations for ψ^e and ψ^h are solved for values of the potentials at the net points, and for this purpose the wave equations for ψ^e and ψ^h may be written in finite difference form as [11]

$$\lambda\psi^e_{m,n} = 2(1+R^2)\psi^e_{m,n} - \psi^e_{m+1,n} - \psi^e_{m-1,n} - R^2\psi^e_{m,n+1} - R^2\psi^e_{m,n-1} \tag{2.65}$$

$$\lambda\psi^h_{m,n} = 2(1+R^2)\psi^h_{m,n} - \psi^h_{m+1,n} - \psi^h_{m-1,n} - R^2\psi^h_{m,n+1} - R^2\psi^h_{m,n-1} \tag{2.66}$$

where $\lambda = (k^2 - \beta^2)(\Delta x)^2, \psi^e_{m,n} = \psi^e(m\Delta x, n\Delta y), \psi^h_{m,n} = \psi^h(m\Delta x, n\Delta y)$ and $R = \Delta x/\Delta y$. Integers m and n in subscripts refer to the coordinates of the grid point. The configuration and the coordinate system are shown in Figure 2.4. After applying boundary and interface conditions, the finite difference equations (2.65) and (2.66) may be written in the form of the matrix equation

$$[\mathbf{A}][\phi] = \lambda[\phi] \tag{2.67}$$

where [**A**] is the coefficient matrix, which is sparse and has the size $2(MN - 1)$ by $2(MN - 1)$ with $M\Delta x = L$ and $N\Delta y = H$ (as shown in Figure 2.4). Potentials $\psi^e_{m,n}$ and $\psi^h_{m,n}$ are elements of vector ϕ. It may be pointed out that λ has different values in regions 1 and 2.

There are several methods of solving (2.67), and a discussion of these techniques is given in [11] and [12]. It may be pointed out that the relaxation method used for quasi-static analysis becomes prohibitively slow in the present case. A method suitable for the present case has been described by Martin and Wilkinson [13]. Also, the matrix resulting from (2.65) and (2.66) is asymmetric, whereas efficient methods are available for the solution of symmetric matrix eigenvalue problems. A symmetric matrix can be obtained by using the variational method [12]. Another advantage of the variational method is that a graded mesh (with closer spacings near the strip and wider spacings near the enclosure walls) can be used.

This permits the analysis of structures of realistic dimensions without prohibitively large computer storage requirements.

The derivation of a variational expression suitable for finite difference equations proceeds from a general variational formulation for an inhomogeneously filled structure. The general expression is obtained directly from Maxwell's curl equations [14] and can be written in terms of the longitudinal field components as

$$\iint \left[\frac{1}{\varepsilon_r} \frac{1}{k_0^2} \left(\omega \varepsilon_0 \varepsilon_r E_z \nabla_t^2 E_z + \omega \mu_0 H_z \nabla_t^2 H_z \right) + \omega \varepsilon_0 \varepsilon_r E_z^2 + \omega \mu_0 H_z^2 \right] dS = 0 \quad (2.68)$$

Applying the divergence theorem, one may obtain a variational expression for the surface integral J of (2.68) as [12]

$$J = \int_S \int \left\{ A\tau\varepsilon_r \left| \nabla_t \psi^e \right|^2 + \tau \left| \nabla_t \psi^h \right|^2 + 2A\tau \left\{ \frac{\partial \psi^e}{\partial x} \frac{\partial \psi^h}{\partial y} - \frac{\partial \psi^h}{\partial x} \frac{\partial \psi^e}{\partial y} \right\} - k_0^2 [(\psi^h)^2 + A\varepsilon_r (\psi^e)^2] \right\} dS \quad (2.69)$$

where

$$\psi^h = H_z, \qquad \psi^e = \frac{\omega \varepsilon_0}{\beta} E_z$$

$$\tau = \frac{\omega^2 \mu_0 \varepsilon_0 - \beta^2}{\omega^2 \mu_0 \varepsilon_0 \varepsilon_r - \beta^2} \qquad A = (\beta c/\omega)^2$$

where c is the velocity of electromagnetic waves in free space. Since (2.69) does not involve derivatives higher than the first order, it can be put in finite difference form using the following formulas (refer to Figure 2.5 with $\Delta_1 = \Delta_2 = \Delta$)

$$\iint_S \left| \nabla_t \phi \right|^2 dS \simeq \left\{ \left[\frac{\phi_1 - \phi_0}{\Delta} \right]^2 + \left[\frac{\phi_2 - \phi_0}{\Delta} \right]^2 \right\} \frac{\Delta^2}{2} \quad (2.70)$$

and

$$\int_S \int \phi^2 \, dS \simeq \frac{1}{3} \left(\phi_0^2 + \phi_1^2 + \phi_2^2 \right) \frac{\Delta^2}{2} \quad (2.71)$$

where ϕ_0, ϕ_1 ... represent values of potential ψ^e or ψ^h at points 0, 1, ... Using approximations described by (2.70) and (2.71), it is possible to arrive at an approximation for the contribution from the elementary triangular region of Figure 2.5 to the integral of (2.69). The surface integral J of (2.69) is then computed as the sum of such approximations for each elemental region in the structure. The stationary property of J is utilized after differentiating with respect to each of the variables $\psi_1^h, \psi_2^h, \ldots, \psi_i^h, \psi_1^e, \psi_2^e, \ldots \psi_i^e$. In this way N linear equations are derived for the system where N is the total number of variables ψ_i^h and ψ_i^e. These relations are put in the form of a matrix equation (2.67), which now becomes a symmetric band structure matrix. The solution of such a matrix may be found by the following three steps: (i) [A] is reduced to a tridiagonal form [15]; (ii) the eigenvalues of the tridiagonal matrix are found by the method of bisection [16]; and (iii) the

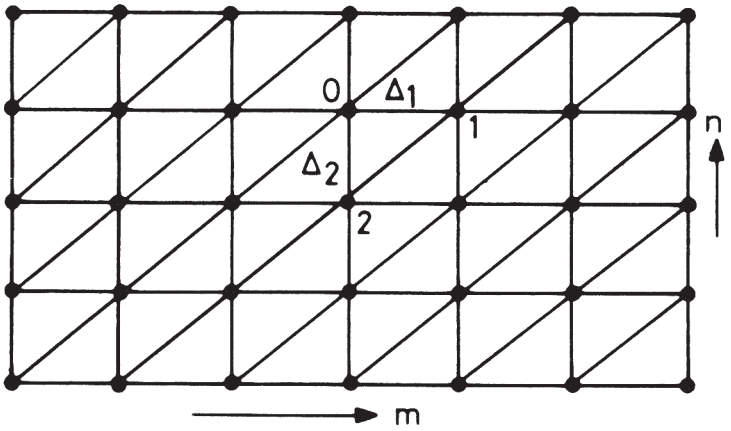

Figure 2.5 A typical region within the finite difference mesh.

eigenvector associated with a specific eigenvalue is found by the method of inverse iterations [17]. References [15–17] give details of these three steps.

A disadvantage of the finite difference method is the large size of the matrix to be handled and the resulting computer storage requirement.

Equation (2.69) can also be solved by the finite element method in place of the finite difference method discussed above. Corr and Davies [12] have tried this technique and found that there are no advantages to be gained by using the finite element method.

2.3.3 Discussion of Results

Methods for fullwave analysis of a microstrip provide information about two aspects of wave propagation along the microstrip, namely, dispersion and higher order modes. The principal features of these results are discussed in this section.

Dispersion

Information regarding the dispersive nature of propagation in a microstrip can be expressed in different ways. Figures 2.6 and 2.7 indicate two ways of representing dispersion. In Figure 2.6, the frequency is plotted against the phase constant β leading to the traditional ω-β diagram. This figure also includes a ω-β curve based on a quasi-static analysis (which is a straight line). Results of the fullwave analysis based on two different methods are shown. These two curves are not straight but lie between the two straight lines, one corresponding to a quasi-static analysis and the other for a homogeneously filled line. At lower frequencies (less than 5 GHz) results given by both methods coincide with the quasi-static results.

Figure 2.7 presents the same results in a different manner. Here the normalized guide wavelength λ_m/λ_0 is plotted as a function of frequency. Two different methods (the integral equation method and the singular integral equation method [8]) are compared. Experimental results for an open microstrip are also included.

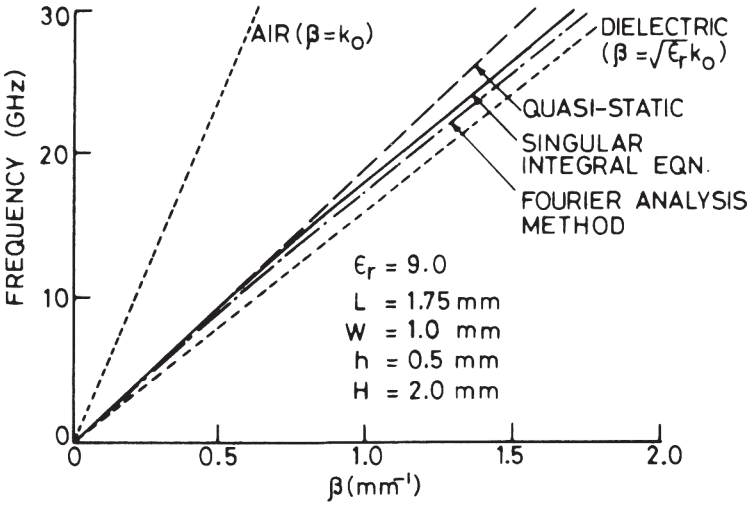

Figure 2.6 Dispersion behavior of a microstrip as computed by different methods (from [8], © 1971 IEEE. Reprinted with permission.).

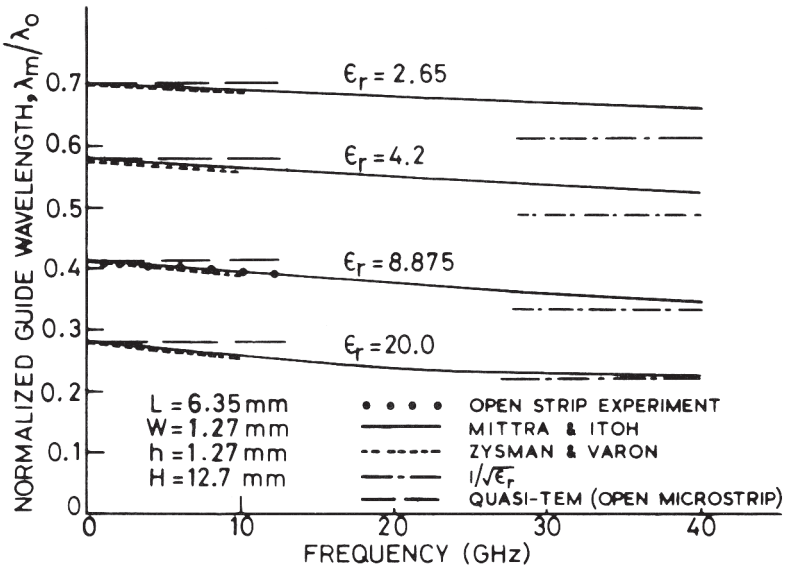

Figure 2.7 Variation of microstrip guide wavelength with frequency (from [8], © 1971 IEEE. Reprinted with permission.).

It is observed that λ_m/λ_0 decreases with an increase in frequency and tends to $1\sqrt{\varepsilon_r}$. It implies that at higher frequencies more and more energy propagates inside the substrate and below the strip.

Higher Order Modes

Plotting the ω-β diagram for higher order modes requires considerable computation time. Thus only limited results are available.

The singular integral equation method has been used to investigate higher order modes [8]. The results for a substrate of dielectric constant 8.875 (alumina) are shown in Figure 2.8. Similar results are available [8] for three other dielectric constant values (2.62, 4.2, and 20.0). The existence of a number of higher order modes is evident in these plots. It should be noted that this mode spectrum is not complete since only the E_z even – H_z odd type of modes are shown. Comparison with similar curves for other values of ε_r indicates that the frequency at which the first higher order mode begins to appear is lower for higher values of ε_r.

Dispersion curves for higher order modes have also been calculated by Corr and Davies [12] using the finite difference method discussed earlier. Their results are presented in Figure 2.9(b) for the microstrip configuration shown in Figure 2.9(a). This plot includes E_z odd – H_z even type of modes also. It is seen that the dispersion curves tend to group in pairs of E_z even and E_z odd modes of the same order. The difference between the static limiting value of ε_{re} for the lowest mode and the TEM value is attributed entirely to discretization errors in the finite difference method.

Higher order microstrip modes have been compared with LSM and LSE modes of the slab line structure formed by the removal of the microstrip conductor [12]. A very close similarity between the power density distributions of E_z odd and LSM modes is noted. Also higher order E_z even and E_z odd modes have very similar power density distributions. It is concluded that because the plane of symmetry makes so little difference to the higher order modes with the same subscript, these modes are strongly associated not with the strip but with the dielectric-air interface. In view of their close similarity to the LSM modes, they can be considered as distorted LSM modes. The specific type of mode correspondences may be grouped together. Using the notation E for E_z even and M for E_z odd modes, it can be said that modes E_1, M_1 and LSM_{12} are similar; modes E_2, M_2, and LSM_{14} are similar; and so on. Thus, for an enclosed microstrip, the approximate cut-off frequency for higher order modes may be obtained from the cut-off frequency of LSM modes.

Considerable information about higher order modes can also be obtained from the planar waveguide model for a microstrip as discussed in Chapter 1. Cutoff frequencies and guide wavelengths for various modes are given by (1.85) and (1.86), respectively.

2.4 Design Considerations

In this section various important design parameters of microstrip lines are discussed. These include attenuation constant, power handling capability, effect of tolerances, and dielectric anisotropy. Various expressions, useful for microstrip design, are summarized in the last subsection.

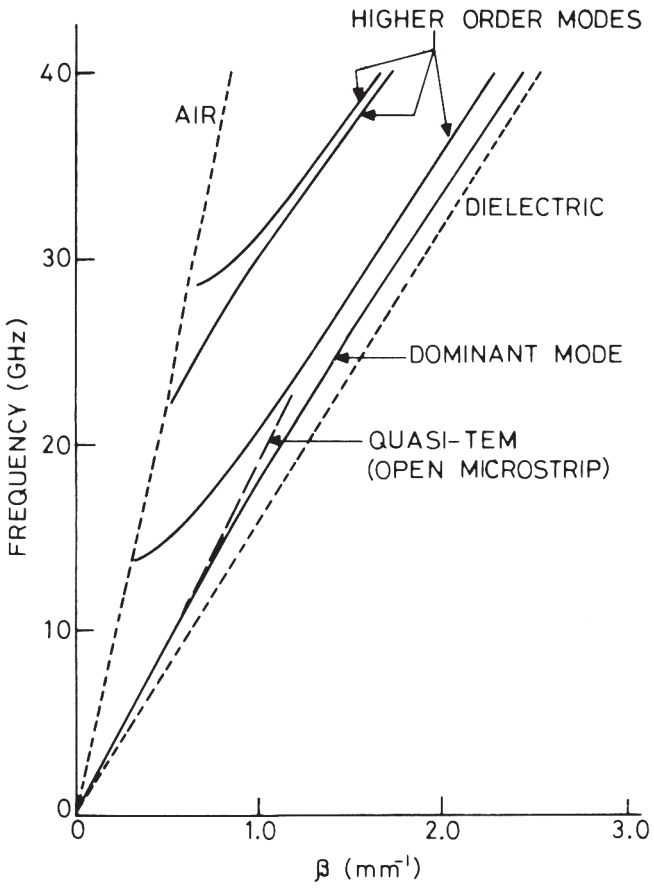

Figure 2.8 Higher order modes in a microstrip (computed by using the singular integral equation method) $\varepsilon_r = 8.875$, $L = 6.35$ mm, $W = 1.27$ mm, $h = 1.27$ mm, and $H = 12.7$ mm (from [8], © 1971 IEEE. Reprinted with permission.).

2.4.1 Microstrip Losses

Attenuation in a microstrip line is caused by two loss components: conductor loss and dielectric loss. If a magnetic substrate is used, a magnetic loss component will also be present. We will discuss losses for nonmagnetic substrates in this subsection.

Conductor Loss

A comprehensive treatment of conductor loss in a microstrip structure is given by Pucel et al. [18] and by Schneider [19]. Both of these analyses are based on the "incremental inductance rule" of Wheeler [20]. In this method the series surface resistance R per unit length is expressed in terms of that part of the total inductance per unit length that is attributable to the skin effect, that is, the inductance L_i produced by the magnetic field within the conductors.

It is well known that for a conductor the surface impedance, $Z_s(=R + jX)$, has a real part R (surface resistance per unit length) that is equal to the imaginary part X. That is,

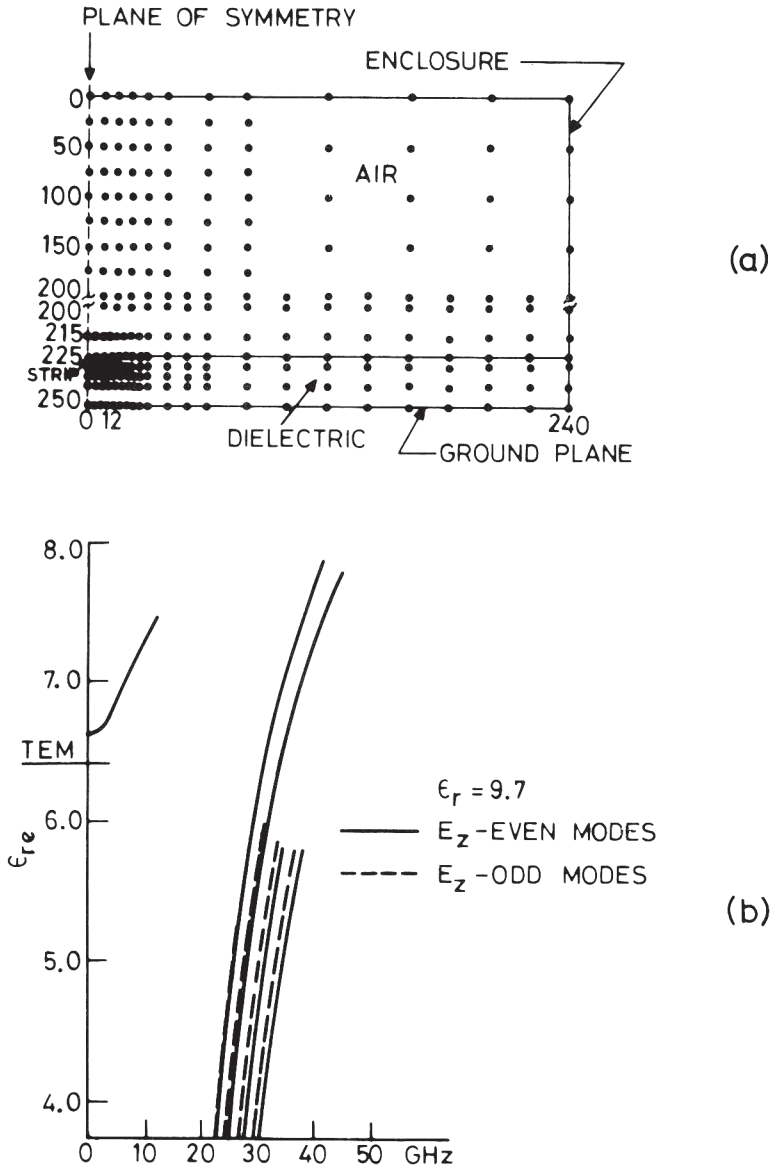

Figure 2.9 (a) Mesh points for microstrip analysis by using the finite difference method (scale 1 unit = 0.002 in) and (b) higher order modes, computed by using the finite difference method (from [12], © 1972 IEEE. Reprinted with permission.).

$$R = X = \omega L_i \tag{2.72}$$

According to Wheeler, L_i can be found from the external inductance L per unit length. L_i is obtained as the incremental increase in L caused by an incremental recession of all metallic walls due to the skin effect. This situation is shown in Figure 2.10. The amount of recession is equal to half the skin depth $\delta = (2/\omega\mu\sigma_c)^{1/2}$. An assumption underlying this rule is that the radius of curvature and the thickness

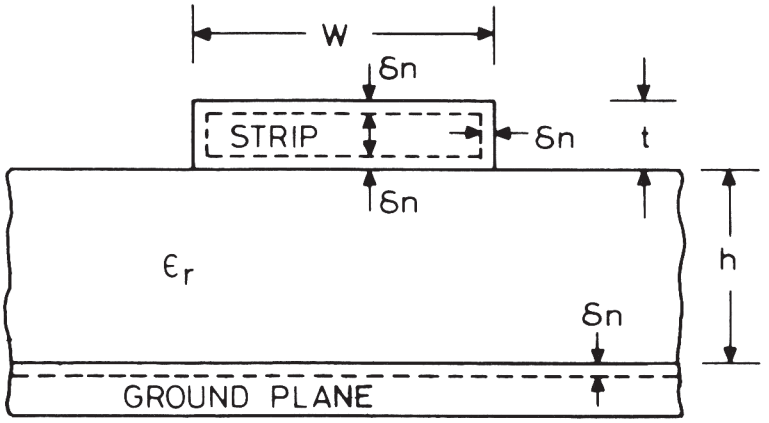

Figure 2.10 Recession of conducting walls of a microstrip for loss calculation using "incremental inductance rule."

of the conductors exposed to the electromagnetic fields are greater than the skin depth, preferably several skin depths. According to Wheeler [20], we have

$$L_i = \sum_m \frac{\mu_m}{\mu_0} \frac{\partial L}{\partial n_m} \frac{\delta_m}{2} \tag{2.73}$$

$$R = \sum_m \frac{R_{sm}}{\mu_0} \frac{\partial L}{\partial n_m} \tag{2.74}$$

where $\partial L/\partial n_m$ denotes the derivative of L with respect to incremental recession of wall m, n_m is the normal direction to this wall, and $R_{sm} = \omega\mu_m\ \delta_m/2$ is the surface. resistance of the wall m.

The attenuation constant because of conductor (ohmic) loss is defined as

$$\alpha_c \simeq \frac{P_c}{2P(z)} = \frac{\text{Power loss in conductors}}{2\ (\text{Power transmitted})}\ (\text{nepers/unit length}) \tag{2.75}$$

In terms of R and Z_{0m} (characteristic impedance), α_c may be written as

$$\alpha_c = \frac{|I|^2 R}{2|I|^2 Z_{0m}} = \frac{1}{2\ \mu_0 Z_{0m}} \sum_m R_{sm} \frac{\partial L}{\partial n_m} \tag{2.76}$$

Inductance L of the microstrip structure can be expressed in terms of the characteristic impedance for the microstrip with the substrate replaced by air (Z^a_{0m}) and is given as

$$L = Z^a_{0m}/c \tag{2.77}$$

where c is the velocity of electromagnetic waves in free space.

Wheeler's incremental inductance rule requires the thickness of the conductors to be greater than about four times the skin depth. The effect of using smaller thicknesses has also been reported [21–23]. It is observed that the conductor losses are reduced by about 9 percent when the conductor thickness is $\pi/2$ times the skin depth.

An expression for the attenuation constant based on (2.76) is presented later in Section 2.4.5 where all other design information is also summarized.

Dielectric Loss

For a uniformly filled transmission line the dielectric loss α_{du} is independent of the geometry of the line and may be written as

$$\alpha_{du} = \frac{gZ_0}{2} = \frac{\omega}{2}\sqrt{\frac{\mu}{\varepsilon'}}\varepsilon'' = \frac{\omega}{2}\sqrt{\mu\varepsilon'}\tan\delta \tag{2.78}$$

where g is the shunt conductance per unit length of the line, ε' is the real part, and ε'' is the imaginary part of the permittivity of the dielectric. However, when the dielectric is not uniform over the cross section of the line, the above expression does not apply. Calculation of the loss for the mixed dielectric case has been considered by Welch and Pratt [21] and by Schneider [24]. In both of these analyses, an effective loss tangent $(\tan\delta)_e$ is derived. The results obtained in these two analyses can be shown to be identical when the difference in the definition of filling factor q in the two cases is taken into account.

When the upper dielectric (air) is assumed to be lossless, the following expression for α_d (attenuation constant considering mixed dielectrics) is obtained [21]

$$\begin{aligned}\alpha_d &= \frac{\omega}{2}\sqrt{\mu\varepsilon_{re}}(\tan\delta)_e \\ &= \frac{\omega}{2}\sqrt{\mu\varepsilon_{re}}\frac{\sigma_e}{\omega\varepsilon_{re}}\end{aligned} \tag{2.79}$$

If σ is the conductivity of the dielectric and σ_0 the conductivity of air, we can write

$$\sigma_e = q\sigma + (1-q)\sigma_0 \simeq q\sigma \qquad (\text{since } \sigma_0 \ll \sigma)$$

Also,

$$\varepsilon_0\varepsilon_{re} = q\varepsilon + (1-q)\varepsilon_0 \qquad \text{with } \varepsilon = \varepsilon_0\varepsilon_r$$

Therefore, (2.79) becomes

$$\alpha_d = q\left\{\frac{\varepsilon}{q\varepsilon + (1-q)\varepsilon_0}\right\}^{\frac{1}{2}}\alpha_{du} = \left(\frac{\varepsilon_r}{\varepsilon_{re}}\right)^{\frac{1}{2}}q\alpha_{du} \tag{2.80}$$

where q is the dielectric filling fraction (see Section 1.2.1) and α_{du} is the attenuation constant for a line uniformly filled with the dielectric ε_r, given by (2.78). Since

$$q = \frac{\partial\varepsilon_{re}}{\partial\varepsilon_r} = \frac{\varepsilon_{re}-1}{\varepsilon_r-1}$$

the attenuation constant α_d may be written as

$$\alpha_d = 27.3\frac{\varepsilon_r}{\sqrt{\varepsilon_{re}}}\frac{\varepsilon_{re}-1}{\varepsilon_r-1}\frac{\tan\delta}{\lambda_0} \quad \text{dB/unit length} \tag{2.81}$$

For microstrip lines on alumina substrate the dielectric loss α_d is negligible compared to the total loss α. But for microstrip lines utilizing semiconductor substrates such as Si, the dielectric loss factor is dominant. For example, a 50-Ω line on a silicon substrate ($\varepsilon_r = 11.7$) with a resistivity of 10^3-Ωcm has a dielectric loss on the order of 0.36 dB/cm while the conductor loss is about 0.19 dB/cm [21]. For these substrates the dielectric conductivity σ is nonzero. In this case, (2.81) can be used with some modification; the final expression is given [21] as

$$\alpha_d = 4.34 \frac{1}{\sqrt{\varepsilon_{re}}} \frac{\varepsilon_{re} - 1}{\varepsilon_r - 1} \left(\frac{\mu_0}{\varepsilon_0} \right)^{1/2} \sigma \qquad \text{dB/unit length} \tag{2.82}$$

Dielectric loss in a microstrip has also been computed numerically using the moment method [25]. In this case, α_d is written as

$$\alpha_d = \frac{(\sigma/2) \int E^2 \, ds}{2P} = \frac{\sigma \int E^2 \, ds}{2V^2 / Z_{0m}} \tag{2.83}$$

Equations (2.81) and (2.82) give a value of α_d, which is about 1 percent higher than that predicted by the numerical method of Simpson and Tseng [25]. Values of the conductor and the dielectric losses per unit length in 50-Ω microstrip lines on various substrates have been calculated using results given in [26] and are shown in Figure 2.11 as function of frequency. Attenuation for lines on quartz substrate has been discussed by Van Reuven [27].

2.4.2 Power Handling Capability [28]

There is a widespread impression that microstrip lines are suitable only for low-power components. Although microstrip lines are not as well suited for high-power applications as are waveguides or coaxial lines of comparable cross section, they could certainly be used for several medium-power applications. A 50-Ω microstrip on a 25-mil-thick alumina substrate can handle a few kilowatts of power.

The power handling capacity of a microstrip, like that of any other dielectric filled transmission line, is limited by heating caused because of ohmic and dielectric losses and by dielectric breakdown. An increase in temperature due to conductor and dielectric losses limits the average power of the microstrip line, while the breakdown between the strip conductor and ground plane limits the peak power.

Average Power

The *average power handling capability* (APHC) of a microstrip is determined by the temperature rise of the strip conductor and the supporting substrate. The parameters that play major roles in the calculation of average power capability are: (i) transmission line losses; (ii) thermal conductivity of the substrate material; (iii) surface area of the strip conductor; and (iv) ambient temperature; that is, temperature of the medium surrounding the microstrip. Therefore, dielectric substrates with low-loss tangent and large thermal conductivity will increase the average power handling capability of microstrip lines.

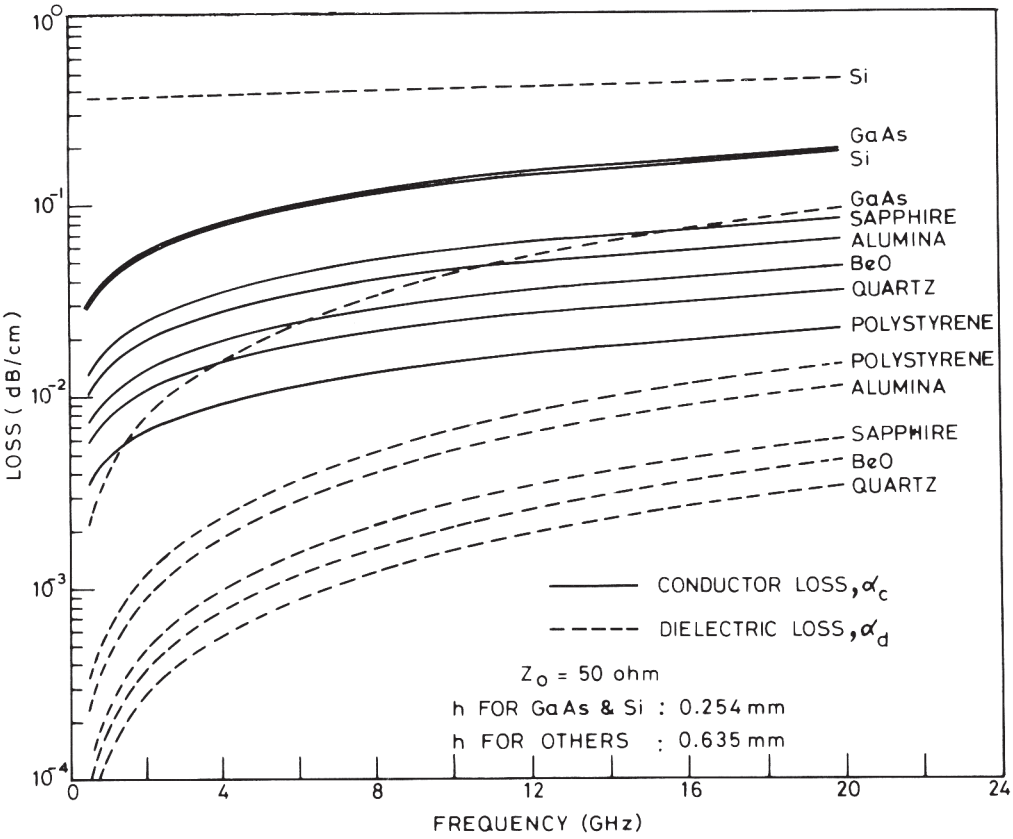

Figure 2.11 Conductor and dielectric losses as a function of frequency for microstrip lines on various substrates.

Table 2.1 Analogy Between Heat Flow Field and Electric Field

Heat Flow Field	*Electric Field*
1. Temperature, T (°C)	Potential, V (V)
2. Temperature gradient, T_g (°C/m)	Electric field, E (V/m)
3. Heat flow rate, Q (W)	Flux, ϕ (coulomb/m^2)
4. Density of heat flow, q (W/m^2)	Flux density, D (coulomb/m^2)
5. Thermal conductivity, K (W/m/°C)	Permittivity, ε (coulomb/m/V)
6. Density of heat generated, ρ_h (W/m^3)	Charge density, ρ (coulomb/m^3)
7. $q = -K\nabla T$	$D = -\varepsilon\nabla V$
8. $\nabla \cdot q = \rho_h$	$\nabla \cdot D = \rho$

The temperature rise of the strip conductor can be calculated from the heat flow field in the cross section. An analogy between the heat flow field and the electric field is described in Table 2.1. The heat generated by the conductor loss and the dielectric loss is discussed separately in the following paragraphs.

Density of Heat Flow Due to Conductor Loss

A loss of electromagnetic power in the strip conductor generates heat in the strip. Because of the good heat conductivity of the strip metal, heat generation is uniform

along the width of the conductor. Since the ground plane is held at ambient temperature (i.e., acts as a heat sink), this heat flows from the strip conductor to the ground plane through the substrate. The heat flow can be calculated by considering the analogous electric field distribution. The heat flow field in the microstrip structure corresponds to the electrostatic field (without any dispersion) of the microstrip. From Figure 1.4 we note that the electric field lines (the thermal field in the case of heat flow) spread near the ground plane.

To account for the increase in area normal to heat flow lines, the parallel plate model of a microstrip is used. For these calculations ε_r (in electrical analog) is assumed to be equal to the ratio of the thermal conductivity of the substrate (Table 2.2) to that of the air. The equivalent width of the strip (W_e) in the parallel plate model is calculated from the electrical analog as

$$W_e = \frac{120\pi h}{Z'_{0m}\sqrt{\varepsilon'_{re}}} \tag{2.84a}$$

where h is the thickness of the substrate and Z'_{0m} is the characteristic impedance of the microstrip (in ohms). Microstrip parameters Z'_{0m} and ε'_r are calculated with ε_r replaced by K_d/K_a (the ratio of thermal conductivity of the dielectric to that of the air). When the impedance of a microstrip with air as the dielectric is written as $Z^a_{0m}(= Z'_{0m}\sqrt{\varepsilon'_{re}})$, (2.84a) becomes

$$W_e = \frac{120\pi h}{Z^a_{0m}} \tag{2.84b}$$

Consider a unit length of the line. The power absorbed (ΔP) in the line, due to conductor loss in the strip when one watt of power is incident, is given by

$$\Delta P = 0.2303\alpha_c \quad (W/m) \tag{2.85}$$

where α_c (dB/m), the attenuation coefficient due to loss in the strip conductor, is assumed small. The density of heat flow due to the conductor loss may be written as

$$q_c = \frac{0.2303\alpha_c}{W_e}(W/m^2) \tag{2.86}$$

Table 2.2 Properties of Various Dielectric Substrates Used for Microstrip Characteristics in Section 2.4

Material	ε_r	*Loss Tangent at 10 GHz*	*K (W/cm/°C)*	*Dielectric Strength (kV/cm)*
Sapphire	11.7	10^{-4}	0.4	4×10^3
Alumina	9.7	2×10^{-4}	0.3	4×10^3
Quartz (fused)	3.8	10^{-4}	0.01	10×10^3
Polystyrene	2.53	4.7×10^{-4}	0.0015	280
Beryllium oxide (BeO)	6.6	10^{-4}	2.5	—
GaAs ($\rho = 10^7\ \Omega$ cm)	12.3	16×10^{-4}	0.3	350
Si ($\rho = 10^3\ \Omega$ cm)	11.7	50×10^{-4}	0.9	300
SiC	9.7	0.003	3.5	$> 2 \times 10^3$
FR4	4.5	0.03	0.0027	> 200
Air	1	≃ 0	0.00024	30

Density of Heat Flow Due to Dielectric Loss

In addition to the conductor loss, heat is generated by dielectric loss in the substrate. The density of the heat generated is proportional to the square of the electric field. However, we can consider a parallel plate model wherein the electric field is uniform and the density of the heat generated can also be considered uniform. This assumption ignores the increased dielectric loss in regions of high electric field near the strip edges. However, since the dielectric loss is a small fraction of the total loss (except for semiconductor substrates like Si), the above assumption should hold. The effective width for this parallel plate model depends on the spread of electric field lines and is a function of frequency. The effective width, $W_{\text{eff}}(f)$, is given by [29, 30]

$$W_{\text{eff}}(f) = W + \frac{W_{\text{eff}}(0) - W}{1 + (f/f_{\text{p}})^2} \tag{2.87}$$

where

$$f_{\text{p}} = \frac{Z_{0\text{m}}}{2\mu_0 h}$$

and $W_{\text{eff}}(0)$ is equal to W_{e} of (2.84). μ_0 is the permeability of free space, ε_{re} is the static value of the effective dielectric constant [31], and Z_{0m} is the characteristic impedance of the microstrip (in ohms).

The heat flow in the y-direction caused by a sheet of heat sources can be evaluated by considering the configuration in Figure 2.12.

The heat conducted away by air is negligible, and the air-dielectric boundary can be considered as an insulating wall (corresponding to a magnetic wall in the electric analog). Therefore, the configuration is modified by removing the insulating wall and incorporating an image source of heat and an image of the ground plane as shown. The space between the two ground planes is filled homogeneously by the dielectric medium. Now the heat flow at a point A is obtained by applying the divergence theorem (for heat flow field) to the volume shown by the dotted lines, that is,

$$\iiint (\nabla \cdot q_{\text{d}})\, dv = \oint\oint_s q_{\text{d}} \cdot ds = \iiint \rho_{\text{h}}\, dv \tag{2.88}$$

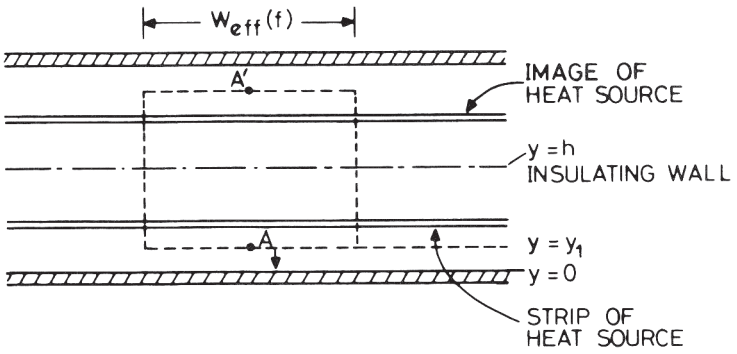

Figure 2.12 Geometry for calculating the density of heat flow due to dielectric loss in microstrip lines.

where s is the enclosed area. The total q_d at $y = y_1$ is contributed by the heat source lying between $y = y_1$ and $y = h$ (and their images). It may be noted that sources located at $y < y_1$ (and their images) do not contribute to the heat flow at $y = y_1$. Thus,

$$q_d(y) = -(h - y)\rho_h \tag{2.89}$$

The negative sign implies that the heat flow is in the $-y$ direction (for $y < h$). If α_d (dB/m) is the attenuation coefficient due to dielectric loss, the density of heat generated, ρ_h, may be written as

$$\rho_h = \frac{0.2303\alpha_d}{W_{eff}(f)h} \tag{2.90}$$

From (2.89) and (2.90)

$$q_d(y) = -\frac{0.2303\alpha_d}{W_{eff}(f)}(1 - y/h) \tag{2.91}$$

Temperature Rise

The total density of the heat flow due to conductor and dielectric losses may be expressed in terms of a temperature gradient as

$$q = q_c + q_d(y) = -K\frac{\partial T}{\partial y} \tag{2.92}$$

where K is the thermal conductivity of the substrate. Therefore, the temperature at $y = h$ (i.e., at the strip conductor) is given by

$$T = \frac{0.2303}{K}\int_0^h \left\{\frac{\alpha_c}{W_e} + \frac{\alpha_d}{W_{eff}(f)}(1 - y/h)\right\} dy + T_{amb} \tag{2.93}$$

The corresponding rise in temperature is

$$\Delta T = \frac{0.2303h}{K}\left\{\frac{\alpha_c}{W_e} + \frac{\alpha_d}{2W_{eff}(f)}\right\} \qquad (^\circ C/W) \tag{2.94}$$

This relation is used for calculating the average power handling capability of the microstrip line.

The properties of various substrates are given in Table 2.2. Strip conductors, except in the case of polystyrene substrates, are of gold ($t = 0.01$ mm) while in the case of polystyrene substrates copper ($t = 0.035$ mm) is used. Conductor loss in the ground plane does not contribute to APHC limitation. However, as the ground plane loss is very small compared to the strip loss [32], formulas for the total loss could be used to calculate APHC. Results shown in Figure 2.13 for variations of ΔT with frequency are based on this assumption. The following interesting observations are noted from this figure. (i) The temperature rise ΔT increases with frequency. (ii) The beryllium oxide (BeO) substrate has a smaller temperature rise due to its higher value of thermal conductivity. Alumina and sapphire have nearly the same ΔT variation, although alumina has about 25 percent lower thermal conductivity compared to sapphire. This is due to the fact that sapphire line has

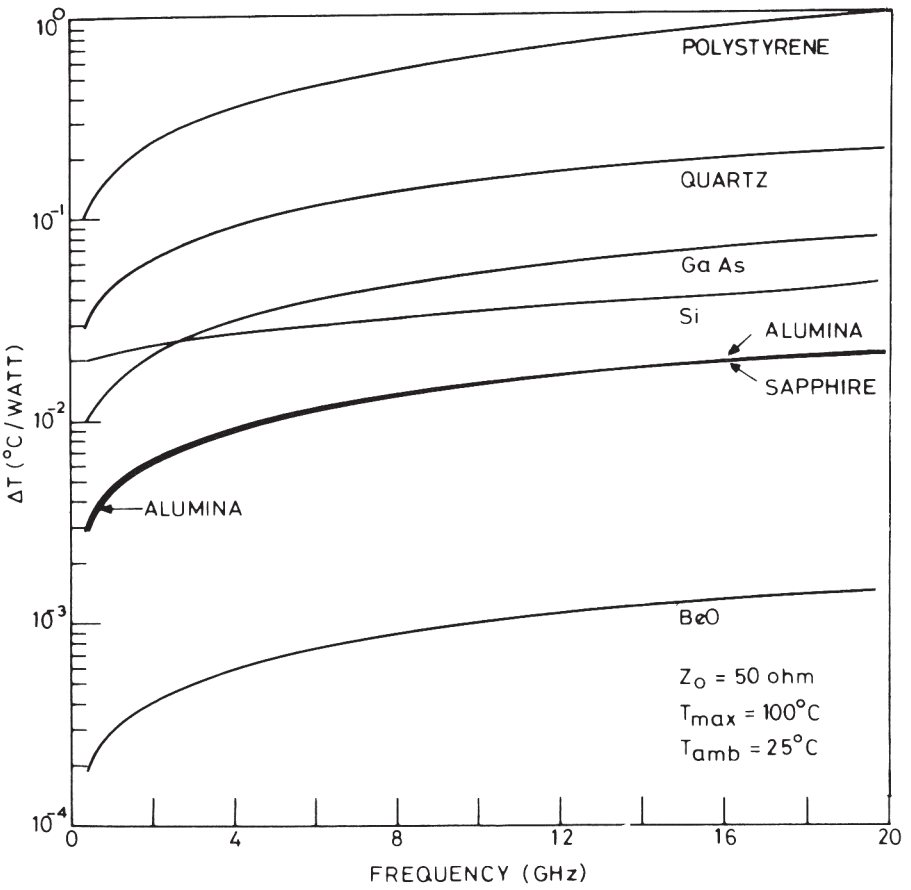

Figure 2.13 Rise in temperature of the strip conductor as a function of frequency for various substrates.

slightly more loss due to a higher dielectric constant. Also W_e and W_{eff} in the case of sapphire are smaller. Therefore, the combined effect of these parameters on ΔT is almost equal in sapphire and alumina. (iii) We note that for frequencies less than 2.6 GHz, ΔT for Si (1000 Ωcm) is larger than that for GaAs (10^7 Ωcm). At 2.6 GHz the two ΔT's are equal, and for frequencies above 2.6 GHz ΔT is smaller for Si. (iv) Plastic substrates (polystyrene etc.) have higher values of ΔT due to poor thermal conductivity, although the losses are smaller (Figure 2.11).

It may be pointed out that the effects of any thermal resistance barriers that may exist between the bonding of the strip and the microstrip dielectric, between the microstrip dielectric and the ground plane, and between the ground plane and any heat sink have not been taken into account in this analysis. This effect can limit the average power handling capability of microstrip lines.

Average Power Handling Capability

The maximum average power for a given line may be calculated from

$$P_{avg} = (T_{max} - T_{amb})/\Delta T \tag{2.95}$$

where ΔT denotes rise in temperature per watt and T_{max} is the maximum operating temperature. For polystyrene, the maximum operating temperature is 100°C, whereas for the rest of the dielectrics (in Table 2.2) it is much more than 100°C. The maximum operating temperature of microstrip circuits is limited due to (i) change of substrate properties with temperature, (ii) change of physical dimensions with temperature, and (iii) connectors. One can assume the maximum operating temperature of microstrip circuits to be the one where its electrical and physical characteristics remain unchanged. Circuits on alumina and glass fiber-reinforced teflon substrates have been tested up to 150°C for about 2000 hours. It has been found [33] that the electrical and physical characteristics remain unchanged.

For $T_{\max} = 100°C$, $T_{\text{amb}} = 25°C$, and $Z_{0\text{m}} = 50\ \Omega$, values of APHC for various substrates at 2 GHz, 10 GHz, and 20 GHz are calculated and given in Table 2.3. Among the dielectrics considered, APHC is the lowest for polystyrene and it is maximum for BeO. At lower frequencies, GaAs microstrip lines have better APHC than Si microstrip lines, but at higher frequencies (>2.6 GHz) APHC is better in the case of Si. For commonly used alumina (or sapphire) substrates, a 50-Ω microstrip can carry about 5.14 kW of CW power at 10 GHz.

The APHC analysis presented above has been extended to multilayer microstrip lines [34–36]. As a first-order approximation for a two-layered microstrip configuration, the heat flow from the microstrip conductor was considered to follow the rule of 45° thermal spread angle. Table 2.4 shows the APHC values of several multilayer 50-Ω microstrip lines on 75-μm thick GaAs at several frequencies. The APHC decreases with increasing frequency.

Peak Power Handling Capability

The calculation of peak power handling capability of microstrip lines is more complicated. The peak voltage that can be applied without causing dielectric breakdown determines the peak power handling capability (PPHC) of the microstrip. If Z_{0m} is the characteristic impedance of the microstrip and V_0 is the maximum voltage the line can withstand, the maximum peak power is given by

$$P_{\text{p}} = \frac{V_0^2}{2Z_{0\text{m}}} \tag{2.96}$$

Thick substrates can support higher voltages (for the same breakdown field). Therefore, low impedance lines and lines on thick substrates have higher peak power handling capability.

Table 2.3 Comparison of APHC for Various Substrates

	Maximum Average Power (kW)		
Substrate	*2.0 GHz*	*10 GHz*	*20 GHz*
Polystyrene	0.321	0.124	0.075
Quartz	1.200	0.523	0.357
Si	3.19	2.23	1.64
GaAs	3.55	1.47	0.934
Sapphire	11.65	5.10	3.46
Alumina	12.12	5.17	3.40
BeO	174.5	75.7	51.5

Table 2.4 Comparison of APHC of 50-Ω Multilayer Microstrip Lines on 75-μm Thick GaAs. Gold Conductors are 4.5 μm Thick Except in the 3-μm Polyimide ($\varepsilon_{rd} = 3.2$) Case, Where Thickness Is 9 μm.

	Maximum Average Power (W)			
Polyimide Thickness, d (μm)	*5 GHz*	*10 GHz*	*20 GHz*	*40 GHz*
0	2049	1445	1020	720
1	260	181	129	91
3	107	76	53	38
7	71	51	36	25
10	63	44	31	22

The sharp edges of the strip conductor serve as field concentrators. The electric field tends to a large value at the sharp edges of the conductor if it is a flat strip and decreases as the edge of the conductor is rounded off more and more. Therefore, thick and rounded strip conductors will increase breakdown voltage.

The dielectric strengths of the substrate material as well as of the air play important roles. The breakdown strength of dry air is approximately 30 kV/ cm. Thus the maximum (tangential) electric field near the strip edge should be less than 30 kV/ cm. To avoid air breakdown near the strip edge, the edge of the strip conductor can be painted with a dielectric paint that has the same dielectric constant as that of the substrate and is lossless. The dielectric strength of various dielectrics is also given in Table 2.2. This table shows that, among the dielectrics considered, fused quartz has the maximum dielectric strength while polystyrene has the minimum.

In some cases connectors or launchers decide the PPHC of the microstrip line. The 3-mm subminiature connectors and their transitions will breakdown before the line [37] itself. *N*-type connectors and transitions have higher PPHC. An additional factor, which may reduce PPHC, is the effect of internal mismatches. Experimental data for PPHC are not readily available. Howe [37] has reported successful operation of microstrip lines up to 10 kW at S-band and 4 kW at X-band.

2.4.3 Effect of Tolerances [38]

Characteristics of microstrip lines (namely, Z_{0m} and ε_{re}) are primarily functions of strip width W and substrate parameters ε_r and h. These are also influenced by factors such as strip thickness, frequency of operation (dispersion), and size of enclosure. Any changes in the values of W, ε_r or h give rise to corresponding changes in Z_{0m} and ε_{re}.

Substrate properties, like surface finish, metallization thickness, and the fabrication process, determine the accuracy of fabrication of the strip width. In addition to the error in fabrication of the strip width, the thickness and the dielectric constant of the substrate have some manufacturing tolerances. All these factors contribute to variations in Z_{0m} and ε_{re} of the microstrip. Since it is very difficult to incorporate arrangements for post-fabrication adjustments in MICs, it is necessary to take into account the effect of tolerances at the design stage itself. However, unlike the effects of deterministic parameters like dispersion and strip thickness, the effect of tolerances cannot be incorporated exactly because of the uncertainty in Z_{0m} and ε_{re} arising from tolerances.

The effect of tolerances on the performance of a microstrip can be analyzed using the sensitivity approach. This approach is the easiest method of predicting

the worst case behavior corresponding to a given set of tolerances. It does not require the actual statistical distribution of tolerances. Only their maximum absolute values are needed. Sensitivity analysis is useful in situations where deviations in parameters can be considered incremental. This implies that the circuit characteristics should be slowly varying functions in the domain of parameter variation around the exact parameter values.

It has been observed that the maximum change in the characteristics of a microstrip due to tolerances can be evaluated using the equations

$$\frac{|\Delta Z_{0\mathrm{m}}|_{\max}}{Z_{0\mathrm{m}}} = \left|\frac{\Delta W}{W} S_W^{Z_{0\mathrm{m}}}\right| + \left|\frac{\Delta h}{h} S_h^{Z_{0\mathrm{m}}}\right| + \left|\frac{\Delta \varepsilon_{\mathrm{r}}}{\varepsilon_{\mathrm{r}}} S_{\varepsilon_{\mathrm{r}}}^{Z_{0\mathrm{m}}}\right| \tag{2.97}$$

and

$$\frac{|\Delta \varepsilon_{\mathrm{re}}|_{\max}}{\varepsilon_{\mathrm{re}}} = \left|\frac{\Delta W}{W} S_{\mathrm{W}}^{\varepsilon_{\mathrm{re}}}\right| + \left|\frac{\Delta h}{h} S_h^{\varepsilon_{\mathrm{re}}}\right| + \left|\frac{\Delta \varepsilon_{\mathrm{r}}}{\varepsilon_{\mathrm{r}}} S_{\varepsilon_{\mathrm{r}}}^{\varepsilon_{\mathrm{re}}}\right| \tag{2.98}$$

where ΔW, Δh, and $\Delta \varepsilon_{\mathrm{r}}$ are the tolerances in W, h, and ε_{r}, respectively. The sensitivity S_B^A is defined as

$$S_B^A = \frac{B}{A}\frac{\partial A}{\partial B} \tag{2.99}$$

The influence of tolerances can be reduced by using improved fabrication techniques and using substrates with better tolerances. The required fabrication accuracy for the strip width will be a function of the specified accuracy in transmission line characteristics and given tolerances in substrate parameters.

It can be determined from the equations

$$\left|S_{\mathrm{W}}^{Z_{0\mathrm{m}}}\right| \frac{|\Delta W|}{W} = \frac{|\Delta Z_{0\mathrm{m}}|}{Z_{0\mathrm{m}}} - \left|\frac{\Delta h}{h} S_{\mathrm{h}}^{Z_{0\mathrm{m}}}\right| - \left|\frac{\Delta \varepsilon_{\mathrm{r}}}{\varepsilon_{\mathrm{r}}} S_{\varepsilon_{\mathrm{r}}}^{Z_{0\mathrm{m}}}\right| \tag{2.100}$$

$$\left|S_{\mathrm{W}}^{\varepsilon_{\mathrm{re}}}\right| \frac{|\Delta W|}{W} = \frac{|\Delta \varepsilon_{\mathrm{re}}|}{\varepsilon_{\mathrm{re}}} - \left|\frac{\Delta h}{h} S_h^{\varepsilon_{\mathrm{re}}}\right| - \left|\frac{\Delta \varepsilon_{\mathrm{r}}}{\varepsilon_{\mathrm{r}}} S_{\varepsilon_{\mathrm{r}}}^{\varepsilon_{\mathrm{re}}}\right| \tag{2.101}$$

The required fabrication accuracy for the strip width is the minimum of the two values of ΔW obtained from the above equations. The fabrication accuracy of h or tolerance in ε_{r} can be determined in a similar manner provided that the tolerances for the other two parameters are known.

Expressions for the sensitivity of microstrip characteristics (Z_{0m} and $\varepsilon_{\mathrm{re}}$) with respect to various parameters (for example, W, h, and ε_{r}) can be calculated using the closed-form expressions for Z_{0m} and $\varepsilon_{\mathrm{re}}$ given by Schneider [19] and the definition of sensitivity given in (2.99). Various sensitivities may thus be written as

$$\begin{aligned} S_W^{Z_{0\mathrm{m}}} = -S_h^{Z_{0\mathrm{m}}} = \frac{-1}{Z_{0\mathrm{m}}\sqrt{\varepsilon_{\mathrm{re}}}} \Bigg\{ & \frac{60\left(8h/W - W/4h\right)}{8h/W + W/4h} \\ & + 1.25 Z_{0\mathrm{m}} \frac{\varepsilon_{\mathrm{r}} - 1}{\sqrt{\varepsilon_{\mathrm{re}}}} \frac{h/W}{\left(1 + 10h/W\right)^{3/2}} \Bigg\} \quad \text{for } \left(W/h \le 1\right) \end{aligned} \tag{2.102}$$

$$S_W^{Z_{0m}} = -S_h^{Z_{0m}} = -\left[\frac{Z_{0m}\sqrt{\varepsilon_{re}}}{120\pi} \left\{ \frac{W}{h} + 0.44\frac{h}{W} + 6\frac{h}{W}\left(1 - \frac{h}{W}\right)^5 \right\} + 1.25\frac{\varepsilon_r - 1}{\varepsilon_{re}} \frac{h/W}{(1 + 10h/W)^{3/2}} \right] \quad \text{for } (W/h \geq 1) \tag{2.103}$$

$$S_W^{\varepsilon_{re}} = -S_h^{\varepsilon_{re}} = \frac{2.5}{W/h}\frac{\varepsilon_r - 1}{\varepsilon_{re}}(1 + 10h/W)^{-\frac{3}{2}} \tag{2.104}$$

$$S_{\varepsilon_r}^{Z_{0m}} = -0.25\frac{\varepsilon_r}{\varepsilon_{re}}\left[1 + (1 + 10h/W)^{-\frac{1}{2}}\right] \tag{2.105}$$

$$S_{\varepsilon_r}^{\varepsilon_{re}} = 0.5\frac{\varepsilon_r}{\varepsilon_{re}}\left[1 + (1 + 10h/W)^{-\frac{1}{2}}\right] \tag{2.106}$$

The sensitivity curves for impedance and effective dielectric constants are shown in Figure 2.14 and Figure 2.15, respectively, for $\varepsilon_r = 9.7$.

The sensitivity values thus obtained are used in (2.97) to determine the maximum change in Z_{0m}. From $(\Delta Z_{0m})_{max}$ the maximum value of VSWR is obtained using the relation

$$\text{VSWR} = \left[1 - \frac{|\Delta Z_{0m}|_{max}}{Z_{0m}}\right]^{-1} \tag{2.107}$$

It may be observed from (2.97) that there is a tradeoff between tolerances; that is, the tolerance value for one parameter can be increased or decreased at the cost of other parameters. This helps in the optimum use of fabrication technologies.

The effect of tolerances on the characteristics of a microstrip has been compared with the effects of finite thickness of metal strip, dispersion, discontinuity, and an imperfect measurement system and is detailed later in Section 2.4.5.

2.4.4 Effect of Dielectric Anisotropy

Some of the dielectric substrates used for microstrip circuits exhibit anisotropy in permittivity. The most common examples are sapphire (especially when single crystal) and Epsilam-10 (trade name for a ceramic-loaded resin). In both these cases, the substrates are manufactured such that one of the principal axes of the permittivity tensor is perpendicular to the dielectric interface $y = h$. If there were no fringing electric fields (in microstrip configuration), all the field lines would coincide with this axis, and the capacitance is determined by the value of permittivity in this direction. In such a case there is no effect of anisotropy.

If the line parameters are to be independent of line orientation in the xz-plane, the permittivity tensor in the x- and z-directions must be equal. For sapphire we take $\varepsilon_x = \varepsilon_z = 11.6$ and $\varepsilon_y = 9.4$, whereas for Epsilam-10 $\varepsilon_x = \varepsilon_z = 15.0$ and $\varepsilon_y = 10.0$.

Quasi-static analysis of a microstrip on anisotropic substrates has been carried out by using the finite difference method [39] and also by using a transformation

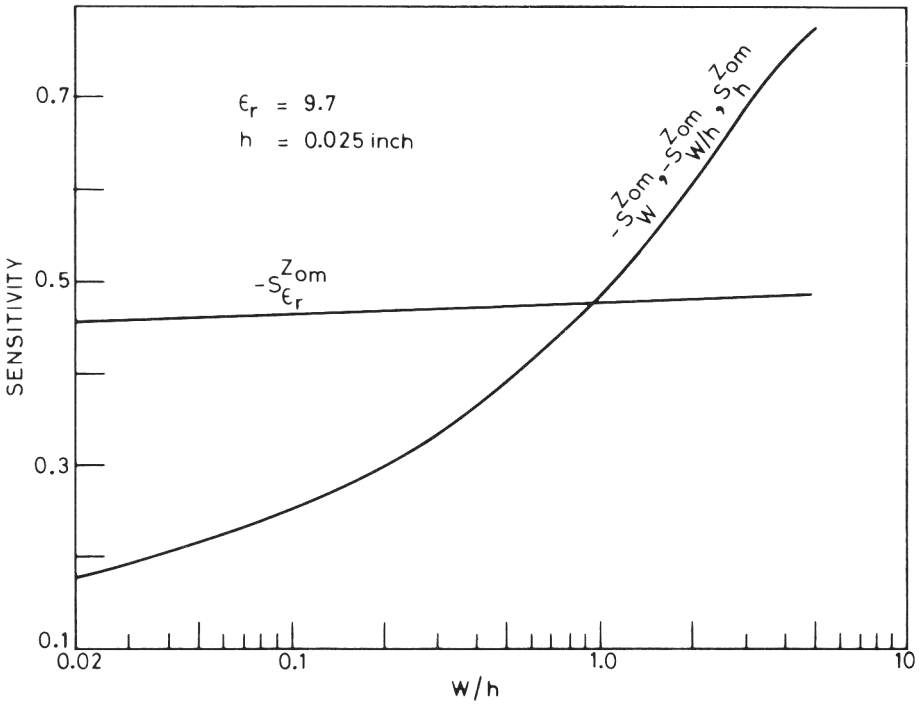

Figure 2.14 Sensitivity of microstrip impedance with respect to *W*, *h*, and ε_r (from [38], © 1978 IEEE. Reprinted with permission.).

[40] that enables the capacitance for anisotropic substrates to be derived from microstrip formulas for isotropic substrates.

Finite Difference Method [39]

This method is a straightforward solution of the Laplace equation by finite difference techniques. When the dielectric is anisotropic, the Laplace equation may be written

$$\varepsilon_x \frac{\partial^2 \phi(x,y)}{\partial x^2} + \varepsilon_y \frac{\partial^2 \phi(x,y)}{\partial y^2} = 0 \tag{2.108}$$

In finite difference form this may be written as follows for all net points in the dielectric material (see Figure 1.9)

$$\varepsilon_x(\phi_B + \phi_A) + \varepsilon_y(\phi_D + \phi_C) - 2(\varepsilon_x + \varepsilon_y)\phi_p = 0 \tag{2.109}$$

and when the point P lies on the dielectric-air interface

$$\frac{1}{2}(1 + \varepsilon_x)(\phi_B + \phi_A) + \phi_D + \varepsilon_y\phi_C - (2 + \varepsilon_x + \varepsilon_y)\phi_p = 0 \tag{2.110}$$

The rest of the procedure for evaluating capacitances is the same as outlined in Section 1.2.2.

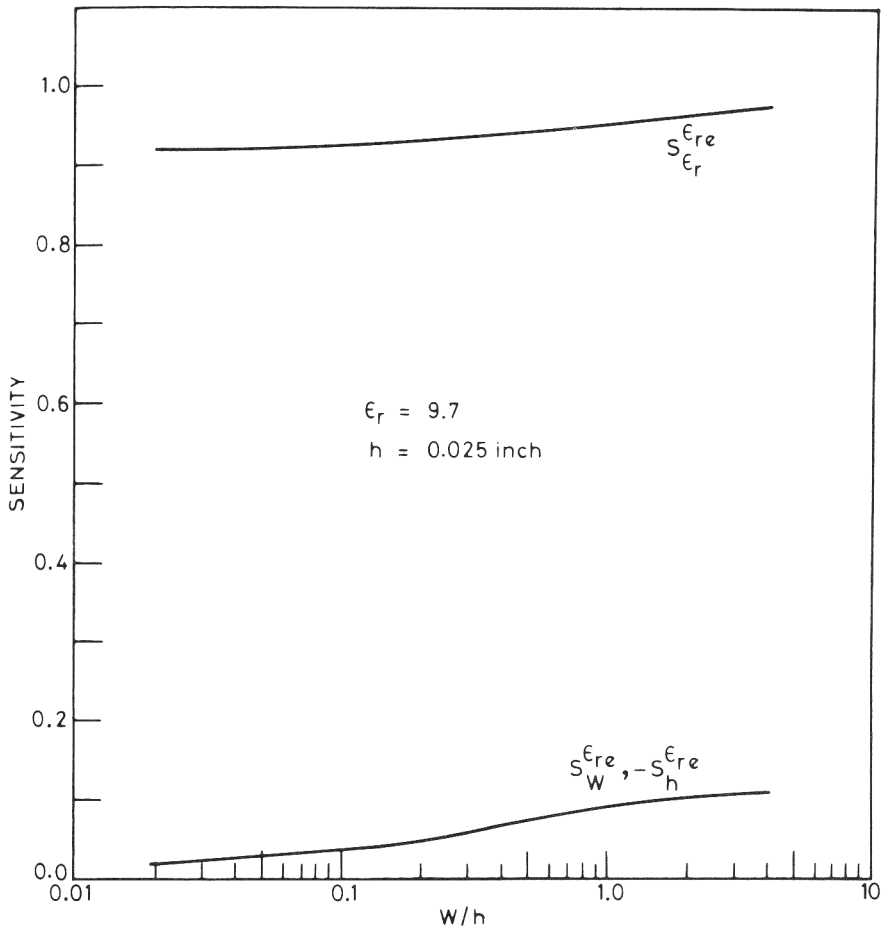

Figure 2.15 Sensitivity of the effective dielectric constant of a microstrip with respect to *W*, *h*, and ε_r (from [38], © 1978 IEEE. Reprinted with permission.).

Transform Method [40]

A simple, but rigorous transformation that converts the anisotropic electrostatic field into an isotropic one with similar shape has been reported by Szentkuti [40]. This transformation may be described as follows.

For the substrate ($y \le h$) let

$$\overline{x} = x,\ \overline{y} = y\sqrt{(\varepsilon_x/\varepsilon_y)} \text{ that is, } \overline{h} = h\sqrt{(\varepsilon_x/\varepsilon_y)} \tag{2.111}$$

$$\overline{\varepsilon}_r = \overline{\varepsilon}_x = \overline{\varepsilon}_y = \sqrt{(\varepsilon_x \varepsilon_y)} \tag{2.112}$$

Potentials and their derivatives at the original and transformed points (P and $\bar{P}$) are related by

$$\phi_p = \overline{\phi}_{\overline{p}} \tag{2.113}$$

$$\partial\phi_p/\partial y = \sqrt{\varepsilon_x/\varepsilon_y}\left(\partial\overline{\phi}_{\overline{p}}/\partial\overline{y}\right) \tag{2.114}$$

Expressing (2.108) in terms of $\bar{x}$ and $\bar{y}$ leads to an isotropic Laplace equation for $\phi(\bar{x}, \bar{y})$. Also

$$E_x = -\partial\bar{\phi}/\partial\bar{x} = \bar{E}_{\bar{x}} \qquad D_y = -\bar{\varepsilon}_r\varepsilon_0\,\partial\bar{\phi}\,/\,\partial\bar{y} = \bar{D}_{\bar{y}} \tag{2.115}$$

Thus we note that: (i) values of the tangential component of **E** and the normal component of flux at the interface $y = h$ are not affected by the transformation, (ii) all potential and charges are not altered within the region $y \leq h$, and (iii) the potential of the transformed ground plane is conserved. Therefore, capacitances of the original anisotropic and the transformed isotropic structures are equal.

Effective dielectric constants for anisotropic substrates are compared with the corresponding values for isotropic substrates ($\varepsilon_r = \varepsilon_y$) as a function of W/h in Figure 2.16. We note that considerable difference exists for thin lines (small W/h), whereas the two results tend to identical values as W/h increases. This can be explained by noting that the fringing field values are larger for narrow strips, and it is only the E_x component of the fringing field that is affected by ε_x.

2.4.5 Design Equations

The numerical methods for the characterization of microstrip lines discussed so far involve extensive computations. Closed-form expressions are necessary for the optimization and computer-aided-design of microstrip circuits. A complete set of design equations for a microstrip is presented in this section. This includes closed

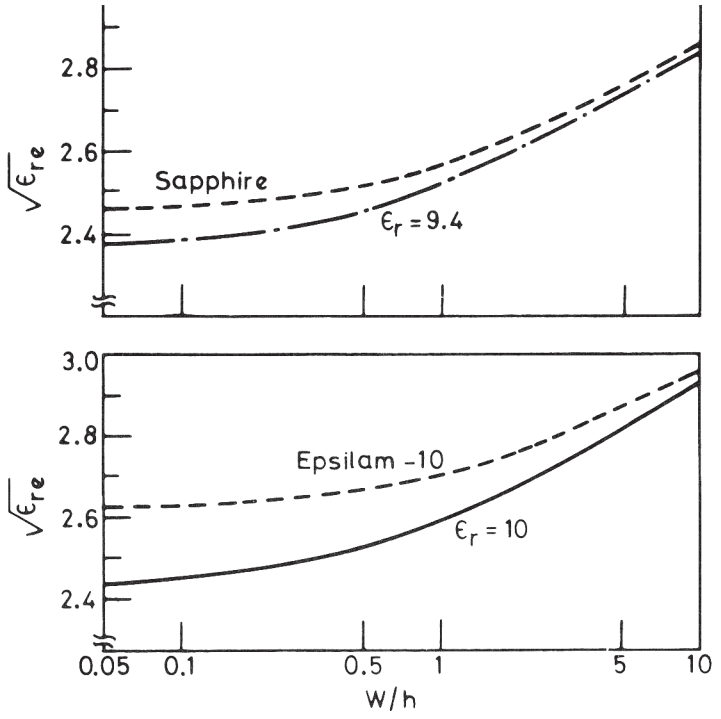

Figure 2.16 Effect of dielectric anisotropy on effective dielectric constants of microstrip lines on sapphire ($\varepsilon_x = \varepsilon_z = 11.6$, $\varepsilon_y = 9.9$) and Epsilam-10 substrates (from [40], © 1976 IEE (U.K.). Reprinted with permission.).

form expressions for the characteristic impedance and effective dielectric constant and their variation with metal strip thickness, enclosure size, and dispersion. Expressions for microstrip loss and quality factor Q are also described.

Characteristic Impedance and Effective Dielectric Constant

Closed-form expressions for Z_{0m} and ε_{re} have been reported by Wheeler [41], Schneider [19], and Hammerstad [42]. Wheeler and Hammerstad have also given synthesis expressions for Z_{0m}. The closed-form expressions based on the works of Wheeler and Schneider are given [42] as

$$Z_{0m} = \frac{\eta}{2\pi\sqrt{\varepsilon_{re}}}\ell n\left(\frac{8h}{W} + 0.25\frac{W}{h}\right) \qquad \left(\frac{W}{h} \le 1\right) \tag{2.116a}$$

$$Z_{0m} = \frac{\eta}{\sqrt{\varepsilon_{re}}}\left\{\frac{W}{h} + 1.393 + 0.667\ell n\left(\frac{W}{h} + 1.444\right)\right\}^{-1} \tag{2.116b}$$

where $\eta = 120\pi\Omega$

$$\varepsilon_{re} = \frac{\varepsilon_r + 1}{2} + \frac{\varepsilon_r - 1}{2}F(W/h) \tag{2.117}$$

$$F(W/h) = \begin{cases} (1 + 12h/W)^{-1/2} + 0.04(1 - W/h)^2 & (W/h) \le 1 \\ (1 + 12h/W)^{-1/2} & (W/h) \ge 1 \end{cases}$$

Hammerstad [43] noted that the maximum relative error in ε_{re} and Z_{0m} is less than 1 percent. The expressions for W/h in terms of Z_{0m} and ε_r are as follows. For $Z_{0m}\sqrt{\varepsilon_{re}} > 89.91$, that is, $A > 1.52$

$$W/h = \frac{8\exp(A)}{\exp(2A) - 2} \tag{2.118a}$$

for $Z_{0m}\sqrt{\varepsilon_{re}} \le 89.91$, that is, $A \le 1.52$

$$W/h = \frac{2}{\pi}\left\{B - 1 - \ell n(2B - 1) + \frac{\varepsilon_r - 1}{2\varepsilon_r}\left[\ell n(B - 1) + 0.39 - \frac{0.61}{\varepsilon_r}\right]\right\} \tag{2.118b}$$

where

$$A = \frac{Z_{0m}}{60}\left\{\frac{\varepsilon_r + 1}{2}\right\}^{1/2} + \frac{\varepsilon_r - 1}{\varepsilon_r + 1}\left\{0.23 + \frac{0.11}{\varepsilon_r}\right\}$$

$$B = \frac{60\pi^2}{Z_{0m}\sqrt{\varepsilon_r}}$$

These expressions also provide an accuracy better than one percent.

A more accurate expression for the characteristic impedance Z_{0m}^a of a microstrip for $t = 0$ and $\varepsilon_r = 1$ is given by [44]

$$Z_{0m}^a = \frac{\eta}{2\pi}\ell n\left[\frac{f(u)}{u} + \sqrt{1 + \left(\frac{2}{u}\right)^2}\right] \tag{2.119}$$

where

$$f(u) = 6 + (2\pi - 6)\exp\left[-\left(\frac{30.666}{u}\right)^{0.7528}\right] \tag{2.120}$$

and $u = W/h$ and $\eta = 120\pi\ \Omega$. The accuracy of this expression is better than 0.01 percent for $u \le 1$ and 0.03 percent for $u \le 1000$. The effective dielectric constant ε_{re} may be expressed as

$$\varepsilon_{re} = \frac{\varepsilon_r + 1}{2} + \frac{\varepsilon_r - 1}{2}\left(1 + \frac{10}{u}\right)^{-a(u)b(\varepsilon_r)} \tag{2.121}$$

$$a(u) = 1 + \frac{1}{49}\ell n\left(\frac{u^4 + (u/52)^2}{u^4 + 0.432}\right) + \frac{1}{18.7}\ell n\left[1 + \left(\frac{u}{18.1}\right)^3\right] \tag{2.122a}$$

$$b(\varepsilon_r) = 0.564\left(\frac{\varepsilon_r - 0.9}{\varepsilon_r + 3}\right)^{0.053} \tag{2.122b}$$

The accuracy of this model is better than 0.2 percent for $\varepsilon_r \le 128$ and $0.01 \le u \le 100$. Finally, the characteristic impedance is

$$Z_{0m} = \frac{Z_{0m}^a}{\sqrt{\varepsilon_{re}}} \tag{2.123}$$

The results discussed above are based on the assumption that the thickness of the strip conductor is negligible. But, in practice, the strip has a finite thickness t that affects the characteristics.

Effect of Strip Thickness

The effect of strip thickness on Z_{0m} and ε_{re} of microstrip lines has been reported by a number of investigators [19, 31, 41, 44–54]. Simple and accurate formulas for Z_{0m} and ε_{re} with finite strip thickness are [31]

$$Z_{0m} = \frac{\eta}{2\pi\sqrt{\varepsilon_r}}\ell n\left\{\frac{8h}{W_e} + 0.25\frac{W_e}{h}\right\} \qquad (W/h \le 1) \tag{2.124a}$$

$$Z_{0m} = \frac{\eta}{\sqrt{\varepsilon_{re}}}\left\{\frac{W_e}{h} + 1.393 + 0.667\ell n\left(\frac{W_e}{h} + 1.444\right)\right\}^{-1} \quad (Wh \ge 1) \tag{2.124b}$$

where

$$\frac{W_e}{h} = \frac{W}{h} + \frac{1.25}{\pi}\frac{t}{h}\left(1 + \ell n\frac{4\pi W}{t}\right) \qquad (W/h \le 1/2\pi) \tag{2.125a}$$

$$\frac{W_e}{h} = \frac{W}{h} + \frac{1.25}{\pi}\frac{t}{h}\left(1 + \ell n\frac{2h}{t}\right) \quad (W/h \ge 1/2\pi) \tag{2.125b}$$

$$\varepsilon_{re} = \frac{\varepsilon_r + 1}{2} + \frac{\varepsilon_r - 1}{2}F(W/h) - C \tag{2.126}$$

in which

$$C = \frac{\varepsilon_r - 1}{4.6} \frac{t/h}{\sqrt{W/h}} \tag{2.127}$$

It can be observed that the effect of thickness on Z_{0m} and ε_{re} is insignificant for small values of t/h. This agrees with the experimental results reported in [45] for $t/h \leq 0.005$, $2 \leq \varepsilon_r \leq 10$, and $W/h \geq 0.1$. However, the effect of strip thickness is significant on conductor loss in the microstrip line.

Effect of Enclosure

Most microstrip circuit applications require a metallic enclosure for hermetic sealing, mechanical strength, electromagnetic shielding, mounting connectors, and ease of handling. The effect of the top cover alone [55–57] as well as of the top cover and side walls [51, 58] has been reported in the literature. Both the top cover and side walls tend to lower impedance and effective dielectric constant. This is because the fringing flux lines are prematurely terminated on the enclosure walls. This increases the electric flux in air. The closed-form equations for a microstrip with top cover (without side walls) are obtained as [56, 57]

$$Z_{0m}^a = Z_{0\infty}^a - \Delta Z_{0m}^a \tag{2.128a}$$

where $Z_{0\infty}^a$ is the characteristic impedance with infinite shield height and superscript a designates air as dielectric. The decrease in impedance ΔZ_{0m}^a is given by

$$\Delta Z_{0m}^a = \begin{cases} P & \text{for } W/h \leq 1 \\ P \cdot Q & \text{for } W/h \geq 1 \end{cases} \tag{2.128b}$$

where

$$P = 270\left[1 - \tanh\left(0.28 + 1.2\sqrt{\frac{h'}{h}}\right)\right]$$

$$Q = 1 - \tanh^{-1}\left(\frac{0.48\sqrt{W/h - 1}}{\left(1 + h'/h\right)^2}\right)$$

and h' is the height of the top cover above the strip conductor. In this expression, the distance between the ground plane and the top cover is $h + h'$. The effective dielectric constant is calculated from the concept of the filling factor q as

$$\varepsilon_{re} = \frac{\varepsilon_r + 1}{2} + q\frac{\varepsilon_r - 1}{2} \tag{2.129a}$$

$$q = (q_\infty - q_T)q_c \tag{2.129b}$$

where

$$q_\infty - q_T = \left(1 + \frac{10}{u}\right)^{-a(u)b(\varepsilon_r)}$$

$$q_T = \frac{2}{\pi}\frac{\ell n 2}{\sqrt{W/h}}\frac{t}{h}$$

$$q_c = \tanh\left(1.043 + 0.121\frac{h'}{h} - 1.164\frac{h}{h'}\right)$$

and $a(u)$ and $b(\varepsilon_r)$ are obtained from (2.122).

Using the preceding equations, the characteristic impedance of the shielded microstrip can be calculated from $Z_{0m} = Z_{0m}^a/\sqrt{\varepsilon_{re}}$.

For the range of parameters, $1 \le \varepsilon_r \le 30$, $0.05 \le W/h \le 20$, $t/h \le 0.1$, and $1 < h'/h < \infty$, the maximum error in Z_{0m} and ε_{re} is found to be less than ±1 percent.

When $h'/h \ge 5$, the effect of the top cover on the microstrip characteristics becomes negligible.

Effect of Dispersion

The effect of frequency (dispersion) on ε_{re} has been described, accurately by the dispersion models given by Getsinger [59], Edwards and Owens [60], Kirschning and Jansen [61], and Kobayashi [62], as discussed in Section 1.3. The effect of frequency on Z_{0m} has been described by several investigators [3, 29, 30, 44, 63]. The accurate expressions of Hammerstad and Jensen [44] for $Z_{0m}(f)$ and Kobayashi [62] for $\varepsilon_{re}(f)$ are

$$Z_{0m}(f) = Z_{0m}\frac{\varepsilon_{re}(f) - 1}{\varepsilon_{re} - 1}\sqrt{\frac{\varepsilon_{re}}{\varepsilon_{re}(f)}} \tag{2.130}$$

$$\varepsilon_{re}(f) = \varepsilon_r - \frac{\varepsilon_r - \varepsilon_{re}}{1 + (f/f_{50})^m} \tag{2.131}$$

where

$$f_{50} = \frac{f_{k,TM_0}}{0.75 + \{0.75 - (0.332/\varepsilon_r^{1.73})\}W/h}$$

$$f_{k,TM_0} = \frac{c\tan^{-1}\left(\varepsilon_r\sqrt{\dfrac{\varepsilon_{re} - 1}{\varepsilon_r - \varepsilon_{re}}}\right)}{2\pi h\sqrt{\varepsilon_r - \varepsilon_{re}}}$$

$$m = m_0 m_c$$

$$m_0 = 1 + \frac{1}{1 + \sqrt{W/h}} + 0.32\left(\frac{1}{1 + \sqrt{W/h}}\right)^3$$

$$m_c = \begin{cases} 1 + \dfrac{1.4}{1 + W/h}\left\{0.15 - 0.235\exp\left(\dfrac{-0.45f}{f_{50}}\right)\right\} & \text{for } W/h \le 0.7 \\ 1 & \text{for } W/h > 0.7 \end{cases}$$

Z_{0m}, ε_{re} are the quasi-static values obtained earlier, and c is the velocity of light.

Losses

Closed-form expressions for total loss have been reported in the literature [18, 19, 64]. An expression for loss, derived using (2.124) to (2.127), may be written as

$$\alpha_T = \alpha_c + \alpha_d \tag{2.132}$$

The two components α_c and α_d are given by

$$\alpha = \begin{cases} 1.38A\dfrac{R_s}{hZ_{0m}}\dfrac{32-(W_e/h)^2}{32+(W_e/h)^2} & \text{dB/unit length } (W/h \le 1) \\ 6.1\times10^{-5}A\dfrac{R_sZ_{0m}\varepsilon_{re}(f)}{h}\left[W_e/h+\dfrac{0.667W_e/h}{W_e/h+1.444}\right] & \text{dB/unit length } (W/h \ge 1) \end{cases} \tag{2.133}$$

and

$$\alpha_d = \begin{cases} 4.34\eta\sigma\dfrac{\varepsilon_{re}(f)-1}{\sqrt{\varepsilon_{re}(f)}\,(\varepsilon_r-1)} & \text{dB/ unit length} \\ 27.3\dfrac{\varepsilon_r}{\varepsilon_r-1}\dfrac{\varepsilon_{re}(f)-1}{\sqrt{\varepsilon_{re}(f)}}\dfrac{\tan\delta}{\lambda_0} & \text{dB/unit length} \end{cases} \tag{2.134}$$

where

$$A = 1+\frac{h}{W_e}\left\{1+\frac{1.25}{\pi}\ell n\frac{2B}{t}\right\}$$

$R_s = \sqrt{\pi f\mu_0\rho_c}$; ρ_c = resistivity of the strip coductor
$\sigma = \omega\varepsilon_0\varepsilon_r\tan\delta$ = conductivity of the dielectric substrate;

and

$$B = \begin{cases} h & \left(W/h \ge \dfrac{1}{2\pi}\right) \\ 2\pi W & \left(W/h \le \dfrac{2}{2\pi}\right) \end{cases}$$

Effect of Surface-Roughness of Conductor on Loss

In general, the metallization on the substrate is not smooth and may result in increased conductor loss. The undulations or roughness of metal surface depends on the roughness of the substrate and the technique used to metallize the substrate. The rough metal surface can be modeled as a surface with triangular grooves, with groove depth varying randomly, and can be characterized by rms depth. The current flowing across the grooves will therefore travel a larger distance compared to the smooth surface, resulting in an increased conductor loss. When the rms depths are small compared with the skin depth, the surface finish of conductors has lit-

tle effect on the conductor loss. If the rms depth has dimensions comparable with the skin depth, the additional loss becomes significant depending on the direction of roughness (grooves). The adverse effect on the loss of grooves parallel to the conductor current is much less than that produced by transverse grooves of similar size. The surface roughness of the conductor equivalently increases the surface resistance beyond the intrinsic value obtained for optimally flat and pure conductor surfaces. The effect of surface roughness on the conductor loss may easily be calculated by replacing R_S in (2.133) with R_s^s, which is given below [18]:

$$R_s^s = R_S\left\{1+\frac{2}{\pi}\tan^{-1}\left[1.4\left(\frac{\Delta}{\delta}\right)^2\right]\right\} \tag{2.135}$$

where δ is the skin depth and Δ is the rms surface roughness. Since, at millimeter wavelengths, the skin depth is only a few tenths of a micron, the surface roughness must be preserved at less than 0.1 μm in order to keep conductor loss low in the microstrip.

The dielectric loss is normally very small compared with the conductor loss for dielectric substrates. The dielectric loss in silicon substrates (used for RFICs), however, is usually of the same order or even larger than the conductor loss. This is because of the lower resistivity available in silicon wafers. However, higher resistivity can be obtained in GaAs, and therefore the dielectric loss is lower for this material. Values of conductor and dielectric losses per unit length for 50-Ω microstrip lines on various substrates (dielectric as well as semiconductor) are plotted in Figure 2.11 (in Section 2.4.1) as functions of frequency. At a given frequency the total loss can be obtained by adding the two values.

Figure 2.17 compares the total loss for 50-Ω microstrip lines on RT/duroid, quartz, and alumina substrates. At the same h/λ_0 ratio, high dielectric constant substrates result in greater loss.

Microstrip loss data presented above require that the conductor thickness be greater than about four times the skin depth. The microstrip conductor loss calculation for any metalization thickness has been reported by Lee and Itoh [65] based on the phenomenological loss equivalence method and by Faraji-Dana and Chow [66, 67] based on ac resistance. Faraji-Dana and Chow's calculated conductor loss data for thick conductors agree very well with the calculated results obtained using expressions reported by Pucel et al. [18]. Aksun and Morkoc [68] have reported dielectric loss results for microstrip substrates. consisting of different GaAs layer thicknesses on an Si substrate.

In order to reduce insertion loss in the microstrip matching networks, a ridged microstrip structure, as shown in Figure 2.18, has been used [69]. In this structure, the strip conductor is fabricated on a thin polyimide dielectric (ε_{rd} = 3.2) layer, which is placed on top of the GaAs substrate. The electric flux lines in this case are more in the air, and the structure resembles a suspended microstrip line, which has much lower insertion loss than the conventional microstrip. The loss has been reported to be reduced by a factor of two [69] by placing 14-μm thick polyimide between the conductor and the 125-μm thick GaAs substrate.

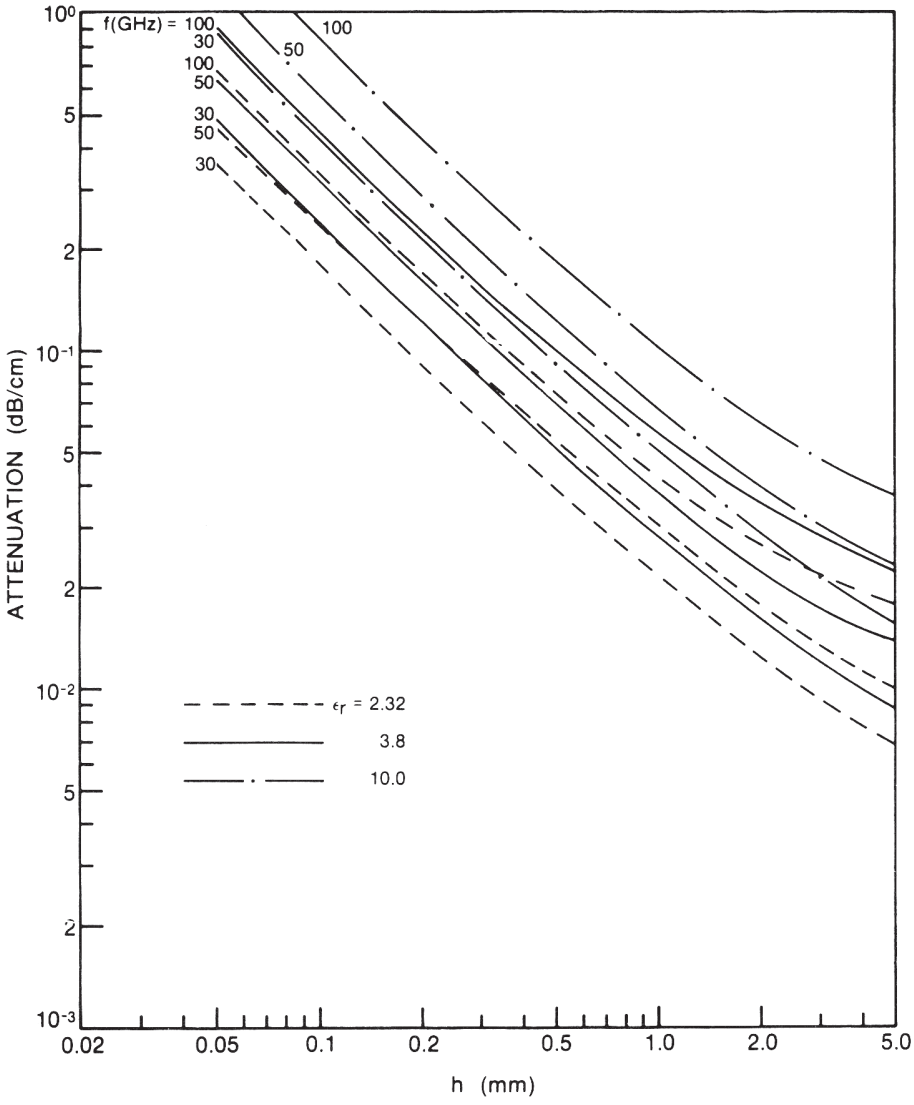

Figure 2.17 Total loss versus substrate thickness (h) for RT/Duroid ($\varepsilon_r = 2.32$), Quartz ($\varepsilon_r = 3.8$), and Alumina ($\varepsilon_r = 10.0$) at various frequencies.

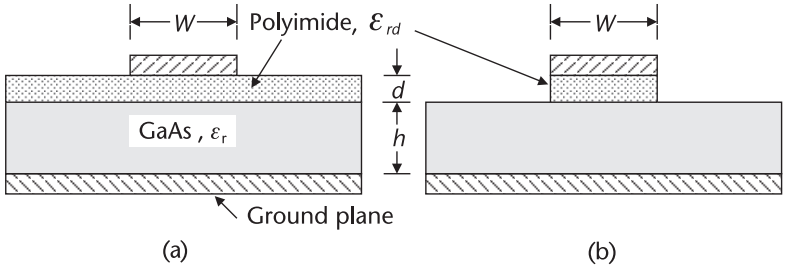

Figure 2.18 Low-loss microstrip configurations. (a) Multilayer and (b) ridged.

Quality Factor Q

The quality factor, Q, of a microstrip can be related to the total loss in the line by [70]

$$Q_T = \frac{\beta}{2\alpha_T} \tag{2.136}$$

where Q_T is the total Q of the resonator (quarter wavelength), α_T is the total loss in the resonator, and $\beta = 2\pi/\lambda_m$. When losses in a resonant line are considered, another loss factor, α_r due to radiation at the open-end discontinuities must also be taken into account [70, 71]. The corresponding radiation Q-factor is given by [70]

$$Q_r = \frac{Z_{0m}}{480\pi(h/\lambda_0)^2 R} \tag{2.137a}$$

where

$$R = \frac{\varepsilon_{re}(f)+1}{\varepsilon_{re}(f)} - \frac{\left[\varepsilon_{re}(f)-1\right]^2}{2\left[\varepsilon_{re}(f)\right]^{3/2}} \ell n\left\{\frac{\sqrt{\varepsilon_{re}(f)}+1}{\sqrt{\varepsilon_{re}(f)}-1}\right\} \tag{2.137b}$$

Note that the effect of dispersion is considered, as described by (2.131).

The total Q of the resonator can be expressed by

$$\frac{1}{Q_T} = \frac{1}{Q_c} + \frac{1}{Q_d} + \frac{1}{Q_r} \tag{2.138}$$

Here, Q_c, Q_d, and Q_r are the quality factors corresponding to conductor, dielectric, and radiation losses, respectively. Finally, the circuit quality factor, Q_0, is defined as

$$\frac{1}{Q_0} = \frac{1}{Q_c} + \frac{1}{Q_d} = \frac{\lambda_0\left(\alpha_c + \alpha_d\right)}{\pi\sqrt{\varepsilon_{re}(f)}} \tag{2.139}$$

The variation with frequency of Q_0, Q_r, and Q_T for a quarter-wave resonator on GaAs, alumina, and quartz substrates is shown in Figure 2.19. A quarter-wave 50-Ω resonator on a 25-mil-thick alumina substrate has a Q_0 of about 240 at 2.0 GHz and 550 at 10.0 GHz, whereas Q_T is 230 at 2.0 GHz and nearly 160 at 10.0 GHz. This is due to the fact that the radiation losses are higher than conductor and dielectric losses at higher frequencies. On the other hand, a quarter-wave 50-Ω resonator on a 10-mil GaAs substrate has Q_0 of about 82 at 2.0 GHz and 160 at 10.0 GHz, whereas Q_T is 82 at 2.0 GHz and nearly 145 at 10.0 GHz. This is explained by smaller radiation losses for thin substrates. Thus, the commonly accepted rule that thick substrates should be used for high Q circuits does not apply to microstrip lines because of high radiation losses incurred under this condition.

The variation, with substrate thickness, of the total Q for half-wave resonators on RT/duroid, quartz, and alumina is shown in Figure 2.20 for f = 30 GHz, 50 GHz, and 100 GHz. For a given frequency, there is an optimum substrate thickness at which the Q is maximum. This optimum value of h decreases with increasing frequency and decreasing dielectric constant value, mainly because of radiation.

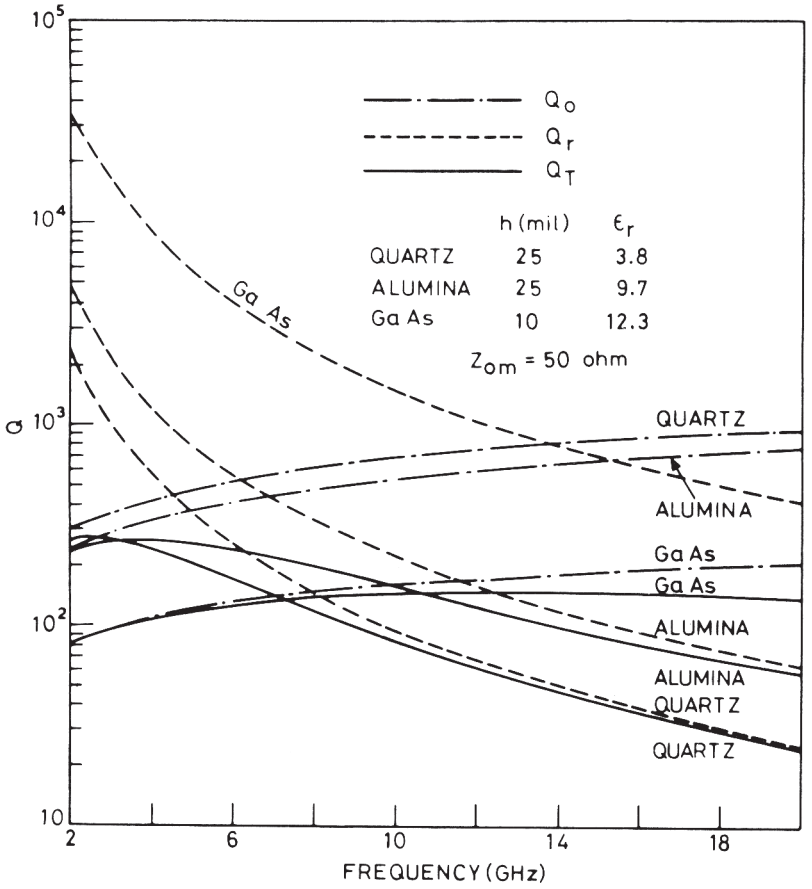

Figure 2.19 Variation of *Q*-factors with frequency for quarterwave microstrip resonators on Quartz, Alumina, and GaAs substrates.

Comparison of Various Factors Affecting Microstrip Characteristics

The effect of tolerances on the characteristics of a microstrip has been compared in [72] with the effects of finite thickness of a metal strip, dispersion, discontinuities, and an imperfect measurement system. These are included here as Tables 2.5 and 2.6 for a 50-Ω microstrip on alumina and polystyrene substrates, respectively.

It may be observed from the tables that the change in Z_{0m} is relatively higher due to the dimensional tolerances and the imperfect measurement system. For a microstrip on polystyrene substrate, the change in characteristics due to dimensional tolerances dominates the change due to other factors. However, at 10 GHz and for microstrip on alumina substrate, dispersion gives rise to the largest change in ε_{re}.

2.4.6 Frequency Range of Operation

The maximum frequency of operation of a microstrip is limited due to several factors such as excitation of spurious modes, higher losses, pronounced discontinuity effects, low Q due to radiation from discontinuities, effect of dispersion on pulse

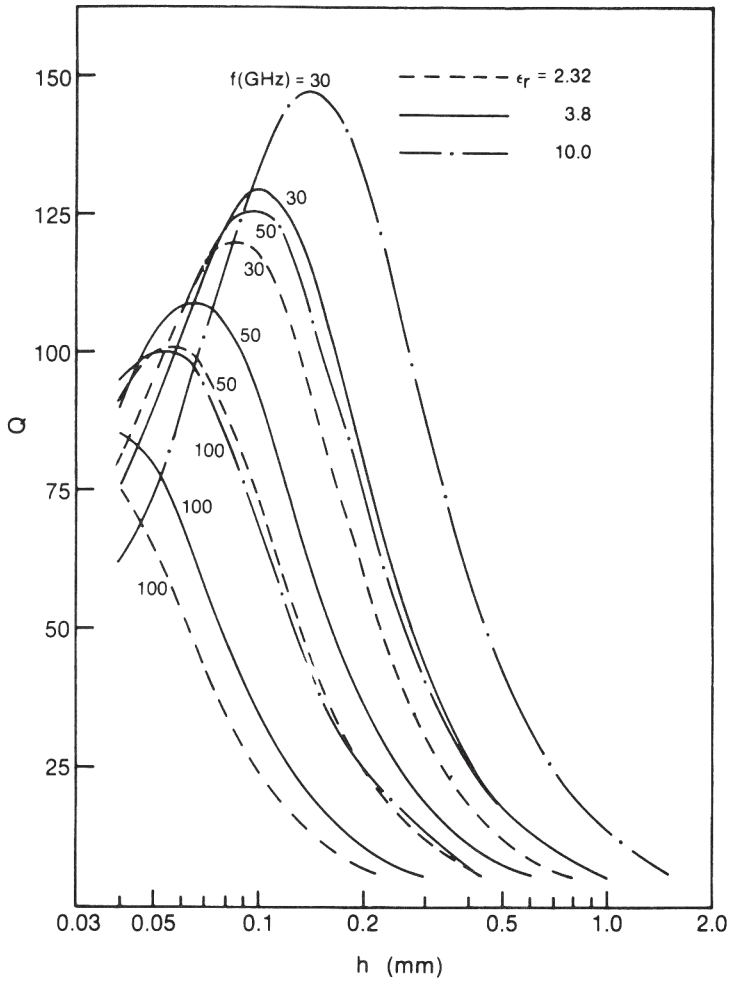

Figure 2.20 Total Q for a half-wave resonator on RT/Duroid ($\varepsilon_r = 2.32$), Quartz ($\varepsilon_r = 3.8$) and Alumina ($\varepsilon_r = 10.0$) versus substrate thickness.

distortion, tight fabrication tolerances, handling fragility, and, of course, technological processes. The frequency at which significant coupling occurs between the quasi-TEM mode and the lowest order surface wave spurious mode is given below [73].

$$f_T = \frac{150}{\pi h}\sqrt{\frac{2}{\varepsilon_r - 1}}\tan^{-1}(\varepsilon_r) \tag{2.140}$$

where f_T is in gigahertz and h is in millimeters. Thus the maximum thickness of the quartz substrate ($\varepsilon_r \cong 3.8$) for microstrip circuits designed at 100 GHz is less than 0.5 mm. The inverse tangent is expressed in radians.

Table 2.5 Change in the Characteristics of Microstrip on Alumina Substrate (Z_{0m} = 50 Ω, ε_r = 9.7, h = 0.025 in)

Effect of Various Factors		VSWR *(due to change in Z_{0m}*	$\Delta\varepsilon_{re}$
Effect of thickness	t/h = 0.004	1.013	– 0.029
(compared with t = 0 case)	t/h = 0.040	1.029	– 0.075
Effect of dispersion	f = 3 GHz	1.003	+ 0.033
(compared to quasi-static value)	f = 10 GHz	1.03	+ 0.303
Effect of dimensional tolerances	ΔW= ± 0.0002 in	≤ 1.037	≤ + 0.1919
($\Delta\varepsilon$ = ±0.25, Δh = ±0.001 in)	ΔW= ±0.0020 in	≤ 1.076	≤ + 0.2347
Effect of step discontinuity			
W_2/W_1 = 2.0 (W_1 = 0.025 in)	f = 3 GHz	1.008	
$C_{step} = 8.9 \times 10^{-3}$ pF	f = 10 GHz	1.028	—
Launchers, connectors, or	f = 3 GHz	1.065	—
transitions	f = 10 GHz	1.100	

Table 2.6 Change in the Characteristics of a Microstrip on Polystyrene Substrate (Z_{0m} = 50 Ω, ε_r = 2.55, h = 0.0625 in)

Effects of Various Factors		VSWR *(due to change in Z_{0m}*	$\Delta\varepsilon_{re}$
Effect of thickness	t/h = 0.022	1.009	– 0.004
(compared with t = 0 case)	t/h = 0.044	1.017	– 0.009
Effect of dispersion	f = 2 GHz	1.007	+ 0.011
(compared to quasi-static value)	f = 4 GHz	1.027	+ 0.043
Effect of dimensional tolerances	ΔW= ± 0.0001 in	≤ 1.097	≤ + 0.1596
($\Delta\varepsilon$ = ± 0.2, Δh = ± 0.005 in)	ΔW= ±0.0030 in	≤ 1.110	≤ + 0.1619
Effect of step discontinuity	f = 2 GHz	1.016	—
W_2/W_1 = 2.0	f = 4 GHz	1.032	—
$C_{step} = 2.66 \times 10^{-2}$ pF			
Launchers, connectors, or	f = 2 GHz	1.060	—
transitions	f = 4 GHz	1.070	—

The excitation of higher order modes in a microstrip can be avoided by operating it below the cut-off frequency of the first higher order mode, which is given approximately by [73].

$$f_c \cong \frac{300}{\sqrt{\varepsilon_r}(2W + 0.8h)} \tag{2.141}$$

where f_c is in gigahertz and W and h are in millimeters. This limitation is mostly applicable to low impedance lines that have wide microstrip conductors and/or thick substrates commonly used for microstrip patch antenna elements.

An infinitely long microstrip does not radiate as there is no coupling between the dominant mode and the higher order radiating modes. However, whenever there is some discontinuity in the line, namely an open end, slit, step in width, bend, or a gap, higher order radiating modes are excited, which depend upon the substrate thickness and frequency of operation. The operating frequency at which the radiation becomes significant may be calculated from the radiation Q factor of a $\lambda/2$ resonator, approximately given by

$$Q_r = \frac{3\varepsilon_r Z_{0m}\lambda_0^2}{32\eta h^2} \tag{2.142}$$

where $\eta = 120\pi$. Thus for thicker substrates, where $Q \cong Q_r$, the variation of Q is proportional to $1/(fh)^2$. For example, a 50-Ω resonator on a quartz substrate has a $Q_r \cong 0.4252 \times 10^4/(fh)^2$ where f is in gigahertz and h is in millimeters. At 100 GHz, the substrate thickness is less than 0.065 mm for Q_r greater than 100. A substrate thickness of this order results in attenuation on the order of 1 dB/cm. Thus not only do thin substrates give rise to high losses, but they are also difficult to handle and result in narrow conducting strips. Fabrication tolerances and technological processes such as photoetching limit the minimum strip width and the spacing between two adjacent strips in the case of coupled lines. High impedance lines of about 120 Ω require strip widths on the order of 0.02 mm on a 0.065-mm thick quartz substrate, thereby also setting a limit on the frequency of operation of microstrip lines because of low radiation Q_r.

On a microstrip, phase and group velocities are frequency dependent. Therefore, a digital pulse signal is distorted due to different velocities of the signals' frequency components. To minimize distortion, the dispersion effects must be minimized by keeping the fh product as small as possible.

2.4.7 Lumped Element Model of Microstrip Interconnect

Microstrip lines are integral parts of packaging and interconnect for high-speed electronics. In order to increase the transmission bandwidth of sub-nanosecond digital signals and enhance the simulation efficiency, a lumped element model of microstrip is needed. The lumped element equivalent-circuit model (unit cell) of a microstrip interconnect is shown in Figure 2.21. The equivalent-circuit parameters consist of series resistance ($\overline{\mathrm{R}}$), series inductance ($\overline{\mathrm{L}}$), shunt capacitance ($\overline{\mathrm{C}}$), and shunt conductance ($\overline{\mathrm{G}}$), all defined per unit length of the line. For the lumped element analysis of a distributed line, the line length ℓ is divided into small sections of length $\Delta\ell \ll \lambda$. The distributed parameters, characteristic impedance Z_{0m} and the propagation constant of the microstrip line, are related to the lumped parameters as

$$Z_{0m} = \sqrt{\frac{\overline{R} + j\omega\overline{L}}{\overline{G} + j\omega\overline{C}}} \tag{2.143a}$$

$$\gamma = \sqrt{\left(\overline{R} + j\omega\overline{L}\right)\left(\overline{G} + j\omega\overline{C}\right)} = \alpha + j\beta \tag{2.143b}$$

where α and β are the attenuation and phase constants, respectively.

Various methods [74–81] have been used to determine the lumped element model parameters of microstrip lines. They are based on empirical methods, measured S-parameters, quasi-static techniques, and full-wave methods.

In the empirical approach, one can extract the LE model parameters, such as inductance and capacitance, using closed form expressions given in Section 2.4.5 as follows:

$$\overline{L} = \frac{Z_{0m}\sqrt{\varepsilon_{re}}}{c} \tag{2.144a}$$

$$\overline{C} = \frac{\sqrt{\varepsilon_{re}}}{cZ_{0m}} \tag{2.144b}$$

where c is the velocity of electromagnetic waves in free space. Expressions for resistance and conductance are given as

$$\overline{R} = R_{dc} = \frac{1}{\sigma W t} \tag{2.145a}$$

$$\overline{R} = R_{rf} = \frac{1}{\sigma W \delta\left[1 - e^{-t/\delta}\right]\left[1 + t/W\right]} \tag{2.145b}$$

$$\overline{G} = \frac{2\pi f\sqrt{\varepsilon_{re}}}{\lambda_0 Z_{0m}} \tan\delta \tag{2.146a}$$

$$\delta = \frac{1}{\sqrt{\pi f \mu_0 \sigma}} \tag{2.146b}$$

where δ is the conductivity of the conductor metal and λ_0 is the free space wavelength.

In the S-parameter measurement method, several fabricated lines are tested and the LE model parameters are extracted. It starts with the extraction of characteristic impedances and propagation constants by using the following equations [79]:

$$e^{-\gamma\ell} = \left[\frac{1 - S_{11}^2 + S_{21}^2}{2S_{21}} \pm K\right]^{-1} \tag{2.147a}$$

$$K = \left[\frac{\left(S_{11}^2 - S_{21}^2 + 1\right)^2 - 4S_{11}^2}{4S_{11}^2}\right]^{0.5} \tag{2.147b}$$

$$Z_{0m} = Z_0\left[\frac{(1 + S_{11})^2 - S_{21}^2}{(1 - S_{11})^2 - S_{21}^2}\right]^{0.5} \tag{2.147c}$$

where Z_0 is the system or terminal impedance. From (2.143) and (2.147),

$$\overline{R} = \mathrm{Re}[\gamma Z_{0m}] \tag{2.148a}$$

$$\overline{L} = \mathrm{Im}[\gamma Z_{0m}]/\omega \tag{2.148b}$$

$$\overline{C} = \mathrm{Re}[\gamma / Z_{0m}]/\omega \tag{2.148c}$$

$$\overline{G} = \mathrm{Im}[\gamma / Z_{0m}] \tag{2.148d}$$

The next step is to use this data to modify the existing analytical expressions (2.144–2.146), by adding empirical corrections, to improve their accuracy.

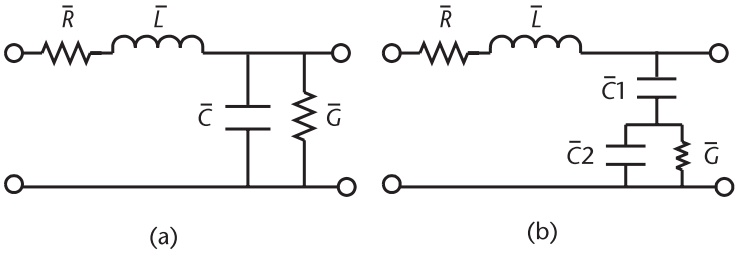

Figure 2.21 Lumped element equivalent of a microstrip interconnect: (a) single dielectric substrate and (b) oxide-silicon substrate.

The equivalent-circuit model parameters were also obtained by using quasi-static analysis of a microstrip line [78]. Closed form expressions for frequency-dependent resistance and inductance of microstrip were derived. The variations of resistance and inductance per unit length of a microstrip are shown in Figure 2.22. The line parameters are $W = 0.2$ mm, $h = 0.1$ mm, $t = 10$ μm, ground plane width = 2 mm, $\varepsilon_r = 4$, and copper conductors ($\sigma = 56$ MS/m). The dc resistance and inductance values of the line are 0.0982 Ω/cm and 4.392 nH/cm, respectively. These values become 0.1462 Ω/cm and 3.001 nH/cm at 100 MHz. Above 1 GHz, the resistance increases as $\sqrt{f}$ and the inductance becomes constant with frequency.

For silicon based interconnects shown in Figure 2.23, the LE model parameters are given as [77]:

$$\overline{L} = \mu_0 F(h + d, W) \tag{2.149a}$$

$$\overline{C}1 = \frac{\varepsilon_0 \varepsilon_{re}(\varepsilon_{rd}, d, W)}{F(d, W)} \tag{2.149b}$$

$$\overline{C}2 = \frac{\varepsilon_0 \varepsilon_{re}(\varepsilon_r, h, W)}{F(h, W)} \tag{2.149c}$$

$$\overline{G} = \frac{\sigma_{si}[1 + (1 + 10h/W)^{-0.5}]}{2F(h, W)} \tag{2.149d}$$

$$F(v, W) = \begin{cases} \ln(8v/W + W/4v)/2\pi & v/W \geq 1 \\ \left[W/v + 2.42 - 0.44v/W + (1 - v/W)^6 \right]^{-1} & v/W \leq 1 \end{cases} \tag{2.149e}$$

$$\varepsilon_{re}(\varepsilon_u, v, W) = \frac{\varepsilon_u + 1}{2} + \frac{\varepsilon_u - 1}{2(1 + 10v/W)^{0.5}} \tag{2.149f}$$

where v is a variable height and has a value of d, h, or $h + d$. The other variable u designates ε_r or ε_{rd}. The series resistance is calculated using (2.145). The capacitance value agrees with the measured data, however, for very narrow lines more accurate model is required [77].

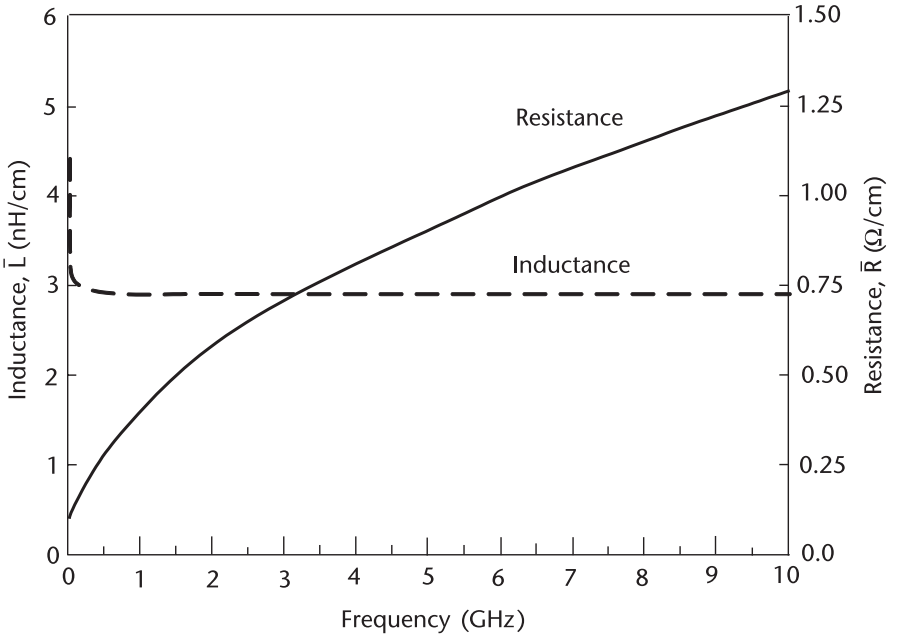

Figure 2.22 Variations of calculated resistance and inductance of a microstrip line versus frequency.

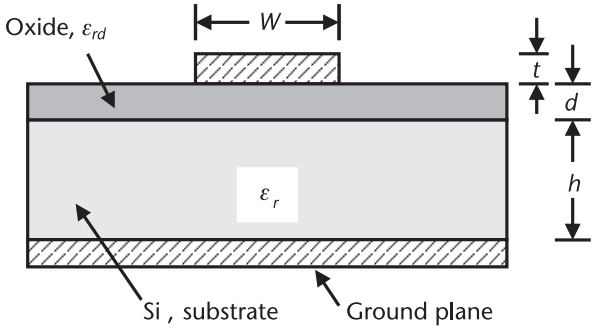

Figure 2.23 Configuration of an oxide-silicon substrate microstrip line.

2.5 Other Types of Microstrip Lines

There are several derivatives of microstrip lines being used in ICs. These include inverted and suspended microstrip lines, a multilayered microstrip, a thin film microstrip, and valley microstrip. These structures are briefly described in this section.

2.5.1 Suspended and Inverted Microstrip Lines

Suspended and inverted microstrip lines (shown in Figure 2.24) provide a higher Q (500 to 1500) than the conventional microstrip lines. The wide range of achiev-

able impedance values makes these media particularly suitable for filters. Expressions for the characteristic impedance and effective dielectric constant for $t/h \ll 1$ are given as [81]

$$Z_0 = \frac{60}{\sqrt{\varepsilon_{re}}} \ell n \left[\frac{f(u)}{u} + \sqrt{1 + \left(\frac{2}{u}\right)^2} \right] \tag{2.150}$$

where

$$f(u) = 6 + (2\pi - 6)\exp\left[-\left(\frac{30.666}{u} \right)^{0.7528} \right]$$

For the suspended microstrip $u = W/(a + b)$ and for the inverted microstrip $u = W/b$, where all the variables are defined in Figure 2.24.

For a suspended microstrip the effective dielectric constant ε_{re} is obtained from

$$\sqrt{\varepsilon_{re}} = \left[1 + \frac{a}{b}\left(a_1 - b_1 \ell n \frac{W}{b} \right)\left(\frac{1}{\sqrt{\varepsilon_r}} - 1 \right) \right]^{-1} \tag{2.151}$$

where

$$a_1 = \left(0.8621 - 0.1251 \ell n \frac{a}{b} \right)^4$$

$$b_1 = \left(0.4986 - 0.1397 \ell n \frac{a}{b} \right)^4$$

and for an inverted microstrip the effective dielectric constant is given by

$$\sqrt{\varepsilon_{re}} = 1 + \frac{a}{b}\left(\overline{a}_1 - \overline{b}_1 \ell n \frac{W}{b} \right)\left(\sqrt{\varepsilon_r} - 1 \right) \tag{2.152}$$

where

$$\overline{a}_1 = \left(0.5173 - 0.1515 \ell n \frac{a}{b} \right)^2$$

$$\overline{b}_1 = \left(0.3092 - 0.1047 \ell n \frac{a}{b} \right)^2$$

The accuracy of (2.144) and (2.145) is within ±1 percent for $1 < W/b \leq 8$, $0.2 \leq a/b \leq 1$, and $\varepsilon_r \leq 6$. For $\varepsilon_r \simeq 10$, the error is less than ±2 percent.

2.5.2 Multilayered Dielectric Microstrip

Multilayered dielectric microstrip lines are becoming an integral part of ICs. Several applications of such structures include circuit passivation or scratch protection, high-speed digital circuit crossover interconnects, MMIC crossover interconnects, metal-insulator-metal capacitors, high directivity couplers [82, 83], tightly coupled structures [84–86], improving pulse characteristic propagation [87], and many others. Analysis of multilayered dielectric microstrip lines has been performed using quasi-static analyses such as the variational method [88, 89], the potential theory method, and full wave spectral domain methods [90, 91].

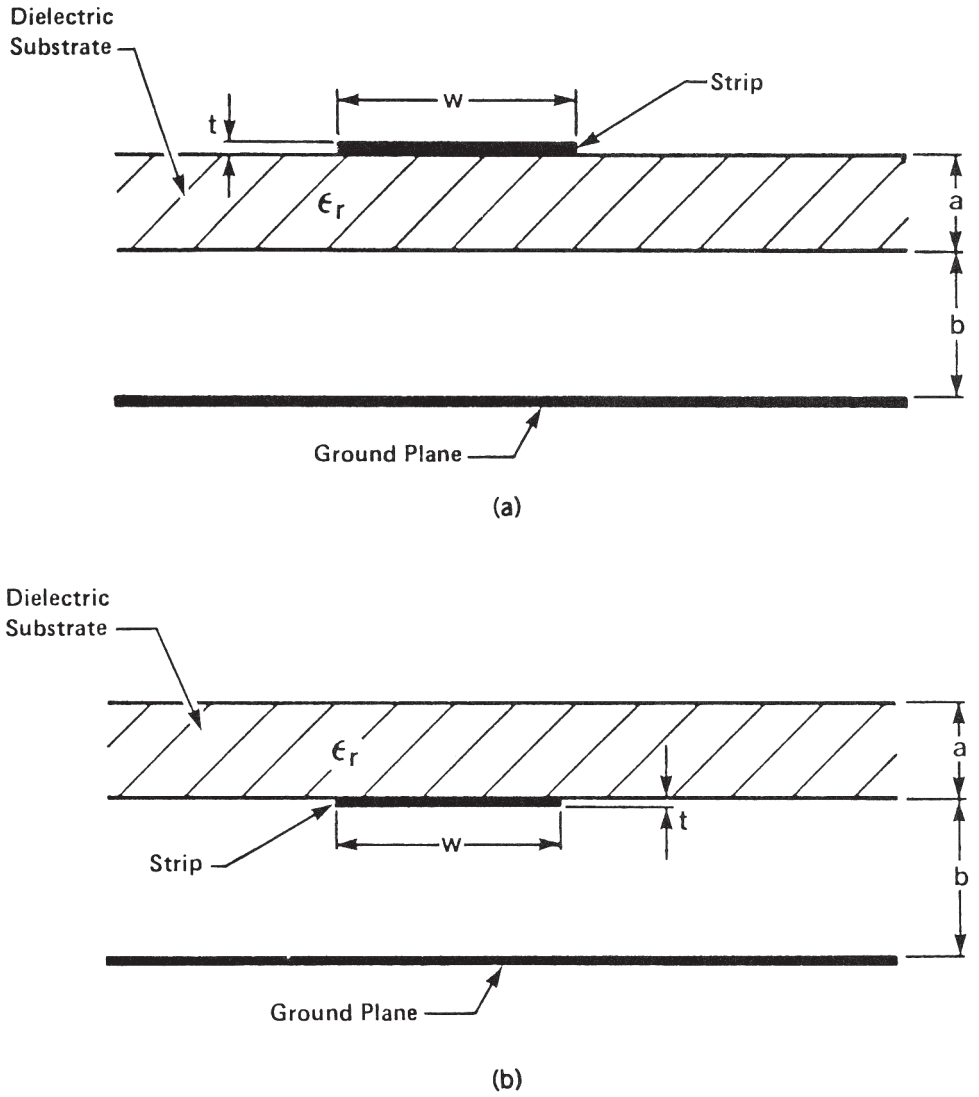

Figure 2.24 Suspended-substrate microstrip line configurations: (a) suspended and (b) inverted.

Multilayered structures are generally fabricated in MMICs using very thin dielectric layers of insulating materials such as silicon nitride ($\varepsilon_r \cong 6.7$) and polyimide ($\varepsilon_r \cong 3.0$). The dielectric constant of these materials might vary from foundry to foundry depending upon the composition used. The characteristic impedance and effective dielectric constant of a multilayered structure using polyimide are calculated utilizing the variational method, and the results are plotted in Figures 2.25 and 2.26 for several values of dielectric thicknesses. It may be noted from these figures that the lower polyimide dielectric layer has a significant effect on these characteristics as compared to that of the upper layer. Figure 2.27 shows the calculated capacitance per unit length of a microstrip line for various values of the

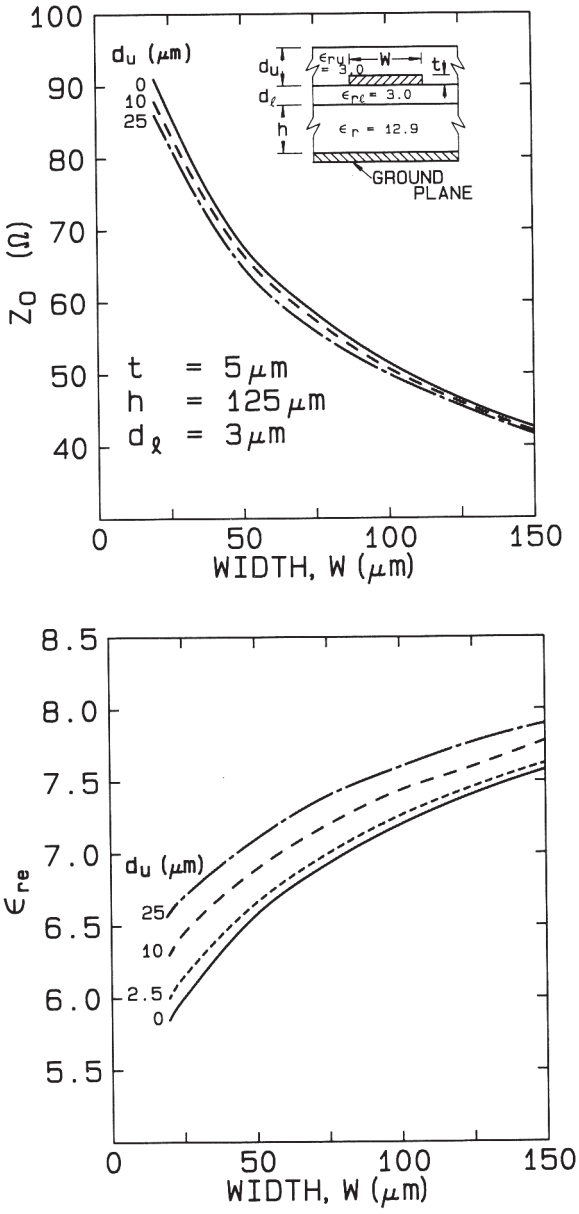

Figure 2.25 Calculated Z_0 and ε_{re} for various values of d_u and W: $\varepsilon_r = 12.9$, $t = 5$ μm, and $h = 125$ μm.

lower dielectric layer thickness and fixed value of upper layer thickness. Even thin layers of low dielectric constant under the microstrip conductors reduce its capacitance significantly. This feature can be used to reduce the parasitic capacitance of a lumped inductor realized in this configuration in order to extend its maximum operating frequency to higher values. The effects of uncertainties in the polyimide layer's thickness and dielectric constant values on the effective dielectric constant and characterstic impedance are given in Table 2.7.

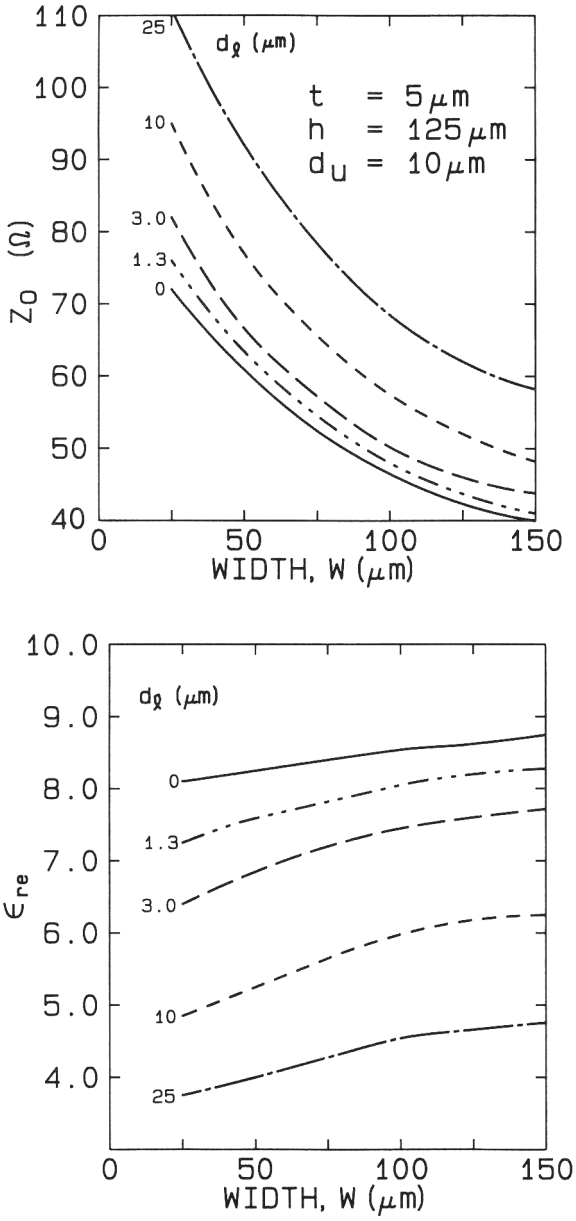

Figure 2.26 Calculated Z_0 and ε_{re} for various values of d_1 and W:$\varepsilon_r = 12.9$, $t = 5$ μm, and $h = 125$ μm.

Figure 2.28 shows the calculated capacitance and inductance per unit length of a microstrip as a function of strip width for various values of air thickness under the conductor. The capacitance reduces significantly even for small thicknesses, while the inductance is almost constant.

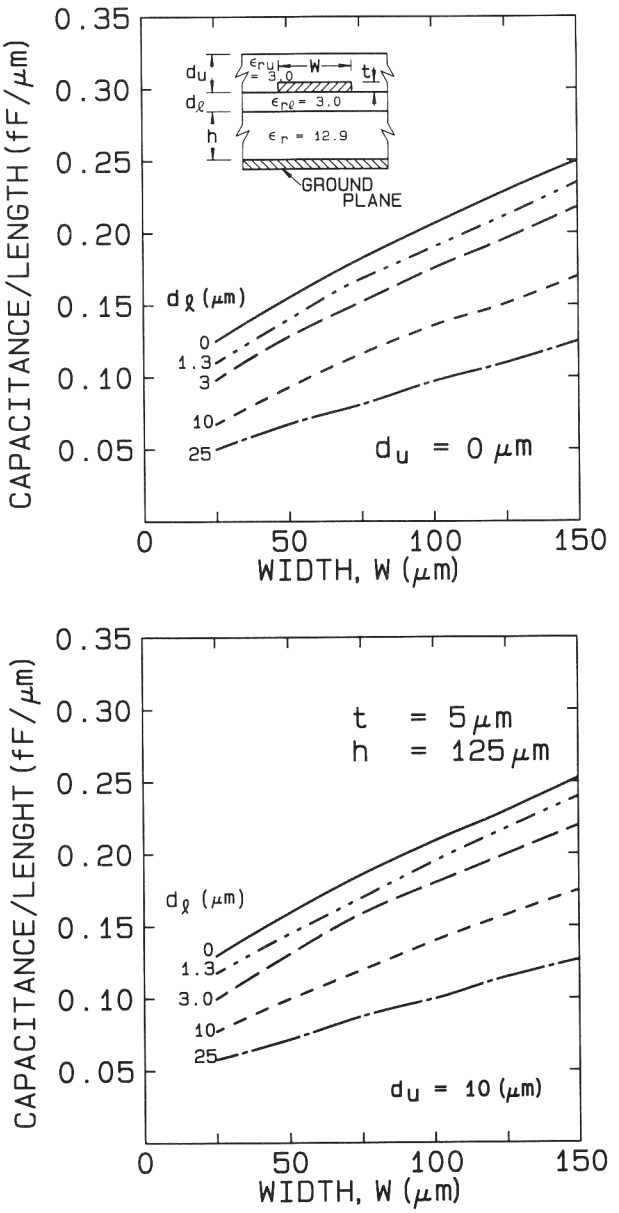

Figure 2.27 Calculated capacitance per unit length of a multilayered microstrip.

2.5.3 Thin Film Microstrip (TFM)

In order to make MMICs compact and low cost, a *thin film microstrip* (TFM) structure has also been used [92–96]. Both active and passive miniature circuits have been successfully realized with TFM employing a narrow-width microstrip conductor on thin low-dielectric constant materials, fabricated on semi-insulating GaAs substrate. As shown in Figure 2.29, a ground plane is placed between a thin dielectric layer and the GaAs substrate. The GaAs substrate provides support as

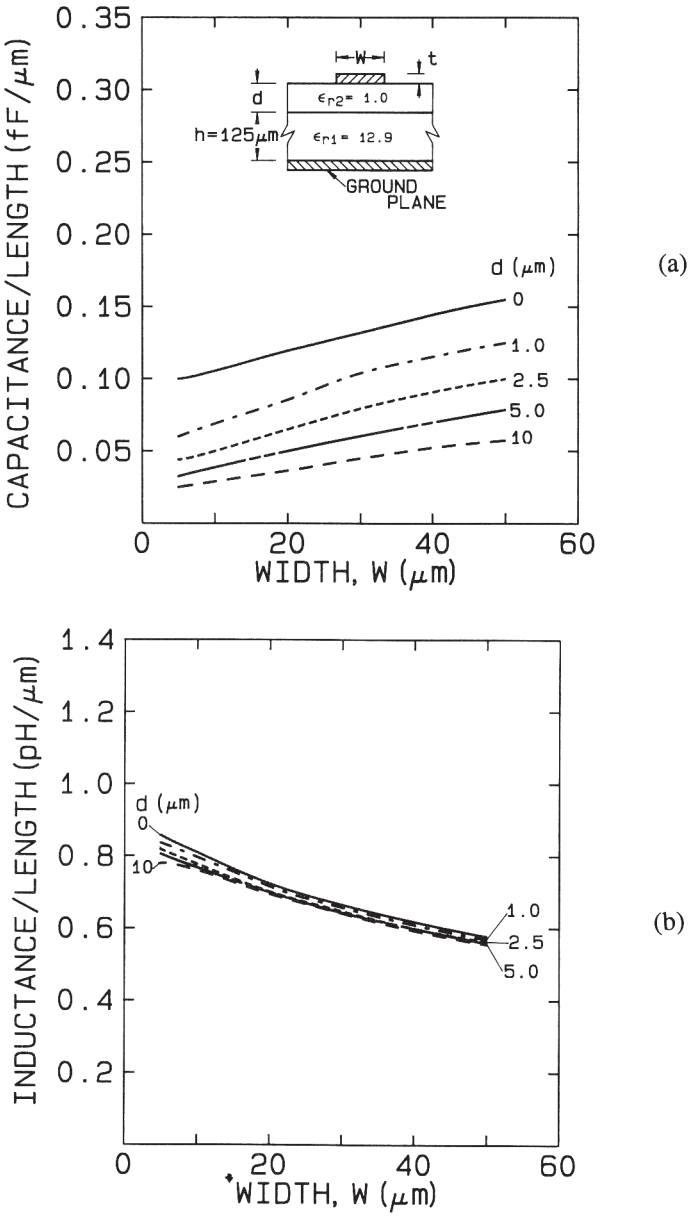

Figure 2.28 (a) Calculated capacitance per unit length of a multilayered microstrip and (b) calculated inductance per unit length of a multilayered microstrip.

well as a semiconductor medium for active devices. Due to the thin microstrip conductors, TFM has relatively high insertion loss as compared to a conventional microstrip.

The loss characteristics of a TFM and a conventional microstrip on GaAs are compared [92] in Figure 2.30. The metal thickness t of the TFM is assumed to be one-third of the thin film thickness ($H/3$). The thin film dielectric is SiON, having

Table 2.7 Sensitivity Analysis of a Multilayered Microstrip Line ε_{r1} (GaAs) = 12.9, Substrate Thickness, $h = 125$ μm

		Uncertainty in Polyimide Layers		
Microstrip Parameter Change (%)	*Line Width (μm)*	$\Delta\varepsilon_{ru} = +10\%$ $\Delta\varepsilon_{r1} = +10\%$ *(Dielectric Constant)*	$\Delta d_1 = +10\%$ *(Under layer)*	$\Delta d_u = +10\%$ *(Over layer)*
$\Delta\varepsilon_{re}$	20	+3.3	–1.9	+0.4
$\Delta Z_{0m}(\Omega)$	20	–1.5	+1.0	–0.2
$\Delta\varepsilon_{re}$	90	+1.8	–1.2	+0.2
$\Delta Z_{0m}(\Omega)$	90	–0.9	+0.7	–0.1

a dielectric constant value of 5. Three micron-thick conductors were used in the calculation of conventional microstrip line characteristics. Loss calculations were performed for 50-Ω lines. Figure 2.31 shows measured data obtained at 10 GHz for the TFM lines. Here the thin film dielectric is polyimide ($\varepsilon_{rd} \cong 3$, $H \cong 3$ μm). TFM lines can readily be realized to achieve very low characteristic impedances 3 Ω to 4 Ω, by using microstrip conductor widths on the order of 100 μm, without exciting higher order modes. Thus TFM overcomes the low characteristic impedance limit problem of a conventional microstrip and has an important application in the design of power amplifier matching networks where very low characteristic impedance is required to match very low device input impedance.

Closed form expressions for the characteristic impedance, effective dielectric constant, and dispersion of the TFM are reported by Schnieder and Heinrich [97]. The expressions have been validated by comparing with the full-wave simulated results. Typical errors for the characteristic impedance and phase constant were 3 percent and 2 percent, respectively. A modification of Wheeler's incremental inductance rule to calculate conductor loss in a TFM is given by Stracca [98]. The conductor loss was calculated by using the proposed method agrees with the available numerical results.

The lumped element equivalent-circuit model for the TFM has been discussed in [97]. The closed form formulas for the equivalent-circuit elements *R, L, C,* and *G* were provided. First, existing closed form equations for microstrip characteristics were chosen based on their accuracy; then they were modified based on the extensive data collected using electromagnetic simulations employing full-wave mode matching method. This lead to more accurate closed form expressions for the TFM.

2.5.4 Valley Microstrip Lines

Valley microstrip lines have been used to realize low loss and miniature MMIC components using multilayer techniques. Figure 2.32 shows cross sections of valley microstrip lines with and without slits. These lines have lower insertion loss than TFM [99–103]. These structures have been analyzed using quasi-TEM techniques [102, 103]. The calculated value of the characteristic impedance of a valley microstrip as a function of strip width for several values of slit widths is shown in Figure 2.33 [101]. The thin film dielectric is polyimide ($\varepsilon_{rd} = 3.3$), having a thickness of 10 μm. The insertion loss is about 0.5 dB/mm at 10 GHz.

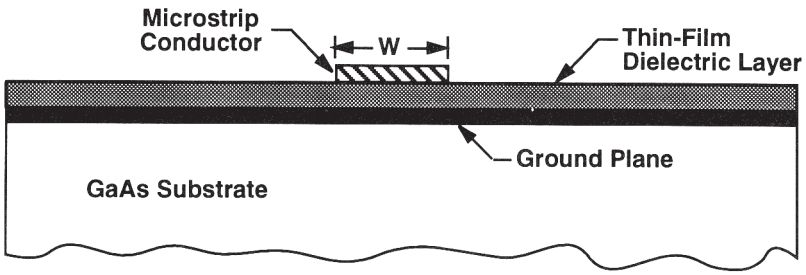

Figure 2.29 Cross section of a low impedance thin film microstrip transmission line (TFMS).

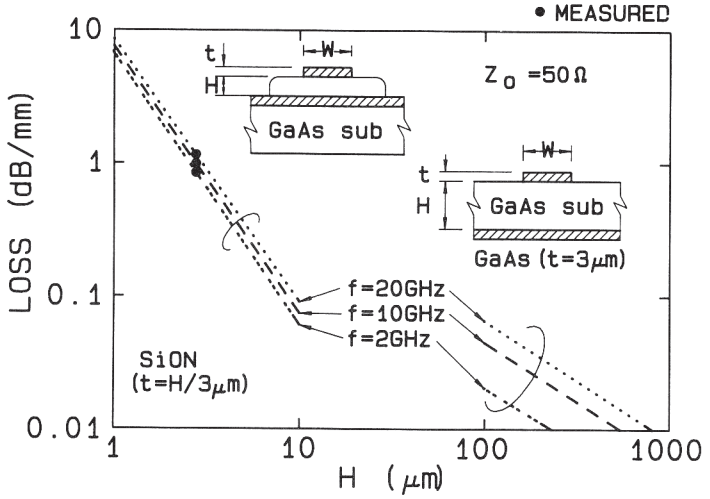

Figure 2.30 Characteristics of TFMS and conventional microstrip lines (from [85], © 1989 IEEE. Reprinted with permission.).

2.5.5 Buried Microstrip Line

The configuration of a buried microstrip line (BML) is shown in Figure 2.34. In this case, the microstrip conductor is placed on a dielectric slab that is surrounded by conductor walls. The BML geometry may be considered as a modification of TFM. The structure was analyzed using FDTD method. It was found that the cross-talk between buried microstrip lines is at much lower levels than the cross-talk between the conventional microstrip lines; this is due to the presence of the ground between them. In practical circuits, the isolation improvement could be as large as 50–60 dB [104]. High isolation in BML structure is very desirable for constructing high-density and millimeter-wave integrated circuits.

2.5.6 Superconducting Microstrip Circuits

Most planar transmission lines are lossy (due to high conductor loss) to varying degrees when compared with coaxial lines and waveguides, which precludes their use

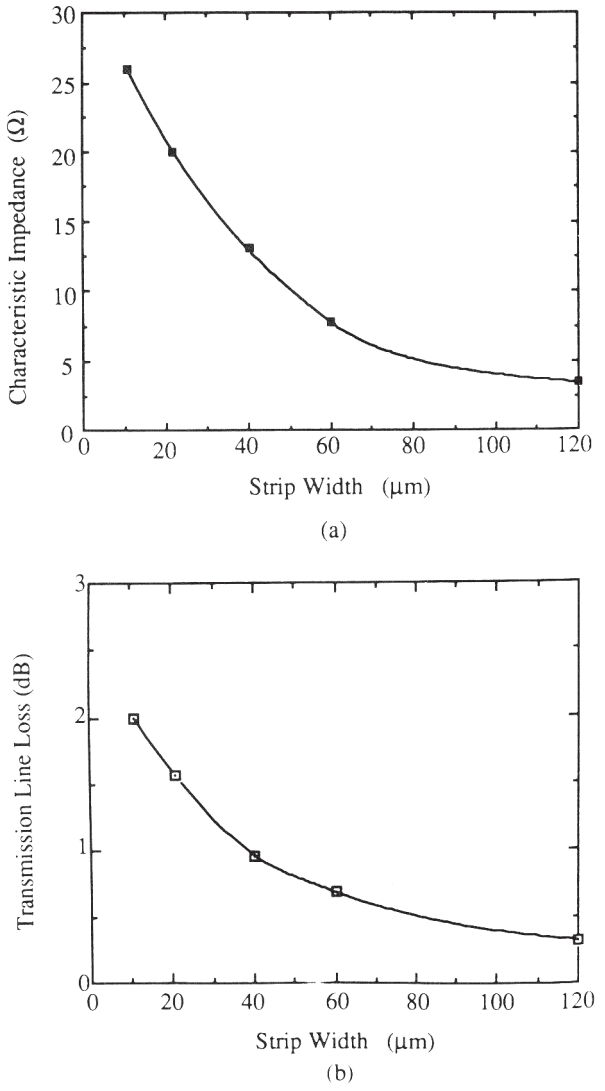

Figure 2.31 Characteristic impedance and (b) transmission loss (per millimeter) at 10 GHz for various widths of TFM lines (from [88], © 1993 IEEE. Reprinted with permission.).

for the realization of narrow-band filters and low-loss delay lines. The low surface resistance of superconducting materials at microwave frequencies is attractive to realize nearly lossless planar passive components. Materials exhibiting superconducting behavior at temperatures as high as 125K have generated a great deal of interest in microwave circuitry for the realization of low-loss passive components. The high-temperature superconducting materials are referred to as HTS, and the temperature at which the materials exhibit this property is referred to as the transition temperature, T_c, and is commonly measured in Kelvin (K). The growth of good quality HTS films compatible with hybrid and monolithic microwave integrate circuits has made HTS readily usable. Several HTS materials are listed in Table 2.8. It. Yttrium barium copper oxide (YBCO) has the lowest T_c. In order to maintain

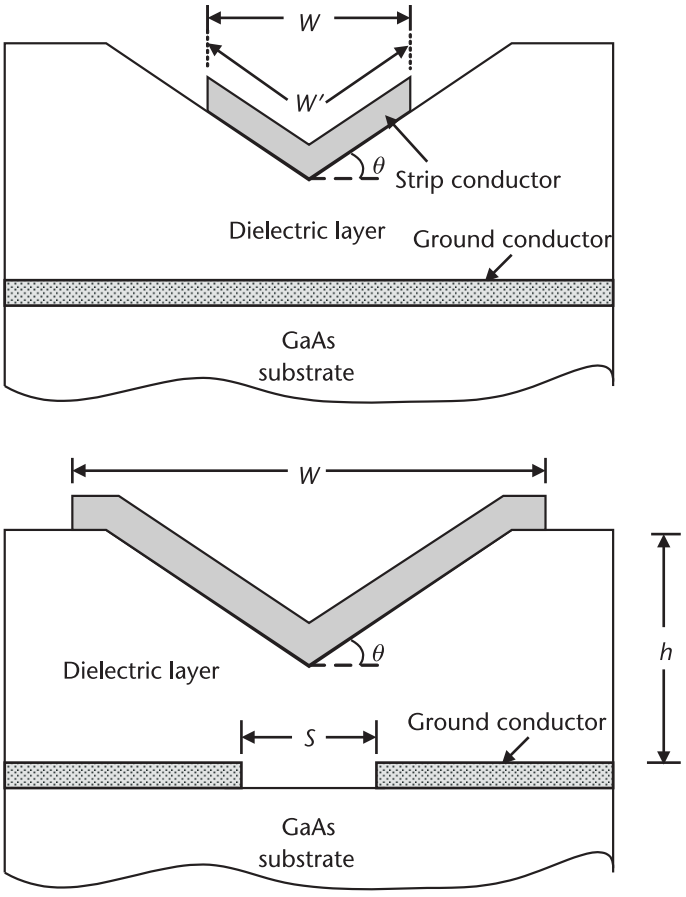

Figure 2.32 Cross section of the valley microstrip line with and without slit.

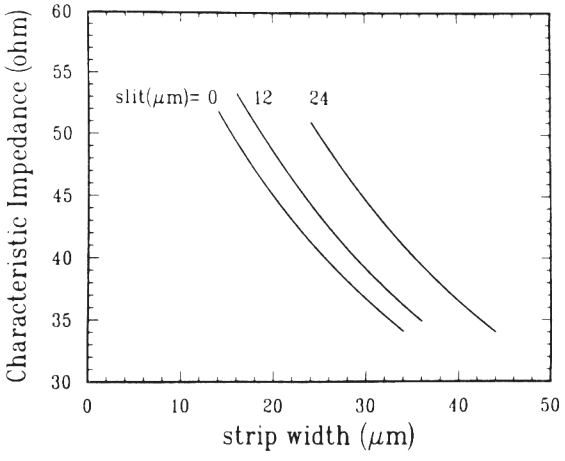

Figure 2.33 Calculated value of the characteristic impedance of a valley microstrip line as a function of the strip width for slit widths = 0, 12 μm, and 24 μm. The dielectric film thickness, H, is 10 μm, and the valley taper, θ, is 35° (from [92], © 1992 IEEE. Reprinted with permission.).

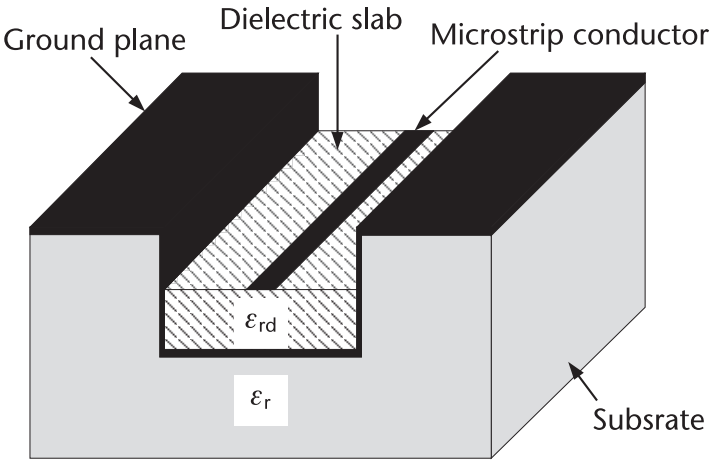

Figure 2.34 Configuration of the buried microstrip line.

Table 2.8 Material Parameters for High-Temperature Superconductors

Material	$T_c(K)$	$\lambda(\mu m)$
$YBa_2Cu_3O_7$	95	0.150
$Bi_2Sr_2CaCu_2O_8$	85	0.300
$Bi_2Sr_2Ca_2Cu_3O_{10}$	110	
$Tl_2Ba_2CaCu_2O_8$	108	
$Tl_2Ba_2Ca_2Cu_2O_{10}$	125	0.200

Note: Here λ is the zero-temperature penetration depth of the fields into superconductors.

stable circuit operation, the material should be selected to have a T_c substantially higher than the operating temperature. The materials shown in Table 2.8 have a T_c higher than liquid nitrogen (77K) and also have larger energy gaps that make them usable at liquid nitrogen and at high power levels, respectively. HTS films can easily be deposited on low-loss tangent ($\tan \delta \leq 0.0001$ at microwave frequencies) substrates such as sapphire, silica, MgO, lithium nitrate, and lanthanum aluminate ($LaAlO_3$) with good lattice match to realize low-loss HTS microstrip lines. Sapphire is one of the most commonly used materials for depositing HTS films. At room temperature the dielectric constant along its *c*-(optic) axis is $\varepsilon_{r11} = 11.6$ and perpendicular to this axis (*z*-axis) the dielectric constant is $\varepsilon_{r\perp} = 9.4$. The planar surface lies in the optic axis called the *c*-plane. At 77K the values are slighty lower, but for a first-order approximation one can still use these values.

Superconductor Technologies [105, 106] have characterized HTS microstrip using thin films of thallium barium calcium copper oxide (TlBaCaCuO) grown on lanthanum aluminate ($LaAlO_3$) substrate. Typical specifications for such substrates are given in Table 2.9. Figure 2.35 shows the surface resistance measured at 10 GHz as a function of temperature. The sample used was l-cm^2 and was much thicker than the penetration depth. Figure 2.36 shows the loaded Q of microstrip resonators measured at 5 GHz as a function of input power for 6-mil- and 40-mil-wide microstrip conductors. The loaded Q for HTS microstrip resonators at small

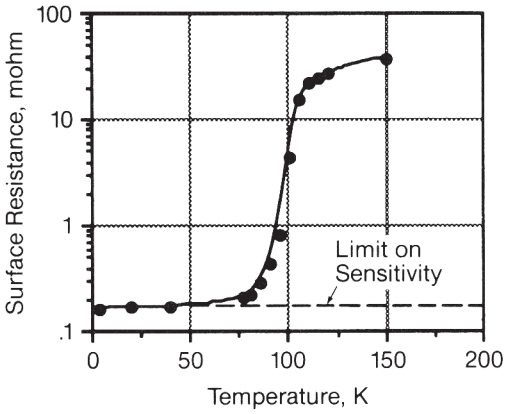

Figure 2.35 R_s versus temperature of TlCaBaCuO HTS measured at 10 GHz (from [106]).

Table 2.9 Typical Substrate and HTS Film Specifications

Substrate
TYPE: Lanthanum Aluminate ($LaAlO_3$)
DIELECTRIC CONSTANT: 24 typical
DIELECTRIC LOSS TANGENT: 3×10^{-5} typical
THICKNESS: 0.010″ ± 0.0005″
0.020″ ± 0.0005″
DIMENSIONS: 1.00 cm ±0.01 cm
2.00″ ± 0.0005″
HTS Film
COMPOSITION: TlBaCaCuO
THICKNESS: 0.75 μm ± 0.1 μm, typical
PENETRATION DEPTH: 0.3 μm, typical @ 77K
CRITICAL CURRENT: 5×10^5 A/cm^2, typical @ 77K
R_s (at 10 GHz): 0.25 mohm, typical @ 77K
T_c: 100 K, minimum
Q_0 (at 5 GHz): 10,000 minimum

power levels are 25 to 100 times more than that for conventional microstrip resonators.

For a superconductor, the conductivity based on a two-fluid theory is given by

$$\sigma = \sigma_1 - j\sigma_2 = \sigma_n \left(\frac{T}{T_c}\right)^4 - j\frac{1-(T/T_c)^4}{2\pi f \mu_0 \lambda^2} \qquad \text{for } T < T_c \tag{2.153}$$

where σ_n is the normal part of the conductivity, f is the operating frequency, μ_0 is the free-space permeability, λ is the penetration depth, T is the temperature, and T_c is the critical temperature of the HTS. The real and imaginary parts of the conductivity correspond to the normal electrons and superconducting electron pairs, respectively [107]. Using (2.153) one can modify the surface impedance and calculate approximately the microstrip characteristics. The analysis of the superconducting microstrip line has been described in the literature [107–112]. Antsos et al. [107] reported closed-form expressions for the characteristic impedance, effective dielectric constant, and attenuation constant based on quasi-TEM analysis of HTS.

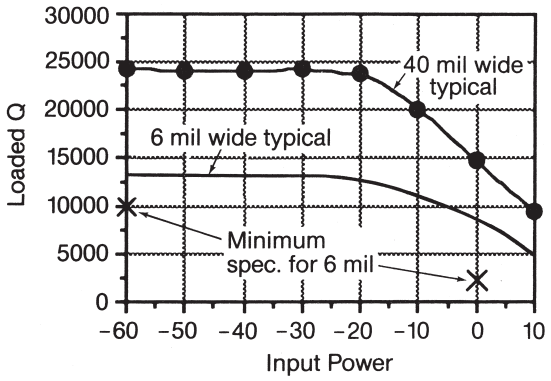

Figure 2.36 Loaded Q of microstrip resonators measured at 5 GHz [106].

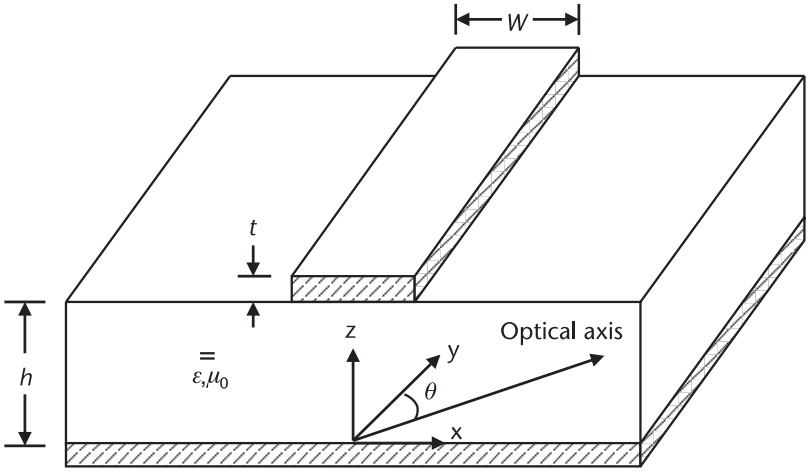

Figure 2.37 Superconducting micostrip line with a perfectly conducting ground plane on an anisotropic substrate.

Lee et al. [113] described fullwave analysis of HTS microstrip lines on anisotropic substrates using an equivalent surface impedance approach. A superconducting microstrip line with a perfectly conducting ground plane on an anisotropic substrate for which the optic axis is the (x-y)-plane is shown in Figure 2.37. In this case, high-quality $YBa_2Cu_3O_7$ (YBCO) films have been deposited on m-plane sapphire (the angle between the c-plane and the m-plane is 90°). The characteristic impedance, effective dielectric constant, and attenuation constant, calculated using the fullwave method for YBCO microstrip lines on a 430-μm-thick m-plane sapphire substrate, are shown in Figure 2.38 as a function of the rotation angle of the optic axis. Other parameters used in the calculations are the zero temperature penetration depth of the fields into the superconductor $\lambda = 0.323$ μm, the real part of conductivity $\sigma = 3.5$S/μm, conductor thickness t = 0.4 μm, transition temperature $T_c = 90$K, and operating temperature $T = 77$K. The characteristic impedance and effective dielectric constant values shown in Figure 2.38 for an HTS microstrip are very close to the conventional microstrip results on a sapphire substrate. Thus

approximate expressions for the microstrip on an anisotropic substrate in Section 2.4.4 may be used to calculate HTS microstrip characteristics.

Microwave circuits, including filters, delay lines, resonators, dividers, combiners, and Lange couplers, have been developed using an HTS microstrip [105, 114–122]. Specific applications of HTS microstrip lines include narrow-band filters, low-loss delay lines, high Q resonators, and a low-loss receiver front end consisting of a microstrip antenna, a low-noise amplifier, and a mixer for improved sensitivity.

2.6 Microstrip Applications

Satellite, airborne communications, and EW systems have requirements for small size, lightweight, and low-cost microwave passive components. Microstrip line-based filters, impedance transformers, hybrids, couplers, power dividers/combiners, delay lines, baluns, circulators, and antennas are used extensively in microwave systems, including measurement instruments where the demand on low-loss and high-power characteristics is not severe. The suspended microstrip provides a higher Q than the microstrip, as most of the energy is propagating in air. This results in lower loss passive components.

Sections of microstrip lines constitute the basic building blocks of microwave integrated circuits. When the size of the microstrip section is reduced to dimensions much smaller than the wavelength, it can be used as a lumped element. Examples of lumped microstrip elements are spiral inductors, thin film resistors, interdigital capacitors, *metal-insulator-metal* (MIM) capacitors, via holes, and airbridges as shown in Figure 2.39. Microstrip sections in lumped and distributed forms are commonly used in passive and active hybrid and monolithic integrated circuits. Examples of passive circuits include filters, impedance transformers, hybrids, couplers, power dividers/combiners, delay lines, and baluns. Amplifiers, oscillators, mixers, and control circuits employing solid state devices constitute the other class. Microwave packages and assembly techniques frequently use microstrip transmission medium in the feedthroughs and interconnects. Another important application of microstrip lines is in high-temperature superconducting microwave integrated circuits. This section provides a brief introduction to the design of microstrip elements for the above-mentioned applications.

2.6.1 Lumped Elements

Lumped-element circuits that have lower Q than distributed circuits have the advantage of smaller size, lower cost, and wide-band characteristics. These are especially suitable for monolithic MICs and for broadband hybrid MICs where realestate requirements are of prime importance. Impedance transformations on the order of 20:1 can be easily accomplished using the lumped-element approach. Therefore, high-power devices that have very low impedance values can easily be tuned with large impedance transformers using lumped elements. Consequently, lumped elements find applications in high-power oscillators, power amplifiers, and broadband circuits.

With the advent of new photolithographic techniques, the fabrication of lumped elements that was limited to X-band frequencies can now be extended

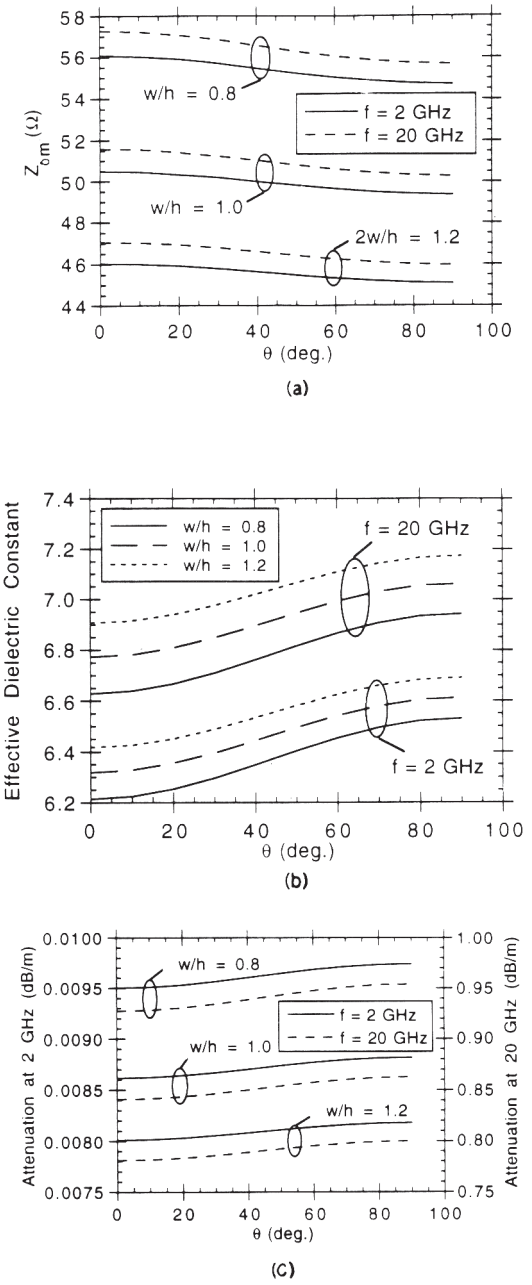

Figure 2.38 Calculated HTS microstrip line characteristics as a function of the rotation angle of the optic axis using the fullwave method: (a) characteristic impedance; (b) effective dielectric; (c) attenuation constant (from [113], © 1993 IEEE. Reprinted with permission.

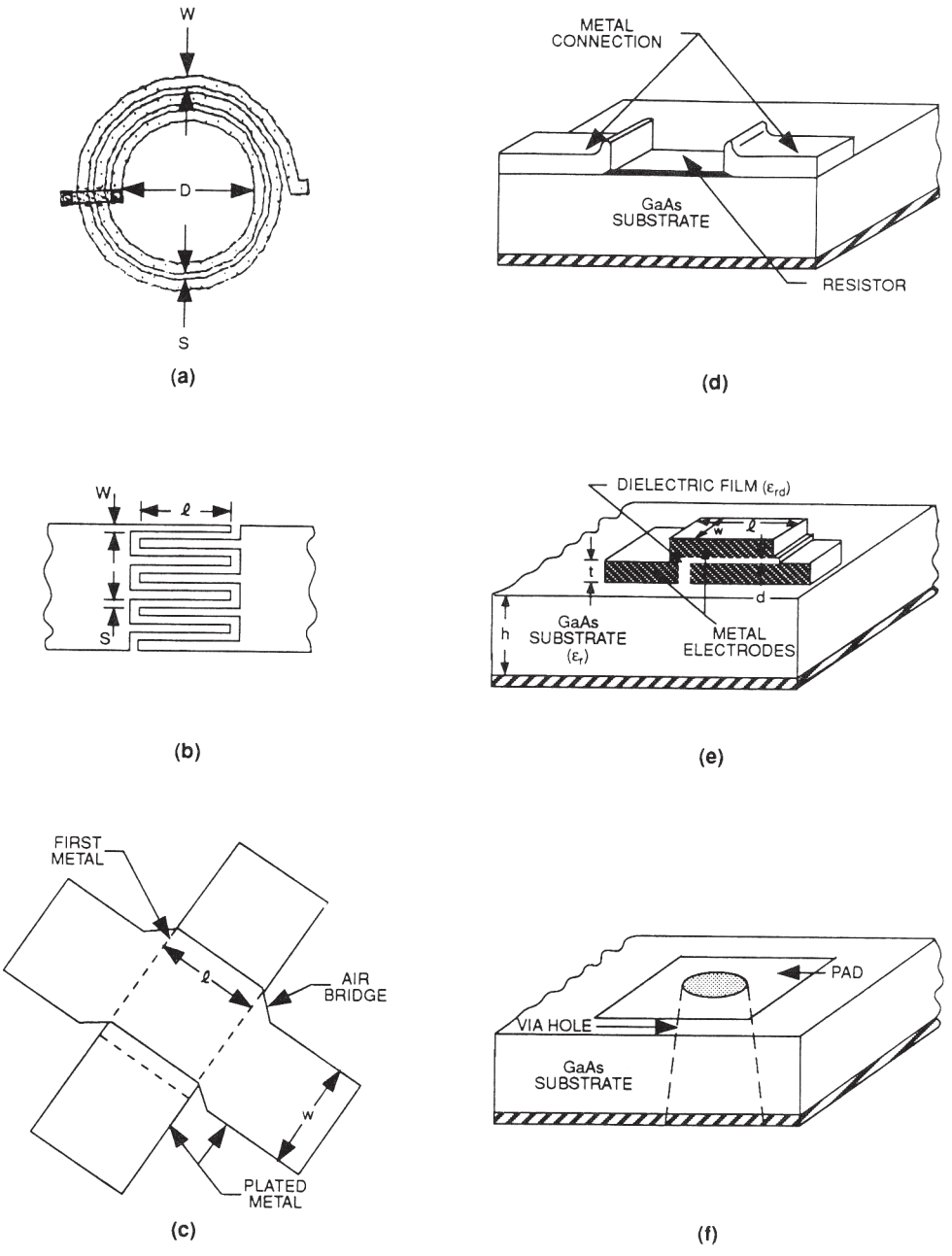

Figure 2.39 MMIC circuits use passive lumped elements: (a) spiral inductor; (b) interdigital capacitor; (c) airbridge crossover; (d) thin film resistor; (e) MIM capacitor; and (f) via hole.

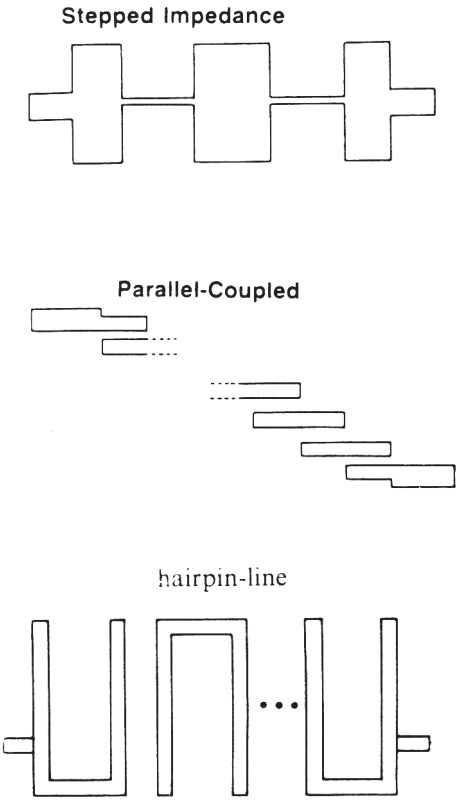

Figure 2.40 Microstrip filter configurations.

to about 60 GHz. The three basic building blocks for circuit design—inductors, capacitors, and resistors—are available in lumped form. Computer-aided design of circuits using lumped elements requires a complete and accurate characterization of lumped elements at microwave frequencies. This necessitates the development of comprehensive mathematical models that take into account the presence, for example, of ground planes, proximity effect, fringing fields, and parasitics. The design, fabrication, and applications of lumped elements have been thoroughly discussed in the literature [123–127]. Bahl [127] exclusively discusses the subject of lumped element realization, characterization, and lumped element circuits.

2.6.2 Passive Components

Microstrip passive components are fabricated using both hybrid and monolithic microwave integrated circuit techniques. Most commonly used substrate materials are RT Duroid, alumina, and GaAs. Use of a high dielectric constant substrate $\varepsilon_r \cong 10$ is highly desirable. However, the substrate thickness is limited by modal problems. High-impedance lines on thin substrates require very narrow conductors, which become lossy, and the fabrication of narrow conductors can be difficult. For low frequencies up to about 4 GHz to 6 GHz for circuits and up to and beyond 20 GHz for microstrip antennas, plastic substrates ($\varepsilon_r \cong 2$ to 4) are often used. Alu-

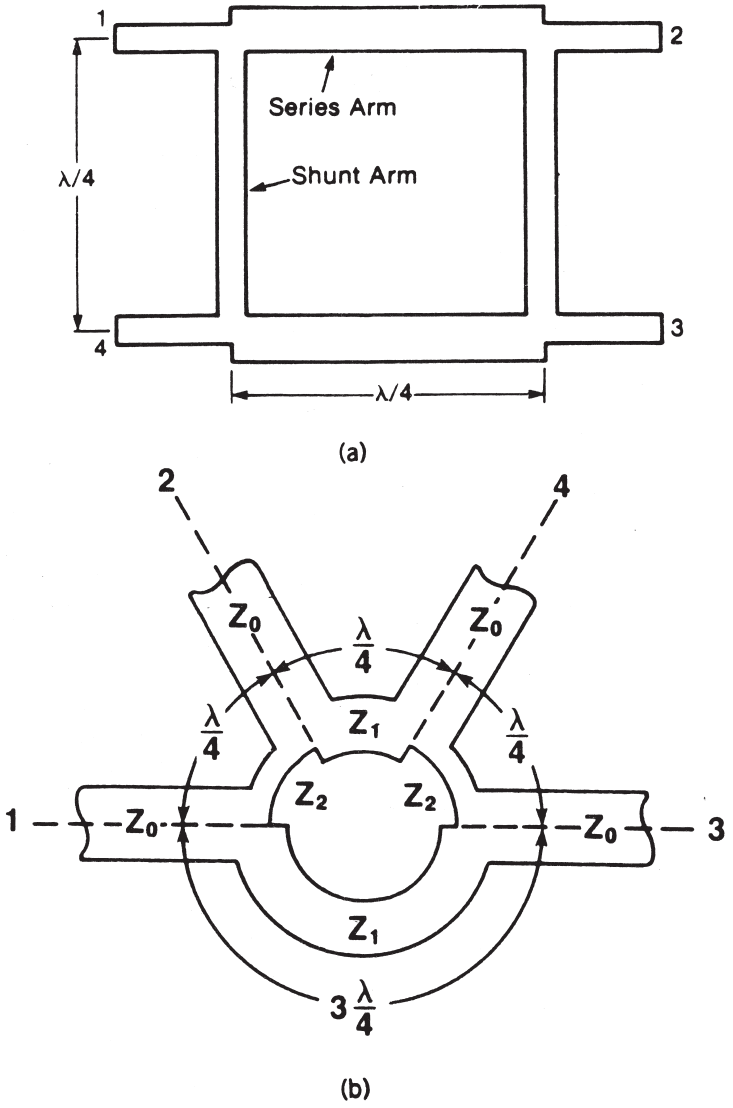

Figure 2.41 Microstrip hybrids: (a) branch line and (b) ring.

mina (Al_2O_3) is one of the most suitable substrate materials for use up to 20 GHz. The grade of the Al_2O_3 used depends upon the fabrication technology employed: thin or thick film. The dielectric constant of alumina may be high for millimeter-wave circuits because high impedance lines with required tolerances are difficult to fabricate and are lossy. Quartz with a dielectric constant of 4 is more suitable and widely used for high-frequency (>20 GHz) microwave and millimeter-wave integrated circuits. Beryllia is a good conductor of thermal energy and is suitable for power applications where heat dissipation is large and a low thermal resistance substrate is required. GaAs is one of the most suitable substrates for MMICs, since

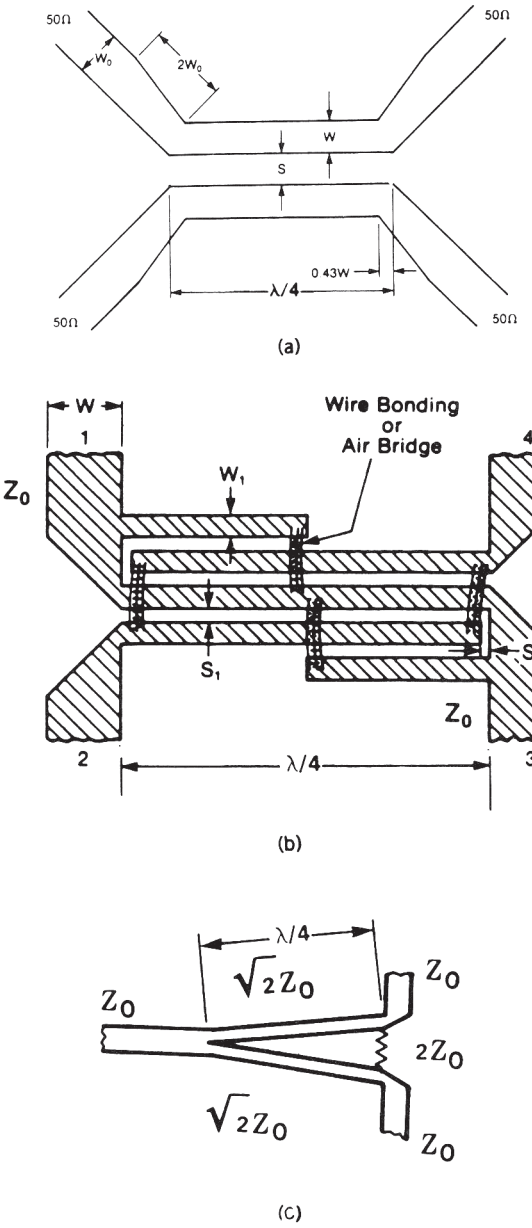

Figure 2.42 Microstrip couplers and combiner: (a) coupled line; (b) Lange coupler; and (c) Wilkinson.

most of the active devices, such as low-noise MESFETs, power MESFETs, and Schottky diodes, are fabricated on a semi-insulating GaAs substrate along with the passive components.

Figures 2.40, 2.41 and 2.42 show many popular microstrip passive components. The design of such components has been thoroughly discussed in references [126, 128–132]. To predict the performance of microstrip passive components, the

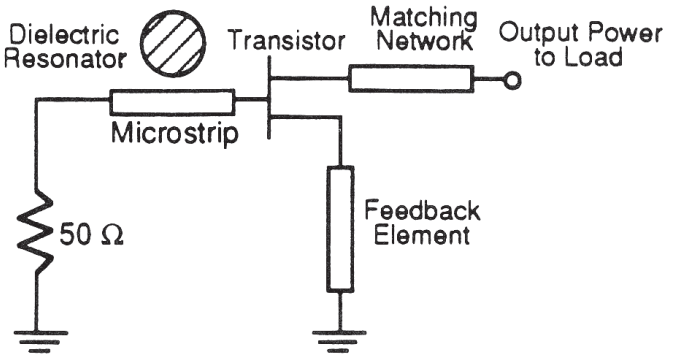

(a)

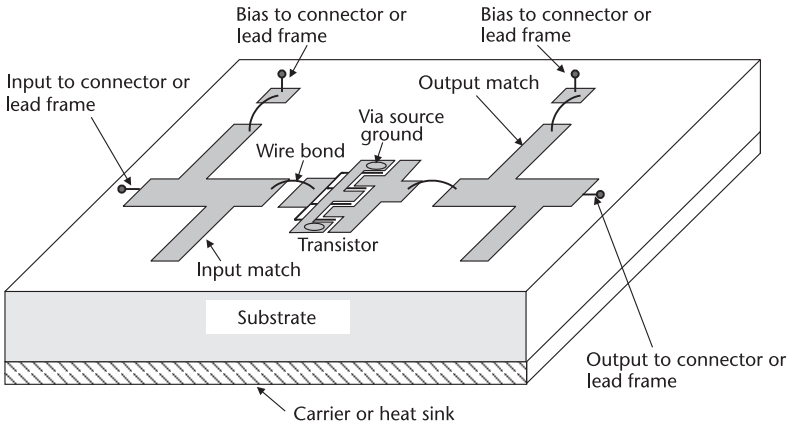

(b)

Figure 2.43 (a) Basic configuration of a dielectric resontor oscillator. The feedback element is used to make the active device unstable, the matching network allows the transfer of maximum power to the load, and the dielectric resonator provides frequency stability. (b) Schematic representation of a transistor amplifier.

effects of junction and layout discontinuities and interaction effects between circuit elements due to close proximity must be included in the circuit analysis.

2.6.3 Active Components

Over the past three decades microwave active circuits have evolved from individual solid-state transistors, diodes, and passive elements housed in conventional waveguides and/or coaxial lines to integrated fully planar assemblies, fabricated using the microstrip medium. A hybrid microwave integrated circuit (MIC) consists of a microstrip interconnect pattern and microstrip distributed circuit components printed on a suitable substrate with active and lumped circuit components (in pack-

aged or chip form) attached individually to the printed interconnect circuit by using soldering and wire bonding techniques. Solid-state active elements are either silicon or gallium arsenide (or other III-V compound) devices. More recently, the solid state monolithic microwave integrated circuit (MMIC) approach is becoming commonplace. In MMICs all interconnections and components, both active and passive, are fabricated simultaneously on a semi-insulating semiconductor substrate (usually gallium arsenide (GaAs) using deposition and etching processes, thereby eliminating discrete components and wire bond interconnects. Microstrip is commonly used for passive components. The term MMIC is used for circuits operating in the microwave (1 GHz to 30 GHz) region of the frequency spectrum as well as the millimeter wave (30 GHz to 300 GHz) region. Major advantages of MMICs include low cost, small size, low weight, circuit design flexibility, broadband performance, elimination of circuit tweaking, high-volume manufacturing capability, package simplification, improved reproducibility, improved reliability, and multifunction performance on a single chip.

Microwave integrated circuits use two types of active devices: two-terminal devices referred to as diodes such as Schottky, Gunn, tunnel, impact avalanche and transit time (IMPATT), varactor, and PIN; and three-terminal devices referred to as transistors such as the bipolar junction transistor (BJT), metal semiconductor field effect transistor (MESFET), high electron mobility transistor (HEMT), and heterojunction bipolar transistor (HBT). Microwave circuits using these devices include amplifiers, oscillators, multipliers, mixers, switches, phase shifters, attenuators, modulators, and many others used for receiver or transmitter applications covering microwave and millimeter-wave frequency bands. The theory and performance of most of these circuits have been well documented [126, 132–140]. Examples of some active circuits using the microstrip medium are shown in Figure 2.43. Solid-state circuits are extensively used in applications such as radar, communication, navigation, electronic warfare (EW), smart weapons, consumer electronics, and microwave instruments.

2.6.4 Packages and Assemblies

Microwave packaging and assembly techniques play a very important role in the performance, cost, and reliability of packaged monolithic microwave integrated circuits. MMIC packages provide the necessary support structure and a protective enclosure without affecting its electrical and thermal characteristics appreciably. The affordability requirements on packages mandate that their complexity be minimized.

The microstrip is the commonly used transmission medium in MICs and MMICs. It also provides excellent layout flexibility. Therefore, in order to provide a good interface between the MMIC and other circuitry in the package or between the MMIC and subsystem, a microstrip line is desired as an interconnect medium in microwave packages. The design of microwave packages has been treated extensively in the literature [141–147]. The most important electrical characteristics of microwave packages are low insertion loss, high return loss and isolation, and no cavity or feedthrough resonance over the operating frequency range. When a chip

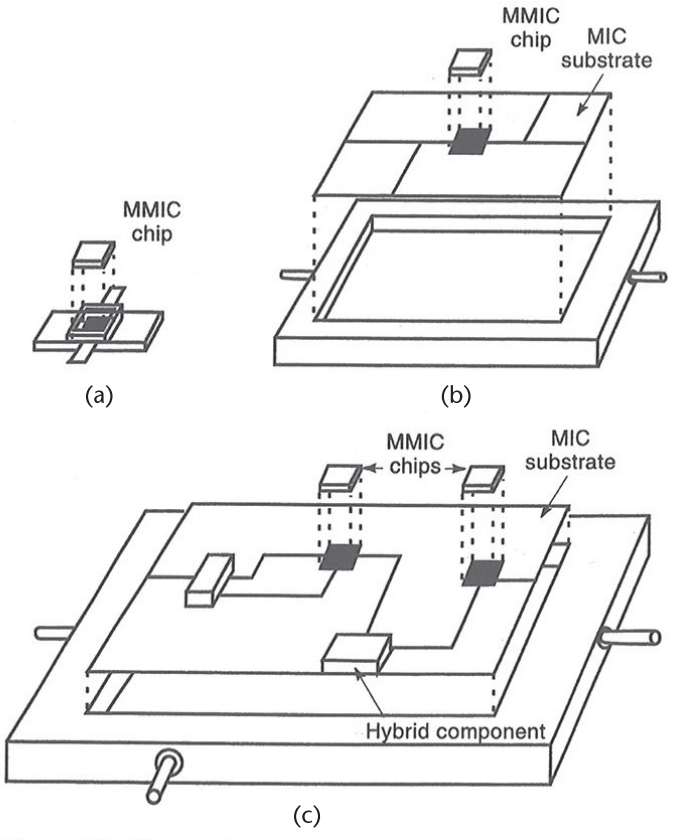

Figure 2.44 Three MMIC packaging levels: (a) MMIC in package, (b) MMIC with support circuitry, and (c) MMICs with hybrid and support circuitry.

set is placed in the cavity of a microwave package, there should be minimum degradation in the chip's performance. Generally this cannot be accomplished without accurate electrical and electromagnetic modeling of the critical package elements. Microwave design principles must be applied to three parts of the package: RF feedthrough, cavity, and dc bias lines. Of the three, the design of the RF feedthrough is the most critical in determining the performance of packaged MMIC chips. As an example, Figure 2.44 shows some of the typical packaging techniques used for microwave circuits. An overview of RF and microwave packages has been included in [140].

References

[1] Denlinger, E. J., "A Frequency Dependent Solution for Microstrip Transmission Lines," *IEEE Trans.*, Vol. MTT-19, 1971, pp. 30–39.

[2] Itoh, T., and R. Mittra, "Spectral-Domain Approach for Calculating Dispersion Characteristics of Microstrip Lines," *IEEE Trans.*, Vol. MTT-21, 1973, pp. 496–498.

[3] Knorr, J. B., and A. Tufekcioglu, "Spectral-Domain Calculation of Microstrip Characteristics Impedance," *IEEE Trans.*, Vol. MTT-23, 1975, pp. 725–728.

[4] Itoh, T., "Spectral Domain Approach for Dispersion Characteristics of Generalized Printed Transmission Lines," *IEEE Trans.*, Vol. MTT-28, No.7, July 1980, pp. 733–736.

[5] Uwano, T., and T. Itoh, "Spectral Domain Analysis," *Numerical Techniques in Microwaves and Millimeterwave Passive Structures* (ed. T. Itoh) New York: John Wiley and Sons, 1989, pp. 334–380.

[6] Zysman, G. I., and D. Varon, "Wave Propagation in Microstrip Transmission Lines," *IEEE G-MTT Int. Microwave Symp. Digest*, 1969, pp. 2–9.

[7] Hornsby, J. S., and A. Gopinath, "Fourier Analysis of a Dielectric-Loaded Waveguide with a Microstrip," *Electron. Lett.*, Vol. 5, 1969, pp. 265–267.

[8] Mittra, R., and T. Itoh, "A New Technique for the Analysis of the Dispersion Characteristics of Microstrip Lines," *IEEE Trans.*, Vol. MTT-19, 1971, pp. 47–56.

[9] Lewin, L., "The Use of Singular Integral Equations in the Solution of Waveguide Problems,"*Advances in Microwaves*, Vol. 1, (ed. L. Young), New York: Academic Press, 1966, pp. 211–284.

[10] Itoh, T., and R. Mittra, "A Technique for Computing Dispersion Characteristics of Shielded Microstrip Lines," *IEEE Trans.*, Vol. MTT-22, 1974, pp. 896–898.

[11] Hornsby, J. S., and A. Gopinath, "Numerical Analysis of a Dielectric Loaded Waveguide with a Microstrip Line-Finite Difference Methods," *IEEE Trans.*, Vol. MTT-17, 1969, pp. 684–690.

[12] Corr, D. G., and J. B. Davies, "Computer Analysis of the Fundamental and Higher Order Modes in Single and Coupled Microstrip," *IEEE Trans.*, Vol. MTT-20, 1972, pp. 669–678.

[13] Martin, R. S., and J. H. Wilkinson, "Reduction of the Symmetric Eigenproblem $Ax = \lambda Bx$ and Related Problems to Standard Form," *Numer. Math.*, Vol. 11, 1968, pp. 99–110.

[14] Berk, A. D., "Variational Principles for Electromagnetic Resonators and Waveguides," *IRE Trans.*, Vol. AP-4, 1956, pp. 104–111.

[15] Schwartz, H. R., "Tridiagonalization of a Symmetric Band Matrix," *Numer. Math.*, Vol. 12, 1968, pp. 231–241.

[16] Barth, W., et al., "Calculation of the Eigenvalues of a Symmetric Tridiagonal Matrix by the Method of Bisection," *Numer. Math.*, Vol. 9, 1967, pp. 336–393.

[17] Wilkinson, J. H., "Calculation of the Eigenvectors of a Symmetric Tridiagonal Matrix by Inverse Iteration," *Numer. Math.*, Vol. 4,1962, pp. 368–376.

[18] Pucel, R. A., et al., "Losses in Microstrip," *IEEE Trans.*, Vol. MTT-16, 1968, pp. 342–350. Correction in *IEEE Trans.*, Vol. MTT-16, 1968, p. 1064.

[19] Schneider, M. V., "Microstrip Lines for Microwave Integrated Circuits," *Bell System Technical Journal*, Vol. 48, 1969, pp. 1422–1444.

[20] Wheeler, H. A., "Formulas for the Skin Effect," *Proc. IRE*, Vol. 30, 1942, pp. 412–424.

[21] Welch, J. D., and H. J. Pratt, "Losses in Microstrip Transmission Systems for Integrated Microwave Circuits," *NEREM Rec.*, Vol. 8, 1966, pp. 100–101.

[22] Horton, R., et al., "Variation of Microstrip Losses with Thickness of Strip," *Electron. Lett.*, Vol. 7, 1971, p. 490.

[23] Garg, R., et al., "Optimum Thickness of Metal in Waveguiding Structures, Ground Planes and Reflectors," *Int. J. Electron.*, Vol. 39, 1975, pp. 525–527.

[24] Schneider, M. V., "Dielectric Loss in Integrated Microwave Circuits," *Bell System Technical Journal*, Vol. 48, 1969, pp. 2325–2332.

[25] Simpson, T. L., and B. Tseng, "Dielectric Loss in Microstrip Lines," *IEEE Trans.*, Vol. MTT-24, 1976, pp. 106–108.

[26] Bahl, I. J., and D. K. Trivedi, "A Designer's Guide to Microstrip Line," *Microwaves*, Vol. 16, May 1977, pp. 174–182.

[27] Van Heuven, J., "Properties of Microstrip Lines on Fused Quartz," *IEEE Trans.*, Vol. MTT-18, 1970, pp. 113–114.

[28] Bahl, I. J., and K. C. Gupta, "Average Power Handling Capability of Microstrip Lines," *IEE Journal on Microwaves, Optics and Acoustics*, January 1979, pp. 1–4.

[29] Owens, R. P., "Predicted Frequency Dependence of Microstrip Characteristic Impedance Using the Planar-Waveguide Model," *Electron. Lett.*, Vol. 12, 1976, pp. 269–270.

[30] Bianco, B., et al., "Frequency Dependence of Microstrip Parameters," *Alta Freq.*, Vol. 43, 1974, pp. 413–416.

[31] Bahl, I.J., and R. Garg, "Simple and Accurate Formulas for Microstrip with Finite Strip Thickness," *Proc. IEEE*, Vol. 65, 1977, pp. 1611–1612.

[32] Frey, J., "Hybrid and Monolithic Microwave Integrated Circuits," *Microwave Integrated Circuits*, (ed.J. Frey), Dedham, MA: Artech House, 1975, pp. xvii-xxi.

[33] Heckl, H., and O. Schweiger, "Evaluation and Space Qualification of MIC on Alumina and Glass Fiber Reinforced Teflon Substrates," ESA session on "Space Qualified MIC" at *6th European Microwave Conf.*, 1976, Rome.

[34] Bahl, I. J., "Average Power Handling Capability of Multilayer Microstrip Lines," *Int. J. RF and Microwave Computer-Aided Engineering*, Vol. 11, 2001, pp. 385–395.

[35] Yin, W.-Y., et al., "Average Power-Handling Capability of the Signal Line in Coplanar Waveguides on Polyimide and GaAs Substrates Including the Irregular Line Edge Shape Effects", *Int. J. RF and Microwave Computer-Aided Engineering*, Vol. 15, 2005, pp. 156–162.

[36] Yin, W. -Y., and X. T. Dong, "Wide-Band Characterization of Average Power Handling Capabilities of Some Microstrip Interconnects on Polyimide and Polyimide/GaAs Substrates," *IEEE Trans. Advanced Packaging*, Vol. 28, 2005, pp. 328–336.

[37] Howe, Jr., H., "Stripline is Alive and Well—," Microwave *J.*, Vol. 14, July 1971, p. 25.

[38] Garg R., "The Effect of Tolerances on Microstrip Line and Slotline Performance," *IEEE Trans.*, Vol. MTT-26, 1978, pp. 16–19.

[39] Owens, R. P., et al., "Quasi-static Characteristics of Microstrips on an Anistropic Sapphire Substrate," *IEEE Trans.*, Vol. MTT-24, 1976, pp. 499–505.

[40] Szentkuti, B. T., "Simple Analysis of Anisotropic Microstrip Lines by a Transform Method," *Electron. Lett.*, Vol. 12, 1976, pp. 672–673.

[41] Wheeler, H. A., "Transmission Line Properties of Parallel Strips Separated by a Dielectric Sheet," IEEE Trans., Vol. MTT-13, 1965, pp. 172–185; "Transmission Line Properties of a Strip on a Dielectric Sheet on a Plane," *IEEE Trans.*, Vol. MTT-25, 1977, pp. 631–647.

[42] Hammerstad, E. O., "Equations for Microstrip Circuit Design," *Proc. European Microwave Conf.*, 1975, pp. 268–272.

[43] Hammerstad, E. O., Private communication.

[44] Hammerstad, E., and O. Jensen, "Accurate Models for Microstrip Computer-Aided Design," *IEEE MTT-S Int. Microwave Symp. Dig.*, 1980, pp. 407–409.

[45] Gunston, M. A. R., and J. R. Weale, "Variation of Microstrip Impedances with Strip Thickness," *Electron. Lett.*, Vol. 5, 1969, pp. 697–698.

[46] Kaupp, H. P., "Characteristics of Microstrip Transmission Lines," *IEEE Trans.*, Vol. EC-16, 1967, pp. 185–193.

[47] Schwarzmann, A., "Microstrip Plus Equations Add Up to Fast Designs," *Electronics*, Vol. 40, October 1967, pp. 109–112.

[48] John, S., and P. Arlett, "Simple Method for the Calculation of the Characteristic Impedance of Microstrip," *Electron. Lett.*, Vol. 10, 1974, pp. 188–190.

[49] Kumar, A., et al., "A Method for the Calculation of the Characteristic Impedance of Microstrip," *Int. J Electron.*, Vol. 40, 1976, pp. 45–47.

[50] Ross, R. F. G., and M. J. Howes, "Simple Formulas for Microstrip Lines," *Electron. Lett.*, Vol. 12, 1976, p. 410.

[51] Gunston, M. A. R., *Microwave Transmission-line Impedance Data*, London: Van Nostrand, 1972, p. 48.

[52] Yamashita, E., and R. Mittra, "Variation Method for the Analysis of Microstrip Lines," *IEEE Trans.*, Vol. MTT-16, 1968, pp. 251–256.

[53] Stinehelfer, H. E., "An Accurate Calculation of Uniform Microstrip Transmission Lines," *IEEE Trans.*, Vol. MTT-16, 1968, pp. 439–444.

[54] Silvester, P., "TEM Wave Properties of Microstrip Transmission Lines," *Proc. IEEE*, Vol. 115, 1968, pp. 43–48.

[55] Yamashita, E., "Variation Method for the Analysis of Microstrip Line Transmission Lines," *IEEE Trans.*, Vol. MTT-16, 1968, pp. 529–539.

[56] Bahl, I. J., "Easy and Exact Methods for Shielded Microstrip Design" *Microwaves*, Vol. 17, December 1978, pp. 61–62.

[57] March, S. L., "Empirical Formulas for the Impedance and Effective Dielectric Constant of Covered Microstrip for Use in the Computer-Aided Design of Microwave Integrated Circuits," *Proc. European Microwave Conf.*, Microwave Exhibitors & Publishers Ltd., Kent, United Kingdom, 1981, pp. 671–676.

[58] Gish, D. L., and O. Graham, "Characteristic Impedance and Phase Velocity of a Dielectric Supported Air Strip Transmission Line with Side Walls," *IEEE Trans.*, Vol. MTT-18, 1970, pp. 131–148.

[59] Getsinger, W. J., "Microstrip Dispersion Model," *IEEE Trans.*, Vol. MTT-21, 1973, pp. 34–39.

[60] Edwards, T. C., and R. P. Owens, "2–18 GHz Dispersion Measurements on 10–100 ohm Microstrip Line on Sapphire," *IEEE Trans.*, Vol. MTT-24, 1976, pp. 506–513.

[61] Kirschning, M., and R. H. Jansen, "Accurate Model for Effective Dielectric Constant of Microstrip and Validity up to Millimeter-wave Frequencies," *Electron. Lett.*, Vol. 25, 18 March 1982, pp. 272–273.

[62] Kobayashi, M., "A Dispersion Formula Satisfying Recent Requirements in Microstrip CAD," *IEEE Trans.*, Vol. MTT-36, August 1988, pp. 1246–1250.

[63] Krage, M. K., and G. I. Haddad, "Frequency Dependent Characteristics of Microstrip Transmission Lines," *IEEE Trans.*, Vol. MTT-20, 1972, pp. 678–688.

[64] Denlinger, E. J., "Losses in Microstrip Lines," *IEEE Trans. on Microwave Theory Tech.*, Vol. MTT-28, June 1980, pp. 513–522.

[65] Lee, H. Y., and T. Itoh, "Wideband Conductor Loss Calculation of Planar Quasi-TEM Transmission Lines with Thin Conductors Using Phenomenological Loss Equivalence Method," *IEEE MTT-Int. Microwave Symp. Digest*, 1989, pp. 367–370.

[66] Faraji-Dana, R., and Y. Chow, "Edge Condition of the Field and A.C. Resistance of a Rectangular Strip Conductor," *IEE Proc.*, Vol. 137, Pte H., April 1990, pp. 133–140.

[67] Faraji-Dana, R., and Y. Chow, "The Current Distribution and AC Resistance of a Microstrip Structure," *IEEE Trans.*, Vol. MTT-38, September 1990, pp. 1268–1277.

[68] Aksun, M. I., and H. Morkoc, "GaAs on Si as Substrate for Microwave and Millimeter-Wave Monolithic Integration," *IEEE Trans.*, Vol. MTT-36, January 1988, pp. 160–162.

[69] Bahl, I. J., et al., "Low Loss Multilayer Microstrip Line for Monolithic Microwave Integrated Circuits Applications," *Int. J RF and Microwave Computer-Aided Engineering*, Vol. 8, 1998, pp. 441–454.

[70] Belohoubek, E., and E. J. Denlinger, "Loss Considerations for Microstrip Resonators," *IEEE Trans.*, Vol. MTT-23, 1975, pp. 522–526.

[71] Denlinger, E., "Radiation from Microstrip Resonators," *IEEE Trans.*, Vol. MTT-16, 196, pp. 235–236.

[72] Garg, R., "A Microstrip Design Guide," *Int. J. Electron.*, Vol. 46, 1979, pp. 187–192.

[73] Vendelin, G. D., "Limitations on Stripline Q," *Microwave J.*,Vol. 13, May 1970, pp. 63–69.

[74] Bogatin, E., "Design Rules for Microstrip Capacitance", *IEEE Trans. Components Hybrids Manufacturing Technol.*, Vol. 11, 1988, pp. 253–259.

[75] Bogatin, E., "A Closed Form Analytical Model for the Electrical Properties of Microstrip Interconnects," *IEEE Trans. Components Hybrids Manufacturing Technol.*, Vol. 13, 1990, pp. 258–266.

[76] Eisenstadt, W. R., and Y. Eo, "S-Parameter-Based Interconnect Transmission Line Characterization," *IEEE Trans. Components Hybrids Manufacturing Technol.*, Vol. 15, 1992, pp. 483–490.

[77] Eo, Y., and W. R. Eisenstadt, "High Speed VLSI Interconnect Modeling Based on S-Parameter Measurements," *IEEE Trans. Components Hybrids Manufacturing Technol.*, Vol. 16, 1993, pp. 555–562.

[78] Djordjevic, A. R., and T. K. Sarkar, "Closed-Form Formulas for Frequency-Dependent Resistance and Inductance per Unit Length of Microstrip and Strip Transmission Lines," *IEEE Trans. Microwave Theory Tech.*, Vol. 42, 1994, pp. 241–248.

[79] Ryu, W., et al., " Embedded Microstrip Interconnect Lines for Gigahertz Digital Circuits," *IEEE Trans Advanced Packaging*, Vol. 23, 2000, pp. 495–503.

[80] Verma, A. K., and Nasimuddin, "Quasistatic RLCG Parameters of Lossy Microstrip Line for CAD Applications," *Microwave Optical Technol. Letts.*, Vol. 28, 2001, pp. 209–212.

[81] Pramanick, P., and P. Bhartia, "CAD Models for Millimeter-wave Finlines and Suspended-Substrate Microstrip Lines," *IEEE Trans.*, Vol. MTT-33, December 1985, pp. 1429–1435.

[82] Buntschuh, C., "High Directivity Microstrip Couplers Using Dielectric Overlays," *IEEE G-MTT Symp. Digest*, 1975, pp. 125–127.

[83] Houpt, G., and H. Delys, "High Directivity Microstrip Directional Couplers," *Electron. Lett.*, VoL, 10, May 2, 1974, pp. 142–143.

[84] Izadian, J. S., "A New 6–18 GHz, -3 dB Multisection Hybrid Coupler Using Asymmetric Broadside, and Edge Coupled Lines," *IEEE MIT-S Int. Microwave Symp. Digest*, 1989, pp. 243–247.

[85] Nakajima, M. and E. Yamashita, "A Quasi-TEM Design Method for 3 dB Hybrid Couplers Using a Semi-Reentrant Coupling Section," *IEEE Trans.*, Vol. MTT-38, November 1990, pp. 1731–1736.

[86] Willems, D., and I. Bahl, "A MMIC Compatible Tightly Coupled Line Structure Using Embedded Microstrip," *IEEE Trans.*, Vol. MTT-41, December 1993, pp. 2303–2310.

[87] Quian, Y., and E. Yamashita, "Low-Distortion and Low-Crosstalk Characteristics of Picosecond Pulses in a Dual-Plane Coupled Microstrip Lines Structure," *IEEE Microwave and Guided Wave Letters*,Vol. 3, August 1993, pp. 273–275.

[88] Yamashita, E., "Variational Method for the Analysis of Microstrip Like Transmission Lines," *IEEE Trans.*, Vol. MTT-16, August 1968, pp. 529–535.

[89] Bahl, I. J., and S. S. Stuchly, "Analysis of Microstrip Covered with Lossy Dielectric," *IEEE Trans. on Microwave Theory Tech.*, Vol. MTT-28, February 1980, pp. 104–109.

[90] Das, N. K., and D. M. Pozar, "Generalized Spectral Domain Green's Function for Multilayer Dielectric Substrates with Applications to Multilayer Transmission Lines," *IEEE Trans.*, Vol. MTT-35, March 1987, pp. 326–335.

[91] Finlay, H. J., et al., "Accurate Characterization and Modeling of Transmission Lines for GaAs MMICs," *IEEE Trans.*, Vol. MTT-36, June 1988, pp. 961–967.

[92] Hiraoka, T., T. Tokumitsu, and M. Akaike, "Very Small Wide-band MMIC Magic-Ts Using Microstrip Lines on a Thin Dielectric Film," *IEEE Trans.*, Vol. MTT-37, October 1989, pp. 1569–1575.

[93] Tokumitsu, T., et al., "Multilayer MMICUsing a 3 μm × 3–layer Dielectric Film Structure," *IEEE MTT-S Int. Microwave Symp. Digest*, 1990, pp. 831–834.

[94] Gillick, M., and I. D. Robertson, "An X-band Monolithic Power Amplifier Using Low Characteristic Impedance Thin-Film Microstrip Transformers," *IEEE Microwave and Guided Wave Lett.*, August 1992, pp. 328–330.

[95] Gillick, M., and I. D. Robertson, "Ultra Low Impedance CPW Transmission Lines for Multilayer MMICs," *IEEE Microwave and Millimeter-wave Monolithic Circuits Symp. Digest*, 1993, pp. 127–130.

[96] Banba, S., and H. Ogawa, "Small-Sized MMIC Amplifiers Using Thin Dielectric Layers," *IEEE Trans. on Microwave Theory Tech.*, Vol. 43, March 1995, pp. 485–492.

[97] Schnieder, F., and W. Heinrich, "Model of Thin-Film Microstrip Line for Circuit Design," *IEEE Trans. Microwave Theory Tech.*, Vol. 49, 2001, pp. 104–110.

[98] Stracca, G. B., "A Simple Evaluation of Losses in Thin Microstrips," *IEEE Trans. Microwave Theory Tech.*, Vol. 45, 1997, pp. 281–283.

[99] Ogawa, H., et al., "MMIC Transmission Lines for Multi-Layered MMICs," *IEEE MTT-S Int. Microwave Symp. Digest*, 1991, pp. 1067–1070.

[100] Hasegawa, T., et al., "Characteristics of Valley Microstrip Lines for Use in Multilayer MMICs," *IEEE Microwave and Guided Wave Lett.*, Vol. 1, October 1991, pp. 275–277.

[101] Hasegawa, T., S. Banda, and H. Ogawa, "A Branchline Hybrid Using Valley Microstrip Lines," *IEEE Microwave and Guided Wave Lett.*, Vol. 2, February 1992, pp. 76–78.

[102] Rong, A. S., and Z. L. Sun, "A Novel Quasi-TEM Analysis of Valley Microstrip Lines with Slit for Use in Multilayered MMICs," *IEEE MTT-S Int. Microwave Symp. Digest*, Vol. 2,1993, pp. 955–958.

[103] Rong, A. S., and Z. L. Sun, "Packaging and Metallization Effects of Valley Microstrip Line with Slit for Use in Very Small Multilayer MMICs," *IEEE MTT-S Int. Microwave Symp. Digest*, 1994, pp. 1723–1726.

[104] Ishikawa, T., and E. Yamashita, "Experimental Results on Buried Microstrip Lines for Constructing High-Density Microwave Integrated Circuits," *IEEE Microwave Guided Wave Letters*, Vol. 5, 1995, pp. 437–438.

[105] Madden, J., and N. Fenzi, "HTS Filters and Delay Lines Suit EW Systems," *Microwaves & RF*, Vol. 33, May 1994, pp. 79–84.

[106] Superconductor Technologies Data Sheet, 460 Ward Dr., Santa Barbara, CA, 1994.

[107] Antsos, D., et al., "Modeling of Planar Quasi-TEM Superconducting Transmission Lines," *IEEE Trans.*, Vol. MTT-40, June 1992, pp. 1128–1132.

[108] Lee, H. Y., and T. Itoh, "Phenomenological Loss Equivalence Method for Planar Quasi-TEM Transmission Lines with a Thin Normal Conductor or Superconductor," *IEEE Trans.*, Vol. MTT-37, December 1989, pp. 1904–1909.

[109] Ekholm, E. B., and S. W. McKnight, "Attenuation and Dispersion for High-Tc Superconducting Microstrip Lines," *IEEE Trans.*, Vol. MTT-38, April 1990, pp. 387–395.

[110] Van Deventer, T. E., et al., "High Frequency Characterization of High-Temperature Superconducting Thin Film Lines," *IEEE MTT-S Int. Microwave Symp. Digest*, 1990, pp. 285–288.

[111] Vendik, I. B., et al., "A CAD Model for Microstrips on r-cut Sapphire Substrates," *Int. J. Microwave and Millimeter-Wave Computer-Aided Engineering*, Vol. 4, October 1994, pp. 274–383.

[112] Vendik, O., and E. Kollberg,. "Software Models HTSC Microstrip and Coplanar Lines," *Microwaves & RF*, Vol. 32, July 1993, pp. 118–120.

[113] Lee, L. H., et al., "Full-Wave Analysis of Superconducting Microstrip Lines on Anisotropic Substrates Using Equivalent Surface Impedance Approach," *IEEE Trans.*, Vol. MTT-41, December 1993, pp. 2359–2367.

[114] Bybokas, J., and B. Hammond, "High Temperature Superconductors," *Microwave J.*, Vol. 23, February 1990, pp. 127–138.

[115] Williams, J. T., and S. A. Long, "High Temperature Superconductors and Their Application in Passive Antenna System," *IEEE Antenna Propagation Mag.*, August 1990, pp. 7–18.

[116] Agarwal, K. K., "Superconductors and MMICs in Microwave Systems," *Appl. Microwave*, Vol. 4, Spring 1992, pp. 72–81.

[117] Hammond, R. B., G. L. Hey-Shipton, and G. L. Matthaei, "Designing with Superconductors," *IEEE Spectrum*, April 1993, pp. 34–39.

[118] Delin, K. A., and T. P. Orlando, "Superconductivity," *The Electrical Engineering Handbook* (R. C. Dorf, Editor-in-Chief), Boca Raton, FL: CRC Press, 1993.

[119] Shen, Z. Y., et al., "High-Temperature Superconductor/II-V Hybrid Microwave Circuits," *Microwave Opt. Tech Letts.*, Vol. 6, October 1993, pp. 732–736.

[120] Liang, G. C., et al., "High-Power HTS Microstrip Filters for Wireless Communication," *IEEE MTT-S Int. Microwave Symp. Digest*, 1994, pp. 183–186.

[121] Shen, Z. Y., *High-Temperature Superconducting Microwave Circuits*, Norwood, MA: Artech House, 1994.

[122] Madden, J., "Microwave HTS Application Notes," Superconductor Technologies, Santa Barbara, CA,1994.

[123] Alley, G. D., "Interdigital Capacitors and Their Application to Lumped-Element Microwave Integrated Circuits," *IEEE Trans.*, Vol. MTT-18, 1970, pp. 1028–1033.

[124] Pettenpaul, E., et al., "CAD Models of Lumped Elements on GaAs Up to 18 GHz," *IEEE Trans.*, 'Vol. MTT-36, February 1988, pp. 294–304.

[125] Sadhir, V. K., I. J. Bahl, and D. A. Willems, "CAD Compatible Accurate Models of Microwave Passive Lumped Elements for MMIC Applications," *Int. J Microwave and Millimeter-Wave Computer-Aided Engineering*, Vol. 4, April 1994, pp. 148–162.

[126] Bahl, I. J., and P. Bhartia, *Microwave Solid State Circuit Design, Second Edition*, Hoboken, NJ: John Wiley, 2003, Chapter 2.

[127] Bahl, I., *Lumped Elements for RF and Microwave Circuits*, Norwood, MA: Artech House, 2003.

[128] Bhartia, P., and I. J. Bahl, *Millimeter Wave Engineering and Applications*, New York: John Wiley, 1984.

[129] Rizzi, P. A., *Microwave Engineering Passive Circuits*, Englewood Cliffs, NJ: Prentice Hall, 1988.

[130] Chang, K. (ed.), *Handbook of Microwave and optical Components*, Vol. 1, New York: John Wiley, 1989.

[131] Pozar, D. M., *Microwave Engineering*, Reading, PA: Addison-Wesley, 1990.

[132] Chang, K., *Microwave Solid-State Circuits and Applications*, New York: John Wiley & Sons, 1994.

[133] Kollberg, E. L. (ed.), *Microwave and Millimeter-Wave Mixers*, New York: IEEE Press, 1984.

[134] Pucel, R. A. (ed.), *Monolithic Microwave Integrated Circuits*, New York: IEEE Press, 1985.

[135] Goyal, R. (ed.), *Monolithic Microwave Integrated Circuits: Technology and Design*, Norwood, MA: Artech House, 1989.

[136] Chang, K. (ed.), *Handbook of Microwave and Optical Components*, Vol. 2, New York: John Wiley, 1990.

[137] Ali, F., and A. Gupta (eds.), *HEMTs and HBTs: Devices, Fabrication and Circuits*, Norwood, MA: Artech House, 1991.

[138] Chang, K., I. Bahl, and V. Nair, *RF and Microwave Circuit and Component Design for Wireless Systems*, Hoboken, NJ: John Wiley, 2002.

[139] Vendelin, G. D., A. Pavio, and U. L. Rohde, *Microwave Circuit Design Using Linear and Nonlinear Techniques, Second Edition*, Hoboken, NJ: John Wiley, 2005.

[140] Bahl, I. J., *Fundamental of RF and Microwave Transistor Amplifiers*, Hoboken, NJ: John Wiley, 2009.

[141] Tummala, R. R., and E.J. Rayaszewski (Eds.), *Microelectronic Packaging Handbook*, New York: Van Nostrand Reinhold, 1989.

[142] Chai, S., et al., "Low-Cost Package Technology for Advanced MMIC Applications," *IEEE Int. Microwave Symp. Digest*, 1990, pp. 625–628.

[143] Shih, Y. C., et al., "A High Performance Quartz Package for Millimeter Wave Applications," *IEEE Int. Microwave Symp. Digest*, 1991, pp. 1063–1066.

[144] Smith, S. R., and M. T. Murphy, "Electrical Characterization of Packages for Use with GaAs MMIC Amplifiers," *IEEE MTT-S Int. Microwave Symp. Digest*, 1993, pp. 131–134.

[145] Ndagijimana, F., et al., "The Inductive Connection Effects of a Mounted SPDT in a Plastic S08 Package," *IEEE MTT-S Int. Microwave Symp. Digest*, 1993, pp. 91–94.

[146] Wein, D., et al., "Microwave and Millimeter-Wave Packaging and Interconnection Methods for Single and Multiple Chip Modules," *IEEE GaAs IC Symp. Digest*, 1993, pp. 333–336.

[147] Strauss, G., and W. Menzel, "A Novel Concept for mm-Wave Interconnects and Packaging," *IEEE MTT-S Int. Microwave Symp. Digest*, 1994, pp. 1141–1144.

CHAPTER 3

Microstrip Discontinuities I: Quasi-Static Analysis and Characterization

3.1 Introduction

Microstrip circuits invariably incorporate transmission line discontinuities of one type or another. Some of the most common forms of microstrip discontinuities are open ends, gaps, steps in width, right-angled bends, T junctions, and cross junctions. These are shown in Figure 3.1. Examples of circuits or circuit elements, wherein these discontinuities occur frequently, are also listed in this figure. A complete understanding and design of microstrip circuits require characterization of various discontinuities included in the circuit. Since discontinuity dimensions are usually much smaller than the wavelength in microstrip, they may be modelled by lumped element equivalent circuits. A more complete characterization involves determination of frequency-dependent scattering matrix coefficients associated with the discontinuity. Various methods of characterization of microstrip discontinuities are discussed in this and the next chapter.

Discontinuities appear in conventional microwave circuits (using coaxial lines and waveguides) also. However, it may be pointed out that it is much more important to characterize discontinuities in microstrip circuits accurately. This is because of the fact that the microstrip circuits do not lend themselves to easy adjustments or tuning after the fabrication of the circuit is completed. If a provision is made for adjustments, the main advantages of compactness and reliability gained by the use of microstrip circuits are lost (at least partially). In monolithic circuits the first-pass success of design is heavily dependent on accurate characterization of microstrip and other discontinuities. Recent developments in microwave CAD have emphasized the introduction of accurate models for microstrip discontinuities.

A discontinuity in a microstrip is caused by an abrupt change in the geometry of the strip conductor. Therefore, electric and magnetic field distributions are modified near the discontinuity. The altered electric field distribution gives rise to a change in capacitance, and the changed magnetic field distribution can be expressed in terms of an equivalent inductance. The analysis of a microstrip discontinuity involves the evaluation of these capacitances and inductances and can either be based on quasi-static considerations or carried out more rigorously by fullwave analysis.

Quasi-static analysis involves calculations of static capacitances and low-frequency inductances. Equivalent circuits for discontinuities may be derived from these results. Alternatively, a waveguide type dynamic analysis taking dispersion (and possibly higher order modes) into account may be carried out. This can be based on the planar waveguide model of the microstrip line or one of the more

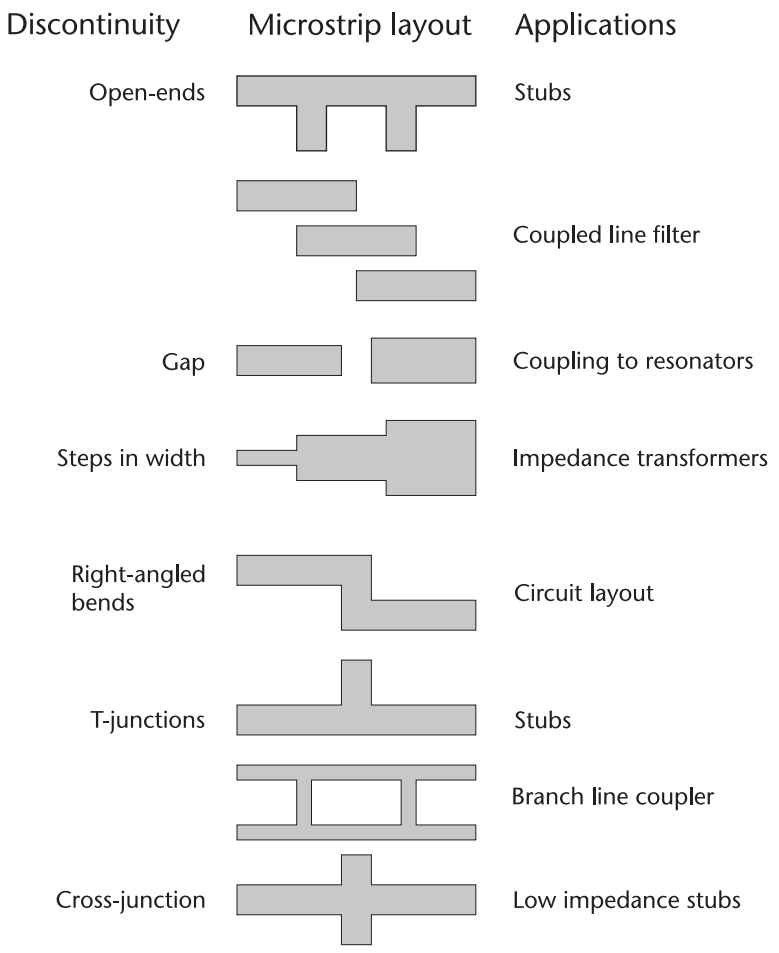

Figure 3.1 Various types of microstrip discontinuities and their typical applications.

rigorous full-wave electromagnetic analyses. Such a dynamic analysis leads to a frequency-dependent scattering matrix. Again, equivalent circuits for discontinuities can be based on these results. Methods for the calculation of quasi-static capacitances and inductances for a discontinuity will be discussed in this chapter. Methods of dynamic analysis of the discontinuities are included in Chapter 4.

3.2 Discontinuity Capacitance Evaluation

The static values of capacitances associated with discontinuities can be evaluated by finding the excess charge distribution near the discontinuity. The quasi-static methods for the evaluation of discontinuity capacitance have been treated by Farrar and Adams [1–3], Maeda [4], Itoh et al. [5, 6], Silvester and Benedek [7, 8], Benedek and Silvester [9], and Horton [10,11]. The different methods used for these calculations are:

1. Matrix inversion method [1–3];
2. Variational method [4];
3. Galerkin's method in the spectral domain [5, 6];
4. Use of line sources with charge reversal [7–9].

These methods are discussed briefly in the following subsections. In all these methods, the following assumptions are implied: (i) the size of the discontinuity is small compared to the wavelength so that the phase variation across the discontinuity can be neglected; (ii) the current on the strip has zero divergence; and (iii) the strip conductor is infinitely thin.

3.2.1 Matrix Inversion Method

The matrix inversion method [3] is a very general approach for determining the static capacitance of a conductor of any arbitrary shape on the top surface of the microstrip substrate. The total conductor area is divided into small subsections over which the charge density can be assumed to be uniform. This subdivision for a microstrip rectangular section of length L and width W is shown in Figure 3.2. The typical subsection Δs_j, of sides Δx_j and Δz_j, is assumed to bear a uniform surface charge density σ_j. The potential at subsection Δs_i due to n number of subsections may be written as

$$V_i = \sum_{j=1}^{n} \sigma_j D_{ij} \tag{3.1}$$

where D_{ij} is a function representing the potential at subsection Δs_i, due to a uniform charge density of magnitude unity on Δs_j. One can write a Green's function expressing potential due to a unit charge at Δs_j. Since the potential varies in all three directions, the Green's function becomes three-dimensional. Values of D_{ij} correspond to values of this Green's function at $y = h$. Equation (3.1 may be put in matrix form as

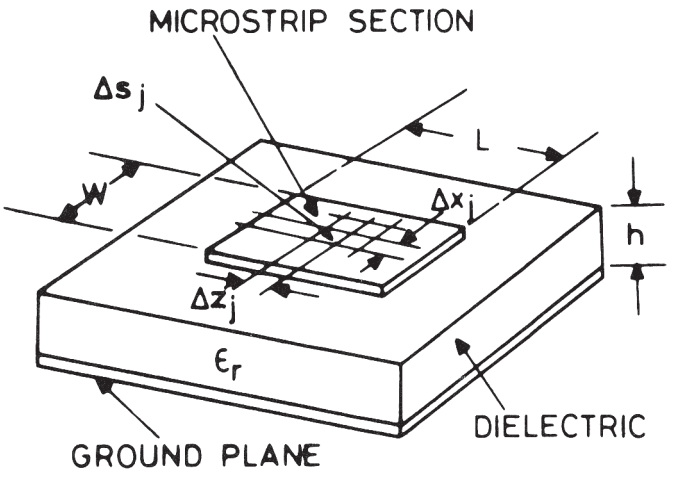

Figure 3.2 A typical microstrip discontinuity area divided into small sections.

$$[\mathbf{V}] = [\mathbf{D}][\boldsymbol{\sigma}] \tag{3.2}$$

The unknown charge densities $[\sigma]$ are obtained by matrix inversion

$$[\boldsymbol{\sigma}] = [\mathbf{D}]^{-1}[\mathbf{V}] \tag{3.3}$$

If the voltage over the conductor with respect to the ground plane is taken as unity, the total capacitance of the conductor may be written as

$$C = \sum_{j=1}^{n} \sigma_j = \sum_{i=j}^{n} \sum_{j=1}^{n} D'_{ij} \tag{3.4}$$

where D'_{ij} represents an element of matrix $[\mathbf{D}]^{-1}$.

In order to implement this method, an expression for D_{ij} is needed. D_{ij} for a rectangular subsection is derived by using the theory of images [3]. A rectangular subsection has been selected because of its frequent occurrence in discontinuity problems. For evaluation of D_{ij}, the potential due to a uniformly charged plate in free space is obtained first. D_{ij} for the microstrip section is then evaluated by using the principle of multiple images. The resulting expression is a series, each term of which is contributed by an image of the charge. This series expression may be written as

$$\begin{aligned}
D_{ij} = & \sum_{n=1}^{\infty} \frac{K^{n-1}}{2\pi\varepsilon_0(1+\varepsilon_r)} \\
& \cdot \Bigg\{ (z_j - z_i)\, \ell n \frac{(c+A)(d+B)(d+G)(c+H)}{(d+C)(c+D)(c+E)(d+F)} \\
& + \frac{\Delta z_j}{2}\, \ell n \frac{(d+B)(d+C)(c+E)(c+H)}{(c+D)(c+A)(d+G)(d+F)} \\
& + (x_j - x_i)\, \ell n \frac{(a+A)(b+B)(b+H)(a+G)}{(b+D)(a+C)(a+E)(b+F)} \\
& + \frac{\Delta x_j}{2}\, \ell n \frac{(b+B)(b+D)(a+E)(a+G)}{(a+C)(a+A)(b+G)(b+F)} \\
& - (2n-2)h \left[\tan^{-1} \frac{ac}{(2n-2)hA} \right. \\
& \left. + \tan^{-1} \frac{bd}{(2n-2)hB} \right] + (2n-2)h \\
& \cdot \left[\tan^{-1} \frac{ad}{(2n-2)hC} + \tan^{-1} \frac{bc}{(2n-2)hD} \right] \\
& + 2nh \left[\tan^{-1} \frac{ac}{2nhE} + \tan^{-1} \frac{bd}{2nhF} \right] \\
& - 2nh \left[\tan^{-1} \frac{ad}{2nhG} + \tan^{-1} \frac{bc}{2nhH} \right] \Bigg\}
\end{aligned} \tag{3.5}$$

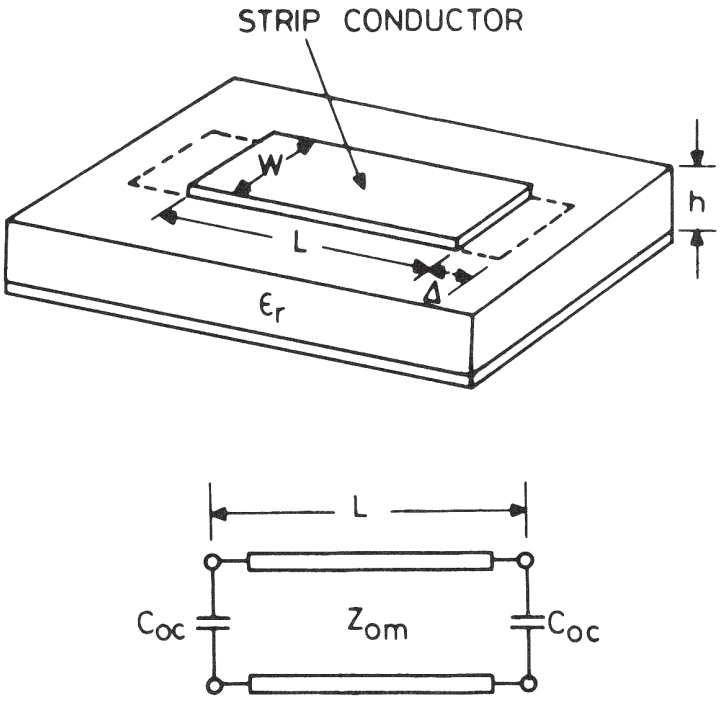

Figure 3.3 Configuration for calculating the microstrip open-end capacitance and its equivalent circuit.

where

$$A = \sqrt{a^2 + c^2 + (2n-2)^2 h^2} \qquad E = \sqrt{a^2 + c^2 + (2nh)^2}$$
$$B = \sqrt{b^2 + d^2 + (2n-2)^2 h^2} \qquad F = \sqrt{b^2 + d^2 + (2nh)^2}$$
$$C = \sqrt{a^2 + d^2 + (2n-2)^2 h^2} \qquad G = \sqrt{a^2 + d^2 + (2nh)^2}$$
$$D = \sqrt{b^2 + c^2 + (2n-2)^2 h^2} \qquad H = \sqrt{b^2 + c^2 + (2nh)^2}$$

and

$$a = z_j - \frac{\Delta z_j}{2} - z_i \qquad b = z_j + \frac{\Delta z_j}{2} - z_i$$
$$c = x_j - \frac{\Delta x_j}{2} - x_i \qquad d = x_j + \frac{\Delta x_j}{2} - x_i$$
$$K = \frac{1 - \varepsilon_r}{1 + \varepsilon_r}$$

Slow convergence of the series in (3.5) is a drawback of this method. About 40 terms of the series have been used in the computation of discontinuity capacitances [3].

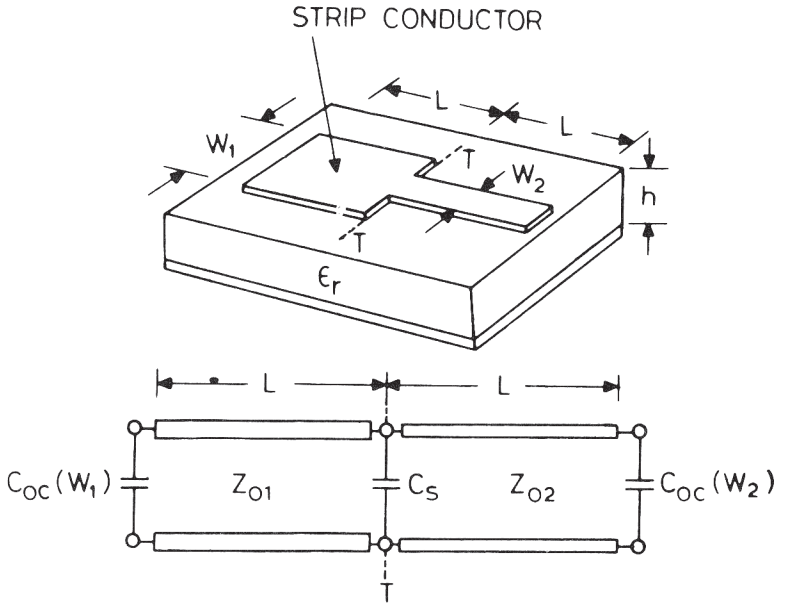

Figure 3.4 Geometry for calculating the capacitance of a step discontinuity and its equivalent circuit.

The method has been used for finding capacitances associated with microstrip open ends, steps, and gaps. The capacitance associated with an open end (shown in Figure 3.3) may be written as

$$C_{oc} = \frac{1}{2}\lim_{L\to\infty}\left[C_t(L) - CL\right] \tag{3.6}$$

$C_t(L)$ is the total capacitance of a microstrip section of total length L and C is the capacitance per unit length of an infinite line of the same width. In order to find the limit in (3.6), the length L is increased iteratively and the total capacitance is computed until the open-end capacitance given by (3.6) converges. A difficulty with this procedure is that (3.6) involves subtraction of two nearly equal large numbers, and therefore very accurate computations of $C_t(L)$ and CL are necessary.

The configuration for calculating the capacitance associated with a step in the width of a microstrip is shown in Figure 3.4. Its equivalent circuit is also shown in this figure. The capacitance associated with the step is evaluated as

$$C_s = \lim_{L\to\infty}\left[C_t(L) - C_{oc}(W_1) - C_{oc}(W_2) - C_1L - C_2L\right] \tag{3.7}$$

where $C_{oc}(W_1)$ and $C_{oc}(W_2)$ are open-end capacitances of lines of width W_1 and W_2, respectively, and C_1 and C_2 are capacitances per unit length for these lines.

In the case of a microstrip gap, the equivalent circuit consists of three capacitances in a π-configuration as shown in Figure 3.5.

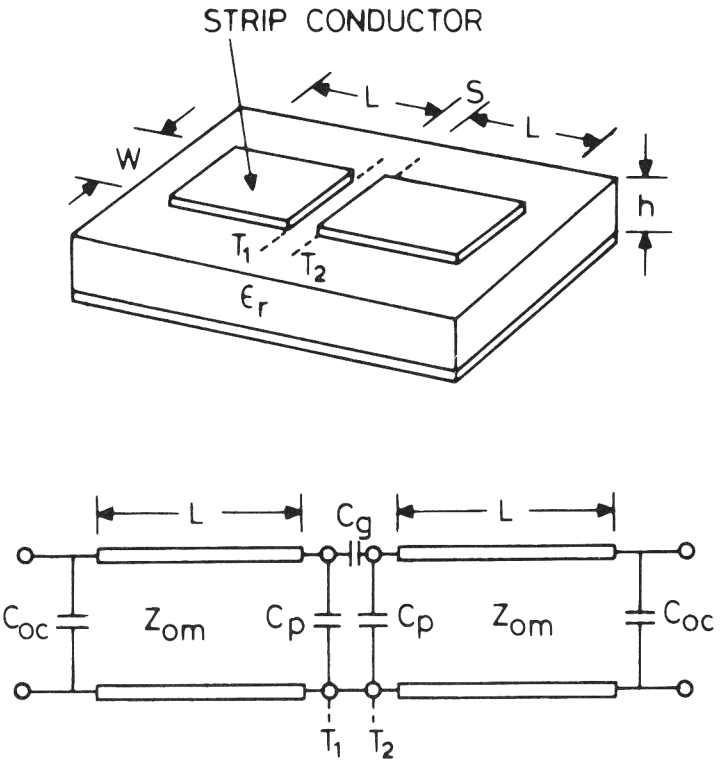

Figure 3.5 Configuration for characterizing a microstrip gap and its equivalent circuit.

To evaluate these capacitances, a capacitance matrix [C(L)] is computed as

$$[\mathbf{C}(\mathrm{L})] = \begin{bmatrix} C_{11}(L) & C_{12}(L) \\ C_{21}(L) & C_{22}(L) \end{bmatrix} \tag{3.8}$$

where $C_{ij}(L)$ are related to the elements of the admittance matrix of the two-port network (shown in Figure 3.5) by

$$C_{ij}(L) = Y_{ij}/j\omega \tag{3.9}$$

Capacitances C_p and C_g are then computed by using

$$C_p = \lim_{L\to\infty} \left[C_{11}(L) - CL - C_{oc}\right] \tag{3.10a}$$

$$C_g = \lim_{L\to\infty} C_{12}(L) \tag{3.10b}$$

It may be noted that the subtraction of two nearly equal large numbers is involved in (3.7) and (3.10a). But such a subtraction is not involved in the computation of C_g, and thus an accurate computation of C_g is much less time consuming.

One can conclude that the method described above is a general one and can be used to compute the excess capacitance of any microstrip discontinuity. The difficulties faced in this method are slow convergence of infinite series in the three-dimensional Green's function and the subtraction of two nearly equal large numbers. The accuracy of capacitance results can be improved at the expense of increased computer time.

3.2.2 Variational Method

This method [4] uses the variational principle to formulate the capacitance problem. It is known that the capacitance can be expressed by a variational expression that is stationary with respect to arbitrary first-order variations in the charge distribution on the strip conductor [12]. If the charge distribution is $\rho(r)$, the capacitance C may be expressed as

$$\frac{1}{C} = \frac{\iint \rho(r) G(r;r') \rho(r') dv' dv}{\left[\int \rho(r') dv'\right]^2} \tag{3.11}$$

where the integrals are over all the volume in which the charge is distributed. Source and observation point coordinates are shown in Figure 3.6. Since (3.11) is a lower bound type of expression, the capacitance can be obtained by maximizing with a suitable choice of charge distribution as a trial function.

Therefore, the charge distribution does not need to be known exactly when using this method. G is a three-dimensional Green's function for potential and satisfies the relation

$$\nabla^2 G(x,y,z;x',y',z') = -\frac{1}{\varepsilon_0 \varepsilon_r} \delta(x-x') \delta(y-y') \delta(z-z') \tag{3.12}$$

where δ indicates a Dirac's delta function. Green's functions for the case $y = h$ are adequate for the evaluation of excess capacitance of a discontinuity using the variational expression (3.11).

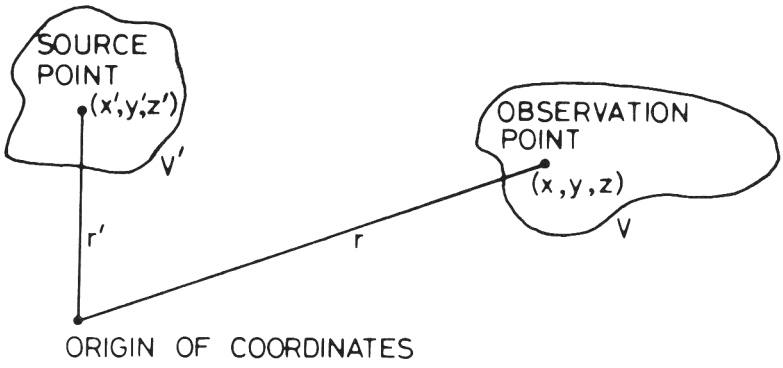

Figure 3.6 Coordinate system for source and observation points.

The variational method has been used to characterize two types of discontinuities: an open end and a gap, for which suitable Green's functions have been developed. As shown in Figure 3.7(a), a gap in the strip conductor of a microstrip line, which is represented by a π equivalent circuit, can be analyzed by placing an electric wall and a magnetic wall successively along the plane of symmetry A. This corresponds to a short circuit and an open circuit, respectively, in the equivalent circuit representation. The capacitances between the microstrip end and the plane A are denoted C_e for electric wall and C_m for magnetic wall. The parameters of the equivalent π circuit, C_p (shunt gap capacitance) and C_g (coupling capacitance between the adjacent strip conductors), may be written in terms of C_e and C_m as

$$C_e = C_p + 2C_g \quad \text{and} \qquad C_m = C_p \tag{3.13}$$

The capacitances C_e and C_m can be evaluated using (3.11) with suitable G and ρ. The configuration considered for evaluation of G for the two cases is shown in Figure 3.7(b). The portion of the microstrip betwen the planes of symmetry located at $z = 0$ and $z = -c$ is enclosed in a box as shown in this figure. Two Green's functions G_e and G_m are evaluated for electric wall and magnetic wall cases by writing the solution of (3.12) as a linear combination of hyperbolic sinusoidal functions and applying boundary and continuity conditions. The expressions obtained for G_e and G_m may be written as [4]

$$G_e(x,y,z;x',h,z') = \begin{cases} \displaystyle\sum_{m=1}^{\infty}\sum_{n=1}^{\infty} PQ\sinh(\gamma_{mn}y)\sinh\left[\gamma_{mn}(b-h)\right] & (0 \le y \le h) \quad (3.14a) \\ \displaystyle\sum_{m=1}^{\infty}\sum_{n=1}^{\infty} PQ\sinh\left[\gamma_{mn}(b-y)\right]\sinh(\gamma_{mn}h) & (h \le y \le b) \quad (3.14b) \end{cases}$$

and

$$G_m(x,y,z;x',h,z') = \begin{cases} \displaystyle\sum_{m=1}^{\infty}\sum_{n=0}^{\infty} \sigma_n PR\,\sinh(\gamma_{mn}y)\sinh\left[\gamma_{mn}(b-h)\right] & (0 \le y \le h) \quad (3.15a) \\ \displaystyle\sum_{m=1}^{\infty}\sum_{n=0}^{\infty} \sigma_n PR\,\sinh\left[\gamma_{mn}(b-y)\right]\sinh(\gamma_{mn}h) & (h \le y \le b) \quad (3.15b) \end{cases}$$

where

$$P = \frac{4}{ac\gamma_{mn}\Gamma_{mn}}\sin\left(\frac{m\pi x}{a}\right)\sin\left(\frac{m\pi x'}{a}\right)$$

$$Q = \sin\left(\frac{n\pi z}{c}\right)\sin\left(\frac{n\pi z'}{c}\right)$$

$$R = \cos\left(\frac{n\pi z}{c}\right)\cos\left(\frac{n\pi z'}{c}\right)$$

$$\gamma_{mn} = \left[\left(\frac{m\pi}{a}\right)^2 + \left(\frac{n\pi}{c}\right)^2\right]^{1/2}$$

$$\Gamma_{mn} = \varepsilon_r \cosh(\gamma_{mn}h)\sinh\left[\gamma_{mn}(b-h)\right] + \sinh(\gamma_{mn}h)\cosh\left[\gamma_{mn}(b-h)\right]$$

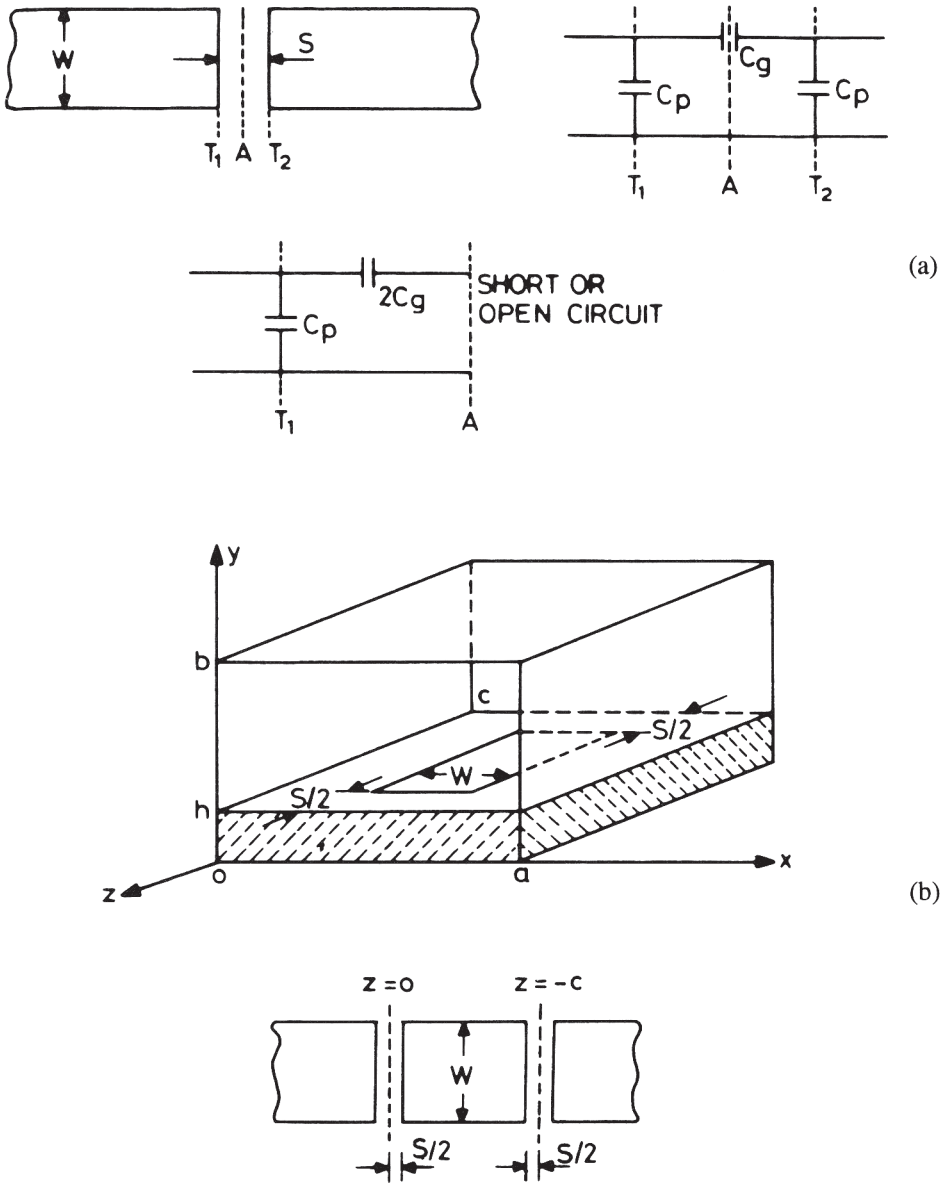

Figure 3.7 (a) Representation of a gap in microstrip and its equivalent circuit and (b) configuration for evaluating Green's functions for gap capacitances.

and σ_n is $\frac{1}{2}$ for $n = 0$ and is 1 for $n \neq 0$. The only additional information required to solve (3.11) is an estimate for the charge distribution ρ. If it is assumed that $\rho(x, z)$ is separable in the x- and z-directions we can write

$$\rho(x, z) = f(x)g(z) \tag{3.16}$$

where $f(x)$ corresponds to the charge distribution of a uniform microstrip and may be written as [13]

$$f(x)=\begin{cases} 1+\left|\dfrac{2}{W}\left(x-\dfrac{a}{2}\right)\right|^3 & \text{for}\left|x-\dfrac{a}{2}\right|\le\dfrac{W}{2} \\ 0 & \text{elsewhere}\end{cases} \tag{3.17}$$

Charge density in the longitudinal direction also increases near the edge of the strip conductor, and $g(z)$ may be assumed to be of the form

$$g(z)=\begin{cases} 0 & \dfrac{c}{2}-\dfrac{S}{2}\le\left|z-\dfrac{c}{2}\right|\le\dfrac{c}{2} \\ 1+\dfrac{K}{h}\left\{\left|z-\dfrac{c}{2}\right|-\dfrac{c}{2}+\dfrac{S}{2}+h\right\} & \dfrac{c}{2}-\dfrac{S}{2}-h\le\left|z-\dfrac{c}{2}\right|\le\dfrac{c}{2}-\dfrac{S}{2} \\ 1 & \left|z-\dfrac{c}{2}\right|\le\dfrac{c}{2}-\dfrac{S}{2}-h\end{cases} \tag{3.18}$$

The coefficient K is determined so as to maximize the capacitance. A table of optimum values of coefficient K for the electric and magnetic walls for various values of ε_r and S/h is given by Maeda [4]. When S/h is large (or in the case of an open-circuit discontinuity), K becomes unity for the electric as well as the magnetic walls.

This method has been used to characterize gaps and open ends. The open end capacitance is evaluated as a limit of the gap capacitance C_g when the gap width becomes very large. A fairly good agreement with experimental results is reported in [4].

3.2.3 Galerkin's Method in the Fourier Transform Domain [5, 6]

This method is similar to Galerkin's method in FTD used for fullwave analysis of microstrip lines discussed in Chapter 2 and the variational method in FTD used for quasi-static analysis in Chapter 1. The microstrip configuration and the coordinate system are shown in Figure 3.8.

In this case a two-dimensional Fourier transform in the (x-z)-plane is used. Transforms of potential and charge are defined by

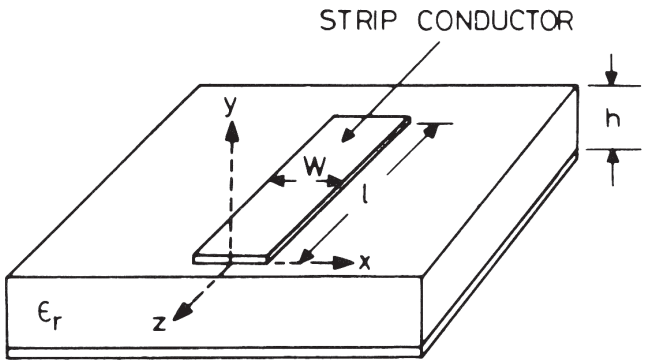

Figure 3.8 Microstrip geometry and the coordinate system used for Galerkin's method in spectral domain.

$$\tilde{\phi}(\alpha,y,\beta) = \int_{-\infty}^{\infty}\int_{-\infty}^{\infty} \phi(x,y,z)\exp\left(j\{\alpha x + \beta z\}\right)dx\,dz \tag{3.19}$$

$$\tilde{\rho}(\alpha,\beta) = \int_{-\ell/2}^{\ell/2}\int_{-W/2}^{W/2} \rho(x,z)\exp\left(j\{\alpha x + \beta z\}\right)dx\,dz \tag{3.20}$$

In the spectral domain, Poisson's equation is written as

$$\left[\frac{\partial^2}{\partial y^2} - \left(\alpha^2 + \beta^2\right)\right]\tilde{\phi}(\alpha,y,\beta) = -\frac{1}{\varepsilon_0}\rho(\alpha,\beta)\delta(y) \tag{3.21}$$

Boundary conditions at $y = -h$ and $y \to \infty$ and the interface conditions across $y = 0$ are written in the spectral domain. When these conditions are applied to (3.21), we obtain

$$G(\alpha,\beta)\tilde{\rho}(\alpha,\beta) = \tilde{\phi}_i(\alpha,0,\beta) + \tilde{\phi}_0(\alpha,0,\beta) \tag{3.22}$$

where

$$G(\alpha,\beta) = \frac{1}{\varepsilon_0\sqrt{\left(\alpha^2+\beta^2\right)}\left[1 + \varepsilon_r \coth\left\{\sqrt{\left(\alpha^2+\beta^2\right)}h\right\}\right]} \tag{3.23}$$

and $\tilde{\phi}_1$ and $\tilde{\phi}_0$ are the transforms of the potential functions on the strip and outside the strip at $y = 0$, respectively. We assume that the potentials on the strip and the ground plane are 1 and 0 V, respectively. Using (3.19),

$$\tilde{\phi}_i = \frac{4}{\alpha\beta}\sin\frac{\alpha W}{2}\sin\frac{\beta\ell}{2} \tag{3.24}$$

Now (3.22) contains two unknowns: the transforms of charge on the strip $\tilde{\rho}$ and the potential outside the strip $\tilde{\phi}_0$.

At this stage Galerkin's method is applied, which eliminates one of the unknowns $\tilde{\phi}_0$ and converts (3.22) into a small-sized matrix equation. This is subsequently solved for the unknown coefficients. The matrix equation is

$$\sum_{n=1}^{N} K_{mn} d_n = f_m \qquad m = 1,2,\ldots,N \tag{3.25}$$

where

$$K_{mn} = \int_{-\infty}^{\infty}\int_{-\infty}^{\infty} \tilde{\zeta}_m(\alpha,\beta)G(\alpha,\beta)\tilde{\zeta}_n(\alpha,\beta)d\alpha\,d\beta$$

$$f_m = \int_{-\infty}^{\infty}\int_{-\infty}^{\infty} \tilde{\zeta}_m(\alpha,\beta)\tilde{\phi}_i(\alpha,0,\beta)d\alpha\,d\beta$$

and ζ'_m are the basis functions for $\tilde{\rho}$. Equation (3.25) is solved for d_n. Finally, the charge distribution in the space domain is expressed in terms of the superposition of the inverse transforms of the basis functions weighted by the coefficients d_n.

The choice of the basis functions is arbitary as long as they satisfy the required condition that they are zero in the appropriate range. The basic functions chosen are transforms of the following:

$$\zeta_m(x,z) = \begin{cases} |x|^{k-1}|z|^{j-1} & \text{on the strip} \\ 0 & \text{otherwise} \end{cases} \tag{3.26}$$

where $m = 1$ for $k = 1$, $j = 1$; $m = 2$ for $k = 2$, $j = 1$ and so on. In actual numerical computations one or two terms in ζ_m are sufficient. Total capacitance for the strip is obtained from the expression

$$C = \int_{-\ell/2}^{\ell/2} \int_{-W/2}^{W/2} \rho(x,z)\,dx\,dz = (2\pi)^2 \sum_{n=1}^{N} d_n f_n \tag{3.27}$$

The fringing capacitance at the end of the open-circuited microstrip may again be evaluated using (3.6).

Comparing with the variational method of the last subsection, one notes that Green's function in the transform domain is a closed-form expression in contrast to a slowly converging series in the space domain.

Although this method could, in principle, be applied to other discontinuities also, the results are available for microstrip open ends only.

3.2.4 Use of Line Sources with Charge Reversal

All three methods for the evaluation of discontinuity capacitance discussed so far involve subtraction of two nearly equal large quantities. This factor limits the computational accuracy. A method using line sources with charge reversal [7–9] overcomes this difficulty. This method uses line sources (not subareas) to develop Green's functions suitable for discontinuity problems. The basic element common to all the discontinuities considered using this method is a semi-infinite line charge. Formulation of Green's function for a semi-infinite line charge is shown in Figure 3.9. Here, the semi-infinite line charge (c) is considered as a superposition of two line charges (a) and (b). Figure 3.9(a) shows a uniform and infinitely long line charge such as present in the case of an infinite microstrip. This charge distribution can be obtained by solving

$$\phi_e(x) = \int_{-\infty}^{\infty} \sigma_\infty(\xi) G_e(x,\xi)\,d\xi \tag{3.28}$$

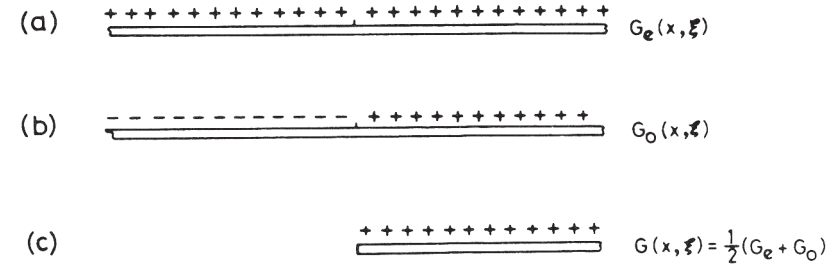

Figure 3.9 Formulation of Green's functions for a semi-infinite line source.

where G_e is the two-dimensional Green's function of the microstrip problem discussed in Section 1.2.3 and σ_∞ is the charge density on an infinitely extended microstrip line. We also consider a charge distribution shown in Figure 3.9(b) that is exactly similar to $\sigma_\infty(\zeta)$ on half the infinite strip and exactly $-\sigma_\infty(\zeta)$ on the other half. While this situation is physically difficult to realize, there is no mathematical objection to it, and the potential distribution in this case may be written as

$$\phi_0(x) = \int_{-\infty}^{\infty} \sigma_\infty(\xi) G_0(x, \xi)\ d\xi \tag{3.29}$$

where $G_0(x, \zeta)$ is the appropriate Green's function. When the charge distributions given by (3.28) and (3.29) are combined, we obtain the configuration of a semi-infinite line charge, Figure 3.9(c), and the potential distribution is now given by

$$\phi_{si} = \frac{1}{2}\{\phi_e + \phi_0\} = \frac{1}{2}\int \sigma_\infty(\xi)\{G_e(x,\xi) + G_0(x,\xi)\}\, d\xi \tag{3.30}$$

where ϕ_{si} is the potential associated with a charge distribution exactly like that of an infinite microstrip but terminating at the origin. The potential ϕ_{si} cannot satisfy the requirement of constant potential everywhere on the semi-infinite strip. To obtain a constant potential, a certain amount of extra charge, say σ_e, must be placed on half the strip. This excess charge σ_e may be obtained from the equation

$$\phi - \phi_{si} = \int \sigma_e(\xi) G(x;\xi)\, d\xi \tag{3.31}$$

where ϕ is a constant potential ($= \phi_e$) over the semi-infinite length and $G = 1/2(G_e + G_0)$. It may be noted that the excess charge $\sigma_e(\zeta)$ is responsible for the discontinuity capacitance C, which may now be written as

$$C = \frac{1}{\phi}\int \sigma_e\, dx \tag{3.32}$$

Using the concepts outlined above, computing the capacitance associated with a microstrip open end involves:

1. Constructing G_e and G_0;
2. Evaluating ϕ_{si} from (3.30);
3. Solving integral equation (3.31) for σ_e;
4. Finding the capacitance from (3.32).

Although the integration (3.31) is over a semi-infinite length, it may be noted that both the potential residual and the excess charge approach zero asymptotically (and rather rapidly) for points at increasing distances from the strip end. Also, (3.31) and (3.32) permit the solution for excess charge density and excess capacitance directly, and the subtraction of two equally large quantities is not involved.

Green's functions G_e and G_0 are obtained [7] by considering the multiple images of a line charge when placed parallel to a dielectric slab. Green's function G_e for a microstrip is given by (1.36) of Chapter 1, and G_0 may be written as

$$G_0(x,h,z;x_0) = \frac{1-K}{4\pi\,\varepsilon_0\,\varepsilon_r}\left[f(0) - (1-K)\sum_{n=1}^{\infty} K^{n-1} f(n)\right] \tag{3.33}$$

where $K = (1 - \varepsilon_r)/(1 + \varepsilon_r)$ and

$$f(n) = \ell n \frac{\sqrt{z^2 + 4n^2h^2 + (x - x_0)^2} + z}{\sqrt{z^2 + 4n^2h^2 + (x - x_0)^2} - z}$$

The line source configuration used is shown in Figure 3.10 and h is the height of the dielectric substrate.

This method is very general and is used for all types of microstrip discontinuities [8, 9] shown in Figure 3.1. The formulation for a microstrip gap is sketched in Figure 3.11. Green's functions G_{even} and G_{odd} are used in equations similar to (3.31) to calculate the residual potentials which lead to excess charges and discontinuity capacitances. Similar formulations may be carried out for other discontinuities also.

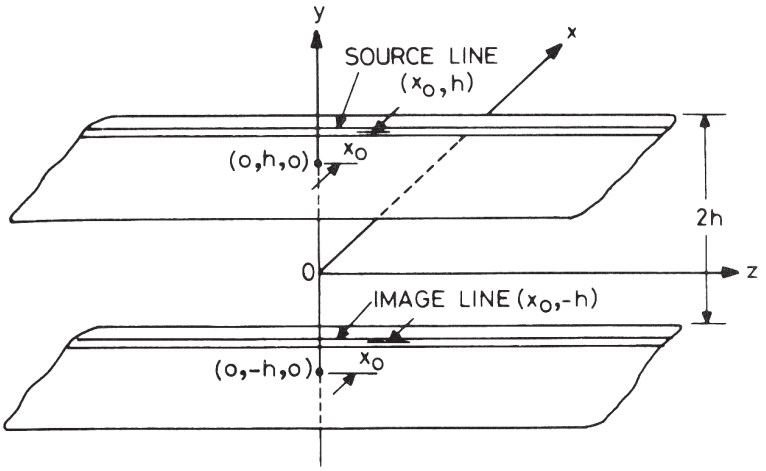

Figure 3.10 Configuration for calculating G_e and G_o of Figure 3.9.

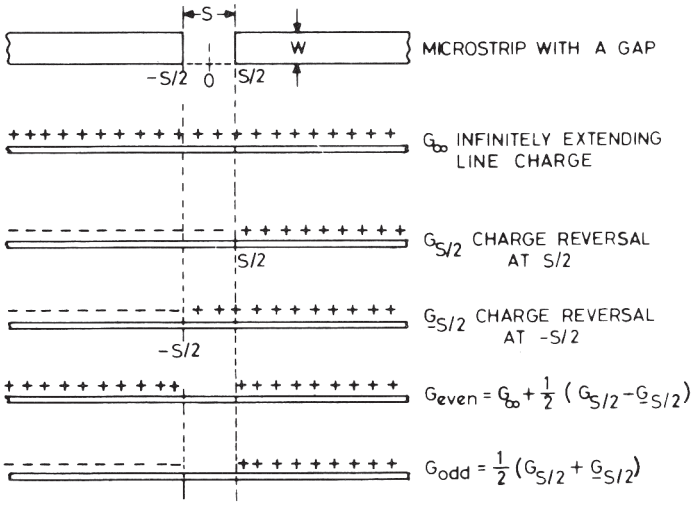

Figure 3.11 Representation of a microstrip gap in terms of line charges.

3.3 Discontinuity Inductance Evaluation

The calculation of capacitances associated with microstrip discontinuities has been discussed in the above section. However, in several cases, for example, bends, steps, and T-junctions, inductive effects also become significant. Evaluation of inductive reactances in the equivalent circuit of microstrip discontinuities using the quasi-static method [14, 15] will be discussed in this section. These inductive components are frequency dependent, and quasi-static calculations can only provide their low frequency values.

When inductances are being calculated, the presence of the dielectric substrate (provided it is nonmagnetic) may be disregarded, and only the discontinuity structure and its image in the ground plane are considered. For magnetic substrates it will be necessary to consider the multiple images formed.

The magnetic vector potential A due to the current density J on any section of the line or discontinuity can be written as

$$A = \mu_0 \int GJ\, dV \tag{3.34}$$

where G is Green's function given by

$$G = \frac{1}{4\pi \left[(x - x_0)^2 + (y - y_0)^2 + (z - z_0)^2 \right]^{1/2}} \tag{3.35}$$

From Maxwell's equation, the electric field may be written as

$$E = -\frac{\partial A}{\partial t} - \nabla\phi \tag{3.36}$$

where ϕ is the impressed voltage on the strip that causes current to flow. Also from Ohm's law we have

$$J = \sigma E \tag{3.37}$$

where σ is the strip conductivity. Combining (3.34), (3.36), and (3.37) we may write

$$J + \mu_0 \sigma \frac{\partial}{\partial t} \int GJ\, dV = -\sigma \nabla\phi \tag{3.38}$$

For good conductors $\sigma \to \infty$ and (3.38) may be rewritten as

$$\mu_0 \frac{\partial}{\partial t} \int GJ\, dV \simeq -\nabla\phi \tag{3.39}$$

Divergence of (3.39) yields (under quasi-static assumptions)

$$\nabla^2 \phi = 0 \tag{3.40}$$

which implies that the impressed potential satisfies Laplace's equation on the strip conductor. The current density distribution on the microstrip structure can be found by solving (3.40) for ϕ (or $\nabla\phi$) and then (3.39) for J. Knowledge of current density distribution J enables the inductance L of the microstrip structure to be obtained from the relation

$$\int\left(\bar{A}\cdot\bar{J}\right)dV = I^2L \qquad \text{where } I = \int\bar{J}\cdot d\bar{S} \tag{3.41}$$

A straightforward implementation of the procedure indicated above will yield a value of discontinuity inductance as the difference between two large numbers corresponding to the inductance of the total structure including the discontinuity and the inductance contributed by the uniform line portion of the discontinuity structure. In this procedure it becomes difficult to obtain accurate values of L. This can be overcome using an excess current technique [14] similar to the excess charge formulation [7] used in Section 3.2.4. We will discuss this technique for the case of a right-angled bend.

For the purpose of inductance calculation, the configuration of the right-angled bend is divided into five sections (S1 to S5) as shown in Figure 3.12. The planes PP' and QQ' are located such that the currents in S1 and S5 are practically the same as for infinitely long lines, that is, $J_{z\infty}$ or $J_{x\infty}$, respectively. In S_2 and S_4, the current distribution is considered to consist of two components $J_{z\infty}$ or $J_{x\infty}$ and J_{e2} or J_{e4}, the latter being excess circulating current because of the discontinuity. In S3 the only current component present is the excess circulating current J_{e3}. The magnitude and the distribution of excess circulating currents J_{e2}, J_{e3} and J_{e4} are to be determined. Equation (3.39) becomes (for the configuration in Figure 3.12),

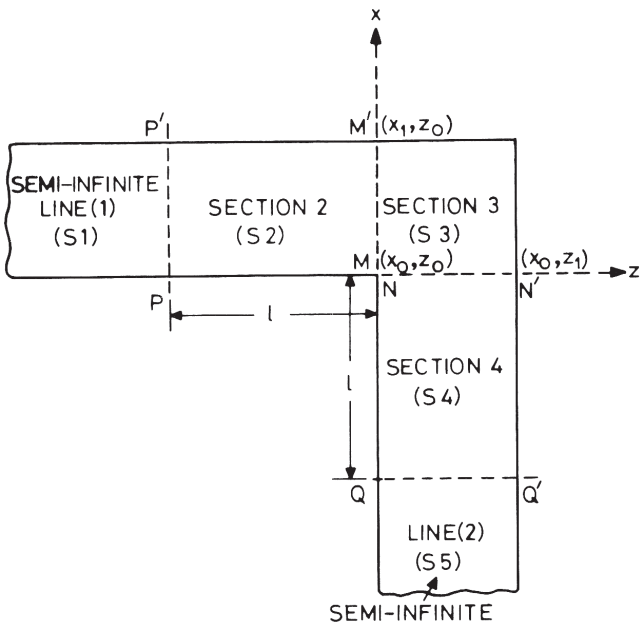

Figure 3.12 Subdivision of a right-angled bend structure for calculating the discontinuity inductance.

$$\int_{S1} G_i J_{z\infty}\, dS + \int_{S2} G_i (J_{z\infty} + J_{e2})\, dS + \int_{S3} G_i J_{e3}\, dS + \int_{S4} G_i (J_{x\infty} + J_{e4})\, dS + \int_{S5} G_i J_{x\infty}\, dS = \frac{-1}{\mu_0} \Delta \Phi \tag{3.42}$$

where $\Phi = \phi/(jt\omega)$, t is the thickness of the strip conductor, and ω is the angular frequency. $J_{z\infty}$ and $J_{x\infty}$ are current distributions for infinite lines and vary only along x and z, respectively. Thus, they can be integrated analytically with respect to x and z, respectively. G_i is Green's function for the line current element and its image and may be written as

$$G_i = \frac{1}{4\pi\left[(x - x_0)^2 + (z - z_0)^2\right]^{1/2}} - \frac{1}{4\pi\left[(x - x_0)^2 + (2h)^2 + (z - z_0)^2\right]^{1/2}} \tag{3.43}$$

When Green's functions for semi-infinite line currents (along with their images in the ground plane) are introduced, (3.42) may be rewritten as

$$\int_{S2+S3+S4} G_i J_e\, dS = \frac{-1}{\mu_0} \nabla \Phi - \int_{z_0}^{z_1} G_2 J_{x\infty}\, dz - \int_{x_0}^{x_1} G_1 J_{z\infty}\, dx \tag{3.44}$$

Green's functions G_1 and G_2 are given by

$$G_1 = \ell n \left[\frac{(x_0 - x) + \left\{(x_0 - x)^2 + (2h)^2 + (z_0 - z)^2\right\}^{1/2}}{(x_0 - x) + \left\{(x_0 - x)^2 + (z_0 - z)^2\right\}^{1/2}} \right] \tag{3.45}$$

and

$$G_2 = \ell n \left[\frac{(z_0 - z) + \left\{(x_0 - x)^2 + (2h)^2 + (z_0 - z)^2\right\}^{1/2}}{(z_0 - z) + \left\{(x_0 - x)^2 + (z_0 - z)^2\right\}^{1/2}} \right] \tag{3.46}$$

Equation (3.44) is solved by Galerkin's method, and the solution for J_e in each region is used to calculate the excess inductance.

This method has also been used for a T-junction [14], a step discontinuity, and a cross junction [15].

3.4 Characterization of Various Discontinuities

Quasi-static techniques for evaluating discontinuity capacitances and inductances were described in the previous section. The results of these types of analyses for various microstrip discontinuities will be presented now. Closed-form expressions for these discontinuities (wherever available) and the ranges of their validity are included here. Some of these closed-form expressions are based on the fullwave analysis data, methods for which are discussed in Chapter 4. Techniques of compensation of the reactive effects of these discontinuities to obtain better circuit performance are also described in this section.

3.4.1 Open Ends

An open-end discontinuity occurs frequently in a number of circuits such as resonators, matching stubs, parallel coupled filters, and in microstrip antennas. The equivalent circuit of an open end is represented by an excess capacitance C_{oc} which can be transformed into an equivalent length of transmission line, $\Delta\ell_{oc}$ as shown in Figure 3.13. The equivalent capacitance shown in Figure 3.13(b) is what is usually calculated, whereas the equivalent line length representation (Figure 3.13(c)) is more convenient for circuit design.

The most extensive data set on the microstrip open circuit has been obtained by Silvester and Benedek [7] using the method of line sources with charge reversal. Their results are presented in Figure 3.14. Also they have given an empirical expression that is very useful for computational purposes and may be written as

$$\frac{C_{oc}}{W} = \exp\left\{2.3026\sum_{i=1}^{5} C_i(\varepsilon_r)\left[\log\frac{W}{h}\right]^{i-1}\right\} \quad \text{(pF/m)} \tag{3.47}$$

where C_i's are numerical constants tabulated in [7] for $\varepsilon_r = 1.0$, 2.5, 4.2, 9.6, 16.0, and 51.0. For example, for $\varepsilon_r = 9.6$, values of C_i are 1.738, –0.2538, 0.1308, –0.0087, –0.0113 for $i = 1, \ldots, 5$ respectively.

The equivalent additional line length $\Delta\ell_{oc}$ for an open-circuit discontinuity may be obtained from C_{oc} by using the relation

$$\frac{\Delta\ell_{oc}}{h} = \frac{C_{oc}}{W}\frac{cZ_{0m}W/h}{\sqrt{\varepsilon_{re}}} \tag{3.48}$$

where c is the velocity of wave propagation in free space. An empirical expression for $\Delta\ell_{oc}/h$ has been obtained by modifying the expression derived by Hamerstad and Bekkadal [16]. The expression is given [17] as

$$\frac{\Delta\ell_{oc}}{h} = 0.412\frac{\varepsilon_{re}+0.3}{\varepsilon_{re}-0.258}\left[\frac{W/h+0.264}{W/h+0.8}\right] \tag{3.49}$$

Maximum relative error in this expression, as compared to (3.47), is less than 4 percent for $W/h \geq 0.2$ and $2 \leq \varepsilon_r \leq 50$. However, the result above is not valid [18] for wide microstrip lines (say $W/h > 3$) used extensively for microstrip antennas.

A more accurate expression, with accuracy better than 0.2 percent for the range of normalized widths $0.01 \leq W/h \leq 100$ and $\varepsilon_r \leq 128$, has been derived [19] by curve fitting the numerical results based on hybrid-mode fullwave analysis [20, 21]. According to this,

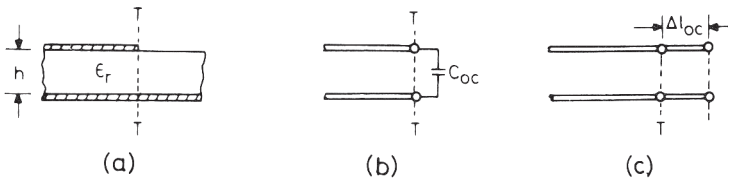

Figure 3.13 (a) Microstrip open-end discontinuity, (b) equivalent capacitance representation, and (c) equivalent line length representation.

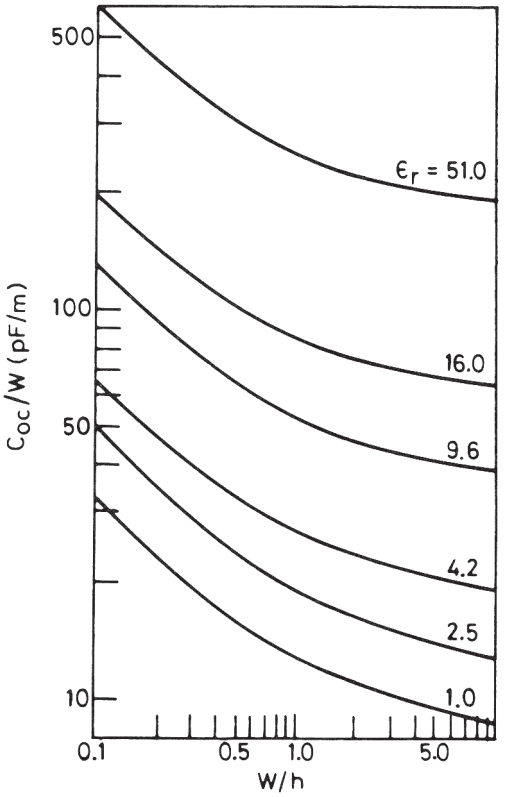

Figure 3.14 Capacitance associated with an open-end discontinuity (from [7], © 1972 IEEE. Reprinted with permission.).

$$\frac{\Delta \ell_{oc}}{h} = \xi_1 \xi_3 \xi_5 / \xi_4 \tag{3.50}$$

where

$$\xi_1 = 0.434907 \frac{\varepsilon_{re}^{0.81} + 0.26(W/h)^{0.8544} + 0.236}{\varepsilon_{re}^{0.81} - 0.189(W/h)^{0.8544} + 0.87}$$

$$\xi_2 = 1 + \frac{(W/h)^{0.371}}{2.358\ \varepsilon_r + 1}$$

$$\xi_3 = 1 + \frac{0.5274 \arctan[0.084(W/h)^{1.9413/\xi_2}]}{\varepsilon_{re}^{0.9236}}$$

$$\xi_4 = 1 + 0.0377 \arctan[0.067(W/h)^{1.456}] \cdot \{6 - 5\exp[0.036(1 - \varepsilon_r)]\}$$

$$\xi_5 = 1 - 0.218 \exp(-7.5W/h)$$

and the expressions for effective dielectric constant ε_{re} given in [22] are used.

The effect of dispersion on $\Delta \ell_{oc}$ has been analyzed by Itoh [23]. At millimeter wavelengths the value of $\Delta \ell_{oc}$ is considerably smaller than that computed by using

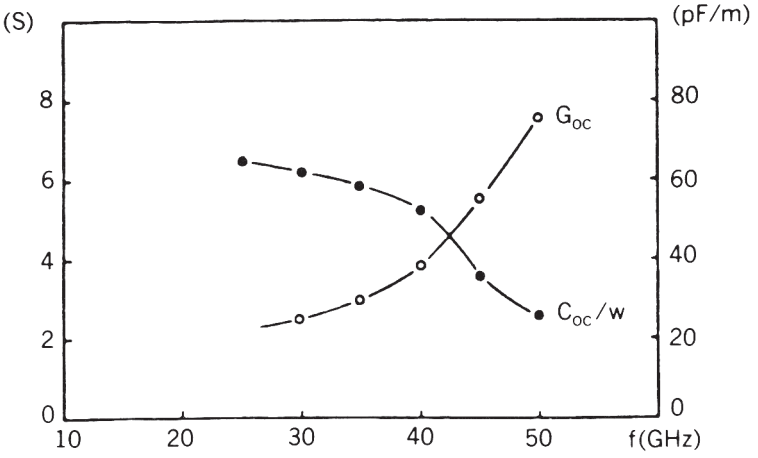

Figure 3.15 Normalized capacitance and radiation conductance of an open-ended microstrip line: $\varepsilon_r = 9.6$, $W/h = 1$, and $h = 0.6$ mm (from [26], © 1985 IEEE. Reprinted with permission.).

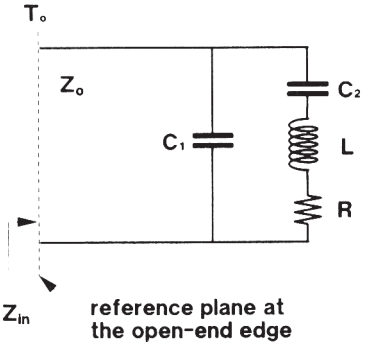

Figure 3.16 Equivalent circuit model for a microstrip open-end discontinuity (from [28], © 1994 IEEE. Reprinted with permission.).

the quasi-static approximation. However, for frequencies up to about 10 GHz, the quasi-static approach gives reasonably good results.

For thicker substrates and for wider microstrip lines, radiation from an open end discontinuity becomes significant [24, 25]. Rigorous fullwave analyses based on the method of moments [26, 27] and spectral domain [28] for characterization of a microstrip open end have also been reported. Figure 3.15 is a typical example of the very few results available from such analyses. In this case, the open-end capacitance is replaced with a parallel combination of open-end capacitance (C_{oc}) and radiation conductance (G_{oc}). We note that as frequency increases, the radiation conductance associated with the open end increases while the capacitance decreases. A more elaborate equivalent circuit model, based on fullwave analysis of open-end discontinuity, is shown in Figure 3.16. Closed-form expressions for the circuit element values are given as [28]:

$$C_1\left(\frac{25Z_{0m}}{h}\right) = 1.125\tanh\left(1.358\frac{W}{h}\right) - 0.315 \quad (\text{pF}\cdot\Omega) \tag{3.51a}$$

$$C_2\left(\frac{25Z_{0m}}{h}\right) = 6.832\tanh\left(0.0109\frac{W}{h}\right) - 0.910 \quad (\text{pF}\cdot\Omega) \tag{3.51b}$$

$$L\left(\frac{25}{hZ_{0m}}\right) = 0.008285\tanh\left(0.5665\frac{W}{h}\right) + 0.0103 \quad (\text{nH}/\Omega) \tag{3.51c}$$

$$R/Z_{0m} = 1.024\tanh\left(2.025\frac{W}{h}\right) \tag{3.51d}$$

where both h and W are in milli-inches and Z_{0m} is the characteristic impedance of the microstrip line.

3.4.2 Gaps in a Microstrip

The characterization of a gap in a microstrip is useful in the design of, for example, dc blocks, end coupled filters, and coupling elements to resonators. A microstrip gap and its equivalent circuits are shown in Figure 3.17. There are three sets of published data for gap capacitance [1, 4, 9]. Perhaps the results of Benedek and Silvester are the most accurate as the other two involve the subtraction of nearly equal large numbers. The available results are shown in Figure 3.18. The two sets of points shown in Figure 3.18(b) correspond to results of Maeda [4] and Farrar and Adam [1]. The capacitances C_{odd} and C_{even} are related to C_p and C_g by

$$\begin{aligned} C_{even} &= 2\,C_p \\ C_{odd} &= 2C_g + C_p \end{aligned} \tag{3.52}$$

Equivalent line length $\Delta\ell_g$ of Figure 3.17 may be calculated as

$$\frac{\Delta\ell_g}{h} = \frac{C_p}{W}\frac{cZ_{0m}W/h}{\sqrt{\varepsilon_{re}}} \tag{3.53}$$

A comparison of computed and experimental results given by Maeda [4] is shown in Figure 3.19. Experimental results for C_g are derived from [29]. The agreement between the experimental results and computed values is reasonably good.

It may be noted that the curves of Figure 3.18 are well suited for polynomial approximation as has been done for the open-end capacitance discussed in the previous section. The closed-form expressions for C_{even} and C_{odd} for $\varepsilon_r = 9.6$ and $0.5 \leq$

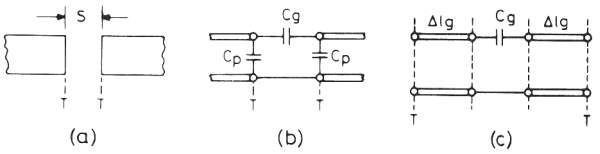

Figure 3.17 (a) A microstrip gap and (b, c) its equivalent circuits.

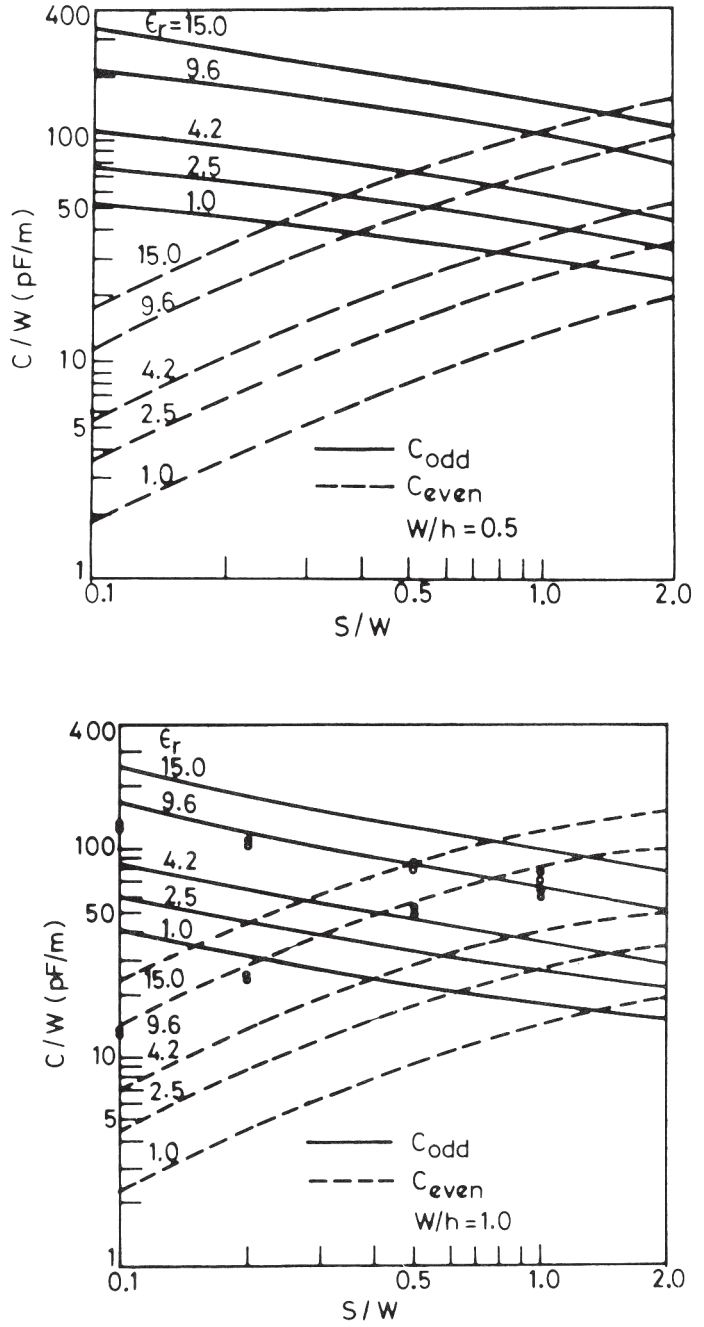

Figure 3.18 (a) Capacitances for a microstrip gap evaluated by using line sources with charge reversal ($W/h = 0.5$), (b) capacitances for a microstrip gap evaluated by using line sources with charge reversal ($W/h = 1.0$), and (c) capacitances for a microstrip gap evaluated by using line sources with charge reversal ($W/h = 2.0$) (from [9], © 1972 IEEE. Reprinted with permission.).

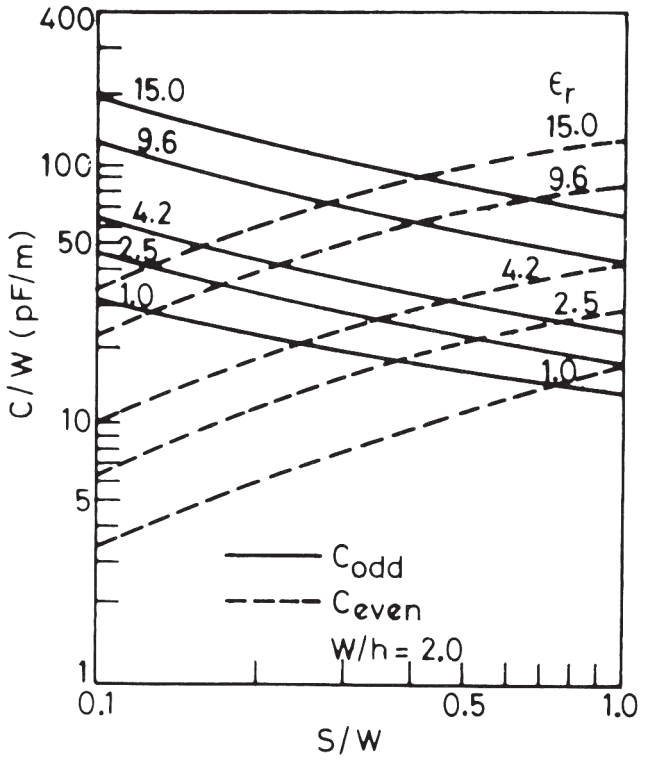

(c)

Figure 3.18 (continued).

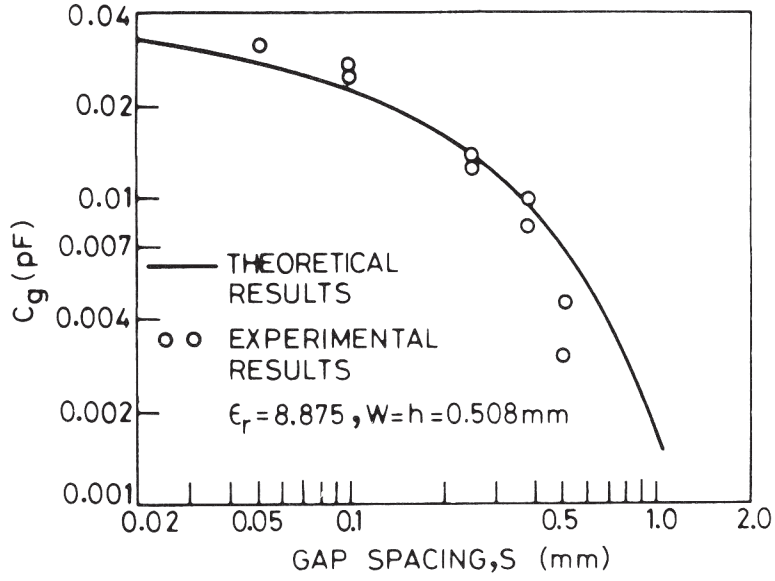

Figure 3.19 Comparison of theoretical and experimental results for gap capacitance (from [4], © 1972 IEEE. Reprinted with permission.).

$W/h \le 2$ have been determined [17] by curve fitting the available numerical results [9]. The expressions are

$$C_{\text{odd}}/W\left(\text{pF/m}\right) = \left(\frac{S}{W}\right)^{m_0} \exp(k_0) \tag{3.54}$$

$$C_{\text{even}}/W(\text{pF/m}) = 12\left(\frac{S}{W}\right)^{m_e} \exp(k_e) \tag{3.55}$$

where

$$\left.\begin{aligned} m_0 &= \frac{W}{h}\left(0.619\log W/h - 0.3853\right) \\ k_0 &= 4.26 - 1.453\log W/h \end{aligned}\right\} \qquad (0.1 \le S/W \le 1.0)$$

$$m_e = 0.8675 \qquad k_e = 2.043\left(\frac{W}{h}\right)^{0.12} \qquad (0.1 \le S/W \le 0.3)$$

$$m_e = \frac{1.565}{\left(W/h\right)^{0.16}} - 1 \qquad k_e = 1.97 - \frac{0.03}{W/h} \qquad (0.3 \le S/W \le 1.0)$$

The values of C_{odd} and C_{even} for other values of ε_r in the range $2.5 \le \varepsilon_r \le 15$ can be calculated by scaling according to the relations

$$C_{\text{odd}}(\varepsilon_r) = C_{\text{odd}}(9.6)(\varepsilon_r/9.6)^{0.8} \tag{3.56}$$

$$C_{\text{even}}(\varepsilon_r) = C_{\text{even}}(9.6)(\varepsilon_r/9.6)^{0.9} \tag{3.57}$$

The accuracy of these expressions is within 7 percent for the above-mentioned set of parameters.

Closed-form expressions for a microstrip gap discontinuity based on the spectral domain method have been reported by Alexopoulos and Wu [28]. The model parameters shown in Figure 3.20 are evaluated for $\varepsilon_r = 9.9$ using the following equations:

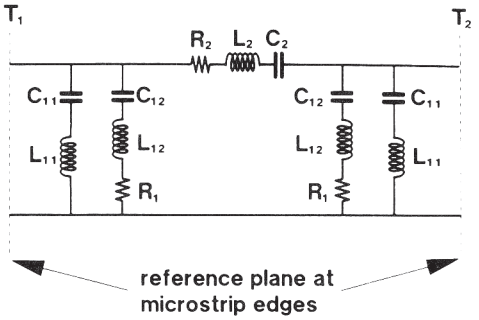

Figure 3.20 Equivalent circuit model for a microstrip gap discontinuity (from [28], © 1994 IEEE. Reprinted with permission.).

$$R_1 Z_{0m} = 1.024 \tanh\left(2.025\frac{W}{h}\right) \cdot \tanh\left[\left(0.01584 + 0.0187\frac{h}{W}\right)\frac{S}{h} + \left(0.1246 + 0.0394\sinh\left(\frac{W}{h}\right)\right)\right] \tag{3.58a}$$

$$C_2\left(\frac{25Z_{0m}}{h}\right) = \left[0.1776 + 0.05104\ \ell n\left(\frac{W}{h}\right)\right]\frac{h}{S} + \left[0.574 + 0.3615\frac{h}{W} + 1.156\ \ell n\left(\frac{W}{h}\right)\right] \cdot \operatorname{sech}\left(2.3345\frac{S}{h}\right) \quad (\mathrm{pF}\cdot\Omega) \tag{3.58b}$$

$$L_2\left(\frac{25}{hZ_{0m}}\right) = \left[0.00228 + \frac{0.0873}{7.52W/h + \cosh(W/h)}\right] \cdot \sinh\left(2.3345\frac{S}{h}\right) \quad (\mathrm{nH}/\Omega) \tag{3.58c}$$

$$R_2/Z_{0m} = \left[-1.78 + 0.749\frac{W}{h}\right]\frac{S}{h} + \left[1.196 - 0.971\ \ell n\left(\frac{W}{h}\right)\right] \cdot \sinh\left(2.3345\frac{S}{h}\right) \tag{3.58d}$$

$$C_{11}\left(\frac{25Z_{0m}}{h}\right) = \left[1.125\tanh\left(1.358\frac{W}{h}\right) - 0.315\right] \cdot \tanh\left[\left(0.0262 + 0.184\frac{h}{W}\right) + \left(0.217 + 0.0619\ \ell n\frac{W}{h}\right)\frac{S}{h}\right] \quad (\mathrm{pF}\cdot\Omega) \tag{3.59a}$$

$$C_{12}\left(\frac{25Z_{0m}}{h}\right) = \left[6.832\tanh\left(0.0109\frac{W}{h}\right) + 0.910\right] \cdot \tanh\left[\left(1.411 + 0.314\frac{h}{W}\right) + \left(\frac{S}{h}\right)^{1.248+0.360\tan^{-1}(W/h)}\right] \quad (\mathrm{pF}\cdot\Omega) \tag{3.59b}$$

$$L_{11}\left(\frac{25}{hZ_{0m}}\right) = \left[0.134 + 0.0436\ \ell n\frac{h}{W}\right] \cdot \exp\left\{-\left(3.656 + 0.246\frac{h}{W}\right) \cdot \left(\frac{S}{h}\right)^{1.739+0.390\ell n(W/h)}\right\} \quad (\text{nH}/\Omega) \tag{3.59c}$$

$$L_{12}\left(\frac{25}{hZ_{0m}}\right) = \left[0.008285\tanh\left(0.5665\frac{W}{h}\right) + 0.0103\right] + \left[0.1827 + 0.00715\ \ell n\frac{W}{h}\right] \cdot \exp\left\{-\left(5.207 + 1.283\tanh\left(1.656\frac{h}{W}\right)\right) \cdot \left(\frac{S}{h}\right)^{0.542+0.873\tan^{-1}(W/h)}\right\} \quad (\text{nH}/\Omega) \tag{3.59d}$$

3.4.3 Steps in Width

Steps in width exist at junctions of two microstrip lines that have different impedances. This type of discontinuity is encountered when designing matching transformers, couplers, filters, and transitions. The configurations of a step discontinuity and its equivalent circuit are shown in Figure 3.21. Results for excess capacitance C_s have been given by Farrar and Adams [1], Benedek and Silvester [9], and Gupta and Gopinath [30]. Data for C_s given by Gupta and Gopinath are most extensive and are presented in Figure 3.22 for $\varepsilon_r = 2.3$ and 9.6. The small dotted curve in Figure 3.22(b) corresponds to [9] and has been inserted to compare the two sets of results. In terms of distributed elements, the discontinuity capacitance C_s has the effect of an increase in the wide line's length and an equal decrease in the narrow line's length. As these effects are small, the change in lengths may be approximated

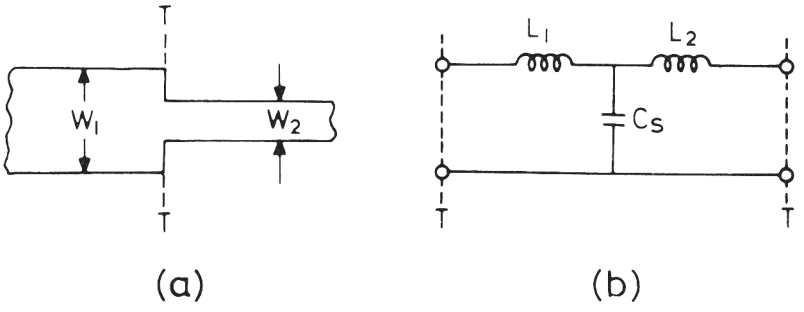

Figure 3.21 (a) A microstrip step discontinuity and (b) its equivalent circuit.

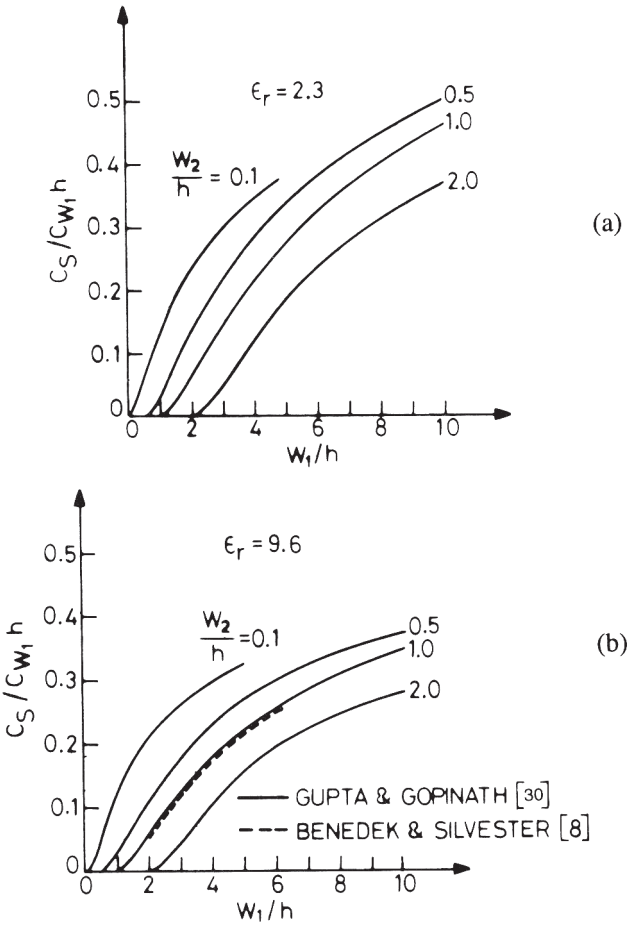

Figure 3.22 Shunt capacitance for a step discontinuity. $C_{w1}(= \sqrt{\varepsilon_{re}}/cZ_{0m})$ denotes capacitance per unit length of the line of width W_1 (from [30], © 1977 IEEE. Reprinted with permission.).

by $\Delta\ell_{oc}(1 - W_2/W_1)$ [16] where $\Delta\ell_{oc}$ is the open-circuit line extension calculated from (3.48) for line width W_1. A more accurate expression for the change in lengths that is applicable for a wide range of ε_r values is given by Rizzoli et al. [31] as $\Delta\ell_{oc}$ $f(\varepsilon_r)$ $[1 - W_2/W_1]$, where the function $f(\varepsilon_r)$ has the form

$$f(\varepsilon_r) = 1.25 + 0.19\tan^{-1}\left(6.16 - \varepsilon_r\right) \tag{3.60}$$

Measurement of the step capacitance has been reported by Easter et al. [32]. A comparison with the results in Figure 3.22 is difficult because of insufficient information about the experimental data.

Some results for the inductance associated with a step discontinuity in a microstrip are also available [15]. These are based on the method of quasi-static computation of inductance discussed in Section 3.3. Inductance L_s plotted in Figure 3.23 is the total of inductances L_1 and L_2 shown in Figure 3.21 and has been normalized

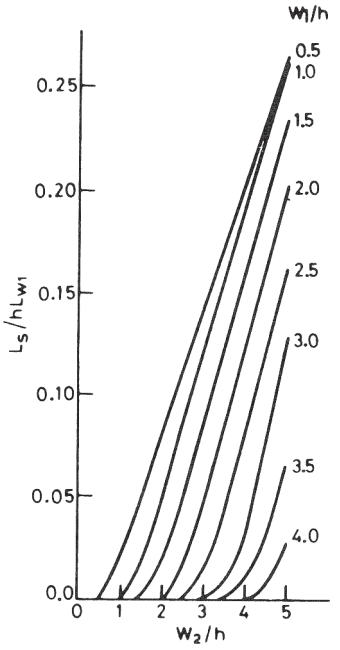

Figure 3.23 Calculated inductance values for a microstrip step discontinuity. $L_{w1}(=\sqrt{\varepsilon_{re}}Z_{0m}/c)$ denotes inductance per unit length of the line of width W_1 (from [15], © 1976 IEEE. Reprinted with permission.).

with respect to (L_{w1}/h) where L_{w1} is the inductance per unit length of microstrip of width W_1 given by

$$L_{w1} = \frac{Z_{0m}\sqrt{\varepsilon_{re}}}{c} \text{ (H/m)} \tag{3.61}$$

where Z_{0m} and ε_{re} correspond to width W_1 and $c = 3 \times 10^8$ m/s. A comparison of theoretical and experimental results is also available [15] and is shown in Figure 3.24. The experiments were carried out in the frequency range of 6.5 GHz to 10 GHz. It may be pointed out that inductance values are in the range of 1.4×10^{-11} H to 9.6×10^{-11} H.

To factor in the effect of discontinuity inductances in the circuit design, the total inductance L_s may be separated into L_1 and L_2 (as a first-order approximation) as follows:

$$L_1 = \frac{L_{w1}}{L_{w1} + L_{w2}} L_s \tag{3.62a}$$

$$L_2 = \frac{L_{w2}}{L_{w1} + L_{w2}} L_s \tag{3.62b}$$

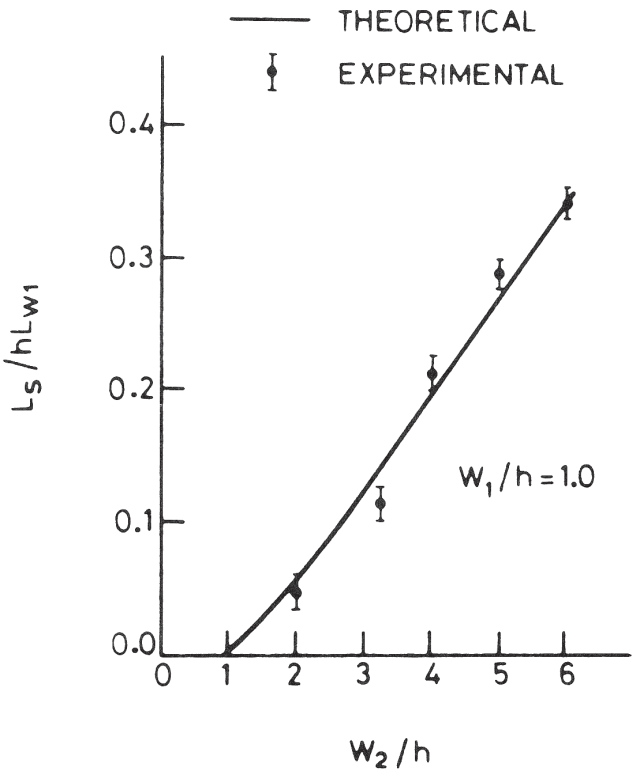

Figure 3.24 Comparison of theoretical and experimental results for step discontinuity inductance. Bars indicate the experimental error range (from [15], © 1976 IEEE. Reprinted with permission.).

and corresponding additional line lengths may be written as

$$\frac{\Delta \ell_1}{h} = \frac{\Delta \ell_2}{h} = \frac{L_S}{(L_{w1} + L_{w2})h} \tag{3.63}$$

The closed-form expressions for C_s and L_s have been derived by curve fitting the numerical results. The expressions are given as

$$\frac{C_S}{\sqrt{W_1 W_2}}\,(\text{pF/m}) = (10.1 \log\, \varepsilon_r + 2.33)\frac{W_1}{W_2} - 12.6 \log\, \varepsilon_r - 3.17 \qquad (\text{for } \varepsilon_r \le 10;\ 1.5 \le W_1/W_2 \le 3.5) \tag{3.64}$$

This expression yields a percentage error of less than 10 percent. A more accurate expression can be written for alumina substrates ($\varepsilon_r = 9.6$) as

$$\frac{C_S}{\sqrt{W_1 W_2}}\,(\text{pF/m}) = 130 \log\left(\frac{W_1}{W_2}\right) - 44 \qquad (\text{for } 3.5 \le W_1/W_2 \le 10) \tag{3.65}$$

The above relation is accurate to within 0.5 percent. The expression for inductance is given by

$$\frac{L_s}{h}(\text{nH/m}) = 40.5\left(\frac{W_1}{W_2} - 1.0\right) - 75\log\frac{W_1}{W_2} + 0.2\left(\frac{W_1}{W_2} - 1\right)^2 \tag{3.66}$$

Equation (3.66) has an error of less than 5 percent for $W_1/W_2 \leq 5$ and $W_1/h = 1.0$. More general expressions for C_s and L_s are given as

$$C_s = 0.00137\frac{\sqrt{\varepsilon_{re1}}}{Z_{0m1}}\left(1 - \frac{W_2}{W_1}\right)h\left[\frac{\varepsilon_{re1} + 0.3}{\varepsilon_{re1} - 0.258}\right]\left[\frac{W_1/h + 0.264}{W_1/h + 0.8}\right] \quad \text{(pF)} \tag{3.67a}$$

$$L_s = 0.000987h\left(1 - \frac{Z_{0m1}}{Z_{0m2}}\sqrt{\frac{\varepsilon_{re1}}{\varepsilon_{re2}}}\right)^2 \text{(nH)} \tag{3.67b}$$

where Z_{0m} and ε_{re} are the microstrip line characteristic impedance and effective dielectric constant, respectively, and the substrate thickness h is in micrometers.

3.4.4 Bends

A microstrip bend may be formed by two lines of equal or unequal impedances and is normally used for introducing flexibility in the layout of the circuit design. The equivalent circuit of a microstrip bend with lines of equal impedances is shown in Figure 3.25. The most common form of microstrip bend used in circuits and investigated analytically is a right-angled bend ($\phi_b = 90°$).

Silvester and Benedek [8] have computed the electrostatic value of the excess capacitance of right-angled bends; their results are shown in Figure 3.26. Experimental results given by Easter [33] are shown as three small circles in this figure. It is observed that the agreement between the theoretical and experimental results is reasonably good only for microstrips with 50-Ω impedance.

Inductance for right-angled bends has been computed by Thomson and Gopinath [14], and their results are shown in Figure 3.27, wherein the normalized inductance ($L_b/L_w h$) is plotted for different width: height ratios. A comparison to the experimental results of Easter [33] is also shown, but the agreement is not very good.

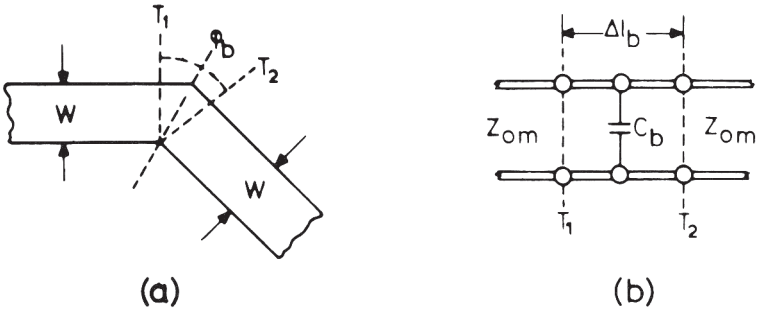

Figure 3.25 (a) Geometry and (b) equivalent circuit of a microstrip bend.

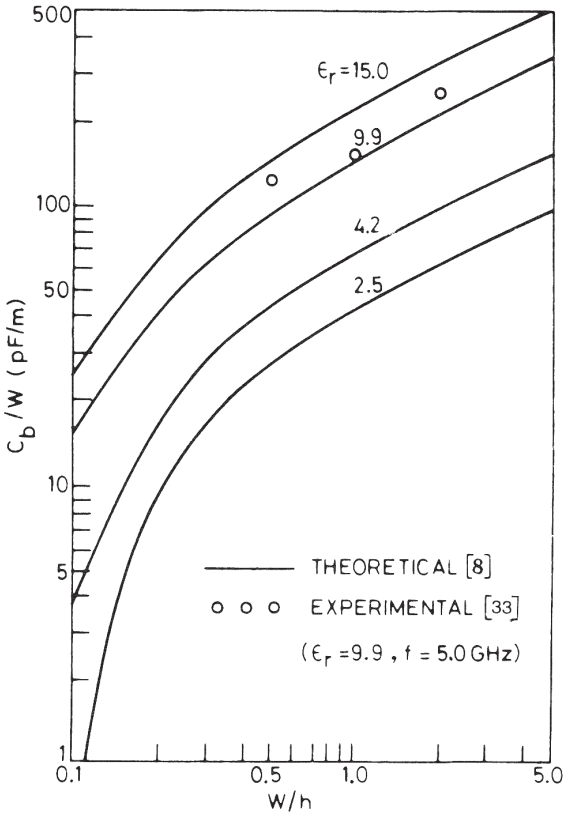

Figure 3.26 Discontinuity capacitance of a microstrip right-angled bend (from [8], © 1973 IEEE. Reprinted with permission.)

Closed-form expressions for right-angled bend discontinuities are given [17] as

$$\frac{C_b}{W}(\text{pF/M}) = \begin{cases} \dfrac{(14\varepsilon_r + 12.5)W/h - (1.83\varepsilon_r - 2.25)}{\sqrt{W/h}} + \dfrac{0.02\varepsilon_r}{W/h} & (W/h < 1) \quad (3.68a) \\ (9.5\varepsilon_r + 1.25)W/h + 5.2\varepsilon_r + 7.0) & (W/h \geq 1) \quad (3.68b) \end{cases}$$

$$\frac{L_b}{h}(\text{nH/m}) = 100(4\sqrt{W/h} - 4.21) \quad (3.69)$$

Equations (3.68) are accurate to within 5 percent for $2.5 \leq \varepsilon_r \leq 15$ and $0.1 \leq W/h \leq 5$. The accuracy of (3.69) is about 3 percent for $0.5 \leq W/h \leq 2.0$.

3.4.5 T-Junctions

The T-junction is perhaps the most important discontinuity in a microstrip as it is found in most circuits such as impedance networks, stub filters, and branch-line couplers. A microstrip T-junction and its equivalent circuit are shown in Figure 3.28. The discontinuity capacitance C_T for this structure has been calculated by Silvester and Benedek [8]. Their results are shown in Figure 3.29. Capacitances

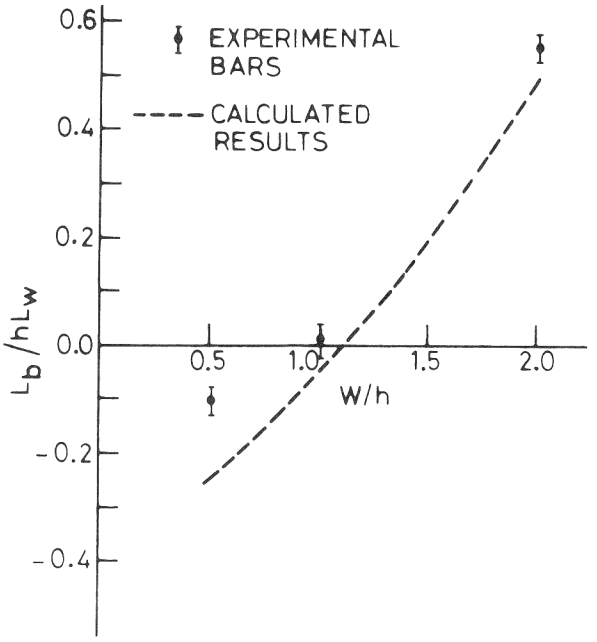

Figure 3.27 Discontinuity inductance of a microstrip right-angled bend. Bars indicate the experimental error range (from [14], © 1968 IEEE. Reprinted with permission.)

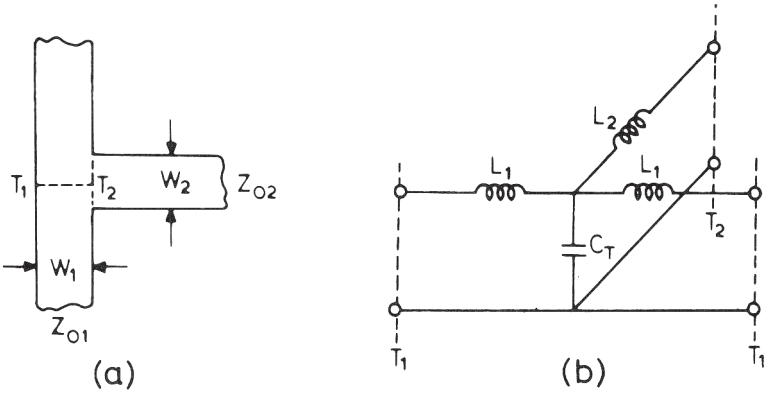

Figure 3.28 (a) A microstrip T-junction and (b) its equivalent circuit.

shown in this figure are for per-unit main-line width. The inductance calculation for T-junctions have been carried out by Thomson and Gopinath [14]. Their results are shown in Figure 3.30. A comparison with the experimental results of Easter [33] is also shown. The agreement between the experimental and theoretical results for L_2 is not as good as for L_1.

Closed-form expressions for the discontinuity reactances of the equivalent circuit shown in Figure 3.28(b) with a main-line impedance of 50 Ω and for $\varepsilon_r = 9.9$ have also been derived [17] as follows:

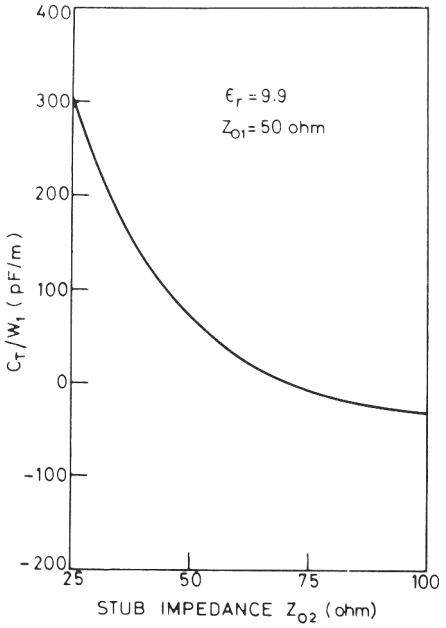

Figure 3.29 Discontinuity capacitance of a microstrip T-junction (from [8], © 1973 IEEE. Reprinted with permission.)

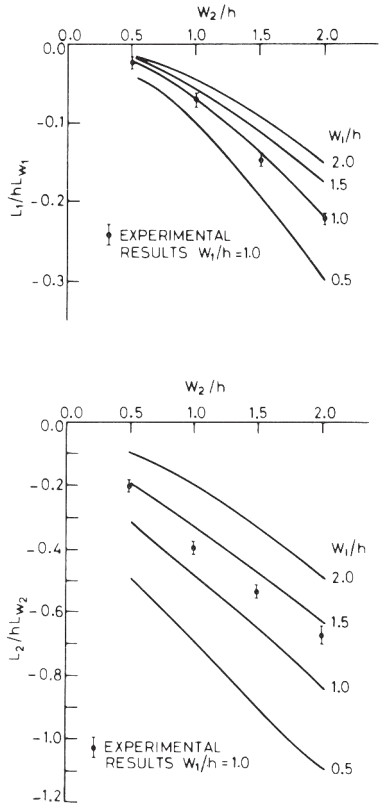

Figure 3.30 Discontinuity inductances of a microstrip T-junction (from [14], © 1968 IEEE. Reprinted with permission.)

$$\frac{C_T}{W_1}(\text{pF/m}) = \frac{100}{\tanh(0.0072\,Z_0)} + 0.64\,Z_0 - 261 \qquad (25 \le Z_0 \le 100) \tag{3.70}$$

where Z_0 is the characteristic impedance of the stub

$$\frac{L_1}{h}(\text{nH/m}) = \frac{W_2}{h}\left\{\frac{W_2}{h}\left(-0.016\frac{W_1}{h} + 0.064\right) + \frac{0.016}{W_1/h}\right\}L_{w1} \tag{3.71}$$

$$(0.5 \le (W_1/h,\, W_2/h) \ge 2.0)$$

$$\frac{L_2}{h}(\text{nH/m}) = \left\{\left(0.12\frac{W_1}{h} - 0.47\right)\frac{W_2}{h} + 0.195\frac{W_1}{h} - 0.357 + 0.0283\sin\left(\pi\frac{W_1}{h} = 0.75\pi\right)\right\}L_{w2} \tag{3.72}$$

$$(1 \le W_1/h \le 2.0;\; 0.5 \le W_2/h \le 2)$$

where L_w is the inductance per unit length for a microstrip of width W. The equations have an error of less than 5 percent.

Equations (3.70) to (3.72) hold for the symmetric T-junction shown in Figure 3.28(a). For a nonsymmetrical T-junction (Figure 3.31a), an equivalent circuit like that shown in Figure 3.31 (b) has been proposed [18]. It has been suggested that for moderate nonsymmetry, the results for the symmetrical case may be extended to the nonsymmetrical case as follows. For the main arm turns ratio, use the mainline impedance of the side being calculated. For the sidearm reference plane displacement and the shunt susceptance, use the main line impedance equal to the geometric mean of the two actual ones. The expressions for the symmetric case are

$$\frac{d_1}{D_2} = 0.055\left[1 - 2\frac{Z_1}{Z_2}\left(\frac{f}{f_{p1}}\right)^2\right]\frac{Z_1}{Z_2} \tag{3.73}$$

$$\frac{d_2}{D_1} = 0.5 - \left[0.05 + 0.7\exp\left(-1.6\frac{Z_1}{Z_2}\right) + 0.25\frac{Z_1}{Z_2}\left(\frac{f}{f_{pl}}\right)^2 - 0.17\ell n\frac{Z_1}{Z_2}\right]\frac{Z_1}{Z_2} \tag{3.74}$$

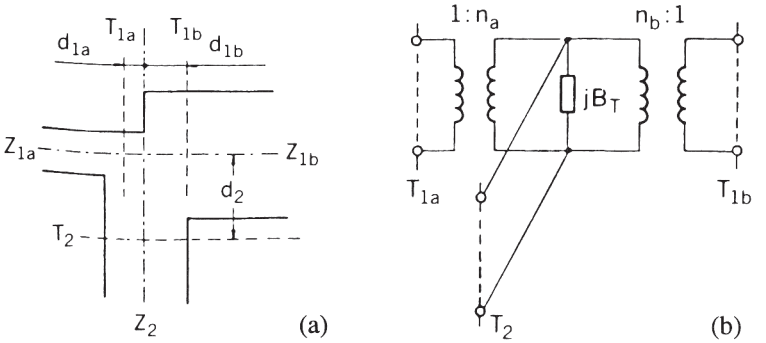

Figure 3.31 Equivalent circuit for modeling a nonsymmetric T-junction in microstriplines (from [18], © 1981 IEEE. Reprinted with permission.).

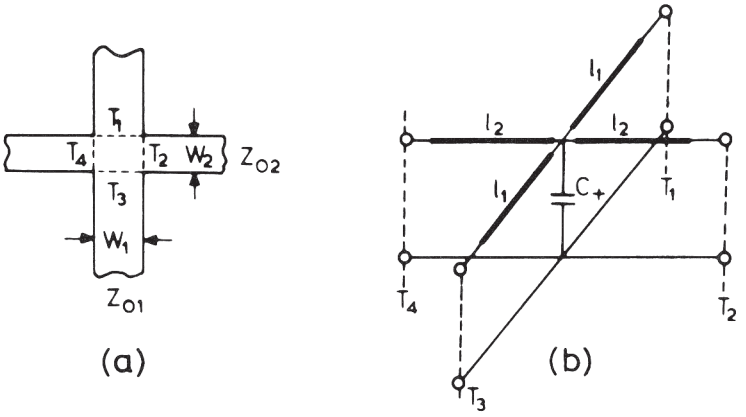

Figure 3.32 (a) Geometry and (b) equivalent circuit of a microstrip cross junction.

$$n^2 = 1 - \pi\left(\frac{f}{f_{p1}}\right)^2\left[\frac{1}{12}\left(\frac{Z_1}{Z_2}\right)^2 + \left(0.5 - \frac{d_2}{D_1}\right)^2\right] \tag{3.75}$$

$$\begin{aligned}\frac{B_T}{Y_2}\frac{\lambda_1}{D_1} = 5.5\frac{\varepsilon_r + 2}{\varepsilon_r}\Bigg[1 + 0.9\ell n\frac{Z_1}{Z_2} + 4.5\frac{Z_1}{Z_2}\left(\frac{f}{f_{p1}}\right)^2 \\ -4.4\exp\left(-1.3\frac{Z_1}{Z_2}\right) - 20\left(\frac{Z_2}{\eta_0}\right)^2\Bigg]n^{-2}\frac{d_1}{D_2}\end{aligned} \tag{3.76}$$

where D, f_p, Z, and λ are the equivalent parallel plate line width, first higher order mode cut-off frequency, characteristic impedance, and guide wavelength of the microstrip line. The subscripts 1 and 2 represent series and shunt lines. Expressions for D and f_p are given as

$$D = \eta_0 h/(\sqrt{\varepsilon_{re}}Z) \tag{3.77}$$

$$f_P\,(\text{GHz}) = 0.4Z/h \tag{3.78}$$

where $\eta_0 = 377\ \Omega$ and h is in millimeters.

3.4.6 Cross Junctions

One of the most common applications of a cross junction is for the realization of low impedance stubs. When a low impedance stub has a strip width large enough to sustain transverse resonance modes, one of the possible solutions is to employ two stubs in parallel, connected on either side of the main line. The impedance of each of the equivalent stubs is equal to twice the impedance of the simulated stub.

The geometery of a microstrip cross junction and its equivalent circuit are shown in Figure 3.32. Capacitance C_+ has been calculated by Silvester and Benedek [8], and their results are shown in Figure 3.33. Inductances associated with a cross junction have been computed by Gopinath et al. [15] but are expressed in terms of

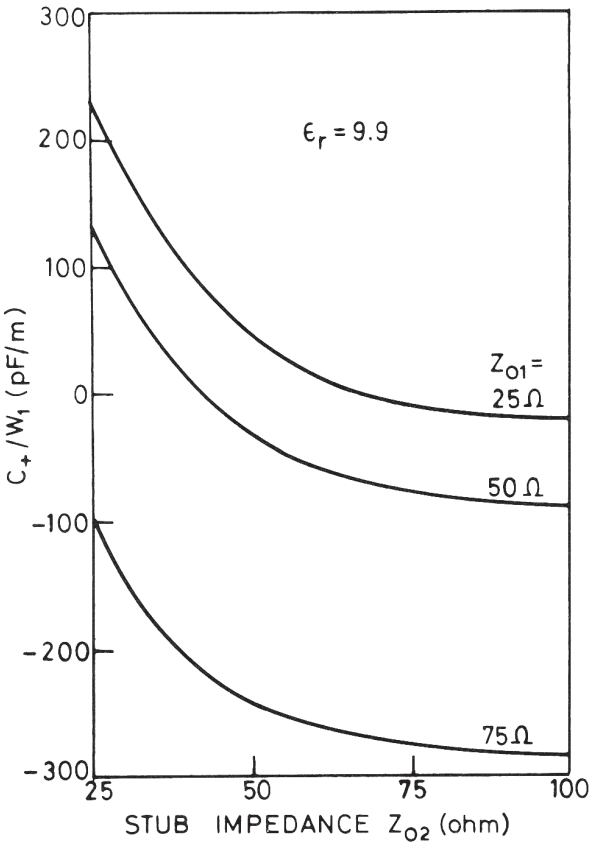

Figure 3.33 Discontinuity capacitance of a microstrip cross junction (from [8], © 1973 IEEE. Reprinted with permission.).

a somewhat different equivalent circuit (shown in Figure 3.34). Inductance results are shown in Figure 3.35(a, b). Figure 3.35(a) presents calculated values of L_1 normalized to $L_{w1}h$ of the cross junction for different W_1/h and W_2/h. This same set of curves is to be used to estimate normalized L_2 by interchanging W_1 and W_2. Calculated values of L_3 normalized to $L_{w1}h$ are shown in Figure 3.35(b). Only one experimental point due to Easter [33] is available for comparison and is shown in these figures. The agreement is good for L_1 and L_2 but not for L_3.

Closed-form expressions for cross-junction discontinuities have been derived [17] by curve fitting the available numerical results for capacitances and inductances for $\varepsilon_r = 9.9$. The expressions are accurate to within 5 percent and are given as

$$\frac{C_+}{W_1}(\text{pF/m}) = \left[\log\frac{W_1}{h}\left\{86.6\frac{W_2}{h} - 30.9\left(\frac{W_2}{h}\right)^{1/2} + 367\right\} + \left(\frac{W_2}{h}\right)^3 + 74\frac{W_2}{h} + 130\right]\left(\frac{W_1}{h}\right)^{-1/3} - 240 + \frac{2}{W_2/h} - 1.5\frac{W_1}{h}\left(1 - \frac{W_2}{h}\right) \tag{3.79}$$

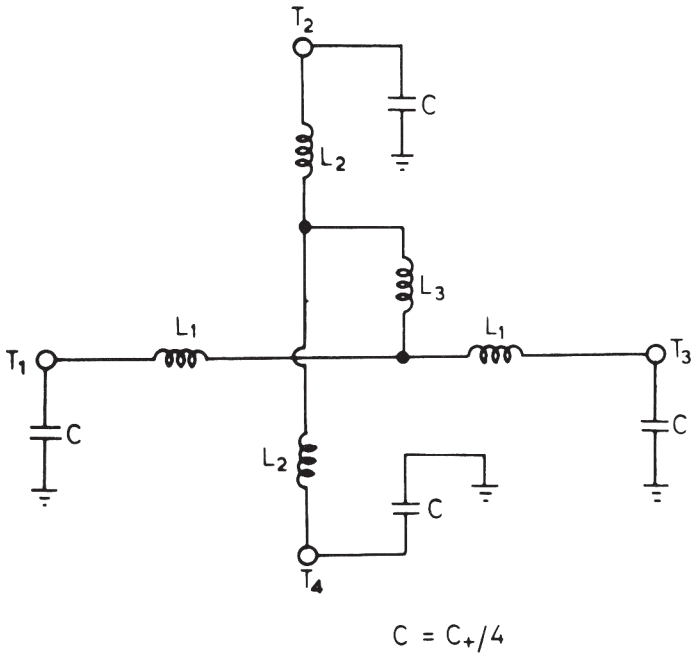

Figure 3.34 An equivalent circuit for a microstrip cross junction using lumped inductors (from [15], © 1976 IEEE. Reprinted with permission.).

$$\frac{L_1}{h}(\text{nH/m}) = \left\{\frac{W_1}{h}\left[165.6\frac{W_2}{h} + 31.2\sqrt{\frac{W_2}{h}} - 11.8\left(\frac{W_2}{h}\right)^2\right] - 32\frac{W_2}{h} + 3\right\}\left(\frac{W_1}{h}\right)^{-3/2} \quad (3.80)$$

$$(0.3 \le W_1 h \le 3.0 \text{ and } 0.1 < W_2/h \le 3.0)$$

The expression for L_2/h (nH/m) can be developed by interchanging W_1 and W_2 in (3.80)

$$-\frac{L_3}{h}(\text{nH/m}) = 337.5 + \left(1 + \frac{7}{W_1/h}\right)\frac{1}{W_2/h} - 5\frac{W_2}{h}\cos\left[\frac{\pi}{2}\left(1.5 - \frac{W_1}{h}\right)\right] \quad (3.81)$$

$$(0.5 \le (W_1/h, W_2/h) \le 2.0)$$

where $C = C_+/4$. The unsymmetric cross junction has been studied experimentally [34] and compared with the T-junction. This comparison indicates that the T-junction data may be used as a first step to estimate the properties of the cross-junction. An approximate value of C_+ may be calculated by using $C_+ = 0.75\ C_m$ where C_m is the capacitance of the uniform microstrip line of widest width in the cross junction.

3.4.7 Notch

A notch or a narrow transverse slit in the strip conductor of a microstrip line can be introduced to realize a series inductance. The configuration of this discontinuity

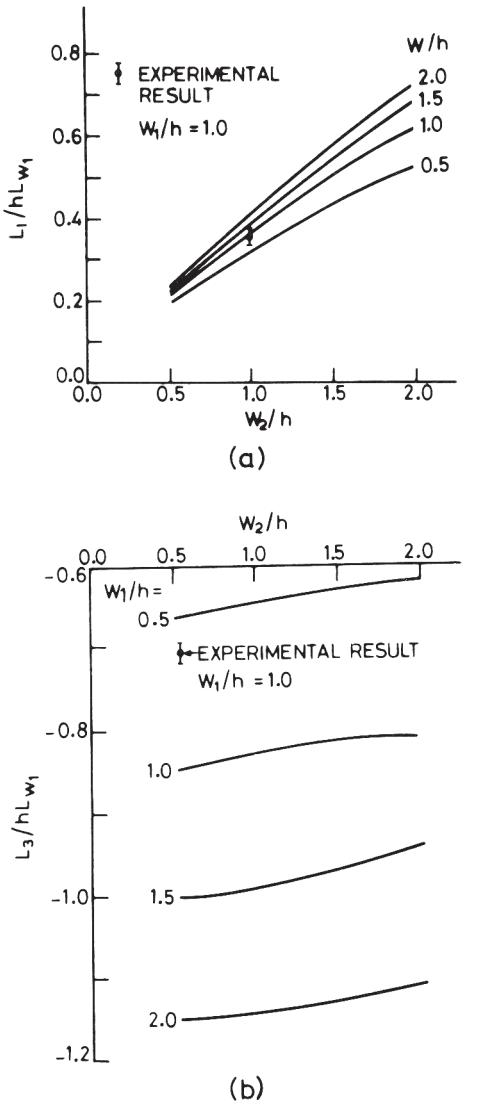

Figure 3.35 Discontinuity inductances L_1, shown in (a), and L_3, in (b), for a cross junction (from [15], © 1976 IEEE. Reprinted with permission.).

and that of its equivalent circuit are shown in Figure 3.36. The value of the series inductance L_N can be obtained from the approximate relation [35]

$$\frac{L_N}{h}(\text{nH/mm}) = 2\left(1 - \frac{Z_{0\text{m}}}{Z'_{0\text{m}}}\sqrt{\frac{\varepsilon_{re}}{\varepsilon'_{\text{re}}}}\right)^2 \tag{3.82}$$

where ε_{re} and ε'_{re} are the effective dielectric constants for microstrip lines with widths W and $(W - b)$, respectively, and $Z_{0\text{m}}$ and $Z'_{0\text{m}}$ are the corresponding impedances. The substrate thickness h is measured in millimeters. The expression for L_N above is valid for $0 \le b/W \le 0.9$ and $a \le h$.

Figure 3.36 Notch discontinuity and its equivalent circuit.

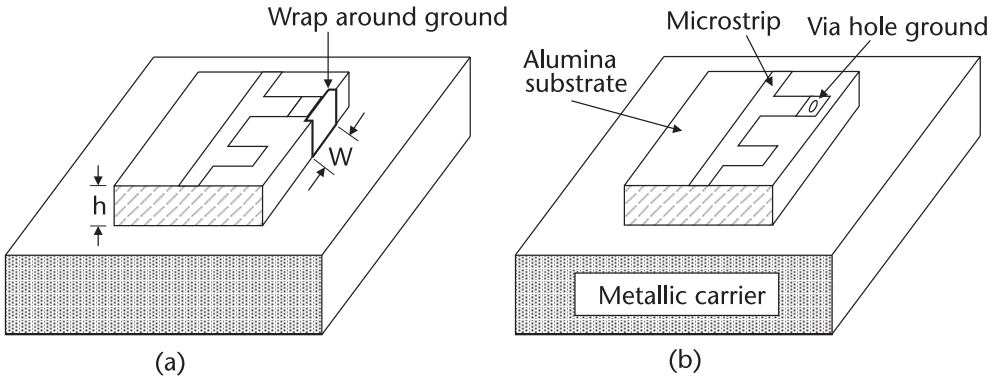

Figure 3.37 Various ground connection techniques in ICs: (a) wrap-around and (b) via hole.

3.4.8 RF Short and Via Hole

In RF and microwave circuits, shorts and via holes are frequently used for dc and RF ground connections. Via holes are also used for interconnections of metal layers in a multilayer technology. Low-loss and low-inductance grounds are very important to achieve good gain, noise figure, insertion loss, VSWR, output power, PAE, stability, and wide bandwidth performance in amplifiers. In MICs/MMICs, one needs the backside ground metalization to be connected with the minimum possible inductance path to the top side of the substrate having RF microstrip ground pads. In MICs, there are two basic techniques used to achieve such ground connections. These are via hole and wrap-around grounds, and their typical configurations are shown in Figure 3.37.

Wrap-Around Ground

Wrap-around ribbons, or ground straps, are used for low-inductance ground connections in hybrid MICs, and their equivalent circuit model may be represented by a simple inductor. The inductance of the ribbon/strap is given by

$$L(nH) = \ell \times 10^{-4}\left[\ln\left(\frac{\ell}{W+t}\right) + 1.193 + 0.2235\frac{W+t}{\ell}\right] \tag{3.83}$$

where W, t, and ℓ are the width, thickness, and length of the strap expressed in microns, respectively. For $W = 380$ μm, t = 15 μm, and $\ell = 380$ μm, the calculated value of L is 0.053 nH.

Via Hole Connection

In multilayer MMICs, RFICs, and digital ICs, the interconnection between different level metals is realized using via holes in the separating dielectric layer or layers, which are generally of 1–3 μm thick polyimide. For a 3μm × 3μm contact via hole, the dc resistance is about 0.1 Ω. They have minimum parasitic inductance. Via hole connections are integral parts of transistors, inductors, transformers, and Lange couplers. In multilayer MICs, the thickness of separating dielectric layers is much larger than polyimide thickness. In this case, the lumped element model described next may be used.

Via Hole Ground Model

Several different techniques have been applied to develop via hole models. These include analytical methods [36], quasistatic approach [37], fullwave analysis [38–47], time domain measurements [48, 49], and S-parameter measurement-based models [50]. Analytical models have limited accuracy; quasi-static models are valid for dimensions much smaller than the operating wavelengths; fullwave techniques provide accurate results but require long computational time; and measurement-based models are valid for only those geometries used in the characterization. Analytical models are discussed in this section.

An analytical model of a via hole is a series combination of an inductance L_{via} and resistance R_{via} of a cylindrical via hole shown in Figure 3.38. Expressions for L_{via} and R_{via} were obtained by Goldfarb and Pucel [36] and are given below.

$$L_{via} = 0.2\left[h\,\ell n\left(\frac{h+\sqrt{r^2+h^2}}{r}\right)+\frac{3}{2}\left(r-\sqrt{r^2+h^2}\right)\right] \quad \text{(pH)} \tag{3.84}$$

$$R_{via} = R_{dc}\sqrt{1+\frac{f}{f_\delta}} \tag{3.85a}$$

where

$$f_\delta = \frac{1}{\pi\mu_0\sigma\delta^2} \tag{3.85b}$$

and r and h, the radius and height of the via hole (respectively), are expressed in μm. Here, f is the operating frequency, R_{dc} the dc resistance, μ_0 the free space permeability, σ is the conductivity of the metal, and δ is its skin depth. For $h = 380$ μm and $r = 100$ μm, the calculated value of L_{via} is 0.067 nH, which is larger than the strap inductance value because of smaller via hole diameter.

A more accurate model for a via hole includes the reactance of the microstrip via pad section between the microstrip feed and via hole, and is shown as inductance L_p in Figure 3.38. The value of L_p can be determined as described in Chapter 2.

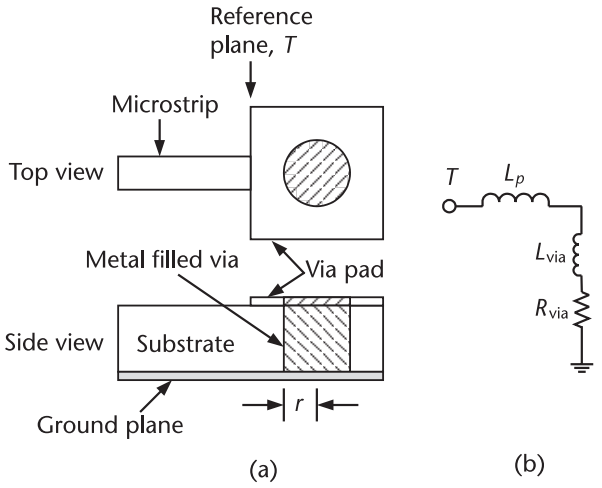

Figure 3.38 (a) Top and side views of a cylindrical via in microstrip configuration and (b) equivalent circuit model for a ground via hole.

3.5 Compensated Microstrip Discontinuities

In microwave integrated circuit designs, the reactances introduced by microstrip discontinuities should either be taken into account or microstrip structures with compensated discontinuities should be used. In general, compensated discontinuities improve the circuit performance as well as the bandwidth. Usually chamfered bends or rounded corners are used in MICs and MMICs. The chamfered discontinuity technique is also known as the discontinuity compensation in which the discontinuity reactances are minimized by removing appropriate portions of the microstrip conductor near the discontinuity location. In this section we describe briefly the step in width, right-angled bend, and T-junction compensated microstrip discontinuities.

3.5.1 Step in Width

The compensation of a step discontinuity using appropriate tapers has been, reported [51–54]. In this case the effect of discontinuity reactances is reduced by chamfering the large width. The taper length depends upon the step ratio, dieletric constant value, and the substrate thickness (h). For $h/\lambda \leq 0.01$ and a step ratio less than 3, the step discontinuity reactance is negligible and generally no compensation technique is needed. Figure 3.39 shows three types of tapers. The taper shown in Figure 3.39(a) has been studied using a planar waveguide model and is described in Section 4.1.2. For a gradual taper, as shown in Figure 3.39(b), closed form expressions for the contour of taper compensating step discontinuities in microstrip lines are given by Raicu [54]. For a partial taper, as shown in Figure 3.39(c), discontinuity compensation on the 75-μm- to 125-μm-thick GaAs substrate has been arrived at by using a commerical fullwave analysis CAD tool. For a step-width ratio ranging from 3 to 13, the step discontinuity reactance is negligible when $L = W_1/8$ and $W_1' = 0.33\ W_1$.

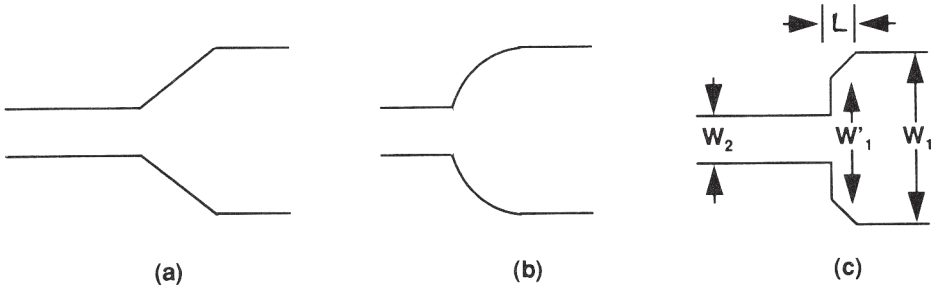

Figure 3.39 Three different kinds of compensated step-in-width discontinuity configurations with (a) linear taper, (b) curved taper, and (c) partial linear taper.

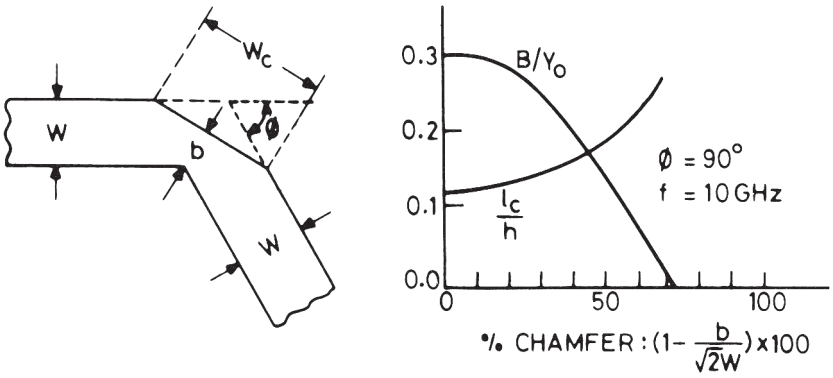

Figure 3.40 A chamfered bend and variations of shunt susceptance and series equivalent length of a chamfered right-angled bend as a function of percentage chamfer (from [32], © 1973 Microwave Exhibitions & Publishers (U.K.). Reprinted with permission.).

3.5.2 Bends

In practical circuits, microstrip bends are chamfered (see Figure 3.40) to compensate for the excess capacitance Measurements by Easter et al. [32] indicate that a chamfer of approximately 72 percent as defined in Figure 3.40 is needed for a bend in a 50-Ω line on alumina substrate. This figure includes variation of normalized discontinuity susceptance (B/Y_0) as a function of percentage chamfer and shows that 72 percent chamfering will increase the length correction in the equivalent circuit to approximately 0.3 of the substrate thickness. The length of the chamfer (W_c) is approximately $1.8W$. Groll and Weidmann [55] have also found the optimum length of the chamfer using TDR measurements for a 50-Ω line on alumina substrate. They observed that $W_c = \text{I.83}W$ gives a VSWR less than 1.11 up to 12 GHz. Hammerstad and Bekkadal [16] have found optimum lengths of the chamfer for 50-Ω microstrips on rexolite substrates having various bend angles ($\phi = 30°$, 60°, 90°, and 120°). The value of W_c comes out to be about $1.8W$ in all of these cases.

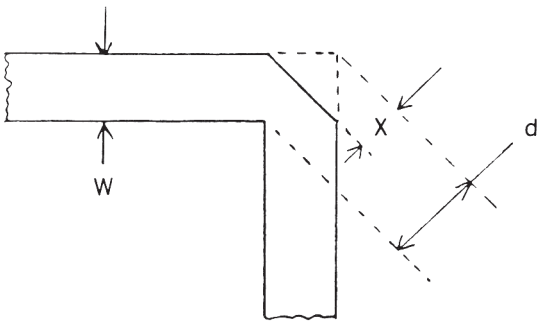

Figure 3.41 Geometry of a chamfered bend.

Data on the optimum amount of chamfering have been given in [56] as

$$M = 52 + 65\exp(-1.35W/h) \tag{3.86}$$

for $W/h \geq 0.25$ and $\varepsilon_r \leq 25$, where M is the percentage chamfer given by $(X/d) \times 100\%$ with X and d as shown in Figure 3.41. For a chamfered bend, the reflection coefficient $S_{11} \sim 0$, when the transmission line is terminated by an impedance equal to its characteristic impedance, but the discontinuity reactances cause a reduction Δb in length compared to that measured along the centerlines of the microstrip lines. A closed-form expression for this reduction in length may be written as [18]

$$\Delta b/D = 0.16\{2 - (f/f_p)^2\} \tag{3.87}$$

where D and f_p are given by (3.77) and (3.78), respectively.

Several other types of chamfering, as shown in Figure 3.42, have been studied. Figure 3.43 compares calculated S_{11} for an uncompensated right-angled bend discontinuity with different compensated topologies. The configuration of Figure 4.42(c) provides the best compensation for this example.

3.5.3 T-Junction

The T-junction discontinuity compensation is much more difficult than the step-in width and right-angled bend discontinuity compensation techniques described in the previous subsections. Figure 3.44(a) shows T-junction compensation configurations using rectangular and triangular notches and their approximate dimensions for $h/\lambda \ll 1$. However, accurate dimensions of the compensated configuration depend upon the line widths, dielectric constant, and the substrate thickness. Figure 3.44(b) illustrates T-junction discontinuity minimization configurations in which the line widths are tapered to minimize the junction effect. In this case the taper length is about twice the line width or substrate thickness, whichever is larger.

T-junction discontinuities can also be compensated for by adjusting the lengths of the three microstrip lines forming the junction. The effect of the shunt susceptance can be compensated for by changing the microstrip widths near the junction

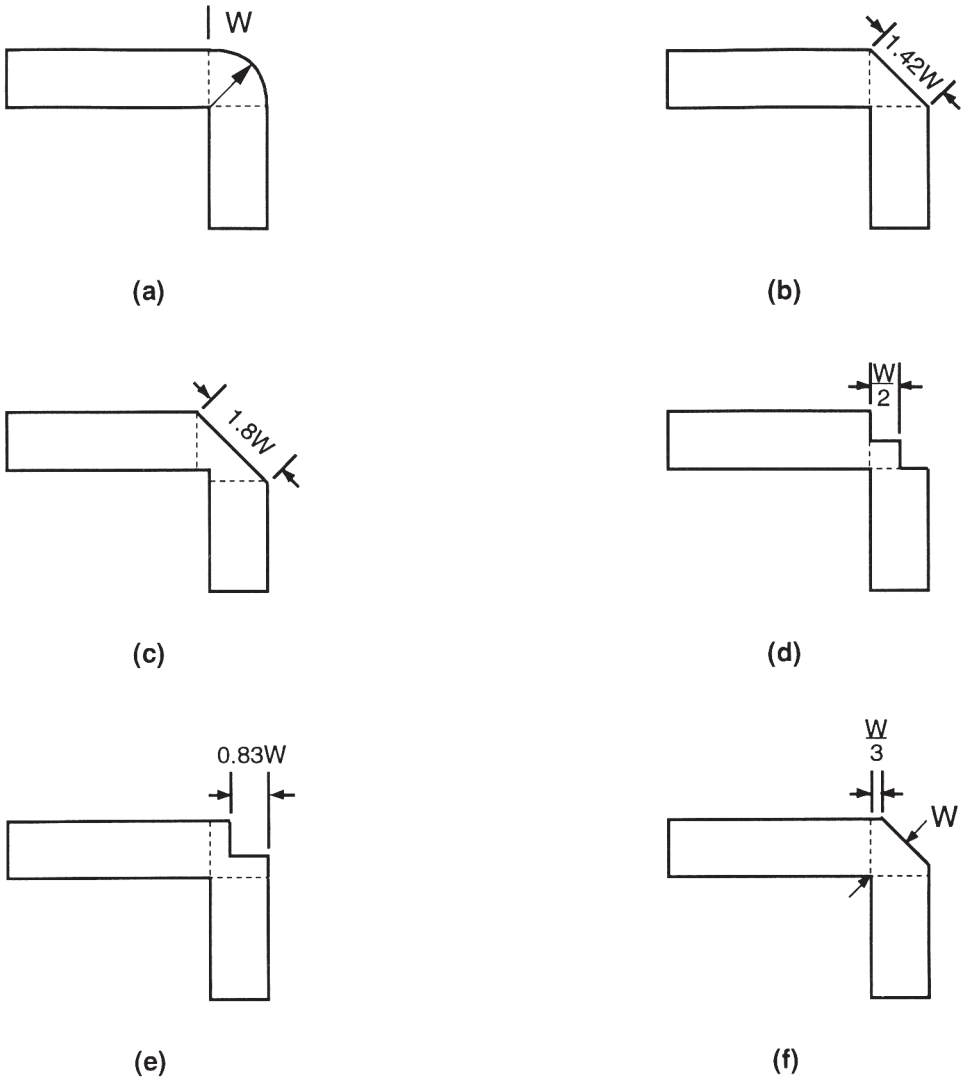

Figure 3.42 Six different configurations for compensated right-angled bends: (a, b, c, d, e, f).

as shown in Figure 3.45. The lengths θ_1, θ_2 and the characteristic impedances (Z_{m1} Z_{m2}) of the modified portions near the junctions can be derived from the values of the, discontinuity reactances [57]. The microstrip discontinuity compensation using defected ground structures has been described recently [58]. The defected ground structures are discussed in Chapter 6.

The discussion on microstrip discontinuities is continued in Chapter 4, where fullwave analyses for discontinuities and the techniques for experimental measurements of discontinuity parameters are discussed.

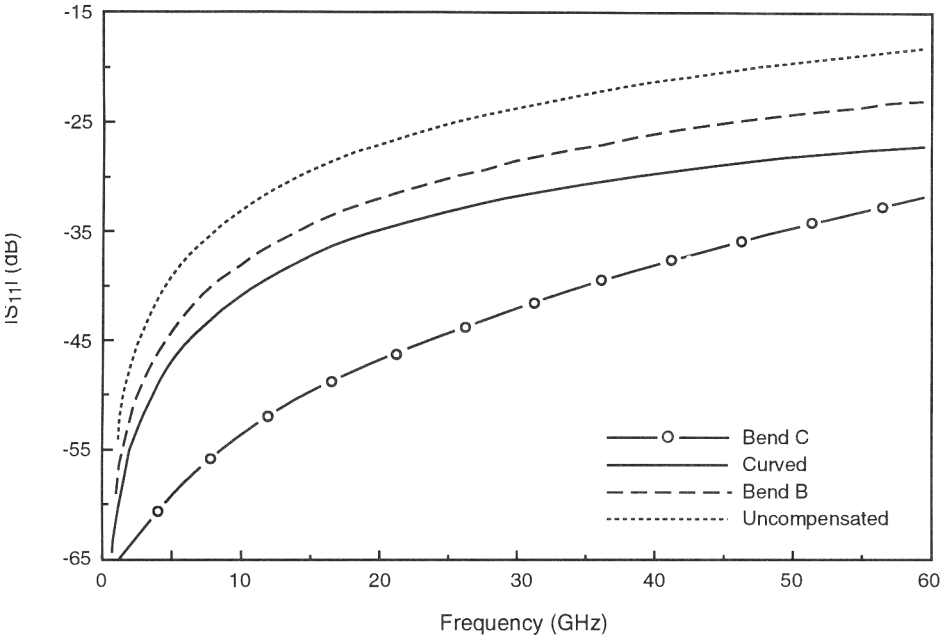

Figure 3.43 Magnitude of the reflection coefficient as a function of frequency for several compensated and uncompensated right-angled bends: W = 73 μm, h = 100 μm, ε_r = 12.9, and the curved line has a mean radius = 2W.

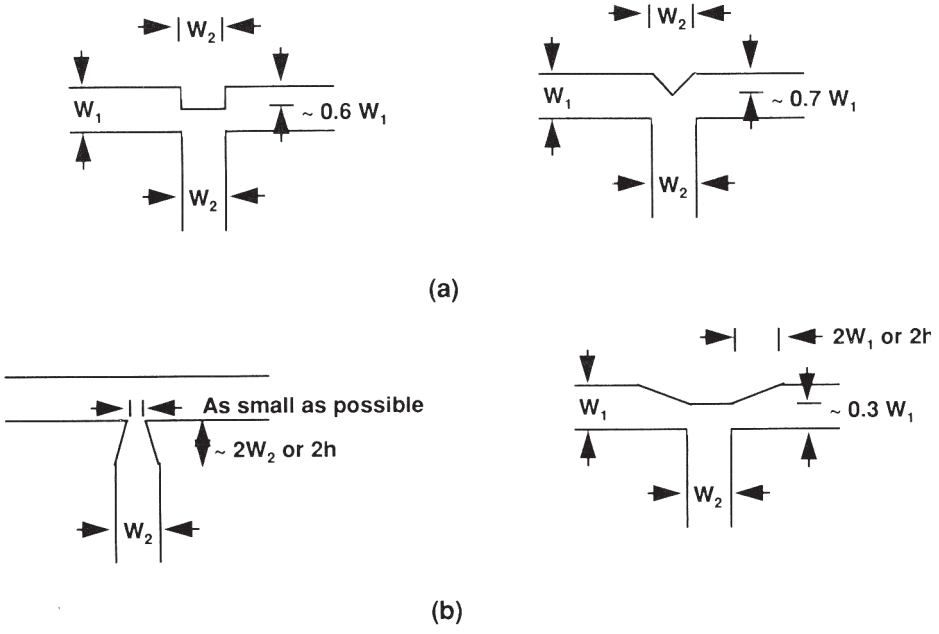

Figure 3.44 (a) T-junction discontinuity compensation configurations and (b) minimized T-junction discontinuity effect configuration.

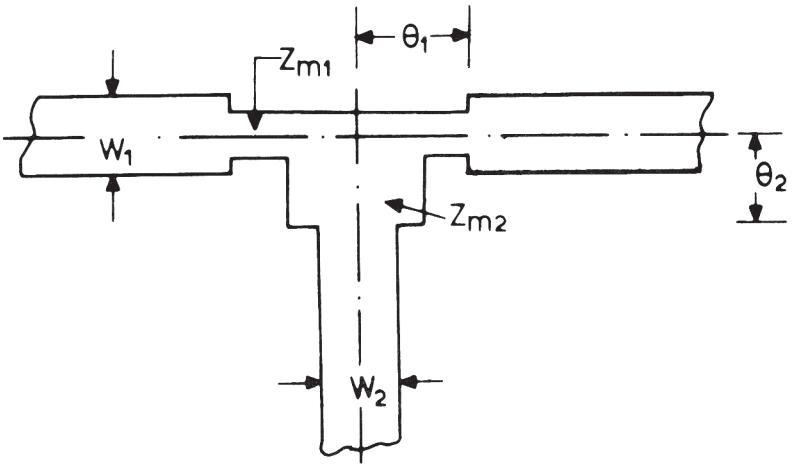

Figure 3.45 A T-junction with compensation for junction discontinuity reactances.

References

[1] Farrar, A., and A. T. Adams, "Matrix Methods for Microstrip three-dimensional Problems," *IEEE Trans.*, Vol. MTT-20, 1972, pp. 497–504.

[2] Farrar, A., and A. T. Adams, "Computation of Static Capacitance Data for Single, Double and Triple Microstrip Line," *IEEE-GMTT Int. Microwave Symp. Digest*, 1970, pp. 257–261.

[3] Farrar, A., and A. T. Adams, "Computation of Lumped Microstrip Capacities by Matrix Methods: Rectangular Sections and End Effect," *IEEE Trans.*, Vol. MTT-19, 1971, pp. 495–497; Also see correction *IEEE Trans.*, Vol. MTT-20, 1972, p. 294.

[4] Maeda, M., "An Analysis of Gap in Microstrip Transmission Lines," *IEEE Trans.*, Vol. MTT-20, 1972, pp. 390–396.

[5] Itoh, T., R. Mittra, and R. D. Ward, "A New Method for Solving Discontinuity Problems in Microstrip Lines," 1972 IEEE-GMIT Int. Microwave Symp. Digest, pp. 68–70.

[6] Itoh, T., R. Mittra, and R. D. Ward, "A Method for Computing Edge Capacitance of Finite and Semi-Finite Microstrip Lines," *IEEE Trans.*, Vol. MTT-20, 1972, pp. 847–849.

[7] Silvester, P., and P. Benedek, "Equivalent Capacitance of Microstrip Open Circuits," *IEEE Trans.*, Vol. MTT-20, 1972, pp. 511–516.

[8] Silvester, P., and P. Benedek, "Microstrip Discontinuity Capacitances for Right-angle' Bends, T-junctions and Crossings," *IEEE Trans.*, Vol. MTT-21, 1973, pp. 341–346; see correction IEEE Trans., Vol. MTT-23, 1975, p. 456.

[9] Benedek, P., and P. Silvester, "Equivalent Capacitance for Microstrip Gaps and Steps," *IEEE Trans.*, Vol. MTT-20, 1972, pp. 729–733.

[10] Horton, R., "The Electrical Characterization of a right-angled Bend in Microstrip Line," *IEEE Trans.*, Vol. MTT-21, 1973, pp. 427–429.

[11] Horton, R., "Equivalent Representation of an Abrupt Impedance Step in Microstrip Line," *IEEE Trans.*, Vol. MTT-21, 1973, pp. 562–564.

[12] Collin, R. E., Field Theory of Guided Waves, New York: McGraw-Hill, 1960, p. 148.

[13] Yamashita, E., "Variational Method for the Analysis of Microstrip-like Transmission Lines," *IEEE Trans.*, Vol. MTT-16, 1968, pp. 529–535.

[14] Thompson, A. F., and A. Gopinath, "Calculation of Microstrip Discontinuity Inductances," *IEEE Trans.*, Vol. MTT-23, 1975, pp. 648–655.

[15] Gopinath, A., et al., "Equivalent Circuit Parameters of Microstrip Step Change in Width and Cross Junctions," *IEEE Trans.*, Vol. MTT-24, 1976, pp. 142–144.

[16] Hammerstad, E. O., and F. Bekkadal, Microstrip Handbook, ELAB report STF 44 A74169, The University of Trondheim, The Norwegian Institute of Technology, 1975.

[17] Garg, R., and I.J. Bahl, "Microstrip Discontinuities," *Int. J. Electron.*, Vol. 45, July 1978, pp. 81–87.

[18] Hammerstad, E., "Computer-Aided Design of Microstrip Couplers with Accurate Discontinuity Models," *IEEE MTT-S Int. Microwave Symp. Digest*, 1981, pp. 54–56.

[19] Kirschning, M., R. H. Jansen, and N. H. L. Koster, "Accurate Model for Open End Effect of Microstrip Lines," *Electron Lett.*, Vol. 17, February 1981, pp. 123–125.

[20] Jansen, R. H., and N. H. L. Koster, "Accurate Results on the End Effect of Single and Coupled Microstrip Lines for Use in Microwave Circuit Design," *Arch. Elektr. Ubertr.*, Vol. 34, 1980, pp. 453–459.

[21] Jansen, R. H., "Hybrid Mode Analysis of End Effects of Planar Microwave and Millimeter Wave Transmission Lines," *Proc. Inst. Electr. Eng.*, Vol. 128, Part H, 1981, pp. 77–86.

[22] Hammerstad, E., and O. Jansen, "Accurate Models for Microstrip Computer-Aided Design," *IEEE MTT-S Int. Microwave Symp. Digest*, 1980, pp. 407–409.

[23] Itoh, T., "Analysis of Microstrip Resonators," *IEEE Trans.*, Vol. MTT-22, November 1974, pp. 946–952.

[24] James, J. R., and A. Henderson,"High Frequency Behavior of Microstrip Open-End Terminations," *IEEE Microwaves, Opt. Acoust.*, Vol. 3, 1979, pp. 205–211.

[25] Boukamp, J., and R. H. Jansen, "The High-Frequency Behavior of Microstrip Open-Ends in Microwave Integrated Circuits Including Energy Leakage," *Proc. 14th European Microwave Conf.*, 1984, pp. 142–147.

[26] Katehi, P. B., and N. G. Alexopoulos, "Frequency-Dependent Characteristics of Microstrip Discontinuities in Millimeter-Wave Integrated Circuits," *IEEE Trans.*, Vol. MTT-33, October 1985, pp. 1029–1035.

[27] Jackson, R. W., and D. M. Pozar, "Full-Wave Analysis of Microstrip Open-End and Gap Discontinuities," *IEEE Trans.*; Vol. MTT-33, 1985, pp. 1036–1042.

[28] Alexopoulos, N. G., and S.-C. Wu, "Frequency-Independent Equivalent Circuit Model for Microstrip Open-end and Gap Discontinuity," *IEEE Trans.*, Vol. MTT-42, July 1994, pp. 1268–1272.

[29] *The Microwave Engineer's Handbook and Buyers Guide*, Dedham, MA: Horizon House, 1969, p. 72.

[30] Gupta, C., and A. Gopinath, "Equivalent Circuit Capacitance of Microstrip Step Change in Width," *IEEE Trans.*, Vol. MTT-25, 1977, pp. 819–822.

[31] Rizzoli, V., F. Mastri, and D. Masotti, "Modeling the Microstrip Impedance Step from Direct Measurements in the 1–27 GHz Band," *Microwave and Opt. Tech. Lett.*, Vol. 4, December 1991, pp. 562–566.

[32] Easter, B., et al., "Resonant Techniques for the Accurate Measurement of Microstrip Properties and Equivalent Circuits," Proc. 1973 European Microwave Conf., paper B. 7.5.

[33] Easter, B., "The Equivalent Circuit of some Microstrip Discontinuities," *IEEE Trans.*, Vol. MTT-23, 1975, pp. 655–660.

[34] Akello, R. J., et al., "Equivalent Circuit of the Asymmetric Cross Over Junction," *Electron, Lett.*, Vol. 13, 1977, pp. 117–118.

[35] Hoefer, W. J. R., "Equivalent Series Inductivity of a Narrow Transverse Slit in Microstrip," *IEEE Trans.*, Vol. MTT-25, October 1977, pp. 822–824.

[36] Goldfarb, M. E., and R. A. Pucel, "Modeling Via Hole Grounds in Microstrip," *IEEE Microwave and Guided Wave Letters*, Vol. 1, 1991, pp. 135–137.

[37] Wang, T., R. F. Harrington, and J. Mautz, "Quasi-static Analysis of a Microstrip Via Through a Hole in a Ground Plane," *IEEE Trans. Microwave Theory Tech.*, Vol. 36, 1988, pp. 1008–1013.

[38] Rautio, J. C., and R. F. Harrington, "An Electromagnetic Time-Harmonic Analysis of Shielded Microstrip Circuits," *IEEE Trans. Microwave Theory Tech.*, Vol. MTT-35, 1987, pp. 726–730.

[39] Finch, K. L., and N. G. Alexopoulos, "Shunt Posts in Microstrip Transmission Lines," *IEEE Trans. Microwave Theory Tech.*, Vol. 38, 1990, pp. 1585–1594.

[40] Maeda, S., T. Kashiwa, and I. Fukai, "Full Wave Analysis of Propagation Characteristics of a Through Hole Using the Finite Difference Time-Domain Method," *IEEE Trans. Microwave Theory Tech.*, Vol. MTT-39, 1991, pp. 2154–2159.

[41] Tsai, W. J., and J. T. Aberle, "Analysis of a Microstrip Line Terminated With a Shorting Pin," *IEEE Trans. Microwave Theory Tech.*, Vol. MTT-40, 1992, pp. 645–651.

[42] Becker, W. D., P. Harms, and R. Miltra, "Time Domain Electromagnetic Analysis of a Via in a Multilayer Computer Chip Package," *IEEE MTT-S Int. Microwave Symp. Digest*, 1992, pp. 1129–1232.

[43] Jansen, R. H., "A Full-Wave Electromagnetic Model of Cylindrical and Conical Via hole Grounds for Use in Interactive MIC/MMIC Design," *IEEE MTT-S Int. Microwave Symp. Dig.*, 1992, pp. 1233–1236.

[44] Sorrentino, R., et al., "Full Wave Modeling of Via-Hole Grounds in Microstrip by Three Dimensional Mode Matching Technique," *IEEE Trans. Microwave Theory Tech.*, Vol. MTT-40, 1992, pp. 2228–2234.

[45] Visan, S., O. Picon, and V. Fouad Hanna, "3D Characterization of Air Bridges and Via Holes in Conductor-Backed Coplanar Waveguides for MMIC Applications," *IEEE MTT-S Int. Microwave Symp. Dig.*, 1993, pp. 709–712.

[46] Eswarappa, C., and W. J. R. Hoefer, "Time Domain Analysis of Shorting Pins in Microstrip Using 3–D SCN TLM," *IEEE MTT-S Int. Microwave Symp. Digest*, 1993, pp. 917–920.

[47] Cerri, G., M. Mongiardo, and T. Rozzi, "Full-Wave Equivalent Circuit of Via Hole Grounds in Microstrip," *Proc. 23rd European Microwave Conference*, 1993, pp. 207–208.

[48] Tsai, M. J., et al, "Multiple Arbitrary Shape Via-Hole and Air-Bridge Transitions in Multi-Layered Structures," *IEEE Trans. Microwave Theory Tech.*, Vol. 44, 1996, pp. 2504–2511.

[49] LaMeres, B. J., and T. S. Kalkur, "Time Domain Analysis of Printed Circuit Board Via," *Microwave J.*, Vol. 43, 2000, pp. 76–84.

[50] LaMeres, B. J., and T. S. Kalkur, "The Effect of Ground Vias on Changing Signal Layers in a Multilayered PCB," *Microwave Opt. Tech. Letters*, Vol. 28, 2001, pp. 257–260.

[51] Malherbe, J. A. G., "The Compensation of Step Discontinuities in TEM-Mode Transmission Lines," IEEE Trans., Vol. MTT-26, November 1978, pp. 883–885.

[52] Chadha, R., and K. C. Gupta, "Compensation of Discontinuities in Planar Transmission Lines," *IEEE Trans. on Microwave Theory Tech.*, Vol. MTT-30, December 1982, pp. 2151–2156.

[53] Hoefer, W. J. R., "A Contour Formula for Compensated Microstrip Steps and Open Ends," *IEEE MTT-S Int. Microwave Symp. Digest*, Boston, 1983, pp. 524–526.

[54] Raicu, D., "Universal Taper for Compensation of Step Discontinuities in Microstrip Lines," *IEEE Microwave Guided Lett.*, Vol. 1, September 1991, pp. 249–251.

[55] Groll, H., and W. Weidmann, "Measurement of Equivalent Circuit Elements of Microstrip Discontinuities by a Resonant Method," *Nachrichtentechnische Zeitschrift*, Vol. 28; 1975, pp. 74–77.

[56] Douville, R. J. P., and D. J. James, "Experimental Study of Symmetric Microstrip Bends and Their Compensation," *IEEE Trans. on Microwave Theory Tech.*, Vol. MTT-26, 1978, pp. 175–182.

[57] Dydyk, M., "Master the T-junction and Sharpen Your MIC Designs," *Microwaves*, Vol. 16, May 1977, pp. 184–186.

[58] Izadi, O. H., and M. Khalaj-Amirhosseini, "Microstrip Discontinuity Compensation using DGS," *Int. J. RF and Microwave Computer-Aided Engineering*, Vol. 23, March 2013, pp. 260–271.

CHAPTER 4

Microstrip Discontinuities II: Fullwave Analysis and Measurements

The quasi-static characterization of capacitances and inductances associated with microstrip discontinuities was discussed in Chapter 3. Results based on quasi-static analysis are valid, with sufficient accuracy, only up to frequencies of a few gigahertz. For a complete characterization of discontinuities, the frequency dependence of various parameters must be determined. This information is obtained from dynamic analyses, which are discussed in this chapter. Two-dimensional analysis, based on a planar waveguide model of a microstrip line, is presented in Section 4.1. Methods for more rigorous fullwave analysis are described in Section 4.2. Techniques for measuring microstrip discontinuities are also included in this chapter.

4.1 Planar Waveguide Analysis

4.1.1 Discontinuity Characterization

The planar waveguide model [1–3] for the microstrip line discussed in Section 1.3 is a very powerful technique for analyzing a number of microstrip discontinuities. Steps in width, T-junctions, bends, and cross junctions have been analyzed using this method and are discussed in this section. The equivalent circuits of these discontinuities can be obtained by using the derived scattering parameters and the theory of linear networks.

Step in Width [4]

The planar waveguide model of a step discontinuity is shown in Figure 4.1. Dimensions a and b are widths of planar waveguides corresponding to the microstrip lines "a" and "b," respectively. The cross-sectional areas of these guides are denoted by A^a ($= a \times h$) and A^b ($= b \times h$).

Since the height of the substrate, h, is much less than the wavelength in the microstrip, the fields are uniform along the y-direction in the equivalent planar waveguide model. Under this condition only TEM and TE_{m0} modes can be excited. (TM_{mn} modes do not exist because a small value of the substrate height requires $n = 0$, whereas the lowest value of n for TM modes is unity.) For TE_{m0} modes, the transverse fields in the planar waveguide model can be expressed in terms of orthogonal series expansions as

$$E_t = \sum_{m=0}^{\infty} U_{m0} \left\{ \hat{z} \times \nabla_t \psi_{m0}(x, y) \right\} \tag{4.1}$$

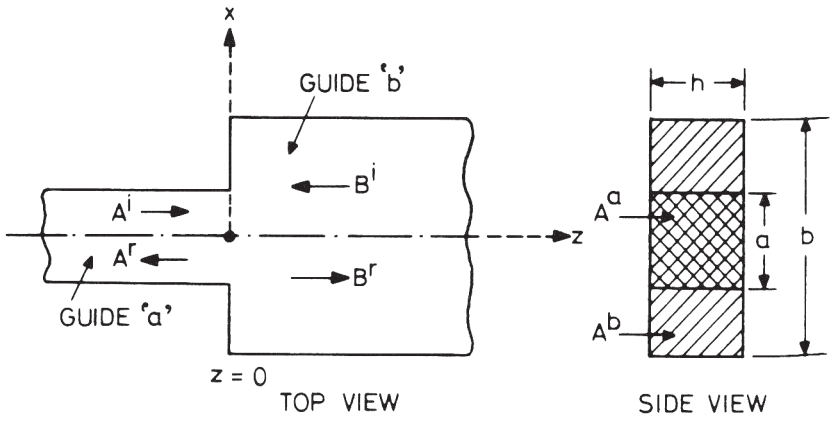

Figure 4.1 Top and side views of a step (in width) discontinuity.

$$H_t = \sum_{m=0}^{\infty} I_{m0} \left\{ -\nabla_t \psi_{m0}(x,y) \right\} \tag{4.2}$$

where U_{m0} and I_{m0} are the expansion coefficients and ψ_{m0} are the scalar potentials for TE modes. The unit vector along the z-axis is denoted by $\hat{z}$, and $m = 0$ corresponds to the dominant mode (TEM). The symbol ∇_t designates the transverse component of the gradient.

In the discontinuity plane ($z = 0$) the following boundary and interface conditions must be satisfied:

$$H_t^b = 0 \qquad \text{in region } \left(A^b - A^a \right) \tag{4.3a}$$

$$H_t^a = H_t^b \qquad \text{in region } A^a \tag{4.3b}$$

$$E_t^a = E_t^b \qquad \text{in region } A^a \tag{4.3c}$$

It can be shown that the conditions given by (4.3) can only be satisfied if the transverse magnetic field of guide "a" is expanded in terms of the modes of guide "b." While expanding the magnetic field H_t^a in terms of the modes of guide "b," the expansion coefficients I^b are chosen in such a way that $H_t^b = 0$ in region $A^b - A^a$ and will be equal to H_t^a in the discontinuity plane. On the other hand, no special boundary condition exists for the transverse electric field in the region $A^b - A^a$, so that the electric field E_t^b in the discontinuity cross section can be expanded in terms of the modes of guide "a."

Multiplying (4.3c) by $(\hat{z} \times \nabla_t \psi_{M0}^a)$ for various values of M (= 0, 1, 2 ...) and integrating over the aperture A^a leads to the equation

$$U_{M0}^a = \iint_{A^a} E_t^b \cdot \left(\hat{z} \times \nabla_t \psi_{M0}^a \right) dA \tag{4.4}$$

Due to the orthogonality property of the employed functions only coefficients U^{a}_{M0} will be nonzero. Similarly the following expression is found for the expansion coefficients I^{b}:

$$I^{b}_{P0} = \iint_{A^a} H^{a}_{t} \cdot \left(-\nabla_t \psi^{b}_{P0}\right) dA \tag{4.5}$$

Substituting the expansions of E^{b}_{t} and H^{a}_{t} from (4.1) and (4.2), respectively, one gets the following expressions for U^{a}_{M0} and I^{b}_{P0}:

$$U^{a}_{M0} = \sum_{p=0}^{\infty} U^{b}_{p0} K_{(M0)(p0)} \tag{4.6}$$

$$I^{b}_{P0} = \sum_{m=0}^{\infty} I^{a}_{m0} K_{(m0)(P0)} \tag{4.7}$$

where M, m and P, p correspond to the models in the guides "a" and "b" respectively. K's are called the coupling integrals, and the evaluation of these integrals provides information about the degree of interaction between the modes in the two guides. The coupling integrals are given by

$$K = K_{(M0)(p0)} = \iint_{A^a} \left(\hat{z} \times \nabla_t \psi^{b}_{p0}\right) \cdot \left(\hat{z} \times \nabla_t \psi^{a}_{M0}\right) dA \tag{4.8a}$$

$$K^{T} = K_{(m0)(P0)} = \iint_{A^a} \left(\nabla_t \psi^{a}_{m0}\right) \cdot \left(\nabla_t \psi^{b}_{P0}\right) dA \tag{4.8b}$$

The expansion coefficients U and I can be replaced by the normal modes coefficients A^{i}, A^{r} and B^{i}, B^{r} (see Figure 4.1). The resulting equations are

$$\sqrt{Z^{a}_{M0}}\left(A^{i}_{M0} + A^{r}_{M0}\right) = \sum_{p=0}^{\infty} \sqrt{Z^{b}_{p0}} K_{(M0)(p0)} \left(B^{i}_{p0} + B^{r}_{p0}\right) \tag{4.9a}$$

$$\sqrt{Y^{b}_{P0}}\left(B^{i}_{P0} - B^{r}_{P0}\right) = \sum_{m=0}^{\infty} \sqrt{Y^{a}_{m0}} K_{(m0)(P0)} \left(A^{i}_{m0} - A^{r}_{m0}\right) \tag{4.9b}$$

where m, M, p, $P = 0, 1, 2, \ldots$ and Z (= $1/Y$) is the wave impedance for TE mode given by

$$Z = \frac{\omega\mu}{\beta_z}$$

Here β_z is the propagation constant along the z-axis. For compactness, (4.9) may be written as

$$\sqrt{Z^{a}}\left(A^{i} + A^{r}\right) = \sqrt{Z^{b}} K \left(B^{i} + B^{r}\right) \tag{4.10a}$$

$$\sqrt{Y^{b}}\left(B^{i} - B^{r}\right) = \sqrt{Y^{a}} K^{T} \left(A^{i} - A^{r}\right) \tag{4.10b}$$

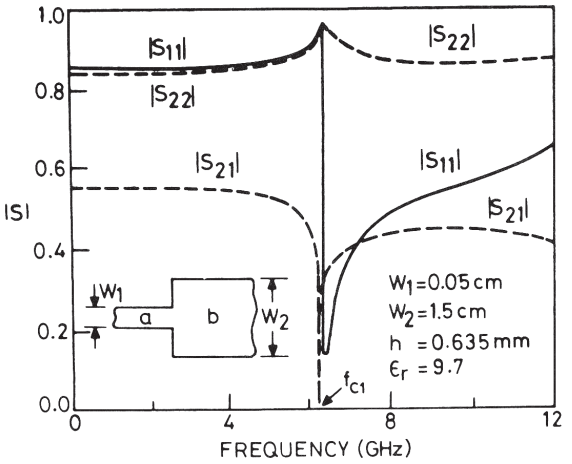

Figure 4.2 Computed scattering coefficients for a step discontinuity as a function of frequency (from [4], © 1976 S. Hirzel Verlag. Reprinted with permission.).

The incident and the reflected modes may be related by an **S**-matrix as

$$\begin{bmatrix} A^{r} \\ B^{r} \end{bmatrix} = [\mathrm{S}] \begin{bmatrix} A^{i} \\ B^{i} \end{bmatrix} \tag{4.11}$$

By knowing K, K^{T}, Z^{a}, and Z^{b} one can calculate the S-parameters of the step discontinuity.

Results and Equivalent Circuit

Numerical results of the scattering parameters of a symmetric step discontinuity have been reported by Kompa [4]. Typical results for frequency-dependent scattering matrix coefficients are shown in Figure 4.2. The incident mode considered here is the dominant TEM mode, while only even modes with $m = 0, 2, 4$ are assumed to be excited by the discontinuity. Figure 4.2 shows that, at frequencies well below the cut-off frequency of the first higher order mode ($m = 2$), the transmission and reflection coefficients are fairly constant. At the cut-off frequency of the TE_{20} mode (f_{c1}) the incident TEM mode is rejected and no transmission is possible. Assuming the step to be lossless, the reflection coefficient becomes equal to unity. For frequencies greater than the cut-off frequency, a part of the power is transmitted by the TE_{20} mode due to mode conversion, so that the transmission coefficient S_{21} for the dominant mode is always smaller than that for $f = 0$ (quasi-static case).

The equivalent circuit of a step discontinuity is determined from the known **S**-matrix by converting it into the **Y**-matrix. The **Y**-matrix elements y_{ik} which are normalized with respect to the characteristic admittance of guide "a," can be obtained from the relation

$$\mathbf{Y} = (\bar{\mathbf{I}} + \mathbf{S})^{-1} (\bar{\mathbf{I}} - \mathbf{S}) \tag{4.12}$$

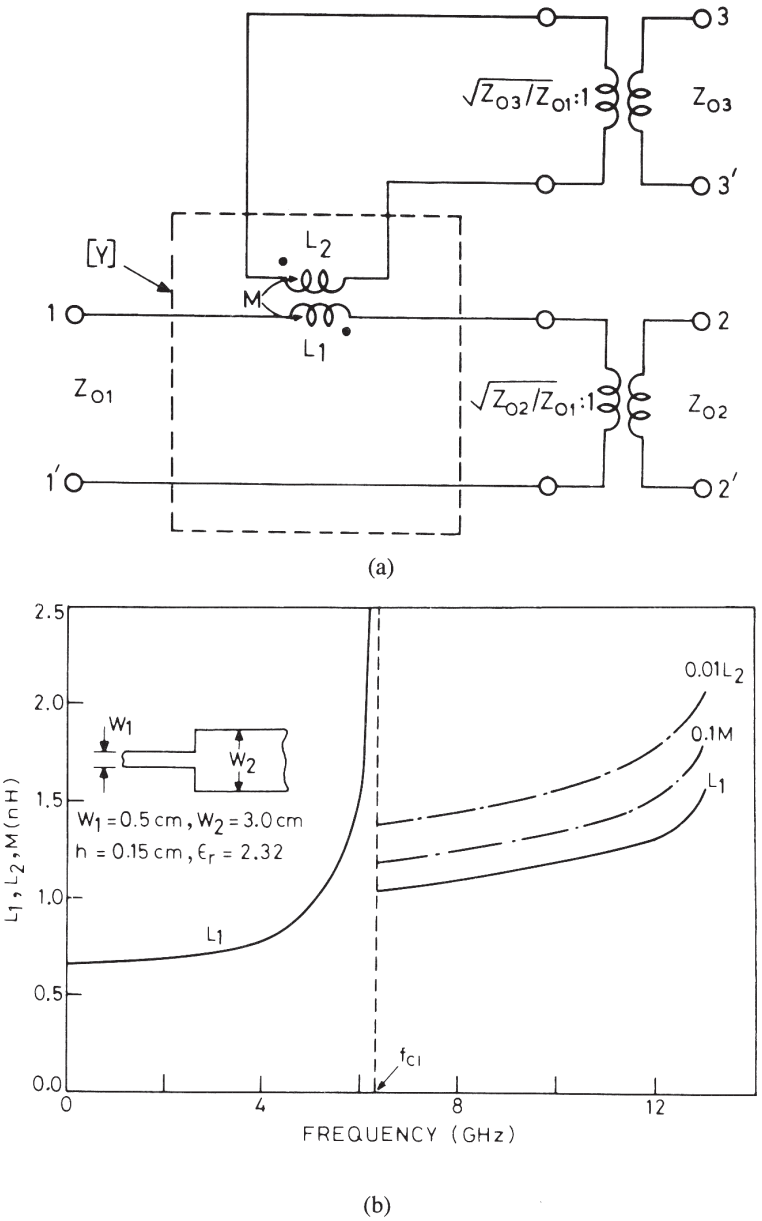

Figure 4.3 (a) Frequency-dependent equivalent circuit for a step discontinuity and (b) variations of equivalent circuit parameters of a step discontinuity with frequency (from [4], © 1976 S. Hirzel Verlag. Reprinted with permission.).

where $\bar{\mathrm{I}}$ is the identity matrix. The equivalent circuit is shown in Figure 4.3(a). Ports 1-1′ and 2-2′ refer to the TEM mode, while the port 3-3′ corresponds to the first higher order mode. The characteristic impedance Z_{03} for this mode is defined by the axial power flow of the first higher order mode in guide "b," that is,

$$Z_{03} = \frac{h^2 \left| E_{\max} \right|^2}{2 P_{p0}} \tag{4.13}$$

where P_{p0} is the axial power flowing in the $(p0)$ mode.

Figure 4.3(b) shows computed results for the equivalent circuit parameters. It can be seen that under single-mode propagation conditions, the discontinuity can be represented by a simple series inductance.

T-Junction [5]

The fullwave analysis of a T-junction using the planar waveguide model has been reported by Mehran [5]. The other two discontinuities (the right-angled bend and the cross junction) can be considered in terms of the T-junction by making use of symmetry considerations. Therefore the T-junction will be considered in detail for formulating the boundary value problem.

The T-junction geometry (shown in Figure 4.4) is subdivided into regions "a" and "b" wherein the transverse fields are expressed in terms of an orthogonal series expansion. The fields are matched at the discontinuity interface $z = 0$, which results in an infinite system of linear equations. The wave amplitudes in region "a," for arbitrary excitation, can be calculated by truncating the system of linear equations. To obtain the scattering parameters of the T-junction, the wave amplitudes of the transmitted waves in region "b" are evaluated.

The height of the substrate, h, is again much less than the wavelength in the microstrip, and the magnetic field does not have a component in the y-direction. Therefore, as was the case for step discontinuity, the description of the total field is complete in terms of an expansion using TE_{m0} modes only ($m = 0$ corresponds to the TEM-mode).

In region "a," the transverse field components may be written in terms of the series of the scalar potentials used in (4.1) and (4.2) as

$$E_t^a = U_{00}\nabla_t\psi_{00}^a + \sum_{m=1}^{\infty} U_{m0}\left(\hat{z} \times \nabla_t\psi_{m0}^a\right) \tag{4.14}$$

$$H_t^a = I_{00}\left(\hat{z} \times \nabla_t\psi_{00}^a\right) + \sum_{m=1}^{\infty} I_{m0}\left(-\nabla_t\psi_{m0}^a\right) \tag{4.15}$$

These field components satisfy the boundary conditions on the guide walls. ψ_{00}^a represents the scalar potential for the TEM mode and is given by

$$\psi_{00}^a = \frac{1}{\sqrt{W_1 h}}\, y \tag{4.16a}$$

The scalar potentials ψ_{m0}^a (which are also known as the orthonormalized vector mode functions of guide "a") are given by

$$\psi_{m0}^a = \frac{1}{m\pi}\sqrt{\frac{2W_1}{h}}\sin\left\{\frac{m\pi}{W_1}\left(x + \frac{W_1}{2}\right)\right\} \quad m \neq 0 \tag{4.16b}$$

Further, the expansion coefficients U_{m0} and I_{m0} for the field components E_t^a and H_t^a, respectively, are related to wave amplitudes $a_{1(m0)}$ and $b_{1(m0)}$ by

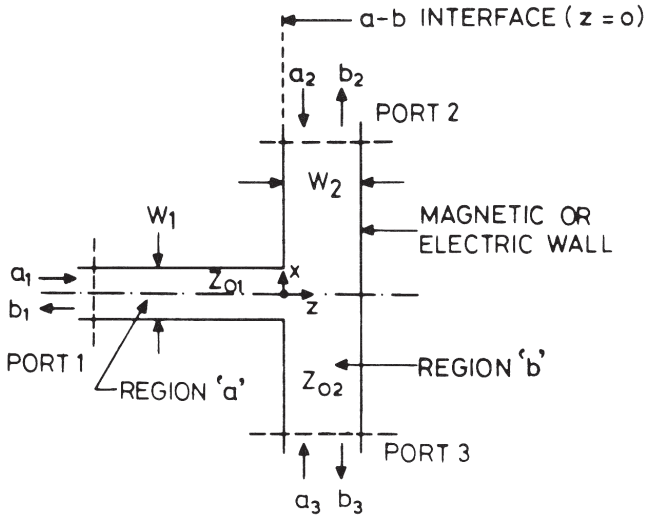

Figure 4.4 Configuration for analyzing a T-junction.

$$\sqrt{Y^{a}_{m0}}\,U_{m0} = a_{1(m0)}\exp(-j\beta^{a}_{z}z) + b_{1(m0)}\exp(j\beta^{a}_{z}z) \tag{4.17}$$

$$\sqrt{Z^{a}_{m0}}\,I_{m0} = a_{1(m0)}\exp(-j\beta^{a}_{z}z) - b_{1(m0)}\exp(j\beta^{a}_{z}z) \tag{4.18}$$

where Z^{a}_{m0} and Y^{a}_{m0} are wave impedances and admittances, respectively, for TE modes in region "a" and are given by

$$Z^{a}_{m0} = \frac{1}{Y^{a}_{m0}} = \frac{\omega\mu}{\beta^{a}_{z}} \tag{4.19}$$

where β^{a}_{z} is the propagation constant along the z-axis in region "a." The fields in region "b" may also be expanded by writing relations analogous to (4.14) and (4.15). However, by using an expansion of this type, matching of the fields at the interface cannot be achieved because the functions ψ^{b}_{m0} of guide "b" will vanish in the $(z = 0)$-plane. Hence an additional continuous spectrum is taken into account in region "b." This yields

$$E^{b}_{t} = E^{eb}_{e} + \int_{-\infty}^{\infty} F\left(\beta^{b}_{x}\right)\sqrt{\frac{\omega\mu}{\beta^{b}_{z}}}\left\{\begin{array}{c}\cos\left[\beta^{b}_{z}\left(z - W_2\right)\right]\\ \sin\left[\beta^{b}_{z}\left(z - W_2\right)\right]\end{array}\right\}\left[\hat{z}\times\nabla_{t}\psi^{b}\left(\beta_{x}\right)\right]d\beta^{b}_{x} \tag{4.20}$$

$$H^{b}_{t} = H^{eb}_{t} + j\int_{-\infty}^{\infty} F\left(\beta^{b}_{x}\right)\sqrt{\frac{\beta^{b}_{z}}{\omega\mu}}\left\{\begin{array}{c}\sin\left[\beta^{b}_{z}\left(z - W_2\right)\right]\\ -\cos\left[\beta^{b}_{z}\left(z - W_2\right)\right]\end{array}\right\}\left[\nabla_{t}\psi^{b}\left(\beta_{x}\right)\right]d\beta^{b}_{x} \tag{4.21}$$

where β^{b}_{x} is the propagation constant in the x-direction in region "b." The superscript e denotes a set of discrete incident modes, and $F(\beta^{b}_{x})$ is a weighting function to be determined. The function $\psi^{b}(\beta_{x})$ is defined by

$$\psi^{\mathrm{b}}(\beta_x) = \frac{\exp\left(j\beta_x^{\mathrm{b}} x\right)}{\beta_x^{\mathrm{b}}\sqrt{h}} \tag{4.22}$$

In (4.20) and (4.21), and also in the equations appearing later in this section, the upper functions are used if a T-junction with a magnetic side wall opposite to guide "a" is analyzed. For an electric wall, the lower functions are valid. The latter configuration is useful for extending the results of a T-junction discontinuity to the case of a cross junction.

The boundary condition that must be fulfilled by the transverse field components given by (4.14), (4.15) and (4.20), (4.21) is the continuity relation at the interface ($z = 0$)-plane. However, the unknown weighting function $F(\beta_{\mathrm{x}}^{\mathrm{b}})$ must be derived first. This is done by choosing the magnetic field components at the interface a – b in the following way

$$H_t^{\mathrm{b}}(z=0) = \begin{cases} H_{\mathrm{t}}^{\mathrm{a}}(z=0) & \text{for } \mathrm{W}_1/2 \geq x \geq -W_1/2 \\ 0 & \text{for } \mathrm{W}_1/2 \leq x \leq -W_1/2 \end{cases} \tag{4.23}$$

When (4.23) is multiplied by $\nabla_{\mathrm{t}}\psi^{\mathrm{b}^*}(\beta_{\mathrm{x}})$ and integrated with respect to y from 0 to h, the weighting function $F(\beta_{\mathrm{x}}^{\mathrm{b}})$ is obtained through the orthogonality of the employed functions. This results in

$$F\left(\beta_x^{\mathrm{b}}\right) = \frac{j\sqrt{\omega\mu/\beta_z^{\mathrm{b}}}}{2\pi\left\{\begin{array}{c}\sin\beta_z^{\mathrm{b}}W_2 \\ \cos\beta_z^{\mathrm{b}}W_2\end{array}\right\}} \int_{-W_1/2}^{W_1/2}\int_0^h H_{\mathrm{t}}^{\mathrm{a}}(z=0)\left\{\nabla_{\mathrm{t}}\psi^{\mathrm{b}^*}(\beta_x)\right\} dx\,dy \tag{4.24}$$

where the asterisk * denotes the complex conjugate.

Finally, expressions for $E_{\mathrm{t}}^{\mathrm{a}}$ and $E_{\mathrm{t}}^{\mathrm{b}}$, (4.14) and (4.20), at the interface a – b are equated. The resulting equation is solved by projecting the series in (4.14) and (4.20) into the function space spanned by the elements $\nabla_{\mathrm{t}}\psi^{\mathrm{b}^*}(\beta_{\mathrm{x}})$. The integration is performed with respect to the strip $-\infty \leq x \leq \infty$, $0 \leq y \leq h$. This procedure results in an infinite system of linear equations. The wave amplitudes $a_{1(m0)}$ and $b_{1(m0)}$ of region "a" for arbitrary excitation can be calculated by truncating the infinite system of linear equations. Thus the field component $H_{\mathrm{t}}^{\mathrm{a}}(z=0)$ is known and (4.24) yields the weighting function $F(\beta_{\mathrm{x}}^{\mathrm{b}})$.

To obtain the scattering parameters of the T-junction, the wave amplitude of the transmitted wave in region "b" is calculated. It is known that the integral representation of $E_{\mathrm{t}}^{\mathrm{b}}$ has to decompose into the discrete modes of waveguide "b" for $|x| \geq \mathrm{W}_1/2$. This decomposition is achieved by inserting the known function $F(\beta_{\mathrm{x}}^{\mathrm{b}})$ in (4.20) and evaluating the resulting integral. The field amplitudes can then be recognized as the coefficients of the constituent modal terms.

For TE_{m0} modes the expansion coefficients for guide "a" are related by the equation

$$U_{M0} = \frac{-j\omega\mu}{\beta^{b}_{z(M0)}} \begin{Bmatrix} \cot\left(\beta^{b}_{z(M0)} W_2\right) \\ -\tan\left(\beta^{b}_{z(M0)} W_2\right) \end{Bmatrix} I_{M0}$$
$$+ \sum_{m=0}^{\infty}\sum_{p=0}^{\infty} \frac{j\omega\mu \begin{Bmatrix} \varepsilon_{0p} \\ 2 \end{Bmatrix} \sqrt{\varepsilon_{0m}\varepsilon_{0M}} \exp\left(-j\beta^{b}_{x} W_1/2\right)}{W_1 W_2 \left\{ \left[\beta^{b}_{x(p0)}\right]^2 - \left(\frac{m\pi}{W_1}\right)^2 \right\}} \tag{4.25a}$$
$$\cdot\, H\left(M, \beta^{b}_{x}\right) I_{m0} + R_{M0}$$

with $\varepsilon_{0i} = \begin{cases} 2 \text{ for } i \neq 0 \\ 1 \text{ for } i = 0 \end{cases}$

$$H\left(M, \beta^{b}_{x}\right) = \begin{cases} \dfrac{2\beta^{b}_{x(p0)} \sin\left(\beta^{b}_{x(p0)} W_1/2\right)}{\left(\beta^{b}_{x(p0)}\right)^2 - \left(M\pi/W_1\right)^2} & \text{for } \dfrac{M\pi}{W_1} \neq \beta^{b}_{x(p0)} \\ \dfrac{1}{2} W_1 \cos\dfrac{M\pi}{2} & \text{for } \dfrac{M\pi}{W_1} = \beta^{b}_{x(p0)} \end{cases} \tag{4.25b}$$

$$R_{M0} = \begin{cases} \int_0^h \int_{-W_1/2}^{W_1/2} E^{eb}_{t}(z=0)\left(\hat{z} \times \nabla_t \psi^{a}_{M0}\right)\, dx dy & \text{for } M \neq 0 \\ \int_0^h \int_{-W_1/2}^{W_1/2} E^{eb}_{t}(z=0)\left(\hat{z} \times \nabla_t \psi^{a}_{00}\right)\, dx\, dy & \text{for } M = 0 \end{cases} \tag{4.25c}$$

where $M = 0, 2, 4 \ldots$ and M and p denote modes present in regions "a" and "b," respectively. Since the amplitudes of the incident waves are known, the amplitudes of the reflected waves in region "a" can be computed from (4.17), (4.18), and (4.25). The amplitudes of the waves transmitted into region "b" can also be calculated. For the waves transmitted in region "b," the amplitudes are described by

$$b_{2(p0)} = \exp\left[-j\beta^{b}_{x(p0)} W_1\right] \begin{Bmatrix} 1 \\ 0 \end{Bmatrix} a_{3(p0)} + \sum_{m=0}^{\infty} I_{m0}$$
$$\frac{\omega\mu(-1)^{p} \begin{Bmatrix} \sqrt{\varepsilon_{0p}\varepsilon_{0m}} \\ \sqrt{2\varepsilon_{0m}} \end{Bmatrix} \sin\left[\beta^{b}_{x(po)} W_1/2\right]}{\sqrt{W_1 W_2}\sqrt{Z^{b}_{p0}}\left[\left(\beta^{b}_{x(p0)}\right)^2 - \left(\frac{m\pi}{W_1}\right)^2\right]} \exp\left[-j\beta^{b}_{x(p0)} W_1/2\right] \tag{4.26a}$$

and

$$b_{3(p0)} = \exp\left[-j\beta^{b}_{x(p0)}W_1\right]\begin{Bmatrix}1\\0\end{Bmatrix}a_{2(p0)} + \sum_{m=0}^{\infty} I_{m0}$$
$$\cdot \frac{\omega\mu(-1)^p \begin{Bmatrix}\sqrt{\varepsilon_{0p}\varepsilon_{0m}}\\ \sqrt{2\varepsilon_{0m}}\end{Bmatrix}\sin\left[\beta^{b}_{x(p0)}W_1/2\right]}{\sqrt{W_1W_2}\sqrt{Z^{b}_{p0}}\left[\left(\beta^{b}_{x(p0)}\right)^2 - \left(\frac{m\pi}{W_1}\right)^2\right]}\exp\left[j\beta^{b}_{x(p0)}W_1/2\right] \tag{4.26b}$$

with $p = 0, 1, 2, \ldots$ and $m = 0, 2, 4, \ldots$.

In the above equations also, the upper functions are used when a T-junction is analyzed with a magnetic side wall opposite to guide "a." For an electric wall, the lower functions are valid.

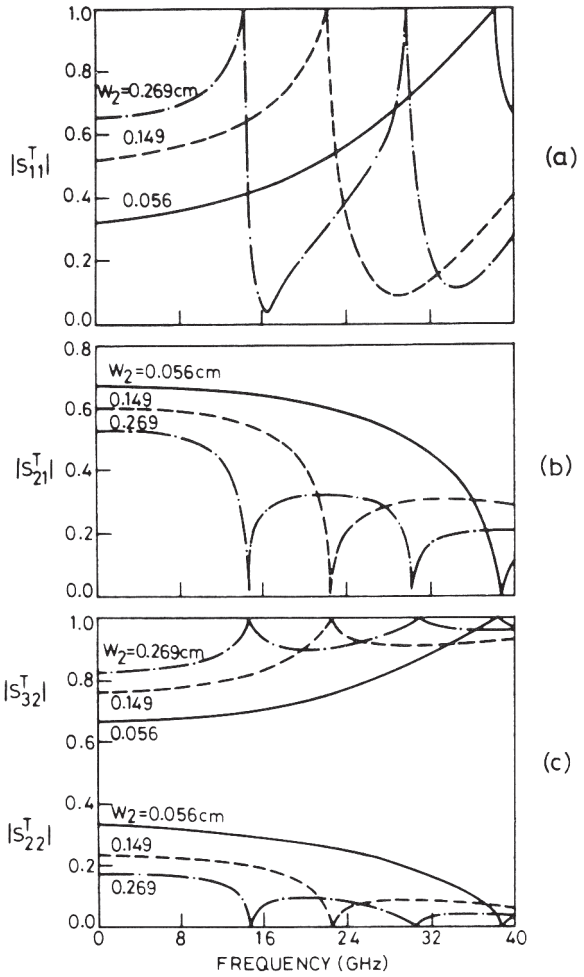

Figure 4.5 Numerical results for scattering coefficients of a T-junction: $\varepsilon_r = 9.7$, $h = 0.0635$ cm, $W_1 = 0.056$ cm (from [5], © 1975 S. Hirzel Verlag. Reprinted with permission.).

For odd values of m and M the expression $\sin\left[\beta^b_{x(po)}W_1/2\right]$ in (4.25) and (4.26) must be replaced by $-j\cos\left[\beta^b_{x(po)}W_1/2\right]$. Using (4.25) and (4.26), the scattering parameters of a T-junction can be calculated.

Results and Equivalent Circuit

Numerical results for the scattering parameters have been reported by Mehran [5]. If the incident wave is the dominant TEM mode, at least four modes should be considered in region "b" and at least two modes in region "a" when the transmission coefficient is to be calculated with an accuracy of 1 percent. The two modes in region "a" describe the total field and account for the reflected wave also.

Typical results for frequency-dependent scattering matrix coefficients of a T-junction are shown in Figure 4.5. We note that $|S^T_{11}|$, and therefore the power reflected by the T-junction discontinuity at $z = 0$ increases with frequency in the range $0 \le f \le f_{c1}$, where f_{c1} is the cut-off frequency of the first higher order (TE_{10}) mode in region "b." Correspondingly, the power transmitted into region "b" decreases with frequency (Figure 4.5(b)). For frequencies greater than f_{c1} a part of the power is transmitted by the TE_{10} mode, so that the transmission coefficient $|S^T_{11}|$ for the TEM mode is always smaller than that for $f = 0$. Figure 4.5(c) indicates that if the TEM mode is incident at port 2, the power reflected into guide "b" decreases

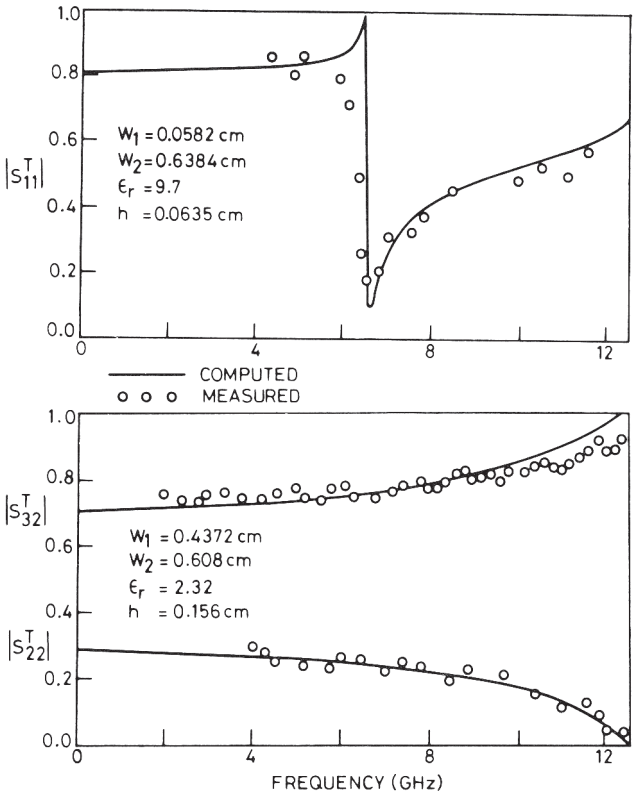

Figure 4.6 Comparison of computed results of fullwave analysis of a T-junction with experimental results (from [5], © 1975 S. Hirzel Verlag. Reprinted with permission.).

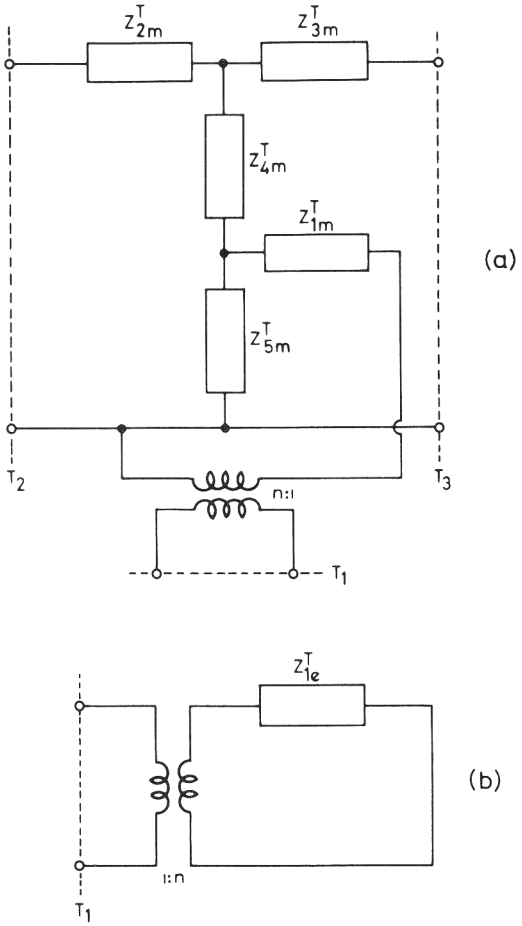

Figure 4.7 Frequency-dependent equivalent circuit for a microstrip T-junction: (a) with magnetic wall and (b) with electric wall (from [6], © 1975 S. Hirzel Verlag. Reprinted with permission.).

with increasing frequency. Also the power transmitted into guide "a" decreases, whereas the power transmitted into port 3 behaves in the opposite manner. It may be pointed out that the information contained in Figure 4.5 provides *S*-parameters for the TEM-mode since the incident power has been assumed to propagate in the dominant TEM-mode. For frequencies greater than f_{c1} (cut-off for the TE_{10} mode) a part of the power is transmitted in the TE_{10} mode also. Therefore, *S*-parameters for the TEM-mode do not describe the circuit completely for frequencies greater than f_{c1}.

A comparison between theoretical and experimental results is shown in Figure 4.6. Small circles show the experimental points. Discrepancies near the cut-off frequencies of higher order modes in microstrip of width *W* are attributed to the radiation effects.

The frequency-dependent equivalent circuit of a discontinuity can be derived from the scattering parameters. The equivalent circuits of a T-junction with a mag-

netic wall and an electric wall at $z = W_2$ can be represented as shown in Figure 4.7(a) and 4.7(b), respectively.

The impedances Z_{im}^{T} of the equivalent circuit elements can be determined using the relation between the short-circuit admittance matrix and the scattering matrix. These impedances may be written in terms of *S*-parameters as [6]

$$
\begin{aligned}
Z_{1m}^{T} &= \frac{n\left[\left(1 - S_{22}^{T} + S_{32}^{T}\right)\left\{2S_{12}^{T}\left(nS_{12}^{T} - 1\right) + n\left(1 + S_{11}^{T}\right)\left(1 - S_{22}^{T} - S_{23}^{T}\right)\right\}\right]}{D^{T}} \\
Z_{3m}^{T} &= Z_{2m}^{T} = \frac{\left(1 + S_{22}^{T} - S_{23}^{T}\right)\left[\left(1 - S_{11}^{T}\right)\left(1 - S_{22}^{T} - S_{23}^{T}\right) - 2\left(S_{12}^{T}\right)^{2}\right]}{D^{T}} \\
Z_{4m}^{T} &= 2\frac{\left(S_{12}^{T}\right)^{2} - 2nS_{12}^{T}\left(1 - S_{22}^{T} + S_{23}^{T}\right) + S_{23}^{T}\left(1 - S_{11}^{T}\right)}{D^{T}} \\
Z_{5m}^{T} &= \frac{2nS_{12}^{T}\left(1 - S_{22}^{T} + S_{23}^{T}\right)}{D^{T}}
\end{aligned}
\tag{4.27}
$$

where

$$
D^{t} = (1 - S_{22}^{T} + S_{23}^{T})[(1 - S_{11}^{T})(1 - S_{22}^{T} - S_{23}^{T}) - 2(S_{12}^{T})^{2}]
$$

$$
n^{2} = Z_{01}/Z_{02}
$$

In the above equation, the subscript m denotes a magnetic wall. The impedances Z_{im}^{T} are normalized with respect to Z_{02}. For frequencies lower than the cut-off frequency of the first higher order mode, all elements of the equivalent circuit are reactances (capacitive or inductive). The reactance representation of the equivalent circuit is shown in Figure 4.8(a). For a typical set of T-junction parameters the variations of these reactances with frequency are shown in Figure 4.8(b). This figure shows that except for C_{4T}, other capacitances and inductances of the equivalent circuit do not vary much with frequency up to about 10 GHz.

For a T-junction with electric wall, Z_{le}^{T} is given by the expression for Z_{lm}^{T} when *S*-parameters corresponding to a T-junction with electric wall (Figure 4.4) are used.

Right-Angled Bend and Cross Junction [5]

The scattering parameters for right-angled bends and cross junctions can be derived from those for the T-junction. This is achieved by an even- and odd-mode excitation at the opposite ports (ports 2 and 3 in Figure 4.4). Right-angled bends and cross junctions are discussed in the following paragraphs.

The scattering parameters of a right-angled bend can be arrived at from the analysis of a T-junction with a magnetic wall at z = W_2. When the T-junction is excited symmetrically at ports 2 and 3 ($a_2 = a_3 = v_2$ as shown in Figure 4.9), the symmetry plane $x = 0$ (which bisects the T-junction into two identical right-angled bends) can be replaced by a magnetic wall. Using the symmetry and reciprocity properties of the structure, the relationship between the scattering parameters of the T-junction and the bend may be written as

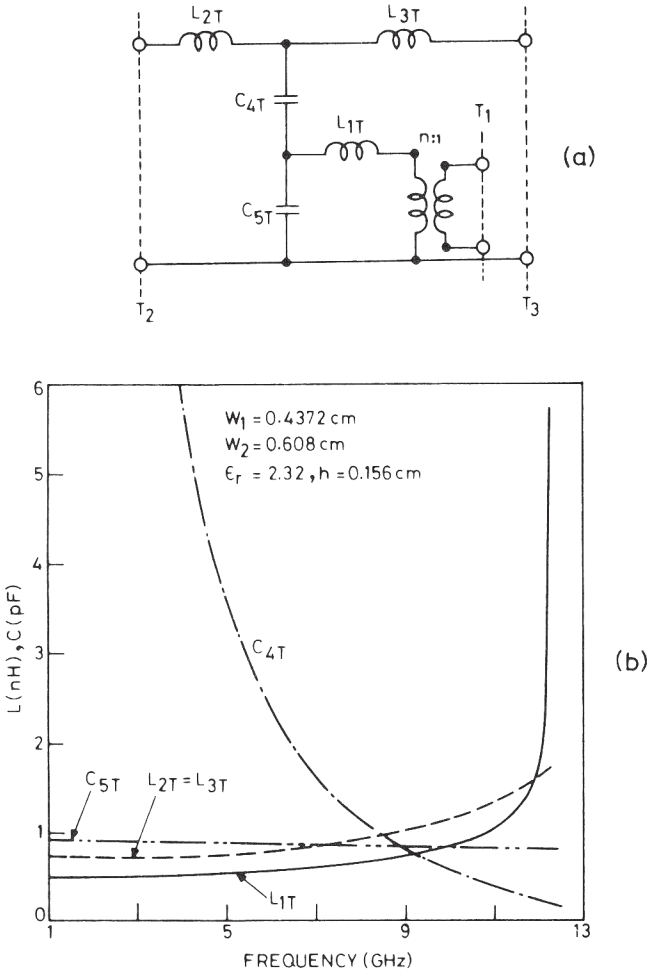

Figure 4.8 (a) Microstrip T-junction discontinuity capacitances and inductances and (b) variations of equivalent circuit parameters with frequency (from [6], © 1975 S. Hirzel Verlag. Reprinted with permission.).

$$
\begin{aligned}
S_{12}^{\mathrm{B}} &= \sqrt{2} S_{12\mathrm{m}}^{\mathrm{T}} \\
S_{21}^{\mathrm{B}} &= \sqrt{2} S_{21\mathrm{m}}^{\mathrm{T}} \\
S_{11}^{\mathrm{B}} &= S_{11\mathrm{m}}^{\mathrm{T}} \\
S_{22}^{\mathrm{B}} &= S_{23\mathrm{m}}^{\mathrm{T}} + S_{22\mathrm{m}}^{\mathrm{T}}
\end{aligned}
\tag{4.28}
$$

The superscripts B and T denote the bend and the T-junction, respectively. The subscript m indicates a T-junction with a magnetic wall at $z = W_2$. Equations (4.28) constitute a correspondence between a right-angled bend and a T-junction whose W_1 is chosen such that

$$Z_{01}^{\mathrm{T}} = Z_{01}^{\mathrm{B}}/2$$

or

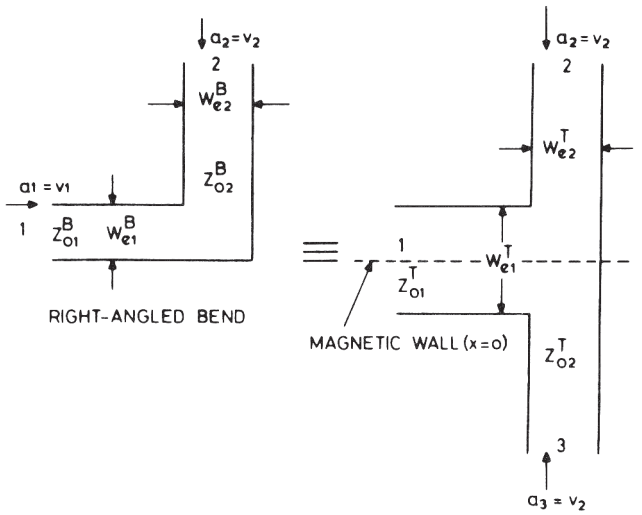

Figure 4.9 Derivation of right-angled bend from symmetrically excited T-junction.

$$W_{e1}^{T}(f) = 2W_{e1}^{B}(f) \tag{4.29}$$

The *S*-parameters of a cross junction are calculated in the following manner. Any arbitrary excitation v at port 1 can be considered as a superposition of a symmetric ($a_1 = v/2$, $a_3 = v/2$) excitation and an antisymmetric excitation ($a_1 = v/2$, $a_3 = -v/2$) at ports 1 and 3. This situation is shown in Figure 4.10. The cross junction with symmetric excitation is a combination of two T-junctions with magnetic walls placed back to back. Similarly, for antisymmetric excitation, a cross junction corresponds to two T-junctions with an electric wall as shown in Figure 4.10. These T-junctions have the effective width of the through arm equal to $W_{e2}^{C}/2$. The above considerations allow us to write the *S*-parameters of a cross junction as

$$\begin{aligned} S_{11}^{C} &= (S_{11m}^{T} + S_{11e}^{T})/2 \\ S_{13}^{C} &= (S_{11m}^{T} - S_{11e}^{T})/2 \\ S_{12}^{C} &= (1/\sqrt{2})\, S_{12m}^{T} \qquad S_{22}^{C} = S_{22m}^{T} \qquad S_{24}^{C} = S_{23m}^{T} \end{aligned} \tag{4.30}$$

The effective width of the T-junction has to be determined so that

$$Z_{02}^{C} = Z_{02}^{T}/2 \quad \text{or} \quad W_{e2}^{C}(f) = 2W_{e2}^{T}(f) \tag{4.31}$$

The superscript C denotes cross junction.

Results and Equivalent Circuit

S-parameters for right-angled bends are calculated using (4.28) and (4.29). For cross junctions, (4.30) and (4.31) are used. The equivalent circuits for these discontinuities are derived from the equivalent circuit impedances Z_{im}^{T} of the T-junction.

The frequency-dependent equivalent circuit of the right-angled bend, based on the conversion procedure from the T-junction (with magnetic wall at $z = W_2$) to

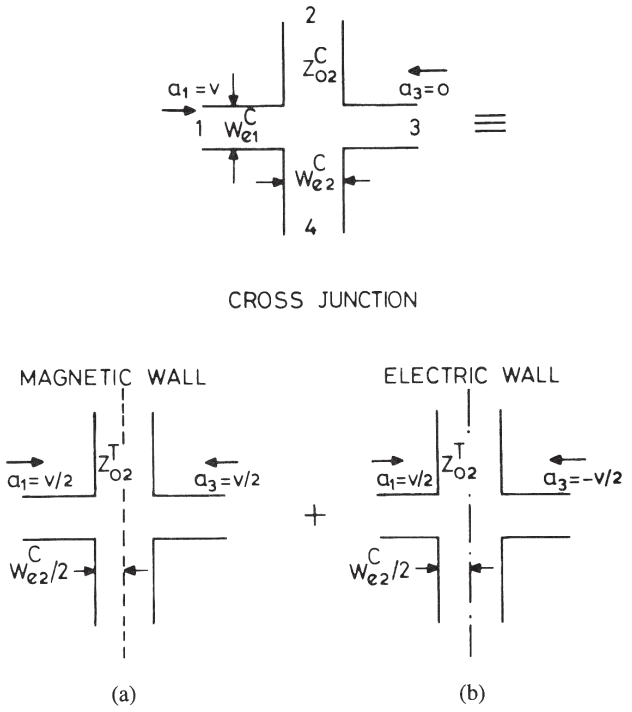

Figure 4.10 Derivation of a cross junction from superposition of (a) symmetrically and (b) antisymmetrically excited T-junctions.

the right-angled bend discussed above is shown in Figure 4.11(a). The equivalent circuit element impedances are obtained from the relations (see also Figure 4.7a)

$$\begin{aligned} Z_1^B &= Z_{2m}^T + 2Z_{4m}^T \\ Z_2^B &= 2Z_{5m}^T \\ Z_3^B &= 2Z_{1m}^T \end{aligned} \tag{4.32}$$

The superscript B denotes a right-angled bend, while subscript m denotes a magnetic wall. The variations of capacitive and inductive components of an equivalent circuit (shown in Figure 4.11(b)) with frequency are shown in Figure 4.11(c). This figure shows that the capacitive and inductive values are almost constant up to 10 GHz.

The frequency-dependent equivalent circuit of the cross junction, derived from the T-junctions (with magnetic and electric walls at $z = W_2/2$), is shown in Figure 4.12(a). The relations between the elements of the equivalent circuit of the T-junction and the cross junction can be written as (see also Figure 4.7)

$$\begin{aligned} Z_1^C &= 2\,Z_{1e}^T \\ Z_2^C &= Z_{2m}^T \\ Z_3^C &= Z_{4m}^T\left(Z_{1m}^T - Z_{1e}^T\right)\left\{\frac{1}{Z_{4m}^T} + \frac{1}{Z_{1m}^T - Z_{1e}^T} + \frac{1}{Z_{5m}^T}\right\} \\ Z_4^C &= Z_{5m}^T \cdot Z_3^C / Z_{4m}^T \\ Z_5^C &= Z_{5m}^T \cdot Z_3^C / \left(Z_{1m}^T - Z_{1e}^T\right) \end{aligned} \tag{4.33}$$

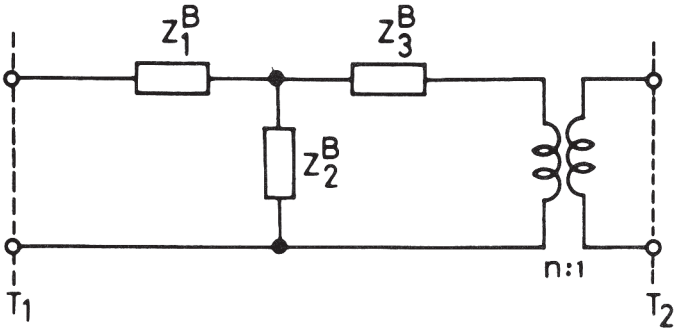

(a)

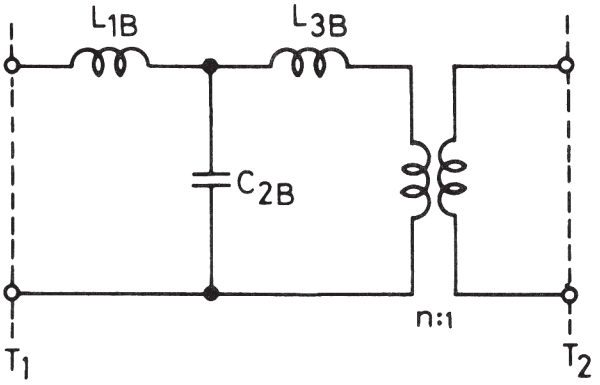

(b)

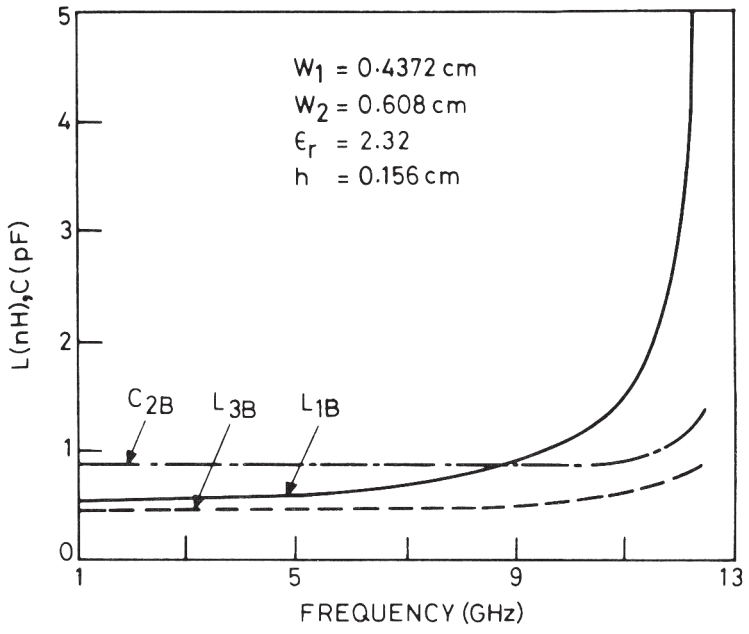

(c)

Figure 4.11 (a) and (b) Equivalent circuits of a right-angled bend based on fullwave analysis and (c) variations of computed results for capacitance and inductances as a function of frequency (from [6], © 1975 S. Hirzel Verlag. Reprinted with permission.).

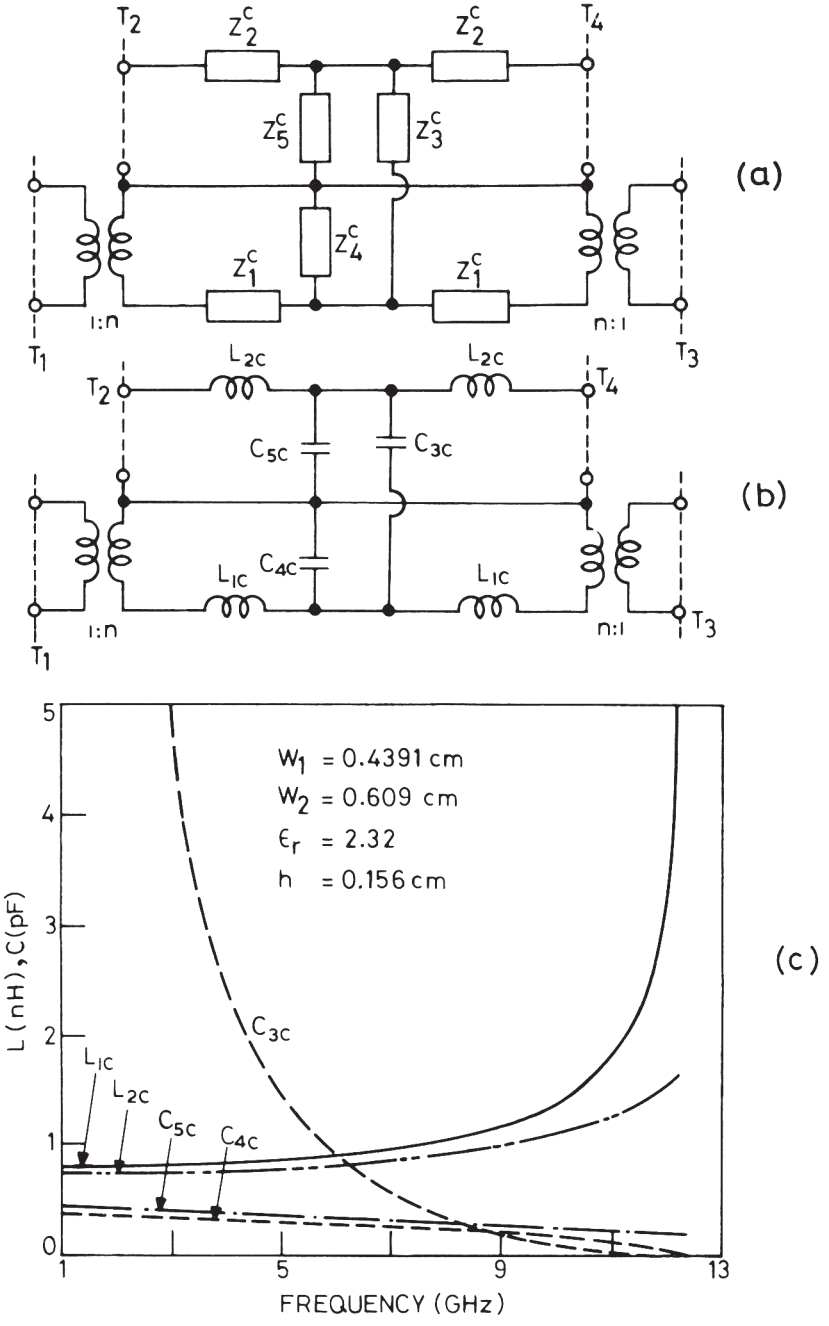

Figure 4.12 (a) and (b) Frequency-dependent equivalent circuits of a cross junction and (c) discontinuity capacitances and inductances as a function of frequency (from [6], © 1975 S. Hirzel Verlag. Reprinted with permission.).

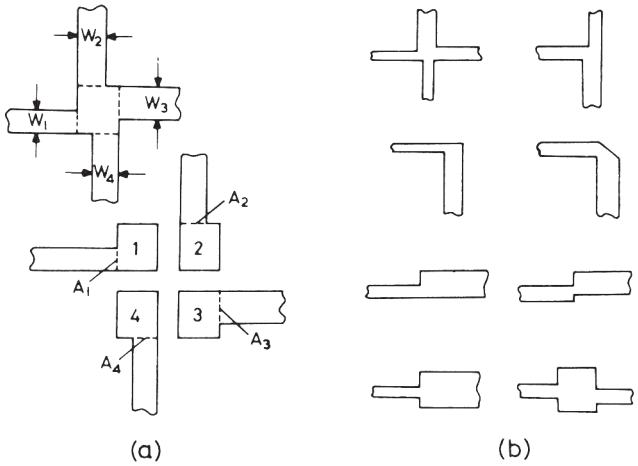

Figure 4.13 (a) Configuration for calculation of dynamic properties of an unsymmetric cross junction and (b) other types of discontinuities that could be analyzed by the parallel plate waveguide model.

with superscript C denoting the cross junction. The subscript e indicates electric wall at $z = W_2/2$ opposite to guide "a" of the T-junction. The equivalent circuit in terms of capacitances and inductances, based on the results of (4.33), is shown in Figure 4.12(b). The variations of these components with frequency are shown in Figure 4.12(c). In this case also, the variation of inductances with frequency is small, up to 10 GHz.

The planar waveguide model of a microstrip can also be used to analyze more general unsymmetrical discontinuities [7]. An example of an unsymmetrical crossing is shown in Figure 4.13(a). The microstrip lines are replaced by the equivalent planar waveguides, and the connnecting field region is treated as a rectangular disc resonator. The fields of the rectangular disc resonator can also be approximated by a magnetic wall model. The magnetic fields in various regions are matched at the subareas A_i ($i = 1, 2, 3, 4$), all other boundaries being magnetic walls. By superposition of the fields of the four subproblems and matching the electric fields in the area A_i, the scattering matrix of the discontinuity can be calculated, taking into account the influence of dispersion effects and higher order modes. Figure 4.13(b) shows some other types of discontinuities that can be analyzed using this method.

Curved Microstrip Bend

Curved microstrip bends are frequently used in MMICs and MICs. For high impedance microstrip lines they offer better alternative to chamfered microstrip bends. The curved microstrip bends have been analyzed using magnetic wall planar waveguide model [15]. Figure 4.14 shows the curved microstrip bend and its equivalent waveguide model. When the curvature is large (i.e., R/W is greater than 3), the parasitic effect (due to the curvature discontinuity) is negligible. However, the

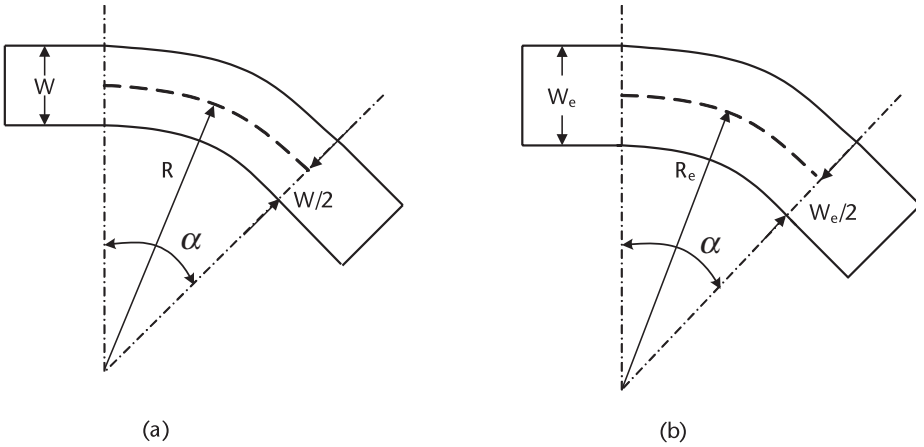

Figure 4.14 (a) Curved microstrip bend configuration and (b) equivalent waveguide model for the microstrip bend.

curvature affects the length of the curved section. The effective radius of curvature is given by [15]:

$$R_e = \frac{R}{2} + \frac{1}{2}\sqrt{R^2 + (W_e - W)W_e} \tag{4.34a}$$

where W_e is the effective width of the microstrip constituting the bend. When $(We - W)We/R \ll 1$, (4.34a) becomes

$$R_e = R + \frac{(W_e - W)W_e}{4R} \tag{4.34b}$$

$$\Delta\ell = \frac{2\pi\alpha(R_e - R)}{360} = \frac{2\pi\alpha}{360}\Delta R = \frac{\pi\alpha}{720}\frac{(W_e - W)W_e}{R} \tag{4.34c}$$

where the angle α is measured in degrees. Thus, the curvature increases the curved section's line length. Therefore, in the design of microstrip circuits one needs a correction $(-\Delta\ell)$ in the line length corresponding to the difference in the electrical length of the physical curved line and the equivalent waveguide model line. For a right-angled bend with 3<R/W<7, the increased line length is about 0.3W [16]. For larger radius of curvatures and narrow line widths, the increased line length becomes negligible.

4.1.2 Compensation of Discontinuity Reactances

The planar waveguide analysis approach discussed in Section. 4.1.1 has been used not only for characterizing microstrip discontinuities but also for the compensation of microstrip discontinuity reactances. The compensation of discontinuity reactances [8] involves a modification of the discontinuity's geometrical configuration so as to minimize its adverse effects on the performance of microstrip circuits. This compensation has been reported [8] for three types of discontinuities: step junc-

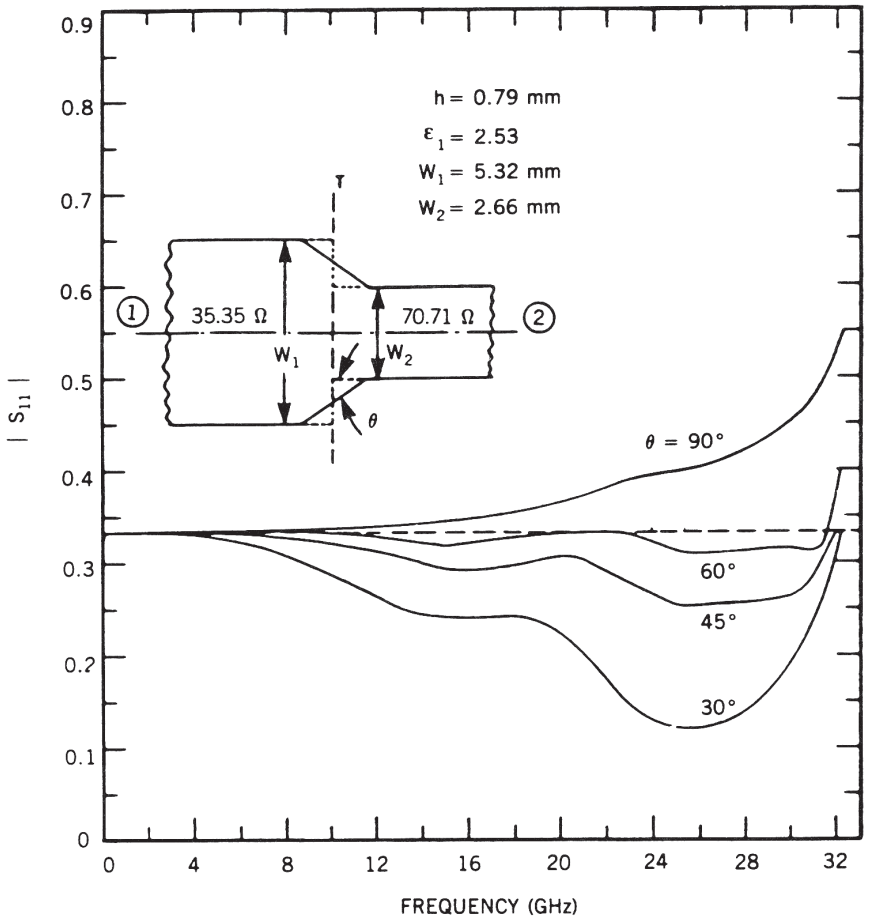

Figure 4.15 Reflection coefficients for the uncompensated and compensated step discontinuities with 1:2 impedance ratio (from [8], © 1982 IEEE. Reprinted with permission.).

tions, right-angled bends, and T-junctions. A combination of the segmentation and desegmentation methods [3] has been used in these cases. The computed results for these three types of compensated discontinuities are shown in Figures 4.15 to 4.17. For the sake of comparison, the characteristics of the uncompensated discontinuities are also shown in these three cases.

4.1.3 Radiation and Parasitic Coupling

Because of the open nature of the microstrip configuration, hybrid and monolithic microwave circuits suffer from radiation originating at various geometrical discontinuities. Two consequences of this radiation phenomenon are additional signal loss in the circuit and undesired interactions between different parts of the circuit due to external electromagnetic coupling. These phenomena can become significant in three different situations. First, when attempts are made to increase circuit density in monolithic microwave circuits, more bends and other discontinuities are introduced and spurious electromagnetic coupling increases considerably. Second,

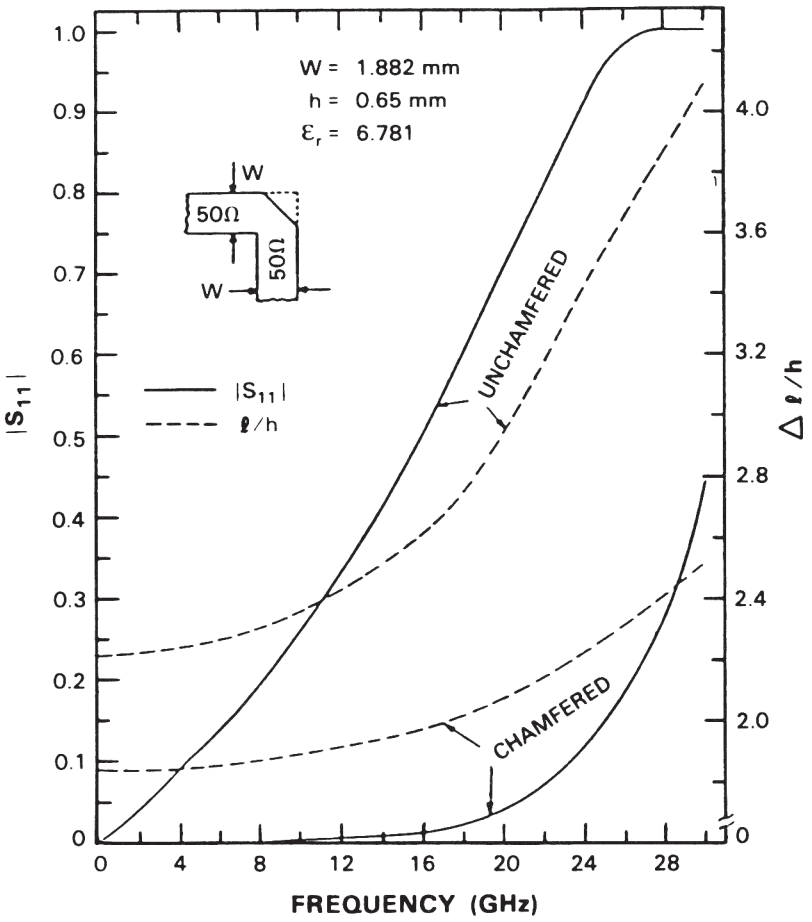

Figure 4.16 Reflection coefficients and normalized electrical lengths for uncompensated and optimally compensated right-angled bends (from [8], © 1982 IEEE. Reprinted with permission.).

in microstrip antenna arrays, relatively thicker substrates are used and the feed networks printed on these substrates can result in substantial spurious radiation. Third, in multichip modules, microstrip interconnects that have bends and junction discontinuities introduce EM coupling between various parts of the module, which degrades RF performance.

Radiation from Microstrip Discontinuities

Three different approaches for addressing the issue of radiation from microstrip discontinuities have been reported in the literature. These are:

1. The Poynting vector method based on longitudinal electric currents and polarization currents associated with discontinuities [9, 10];
2. The equivalent magnetic current formulation based on two-dimensional planar analysis [11];
3. Fullwave analysis methods incorporating radiation phenomenon [12].

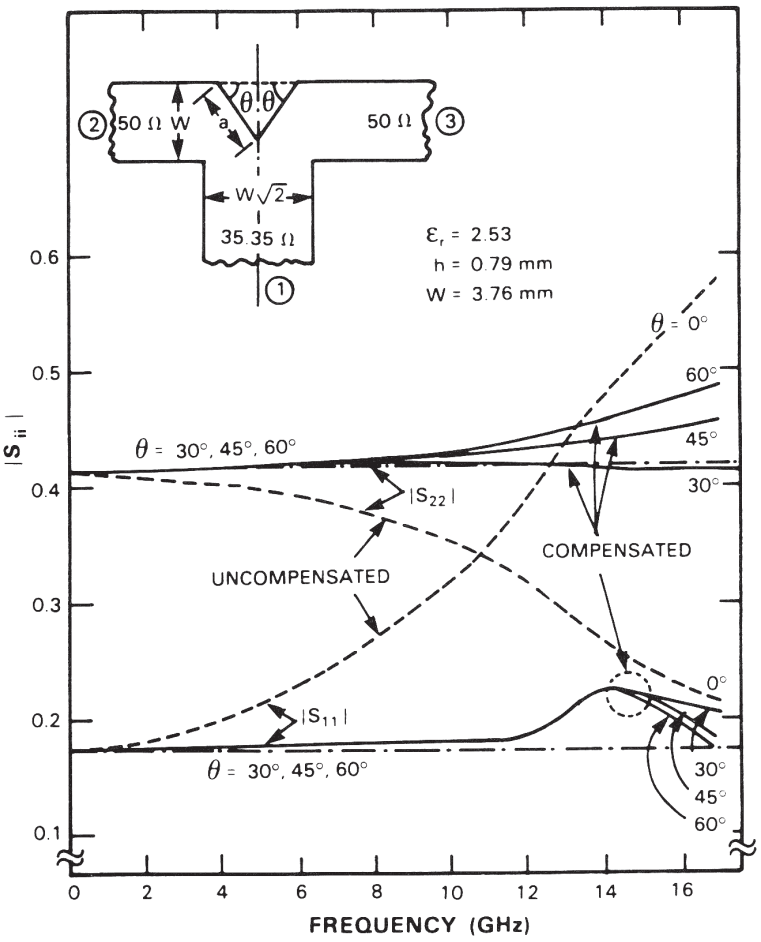

Figure 4.17 Main line and branch line reflection coefficients for uncompensated and compensated T-junctions (impedance ratio $1/\sqrt{2}$:1:1) (from [8], © 1982 IEEE. Reprinted with permission.).

Poynting Vector Method

In this approach, the source of radiation is described as a line current in the middle of the strip conductor, and, in the case of a microstrip open circuit, a polarization current flowing perpendicular to it. For other discontinuities, different polarization effects are associated with the longitudinal currents. The Poynting vector is calculated in the far field, and the total radiated power is calculated there from. The method is limited to narrow strip transmission lines with $W \ll \lambda_0$ and thin substrates with $h \ll \lambda_0$ having discontinuities of small extent. The air-substrate layers are represented by a homogeneous dielectric with a relative dielectric constant equal to ε_{re} of the microstrip line. Using this approach, the ratio of the radiated power to the incident power can be expressed as

$$P_{rad}/P_{inc} = 2\pi\eta_0 \cdot \left(h/\lambda_0\right)^2 \cdot F_i/Z_{0m} \tag{4.35}$$

where F_i is the dimensionless radiation factor that characterizes the specific radiation properties of the discontinuity and is dependent only on ε_r. The expressions

for F_i for various discontinuities are summarized in [10]. The microstrip line is described by its characteristic impedance Z_{0m}. The power radiated by surface waves is ignored (as $h/\lambda_0 \ll 1$) as compared with the free-space power. It is important to note that the radiated power is proportional to $(h/\lambda_0)^2$, a result that is consistent with the behavior of narrow-width rectangular microstrip patch antennas [13].

Equivalent Magnetic Current Formulation [11]

This approach is an extension of the planar waveguide model used for characterization of microstrip discontinuities discussed in Section 4.1.1. To evaluate the radiation field produced by microstrip discontinuities, the multiport network model is used to find the voltage distribution around the edges of the discontinuity configuration. This voltage distribution is expressed as an equivalent magnetic current distribution, which is used to compute the resultant radiation fields.

The procedure is similar to that developed earlier [14] for microstrip patch antennas. To implement this method, we add a number of open ports at the edges of the discontinuity structure from which the radiation (or spurious external coupling) is being evaluated. This is shown in Figure 4.18(a, b) for a right-angled bend and a compensated right-angled bend, respectively.

Lengths of transmission lines on two sides of the junction are made large enough so that the higher order evanescent modes produced by the discontinuities decay out at the locations of external ports 1 and 2. The circuit behavior is simulated by terminating port 2 in a matched load and adding a matched source to port 1. Voltages at the N ports at the edges are computed by using the following procedure.

1. The configuration is broken down in elementary regular segments, connected at the interfaces by a discrete number of interconnections.
2. **Z**-matrices for each of these elementary segments are evaluated by using the Green's function approach for individual geometries.
3. Individual **Z**-matrices obtained in step 2 are combined by using the segmentation formula.
4. The overall multiport **Z**-matrix is used to calculate voltages at the N edge ports for a unit current input at port 1.

As mentioned earlier, a similar procedure has been used for the design of microstrip patch antennas [14] also. The only distinction in the latter case is the use of edge admittance networks (containing equivalent radiation conductances) that are connected to the edge ports. Because of the nonresonant nature of the microstrip discontinuity structures, the radiated power is small and the edge voltages may be assumed to be unaffected by radiation conductances involved. However, for a more accurate assessment of the radiated power, radiation conductance networks may be added to edge ports and iterative computations may be carried out to evaluate radiation fields.

Voltages at the discontinuity edges are represented by equivalent magnetic current sources as shown in Figure 4.18(c, d). Each of the magnetic current line sources is divided into small sections over which the field may be assumed to be uniform. The amplitude M of each of the magnetic current elements is twice that of the edge voltage at that location, and the phase of M is equal to the phase of the

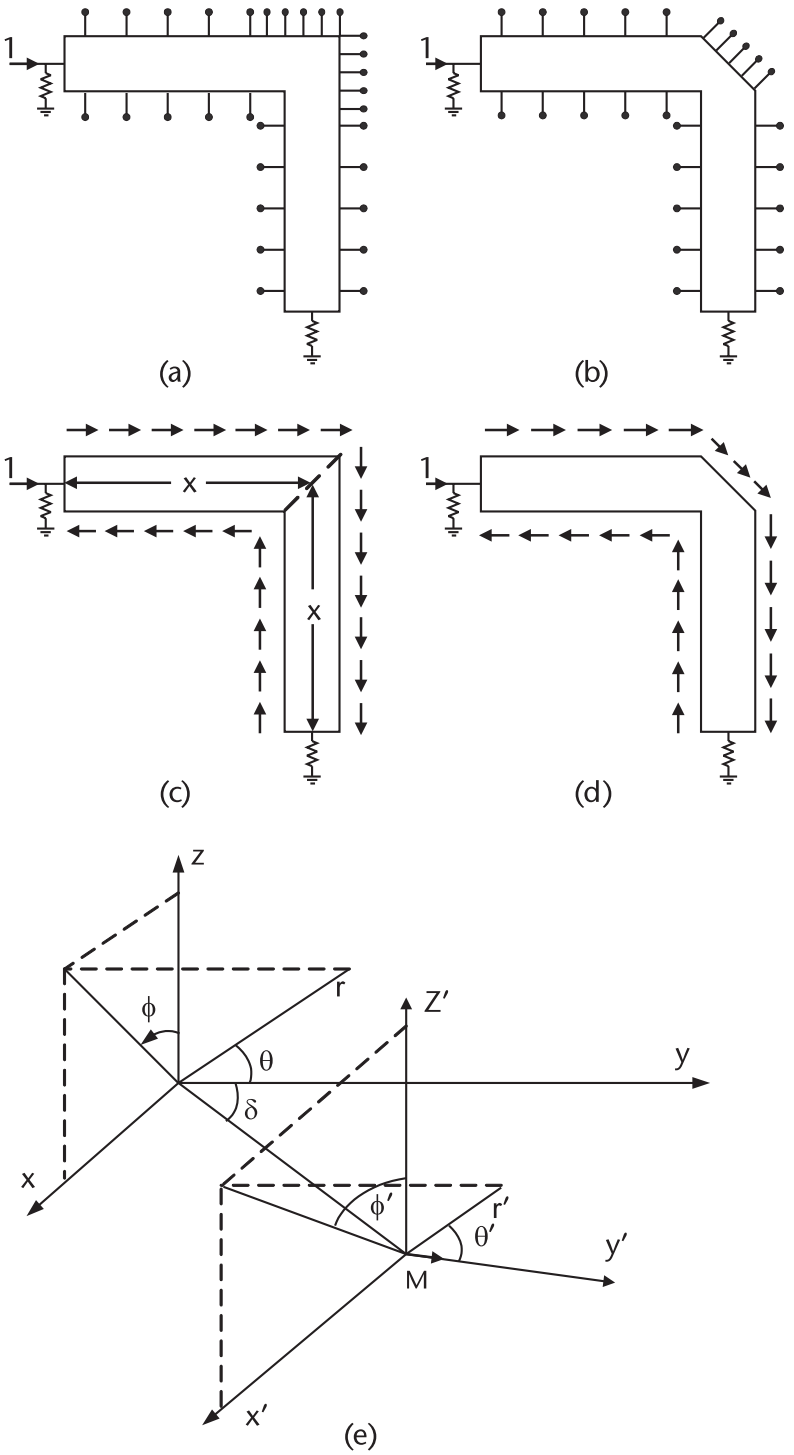

Figure 4.18 Multiple ports located at the edges of the microstrip discontinuities for (a) a right-angled bend and (b) a compensated right-angled bend. Voltages at these ports are expressed as an equivalent magnetic current distribution. Equivalent magnetic current distribution at discontinuity edges, (c) for a sharp bend and (d) for a chamfered bend. (e) Coordinate system for external field calculations.

corresponding voltage. The total radiation is computed using the superposition of the far field radiated by each section. Referring to the coordinate system, shown in Figure 4.18(e), the far-field pattern may be written in terms of voltages at the various elements. With the voltage at the ith element expressed as $V(i)\, e^{j\alpha(i)}$, we have

$$F(\theta,\phi) = \sum_{i=1}^{N} V(i)\; W(i) \exp\left\{k_0 \gamma_0(i) + \alpha(i)\right\} F_i(\theta,\phi) \tag{4.36a}$$

where

$$F_i(\theta,\phi) = \frac{\sin\left\{\left(k_0 W(i)/2\right)\cos\theta\right\}}{\left(k_0 W(i)/2\right)\cos\theta} \sin\theta \tag{4.36b}$$

$$\gamma_0(i) = X_0(i)\sin\theta\cos\phi + Y_0(i)\cos\theta \tag{4.37}$$

N is the number of ports, X_0(i), $Y_0(i)$ specify the location of the ith magnetic current element, and W(i) is the width of the ith element.

The radiated power is calculated by integrating the Poynting vector over the half-space and may be written as

$$P_r = \frac{1}{240\pi} \int_{-\pi/2}^{\pi/2} \int_0^{\pi} \left(\left|E_\theta\right|^2 + \left|E_\phi\right|^2\right) r^2 \sin\theta \, d\theta \, d\phi \tag{4.38}$$

The fields E_θ and E_ϕ are expressed in terms of F (θ, ϕ) as

$$E_\theta = \hat{a}_\theta \left(-jkF(\theta, \phi) F_\theta / 4\pi r\right) \tag{4.39}$$

$$E_\phi = \hat{a}_\phi \left(-jkF(\theta,\phi) F_\phi / 4\pi \mathrm{r}\right) \tag{4.40}$$

where

$$F_\phi = \sin\phi' \sin\phi + \cos\delta \cos\phi \cos\phi' \tag{4.41}$$

$$F_\theta = -\sin\phi' \cos\theta \cos\phi + \cos\delta \cos\theta \sin\phi + \sin\delta \cos\phi' \sin\theta \tag{4.42}$$

and

$$\begin{aligned} \cos\theta' &= \sin\theta \sin\phi \sin\delta + \cos\theta \cos\delta \\ \cos\phi' &= \sin\theta \cos\phi / \sqrt{1 - \cos^2\theta'} \end{aligned} \tag{4.43}$$

The radiation loss may be expressed as

$$\text{Power loss } (\text{dB}) = 10 \log_{10}\left(1 - \frac{P_r}{P_i}\right) \tag{4.44}$$

where P_i is the input power at port 1.

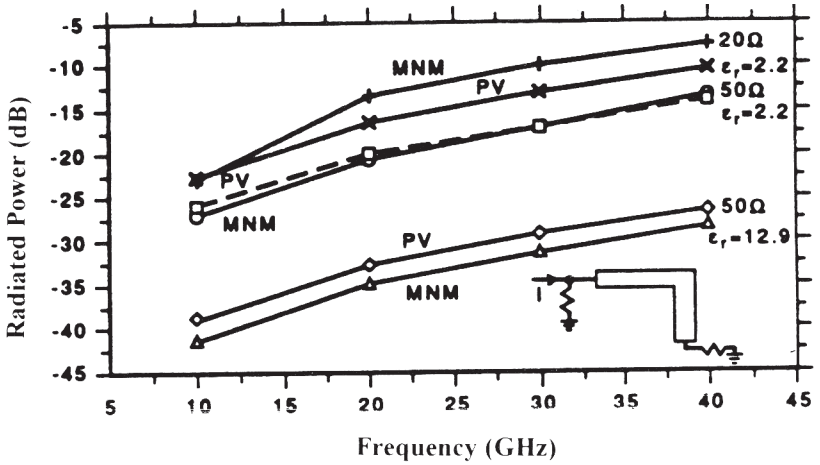

Figure 4.19 Normalized radiated power from a right-angled bend (MNM: Multiport Network Model and PV: Poynting Vector method).

To identify the regions of the discontinuity configuration that contribute dominantly to the radiated power, several computations were performed by taking different regions around the discontinuity. These computations show that in most of the cases the biggest contribution to the radiated power is due to ports in the region of the discontinuity itself. The results for a 50-Ω, right-angled bend, as shown in Table 4.1, illustrate this point.

Radiation from a Right-Angled Microstrip Bend: Results for the power radiated by a 90° bend normalized with respect to the input power are shown in Figure 4.19 for frequency ranges from 10 GHz to 40 GHz. These results are in good agreement, with results based on the complex Poynting vector method, which are also plotted in Figure 4.19. The radiation loss at 40 GHz is a 0.0062 dB for a 50-Ω line bend on a GaAs (ε_r = 12.9) substrate. The values for radiation loss from a 90° bend in a 50-Ω line on a substrate with ε_r = 2.2 at 30 GHz and 40 GHz are 0.1 dB and 0.17 dB, respectively.

Radiation from a Microstrip Step Junction: The power radiated from a step junction discontinuity, with a change in impedance from 50 Ω to 10 Ω, on a ε_r = 2.2 substrate with a thickness of 0.79 mm is plotted in Figure 4.20. A similar computation for a 50-Ω to 70.7-Ω junction (at 30 GHz, ε_r = 2.2, thickness 0.02 in) yields

Table 4.1: Radiated Power as a Function of Microstrip Line Length (ε_r = 12.9, h = 127.1 μm, f = 10 GHz)

Length X (shown in Figure 4.18)	P_r/P_1 *(dB)*
(0.4 × 0.4) λ	–40.64
(0.35 × 0.35) λ	–40.67
(0.3 × 0.3) λ	–40.77
(0.25 × 0.25) λ	–40.84
(0.2 × 0.2) λ	–41.1
Ports on bend only	–41.1

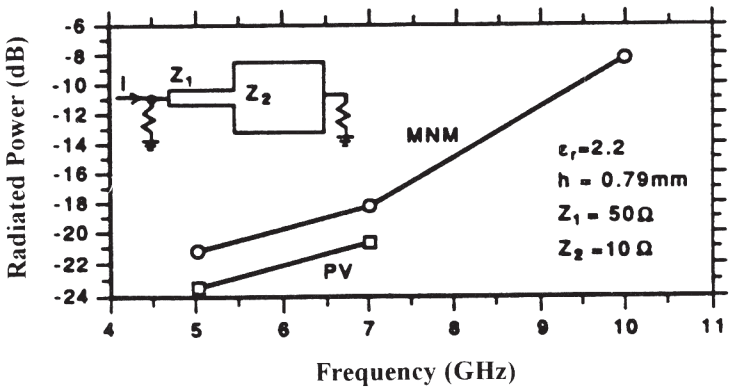

Figure 4.20 Normalized radiated power from a step (MNM: Multiport Network Model and PV: Poynting Vector method).

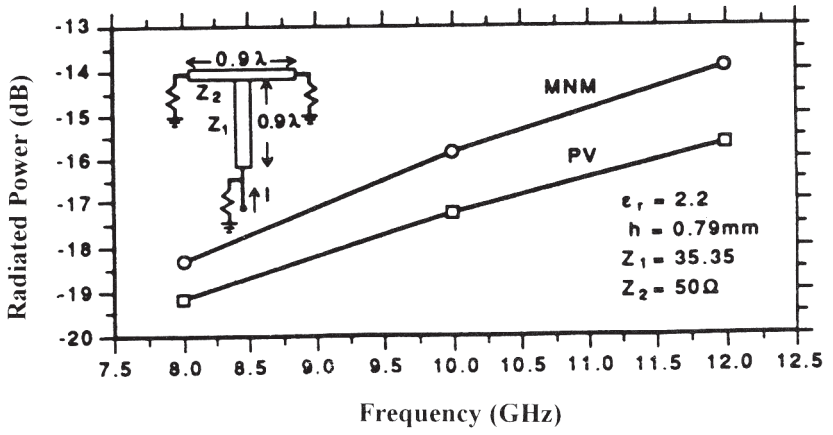

Figure 4.21 Normalized radiated power from a T-junction (MNM: Multipart Network Model and PV: Poynting Vector method).

the normalized radiated power to be –24.8 dB when the input power is fed from the 50-Ω line and –33 dB when the power is fed from the 70.7-Ω line.

Radiation from a T-Junction Discontinuity: Computed results for power radiated from a T-junction (50-Ω main line with 35.35-Ω branch line on a substrate, thickness 1/32 in, $\varepsilon_r = 2.2$) are shown in Figure 4.21. The radiation loss at 12 GHz is 0.18 dB. It is found that for such a T-junction most of the contribution to the radiation loss originates from the region of the junction.

Radiation Evaluated from Fullwave Analysis

Fullwave analysis methods for the characterization of microstrip discontinuities are discussed in Section 4.2. When these analyses are conducted without using any enclosure or shield above the microstrip structure [12], the radiation effect gets incorporated in the discontinuity characterization. However, the computation of power radiated by discontinuities based on fullwave analysis has not been reported

extensively. A general consensus is that for thin substrates used for microwave hybrid and monolithic circuit applications, radiation loss from microstrip discontinuities can be neglected.

Spurious Coupling Among Discontinuities

Parasitic coupling among different parts of a microstrip circuit caused by external fields produced by discontinuities is considered a more significant phenomenon than the radiation loss discussed above. Generally, in MMICs, matching networks are packed very closely together and have layout and junction discontinuity reactances. Coupling occurs between the matching elements due to close proximity and can be accounted for by using EM simulators [17–22]. For long coupled lines on the order of a quarter wavelength, spacing between the lines must be $3W$ (width of line) or $3h$ (height of substrate)—whichever is greater—in order to reduce coupling effects. For short lines on the order of 1/10 wavelength, $1W$ or $1h$ spacing between the lines is adequate for most applications.

As shown in Figure 4.22, interaction effects take place between the closely-spaced discontinuities due to coupling of fields from one discontinuity to another. The interaction between two discontinuities affects the isolated discontinuity reactance and must be accurately determined using EM simulators. The minimum distance between two discontinuities with the potential for coupling is $2W$ or $2h$, whichever is greater. For T-junction and cross-junction discontinuities on thick substrates (≥ 100 μm for GaAs and ≥ 250 μm for alumina), EM simulators are commonly used to accurately include their effects in the circuit design.

The spurious coupling between two discontinuities (due to the external fields) may be incorporated in the planar waveguide model-based analysis by connecting an additional multiport network between the two discontinuities as shown in Figure 4.23. The *multiport coupling network* (MCN) is characterized in terms of an admittance matrix Y_m. Elements of this matrix represent mutual admittances between various sections of the edges of the two discontinuities. The elements of the matrix Y_m are obtained by representing the edge fields by small sections of length, $d\ell$, of equivalent magnetic current and by computing the magnetic field components H_θ and H_r produced at the jth subsection of the nearby discontinuity. We have

$$H_\theta = j\frac{k_0 M d\ell \sin\theta}{4\pi\eta_0 r}\left(1+\frac{1}{jk_0 r}-\frac{1}{(k_0 r)^2}\right)e^{-jk_0 r} \tag{4.45}$$

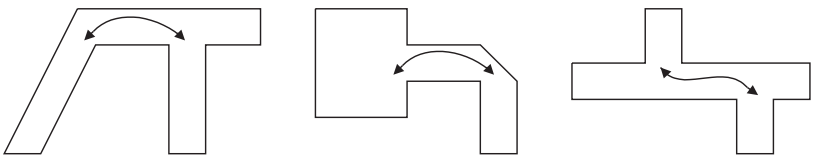

Figure 4.22 Examples of interactions between discontinuities. Arrows point at junction discontinuities.

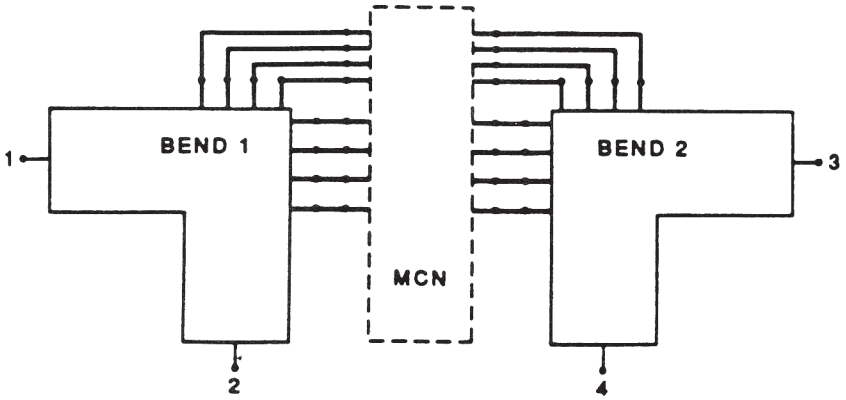

Figure 4.23 A multiport coupling network (MCN) incorporated for modeling spurious coupling between discontinuities.

$$H_r = \frac{Md\ell\cos\theta}{4\pi\eta_0 r^2}\left(1+\frac{1}{jk_0 r}\right)e^{-jk_0 r} \tag{4.46}$$

The induced current in the jth element is calculated from the magnetic field as

$$J_j = \left(\hat{z}\times\overline{H}\right)\cdot\hat{j} \tag{4.47}$$

where $\hat{j}$ is a unit vector normal to the jth element. The value of Y_{ji} is obtained from the current induced in the jth subsection as a result of voltage, V_i, at the ith subsection.

$$Y_{ji} = J_j d\ell_j / V_i \tag{4.48}$$

The **Z** matrix of the mutual coupling network is the inverse of Y_m. The segmentation method is used to combine the **Z** matrix representations of the discontinuities and the coupling network to yield the overall **Z** matrix. The **Z** matrix is converted to S parameters. The effect of the coupling on the circuit performance is obtained from these S parameters. Cascaded step discontinuities have been treated by Kompa [16].

In addition to the above-mentioned approach, the spurious coupling among microstrip discontinuities can be derived from the fullwave electromagnetic analysis discussed in the next section.

4.2 Fullwave Analysis of Discontinuities

As the operating frequency of microwave and millimeter-wave integrated circuits increases, the surface wave and radiation effects become more significant. To account for these phenomena and to accurately characterize various discontinuities, fullwave solutions (without making any assumptions) become essential. A num-

ber of electromagnetic analysis software packages based on fullwave analysis are now available commercially [17–22] for analyzing microstrip discontinuities and circuits.

The development of fullwave simulation techniques has enabled microwave designers and software vendors to characterize microstrip discontinuities accurately by using rigorous numerical methods with minimum analytical and numerical approximations.

One of the earliest fullwave analyses reported for microstrip discontinuities is Galerkin's Method in Spectral Domain [23], which is an extension of the spectral domain analysis procedure discussed for a uniform microstrip line in Chapter 2. The integral equation approach based on the moment method solution in space domain [24, 25] has been more popular. Other fullwave numerical electromagnetic methods (such as the finite difference time domain technique [26]) have also been used to characterize microstrip discontinuities. These fullwave analysis methods are reviewed in this section.

4.2.1 Galerkin's Method in the Spectral Domain [23]

Galerkin's method in the spectral domain has been used for the fullwave analysis of microstrip open ends and gaps. The characterization of these two discontinuities can be carried out by analyzing suitably designed linear resonators. For an open end, one can consider a section of microstrip with open ends on each side, as shown in Figure 4.24. By carrying out a fullwave analysis for the resonance frequency of this structure, one can obtain the equivalent line length contributed by the open end. The extent of the substrate can be finite in either one or both of the dimensions x and z. In the analysis reported in [23] the substrate is considered to be infinite along z and finite along the x-direction. In the x-direction two conducting planes ($2L$ apart) are placed symmetrically with respect to the microstrip. A cover plate is located at y = H. The analysis of such a structure in the spectral domain requires a Fourier transform along the z-direction and a finite Fourier transform along x.

Details of Galerkin's method in the spectral domain were discussed in Chapter 2. The choice of the basis functions for currents on the strip is important for the numerical efficiency of the method. For the dominant mode of resonance, the following forms for J_z and J_x are suitable:

$$J_z(x,z) = J_1(x)\,J_2(z) \tag{4.49}$$

$$J_x(x,z) = J_3(x)\,J_4(z) \tag{4.50}$$

where

$$J_1(x) = \begin{cases} \dfrac{1}{W}\left[1+\left|\dfrac{2x}{W}\right|^3\right] & |x| \le W/2 \\ 0 & \text{elsewhere} \end{cases} \tag{4.51a}$$

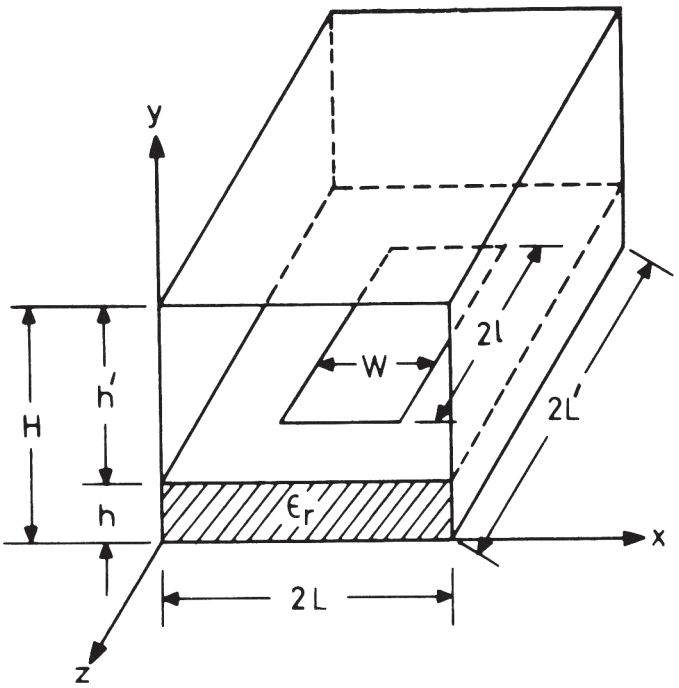

Figure 4.24 Geometry for analysis of microstrip open ends and gaps.

$$J_2(z) = \begin{cases} \dfrac{1}{\ell}\cos\left(\dfrac{\pi z}{2\ell}\right) & |z| \le \ell \\ 0 & \text{elsewhere} \end{cases} \tag{4.51b}$$

$$J_3(x) = \begin{cases} \dfrac{2}{W}\sin\left(\dfrac{2\pi x}{W}\right) & |x \le W/2| \\ 0 & \text{elsewhere} \end{cases} \tag{4.51c}$$

$$J_4(z) = \begin{cases} \dfrac{z}{2\ell^2} & |z| \le \ell \\ 0 & \text{elsewhere} \end{cases} \tag{4.51d}$$

After performing various steps of Galerkin's method in the spectral domain discussed in Section 2.3.1, a dispersion relation for the microstrip resonator is developed. This dispersion relation is solved for the resonant frequency. The microstrip open-end and gap discontinuities can be characterized by calculating the effective increase in length, $\Delta\ell$, of suitably designed microstrip resonators. For resonance one can write

$$2(\ell + \Delta\ell) = \lambda_m/2 \tag{4.52}$$

where

$$\lambda_m = \lambda_0 / \sqrt{\varepsilon_{re}} = c / \left(\sqrt{\varepsilon_{re}} f_{res} \right)$$

Open End

The effective increase in length, $2\Delta\ell_{oc}$, for a microstrip resonator is determined from the method described above. From $\Delta\ell_{oc}$ one can find the open-end discontinuity capacitance, C_{oc} by using (3.48). The frequency-dependent behavior of C_{oc} can be found by calculating the resonant frequencies of microstrip resonators of different lengths.

It may be pointed out that for frequencies up to about 10 GHz the quasi-static approach gives reasonably reliable results. At 8 GHz, for $h = 0.66$ mm, $W/h = 1.0$, and $\varepsilon_r = 9.8$, the measured value of $\Delta\ell_{oc}$ is 0.021 ±0.001 mm [27], whereas the corresponding quasi-static value of $\Delta\ell_{oc}$ calculated using (3.49) is 0.0206 mm.

Gap

Fullwave analysis of a gap discontinuity can also be carried out by using Galerkin's method in the spectral domain. In this case, one considers two types of resonators. First, an analysis is carried out with conducting planes (electric walls) at $z = 0$ and $z = 2L'$. The latter dimension is chosen such that $(2L' - 2\ell)$ is equal to the gap spacing. A second computation is carried out for magnetic walls at $z = 0$ and $z = 2L'$. For both of these computations, finite Fourier transforms are used along the x- and z-directions. Equivalent lengths, $\Delta\ell_e$ and $\Delta\ell_m$, for electric and magnetic walls, respectively, are determined from the respective resonance frequencies of resonators. From $\Delta\ell_e$ and $\Delta\ell_m$ two equivalent capacitances, C_e and C_m, are calculated. These capacitances are related to the discontinuity capacitances of π equivalent circuits of a gap (Figure 3.7a) by the following equations:

$$C_g = \left(C_e - C_m \right) / 2 \tag{4.53a}$$

$$C_p = C_m \tag{4.53b}$$

The spectral domain approach has also been used for discontinuities in open microstrips (without any shield or enclosing box). Again, open-end and gap discontinuities have recieved more detailed attention [28–33].

The spectral domain approach is best suited for treating microstrip discontinuities of simple shape, where the current distribution can be expanded using a set of basis functions having closed-form Fourier transform counterparts. Analysis involving semi-infinite long lines are ideal for this method since the current on these lines can be represented by a pair of forward and backward travelling waves, which in the Fourier transform plane are simple delta functions. Therefore, semi-infinite lines have been used as standard feeds in analyzing discontinuities in [30, 33]. However, since the current in and near the discontinuity region is not uniform, a different set of subsectional basis functions is needed to capture the junction effect.

This hybrid use of basis functions implies that each set of basis functions must be carefully defined over the structure, and different algorithms are needed to evaluate the moment integrals associated with each type of basis function. Also, to obtain accurate results, the spectral domain approach requires the precomputation of the propagation constant and/or transverse distribution of the current on each distinct feed strip [30, 33, 34].

4.2.2 Integral Equation Solution in the Space Domain

As mentioned earlier, the space domain solution of the integral equation for discontinuity structures is a very versatile alternative to the spectral domain method. Spatial domain evaluation provides more physical insight since the problem remains in the physical domain. For this approach, Green's functions are numerically evaluated first and treated as known functions in the integral equation. This implies that the selection of the expansion functions for the current is arbitrary, which renders the approach very versatile. Moreover, subsectional basis functions of simple form can be implemented with straightforward numerical algorithms using the spatial domain approach. Therefore, this approach provides an ideal base for a general solver and has been used in several electromagnetic simulators for microwave circuits. The groundwork for a mixed potential integral equation MPIE-based, spatial domain microstrip solver can be attributed to Mosig and Gardiol [24, 35].

The use of potentials is generally preferred in the spatial domain approach because the associated Green's functions are better suited for numerical evaluations. Using an $e^{j\omega t}$ time convention, the MPIE can be expressed as

$$\begin{aligned}\vec{E}^{s} &= \frac{-j\omega\mu_0}{4\pi}\int_S \left[G_m(\bar{x},\bar{x}')\,\vec{J}(\bar{x}')\,ds' - \frac{1}{k_0^2}\nabla\nabla' G_e(\bar{x},\bar{x}')\,\vec{J}(\bar{x}') \right] dS' \qquad (4.54)\\ &= -\vec{E}^{inc}(\bar{x}) \qquad\qquad \bar{x} \text{ on } S\end{aligned}$$

where J is the unknown current density on the microstrip discontinuity surface S and $\vec{E^s}$ and $\vec{E^{inc}}$ denote the scattered and incident fields, respectively. The scalar Green's functions, G_m and G_e, are associated with the potentials produced by a unit source on top of the grounded substrate. They are identified as Green's functions of the magnetic and electric types, respectively. By evoking the continuity equation

$$\nabla \cdot \vec{J} + j\omega q = 0$$

it can be shown that G_m is related to the surface current density while G_e is related to the surface charge density q. Thus, (4.54) can also be expressed in terms of the surface current and charge densities. For a single-layer grounded dielectric slab in open space, these Green's functions can be expressed in terms of Sommerfeld integrals as [36, 37]

$$G_m(R) = \int_0^\infty 2J_0(\xi R)\frac{\xi}{D_{TE}}d\xi \qquad (4.55)$$

$$G_e(R) = \int_0^\infty 2J_0(\xi R)\frac{\xi\left[u_0 + u\tanh(ut)\right]}{D_{TE}D_{TM}}d\xi \tag{4.56}$$

for $R = |\bar{x} - \bar{x}'|$, where

$$\begin{aligned} D_{TE} &= u_0 + u\coth(ut) \\ D_{TM} &= \varepsilon_r u_0 + u\tanh(ut) \end{aligned} \tag{4.57}$$

$$u_0 = \sqrt{\xi^2 - 1} \qquad u = \sqrt{\xi^2 - \varepsilon_r} \tag{4.58}$$

R is the distance between the source and observation points, t is the slab thickness, and k_0 is the free-space propagation constant. Since these kernels are a function of R, they can be precomputed for a given range of R. Once they are known, the integral equation (4.54) can be solved readily in the spatial domain.

Several results for discontinuities' characterizations based on this method are available in [24, 25]. Electromagnetic simulators based on this approach have been used by several microwave circuit CAD software developers to derive models for microstrip discontinuities.

4.2.3 Time Domain Methods for Microstrip Discontinuity Characterization

In addition to the frequency domain methods discussed so far, time domain techniques for electromagnetic analysis can be used for the characterization of microstrip discontinuities and, in general, for the characterization of microstrip circuits. The *finite-difference time domain* (FDTD) approach [26, 38] is most popular among the various time domain methods available. The *transmission line matrix* (TLM) approach could be used as well for this purpose [39].

The key feature of the time domain analysis results from the fact that an impulse response contains all the information of a system for the whole frequency range. Thus, a wide frequency range characterization of discontinuities can be obtained by using a pulse excitation in the time domain and evaluating the Fourier transform of the time domain pulse response.

Among various time domain methods, FDTD is the most direct from a mathematical point of view and is based on time and space discretizations of Maxwell's equations:

$$\frac{\partial\vec{E}}{\partial t} = \frac{1}{\varepsilon_i}\nabla\times\vec{H} \tag{4.59}$$

$$\frac{\partial\vec{H}}{\partial t} = -\frac{1}{\mu_0}\nabla\times\vec{E} \tag{4.60}$$

where the subscript i emphasizes different values of ε_r to be used in substrate and air regions. To simulate the wave propagation in three dimensions, the spatial node points where different values of **E** and **H** are to be calculated are arranged in a mesh configuration. A unit cell of this mesh is shown in Figure 4.25. A repetitive arrangement of such cells fills the computational domain. Every component of the

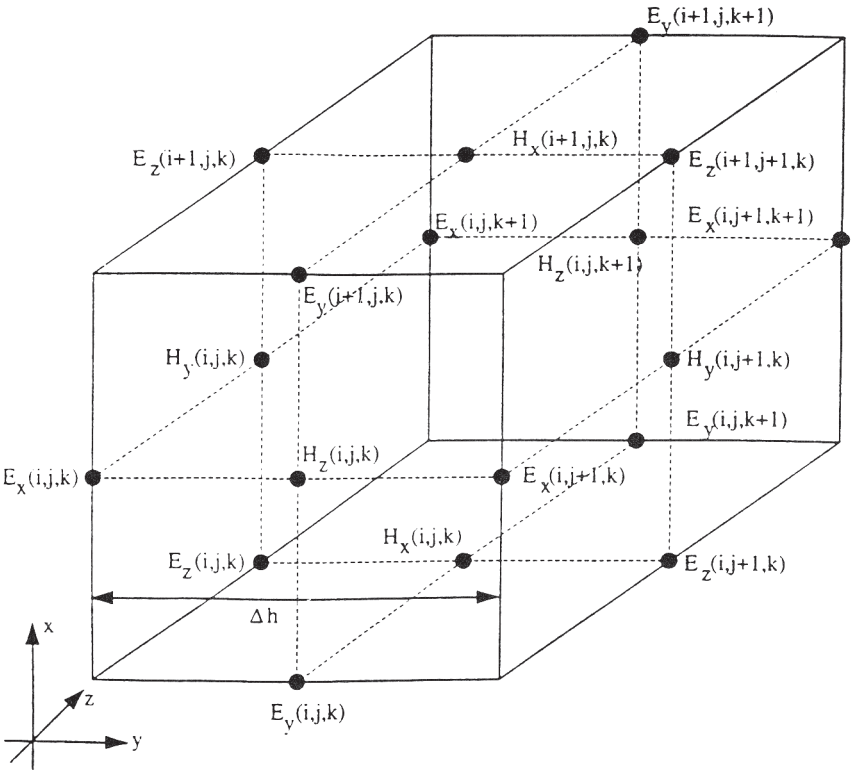

Figure 4.25 One cell of a typical mesh used for FDTD computations.

magnetic field **H** can be obtained by the loop integral of the electric field **E** using the four surrounding nodal **E** values according to Maxwell's curl equation for **E**. A similar approach is used for the calculation of **H**. As a result of this procedure, not only the placements of the **E** and **H** nodes are off in space by half a space step, but the time instants when the **E** or **H** field are calculated are also off by half a time step. This gives rise to a "leap frog" algorithm with components of **E** being calculated at $n\Delta t$ and components of **H** being calculated at $(n + 1/2)\,\Delta t$, where Δt is the discretization unit in time. The resulting finite difference equations are of central difference form and of second-order accuracy. They are given by

$$E_x^{n+1}(i,j,k) = E_x^n(i,j,k) + \frac{\Delta t}{\varepsilon \Delta h}\left(H_z^{n+1/2}(i,j,k) - H_z^{n+1/2}(i,j-1,k) - H_y^{n+1/2}(i,j,k) + H_y^{n+1/2}(i,j,k-1)\right)$$

$$E_y^{n+1}(i,j,k) = E_y^n(i,j,k) + \frac{\Delta t}{\varepsilon \Delta h}\left(H_x^{n+1/2}(i,j,k) - H_x^{n+1/2}(i,j,k-1) - H_z^{n+1/2}(i,j,k) + H_z^{n+1/2}(i-1,j,k)\right)$$

$$E_z^{n+1}(i,j,k) = E_z^n(i,j,k) + \frac{\Delta t}{\varepsilon \Delta h}\left(H_y^{n+1/2}(i,j,k) - H_y^{n+1/2}(i-1,j,k) - H_x^{n+1/2}(i,j,k) + H_x^{n+1/2}(i,j-1,k)\right)$$

$$H_x^{n+1/2}(i,j,k) = H_x^{n-1/2}(i,j,k) - \frac{\Delta t}{\mu \Delta h}\left(E_z^n(i,j+1,k) - E_z^n(i,j,k) - E_y^{\mathrm{n}}(i,j,k+1) + E_y^{\mathrm{n}}(i,j,k)\right)$$

$$H_y^{n+1/2}(i,j,k) = H_y^{n-1/2}(i,j,k) - \frac{\Delta t}{\mu \Delta h}\left(E_x^n(i,j,k+1) - E_x^n(i,j,k) - E_z^{\mathrm{n}}(i+1,j,k) + E_z^{\mathrm{n}}(i,j,k)\right)$$

$$H_z^{n+1/2}(i,j,k) = H_z^{n-1/2}(i,j,k) - \frac{\Delta t}{\mu \Delta h}\left(E_y^n(i+1,j,k) - E_y^n(i,j,k) - E_x^n(i,j+1,k) + E_x^n(i,j,k)\right) \tag{4.61}$$

The indices i, j, and k define the positions of the field nodes. Distances between the nodes are $\Delta x = \Delta y = \Delta z = \Delta h$. For any finite-difference scheme, a stability condition must be found that guarantees that the numerical error generated in one step of the calculation does not accumulate and grow. The stability condition for the "leap frog" algorithm is given by

$$v_{\max} \cdot \Delta t \le \frac{1}{\sqrt{1/\Delta x^2 + 1/\Delta y^2 + 1/\Delta z^2}} \tag{4.62}$$

For the special case of $\Delta x = \Delta y = \Delta z = \Delta h$, the above condition becomes

$$v_{\max} \cdot \Delta t \le \frac{1}{\sqrt{3}} \cdot \Delta h \tag{4.63}$$

where $v_{\max}$ is the maximum signal phase velocity in the configuration being considered.

The excitation pulse most commonly used for FDTD computations is Gaussian in shape. It has a smooth waveform in time, and its Fourier transform is also a Gaussian pulse centered at zero frequency. This property makes a Gaussian pulse a perfect choice for investigating the frequency-dependent characteristics of microstrip discontinuities.

Another important consideration in implementing a FDTD algorithm is the use of an "absorbing boundary condition" to confine the computational space and thus keep the computer memory requirements to a reasonable size. Until recently, approximations in the absorbing boundary were the principal bottleneck, responsible for the limited accuracy of FDTD results. However, the introduction of the *perfectly matched layer* (PML) by Berenger [40, 41] is a major breakthrough in reducing the FDTD errors due to the absorbing boundary condition. The basic concept of this PML can be considered as an extension of the well-known fact that the condition

$$\sigma/\varepsilon_0 = \sigma^*/\mu_0 \tag{4.64}$$

provides for the reflectionless transmission of a plane wave propagating normally across the interface between free space (ε_0, μ_0, $\sigma = 0$) and the outer boundary layer (with σ and σ^* as electric conductivity and magnetic conductivity, respectively.)

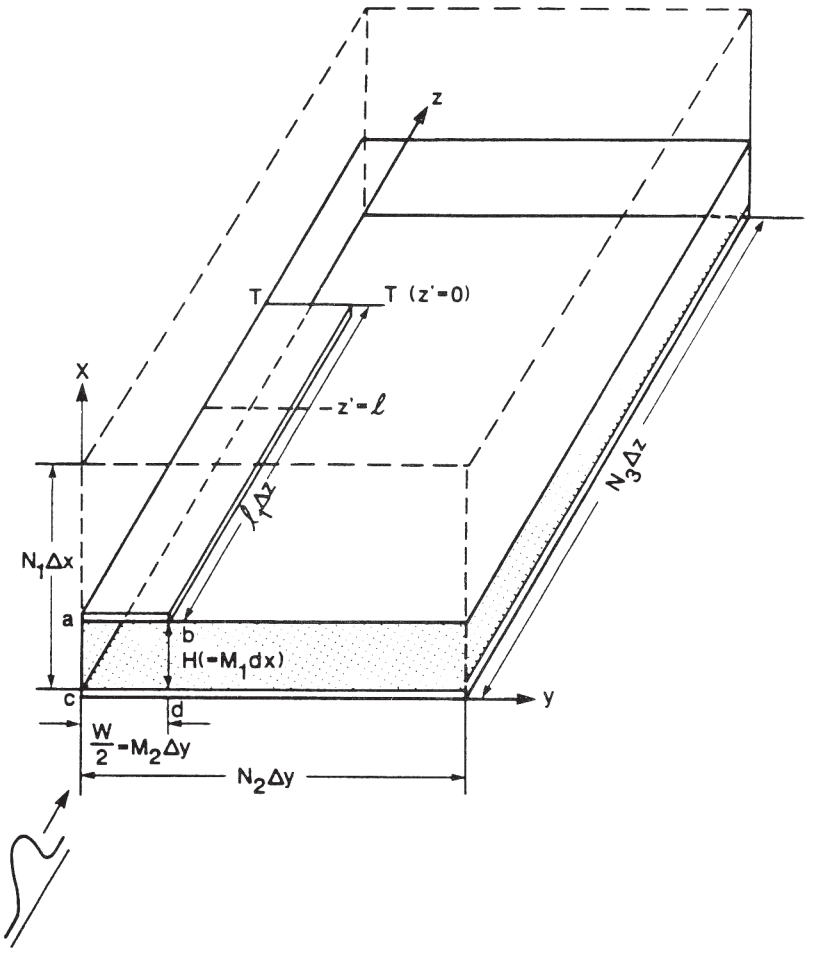

Figure 4.26 Configuration for characterization of a microstrip open end by FDTD (from [26], © 1988 IEEE. Reprinted with permission.).

Let us consider the extension of (4.64) to PMLfor a two-dimensional transverse electric (TE to z-direction) case with field components E_x, E_y, and H_z and with the computation grid in the (x-y)-plane. The PML technique splits the H_z field into two components, H_{zx} and H_{zy}, and introduces (σ_x, σ_x^*) and (σ_y, σ_y^*) pairs both of which satisfy the relation (4.64). Under these conditions, it can be shown that the wave in the PML medium propagates with exactly the speed of light but decays exponentially along x and y. Also, the wave impedance of the PML medium exactly equals that of vacuum, regardless of the angle of propagation or frequency. The TM case can be treated by duality by splitting E_z into E_{zx} and E_{zy}. In the three dimensional case, all six components of the field vectors are split and the resulting PML modification of Maxwell's equations yields 12 equations. PML matching conditions are analogous.

Figure 4.26 shows the finite-difference computational domain used for the microstrip open-end discontinuity characterization problem [26]. Due to symmetry, only half of the structure is placed in the mesh domain with a magnetic wall at the plane of symmetry. These computations yield the total E-field at the open end.

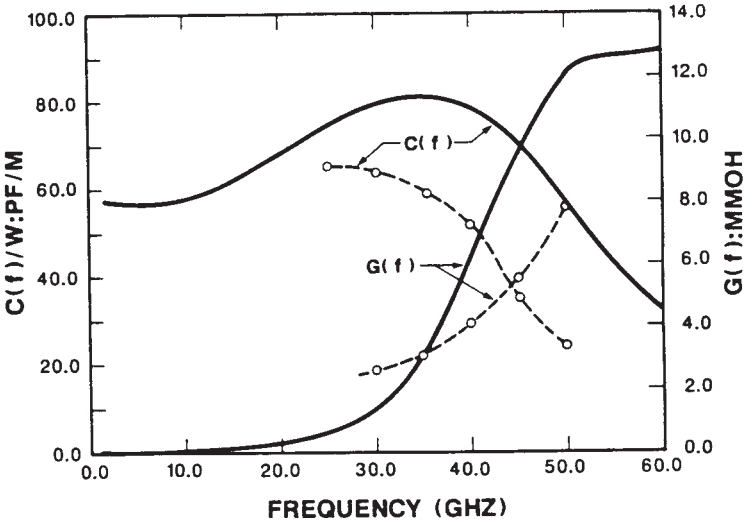

Figure 4.27 Wide frequency range modeling of a microstrip open end as obtained from FDTD: (__) and spectral domain (----) methods (from [26], © 1988 IEEE. Reprinted with permission.)

For S_{11} calculations, the incident field is obtained from that of an infinitely long microstrip, and the reflected field from the open end is obtained from the difference between the total open-end field and the incident field. When an equivalent circuit (a parallel combination of $G(f)$ and $C(f)$) is used to model the microstrip open end, the resulting values are plotted in Figure 4.27 [26]. Spectral domain analysis results of [31] are also shown in the figure. The amount of discrepancy seen, especially for higher frequencies, raises question about both sets of results. $G(f)$ values given in [31] do not exhibit a trend to go down smoothly to zero as the frequency goes to dc. The major difference in $C(f)$ behavior is in the increase in $C(f)$ value with frequency (before ultimately going down) seen in time domain analysis results. Such a behavior has also been seen in some other frequency domain analysis [42, 43]. Perhaps, refinements in implementation of both of these approaches are needed before any comparative conclusions can be drawn.

4.3 Discontinuity Measurements

Often experimental validation of microstrip discontinuities becomes necessary to test the accuracy of numerical results. Methods for accurately measuring microstrip discontinuities are based on the technique of incorporating discontinuities in microstrip resonators and measuring the change in the resonance frequency. Since these resonators are coupled very loosely to the test equipment, the measurements are not affected by the uncertain characteristics of coaxial-to-microstrip transitions. Both linear and ring resonators have been used for discontinuity measurements.

Two (or more) resonators need to be fabricated and tested for complete discontinuity characterization. The use of these resonators to measure the phase velocity in a microstrip was discussed in Section 1.5.3. The effect of microstrip disconti-

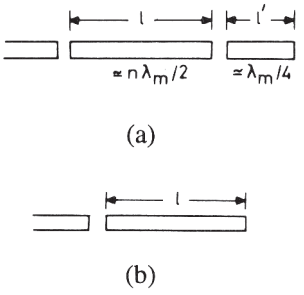

Figure 4.28 Arrangements for experimental characterization of an open end and a gap: (a) with two gaps and (b) with one gap and one open end.

nuities can also be determined accurately by measuring the scattering parameters. Measurements of discontinuities using resonators and scattering parameters methods are discussed in this section.

4.3.1 Linear Resonator Method

This method [27, 44, 45] uses a linear microstrip resonator that incorporates the discontinuity to be tested and is lightly coupled to the measuring instrumentation through a microstrip gap. The linear resonator is obtained by a $n\lambda_m/2$ length of a microstrip section open at the two ends. Thus the microstrip open end and the microstrip gap constitute essential parts of this measuring arrangement and must be calibrated before measurements on any other discontinuity may be carried out.

To minimize significant effects due to the change in substrate properties and fabrication, it is necessary to measure the effective dielectric constant ε_{re} for each circuit either by adding a linear resonator alongside each test configuration or by etching the test configuration to a suitable form and making a second measurement of the resonant frequency. The careful use of the latter strategy realizes the advantages of a substitutional method and will be illustrated in the method for characterization of microstrip gaps discussed in the following paragraph.

Open Ends and Gaps

An arrangement for characterization of the open end and the gap is shown in Figure 4.28(a). The length ℓ is chosen so that the effective length of this section at the frequency of measurement is $n\lambda_m/2$ where n is an integer and λ_m the microstrip wavelength. The length ℓ' should have an effective length of $\lambda_m/4$. The free-space wavelength for the resonance of the structure, as shown in Figure 4.28(a), is then given by

$$\left(\ell + 2\Delta\ell_g\right) = \frac{n}{2}\frac{\lambda_0}{\sqrt{\varepsilon_{re}}} \tag{4.65}$$

where $\Delta\ell_g$ is the extra length contributed by the microstrip gap. The equivalent circuit used for the gap is shown in Figure 3.17. The next step involves selective etching of length ℓ'. The resonance wavelength is measured again after ℓ' is removed (Figure 4.28(b)). Equation (4.65) can now be modified as

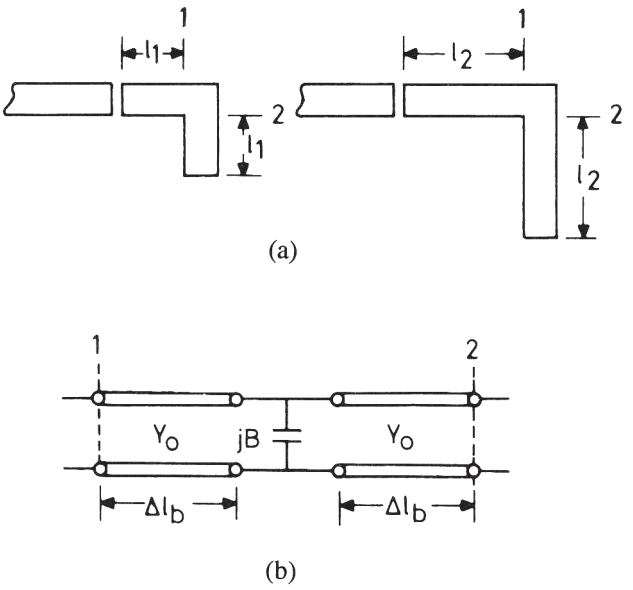

Figure 4.29 (a) An arrangement of experimental characterization of a right-angled bend and (b) equivalent circuit of the right-angled bend.

$$\left(\ell + \Delta\ell_{oc} + \ell\Delta_g\right) = \frac{n}{2}\frac{\lambda_0}{\sqrt{\varepsilon_{re}}} \tag{4.66}$$

where $\Delta\ell_{oc}$ is the equivalent line length associated with an open end. There are three unknowns appearing in (4.65) and (4.66), namely, $\Delta\ell_g$, $\Delta\ell_{oc}$ and ε_{re}. So an additional measurement is required. If two values of ℓ are chosen to given resonance frequencies for different n close to the normal frequency of measurement, then one measurement with ℓ' present, together with two measurements (for different values of ℓ) with the extra section ℓ' removed, are sufficient to give ε_{re}, $\Delta\ell_{oc}$, and $\Delta\ell_g$. Suitable choices of resonant mode, n, and lengths ℓ have to be made such that various resonant frequencies are close together and ε_{re} can be taken as constant over this frequency range.

It has been mentioned [27] that this method has an experimental uncertainty of ±10 μm, which is largely attributable to substrate variations. This uncertainty corresponds to about $\pm 0.005 Y_0$ at 10 GHz.

Right-Angled Bends and Steps in Width

Variations of the procedure described above may also be used for other discontinuities. The arrangement for characterization of a right-angled bend [27, 44] and its equivalent circuit are shown in Figure 4.29. Two resonators of different lengths are needed to determine the two unknowns (B and $\Delta\ell_b$) in the equivalent circuit. These resonators will either have a voltage minimum or a voltage maximum at the corner, according to whether the effective overall length $(2\ell_1 + 2\Delta\ell_b + \Delta\ell_{oc} + \Delta\ell_g)$ or $(2\ell_2 + 2\Delta\ell_b + \Delta\ell_{oc} + \Delta\ell_g)$ at resonance is an odd or an even number of half wavelengths. For example, in the case of a half-wave resona-

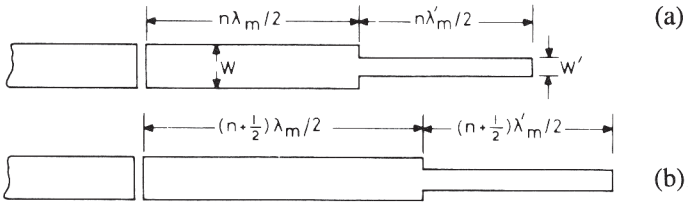

Figure 4.30 Circuit layouts for measuring the equivalent circuit of a step discontinuity: (a) with voltage maximum at the step and (b) with voltage minimum at the step.

tor, there will be a voltage minimum at the corner of the bend and the effective increase in length will be $2\Delta\ell_b$. On the other hand, for a fullwave resonator the presence of a voltage maximum at the corner will cause the shunt susceptance B to increase the effective length of the fullwave resonator by an amount $(\lambda_m/\pi) \cdot \tan^{-1}(B/2Y_0)$. The relation for resonance frequency may now be written as

$$\ell_2 + \Delta\ell_b + \frac{\Delta\ell_{oc} + \Delta\ell_g}{2} + \frac{\lambda_m}{2\pi}\tan^{-1}\left(\frac{B}{2Y_0}\right) = (2n+1)\frac{\lambda_m}{2} \tag{4.67}$$

Thus the series and the shunt components of the equivalent circuit can be separated. Since ε_{re}, $\Delta\ell_{oc}$ and $\Delta\ell_g$ are known from previous measurements, the parameters of the equivalent circuit shown in Figure 4.29(b) may be determined from the two frequencies of resonance.

A similar arrangement can be used to determine equivalent circuit parameters of a step continuity. The circuit arrangement is shown in Figure 4.30. Two resonators are used. Their lengths are adjusted so that in one case (i) we have a voltage maximum at the step, while in the other case (ii) we have a voltage minimum at the step. Note that microstrip wavelengths λ_m and λ'_m correspond to microstrip lines of widths W and W', respectively, and are not equal. Also in this case, we need the previous characterization of ε_{re}, $\Delta\ell_{oc}$, and $\Delta\ell_g$ for two widths W and W'.

T-Junctions

A T-junction, its equivalent circuit, and circuit arrangement for its characterization [27] are shown in Figure 4.31. Only a symmetrical T-junction, with its through arm having the same impedance on either side of the branch, is considered.

The circuit of Figure 4.31(b) enables an accurate determination of the line length ℓ_a by determining the resonance of the half wavelength along the through arm before and after removing the stub. It may be pointed out that the susceptance B is ineffective because of the presence of a voltage minimum at the location of B. The length ℓ_b may be obtained from the frequency of peak attenuation when the stub arm of Figure 4.31(c) is an odd number of quarter wavelengths long. Due to the shunt resonance of the stub, peak attenuation is a strong function of stub length. The end effect of the open end of the stub is assumed to be known from previous measurements. The configuration of Figure 4.31(d) enables B to be determined. The impedance ratio n^2 is measured by using the configuration shown in Figure

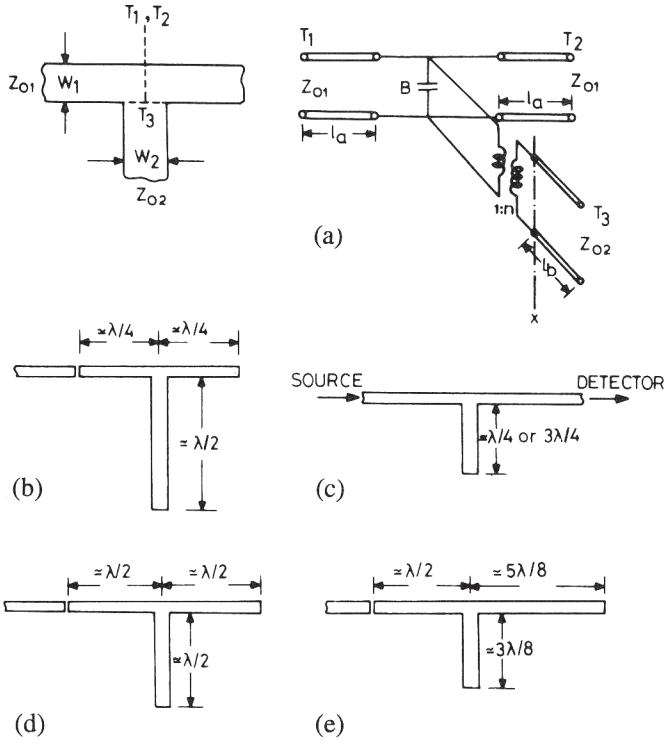

Figure 4.31 Circuit arrangement required for characterization of a T-junction: (a) discontinuity geometry and equivalent circuit, (b) set-up for determination of ℓ_a, (c) set-up for obtaining ℓ_b, (d) set-up for determination of *B*, and (e) set-up for determination of n^2 (from [27], © 1975 IEEE. Reprinted with permission.).

4.31(e). Values of B and n^2 depend on previous measurements, but some cancellation in the uncertainty can be obtained if the stub in Figure 4.31(d) is etched off and measurements carried out to obtain ε_{re} from resonance of the "through arm." The accuracy of determining n^2 has been estimated [27] as ±2 percent. It may be noted that the transformation ratio n does not affect the resonance frequency for the configurations (b) to (d) because of the presence of an open or short circuit at plane XX (Figure 4.31(a)).

Measurements for a symmetrical cross junction may also be made by using circuits of Figures 4.31(b, c, d, and e) and taking advantage of the symmetry of the junction. Similar measurement techniques may also be designed for other discontinuity structures.

The main advantage of the linear resonator method is that it involves shorter lengths that result in better accuracy. Since this method uses the open ends of the resonator, it is necessary to characterize the open ends accurately. This is one of the disadvantages associated with this method. The other disadvantage of this method is the need for fabricating a set of resonators for each frequency of interest. These problems are overcome in the ring resonator method, which is discussed in the next section.

4.3.2 Ring Resonator Method

Ring resonators were described in Section 1.5 during the discussion of measurement of microstrip phase velocities. When a ring resonator is used in place of a linear resonator as discussed above, the open-end and gap reactances need not be calibrated and taken into account. This method is convenient particularly for symmetrical two-port discontinuities (with $S_{11} = S_{22}$).

A microstrip ring structure resonates if its electrical length is an integral multiple of the guide wavelength. When a discontinuity is introduced into the ring, each resonance degenerates into two distinct modes. This splitting is conveniently interpreted in terms of even and odd excitations of the discontinuity [46]. The even mode corresponds to the incidence of two waves of equal magnitude and phase upon the discontinuity; while in the odd mode, waves of equal magnitude but opposite phase are incident from two sides. Anyone of these resonances can be excited by an appropriate choice of the point of excitation along the ring. In an experimental setup [46], this is achieved by shifting the position of the launcher along the ring as shown in Figure 4.32.

A symmetrical discontinuity, may be represented in terms of a T-network as shown in Figure 4.33(a). Parameters of the T-network can be evaluated from the two impedances Z_{ie} and Z_{io} shown in Figure 4.33(b) and obtained by introducing an open circuit and a short circuit, respectively, at the $z = 0$ plane. These impedances can be expressed in terms of two fictitious electrical lenghts ℓ_e and ℓ_o (shown in Figure 4.33(c)) as

$$\text{(even case)} \quad Z_{ie} = Z_{11} + Z_{12} = -j\cot k\ell_e \qquad \text{(even case)} \tag{4.68a}$$

$$\text{(odd case)} \quad Z_{io} = Z_{11} - Z_{12} = j\tan k\ell_o \qquad \text{(odd case)} \tag{4.68b}$$

where $k = 2\pi/\lambda_m$ is the propagation constant along the ring resonator and all the impedances have been normalized to the characteristic impedance of the microstrip ring. These equivalent lengths ℓ_e and ℓ_o add to the total length of the ring for even

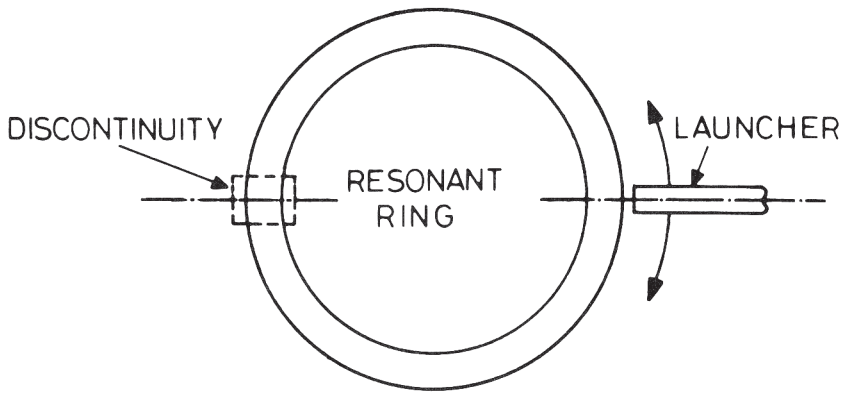

Figure 4.32 Ring resonator method for measurement on a two-port symmetrical discontinuity.

and odd excitations, respectively, as shown in Figure 4.34(a, b). Resonance conditions for the two cases may be written as

$$\ell_{\text{ring}} + 2\ell_{\text{e}} = n\lambda_{\text{me}} \tag{4.69}$$

and

$$\ell_{\text{ring}} + 2\ell_{\text{o}} = n\lambda_{\text{mo}} \tag{4.70}$$

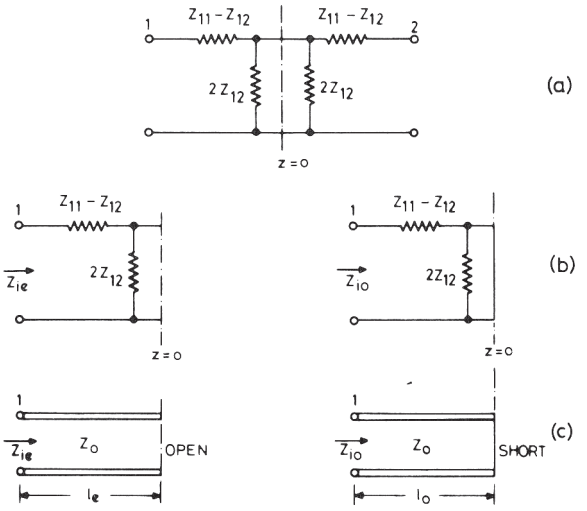

Figure 4.33 (a) Representation of a symmetrical discontinuity by a T-network, (b) equivalent circuits for even and odd modes and (c) equivalent line lengths for these modes.

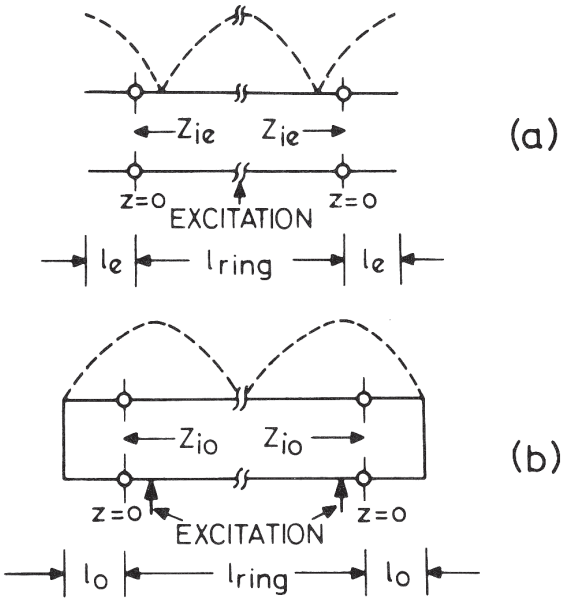

Figure 4.34 Standing wave patterns on the ring for (a) even and (b) odd modes of excitation.

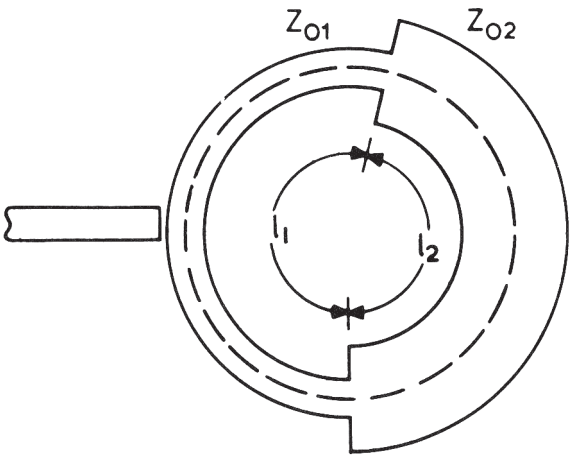

Figure 4.35 An arrangement for the characterization of step discontinuity by ring resonator method.

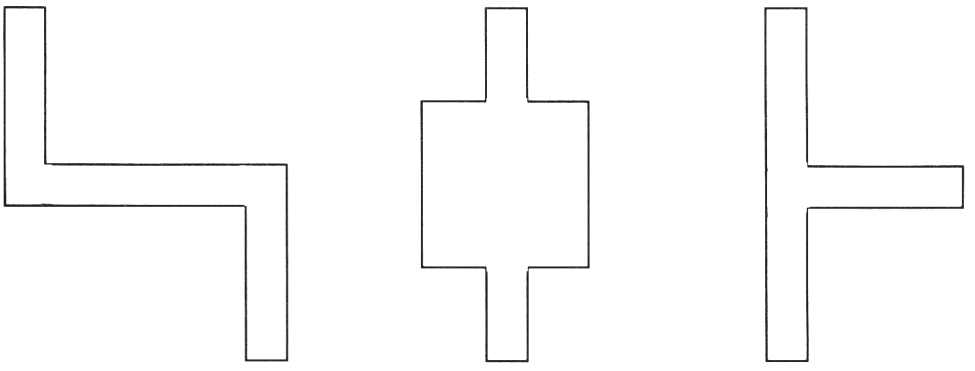

Figure 4.36 Examples of microstrip discontinuity measurement structures.

where λ_{me} and λ_{mo} are guide wavelengths corresponding to the even and odd mode resonance frequencies, respectively. ℓ_{ring} is the physical length of the ring resonator along the mean circumference. Equations (4.68) to (4.70) may be used to evaluate Z_{11} and Z_{12} and hence the equivalent circuit.

This method can also be extended for unsymmetrical discontinuities. An example of characterization of impedance steps in a ring resonator is given in reference [47]. The circuit arrangement used is shown in Figure 4.35. Two steps are located such that lengths ℓ_1 and ℓ_2 are electrically equal. A voltage maximum or minimum can be arranged to appear at the discontinuity locations successively by changing the point of excitation. Shunt and series parts of equivalent circuits are thus separated.

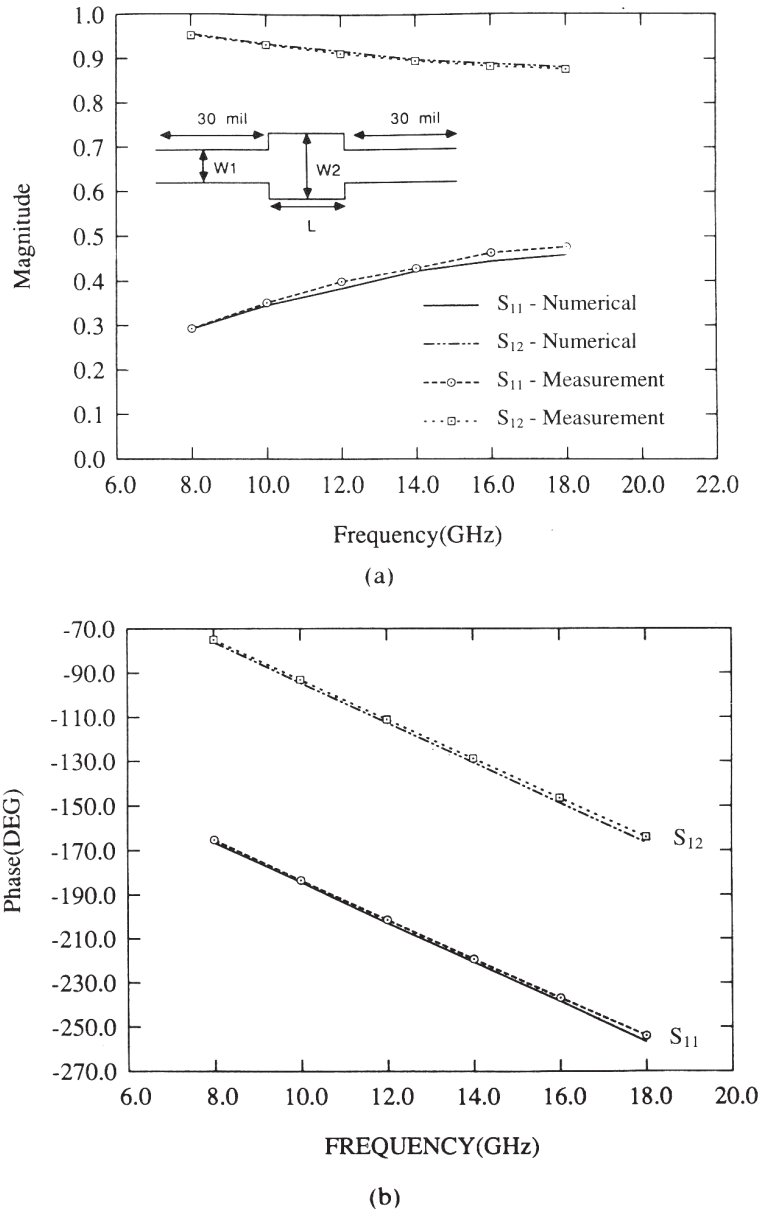

Figure 4.37 Scattering parameters of the two-step configuration shown. Numerical (experimental) dimensions: *W*1 = 9.2 (9.2) mil, *W*2 = 23 (23.1) mil, L = 50.6 (50.0) mil, ε_r = 9.9, *h* = 10 mil. (a) Magnitude and (b) phase (from [48], © 1989 IEEE. Reprinted with permission.).

4.3.3 Scattering Parameters Measurement Method

With recent advancements in de-embedding techniques and RF probes, the discontinuity equivalent circuit model parameters can also be determined accurately from 1-port or 2-port scattering parameter measurements. The model parameters are extracted by computer optimization, which correlates the calculated and measured *S*-parameters. The model parameter values can be obtained to the same accuracy as

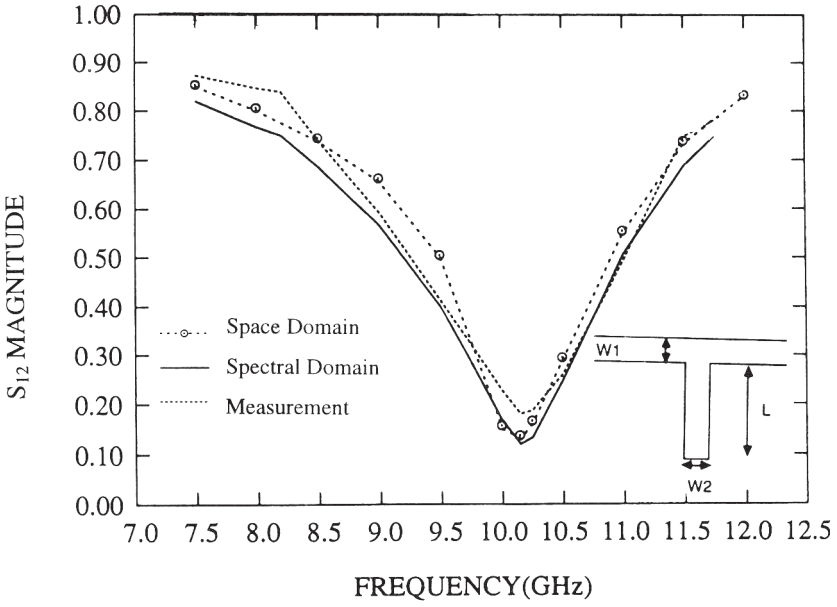

Figure 4.38 Scattering parameters S_{12} for microstrip stub. Parameters for space (spectral) domain analysis: $W1$ = 1.44 (1.40), $W2$ = 1.44 (1.40); L = 2.16 (2.16), ε_r = 10.65, h = 1.27. All dimensions are in millimeters (from [48], © 1989 IEEE. Reprinted with permission.).

the measurement accuracy by using recently developed on-wafer sapphire substrate calibration standards and the *thru-reflect-line* (TRL) calibration method. The TRL calibration method is based on the transmission line calibration standards, which include nonzero thru, a reflect (open or short), and delay line standards (one or more dictated by the frequency range over which the calibration is performed). The advantage of the TRL calibration lies in simple standards that can be placed on the same substrate as the components ensuring a common transmission medium.

Figure 4.36 shows examples of structures that can be tested for 2-port *S*-parameters to characterize right-angle bend, step-in-width, and T-junction microstrip discontinuities. The minimum distance between the two discontinuities (right angle bend and step-in width) must be kept to 2 to 3 line widths or substrate thicknesses, whichever is greater, so that the interaction effects between the discontinuities due to evanescent modes are negligible. Figures 4.37 and 4.38 show a comparison between the numerical and measured *S*-parameters for the step-in width and T-junction discontinuities, respectively [48]. The measured results were obtained using RF probes and agrees very well with the fullwave analysis values.

References

[1] Wolff, I., G. Kompa, and R. Mehran, "Calculation Method for Microstrip Discontinuities and T-Junctions," *Electron. Lett.*, Vol. 8, 1972, pp. 177–179.

[2] Kompa, G., and R. Mehran, "Planar Waveguide Model for Calculating Microstrip Components," *Electron. Lett.*, Vol. 11, 1975, pp. 459–460.

[3] Gupta, K. C., and M. D. Abouzahra, "Planar Circuit Analysis," *Numerical Technique for Microwave and Millimeter-Wave Passive Structures* (ed. T. Itoh), New York: John Wiley & Sons, 1989, pp. 273–278.

[4] Kompa, G., "S-matrix Computation of Microstrip Discontinuities with a Planar Waveguide Model," *Archiv. Elektr. Obertr.,* Vol. 30, 1976, pp. 58–64.

[5] Mehran, R., "The Frequency-dependent Scattering Matrix of Microstrip Right-Angle Bends, T-Junctions and Crossings," *Archiv. Elektr. Obertr.,* Vol. 29, 1975, pp. 454–460.

[6] Mehran, R., "The Frequency-dependent Equivalent Circuits for Microstrip Right-Angle Bends, T-Junctions and Crossings," *Archiv. Elektr. Obertr.,* Vol. 30, 1976, pp. 80–82.

[7] Menzel, W., and I. Wolff, "A Method for Calculating the Frequency Dependent Properties of Microstrip Discontinuities," *IEEE Trans*., Vol. MTT-25, 1977, pp. 107–112.

[8] Chadha, R., and K. C. Gupta, "Compensation of Discontinuities in Planar Transmission Lines," *IEEE Trans*., Vol. MTT-30, December 1982, pp. 2151–2156.

[9] Abouzahra, M. D., "On the Radiation from Microstrip Discontinuities," *IEEE Trans*., Vol. MTT-29; 1981, pp. 666–668.

[10] Hoffman, K., "Radiation from Microwave Circuits," *Handbook of Microwave Integrated Circuits,* Norwood, MA: Artech House, 1987, pp. 311–324.

[11] Sabban, A., and K. C. Gupta, "Characterization of Radiation Loss from Microstrip Discontinuities Using a Multiport Network Modeling Approach," *IEEE Trans*., Vol. MTT-39, April 1991, pp. 705–712.

[12] Gardiol, F. E., "Radiation from Microstrip Circuits: an Introduction," *Intl. J. MIMICAE*, Vol. 1 (2), 1991, pp. 225–235.

[13] James, J. R., et al., *Microstrip Antennas, Theory and Design*, Stevenage, UK: Peter Peregrinus, Ltd., 1981, p. 90.

[14] Benalla, A., and K. C. Gupta, "Multiport Network Model and Transmission Characteristics of Two Port Rectangular Microstrip Antennas," *IEEE Trans. on Antennas Propagation*, Vol. AP-36, October C. 1988, pp. 1337–1342.

[15] Weisshaar, A., and V. K. Tripathi, "Pertubation Analysis and Modeling of Curved Microstrip Bends," *IEEE Trans. Microwave Theory Tech.,* Vol. 38, 1990, pp. 1449–1454.

[16] Kompa, G., *Practical Microstrip Design and Applications*, Norwood, MA: Artech House, 2005.

[17] Momentum, Agilent EEsof, Santa Clara, CA.

[18] HFSS, Ansoft, Pittsburgh, PA.

[19] AXIEM, AWR, El Segundo, CA.

[20] IE3D, Zeland Software, Freemont, CA.

[21] Em, Sonnett Software, North Syracuse, NY.

[22] CST Microwave Studio, CST, Framingham, MA.

[23] Itoh, T., "Analysis of Microstrip Resonators," *IEEE Trans*., Vol. MTT-22, 1974, pp. 946–952.

[24] Mosig, J. R., and F. E. Gardiol, "Integral Equation Techniques for Dynamic Analysis of Microstrip Discontinuities," *Alta Freq*., Vol. LVII, June 1988, pp. 171–181.

[25] Wu, D. I., D. C. Chang, and B. L. Brim, "Accurate Numerical Modeling of Microstrip Junctions and Discontinuities," *Intl. J. MIMICAE*, Vol. 1, 1991, pp. 48–58.

[26] Zhang, X., and K. K. Mei, "Time-Domain Finite Difference Approach to the Calculation of Frequency-Dependent Characteristics of Microstrip Discontinuities," *IEEE Trans*., Vol. MTT-36, December 1988, pp. 1775–1786.

[27] Easter, B., "The Equivalent Circuits of Some Microstrip Discontinuities," *IEEE Trans*., MTT-23, 1975, pp. 655–660.

[28] Jansen, R. H., "Hybrid Mode Analysis of End Effects of Planar Microwave and Millimeter Wave Transmission Lines," *Proc. Inst. Elec. Engr.,* Vol. 128, Part H, April 1978, pp. 77–86.

[29] Boukamp, J., and R. H. Jansen, "The High Frequency Behavior of Microstrip Open Ends in Microwave Integrated Circuits Including Energy Leakage," *Proc. 14th European Microwave Conf.*, 1984, pp. 142–147.

[30] Jackson, R. W., and D. M. Pozar, "Microstrip Open-End and Gap Discontinuities," *IEEE Trans.,* Vol. MTT-33, October 1985, pp. 1036–1042.

[31] Katehi, P. B., and N. C. Alexopoulos, "Frequency-Dependent Characteristics of Microstrip Discontinuities in Millimeter-Wave Integrated Circuits," IEEE Trans., Vol. MTT-33, October 1985, pp. 1029–1035.

[32] Koster, N. H. L., and R. H. Jansen, "The Microstrip Step Discontinuity: A Revised Description," *IEEE Trans*., Vol. MTT-34, February 1986, pp. 213–223.

[33] Jackson, R. W., "Full-wave, Finite Element Analysis of Irregular Microstrip Discontinuities," *IEEE Trans*., Vol. MTT-37, 1989, pp. 81–89.

[34] Jansen, R. H., "The Spectral-domain Approach for Microwave Integrated Circuits," IEEE Trans., Vol. MTT-33, 1985, pp. 1043–1056.

[35] Mosig, J. R., and F. E. Gardiol, "A Dynamic Radiation Model for Microstrip Structures," *Advances in Electronics and Electron Physics* (ed. P. W. Hawkes), Vol. 59, New York: Academic Press, 1982.

[36] Mosig, J. R., "Arbitrarily Shaped Microstrip Structures and Their Analysis with a Mixed Potential Integral Equation," *IEEE Trans*., Vol. MTI-36, 1988, pp. 314–323.

[37] Chang, D. C., and J. X. Zheng, "Electromagnetic Modeling of Passive Circuit Elements in MMIC," *IEEE Trans*., Vol. MTT-40, September 1992, pp. 1741–1747.

[38] Wolff, I., "Finite Difference Time-domain Simulation of Electromagnetic Fields and Microwave Circuits," *Intl. J. Numerical Modeling: Electronic Networks, Devices and Fields*, Vol. 5,1992, pp. 163–182.

[39] Eswarappa, C., and W. J. R. Hoefer, "Time Domain Analysis of Via Holes and Shorting Pins in Microstrip Using 3–D SCN TLM," *IEEE MTT-S Symp. Digest*, Vol. 2, June 1993, pp. 917–920.

[40] Berenger, J., "A Perfectly Matched Layer for the Absorption of Electromagnetic Waves," *J. Comp. Phys.,* Vol. 114, October 1994, pp. 185–200.

[41] Katz, D., E. Thiele, and A. Taflove, "Validation and Extension to Three Dimensions of the Berenger PML Absorbing Boundary Condition for FDTD Meshes," *IEEE Microwave & Guided Wave Lett*., Vol. 4, August 1994, pp. 268–270.

[42] James, J. R., and A. Henderson, "High-Frequency Behavior of Microstrip Open-End Terminations," IEE J. *Microwave Opt. Acoustics*, Vol. 3, September 1979, pp. 205–211.

[43] James, D. S., and S. H. Te, "Microstrip End Effects," *Electron. Lett.*, Vol. 8, January 27, 1972, pp. 46–47.

[44] Easter, B., et al., "Resonant Techniques for the Accurate Measurement of Microstrip Properties and Equivalent Circuits," *Proc. 1973 European Microwave Conf.,* paper B 7.6.

[45] Stephenson, I. W., and B. Easter, "Resonant Techniques for Establishing the Equivalent Circuits of Small Discontinuities in Microstrip," *Electron. Lett.*, Vol. 7, 1971, pp. 582–584.

[46] Hoefer, W. J. R., and A. Chattopadhyay, "Evaluation of the Equivalent Circuit Parameters of Microstrip Discontinuities Through Perturbation of a Resonant Ring," *IEEE Trans.,* Vol. MTT-23, 1975, pp. 1067–1071.

[47] Groll, H., and W. Weidmann, "Measurement of Equivalent Circuit Elements of Microstrip Discontinuities by a Resonant Method," *Nachr. Zeit*., Vol. 28, 1975, pp. 74–77.

[48] Harokopus, Jr., W. P., and P. B. Ketehi, "Characterization of Microstrip Discontinuities on Multilayer Dielectric Substrates Including Radiation Losses," *IEEE Trans. on Microwave Theory Tech*., Vol. MTT-37, December 1989, pp. 2058–2066.

CHAPTER 5

Slotlines

5.1 Introduction

A slotline is a planar transmission structure proposed for use in MICs by Cohn in 1968 [1]. The basic slotline configuration is shown in Figure 5.1. It consists of a dielectric substrate with a narrow slot etched in the metallization on one side of the substrate. The other side of the substrate is without any metallization. The geometry is planar and, as mentioned earlier in Chapter 1, is well suited for its usage in microwave integrated circuits.

Slotlines can be included in microstrip circuits by etching the slotline circuit in the ground plane of the substrate for microstrip circuits. This type of hybrid combination allows flexibility in the design of microwave circuits and has led to some new types of circuits such as hybrid branchline directional couplers. Also, some of the circuit elements, which cannot easily be achieved in microstrip configuration, can be incorporated in the slotline part of the circuit. These, for example, could be short circuits, high impedance lines, series stubs, and baluns. Slotlines can also be employed as a resonant or nonresonant antenna.

In a slotline, the wave propagates along the slot with the major electric field component oriented across the slot in the plane of metallization on the dielectric substrate. The mode of propagation is non-TEM and almost transverse electric in nature. However, unlike conventional waveguides, there is no low-frequency cutoff, because the slotline is a two-conductor structure. The approximate field distribution in a slotline is shown in Figure 5.2. This near-field distribution has been discussed by Cohn [2].

The various methods used for the analysis of a slotline are described in the following section. Design considerations for the slotline, short-end and open-end discontinuities, transitions from slotline to microstrip and coaxial line, and some circuit applications of slotlines are discussed in this chapter.

5.2 Slotline Analysis

The slotline was first analyzed by Cohn [1]. He employed the transverse resonance approach after converting the slotline into a waveguide configuration. Since then, a number of other techniques have been employed. Some of these analytical techniques are:

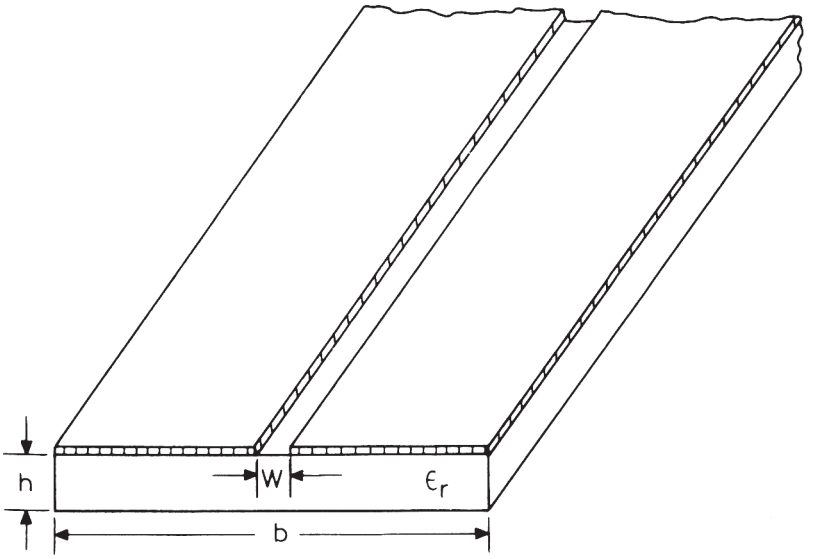

Figure 5.1 Slotline configuration.

------ MAGNETIC FIELD LINES
—— ELECTRIC FIELD LINES

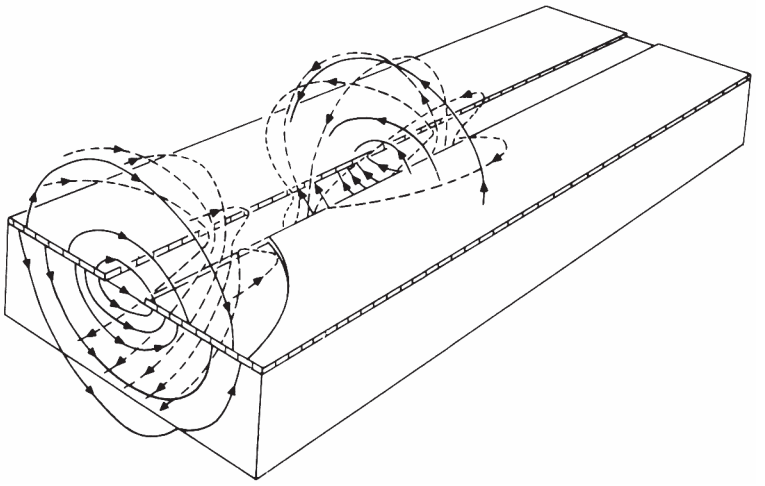

Figure 5.2 Field distribution in a slotline.

1. Approximate analysis [1];
2. The transverse resonance approach [1];
3. Galerkin's method in Fourier transform domain [3–7];
4. Finite-difference time domain technique [8].

The first three methods are discussed in the following sections.

5.2.1 Approximate Analysis

Before attempting a rigorous analysis, it is worthwhile to look at an approximate solution for slotline characteristics. This has the advantage of mathematical simplicity and provides a better qualitative picture. An approximate analysis for the field distribution, polarization of magnetic field, and expression for slot wavelength are presented below.

Field Distribution

For a waveguiding structure to be useful as a transmission line or a circuit element, it is necessary to confine the fields near the structure. An analysis of the field distribution of the transmission line structure is helpful in determining the parameters necessary to prevent the spreading of the fields.

The slotline field contains six components: three electric field components and three magnetic field components. The longitudinal component of the electric field is very weak since the energy propagates between the two conductors. If the slot width W is much smaller than the free-space wavelength λ_0, the electric field across the slot may be represented by an equivalent line source of magnetic current, and then the far-field contains only three components: H_x, H_r, and E_ϕ. At a distance r ($\gg W$) in the air region above the slot (Figure 5.3), these may be written as [1]

$$H_x = AH_0^{(1)}(k_c r) \tag{5.1}$$

$$H_r = -\frac{\gamma_x}{k_c^2}\frac{\partial H_x}{\partial r} = \frac{A}{\sqrt{1-(\lambda_s/\lambda_0)^2}}H_1^{(1)}(k_c r) \tag{5.2}$$

$$E_\phi = \frac{j\omega\mu}{k_c^2}\frac{\partial H_x}{\partial r} = -\eta H_r \lambda_s/\lambda_0 \tag{5.3}$$

where γ_x is the propagation constant along the x-direction, which is the direction of propagation, and k_c is related to the slot wavelength λ_s by the equation

$$k_c = j\frac{2\pi}{\lambda_0}\sqrt{\left(\frac{\lambda_0}{\lambda_s}\right)^2 - 1} \tag{5.4}$$

From the above expressions for the field components the following information may be obtained.

Rate of Decay of Field

For large values of r, $H_0^{(1)}(j|r|)$ and $H_1^{(1)}(j|r|)$ may be expressed as

$$H_n^{(1)}\left(j|r|\right) = \frac{2}{\sqrt{j\pi|r|}}\exp\left(-|r| - j\frac{n\pi}{2} - j\frac{\pi}{4}\right) \tag{5.5}$$

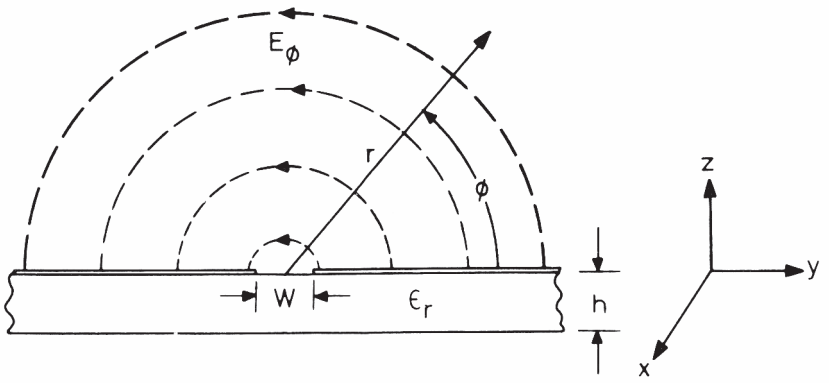

Figure 5.3 Cylindrical coordinates configuration for the approximate analysis of slotline.

Therefore, if $k_c r$ is imaginary, the field will decay with distance r. Equation (5.4) shows that $k_c r$ is imaginary for $\lambda_s/\lambda_0 < 1$. Hence a relative wavelength ratio less than unity is a sufficient condition to ensure transverse decay of the field. To a zero-order approximation, λ_s/λ_0 is equal to $\sqrt{2/(\varepsilon_r + 1)}$. As λ_s/λ_0 is decreased, that is, ε_r increased, the rate of decay becomes faster and fields become more tightly bound to the slot. For example, the ratio of voltage $V(r)$ at a distance r equal to one inch (2.54 cm) to the voltage V directly across the slot on a substrate with $\varepsilon_r = 16$ is calculated (at 3 GHz) to be

$$V(r)/V = \frac{\pi}{2}\left|k_c r H_1^{(1)}(k_c r)\right| = 0.038 \tag{5.6}$$

Information regarding the rate of decay of fields is also helpful in determining the size of the enclosure needed for the slotline.

Polarization of the Magnetic Field

The polarization of the magnetic field in a slotline can be obtained from the ratio $|H_x/H_r|$. Equations (5.1) and (5.2) give

$$\left|\frac{H_x}{H_r}\right| = \left|\frac{H_0^{(1)}(k_c r)}{H_1^{(1)}(k_c r)}\right|\sqrt{1-(\lambda_s/\lambda_0)^2} \tag{5.7}$$

From the mathematical tables it is evident that $H_1^{(1)}(j|r|)$ is always greater than $H_0^{(1)}(j|r|)$ and also $\lambda_s < \lambda_0$. Therefore, $|H_x|$ is always less than $|H_r|$, and the magnetic field cannot have circular polarization. Nevertheless elliptical polarization exists for all values of r.

The field configuration shown in Figure 5.2 indicates that the magnetic field has regions of elliptical polarization both in the air region above the slot and on the conducting surface constituting the slot. These regions of elliptical polarization can be utilized for the construction of nonreciprocal ferrite components. Robinson and Allen [9] have used slotline in the construction of ferrite devices.

Slot Wavelength

As shown in Figure 5.2, slotline field components are not confined to the substrate alone. They extend into the air regions above the slot and below the substrate also. Therefore, the energy is distributed between the substrate and the air regions. Consequently, the effective dielectric constant for a slotline (ε_{re}) is less than the substrate permittivity ε_{re} Galejs [10] has shown that the zeroth-order value of ε_r for a slot on an infinitely thick substrate is the average dielectric constant of the two media, that is,

$$\varepsilon_{re} = \frac{\varepsilon_r + 1}{2} \tag{5.8}$$

and therefore,

$$\frac{\lambda_s}{\lambda_0} = \sqrt{\frac{2}{\varepsilon_r + 1}} \tag{5.9}$$

It has been observed by Garg and Gupta [11] that for slotline on a finite thickness substrate, the above value of λ_s/λ_0 is approached for the cutoff thickness for the TE_0 surface wave mode. The cutoff thickness $(h/\lambda_0)_c$ is given by

$$(h/\lambda_0)_c = 0.25/\sqrt{\varepsilon_r - 1} \tag{5.10}$$

The approximate analysis discussed above gives a good physical picture of the field configuration of the slotline. But it does not lead to an evaluation of the characteristic impedance of the slotline. Moreover, the variation of slot wavelength λ_s with different geometrical parameters of the slotline, that is, h, W and b, is not provided by this analysis. To overcome these shortcomings, several rigorous analyses of slotline have been carried out [1–8, 12–15]. These analyses take into account the effects of various parameters on the slotline impedance Z_{0s} and the wavelength λ_s. Some of these analyses are described next.

5.2.2 Transverse Resonance Method

In this method, a slotline is analyzed as a rectangular waveguide configuration. The key feature of this analysis is the introduction of boundary walls such that a rectangular waveguide configuration with a capacitive iris is obtained. It is then analyzed in terms of waveguide modes propagating perpendicular to the slotline plane.

Development of Waveguide Model

A waveguide model for a slotline is obtained by introducing (i) conducting planes normal to the slot and the substrate at $x = 0$ and $x =$ a such that $a = \lambda_s/2$ as shown in Figure 5.4(a). Since the spacing between the two planes is $\lambda_s/2$, the introduction of these planes does not disturb the field variations. A standing wave field configuration with E_y and E_z equal to zero at $x = 0$ and $x = a$ is obtained. (ii) Next, electric walls or magnetic walls are inserted in planes parallel to the slot and perpendicular

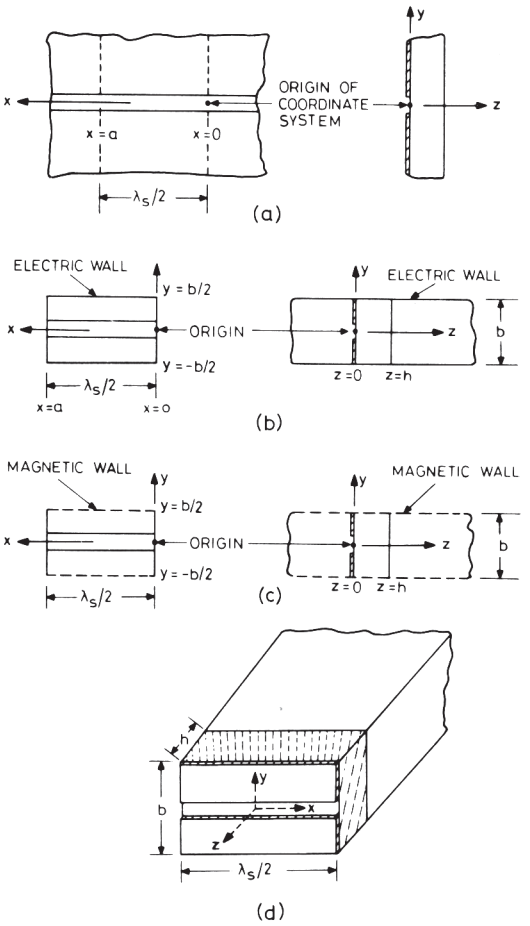

Figure 5.4 Development of the rectangular waveguide model for slotline analysis using the transverse resonance method: (a) The configuration, (b) model with electric walls, (c) model with magnetic walls, and (d) resulting configuration of an iris in a waveguide.

to the substrate at $y = \pm b/2$ as shown in Figure 5.4(b, c). Since the fields are tightly bound to the slot, the walls at $y = \pm b/2$ will have a negligible effect when the distance b is sufficiently large. Introduction of electric walls creates a configuration of a capacitive iris in a rectangular waveguide as shown in Figure 5.4(d). The two cases of electric walls and magnetic walls are analyzed separately.

Slot Wavelength

Having developed the capacitive iris waveguide model the method of transverse resonance is applied to determine the slot wavelength. In this method the sum of susceptances at the iris plane is equated to zero.

This sum includes the susceptances of the TE_{10} mode looking in the $+z$ and $-z$ directions and the capacitive iris susceptance due to higher order modes on

both sides of the iris (the TE_{10} mode cannot exist for the magnetic wall case). The introduction of magnetic walls or electric walls at $y = \pm b/2$ gives rise to different sets of modes. These sets are $TE_{1,\,2n}$ and $TM_{1,2m}$ where n is an integer ≥ 0 and $m \geq 1$ for electric walls, and n or $m = 1/2, 3/2, 5/2$ for magnetic walls.

Two separate expressions for the total susceptance ηB_t for the electric wall and magnetic wall cases are obtained. These are given in Appendix 5.A.

Evaluation of Slot Wavelength

Roots of the equation $\eta B_t = 0$, with ηB_t given by (A.1) or (A.2) for the electric wall case or magnetic wall case, respectively, give the slot wavelength λ_s. It is a function of λ_0 also, unlike in a microstrip because the mode of propagation in the slotline is hybrid in nature.

Numerical computations by Cohn [1] show that, for large values of b, identical results are obtained for both the electric wall and magnetic wall models. In the specific case when $\varepsilon_r = 20$, $h = 3.48$ mm, $W = 0.625$ mm, $\lambda_0 = 10.67$ cm, and $\lambda_s = 3.45$ cm, the solutions for electric and magnetic walls approach each other for $b > 38.1$ mm and are only slightly different for $b = 25.4$ mm.

Slotline Impedance

Because of the non-TEM nature of the mode in a slotline, the characteristic impedance Z_{0s} cannot be defined uniquely. The definition based on the power-voltage relationship is used more frequently and may be written as [6]

$$Z_{0s} = |V|^2/2P \tag{5.11}$$

where V is the peak voltage across the slot. The average power P can be expressed in terms of energy storage W_t, which may be related to the rate of change of total susceptance B_t with frequency. For resonant cavities [16]

$$W_t = \left(\frac{V^2}{4}\right)\left(\frac{\partial B_t}{\partial \omega}\right) \tag{5.12}$$

and also since

$$W_t = \frac{\pi P}{2\omega}\frac{v}{v_g} \tag{5.13}$$

we can write

$$Z_{0s} = (v/v_g)\pi/(\omega\,\partial B_t/\partial\omega)$$

With $p = \lambda_0/\lambda_s$ it may be also expressed as

$$Z_{0s} = \eta\frac{v}{v_g}\frac{\pi}{p}\left\{\frac{\Delta p}{-\Delta(\eta B_t)}\right\} \tag{5.14}$$

The ratio of the phase velocity v to the group velocity v_g can be evaluated from the sensitivity of (λ_0/λ_s) with respect to frequency f. It is given by

$$\frac{v}{v_g} = 1 - \frac{f}{\lambda_s/\lambda_0}\frac{\Delta(\lambda_s/\lambda_0)}{\Delta f} \tag{5.15}$$

Evaluation of Slotline Impedance

For the given set of slotline parameters ε_r, W, h, and b choose a small frequency interval Δf centered around f, the frequency of operation. The value of $\Delta(\lambda_s/\lambda_0)$ is computed from two separate solutions of $\eta B_t = 0$ for the two values of h/λ_0 corresponding to the ends of the frequency interval. Using the value of $\Delta(\lambda_s/\lambda_0)$ in (5.15) gives the value of v/v_g. The change in susceptance $\Delta(\eta B_t)$ (needed for evaluating Z_{0s}) is computed from (A.l) or (A.2) with λ_s held constant (λ_s is obtained from the value of λ_s/λ_0 at the frequency f) and p incremented slightly plus and minus from the value $p = \lambda_0/\lambda_s$ at $\eta B_t = 0$. (The two values of p are obtained from the two end values of λ_0 for the frequency interval Δf selected.)

Computations of slot wavelength and impedance, based on the above method, have been carried out. They are shown in Figure 5.5 for $\varepsilon_r = 9.7$. Mariani et al. [17] have also reported slotline characteristics for $\varepsilon_r = 9.6$, 11.0, 13.0, 16.0, and 20.0.

The method of transverse resonance is valid for the following range of parameters

$$W < 0.25\lambda_0/\sqrt{\varepsilon_r} \tag{5.16a}$$

$$W/h \leq 1 \tag{5.16b}$$

$$b \geq 7W \tag{5.16c}$$

Condition (5.16a) is necessary to avoid resonance across the slot. Although this method can also be used to determine the effect of the finite size of metal sheets enclosing the slot, it cannot be employed for wide slots ($W/h > 1$). The method described next does not suffer from this limitation.

5.2.3 Galerkin's Method in the Spectral Domain

An accurate analysis of the slotline is based on the use of Galerkin's method in the Fourier transform domain. This method is very popular and is similar to those used for fullwave analysis of microstrip lines (in Section 2.3.1) and for analysis of microstrip discontinuities (in Section 3.2.3).

Field components in a slotline are expressed in terms of two scalar potentials $\psi^e(x, y)$ and $\psi^h(x, y)$. The longitudinal components are proportional to these potentials and are written as

$$E_z = k_c^2 \psi^e(x, y)\exp(\pm j\beta z) \tag{5.17}$$

$$H_z = k_c^2 \psi^h(x, y)\exp(\pm j\beta z) \tag{5.18}$$

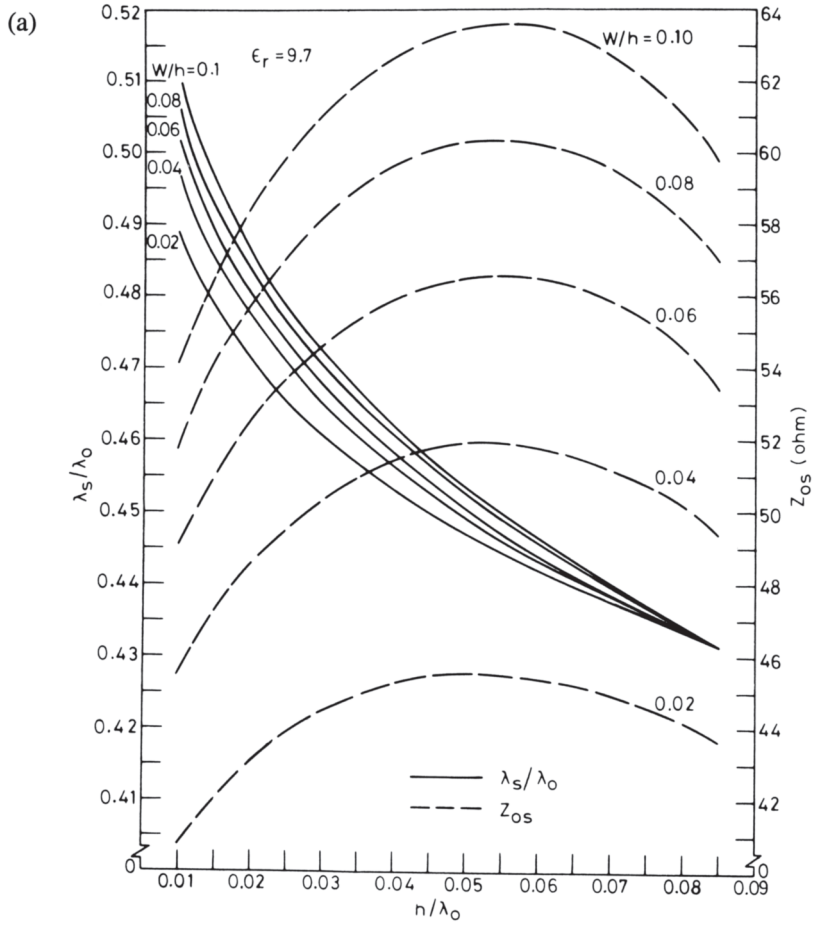

Figure 5.5 (a) Characteristics of slotline ($\varepsilon_r = 9.7$, $W/h = 0.02$ to 0.1, $h/\lambda_0 = 0.01$ to 0.085) and (b) characteristics of slotline ($\varepsilon_r = 9.7$, $W/h = 0.2$ to 1.0, $h/\lambda_0 = 0.01$ to 0.085).

where β is the propagation constant and

$$k_c^2 = k_i^2 - \beta^2$$

$$k_i = (\varepsilon_i \mu_i)^{1/2} \qquad i = 1,2,3 \tag{5.19}$$

Values of i specify the three regions of the slotline cross section as shown in Figure 5.6. The next step is the Fourier transformation of the scalar wave equation along x. This transformation converts the second-order partial differential equation into an ordinary differential equation that can be solved easily. The solutions for transforms of scalar potentials in the three regions may be written as

$$\begin{aligned}
\psi_1^e(\alpha, y) &= A^e(\alpha)\exp\left[-\gamma_1(y-h)\right] \\
\psi_2^e(\alpha, y) &= B^e(\alpha)\sinh\gamma_2 y + C^e(\alpha)\cosh\gamma_2 y \\
\psi_3^e(\alpha, y) &= D^e(\alpha)\exp\left(\gamma_1 y\right)
\end{aligned} \tag{5.20}$$

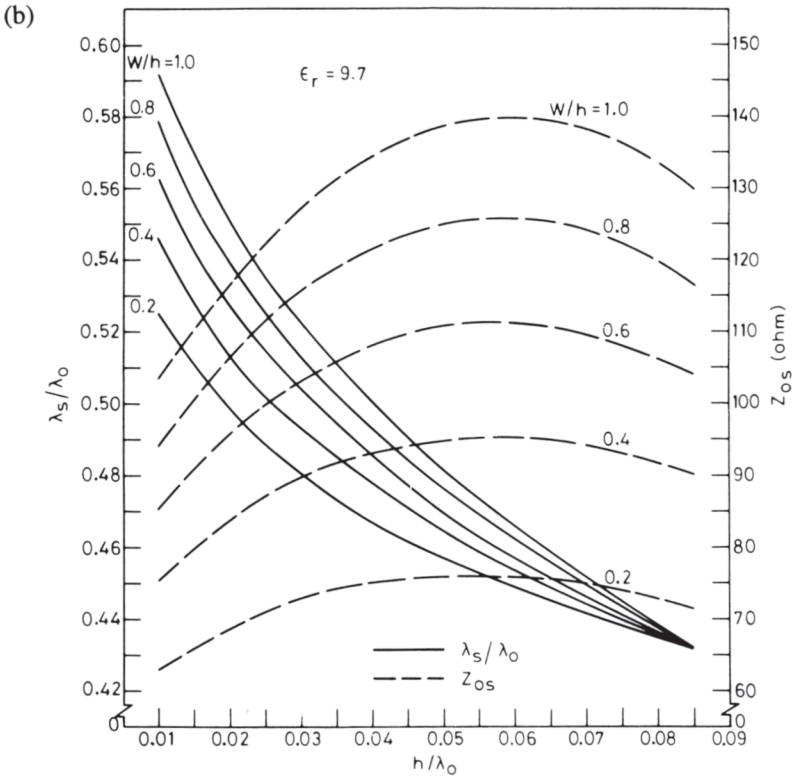

Figure 5.5 (continued).

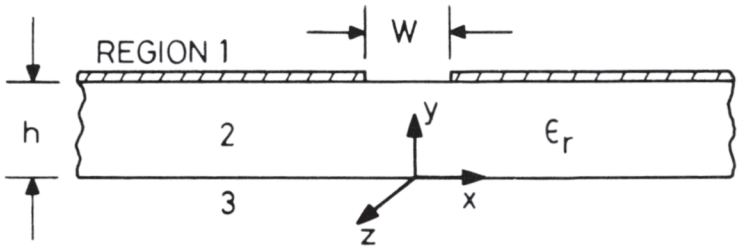

Figure 5.6 Configuration of slotline for analysis using Galerkin's method in FTD.

and

$$\begin{aligned}\psi_1^{\mathrm{h}}(\alpha,y) &= A^{\mathrm{h}}(\alpha)\exp\left[-\gamma_1(y-h)\right]\\ \psi_2^{\mathrm{h}}(\alpha,y) &= B^{\mathrm{h}}(\alpha)\sinh\gamma_2 y + C^{\mathrm{h}}(\alpha)\cosh\gamma_2 y\\ \psi_3^{\mathrm{h}}(\alpha,y) &= D^{\mathrm{h}}(\alpha)\exp(\gamma_1 y)\end{aligned} \tag{5.21}$$

where

$$\gamma_i^2 = \alpha^2 + \beta^2 - k_i^2$$

The eight unknown coefficients A^e through D^h are related to the tangential electric and magnetic field components at the interfaces $y = 0$ and $y = h$ by the continuity conditions and can also be related to the surface current density on the metal and the electric fields in the slot at $y = h$. If the Fourier transforms of the x- and z-directed current densities are denoted by $\tilde{J}_x(\alpha)$ and $\tilde{J}_z(\alpha)$ and electric field components by $\tilde{E}_x(\alpha)$ and $\tilde{E}_z(\alpha)$, one obtains a set of coupled equations of the form

$$\begin{bmatrix} M_1(\alpha,\beta), M_2(\alpha,\beta) \\ M_3(\alpha,\beta), M_4(\alpha,\beta) \end{bmatrix} \begin{bmatrix} \tilde{J}_x(\alpha) \\ \tilde{J}_z(\alpha) \end{bmatrix} = \begin{bmatrix} \tilde{E}_x(\alpha) \\ \tilde{E}_z(\alpha) \end{bmatrix} \tag{5.22}$$

The matrix **M** is now inverted to express transforms of current densities in terms of electric field transforms. If the **N**-matrix is the inverse of the **M**-matrix, (5.22) gives

$$\begin{bmatrix} N_1(\alpha,\beta), N_2(\alpha,\beta) \\ N_3(\alpha,\beta), N_4(\alpha,\beta) \end{bmatrix} \begin{bmatrix} \tilde{E}_x(\alpha) \\ \tilde{E}_z(\alpha) \end{bmatrix} = \begin{bmatrix} \tilde{J}_x(\alpha) \\ \tilde{J}_z(\alpha) \end{bmatrix} \tag{5.23}$$

The matrix elements $N_1, \ldots, N_4$ are known functions of α and β. Now $\tilde{E}_x(\alpha)$ and $\tilde{E}_z(\alpha)$ are expanded in terms of the Fourier transforms of basis functions, and Galerkin's method is applied to yield a homogeneous system of linear equations. The determinant of the coefficient matrix, corresponding to this set of linear equations, equated to zero gives the dispersion relation. An iteration scheme for β can be used to find a nontrivial solution of this dispersion relation.

The rate of convergence of this series representation depends upon the choice of basis functions. A frequently used choice [6] is

$$E_x = \sum_{n=0}^{N} a_n E_{xn} \tag{5.24}$$

$$E_{xn} = \begin{cases} \dfrac{2}{\pi W} \dfrac{T_{2n}(2x/W)}{\sqrt{1-(2x/W)^2}} & n = 0,1,2,\ldots; |x| \le W/2 \\ 0 & \text{elsewhere} \end{cases} \tag{5.25}$$

$$E_z = \sum_{m=1}^{M} b_m E_{zm} \tag{5.26}$$

$$E_{zm} = \begin{cases} \dfrac{2}{\pi W} \sqrt{1-(2x/W)^2}\, U_{2m-1}(2x/W) & m = 1,2,\ldots; |x| \le W/2 \\ 0 & \text{elsewhere} \end{cases} \tag{5.27}$$

where $T_n(\bullet)$ and $U_n(\bullet)$ are Chebyshev polynomials of the first and second kind, respectively. The Fourier transforms of the above basis functions can be found readily in closed form as

$$\tilde{E}_{xn} = (-1)^n J_{2n}\left(\frac{\alpha W}{2}\right) \quad n = 0,1,\ldots \tag{5.28}$$

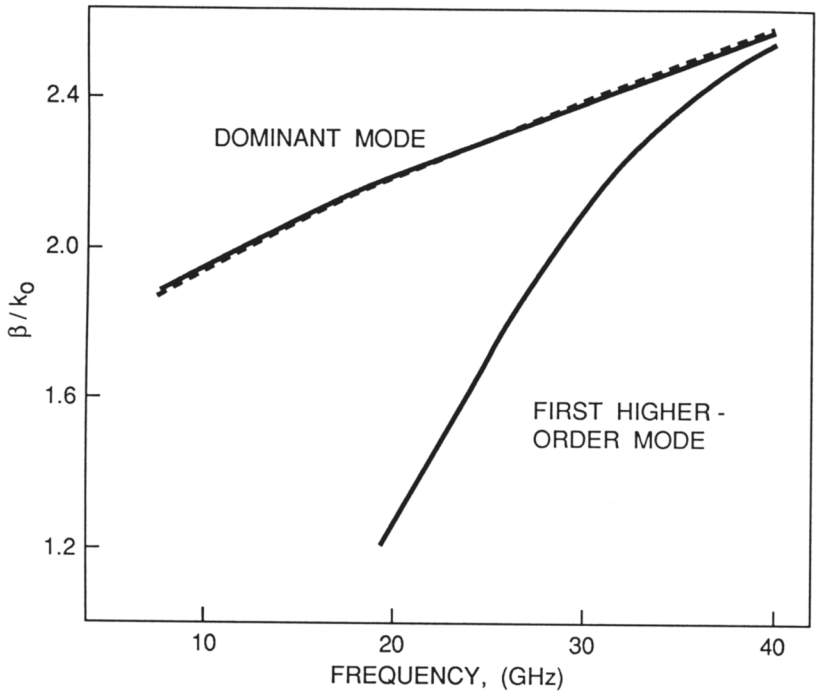

Figure 5.7 Normalized propagation constant for the dominant and first higher order mode in a slotline: $\varepsilon_r = 9.6$, h = 1 mm, W = 1 mm. A broken line represents Cohn's method [1] (from [14], © 1980 IEEE. Reprinted with permission.)

and

$$\tilde{E}_{zm} = \; j(-1)^{m+1} 2m \frac{J_{2m}(\alpha W/2)}{(\alpha W/2)} \quad m = 1,2... \tag{5.29}$$

The computations involved can be simplified by assuming $E_z = 0$. A comparison of the magnitudes of the x and z components of the electric field shows that E_z is about one-tenth of E_x and can therefore be neglected [4].

This method has also been used to evaluate the characteristic impedance of slotlines [6]. In the definition of characteristic impedance (5.11) the voltage across the slot is obtained by integrating the transverse electric field component E_x as

$$V = \int_{-W/2}^{W/2} E_x(x)\, dx = \tilde{E}_x(\alpha)\Big|_{\alpha=0} = \tilde{E}_x(0) \tag{5.30}$$

The time-averaged power flow P along the slotline can be obtained as in (2.37). Again the computations involved can be simplified by neglecting $E_z(x)$.

A comparison of results obtained by Galerkin's method in the spectral domain with Cohn's method [1] indicates that the transverse resonance method used by Cohn yields accurate results for a slotline within the limits prescribed in (5.16). However, for wider slots one should use Galerkin's method in the spectral domain.

Higher order modes in a slotline can also be determined using the above method. Citerne et al. [13] and Kitazawa et al. [14] have determined the propagation constant for the first higher order mode in a slotline using different techniques. Figure 5.7 shows the dispersion characteristics of the normalized propagation constant β/k_0 for the dominant and first higher order mode [14]. Computations show that one basis function is sufficient for the dominant mode, while two basis functions are necessary for the first higher order mode. The numerical data are compared with the results of Cohn [1], and the agreement is quite good.

5.3 Design Considerations

5.3.1 Closed-Form Expressions

The various methods of analysis discussed above do not lead to any closed-form expressions for slotline wavelength and impedance. This becomes a serious handicap for circuit analysis and design especially when computer-aided design techniques are used. Some attempts to overcome this difficulty have been reported [11]. Closed-form expressions given below have been obtained by curve fitting the result based on Cohn's analysis. These expressions have an accuracy of about 2 percent for the following range of parameters

$$\begin{aligned} &9.7 \le \varepsilon_r \le 20 \\ &0.02 \le W/h \le 1.0 \\ &0.01 \le h/\lambda_0 \le (h/\lambda_0)_c \end{aligned} \tag{5.31}$$

where $(h/\lambda_0)_c$ is the cutoff value for the TE_0 surface-wave mode on the grounded substrate and is given by (5.10).

The expressions obtained are:

- For $0.02 \le W/h < 0.2$

$$\begin{aligned} \lambda_s/\lambda_0 = {} & 0.923 - 0.448\log\varepsilon_r + 0.2W/h \\ & - (0.29W/h + 0.047)\log(h/\lambda_0 \times 10^2) \end{aligned} \tag{5.32}$$

$$\begin{aligned} Z_{0s} = {} & 72.62 - 35.29\log\varepsilon_r + 50\frac{(W/h - 0.02)(W/h - 0.1)}{W/h} \\ & + \log(W/h \times 10^2)\left[44.28 - 19.58\log\varepsilon_r\right] \\ & - \left[0.32\log\varepsilon_r - 0.11 + W/h(1.07\log\varepsilon_r + 1.44)\right] \\ & \cdot (11.4 - 6.07\log\varepsilon_r - h/\lambda_0 \times 10^2)^2 \end{aligned} \tag{5.33}$$

- For $0.2 \le W/h \le 1.0$

$$\begin{aligned} \lambda_s/\lambda_0 = {} & 0.987 - 0.483\log\varepsilon_r + W/h(0.111 - 0.0022\varepsilon_r) \\ & - (0.121 + 0.094W/h - 0.0032\varepsilon_r)\log(h/\lambda_0 - 10^2) \end{aligned} \tag{5.34}$$

$$
\begin{aligned}
Z_{0s} = {} & 113.19 - 53.55\log\varepsilon_r + 1.25W/h(114.59 - 51.88\log\varepsilon_r) \\
& + 20(W/h \times 0.2)(1 - W/h) \\
& - \left[0.15 + 0.23\log\varepsilon_r + W/h(-0.79 + 2.07\log\varepsilon_r)\right] \\
& \cdot \left[10.25 - 5\log\varepsilon_r + W/h(2.1 - 1.42\log\varepsilon_r)\right. \\
& \left. - h/\lambda_0 \times 10^2\right]^2
\end{aligned}
\tag{5.35}
$$

It is possible to derive more accurate expressions for the slotline wavelength when the dielectric constant of the substrate is fixed. Expressions with 1 percent accuracy for dielectric constant values of 9.7 and 20.0 are

1. $\varepsilon_r = 9.7, 0.01 \le h/\lambda_0 \le (h/\lambda_0)_c$ (5.36)

(i) $0.02 \le W/h \le 0.1$

$$\lambda_s/\lambda_0 = -(0.29W/h + 0.057)\log\left(h/\lambda_0 \times 10^2\right) + 0.283W/h + 0.485$$

(ii) $0.1 \le W/h \le 1.0$ (5.37)

$$\lambda_s/\lambda_0 = -(0.11W/h + 0.077)\log(h/\lambda_0 \times 10^2) + 0.104W/h + 0.507$$

2. $\varepsilon_r = 20, 0.01 \le h/\lambda_0 \le (h/\lambda_0)_c$ (5.38)

(i) $0.02 \le W/h \le 0.1$

$$\lambda_s/\lambda_0 = -(0.269W/h + 0.047)\log(h/\lambda_0 \times 10^2) + 0.2W/h + 0.345$$

(ii) $0.1 < W/h \le 1.0$ (5.39)

$$\lambda_s/\lambda_0 = -(0.094W/h + 0.072)\log(h/\lambda_0 \times 10^2) + 0.075W/h + 0.362$$

The logarithms in expressions (5.32) through (5.39) are to the base 10.

High ε_r substrates are used for circuit applications to confine the field near the slot. Slotlines on low ε_r substrates have interesting applications in antennas. Janaswamy and Schaubert [6] have obtained closed-form expressions for low ε_r substrates by curve fitting the numerical results obtained from Galerkin's method in FTD. These expressions are as follows and are valid for the range of parameters [6]

$$2.22 \le \varepsilon_r \le 9.8$$
$$0.0015 \le W/\lambda_0 \le 1.0$$
$$0.006 \le h/\lambda_0 \le 0.06$$

1. For $0.0015 \le W/\lambda_0 \le 0.075$ and $2.22 \le \varepsilon_r \le 3.8$

$$\lambda_s/\lambda_0 = 1.045 - 0.365\ell n\varepsilon_r + \frac{6.3(W/h)\varepsilon_r^{0.945}}{(238.64 + 100W/h)} - \left[0.148 - \frac{8.81(\varepsilon_r + 0.95)}{100\varepsilon_r}\right] \cdot \ell n(h/\lambda_0) \tag{5.40}$$

av = 0.37 percent, max = 2.2 percent (at one point)

$$\begin{aligned} Z_{0s} \;=\; & 60 + 3.69\sin\left[\frac{(\varepsilon_r - 2.22)\pi}{2.36}\right] + 133.5\ell n(10\varepsilon_r)\sqrt{W/\lambda_0} \\ & + 2.81\left[1 - 0.011\varepsilon_r(4.48 - \ell n\varepsilon_r)\right](W/h)\ell n(100h/\lambda_0) \\ & + 131.1(1.028 - \ell n\varepsilon_r)\sqrt{h/\lambda_0} \\ & + 12.48(1 + 0.18\ell n\varepsilon_r)\frac{W/h}{\sqrt{\varepsilon_r - 2.06 + 0.85(W/h)^2}} \end{aligned} \tag{5.41}$$

av = 0.67 percent, max = 2.7 percent (at one point)

2. For $0.0015 \le W/\lambda_0 \le 0.075$ and $3.8 \le \varepsilon_r \le 9.8$

$$\lambda_S/\lambda_0 = 0.9217 - 0.277\ell n\varepsilon_r + 0.0322(W/h)\left[\frac{\varepsilon_r}{(W/h + 0.435)}\right]^{1/2} - 0.01\ell n(h/\lambda_0)\left[4.6 - \frac{3.65}{\varepsilon_r^2\sqrt{W/\lambda_0}(9.06 - 100W/\lambda_0)}\right] \tag{5.42}$$

av = 0.6 percent, $|\max|$ = 3 percent (at three points, occurs for $W/h > 1$ and $\varepsilon_r > 6.0$)

$$\begin{aligned} Z_{0s} = {} & 73.6 - 2.15\varepsilon_r + (638.9 - 31.37\varepsilon_r)(W/\lambda_0)^{0.6} \\ & + \left(36.23\sqrt{\varepsilon_r^2 + 41} - 225\right)\frac{W/h}{(W/h + 0.876\varepsilon_r - 2)} \\ & + 0.51(\varepsilon_r + 2.12)(W/h)\ell n(100h/\lambda_0) \\ & - 0.753\varepsilon_r(h/\lambda_0)/\sqrt{W/\lambda_0} \end{aligned} \tag{5.43}$$

av = 1.58 percent, max = 5.4 percent (at three points, occurs for $W/h > 1.67$)

3. For $0.075 \le W/\lambda_0 \le 1.0$ and $2.22 \le \varepsilon_r \le 3.8$

$$\lambda_S/\lambda_0 = 1.194 - 0.24\ell n\varepsilon_r - \frac{0.621\varepsilon_r^{0.835}(W/\lambda_0)^{0.48}}{(1.344 + W/h)} - 0.0617\left[1.91 - \frac{(\varepsilon_r + 2)}{\varepsilon_r}\right]\ell n(h/\lambda_0) \tag{5.44}$$

av = 0.69 percent, max = –2.6 percent (at two points, for $W/\lambda_0 > 0.80$)

$$Z_{0S} = 133 + 10.34(\varepsilon_r - 1.8)^2 + 2.87[2.96 + (\varepsilon_r - 1.582)^2] \quad (5.45)$$
$$\cdot [\{W/h + 2.32\varepsilon_r - 0.56\}$$
$$\cdot \{(32.5 - 6.67\varepsilon_r)(100h/\lambda_0)^2 - 1\}]^{1/2}$$
$$- (684.45h/\lambda_0)(\varepsilon_r + 1.35)^2$$
$$+ 13.23[(\varepsilon_r - 1.722)W/\lambda_0]^2$$

av = 1.9 percent, $|\max|$ = 5.4 percent (at three points, for $W/\lambda_0 > 0.8$)

4. For $0.075 \le W/\lambda_0 \le 1.0$ and $3.8 \le \varepsilon_r \le 9.8$

$$\lambda_S/\lambda_0 = 1.05 - 0.04\varepsilon_r + 1.411 \times 10^{-2}(\varepsilon_r - 1.421) \quad (5.46)$$
$$\cdot \ell n\{W/h - 2.012(1 - 0.146\varepsilon_r)\}$$
$$+ 0.111(1 - 0.366\varepsilon_r)\sqrt{W/\lambda_0}$$
$$+ 0.139 + 0.52\varepsilon_r \ell n(14.7 - \varepsilon_r))(h/\lambda_0)\ell n(h/\lambda_0)$$

av = 0.75 percent, $|\max|$ = 3.2 percent (at two points, occurs for $W/\lambda_0 = 0.075, h/\lambda_0 > 0.03$)

$$Z_{0S} = 120.75 - 3.74\varepsilon_r + 50[\tan^{-1}(2\varepsilon_r) - 0.8] \quad (5.47)$$
$$\cdot (W/h)^{[1.11+(0.132(\varepsilon_r - 27.7)/(100h/\lambda_0 + 5))]}$$
$$\cdot \ell n[100h/\lambda_0 + \sqrt{(100h/\lambda_0)^2 + 1}]$$
$$+ 14.21(1 - 0.458\varepsilon_r)(100h/\lambda_0 + 5.1\ell n\varepsilon_r - 13.1)$$
$$\cdot (W/\lambda_0 + 0.33)^2$$

av = 2.0 percent, $|\max|$ = 5.8 percent (at two points, occurs for $W/\lambda_0 < 0.1$). In the above formula, $\tan^{-1}(\cdot)$ assumes its principal value.

In the expressions (5.40) to (5.47) "av" stands for the average of the absolute percentage error and "max" for the maximum percentage error in a sample of 120 data points.

The values obtained from the closed-form expressions (5.40) to (5.47) have been compared with the numerical data in [12]. The comparison covers the microwave and millimeter-wave frequency range.

5.3.2 Effect of Metal Thickness

It has been assumed in the analysis presented in Section 5.2 that the metal conductors constituting the slot have zero thickness, which does not reflect reality. Kitazawa et al. [14, 15] have evaluated the effect of finite metal thickness on the phase constant and characteristic impedance. It is observed that λ_s increases and the characteristic impedance decreases with the increase in metal thickness t. For $\varepsilon_r = 20$, the increase in λ_s is about 1 percent, and the decrease in characteristic impedance is about 2 percent for a t/W ratio of 0.02.

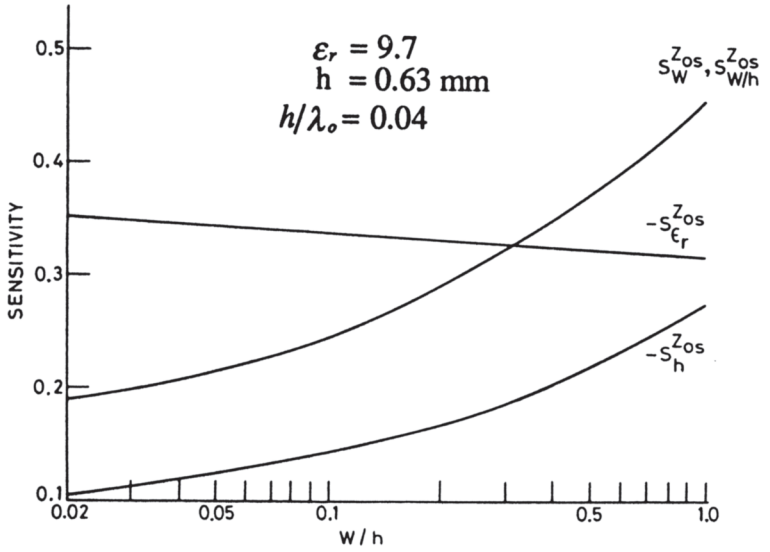

Figure 5.8 Sensitivity of the characteristic impedance of a slotline with respect to its parameters (from [18], © 1978 IEEE. Reprinted with permission.)

5.3.3 Effect of Tolerances

The effect of tolerances in various parameters on the performance of a slotline can be carried out using sensitivity analysis, as we did for the microstrip in Section 2.4.3. The worst case behavior for a given set of tolerances is represented by the maximum change in characteristic impedance and slot wavelength. Expressions for these quantities are (for a fixed λ_0)

$$\frac{|\Delta Z_{0s}|_{\max}}{Z_{0s}} = \left|\frac{\Delta W}{W} S_W^{Z_{0s}}\right| + \left|\frac{\Delta h}{h} S_h^{Z_{0s}}\right| + \left|\frac{\Delta \varepsilon_r}{\varepsilon_r} S_{\varepsilon_r}^{Z_{0s}}\right| \tag{5.48}$$

$$\frac{|\Delta \varepsilon_{re}|_{\max}}{\varepsilon_{re}} = \left|\frac{\Delta W}{W} S_W^{\varepsilon_{re}}\right| + \left|\frac{\Delta h}{h} S_h^{\varepsilon_{re}}\right| + \left|\frac{\Delta \varepsilon_r}{\varepsilon_r} S_{\varepsilon_r}^{\varepsilon_{re}}\right| \tag{5.49}$$

$$\text{where } \varepsilon_{re} = (\lambda_0/\lambda_s)^2 \tag{5.50}$$

The sensitivity expressions can be obtained by using closed-form equations for Z_{0s} and λ_s/λ_0. These expressions are given in Appendix 5.B for high ε_r values and plotted as sensitivity curves in Figure 5.8 and 5.9 [18]. Sensitivity expressions for low ε_r values can be similarly derived by using (5.40) to (5.47).

For a given set of slotline parameters the sensitivity values are calculated and substituted in (5.48) to determine $(\Delta Z_{0s})_{\max}$. This value of $(\Delta Z_{0s})_{\max}$ may be used to calculate slotline VSWR. The inverse problem of determining the fabrication tolerance for a given set of other tolerances can be solved in the same manner as has been done for a microstrip in Section 2.4.3.

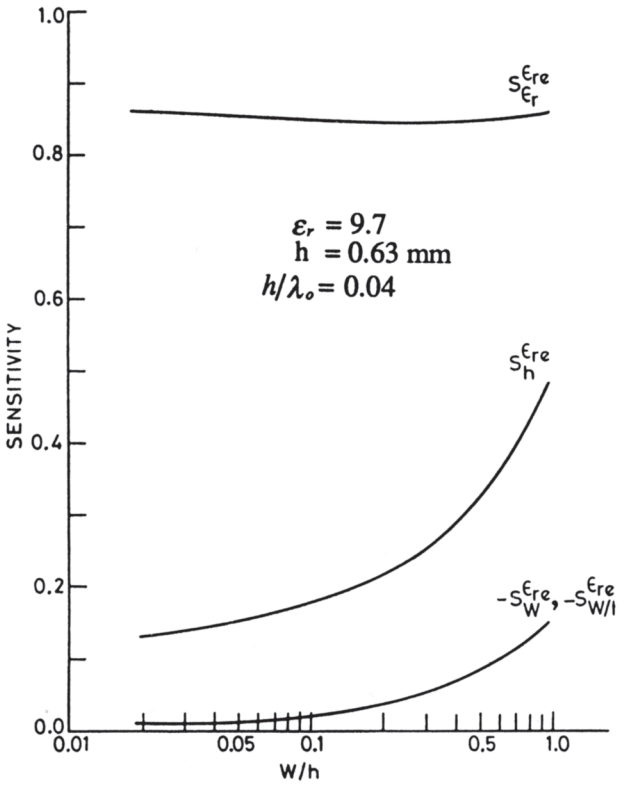

Figure 5.9 Sensitivity of the effective dielectric constant of a slotline with respect to its parameters (from , [18], © 1978 IEEE. Reprinted with permission.)

5.3.4 Losses in Slotline

The losses in a slotline, like those in a microstrip, are the result of the lossy dielectric and the conductors with finite conductivity σ. Dielectric loss α_d can be computed by using a complex value for the relative permittivity, ε_r, of the substrate in the evaluation of the propagation constant of the slotline. Due to the lossy substrate the propagation constant becomes complex, $\gamma = \beta + j\alpha$, with α representing the dielectric loss α_d in nepers/meter of the line. The dielectric loss in a slotline has been found to be of the same order as the loss tangent of the substrate [12].

Conductor loss α_c cannot be obtained from Wheeler's incremental inductance rule because the mode of propagation in a slotline is non-TEM in nature. In such a case one can follow the classical perturbation approach. In this approach conductor loss is evaluated by means of the energy dissipated by the *lossless fields* while propagating through the conductors with surface resistance $R_s = \sqrt{\omega\pi_0/2\sigma}$. The conductor attenuation constant α_c, expressed in nepers/meter, is defined as

$$\begin{aligned}\alpha_c &= \frac{1}{2}\frac{\text{Power dissipated in the conductors}}{\text{Power transmitted along the guide}} \\ &= \frac{P_c}{2P}\end{aligned} \tag{5.51}$$

The power dissipated in the conductors per unit length of the slotline (Figure 5.6) is given by

$$P_c = \frac{R_s}{2}\int_{W/2}^{\infty}\left(\left|H_x^+\right|^2 + \left|H_x^-\right|^2 + \left|H_z^+\right|^2 + \left|H_z^-\right|^2\right) dy \tag{5.52}$$

where $H_x^{\pm}$, . . . are the magnetic fields just above and below the conductor surface, respectively. The power transmitted along the guide is obtained as

$$P = \frac{1}{2}\mathrm{Re}\int\int_{-\infty}^{\infty}\left(E_x H_y^* - E_y H_x^*\right) dx\ dy \tag{5.53}$$

The field components E_x, H_y, . . . are obtained from an analysis of the slotline for the given set of parameters. The overall attenuation per unit length α is then given by

$$\alpha = \alpha_c + \alpha_d \tag{5.54}$$

The actual evaluation of the integrals in (5.52) does not pose any problem as far as $|H_z|^2$ is concerned, because this field component is regular along the edges $|x| = W/2$. However, $|H_x|^2 = |J_z|^2$ is singular along the edges and diverges as $(x^2 - [W/2]^2)^{-1}$. This is a nonintegrable singularity. Rozzi et al. [12] overcame this difficulty by arguing that due to the effect of the small but finite thickness of the conductors, the actual edge behavior of the longitudinal current falls between the $r^{-1/2}$ type and $r^{-1/3}$ type. They assumed a current distribution of the following type (for $|x| \geq W/2$)

$$J_z \propto \left(\frac{2|x|}{W} - 1\right)^{-1/3} \cdot e^{-(2|x|/W-1)/2} \tag{5.55}$$

The above current distribution has the required edge behavior and qualitatively correct far field dependence. Now, the singularity of $|J_z|^2$ is of the type $(x^2 - [W/2]^2)^{-2/3}$, which poses no convergence problem.

Das and Pozar [19] have circumvented the problem of singularity of a current at the slot edges by using the finite conductivity of metal conductors and enforcing the proper impedance boundary conditions and by solving for the complex propagation constant. Results for the conductor loss of a slotline [19, Figure 10] have been compared with the traditional perturbation analysis. The comparison is found to be fairly good except for narrow slots where the conductor loss is found to be relatively smaller.

The conductor and dielectric losses obtained by Rozzi et al. [12] are plotted in Figure 5.10 for a slotline on alumina substrate with $h = 0.635$ mm, $\varepsilon_r = 9.8$, $\sigma = 4.1 \times 10^7$ S/m, and $\tan\delta = 2 \times 10^{-4}$. It is seen that the conductor loss is higher than the dielectric loss for all values of slot width and frequency. It increases with frequency but decreases with slot width. Consequently, in the millimetric wave region narrow slots will be very lossy. An increase in the substrate thickness and/or dielectric constant will allow larger slot widths for the same impedance. A

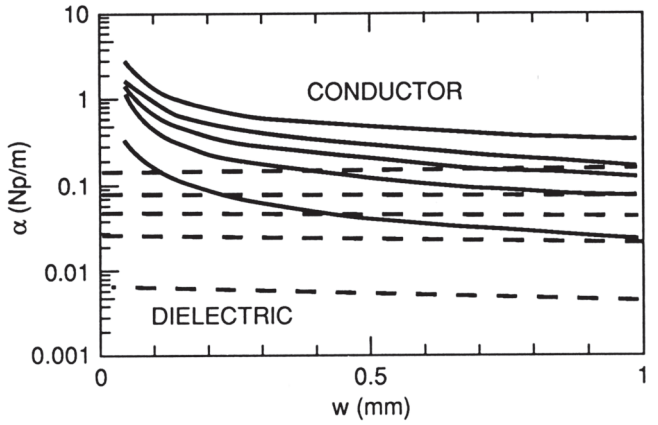

Figure 5.10 Dielectric loss (- - - -) and conductor loss (___) in the slotline as a function of slot width at 2 GHz, 7 GHz, 12 GHz, 18 GHz, and 30 GHz; losses increase with frequency (from [12], © 1990 IEEE. Reprinted with permission.)

limit to the substrate thickness and permittivity is set by the excitation of TM surface waves in the substrate [12].

Experimental results by Kurpis [20] show that the relative value for unloaded Q-factors of microstrip and slotline resonators are 280 and 120, respectively.

5.4 Slotline Discontinuities

As in the case of microstrip circuits, the characterization of slotline discontinuities is needed for the design of slotline circuits. However, only two types of discontinuities in the slotline have been studied. These are short-end and open-end discontinuities. The experimental data is available for both types of discontinuities, but only short-end discontinuity has been analyzed.

5.4.1 Short End Discontinuty

A short end (shown in Figure 5.11) is created by merely ending the slot or equivalently filling the slot with a conducting surface lying in the plane of the slot. The current flows in the metal surface around the end of the slot, and there is appreciable energy stored beyond the termination. This is illustrated in Figure 5.11. The net result is a predominance of stored magnetic energy, which gives rise to an inductive reactance as seen at a reference plane normal to the slot axis and coincident with the end of the slot.

Fullwave analysis of the short end has been carried out in [21, 22]. Experimental characteristics of this discontinuity have been reported by Knorr and Saenz [23] and Chramiec [24]. Yang and Alexopoulos [22] have compared their theoretical results with those of Jansen [21] and measurements of Knorr [23]. This comparison is plotted in Figure 5.12 for the normalized end reactance of the slot. As expected, the end reactance of a shorted slot is inductive and significant. It increases with the increase in slot width and h/λ_0 ratio. The equivalent length of the short end may be

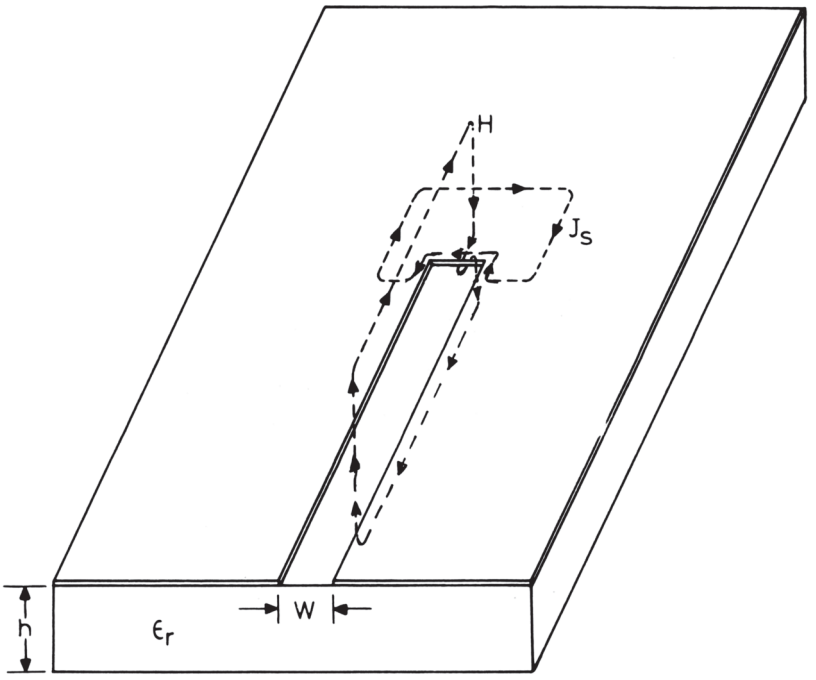

Figure 5.11 Field and current distributions in the vicinity of a slotline short end.

up to 0.1 λ_s. Figure 5.12 also shows good agreement between the theoretical results of two different authors. However, the agreement with the measured values of the end reactance is not so good. Measurement results are subject to various kinds of errors such as tolerances in fabrication, measurement accuracy, substrate tolerances, and coaxial-to-slotline transition.

Like an open end in a microstrip line, the short end in a slotline is not purely reactive. There are losses associated with the short end that are due to the propagation of power in surface waves and radiation in the form of space waves and can be described in terms of an equivalent resistance R presented by the discontinuity to the rest of the circut. Yang and Alexopoulos [22] have calculated the normalized end resistance for a shorted slot on the $\varepsilon_r = 12$ substrate. These results are plotted in Figure 5.13. A comparison of Figure 5.12 for X/Z_{0s} and Figure 5.13 for R/Z_{0s} shows that for the chosen substrate thickness of $h = 3.07$ mm, the resistance and reactance are of the same order, which means that in this case radiated space waves and surface waves are strongly excited. The equivalent circuit of a short end is, therefore, a series combination of an inductor and a resistor. It may be mentioned that a slotline short end is frequently used in slotline circuits and has the same significance as an open end in microstrip circuits.

5.4.2 Open End Discontinuity

For some circuit applications an open end in slotline circuits is required. An open circuit can be achieved by slowly tapering the metallizations constituting the slot.

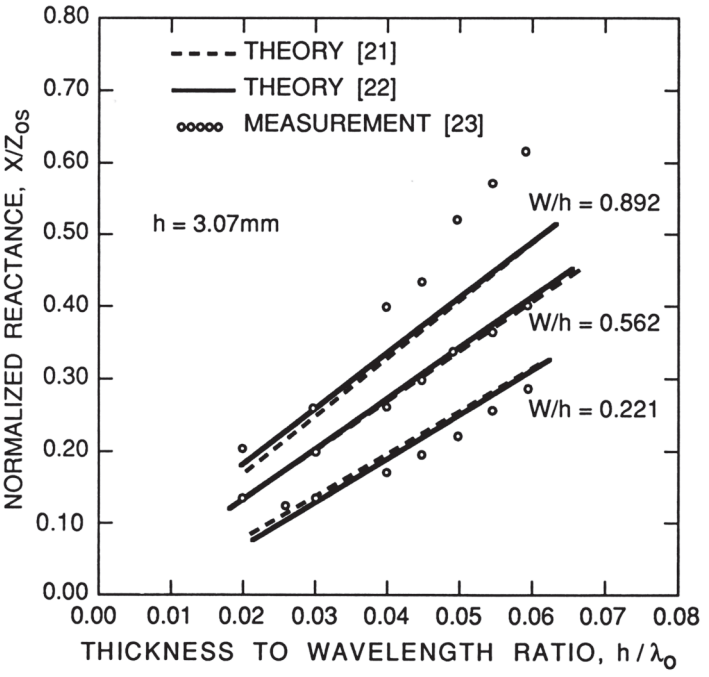

Figure 5.12 Normalized end reactance of a shorted slot, $\varepsilon_r = 12$ (from [22], © 1988 IEEE. Reprinted with permission.)

This is shown in Figure 5.14(a). This type of open circuit is impractical because it requires a lot of substrate area and cannot be implemented at any position in the circuit. Moreover, this type of open circuit produces a lot of radiation. In practice, an open circuit in a slotline is simulated by means of a circular disc opening (no metallization) at the end of the slotline. This is shown in Figure 5.14(b). The larger the radius of the disc, the better will be the open-circuit behavior. Theoretically, the circular disc will behave like a resonator especially if the width of the connecting slotline is narrow compared to the radius of the disc. Experimental studies carried out by Chramiec [24] on alumina substrate confirm this behavior. It is observed that if the operating frequency is higher than the resonant frequency, the circular disc behaves like an open circuit, that is, it is capacitive in nature. Chramiec has also studied a slotline discontinuity that is a combination of a flared slot and a half disc. This is shown in Figure 5.14(c). This discontinuity has a resonant behavior very similar to the circular slot/disc. But this discontinuity has the advantage that it requires lesser surface area and therefore can be used to minimize the overlap between microstrip and slotline portions of the circuit resulting in reduced proximity effects. Chramiec has used this slotline discontinuity to develop a 1.5-GHz to 6-GHz low VSWR microsttip-to-slotline transition [24].

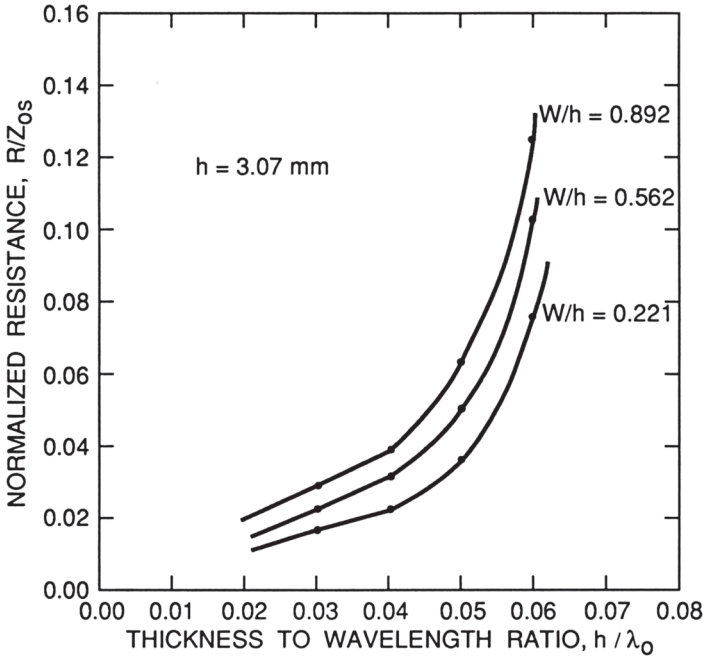

Figure 5.13 Normalized end resistance of a shorted slot, $\varepsilon_r = 12$ (from [22], © 1988 IEEE. Reprinted with permission.)

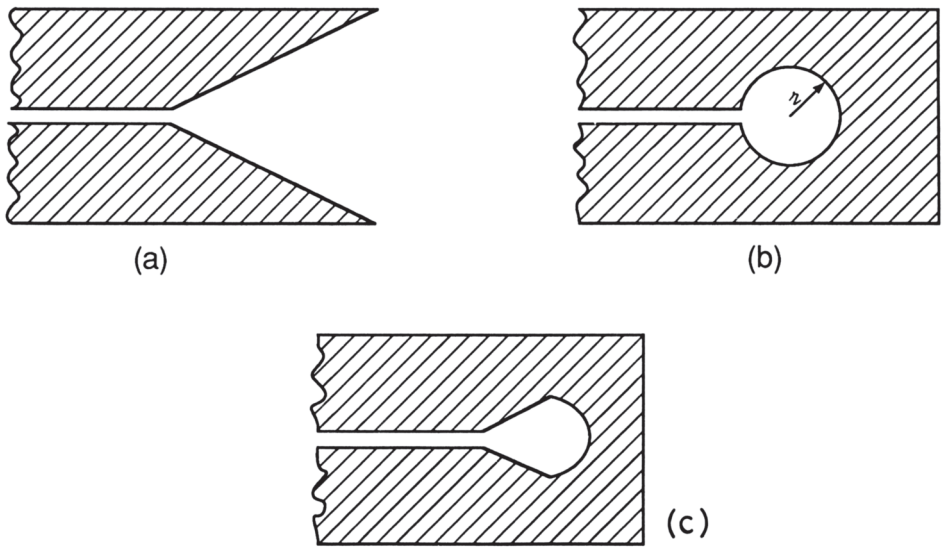

Figure 5.14 Various types of open-end discontinuity in a slotline: (a) a flared open end; (b) circular disc open end; and (c) combination of flared slot and half-disc open end.

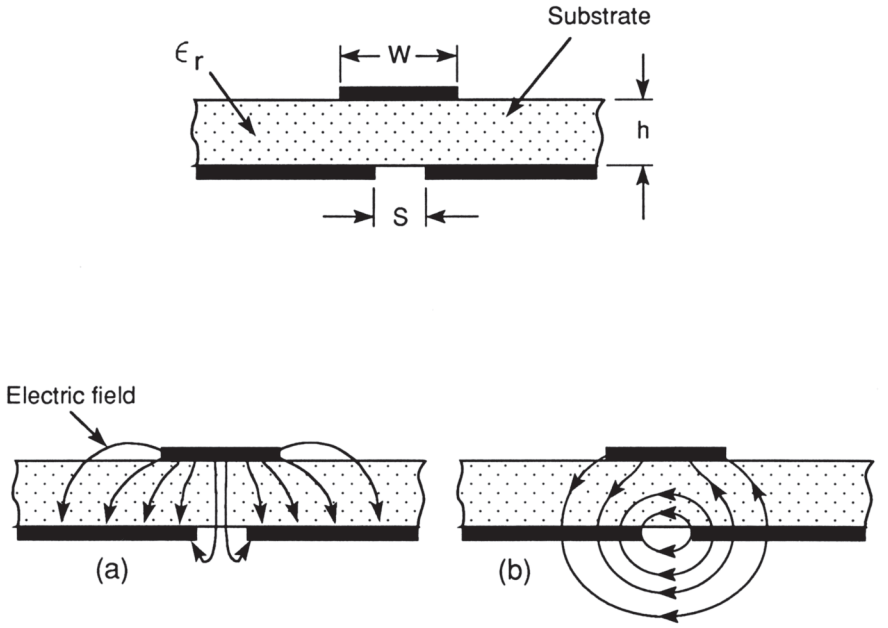

Figure 5.15 Cross section of a coupled microstrip-slotline, and the electric field distributions for (a) even mode and (b) odd mode (from [28], © 1982 IEEE. Reprinted with permission.)

5.5 Variants of Slotline

5.5.1 Coupled Microstrip-Slotline

The cross section of a coupled microstrip-slotline is shown in Figure 5.15. It consists of a slot in the ground plane of a microstrip line. This configuration has been used in the hybrid branchline coupler discussed in Section 5.7.1.

A coupled microstrip-slotline has been analyzed by a number of investigators [25–30]. The method of analysis used most frequently is Galerkin's method in the spectral domain. It was observed that two types of modes propagate in this transmission line: quasi-microstrip mode and the quasi-slotline mode. The electric field distribution for these modes is shown in Figure 5.15. The mode in Figure 5.15(a) has the field disttibution similar to that of a microstrip line. Since it has even symmetry, it is also called the even mode. Similarly, the mode in Figure 5.15(b) is called the odd mode, and the field distribution is similar to that in a slotline. Figures 5.16 and 5.17 show the effective dielectric constants and the characteristic impedances of these modes [30]. It is observed from these figures that for the even mode, the effective dielectric constant decreases and the characteristic impedance increases with increasing slot width. This is because the effect of free space below the slot becomes more pronounced [25]. This mode can be used to realize very high impedances, in the order of 200 Ω to 300 Ω. Quite the opposite is true of the behavior of the odd mode or the slot mode with respect to the increase in strip width. This mode is less sensitive to the presence of the strip. It may be due to the fact that most of the energy in this mode is confined near the slot.

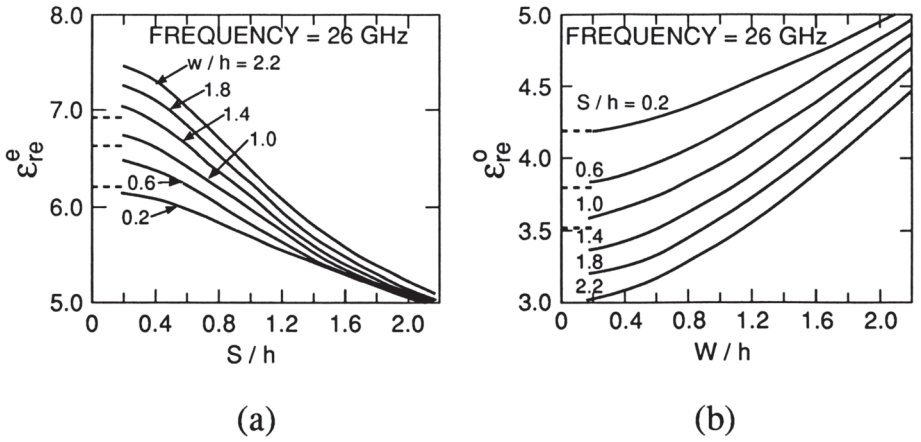

Figure 5.16 Effective dielectric constant of coupled mierostrip-slotline (ε_r =9.6): (a) even mode (... Itoh's result [25]) and (b) odd mode (... Cohn's result [1] (from [30], © 1989 IEEE. Reprinted with permission.)

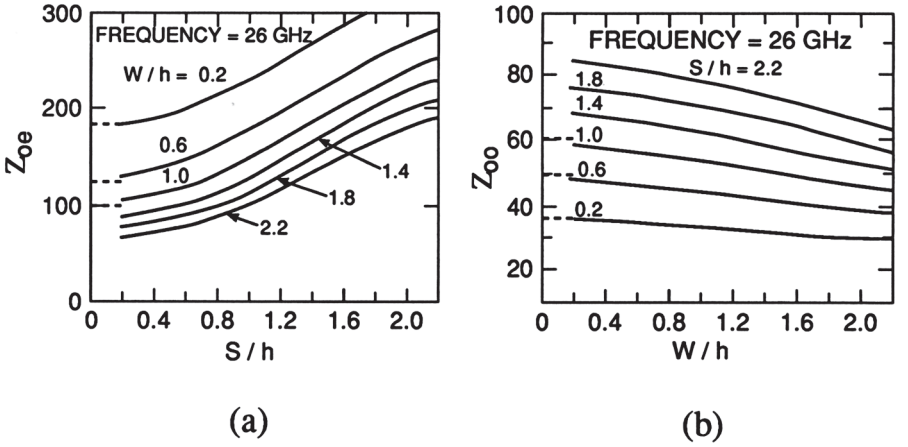

Figure 5.17 Characteristic impedance of coupled microstrip-slotline (ε_r=9.6): (a) even mode (... Itoh's result [25]) and (b) odd mode (... Cohn's result [1]) (from [30], © 1989 IEEE. Reprinted with permission.)

A variation of coupled microstrip-slotline is used in the design of double substrate directional couplers [31]. In this configuration, the slotline is sandwiched between two microstrips by placing another microstrip on the slotline side of the coupled microstrip-slotline. This configuration is discussed later in Section 5.7.3.

5.5.2 Conductor-Backed Slotline

It is very tempting to introduce a conductor backing to the slotline. Among the many advantages that are envisaged are improved mechanical strength, easier implementation of microstrip-slotline circuits, help in grounding floating regions, convenience in dc biasing, and heat sink.

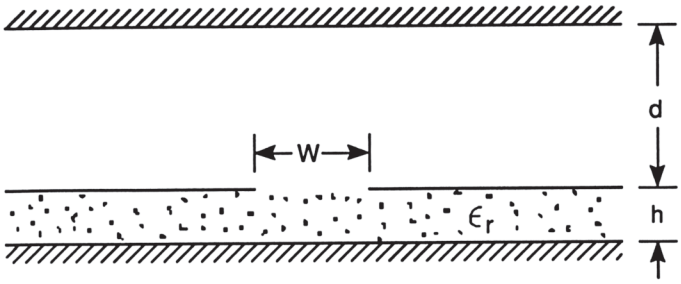

Figure 5.18 Cross section of a conductor-backed slotline.

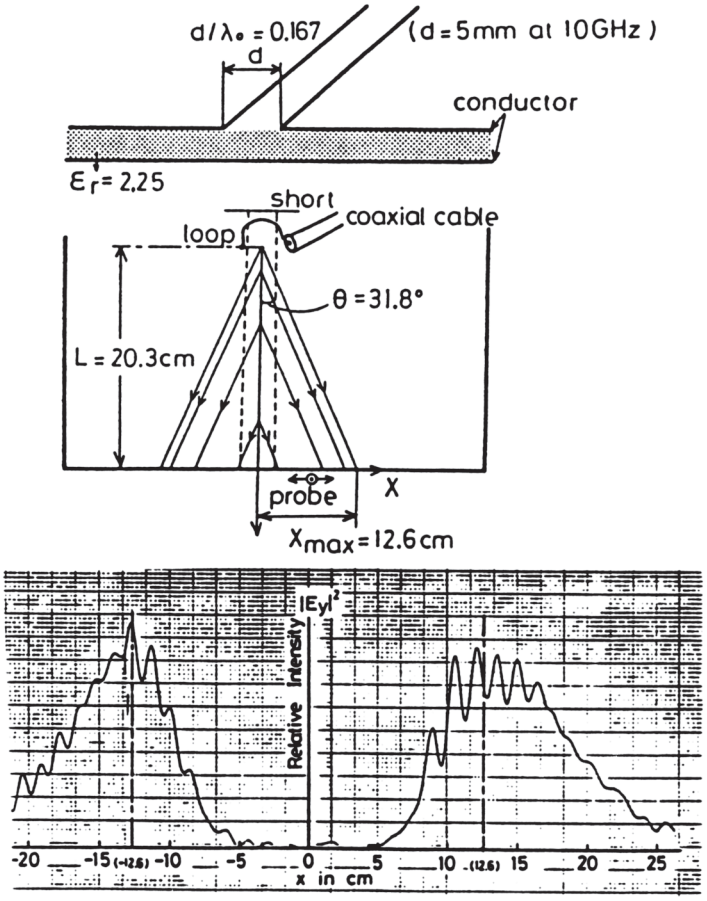

Figure 5.19 Sketch of the measurement set-up, and a plot of the leaky wave field across the width of a slotline (h =5 mm, f = 10 GHz, ε_r =2.25) (from [32]. © 1988 IEEE. Reprinted with permission.)

Shigesawa, et al., [32] and Das and Pozar [19] have carried out fullwave analysis of a conductor-backed slotline with a cover plate (see Figure 5.18). The analysis shows that for a conductor-backed slotline of infinite lateral dimension, power leaks into the dielectric-filled parallel plate region away from the slot. The loss of

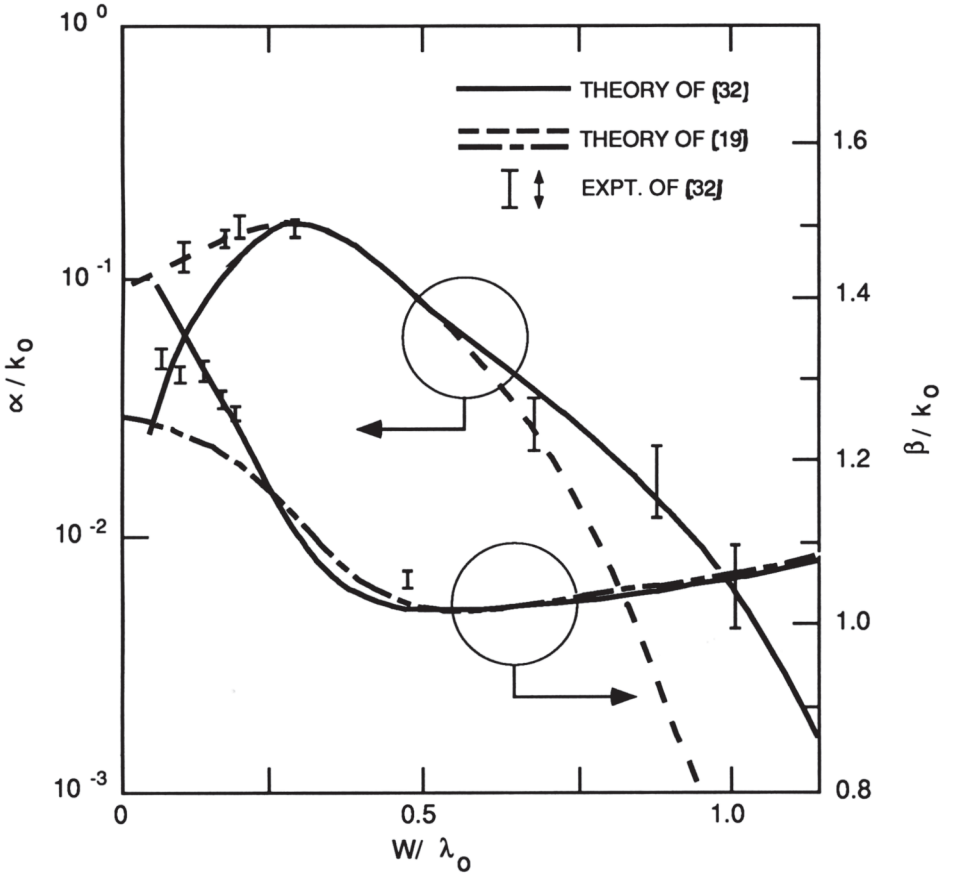

Figure 5.20 Phase constant (β/k_0) and attenuation constant (α/k_0) of a conductor-backed slotline as a function of slot width for $\varepsilon_r = 2.55$. $h/\lambda_0 = 0.267$, $f = 10$ GHz (from [19], © 1991 IEEE. Reprinted with permission.)

power can be explained by a leaky mode characterized by the complex propagation constant $\gamma = \beta + j\alpha$, the imaginary part α accounting for the power loss. The leakage phenomenon is explained as follows.

Far away from the slot, the conductor-backed slotline resembles a conventional dielectric filled parallel plate waveguide formed by the electric conductors on both sides of the substrate. This waveguide supports a TEM mode for which there is no cut-off frequency. Therefore, there are two modes in the conductor-backed slotline: the slotline mode and the TEM mode. Leakage occurs for that range of parameters for which the propagation constant β of the slot mode is less than that of the parallel plate mode [19]. In the structure under study, the propagation constant β/k_0 for the slot mode lies between $\sqrt{\varepsilon_r}$ and 1. The TEM mode for the parallel plate waveguide has the propagation constant $\beta_{TEM}/k_0 = \sqrt{\varepsilon_r}$. Since $\beta_{TEM} > \beta$, leakage occurs independent of frequency or parallel plate separation.

Shigesawa et al. [32] have carried out the analysis of a conductor-backed slotline using two different approaches: a mode-matching technique and the transverse equivalent network approach. Das and Pozar [19] used the fullwave spectral

domain moment method. Measurements were also carried out to determine the leaky wave aspect of the leakage phenomenon [32]. For this purpose, the electric field distribution was probed across the width of slotline at a distance far away from the point of excitation. A sketch of the measurement set-up and a plot of the leaky wave field across the width of the slotline are shown in Figure 5.19. It was observed that the maximum of the electric field occurred at an angle θ from the slot axis given by $\cos^{-1}(\beta/(k_0\sqrt{\varepsilon_r})$. Das and Pozar [19] have compared the theoretical values of β/k_0 and α/k_0 with the computed and measured values in [32]. This is plotted in Figure 5.20. It is observed that the agreement is very good for wider slots between the measured values of [32] and theoretical calculations in [19]. Also, the attenuation constant is fairly high for the narrow slots. The effect of finite plate widths of the slotline and the conductor backing is also discussed by the authors [32]. In this case the propagation constant is found to be purely real.

The leaky slotline mode is one of the unwanted features of a conductor backed slotline. Another aspect of this transmission line becomes important when either the top plates or bottom plate of the structure is finite in the lateral direction but the substrate is thick enough electrically to support a surface wave also. At higher frequencies the value of β for the slotline mode can become lower than the value of β for the surface wave. When this happens the power from the slotline mode will couple to the surface wave, and β for the slotline mode will become complex. Surface wave propagation could produce unexpected cross talk with neighboring circuits. Shigesawa et al. [32] have calculated the crossover frequency between the slotline mode and the TM_0 surface wave mode.

In addition to the discrete modes, a slotline also supports a continuum of radiation modes due to its open nature. These modes can get excited at a discontinuity and are utilized to develop slot antennas. Rozzi et al. [33] have studied these modes for a conductor-backed slotline.

5.5.3 Conductor-Backed Slotline with Superstrate

This modification of the conductor-backed slotline has been suggested by Das [34] to eliminate leakage. The cross section of the conductor-backed slotline with a superstrate is shown in the inset of Figure 5.21. Here, the superstrate parameters are described by the thickness d and the relative dielectric constant ε_{r2}. The substrate parameters are the thickness h and the relative dielectric constant ε_{r1}. As described in Section 5.5.2, leakage occurs because the propagation constant of the slotline mode is lower than the propagation constant of the parallel plate TEM mode. The propagation constant β of the slotline mode can be increased by loading the conductor-backed slotline by means of a superstrate. The loading is increased to an extent such that $\beta > \beta_{TEM}(= k_0\sqrt{\varepsilon_r})$. Loading by the superstrate increases with the increases in its dielectric thickness d and relative dielectric constant ε_{r2}, thickness h of the substrate, and frequency. This is shown in Figure 5.21 for the effective dielectric constant ε_{re}. The increase in ε_{re} is almost linear with d when d is greater than a certain minimum value.

The effect of superstrate on the characteristic impedance Z_{0s} has also been determined by Das [34]. It is plotted in Figure 5.22. This figure shows that for a given

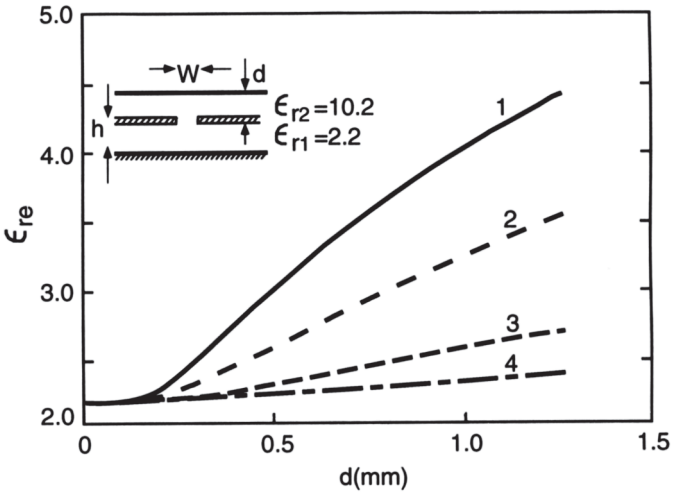

Figure 5.21 Effective dielectric constant of conductor-backed slotline with superstrate with W= 1 mm (1 : h =0.157 cm, f = 10 GHz; 2: h = 0.076 cm, f = 10 GHz; 3: h = 0.157 cm, f = 3 GHz; 4 : h =0.076 cm, f = 3 GHz) (from [34], © 1973 IEEE. Reprinted with permission.)

set of parameters there is a minimum value of superstrate thickness d below which Z_{0s} decreases sharply to small values. This low value of Z_{0s} is interpreted as indicative of onset of leakage, that is, transition from the bound mode to unbound (leaky) mode. The evaluation of the field distribution as a function of d confirms the corresponding field spreading about the slot. Using such studies on field spreading and/or impedance variation, a suitable set of parameters for a conductor-backed slotline can be chosen so that leakage effects are avoided. For example, for the parameters of curve 1 of Figure 5.22, the value of d should be greater than 0.5 mm.

5.5.4 Slotlines with Double-Layered Dielectric

Slotlines on two layers of dielectric and sandwich slot configuration have been studied to introduce flexibility in design [52, 56–58]. The cross-section of these slotlines is shown in Figure 5.23. The sandwich slotline, Figure 5.23(a), confines the fields better in the dielectric layers compared to the single-layer slotline. Therefore, it has a shorter guide wavelength. The double-layered slotline, Figure 5.23(b), may be employed to realize higher values of characteristic impedance compared to single-layer slotlines [58]. The double-layered slotlines have been analyzed using Cohn's transverse resonance method [56, 58] and analysis in spectral domain [57]. The transverse resonance method (discussed in Section 5.2.2) is formulated for the slotline in an enclosure, and the results for open configuration are retrieved when the enclosure dimensions approach infinity. This technique can be extended to any number of dielectric layers around the slot. Numerical results for the guide wavelength and characteristic impedance of these slotlines are available as a function of frequency [58]. Empirical expressions for these characteristics are derived in [59].

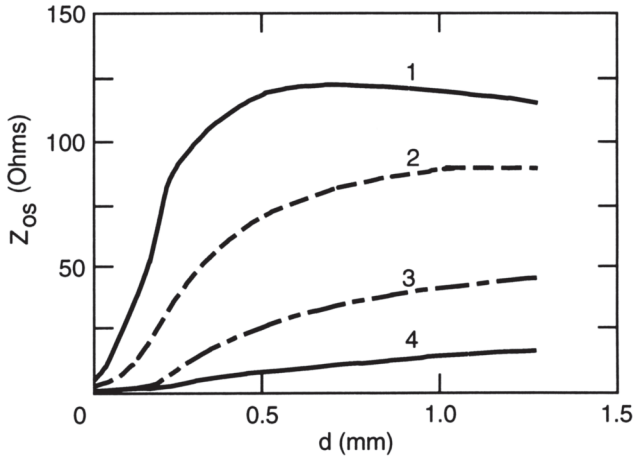

Figure 5.22 Characteristic impedance Z_{0s} for the geometries of Figure 5.21 (from [34], © 1991 IEEE. Reprinted with permission.)

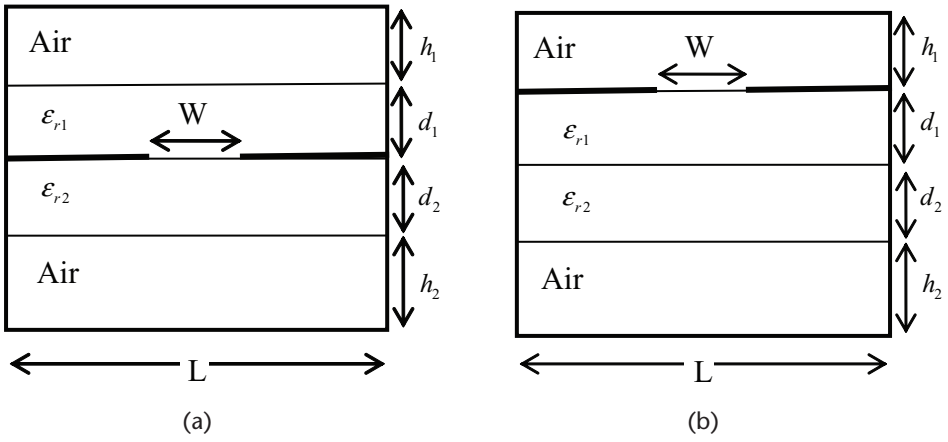

Figure 5.23 Cross-section of double-layered slotline configurations. (a) sandwich slotline and (b) double-layered slotline.

5.6 Slotline Transitions

To test and design slotline circuits it is necessary to have a transition between a slotline and the measuring equipment. A coaxial-to-slotline transition is commonly used for this purpose. Transitions between slotline and other transmission lines are also useful and increase the applications of slotlines. One such transition is slotline-to-microstrip. These two types of transitions are discussed in this section. Slotline-to-CPW transition is discussed in Chapter 7.

5.6.1 Coaxial-to-Slotline Transition

A commonly used coaxial line-to-slotline transition is shown in Figure 5.24(a). It consists of a miniature coaxial line placed perpendicular to and at the end of an

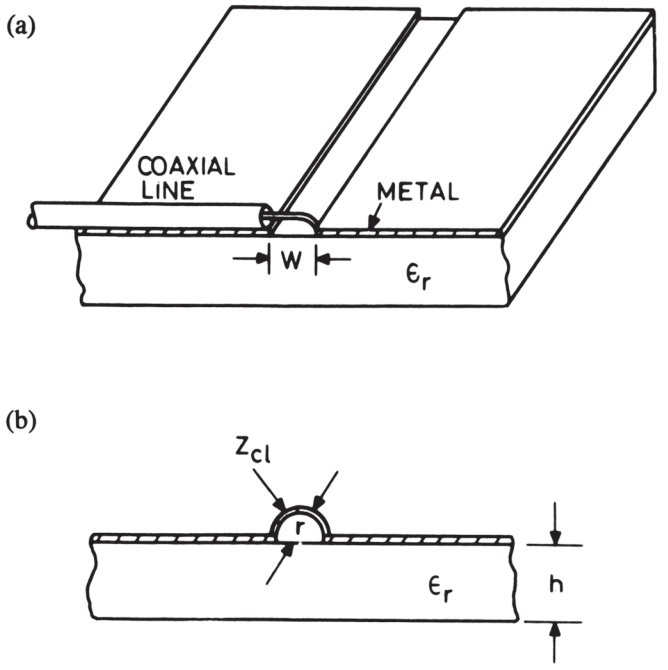

Figure 5.24 A coaxial-to-slotline transition and its analysis model.

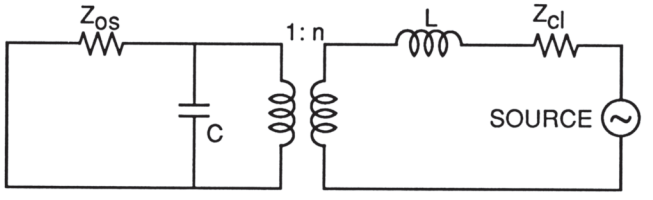

Figure 5.25 Equivalent circuit of the transition shown in Figure 5.24.

open-circuited slotline. The outer conductor of the cable is electrically connected (with solder or epoxy) to the metallization in the left half of the slot plane. The inner conductor is extended over the slot and connected to the metallization on the opposite side of the slot. This transition has been analyzed in [35] by assuming that the inner conductor of the coaxial line has a semicircular shape over the slot as shown in Figure 5.24(b).

An equivalent circuit suggested in [35] for the coax-slot transition of Figure 5.24 is shown in Figure 5.25. The impedances Z_{0s} and Z_d are the characteristic impedances of the slotline and coaxial line, respectively. The fringe capacitance at the open end of the slot is represented by the lumped capacitor C. The inductance presents the self-inductance of the semicircular loop. The transformation ratio can be evaluated approximately by using (5.6), which gives the ratio of the voltage distance r to the voltage across the slot. We have

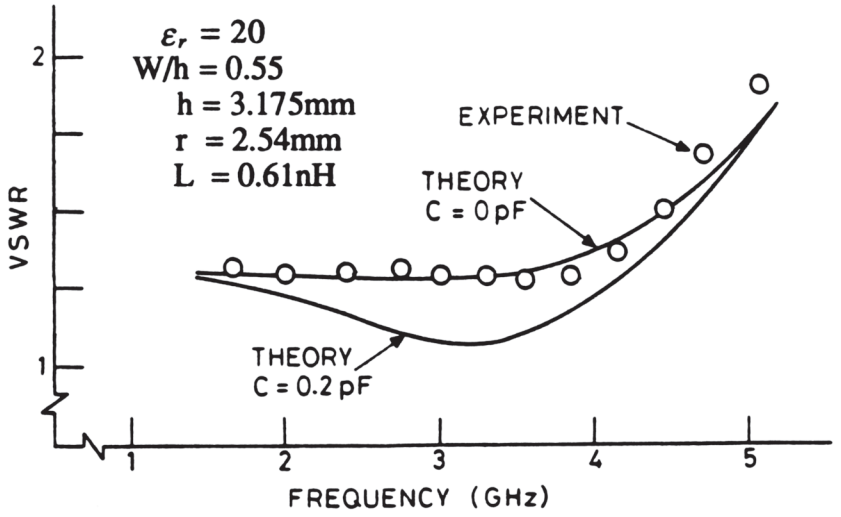

Figure 5.26 Comparison of theoretical and experimental VSWR for coaxial-to-slotline transition (from [35], © 1974 IEEE. Reprinted with permission.)

$$n = \frac{\pi}{2}\left|k_c r H_1^{(1)}(k_c r)\right| \tag{5.56}$$

where k_c is defined by (5.4).

From (5.56), it may be noted that the value of the transformer ratio n decreases with increases in frequency. Thus we can expect the performance of the transition to worsen at higher frequencies.

A comparison between experimental VSWR for a coaxial-to-slotline transition and the values based on the above model is shown in Figure 5.26. This transition has been constructed with a 50-Ω 3.58-mm semirigid coaxial cable that is coupled to a slotline etched from a 3.175-mm-thick substrate with $\varepsilon_r = 20$. The slot impedance is about 75 Ω ($W/h = 0.55$). The measured value of L is found to be 0.61 nH, and the capacitance C has a typical value of 0.2 pF. It is seen that the experimental curve is in reasonable agreement with the theoretical curve for $C = 0$ pF. Also, to achieve this agreement, the value of r used is 2.54 mm, which is about 50 percent greater than the actual height of the inner conductor of the coaxial line above the slot. There are two possible reasons for the lack of any better agreement between the model and the actual performance. First, the inner conductor of the coaxial line does not form a loop of exactly semicircular shape. Second, the Hankel function approximation does not describe accurately the variations of the electric field near the slot [2].

The transition described above has been successfully used in the S-band as it presents a good VSWR (less than 1.15) in the frequency range of 1.65 GHz to 4.0 GHz. A lower VSWR value over a narrow frequency range can be obtained by using a movable short as shown in Figure 5.27. This transition is very useful for feeding and testing slotline circuits.

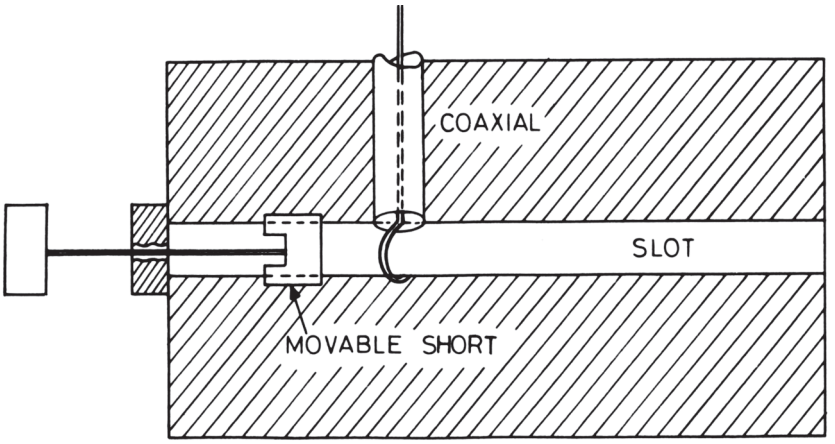

Figure 5.27 Coaxial-to-slotline transition with a movable short.

5.6.2 Microstrip-to-Slotline Cross-Junction Transition

Most of the circuits, wherein a slotline is used, also incorporate microstrip lines. Thus a microstrip-to-slotline transition is desired. Also the fabrication of the microstrip-to-slotline transition can easily be included in the MIC fabrication routine when an arrangement is made for etching the substrate on both sides. This transition has been comprehensively analyzed by many investigators [35–42]. A layout of this transition is shown in Figure 5.28.

The slotline, which is etched on one side of the substrate, is crossed at a right angle by a microstrip conductor on the opposite side. The microstrip extends about one quarter of a wavelength beyond the slot. The transition can be fabricated using the usual photoetching process and is thus easily reproducible. Also, as the microstrip part of the circuit can be placed on one side of the substrate and the slotline part on the other side, this transition makes two-level circuit design possible. Coupling between the slotline and microstrip line occurs by means of the magnetic field (see Figures 1.4(d) and 5.2).

A transmission line equivalent circuit of the transition (Figure 5.28(a)) proposed by Chambers et al. [36] is shown in Figure 5.28(b). The reactance X_{0s} represents the inductance of a shorted slotline (see Section 5.4.1), and C_{0c} is the capacitance of an open microstrip (see Section 3.4.1). Z_{0s} and Z_{0m} are slotline and microstrip characteristic impedances respectively. θ_s and θ_m represent the electrical lengths (quarter-wave at the center frequency) of the extended portions of the slotline and the microstrip, respectively, measured from the reference planes as shown in Figure 5.28(a). The transformer turns ratio n describes the magnitude of the coupling between the microstrip and slotline.

For further analysis the equivalent circuit in Figure 5.28(b) may be redrawn as in Figure 5.28(c). Here,

$$jX_s = Z_{0s}\frac{jX_{0s} + jZ_{0s}\tan\theta_s}{Z_{0s} - X_{0s}\tan\theta_s} \tag{5.57}$$

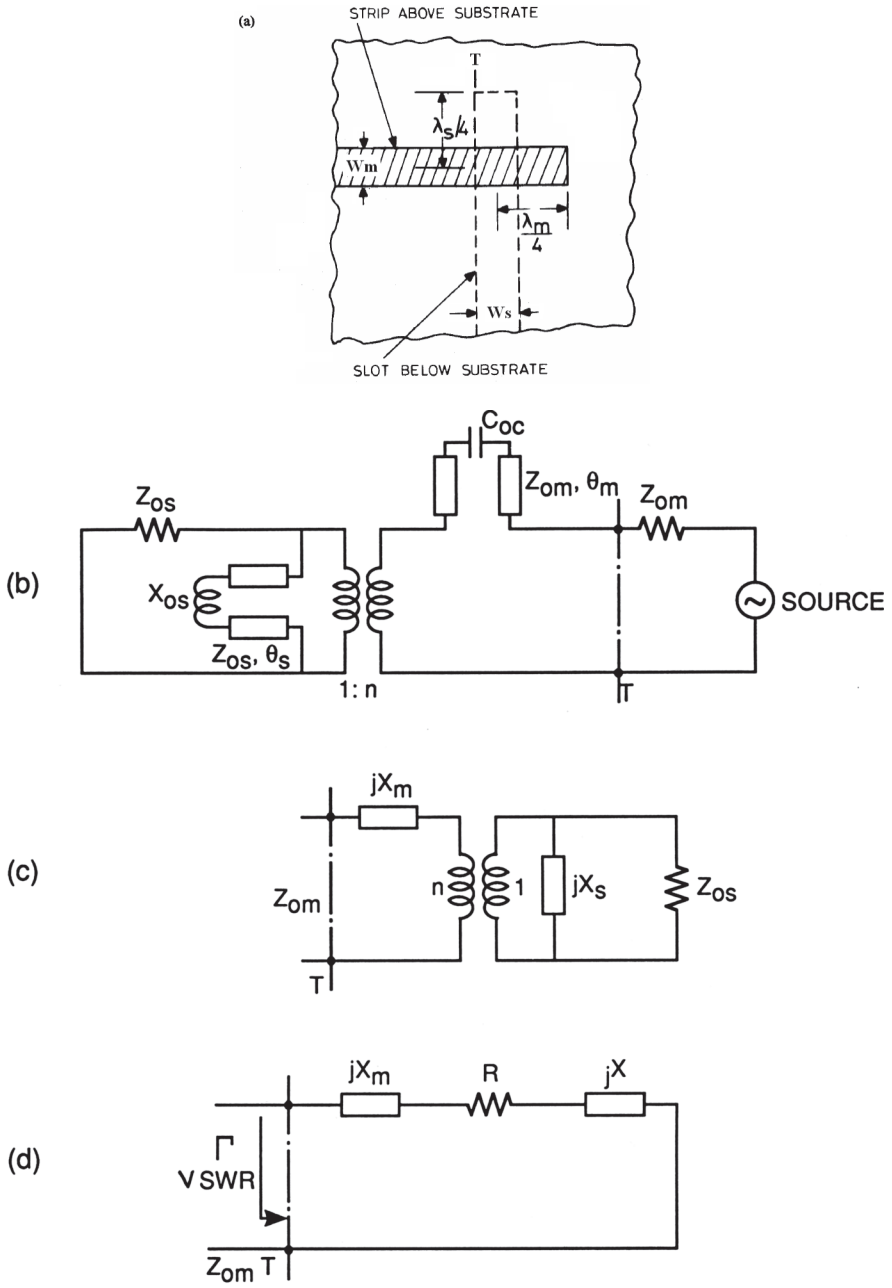

Figure 5.28 (a) Microstrip-to-slotline transition; (b) transmission line equivalent circuit for the transition of (a); (c) reduced equivalent circuit of (b); and (d) transformed equivalent circuit of (c).

and

$$jX_{\mathrm{m}} = Z_{0\mathrm{m}} \frac{1/j\omega C_{0\mathrm{c}} + jZ_{0\mathrm{m}} \tan\theta_{\mathrm{m}}}{Z_{0\mathrm{m}} + \tan\theta_{\mathrm{m}}/\omega C_{0\mathrm{c}}} \tag{5.58}$$

After transformation to the microstrip side, the equivalent circuit of Figure 5.28(c) reduces to that shown in Figure 5.28(d). In this circuit,

$$R = n^2 \frac{Z_{0s} X_s^2}{Z_{0s}^2 + X_s^2} \tag{5.59}$$

and

$$X = n^2 \frac{Z_{0s}^2 X_s}{Z_{0s}^2 + X_s^2} \tag{5.60}$$

Finally, the reflection coefficient Γ is given by

$$\Gamma = \frac{R - Z_{0m} + j[X_m + X]}{R + Z_{0m} + j[X_m + X]} \tag{5.61}$$

From the above analysis one can determine the characteristic impedance of the slotline Z_{0s} needed to match the microstrip line impedance Z_{0m}.

In the approximate analysis reported by Knorr [35] the transformer turns ratio n is determined from a knowledge of the slotline field components as

$$n = V(h)/V_0 \tag{5.62}$$

where

$$V(h) = -\int_{-b/2}^{b/2} E_y(h)\, dy \tag{5.63}$$

V_0 is the voltage across the slot and $E_y(h)$ is the electric field of the slotline on the other surface of the dielectric substrate. Limits of integration in (5.63) correspond to the locations of electric (or magnetic) walls in Cohn's analysis discussed in Section 5.2.2 (see Figure 5.4). From Cohn's analysis $E_y(h)$ may be written as

$$E_y(h) = -\frac{V_0}{b}\left\{\cos\frac{2\pi u}{\lambda_0}h - \cot q_0 \sin\frac{2\pi u}{\lambda_0}h\right\} \tag{5.64}$$

where

$$q_0 = \frac{2\pi u}{\lambda_0}h + \tan^{-1}(u/v) \tag{5.65}$$

$$u = [\varepsilon_r - (\lambda_0/\lambda_s)^2\}^{1/2} \qquad v = \{(\lambda_0/\lambda_s)^2 - 1\}^{1/2} \tag{5.66}$$

Yang and Alexopoulos [22], Das [37], and Antar et al. [38] have analyzed the microstrip-to-slotline cross-junction transition comprehensively. The analysis in [22] includes the effects of (i) radiation and surface waves excited by the cross-junction, (ii) the line discontinuities, and (iii) all the mutual couplings due to the dominant and higher order modes of each line. Das [37] has derived a simple closed-form expression for turns ratio n after making a number of approximations in the analysis. This expression is given as

$$n = \frac{J_0(k_{es}W_m/2)J_0(k_{em}W_s/2)}{k_{es}^2 + k_{em}^2} \cdot \left[\frac{k_{em}^2 k_2 \varepsilon_r}{k_2\varepsilon_r \cos k_1 h - k_1 \sin k_1 h} + \frac{k_{es}^2 k_1}{k_1 \cos k_1 h + k_2 \sin k_1 h}\right] \tag{5.67}$$

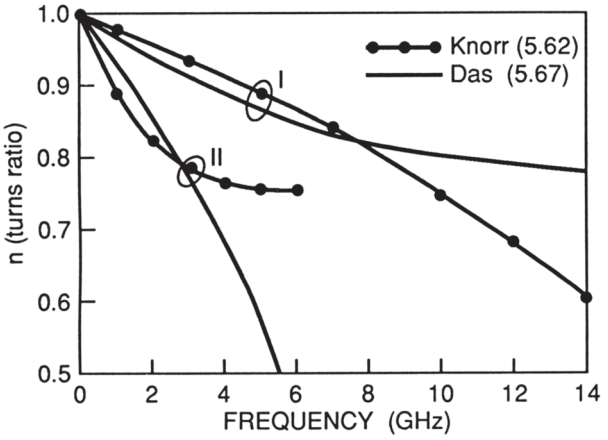

Figure 5.29 Comparison of transformer turns ratio n versus frequency for microstrip-slotline cross-junction obtained from (5.62) and (5.67). Curve I : h 0.3175 cm, ε_r =20, W_m = 0.157 cm, W_s = 0.206 cm; Curve II : h = 0.12 cm, ε_r =10.2, W_m = 0.12 cm, W_s = 0.11 cm (from [37], © 1995 IEEE. Reprinted with permission.)

where $J_o(\bullet)$ is the zeroth-order Bessel function and

$$k_1 = \sqrt{\left|k_0^2\varepsilon_r - k_{es}^2 - k_{em}^2\right|} = k_0\sqrt{\left|\varepsilon_r - \varepsilon_{res} - \varepsilon_{rem}\right|}$$

$$k_2 = k_0\sqrt{\left|\varepsilon_{res} + \varepsilon_{rem} - 1\right|}$$

$$k_{es} = k_0\sqrt{\varepsilon_{res}} \qquad k_{em} = k_0\sqrt{\varepsilon_{rem}}$$

Here, ε_{rem} and ε_{res} are the effective dielectric constants and W_m and W_s are the widths of the microstrip line and the slotline, respectively. Expression (5.67) depends on the microstrip parameters (W_m, ε_{rem}) as well as the slotline parameters (W_s, ε_{res}), whereas the expression (5.62) depends on the slotline parameters only. Das [37] has given an expression for n for a multilayered configuration also in terms of Green's function. The value of n obtained from (5.67) is compared to that obtained from (5.62) in Figure 5.29 for two sets of parameters [37]. It is observed from this figure that the results are comparable at lower frequencies, with $n = 1$ at dc ($f \approx 0$). However, there is a significant deviation at higher frequencies that suggests the inaccuracy of Knorr's analysis for higher frequencies where higher order modes, surface waves, and radiation effects become important.

A comparison of VSWR between the measurements of [35], the transmission line circuit model of Figure 5.28(b), and theoretical values of [22] is shown in Figure 5.30. Again, the agreement is good between the comprehensive analysis and circuit model for lower frequencies and poor for higher frequencies. The reason appears to be the same as discussed earlier for turns ratio n. The measured value of VSWR in Figure 5.30 shows a wider bandwidth than that of either the circuit model or the analytical results in [22]. It is suggested in [22] that the measured value of VSWR is very much influenced by nonideal match load, the coaxial-to-microstrip line transition, and substrate losses. Antar et al. [38] have used a slightly different equivalent circuit for the transition. Their theoretical results are found to have better agreement with the measurements of Knorr [35].

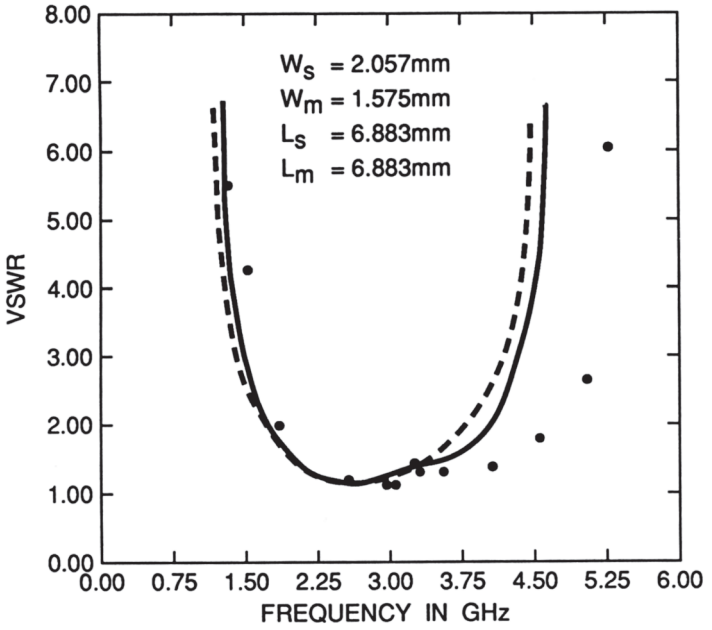

Figure 5.30 Comparison of VSWR versus frequency for microstrip-to-slotline transition, $\varepsilon_r = 20$ and $h = .3.175$ mm (____transmission line circuit model, ...measurement [34], - - - - theory [22]) (from [22], © 1988 IEEE. Reprinted with permission.)

Bandwidth Improvement

Bandwidth limitation of the cross-junction transition results mainly from the frequency dependence of X and X_m (Figure 5.28(d)). These reactances in turn depend on the stub length and turns ratio. A short-circuited microstrip will minimize X_m, and an open-circuited slotline will minimize X. Alternatively, stub reactances can be so designed that there is a mutual cancellation of X and X_m and $R = Z_{0m}$. To achieve this condition various investigators have tried different approaches. Some of these are described next.

In the transition developed by Robinson and Allen [9] the microstrip is terminated in a quarter-wave radial stub as shown in Figure 5.31(a). For this transition, a VSWR value less than 1.10 is obtained from 8.0 GHz to 10.0 GHz (20 percent bandwidth). Chramiec [24] has terminated the slotline in a radial stub, and the microstrip stub is a combination of a radial section and a rectangular section as shown in Figure 5.31(b). Reactances X and X_m are designed to cancel each other (Figure 5.32) when the transition is developed on a 1.5-mm-thick alumina substrate, with $\alpha = 60°$ for the radial slotline stub, $W/h = 0.2$, $W_r = 7.5$ mm, and $\ell_r = 6.5$ mm. The measured VSWR = 1.5 bandwidth of two cascaded transitions separated by a slotline section of 12 mm is found to be two octaves from 1.5 GHz to 6 GHz. This is plotted in Figure 5.33. When this transition was scaled to a 0.7-mm-thick alumina substrate, the VSWR was found to be below 1.45 in the frequency range 2 GHz to 12.7 GHz [24]. The cross-junction transition on an anisotropic substrate has been studied by Podcameni and Coimbra [39].

Schuppert [40] has carried out an extensive study on the transmission line equivalent circuit of the cross-junction. First of all, he simplified the equivalent

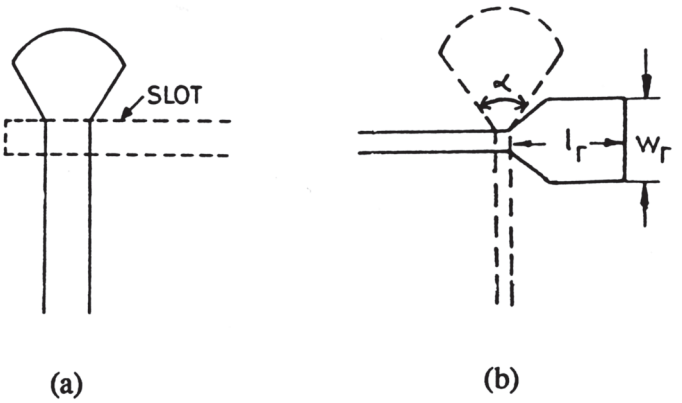

Figure 5.31 Two different types of microstrip slotline transition with nonuniform stubs: (a) microstrip stub and (b) microstrip and slotline stubs.

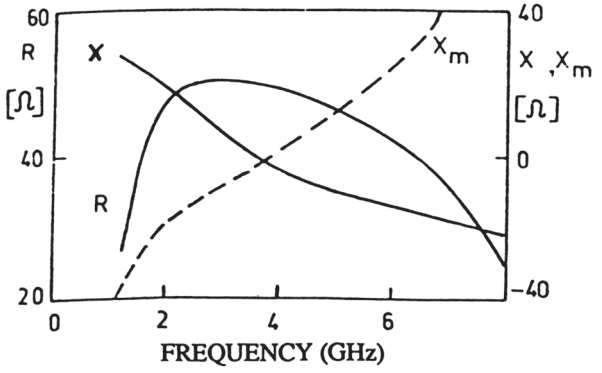

Figure 5.32 Variation of X, X_m, and R with frequency for the transition in Figure 5.31(b) (from [24], © 1989 IEEE. Reprinted with permission.)

circuit of Figure 5.28 by assuming $n = 1$ and by neglecting the open-circuit and short-circuit discontinuity reactances. Using this simplified equivalent circuit, he obtained a simple expression for the insertion loss of the transition as a function of characteristic impedance of the microstrip and slotline stubs assuming that the characteristic impedance of the slotline is the same as that of the microstrip, that is, 50 Ω. The simple analysis of the equivalent circuit shows that the bandwidth of the transition increases with increasing characteristic impedance of the slotline stub and decreasing characteristic impedance of the microstrip stub. Moreover, the bandwidth is at a maximum when the characteristic impedance of the microstrip stub is 2.618 times the characteristic impedance of the slotline stub. Experiments were carried out by Schuppert on uniform and nonuniform impedance stubs. The nonuniform stubs were realized in the form of circular geometry of various diameters. Theoretical and measured transmission coefficient for such a transition on alumina substrate of 0.635 mm thickness is compared in Figure 5.34. The agree-

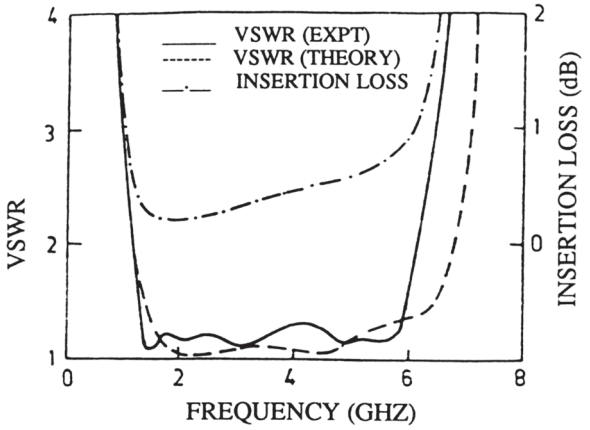

Figure 5.33 Comparison of theoretical VSWR characteristic of a single microstrip-slotline transition and experimental VSWR performance of two cascaded transitions: $h = 1.5$ mm, $\varepsilon_r = 9.8$ (from [24], © 1989 IEEE. Reprinted with permission.)

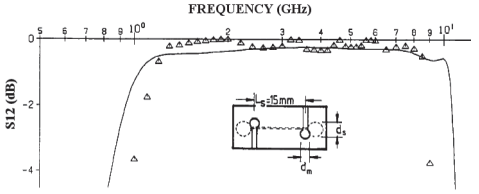

Figure 5.34 Transmission coefficient of a cascade of two microstrip-to-slotline transitions separated by a slotline of length 15 mm, $d_m = 5$ mm, and $d_s = 6$ mm [theoretical (____) and measurements (ΔΔΔ)] (from [40], © 1988 IEEE. Reprinted with permission.)

ment is seen to be fairly good. The cascade connection of two transitions has a bandwidth of approximately one decade. The bandwidth of a single transition will be larger than this. To reduce interaction between the two circular stubs, especially when the diameter increases, it has been suggested that triangular or radial stubs may be used instead [40].

The analysis by Schuppert makes a number of simplifying assumptions that do not appear to be reasonable particularly for a decade bandwidth transition. It appears that mutual cancellation of discontinuity reactances occurs over a broad bandwidth in this case. For example, a circular slot behaves like a resonant circuit [24]. Similarly, a circular microstrip patch will also behave like a resonant circuit, with the resonant frequency adjustable by a proper selection of its diameter. Microstrip-to-slotline cross-junction transition with circular stubs was also studied by de Ronde [43]. The configuration of this transition is different from that in Figure 5.34. In this case, the slotline runs below the microstrip in the form of a spiral. The transition employs a short circuit at the center of a microstrip circular stub. The reported VSWR of this transition is less than 1.1 in the 1.0-GHz to 10-GHz frequency range. A transition with a microstrip short-circuited at the junction has also been studied [40]. It was found to have a larger bandwidth than the

open circuited microstrip stub, but its implementation needs a via-hole grounding that may sometimes be difficult. A microstrip-to-slotline transition using a six-port junction has been described by Schiek and Kohler [44]. Although this transition has good performance between 2 GHz to 9 GHz, it needs more substrate space.

5.7 Slotline Applications

It was mentioned in Section 5.1 that slotlines can be incorporated in microstrip circuits by etching the slotline circuit in the ground plane of the microstrip circuit. This type of hybrid combination has a number of advantages. Most of these advantages are due to the balanced (slotline) and unbalanced (microstrip line) natures of the transmission lines used. Many circuit functions that were not possible or easily realizable in microstrip form can now be implemented. These include short-circuit, series T-junction, balanced circuits, and tight coupling. In addition to these, flexibility in circuit design is introduced, for example, series and parallel device mounting, wider range of line impedance, elimination of line crossings, and substrate space saving, leading to better integration. These features have given rise to some novel circuits like hybrid branchline couplers, magic-T, and balanced circuits in printed form. The hybrid circuits based on microstrip-slotline, microstrip-CPW, and microstrip-slotline-CPW combinations are also called double-sided MICs [30].

5.7.1 Circuits Using T-Junctions

T-junctions and their variations occur very frequently in slotline-microstrip circuits or double-sided MICs. A slotline-microstrip T-junction can be obtained by allowing the microstrip line to run indefinitely in the microstrip-to-slotline transition of Figure 5.28. The resulting T-junction will be as shown in Figure 5.35(a). The equivalent circuit of this T-junction can be obtained from the equivalent circuit of Figure 5.28(b) and will be as shown in Figure 5.35(b). Assuming $n = 1$ simplifies this circuit to that given in Figure 5.35(c).This is the equivalent circuit of a power divider with the slotline appearing in series with the two arms of a microstrip line. Therefore, this T-junction behaves like a series-T. Further, if the slotline is terminated in its matched load, the equivalent circuit will reduce to that shown in Figure 5.35(d), where $R_s = n^2 Z_{0s}$.

Another T-junction can be obtained when the slotline of Figure 5.28 is not terminated in an open circuit but is allowed to run indefinitely. In this case the T-junction will behave like a parallel T-junction, that is, the slotline arms and the microstrip arm of the T-junction are connected in parallel to each other. A configuration of this T-junction, the electric field distribution in the slotline, and the equivalent circuit are shown in Figure 5.36 [30, 45].

Series and parallel T-junctions can be combined to realize magic-T or 180° hybrids, as is discussed next.

Magic-T/180° Hybrid. Magic-T in a microstrip-slotline configuration has been studied by de Ronde [43], Aikawa and Ogawa [30, 45], and Chua [46]. Aikawa and Ogawa have described three different types of magic-T. Two of these magic-T

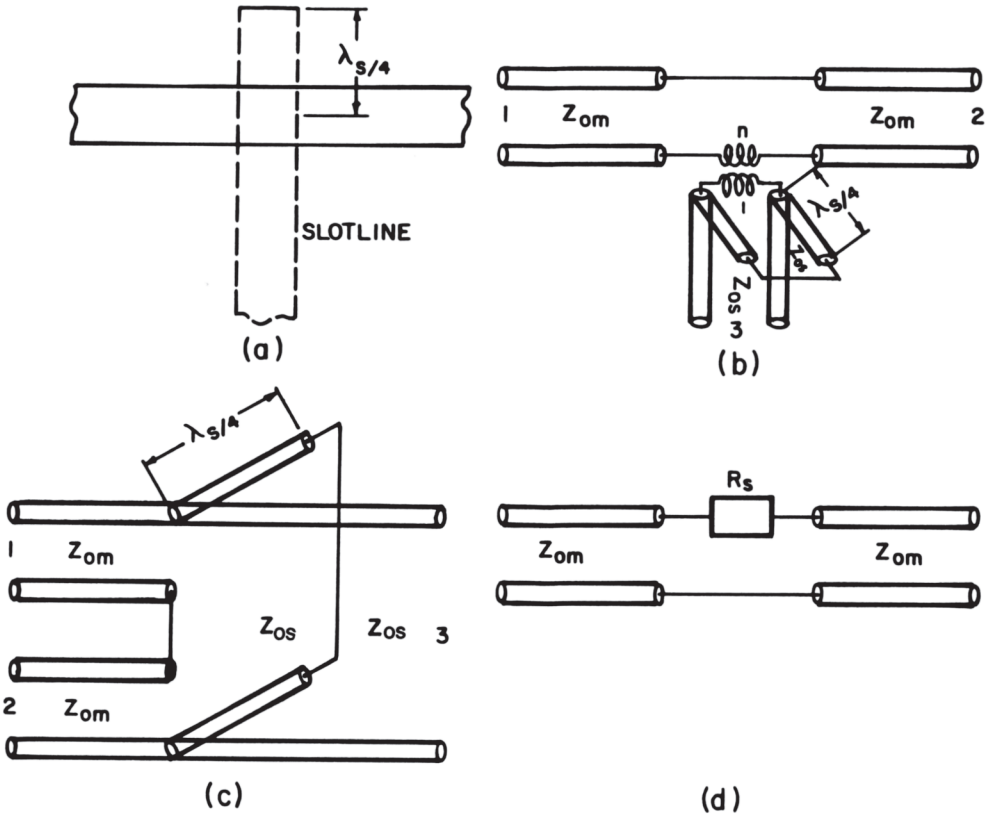

Figures 5.35 Slotline-microstrip series T-junction: (a) schematic; (b) equivalent circuit of (a); (c) equivalent circuit of (a) for $n = 1$; and (d) equivalent circuit of (b) when port 3 is terminated in matched load.

use microstrip lines, slotlines, and coupled slotlines. Another one uses a microstrip line and a slotline only. The three configurations are shown in Figure 5.37. In this figure solid lines represent slotlines and dotted lines represent the microstrip lines on the reverse side of the substrate. Ports Ⓔ and Ⓗ correspond to the *E*- and *H*-arms of a conventional waveguide magic-T, respectively, and ports ①, and ② are the remaining ports. Let us call these magic-T as *microstrip type, slotline type*, and *T-junction type* based on the kinds of transmission lines connected to the coupled slotlines for (a) and (b) and the use of T-junction only for (c). The slotline type magic-T can be used up to millimeter-wave frequencies because it does not need via-holes for grounding. The coupling behavior of *microstrip* and *slotline-types* magic-T is the same in principle. Therefore, we shall only explain the behavior of magic-T in Figure 5.37(a, c).

Figure 5.38 describes the in-phase coupling and out-of-phase coupling behaviors of a *microstrip-type* magic-T. Here, we have drawn the electric field distribution in the slotlines to explain the coupling. Let us first consider Figure 5.38(a). A signal fed to the microstrip port Ⓗ is converted to the slotline mode and gets divided equally into two quarter-wavelength slotlines, and the direction of the

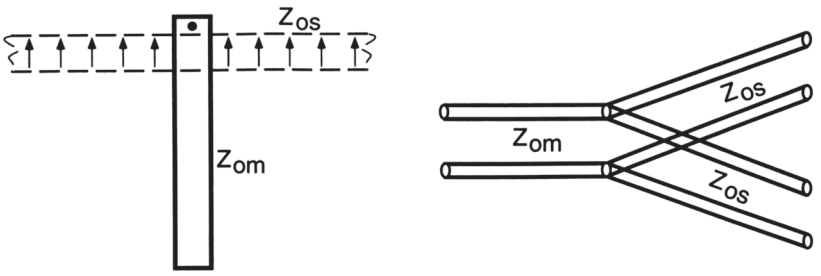

Figure 5.36 Schematic and equivalent circuit of a microstrip-slotline parallel T-junction.

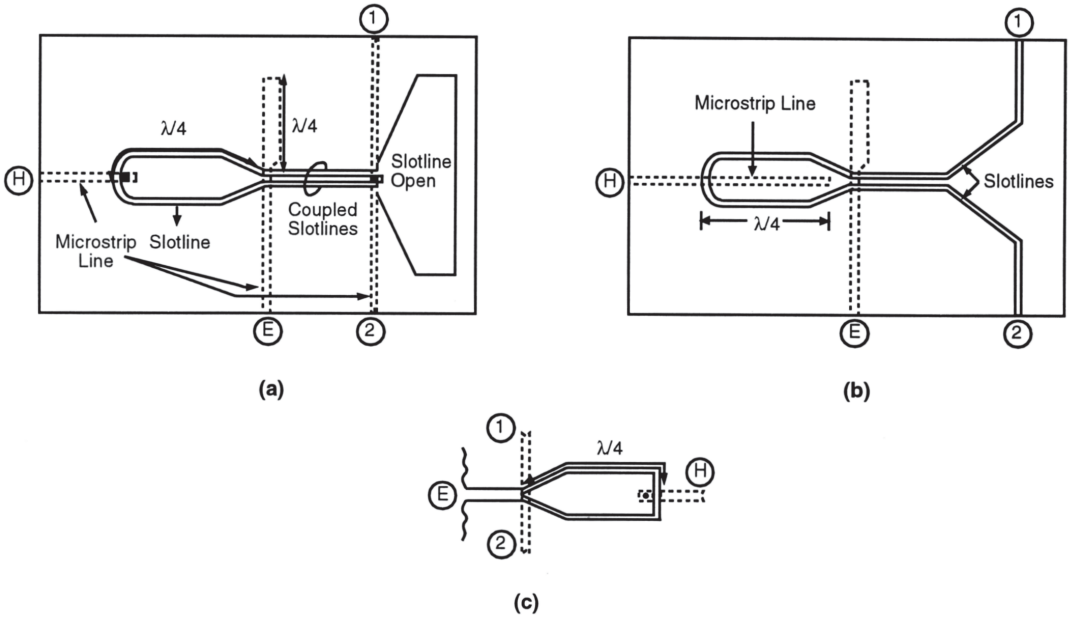

Figure 5.37 Three types of magic-T in a microstrip-slotline configuration: (a) microstrip type; (b) slotline type; and (c) T-junction type (from [30, 45], © 1989, 1980 IEEE. Reprinted with permission.)

electric field is such that the two slotlines are in parallel (very similar to *H*-plane T-junction in the waveguide). These signals cancel each other while coupling to the microstrip port Ⓔ. Therefore, port Ⓔ is the uncoupled port. Then, these signals propagate through the coupled slotlines portion as an odd mode. They get further divided at the microstrip junction and appear as in-phase signals out of the microstrip ports ① and ② because of the even symmetry of the structure and the electric fields.

In Figure 5.38(b), a signal fed to port Ⓔ is converted to the even mode of the coupled, slotlines and thereafter emerges as 180° out-of-phase signals through the ports① and ②. A signal from the Ⓔ port does not couple to the Ⓗ port because

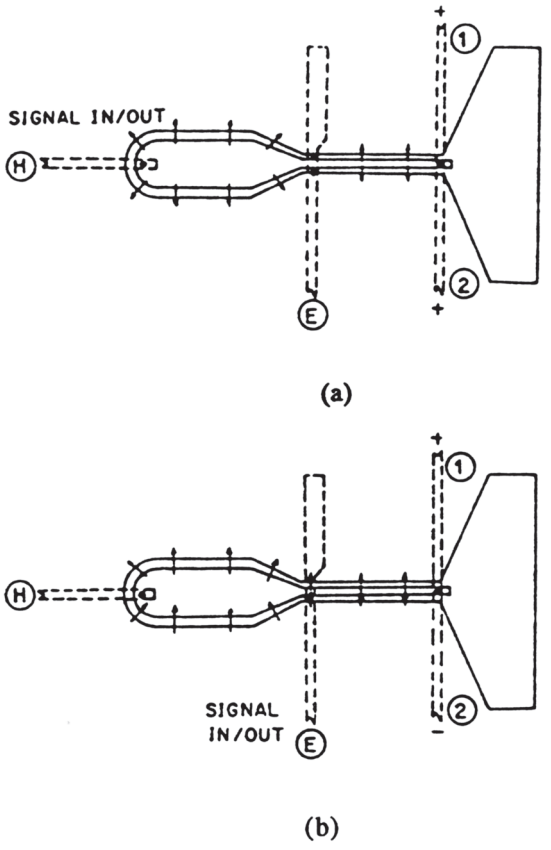

Figure 5.38 Coupling behavior of a microstrip-type magic-T: (a) in-phase coupling and (b) out-of-phase coupling (from [45], © 1980 IEEE. Reprinted with permission.)

the two quarter-wave slotlines are connected in parallel to the microstrip and the electric fields are out-of-phase in these slotline sections.

An equivalent circuit of the microstrip type magic-T is given in Figure 5.39. It is seen that the equivalent circuit is symmetrical with respect to ports Ⓔ and Ⓗ. Consequently, two-port calculations can be used to analyze the four-port circuit. The two-port equivalent circuits for the in-phase and out-of-phase excitations of magic-T are given in Figure 5.40. The analysis of a cascade of two-port circuits can be carried out using the *ABCD* matrix. Theoretical and experimental performances of this magic-T have been calculated. Measured results for a magic-T designed at a center frequency of 6 GHz are plotted in Figure 5.41. The substrate used is alumina with a thickness of 0.635 mm and $\varepsilon_r = 9.6$. All the port impedances are 50 Ω. The coupled slotline is designed such that $Z_{even} = 35.4\ \Omega\ (= Z_0/\sqrt{2})$ and $Z_{odd} = 63.6\ \Omega\ (= Z_H/\sqrt{2})$ because the slotline is designed to be 90 Ω. The open microstrip stub impedance Z_E is designed to be 40 Ω. It may be observed from the figure that the out-of-phase coupling Ⓔ – ①,② bandwidth is very wide. The in-phase coupling Ⓗ – ①, ② is almost flat and can transmit even dc signals. The isolation between the ports Ⓔ and Ⓗ is greater than 30 dB and between ports ① and ② is 25 dB at the center frequency. The insertion loss of the in-phase coupling is 0.7 dB and is 0.9

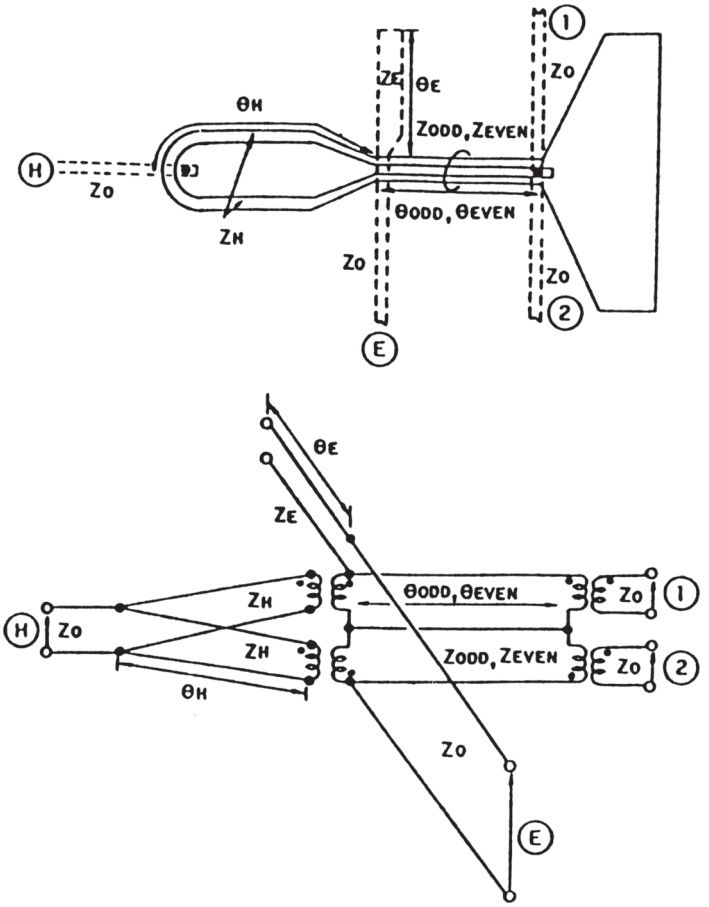

Figure 5.39 Schematic and equivalent circuit of a microstrip-type magic-T (from [45], © 1980 IEEE. Reprinted with permission.)

dB for out-of-phase coupling at the center frequency. The insertion loss is caused mostly by the conductor loss of the transmission lines. The coupling imbalance between ports ① and ② is a maximum 0.3 dB in amplitude and 2.1° in phase over an octave band.

The magic-T described above has a number of practical applications because of the convenient location of the ports. The *E*- and *H*-ports are located on the same side and opposite to the other two ports. This port configuration is quite different from that of a conventional 180° hybrid, such as a rat race. As a result of this, balanced type circuits, such as balanced mixers and balanced modulators, can be implemented with no crossing of transmission lines, which causes signal leakage between the lines and deterioration of the performance.

The magic-T of Figure 5.37(c) can be analyzed in the same manner as the other two. The electric field distributions for out-of-phase excitation and in-phase excitation are shown in Figure 5.42. The theoretical performance can be calculated using the two-port circuit approach described earlier. Theoretical and measured performances of this type of magic-T are compared in [30]. However, the bandwidth of this magic-T is narrower than that of the microstrip type described earlier.

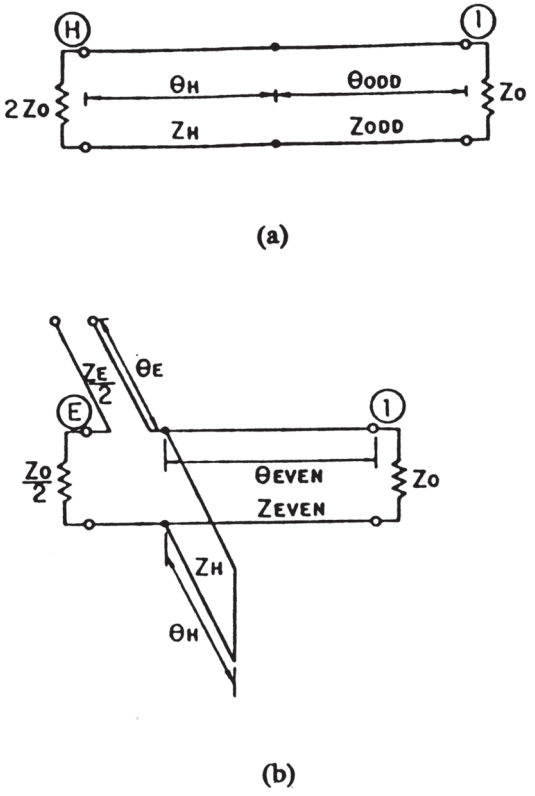

Figure 5.40 Two-port equivalent circuits for the analysis of microstrip type magic-T: (a) in-phase excitation and (b) out-of-phase excitation (from [45], © 1980 IEEE. Reprinted with permission.)

The configuration of de Ronde's magic-T is shown in Figure 5.43. It consists of a series T-junction and a parallel T-junction. The parallel T-junction is realized in the form of a microstrip T. A linear taper in the microstrip line is introduced in this T to act as an impedance transformer. In an experimental model tested at 2 GHz to 4 GHz on 2.54-cm by 2.54-cm alumina substrate the following performance has been reported [43]:

Isolation between shunt and series arm	≥	40 dB
Isolation between collinear arms	≥	20 dB
Imbalance between opposite arms	≤	0.3 dB
Insertion loss between any two ports	≅	3.2 dB

A different type of magic-T, studied by Chua [46], is described in Section 5.7.2.

Balanced Microstrip-Slotline Ciruits [30]. Microstrip-slotline T-junctions have also been used to implement a number of balanced circuits. These include the balanced PSK modulator, phase detector, mixer, ASK modulator, and balanced frequency doubler. The heart of these balanced circuits is the balance-to-unbalance transition or balun between slotline (balanced line) and microstrip line (unbalanced line). A configuration of this balun is shown in Figure 5.44. There are a number of useful features of this balun. These are: (i) very good isolation between the balanced line and the

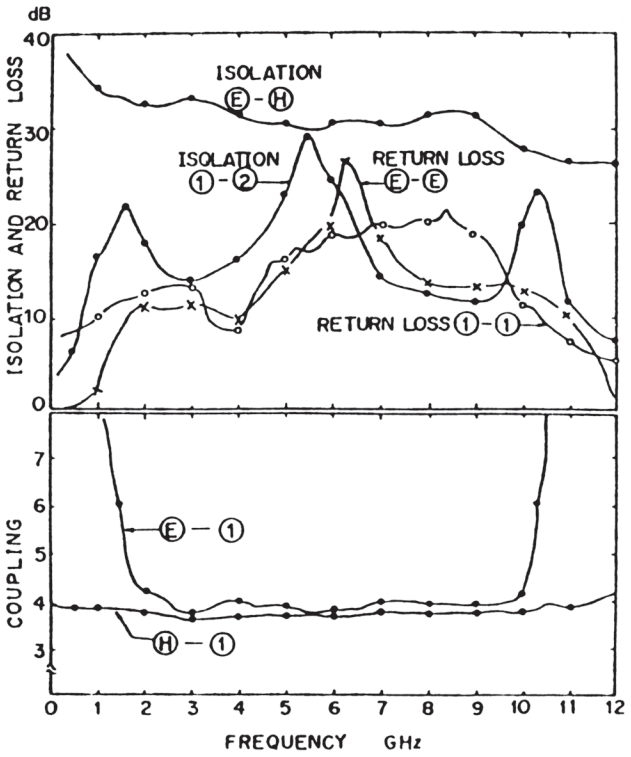

Figure 5.41 Experimental performance of a microstrip-type magic-T designed for the center frequency of 6 GHz (from [45], © 1980 IEEE. Reprinted with permission.)

unbalanced line over a wide range of frequency due to the symmetric configuration, (ii) beam-lead devices can easily be mounted in the slotline portion of the balun, and (iii) a dc return path is not required because of the use of the slotline.

The balun, Figure 5.44, consists of a slotline T-junction, two quarter-wave slotlines, and a slotline-to-microstrip T-junction. In the slotline-to-microstrip T-junction the microstrip end is connected to the slotline by means of a through hole conductor, as shown in the Figure 5.44(a). Alternatively, the microstrip stub can be a quarter-wave long and terminated in an open circuit as shown in Figure 5.44(b). This configuration of a balun is more useful. In this circuit a wire is bonded on the inside conductor of the slotline to supply the modulating signal or to obtain the IF signal. The wire port (or IF port) is isolated from the rf circuit because of the concentration of rf electromagnetic fields in the slotlines and the high series inductance of the wire. The low frequency signals such as the IF and modulating signals do not couple to the microstrip line because (i) a microstrip line does not touch the inside conductor where the wire is bonded and (ii) the quarter-wave open-circuited microstrip line acts as a bandpass filter. Isolation between the rf ports, that is, microstrip line and input slotline, can be understood from the electric field distribution described earlier for the magic-T (Figure 5.42). Consequently, the three ports shown in Figure 5.44 for the balun are isolated from each other without the need for filters.

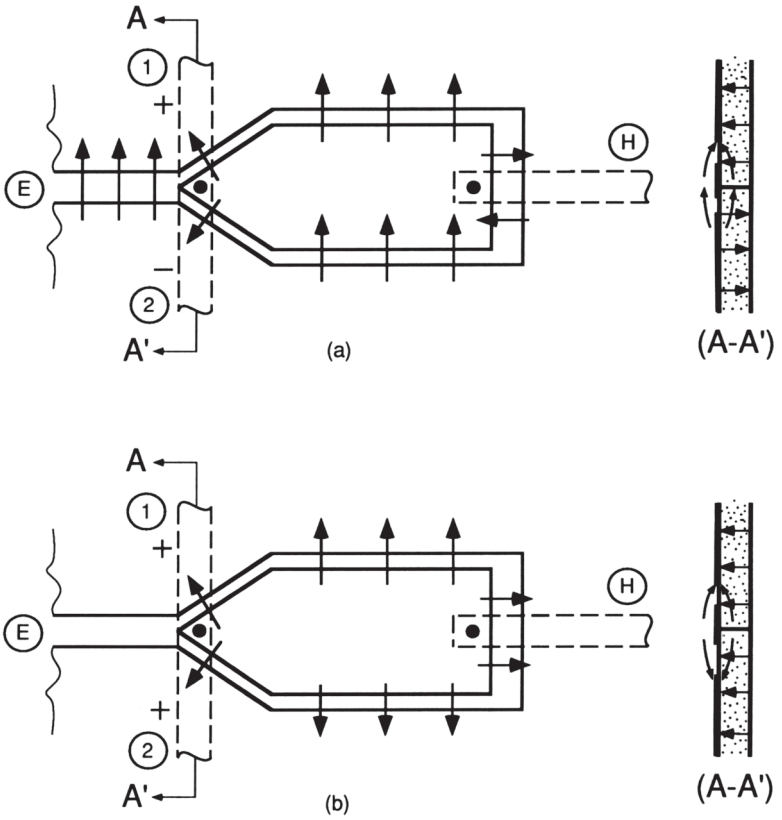

Figure 5.42 Electric field distributions for the T-junction type of magic-T: (a) out-of-phase excitation and (b) in-phase excitation (from [45], © 1980 IEEE. Reprinted with permission.)

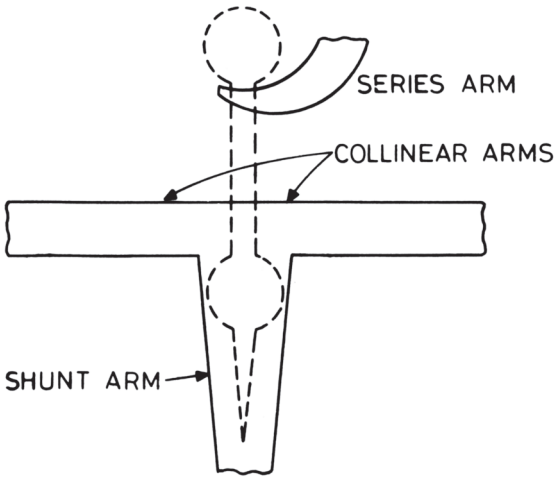

Figure 5.43 Configuration of de Ronde's magic-T (from [43], © 1970 IEEE. Reprinted with permission.)

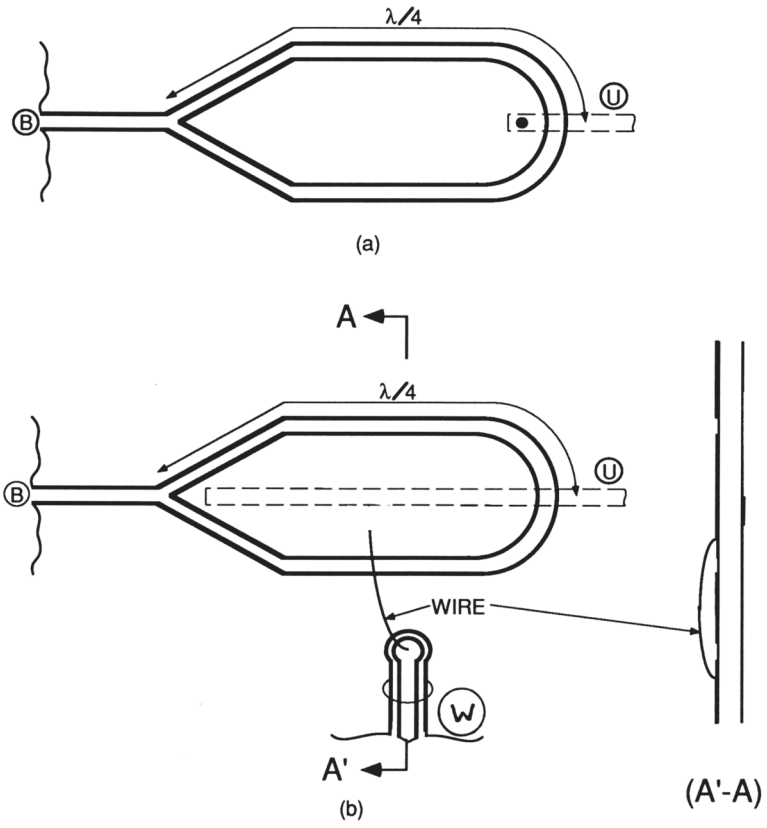

Figure 5.44 Some more configurations of microstrip slotline balun: (a) balun with a shorted microstrip stub and (b) balun with a wire port and an open microstrip stub (from [30], © 1989 IEEE. Reprinted with permission.)

The equivalent circuit of the balun in Figure 5.44(b) is shown in Figure 5.45. Here, the T-junctions are represented by ideal transformers. It may be observed that the slotline T-junction is represented by a series-T circuit and the slotline-microstrip T-junction by a parallel-T circuit. It should be remembered that the microstrip-slotline T-junction with microstrip through ports, described earlier, behaved like a series-T circuit. Applications of the balun are described next.

Figure 5.46 shows some examples of balanced microwave circuits [30]. The circuit of Figure 5.46(a) can be used as a PSK modulator, phase detector, or a mixer. When it is used as a PSK modulator the carrier propagates along each slotline according to the polarity of the modulating pulse. If it is used as a mixer, an IF signal is obtained at the wire port. The isolation between the RF and LO ports is limited by the mismatch between the chartcteristics of two diodes. In the fequency doubler circuit of Figure 5.46(b) the diodes are mounted in such a manner that they are forward biased when dc is applied through the wire. The length of the open-circuited microstrip stub is $\lambda/8$ at the input frequency f_0. When the input signal is applied to the port Ⓑ it gets split equally into two parts and is supplied out of phase to the two diodes. The input signal and its odd-harmonics propagate out of phase along the $\lambda/4$ slotlines and nullify each other at the microstrip-slotline junction. Thus, all odd harmonics are decoupled from the output port Ⓤ. However, the second

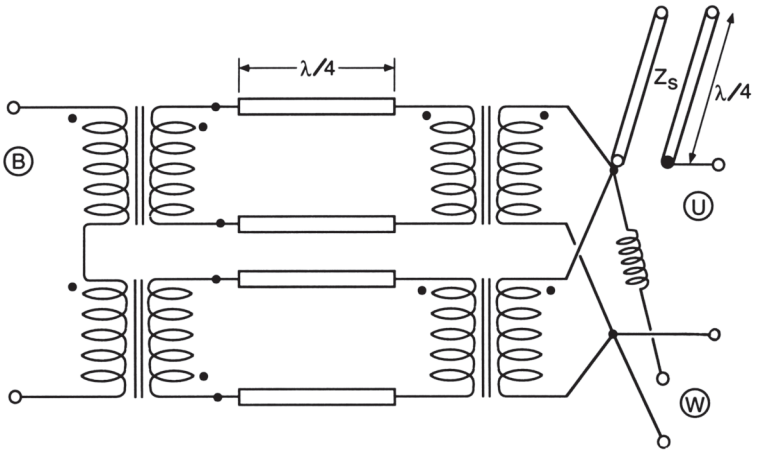

Figure 5.45 Equivalent circuit of the balun in Figure 5.44(b) (from [30], © 1989 IEEE. Reprinted with permission.)

harmonic $2f_0$ as well as higher order even harmonics are generated in phase by the diodes. The second harmonic signal is then obtained from the output port Ⓤ, the $\lambda/8$ microstrip stub playing the role of a bandpass filter at $2f_0$. The circuit of Figure 5.46(c) can be used as an ASK modulator. In this circuit the inside metallization of the slotlines is divided into two parts so that dc bias to the diodes can be applied independently of each other in order to generate the ASK signal. In principle, other devices such as MESFETs can be used in these circuits in place of diodes.

5.7.2 Circuits Using Wideband 180° Phase Shift

When two microstrip-to-slotline transitions are connected back-to-back as shown in Figure 5.47(a), an additional 180° phase shift is introduced in the signal path. This can be explained qualitatively by considering the **E**-field distribution associated with the microstrip-to-slotline transition. Referring to Figure 5.47(b), we note that the E-field in the input microstrip line (near the transition) is in the $-y$-direction. This produces a slotline wave with the E-field in the x-direction. At the second transition an x-directed component of **E** will cause the **E**-field in the output microstrip to lie in the y-direction. Thus, in addition to the phase change introduced by the line length, the **E**-field direction changes from $-y$, to y, which amounts to an equivalent 180° phase change. This phase change is independent of frequency (at least in a first-order analysis) and can thus be used in wide-band circuits. Its application in a rat-race circuit is now discussed.

Rat-Race Hybrid. The usual microstrip rat-race circuit shown in Figure 5.48(a) consists of a $3\lambda/2$ microstrip ring with the four ports located radially as shown. The three adjacent sections are each $\lambda/4$ long while the fourth section is $3\lambda/4$. Typically this circuit will have a bandwidth of 20 percent. A modified version of this circuit [46] involves the replacement of the $3\lambda/4$ microstrip section with a $\lambda/4$ slotline etched on the other side of the substrate as shown in Figure 5.48(b). The remaining 180° electrical length of the microstrip section is compensated for by

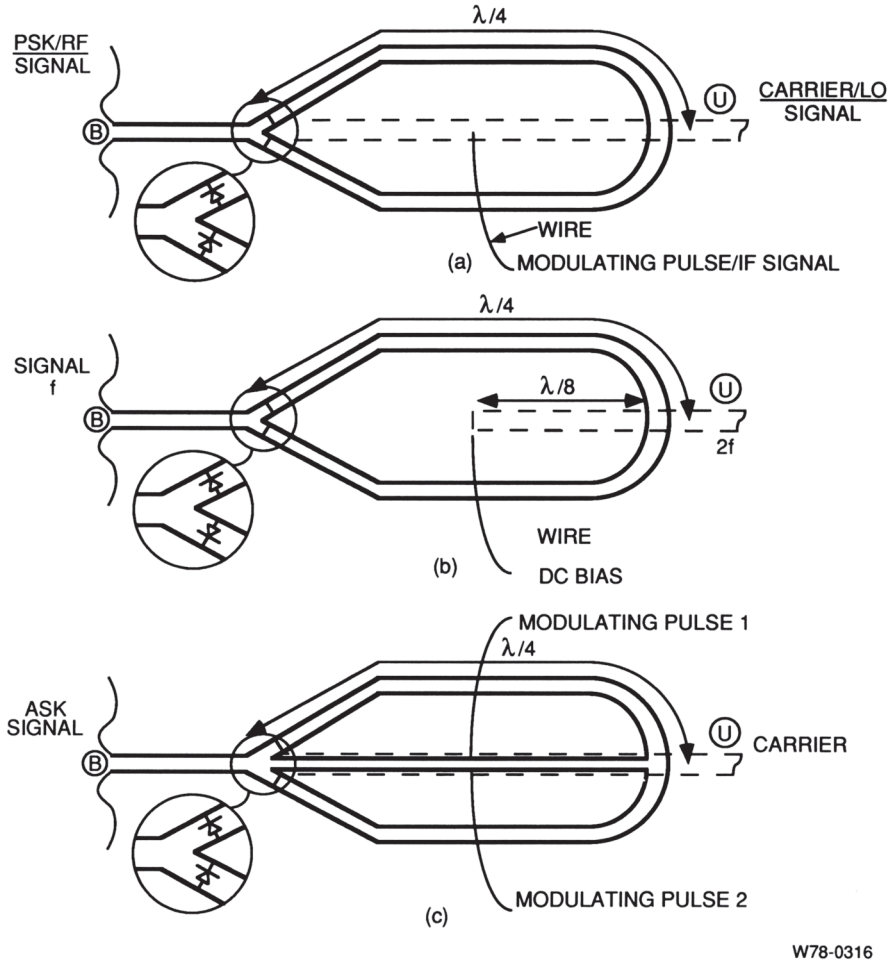

Figure 5.46 Double-sided balanced microwave circuits: (a) balanced PSK modulator/phase detector/mixer; (b) balanced frequency doubler; and (c) ASK modulator (from [30], © 1989 IEEE. Reprinted with permission.)

the two microstrip slotline junctions required to introduce a slotline in the circuit. Since this phase change is frequency independent, the resulting rat-race circuit has a wider bandwidth. Experimental measurements [46] presented in Figure 5.48(c) show that a bandwidth of greater than an octave can be realized.

Pulse Inverter. The use of slotline provides a method of obtaining a broadband 180° phase change. This technique can be used successfully in other circuits where a broadband 180° phase shift may be needed. A broadband pulse inverter has also been designed on this principle [47]. The input pulse is fed to one of the microstrip lines (see Figure 5.49(a)), and the inverted pulse output appears at the other microstrip. This pulse inverter was designed using a 0.625-mm thick alumina substrate. The oscilloscope traces of the input and the output pulse trains at 250 MHz are shown in Figure 5.49(b). As seen in this figure, the output pulses are almost identical to the input pulses except for the change in polarity. The bandwidth measurement of the pulse inverter indicates that the circuit works up to 1 GHz.

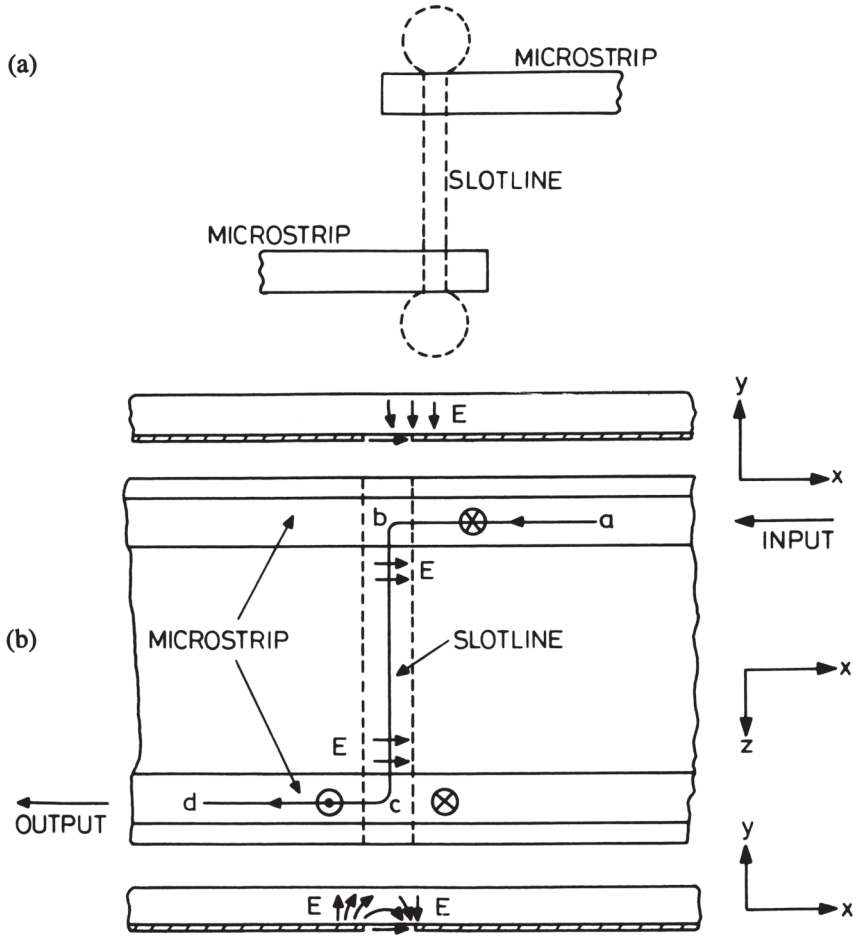

Figure 5.47 (a) Two microstrip-to-slotline transitions connected back-to-back for 180° phase change and (b) mechanism for 180° phase change.

Riblet has developed a microstrip-slotline symmetrical ring eight-port comparator circuit [48]. The size of the ring is 3λ at the center frequency. It can be reduced to a wavelength or less by using shunting capacitors across the slotline stubs.

5.7.3 Hybrid/de Ronde's Branchline Couplers

Let us consider the branchline coupler configuration shown in Figure 5.50. A conventional microstrip branchline coupler is shown in Figure 5.50(a) along with its transmission line equivalent circuit (neglecting junction effects). All the branchlines in this circuit are connected in shunt. Series connections of the branchline are not possible by the use of microstrips. However, the use of slotlines also allows the designer the flexibility of incorporating series-connected branches if desired.

As shown in Figure 5.50(b) a shunt-connected element can be transformed in to an equivalent series-connected element provided two additional quarter-wave

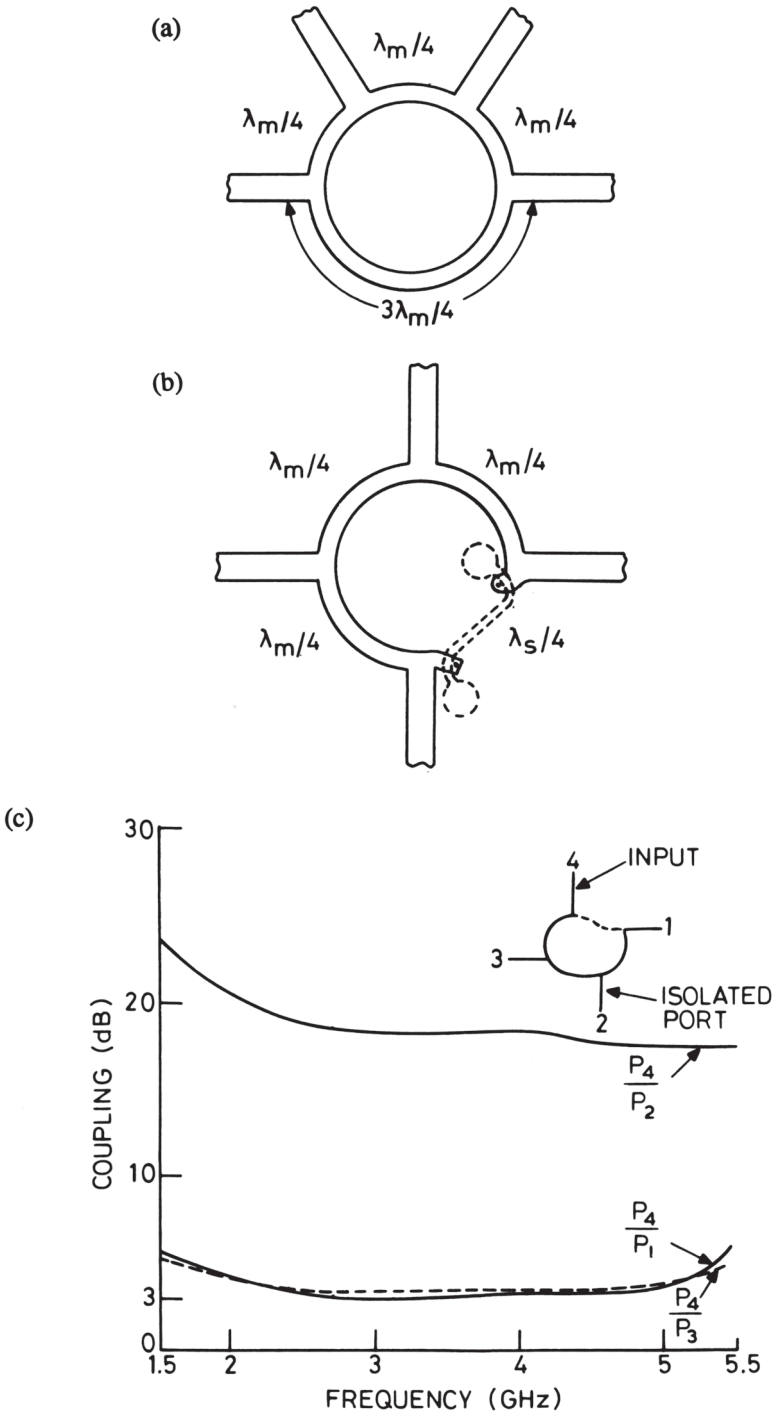

Figure 5.48 (a) A rat-race hybrid using microstrip lines only, (b) rat-race hybrid using slotline in (a) and (c) performance of rat-race hybrid shown in (b) from [46], © 1971 Microwave Exhibitions & Publishers (U.K.) Reprinted with permission.)

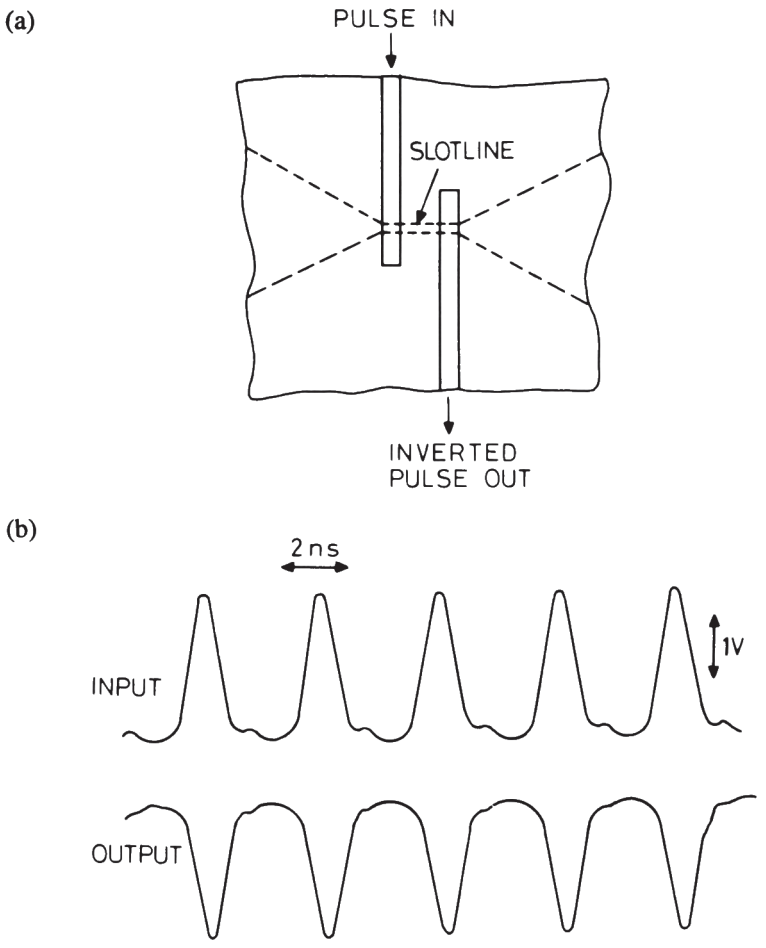

Figure 5.49 (a) Configuration of a microstrip-slotline pulse inverter and (b) oscilloscope trace of the performance of a microstrip-slotline pulse inverter (from [47]).

sections are included on each side of the series-connected element. If the middle branch of the 3-branch coupler, shown in Figure 5.50(a), is replaced by a series connected branch in this manner, we obtain the configuration shown in Figure 5.50(c). In this arrangement, there are two half-wave sections between the shunt- and series-connected branches. These half-wave sections can be eliminated and the three branches put together at one place as shown in Figure 5.50(d). This coupler has been analyzed, like any other branchline coupler, using the method of even- and odd-mode excitations.

The modified branchline coupler has two advantages over the conventional microstrip branchline coupler: smaller size and wider bandwidth. Both of these advantages result from the elimination of the two quarter-wave lengths shown in Figure 5.50(a).

The final version of the hybrid branchline coupler, shown in Figure 5.50(d) is very similar to the coupler configuration shown in Figure 5.51, which was suggested earlier empirically by de Ronde [43] and is named after him. One can consider

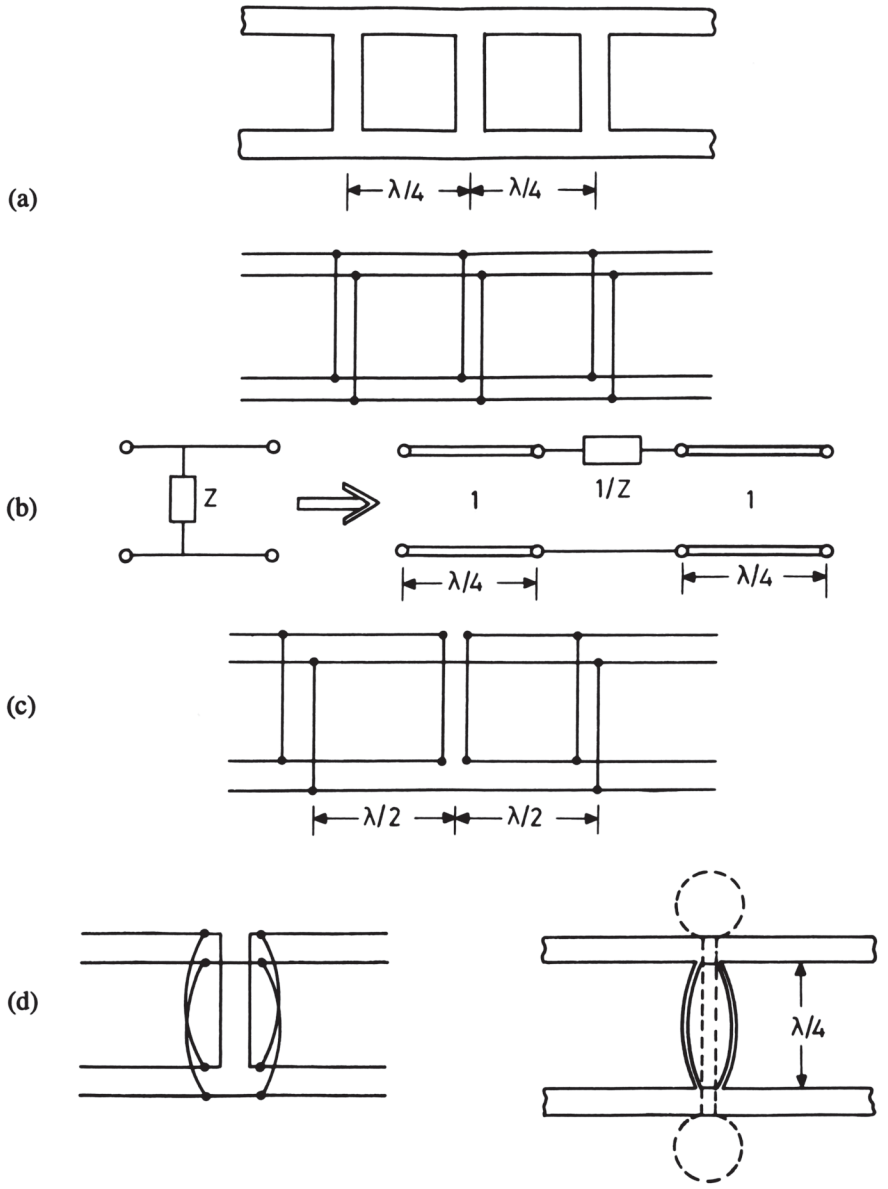

Figure 5.50 (a) Branchline coupler configurations using microstrip lines and two-wire lines, (b) equivalence between a shunt- and a series-connected branch, (c) modified coupler with a series branch, and (d) hybrid branchline coupler.

de Ronde's coupler to be derived from the configuration of Figure 5.50(d) in the following manner. Two shunt-connected branches are combined and realized by the microstrip on the top surface of the dielectric substrate. The series-connected brach is realized by the slotline in the ground plane. Performance of a de Ronde coupler has been measured [49] and the results are shown in Figure 5.52. The circuit designs are as follows:

Substrate thickness	0.38 mm
Slot width	50 μm
ε_r	12
Substrate size	2 cm × 2 cm
Microstrip impedance	60.4 Ω
Slotline impedance	50 Ω
Frequency range	X-band

A thorough analysis of de Ronde's coupler has been carried out by Hoffmann and Siegl [28, 50]. The coupler has been analyzed using the method of even- and odd-mode excitations applied to the coupled microstrip-slotline configuration. Characteristics of this transmission line were described in Section 5.5.1. Let Z_{0e} and ε_{re} be the characteristic impedance and effective dielectric constant for the even-mode (quasi-microstrip mode), respectively, and Z_{0o} and ε_{ro} be the corresponding quantities for the odd-mode (quasi-slot mode), respectively. Synthesis equations for this coupler are obtained as [28]

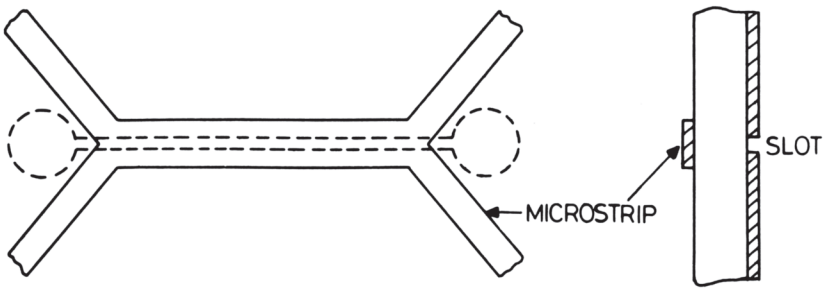

Figure 5.51 Configuration of de Ronde's coupler (from [43], © 1970 IEEE. Reprinted with permission.)

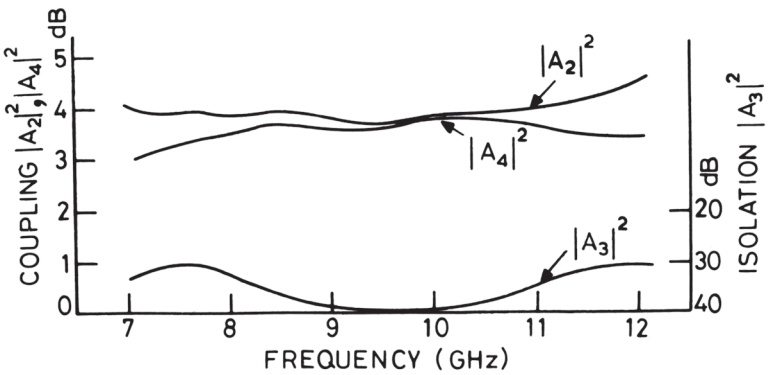

Figure 5.52 Measured performance of de Ronde's coupler (from [49], © 1974 IEEE. Reprinted with permission.)

$$Z_{0e} = \frac{Z_0}{2}\sqrt{\frac{1+k}{1-k}} \tag{5.68}$$

and

$$Z_{0o} = 2Z_0\sqrt{\frac{1+k}{1-k}} = \frac{Z_0^2}{Z_{0e}} \tag{5.69}$$

where Z_0 is the characteristic impedance of the feed lines to the coupler and k is the coupling coefficient. From the odd- and even-mode impedances one can determine the strip width and slot width of the coupler. If the length of the coupled section is chosen to be a quarter-wave at the center frequency, the directivity of the coupler is found to be poor because the phase velocities for the even- and odd-modes are different ($\varepsilon_{ro} < \varepsilon_{re}$). The lower phase for the odd mode can be compensated for, at a particular frequency, by increasing the length of the slotline so that it extends outside the overlapping microstrip [51], as shown in Figure 5.53. The additional slotline leaves the phase associated with the even-mode unchanged, and the total phase of the odd mode can be adjusted such that $\theta_e = \theta_o$. However, this end loading decreases the impedance. To compensate for this the characteristic impedance of the slot mode, Z_{0o}, has to be increased.

Now, let us assume that the phase compensation is to be achieved at the center frequency referenced to the even mode, that is,

$f_c = \dfrac{c}{4\ell\sqrt{\varepsilon_{re}}}$ where ℓ is the length of the coupling section.

Further, assuming that a slight increase in Z_{0o} to Z^*_{0o} required for compensation will not alter ε_{ro}, that is $\varepsilon^*_{ro} = \varepsilon_{ro}$, the increased characteristic impedance Z^*_{0o} and the additional slot length ℓ_s on either end of the coupled section are obtained as [28]

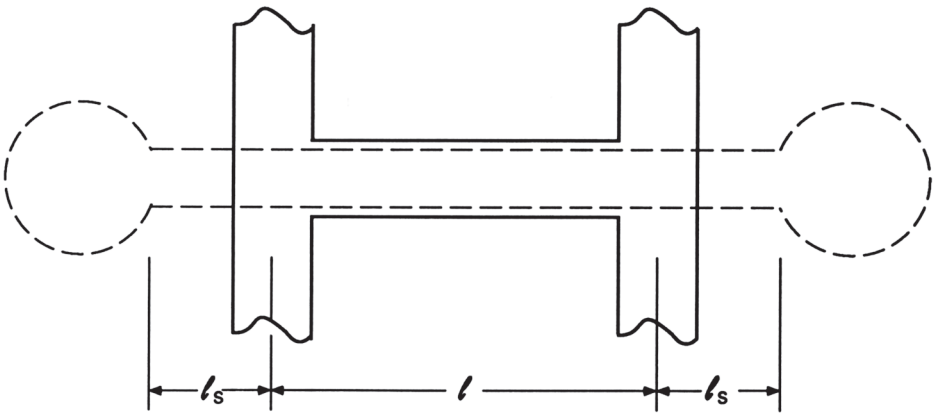

Figure 5.53 de Ronde's coupler with increased length of slotline for improving the isolation (from [50], © 1982 IEEE. Reprinted with permission.)

$$Z_{0o}^{*} = \frac{Z_{0o}}{2}\left[\cot\left(\frac{\pi}{4}\sqrt{\frac{\varepsilon_{ro}}{\varepsilon_{re}}}\right) + \tan\left(\frac{\pi}{4}\sqrt{\frac{\varepsilon_{ro}}{\varepsilon_{re}}}\right)\right] \tag{5.70}$$

$$\ell_s = \frac{2\ell}{\pi}\sqrt{\frac{\varepsilon_{re}}{\varepsilon_{ro}}}\tan^{-1}\left\{\frac{Z_{0o}^{*}}{Z_{0o}}\left[1 - 2\sin^2\left(\frac{\pi}{4}\sqrt{\frac{\varepsilon_{ro}}{\varepsilon_{re}}}\right)\right]\right\} \tag{5.71}$$

Another approach for equalizing the even- and odd-mode velocities for the coupled microstrip-slotline is to cover the slotline with a dielectric sheet as shown in Figure 5.54.

Aikawa and Ogawa [30] have designed a de Ronde's coupler in the millimeter wave region at a center frequency of 26 GHz. It was fabricated on 0.3-mm-thick alumina substrate. The insertion loss variation of the coupler was found to be less than 0.5 dB over the frequency range 25 GHz to 28.5 GHz. The isolation was greater than 18 dB over a bandwidth of 6 GHz.

A two-layer, slotline-coupled microstrip directional coupler—useful for realizing tight and loose couplings—has been discussed by Tanaka et al. [31]. The cross-section of the transmission line used in the coupler is shown in Figure 5.55. It consists of two microstrip lines that couple through a slot line in the common ground plane as shown. The conformal mapping based design of this coupled line configuration is discussed in Chapter 8, Section 8.3. A number of directional couplers were designed for tight coupling (~ 3 dB), as well as loose coupling (such as 10 dB), for a center frequency of 1.5 GHz. The design of this coupler is exactly similar to any coupled-line directional coupler. The substrate thickness was 0.8 mm and the relative permittivity was 2.5. Measurements on these couplers showed >25 dB return loss, >28 dB isolation, and a coupling variation of 0.2 dB over the 1.2–1.8 GHz frequency range [31]. These couplers were then combined to obtain multiport directional couplers, avoiding any microstrip line crossover.

Abbosh and Bialkowski have discussed compact UWB directional couplers that utilize slot-coupled microstrip lines [60]. The couplers employ elliptical-shaped microstrip lines and slotlines to achieve UWB operation. The schematic of the coupler is shown in Figure 5.56 [61]. The elliptical microstrips in the top and bottom layers

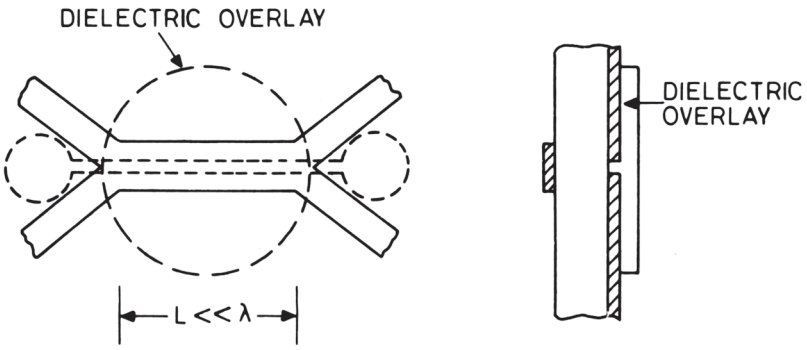

Figure 5.54 de Ronde's coupler with a dielectric overlay for equalizing the even- and odd-mode phase velocities.

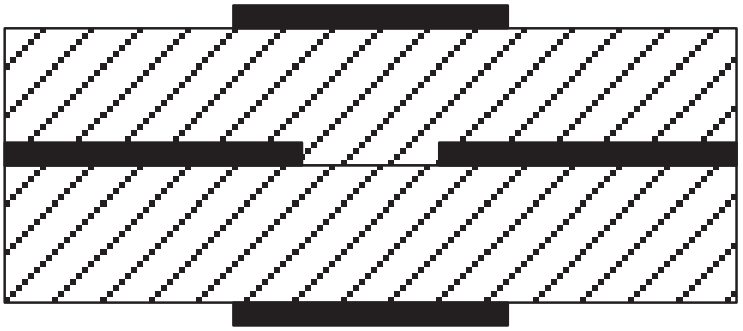

Figure 5.55 Cross-section of slotline-coupled microstrip line geometry.

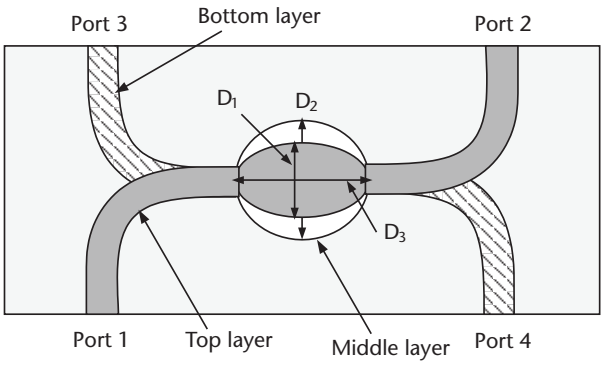

Figure 5.56 Schematic of an UWB directional coupler employing slotline-coupled microstrip lines. (from [60], © 2007 IEEE. Reprinted with permission.)

are defined by D1 and D2, while the elliptical slot in the middle layer is defined by D2 and D3. The measured results for the couplers show 3±0.8 dB, 6±1.4 dB, and 10±1.5 dB coupling across the 3.1–10.5 GHz band. The isolation is better than 23, 20, and 19 dB, whereas the return loss is better than 23, 18, and 19 dB for the 3-, 6- and 10-dB couplers, respectively. A new Marchand balun utilizing slot-coupled microstrip lines is reported [61]. Diamond-shaped microstrip lines and slotlines are employed to achieve broadband operation of the balun. The balun achieves 0.69 dB amplitude balance and 1.4 degree phase balance over 1.11–2.93 GHz.

5.7.4 Other Types of Slotline Circuits

The circuits mentioned in this section are based on the properties of slotlines only. They do not have the hybrid composition as described in earlier circuits using slotlines. These circuits can be classified into two categories: circuits using slotline resonators (for example, filters) and ferrite devices using slotline.

Circuits Using Slotline Resonators

Slotline resonators have been used for the design of filters, both band-pass and band-reject types [52]. The design procedure for slotline filters is the same as that for any other transmission line; that is, it is based on the coupling coefficient be-

tween either two end-coupled or two parallel-coupled sections of transmission line. The experimental results in [52] indicate that the performance of slotline filters is not superior to those using other transmission lines.

Ferrite Devices Using Slotline

When the slotline was introduced as an alternative transmission structure for MICs, it was expected that the slotline would be more suitable than the microstrip line for nonreciprocal ferrite devices. This expectation was based on the existence of an elliptically polarized magnetic field distribution in the slot as discussed in Section 5.2.1. However, the experimental and analytical studies reported so far on circulators and isolators [53–55] have not pointed out any significant advantage of ferrite devices using slotline. A differential phase shifter in a coupled microstrip-slotline configuration (Figure 5.15) holds promise. El-Sharawy and Jackson have reported the analysis and experimental results on this type of phase shifter [29]. A multilayered configuration provides a larger amount of phase shift. A differential phase shift of the order of 45°/cm was measured by them over a 6-GHz to 8.5 GHz frequency range.

References

[1] Cohn, S. B., "Slotline on a Dielectric Substrate," *IEEE Trans.*, Vol. MTT-17, 1969, pp. 768–778.

[2] Cohn, S. B., "Slotline Field Components," *IEEE Trans.*, Vol. MTT-20, 1972, pp. 172–174.

[3] Knorr, J. B., and K. D. Kuchler, "Analysis of Coupled Slots and Coplanar Strips on Dielectric Substrates," *IEEE Trans.*, Vol. MTT-23, 1975, pp. 541–548.

[4] Itoh, T., and R. Mittra. "Dispersion Characteristics of Slotlines," *Electron. Lett.*, Vol. 7. 1971, pp. 364–365.

[5] Janaswamy, R., and D. H. Schaubert, "Dispersion Characteristics for Wide Slotlines on Low Permittivity Substrate," *IEEE Trans.*, Vol. MTT-33, 1985, pp. 723–726.

[6] Janaswamy, R., and D. H. Schaubert, "Characteristic Impedance of a Wide Slotline on Low Permittivity Substrate," *IEEE Trans.*, Vol. MTT-34, 1986, pp. 900–902.

[7] Itoh, T. (Ed), *Numerical Techniques for Microwave and Millimeter-wave Passive Structures*, New York: John Wiley, 1989.

[8] Liang, G. C., et al., "Full-wave Analysis of Coplanar Waveguide and Slotline Using the Time-Domain Finite-Difference Method, *IEEE Trans.*, Vol. MTT-37. 1989, pp. 1949–1957.

[9] Robinson, G. H., and J. L. Allen, "Slotline Application to Miniature Ferrite Devices," *IEEE Trans.*, Vol. MTT-17, 1969, pp. 1097–1101.

[10] Galejs, J., "Excitation of Slots in a Conducting Screen Above a Lossy Dielectric Half Space," *IRE Trans.*, Vol. AP-10, 1962, pp. 436–443.

[11] Garg, R., and K. C. Gupta, "Expressions for Wavelength and Impedance of Slotline." *IEEE Trans.*, Vol. MTT-24, 1976, p. 532.

[12] Rozzi, et al., "Hybrid Modes, Substrate Leakage, and Losses of Slotline at Millimeter-wave Frequencies," *IEEE Trans.*, Vol. MTT-38, 1990, pp. 1069–1078.

[13] Citerne, J., et al., "Fundamental and Higher Order Modes in Microslot Lines," *Proc. 5th European Microwave Conf.*, Hamburg, 1975, pp. 273–277.

[14] Kitazawa, T., et al., "Analysis of the Dispersion Characteristics of Slot Line With Thick Metal Coating," *IEEE Trans.*, Vol. MTT-28, 1980, pp. 387–392.

[15] Kitazawa, T., et al., "Slotline with Thick Metal Coating," *IEEE Trans.*, Vol. MTT-21. 1973, pp. 580–582.

[16] Montgomery, C. G., et al., *Principles of Microwave Circuits*, New York: McGraw-Hill Book Company, 1948, p. 154.

[17] Mariani, E. A., et al., "Slotline Characteristics" *IEEE Trans.*, Vol. MTT-17, 1969, pp. 1091–1096.

[18] Garg, R., "Effect of Tolerances on Microstripline and Slotline Performances," *IEEE Trans.*, Vol. MTT-26, 1978, pp. 16–19.

[19] Das, N. K., and D. M. Pozar, "Full-Wave Spectral-Domain Computation of Material, Radiation, and Guided Wave Losses in Infinite Multilayered Printed Transmission Lines," *IEEE Trans.*, Vol. MTT-39, 1991, pp. 54–63.

[20] Kurpis, G. P., "Coplanar and Slotlines—Are They Here to Stay?," *Proc. Int. Microelectric Symp.*, Washington, 1972, pp. 3B.6.1–3B.6.5.

[21] Jansen, R., "Hybrid Mode Analysis of End Effects of Planar Microwave and Millimeter Wave Transmission Lines," *Proc. Inst. Elec. Eng.,* Vol. 128, pt. H, 1981, pp. 77–86.

[22] Yang, H., and N.G. Alexopoulos, "A Dynamic Model for Microstrip-slotline Transition and Related Structures," *IEEE Trans.*, Vol. MTT-36, 1988, pp. 286–293.

[23] Knorr, J. B., and J. Saenz, "End Effect in a Shorted Slot." *IEEE Trans.*, Vol. MTT-21, 1973, pp. 579–580.

[24] Chramiec, J., "Reactances of Slotline Short and Open Circuits on Alumina Substrate," *IEEE Trans.*, Vol. MTT-37, 1989, pp. 1638–1641.

[25] Itoh, T., "Spectral Domain Immitance Approach for Dispersion Characteristics of Generalized Printed Transmission Lines," *IEEE Trans.*, Vol. MTT-28, 1980, pp. 733–736.

[26] Jansen, R. H., "Microstrip Lines with Partially Removed Ground Metallization, Theory and Applications," *Archiv Elekr. Ubertr.*, Vol. 32, 1978, pp. 485–492.

[27] Ogawa, H., and M. Aikawa, "Analysis of Coupled Microstrip-Slotlines." *Trans. IECE. Jap.*, Vol. 62B, 1979, pp. 269–270.

[28] Hoffmann, R. K., and J. Siegl, "Microstrip-Slot Coupler Design—Part I: S-Parameters of Uncompensated and Compensated Couplers," *IEEE Trans.*, Vol. MTT-30, 1982, pp. 1205–1210.

[29] El-Sharawy, E. B., and R. W. Jackson, "Analysis and Design of Microstrip-slot Line for Phase Shifting Applications," *IEEE Trans.*, Vol. MTT-38, 1990, pp. 276–283.

[30] Aikawa, M., and H. Ogawa, "Double-Sided MIC's and Their Applications," *IEEE Trans.*, Vol. MTT-37, 1989, pp. 406–413.

[31] Tanaka, T., et al., "Slot-Coupled Directional Couplers Between Double Sided Substrate Microstrip Lines and Their Applications," *IEEE Trans.*, Vol. MTT-36, 1986, pp. 1752–1757.

[32] Shigesawa, H., et al., "Conductor-Backed Slot Line and Coplanar Waveguide: Dangers and Full-Wave Analyses," *Proc. Int. Microwave Symp.*, 1988, pp. 199–202.

[33] Rozzi, T., et al., "Radiation Modes of Slotline with Application to Millimetric Circuits," *IEEE MTT-S, Digest,* 1992, pp. 503–506.

[34] Das, N. K., "Characteristics of Modified Slotline Configurations," *Digest Int. Microwave Symp.*, 1991. pp. 777–780.

[35] Knorr, J. B., "Slotline Transitions," *IEEE Trans.*, Vol. MTT-22, 1974, pp. 548–554.

[36] Chamber, D., et al., "Microwave Active Network Synthesis," *Semiannual Report, Stanford Resr. lnst.*, June 1970.

[37] Das, N. K., "Generalized Multiport Reciprocity Analysis of Surface-to-surface Transitions Between Multiple Printed Transmission Lines," *IEEE Trans.*, Vol. MTT-41, 1993, pp. 1164–1177.

[38] Antar, Y. M. M., et al., "Microstrip-Slotline Transition Analysis Using the Spectral Domain Technique," *IEEE Trans.*, Vol. MTT-40. 1992, pp. 515–523.

[39] Podcameni, A., and M. L. Coimbra, "Slotline-Microstrip Transition on Iso/Anisotropic Substrate: A More Accurate Design," *Electron. Lett.*, Vol. 16, 1980, pp. 780–781.

[40] Schuppert, B., "Microstrip/Slotline Transitions: Modeling and Experimental Investigations," *IEEE Trans.*, Vol. MTT-36, 1988, pp. 1272–1282.

[41] Schwab, W., and W. Menzel, "On the Design of Planar Microwave Components Using Multilayer Structures," *IEEE Trans.*, Vol. MTT-40, 1992, pp. 67–72.

[42] Uwano, T., et al., "Characterization of Microstrip-to-Slotline Transition Discontinuities by Transverse Resonance Analysis,"*Alta Freq.*, Vol. 57. No. 5, 1988, pp. 183–191.

[43] de Ronde, F. C., "A New Class of Microstrip Directional Couplers," *Digest of Tech. Papers, G-MTT Symp.*, 1970, pp. 184–189.

[44] Schiek, B., and J. Kohler. "An Improved Microstrip-to-Microslot Transition," *IEEE Trans.*, Vol. MTT-24, 1976, pp. 231–233.

[45] Aikawa, M., and H. Ogawa, "A New MIC Magic-T Using Coupled Slot Lines," *IEEE Trans.*, Vol. MTT-28, 1980, pp. 523–528.

[46] Chua, L. W., "New Broadband Matched Hybrids for Microwave Integrated Circuits," *Proc. European Microwave Conf.* (Stockholm), 1971, pp. C4/5.1–C4/5.4.

[47] Hede, C., "High Speed Logic, Part 3," Tech. Report IR 127, Electromagnetics Institute, Technical University of Denmark, 1977.

[48] Riblet, G. P., "Compact Planar Microstrip-slotline Symmetrical Ring Eightport Comparator Circuits," *IEEE Trans.*, Vol. MTT-38, 1990, pp. 1421–1426.

[49] Schiek, B., "Hybrid Branchline Couplers—A Useful New Class of Directional Couplers," *IEEE Trans.*, Vol. MTT-22, 1974, pp. 864–869.

[50] Hoffmann, R. K., and J. Siegl, "Microstrip-slot Coupler Design-Part II: Practical Design Aspects." *IEEE Trans.*, Vol. MTT-30, 1982, pp. 1211–1215.

[51] Schick, B., and J. Kohler, "Improving the Isolation of 3–dB Couplers in Microstrip-Slotline Technique," *IEEE Trans.*, Vol. MTT-26, 1978, pp. 5–7.

[52] Mariani, E. A., and J. P. Agrios, "Slotline Filters and Couplers," *IEEE Trans.*, Vol. MTT-18, 1970, pp. 1089–1095.

[53] Ogasawara, N., and M. Kaji, "Coplanar-Guide and Slot-Guide Junction Circulators," *Electron. Lett.,* Vol. 7, 1971, pp. 220–221.

[54] De Vecchis, M., et al., "A New Slotline Broadband Isolator," *Proc. European Microwave Conf.* (Brussels), 1973, Paper B.9.6.

[55] Courtois, L., and M. de Vecchis, "A New Class of Non-Reciprocal Components Using Slotline," *IEEE Trans.*, Vol. MTT-23, 1975, pp. 511–516.

[56] Cohn, S. B., "Sandwich Slotline," *IEEE Trans.*, Vol. MTT-19, 1971, pp. 773–774.

[57] Samardzija, N., and T. Itoh, "Double-Layered Slot-Line for Millimeter-Wave Integrated Circuits," *IEEE Trans.*, Vol. MTT-24, 1976, pp. 827–831.

[58] Simons, R., "Suspended Slot Line Using Double Layer Dielectric," *IEEE Trans.*, Vol. MTT-29, 1981, pp. 1102–1107.

[59] Svacina, J., "Dispersion Characteristics of Multilayered Slotline-A Simple Approach," *IEEE Trans. Microwave Theory Tech.*,Vol. 47, 1999, pp. 1826–1829.

[60] Abbosh, A. M., and Bialkowski, "Design of Compact Directional Couplers for UWB Applications," *IEEE Trans. Microwave Theory Tech.*, Vol. 55, 2007, pp. 189–194.

[61] Tseng, C.-H., and Y.-C. Hsiao, "A New Broadband Marchand Balun Using Slot-Coupled Microstrip Lines," *IEEE Microwave Wireless Comp. Lett.*, Vol. 20, 2010, pp. 157–159.

Apendix 5.A: Susceptance Calculation for the Transverse Resonance Method

The formula for susceptance ηB_t for the case of electric walls at $y = \pm b/2$ is given as

$$\begin{aligned}\eta B_t = \frac{a}{2b}\left[-v + u\tan\left(\frac{\pi h u}{ap} - \tan^{-1}\frac{v}{u}\right)\right] \\ + \frac{1}{p}\left\{\left(\frac{\varepsilon_r + 1}{2} - p^2\right)\ell n\frac{2}{\pi\delta}\right. \\ \left. + \frac{1}{2}\sum_{n=1,2,3,\ldots}\left[v^2\left(1 - \frac{1}{F_n}\right) + M_n\right]\frac{\sin^2(\pi n\delta)}{n(\pi n\delta)^2}\right\}\end{aligned} \tag{A.1}$$

For magnetic walls at $y = \pm b/2$ the expression for B_t is

$$\begin{aligned}\eta B_t = \frac{1}{p}\left\{\left(\frac{\varepsilon_r + 1}{2} - p^2\right)\ell n\frac{8}{\pi\delta}\right. \\ \left. + \frac{1}{2}\sum_{n=1/2,3/2,5/2,\ldots}\left[v^2\left(1 - \frac{1}{F_n}\right) + M_n\right]\frac{\sin^2(\pi n\delta)}{n(\pi n\delta)^2}\right\}\end{aligned} \tag{A.2}$$

where $\eta = \sqrt{\mu_0/\varepsilon_0} = 376.7\ \Omega$, $\delta = W/b$, $p = \lambda_0/\lambda_s$, and

$$u = \sqrt{\varepsilon_r - p^2} \qquad v = \sqrt{p^2 - 1} \tag{A.3}$$

$$F_n = \sqrt{1 + \left(\frac{b}{2an}\frac{v}{p}\right)^2} \tag{A.4}$$

$$F_{n1} = \sqrt{1 - \left(\frac{b}{2an}\frac{u}{p}\right)^2} \tag{A.5}$$

(A.6)

For F_{nl} real, M_n is

$$M_n = \frac{\varepsilon_r \tanh r_n - p^2 F_{n1}^2 \coth q_n}{[1 + (b/2an)^2]F_{n1}} - u_2$$

where

$$r_n = \frac{2\pi n h F_{n1}}{b} + \tanh^{-1}\left(\frac{F_{n1}}{\varepsilon_r F_n}\right) \tag{A.7}$$

$$q_n = \frac{2\pi nhF_{n1}}{b} + \coth^{-1}\left(\frac{F_n}{F_{n1}}\right) \tag{A.8}$$

For F_{nl} imaginary, M_{n} is

$$M_n = \frac{\varepsilon_{\mathrm{r}} \tanh r_n' - p^2 |F_{n1}|^2 \cot q_n'}{[1 + (b/2an)^2]|F_{n1}|} - u_2 \tag{A.9}$$

where

$$r_n' = \frac{2\pi nh|F_{n1}|}{b} + \tan^{-1}\left(\frac{|F_{n1}|}{\varepsilon_{\mathrm{r}} F_n}\right) \tag{A.10}$$

$$q_n' = \frac{2\pi nh|F_{n1}|}{b} + \cot^{-1}\left(\frac{F_n}{|F_{n1}|}\right) \tag{A.11}$$

Appendix 5.B: Sensitivity Expressions for Slotline Impedance and Wavelength

The following expressions can be obtained by using the definition of sensitivity, (2.99), and the expressions for slotline impedance and wavelength, (5.31) to (5.39).

1. For $0.02 \le W/h \le 0.2$

$$S_W^{Z_{0s}} = \frac{50}{Z_{0s}}\left\{2\frac{W}{h} - 0.12 - \frac{(W/h - 0.02)(W/h - 0.1)}{W/h} + \frac{0.4343}{50} \cdot (44.28 - 19.58\log\varepsilon_{\mathrm{r}})\right\} - \frac{W/h}{Z_{0s}}(1.07\log\varepsilon_{\mathrm{r}} + 1.44) \cdot (11.4 - 6.072\log\varepsilon_{\mathrm{r}} - h/\lambda_0 \times 10^2)^2 \tag{B.1}$$

$$S_h^{Z_{0s}} = -S_W^{Z_{0s}} + \frac{h}{Z_{0s}}\frac{1}{\lambda_0}\frac{\partial Z_{0s}}{\partial(h/\lambda_0)} \tag{B.2}$$

where

$$\frac{\partial Z_{0s}}{\partial(h/\lambda_0)} = -200(11.4 - 6.07\log\varepsilon_r - h/\lambda_0 \times 10^2) \cdot [0.32\log\varepsilon_r - 0.11 + \frac{W}{h}(1.07\log\varepsilon_r + 1.44)]$$

$$S_{\varepsilon_r}^{Z_{0s}} = \frac{0.4343\varepsilon_r}{Z_{0s}}[35.19 + 19.58\log(W/h) \times 10^2) + (0.32 + 1.07W/h)(11.4 - 6.07\log\varepsilon_r - h/\lambda_0 \times 10^2)^2 - 12.14(11.4 - 6.07\log\varepsilon_r - h/\lambda_0 \times 10^2) \cdot [0.32\log\varepsilon_r - 0.11 + W/h(1.07\log\varepsilon_r + 1.44)]] \quad \text{(B.3)}$$

$$S_W^{\varepsilon_{re}} = -2S_W^{\lambda_s/\lambda_0} = -\frac{2W/h}{\varepsilon_{re}}[0.2 - 0.29\log(h/\lambda_0) \times 10^2)] \quad \text{(B.4)}$$

$$S_h^{\varepsilon_{re}} = -S_W^{\varepsilon_{re}} + \frac{0.8686}{\varepsilon_{re}}(0.29W/h + 0.047) \quad \text{(B.5)}$$

$$S_{\varepsilon_r}^{\varepsilon_{re}} = 0.389/\varepsilon_{re} \quad \text{(B.6)}$$

2. For $0.2 \le W/h \le 1.0$

$$S_W^{Z_{0s}} = \frac{W/h}{Z_{0s}}\big[1.25(114.59 - 51.88\log\varepsilon_r) + 24 - 40W/h - \{10.25 - 5\log\varepsilon_r + W/h)(2.1 - 1.42\log\varepsilon_r) - h/\lambda_0 \times 10^2\} \cdot \{(2.07\log\varepsilon_r - 0.79)[10.25 - 5\log\varepsilon_r + W/h(2.1 - 1.42\log\varepsilon_r) - h/\lambda_0 \times 10^2] + 2(2.1 - 1.42\log\varepsilon_r)[0.15 + 0.23\log\varepsilon_r + W/h(2.07\log\varepsilon_r - 0.79)]\}\big] \quad \text{(B.7)}$$

$$S_h^{Z_{0s}} = -S_W^{Z_{0s}} + \frac{h}{Z_{0s}}\frac{1}{\lambda_0}\frac{\partial Z_{0s}}{\partial(h/\lambda_0)} \quad \text{(B.8)}$$

where

$$\frac{\partial Z_{0s}}{\partial(h/\lambda_0)} = 200[10.25 - 5\log\varepsilon_r + W/h\,(2.1 - 1.42\log\varepsilon_r) - h/\lambda_0 \times 10^2] \cdot [0.15 + 0.23\log\varepsilon_r + W/h\,(2.07\log\varepsilon_r - 0.79)]$$

$$S_{\varepsilon_r}^{Z_{0s}} = \frac{0.4343}{Z_{0s}}\{53.55 + 64.84W/h + (0.23 + 2.07W/h) \cdot [10.25 - 5\log\varepsilon_r + W/h(2.1 - 1.42\log\varepsilon_r) - h/\lambda_0 \times 10^2]^2 - 2(5 + 1.42W/h)[0.15 + 0.23\log\varepsilon_r + W/h(2.07\log\varepsilon_r - 0.79)] \cdot [10.25 - 5\log\varepsilon_r + W/h(2.1 - 1.42\log\varepsilon_r) - h/\lambda_0 \times 10^2]\} \quad \text{(B.9)}$$

$$-S_W^{\varepsilon_{re}} = \frac{2W/h}{\varepsilon_{re}}[0.111 - 0.0022\varepsilon_r - 0.094\log(h/\lambda_0 \times 10^2)] \quad \text{(B.10)}$$

$$S_h^{\varepsilon_{re}} = -S_W^{\varepsilon_{re}} + \frac{0.8686}{\varepsilon_{re}}(0.121 + 0.094W/h - 0.0032\varepsilon_r) \tag{B.11}$$

$$S_{\varepsilon_{re}}^{\varepsilon_{re}} = \frac{2}{\varepsilon_{re}}[0.21 + 0.0022\varepsilon_r W/h - 0.0032\varepsilon_r \log(h/\lambda_0 \times 10^2)] \tag{B.12}$$

The logarithms are to the base 10 in the above expressions.

CHAPTER 6

Defected Ground Structure (DGS)

6.1 Introduction

In the design of microstrip components and circuits, the frequency response is usually optimized by properly selecting the shape and size of the conductor lines: the backside ground plane is typically a solid metal sheet, and it does not represent a degree of freedom in the design phase.

Defected ground structures (DGS) offer an alternative solution for improving the performance of several printed microwave circuits, based on microstrip lines and coplanar waveguides [1–4]. In DGS, the ground plane is intentionally modified to improve the frequency response of the component. The modifications of the ground plane are usually called "defects," and these defects in the ground plane give the name to this class of components. A defect typically consists of a slot or an aperture in the ground plane, located directly under the microstrip line or besides the coplanar waveguide. The geometry of the aperture/slot is carefully selected, in order to create a proper perturbation of the current distribution in the ground plane and to achieve the desired electromagnetic effect.

There are two major classes of DGS: the first group comprises structures based on a single defect, whereas the second group encompasses structures based on a small number of defects, in a periodic or non-periodic arrangement. DGS based on a single defect [5–8] exploit the additional inductance and capacitance effect of an aperture in the ground plane to modify the frequency response of a printed circuit, for instance by introducing a transmission zero in the frequency response of a microstrip filter. Conversely, DGS based on a small number of defects [9–11] (either periodic or non-periodic) allow enhancing the characteristics of single defects. In the case of small periodic arrays of defects, they exploit the propagation band–gap to modify the characteristics of a printed circuit or a patch antenna. In the majority of cases, components based on a single defect (or few defects) are preferred, due to the easier modeling, more compact size, and smaller radiation issues.

The use of DGS was first proposed around year 2001 [5], as an evolution of the research activities on photonic band-gap structures (PBG) and electromagnetic band–gap structures (EBG) [12–14]. There is a substantial difference between DGS and PBG structures (or the term EBG, usually preferred in the microwave community): PGB/EBG structures are large periodic arrays of defects and exploit their periodicity to prevent the propagation of electromagnetic waves in a certain frequency band (band-gap effect). In DGS, the periodicity is usually not implemented and the structures are based on a single defect (or a few defects).

DGS open a variety of new perspectives for the development of printed planar circuits and antennas, as they break the traditional design approach of microstrip and coplanar waveguide components and add an extra degree of freedom in the design phase. The applications of DGS range from microstrip filters with additional transmission zeros to transmission lines supporting slow–wave propagation or with high characteristic impedance, to hybrid couplers, oscillators, power amplifiers and antennas with improved performance.

The main advantage of DGS is related to their easy technological implementation: in fact, the processing of DGS–loaded circuits is based on standard printed circuit board (PCB) technology, the same manufacturing technique adopted for printed microwave components. In the case of DGS components, the only additional requirement can be the processing of the ground metal layer. Conversely, the main disadvantage of DGS is the increase in radiation leakage: for instance, when a defect produces reflection of the incident wave, part of the energy is radiated into the free space. The radiation effect can be a critical issue, as it determines the coupling between adjacent circuits and may lower the Q of the component. In addition, there is the need of some free space underneath the defected ground plane, not to perturb the electromagnetic behavior of the apertures. For this reason, and in order to keep the radiation levels negligible, special housing for such circuits are required in most cases.

6.1.1 Basic Structure of DGS

The basic configuration of DGS is represented by a microstrip line combined with a slot etched in the metallic ground plane (Figure 6.1). The shape and size of the aperture in the ground plane play a critical role in the determination of the frequency response, which is similar to the way in which the geometry of conductors affects the frequency response of conventional microstrip circuits.

A simple yet significant example of DGS was first presented in [5, 9], where a band–stop filter is designed by adopting a conventional straight microstrip transmission line with a dumbbell aperture etched in the backside metallic ground plane (Figure 6.1). The dumbbell defect consists of two rectangular apertures of dimensions $a \times b$ connected by a thin slot of width g and length w. The dimensions of the aperture in the ground plane are quite small: in [5], a defect with $a = b = 2.5$ mm, $g = 0.2$ mm, and $w = 1.62$ mm was adopted to obtain a stop–band effect at 7.5 GHz, in conjunction with a 50 Ω microstrip line of width w on a substrate of thickness $h = 1.5748$ mm and relative dielectric permittivity $\varepsilon_r = 10$ (Figure 6.1).

A variety of shapes have been adopted for the design of DGS (Figure 6.2). The most common aperture geometries are rectangular dumbbell [5], circular dumbbell [15], arrowhead [16], cross [17], H-shape [18], square open-loop with a slot in the middle section [19], V-shape [20], U-shape [20], spiral [21], concentric ring [22], split-ring resonator [23], and fractals [24]. In all cases, the geometry is optimized to achieve the required electromagnetic performance with the minimization of the circuit footprint.

The first geometry adopted for a DGS circuit was the rectangular dumbbell shape (Figure 6.1) [5]. This shape presents a sufficient number of degrees of free-

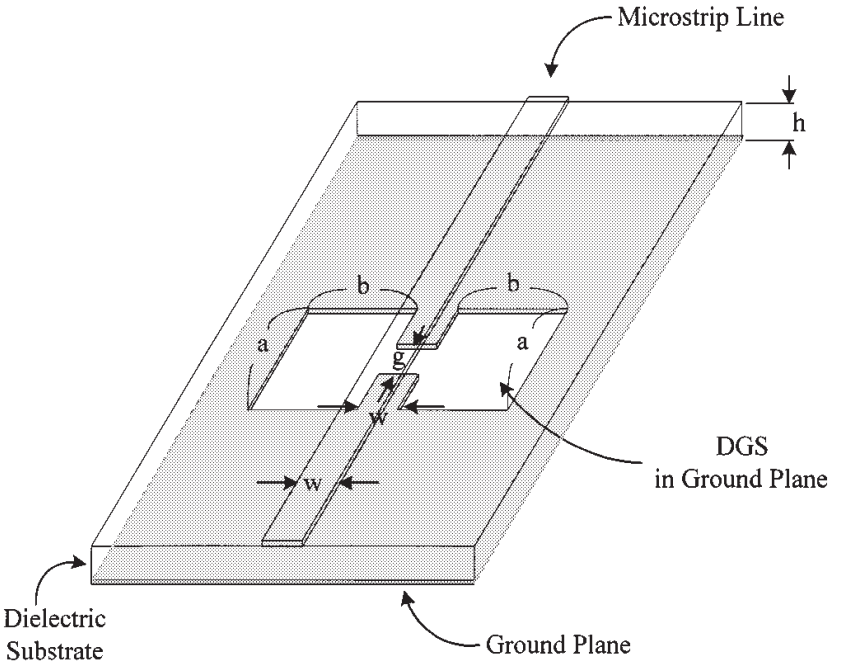

Figure 6.1 Defected ground structure, consisting of a straight microstrip line with a dumbbell-shaped aperture (defect) in the backside ground plane (from [5], © 2001 IEEE. Reprinted with permission.).

dom, and this permits achieving the desired electromagnetic effect and optimizing the frequency response of the component. The circular dumbbell shape, proposed in [15], exhibits a very similar geometry, with two circular apertures connected by a thin slot, etched in the ground plane of a microstrip line. In both cases, the use of a single defect allows introducing a distinct stop-band property in the transmission frequency response of the microstrip line.

The use of a spiral-shaped defect, proposed in [21], appears particularly interesting, as it leads to very compact structures. More specifically, when a spiral defect and a dumbbell defect with the same size are implemented on identical substrates, the stop-band frequency of the spiral-loaded microstrip line is much lower than that of the dumbbell loaded line.

The H-shaped DGS offers very attractive features, as its size is very compact and the quality factor of the stop-band resonance is higher than rectangular and circular dumbbell, thus providing a sharper transition from pass-band to stop-band [18]. V-shaped and U-shaped DGS also present stop-band resonances with high quality factors [20]. The quality factor can be increased by decreasing the distance between the two arms of U-shaped defects or by reducing the angle between the two arms of V-shaped DGS.

Concentric ring-shaped defects, proposed in [22], permit achieving a particularly broad stop-band. The band-stop properties can be controlled by varying their radius and thickness of the concentric rings.

Due to the presence of defects, the electromagnetic field is not completely confined and may have significant values below the ground plane. For this reason,

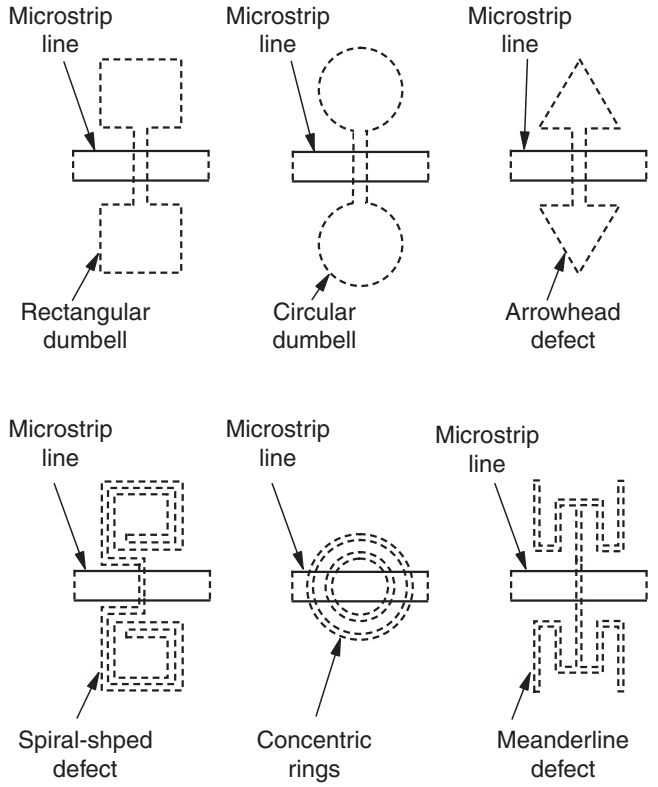

Figure 6.2 Commonly adopted DGS shapes: rectangular and circular dumbbell shapes, arrowhead defect, spiral-shape, concentric rings, and meander line.

proper housing structures are needed to avoid perturbing the field. The minimum dimensions of these structures and the needed clearance below the ground plane depend on the shape and size of the defect and on the characteristics of the dielectric substrate, and they need to be evaluated for each specific case.

The microstrip–based DGS shown in Figure 6.1 has also its counterpart in coplanar waveguide technology. A dumbbell–shaped aperture can be integrated on the ground plane of a coplanar waveguide (Figure 6.3), with the aim to design a band–stop filter [25]. The dumbbell–shaped defect consists of two square apertures of side a, connected by short gaps of length l and width d to the slots of the coplanar waveguide (Figure 6.3a). In this case, the circuit can be realized in uni-planar technology, as the defect is located on the same plane of the slots of the coplanar waveguide. In addition, different topologies can be adopted: instead of removing completely the metal in the square apertures, only a peripheral strip can be removed, thus leaving an internal square metal patch (Figure 6.3b). This latter topology is suitable for integration with control elements (e.g., varactor diodes), which allow the tuning of the stop-band frequency (Figure 6.3c).

Other examples of DGS based on a coplanar waveguide were proposed in [21], where a spiral-shaped defect is integrated on the ground plane of the coplanar waveguide, and in [26], where a meander line connected to the coplanar waveguide was adopted to design band-stop filters with broad rejection bandwidth.

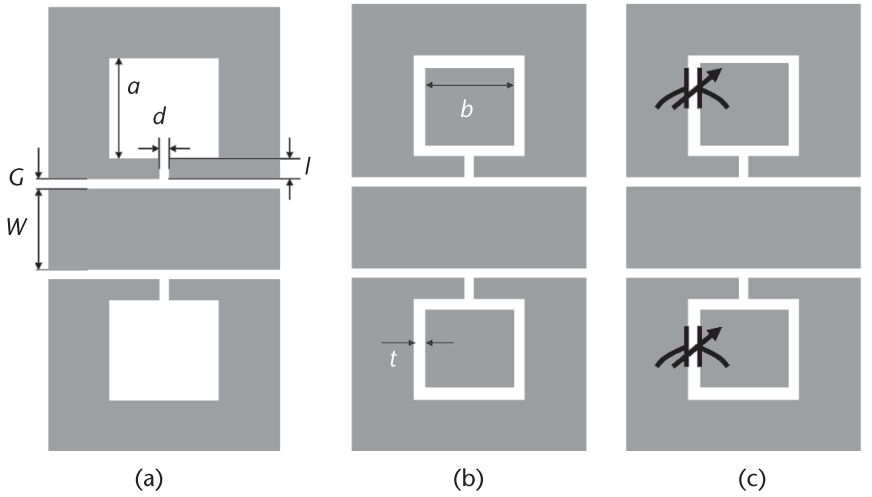

Figure 6.3 Defected ground structure in coplanar waveguide: (a) dumbbell-shaped defect; (b) slot ring defect; (c) tunable slot ring defect, integrated with a varactor diode. (from [25], © 2006 IEEE. Reprinted with permission.).

6.1.2 Unit Cell and Periodic DGS

In several cases, a single defect represents the unit cell of a periodic pattern of apertures, etched in the ground plane of a microstrip line or a coplanar waveguide [9–10]. Periodic DGS allow achieving a more selective frequency response, enhancing the band-stop properties and getting more pronounced slow-wave effect, compared to structures based on a single defect.

Two major topologies have been investigated for periodic DGS-based components: one with longitudinal periodicity and the other with transversal (or vertical) periodicity. The first solution is represented by an array of identical defects, longitudinally aligned along the propagation direction of the transmission line (Figure 6.4a). This structure allows, for instance, designing band-stop filters with broad rejection bandwidth: the central frequency mainly depends on the geometry of the unit cell and (partially) on the longitudinal spacing of the defects, while the depth and the bandwidth of the stop band are mainly related to the number of periods [9].

In the second topology of periodic DGS, a number of identical defects are periodically aligned transversally with respect to the propagation direction of the transmission line (Figure 6.4b). Compared to longitudinally periodic DGS, the transversal topology provides a much higher slow-wave effect and leads to a significant reduction in length, at the cost of an increased width. A combination of longitudinal and transversal configurations can also be adopted (Figure 6.4c): in particular, in [10] it was demonstrated that this structure permits to reduce the length of the matching network of an amplifier by almost 50%.

In some cases, it has been shown that improved performance can be achieved by adopting a non-periodic pattern of defects: by properly optimizing the size of each single defect, the frequency response of a band-stop filter can be improved by reducing the ripple and broadening the rejection bandwidth [11].

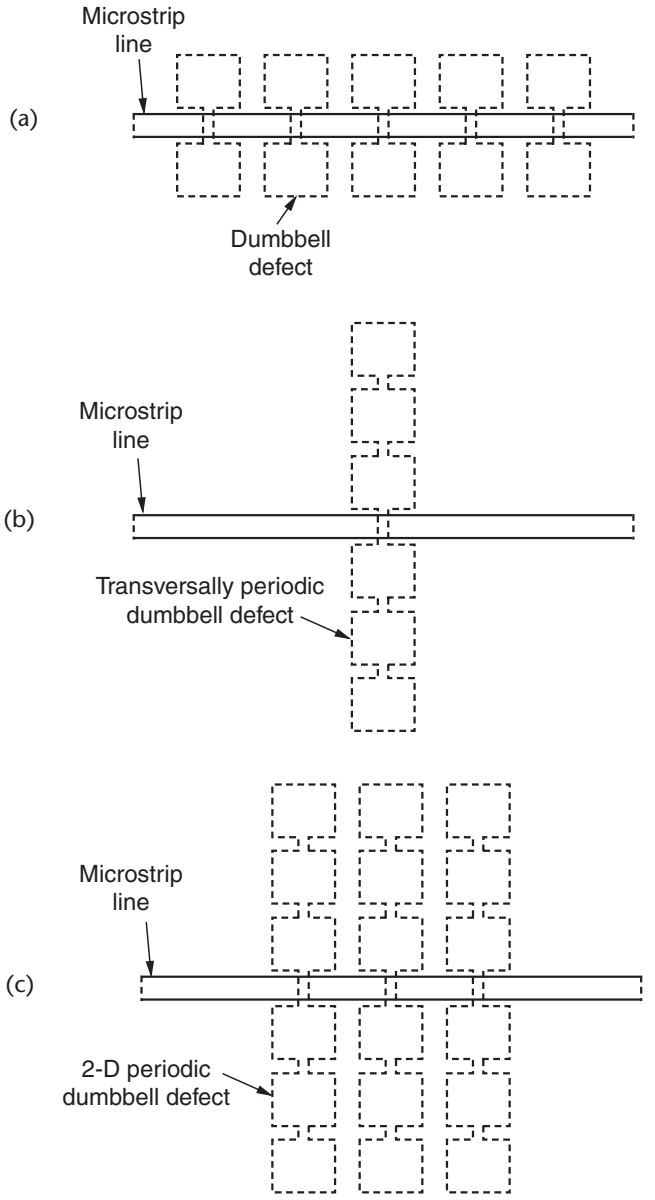

Figure 6.4 Circuit topologies of periodic DGS: (a) longitudinal configuration [9]; (b) transversal configuration; (c) 2-D configuration [10].

A class of components based on periodic defects, similar to periodic DGS and their precursors, is represented by the electromagnetic band-gap (EBG) structures. In EBG structures, the defects are arranged according to a two-dimensional periodic pattern in the ground plane of microstrip line or coplanar waveguide circuits. EBG structures exploit the periodicity to prevent the electromagnetic wave propagation in certain frequency bands and certain directions, and to synthesize artificial magnetic conductors and negative index materials. However, these structures are beyond the scope of this chapter: a thorough description of their properties and applications can be found in papers [12–14] and books [27–29].

6.1.3 Advantages and Disadvantages of DGS

DGS represent a significant advance in the field of microstrip line and coplanar waveguide components, as they allow improving the performance of a large variety of passive components, active circuits, and antennas, with a minimum increase in the manufacturing complexity. They permit to enhance the frequency response of filters, to improve the efficiency of power amplifiers, to control harmonic frequencies in active circuits and antennas, and to reduce the size of hybrid couplers and power dividers. All these applications will be described in Sec. 6.4.

Nonetheless, some disadvantages are associated with the use of DGS–based circuits. The major drawback of this class of structures, which often is not fully considered in the literature, is the effect of spurious radiation leakage and consequent decrease in Q, due to the presence of apertures in the ground plane. Radiation causes two major problems; one is the power loss, which reduces the overall efficiency of the component, and the other is the undesired parasitic coupling between adjacent circuits, which can jeopardize the proper operation of large or complex circuits. Furthermore, an additional step is needed to design and etch ground plane, and the circuit needs special housing or enclosure.

In addition, the numerical modeling of DGS circuits is more complex compared to classical microstrip line and coplanar waveguide structures: due to the radiation and parasitic coupling effects, the approximation of boxed printed circuits (often adopted in the modeling of classical microstrip components) cannot be applied, and radiation boundary conditions need to be employed in the electromagnetic simulation. In addition, there is a lack of equivalent circuit models of classical DGS in commercial software, and this makes the design phase of DGS–based circuits more time consuming. The modeling issues are even more significant in the case of circuits based on periodic DGS.

6.2 DGS Characteristics

DGS exhibit unique important features, which are particularly useful to improve the performance of printed components and systems. Among them, one of the most interesting characteristics is the possibility to introduce transmission zeros in the frequency response of microstrip-line and coplanar-waveguide components. This stop-band property can be exploited to increase the selectivity of filters and to improve the out-of-band frequency response of several active and passive components.

The second useful characteristic of DGS is related to the possibility to support slow-wave propagation; this means that DGS-loaded transmission lines support guided waves with phase velocity slower than the corresponding transmission lines without defects. The slow-wave characteristic of DGS allows reducing the dimension of printed microwave circuits.

The third important feature of DGS is the possibility to implement high-impedance transmission lines. This is typically a critical task, especially in the case of microstrip lines, as transmission lines with high characteristic impedance require very thin conductor lines. This problem can be overcome by the use of DGS, thus relaxing the requirements in accuracy of the fabrication process.

In this Section, various DGS characteristics are carefully investigated, through the use of a simple equivalent circuit model, and a physical interpretation of the different phenomena is provided.

6.2.1 Stop-Band Properties

The stop-band properties of DGS were first exploited in [5, 9] to design a band-stop filter. The filter is based on a conventional straight microstrip transmission line with a dumbbell aperture etched in the backside metallic ground plane (Figure 6.1). The dumbbell defect consists of two rectangular apertures of dimensions $a \times b$ connected by a thin slot of width g and length w. The presence of the defect determines the stop-band effect, introducing a transmission zero in the frequency response with no need of any modification of the conductor line. The frequency of this transmission zero depends on the shape and size of the defect, and can be modified accordingly: in particular, the stop-band frequency decreases when increasing the size of the defect, namely the dimensions a and b.

A straightforward physical explanation of this phenomenon can be provided. In fact, the presence of the aperture in the ground plane determines two major effects, which can be combined and optimized to achieve the desired frequency response of the circuit.

The first relevant effect is due to the perturbation of the shield current distribution in the ground plane: because of the aperture etched in the ground plane, the electric current flowing on the metallic ground has to face a longer path. If the size of the aperture is small compared to wavelength and the quasi-static approximation can be applied, this perturbation of the path determines an additional series inductance L. Increasing the size of the aperture (more specifically, increasing the sides a and b of the two squares of the dumbbell, see Figure 6.5a) determines a longer path of the current and consequently a larger series inductance.

The second significant effect of the aperture in the ground plane is due to the thin gap located below the strip conductor: the thin gap determines an accumulation of charge and consequently (if the aperture is small compared to wavelength and the quasi-static approximation is applicable) a series capacitance C. In particular, a smaller gap corresponds to a larger value of the series capacitance, while keeping the same size of the two squares of the dumbbell aperture (dimensions a and b, Figure 6.5a).

The combined effect of these two phenomena can be modeled by an equivalent LC-parallel lumped element circuit (Figure 6.5b), where the inductance L is due to the perturbation of the current path and the capacitance C depends on the accumulation of charge near the gap. In this equivalent circuit, Z_0 represents the characteristic impedance of the transmission line. This LC-parallel circuit exhibits a resonance at frequency f_0, which can explain the transmission zero in the frequency response of the microstrip line with the defect located below the conductor line. Obviously, the stop-band frequency f_0 depends on L and C and can be computed as

$$f_0 = \frac{1}{2\pi\sqrt{LC}} \tag{6.1}$$

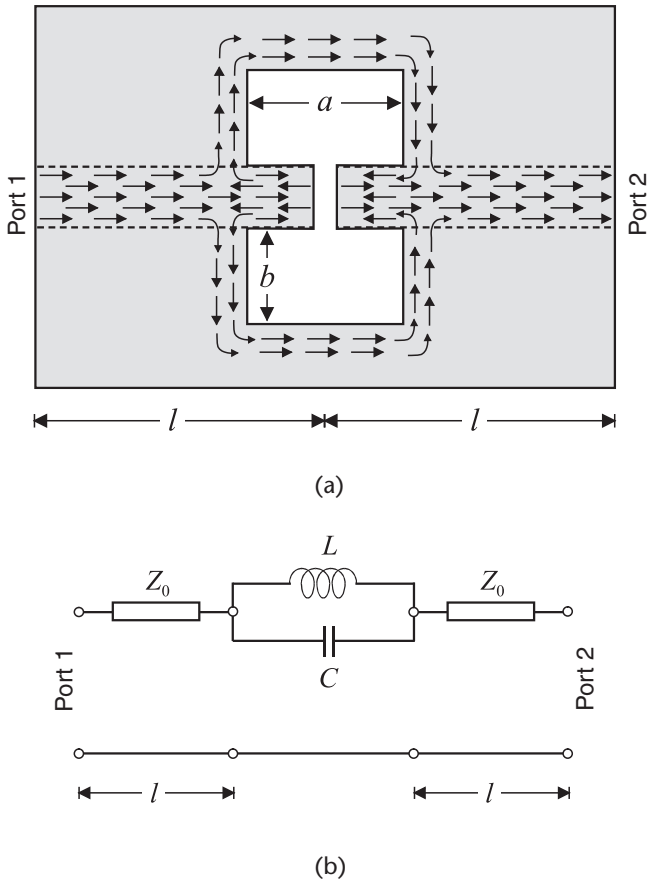

Figure 6.5 Band-stop properties of DGS components: (a) modification of the shield current distribution in the ground plane, due to the presence of the dumbbell-shaped aperture; (b) equivalent circuit of the dumbbell DGS, corresponding to a lumped-element *LC*-parallel resonator.

This effect is particularly useful for the design of band-stop filters, as well as for improving the selectivity of band-pass filters, where out-of-band transmission zeros help improving the response selectivity and eliminating undesired spurious bands. The values of inductance L and capacitance C can be almost independently controlled, thus providing two important degrees of freedom in the circuit design.

An example to clarify these concepts is described next. The microstrip line coupled with the dumbbell defect shown in Figure 6.1 was analyzed by a full-wave simulator, and the parameters L and C of the equivalent circuit model were derived by fitting procedure [5]. The frequency response obtained from the equivalent circuit model of Figure 6.5b shows very good agreement with the result of the full-wave simulation [5]. In all cases, the dielectric substrate has a thickness $h = 1.5748$ mm and relative dielectric permittivity $\varepsilon_r = 10$. The width of the 50 Ω microstrip line is $w = 1.62$ mm. The values of the other geometrical dimensions (namely, $a = b$, and g) are variables, and their effect on the values of L and C and consequently on the stop-band frequency f_0 are investigated.

As a first step, the gap distance is kept constant at the value $g = 0.2$ mm and dimensions a and b are modified. Three analyses, with $a = b = 1.3$ mm, 2.5 mm, and 4.6 mm, respectively, have been performed (Figure 6.6a), and the corresponding equivalent circuit models have been derived. The values of L and C, as well as of the stop-band frequency f_0, are reported in Table 6.1 for the three cases. These results show that the value of the inductance L is strongly affected by the dimensions a and b of the dumbbell, which contribute to increase the path length of the shield current; more specifically, L increases when a and b increase. Conversely, the value of C is practically unaffected when varying a and b. Consequently, the stop-band frequency f_0 decreases when the size of defect is increased.

In the second set of analyses, the dimensions a and b are kept constant ($a = b = 2.5$ mm for all cases) and the gap distance g is modified. Also in this case, three analyses have been performed, with $g = 0.2$ mm, 0.4 mm, and 0.6 mm, respectively (Figure 6.6b), and the corresponding equivalent circuit models have been derived. The values of L, C, and f_0, are reported in Table 6.2 for the three values of g. These results show that the value of the capacitance C decreases when the gap distance g becomes larger, as expected from physical considerations. Conversely, dimension g has a minor (although not negligible) effect on the value of the inductance L. The overall effect is a small reduction of the stop-band frequency f_0 when the gap becomes smaller.

All these analyses demonstrate that the stop-band frequency f_0 of the microstrip line loaded with the dumbbell defect can be adjusted by properly modifying the geometrical dimensions of the defect. Moreover, the values of L and C can be controlled quite independently, and this allows to modify the width of the stop band, which is related to $\sqrt{L/C}$. In all cases, the footprint of the complete circuit remains small compared with the wavelength at the operation frequency.

6.2.2 Slow-Wave Propagation

Another important property of DGS-based circuits, strictly related with the stop-band property discussed in Section 6.2.1, is the possibility to support slow-wave propagation [30]. In slow-wave propagation regime, the phase velocity of the waves

Table 6.1 Equivalent circuit model parameters extracted from the analysis of the microstrip line coupled with a dumbbell defect. The gap distance is kept constant at $g = 0.2$ mm [5]

	$a = b = 1.3$ mm	$a = b = 2.5$ mm	$a = b = 4.6$ mm
Inductance L (nH)	0.3675	0.865945	1.97725
Capacitance C (pF)	0.51222	0.52845	0.537948
Stop-band frequency f_0 (GHz)	11.6	7.44	4.88

Table 6.2 Equivalent circuit model parameters extracted from the analysis of the microstrip line coupled with a dumbbell defect. The square side is kept constant at $a = b = 2.5$ mm [5]

	$g = 0.2$ mm	$g = 0.4$ mm	$g = 0.6$ mm
Inductance L (nH)	0.865945	0.90712	0.96825
Capacitance C (pF)	0.52845	0.43306	0.34247
Stop-band frequency f_0 (GHz)	7.44	8.03	8.74

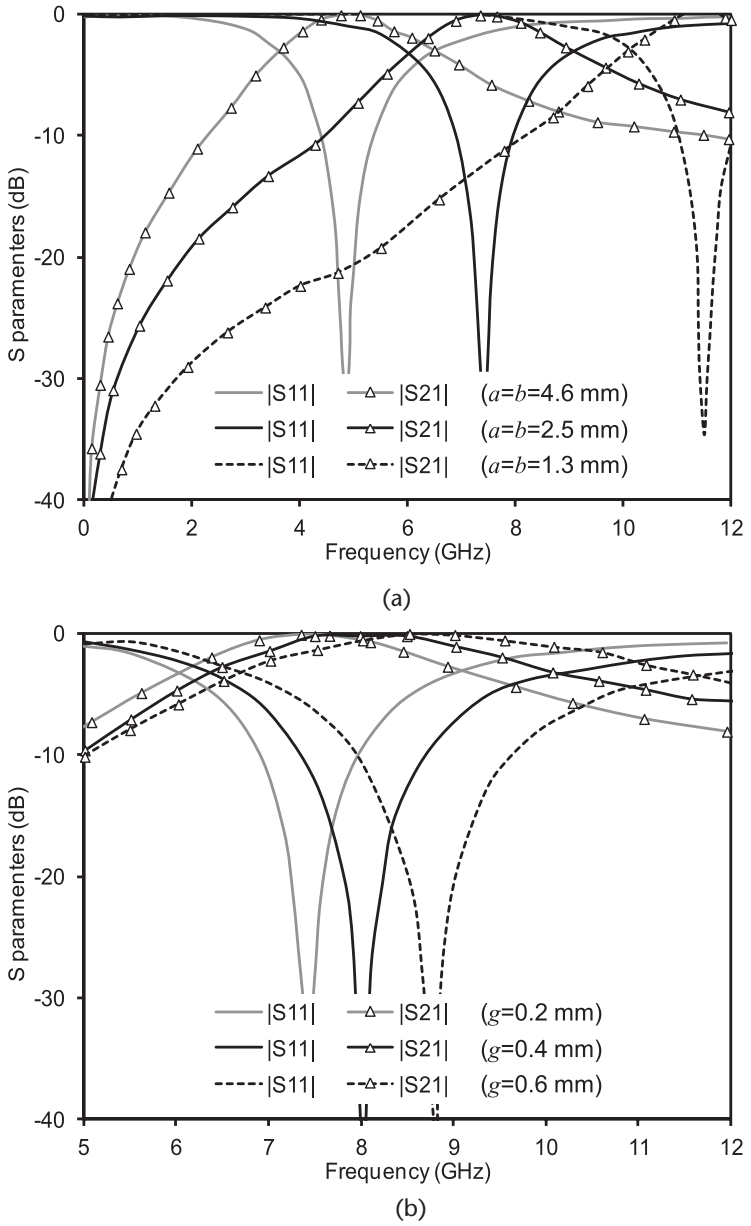

Figure 6.6 Effect of the geometrical dimensions on the stop-band properties of a dumbbell-aperture DGS filter: (a) simulated frequency response for different values of a and b (g = 0.2 mm fixed); (b) simulated frequency response for different values of g (a = b = 2.5 mm fixed). (From [5], ©2001 IEEE. Reprinted with permission.)

propagating in the DGS-loaded microstrip line is smaller than the phase velocity in the corresponding conventional microstrip line (realized on the same dielectric substrate, but with no defects). Likewise, the propagation constant β of the DGS line is larger than the propagation constant k of the conventional microstrip line. Due to this slow-wave effect, the DGS line has longer electrical length than the con-

ventional microstrip line with the same physical length. Therefore, the slow-wave effect can be exploited to reduce the size of printed microwave components and circuits. The slow-wave factor, which can be defined as the ratio β/k, represents a measure of the possible reduction in linear dimension of the circuits.

The LC equivalent circuit shown in Figure 6.5b permits to easily explain the slow-wave propagation phenomenon. In the frequency range below the resonance frequency of the parallel LC resonator ($f < f_0$), the inductance L represents the dominant element, and the effect of the capacitance C can be neglected. Consequently, the equivalent circuit of the DGS (i.e., the parallel LC circuit shown in Figure 6.5b) reduces to the series inductance L. When considering a short section of microstrip line with a defect, this additional series inductance contributes to increase in the inductance per unit length of the transmission line: as a consequence, the propagation constant β (proportional to the square root of the inductance per unit length) becomes larger than the corresponding propagation constant k of the conventional microstrip line ($\beta > k$).

More specifically, the propagation constant k of the conventional microstrip line can be expressed as

$$k = \omega\sqrt{L_0 C_0} \tag{6.2}$$

where ω is the angular frequency and L_0 and C_0 represent the inductance and capacitance per unit length of the conventional microstrip line, respectively.

In a section of DGS-loaded microstrip line of length d (small compared to wavelength, $d \ll \lambda$), the inductance per unit length is increased by L/d, and consequently the propagation constant β is given by

$$\beta = \omega\sqrt{\left(L_0 + \frac{L}{d}\right) C_0} \tag{6.3}$$

The value of β is larger than the value of k for the corresponding conventional microstrip line, thus demonstrating that, for $f < f_0$, the DGS-loaded microstrip line behaves as a slow-wave structure (note that, on the contrary, for $f > f_0$ the capacitor has the dominant effect and the structure supports fast-wave propagation). Expression (6.3) is a good representation of the propagation constant β of the DGS structure, also in the case of periodic DGS, provided that the dimension of the defect (or the short section of microstrip line with a defect) is small compared to wavelength ($d \ll \lambda$). Therefore, this expression is valid only in the low frequency approximation.

The slow-wave factor, defined as the ratio β/k, can be obtained by comparing expressions (6.2) and (6.3). From these equations, however, it appears that the slow-wave factor is independent of frequency: this assumption is not correct, as expression (6.3) is valid only in the low frequency range.

A more accurate study of the slow-wave factor is based on the calculation of the scattering parameters of the DGS-loaded microstrip line, obtained either by a full-wave simulation or by the analysis of the LC equivalent circuit model. By considering the equivalent circuit model of Figure 6.5b, the scattering parameter S_{21} is obtained as

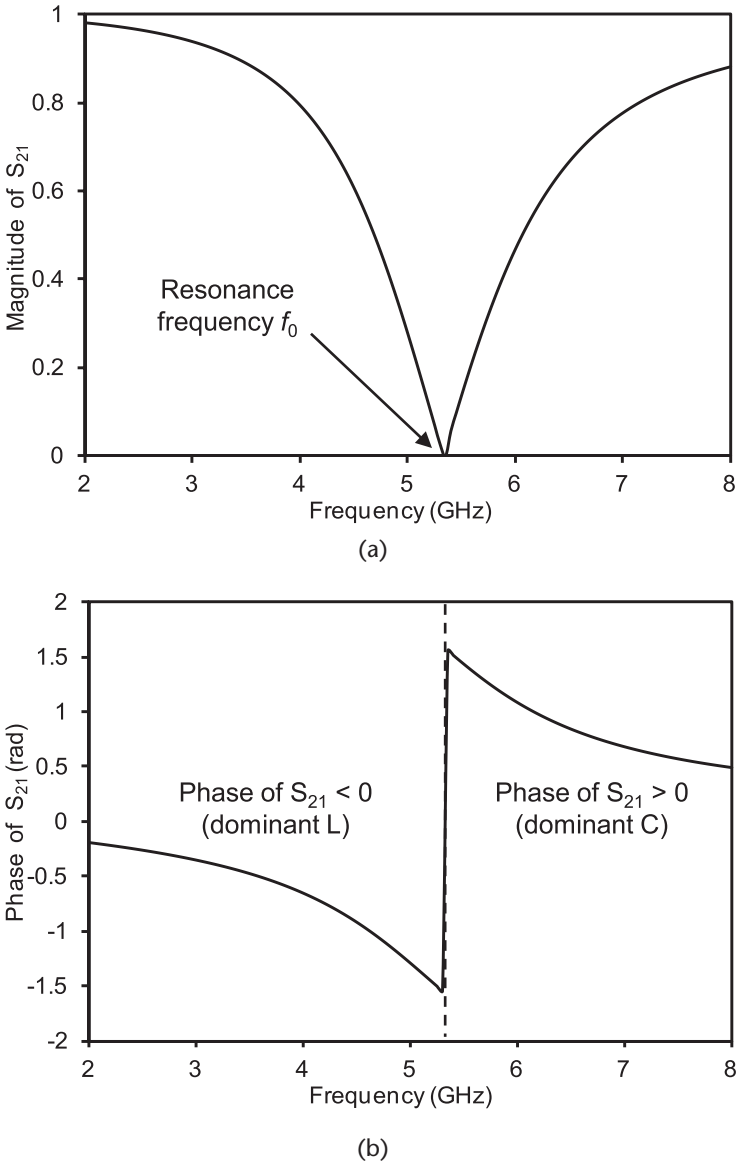

Figure 6.7 Scattering parameter S_{21} of a DGS–based microstrip line, obtained by the analysis of the equivalent circuit model shown in Figure 6.5b (L = 1.33 nH, C = 0.67 pF, and Z_0 = 50 Ω) [30]: (a) amplitude of S_{21}, showing the band-gap frequency range; (b) phase of S_{21} exhibiting a strong variation near the resonance frequency.

$$S_{21} = \frac{2Z_0(1-\omega^2 LC)}{2Z_0(1-\omega^2 LC)+j\omega L} \tag{6.4}$$

where Z_0 represents the reference impedance and is the characteristic impedance of the transmission line in this case. The amplitude and phase of S_{21} are:

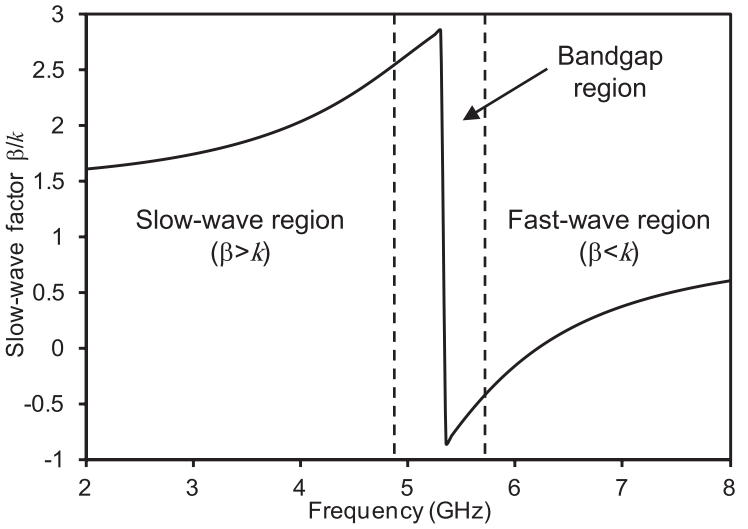

Figure 6.8 Slow-wave factor (β/k) as a function of frequency, calculated by using (6.7) (L = 1.33 nH, C = 0.67 pF, Z_0 = 50 Ω, $k = \omega/c$, and d = 7.5 mm) [30].

$$|S_{21}| = \frac{2Z_0\left|1-\omega^2 LC\right|}{\sqrt{[2Z_0(1-\omega^2 LC)]^2 + (\omega L)^2}} \tag{6.5a}$$

$$\angle S_{21} = -\arctan\left[\frac{\omega L}{2Z_0(1-\omega^2 LC)}\right]. \tag{6.5b}$$

Figs. 6.7a and 6.7b report the amplitude and phase, respectively, of the scattering parameter S_{21} of a DGS-based microstrip line, calculated by using formulas (6.5) and based on the LC equivalent circuit model. The values L = 1.33 nH, C = 0.67 pF, and Z_0 = 50 Ω are adopted in the calculation [30]. The plot of the amplitude $|S_{21}|$ (Figs. 6.7a) shows a minimum of the transmission near the resonance frequency f_0 = 5.32 GHz (center of the band–gap region). Regarding the phase of the scattering parameter S_{21} (Figs. 6.7b), these results show that $\angle S_{21} < 0$ in the frequency range below the resonance frequency f_0, where there is the dominant effect of L (slow–wave propagation region), whereas $\angle S_{21} > 0$ in the frequency range above f_0, where there is the dominant effect of C (fast–wave propagation region).
By using these results, the propagation constant β can be calculated as

$$\beta = k - \frac{\angle S_{21}}{d} = k + \frac{1}{d}\arctan\left[\frac{\omega L}{2Z_0(1-\omega^2 LC)}\right] \tag{6.6}$$

due both to the propagation in the transmission line and to the additional phase change attributed to the DGS. Consequently, the slow-wave factor β/k is obtained as

$$\frac{\beta}{k} = \frac{kd + \arctan\left[\frac{\omega L}{2Z_0(1-\omega^2 LC)}\right]}{kd} \tag{6.7}$$

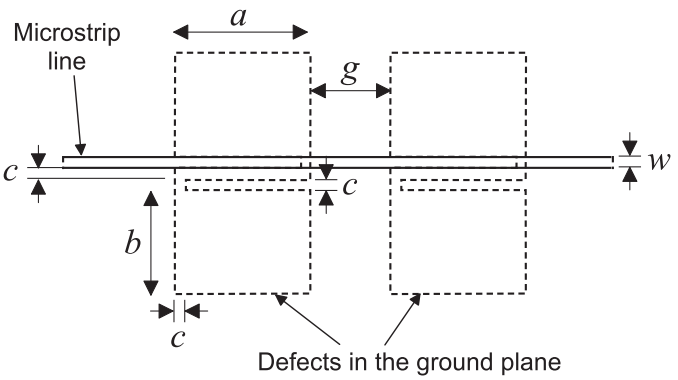

Figure 6.9 High-impedance microstrip line, based on DGS: the DGS dimensions are $a = b = g = 6$ mm and $c = w = 0.4$ mm. (from [6], © 2001 IEEE. Reprinted with permission.).

Figure 6.8 shows the value of the slow–wave factor versus frequency. The maximum value of the slow-wave factor is obtained for frequencies smaller than f_0 and very close to it. Therefore, the slow–wave effect is more pronounced near the stop–band frequency, but only at the price of a reduced $|S_{21}|$: a compromise occurs between transmission performance and slow–wave factor.

6.2.3 Realization of Transmission Lines with High Characteristic Impedance

The realization of transmission lines with high characteristic impedance is typically a serious problem in printed technology: in the case of microstrip lines, for instance, technological constraints limit the highest possible characteristic impedance to 120–130 Ω. For higher values of the characteristic impedance, the conductor width becomes too narrow, and fabrications inaccuracies are an issue. Some applications require the implementation of high impedance transmission lines (e.g., unbalanced power dividers [6]).

The use of DGS allows the realization of high impedance microstrip lines, with conductor width much wider than in the conventional microstrip lines. Using DGS permits to increase the equivalent inductance per unit length, and to decrease the equivalent capacitance, thus finally raising the value of the characteristic impedance up to more than 200 Ω.

An example of high-impedance DGS-based microstrip line is reported in [6], where a transmission line with characteristic impedance $Z_0 = 158$ Ω is required for the design of a 4:1 unequal Wilkinson power divider. For a substrate with $h = 0.787$ mm and $\varepsilon_r = 2.2$, the strip width is $w = 0.17$ mm for a conventional microstrip line, which is extremely challenging for many fabrication technologies. Thanks to the use of DGS, a transmission line with characteristic impedance of 158 Ω was obtained with a strip width $w = 0.4$ mm, almost 2.5 times wider than the conventional microstrip line. The high impedance microstrip line is based on the use of two defects as shown in Figure 6.9.

As a side-effect, the use of defects in the ground planes permits reducing the component dimensions: more specifically, the length of a quarter-wavelength line

section reduces from 38.83 mm in the case of the conventional microstrip line to 32.3 mm in the case of the DGS-loaded line, due to the slow-wave effect discussed in Section 6.2.2.

6.3 Modeling of DGS

The analysis and design of DGS-based circuits is more challenging than the modeling of circuits based on conventional microstrip and coplanar lines. The first reason is that, other than common microstrip line or coplanar waveguide discontinuities, no equivalent circuit models of DGS or DGS-loaded transmission lines are currently available in commercial circuit simulators. The second reason is the intrinsic complexity of the electromagnetic problem: in DGS-based circuits, a number of relevant electromagnetic effects need to be accounted for, like for instance the radiation leakage and the spurious coupling between the DGS and adjacent portions of the circuit.

6.3.1 Full-Wave Modeling

The rigorous electromagnetic modeling of DGS-based circuits requires the use of full-wave simulation tools. A variety of numerical techniques (either 2.5D or 3D) can be adopted for the full-wave modeling of DGS circuits, including the integral equation technique in conjunction with the method of moments, the finite element method, and the finite-difference time domain method.

The complete analysis and (especially) the optimization procedure of DGS-based circuits by a full-wave simulator, however, is a heavy and lengthy process. For this reason, it is avoided whenever possible, and it is replaced by the use of equivalent circuit models.

Nevertheless, the use of full-wave simulators is important, because it permits to precisely understand and evaluate the physical aspects of DGS circuits (like the electric current path and the charge distribution): this analysis process has a paramount importance in the study of DGS circuits, as it allows deriving physical-based equivalent circuit models.

6.3.2 Equivalent Circuit Models

The development of accurate and physical-based equivalent circuit models allows for the fast modeling and design of DGS-loaded circuits, both in the case of isolated and of periodic defects. Currently, equivalent circuit models of DGS are not included in the most used commercial simulators, and for this reason a significant amount of research has been devoted to the development of simple and accurate DGS equivalent models [5, 8, 10, 31–36].

Equivalent circuit models of DGS are usually derived from the frequency response of a DGS-based circuit, computed by a full-wave simulator. In all cases, parametric equivalent models are needed, where the element values of the equivalent models depend on the physical dimensions of the DGS. Physical-based models, which recall the physical geometry and current distribution of the DGS circuit,

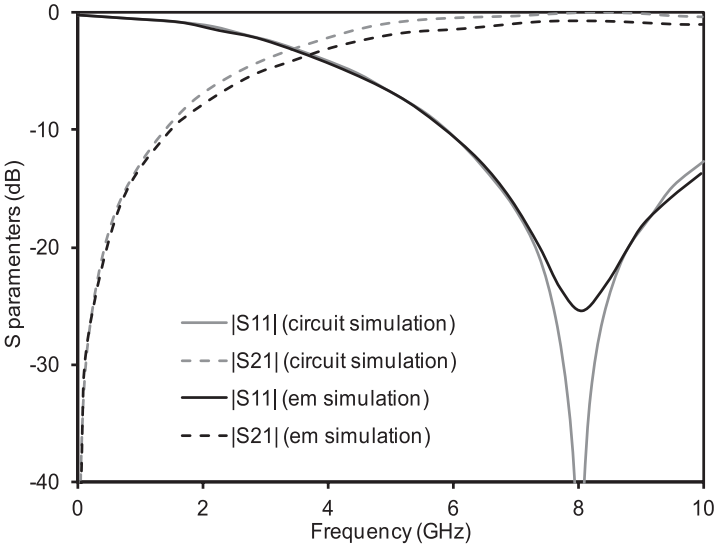

Figure 6.10 Full-wave and LC circuit simulation results of the dumbbell DGS shown in Figure 6.1 (from [5], © 2001 IEEE. Reprinted with permission.)

allow for a better understanding of the behavior of the components and permit to exploit these physical insights in the optimization process.

Simple LC Equivalent Circuit Model of DGS

The simplest equivalent circuit model of DGS consists of a parallel *LC* circuit, already discussed in Sec. 6.2 to introduce the fundamental properties of DGS-based circuits (Figure 6.5b). This *LC* equivalent model is inspired by the resonance properties of DGS, which exhibit a stop-band at frequency f_0 [5]. The element values L and C of the equivalent circuit model are directly obtained from the full-wave simulation of the structure as:

$$C = \frac{\omega_c}{2Z_0\ (\omega_0^2 - \omega_c^2)} \tag{6.8a}$$

$$L = \frac{1}{\omega_0^2\ C} \tag{6.8b}$$

where ω_0 is the stop-band angular frequency and ω_c is the 3-dB cutoff angular frequency, and Z_0 represents the characteristic impedance of the input/output transmission line [31]. This equivalent circuit model does not take into account any type of loss (possibly due to metal finite conductivity, dielectric loss angle, or radiation effects).

As an example of this equivalent circuit model of DGS, the circuit based on the dumbbell-shaped DGS coupled with a microstrip line (introduced in Figure 6.1) is considered. The dimensions of the dumbbell defect are $a = b = 5$ mm, $w = 2.4$ mm, $g = 0.5$ mm, and the substrate has a thickness $h = 31$ mil and a dielectric permittivity $\varepsilon_r = 2.2$. This circuit exhibits a stop-band frequency $f_0 = \omega_0/(2\pi) = 8$ GHz and

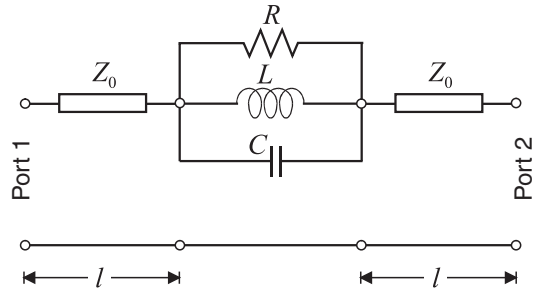

Figure 6.11 Equivalent circuit model of a DGS-loaded transmission line, consisting of a parallel RLC resonator.

a 3-dB cutoff frequency $f_c = \omega_c/(2\pi) = 3.5$ GHz. The characteristic impedance of the microstrip line is $Z_0 = 50\ \Omega$. After calculating the values of C and L by using equations (6.8), the frequency response of the circuits can be computed through the equivalent circuit model shown in Figure 6.5b: the circuit simulation compares very well with the full-wave analysis results, as shown in Figure 6.10 [5].

In the design phase, the effect of the shape and size of the defect on L and C is taken into account, as discussed in Sec. 6.2. In the case of the dumbbell-shaped DGS, increasing the size of the DGS usually shifts down the resonance frequency f_0, mainly due to the increased path length of the electric current density in the ground plane (that increases the value of inductance).

Losses can be easily accounted for by adding a resistor in parallel to the LC resonator (Figure 6.11). Similarly to the case of L and C, the value of the resistance R can be obtained by the full-wave analysis:

$$R = \frac{2Z_0}{\sqrt{\frac{1}{|S_{11}(\omega_0)|^2} - \left[2Z_0\left(\omega_0 C - \frac{1}{\omega_0 L}\right)\right]^2 - 1}} \tag{6.9}$$

where $|S_{11}(\omega_0)|$ represents the magnitude of the input reflection coefficient, calculated at the stop-band angular frequency ω_0 [31]. In this case, the resistance R permits to take into account all types of losses, including dielectric, conductor, and radiation losses.

In the case of asymmetric DGS configuration, the frequency response can exhibit two different resonance frequencies: consequently, the equivalent circuit should be modified to deal with this structure, by considering two parallel RLC resonators connected in series [8].

Broadband Equivalent Circuit Models of DGS

The parallel LC circuits (or the parallel RLC if losses need to be accounted for) represent easy and effective solutions for the equivalent circuit modeling of DGS. Nevertheless, as they are based on lumped elements, these equivalent circuits are able to exhibit only one pole. In some applications, conversely, it is important to carefully represent the broadband frequency behavior of the circuit, including peri-

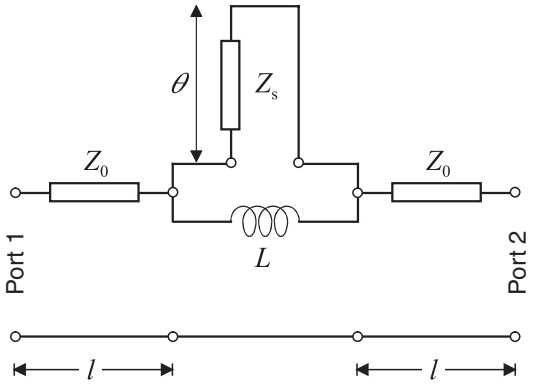

Figure 6.12 Equivalent circuit model of DGS, based on an inductor in parallel with a shorted stub.

odic replicas and spurious bands. For this reason, a different equivalent circuit has been developed, based on an inductor in parallel with a shorted stub (Figure 6.12). This type of equivalent circuit has been widely adopted in the literature, especially for the modeling of spiral defects in coplanar waveguide technology [10, 32–35]. In this model, the inductance L represents the quasi-static behavior, and the stub accounts for the effects of the resonances at high frequency. The values of the inductance L and of the length and characteristic impedance of the stub are usually obtained by curve fitting of full-wave simulation data.

More complex circuit topologies have also been proposed, with the aim to increase the number of degrees of freedom and, consequently, to guarantee the accuracy of the model over a broader band. The broadband validity of the equivalent circuit models is particularly important for certain applications, like the design of power amplifiers, where the active devices need to be terminated with the proper impedance values at the harmonic frequencies.

A π-type equivalent circuit model was proposed in [37]: in this equivalent model, the series element is a classical parallel RLC resonator, and the shunt elements are parallel RC circuits, which permit to take into account the fringing fields (and associated losses) at the discontinuity between the unperturbed transmission line and the DGS (Figure 6.13).

In this equivalent circuit model, the value of the lumped elements can be derived either from the full-wave analysis of the structure [37], or from measured data of a prototype. The method is briefly described below.

Once the S-parameters of the structure have been determined, by either simulations or measurements, the $ABCD$-parameters can be derived as:

$$A = \frac{(1 + S_{11})(1 - S_{22}) + S_{12}S_{21}}{2S_{21}} = 1 + \frac{Y_b}{Y_a} \tag{6.10a}$$

$$B = \frac{(1 + S_{11})(1 + S_{22}) - S_{12}S_{21}}{2S_{21}} = \frac{1}{Y_a} \tag{6. 10b}$$

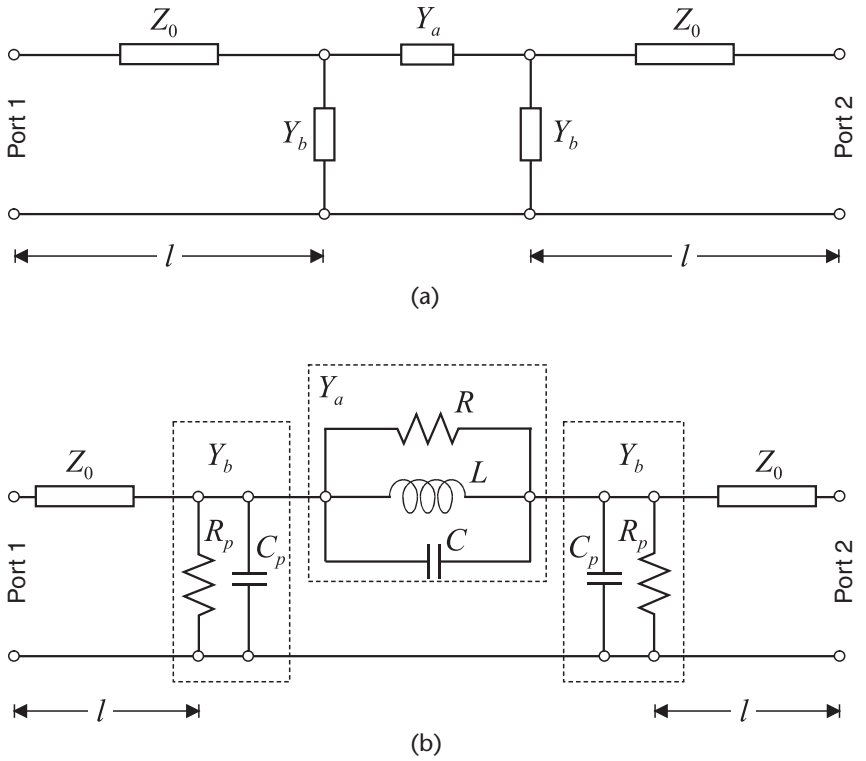

Figure 6.13 π-type equivalent circuit model of DGS.

$$C = \frac{1}{Z_0}\frac{(1-S_{11})(1-S_{22})-S_{12}S_{21}}{2S_{21}} = 2Y_b + \frac{Y_b^2}{Y_a} \tag{6. 10c}$$

$$D = \frac{(1-S_{11})(1+S_{22})+S_{12}S_{21}}{2S_{21}} = 1 + \frac{Y_b}{Y_a} \tag{6. 10d}$$

The *ABCD*-parameters are related to the admittances of the π-type equivalent circuit model shown in Figure 6.13a:

$$Y_a = \frac{1}{B} = \frac{1}{R} + j\left(\omega C - \frac{1}{\omega L}\right) \tag{6. 11a}$$

$$Y_b = \frac{A-1}{B} = \frac{-1 \pm \sqrt{1+BC}}{B} = \frac{D-1}{B} = \frac{1}{R_p} + j\omega C_p \tag{6. 11b}$$

In principle, the values of the lumped elements appearing in Figure 6.13b can be obtained from the admittances Y_a and Y_b at the angular frequency ω_1, and from the knowledge of the resonance angular frequency ω_0

$$\omega_0 = \frac{1}{\sqrt{LC}} \tag{6.12}$$

corresponding to the frequency where the imaginary part of Y_a vanishes. More specifically, the value of the lumped elements are given by:

$$R = \frac{1}{\mathrm{Re}\{Y_a\}} \tag{6. 13a}$$

$$C = \frac{\mathrm{Im}\{Y_a\}}{\omega_0\left(\frac{\omega_1}{\omega_0} - \frac{\omega_0}{\omega_1}\right)} \tag{6. 13b}$$

$$L = \frac{1}{\omega_0^2\, C} \tag{6. 13c}$$

$$R_p = \frac{1}{\mathrm{Re}\{Y_b\}} \tag{6. 13d}$$

$$C_p = \frac{\mathrm{Im}\{Y_b\}}{\omega_1} \tag{6. 13e}$$

In most cases, however, the values obtained by equations (6.13) represent a starting point, and they are subsequently optimized by fitting the frequency response calculated with a full-wave simulation or measured data, with the aim to improve the accuracy of the model and its validity over a broad frequency band.

Quasi-Static Equivalent Circuit Model of DGS

A quasi-static equivalent circuit model of DGS was proposed in [38], based on a derivation approach that is quite different from the previous models. This equivalent circuit was developed specifically for the case of the dumbbell-shaped defect shown in Figure 6.1, and it is based on the observation of the current path in the defected ground plane. As it appears from Figure 6.5a, the electric current density on the ground plane flows in a narrow strip along the periphery of the defect, being practically negligible elsewhere. For this reason, the structure can be simplified as shown in Figure 6.14a, where the defected ground plane is replaced by a set of narrow metal strips, located in the region where the current is more concentrated. The width of the metal strips, which is related to the inductance in the equivalent model, is selected on the basis of the current path observation. The filament model of the simplified ground plane is shown in Figure 6.14b: it includes a cross, located at the junction of the microstrip line and the DGS, two arms with straight sections and 90° bends, and another cross at the opposite side of the DGS. In the middle there is a gap, responsible for the capacitance in the equivalent model.

The use of this filament model of the simplified geometry allows for developing the equivalent circuit model (Figure 6.15): the values of inductance and capacitance elements are derived from the physical dimensions, by adopting quasi-static expressions for microstrip crosses, straight lines, bends, and gaps available in the literature. This approach guarantees a direct relation between the geometry of the

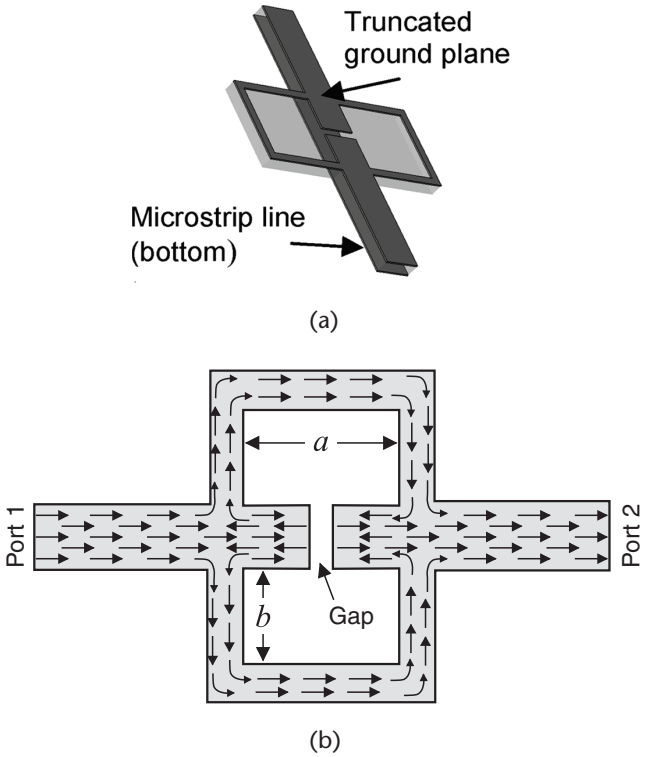

Figure 6.14 Geometry of the structure used to derive a quasi-static model of a dumbbell DGS circuit: (a) truncated structure, showing the path of the electric current density; (b) filament model of the simplified structure. (from [38], © 2006 IEEE. Reprinted with permission.)

circuit and the equivalent model, with a clear physical understanding of the role of each geometrical dimension.

This quasi-static approach permits to derive an equivalent circuit model with no need of full-wave simulations of the structure (except for a qualitative observation of the current path). However, also in this case, a better result can be achieved by adopting correction of the parameter values, based on the curve fitting of full-wave simulations.

6.4 Applications of DGS

A variety of components have been developed to exploit the useful features of DGS: in some cases, the frequency response of the components takes advantage of the band-stop properties of the DGS, in other structures the slow-wave characteristics of the DGS are exploited to reduce the size of the circuits, and in some components high-impedance transmission lines based on DGS allow overcoming possible fabrication issues.

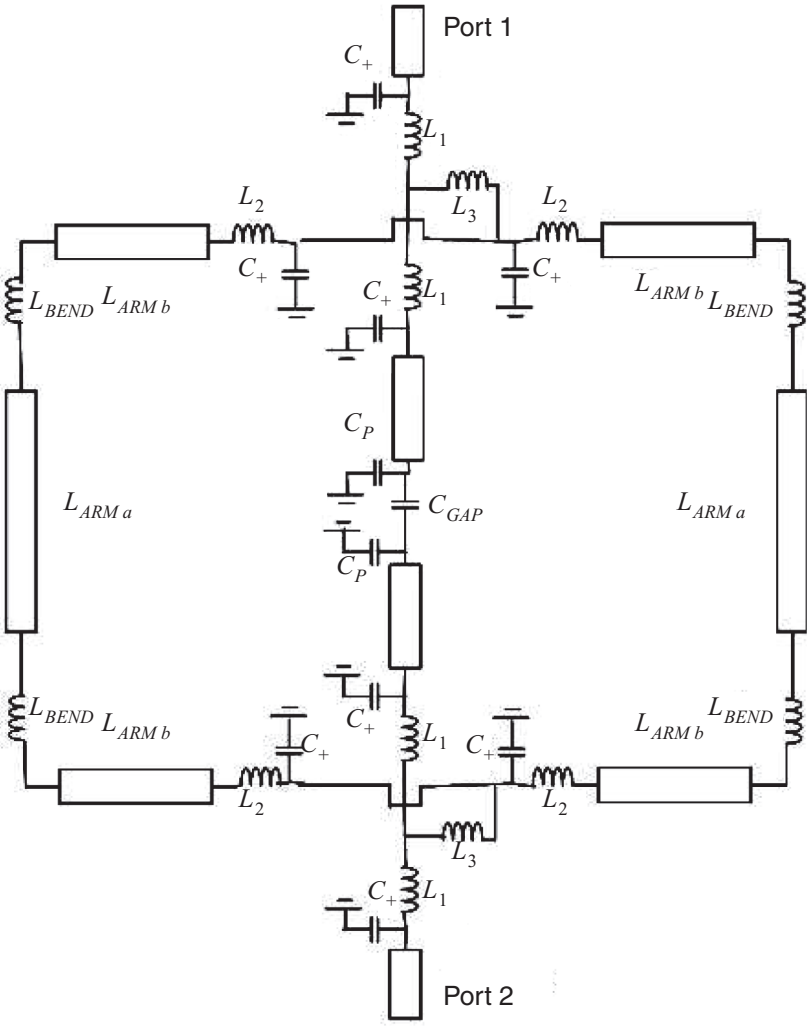

Figure 6.15 Quasi-static equivalent circuit model of a dumbbell DGS circuit (from [38], © 2006 IEEE. Reprinted with permission.)

6.4.1 DGS-Based Filters

The first and most common application of DGS has been the implementation of planar filters, either in microstrip or in coplanar waveguide technology [5, 7, 20, 26, 39–40]. In the framework of filter design, DGS have been adopted to exploit their band-stop effect with the aim to realize band-stop filters, as well as to improve the out-of-band performance of band-pass filters.

Microstrip Low-Pass Filter

A three-pole low-pass filter based on DGS and microstrip technology was proposed in [5]: it consists of a 50 Ω microstrip line with a pair of symmetric open stubs and two dumbbell defects etched in the ground plane (Figure 6.16a). The equivalent cir-

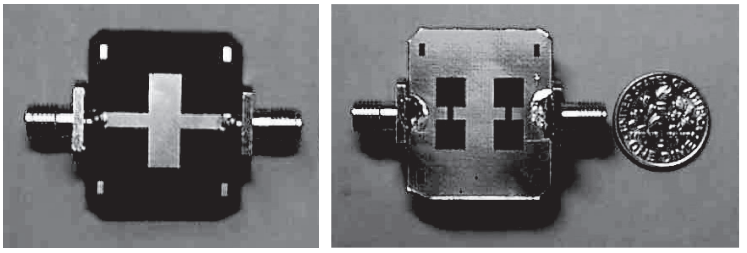

(a)

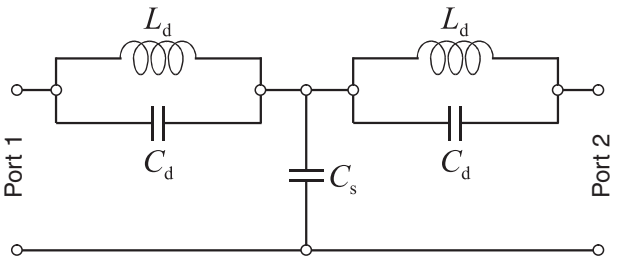

(b)

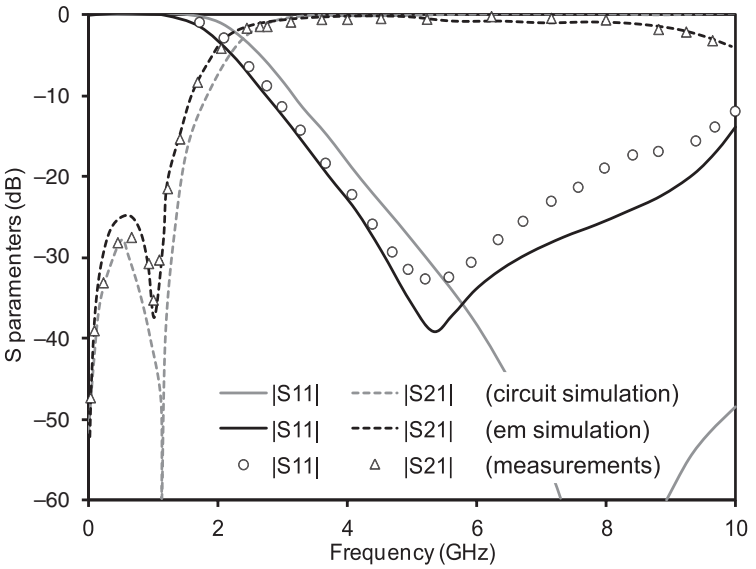

(c)

Figure 6.16 Low-pass filter based on a microstrip line with two open stubs, combined with dumbbell DGS: (a) photographs of the top view (conductor lines) and of the bottom view (defected ground plane); (b) equivalent circuit model of the filter; (c) simulated and measured frequency response of the filter. (from [5], © 2001 IEEE. Reprinted with permission.)

cuit model of this filter is shown in Figure 6.16b: each dumbbell defect is modeled as a parallel LC circuit (with inductance L_d and capacitance C_d), and the open stub is represented by a shunt capacitor (with capacitance C_s). At low frequency, the parallel LC circuits can be simplified and only the inductance L_d can be considered.

Therefore, with concern to the in-band frequency response, this filter topology allows to implement an equivalent circuit consisting of two series inductors and a shunt capacitor: the classical microstrip implementation of such a filter would require the use of a very thin (high impedance) microstrip line for realizing series inductors, which is not suited to high-power applications. Conversely, in this case, the same effect can be realized by using the DGS and 50 Ω microstrip line.

On the basis of the simplified equivalent circuit model, the value L_d (in conjunction with the stub capacitance C_s) can be selected to optimize the in-band filter performance. More specifically, this filter was designed for a cutoff frequency of 1.3 GHz and 0.01 dB ripple level. The resulting values for circuit elements are L_d = 3.678 nH and C_s = 2.33 pF.

The presence of the capacitance C_d in parallel with L_d plays an important role in the out-of-band frequency response, because it allows to locate a transmission zero at the resonance frequency of the parallel LC circuit. The value C_d = 0.107 pF was selected to provide a band-stop frequency of 8 GHz. Thanks to the DGS, the out-of-band attenuation of this filter is better than a conventional microstrip filter. In [5], a measured out-of-band attenuation of 20 dB was achieved up to 8 GHz (Figure 6.16c). Moreover, in-band measured insertion and return losses are better than 0.15 and 20 dB, respectively, demonstrating a very low level of loss.

Band-Stop Filter in Coplanar Waveguide Technology

Periodic DGS can be adopted to design wideband band-stop filters. Specifically, the implementation of wideband band-stop filters based on DGS in coplanar waveguide technology was proposed in [26]. The DGS in this case consists of cascaded meander lines integrated in the ground plane of the coplanar waveguide.

The use of a coplanar waveguide section with one single defect allows designing a narrow band-stop filter [26]. In this case, the size of the defect practically determines the stop-band frequency: a larger defect corresponds to a lower band-stop frequency, as well as to a more significant radiation loss. The cell with one single defect can be cascaded to obtain periodic DGS circuits, which exhibit more flexible characteristics. In particular, circuits based on four cells were designed in [26] to obtain wideband filters. The longitudinal separation of the DGS was optimized to achieve the deepest rejection, the widest bandwidth and the sharpest edges.

Two filters with different geometries of the DGS were designed and fabricated in [26], with different stop-band frequencies (Figure 6.17a). The first filter with smaller defects exhibits the stop band at 6 GHz, a bandwidth of 2.8 GHz, and a rejection better than 30 dB (Figure 6.17b). The second filter has larger defects: in this case, the stop band frequency is 3.7 GHz, the bandwidth is approximately 2.0 GHz, and the rejection is larger than 25 dB (Figure 6.17c). In both cases, radiation loss appears to be very limited.

Tunable Filters

Tunable filters based on DGS and varactor diodes have been proposed in [25, 41]. A tunable band-stop filter based on slot-ring DGS and coplanar waveguide technol-

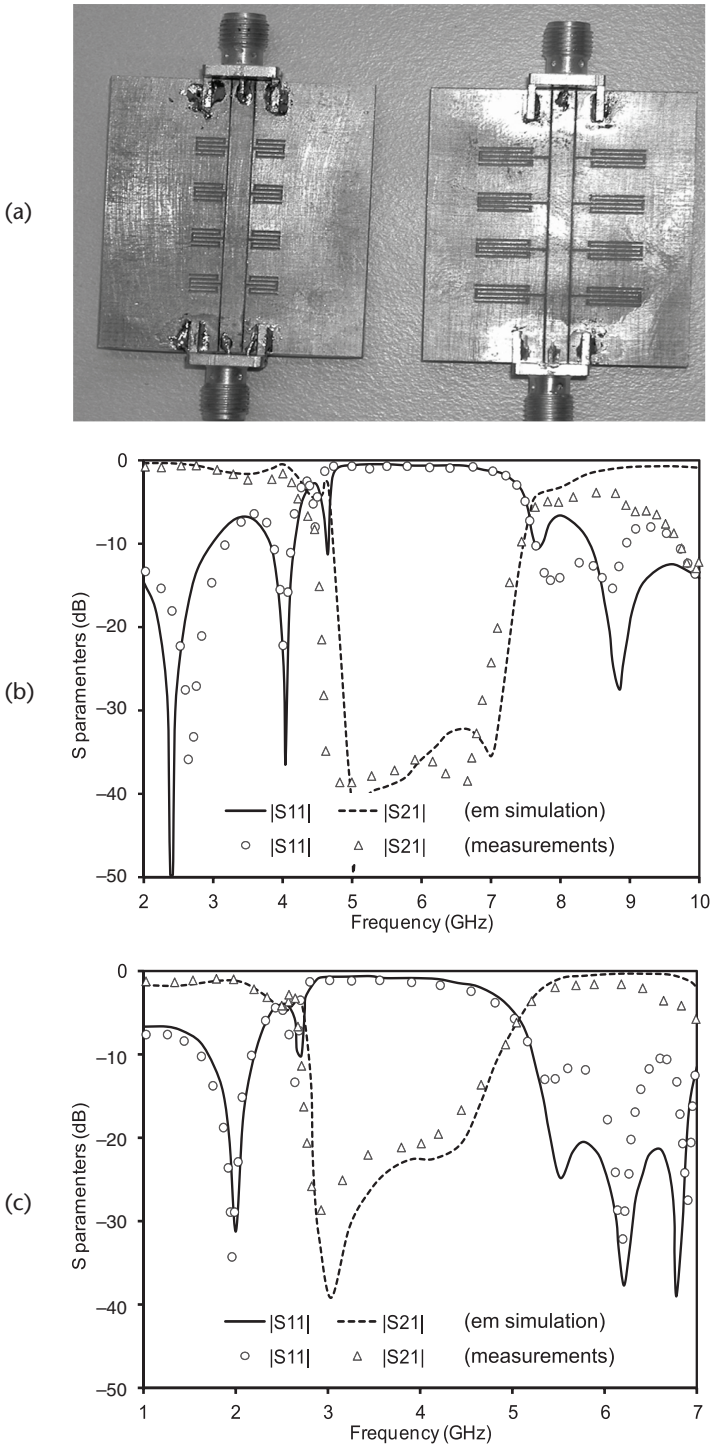

Figure 6.17 Wideband band-stop filters based on a coplanar waveguide with four cells of L-shaped DGS : (a) photograph of the filters; (b) frequency response of the filter with smaller defects; (c) frequency response of the filter with larger defects. (from [26], © The Institution of Engineering and Technology 2005. Reprinted with permission.)

ogy was proposed in [25]. The slot ring geometry allows to mount a varactor diode that provides frequency tuning capabilities: the varactor diode is mounted across the slot (Figure 6.3c), and the presence of the internal rectangular patch permits to connect a DC wire for biasing the varactor. In this modified configuration, the band-stop effect is due to the presence of the slot-ring DGS, and its stop-band frequency depends not only on the geometry of the DGS, but also on the capacitance of the varactor diode: in the equivalent circuit model, the equivalent circuit of the varactor is located in parallel with the *LC* circuit that represents the DGS (shown in Figure 6.5b). The filter proposed in [25] exhibits two rejection bands, located at 3.7 GHz and at 7.4 GHz, respectively. When changing the bias voltage, the varactor diode allows achieving a relative tuning range of 19% of the rejection frequency in both bands, thus resulting in a tuning range of 700 MHz for the first band and 1.4 GHz for the second.

A tunable band-pass filter with very broadband harmonic suppression, based on DGS loaded microstrip lines, was proposed in [41]. This filter exhibits two tunable bands, whose center frequencies can be modified by means of varactor diodes, connected to the microstrip lines. DGS are adopted to determine band-stop effects in the input and output feeding lines, in order to suppress the harmonics over a broad bandwidth. More specifically, the filter exhibits a tunable range of the first pass-band center frequency of 34% (from 0.85 to 1.2 GHz) with a practically constant 3-dB fractional bandwidth of 13%, and a tunable range of the second pass-band center frequency of 41% (from 1.40 to 2.14 GHz) with a 3-dB fractional bandwidth of 11%. In addition, the DGS determine a measured out-of-band rejection level better than 20 dB up to more than 20 GHz (ten times of second band-pass frequency), thus ensuring the complete suppression of harmonic frequencies over a very broad frequency range.

Coupled–Line Filters

DGS have been adopted to improve the performance and reduce the size of coupled-line microstrip filters [42–43]. The use of DGS in the coupled-line filter design allows adding poles in the frequency response and to improve the out-of-band performance by incorporating additional transmission zeros.

A three-pole coupled-line band-pass filter in microstrip configuration was presented in [42]. The filter is shown in Figs. 6.18a and b: it comprises a microstrip resonator, side-coupled with the input and output microstrip lines, and three defects in the ground plane (two external bigger apertures and a central smaller aperture, located below the microstrip resonator).

This band-pass filter was designed with a center frequency of 3 GHz, a 2.9–3.1 GHz pass-band with a 0.01-dB ripple level and rejection of 40 dB up to 6 GHz. The prototype was fabricated on a dielectric substrate with dielectric permittivity $\varepsilon_r = 10.2$ and thickness 1.27 mm.

The frequency response of the filter is shown in Figs. 6.18c: the microstrip resonator and the two external defects in the ground plane are responsible for the three poles in the frequency response. The third defect, located below the microstrip resonator, determines a transmission zero at 5.9 GHz, which improves the out-of-band rejection of the filter.

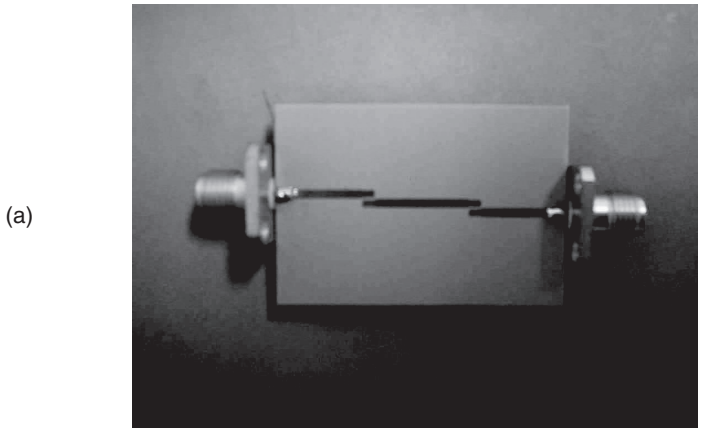

(a)

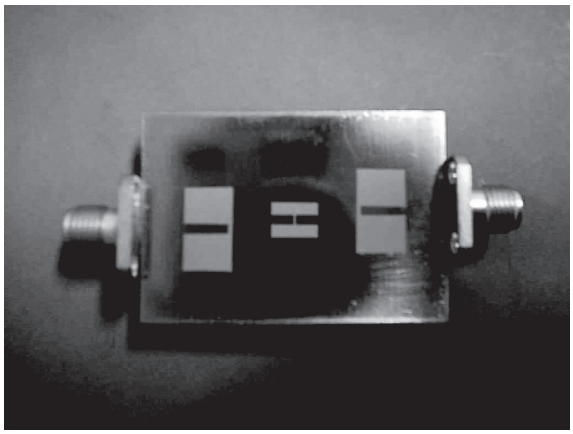

(b)

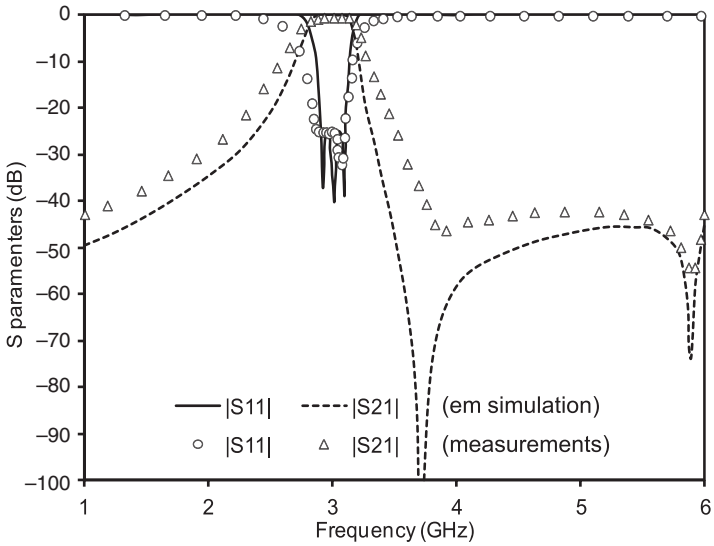

(c)

Figure 6.18 Three-pole coupled-line band-pass filter in microstrip configuration: (a) photograph of the top side of the filter, with a microstrip resonator, side-coupled with the input and output microstrip lines; (b) photograph of the bottom side of the filter, showing three defects in the ground plane; (c) simulated and measured frequency response of the filter. (from [42], © 2002 IEEE. Reprinted with permission.)

Miniaturized Ultra-Wideband (UWB) Filters

The use of DGS has been also investigated with the aim to improve the performance of ultra-wideband (UWB) filters [44–47].

Compact UWB band-pass filters were proposed in [46], to cover the frequency band from 3.1 GHz to 10.6 GHz. The filter topology is based on a quarter-wavelength low-impedance microstrip line, connected to a short-circuited stub, and coupled to the input and output 50–Ω microstrip lines by inter-digital capacitors. The coupling of the inter-digital capacitors is tightened by the presence of H-shaped apertures, located in the ground plane below the capacitors. In addition, three pairs of tapered DGS located below quarter-wavelength microstrip line determine out-of-band transmission zeros, thus suppressing spurious pass bands. The adopted substrate has a relative dielectric constant of 2.65 and the thickness of 1 mm. A prototype of the filter proposed in [46] exhibits a measured 3-dB pass band from 2.8 GHz to 10.8 GHz, and the measured 20 dB rejection bandwidth extends up to more than 20 GHz. A modified version of this filter was also reported in [46], where a meandered slot is introduced in the input microstrip line to reject the undesired wireless local-area network (WLAN) radio (Figure 6.19): this meander line determines a notched band with center frequency of 5.47 GHz and width of about 0.7 GHz, without affecting the remaining part of the frequency response.

6.4.2 Other DGS-Based Passive Components

Apart from filters, several classes of passive components have been proposed, where the application of DGS plays a fundamental role in performance improvement and size reduction [6, 8, 48–49]. They include, for instance, hybrid couplers, rat-race couplers, and Wilkinson power dividers.

DGS-based 10-dB Hybrid Coupler

A 10-dB branch line coupler operating at 1.8 GHz was proposed in [48], and implemented in microstrip technology combined with DGS. This type of component is not very common in microstrip technology: in fact, differently from classical 3-dB and 6–dB hybrid couplers, 10-dB couplers require very thin microstrip lines with a large characteristic impedance. For instance, the branch line coupler with l0-dB coupling presented in [48] requires two pairs of quarter-wavelength transmission lines with characteristic impedances of 150 Ω and of 47.4 Ω, respectively. While the implementation of a microstrip line with characteristic impedance of 47.4 Ω is not an issue, realizing a microstrip line with characteristic impedance of 150 Ω is quite unpractical: on a substrate with a dielectric permittivity of 2.2 and a thickness of 31 mils, the width of the strip would be only 0.2 mm.

The solution found in [48] is based on the use of DGS, which allows implementing high impedance transmission lines. In the branch coupler shown in Figure 6.20, the horizontal lines exhibit 150 Ω characteristic impedance and are implemented by adopting microstrip lines with defects in the ground plane: thanks to the use of the defects, the strips exhibit a width of 1 mm, five times wider than the width of a conventional microstrip line with the same characteristic impedance.

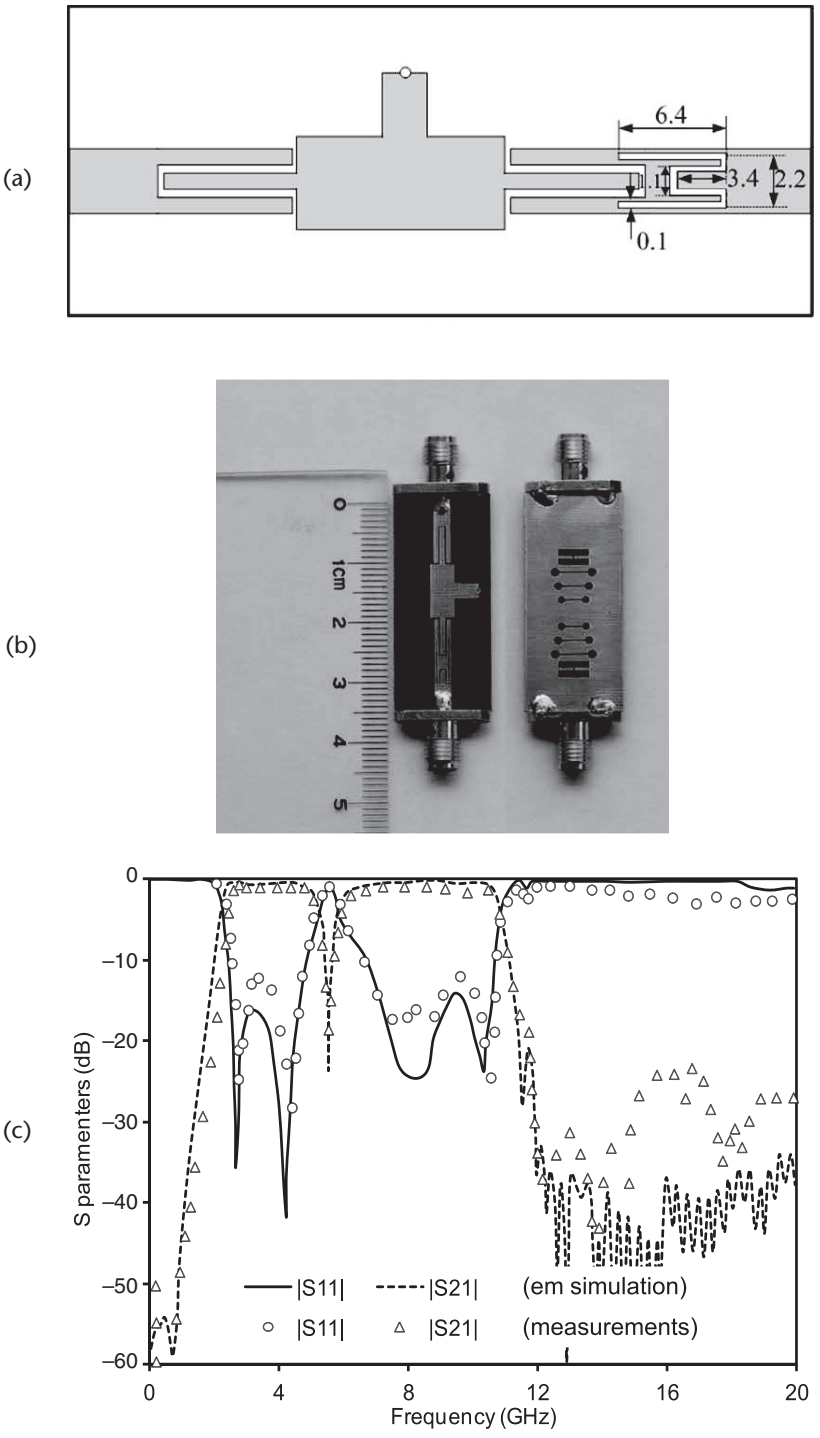

Figure 6.19 Miniaturized ultra-wideband (UWB) filter based on DGS: (a) geometry of the UWB filter with notched band; (b) photograph of the filter prototype (top and bottom views); (c) simulated and measured results of the filter scattering parameters. (from [46], © 2008 IEEE. Reprinted with permission.)

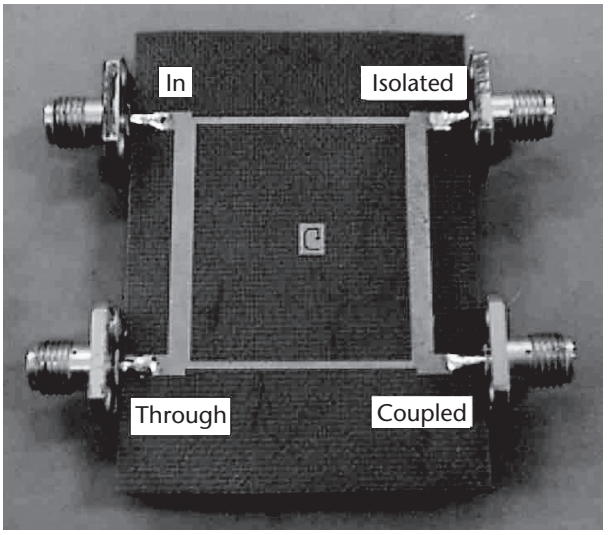

(a)

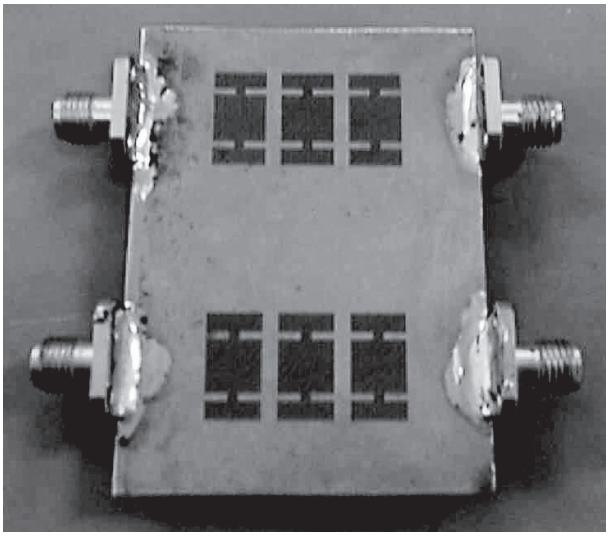

(b)

Figure 6.20 A 10-dB branch line coupler operating at 1.8 GHz, based on microstrip technology and DGS: (a) photograph of the top side of the coupler (conductor lines); (b) photograph of the back side of the coupler (defected ground). (from [48], © The Institution of Engineering and Technology 2000. Reprinted with permission.)

Conversely, the vertical lines present 50 Ω characteristic impedance and are based on conventional microstrip lines.

A further advantage of the defected microstrip line is the higher power handling capability, which is related to larger width of the conductor line. In addition, the quarter wavelength of the defected microstrip line is 26 mm on the adopted substrate, compared to 31 mm when using the conventional microstrip line.

Rat-Race Hybrid Coupler

DGS were applied in [49] to the design of a compact microstrip rat-race hybrid coupler. In these components, the DGS play a two-fold role: they allow achieving a significant reduction in size of the rat-race coupler, and they lead to an improved rejection of the harmonics in the frequency response. It consists of a classical rat-race microstrip coupler, with six dumbbell DGS located in the ground plane below the microstrip ring. The presence of the DGS allows to reduce the size of the component, due to the slow-wave effect, and to suppress the undesired harmonic replicas in the frequency response, thanks to the band-stop effect.

A prototype operating at 1.48 GHz was fabricated on a dielectric substrate with a relative permittivity $\varepsilon_r = 2.5$ and a thickness of 25 mil [49]. The reduction in length of the microstrip ring with respect to a conventional rat-race coupler was approximately 41%. Measurements performed on the prototype showed an insertion loss comparable to that of a conventional rat-race coupler and a suppression of the third harmonic below –30 dB.

Wilkinson Power Divider based on DGS High Impedance Transmission Lines

A 4:1 unequal power divider, based on the Wilkinson topology and operating at 1.5 GHz, was proposed in [6]. This component adopts DGS defects in the ground plane to implement high-impedance microstrip lines.

The circuit topology of a conventional *N*:1 unequal Wilkinson power divider is shown in Figure 6.21a: the divider is based on two quarter-wavelength transmission lines with characteristic impedances Z_2 and Z_3, and a resistor R_{int}. In particular, when considering an input line with characteristic impedance $Z_0 = 50\ \Omega$, the design of a 4:1 divider requires to adopt the characteristic impedance of the first branch $Z_2 = 39.5\ \Omega$ and the characteristic impedance of the second branch $Z_3 = 158.1\ \Omega$.

In [6], two defects in the ground plane were adopted to implement the high-impedance microstrip line (Figs. 6.21b and 6.21c). In this way, the width of the conductor of the DGS-based microstrip line was 0.4 mm (ε_r =2.2 and h = 0.787 mm): a conventional microstrip line with characteristic impedance of 158 Ω, on the same substrate, would require a conductor width of 0.17 mm.

The prototype reported in [6] shows excellent matching and isolation performance, and with very accurate dividing ratios of 1 dB and 7 dB at port 2 and port 3 over the frequency range from 1.2 to 1.8 GHz.

DGS Wilkinson Power Divider with Harmonic Suppression

A 3-dB Wilkinson power divider, proposed in [8], adopts asymmetric spiral defects to effectively suppress the second and third harmonics in the frequency response. The prototype of the power divider is shown in Figure 6.22. The strip side of the circuit resembles a conventional Wilkinson divider, while two spiral defects are etched in the back side ground plane. The spiral DGS are inserted into the quarter-wave transmission lines of the Wilkinson power divider. In particular, asymmetric spiral DGS are adopted in this circuit: the equivalent circuit of each asymmetric spiral defect corresponds to the series of two parallel *LC* circuits: consequently, these defects are able to provide two different resonant frequencies and, consequently,

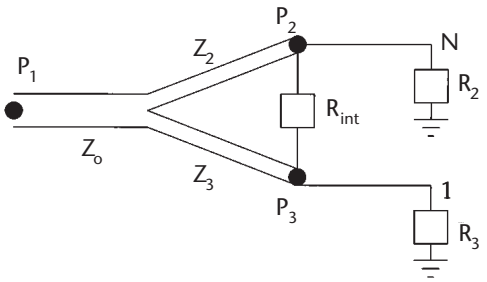

(a)

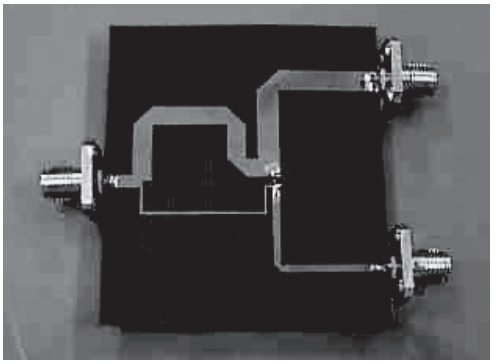

(b)

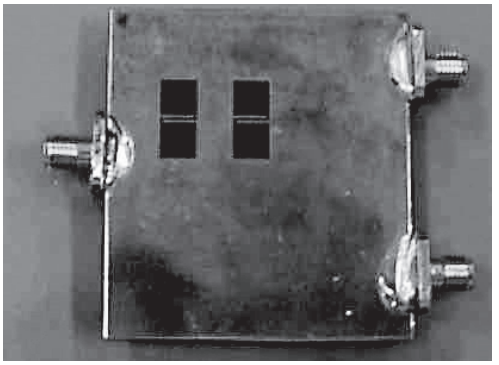

(c)

Figure 6.21 A 4:1 unequal Wilkinson power divider, based on DGS-based high-impedance microstrip lines: (a) circuit topology of the unequal power divider; (b) photograph of the front side of the power divider (conductor lines); (c) photograph of the back side of the power divider (defected ground). (from [6], © 2001 IEEE. Reprinted with permission.)

two rejection bands. This property guarantees the suppression of the second and third harmonics in the frequency response of the circuit. In particular, experimental results from [8] demonstrate an 18-dB suppression of the second harmonic and 15-dB suppression of the third harmonic, respectively. In addition, the use of asymmetric DGS leads to a length reduction of the quarter-wavelength transmission lines by

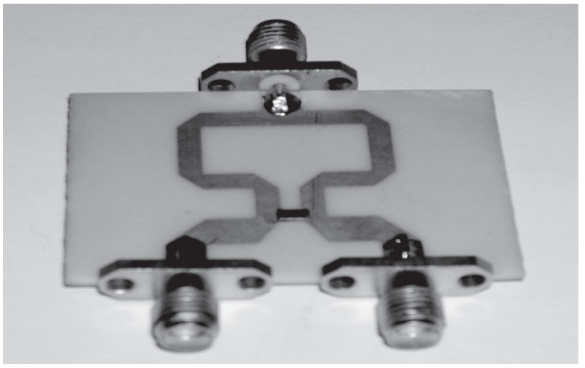

(a)

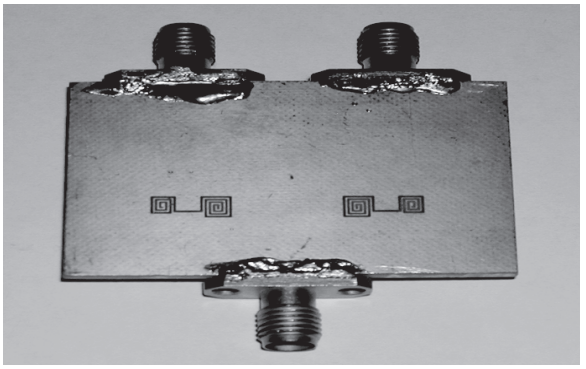

(b)

Figure 6.22 A 3-dB Wilkinson power divider with broadband harmonic suppression: (a) photograph of the front side; (b) photograph of the back side (defected ground). (from [8], © 2005 IEEE. Reprinted with permission).

9.1% compared to length of quarter-wavelength conventional microstrip lines on the same dielectric substrate.

6.4.3 DGS-Based Active Circuits

The use of DGS may be particularly effective in the design of active circuits such as amplifiers and mixers [10, 50–55]. DGS allow improving the performance of active components, as their band-stop properties permits to reduce the detrimental effect of high-order harmonics. In addition, the slow-wave effect of DGS can be exploited to reduce the component dimensions.

DGS-Based Amplifier with Improved Efficiency

The band-stop features of DGS have been adopted to improve the efficiency of power amplifiers [50]. The performance improvement is obtained by adding a DGS-based transmission line with a wide stop band at the output of a class-A power amplifier, based on a GaAs FET and operating in the frequency band from 4.3 GHz to 4.7 GHz. A 50–Ω microstrip line with dumbbell defects in the ground

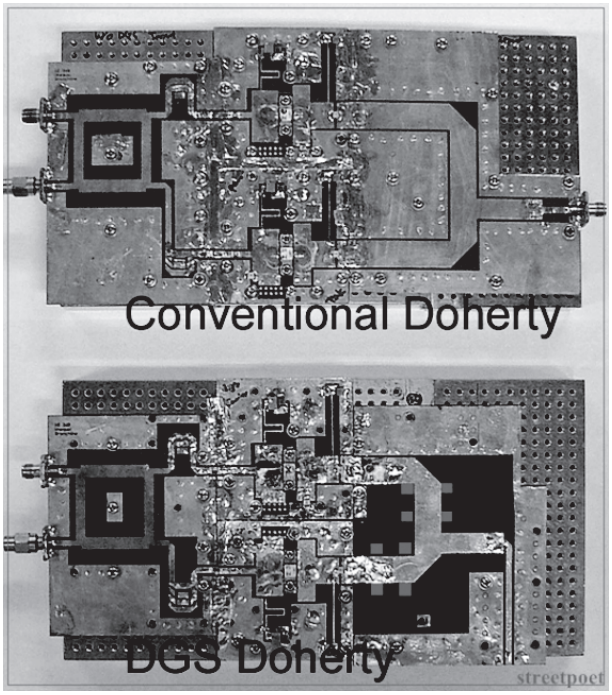

Figure 6.23 Photographs of the Doherty power amplifier based on dumbbell shaped DGS (from [52], © 2006 IEEE. Reprinted with permission.)

plane was adopted. The band-stop effect of the DGS transmission line allows to significantly reduce the amplitude of the undesired harmonic frequencies. In particular, in the case of the amplifier proposed in [50], the amplitude of the output signal at the second harmonic is reduced from around –20 dBm to less than –45 dBm. The power amplifier exhibits an improved output power and power added efficiency up to 5% compared to an identical power amplifier without DGS.

DGS-Based Amplifier with Reduced Size

The size of power amplifiers can be reduced by adopting DGS, by exploiting their properties of slow-wave propagation. An interesting solution was proposed for an amplifier based on a HEMT device, operating in the frequency band from 2 GHz to 2.3 GHz, presented in [51]. In order to reduce the size of the component, dumbbell DGS are introduced in the microstrip lines of the matching networks of the amplifier. Due to the effect of slow-wave propagation, the DGS-loaded microstrip line exhibits a longer electrical length than that of the conventional microstrip line for the same physical length. For this reason, by adopting DGS-loaded microstrip lines in the input and output matching networks of the amplifier, the overall length size of the amplifier in [51] reduces by more than 50%, while keeping practically unchanged electrical performance.

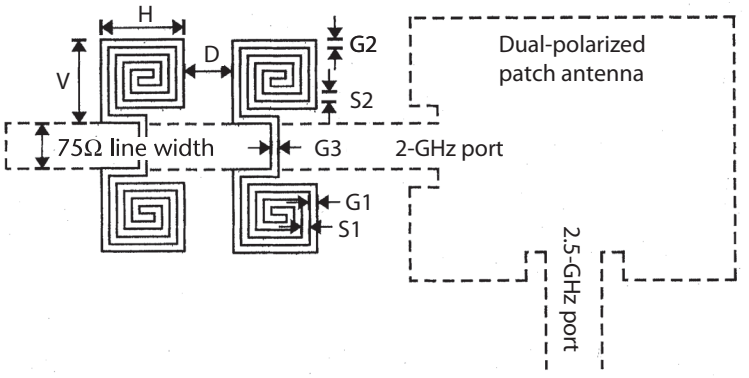

Figure 6.24 Schematic of a high isolation dual-frequency orthogonally polarized rectangular patch antenna, with spiral-shaped DGS located under a feed line (from [57], © 2004 IEEE. Reprinted with permission.)

Doherty Power Amplifier Based on DGS

Both stop-band effect and slow-wave propagation have been exploited in the Doherty power amplifier proposed in [52] (Figure 6.23). Adding dumbbell-shaped DGS in the output quarter-wavelength impedance inverters of the carrier amplifier allows providing a suitable termination impedance at the harmonic frequencies and, at the same time, to shorten the length of the transmission lines, thus reducing the overall circuit dimension.

6.4.4 DGS-Based Antennas

A variety of applications have been proposed for DGS in the field of antennas, in particular patch antennas [56–59]: DGS permit to improve the port isolation in dual-polarized antennas, to suppress undesired cross-polarized radiation, and to reduce higher-order harmonics in active antennas.

High Isolation Dual-Polarized Patch Antenna

DGS can be used in the design of dual-polarized patch antennas, with the aim to significantly improve the port isolation. An example of this application was reported in [57], where a dual-frequency orthogonally polarized rectangular patch antenna is fed by two microstrip lines, connected to two adjacent sides of the patch (Figure 6.24). The patch is designed to resonate at 2 GHz for one polarization and at 2.5 GHz for the other polarization, respectively. The feeding line of the patch are 75-Ω microstrip lines, implemented on a dielectric substrate with relative dielectric permittivity $\varepsilon_r = 2.33$ and thickness of 0.787 mm. To improve the port isolation, two spiral DGS were inserted under the feed line of the 2 GHz port (Figure 6.24): in this way, the defected feed line exhibits a stop band in the frequency range 2.4–2.8 GHz. The position of the defects was optimized, to avoid a variation of the an-

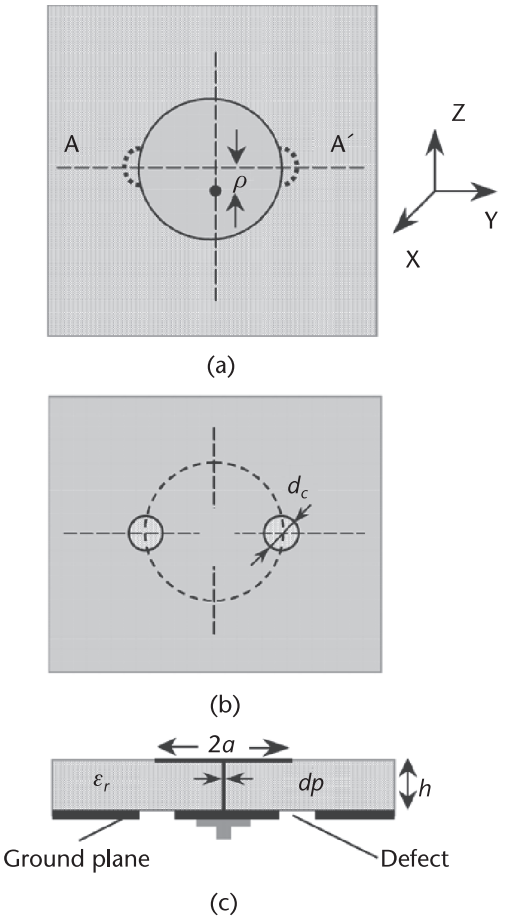

Figure 6.25 Schematic of a circular patch antenna integrated with DGS: the circular apertures in the ground plane contribute to suppress the cross–polarized radiation: (a) top view; (b) bottom view; (c) cross section view. (from [59], © 2005 IEEE. Reprinted with permission.)

tenna input matching. Experimental results in [57] demonstrated an improvement of 20 dB in the port isolation, compared to the case without DGS.

Microstrip Patch Antenna with DGS for Cross Polarization Suppression

Another useful application of DGS in the design of antennas is related to the reduction of cross-polarization in linearly-polarized patch antennas. An example of a patch antenna integrated with DGS was presented in [59]: it consists of a circular metal patch, fed from underneath via a coaxial probe. The DGS consist of two small circular apertures in the ground plane, symmetrically located below the edges of the circular patch (Figure 6.25). The position of circular apertures are selected in such a way that they do now affect the electromagnetic field of the dominant mode, corresponding to the co-polarization contribution of radiation, and they suppress the occurrence of the orthogonal mode, responsible for the cross-polarization ra-

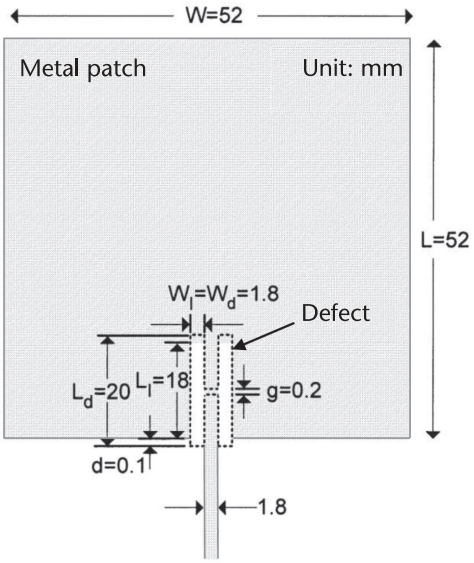

Figure 6.26 Schematic of a rectangular patch antenna with an H-shaped defect in the ground plane (from [56], © 2003 IEEE. Reprinted with permission.)

diation. A prototype presented in [59] was implemented on a dielectric substrate with relative dielectric permittivity $\varepsilon_r = 2.32$ and thickness of 1.575 mm, and it is intended for operation at the frequency of 3.6 GHz. The use of DGS permits a suppression of the cross-polarization contribution by 5 to 8 dB around the broadside direction, with no significant modification of the co-polarized radiation.

Harmonics Reduction with DGS for a Microstrip Patch Antenna

In active patch antennas, the antenna represents the load of the active circuit, and therefore it should provide the proper impedance termination both for the fundamental frequency and for the higher-order harmonics. The use of DGS in active patch antennas results an efficient way to achieve the proper impedance termination and to suppress the radiation at higher-order harmonic frequencies. This effect was demonstrated in [56] by adding an H-shaped slot in the ground plane of a rectangular patch antenna, just below the feed point where the microstrip is connected to the patch (Figure 6.26). The patch antenna is designed to operate at the fundamental frequency of 1.82 GHz, while the H-shaped slot is optimized to attenuate more than 20 dB the input signal of the antenna at the second and third harmonics. A prototype implemented on a dielectric substrate with permittivity $\varepsilon_r = 2.2$ and thickness 0.508 mm was presented in [56]: this solution yields a significant harmonic suppression (>20 dB), and a good performance at the fundamental frequency, with 4.8 dB gain and return loss >10 dB.

References

[1] Breed, G., "An Introduction to Defected Ground Structures in Microstrip Circuits," *High Frequency Electronics*, Vol. 7, No. 11, 2008, pp. 50–54.

[2] Weng, L. H., et al., "An Overview On Defected Ground Structure," *Progress In Electromagnetics Research B*, Vol. 7, 2008, pp. 173–189.

[3] Arya, A. K., M. V. Kartikeyan, and A. Patnaik, "Defected Ground Structure in the perspective of Microstrip Antennas: A Review," *Frequenz*, Vol. 64, No. 5–6, 2010, pp. 79–84.

[4] Guha, D., S. Biswas, and Y. M. M. Antar, "Defected Ground Structure for Microstrip Antennas," in *Microstrip and Printed Antennas: New Trends, Techniques and Applications*. Edited by Debatosh Guha and Yahia M.M. Antar, John Wiley & Sons, Ltd, 2011.

[5] Ahn, D., et al., "A Design of the Lowpass Filter Using the Novel Microstrip Defected Ground Structure," *IEEE Transactions on Microwave Theory and Techniques*, Vol. 49, No. 1, 2001, pp. 86–93.

[6] Lim, J.-S., et al., "A 4:1 Unequal Wilkinson Power Divider," *IEEE Microwave and Wireless Components Letters*, Vol. 11, No. 3, 2001, pp.124–126.

[7] Abdel-Rahman, A. B., et al., "Control of Bandstop Response of Hi-Lo Microstrip Low-Pass Filter Using Slot in Ground Plane," *IEEE Transactions on Microwave Theory and Techniques*, Vol. 52, No. 3, 2004, pp. 1008–1013.

[8] Woo, D.-J., and T.-K. Lee, "Suppression of Harmonics in Wilkinson Power Divider Using Dual-Band Rejection by Asymmetric DGS," *IEEE Transactions on Microwave Theory and Techniques*, Vol. 53, No. 6, 2005, pp. 2139–2144.

[9] Kim, C.-S., et al., "A Novel 1–D Periodic Defected Ground Structure for Planar Circuits," *IEEE Microwave and Guided Wave Letters*, Vol. 10, No. 4, 2000, pp. 131–133.

[10] Lim, J.-S., et al., "A Vertically Periodic Defected Ground Structure and its Application in Reducing the Size of Microwave Circuits," *IEEE Microwave and Wireless Components Letters*, Vol. 12, No. 12, 2002, pp. 479–481.

[11] Liu, H.-W., et al., "An Improved 1D Periodic Defected Ground Structure for Microstrip Line," *IEEE Microwave and Wireless Components Letters*, Vol. 14, No. 4, 2004, pp. 180–182.

[12] Sievenpiper, D., et al., "High-Impedance Electromagnetic Surfaces with a Forbidden Frequency Band," *IEEE Transactions on Microwave Theory and Techniques*, Vol. 47, No. 11, 1999, pp. 2059–2074.

[13] Yang F.-R., et al., "A Uniplanar Compact Photonic-Bandgap (UC-PBG) Structure and its Applications for Microwave Circuit," *IEEE Transactions on Microwave Theory and Techniques*, Vol. 47, No. 8, 1999, pp. 1509–1514.

[14] Yang F.-R., et al., "A Novel TEM Waveguide Using Uniplanar Compact Photonic-Bandgap (UC-PBG) Structure," *IEEE Transactions on Microwave Theory and Techniques*, Vol. 47, No. 11, 1999, pp. 2092–2098.

[15] Abdel-Rahman, A. B., et al., "Control of Bandstop Response of Hi-Lo Microstrip Low-Pass Filter Using Slot in Ground Plane," *IEEE Transactions on Microwave Theory and Techniques*, Vol. 52, No. 3, 2004, pp. 1008–1013.

[16] Boutejdar, A., et al., "Control of Bandstop Response of Cascaded Microstrip Low-Pass-Bandstop Filters Using Arrowhead Slots in Backside Metallic Ground Plane," 2005 *IEEE AP-S International Symposium*, Washington, DC, USA, July 3–8, 2005, pp. 574–577.

[17] Chen, H.-J., et al., "A Novel Cross-Shape DGS Applied to Design Ultra-Wide Stopband Low-Pass Filters," *IEEE Microwave Wireless Component Letters*, Vol. 16, No. 5, 2006, pp. 252–254.

[18] Mandal, M. K., and S. Sanyal, "A Novel Defected Ground Structure for Planar Circuits," *IEEE Microwave Wireless Components. Letters*, Vol. 16, No. 2, 2006, pp. 93–95.

[19] Chen, J. X., et al., "Compact quasi-elliptic function filter based on defected ground structure," *IEE Proc. Microwaves Antennas and Propagation*, Vol. 153, No. 4, 2006, pp. 320–324.

[20] Woo, D.-J., et al., "Novel U–Slot and V–Slot DGSs for Bandstop Filter With Improved Q Factor," *IEEE Transactions on Microwave Theory and Techniques*, Vol. 54, No. 6, 2006, pp. 2840–2847.

[21] Lim, J.–S., et al., "A Spiral-Shaped Defected Ground Structure for Coplanar Waveguide," *IEEE Microwave Wireless Component Letters*, Vol. 12, No. 9, 2002, pp. 330–332.

[22] Guha, D., et al., "Concentric Ring-Shaped Defected Ground Structures for Microstrip Applications," *IEEE Antennas Wireless Propagation Letters*, Vol. 5, 2006, pp. 402–405.

[23] Hou, Z. Z., "Novel Wideband Filter with a Transmission Zero Based on Split-Ring Resonator DGS," *Microwave and Optical Technology Letters*, Vol. 50, No. 6, 2008, pp. 1691–1693.

[24] Liu, H.W., Z. F. Li, and X.W. Sun, "A Novel Fractal Defected Ground Structure and its Application to the Low-Pass Filter," *Microwave and Optical Technology Letters*, Vol. 39, No. 6, 2003, pp. 453–456.

[25] Safwat, A. M. E., et al., "Tunable Bandstop Defected Ground Structure Resonator Using Reconfigurable Dumbbell-Shaped Coplanar Waveguide," *IEEE Transactions on Microwave Theory and Techniques*, Vol. 54, No. 9, 2006, pp. 3559–3564.

[26] Hamad, E. K. I., A. M. E. Safwat, and A. S. Omar, "Controlled Capacitance and Inductance Behaviour of L-shaped Defected Ground Structure for Coplanar Waveguide," *IEE Proceedings Microwaves, Antennas and Propagation*, Vol. 152, No. 5, 2005, pp. 299–304.

[27] Caloz, C., and T. Itoh, *Electromagnetic Metamaterials: Transmission Line Theory and Microwave Applications*, John Wiley & Sons, 2005.

[28] Eleftheriades, G. V., and K. G. Balmain (Editors), *Negative-Refraction Metamaterials: Fundamental Principles and Applications*, Wiley-IEEE Press, 2005.

[29] Engheta, N., and R. W. Ziolkowski (Editors), *Metamaterials: Physics and Engineering Explorations*, Wiley-IEEE Press, 2006.

[30] Kim, H.-M., and B. Lee, "Bandgap and Slow/Fast-Wave Characteristics of Defected Ground Structures (DGSs) Including Left Handed Features," *IEEE Transactions on Microwave Theory and Techniques*, Vol. 54, No. 7, 2006, pp. 3113–3120.

[31] Chang, I., and B. Lee, "Design of defected ground structures for harmonic control of active microstrip antenna," *IEEE Antennas and Propagation Society International Symposium (APS 2002), San Antonio*, Texas, USA, June 16–21, 2002, pp. 852–855.

[32] Kim, C.-S., et al., "Equivalent Circuit Modelling of Spiral Defected Ground Structure for Microstrip Line," *IEE Electronics Letters*, Vol. 38, No. 19, 2002, pp. 1109–1110.

[33] Lim, J.–S., et al., "A Spiral-Shaped Defected Ground Structure for Coplanar Waveguide," *IEEE Microwave and Wireless Components Letters*, Vol. 12, No. 9, 2002, pp. 330–332.

[34] Kim, C.–S., et al., "The Equivalent Circuit Modeling of Defected Ground Structure with Spiral Shape," *IEEE MTT–S International Microwave Symposium Digest* (IMS 2002), Seattle, WA, USA, June 2–7, 2002, pp. 2125–2128.

[35] Chung, Y., et al., "Multifunctional Microstrip Transmission Lines Integrated with Defected Ground Structure for RF Front-End Application," *IEEE Transactions on Microwave Theory and Techniques*, Vol. 52, No. 5, 2004, pp. 1425–1432.

[36] Hong, J.-S., and B. M. Karyamapudi, "A General Circuit Model for Defected Ground Structures in Planar Transmission Lines," *IEEE Microwave and Wireless Components Letters*, Vol. 15, No. 10, 2005, pp. 706–708.

[37] Park, J.-S., et al., "A Novel Equivalent Circuit and Modeling Method for Defected Ground Structure and its Application to Optimization of a DGS Lowpass Filter," *IEEE MTT-S International Microwave Symposium Digest* (IMS 2002), Seattle, WA, USA, June 2–7, 2002, pp.417–420.

[38] Karmakar, N. C., S. M. Roy, and I. Balbin, "Quasi-Static Modeling of Defected Ground Structure," *IEEE Transactions on Microwave Theory and Techniques*, Vol. 54, No. 5, 2006, pp. 2160–2168.

[39] Lim, J.-S., et al., "Design of Low-Pass Filters Using Defected Ground Structure," *IEEE Transactions on Microwave Theory and Techniques*, Vol. 53, No. 8, 2005, pp. 2539–2545.

[40] Balalem, A., et al., "Quasi-Elliptic Microstrip Low-Pass Filters Using an Interdigital DGS Slot," *IEEE Microwave and Wireless Components Letters*, Vol. 17, No. 8, 2007, pp. 586–588.

[41] Chaudhary, G., Y. Jeong, and J. Lim, "Harmonic Suppressed Dual-Band Bandpass Filters With Tunable Passbands," *IEEE Transactions on Microwave Theory and Techniques*, Vol. 60, No. 7, 2012, pp. 2115–2123.

[42] Park, J.-S., J.-S. Yun, and D. Ahn, "A Design of the Novel Coupled-Line Bandpass Filter Using Defected Ground Structure With Wide Stopband Performance," *IEEE Transaction on Microwave Theory and Techniques*, Vol. 50, No. 9, 2002, pp. 2037–2043.

[43] Liang, C.–H., W.-S. Chang, and C.-Y. Chang, "Enhanced Coupling Structures for Tight Couplers and Wideband Filters," *IEEE Transactions on Microwave Theory and Techniques*, Vol. 59, No. 3, 2011, pp. 574–583.

[44] Ting, S.-W., K.-W. Tam, and R. P. Martins, "Miniaturized Microstrip Lowpass Filter With Wide Stopband Using Double Equilateral U-Shaped Defected Ground Structure," *IEEE Microwave and Wireless Components Letters*, Vol. 16, No. 5, 2006, pp. 240–242.

[45] Chen, H.-J., et al., "A Novel Cross-Shape DGS Applied to Design Ultra-Wide Stopband Low-Pass Filters," *IEEE Microwave and Wireless Components Letters*, Vol. 16, No. 5, 2006, pp. 252–254.

[46] Yang, G.-M., et al., "Small Ultra-Wideband (UWB) Bandpass Filter With Notched Band," *IEEE Microwave and Wireless Components Letters*, Vol. 18, No. 3, 2008, pp.176–178.

[47] Lin, W.-J., et al., "Investigation in Open Circuited Metal Lines Embedded in Defected Ground Structure and Its Applications to UWB Filters," *IEEE Microwave and Wireless Components Letters*, Vol. 20, No. 3, 2010, pp. 148–150.

[48] Lim, J.-S., et al., "Design of 10 dB 90° Branch Line Coupler Using Microstrip Line With Defected Ground Structure," *IEE Electronics Letters*, Vol. 36, No. 21, 2000, pp. 1784–1785.

[49] Sung, Y. J., C. S. Ahn, and Y.-S. Kim, "Size reduction and harmonic suppression of rat-race hybrid coupler using defected ground structure," *IEEE Microwave and Wireless Components Letters*, Vol. 14, No. 1, 2004, pp. 7–9.

[50] Lim, J.-S., et al., "A Power Amplifier With Efficiency Improved Using Defected Ground Structure," *IEEE Microwave and Wireless Components Letters*, Vol. 11, No. 4, 2001, pp. 170–172.

[51] Lim, J.-S., at al., "Application of Defected Ground Structure in Reducing the Size of Amplifiers," *IEEE Microwave and Wireless Components Letters*, Vol. 12, No. 7, 2002, pp. 261–263.

[52] Choi, H.-J., J.-S. Lim, and Y.-C. Jeong, "A New Design of Doherty Amplifiers Using Defected Ground Structure," *IEEE Microwave and Wireless Components Letters*, Vol. 16, No. 12, 2006, pp. 687–689.

[53] Kim, K.-B., T.-S. Yun, and J.-C. Lee, "A single balanced diode mixer with defected ground structure (DGS) lowpass filter (LPF)," *34th European Microwave Conference 2004*, Amsterdam, the Netherlands, Oct. 11–14, 2004, pp. 197–200.

[54] Ryu, C. W., et al., "New balanced self oscillating mixer using DGS resonator," *37th European Microwave Conference 2007*, Munich, Germany, Oct. 8–12, 2007, pp. 648–651.

[55] Rehner, R., et al., "Broadband Planar Ring Mixers with DGS-Marchand Baluns in the Millimeter Wave Frequency Range," *German Microwave Conference (GeMIC) 2008*, Hamburg-Harburg, Germany, March 10–12, 2008, pp. 119–122.

[56] Sung, Y. J., M. Kim, and Y. S. Kim, "Harmonics reduction with defected ground structure for a microstrip patch antenna," *IEEE Antennas and Wireless Propagation Letters*, Vol. 2, No. 1, 2003, pp. 111–113.

[57] Chung, Y., et al., "High isolation dual-polarized patch antenna using integrated defected ground structure," *IEEE Microwave and Wireless Components Letters*, Vol. 14, No. 1, 2004, pp. 4–6.

[58] Chung, Y., et al., "Multifunctional microstrip transmission lines integrated with defected ground structure for RF front-end application," *IEEE Transactions on Microwave Theory and Techniques*, Vol. 52, No. 5, 2004, pp. 1425–1432.

[59] Guha, D., M. Biswas, and Y. M. M. Antar, "Microstrip patch antenna with defected ground structure for cross polarization suppression," *IEEE Antennas and Wireless Propagation Letters*, Vol. 4, No. 1, 2005, pp. 455–458.

CHAPTER 7

Coplanar Lines: Coplanar Waveguide and Coplanar Strips

7.1 Introduction

The term *coplanar* is used for those transmission lines/waveguides where all the conductors reside in the same plane; namely, on the top surface of the substrate. These include slotline, coplanar waveguide (CPW), coplanar strips (CPS), and their variants. The slotline has been discussed in Chapter 5. Coplanar waveguide, coplanar strips, and their variants are discussed in this chapter. Some of the advantages of these two lines arise from the fact that the mounting of lumped (active or passive) components in shunt or series configuration is much easier, drilling of holes through the substrate is not needed to reach the ground plane, and transition to slotline is less cumbersome, thereby allowing greater flexibility in the use of mixed transmission media. The performance of coplanar lines is comparable to and sometimes even better than microstrip line in terms of guide wavelength, dispersion, and losses. Active elements such as MESFETs can easily be connected to coplanar lines because they are also coplanar in nature. Consequently, coplanar lines are used commonly in monolithic microwave integrated circuits (MMICs). Coplanar lines have some disadvantages also, such as parasitic modes, lower power-handling capability, and field nonconfinement.

The coplanar waveguide was proposed by Wen [1] in 1969. As shown in Figure 7.1(a) it consists of two slots each of width W printed on a dielectric substrate. The spacing between the slots is denoted by S. The electric and magnetic field configurations for quasi-static approximation are shown in Figure 7.1(b). The coplanar waveguide is not a *waveguide*, but a transmission line, because it is a two-conductor geometry and its dominant mode is TEM. At higher frequencies, the mode of propagation in the CPW becomes non-TEM because a longitudinal component of the magnetic field exists. In such a case the CPW has an elliptically polarized magnetic field in the slots at the air-dielectric interface and becomes suitable for nonreciprocal ferrite devices.

A configuration of coplanar strips, which is complementary to the CPW, is shown in Figure 7.2(a). It consists of two strips, generally of equal width W on a dielectric substrate. The spacing between the strips is denoted by S. The electric and magnetic field configurations are shown in Figure 7.2(b). In the lower range of microwave frequencies, the CPS is also useful for carrying signals for high-speed computer circuits.

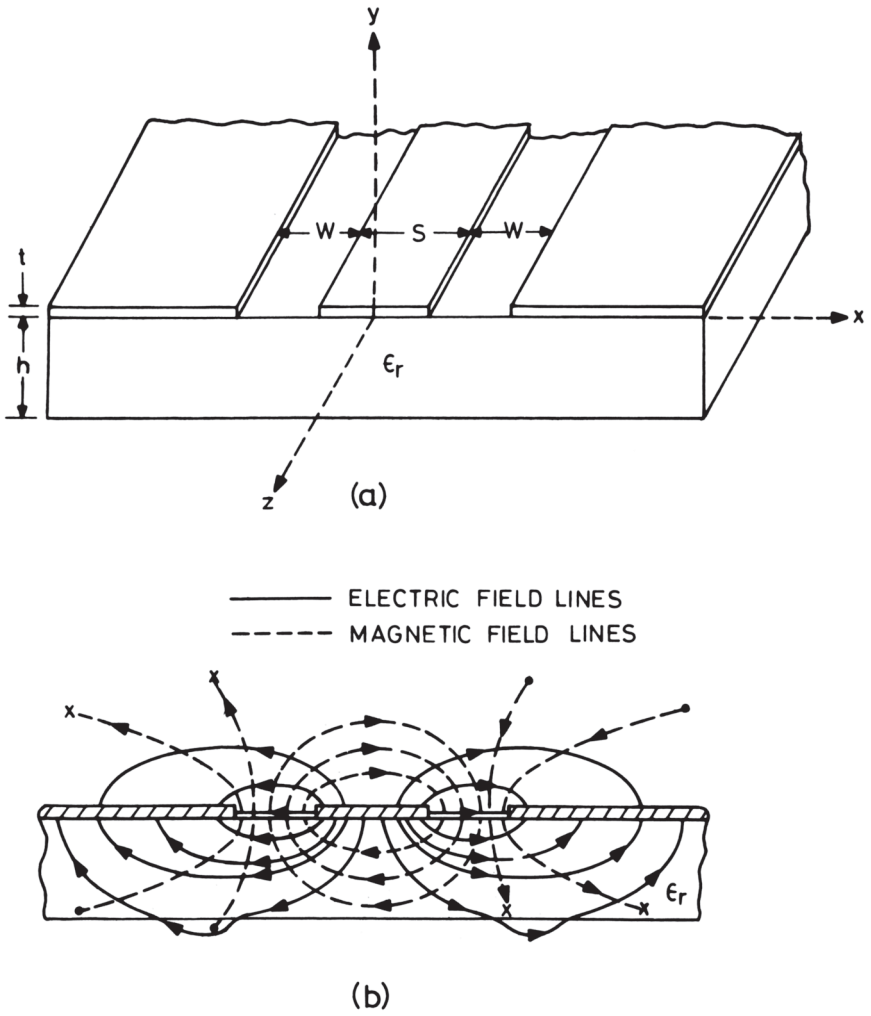

Figure 7.1 (a) Coplanar waveguide (CPW) geometry and (b) electric and magnetic field distributions in CPW.

The conventional coplanar waveguide, introduced by Wen [1], cannot be used as such because of the requirement of infinitely thick substrate. For practical applications substrate thickness has to be finite as in Figure 7.3(a). Also, the ground planes of actual CPW have finite widths as in Figure 7.3(b). The split ground planes are forced at the same potential all along the line by means of conductive air bridges at regular intervals. The spacing between the air bridges should be less than 0.1λ. The width of the ground planes should be kept as small as possible since it has a direct bearing on the maximum line density and the circuit size achievable in coplanar circuits. The fields of a CPW are less confined than those of microstrip lines, thereby making them more sensitive to covers or shields placed above the guide (see Figure 7.3(c)). It is very tempting to introduce a conductor backing (see Figures 7.3(d, e)), to improve both the mechanical strength and the power-

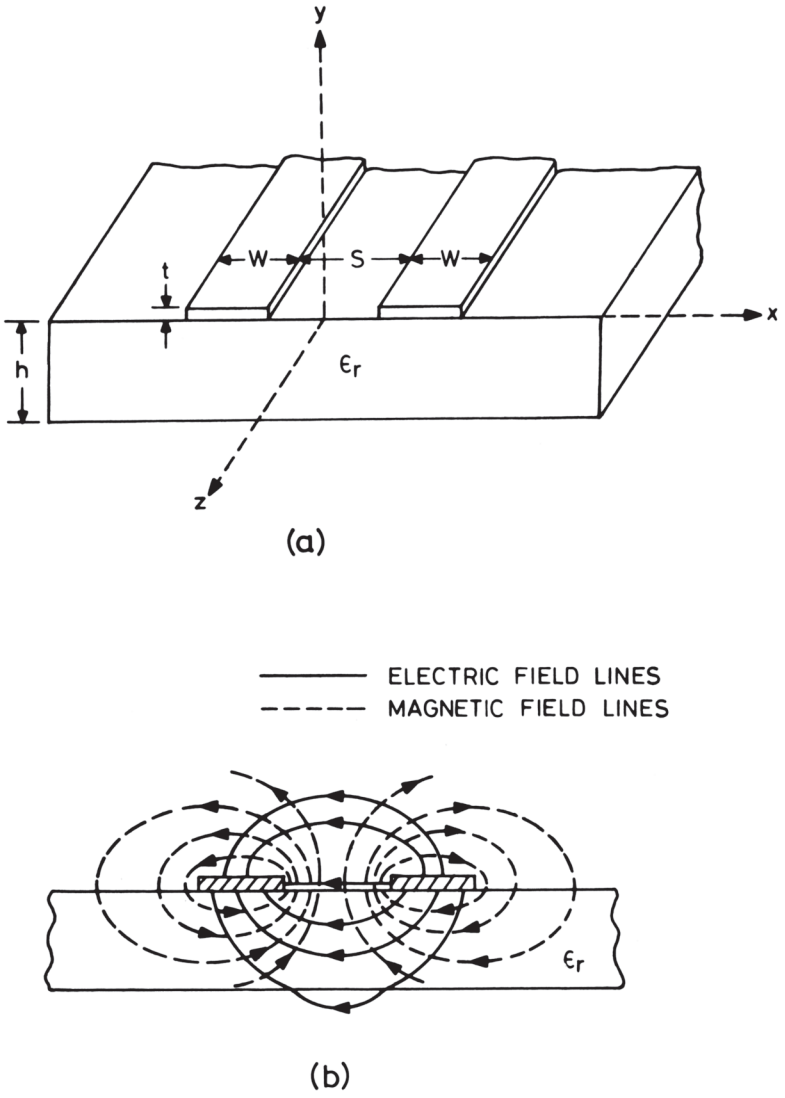

Figure 7.2 (a) Coplanar strips (CPS) geometry and (b) electric and magnetic field distributions in CPS.

handling capability. Moreover, it allows easy implementation of mixed CPW-microstrip circuits. In MMIC applications, the semiconductor substrates are usually thin and fragile. They are mounted on low permittivity materials such as quartz. Some applications may require a dielectric overlay or a multilayered configuration as shown in Figure 7.3(f). Sometimes, it is desirable to adjust the characteristic impedance of a CPW by changing the width of one of the slots, keeping the rest of the parameters unchanged. This configuration is called the asymmetric CPW (see Figures 7.3(g, h)). The effect of all these modifications (in conventional CPW) on propagation will be studied next, in order to exploit the flexibility provided by the additional parameters such as the cover height, lateral ground plane width, asymmetry, and multilayer configuration.

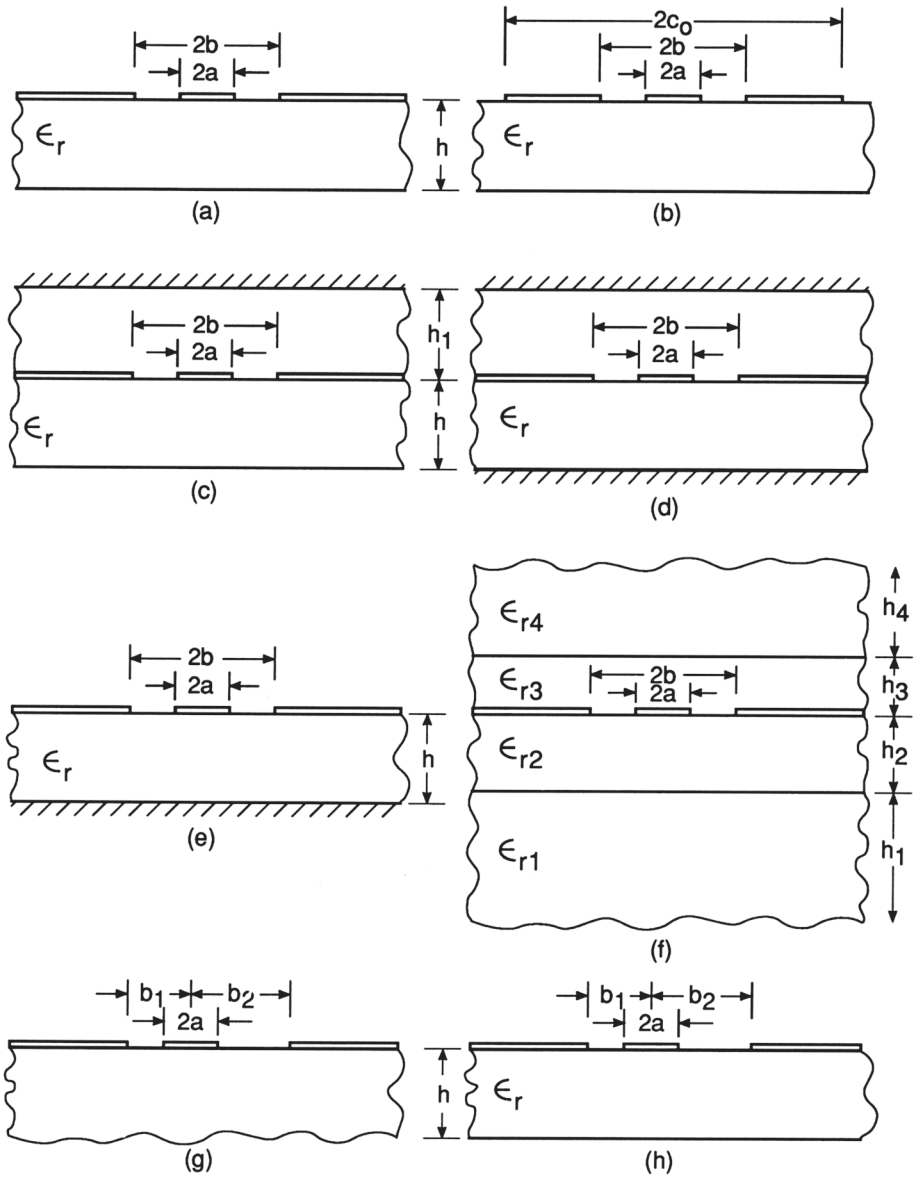

Figure 7.3 Various types of coplanar waveguides: (a) CPW with finite dielectric thickness; (b) CPW with finite width ground planes; (c) CPW with a cover shield; (d) conductor-backed CPW with a cover shiled; (e) conductor-backed CPW; (f) multilayered CPW; (g) asymmetric CPW; and (h) asymmetric CPW with finite dielectric thickness.

Methods of analysis for CPW and CPS are discussed in the following section. Design considerations for these lines are presented in Sections 7.3 through 7.5. Coplanar lines are compared with microstrip and slotline in Section 7.6. Various kinds of CPW transitions are described in Section 7.7, and CPW discontinuities are treated in Section 7.8. Circuits using CPW are included in Section 7.9.

7.2 Analysis

Coplanar lines have been studied using the quasi-static approximation and the fullwave analyses [1–17]. Wen [1] has conducted a quasi-static analysis of these transmission lines using conformal mapping, with the assumption that the dielectric substrate is thick enough to be considered infinite. Conformal transformation has also been applied to take into account the effects of the finite thickness of the dielectric substrate, finite size of the ground planes, upper shield, ground plane below the substrate as in microstrip line, structural asymmetry, and multilayer configuration. A fullwave analysis of coplanar lines, which provides information regarding frequency dependence of phase velocity and characteristic impedance, has been carried out by a number of investigators. The techniques employed include Galerkin's method in the spectral domain [2–12], variational methods [13–15], integral equation [16], relaxation method [17], method of lines [18], mode-matching technique [19], and finite-difference time-domain technique [20–21].

7.2.1 Quasi-Static Conformal Mapping Analysis of CPW

The basic approach used in the conformal transformation method, as applied to coplanar lines, is to assume that all the dielectric interfaces in the structure, including slots, can be replaced by magnetic walls [22]. This assumption is strictly valid for those structure for which the electric field lies along the dielectric interfaces. Under this assumption, half-planes above and below the metallization plane of the structure can be analyzed separately for line capacitance. The total line capacitance is then the algebraic sum of the two capacitances. If the electric field is not symmetric across the slots, the magnetic wall assumption is not justified. However, we can reduce the error associated with this assumption if we employ partial capacitance approximation (PCA) [22].

Partial Capacitance Approximation (PCA)

In PCA, the line capacitance is determined as $C = C^a + C^s$ where C^a is the line capacitance of transmission line geometry obtained by replacing the substrate by air medium, and C^s is the line capacitance contributed by the dielectric layer assumed to have the relative permittivity $(\varepsilon_r - 1)$, and the term -1 compensates for inclusion of similar capacitance in C^a. In PCA, all the interfaces are embedded with magnetic walls. The PCA approximation yields exact results for infinitely thick substrates and for substrate thickness $h \to 0$ [23]; it has been found to provide accuracy better than 3% for multilayered CPW [141]. The magnetic wall assumption at the dielectric interfaces of CPS, however, appears to be suspect in the region outside the slot [142]. The effect of metallization thickness on the validity of magnetic wall assumption is not known.

The conformal mapping of coplanar lines gives rise to analytical expressions for the effective dielectric constant and characteristic impedance in terms of the ratio of complete elliptic integral of the first kind and its complement. These expressions can easily be computed using scientific calculators and the effect of various parameters understood clearly. The accuracy of analytical expressions are comparable with fabrication tolerances and measurement accuracy achievable.

For the various types of coplanar lines discussed in this section one attempts to determine suitable mapping functions so that the given configuration of coplanar lines is transformed into capacitors connected in parallel.

Since we are dealing with the quasi-static approximation of the mode of propagation, the values of phase velocity v_{ph} and the characteristic impedance Z_0 can be written as

$$\varepsilon_{re} = \frac{C}{C^a} \tag{7.1}$$

$$v_{ph} = \frac{c}{\sqrt{\varepsilon_{re}}} \tag{7.2}$$

and

$$Z_0 = \frac{1}{Cv_{ph}} = \frac{1}{c\sqrt{\varepsilon_{re}}C^a} \tag{7.3}$$

where c is the velocity of electromagnetic waves in free space, C is the total capacitance per unit length of the coplanar line, and C^a is the capacitance of the corresponding line with all the dielectrics replaced by air.

Specific coplanar line configurations and the corresponding transformations are discussed next. The strip and the ground plane metallization thickness is considered negligible in deriving the various expressions. The capacitance for the half-plane with air as dielectric is denoted by C_1 and that due to the dielectric layer is denoted by C_2.

CPW with Infinitely Thick Substrate [1]

Making use of the symmetry of the CPW structure, consider only one-half of it for conformal transformation, as shown in Figure 7.4(a). The Schwarz-Christoffel transformation, which maps the dielectric portion of the z-plane of Figure 7.4(a) into the interior of a rectangle in the w-plane of Figure 7.4(b) with the conductor surfaces on the top and the bottom, is given by

$$w = \int_{z_0}^{z} \frac{dz}{\sqrt{(z-a)(z-b)}} \tag{7.4}$$

The size of the rectangle in the w-plane is obtained by carrying out the above integration. It is given by

$$\frac{\overline{12}}{\overline{23}} = \frac{K(k_1)}{K'(k_1)} \tag{7.5}$$

where $\overline{ij}$ is the distance between points i and j in the w-plane and $K(\bullet)$ and $K'(\bullet)$ are the complete elliptic integrals of the first kind and its complement, respectively. They are simply related to each other through the equation

$$K'(k_1) = K(k_1') \qquad \text{with } k_1' = \sqrt{1-k_1^2} \tag{7.6}$$

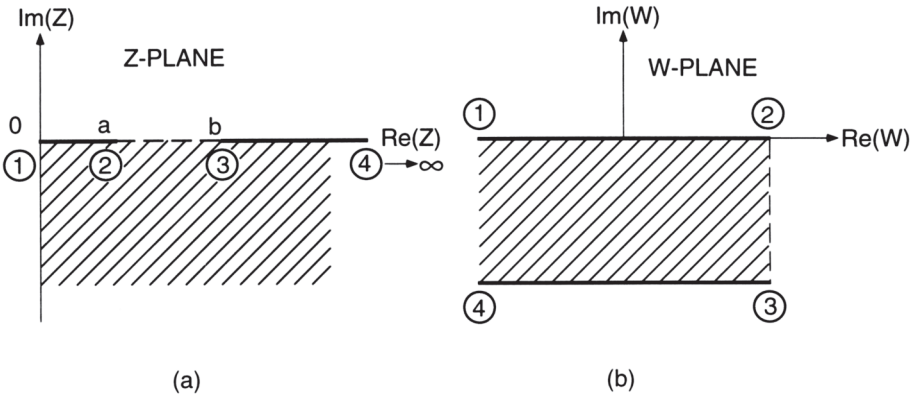

Figure 7.4 Conformal transformation planes for CPW analysis: (a) *z*-plane and (b) *w*-plane.

The argument of the elliptic integrals is obtained as

$$k_1 = a/b = S/(S + 2W) \tag{7.7}$$

The capacitance per unit length of the line contributed by the dielectric half-plane, C_2, is then given by

$$C_2 = 2\varepsilon_0\varepsilon_r \frac{K(k_1)}{K'(k_1)} \tag{7.8a}$$

The capacitance C_1 due to the electric field in the air half-plane follows directly from (7.8a) and is given by

$$C_1 = 2\varepsilon_0 \frac{K(k_1)}{K'(k_1)} \tag{7.8b}$$

The total line capacitance C becomes

$$C = C_1 + C_2 = 2\varepsilon_0(\varepsilon_r + 1)\frac{K(k_1)}{K'(k_1)} \tag{7.8c}$$

The effective dielectric constant of a CPW, obtained using (7.1), is then

$$\varepsilon_{re} = \frac{\varepsilon_r + 1}{2} \qquad C^a = 2C_1 \tag{7.9}$$

Similarly, the phase velocity and the characteristic impedance of a conventional CPW obtained from (7.2) and (7.3) are

$$v_{cp} = c\sqrt{\frac{2}{\varepsilon_r + 1}} \tag{7.10}$$

and

$$Z_{0cp} = \frac{30\pi}{\sqrt{\varepsilon_{re}}}\frac{K'(k_1)}{K(k_1)} \quad \text{(ohm)} \tag{7.11}$$

respectively. An accurate but simple expression of the ratio K/K' is available in the literature [25] and is included here for the reader's convenience.

$$\frac{K(k)}{K'(k)} = \frac{\pi}{\ell n[2(1+\sqrt{k'})/(1-\sqrt{k'})]} \quad \text{for } 0 \le k \le 0.707 \tag{7.12a}$$

$$\frac{K(k)}{K'(k)} = \frac{1}{\pi}\ell n\left[2(1+\sqrt{k})/(1-\sqrt{k})\right] \qquad \text{for } 0.707 \le k \le 1 \tag{7.12b}$$

$$k' = \sqrt{1-k^2} \tag{7.12c}$$

Expressions (7.12) are accurate to within 3 parts per million. The ratio K/K' varies from 0 to ∞ as k varies from 0 to 1.

The value of the characteristic impedance computed using (7.11) and (7.12) is plotted in Figure 7.5(a) for GaAs substrate, $\varepsilon_r = 13$ [26] (see the curve for $h/b = \infty$). The line impedance is found to decrease almost logarithmically as the aspect ratio a/b increases.

For practical applications the substrate thickness of a CPW has to be finite. This configuration is discussed next.

CPW with Finite Dielectric Thickness h

For the analysis of this structure (Figure 7.3a) we invoke the assumption that the capacitance due to the lower half-plane is the sum of the free-space capacitance and the capacitance of the dielectric layer with permittivity $(\varepsilon_r - 1)$. The free-space capacitance for the lower half-plane is exactly the same as that for the upper half-plane. It was calculated earlier and is denoted by C_1. The capacitance of the dielectric layer is calculated next.

A pair of transformations is used to transform the CPW into a parallel plate structure. The first transformation converts this CPW into a conventional CPW, that is, CPW with infinitely thick substrate. This transformation is

$$t = \sinh\left(\frac{\pi z}{2h}\right) \tag{7.13}$$

The resulting configuration in the t-plane is shown in Figure 7.6(b), where

$$t_1 = \sinh\left(\frac{\pi a}{2h}\right) \tag{7.14a}$$

and

$$t_2 = \sinh\left(\frac{\pi b}{2h}\right) \tag{7.14b}$$

The configuration of Figure 7.6(b) is identical to that of the conventional CPW in Figure 7.4(a) that was discussed earlier. Therefore, capacitance C_2 is given by

$$C_2 = 2\varepsilon_0(\varepsilon_r - 1)\frac{K(k_2)}{K'(k_2)} \tag{7.15}$$

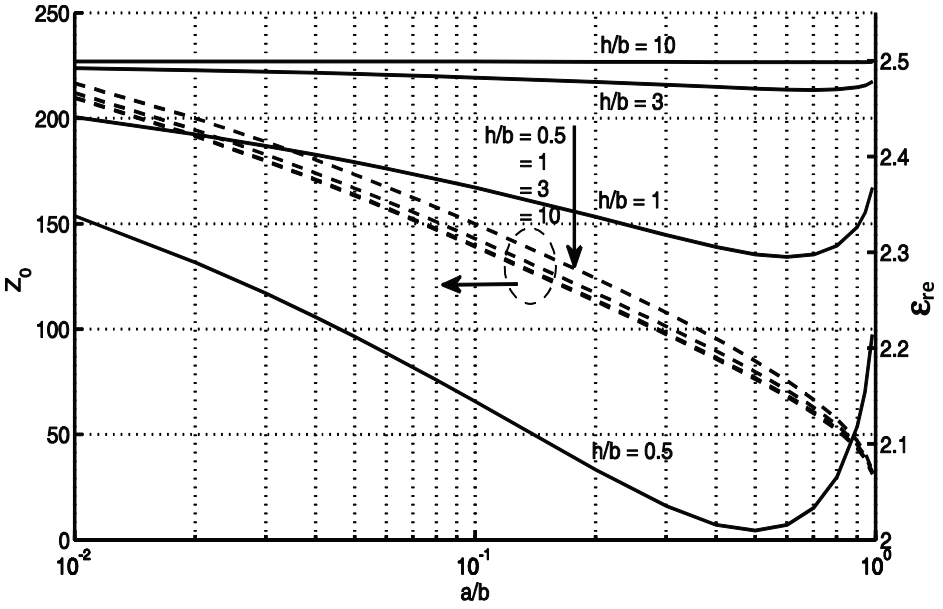

Figure 7.5 Variation of the characteristic impedance and relative effective dielectric constant of CPW (with finite dielectric thickness) as a function of aspect ratio *a/b*, with *h/b* as a parameter, $\varepsilon_r = 4$.

The factor $(\varepsilon_r - 1)$ appears in (7.15) because of the assumptions made in the analysis. The argument k_2 of the elliptic integral follows directly from (7.7), and (7.14),

$$k_2 = \frac{t_1}{t_2} = \frac{\sinh(\pi a/2h)}{\sinh(\pi b/2h)} \tag{7.16}$$

The capacitance C_1 contributed by the upper half-plane is that given by (7.8b). The total capacitance C is therefore given by

$$C = 2C_1 + C_2$$

and

$$C^a = 2C_1$$

Substituting for C and C^a in (7.1) we obtain the following expression for ε_{re}

$$\varepsilon_{re} = 1 + \frac{\varepsilon_r - 1}{2} \frac{K(k_2)}{K'(k_2)} \frac{K'(k_1)}{K(k_1)} \tag{7.17}$$

Quite frequently the effective dielectric constant is expressed in the form

$$\varepsilon_{re} = 1 + q(\varepsilon_r - 1) \tag{7.18}$$

where q is called the filling factor and can be obtained from a comparison of (7.17) and (7.18) as

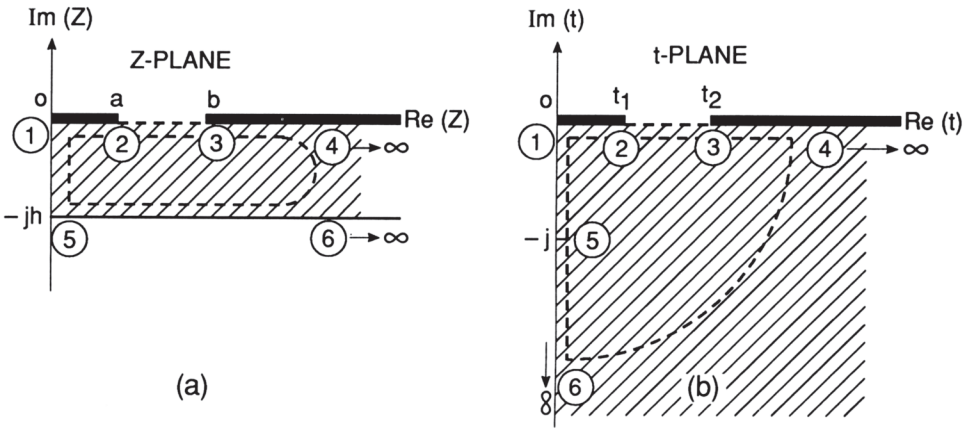

Figure 7.6 Transformation of CPW with substrate thickness h into a CPW with infinitely thick substrate using the mapping function $t = \sinh(\pi z/2h)$: (a) z-plane and (b) t-plane (from [22], © 1980 IEE (U.K.). Reprinted with permission.).

$$q = \frac{1}{2}\frac{K(k_2)}{K'(k_2)}\frac{K'(k_1)}{K(k_1)} \tag{7.19a}$$

It may be observed from (7.19a) that the filling factor does not depend on the relative dielectric constant of the substrate layer. Through k_i, it depends on the dielectric thickness, strip width, and slot width. It may be defined in terms of the capacitances as [24]

$$q = C_s^a / C^a \tag{7.19b}$$

where C^a is the capacitance of the CPW structure with air as dielectric and C_s^a is the capacitance of the substrate layer replaced by air as dielectric. We shall use this definition of q in calculating the effective dielectric constant of a multilayered CPW.

The characteristic impedance can be expressed as

$$Z_{0cp} = \frac{30\pi}{\sqrt{\varepsilon_{re}}}\frac{K'(k_1)}{K(k_1)} \tag{7.20}$$

It may be noted from a comparison of (7.11) and (7.20) that the effect of finite dielectric thickness is to decrease the effective dielectric constant of the CPW. Figure 7.5 shows that the relative effective dielectric constant decreases with a decrease in h and therefore the characteristic impedance increases. Since the impedance curves for $h = 3b$ and $h = 10b$ coincide with each other, $h > 3b$ for Z_{0cp} to be independent of h for $\varepsilon_r = 4$. For a given set of substrate parameters h and ε_r, a given value of characteristic impedance can be realized using different combinations of a and b; the final choice is determined by factors such as conductor loss of line.

Conformal mapping analysis of entire cross-section of CPW with finite thickness substrate has been reported [21,133]. This analysis does not employ partial capacitance decomposition. The lower boundary of the substrate appears as an elliptic void in the lower-half of the parallel plate capacitor in W-plane. The line

capacitance is therefore calculated numerically from the inhomogeneously filled capacitor. The results for $\varepsilon_r = 10{,}120$ are reported in [21].

Practical coplanar waveguides have finite width ground planes. This geometry is analyzed next.

CPW with Finite Dielectric Thickness and Finite Width Ground Planes [23]

The lateral extent of the ground planes of a CPW (Figure 7.3(b)) is denoted by c_0. In this case, the capacitance C_1 for the upper half-plane is determined by transforming the first-quadrant of the CPW (see Figure 7.7(a)) into the upper half of the t-plane (see Figure 7.7(b)) by using the mapping function

$$t = z^2$$

This geometry is now transformed into a parallel plate capacitor in the w-plane as in Figure 7.7(c) through the transformation

$$w = \int_{t_0}^{t} \frac{dt}{\sqrt{t(t-t_1)(t-t_2)(t-t_3)}} \tag{7.21}$$

with

$$t_1 = a^2, \quad t_2 = b^2, \quad t_3 = c_0^2$$

The capacitance per unit length C_1 is then obtained as

$$C_1 = 2\varepsilon_0 \frac{\overline{12}}{\overline{23}} = 2\varepsilon_0 \frac{K(k_3)}{K'(k_3)} \tag{7.22}$$

where

$$k_3 = \frac{a}{b}\sqrt{\frac{1 - b^2/c_0^2}{1 - a^2/c_0^2}} \tag{7.23}$$

The capacitance C_2 is computed by transforming the dielectric region in Figure 7.8(a) into the upper half of the t-plane (see Figure 7.8(b)) by using the mapping function

$$t = \cosh^2\left(\frac{\pi z}{2h}\right) \tag{7.24}$$

The geometry of Figure 7.8(b) is converted into a parallel plate capacitor in the w-plane of Figure 7.7(c) via the transformation

$$w = \int_{t_0}^{t} \frac{dt}{\sqrt{(t-1)(t-t_1)(t-t_2)(t-t_3)}} \tag{7.25}$$

with capacitance C_2 then given by

$$C_2 = 2\varepsilon_0(\varepsilon_r - 1)\frac{\overline{12}}{\overline{23}} = 2\varepsilon_0(\varepsilon_r - 1)\frac{K(k_4)}{K'(k_4)} \tag{7.26}$$

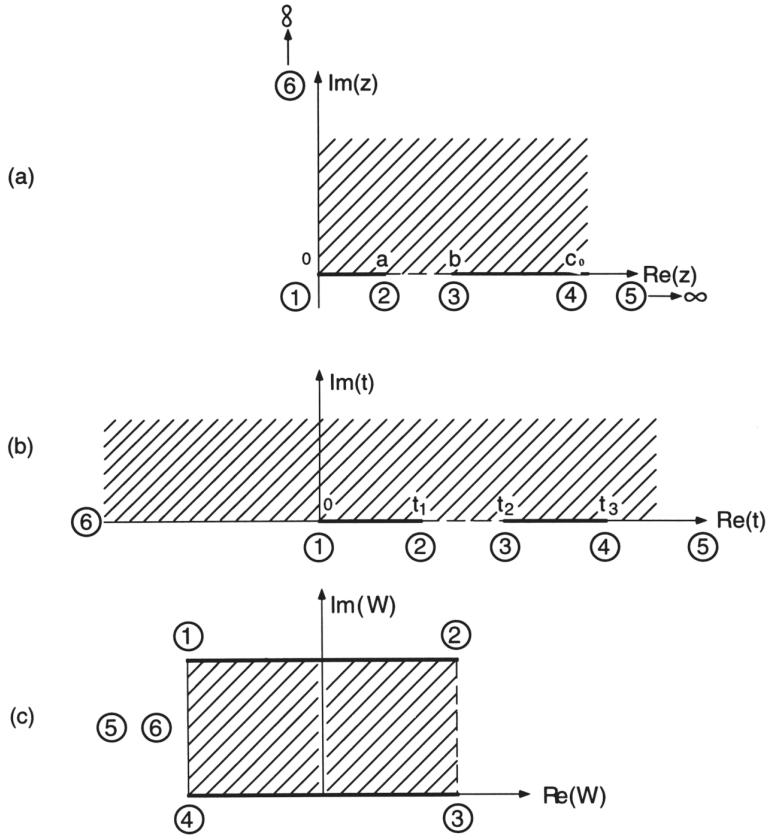

Figure 7.7 Conformal transformation of the first-quadrant of CPW with finite width ground planes into a parallel plate geometry: (a) *z*-plane; (b) *t*-plane; and (c) *w*-plane (from [23], © 1987 IEEE. Reprinted with permission.).

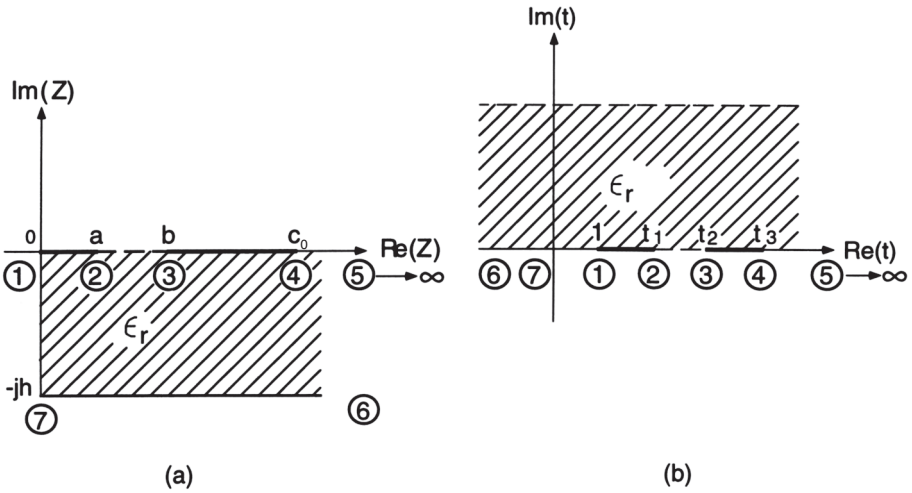

Figure 7.8 Conformal transformation of the fourth quadrant of CPW with finite width ground planes into a parallel plate geometry: (a) *z*-plane and (b) *t*-plane (from [23], © 1987 IEEE. Reprinted with permission.).

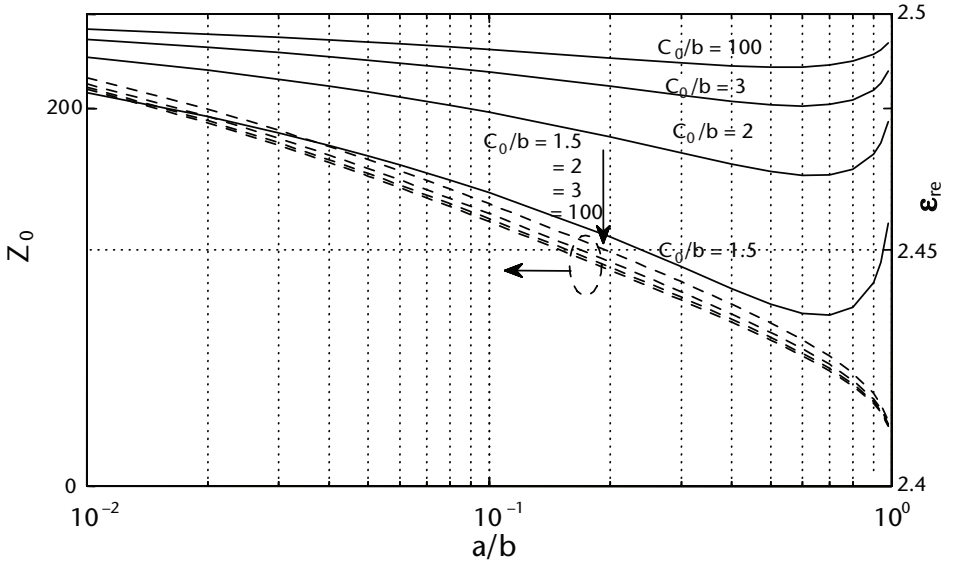

Figure 7.9 Variation of the characteristic impedance and relative effective dielectric constant of CPW (with finite width lateral ground planes) as a function of aspect ratio *a/b*, with c_0/b as a parameter; $\varepsilon_r = 4$, $h = 2b$.

where

$$k_4 = \frac{\sinh(\pi a/2h)}{\sinh(\pi b/2h)}\sqrt{\frac{1-\sinh^2(\pi b/2h)/\sinh^2(\pi c_0/2h)}{1-\sinh^2(\pi a/2h)/\sinh^2(\pi c_0/2h)}} \tag{7.27}$$

Thus,

$$\varepsilon_{re} = 1 + \frac{C_2}{2C_1} = 1 + \frac{\varepsilon_r - 1}{2}\frac{K(k_4)}{K'(k_4)}\frac{K'(k_3)}{K(k_3)} \tag{7.28}$$

and

$$Z_{0cp} = \frac{30\pi}{\sqrt{\varepsilon_{re}}}\frac{K'(k_3)}{K(k_3)} \tag{7.29}$$

Veyres and Fouad Hanna [22] have used different sets of conformal transformations, but the expressions for C_1 and C_2 obtained by them are identical with those obtained above. Evaluating (7.28) and (7.29) shows that the line impedance increases (see Figure 7.9) and relative effective dielectric constant decreases due to the truncation of ground planes. This configuration can also support a quasi-TEM slotline mode, whose characteristic impedance could be comparable to the desired mode. To suppress this mode, lateral ground planes are kept at the same potential by means of properly spaced conductive air bridges [23].

CPW with Finite Dielectric Thickness and a Cover Shield [23]

For this configuration (Figure 7.3(c)) the capacitance C^a can be divided into two portions: that due to the air region in the half-plane below the CPW metalization and that due to the air region between the cover shield and the CPW metalization, or C_1' and C_1''. The expression for C_1' is the same as that of C_1 of (7.8b).

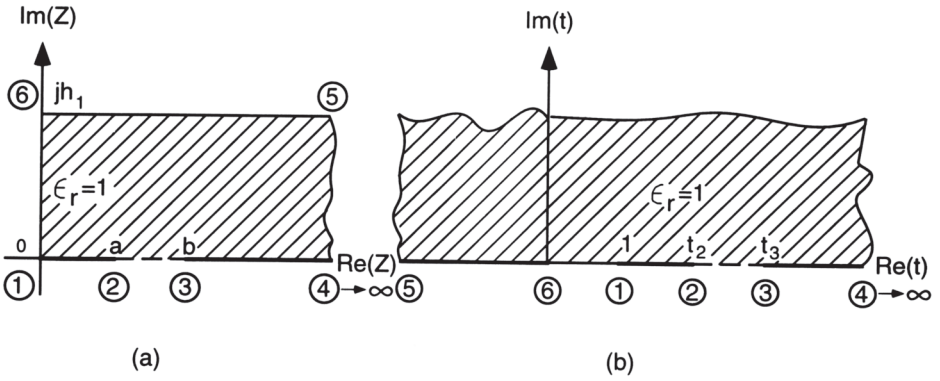

Figure 7.10 Mapping of the first quadrant of a CPW with a cover shield into the upper-half t-plane using the function $t = \cosh^2(\pi z/2h_1)$: (a) z-plane and (b) t-plane (from [25], C 1987 IEEE. Reprinted with permission.).

To obtain an expression for C_1'', let us consider the first quadrant of Figure 7.3(c) as shown in Figure 7.10(a). The dashed region in this figure is first mapped into the upper-half t-plane as in Figure 7.10(b) by means of the mapping function

$$t = \cosh^2\left(\frac{\pi z}{2h_1}\right) \tag{7.30}$$

and then into the parallel plate capacitor in the w-plane through the conformal transformation

$$W = \int_{t_0}^{t} \frac{dt}{\sqrt{t(t-1)(t-t_2)(t-t_3)}} \qquad t_2 = \cosh^2\frac{\pi a}{2h_1}, t_3 = \cosh^2\frac{\pi b}{2h_1} \tag{7.31}$$

The capacitance C_1'' is then given by

$$C_1'' = 2\varepsilon_0 \frac{K(k_5)}{K'(k_5)} \tag{7.32}$$

where

$$k_5 = \frac{\tanh\left(\pi a/2h_1\right)}{\tanh\left(\pi b/2h_1\right)} \tag{7.33}$$

The value of C_2 was obtained earlier and is given by (7.15). The total capacitance per unit length of the line is then

$$\begin{aligned} C &= C_1' + C_1'' + C_2 \\ &= 2\varepsilon_0 \frac{K(k_1)}{K'(k_1)} + 2\varepsilon_0 \frac{K(k_5)}{K'(k_5)} + 2\varepsilon_0\left(\varepsilon_r - 1\right)\frac{K(k_2)}{K'(k_2)} \end{aligned} \tag{7.34}$$

Thus

$$\varepsilon_{re} = 1 + \frac{C_2}{C_1' + C_1''} = 1 + q\left(\varepsilon_r - 1\right) \tag{7.35}$$

where q is called the filling factor and is obtained as

$$q = \frac{K(k_2)/K'(k_2)}{K(k_1)/K'(k_1) + K(k_5)/K'(k_5)} \tag{7.36}$$

and

$$Z_{0cp} = \frac{60\pi}{\sqrt{\varepsilon_{re}}} \frac{1}{K(k_1)/K'(k_1) + K(k_5)/K'(k_5)} \tag{7.37}$$

The effect of cover height h_1 on Z_{0cp} appears through the factor $K(k_5)/K'(k_5)$. For a large value of cover height h_1, (7.37) reduces to (7.20). Due to the additional term in (7.37) compared to (7.20), the line impedance decreases for a shielded CPW. As a conservative estimate the cover height should be at least four times the substrate thickness for the effect of the cover to be negligible.

Conductor-Backed CPW with a Cover Shield [23]

In this configuration (Figure 7.3(d)) the lower surface of the substrate is metalized. Therefore, the lower half and upper half portions of the CPW are similar except for different dielectric constants and thicknesses. Consequently, the capacitance C_2 contributed by the dielectric layer can be obtained from the same transformation that is used for the upper half portion. The resulting capacitance is

$$C_2 = 2\varepsilon_0\varepsilon_r \frac{K(k_6)}{K'(k_6)} \tag{7.38}$$

with

$$k_6 = \frac{\tanh(\pi a/2h)}{\tanh(\pi b/2h)} \tag{7.39}$$

The expression for C_1 in this case is the same as that for C_1'' for the earlier case, (7.32). Thus,

$$\varepsilon_{re} = \frac{C_1 + C_2}{C_1 + C_2\left(\text{for } \varepsilon_r = 1\right)} = 1 + q\left(\varepsilon_r - 1\right)$$

with

$$q = \frac{K(k_6)/K'(k_6)}{K(k_5)/K'(k_5) + K(k_6)/K'(k_6)} \tag{7.40}$$

and

$$Z_{0cp} = \frac{60\pi}{\sqrt{\varepsilon_{re}}} \frac{1}{K(k_5)/K'(k_5) + K(k_6)/K'(k_6)} \tag{7.41}$$

It may be observed from (7.40) that $q = 0.5$ when $k_5 = k_6$, which can be realized by $h_1 = h$; that is, conductor backing and the cover shield are equidistant from CPW metallization. This results in $\varepsilon_{re} = (\varepsilon_r + 1)/2$.

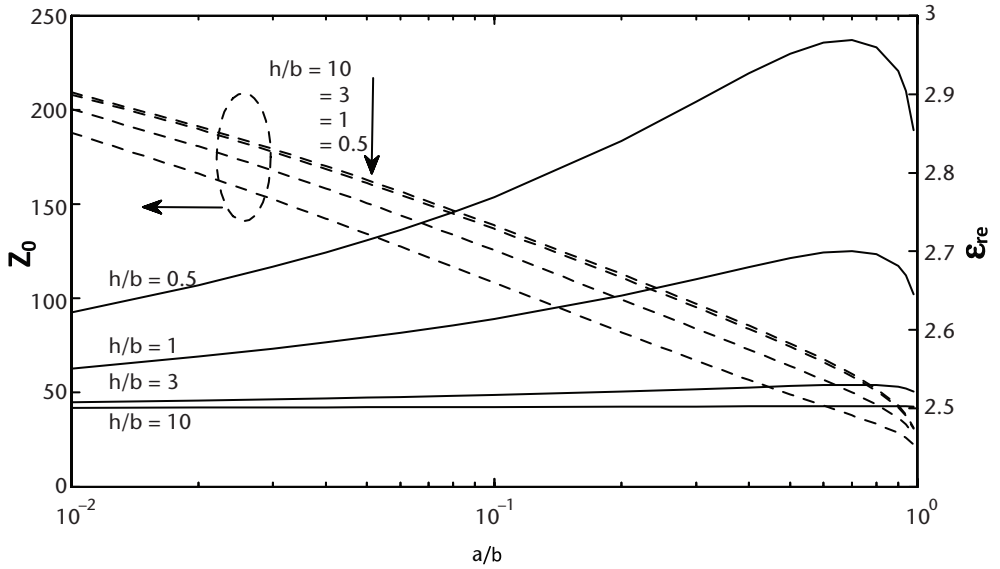

Figure 7.11 Characteristic impedance and relative effective dielectric constant of conductor-backed CPW as a function of aspect ratio a/b, and h/b as parameter; $\varepsilon_r = 4$.

Conductor-Backed CPW [27]

This configuration (shown in Figure 7.3(e)) is the limiting case of Figure 7.3(d) when the cover shield recedes to infinity, that is, $h_1 \to \infty$. Therefore, expressions for q and Z_{0cp} can be obtained from (7.40) and (7.41), respectively. When $h_1 \to \infty$, it follows that $k_5 \to a/b = k_1$ and we obtain

$$q = \frac{K(k_6)/K'(k_6)}{K(k_1)/K'(k_1) + K(k_6)/K'(k_6)} \tag{7.42}$$

and

$$Z_{0cp} = \frac{60\pi}{\sqrt{\varepsilon_{re}}} \frac{1}{K(k_1)/K'(k_1) + K(k_6)/K'(k_6)} \tag{7.43}$$

Conductor backing of the substrate improves the mechanical strength of the line so that thin substrates may be used. However, conductor backing concentrates the fields in the substrate giving rise to increase in effective dielectric constant of the line and the consequent decrease in characteristic impedance; compare Figures 7.11 and 7.5. This is possible if the lower ground conductor is nearer to the central strip than the lateral ground conductors. The mode may become quasi-TEM as in microstrip line. Alternatively, the microstrip-like behavior becomes dominant when the substrate is thin and the slots are wide such that $W/h > 2$. If the aim is to obtain coplanar behavior, the substrate should be thick and the slots should be narrow so that $W/h \ll 1$. For a moderate aspect ratio, for example, $S/2h = 1/3$ and $W/h = 2/3$, the conductor-backed CPW becomes less dispersive than the corresponding microstrip line with the same aspect ratio, $W/h = 2/3$ [8]. Conductor-backed CPW also supports leaky modes, which will be discussed later.

Multilayered CPW Configuration [24]

For a multilayered structure (Figure 7.3(f)) the effective dielectric constant can be expressed as

$$\varepsilon_{re} = q_1\varepsilon_{r1} + q_2\varepsilon_{r2} + q_3\varepsilon_{r3} \ldots + q_n\varepsilon_{rn} \tag{7.44}$$

where $q_1, q_2, \ldots, q_4$ describe the filling factors for the various dielectric regions. To illustrate how to obtain the filling factors for a multilayered CPW we shall first consider the double-layered CPW configurations discussed earlier.

For the double-layered geometries we obtained expressions for ε_{re} in the form

$$\varepsilon_{re} = 1 + q\left(\varepsilon_r - 1\right) \tag{7.45}$$

where

$$q = C_s^a/C^a \tag{7.46}$$

Here C^a is the capacitance of the CPW structure with air as dielectric and $C_s^a = C_2$ (for $\varepsilon_r = 1$) is the capacitance of the substrate layer replaced by air as dielectric. Expressions for C^a and C_s^a were in the form $K(k_i)/K'(k_i)$. These expressions for the capacitances can be used to obtain the general expression for a multilayered CPW configuration.

The general expression for the capacitance of the ith layer with dielectric replaced by air is

$$C_{si}^a = 2\varepsilon_0 \frac{K(k_1)}{K'(k_1)} \tag{7.47}$$

where

$$k_i = \begin{cases} a/b & \text{for the half-plane} \quad (7.48a) \\ \dfrac{\sinh(\pi a/2h)}{\sinh(\pi b/2h)} & \text{for a dielectric layer of thickness } h \quad (7.48b) \\ \dfrac{\tanh(\pi a/2h)}{\tanh(\pi b/2h)} & \text{for a dielectric layer backed by a conductor} \quad (7.48c) \end{cases}$$

Let us now determine the filling factors for the four-layered configuration in Figure 7.3(f). In this case,

$$C^a = 4\varepsilon_0 \frac{K(k)}{K'(k)}, \; k = \frac{a}{b} \tag{7.49}$$

The filling factor for the second layer, defined per (7.46), is

$$q_2 = C_{s2}^a/C^a \tag{7.50}$$

with

$$C_{s2}^{a} = 2\varepsilon_0 \frac{K(k_2)}{K'(k_2)}, \qquad k_2 = \frac{\sinh(\pi a/2h_2)}{\sinh(\pi b/2h_2)} \tag{7.51}$$

Similarly,

$$q_3 = C_{s3}^{a}/C^{a} \tag{7.52}$$

with

$$C_{s3}^{a} = 2\varepsilon_0 \frac{K(k_3)}{K'(k_3)}, \qquad k_3 = \frac{\sinh\left(\pi a/2h_3\right)}{\sinh\left(\pi b/2h_3\right)} \tag{7.53}$$

For the topmost layer, the filling factor is defined as

$$q_4 = \frac{C^{a}/2 - C_{s3}^{a}}{C^{a}} = \frac{1}{2} - \frac{C_{s3}^{a}}{C^{a}} \tag{7.54}$$

Similarly, for the lowest layer

$$q_1 = \frac{C^{a}/2 - C_{s2}^{a}}{C^{a}} = \frac{1}{2} - \frac{C_{s2}^{a}}{C^{a}} \tag{7.55}$$

It can be verified that

$$q_1 + q_2 + q_3 + q_4 = 1 \tag{7.56}$$

The effective dielectric constant of the CPW in Figure 7.3(f) follows from the use of q_1, q_2, q_3, and q_4 in (7.44). The characteristic impedance can be determined from ε_{re} and C^{a}. The parallel plate capacitor in the w-plane, corresponding to Figure 7.3(f), is shown in Figure 7.12.

The above analysis can be extended to any number of dielectric layers in a CPW.

Variants of CPW

(i) Conductor-Backed Asymmetric CPW

This geometry is similar to asymmetric CPW with finite dielectric thickness (Figure 7.3(h)) with the difference that the lower surface of the substrate is metallized as shown in Figure 7.13(a). Unlike a symmetric coplanar waveguide, the slots on either side of the strip are of unequal width in an asymmetric coplanar waveguide (ACPW). Unequal slot widths may occur due to fabrication tolerances. Sometimes unequal slot widths are desirable to introduce flexibility in design. If S_1 and S_2 are the slot widths defined as $S_1 = b_1 - a$ and $S_2 = b_2 - a$, respectively, the asymmetry parameter of the line is defined as S_2/S_1. The conductor backing provides mechanical strength, reduces radiation, and is useful in heat dissipation. Due to the confinement of fields by the conductor backing, the effective dielectric constant increases and characteristic impedance of the line decreases.

For conformal mapping analysis of the line, we make the usual assumption of inserting magnetic wall across the slots [134]. As a result, the line capacitance may be decomposed as $C = C_1 + C_2$ where C_1 is the capacitance contributed by the electric field in the air region, and C_2 is the capacitance contributed by the field in the substrate portion. Two conformal mappings are employed to determine C_2, the first mapping transforms the conductor-backed dielectric into an infinitely thick dielectric without conductor backing, and the second mapping transforms this geometry into parallel plate geometry. The mapping from the z-plane to t-plane in this region is defined as [134]

$$t = \exp(\pi z / h) \qquad -\infty \le x \le \infty, \; -jh \le y \le 0 \tag{7.57}$$

The slots edges in the z-plane are mapped as

$$t_2 = \exp(-\pi b_1 / h), t_3 = \exp(-\pi a / h), t_4 = \exp(\pi a / h), t_5 = \exp(\pi b_2 / h) \tag{7.58}$$

The geometry in the t-plane (Figure 7.13(b)), is an asymmetric CPW with homogeneous dielectric below the strips. The transformation which maps the dielectric region in the t-plane into the interior of a rectangle in the w-plane of Figure 7.13(c) is given by

$$w = \int_{t_2}^{t} \frac{dt}{(t - t_2)(t - t_3)(t - t_4)(t - t_5)} \tag{7.59}$$

Carrying out this integration determines the coordinates of the rectangle, and the capacitance contributed by the dielectric region of ACPW is given by [134]

$$C_2 = \varepsilon_0 \varepsilon_r \frac{K(k_7)}{K'(k_7)} \tag{7.60}$$

where

$$k_7^2 = \frac{(t_4 - t_3)(t_5 - t_2)}{(t_4 - t_2)(t_5 - t_3)} = \frac{(\exp(\pi a / h) - \exp(-\pi a / h))(\exp(\pi b_2 / h) - \exp(-\pi b_1 / h))}{(\exp(\pi a / h) - \exp(-\pi b_1 / h))(\exp(\pi b_2 / h) - \exp(-\pi a / h))} \tag{7.61}$$

The capacitance C_1 due to the fields in the upper-half region of the asymmetric CPW may be obtained from (7.60) in the limit $h \to \infty$, $\varepsilon_r = 1$; one obtains,

$$C_1 = \varepsilon_0 \frac{K(k_8)}{K'(k_8)} \qquad k_8 = \lim_{h \to \infty} k_7 = \sqrt{\frac{2a(b_1 + b_2)}{(a + b_1)(a + b_2)}} \tag{7.62}$$

Therefore, the total line capacitance of the conductor-backed ACPW is

$$C = \varepsilon_0 \frac{K(k_8)}{K'(k_8)} + \varepsilon_0 \varepsilon_r \frac{K(k_7)}{K'(k_7)} \qquad \text{F/unit length} \tag{7.63}$$

The effective relative permittivity and characteristic impedance are then obtained as

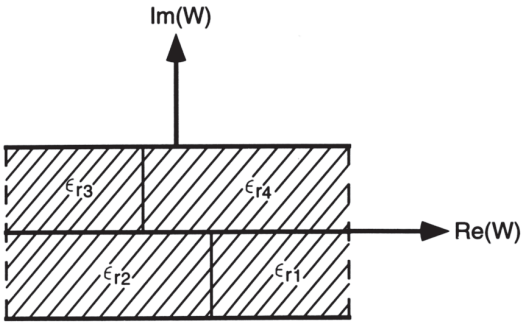

Figure 7.12 Approximate conformal mapped structure corresponding to the CPW of Figure 7.3(f).

$$\varepsilon_{re} = \frac{\dfrac{K(k_8)}{K'(k_8)} + \varepsilon_r \dfrac{K(k_7)}{K'(k_7)}}{\dfrac{K(k_8)}{K'(k_8)} + \dfrac{K(k_7)}{K'(k_7)}}, \qquad Z_{0cp} = \frac{120\pi}{\sqrt{\varepsilon_{re}}\left(\dfrac{K(k_7)}{K'(k_7)} + \dfrac{K(k_8)}{K'(k_8)}\right)} \tag{7.64}$$

The electric field distribution in the line could be useful in understanding the physics of the problem such as conductor loss in the line. The field distribution can be determined by mapping the points from the w-plane to z-plane. It is found that the field is concentrated about the slot edges and the electric field at the conductor backing is very small [134].

(ii) Asymmetric CPW with Infinitely Thick Substrate or No Substrate

The cross-section of this ACPW is shown in Figure 7.3(g). Because of half-space on either side of metallization plane, the electric field is symmetric and we can insert magnetic walls across the slots. The line capacitance C_1 for the fields in upper-half portion is given by (7.62). Similarly, the line capacitance for the fields in lower-half portion is $\varepsilon_r C_1$. The total line capacitance therefore adds to

$$C = \varepsilon_0(\varepsilon_r + 1)\frac{K(k_8)}{K'(k_8)} \tag{7.65}$$

and

$$\varepsilon_{re} = \frac{\varepsilon_r + 1}{2}, \qquad Z_{0cp} = \frac{60\pi}{\sqrt{\varepsilon_{re}}}\frac{K'(k_8)}{K(k_8)} \tag{7.66}$$

Similarly, the characteristic impedance of ACPW with no substrate is given by

$$Z_{0cp} = 60\pi\frac{K'(k_8)}{K(k_8)} \tag{7.67}$$

(iii) Asymmetric CPW with Finite Dielectric Thickness

The cross-section of this ACPW is shown in Figure 7.3(h). The magnetic wall assumption across the slots may not hold well in this case because of finite dielectric

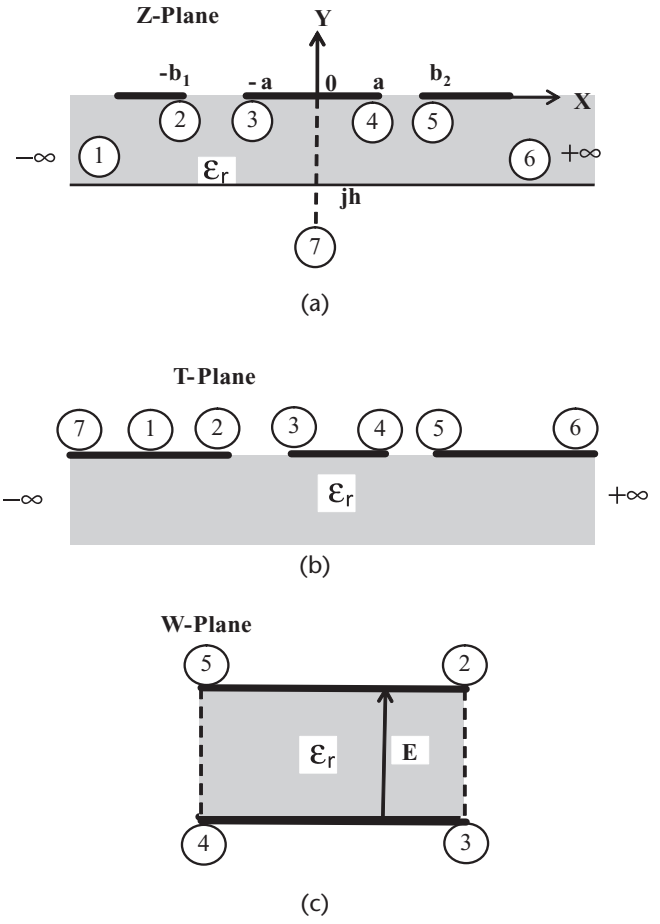

Figure 7.13 Conductor-backed asymmetric CPW and mapping of the dielectric region into the interior of a rectangle. (a) Cross-section of conductor-backed ACPW, (b) *t*-plane geometry, and (c) *w*-plane geometry. (After [143].)

thickness. We employ partial capacitance approximation to write $C = C^a + C^s$. The line capacitance with substrate replaced by air is given by (7.62),

$$C^a = 2\varepsilon_0 \frac{K(k_8)}{K'(k_8)} \tag{7.68}$$

The partial capacitance C^s for ACPW with finite dielectric thickness may be obtained by following the conformal mapping procedure described for conductor-backed ACPW. However, the first mapping is described by

$$t = \sinh\left(\pi z/(2h)\right) \qquad -\infty \le x \le \infty, \; -jh \le y \le 0 \tag{7.69a}$$

The slots edges in the *z*-plane are mapped as

$$t_2 = \sinh\left(-\pi b_1/2h\right), t_3 = \sinh\left(-\pi a/2h\right), t_4 = \sinh\left(\pi a/2h\right), t_5 = \sinh\left(\pi b_2/2h\right) \tag{7.69b}$$

Following mapping (7.59) and algebraic simplification, we obtain

$$C^S = \varepsilon_0(\varepsilon_r - 1)\frac{K(k_9)}{K'(k_9)} \tag{7.70}$$

where

$$k_9 = \sqrt{\frac{2\sinh\left(\frac{\pi a}{2h}\right)\left\{\sinh\left(\frac{\pi b_1}{2h}\right)+\sinh\left(\frac{\pi b_2}{2h}\right)\right\}}{\left\{\sinh\left(\frac{\pi a}{2h}\right)+\sinh\left(\frac{\pi b_1}{2h}\right)\right\}\left\{\sinh\left(\frac{\pi a}{2h}\right)+\sinh\left(\frac{\pi b_2}{2h}\right)\right\}}} \tag{7.71}$$

or

$$k_9^2 = \frac{2(k_{1e} + k_{2e})}{(1 + k_{1e})(1 + k_{2e})} \tag{7.72}$$

where

$$k_{1e} = \frac{\sinh(\pi a/2h)}{\sinh(\pi b_1/2h)}, \quad k_{2e} = \frac{\sinh(\pi a/2h)}{\sinh(\pi b_2/2h)}$$

The relative effective dielectric constant of ACPW with finite dielectric thickness is therefore given by

$$\varepsilon_{re} = \frac{C^a + C^s}{C^a} = 1 + \frac{\varepsilon_r - 1}{2}\frac{K(k_9)}{K'(k_9)}\frac{K'(k_8)}{K(k_8)} \tag{7.73}$$

and the characteristic impedance is obtained as

$$Z_{0cp} = \frac{60\pi}{\sqrt{\varepsilon_{re}}}\frac{K'(k_8)}{K(k_8)} \tag{7.74}$$

The expression (7.73) is similar to that reported in [38].

It may be noted that (7.70) for C^s does not reduce to the corresponding expression for the symmetric case merely by substituting $b_1 = b_2 = b$. This derivation is given next [28]. For the symmetric case, $k_{1e} = k_{2e} = k_e$. Then

$$k_9 = \frac{2\sqrt{k_e}}{(1 + k_e)}, k_e = \frac{\sinh(\pi a/2h)}{\sinh(\pi b/2h)} \tag{7.75}$$

Now, we use the following properties of $K(\bullet)$ and $K'(\bullet)$ [31]:

$$K(k_9) = K\left(\frac{2\sqrt{k_e}}{1 + k_e}\right) = (1 + k_e)K(k_e), \qquad K'(k_9) = K(k_9') = K\left(\frac{1 - k_e}{1 + k_e}\right) = \frac{1 + k_e}{2}K'(k_e) \tag{7.76}$$

Thus

$$\frac{K(k_9)}{K'(k_9)} = 2\frac{K(k_e)}{K'(k_e)} = 2\frac{K(k_2)}{K'(k_2)} \tag{7.77}$$

and (7.70) reduces to (7.15).

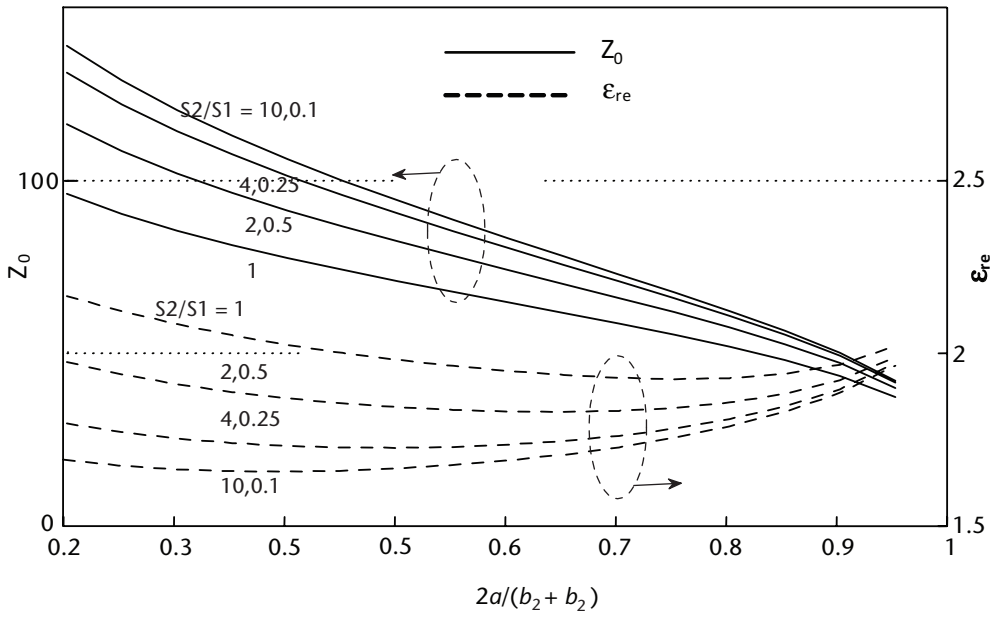

Figure 7.14 Variation of ε_{re} and Z_0 of ACPW with finite dielectric thickness h, $\varepsilon_r = 4$, $b_1 + b_2 = 8h$.

Figure 7.14 shows the effect of slot asymmetry on the relative effective dielectric constant and characteristic impedance of CPW. The asymmetry factor S_2/S_1 is varied from 1 to 10. It is observed that the line asymmetry ($S_2 > S_1$) causes ε_{re} to decrease and Z_0 to increase compared to the symmetric line case, $S_2 = S_1$. However, the increase in strip width $2a$ for the same asymmetry factor reduces this difference perhaps because increased strip width reduces coupling between the slots. The line characteristics remain unchanged if the slots are interchanged. Therefore, the curves of Figure 7.14 are also applicable for the corresponding values of S_1/S_2.

7.2.2 Quasi-Static Conformal Mapping Analysis of CPS

Coplanar strips (CPS), like coplanar waveguide, offer flexibility in the design of planar microwave and millimeter-wave circuits in that lumped devices can be mounted in series as well as in shunt. It is easier to realize high line impedances with CPS than with CPW. Further, CPS is a balanced transmission line such as a slotline and is useful in balanced circuit design such as mixers and modulators and as interconnects in high-speed digital circuits. Coplanar strips are widely used in integrated optic traveling wave modulators [32,33] and optical control microwave attenuators and modulators [34]. Like CPW, practical CPS lines use a finite thickness substrate. The geometry of this line and its field distributions are shown in Figure 7.2. Due to fabrication tolerances we may end up with a CPS in which the two strips do not have the same width. This line is called an asymmetric CPS or ACPS. Sometimes, it is desirable to use an asymmetric CPS to adjust the characteristic impedance by changing the width of one of the strips while keeping the width of the other strip and the slot width fixed. The asymmetric CPS geometry is shown in Figure 7.15(a,b,c).

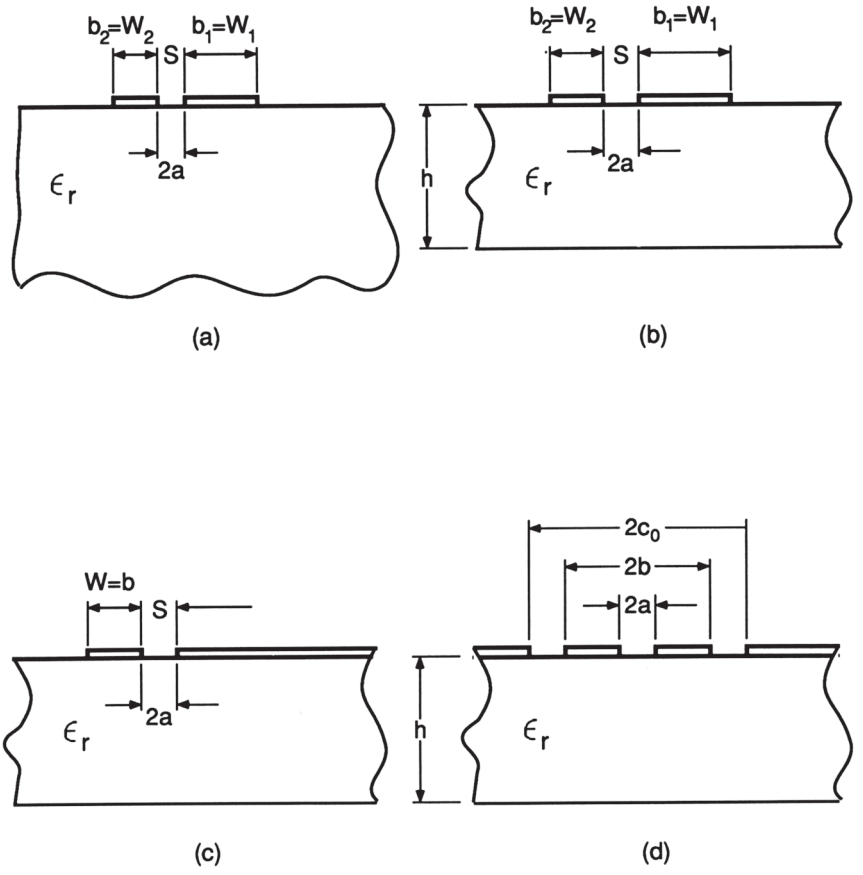

Figure 7.15 Variants of coplanar strips: (a) asymmetric CPS; (b) asymmetric CPS with finite dielectric thickness; (c) asymmetric CPS with one lateral ground plane; and (d) CPS with lateral ground planes.

Conformal mapping analysis of CPS suffers from inaccuracies because the assumption of magnetic walls at the dielectric interfaces is not justified. This assumption works well for CPS with a homogeneous dielectric on either side of strip plane such as an infinitely thick substrate. For finite substrate thickness, it has been observed that the complementary nature of a metallization pattern between CPS and CPW may be utilized along with duality to determine ε_{re} (i.e., the value of ε_{re} obtained for CPW may be used for CPS also for the same value of S/W [24, 40]). According to Zhu et al. [135], duality between CPS and CPW for ε_{re} may be employed provided $h/b > 5$. The assumption of duality for multi-layered coplanar lines has been tested in [132]. For a case study with five layers, the difference between theory and measurements of time delay was 3% for CPW geometry and 6% for the corresponding CPS geometry. The analysis in [133] shows that in general the difference $|\varepsilon_{re}^{cpw} - \varepsilon_{re}^{cps}|$ decreases with increase in dielectric thickness and decrease in $|\varepsilon_{ri} - \varepsilon_{rj}|$ where ε_{ri} and ε_{rj} represent the relative permittivity of contiguous ith and jth layers, respectively.

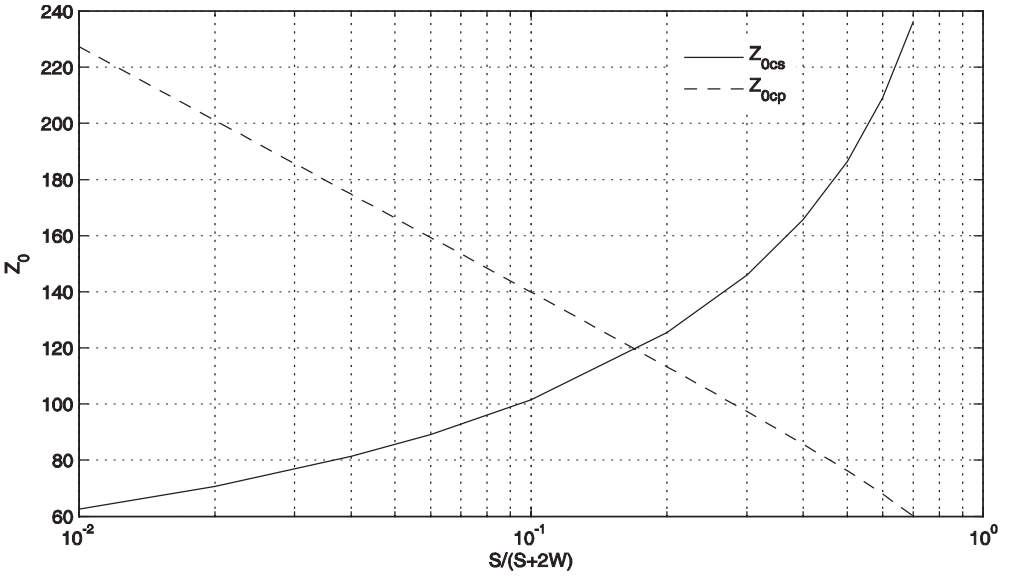

Figure 7.16 Variation of characteristic impedance for CPS and CPW as a function of aspect ratio S/(S+2W), $\varepsilon_r = 4$.

Symmetric CPS with Infinitely Thick Substrate [35]

The geometry of this CPS line is similar to that shown in Figure 7.2(a) with $h \to \infty$. Capacitances C_1 and C_2 contributed by the electric field in the air and dielectric regions, respectively, are given by

$$C_1 = \frac{\varepsilon_0}{2}\frac{K'(k_1)}{K(k_1)}, \qquad k_1 = \frac{S}{S+2W} = \frac{a}{b} \tag{7.78}$$

$$C_2 = \frac{\varepsilon_0\varepsilon_r}{2}\frac{K'(k_1)}{K(k_1)} \tag{7.79}$$

$$\varepsilon_{re} = \frac{C_1 + C_2}{2C_1} = \frac{\varepsilon_r + 1}{2} \tag{7.80}$$

and

$$Z_{0cs} = \frac{120\pi}{\sqrt{\varepsilon_{re}}}\frac{K(k_1)}{K'(k_1)} \tag{7.81}$$

Symmetric CPS and symmetric CPW lines offer complementary impedance values because of the factor $K(k_1)/K'(k_1)$ in the impedance expression for CPS and $K'(k_1)/K(k_1)$ for CPW. The characteristic impedances of CPS and CPW are plotted in Figure 7.16 for the same aspect ratio $S/(S + 2W)$. It is observed that CPW and CPS offer complementary impedance values.

Symmetric CPS with Finite Dielectric Thickness

Conformal transformation analysis of symmetric CPS with finite substrate thickness, (Figure 7.2(a)) has been reported in [38]. Since the electric field is not exactly

tangential to the air-dielectric interface on the strip plane, partial capacitance approximation has been employed along with conformal mapping. The line capacitance with air as dielectric is given by

$$C^a = \varepsilon_0 \frac{K'(k_1)}{K(k_1)} \tag{7.82}$$

The partial capacitance of the substrate region is given by [38]:

$$C^S = \varepsilon_0 \frac{(\varepsilon_r - 1)}{2} \frac{K'(k_{10})}{K(k_{10})} \tag{7.83a}$$

where

$$k_{10} = \tanh\left(\frac{\pi}{4}\frac{S}{h}\right) \Big/ \tanh\left(\frac{\pi}{4}\frac{2W+S}{h}\right) \tag{7.83b}$$

The effective relative dielectric constant and characteristic impedance of symmetric CPS with finite substrate thickness are therefore given by

$$\varepsilon_{re} = \frac{C^a + C^s}{C^a} = 1 + \frac{(\varepsilon_r - 1)}{2} \frac{K'(k_{10})}{K(k_{10})} \frac{K(k_1)}{K'(k_1)} \tag{7.84a}$$

and

$$Z_{0cs} = \frac{120\pi}{\sqrt{\varepsilon_{re}}} \frac{K(k_1)}{K'(k_1)} \tag{7.84b}$$

Variations of relative effective dielectric constant and characteristic impedance of symmetric CPS are plotted in Figure 7.17. The effective dielectric constant increases with substrate thickness and therefore characteristic impedance of the line decreases. Characteristic impedance increases with aspect ratio $S/(S+2W)$ for a given substrate thickness.

Conformal mapping analysis of entire cross-section of CPS with finite thickness substrate has been reported [133]. This analysis does not employ partial capacitance decomposition. The parallel plate capacitor in the W-plane is inhomogeneously filled. The line capacitance is therefore calculated numerically. The results for $\varepsilon_r = 2.2$ are reported.

Variants of Coplanar Strip Line

(i) Asymmetric CPS with Infinitely Thick Substrate [36]

The cross-section of this line is shown in Figure 7.15(a). For determining its characteristics, we make use of the complementary metallization patterns of CPS and CPW. The expression for ε_{re} for ACPS line is assumed to be the same as that of the corresponding ACPW line with the meanings of S and W interchanged. The capacitances obtained from (7.65) are

$$C_1 = \varepsilon_0 \frac{K'(k_{11})}{K(k_{11})}, \qquad C_2 = \varepsilon_0 \varepsilon_r \frac{K'(k_{11})}{K(k_{11})} \tag{7.85}$$

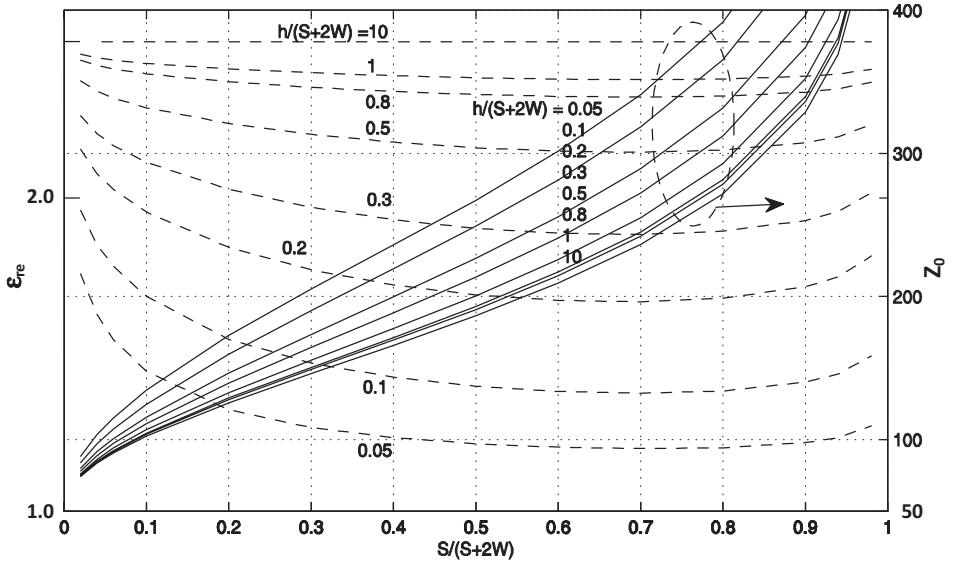

Figure 7.17 Variation of ε_{re} and Z_0 of symmetric CPS with dielectric thickness h, $\varepsilon_r = 4$.

with

$$k_{11} = \sqrt{\frac{S(S+W_1+W_2)}{(W_1+S)(W_2+S)}}, \qquad k'_{11} = \sqrt{\frac{W_1}{(W_1+S)}\frac{W_2}{(W_2+S)}} \tag{7.86}$$

The capacitance expressions (7.85) include the factor $K'(\bullet)/K(\bullet)$ compared to $K(\bullet)/K'(\bullet)$ for CPW in order to preserve the complementary impedance behavior of CPS. The line characteristics are therefore obtained as

$$\varepsilon_{re} = \frac{\varepsilon_r + 1}{2}, \qquad Z_{0cs} = \frac{60\pi}{\sqrt{\varepsilon_{re}}}\frac{K(k_{11})}{K'(k_{11})} \tag{7.87}$$

The above equations are similar to those reported in [37,38].

(ii) Asymmetric CPS with Finite Dielectric Thickness [39]

For this line, Figure 7.15(b), the characteristic impedance is given by

$$Z_{0cs} = \frac{60\pi}{\sqrt{\varepsilon_{re}}}\frac{K(k_{11})}{K'(k_{11})} \tag{7.88}$$

with

$$\varepsilon_{re} = 1 + \frac{\varepsilon_r - 1}{2}\frac{K(k_{12})}{K'(k_{12})}\frac{K(k_{11})}{K'(k_{11})} \tag{7.89}$$

where k_{11} is defined in (7.86) and

$$k_{12} = \sqrt{\frac{\sinh(\pi W_1/2h)}{\sinh(\pi(W_1+S)/2h)}\frac{\sinh(\pi W_2/2h)}{\sinh(\pi(W_2+S)/2h)}} \tag{7.90}$$

These expressions are similar to those available in [38].

(iii) Asymmetric CPS with One Lateral Ground Plane or an Infinitely Wide Strip [38]

The geometry of this line is shown in Figure 7.15(c). It consists of two strips on the dielectric-air interface and may be derived from ACPW with one of the ground planes removed or from ACPS when one of the strips extends to infinity. An asymmetric coplanar line with one ground plane is used in electro-optic modulators [41,42]. It is found that the expressions obtained for ACPS with finite dielectric thickness, (7.88) to (7.90), reduce to the corresponding expressions for this configuration in the limit when one of the strip widths is increased to infinity. Let $W_2 \to \infty$ and $W_1 = W$, then

$$Z_{0cs} = \frac{60\pi}{\sqrt{\varepsilon_{re}}} \frac{K(k_{13})}{K'(k_{13})} \tag{7.91a}$$

with

$$\varepsilon_{re} = 1 + \frac{\varepsilon_r - 1}{2} \frac{K(k_{14})}{K'(k_{14})} \frac{K(k_{13})}{K'(k_{13})} \tag{7.91b}$$

where

$$k_{13} = \lim_{W_2 \to \infty, W_1 = W} k_{11} = \sqrt{\frac{S}{W+S}}, \qquad k_{14} = \lim_{W_2 \to \infty, W_1 = W} k_{12} = \sqrt{\frac{\sinh\left(\pi W / 2h\right)}{\sinh\left(\pi (W+S) / 2h\right)} e^{-\pi S/2h}} \tag{7.92}$$

(iv) CPS with Lateral Ground Planes on Finitely Thick Substrate [43]

The presence of lateral ground planes in this configuration (Figure 7.15(d)) reduces line to line coupling and eliminates the parasitic TE_0 dielectric slab waveguide mode of a conventional CPS. The configuration of this CPS line is complementary to the CPW with finite width ground planes (see Figure 7.3(b)). It may be assumed that the propagation constant is the same for complementary lines in the quasi-static limit [44]. Therefore, the effective dielectric constant of this CPS line is given by (7.28). The characteristic impedance is, however, given by the expression

$$Z_{0\mathrm{cs}} = \frac{120\pi}{\sqrt{\varepsilon_{\mathrm{re}}}} \frac{K(k_3)}{K'(k_3)} \tag{7.93}$$

where k_3 is defined by (7.23). It is found that this line is less dispersive compared to a conventional CPS. Further, lower values of characteristic impedance can be obtained by adjusting the width of the outer slots [40].

We have made two assumptions in this quasi-static analysis: (1) modeling of the slots and dielectric interfaces by magnetic walls, and (2) the filling factor is not a function of the type of dielectric interface but depends only on the physical dimensions of the dielectric layers. The first assumption leads to exact results in the limiting cases when the substrate thickness approaches zero or infinity or when the substrate is replaced by air. For other cases this assumption has been verified in [24]. However, comprehensive comparisons with results from a rigorous fullwave analysis should be carried out to determine the accuracy of the above assumptions. Hybrid-mode analysis is described next, and the propagation characteristics of coplanar lines based on the conformal mapping method and the hybrid-mode approach are compared. Higher order modes are also described.

7.2.3 Fullwave Analysis

Coplanar Waveguide (CPW)

A rigorous fullwave analysis of CPW has been carried out using Galerkin's method in the spectral domain [2–12]. It differs from the fullwave analysis of a single slotline (Section 5.2) only in selection of the basis functions, which now correspond to the physical configuration (Figure 7.1(a)) and the field distribution of a CPW. The slot electric field in the present case may be written as

$$E_x(x) = \sum_x a_x E_{xn}(x) \tag{7.94a}$$

and

$$E_z(x) = \sum_m b_m E_{zm}(x) \tag{7.94b}$$

The basis functions $E_{xn}(x)$ and $E_{xm}(x)$ for a CPW may be obtained from a translation of the corresponding basis functions, (5.25) and (5.27), for the slotline. One obtains [15]

$$E_{xn}(x) = \begin{cases} \dfrac{T_{n-1}(x'/\xi)}{\sqrt{1-(x'/\xi)^2}} & n = 1,2,3\ldots \text{ for a} \le |x| \le b \\ 0 & \text{elsewhere} \end{cases} \tag{7.95a}$$

$$E_{xm}(x) = \begin{cases} U_m(x'/\xi) & n = 1,2,3\ldots \text{ for } a \le |x| \le b \\ 0 & \text{elsewhere} \end{cases} \tag{7.95b}$$

where, $\zeta = (b-a)/2$ and $x_0 = (a-b)/2$. $x' = x + x_0$ for the left slot and $x' = x - x_0$ for the right slot. The sine Fourier transform of $E_{xn}(x)$ and the cosine Fourier transform of $E_{xm}(x)$ are obtained as [3]

$$\tilde{E}_{xn}(\alpha) = \pi\zeta J_{n-1}(\zeta\alpha)\begin{cases} (-1)^{(n-1)/2}\sin(x_0\alpha) & \text{for } n \text{ odd} \\ (-1)^{(n/2)-1}\cos(x_0\alpha) & \text{for } n \text{ even} \end{cases} \tag{7.96a}$$

$$\tilde{E}_{zm}(\alpha) = m\pi\frac{J_m(\zeta\alpha)}{\alpha}\begin{cases} (-1)^{(m-1)/2}\cos(x_0\alpha) & \text{for } m \text{ odd} \\ (-1)^{m/2}\sin(x_0\alpha) & \text{for } m \text{ even} \end{cases} \tag{7.96b}$$

Another set of basis functions has been proposed by Fukuoka et al. [6]. This set is

$$E_{xn}(x) = \begin{cases} \dfrac{\cos\{n\pi x'/2\zeta\}}{\sqrt{\zeta^2 - x'^2}} & n = 0,2,4\ldots \text{for a} \le |x| \le b \\ \dfrac{\sin\{n\pi x'/2\zeta\}}{\sqrt{\zeta^2 - x'^2}} & n = 1,3,5\ldots \text{for a} \le |x| \le b \\ 0 & \text{elsewhere} \end{cases} \tag{7.97}$$

$$E_{zm}(x) = \begin{cases} \dfrac{\cos\{m\pi x'/2\xi\}}{\sqrt{\xi^2 - x'^2}} & m = 1,3,5\ldots \text{for a} \le |x| \le b \\ \dfrac{\sin\{m\pi x'/2\xi\}}{\sqrt{\xi^2 - x'^2}} & m = 2,4,6\ldots \text{for a} \le |x| \le b \\ 0 & \text{elsewhere} \end{cases} \tag{7.98}$$

The Fourier transforms of these basis functions are [6]

$$\tilde{E}_{xn}(\alpha) = \begin{cases} j\sqrt{\pi/2}\sin(\alpha x_0)\left[J_0(r_n) - J_0(s_n)\right] & n = 0,2,4\ldots \\ -j\sqrt{\pi/2}\cos(\alpha x_0)\left[J_0(r_n) - J_0(s_n)\right] & n = 1,3,5\ldots \end{cases} \tag{7.99a}$$

$$\tilde{E}_{zm}(\alpha) = \begin{cases} \sqrt{\pi/2}\cos(\alpha x_0)\left[J_0(r_m) + J_0(s_m)\right] & m = 1,3,5\ldots \\ \sqrt{\pi/2}\sin(\alpha x_0)\left[J_0(r_m) - J_0(s_m)\right] & m = 2,4,6\ldots \end{cases} \tag{7.99b}$$

where $J_0(\bullet)$ denotes the zeroth-order Bessel function of the first kind and

$$r_n = \left|\frac{2\xi a + n\pi}{2}\right| \quad \text{and} \quad s_n = \left|\frac{2\xi a - n\pi}{2}\right|$$

It may be noted that these sets of basis functions account for the edge effects of the slot field.

The characteristic impedance may be calculated using the voltage-current definition as

$$Z_{0\text{cp}} = \frac{V}{I} = \frac{\int_{s/2}^{s/2+w} E_x(x)\,dx}{2\int_0^{s/2} J_z(x)\,dx} \tag{7.100}$$

One could also use a power-voltage definition, which yields

$$Z_{0\text{cp}} = \frac{V^2}{2P_{\text{avg}}} \tag{7.101}$$

As in the case of the slotline, P_{avg} is calculated in the spectral domain from the equation

$$P_{\text{avg}} = \frac{1}{4\pi}\int_{-\infty}^{\infty}\int_{-\infty}^{\infty}\left\{\tilde{E}_x(\alpha,y)\tilde{H}_y^*(\alpha,y) - \tilde{E}_y(\alpha,y)\tilde{H}_x^*(\alpha,y)\right\}d\alpha\,dy \tag{7.102}$$

where α is the variable in the Fourier transform domain and the superscript denotes the transform of the field.

The details of the method are similar to those used for analyzing microstrip lines (Section 2.2.2) and slotlines (Section 5.2) and will not be discussed here. A comparison of fullwave results with the quasi-static values is shown in Figure 7.18

for the guide wavelength of a CPW with finite dielectric thickness [14]. The basis functions used are the Chebyshev polynomials of (7.95). A good agreement is observed. Fullwave analysis for other configurations of CPW have been reported in [8, 45, 46]. Higher order modes in a CPW have also been investigated by using the above method of analysis [3, 14]. In [14] the substrate used is sapphire, which is anisotropic in nature with $\varepsilon_{\perp} = 9.4$ and $\varepsilon_{11} = 11.6$. The results are presented in Figure 7.19 for $h = 1$ mm, $a = 0.25$ mm, and $b = 1.25$ mm. The normalized propagation constant for the dominant even and odd modes, first higher order mode, and TM_0 mode for a grounded sapphire substrate are plotted as functions of frequency. It is seen from the figure that the undesired odd mode can propagate down to dc. However, this mode can be suppressed by connecting both the ground plane conductors together by wires or air bridges. Dispersion characteristics of the first higher order mode of the CPW and the TM_0 mode for a grounded slab are found to be similar. The characteristic impedance calculated using the voltage-current definition of (7.100) compares favourably at low frequencies with those calculated using the quasi-static approximation [14].

Coplanar Strips (CPS)

Fullwave analysis using Galerkin's method in the spectral domain has also been conducted for coplanar strips. In this case, the problem is formulated in terms of surface currents J_x and J_z on the strips. These currents are expressed in terms of sets of basis functions as

$$J_x(x) = \sum_n a_n J_{xn}(x) \tag{7.103a}$$

and

$$J_z(x) = \sum_m b_m J_{zm}(x) \tag{7.103b}$$

A first-order solution, which is accurate enough for narrow strips, is obtained assuming that the transverse surface current J_x is negligible. However, for wide strips and for better accuracy both the components of current density should be considered. The basis functions $J_{xm}(x)$ are of the same form as $E_{xn}(x)$ for CPW. Similarly, $J_{xn}(x)$ are identical with $E_{zm}(x)$. These are given [7] as

$$J_{zm}(x) = \begin{cases} \pm \dfrac{\cos\{m\pi x'/2\xi\}}{\sqrt{\xi^2 - x'^2}} & m = 0,2,4\ldots \text{ for } a \le |x| \le b \\ \dfrac{\sin\{m\pi x'/2\xi\}}{\sqrt{\xi^2 - x'^2}} & m = 1,3,5\ldots \text{ for } a \le |x| \le b \\ 0 & \text{elsewhere} \end{cases} \tag{7.104a}$$

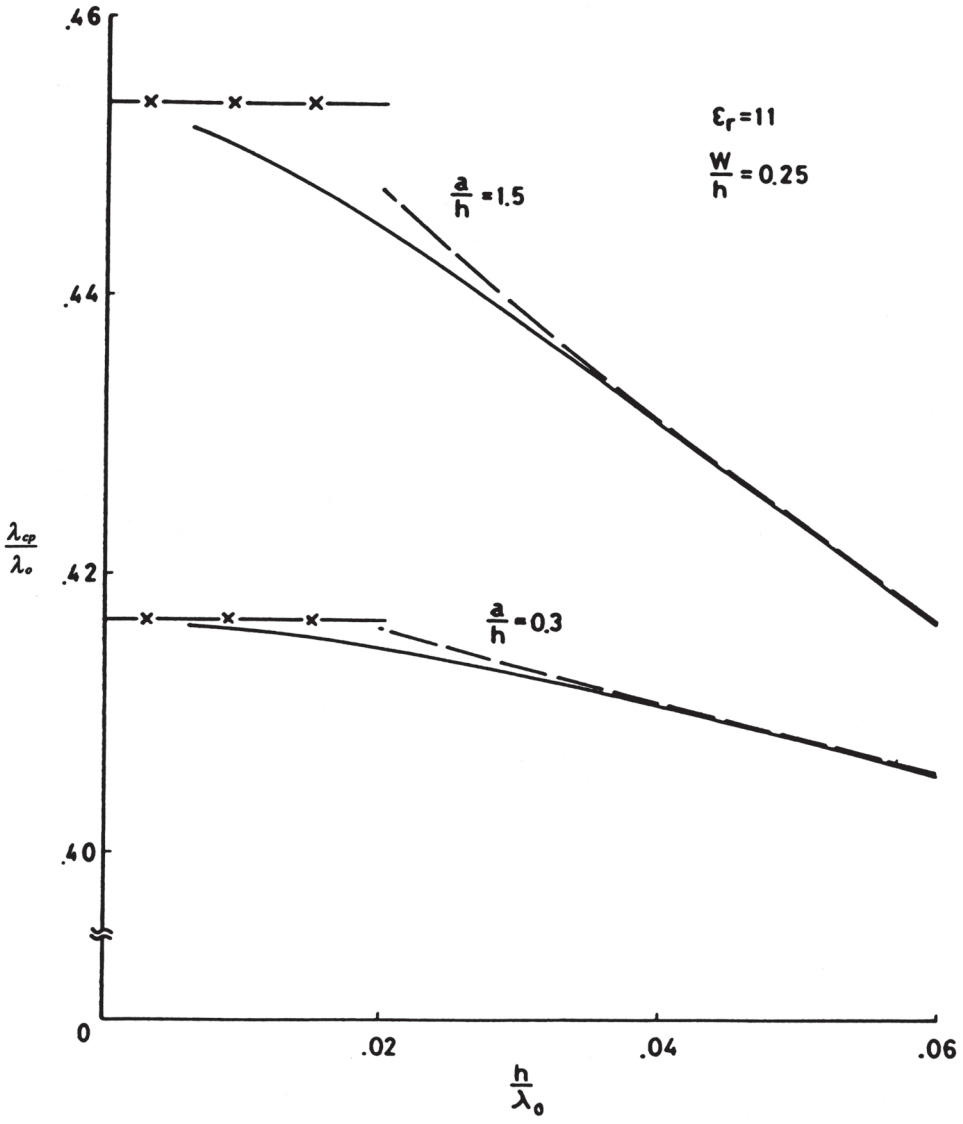

Figure 7.18 Comparison of fullwave and quasi-static results for CPW (from [14], © 1981 IEEE. Reprinted with permission.) (-X-X- quasi-static value,_fullwave value, ... from [2]).

$$J_{xn}(x) = \begin{cases} \dfrac{\cos\{n\pi x'/2\xi\}}{\sqrt{\xi^2 - x'^2}} & n = 1, 3, 4 \ldots \text{for } a \le |x| \le b \\ \dfrac{\pm\sin\{(n+2)\pi x'/2\xi\}}{\sqrt{\xi^2 - x'^2}} & n = 2, 4, 6 \ldots \text{for } a \le |x| \le b \\ 0 & \text{elsewhere} \end{cases} \tag{7.104b}$$

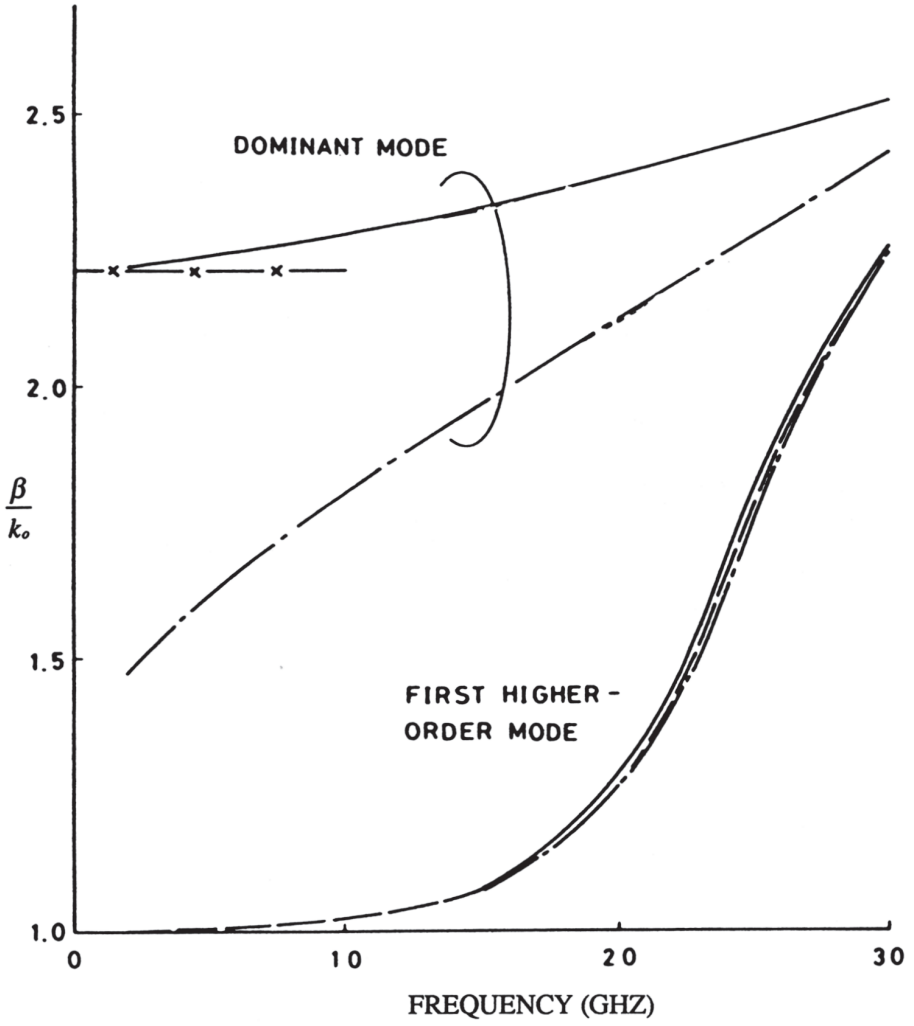

Figure 7.19 Dispersion curves for the dominant and first higher-order modes in CPW (from [14], © 1981 IEEE. Reprinted with permission.) (-X-X- quasi-static value, - even modes, - - - - - odd modes, - - - - - - TM_0 mode of a conductor-coated substrate).

The ± sign for the two different strips, for even values of n and m, accounts for proper symmetry of the current distribution. In (7.104), $x' = x + x_0$ for the left strip and $x' = x - x_0$ for the right strip. The normalized propagation constant for symmetric CPS is plotted as a function of frequency in Figure 7.20 [47] as the substrate chosen has $\varepsilon_r = 10.5$. It is observed that β/k_0 for the CPS mode increases very slowly with frequency. Therefore, over the bandwidth of components, $\varepsilon_{re} = (\beta/k_0)^2$ can be considered to be almost constant. Dispersion curves for the surface wave modes TM_0 and TM_1 are also shown in this figure. Break points in the dispersion curve for the CPS mode occur whenever β/k_0 for the mode becomes lower than that for the surface wave mode. These breaks are indications of strong coupling between the modes. Excitation of surface waves gives rise to an additional loss, as discussed later in Section 7.4.3.

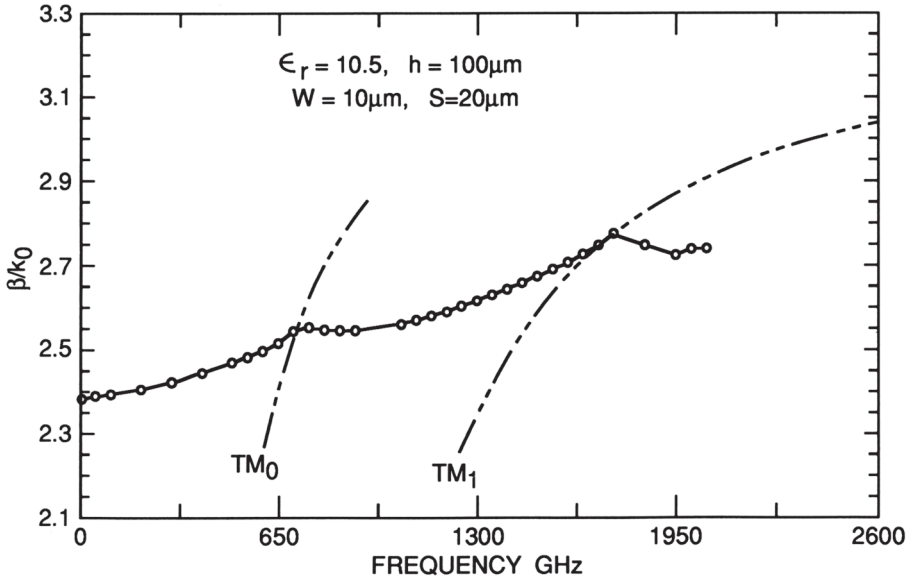

Figure 7.20 Dispersion curves for the dominant CPS mode and surface wave modes (from [47], © 1990 IEEE. Reprinted with permission.).

The basis functions for these slots/strips can be used for the various CPW/CPS geometries discussed in Section 7.2.1. For the asymmetric geometries x_0 should be modified to the corresponding midpoints of the slots/strips.

Study of the numerical data for ε_{re} and Z_0 as a function of frequency and aspect ratio *a/b* for various types of coplanar lines brings out a number of interesting facts about dispersion. These are summarized in Section 7.3.2.

7.3 Design Considerations

Analytical techniques for calculating the effective dielectric constant and characteristic impedance of coplanar lines were described in the last section. The effect of substrate thickness, finite width of the ground planes, conductor backing, cover height, and asymmetry were taken into account. Although the quasi-static values are good enough for some of the structures in the near millimeter region, fullwave analysis should be carried out for frequencies above 40 GHz. Similarly, the losses can be determined using the fullwave approach. But the computations are very time consuming and costly. An alternative to this approach is to use design equations that include the effect of dispersion in quasi-static values. The effect of metallization thickness on the characteristics of coplanar lines becomes important when the substrate ε_r is large and the aspect ratio *a/b* is small. Some of the coplanar line configurations become leaky due to the presence of parasitic modes. Coupling of power from the transmission line mode to the surface wave modes of the substrate may give rise to an increase in losses and unwanted coupling. The effect of dimensional tolerances becomes important when the fabrication limit for very narrow strips and slots is approached. All these aspects that influence the design of coplanar lines are discussed next. Finally, coplanar lines are compared with microstrip lines.

7.3.1 Design Equations

Closed-form expressions for the characteristic impedance and effective dielectric constant for various types of coplanar lines were obtained in the last section. They are simple enough to be calculated using scientific calculators. However, a design engineer requires the value of aspect ratio *a/b* for a desired value of Z_0 and substrate parameters ε_r and h. This type of expression is called the synthesis equation and is not available at present. For synthesis, search algorithms along with the analysis equations may be used. For the initial guess in the search algorithm one can use the value of *a/b* (for a given Z_0) applicable for the infinitely thick substrate. The synthesis expression for this geometry can be obtained very easily by inverting (7.11) as follows.

For $0 \le k_1 \le 0.707$, that is, $K'(k_1)/K(k_1) \ge 1$ or $Z_{0cp}\sqrt{(\varepsilon_r + 1)/2} \ge 30\pi$

$$\frac{a}{b}\left(= k_1\right) = \left[1 - \left(\frac{e^x - 2}{e^x + 2}\right)^4\right]^{1/2} \tag{7.105a}$$

For $0.707 \le k_1 \le 1$, that is, $K'(k_1)/K(k_1) \le 1$ or $Z_{0cp}\sqrt{(\varepsilon_r + 1)/2} \le 30\pi$

$$\frac{a}{b}\left(= k_1\right) = \left(\frac{e^{\pi^2/x} - 2}{e^{\pi^2/x} + 2}\right)^2 \tag{7.105b}$$

where

$$x = \frac{Z_{0cp}}{30}\sqrt{\frac{\varepsilon_r + 1}{2}} \tag{7.105c}$$

The synthesized value of *a/b* for the CPS can be obtained from (7.105) and the following relationship between Z_{0cp} and Z_{0cs} for an infinitely thick substrate (see (7.11) and (7.81)).

$$\frac{Z_{0cp}Z_{0cs}}{(60\pi)^2}\frac{\varepsilon_r + 1}{2} = 1 \tag{7.106}$$

To understand the use of (7.106) let us design a coplanar strip line for a given value of Z_0. The corresponding Z_{0cp} for the CPW obtained from (7.106) is

$$Z_{0cp} = \frac{2}{\varepsilon_r + 1}\frac{(60\pi)^2}{Z_0}$$

Now determine the value of *a/b* from (7.105) corresponding to the value of Z_{0cp} calculated above. The calculated value of *a/b* will yield the desired Z_{0cs}. Alternatively, one can invert (7.81) and obtain expressions similar to (7.105).

7.3.2 Dispersion

The synthesis procedure described above is based on quasi-static values for ε_{re} and Z_0. The resulting design is strictly applicable at the lower end of microwave band

but can be used up to the lower end of the millimeter-wave band, that is, when $h/\lambda_0 \ll 1$. However, at millimeter-wave frequencies or for frequency-selective components, even at lower frequencies the effect of dispersion on Z_0 and especially on ε_{re} should be included in the design. For this purpose, a simple expression, similar to (2.131) for the microstrip line, is available. This expression, obtained by curve fitting the results of numerical simulation, is [48]

$$\sqrt{\varepsilon_{re}(f)} = \sqrt{\varepsilon_{re}(0)} + \frac{\sqrt{\varepsilon_r} - \sqrt{\varepsilon_{re}(0)}}{1 + G(f/f_{TE})^{-1.8}} \tag{7.107}$$

where

$$G = e^{w\ell n(2a/(b-a))+v}$$
$$u = 0.54 - 0.64p + 0.015p^2$$
$$v = 0.43 - 0.86p + 0.54p^2$$
$$p = \ell n(2a/h)$$

In (7.107), $\varepsilon_{re}(0)$ is the quasi-static value of ε_{re} and f_{TE} is the cutoff frequency for the TE_0 surface wave mode for the substrate. Its value can be obtained from (5.10) and is given by

$$f_{TE} = \frac{c}{4h\sqrt{\varepsilon_r - 1}} \tag{7.108}$$

The accuracy of (7.107) is claimed to be 5 percent for the following range of parameters

$$0.1 < W/h < 5 \qquad 0.1 < S/W < 5$$
$$1.5 < \varepsilon_r < 50 \qquad 0 < f/f_{TE} < 10$$

It has been observed that $\varepsilon_{re}(0)$ in (7.107) should be replaced by $(\varepsilon_r + 1)/2$ so as to obtain a better match with experimental data for frequencies above 200 GHz [49].

As with microstrip lines, dispersion in coplanar lines modeled by (7.107) amounts to an increase in ε_{re} from the low-frequency value of $\varepsilon_{re}(0)$ to the asymptote of ε_r. Coplanar lines on thinner substrates are less dispersive due to the larger value of f_{TE}. Moreover, conductor-backed CPW and those with finite width ground planes are found to be less dispersive than others. An analytical expression for the effect of dispersion on Z_0 is not available. But, it is understood that the amount of dispersion in Z_0 is of the same order as for the microstrip line [45]. To a first-order approximation one can include the effect of dispersion on Z_0 through the dispersion in ε_{re}, that is,

$$Z_0(f) = \frac{Z_0^a}{\sqrt{\varepsilon_{re}(f)}}, \; Z_0^a = \frac{1}{cC^a} \tag{7.109}$$

where Z_0^a is the characteristic impedance with air as dielectric.

7.3.3 Effect of Metallization Thickness

The values of Z_0 and ε_{re} obtained earlier are valid for infinitesimally thin metallic strip conductor and ground planes. But in practice, the metallization has a finite thickness t that affects the characteristics. The effect of t on the characteristic impedance and the effective dielectric constant of a CPW has been analyzed in [15, 50–52] based on the quasi-static approximation [50] as well as frequency-dependent solution [15, 51, 52]. It has been observed that an increase in metallization thickness is accompanied by a corresponding decrease in ε_{re} and Z_0. The decrease in ε_{re} is larger for the case of a substrate with higher dielectric constant and lower aspect ratio. On the contrary, the decrease in Z_0 with increase in t is smaller for the higher dielectric constant substrate [15]. For example, for $\varepsilon_{re} = 20$ and $t/W = 0.1$, the decrease in ε_{re} is about 11 percent and the decrease in Z_0 is about 7 percent. For $\varepsilon_r = 2.6$ and for the same value of t/W, the decrease in ε_{re} is about 5 percent and the decrease in Z_0 is about 10 percent. The decrease in ε_{re} and Z_0 with increase in t can be explained from the observation that a higher metallization thickness gives rise to additional concentration of the electric field between the metalized portions of the slots, thus increasing the value of C^a. The increase in C^a is expected to be higher for narrow slots.

The effect of metallization thickness on the characteristics of coplanar lines can be included empirically by defining effective values of strip width and slot width. This is similar to the concept of effective strip width for microstrip line and is discussed in Section 2.4.5.

Metallization Thickness Effect in CPW Design

For a CPW with non-zero conductor thickness (Figure 7.1(a)), we may write

$$S_e^{CPW} = S + \Delta^{CPW} \tag{7.110a}$$

and therefore

$$W_e^{CPW} = W - \Delta^{CPW} \tag{7.110b}$$

where Δ^{CPW} accounts for the effect of metallization thickness. The expression for Δ^{CPW} may be arrived at by curve-fitting the results of conformal mapping analysis of CPW of Figure 7.1(a). For conductors with $t \neq 0$ [133]

$$\frac{\Delta^{CPW}}{t} = \frac{1}{\pi}\left(4.089 + \left\{0.9536 + 3.864 \times 10^{-3}\left[\frac{b}{t}\right]\right\}\ln\left[\frac{4\pi W}{t}\right]\right) \tag{7.111}$$

Based on (7.111), the accuracy of S_e^{CPW} is within 2 percent for $0.002 < t/b \leq 0.2$, $0.05 < W \leq 0.45$, and $0.1 < S \leq 0.9$ (all measured in the same units). On the other hand, the values of W_e^{CPW} matches within 2 percent for $0.002 < t \leq 0.03$, $0.1 \leq S \leq 0.9$, $0.05 \leq W \leq 0.45$ and within 10 percent for $0.03 < t \leq 0.2$, $0.1 < S < 0.8$, $0.1 < W < 0.45$.

Metallization Thickness Effect in CPS Design

For CPS with nonzero conductor thickness (Figure 7.2(a)), we may write

$$W_e^{CPS} = W + \Delta^{CPS} \tag{7.112a}$$

and therefore

$$S_e^{CPS} = S - \Delta^{CPS} \tag{7.112b}$$

The expression for Δ^{CPS} is arrived at by curve fitting the results of the conformal mapping analysis of the CPS of Figure 7.2(a). For conductors with $t \neq 0$ [33]

$$\frac{\Delta^{CPS}}{t} = \frac{1}{\pi}\left(5.188 + \left\{0.9959 + 8.0808 \times 10^{-4}\left[\frac{b}{t}\right]\right\}\ln\left[\frac{4\pi W}{t}\right]\right) \tag{7.113}$$

The values of W_e^{CPS} and S_e^{CPS} obtained using (7.113) were compared with the numerically computed results based on conformal mapping analysis. The accuracy was found to be within 2% for $0.002 < t/b \leq 0.2$, and the following combinations of S and W:

$$0.1 \leq S \leq 0.9,\ 0.05 \leq W \leq 0.45 \text{ and } 0.3 < S < 0.8,\ 0.05 < W < 0.35.$$

CPS Line Capacitance with Nonzero Conductor Thickness

For the design of coplanar lines, we may divide the coplanar line geometry into the upper-half and lower-half regions about the air-dielectric interface. Here, the effect of metal thickness on line capacitance has been assigned to the upper-half region capacitance to simplify the analysis and design. Let C_1 be the line capacitance per unit length for the upper-half region, and C_2 the line capacitance per unit length for the lower-half region.

Capacitance of the upper-half region of coplanar lines: The expression for C_1, which now includes the capacitance associated with strip conductor also is obtained by replacing S and W by the corresponding S_e and W_e, respectively. Specifically, (7.8b) for symmetric CPW now becomes

$$C_1^{CPW} = 2\varepsilon_0 \frac{K(k_{1e})}{K'(k_{1e})}, \qquad k_{1e} = \frac{S_e^{CPW}}{S_e^{CPW} + 2W_e^{CPW}} \tag{7.114}$$

where k_{1e} is the effective value of k_1 due to nonzero conductor thickness. Similarly, (7.78) for symmetric CPS modifies to

$$C_1^{CPS} = \frac{\varepsilon_0}{2}\frac{K'(k_{1e})}{K(k_{1e})}, \qquad k_{1e} = \frac{S_e^{CPS}}{S_e^{CPS} + 2W_e^{CPS}} \tag{7.115}$$

Gap capacitance model for C_1^{CPS} for very thick strips: A simple approach to model C_1^{CPS} is to determine incremental capacitance associated with strip thickness t as [136]

$$\Delta C(t/S) = \varepsilon_0 \frac{t}{S} + f(t/S) \tag{7.116}$$

where $\varepsilon_0 t/S$ is the parallel plate capacitance per unit length between the side walls of coplanar strips. The correction factor $f(t/S)$ is plotted in [127, Figure 4] as a function of t/S. Combining (7.115) and (7.116), one may write

$$C_1^{cps}(t) = C_1^{cps}(t=0) + \varepsilon_0 t/S + q_1 + q_2 \tag{7.117}$$

The first term represents zero thickness capacitance and is given by (7.78). The terms q_1 and q_2 are obtained by curve-fitting and are given by [133]

$$q_1 = \begin{cases} 0.01\varepsilon_0\left(55t/S + 0.065\right) & \text{for } 0.001 \le t/S < 0.017 \\ 0.01\varepsilon_0\left(\ln(t/S) + 5\right) & \text{for } 0.017 \le t/S \le 0.37 \\ 0.0402\varepsilon_0 & \text{for } t/S > 0.37 \end{cases} \tag{7.118}$$

$$q_2 = \varepsilon_0(0.53t/b + 0.048) \tag{7.119}$$

The accuracy of (7.117) using the above approximations is of the order of 5% for $0.02 < t/b < 1.5$ and $t/S < 3.75$.

Capacitance of the lower-half region of coplanar lines: The effect of conductor thickness on the line capacitance has been accounted for through the change in C_1 alone, and the value of capacitance C_2 for the lower-half region therefore remains unaffected by conductor thickness. The expression (7.8a) for symmetric CPW and (7.79) for symmetric CPS may therefore be used to determine C_2.

Effective dielectric constant and Z_0 of coplanar lines with nonzero conductor thickness: By definition, the effective dielectric constant of a line in TEM mode is given by

$$\varepsilon_{re} = \frac{C_1(t) + C_2(\varepsilon_r)}{C_1(t) + C_2(\varepsilon_r = 1)} \tag{7.120}$$

where $C_1(t)$ is the line capacitance for the upper-half region with nonzero conductor thickness, and $C_2(\varepsilon_r)$ is the capacitance for the lower-half region of coplanar line with the given dielectric configuration. The dielectric cover on the line is not considered.

The characteristic impedance for the TEM mode line is simply related to the effective dielectric constant ε_{re} and characteristic impedance in air Z_{0a} as

$$Z_0(\varepsilon_r) = \frac{Z_{0a}}{\sqrt{\varepsilon_{re}}} \tag{7.121a}$$

where Z_{0a} is defined as

$$Z_{0a}^{CPW} = 30\pi \frac{K'(k_{1e})}{K(k_{1e})}, \qquad Z_{0a}^{CPS} = 120\pi \frac{K(k_{1e})}{K'(k_{1e})} \tag{7.121b}$$

The effect of metal thickness on the characteristics of symmetric coplanar lines can be determined from the design of these lines presented above. The variation

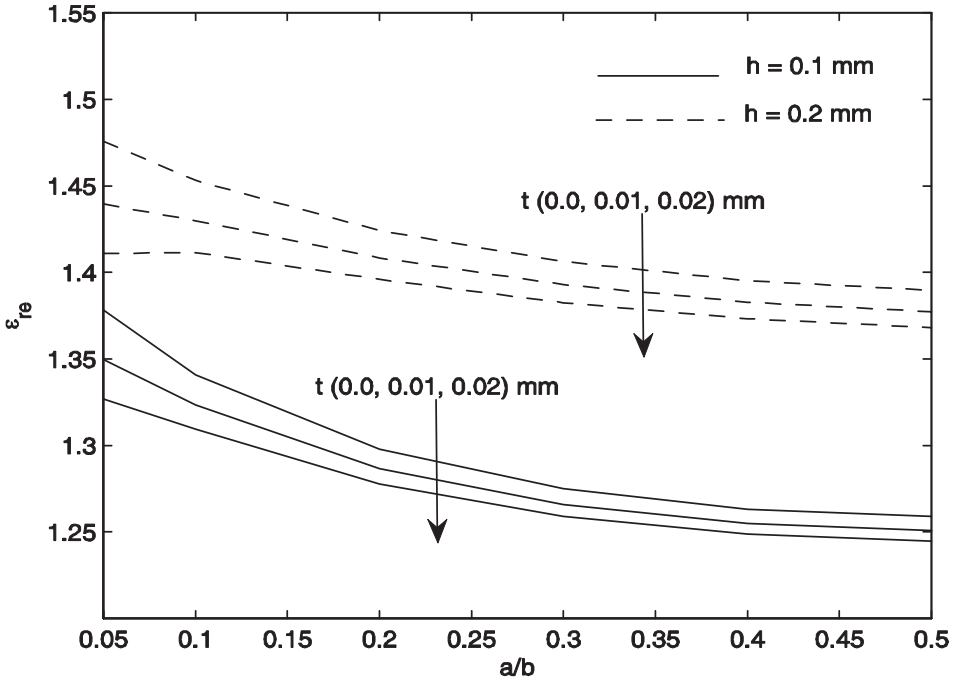

Figure 7.21 Variation of ε_{re} of CPS with aspect ratio a/b and strip thickness t as parameter, ε_r = 2.2. [133].

of ε_{re} for CPS with metal thickness t as parameter is plotted in Figure 7.21 for ε_r = 2.2. It is observed that ε_{re} decreases with increase in thickness t and a/b. This can be explained from (7.120) and the fact that $C_1(t)$ increases with t, and $C_2(\varepsilon_r = 1) < C_2(\varepsilon_r)$. The corresponding percentage change in Z_0^{CPS} with substrate thickness, a/b, and t/b as parameters is plotted in Figure 7.22 for ε_r = 2.2. The impedance of the line decreases with increase in conductor thickness t. The low impedance lines (lower a/b values) are affected more by conductor thickness. Also, the decrease in impedance is almost linearly proportional to t/b.

7.4 Losses in Coplanar Lines

7.4.1 Dielectric Loss

Coplanar lines have three types of losses: dielectric, ohmic, and radiation/surface wave losses. The expression for the attenuation constant due to dielectric loss in CPW is the same as that for a microstrip line. This was discussed in Chapter 2, and is reproduced here

$$\alpha_d = 27.3 \frac{\varepsilon_r}{\sqrt{\varepsilon_{re}}} \frac{\varepsilon_{re} - 1}{\varepsilon_r - 1} \frac{\tan\delta}{\lambda_0} \qquad \text{dB/unit length} \tag{7.122}$$

In this expression, ε_{re} represents the relative effective dielectric constant of the coplanar line.

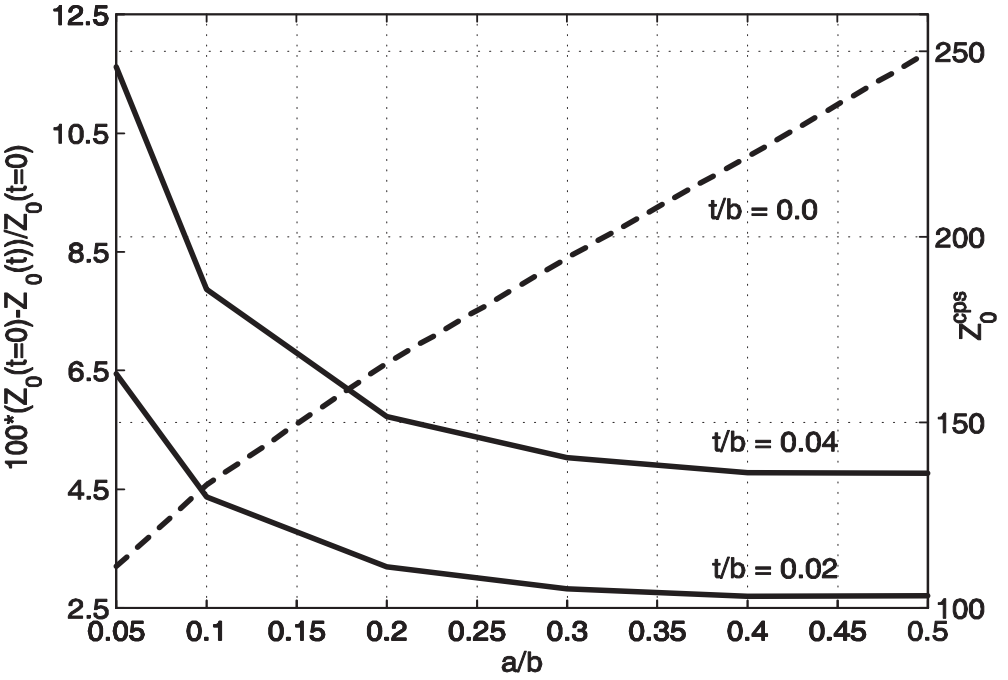

Figure 7.22 Variation of percentage change in Z_0 of CPS with aspect ratio *a/b* and strip thickness *t* as parameter, $\varepsilon_r = 2.2$, $h = 0.2$ mm. (From [133].)

7.4.2 Conductor Loss

A number of different techniques have been reported to determine conductor loss in coplanar lines. These range from techniques such as Wheeler's incremental inductance rule, to calculation of power dissipation in line through conformal mapping of current density in the conductor thickness [54]. These techniques are limited to skin effect frequencies range. For applications to digital signals on coplanar lines, the frequency range of conductor loss has been extended to low frequencies by proper modeling of current density distribution in the strip conductors [55, 137].

Conductor loss calculation based on incremental inductance rule: Following the procedure discussed in Section 2.4.1, one obtains the following expression for the attenuation constant due to ohmic losses for a coplanar line:

$$\alpha_c^{cw} = 0.023 \frac{R_s}{Z_0}\left(\frac{\partial Z_0^a}{\partial W} - \frac{\partial Z_0^a}{\partial S} - \frac{\partial Z_0^a}{\partial t}\right) \quad \text{dB/unit length} \tag{7.123}$$

where Z_0^a is the characteristic impedance of coplanar line with air as dielectric and R_s is the surface resistivity of the conductors.

In the above approach, the value of the attenuation constant is very much dependent on the accuracy of the derivatives of characteristic impedance. The curve fitted expressions for Z_0^a such as (7.121) may be accurate enough for the computation of line impedance but their analytical derivatives may be very approximate for the calculation of conductor loss. Yamashita et al. have proposed numerical evaluation of derivatives to obviate this problem [53]. In this approach, the change in

the inductance per unit length of the line due to recession of all the metal surfaces by half a skin depth δ is evaluated in terms of the change of the line capacitance C^a with air as dielectric. If C_δ^a is the new line capacitance obtained by recessing all the metal surfaces by $\delta/2$, then [53]

$$\sum_m \frac{\partial L}{\partial n_m}\frac{\delta}{2} = \frac{1}{v_p^2}\left(\frac{1}{C^a} - \frac{1}{C_\delta^a}\right) \tag{7.124}$$

where v_p is the phase velocity in the line. Substituting the above expression in (2.76) one obtains for the conductor attenuation as

$$\alpha_c = \frac{\pi}{\lambda_0}\sqrt{\varepsilon_{re}}\left(\frac{C^a - C_\delta^a}{C_\delta^a}\right) \qquad \text{neper/unit length} \tag{7.125}$$

One advantage of the above approach is that one does not need to obtain analytical expressions for the derivatives of Z_0^a. Instead, the technique used to determine C^a can be employed to determine C_δ^a and also to obtain the numerical derivative of C^a implied in (7.124). Moreover, the factor $C^a - C_\delta^a$ in (7.125) cancels the inaccuracies C^a in and C_δ^a that are inherent in the formulation and numerical computations.

Owyang and Wu [54] have used a direct approach to determine the effect of metal thickness on conductor loss. They have evaluated the power dissipated in the line through conformal mapping of the current density in the finite metal thickness structure. Their expression for conductor loss of a CPW has been corrected by Ghione [36] and is given as

$$\alpha_c^{cw} = \frac{8.68R_s\sqrt{\varepsilon_{re}}}{480\pi K(k_1)K'(k_1)(1-k_1^2)} \left\{\frac{1}{b}\left[\pi + \ell n\left(\frac{8\pi b(1-k_1)}{t(1+k_1)}\right)\right] + \frac{1}{b}\left[\pi + \ell n\left(\frac{8\pi b}{t}\frac{1-k_1}{1+k_1}\right)\right]\right\} \quad \text{dB/unit length} \tag{7.126}$$

It is assumed in deriving the above expression that the strip thickness $t > 3\delta$ and $t \ll a$ and $(b - a)$. Equation (7.126) is valid for symmetric CPW configurations with finite and infinite dielectric thickness and for multilayered structures. These effects are manifested in (7.126) through ε_{re}. Due to the complementary nature of a CPW and CPS, (7.126) is applicable for the conductor loss of symmetric CPS also with the appropriate meanings for a, b, and ε_{re}.

Series expansions for $K(k)$, needed for the evaluation of (7.126), are available. These are given as follows [31].

For $0 \le k \le 0.707$

$$K(k) = \frac{\pi}{2}\left\{1 + 2\frac{k^2}{8} + 9\left(\frac{k^2}{8}\right)^2 + 50\left(\frac{k^2}{8}\right)^3 + 306.25\left(\frac{k^2}{8}\right)^4 + \ldots\right\} \tag{7.127a}$$

and, for $0.707 \le k \le 1$

$$K(k) = p + (p-1)(k'^2/4) + 9(p - 7/6)(k'^4/64) + 25(p - 37/30)(k'^6/256) + \ldots \tag{7.127b}$$

where

$$p = \ell n\left(4/k'\right) \tag{7.128}$$

The maximum error in the series of (7.127a) and (7.127b) occurs at the crossover point $k = 0.707$ and is about 0.3 percent. For $k \to 0$ or $k \to 1$ the error also approaches zero.

In many applications such as in processors, printed lines are used as interconnects to carry pulsed signals between two devices. The pulse spectrum includes a broad range of frequencies, from very low to very high frequencies. However, the attenuation constant expression (7.126) is limited to skin effect frequencies ($t > 3\delta$). Holloway and Kuester have obtained a semi-closed form expression for attenuation that extends to low frequencies as well [137]. The attenuation constant is derived from the change in propagation constant of the transmission line with and without lossy conductors as

$$\alpha = \mathrm{Re}(\gamma - \gamma_0) \tag{7.129}$$

where γ is the propagation constant with lossy conductors. It is assumed in (7.129) that losses are small and do not affect the phase constant significantly. In this analysis, the finite thickness strip conductor is modeled by longitudinal current flow on infinitely thin top and bottom surfaces of conductors and the attenuation constant is derived as

$$\alpha = \mathrm{Re}(\gamma - \gamma_0) = -\frac{1}{2Z_0 I^2}\mathrm{Re}\left[\int_{top} \bar{E}^{top}.\bar{J}^{top}\, dl + \int_{bottom} \bar{E}^{bottom}.\bar{J}^{bottom}\, dl\right] \tag{7.130}$$

where I is the central strip current and Z_0 is the characteristic impedance of CPW. The edge condition for longitudinal current on infinitely thin surfaces introduces singularity in the integrals, while the actual current density on real conductors is not singular. This argument is used to avoid singularity and the integration is stopped a distance Δ before the edge. To prevent the associated error in integration, the distance Δ (called the stopping distance) is defined such that the thin surface model provides correct value of α . The current distribution on the CPW is assumed as [137]

$$J = \frac{A}{\sqrt{\left(a^2 - x^2\right)\left(b^2 - x^2\right)}} \qquad |x| < a \text{ (on the central strip)} \tag{7.131a}$$

and

$$J = -\frac{A}{\sqrt{\left(x^2 - a^2\right)\left(x^2 - b^2\right)}}, \qquad |x| > b \text{ (on the ground planes)} \tag{7.131b}$$

where

$$A = \frac{bI}{2K(k_1)} \tag{7.132}$$

The tangential electric fields on the strip surfaces $\bar{\mathrm{E}}^{top}$ and $\bar{\mathrm{E}}^{bottom}$ can be expressed in terms of surface current J and surface impedance [137]. Substituting for the as-

sumed current distribution in (7.130) and carrying out the integrations gives the following final expression for the attenuation constant of CPW [137]

$$\alpha_c^{cpw} \cong \frac{8.68R_{sm}b^2}{16Z_0K^2(k_1)\left(b^2-a^2\right)}\left\{\frac{1}{a}\ln\left[\left(\frac{2a}{\Delta}-1\right)\left(\frac{b-a+\Delta}{b+a+\Delta}\right)\right]+\frac{1}{b}\ln\left[\left(\frac{2b}{\Delta}-1\right)\left(\frac{b-a+\Delta}{b+a-\Delta}\right)\right]\right\} \quad \text{dB/unit length} \qquad (7.133)$$

where

$$R_{sm} = \omega\mu_0 t\,\mathrm{Im}\left(\frac{\cot(k_c t)+\cos ec(k_c t)}{k_c t}\right), \quad k_c = \omega\sqrt{\mu_0(\varepsilon_0 - j\sigma/\omega)}, \quad k_1 = a/b \qquad (7.134)$$

The stopping distance Δ is found to be function of conductor thickness t/δ and the edge shape; its value for an isolated strip is obtained numerically and tabulated in [137] for 90° and 45° edge shapes. For the 90° edge,

$$9.18 \le t/\Delta \le 327 \qquad \text{for } 0.03 \le t/(2\delta) \le 5 \qquad (7.135)$$

The stopping distance Δ is very small compared to a, b and $a - b$, and (7.133) may be approximated as

$$\alpha_c^{cpw} \cong \frac{8.68R_{sm}b^2}{16Z_0K^2(k_1)\left(b^2-a^2\right)}\left\{\frac{1}{a}\ln\left[\left(\frac{2a}{\Delta}\right)\left(\frac{b-a}{b+a}\right)\right]+\frac{1}{b}\ln\left[\left(\frac{2b}{\Delta}\right)\left(\frac{b-a}{b+a}\right)\right]\right\} \quad \text{dB/unit length} \qquad (7.136)$$

This expression reduces to (7.126) in the skin effect limit at which $\Delta = t/(4\pi\exp(\pi))$. The computed values of α are compared with measurements over a broad frequency range in Figure 7.23 for $t = 1.61$ μm, $a = 35.6$ μm, $b = 84.6$ μm, $\varepsilon_r = 12.9$, $\sigma = 3.602\text{e}7$. It is found that the comparison is good for frequencies between 3 and 20 GHz. However, the computed values are found to be higher for $f \le 3$ GHz. At 3GHz, the skin depth is approximately equal to the conductor thickness and the skin effect approximation for line impedance $Z_0 \approx \sqrt{L/C}$ fails. At these and lower frequencies, the characteristic impedance of the line should be calculated from $Z_0 = \sqrt{(R + j\omega L)/j\omega C}$. The increase in the value of Z_0 at these frequencies brings down the value of α. The impedance corrected expression for α is given by [137]

$$\alpha_c^{cpw} \cong \mathrm{Re}\left[\frac{F}{Z_0}\frac{2}{1+\sqrt{1+\dfrac{4F}{Z_0\gamma_{m0}}}}\right] \quad \text{dB/unit length} \qquad (7.137)$$

where

$$F = \frac{8.68(Z_s+Z_m)b^2}{16K^2(k_1)\left(b^2-a^2\right)}\left\{\frac{1}{a}\ln\left[\left(\frac{2a}{\Delta}\right)\left(\frac{b-a}{b+a}\right)\right]+\frac{1}{b}\ln\left[\left(\frac{2b}{\Delta}\right)\left(\frac{b-a}{b+a}\right)\right]\right\} \qquad (7.138a)$$

$$Z_s = -j\cot(k_c t)\sqrt{\frac{\mu_0}{\varepsilon_0 - j\sigma/\omega}}, \quad Z_m = -j\cos ec(k_c t)\sqrt{\frac{\mu_0}{\varepsilon_0 - j\sigma/\omega}}, \quad \gamma_{m0} = jk_0\sqrt{\varepsilon_{re}} \qquad (7.138b)$$

and $Z_0 = \sqrt{L/C}$ is the skin effect characteristic impedance of CPW. The above expression for attenuation constant is found to be valid so long as the assumptions for stopping distance Δ for an isolated strip are satisfied. The isolated strip assumption fails if either the strip is very narrow or the ground plane is very close to the strip [137].

Figure 7.24 shows the comparison of attenuation constant (7.137) as a function of strip width for $t = 3$ μm, $b = 150$ μm, $f = 60$ GHz, $\varepsilon_r = 12.8$, $\sigma = 5.882e7$. The numerical results are based on a MoM solution by Kitazawa and Itoh [58]. The agreement is seen to be fairly good. So, the conductor loss calculations based on conformal mapping method may be used in the millimeter-wave frequency range so long as the assumptions stated there are satisfied; that is, $t > 3\delta$ and $t \ll 2a, t \ll b_2, b_2$. It is observed from Figure 7.24 that conductor loss is minimum near 2a = 0.1 mm ($Z_2 = 50\ \Omega$) and is higher for low-impedance and high-impedance lines. This behavior can be explained from the higher conductor loss in narrow strips and slots. Since the same line impedance can be achieved using different values of b, loss considerations dictate choosing a larger value of b.

Conductor loss calculations for coplanar lines based on conformal mapping and surface impedance model for conductors has been reported by Tuncer et al. [55]. The model used by them correctly predicts the skin effect and proximity effect in conductors of transmission lines, and therefore conductor attenuation over a broad frequency range. However, their results are not available in closed form.

Conductor Loss in Asymmetric Coplanar Lines

Based on the approach described by Owyang and Wu for symmetric coplanar lines [54], an expression for the conductor loss of asymmetric coplanar lines has been reported in [36], and is given next:

$$\alpha_c = \frac{8.68 R_S \sqrt{\varepsilon_{re}}}{480\pi K(k_8) K(k_8')} \left[\Phi(b_1 - a, k_8) + \Phi(b_2 - a, k_8) + \Phi(2a, k_8') - \Phi(b_1 + b_2, k_8') \right] \quad \text{dB/unit length} \tag{7.139}$$

where

$$\Phi(p,k) = \frac{1}{p}\left\{ \ln\left(\frac{4\pi p k}{t}\right) + \pi \right\}, \text{ t: strip thickness} \tag{7.140}$$

and k_8 is defined in (7.62).

Like the symmetric case, (7.139) is also valid for strip thickness much greater than the skin depth, and much less than the strip width and both the slot widths. It may be pointed out that due to the complementary nature of an ACPW and ACPS, (7.139) holds for the conductor loss of ACPS also with the appropriate meanings for a, b_1, b_2 and ε_{re}.

Conductor Loss in Asymmetric Coplanar Lines with One Lateral Ground Plane

The geometry of this line is shown in Figure 7.15(c). Conductor loss for this line may be obtained as the limiting case of an ACPW when $b_1 \to \infty$ and $b_2 = b$ [36]. The attenuation constant (7.139) becomes

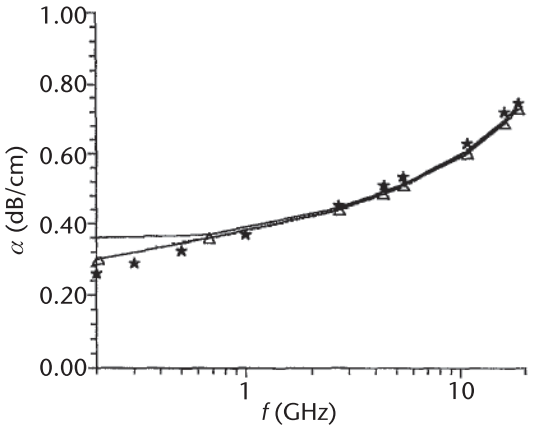

Figure 7.23 Comparison of computed conductor loss with experimental values for a CPW line with $t = 1.61$ μm, $a = 35.6$ μm, $b = 84.6$ μm, $\varepsilon_r = 12.9$, $\sigma = 3.603e07$ ____ (7.133), Δ --- Δ (7.137), *** Measurements. (from [137], © 1995 IEEE. Reprinted with permission.)

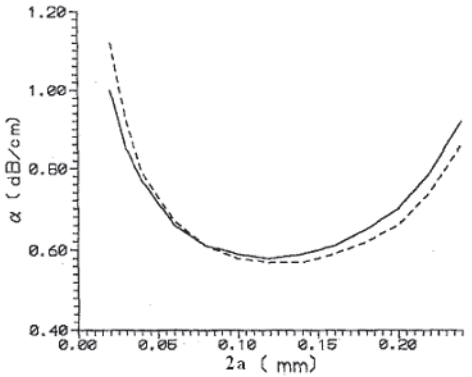

Figure 7.24 Variation of quasi-static and full-wave values of conductor loss in CPW as a function of central strip width $2a$ for symmetric CPW, $t = 3$ μm, $b = 150$ μm, $h = 100$ μm, $\varepsilon_r = 12.8$, $\sigma = 5.882e07$ freq = 60 GHz, ----- quasi-static (7.137), ____full-wave [58]. (from [137], © 1995 IEEE. Reprinted with permission.)

$$\alpha_c = \frac{8.68 R_S \sqrt{\varepsilon_{re}}}{480\pi K(k)K(k')}\left[\Phi\left(b-a,k\right)+\Phi\left(2a,k'\right)\right] \qquad \text{d/B/unit length} \tag{7.141}$$

where $\phi(\bullet)$ is defined by (7.140) and

$$k = \sqrt{2a/(a+b)}, \qquad k' = \sqrt{(b-a)/(b+a)} \tag{7.142}$$

The expressions (7.126) to (7.141) for the conductor loss are based on conformal mapping of the current density in finite thickness conductors. Accuracy for conductor loss in symmetric CPW has been checked against the more accurate full-wave computations [4, 57, 58]. Surface impedance model of conductors is employed in [57]. The perturbation method in spectral-domain is employed in [4,58].

7.4.3 Radiation and Surface Wave Losses

In addition to the dielectric and ohmic losses, coupling of power to surface waves and radiation from unwanted (parasitic) modes contribute to the total loss of the coplanar lines. The parasitic mode in a coplanar waveguide is the odd mode with antiphase voltages in the two slots. This mode can be excited at the discontinuities, and radiation may occur. Radiation from this mode can be minimized by maintaining symmetry of the circuits and thus avoiding its excitation or by using air bridges at regular intervals to short it out [4]. In a conductor-backed coplanar waveguide the parallel plate waveguide mode is another parasitic mode. Surface waves or the substrate modes can give rise to radiation [7]. Some of these losses are important at microwave frequencies, while others become significant in the mm-wave frequency region only.

To understand the physical process involved in radiation through the parasitic modes, let us consider a conductor-backed CPW that has been analyzed exhaustively using different techniques [45, 57, 59–63]. It is found that the leakage in this transmission line occurs when the dominant transmission line mode of the CPW travels faster than the parasitic parallel plate mode, which is TEM in nature [59]. In a conductor-backed CPW, this condition is always satisfied independent of frequency and the dimensions of the structure. Therefore, this type of CPW is said to be unconditionally leaky [57]. This phenomenon is identical to that in a conductor-backed slotline, as discussed in Section 5.5.2. Again, as in a slotline, leakage in a CPW can be controlled by introducing an additional layer of dielectric either as a superstrate, that is, on top of the CPW metallization or between the metallization plane and the substrate. The dielectric constant and the dielectric thickness of this layer are chosen in such a manner that the dominant CPW mode becomes slower than the parasitic LSM_0 mode. Liu and Itoh [62] have analyzed this structure using the fullwave approach. The normalized phase and the attenuation constant for the structure are shown in Figure 7.25 as a function of the thickness of the additional layer. As shown in this figure, β/k_0 for the CPW mode is smaller than that of the parasitic mode, and the structure is leaky for small thickness h_2. The value of β/k_0 increases as layer thickness h_2 is increased and reaches the value for the LSM_0 mode at $h_2 = 0.027$ mm. This thickness is called the critical thickness. As h_2 is increased beyond this value, the CPW mode becomes slower than the parasitic mode. There are corresponding changes in the leakage constant denoted by α/k_0. At the start, $h_2 = 0$ and the structure is leaky with $\alpha/k_0 = 0.003$. As h_2 increases, α/k_0 decreases quickly and goes down abruptly to zero at the critical thickness. Similar behavior for α/k_0 and β/k_0 is observed when the additional layer is used as a superstrate [59].

There are two modes of propagation in a CPW with infinitely thick substrate: (1) CPW guided mode with $\beta/k_0 = \sqrt{(\varepsilon_r + 1)/2}$ and (2) the TEM wave of the substrate with $\beta_s/k_0 = \sqrt{\varepsilon_r}$. In this case $\beta < \beta_s$, therefore the guided mode becomes unconditionally leaky and radiates into the substrate with $v_{ph} = c/\sqrt{\varepsilon_r}$. For constructive interference, the phase velocities of the guided wave and the radiated wave should be the same along the direction of propagation. This is called phase synchronism or phase match condition [63] and leads to the following condition on the direction θ of maximum radiation:

$$\cos\theta = \frac{\beta}{\beta_s} = \sqrt{\frac{\varepsilon_r + 1}{2\varepsilon_r}} \tag{7.143}$$

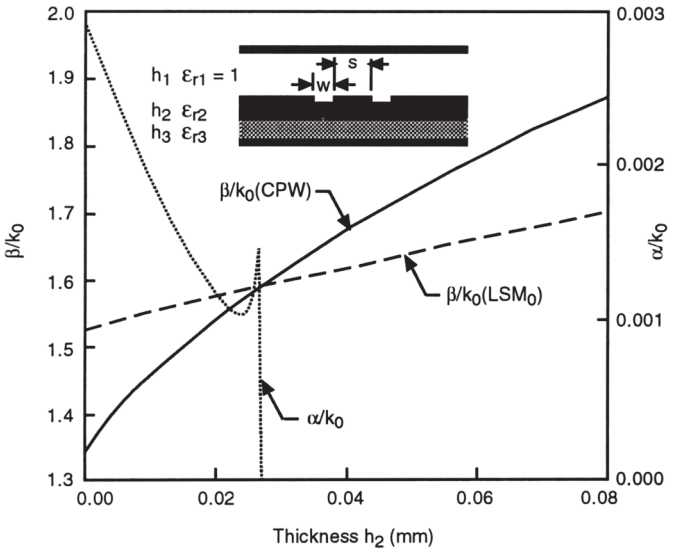

Figure 7.25 Normalized phase and attenuation for different thickness h_2 ($\varepsilon_{r2} = 10.5$, $\varepsilon_{r3} = 2.33$, W = 0.254 mm, S = 0.254 mm, $h_3 = 0.635$ mm, h_1 =15 mm, and f= 10 GHz) (from [62], © 1995 IEEE. Reprinted with permission.).

Energy transfer from the guided wave into the substrate causes attenuation of the guided wave.

Effect of Finite Thickness Substrate

Coplanar lines with finite thickness substrate can also be leaky. Although the mechanism of radiation is similar to the infinite thickness case, the substrate modes are different. It is the surface wave modes of the substrate/slab that are responsible for leakage. Surface waves of the structure are the guided modes of a conductor-backed slab of thickness h. These modes are the same as the odd TE modes and even TM modes of a dielectric slab with thickness $2h$ and no metallization. Dispersion curves for TM modes are plotted in Figures 7.19 and 7.20 along with other modes of CPW and CPS, respectively. These modes are encountered in a microstrip line also. Excitation of substrate modes depends on the polarizations and symmetries of the transmission line mode and the substrate mode. For example, it has been proved analytically that a CPS with narrow strips can lose energy to TM-type substrate modes only because the transverse current on the strips is very weak to excite the TE-type modes [7]. When wider strips are used in the analysis, both TE- and TM-type modes can be excited. Coupling to the substrate modes is expected to be stronger when the substrate thickness is comparable to the wavelength in dielectric λ_d.

The amount of loss due to leakage from coplanar lines on infinitely thick substrates has been calculated using reciprocity [64, 65] as well as the fullwave approach [7, 63, 66, 67]. The reciprocity approach leads to simple expressions for

the attenuation constant. Phatak et al. [7] have modified the expressions for a CPS to fit the numerical results of the fullwave approach. These expressions are given as

$$\alpha_{\text{rad}}^{\text{cps}} = (3-\sqrt{8})\frac{\pi^2}{4}\sqrt{\frac{\varepsilon_{\text{re}}(f)}{\varepsilon_{\text{r}}}}\frac{\sin^4\theta}{K(k_1)K'(k_1)}\frac{W^2}{\lambda_{\text{d}}^3} \qquad \text{neper/unit length, } \lambda_{\text{d}} = \frac{\lambda_0}{\sqrt{\varepsilon_{\text{r}}}} \tag{7.144}$$

where θ, the angle at which maximum radiation occurs, is measured from the direction of propagation, and is defined as

$$\cos\theta = \beta/\beta_{\text{s}} \tag{7.145}$$

where β is the propagation constant for the CPS mode and β_{s} is the propagation constant for the surface mode.

The radiation loss for a coplanar waveguide has also been expressed in a simple form [65, 68]. This expression has been modified by Frankel et al. [49] to fit the experimental data for the attenuation constant of a picosecond pulse. The modified expression is given by [49]

$$\alpha_{\text{rad}}^{\text{cpw}} = \left(\frac{\pi}{2}\right)^5 2\frac{(1-\varepsilon_{\text{re}}(f)/\varepsilon_{\text{r}})^2}{\sqrt{\varepsilon_{\text{re}}(f)/\varepsilon_{\text{r}}}}\frac{(S+2W)^2}{K(k)K'(k)}\frac{1}{\lambda_{\text{d}}^3} \qquad \text{neper/unit length} \tag{7.146}$$

Expressions for the surface mode attenuation constant for a CPW and a CPS on finitely thick substrate are given as [7, 65]

$$\alpha_{\text{SW}}^{\text{TE}} = \frac{\pi^4}{2\sqrt{2}}\frac{\sqrt{1+1/\varepsilon_{\text{r}}}}{K(k)K'(k)h_{\text{e}}}\left(\frac{W}{\lambda_{\text{d}}}\right)^2 \sin^3\theta\sin\theta_{\text{d}}\cos^2\phi_{\text{TE}} \qquad \text{neper/ unit length} \tag{7.147}$$

$$\alpha_{\text{sw}}^{\text{TM}} = \frac{\pi^4}{2\sqrt{2}}\frac{\sqrt{1+1/\varepsilon_{\text{r}}}}{K(k)K'(k)h_{\text{e}}}\left(\frac{W}{\lambda_{\text{d}}}\right)^2 \sin\theta\cos^2\theta\sin\theta_{\text{d}}\cos^2\theta_{\text{d}}\sin^2\phi_{\text{TM}} \qquad \text{neper/ unit length} \tag{7.148}$$

where θ_{d} is the angle of incidence of the ray on the dielectric interface (see Figure 7.26), and is given by [64]

$$\cos\theta_{\text{d}} = \frac{k_{\text{y}}}{k_0\sqrt{\varepsilon_{\text{r}}}} \tag{7.149}$$

Φ_{TE} and Φ_{M} are the phase shifts for TE and TM plane waves, respectively, due to total internal reflection at the dielectric-air interface, and the effective dielectric thickness h_e is defined as [64]

$$h_{\text{e}} = h + 2\Delta \tag{7.150}$$

Δ is the apparent ray penetration in the air region on total internal reflection as shown in Figure 7.26. Leakage from CPW with finite-sized ground planes, with

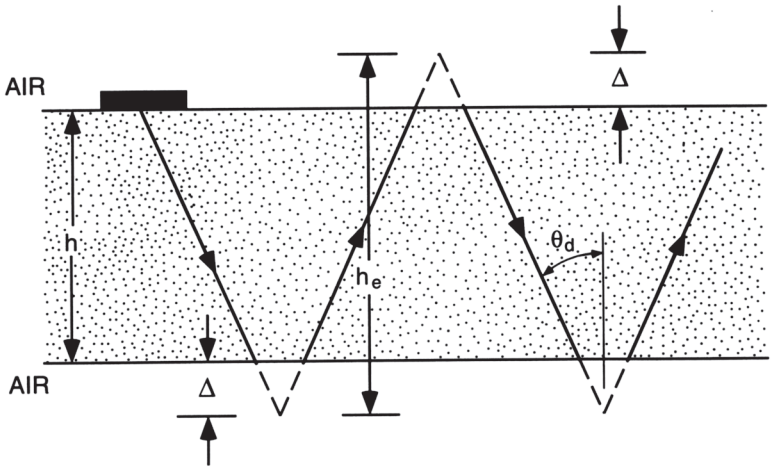

Figure 7.26 Definition of effective thickness, $h_e = h + d\Delta$ (from [64], © 1993 IEEE. Reprinted with permission.).

and without backside metallization, has been studied [63, 66]. Sharp peaks in attenuation are found to occur at the onset of leakage.

Leakage of power not only gives rise to increased attenuation but can also result in cross talk with neighboring portions of the circuit. Power leakage can be avoided if a thin substrate is used so that the cutoff frequency of the surface modes is pushed above the operating frequency. For this, the substrate thickness h should be chosen such that $h\sqrt{\varepsilon_r} < 0.12\ \lambda_0$ [63].

7.5 Effect of Tolerances

The sensitivity analysis described earlier for microstrip line and slotline can also be applied to coplanar lines to evaluate the effect of tolerances. The maximum change in the values of characteristic impedance and effective dielectric constant may be written as

$$\frac{\left|(\Delta Z_0)\right|_{\max}}{Z_0} = \left|\frac{\Delta W}{W} S_W^{Z_0}\right| + \left|\frac{\Delta S}{S} S_S^{Z_0}\right| + \left|\frac{\Delta h}{h} S_h^{Z_0}\right| + \left|\frac{\Delta \varepsilon_r}{\varepsilon_r} S_{\varepsilon_r}^{Z_0}\right| + \left|\frac{\Delta t}{t} S_t^{Z_0}\right| \tag{7.151}$$

$$\frac{\left|(\Delta \varepsilon_{re})\right|_{\max}}{\varepsilon_{re}} = \left|\frac{\Delta W}{W} S_W^{\varepsilon_{re}}\right| + \left|\frac{\Delta S}{S} S_S^{\varepsilon_{re}}\right| + \left|\frac{\Delta h}{h} S_h^{\varepsilon_{re}}\right| + \left|\frac{\Delta \varepsilon_r}{\varepsilon_r} S_{\varepsilon_r}^{\varepsilon_{re}}\right| + \left|\frac{\Delta t}{t} S_t^{\varepsilon_{re}}\right| \tag{7.152}$$

The sensitivity of Z_0 with respect to a parameter y may be evaluated from the sensitivities of Z_0^a and ε_{re} using the relation

$$S_y^{Z_0} = S_y^{Z_0^a} - S_y^{\varepsilon_{re}}/2 \tag{7.153}$$

where Z_0^a ($= Z_0\sqrt{\varepsilon_{re}}$) is the characteristic impedance of a coplanar line with air as dielectric.

Expressions for sensitivities of the characteristics of CPW with respect to various parameters (W, S, h, ε_r, and t) can be calculated using the closed-form expressions for Z_{0cp}^a and ε_{re} derived earlier and the definition of sensitivity given by (2.99). The effect of strip thickness ($t/W \leq 0.005$) on CPW characteristics is very small and therefore has not been included here. Sensitivity expressions for the symmetric coplanar lines with finite dielectric thickness h are given next. Sensitivities for other geometries may be derived in a similar manner.

$$S_W^{Z_{0cp}^a} = -S_S^{Z_{0cp}^a} = \frac{60P}{Z_{0cp}^a}\frac{W}{S}k_1^2 \tag{7.154}$$

where $k_1 = S/(S + 2W)$ and P is defined as

$$P = \begin{cases} \dfrac{k_1}{\left(1-\sqrt{1-k_1^2}\right)\left(1-k_1^2\right)^{3/4}} & \text{for } 0 \leq k_1 \leq 0.707 \\ \dfrac{1}{(1-k_1)\sqrt{k_1}}\left(\dfrac{K'(k_1)}{K(k_1)}\right)^2 & \text{for } 0.707 \leq k_1 \leq 1 \end{cases} \tag{7.155}$$

Sensitivities of Z_{0cp}^a with respect to h and ε_r are zero because characteristics of CPW with air as dielectric do not depend on h and ε_r. Sensitivities of ε_{r_c} with respect to various parameters for $0 \leq k_1 \leq 0.707$ and $0 \leq k_2 \leq 0.707$ are as follows:

$$S_{\varepsilon_r}^{\varepsilon_{re}} = \frac{\varepsilon_r}{\varepsilon_r - 1}\frac{\varepsilon_{re} - 1}{\varepsilon_{re}} \tag{7.156}$$

$$S_S^{\varepsilon_{re}} = \frac{\varepsilon_r - 1}{2\varepsilon_r}\frac{K(k_2)}{K'(k_2)}\left\{\frac{S}{2h}\frac{\varepsilon_{re} - 1}{\varepsilon_{r_c} - 1}\frac{1}{1-k_2'}\frac{k_2}{\sqrt[3]{k_2'}}\frac{\sinh(\pi W/2h)}{\sinh^2\left(\pi(S+2W)/4h\right)} - \frac{2}{\pi}\frac{1}{1-k_1'}\left(\frac{k_1}{k_1'}\right)^3\frac{W}{S}\right\} \tag{7.157}$$

$$S_W^{\varepsilon_{re}} = \frac{W}{2h}\frac{\varepsilon_r - 1}{\varepsilon_{re}}\frac{K(k_2)}{K'(k_2)}\left\{\frac{2}{\pi}\frac{h}{S+2W}\frac{1+k_1'}{\sqrt[3]{k_1'}} - \frac{\varepsilon_{re} - 1}{\varepsilon_r - 1}\frac{1}{1-k_2'}\frac{k_2^2}{\sqrt[3]{k_2'}}\frac{\cosh\left(\pi(S+2W)/4h\right)}{\sinh\left(\pi(S+2W)/4h\right)}\right\} \tag{7.158}$$

$$S_h^{\varepsilon_{re}} = -S_W^{\varepsilon_{re}} - S_S^{\varepsilon_{re}} \tag{7.159}$$

The sensitivities of characteristic impedance and effective dielectric constant of a coplanar waveguide with respect to various parameters are plotted in Figures 7.27 and 7.28. It may be noted from Figure 7.27 that sensitivities of Z_{0cp}, with respect to W and h increase when h/b is decreased. A similar observation can be made for sensitivities of ε_{re} with respect to h, S, and W. Thus the effect of fabrication tolerances is small when thick substrates are used. When $h/b = 0.5$, ε_{re} is very much sensitive to variations in h. For $h/b \geq 3$, the sensitivities of ε_{re} and therefore of Z_{0cp}, with respect to ε_r are independent of the h/b ratio and also the aspect ratio. The values of these two sensitivities are 0.927 and –0.463, respectively, for $\varepsilon_r = 13$.

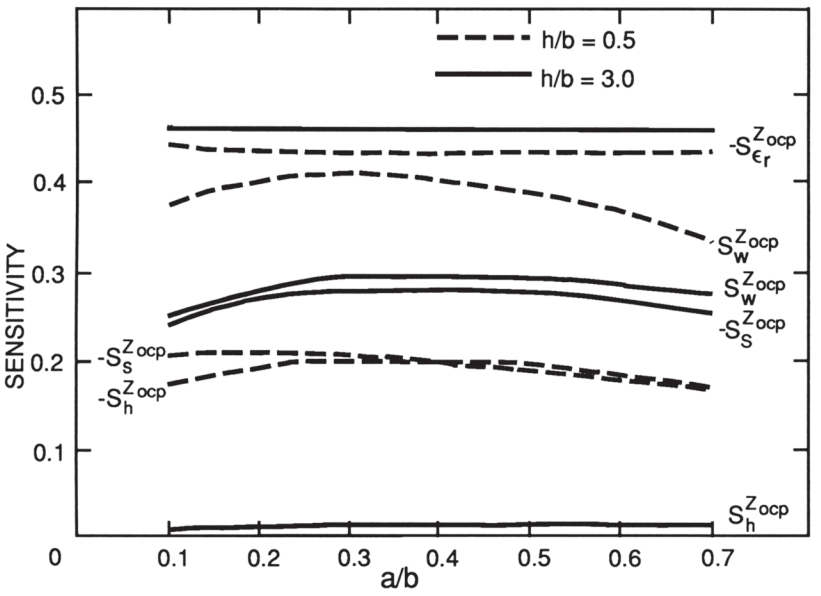

Figure 7.27 Sensitivities of characteristic impedance of CPW with respect to various parameters ($\varepsilon_r = 13.0$).

For coplanar strips, the sensitivities of impedance with air as dielectric (Z_{0cs}^{a}) with respect to parameters S and W are

$$S_W^{Z_{0cs}^{a}} = -S_S^{Z_{0cs}^{a}} = -\frac{120k_1(1-k_1)P'}{Z_{0cs}^{a}} \tag{7.160}$$

where

$$P' = P\left(\frac{K(k_1)}{K'(k_1)}\right)^2 \tag{7.161}$$

As for the CPW, the sensitivities with respect to h and ε_r are zero in this case also. The expression for $S_{\varepsilon_r}^{\varepsilon_{re}}$ is the same as that for a CPW; see (7.156). The rest of the sensitivity expressions for a CPS for $\leq k_1 \leq 0.707$ and $0 \leq k_2 \leq 0.707$ are

$$S_W^{\varepsilon_{re}} = \frac{W}{4h}\frac{\varepsilon_r - 1}{\varepsilon_{re}}\frac{K(k_1)}{K'(k_1)}\left\{\frac{1+k_2'}{\sqrt[3]{k_2'}}\coth\left(\frac{\pi(S+2W)}{4h}\right) - \frac{\varepsilon_{re}-1}{\varepsilon_r - 1}\frac{8h}{\pi(S+2W)}\frac{1+k_1'}{\sqrt[3]{k_1'}}\right\} \tag{7.162}$$

$$S_S^{\varepsilon_{re}} = \frac{S}{8h}\frac{\varepsilon_r - 1}{\varepsilon_{re}}\frac{K(k_1)}{K'(k_1)}\left\{\frac{\varepsilon_{re}-1}{\varepsilon_r - 1}\frac{8h}{\pi(S+2W)}\frac{k_1(1-k_1)}{\sqrt[3]{k_1'}(1-k_1')} - \frac{k_2}{1-k_2'}\frac{1}{\sqrt[3]{k_2'}}\frac{\sinh(\pi W/2h)}{\sinh^2(\pi(S+2W)/4h)}\right\} \tag{7.163}$$

and

$$S_h^{\varepsilon_{re}} = -S_W^{\varepsilon_{re}} - S_S^{\varepsilon_{re}} \tag{7.164}$$

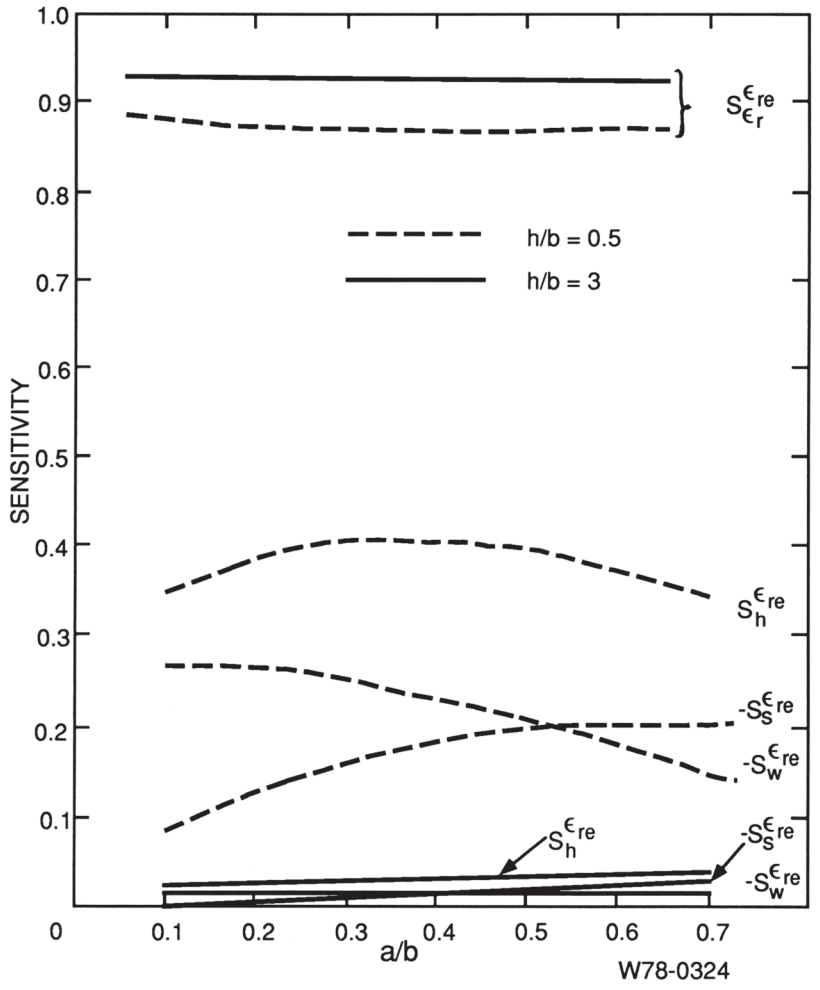

Figure 7.28 Sensitivities of effective dielectric constant of CPW with respect to various parameters ($\varepsilon_r = 13.0$).

7.6 Comparison with Microstrip Line and Slotline

Four types of planar transmission lines suitable for microwave integrated circuits have been discussed so far: (1) microstrip line, (2) slotline, (3) coplanar waveguide, and (4) coplanar strips. In this section we compare the characteristics of these lines. Various features considered include the range of impedance achievable, losses, and effect of tolerances. The microstrip line has been compared with a coplanar waveguide in [4, 26].

Range of Impedance

The range of characteristic impedance that can be practically realized with any particular transmission line is limited by two factors. Technological processes such

as photo etching limit the minimum strip width and the spacing between two adjacent scrips. For comparison, this minimum dimension has been taken as 5 μm (although smaller dimensions are possible with careful processing). The other limitation comes from the possibility of excitation of higher order modes. To avoid the excitation of higher order modes, the substrate thickness and the lateral dimensions should be kept below a quarter wavelength. The impedance limits calculated in this manner are shown in Table 7.1 for three types of lines. In this table the letter "m" in parentheses indicates that the limit is caused by higher order modes and the letter "d" indicates that the limit is due to small dimensions. This comparison indicates that microstrip lines are capable of providing low impedance whereas slotlines and coplanar waveguides may be used for very high impedances.

Losses

Losses or attenuation constant is another important characteristic for the comparison of these lines. Conductor loss in planar lines has been computed and compared by Heinrich in [69, 70]. The value of conductor loss for the microstrip, slotline, and CPW is compared in Figures 7.29 and 7.30 as a function of characteristic impedance. A comparison of the conductor loss in a microstrip line and a CPW (see Figure 9.29) shows that for lower impedance lines the microstrip has lower loss whereas for high impedances a CPW can be designed to have lower loss. For medium impedance lines, the conductor loss in a microstrip and a CPW are substantially similar. The conductor loss for a slotline and a CPW is plotted in Figure 7.30 This comparison shows that high-impedance lines are less lossy if realized in slotline configuration and that a CPW configuration with wider strips should be chosen for low impedance levels. Fabrication constraints are also less stringent if, wider slots and strips are used.

Effect of Tolerances

As discussed earlier, impedance variations caused by tolerances are expressed in terms of the maximum value of VSWR presented to an ideal line connected at the input. The effects of tolerances on the impedance and effective dielectric constant for the three types of lines are compared in Table 7.2. For this comparison, the fabrication accuracy of strip width and gap width has been assumed to be 1 μm. The assumed tolerances in h and ε_r are 5 μm and 0.1, respectively. The table shows that slotline impedance is less sensitive to variations in parameters as compared to other lines.

Table 7.1 Comparison of Z_0 Limits ($\varepsilon_r = 13$, $h = 100$ μm, and frequency = 30 GHz)

Transmission line	*Lower Limit for Z_0 (ohm)*	*Upper Limit for Z_0 (ohm)*
Microstrip	11 (m)	110 (d)
Slotline	35 (d)	250 (m)
Coplanar waveguide	20 (m, d)	250 (m, d)
Coplanar strips	20 (m, d)	250 (m, d)

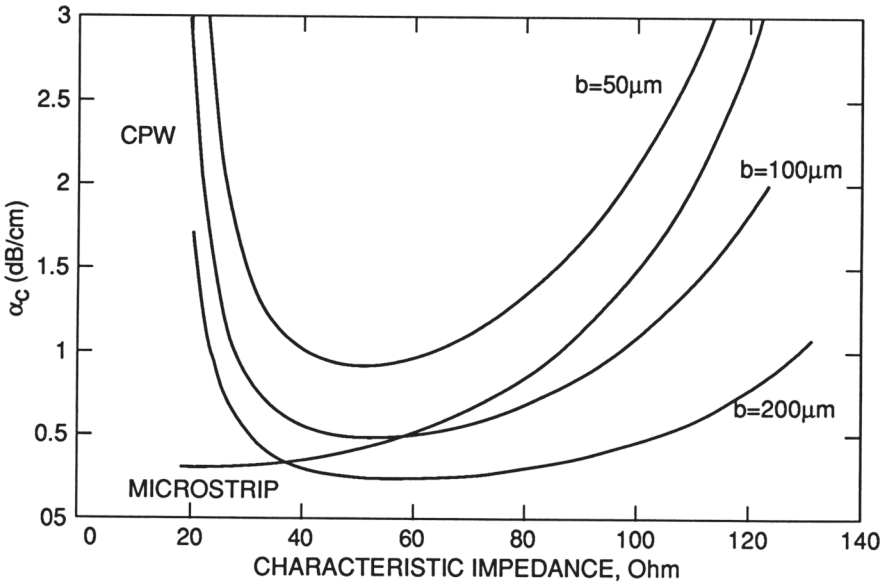

Figure 7.29 Comparison of conductor loss for microstrip and CPW on 100 μm GaAs substrate ($\varepsilon_r = 13$) at $f = 20$ GHz as a function of line impedance. A 3 μm-thick copper metallization is assumed [26].

Other parameters

Several other parameters of the four types of lines are compared qualitatively in Table 7.3. It can generally be seen that CPW and CPS combine some advantageous features of microstrip lines and slotlines. Perhaps the best feature of the coplanar lines is the ease of mounting components in series and shunt configurations, whereas microstrip lines are convenient only for series mounting and slotlines can accommodate only shunt-mounted components. A coplanar waveguide has the advantage of easier fabrication, no via holes, and good grounding for active devices. It suffers from the disadvantages of larger size, parasitic odd mode, and poor heat transfer for active devices [4].

7.7 Transitions

Integration of coplanar lines with other transmission lines requires a suitable transition. Further, transitions between coplanar lines and slotline transform an unbalanced (CPW) mode into a balanced (slotline) mode and is especially useful in balanced circuits such as balanced mixers and modulators. Transitions from CPW to coax, microstrip line, slotline, and CPS, as well as from CPS to slotline, are discussed in this section.

7.7.1 Coax-to-CPW Transitions [71]

This transition is one of the simplest and most frequently used CPW transitions. It is used for testing CPW circuits. Depending upon the sealing requirement, one

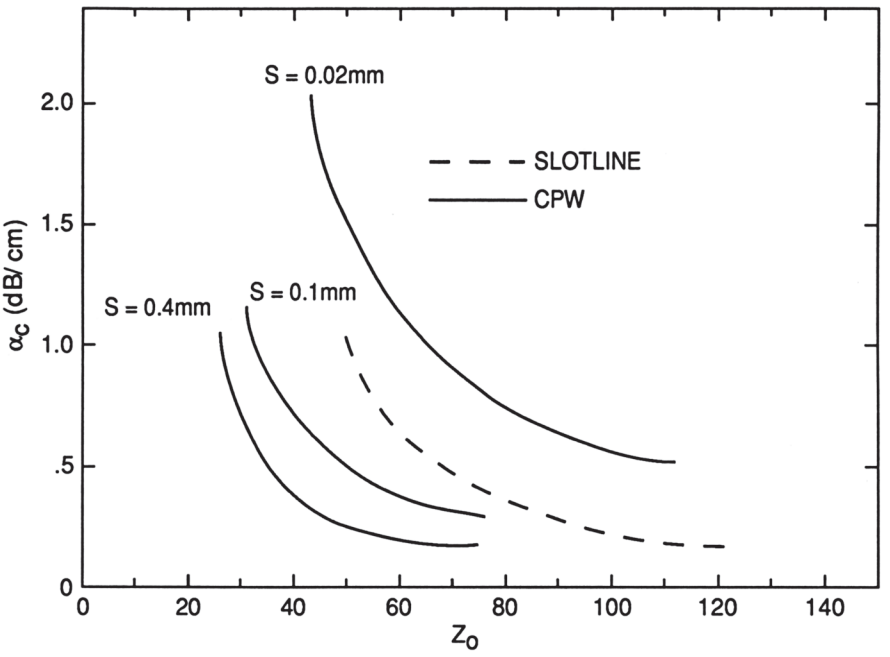

Figure 7.30 Comparison of conductor loss for slotline and CPW on l00 μm GaAs substrate (ε_r = 12.8) at f = 20 GHz as a function of line impedance. A 3-μm-thick conductor with ρ = 1.7 $\mu\Omega$cm is assumed (from [58], © 1991 IEEE. Reprinted with permission.).

Table 7.2 Comparison of the Effect of Tolerances on Various Lines (ε_{re} = 13 ± 0.1, h = 100 ± 5 μm, $\Delta W = \Delta S$ = 1 μm, and Z_0 = 50 Ω)

Transmission Line	*Max. VSWR*	*Max.* $\lvert\Delta \varepsilon_{re} / \varepsilon_{re}\rvert$
Microstrip (W/h = 0.731)	1.033	0.013
Slotline (W/h = 0.1, h/λ_0 = 0.01)	1.015	0.0036
Coplanar waveguide (h/b = 8, a/b = 0.4)	1.07	0.044

of the two transitions shown in Figure 7.31 is used. The transition (a) is useful for the nonhermetic case, while transition (b) is made with a hermetic seal connector. In both the transitions, the pin of the coax connector rests on the strip part of the CPW and the ground planes of the CPW and coax connector make electrical contact with each other. The strip width of the CPW is changed slightly at the beginning to optimize the reflection coefficient of the transition. Houdart and Aury obtained a VSWR less than 1.35 for frequencies below 18 GHz for two transitions connected back-to-back [71].

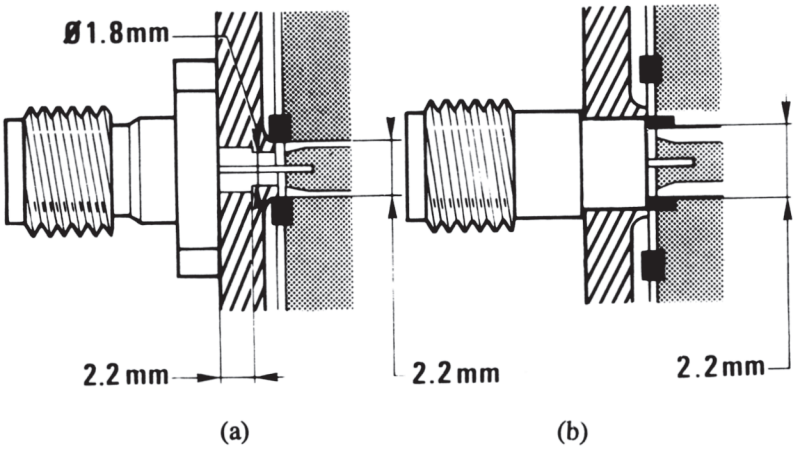

Figure 7.31 Coax-to-CPW transitions: (a) for non-hermetic sealing and (b) hermetic sealing (from [71], © 1979 IEEE. Reprinted with permission.).

Table 7.3 Qualitative Comparison of Various MIC lines

Characteristic	*Microstrips*	*Slotline*	*Coplanar Waveguide*	*Coplanar Strips*
Effective dielectric constant ($\varepsilon_r = 13$ and $h = 100$ μm)	≈ 8.6	≈ 5.07	≈ 7	≈ 7
Power handling capability	High	Medium	Medium	Medium
Radiation loss	Low	Medium	Medium	Medium
Unloaded Q	Medium	Low	Medium	Low (lower impedances)
				High (higher impedances)
Dispersion	Small	Large	Small	Small
Mounting of components:				
in shunt config.	Difficult	Easy	Easy	Easy
in series config.	Easy	Difficult	Easy	Easy
Technological difficulties	Ceramic holes Edge plating	—	—	—
Elliptically polarized magnetic field config.	Not available	Available	Available	Available
Enclosure dimensions	Small	Large	Large	Large

7.7.2 Microstrip-to-CPS Transitions

The transition from microstrip line to coplanar strips (CPS) transforms unbalanced mode of microstrip line to balanced mode of CPS. A standard microstrip-to-CPS transition consists of a 50 ohm microstrip line and a 50 ohm CPS line. However, the impedances of microstrip line and CPS may vary for a specific application. Therefore, the transition design should be applicable to different impedance combinations, and substrate parameters. The polarization of field between the strip and ground plane of microstrip line is vertical whereas it is horizontal across the strips

in CPS. Therefore, the design of microstrip-to-CPS transition involves rotation of fields. A large number of approaches are reported for this transition. We describe next a very broadband transition which includes impedance transformation.

The metallization pattern of the transition is shown in Figure 7.32(a)[138]. As shown there, the metallization can be divided into three distinct portions; microstrip line, transition, and CPS line. The metallization pattern in the transition region is very important for rotating the polarization and impedance transformation from 50-ohm microstrip line to Z_0 of CPS line. This is shown separately as Figure 7.32(b). In the transition region, the microstrip line is converted into coupled microstrip line by adding another strip parallel to it. Vias are added to this strip at periodic intervals. One of the ports of coupled microstrip line is open-circuited. The width of the ground plane underneath the coupled microstrip line is reduced gradually so that the ground plane width equals the strip width at the last via. The CPS line starts after the last via. The coupled microstrip line can support two different modes, even mode and odd mode. The odd-mode field configuration is similar to that in CPS line. The uneven feeding of coupled line and via in one of the strips destroys even symmetry of the geometry and therefore suppresses the even mode. The absence of ground plane after the plane CC' does not permit any vertical component of electric field. The electric field at various sections along the transition region is shown in Figure 7.33.

Transition Design

The line impedance at any position in the transition can be controlled either by the spacings between the strips or by the ground plane width. In this design, the ground plane is optimally tapered to enhance broadband impedance matching; a Klopfenstein taper provides optimum solution between bandwidth and taper length. The characteristic impedance of the line at various positions of the transition may be determined by modeling the geometry as conductor backed asymmetric CPS or by using EM simulation [138]. This helps in the design of transition for any substrate and impedance transformation ratio. A 50 ohm microstrip to 129 ohm CPS transition was designed as per the above guidelines [138]. The insertion loss of the transition was found to be less than 1 dB per transition and return loss was more than 10 dB over 5.39 to 40 GHz. The low frequency end of the transition can be extended by increasing the length of the taper [138]. The simulation studies for this transition show about a 100-GHz bandwidth for 3-dB insertion loss. A microstrip-to-CPS transition without the via but similar to that in Figure 7.32 has been reported [139]. Its insertion loss in X-band is about 1.1 dB.

An ultra wideband (3.1–10.6 GHz) microstrip-to-CPS transition is reported [140]. This transition is completely planar and does not involve via. The transition region is quarter-wave long coupled microstrip line section with partially removed ground plane. Another microstrip-to-CPS transition without via consists of an impedance transformer from microstrip line impedance to CPS line impedance, and a quarter-wave coupled microstrip section with open end for field rotation. The 1-dB insertion loss band covers 1.4–6.6GHz [141].

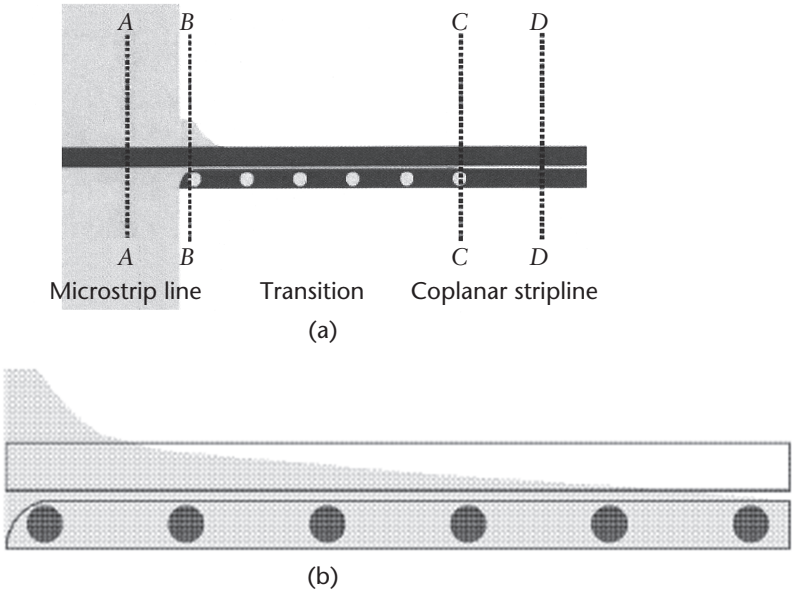

Figure 7.32 (a) Metalization pattern for microstrip line to CPS transition. The gray shade is the ground plane metalization, the dark strips are in the top plane, and the white dots are the vias. (b) Metalization pattern in the transition region of (a). The gray shade is the ground plane metallization, the rectangular strips are in the top plane, and the black dots are the vias. (from [138], © 2007 IEEE. Reprinted with permission).

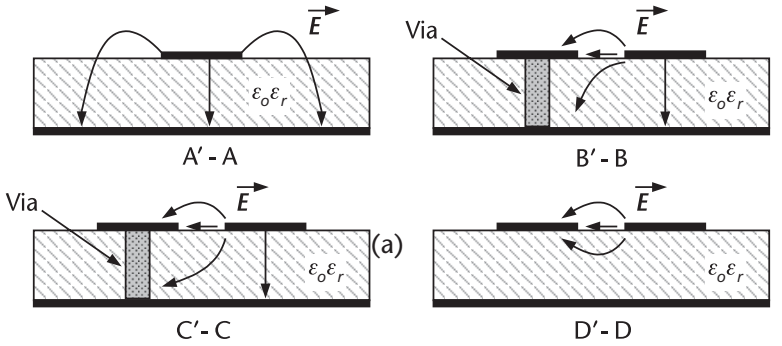

Figure 7.33 Electric field lines at various sections of transition region (from [138], © 2007 IEEE. Reprinted with permission).

7.7.3 Microstrip-to-CPW Transition [142]

The design concepts of microstrip-to-CPS transition of [138] have been extended to microstrip-to-CPW transition. The metallization pattern of this transition is shown in Figure 7.34. Since the CPW line has three strips and the geometry is symmetric about the central strip, the transition region is now symmetric about the central strip. For the design purpose, the characteristic impedance of the line at each of the sections BB, CC, and so forth may be determined using simulation software. For a 50 ohm microstrip to 100 ohm CPW transition, the 10-dB return loss frequency range is found to be 8 to 40 GHz. The lower frequency end can be extended by increasing the length of taper [142]. For a 50-ohm to 50-ohm transition, the return loss and insertion loss bandwidth is found to be 20 GHz (0–20 GHz).

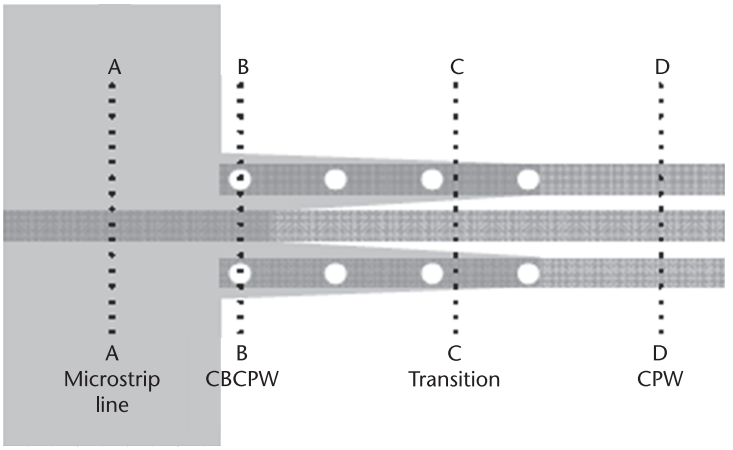

Figure 7.34 Metallization pattern for microstrip line to CPW transition. The gray shade is the ground plane metallization, the dark strips are in the top plane, and the white dots are the vias. (after [142], © 2008 IEEE. Reprinted with permission.)

7.7.4 CPW-to-CPS Transitions

Although CPW-to-CPS transition can be realized by cascading the CPW-to-microstrip and microstrip-to-CPS transitions described earlier, the transition will be long and therefore its insertion loss will be more. A simple layout for CPW-to-CPS transition involves suppressing the unbalanced mode of CPW by connecting the ground strips by an air-bridge and terminating one of the slots of CPW in an open circuit near the air-bridge [143]. This transition is shown in Figure 7.35(a). The transition works well between 1–60 GHz. An improved version of this transition from DC to 110 GHz has also been reported [144]. The modification lies in reworking the ground strip of CPS. The transition consists in joining the ground strips of CPW by an underpass metal line and the *center of this line* is joined to the ground strip of CPS by another line as shown in Figure 7.35(b). This portion utilizes the first metal layer. The signal conductor of CPW passes over this line and is connected to the signal conductor of CPS. The in-phase addition of ground currents in CPW is supposed to improve the performance of this transition to 100 GHz [144].

The microstrip-to-CPW, CPW-to-CPS, and CPS-to-microstrip transitions have been combined to realize a broadband balanced frequency doubler. The doubler had conversion loss less than 10 dB for output frequencies between 9 to 26 GHz, and less than 12 dB for output frequencies between 7 to 38 GHz [142]. The frequency doubler uses 2 GaAs flip-chip Schottky diodes. These transitions have been utilized in designing a three-port wideband planar balun. The input and output ports are microstrip lines. The balun shows return loss > 13 dB, isolation > 10.8 dB, amplitude imbalance <1.1 dB, and phase imbalance < 8 degree between 16.5–40 GHz [145].

7.7.5 CPS-to-Slotline Transitions

The CPS line in microstrip-to-CPS transition can be tapered to realize the slotline, thus achieving a CPS-to-slotline transition [141]. CPS-to-slotline part of this transi-

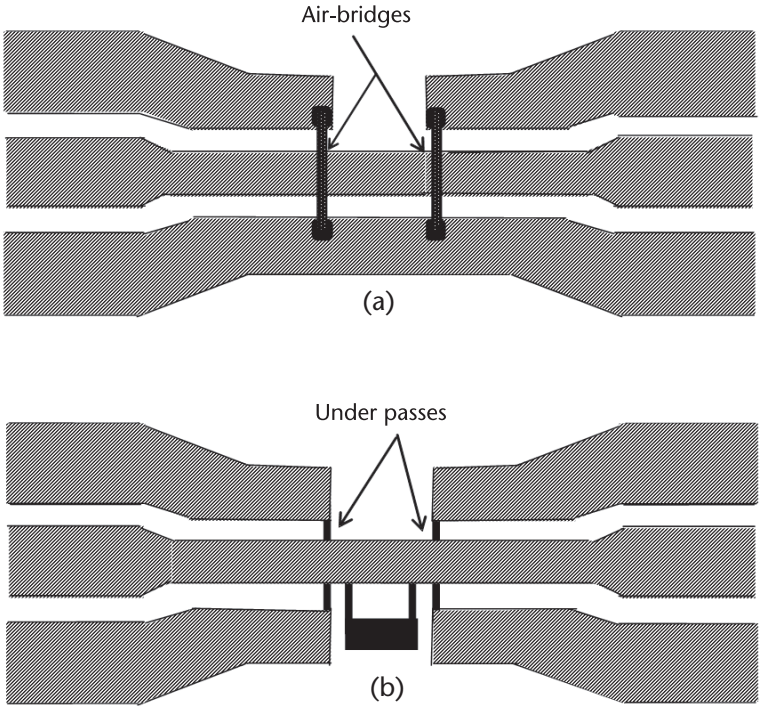

Figure 7.35 Layouts for back-to-back CPW-to CPS transitions. (a) 1–60-GHz transition. (after [143], © 1998 IEEE. Reprinted with permission.) (b) DC-110-GHz transition. (after [144], © 2002 IEEE. Reprinted with permission.)

tion is shown in Figure 7.36. If the slot widths for CPS and slotline are different, the same may also be tapered. A bi-planar transition between CPS and slotline has been reported by Simons [80]. In this transition, the CPS line is first transformed into coupled microstrip lines by using the conductor of slotline as the ground plane for coupled microstrip lines. The spacing between the coupled lines is then slowly flared so that they get uncoupled and cross the slot underneath at right angle, in a way exactly similar to the microstrip-to-slotline transition of Figure 5.29. The layout of the transition is shown in Figure 7.37. The maximum insertion loss per transition was found to be about 1.5 dB over the 8–11.2 GHz band.

7.7.6 Slotline-to-CPW Transitions

This transition has been studied most comprehensively. Various types of transitions that have been proposed are shown in Figure 7.38. The transition in Figure 7.38(a) is based on the CPW-slotline T-junction of Figure 7.48 (b) [72,73]. This junction works like a power divider. If one of the output ports of the power divider is terminated in an open circuit, we obtain the CPW-to-slotline transition of Figure 7.38(a). In this transition there is complete transfer of current from the CPW to the slotline. While current on the strip of the CPW flows into one of the conductors of the slotline, the backward current on the ground planes of the CPW flows from the other conductor of the slotline through a bonding wire. The open circuit on one of the slots of the CPW and the use of a bonding wire (not shown in Figure 7.38), help transform the CPW mode to the slotline mode. A variation of this transition

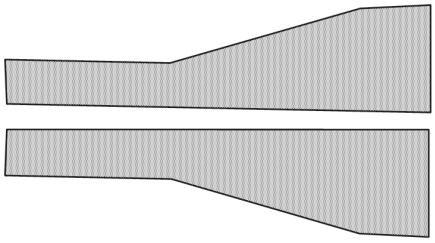

Figure 7.36 CPS-to-slotline transition.

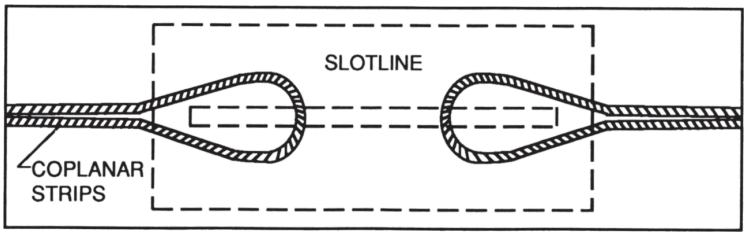

Figure 7.37 CPS-to-slotline transition (from [80],© 1994 IEEE Reprinted with permission.).

uses a slotline open circuit in the form of a circular slot (see Figure 7.38(b)) [74, 75]. In Figure 7.38(c) the open circuits of Figure 7.38(a,b,c) have been replaced by a quarter-wave shorted stub [76], which provides a tuning capability. To improve the bandwidth, the slot in Figure 7.38(d) is terminated in a 90° radial slotline stub. The transitions in Figure 7.38(c–i) borrow the concept of a quarter-wave cross-junction of the microstrip slotline transition of Figure 5.28 [68, 73, 76, 77]. To increase the bandwidth, uniform impedance stubs have been replaced by nonuniform impedance radial stubs. A comparative study of these transitions shows that the transition in Figure 7.38(d) is the best in terms of bandwidth and insertion loss [76]. The 1-dB insertion loss bandwidth for this transition is found to be more than 5.2:1. Further, this transition can be designed such that the CPW and slot lines are colinear, that is, the right-hand slot of the CPW can run straight instead of bending at right angles as shown in the figure. This introduces flexibility in the layout. The idealized equivalent circuit of the transitions in Figures 7.38(e–i) is shown in Figure 7.39; the junction discontinuity effect is neglected here. The equivalent circuit consists of an open-circuited quarter-wave CPW section in series and a shorted quarter-wave slotline section in shunt across the CPW-slotline junction.

For a 50-Ω CPW line the optimum value of Z_{01} is obtained as [73]

$$Z_{01} = \frac{Z_{02}\tan^2\left(\pi f_x/2f_0\right)}{1+\left(Z_{02}/Z_{\text{slot}}\right)^2\tan^2\left(\pi f_x/2f_0\right)} \tag{7.165}$$

where f_x represents either the lower (f_{x1}) or the upper (f_{x2}) band edge of the transition with center frequency $f_0 = (f_{x1}+f_{x2})/2$. A fullwave analysis of the transition in Figure 7.38(e) has been reported in [78].

The transition shown in Figure 7.40(a) employs a six-port junction between the CPW and the slotline [73, 79]. The equivalent circuit of this transition can be expressed in the form of an impedance bridge of Figure 7.40(b). A simple analysis

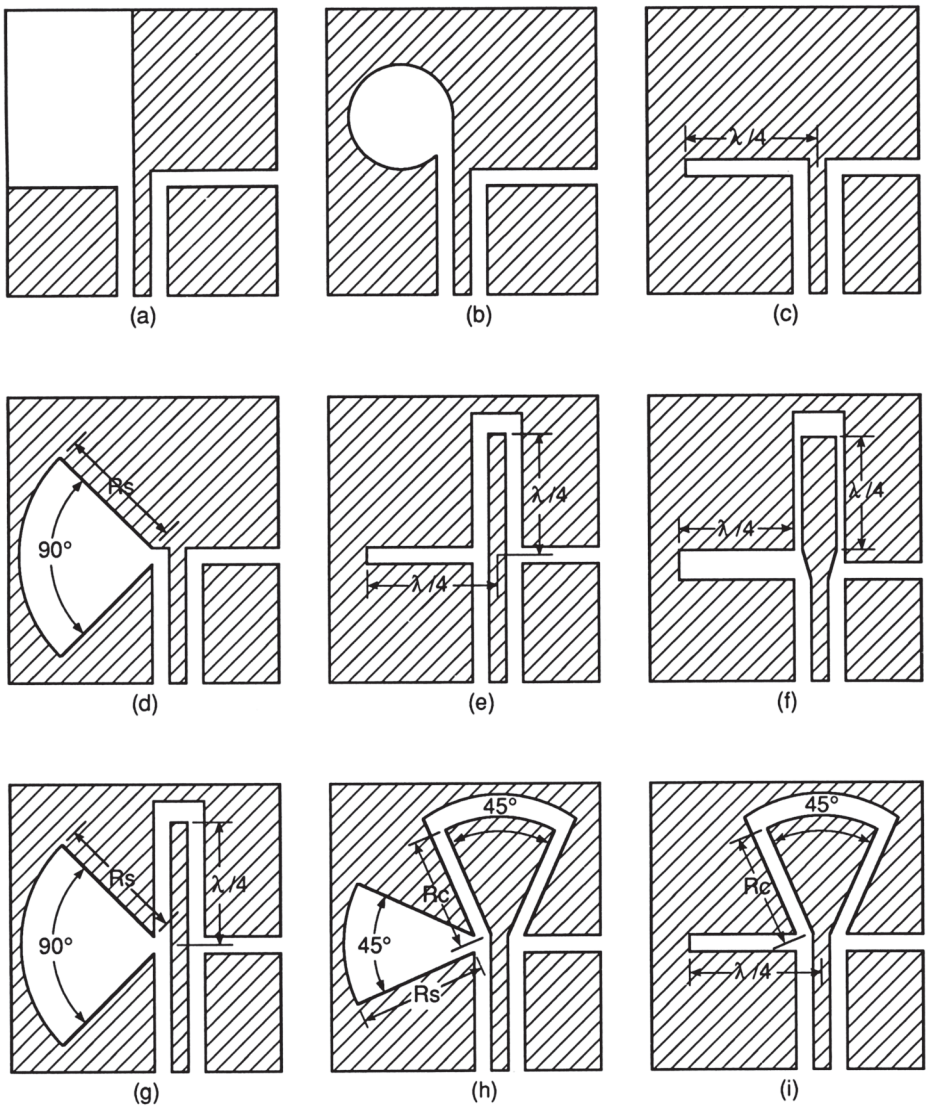

Figure 7.38 (a) through.(i): Slotline-to-CPW transitional with different types of terminations.

of the impedance bridge gives the following expression for the input impedance at the CPW port of the transition:

$$\overline{Z_{\text{in}}} = \frac{1}{\overline{Z_2} + \overline{Z_3} + 1}\left[\overline{Z_2 Z_3} + \frac{\left(\overline{Z_2} + \overline{Z_3}\right)\left(\overline{Z_2} + 1\right)\left(\overline{Z_3} + 1\right)}{\overline{Z_2} + \overline{Z_3} + 2}\right] \tag{7.166}$$

where Z_2, Z_3, Z_5, and Z_6 are input impedances of respective stubs at the junction and all the impedances in (7.166) have been normalized to the characteristic impedance Z_4 of the slotline; and it is assumed that $Z_2 = Z_5$ and $Z_3 = Z_6$. For a perfect match, $\overline{Z\text{in}} = 1$. Equation (7.166) then reduces to the condition

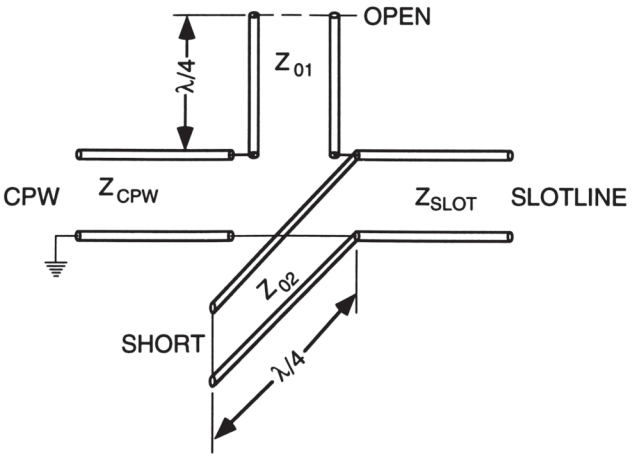

Figure 7.39 Idealized equivalent circuit for the slotline-to-CPW transitions of Figure 7.38(e–i).

$$\overline{Z_2 Z_3} = 1 \tag{7.167}$$

or equivalently

$$\Gamma_2 = -\Gamma_3 \tag{7.168}$$

Equation (7.168) implies that if all the stubs are of the same electrical length, then a perfect match is maintained at all the frequencies. In reality, the bandwidth is limited by unequal dispersion between the slotline and the CPW, junction reactances, and mode conversion. Stub lengths are kept short ($\cong \lambda_g/8$) to minimize dispersion and attenuation effects. Test results of this transition on a 0.33-mm-thick silicon substrate with $\varepsilon_r = 11.9$ are available in [73]. The return loss was found to be greater than 15 dB from 20 GHz to 35 GHz.

All the slotline-CPW transitions discussed above can be modified to introduce biasing of active devices across the slotline as discussed in [65].

7.8 Discontinuities in Coplanar Lines

7.8.1 CAD Models for Discontinuities in Coplanar Waveguide Circuits

Some of the common discontinuities that occur in CPW circuits and antennas are shown in Figure 7.41. The theoretical modeling of these discontinuities has been carried out extensively [81–127]. Both quasi-static as well as full-wave approaches have been reported. However, design information suitable for CAD tools is still lacking for most of the discontinuities; the main reason appears to be that there are a large number of parameters and it is, therefore, difficult to develop expressions covering the useful range of parameters. A complete library for CAD-oriented simulation of CPW lines with discontinuities is available in [113–115]. A comprehensive comparison of CAD models of some of the discontinuities is reported by Dib [123]. Some of these CAD models suitable under quasi-static limit are given next.

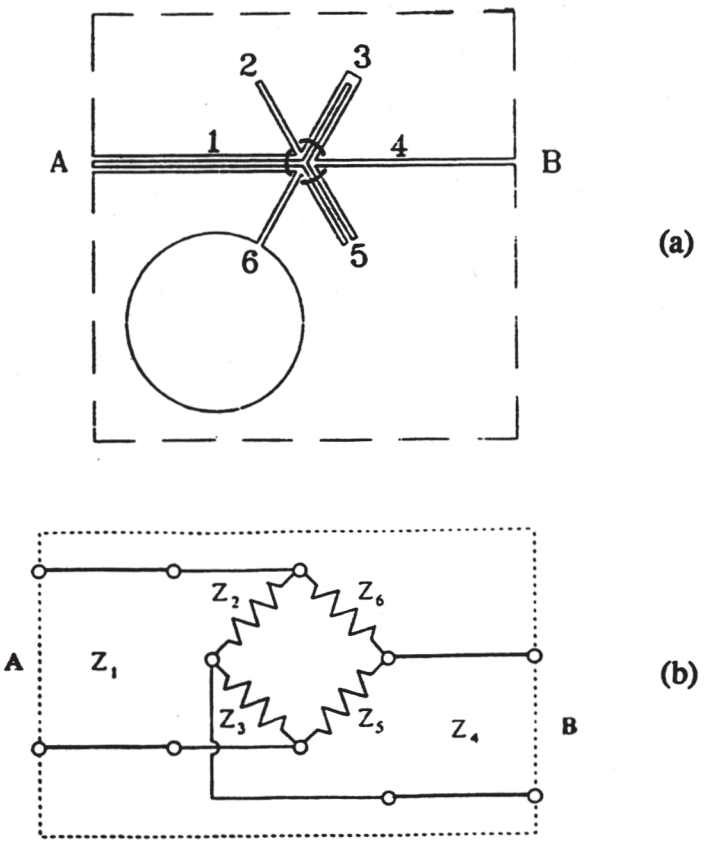

Figure 7.40 Slotline-to-CPW transition using a double junction: (a) schematic and (b) equivalent circuit (from (73], © 1998 IEEE. Reprinted with permission.).

Open and Short Circuit Discontinuities

The open and short circuits in CPW line are shown in Figure 7.41(a) and (b), respectively. The open circuit is capacitive and the short circuit is inductive as shown. A good amount of literature has appeared on the analysis of these continuities [81–97, 104–109, 118, 119, 123–125]. The data for the open end discontinuity has been compared by Dib [123], and it is suggested that the following expression due to Beilenhoff [97] may be employed for wide end-gaps described by $g > 0.2b$,

$$\Delta\ell_{oc} = b/2 \tag{7.169}$$

where $\Delta\ell_{oc}$ is the equivalent length extension of the line terminated by an ideal open circuit, and is related to the capacitance C_{oc} by the approximate expression $C_{oc} = \Delta\ell_{oc}\sqrt{\varepsilon_{re}}/(cZ_0)$. For narrow gaps $g \leq 0.2$b, the following simplified expression for capacitance due to Mao et al. [124] may be used:

$$C_{oc} = \varepsilon_{re}C_{oc}(\varepsilon_r = 1) \tag{7.170}$$

where ε_{re} is the effective dielectric constant of CPW, and

$$
\begin{aligned}
C_{oc}(\varepsilon_r = 1) &= \frac{\varepsilon_0}{\pi}\left(\frac{f_S(g, W+S, 0)}{g^2} + \frac{f_o(W, S, 0)}{W^2}\right) \\
f_S(a,b,c) &= \frac{4}{3}c^3 + f(a,c) + f(b,c) - 4abc\tan^{-1}\left(\frac{ab}{c\tau}\right) - \frac{2\tau}{3}\left(b^2 - 2c^2 + a^2\right) \\
&\quad + b\left(a^2 - c^2\right)\ln\left(\frac{\tau + b}{\tau - b}\right) + a\left(b^2 - a^2\right)\ln\left(\frac{\tau + a}{\tau - a}\right), \qquad \tau = \sqrt{a^2 + b^2 + c^2} \\
f_o(a,b,c) &= \frac{4}{3}c^3 + f(a,c) + f(a+b,c) - 0.5f(b,c) - 0.5f(b+2a,c) \\
&\quad + b\left(a^2 - c^2\right)\ln\left(\frac{\tau + b}{\tau - b}\right) + a\left(b^2 - a^2\right)\ln\left(\frac{\tau + a}{\tau - a}\right) \\
f(x,y) &= \frac{2}{3}\left(x^2 - 2y^2\right)\sqrt{x^2 + y^2} + xy^2\ln\left(\frac{\sqrt{x^2 + y^2} + x}{\sqrt{x^2 + y^2} - x}\right)
\end{aligned}
\tag{7.171}
$$

The accuracy of the above models is about 10% to 20% [123]. The effect of metallization thickness and frequency on open-end effect is found to be very small. At high frequencies, the capacitance is shunted by a resistor representing the power radiated.

The short-circuit discontinuity may be modeled as a lumped inductance L_{sc} or an equivalent line length extension $\Delta\ell_{sc}$ followed by an ideal short. The two are related as $\omega L_{sc} = Z_0 \tan(\beta\Delta\ell_{sc})$. The following expression by Getsinger [125] may be used for determining L_{SC}:

$$
L_{sc} = \frac{2\varepsilon_0\varepsilon_{re}(S+W)Z_0^2}{\pi}\left(1 - \frac{1}{\cosh\left(\dfrac{60\pi^2}{Z_0\sqrt{\varepsilon_{re}}}\right)}\right) \tag{7.172}
$$

where S is the central strip width and W is the slot width of CPW.

The accuracy of the above model is restricted to low impedance lines below 90 ohm. The comparison of values obtained from (7.172) with that due to numerical results of Jansen [81] shows that (7.172) has an accuracy of about 15% [123].

Shunt Inductive Coupling Element

The short circuit of Figure 7.41(b) terminates the line and converts it into one-port. A narrow strip across the CPW conductors, however, may be employed as a coupling element with the following CPW section. The geometry and the equivalent circuit of this inductive discontinuity are shown in Figure 7.41(c). The shunt in-

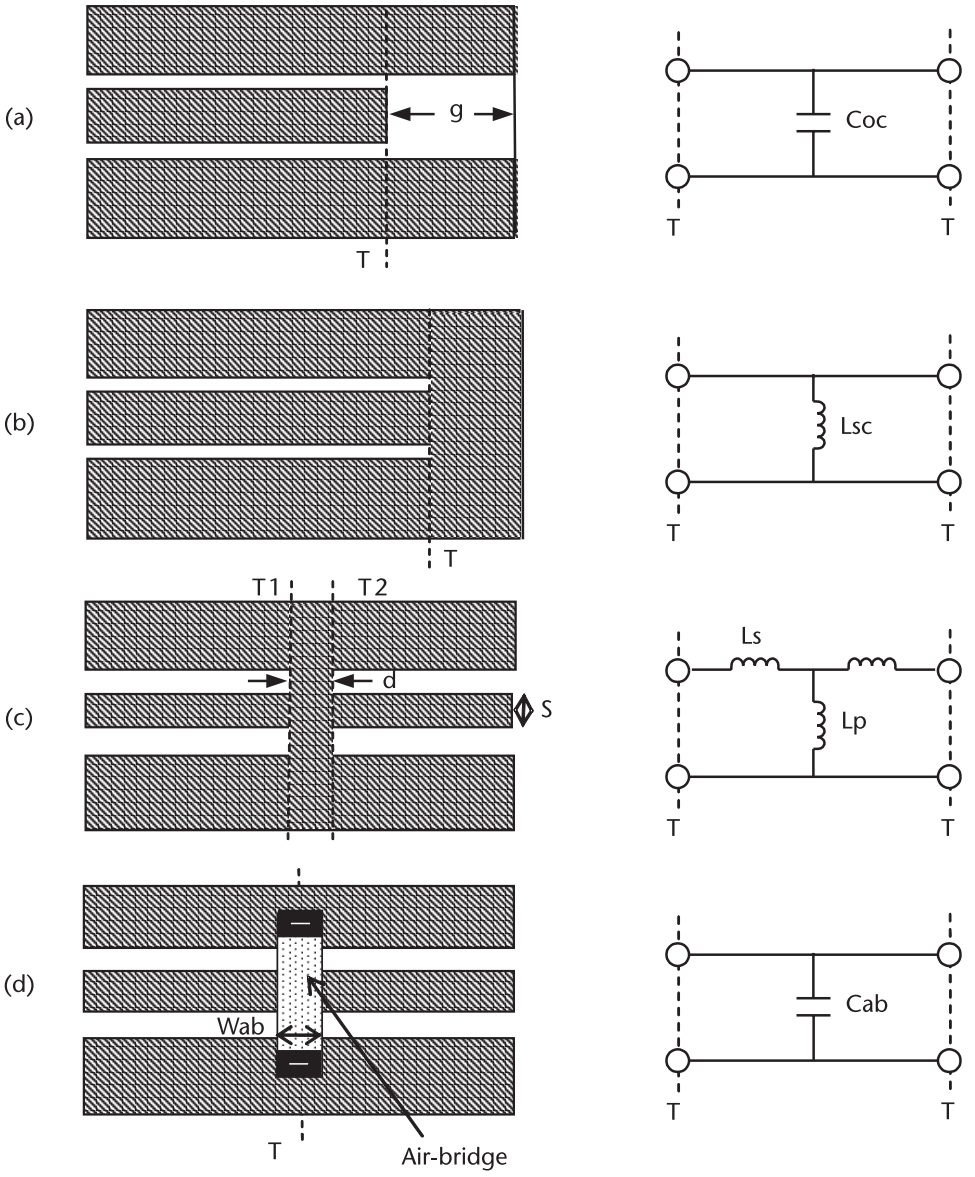

Figure 7.41 Some common discontinuities in CPW circuits and their quasi-static lumped equivalent circuits. (a) Open-end discontinuity, (b) shorted-end discontinuity, (c) shunt inductive discontinuity, and (d) Air-bridge discontinuity.

ductance L_P may be modeled as a ribbon inductor (in free space) with aspect ratio W/d and the corresponding expression is given by

$$L_p = W\left(\ln\left(\frac{1+\sqrt{1+p^2}}{p}\right)+p-\sqrt{1+p^2}\right) \qquad \text{nH} \tag{7.173}$$

where $P = d/(4W)$, d the ribbon width and W the slot width are expressed in centimeters. The expression for series inductor L_S is obtained by curve fitting the numerical results for the discontinuity and is given by [123]

$$\frac{L_{sc}}{L_S} = 1.2193\exp(-5.678t) + 2.3921\exp(-1.0937t) + 1.65653\exp(-0.0423t) \tag{7.174}$$

where $t = d/\Delta\ell_{sc} - 0.45$. In the above expression, L_{sc} and $\Delta\ell_{sc}$ correspond to the short-circuit quantities described earlier. The formula (7.174) may be used for values of d such that L_S/L_{sc}. It is found that for a 50-ohm CPW $0.14 \le L_S \le L_{sc} \le 0.66$ for $0.5 \le d/\Delta\ell_{sc} \le 8$ [123].

Air-Bridge Discontinuity

The CPW line is coupled slotline geometry that can support two modes, even and odd modes. The even mode of propagation, in which the ground planes surrounding the strip conductor is at the same potential, is the preferred mode for circuit realization. However, the odd mode or slot line mode in which all the conductors are at different potentials, may also get excited due to either asymmetry of the line geometry or at discontinuities. This mode can be suppressed if the ground planes are forced at the same potential by connecting a metal ribbon, called an air-bridge, across the center strip. CPW line with air-bridge is shown in Figure 7.41(d). The ribbon creates a capacitive discontinuity due to the electric field between the central strip and ribbon crossover, and can be roughly modeled as a parallel capacitor $C_{//}$ to ground. However, the actual air-bridge capacitance C_{ab} is more than $C_{//}$ because of the fringing field between the strip and ribbon. The detailed study by Weller et al. [126] shows that for air-bridge height of 3 μm, 80 μm $\le 2b \le$ 260 μm, $0.15 \le k \le 0.7$, and 20 μm $\le W_{ab} \le$ 40 μm the ratio $1.5 \le C_{ab}/C_{//} \le 4.2$. Also, $C_{ab}/C_{//}$ is lower for a wide ribbon over a wide strip and vice versa.

Some more discontinuities and their lumped equivalent circuits are discussed in Section 7.9.

Discontinuity Compensation in CPW Circuits

The discontinuity reactance, although small compared to the line reactance, should be included in the design of circuits or antennas; otherwise it may lead to compromise in the performance. An alternative is to compensate for the discontinuity reactance. We illustrate some techniques to compensate for discontinuity reactance.

Air-Bridge Capacitance Compensation

The air-bridge discontinuity is one of the very common discontinuities in CPW circuit realization. As discussed earlier, it can be modeled as shunt capacitance to ground at the mid-point of the cross-over. A simple approach to reduce the air-bridge capacitance is to increase the bridge height or reduce the strip width (resulting in high impedance CPW section) underneath the air-bridge. This compensation is found to be inadequate [126]. However, use of high impedance section beyond

the immediate vicinity of air-bridge may provide sufficient compensation. The compensated air-bridge is shown in Figure 7.42(a). A simple analysis shows that the length L_{high} of the high impedance section is given by [126]

$$L_{high} = \frac{Z_h Z_0^2 C_{ab}}{Z_h^2 - Z_0^2} \frac{c}{\varepsilon_{re}} \tag{7.175}$$

where Z_0 is the impedance of CPW line outside air-bridge, and ε_{re} is the effective dielectric constant of Z_{h} section. It is assumed in deriving the above expression that $\tan(\theta/2) \approx \theta/2$ and $Z_{\text{h}}\omega C_{\text{ab}}\theta/2 \ll 1$, where θ is the electrical length of high impedance section. Iterative approach to fine-tune the values of Z_{h} and L_{high} is required because reducing the strip width below the air-bridge reduces C_{ab} itself. As a rule of thumb, one may use [126]

$$L = L_{high} - 0.7W_{ab} \tag{7.176}$$

where line length L is defined in Figure 7.42(a) and W_{ab} is the width of air-bridge.

Right-Angled Bend Discontinuity Compensation

The right-angled bend in CPW introduces discontinuity reactance similar to that in microstrip line. The compensation technique for CPW right-angled bend is also similar (i.e., the outer corner of the central strip of CPW may be chamfered to reduce the excess capacitance [127]). An alternative compensation approach in the form of reduced strip width in the bend region has been suggested and evaluated [126]. Air-bridges on either side of the bend are included to suppress the possible excitation of coupled slot line mode. The metallization pattern of the compensated right-angled bend with air-bridges is shown in Figure 7.42(b). The high impedance line length L that minimizes the reflection coefficient is given by (7.176). The line step compensation described above for right-angled bends has been extended to the compensation of T-junction discontinuity in CPW circuits [126].

7.8.2 CAD Models for Discontinuities in Coplanar Strips Circuits

Some of the most common discontinuities in CPS circuits have been investigated by Simons et al. [128], and Zhu and Wu [129] to obtain the equivalent circuit models. The layout of these discontinuities and the corresponding circuit models are shown in Figure 7.43. The CAD models in [129] are extracted from the method of moment (MoM) analysis and short-open calibration (SOC) to improve the accuracy of modeling process. The equivalent circuit models therefore include the effects of dispersion, higher-order modes, and radiation loss. Equivalent circuit parameters as a function of frequency are available for $\varepsilon_{\text{r}} = 10.2$ substrate [129]. CAD models for some of these discontinuities in the quasi-static limit are given next. The radiation effect is therefore not included.

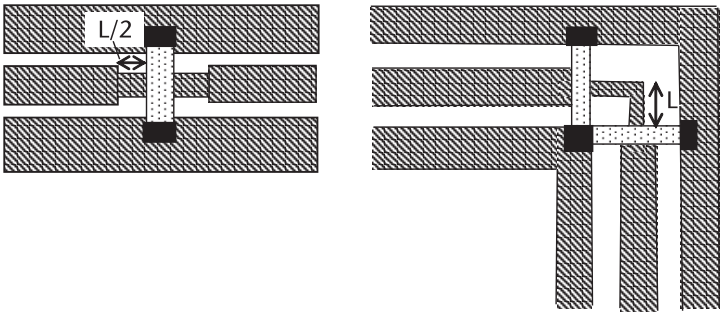

Figure 7.42 Compensation of discontinuity reactance in CPW circuits. (a) Compensation of air-bridge discontinuity, and (b) Compensation of right-angled bend discontinuity. (after [126], © 2000 IEEE. Reprinted with permission.)

Open Circuit Capacitance

Getsinger [125] has proposed a simple expression for the open-end capacitance of CPS line. It is given by

$$C_{oc} = -\frac{2L'}{Z_0^2} \tag{7.177}$$

where

$$L' = -\frac{\mu_0 2S}{4\pi}\left(1 - \frac{\exp(-Z_0^a/60)}{2S}\right), \qquad \text{S: slot width} \tag{7.178}$$

and Z_0^a is the characteristic impedance of CPS line with air as dielectric. Jansen [81] determined the equivalent length for the open end, $\Delta\ell_{oc}$ using computational techniques. Chiu has determined the open-end capacitance based on excess charge and residual potential [130]. The open-end capacitance is plotted as a function of $S/2b$ in Figure 7.44. The capacitance decreases with increase in S provided $2b$ remains constant [130]. Here h is the substrate thickness.

Short-Circuit Inductance

The short-circuit inductance of CPS has been determined by Chiu [130] employing the complementary nature of CPW and CPS lines. The short-circuit discontinuity inductance in CPS is determined from the open-end discontinuity capacitance of CPW and using the relationship $4\varepsilon_0 L_{sc}^{CPS} = \mu_0 C_{oc}^{CPW}$ ($\varepsilon_r = 1$). The equivalent inductance terminating the line is computed as a function of g, the width of shunt strip. The short-circuit inductance L_{sc} is plotted in Figure 7.45; it saturates for large values of g as expected. The inductance is more for narrow strips because of increased current density.

Shunt Inductive Coupling Element

Shunt inductive coupling between sections of symmetric CPS lines (Figure 7.43(e)) has been analyzed for its equivalent circuit inductances [130]. The variation of se-

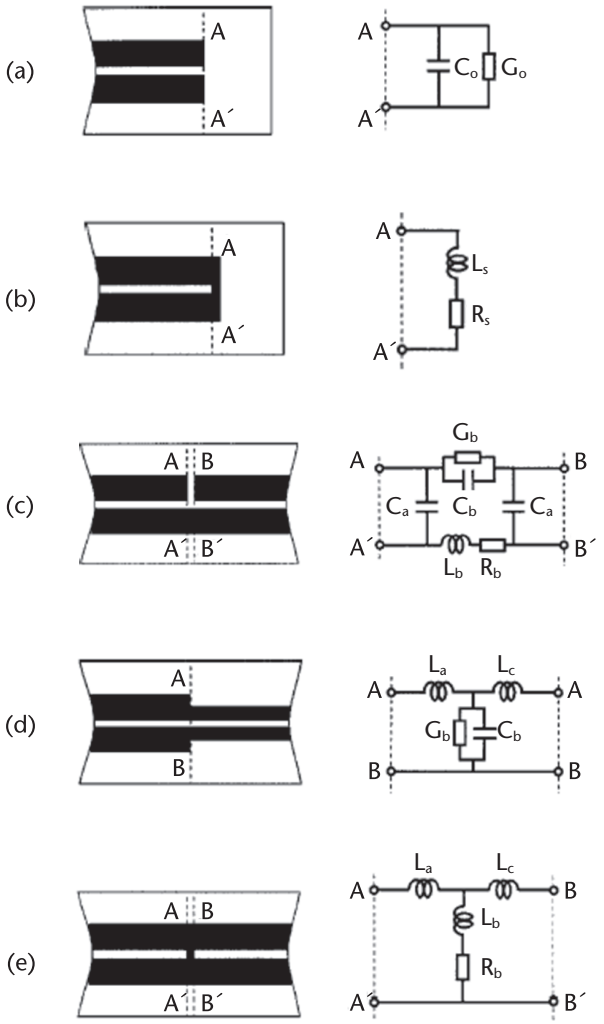

Figure 7.43 Layout and equivalent circuit models of some of the discontinuities in coplanar strips circuits. (a) Open-end, (b) short-circuit, (c) gap, (d) step-in-width, and (e) metallic bridge across the strips. (after [129], © 2002 IEEE. Reprinted with permission.)

ries and shunt inductances is plotted as a function of $g/2b$ in Figure 7.46. The series inductance increases and shunt inductance decreases with increase in the value of $g/2b$, and is consistent with short-circuit inductance results in asymptotic limit.

The paper by Chiu [130] analyzes some more discontinuities in CPS lines.

7.9 Coplanar Line Circuits

Several circuits using CPW have been reported, but CPS circuits have not gained much popularity. Circuit applications of CPW can be grouped as follows:

- Circuits with series and shunt reactances in CPW;
- Circuits using slotline-CPW junctions.

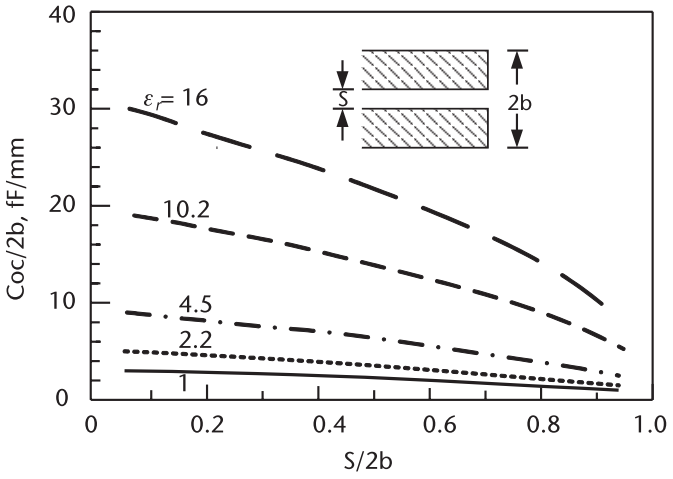

Figure 7.44 Variation of open-end capacitance with slot width S for coplanar strips. h = 0.762 mm, 2b = 1.76 mm. (from [130], © 2002 IEE. Reprinted with permission.)

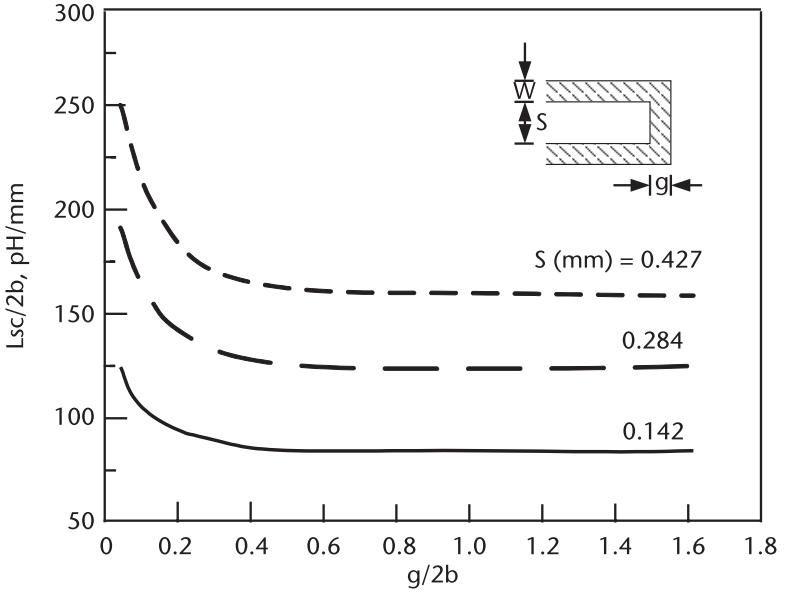

Figure 7.45 Variation of short-circuit inductance with *g* for coplanar strips. 2*b* = 1.59 mm. (from [130], © 2002 IEE. Reprinted with permission.

7.9.1 Circuits with Series and Shunt Reactances in CPW

The first group of CPW circuits uses the flexibility of the coplanar waveguide configuration to accommodate both the series- and the shunt-connected components. Various circuit elements that may be realized in a CPW configuration [116] are shown in Figures 7.47, 7.48, and 7.49. While calculating line lengths it should be remembered that the propagation velocities are not equal for the different impedance sections.

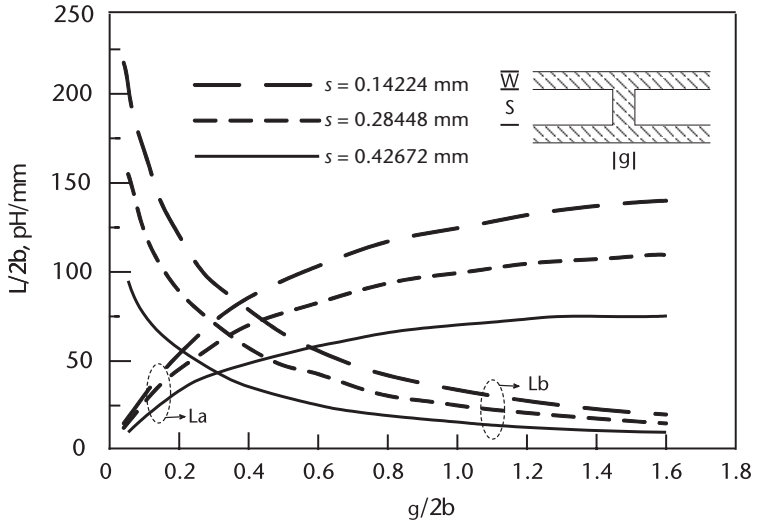

Figure 7.46 Variation of equivalent circuit inductances of inductive coupling element between sections of CPS lines. 2b = 1.59 mm. (from [130], © 2002 IEE. Reprinted with permission.)

Figure 7.47 represents the realization of series-connected inductances and capacitances. Circuit representations in Figure 7.47(b) use another coplanar waveguide configuration inside the central strip of the main CPW. The basic idea is borrowed from similar coaxial line circuits [117]. The series inductance is obtained by a CPW section (smaller than $\lambda_{cp}/4$) shorted at the far end, whereas the series capacitance is realized by a CPW section (again smaller than $\lambda_{cp}/4$) open at the far end.

Use of slotline sections, as shown in Figure 7.47(c), is another way of obtaining series-connected elements. Short-circuited slotlines are used for inductances and open-circuited slotlines for capacitances.

Figure 7.48 represents a realization of shunt-connected reactances obtained by adding coplanar waveguide stubs to the main CPW. Open-circuited stubs are used for capacitance and short-circuited stubs for inductance. The conducting straps are bonded at the junction of the main line and the stubs to ensure that the two ground planes of the CPW stubs are at the same potential. A shunt-mounted series-resonant circuit can be realized by using stubs comprising two CPWs of different impedances. An open-circuit high-impedance section provides the capacitance, whereas the low-impedance section provides inductance. The shunt-mounted series-resonant circuit is useful for designing stop-band filters.

It is also possible to realize pi or tee shaped reactance networks by using CPW stubs. Figure 7.49(b) shows a short CPW stub without any strap to equalize the potentials of the two ground planes of the stub. Thus the stub can support two types of modes: normal CPW mode and the odd mode of coupled slotlines. The latter mode presents an inductance L that appears in series with the main line. When the straps are added, the odd mode of coupled slotlines cannot exist (that is, the inductance L gets shorted) and the equivalent circuit reduces to that shown in Figure 7.48(a). An external capacitance C can be connected in parallel to the series inductance *L* by bonding chip capacitors across the stubs as shown in Figure

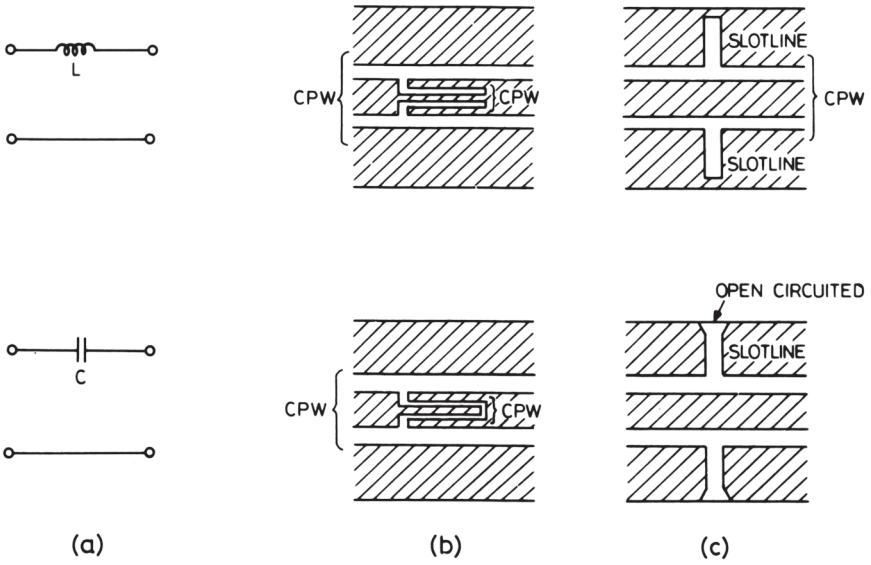

Figure 7.47 Series circuit elements in a CPW configuration: (a) circuit element; (b) realization using CPWs; and (c) realization using CPW and slotline.

7.49(b). This provides a useful circuit element for filter circuits. A pi-network having shunt capacitances can be realized by using an open circuited stub without the shorting strap. One can use chip capacitors to provide a capacitance in parallel to L in this case also.

Schematic diagrams of the Schottky diode detector and the CPW equivalent are shown in Figure 7.50. The circuit uses series and shunt reactances realized by using CPW sections as discussed above. This detector circuit has a VSWR less than 2.0 and a tangential sensitivity less than –52 dBm in the 2-GHz to 4.5-GHz band [116].

7.9.2 Circuits Using Slotline-CPW Junctions

CPW-slotline T-junctions are used frequently in MMICs. There are various types of T-junctions [72], and four of these are illustrated in Figure 7.51. Bonding wires are used to allow the current flow and to equalize the potential of conductors. Idealized equivalent circuits of these T-junctions are shown in Figure 7.52. A better equivalent circuit for the T-junction of Figure 7.51(b) is available in [131]. The circuit includes a series reactance X, representing the junction reactance, in the input line. A closed-form expression for X is obtained by modeling the signal strip (at the junction of slots) as a delta-function current source. Applications of these T-junctions in realizing a magic-T is described next.

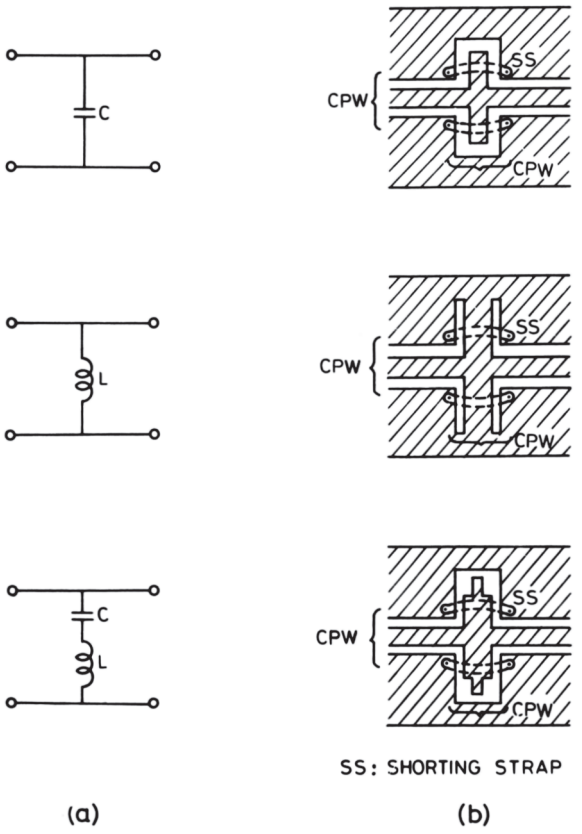

Figure 7.48 Shunt circuit elements in a CPW configuration: (a) circuit element and (b) realization using CPWs.

Magic-T [76]

The magic-T can be realized in a CPW-slotline configuration. It makes use of the properties of a slotline (parallel) T-junction and a CPW-slotline (series) T-junction along with the concept of a rat-race hybrid ring. A configuration of the magic-T is illustrated in Figure 7.53. It consists of a slot ring of radius r such that the circumference of the ring is equal to one guide wavelength of slotline. This circumference is divided equally into four quarter-wave sections. Each of these sections constitutes the output arms of the T-junction associated with them as shown in the figure. Ports 1, 2, and H are the CPW feed ports, and port E is the slotline feed port. The slotline T-junction has the property that outputs have 180° phase difference between them (see Figure 7.51(d)). As a consequence of this the separation between port E and port 2 can be reduced to $\lambda_s/4$ from the value of $3\lambda_s/4$ in a conventional hybrid ring. Other design aspects of magic-T remain the same, namely, $Z_{\text{alot}} = \sqrt{2}$

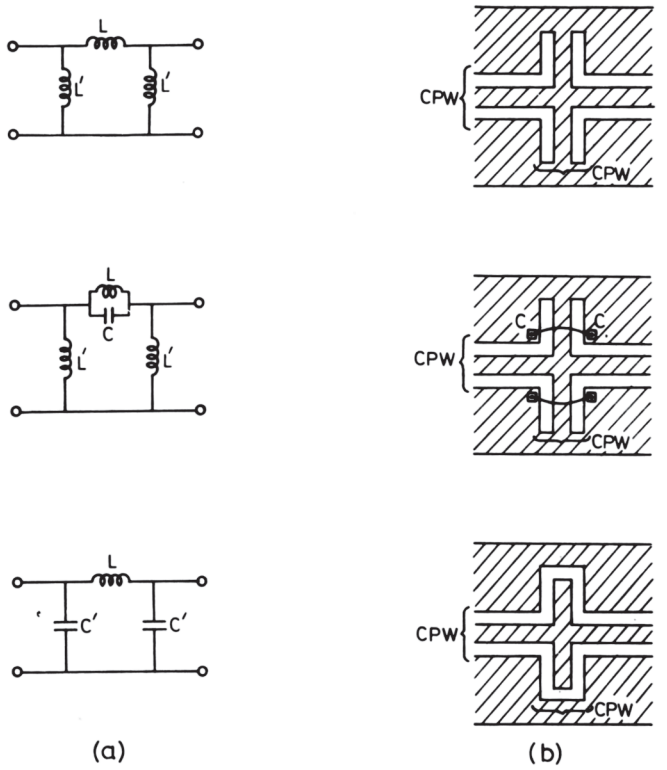

Figure 7.49 Series and shunt circuit elements in a CPW configuration: (a) circuit element and (b) realization using CPWs.

Z_{cpw}. Measurements carried out on a magic-T built on a 1.27-mm-thick substrate with $\varepsilon_r = 10.8$ provided the following characteristics in the S-band [76]:

Power dividing balance of the E-arm	< ±0.4 dB
Isolation between E- and H-arms	>36 dB
Power dividing balance of the H-arm	≤ ±0.3 dB
Isolation between ports 1 and 2	>12 dB
Phase balance of H-arm	–0.75° ±0.75°
Phase balance of E-arm	–181° ±1°

Circuits Using Both Balanced and Unbalanced Signals

A CPW can propagate a signal in two modes: (1) an unbalanced signal in the even mode of coupled slotlines and (2) a balanced signal in the odd mode of coupled slotlines. The impedances for these modes (balanced and unbalanced) are different.

The slotline-to-CPW junction shown in Figure 7.54(a) excites a balanced signal in CPW. On the other hand, when a CPW is fed from a coaxial line as in Figure 7.54(b) or through a microstrip as in Figure 7.54(c), an unbalanced signal is launched on the CPW. Therefore, a microstrip-CPW-slotline (or a coax-CPW-slot-

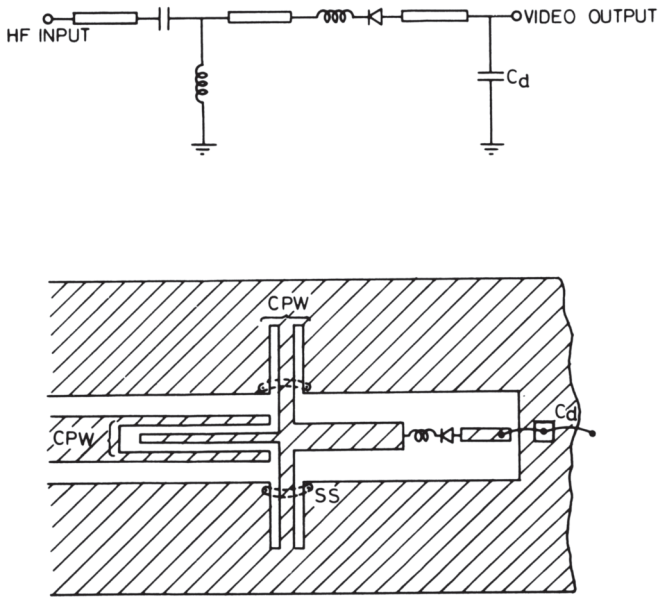

Figure 7.50 Coplanar waveguide detector (from [116], © 1976 Microwave Exhibitions & Publishers (U.K.). Reprinted with permission.).

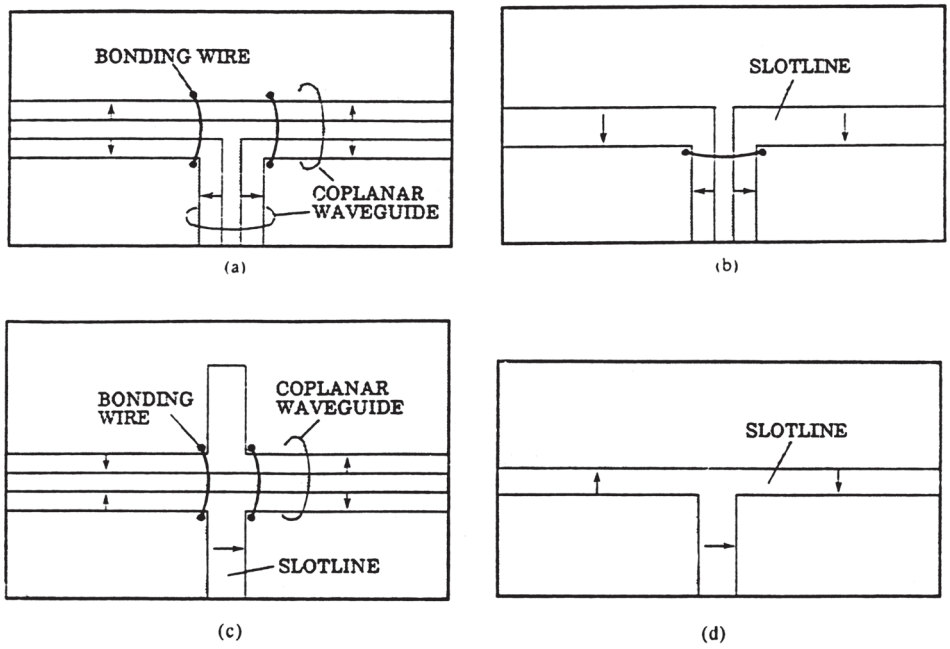

Figure 7.51 Various types of CPW, slotline T-junctions: (a) CPW-CPW T-junction; (b) CPW-slotline T-junction; (c) slotline-CPW T-junction; and (d) slotline-slotline T-junetion (from [72], © 1987 IEEE. Reprinted with permission.).

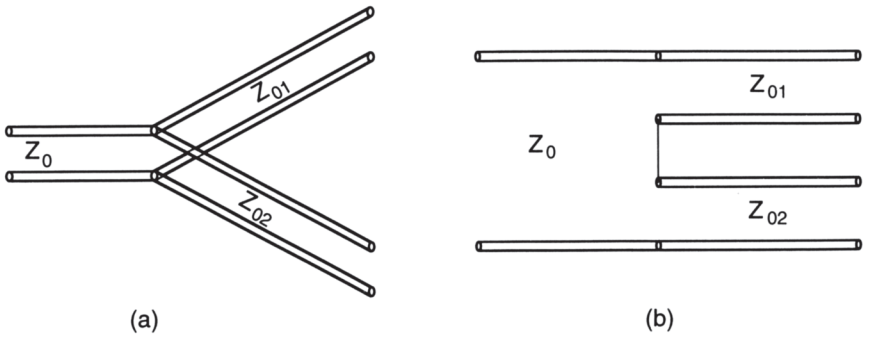

Figure 7.52 Equivalent circuit for T-junctions of Figure 7.51: (a) equivalent circuit for T-junctions with CPW as input transmission line and (b) equivalent circuit for T-junctions with slotline as input transmission line.

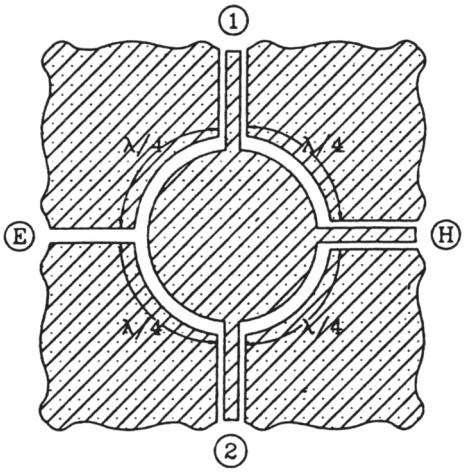

Figure 7.53 Coplanar magic-T (from [76], © 1995 IEEE. Reprinted with permission.).

line) combination may be used in circuits where both the balanced and the unbalanced signals are employed. Such circuits are balanced mixers, double balanced mixers, balanced modulators, balanced frequency multipliers. A number of these circuits in coplanar configuration have been reported [72, 77, 118–122]. A detailed account of some of the topics covered in this chapter may be found in the books by Simons [118], and Wolff [119].

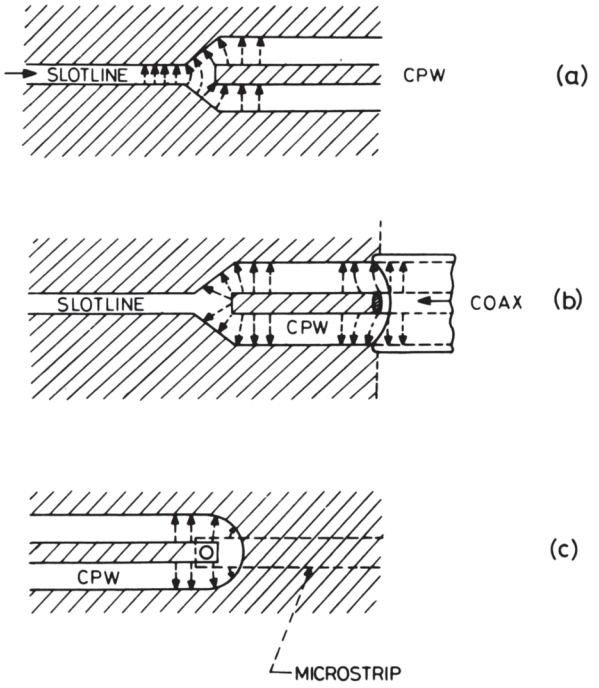

Figure 7.54 (a) Excitation of a balanced mode in CPW by a slotline, (b) an unbalanced mode in CPW excited by a coaxial line, and (c) an unbalanced mode in CPW excited by a microstrip.

References

[1] Wen, C. P., "Coplanar Waveguide: A Surface Strip Transmission Line Suitable for Non-Reciprocal Gyromagnetic Device Application," *IEEE Trans.*, Vol. MTT-I7, 1969, pp. 1087–1090.

[2] Knorr, J. B., and K. D. Kuchler, "Analysis of Coupled Slots and Coplanar Strips on Dielectric Substrate," *IEEE Trans.*, Vol. MTT-23, 1975, pp. 541–548.

[3] Fujiki, Y., et al., "Higher-Order Modes in Coplanar-Type Transmission Lines," *Electron. Comm. in Japan*, Vol. 58–B, Number 2, 1975, pp. 74–80.

[4] Jackson, R. W., "Considerations in the Use of Coplanar Waveguide for Millimeter-Wave Integrated Circuits." *IEEE Trans.*, Vol. MTT-34, 1986. pp. 1450–1456.

[5] Itoh. T., and R. Mittra, "Spectral-Domain Approach for Calculating Dispersion Characteristics of Microstrip Lines," *IEEE Trans.* Vol. MTT-21, 1978, pp. 496–498.

[6] Fukuoka, Y., et al., "Analysis of Slow-Wave Coplanar Waveguide for Monolithic Integrated Circuits," *IEEE Trans.*, Vol. MTT-31, 1983, pp. 567–573.

[7] Phatak, D. S., et al., "Dispersion Characteristics of Optically Excited Coplanar Striplines: Comprehensive Full-Wave Analysis," *IEEE Trans.*, Vol. MTT-38, 1990, pp. 1719–1780.

[8] Shih, Y. C., and T. Itoh, "Analysis of Conductor-Backed Coplanar Waveguide," *Electron. Lett.*, Vol. 18, 1982, pp. 538–540.

[9] Itoh, T. (Ed.), *Numerical Techniques for Microwave and Millimeter-Wave Passive Structures*, New York: Wiley, 1989.

[10] Das, N. K., and D. M. Pozar, "Generalized Spectral-Domain Green's Function for Multilayered Dielectric Substrates with Application to Multilayer Transmission Lines," *IEEE Trans.*, Vol. MTT-35, 1987, pp. 326–335.

[11] Mirshekar-Syahkal, D., and J. B. Davies, "Accurate Solution of Microsttip and Coplanar Structures for Dispersion and for Dielectric and Conductor Losses," *IEEE Trans.*, Vol. MTT-27, 1979, pp. 694–699.

[12] Pintzos, S. G., "Full-Wave Spectral Domain Analysis of Coplanar Strips," *IEEE Trans.*, Vol. MTT-39, 1991, pp. 239–246.

[13] Pregla, R., and S. G. Pintzos, "Determination of the Propagation Constants in Coupled Microslots by a Variational Method," *Proc. V Colloq. Microwave Comm.*, Budapest, June, 1974, pp. Mt-491–500.

[14] Kitazawa, T., and Y. Hayashi, "Coupled Slots on an Anisotropic Sapphire Substrate," *IEEE Trans.*, Vol. MTT-29, 1981, pp. -1035–1040.

[15] Kitazawa, T., and Y. Hayashi, "Quasistatic Characteristics of a Coplanar Waveguide with Thick Metal Coating," *Proc. IEE, Part H*, Vol. 133, 1986, pp. 18–20.

[16] Yamashita, E., and K. Atsuki, "Analysis of Microstrip-Like Transmission Lines by Nonuniform Discretization of Integral Equations," *IEEE Trans.*, Vol. MTT-24. 1976, pp. 195–200.

[17] Hatsuda, T., "Computation of Coplanar-Type Strip Line Characteristics by Relaxation Method and Its Applications to Microwave Circuits," *IEEE Trans.*, Vol. MTT-23, 1975, pp. 795–802.

[18] Diestel, H., and S. B. Worm, "Analysis of Hybrid Field Problems by the Method of Lines with Nonequidistant Discretization," *IEEE Trans.*, Vol. MTT-32, 1984, pp. 633–638.

[19] Sorrentino, R., et al., "Characteristics of Metal-lnsulator-Semiconductor Coplanar Waveguides for Monolithic Microwave Circuits," *IEEE Trans.*, Vol. MTT-32, 1984, pp. 410–416.

[20] Liang, G. C., et al., "Analysis of Coplanar Waveguides and Slotlines using Time-Domain Finite-Difference Method," *IEEE Trans.*, Vol. MTT-37, 1989, pp. 1949–1957.

[21] Davis, M. E. et al., "Finite-Boundary Corrections to the Coplanar Waveguide Analysis," *IEEE Trans.*, Vol. MTT-21, 1973, pp. 594–596.

[22] Veyres, C., and V. F. Hanna, "Extension of the Application of Conformal Mapping Techniques to Coplanar Lines with Finite Dimensions," *Int. J. Electron.*, Vol. 48, 1980, pp. 47–56.

[23] Ghione, G., and C. U. Naldi, "Coplanar Waveguides for MMIC Applications: Effect of Upper Shielding, Conductor Backing, Finite Extent Ground Planes, and Line-to-Line Coupling," *IEEE Trans.*, Vol. MTT-85, 1987, pp. 260–267.

[24] Bedair, S. S., and I. Wolff, "Fast, Accurate and Simple Approximate Analytic Formulas for Calculating the Parameters of Supported Coplanar Waveguides," *IEEE Trans.*, Vol. MTT-40, 1992, pp. 41–48.

[25] Hilberg, W., "From Approximations to Exact Relations for Characteristic Impedances," *IEEE Trans.*, Vol. MTT-17, 1969, pp. 259–265.

[26] Goyal, R., (Ed.), *Monolithic Microwave Integrated Circuits: Technology and Design*, Norwood, MA: Artech House, 1989, Section 4.7.

[27] Ghione, G., and C. Naldi, "Parameters of Coplanar Waveguides with Lower Ground Plane," *Electron Lett.*, Vol. 19, 1983, pp. 734–735.

[28] Svacina, J., Private Communication.

[29] Hanna, V. F., and D. Thebault, "Theoretical and Experimental Investigations of Asymmetric Coplanar Waveguides," *IEEE Trans.*, Vol. MTT-32, 1984, pp. 1649–1651.

[30] Svacina, J., "A Simple Quasi-static Determination of Basic Parameters of Multilayer Microstrip and Coplanar Waveguide," *IEEE Microwave Guided Wave Lett.*, Vol. 2, 1992, pp. 885–387.

[31] Jahnke, E., F. Emde, and F. Losch, *Tables of Higher Functions*, New York: McGraw-Hill, 1960.

[32] Haga, H., et al., "Travelling Wave Modulator Switch with an Etched Grave," *IEEE J. Quantum Electron.*, Vol. QE-22, 1986, pp. 902–906.

[33] Izutsu, M., et al., "Broad-Band Travelling-Wave Modulator Using a LiNbO, Optical Waveguide," *IEEE J. Quantum Electron.*, Vol. QE-13, 1977, pp. 287–290.

[34] Platle, W., and B. Saurer, "Optically CW-Induced Losses in Semiconductor Waveguides," *IEEE Trans.*, Vol. MTT-37, 1989, pp. 139–149.

[35] Crampagne, R., and G. Khoo, "Synthesis of Certain Transmission Lines Employed in Microwave Integrated Circuits," *IEEE Trans.*, Vol. MTT-25, 1977, pp. 440–442.

[36] Ghione, G., "A CAD-Oriented Analytical Model for the Losses of General Asymmetric Coplanar Lines in Hybrid and Monolithic MICs," *IEEE Trans.*, Vol. MTT-41, 1998, pp. 1499–1510.

[37] Bedair, S. S., "Characteristics of Some Asymmetrical Coupled Transmission Lines," *IEEE Trans.*, Vol. MTT-32, 1984, pp. 108–110.

[38] Hoffmann, R. K., *Handbook of Microwave Integrated Circuits*, Norwood, MA: Artech House, 1987.

[39] Gevorgian, S. S., and I. G. Mironenko, "Asymmetric Coplanar-Strip Transmission Lines for MMIC and Integrated Optic Applications," *Electron. Lett.*, Vol. 26, 1990, pp. 1916–1918.

[40] Ghione, G., and C. Naldi, "Analytical Formulas for Coplanar Lines in Hybrid and Monolithic MICs," *Electron. Lett.*, Vol. 20, 1984, pp. 179–181.

[41] Chung, H., et al., "Modeling and Optimization of Traveling Wave LiNbO, Interferometric Modulators," *IEEE J. Quantum Electron.*, Vol. QE-27, 1991, pp. 608–617.

[42] Donnelly, J. P. and A. Gopinath, "A Comparison of Power Requirements of Traveling-Wave $LiNbO_3$ Optical Couplers and Interferometric Modulators," *IEEE Quantum Electron.*, Vol. QE-28, 1987, pp. 30–41.

[43] McLean, J. S., and T. Itoh, "Analysis of a New Configuration of Coplanar Stripline," *IEEE Trans.*, Vol. MTT-40, 1992, pp. 772–774.

[44] Hanna, V. F., "Finite Boundary Corrections to Coplanar Stripline Analysis," *Electron. Lett.*, Vol. 16, 1980, pp. 604–606.

[45] Chou, L., et al., "A WH/GSMT Based Full-Wave Analysis of the Power Leakage from Conductor Backed Coplanar Waveguide," *IEEE MTT-S Digest*, 1992, pp. 219–222.

[46] Janiczak. B. J., "Analysis of Coplanar Waveguide with Finite Ground Planes." *AEU*, Vol. 38, 1984, pp. 341–342.

[47] Phatak, D. S., and A. P. Defonzo, "Dispersion Characteristics of Optically Excited Coplanar Striplines: Pulse Propagation," *IEEE Trans.*, Vol. MTT-38, 1990. pp. 654–661.

[48] Hasnain, G., et al., "Dispersion of Picosecond Pulses in Coplanar Transmission Lines," *IEEE Trans.*, Vol. MTT-54, 1986, pp. 738–741.

[49] Frankel, M. Y., et al., "Terahertz Attenuation and Dispersion Characteristics of Coplanar Transmission Lines," *IEEE Trans.*, Vol. MTT-39, 1991, pp. 910–916.

[50] Kitazawa, T., et al., "A Coplanar Waveguide with Thick Metal-Coating," *IEEE Trans.*, Vol. MTT-24, 1976, pp. 604–608.

[51] Wu. K., et al., "The Influence of Finite Conductor Thickness and Conductivity on Fundamental and Higher-Order Modes in Miniature Hybrid MICs (MHMICs) and MMICs," *IEEE Trans.*, Vol. MTT-41, 1993, pp. 421–430.

[52] Ke, J. Y., and C. H. Chen, "The Coplanar Waveguides with Finite Metal Thickness and Conductivity," *IEEE MTT-S Digest*, 1994, pp. 1681–1684.

[53] Yamashita, E., et al., "Characterization Method and Simple Design Formulas of MCS Lines Proposed for MMICs," *IEEE Trans.*, Vol. MTT-35, 1987, pp. 1355–1362.

[54] Owyang, O. H., and T. T. Wu, "The Approximate Parameters of Slot Lines and Their Complement," *IRE Trans.*, Vol. AP-6, 1958, pp. 49–55.

[55] Tuncer, E., et al., "Quasi-Static Conductor Loss Calculations in Transmission Lines Using a New Conformal Mapping Technique," *IEEE Trans.*, Vol. MTT-42, 1994, pp. 1807–1815.

[56] Gopinath, A, "Losses in Coplanar Waveguides," *IEEE Trans.*, Vol. MTT-80, 1982, pp. 1101–1104.

[57] Das, N. K., and D. M. Pozar, "Full-Wave Spectral Domain Computation of Material, Radiation, and Guided Wave Losses in Infinite Multilayered Printed Transmission Lines," *IEEE Trans.*, Vol. MTT-89, 1991, pp. 54–63.

[58] Kitazawa, T., and T. Itoh, "Propagation Characteristics of Coplanar-Type Transmission Lines with Lossy Media," *IEEE Trans.*, Vol. MTT-39, 1991, pp. 1694–1700.

[59] Shigesawa, H., et al., "Conductor-Backed Slot Line and Coplanar Waveguide: Dangers and Full-Wave Analysis," *IEEE MTT-S Digest*, 1988, pp. 199–202.

[60] Shigesawa, H., et al., "Dominant Mode Power Leakage from Printed-Circuit Waveguides," *Radio Sci.*, Vol. 26, 1991, pp. 559–564.

[61] McKinzie, W. E., and N. G. Alexopoulos, "Leakage Loss for the Dominant Mode of Conductor Backed Coplanar Waveguide," *IEEE Microwave Guided Wave Lett.*, Vol. 2, 1992, pp. 65–67.

[62] Liu, Y., and T. ltoh, "Leakage Phenomena in Multilayered Conductor-Backed Coplanar Waveguides;" *IEEE Microwave Guided Wave Lett.*, Vol. 3, 1993, pp. 426–427.

[63] Riaziat, M., et al., "Propagation Modes and Dispersion Characteristics of Coplanar Waveguides," *IEEE Trans.*, Vol. MTT-38, 1990, pp. 245–251.

[64] Kasiliilgam, D. P., and D. B. Rutledge, "Surface Wave Losses of Coplanar Transmission Lines," *IEEE MTT-S Digest*, 1983, pp. 113–116.

[65] Rutledge, D. B., et al., *Planar Integrated Circuit Antennas*, Vol. 10, *Millimeter Components and Techniques*, Infrared and Millimeter Waves, Part II, (ed. K. Button), New York: Academic Press, 1983, Chapter 1.

[66] Tsuji, M., et al., "New Interesting Leakage Behavior on Coplanar Waveguides of Finite and Infinite Widths," *IEEE Trans.*, Vol. MTT-39, 1991, pp. 2130–2137.

[67] Ke, J.Y., et al., "Dispersion and Leakage Characteristics of Coplanar Waveguides," *IEEE Trans.*, Vol. MTT-40, 1992, pp. 1970–1973.

[68] Grischkowsky, D., et al., "Electromagnetic Shock Waves from Transmission Lines," *Phys Rev. Lett.*, Vol. 59, 1987, pp. 1663–1666.

[69] Heinrich, W., "Full-Wave Analysis of Conductor Losses on MMIC Transmission Lines," *IEEE Trans.*, Vol. MTT-38, 1990, pp. 1468–1472.

[70] Heinrich, W., "Conductor Loss on Transmission lines in Monolithic Microwave and Millimeter Wave Integrated Circuits," *Int. J. Microwave MM-Wave CAE*, Vol. 2, No.3, 1992, pp. 155–167.

[71] Houdart, M., and C. Aury, "Various Excitations of Coplanar Waveguide," IEEE *MTT-S Digest*, 1979, pp. 116–118.

[72] Ogawa, H., and A. Minagawa, "Uniplanar MIC Balanced Multiplier-A Proposed New Structure for MICs," *IEEE Trans.*, Vol. MTT-35, 1987, pp. 1363–1368.

[73] Grammer, W., and K. S. Yngvesson, "Coplanar Waveguide Transitions to Slotline: Design and Microprobe Characterization,"*IEEE Trans.*, Vol. MTT-41, 1993, pp. 1653–1658.

[74] Ho, T. Q., and S. M. Hart, "A Broad-Band Coplanar Waveguide to Slotline Transition," *IEEE Microwave Guided Wave Lett.*, Vol. 2, 1992, pp. 415–416.

[75] Ho, C. H., et al., "Broadband Uniplanar Hybrid-Ring Couplers," *Electron. Lett.*, Vol. 29, 1993, pp. 44–45.

[76] Ho. C. H., et al., "Broadband Uniplanar Hybrid-Ring and Branch-Line Couplers," *IEEE Trans.*, Vol. MTT-41, 1999, pp. 2116–2125.

[77] Cahana, D., "A New Coplanar Waveguide/Slotline Double-Balanced Mixer," *IEEE MTT-S Digest*, 1989, pp. 967–968.

[78] Vourch, E., et al., "A Full-Wave Analysis of Coplanar Waveguide-Slotline Transition," *IEEE MTT-S Digest*, 1994, pp. 1309–1312.

[79] Trifunovic, V., and B. Jokanovic, "New Uniplanar Balun," *Electron. Lett.*, Vol. 27, 1991, pp. 813–815.

[80] Simons, R. N., "Novel Coplanar Stripline to Slotline Transition on High Resistivity Silicon," *Electron. Lett.*, Vol. 30, 1994, pp. 654–655.

[81] Jansen, R. H., "Hybrid Mode Analysis of End Effects of Microwave and Millimeter Wave Transmission Lines," *Proc. IEE, Part H*, Vol. 128, No. 2, 1981, pp. 77–86.

[82] Dib, N., et al., "A Comparative Study Between Shielded and Open Coplanar Waveguide Discontinuities," *Int. J. Microwave MM-Wave Computer Aided Eng.*, Vol. 2, No. 4, 1992, pp. 331–341.

[83] Dib, N., et al., "A Theoretical and Experimental Study of CPW Shunt Stubs," *IEEE Trans.*, Vol. MTT-41, 1993, pp. 38–44.

[84] Dib, N., et al., "Theoretical and Experimental Characterization of Coplanar Waveguide Discontinuities for Filter Applications," *IEEE Trans.*, Vol. MTT-39, 1991, pp. 873–882.

[85] Naghed, M., and I. Wolff, "Equivalent Capacitances of Coplanar Waveguide Discontinuities and Interdigitated Capacitors Using a 3-Dimensional Finite Difference Method," *IEEE Trans.*, Vol. MTT-38, 1990, pp. 1808–1815.

[86] Kuo, W. W., and T. Ttoh, "Characterization of Shielded Coplanar Type Transmission Line Junction Discontinuities Incorporating the Finite Metalization Thickness Effect," *IEFE Trans.*, Vol. MTT40, 1992, pp. 72–80.

[87] Jackson, R. W., "Mode Conversion at Discontinuities in Finite Width Conductor-Backed Coplanar Waveguide," *IEEE Trans.*, Vol. MTT-37, 1989, pp. 1582–1589.

[88] Drissi, M., et al., "Analysis of Coplanar Waveguide Radiating End Effects Using the Integral Equation Technique," *IEEE Trans.*, Vol. MTT-39, 1991, pp. 112–116.

[89] Simons, R. N., and G. E. Ponchak, "Modeling of Some Coplanar Waveguide Discontinuities," *IEEE Trans.*, Vol. MTT-36, 1988, pp. 1796–1803.

[90] Beilenhoff, K., et al. "Open and Short Circuits in Coplanar MMIC's," *IEEE Trans.*, Vol. MTT-41, 1993, pp. 1534–1537.

[91] Bartolucci, G., and J. Piotrowski, "Full-Wave Analysis of Shielded Coplanar Waveguide Short-End," *Electron. Lett.*, Vol. 26, 1990, pp. 1615–1616.

[92] Naghed, M., and I. Wolff, "A Three-Dimensional Finite-Difference Calculation of Equivalent Capacitances of Coplanar Waveguide Discontinuities," *IEEE MTT-S Digest*, 1990, pp. 1143–1146.

[93] Jin, H., and R. Vahldieck, "Calculation of Frequency Dependent S-Parameters of CPW Air Bridges Considering Finite Metalization Thickness and Conductivity," *IEEE MTT-S Digest*, 1992, pp. 207–210.

[94] Sinclair, C., and S. Nightingale, "An Equivalent Model for the Coplanar Waveguide Step Discontinuity," *IEEE MTT-5 Digest*, 1992, pp. 1461–1464.

[95] Naghed. M., et al., "A New Method for the Calculation of the Equivalent Inductances of Coplanar. Waveguide Discontinuities," *IEEE MTT-S Digest*, 1991, pp. 747–750.

[96] Rittweger, M., et al., "Full-Wave Analysis of Coplanar Discontinuities Considering Three-Dimensional Bond Wires," *IEEE MTT-S Digest*, 1991, pp. 465–468.

[97] Beilenhoff K., et al., "Analysis of T-Junctions for Coplanar MMICs," *IEEE MTT-S Digest*, 1994, pp. 1301–1304.

[98] Dib N., et al., "Analysis of Shielded CPW Discontinuities with Air Bridges: *IEEE MTT-S Digest*, 1991, pp. 469–472.

[99] Rittweger, M., et al., "FuIl-Wave Analysis of a Modified Coplanar Air Bridge T-Junction," *Proc. 21st European Microwave Conf.*, 1991, pp. 993–998.

[100] Dib, N., and L. P. Katehi, "Modeling of Shielded CPW Discontinuities Using the Space Domain Integral Equation Method (SDIE)," *J. Electromagnetic Waves Appl.*, Vol. 5, Nos 4/5, 1991, pp. 503–523.

[101] Dib, N., and L. P. Katehi, "The Effect of Mitering on CPW Discontinuities," *Proc. 21st European Microwave Conf.*, 1991, pp. 223–228.

[102] Harokopus, W., and L. P. Katehi, "Radiation Loss from Open Coplanar Waveguide Discontinuities," *IEEE MTT-S Digest*. 1991, pp. 743–746.

[103] Rahman, K. M., and C. Nguyen, "On the Analysis of Single- and Multiple-Step Discontinuities for a Shielded Three-Layer Coplanar Waveguide," *IEEE Trans.*, Vol. MTT-41, 1993, pp. 1484–1488.

[104] Chiu, C. W., and R. B. Wu, "A Moment Method Analysis for Coplanar Waveguide Discontinuity Inductances," *IEEE Trans.*, Vol. MTT-41, 1998, pp. 1511–1514.

[105] Radisic, V., et al., "Experimentally Verifiable Modeling of Coplanar Waveguide Discontinuities," *IEEE Trans.*, Vol. MTT-41, 1993, pp. 1524–1588.

[106] Jin, H., and R. Vahldieck, "Full-Wave Analysis of Coplanar Waveguide Discontinuities Using the Frequency Domain TLM Method," *IEEE Trans.*, Vol. MTT-41, 1995, pp. 1588–1542.

[107] Dib, N. I., et al., "Characterization of Asymmetric Coplanar Waveguide Discontinuities," *IEEE Trans.*, Vol. MTT-41, 1998, pp. 1549–1558.

[108] Chung, S. J., and T. R. Chrang,. "Full-Wave Analysis of Discontinuities in Conductor-Backed Coplanar Waveguides Using the Method of Lines," *IEEE Trans.*, Vol. MTT-41, 1993, pp. 1601–1605.

[109] Tran, A. M., and T. ltoh, "Full-Wave Modeling of Coplanar Waveguide Discontinuities with Finite Conductor Thickness," *IEEE Trans.*, Vol. MTT-41, 1998, pp. 1611–1615.

[110] Alesaandri, F., et al., "A 3–D Mode Matching Technique for the Efficient Analysis of Coplanar MMIC Discontinuities with Finite Metalization Thickness," *IEEE Trans.*, Vol. MTT-41, 1993, pp. 1625–1629.

[111] Yu, M., et al., "Theoretical and Experimental Characterization of Coplanar Waveguide Discontinuities," *IEEE Trans.*, Vol. MTT-41, 1993, pp. 1688–1641.

[112] Wu, K., et al., "Rigorous Analysis of 3–D Planar Circuit Discontinuities Using the Space-Spectral Domam Approach (SSDA)," *IEEE Trans.*, MTT-40, 1992, pp. 1475–1483.

[113] Kulke, R., and T. Sporkmann, "Coplanar Waveguide Elements for a European CAD Environment," *Proc. 23rd European Microwave Conf.*, 1993, pp. 209–211.

[114] Pogatzki, P., and O. Kramer, "A Coplanar Element Library for the Accurate CAD of (M) MICs," *Microwave Eng. Europe*, December/January 1994.

[115] Pogatzki, P., et al., "A Comprehensive Evaluation of Quasi-Static 3D-FD Calculation for More Than 14 CPW Structures—Lines, Discontinuities and Lumped Elements," *IEEE MTT-S Digest*, 1994, pp. 1289–1292.

[116] Houdart, M., "Coplanar Lines: Applications to Broadband Microwave Integrated Circuits," *Proc. Sixth European Microwave Conference* (Rome), 1976, pp. 49–53.

[117] Saad, T. S., et al. (Eds.), *Microwave Engineers Handbook*, Vol. I, Dedham, MA: Artech House, Inc., 1971, p. 114.

[118] Simons, R. N., *Coplanar Waveguide Circuits, Components, and Systems*, New York: John Wiley, 2001.

[119] Wolff, I., *Coplanar Microwave Integrated Circuits*, New York: John Wiley, 2006.

[120] Merkee, J., "A DC to 20GHz Thin Film Signal Sampler for Microwave Instrumentation," *H. P. J.*, Vol. 24, 1973, pp. 10–13.

[121] Hoss, B., and F. Reisch, "Behind the Design of a Portable Analyser," *Microwaves*, Vol. 14, January 1975, pp. 36–40.

[122] Dickens, L. E., and D. W. Maki, "An Integrated-Circuit Balanced Mixer Image and Sum Enhanced," *IEEE Trans. Microwave Theory Tech.*, Vol. 23, 1975, pp. 276–281.

[123] Dib, N., "Comprehensive Study of CAD Models of Several Coplanar Waveguide (CPW) Discontinuities," *IEE Proc.-Microw. Ant. Propagat.*, Vol. 152, April, 2005, pp. 69–76.

[124] Mao, M.-H., et. al., "Characterization of Coplanar Waveguide Open End Capacitance—Theory and Experiment," *IEEE Trans. Microwave Theory Tech.*, Vol. 42, 1994, pp. 1016–1024.

[125] Getsinger, W. J., "End-Effects in Quasi-TEM Transmission Lines," *IEEE Trans. Microwave Theory Tech.*, Vol. 41, 1993, pp. 666–672.

[126] Weller, T. M., et al., "Three-Dimensional High-Frequency Distribution Networks—Part I: Optimization of CPW Discontinuities," *IEEE Trans. Microwave Theory Tech.*, Vol. 48, 2000, pp. 1635–1642.

[127] Watson, P. M., and K. C. Gupta, "EM-ANN Modeling and Optimum Chamfering of 90 degree Bends with Air-Bridges," *IEEE MTT-S Int.Microwave Symp. Digest*, 1996, pp. 1603–1606.

[128] Simons, R. N., N. I. Dib., and L. P. B. Katahi, "Modeling of Coplanar Stripline Discontinuities," *IEEE Trans. Microwave Theory Tech.*, Vol. 44, 1996, pp. 711–716.

[129] L. Zhu, and K. Wu, "Field-Extracted Lumped-Element Models of Coplanar Stripline Circuits and Discontinuities for Radio-Frequency Design and Optimization," *IEEE Trans. Microwave Theory Tech.*, Vol. 50, 2002, pp. 1207–1215.

[130] Chiu, C. W., "Equivalent Circuit Parameters of Coplanar Stripline Discontinuities," *IEEE Proc.- Microw. Ant. Propagat.*, Vol. 149, Feb., 2002, pp. 11–16.

[131] Wang., C.H., et al., "An Input-Impedance-Based Circuit Model for Coplanar Waveguide-to-Slotline T-Junction," *IEEE Trans. Microwave Theory Tech.*, Vol. 52, 2004, pp. 1585–1591.

[132] Chen, E., and S. Y. Chou, "Characteristics of Coplanar Transmission Lines on Multilayer Substrates: Modeling and Experiments," *IEEE Trans. Microwave Theory Tech.*, Vol. 45, 1997, pp. 939–945.

[133] Ashesh, C. B., *Analysis and Design of Symmetric Coplanar Lines with Thick Conductors*, Ph.D. dissertation, 2007, Indian Institute of Technology, Kharagpur (India).

[134] Fang, S.J., and Wang, B.S., "Analysis of Asymmetric Coplanar Waveguide with Conductor Backing," *IEEE Trans. Microwave Theory Tech.*, Vol. 47, 1999, pp. 238–240.

[135] Zhu, N. H., Z. Q. Wang, and W. Lin, "On the Accuracy of Analytical Expressions for Calculating the Parameters of Coplanar Strips on a Finitely Thick Substrate," *Microwave Optical Tech., Lett.*, Vol. 8, 1995, pp. 160–164.

[136] Cohn, S. B., "Thickness Corrections for Capacitive Obstacles and Strip Conductors," *IRE Trans. Microwave Theory Tech.*, Vol. MTT-8, Nov.,1960, pp. 638–644.

[137] Holloway, C. L., and E. F. Kuester, "A Quasi-Closed Form Expression for the Conductor Loss of CPW Lines, with an Investigation of Edge Shape Effects," *IEEE Trans. Microwave Theory Tech.*, Vol. 43, 1995, pp. 2695–2701.

[138] Kim, Y. G., et al., "A New Ultra-Wideband Microstrip-to-CPS Transition," 2007 *IEEE MTTS Int. Microwave Symp. Digest*, pp. 1563–1566.

[139] Chiu, T., "A Buildind-Block Design Scheme for Planar Transmission-Line Transitions," *IEE Proc. Microwave Ant. Propagat.*, Vol. 150, 2003, pp. 405–410.

[140] Lim, T. B., and L. Zhu, "Compact Microstrip-to-CPS Transition for UWB Application," *2008 Int. Microwave Symp. Workshop (Art of Miniaturizing RF and Microwave Passive Components)*, pp. 153–156.

[141] Tu, W. H., and K. Chang, "Wide-Band Microstrip-to-Coplanar Stripline/Slotline Transitions," *IEEE Transac. Microwave Theory Tech.*, Vol. 54, 2006, pp. 1084–1089.

[142] Kim, Y. G., K. W. Kim, and Y. K. Cho, "A Planar Ultra-wideband Balanced Doubler," *2008 IEEE MTTS Int. Microwave Symp. Digest*, pp. 1243–1246.

[143] Prieto, D., et al., "CPS Structure Potentialities for MMICs: A CPS/CPW Transition and Bias Network," *1998 IEEE MTT-S Digest*, pp. 111–114.

[144] Kim, S., et al, "Ultra-Wideband (from DC to 110 GHz) CPW to CPS Transition," *Electron. Lett.*, Vol. 38, 2002, pp.622–623.

[145] Wu, P., Z. Wang, and Y. Zhang, "Wideband Planar Balun Using Microstrip to CPW and Microstrip to CPS Transitions," *Electron. Lett.*, Vol. 46, 2010, pp. 1611–1613.

CHAPTER 8

Coupled Microstrip Lines

8.1 Introduction

A "coupled line" configuration consists of two transmission lines placed parallel to each other and in close proximity as shown in Figure 8.1. In such a configuration there is a continuous coupling between the electromagnetic fields of the two lines. Coupled lines are utilized extensively as basic elements for directional couplers, filters, and a variety of other useful circuits.

Because of the coupling of electromagnetic fields, a pair of coupled lines can support two different modes of propagation. These modes have different characteristic impedances. The velocity of propagation of these two modes is equal when the lines are imbedded in a homogeneous dielectric medium (as, for example, in a triplate stripline structure). This is a desirable property for the design of circuits such as directional couplers and filters. However, for transmission lines such as coupled microstrip lines, the dielectric medium is not homogeneous. A part of the field extends into the air above the substrate. This fraction is different for the two modes of coupled lines. Consequently, the effective dielectric constants (and the phase velocities) are not equal for the two modes. This nonsynchronous feature deteriorates the performance of circuits using these types of coupled lines.

When the two conductors of a coupled line pair are identical we have a symmetrical configuration. This symmetry is very useful for simplifying the analysis and design of such coupled lines. If the two lines do not have the same impedance, the configuration is called asymmetric.

For the lines operating in the TEM mode or when the analysis can be based on quasi-static approximation, the properties of coupled lines can be determined from the self- and mutual inductances and capacitances for the lines. In the case of lines operating in the non-TEM mode (for example, coupled slotlines), a fullwave analysis is needed for the two modes of propagation.

In this chapter, coupled microstrip lines are discussed. The configuration for these lines is shown in Figure 8.1. Some of the important techniques for analyzing coupled lines are outlined. Coupled mode formulation and the even- and odd-mode method are described. Both quasi-static and fullwave analyses are used to evaluate the characteristics of symmetric and asymmetric coupled microstrip lines. The effects of nonzero strip thickness, dispersion, enclosure, fabrication tolerances, dielectric overlay, and dielectric anisotropy on the characteristics are presented Methods of measuring the characteristics of coupled microstrip lines are included.

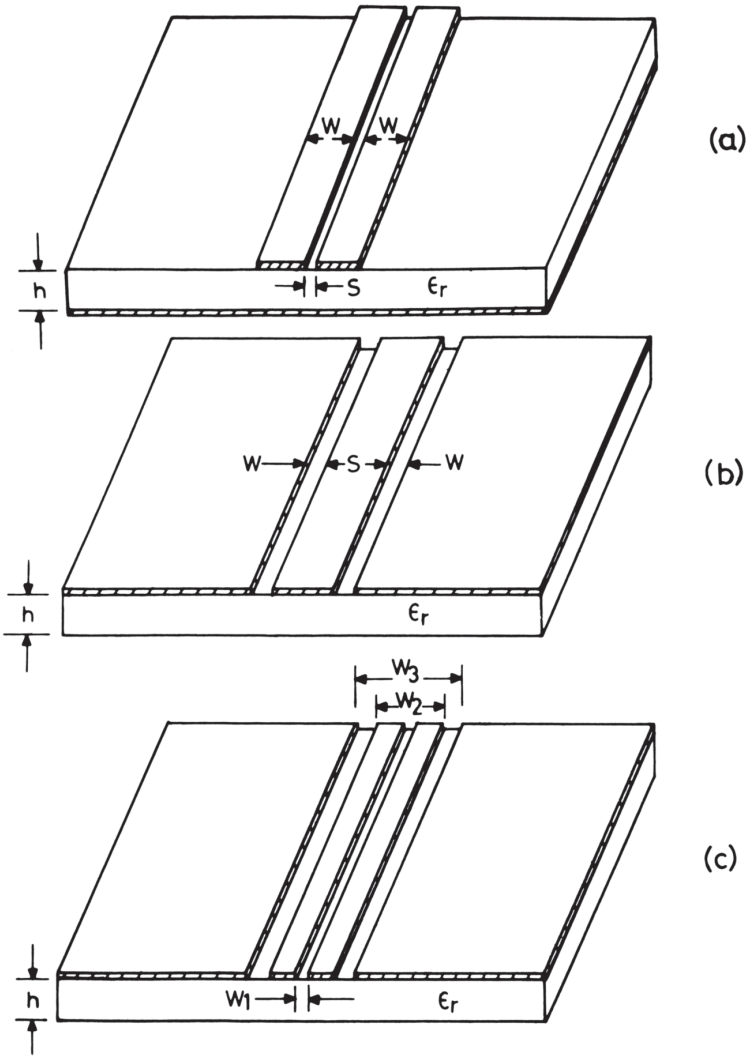

Figure 8.1 Configuration of coupled lines: (a) coupled microstrips, (b) coupled slotlines, and (c) coupled coplanar waveguides.

The last section of this chapter contains a discussion of discontinuities in coupled microstrip lines.

8.2 General Analysis of Coupled Lines

8.2.1 Methods of Analysis

Several analytical techniques are available for determining the propagation characteristics of the coupled lines shown in Figure 8.1(a). The four different methods

that are generally employed are the even- and odd-mode method [1], the coupled mode formulation [2, 3], the graph transformation technique [4], and the congruent transformation technique [5, 6].

The even- and odd-mode method is the most convenient way of describing the behavior of symmetrical coupled lines. In this method wave propagation along a coupled pair of lines is expressed in terms of two modes corresponding to an even or an odd symmetry about a plane that can, therefore, be replaced by a magnetic or electric wall for the purpose of analysis.

In the coupled mode approach, the wave propagation is expressed in terms of the modes of propagation on individual uncoupled lines modified by the coupling because of mutual capacitances and inductances. This approach, therefore, provides an insight into the mechanism of coupling. The method is quite general and is applicable to asymmetric coupled lines also. This approach finds applications in all types of coupled systems used in various disciplines.

The other two approaches employ the representation of coupled line systems in terms of equivalent networks. The "graph transformation technique" involves the use of a graph equivalent to the general coupled transmission line network for analysis [4]. The use of Richards's transformation [7] allows the coupled line structures to be treated in exactly the same manner as lumped networks.

The equivalent circuit for the coupled lines can also be established using the congruent transformation technique [8]. This is believed to be a powerful method for establishing coupled line properties when there is a large number of lines coupled together. Using this technique, n-conductor coupled transmission lines can be reduced to a set of n decoupled transmission lines connected to two congruent transformers.

Graph transformation and congruent transformation methods are very useful when one deals with a number of lines (more than two) coupled together. Of the remaining two approaches, the coupled mode technique is more powerful as it can be applied to asymmetric coupled structures also. This approach is discussed in Section 8.2.2 and the even- and odd-mode method is discussed in Section 8.2.3.

8.2.2 Coupled Mode Approach [9–11]

In this approach coupled lines are characterized by the characteristic impedances (or admittances) and phase velocities for the two modes. These two modes are obtained by considering the effect of the self- and the mutual inductances and capacitances on the modes in the individual uncoupled lines.

For coupled mode analysis, the voltage on one line is written in terms of the currents on both lines and the self- and mutual impedances. Similarly the current is written in terms of voltages and admittances. Eliminating currents or voltages yields the coupled equations. The solution of these coupled equations determines the propagation constants for the two modes.

The coupled mode analysis for coupled lines with unequal impedances, shown in Figure 8.2, is described next.

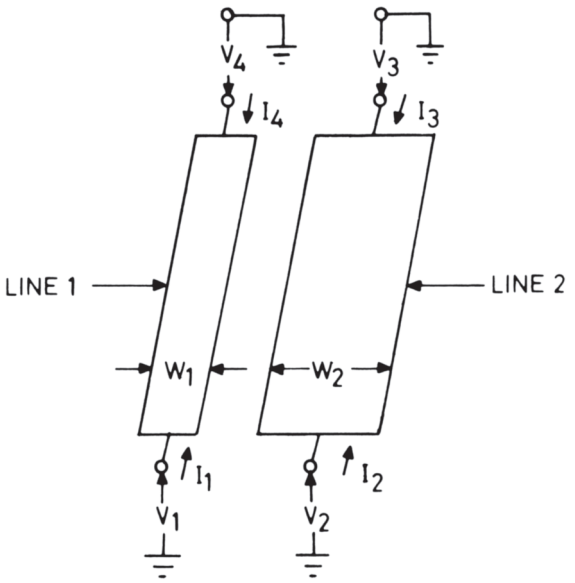

Figure 8.2 A pair of coupled lines with unequal impedances.

Analysis

The behavior of two lossless coupled transmission lines is described in general by the following set of differential equations:

$$-\frac{dv_1}{dz} = Z_1 i_1 + Z_m i_2 \tag{8.1}$$

$$-\frac{dv_2}{dz} = Z_m i_1 + Z_2 i_2 \tag{8.2}$$

$$-\frac{di_1}{dz} = Y_1 v_1 + Y_m v_2 \tag{8.3}$$

$$-\frac{di_2}{dz} = Y_m v_1 + Y_2 v_2 \tag{8.4}$$

where Z_j, Y_j ($j = 1, 2$) are self-impedances and self-admittances per unit length of lines 1 and 2 and Z_m and Y_m are mutual impedance and mutual admittance per unit length, respectively. Voltages and currents, which are functions of z, are represented by v_k and i_k ($k = 1, 2$), respectively. A time variation $e^{j\omega t}$ is assumed.

Eliminating i_1 and i_2 from (8.1) to (8.4) gives the following set of coupled equations for the voltages v_1 and v_2:

$$\frac{d^2 v_1}{dz^2} - a_1 v_1 - b_1 v_2 = 0 \tag{8.5}$$

$$\frac{d^2 v_2}{dz^2} - a_2 v_2 - b_2 v_1 = 0 \tag{8.6}$$

where

$$\begin{aligned} a_1 &= Y_1 Z_1 + Y_m Z_m \\ b_1 &= Z_1 Y_m + Y_2 Z_m \\ a_2 &= Y_2 Z_2 + Y_m Z_m \\ b_2 &= Z_2 Y_m + Y_1 Z_m \end{aligned} \tag{8.7}$$

The coefficients a_1, a_2, b_1, and b_2 are constants.

Assuming a variation of the type $v(z) = v_0\, e^{-\gamma z}$ for the voltages v_1 and v_2, the coupled equations (8.5) and (8.6) reduce to the eigenvalue equation

$$\left[\gamma^4 - \gamma^2 (a_1 + a_2) + a_1 a_2 - b_1 b_2\right] v_0 = 0 \tag{8.8}$$

The solution of (8.8) leads to the following four roots for γ:

$$\gamma_{1,2} = \pm\gamma_c \quad \text{and} \quad \gamma_{3,4} = \pm\gamma_\pi \tag{8.9}$$

where

$$\gamma_{c,\pi}^2 = \frac{a_1 + a_2}{2} \pm \frac{1}{2}\left[(a_1 - a_2)^2 + 4 b_1 b_2\right]^{1/2} \tag{8.10}$$

The subscripts "c" and "π" refer to the c and π modes for asymmetric coupled lines. The propagation constants for these modes, γ_c and γ_π, correspond to in-phase and anti-phase waves, which reduce to even- and odd-mode waves, respectively, for symmetrical lines. The roots with plus and minus signs in (8.9) represent waves travelling in the $+z$- and $-z$-directions, respectively.

The ratio of voltages v_2 and v_1 on the two lines for the c and π modes is obtained from (8.5), (8.6), and (8.10) and is given as

$$\frac{v_2}{v_1} = \frac{\gamma^2 - a_1}{b_1} = \frac{b_2}{\gamma^2 - a_2} \tag{8.11}$$

If the corresponding ratios for the c and π modes are represented by R_c and R_π, then

$$R_c \left(= \frac{v_2}{v_1} \text{ for } \gamma = \pm\gamma_c \right) = \frac{1}{2b_1}\left[(a_2 - a_1) + \left\{(a_2 - a_1)^2 + 4 b_1 b_2\right\}^{1/2}\right] \tag{8.12}$$

and

$$R_\pi \left(= \frac{v_2}{v_1} \text{ for } \gamma = \pm\gamma_\pi \right) = \frac{1}{2b_1}\left[(a_2 - a_1) - \left\{(a_2 - a_1)^2 + 4 b_1 b_2\right\}^{1/2}\right] \tag{8.13}$$

It may be observed from (8.12) and (8.13) that R_c is positive real and R_π is negative real, thus representing in-phase and anti-phase waves.

In terms of the four waves, with propagation constants $\pm\gamma_c$ and $\pm\gamma_\pi$, the general solution for the voltages on the two lines may be written as

$$v_1 = A_1 e^{-\gamma_c z} + A_2 e^{\gamma_c z} + A_3 e^{-\gamma_\pi z} + A_4 e^{\gamma_\pi z} \tag{8.14}$$

$$v_2 = R_c\left(A_1 e^{-\gamma_c z} + A_2 e^{\gamma_c z}\right) + R_\pi\left(A_3 e^{-\gamma_\pi z} + A_4 e^{\gamma_\pi z}\right) \tag{8.15}$$

The currents i_1 and i_2 are obtained by substituting the corresponding voltages v_1 and v_2 from (8.14) and (8.15) in (8.1) and (8.2) and may be written as

$$i_1 = Y_{c1}\left(A_1 e^{-\gamma_c z} - A_2 e^{\gamma_c z}\right) + Y_{\pi 1}\left(A_3 e^{-\gamma_\pi z} - A_4 e^{\gamma_\pi z}\right) \tag{8.16}$$

$$i_2 = Y_{c2}R_c\left(A_1 e^{-\gamma_c z} - A_2 e^{\gamma_c z}\right) + Y_{\pi 2}R_\pi\left(A_3 e^{-\gamma_\pi z} - A_4 e^{\gamma_\pi z}\right) \tag{8.17}$$

where Y_{c1}, Y_{c2}, $Y_{\pi 1}$, and $Y_{\pi 2}$ are the characteristic admittances of lines 1 and 2 for the two modes. These are given by

$$Y_{c1} = \gamma_c \frac{Z_2 - Z_m R_c}{Z_1 Z_2 - Z_m^2} = \frac{1}{Z_{c1}} \tag{8.18}$$

$$Y_{c2} = \frac{\gamma_c}{R_c}\frac{Z_1 R_c - Z_m}{Z_1 Z_2 - Z_m^2} = \frac{1}{Z_{c2}} \tag{8.19}$$

Similar relations hold for the π mode. Substituting the value of R_c in (8.18) and (8.19) gives

$$\frac{Y_{c1}}{Y_{c2}} = -R_c R_\pi = \frac{Y_{\pi 1}}{Y_{\pi 2}} \tag{8.20}$$

The above analysis has been carried out in terms of the two independent modes of propagation termed "c" and "π" modes with propagation constants γ_c and γ_π. The voltages v_1 and v_2 on the two lines are related through $v_2/v_1 = R_c$ and R_π. The corresponding ratios for the currents are given by $i_2/i_1 = -1/R_\pi$ and $-1/R_c$, respectively. For symmetric lines, "c" and "π" modes reduce to even and odd modes, respectively.

Symmetric Lines

For the case of symmetric lines, $a_2 = a_1$ and $b_2 = b_1$. Therefore, (8.12) and (8.13) give for v_2/v_1

$$\begin{aligned} v_2/v_1 &= R_c = +1 \quad \text{for c mode (even mode)} \\ v_2/v_1 &= R_\pi = -1 \quad \text{for } \pi \text{ mode (odd mode)} \end{aligned} \tag{8.21}$$

Also, (8.16) and (8.17) yield

$$\begin{aligned} i_2/i_1 &= +1 \quad \text{for c mode (even mode)} \\ i_2/i_1 &= -1 \quad \text{for } \pi \text{ mode (odd mode)} \end{aligned} \tag{8.22}$$

Evaluation of Characteristics for c and π Modes

As discussed above, asymmetric coupled lines can be represented in terms of two modes called c and π modes. The phase constants and the characteristic impedances of these modes are related to the line constants in the following manner [10]:

$$\gamma_{c,\pi,} = j\beta_{c,\pi,} = j\frac{\omega}{\sqrt{2}}\Big[L_1C_1 + L_2C_2 - 2L_mC_m \pm\sqrt{\left(L_2C_2 - L_1C_1\right)^2 + 4\left(L_mC_1 - L_2C_m\right)\left(L_mC_2 - L_1C_m\right)}\Big]^{1/2} \tag{8.23}$$

$$Z_{c1} = \frac{\omega}{\beta_c}\left(L_1 - \frac{L_m}{R_\pi}\right) = \frac{\beta_c}{\omega}\left(\frac{1}{C_1 - R_cC_m}\right) \tag{8.24}$$

$$Z_{\pi 1} = \frac{\omega}{\beta_\pi}\left(L_1 - \frac{L_m}{R_c}\right) = \frac{\beta_\pi}{\omega}\left(\frac{1}{C_1 - R_\pi C_m}\right) \tag{8.25}$$

and

$$R_{c,\pi} = \frac{L_2C_2 - L_1C_1 \pm \sqrt{\left(L_2C_2 - L_1C_1\right)^2 + 4\left(L_mC_2 - L_1C_m\right)\left(L_mC_1 - L_2C_m\right)}}{2\left(L_mC_2 - L_1C_m\right)} \tag{8.26}$$

Self-capacitances C_1 and C_2, self-inductances L_1 and L_2 as well as mutual capacitance C_m and mutual inductance L_m can be determined from quasi-static analysis.

8.2.3 Even- and Odd-Mode Approach

Thus far the analysis of coupled lines has been very general. Now we will restrict our attention to the case of symmetric coupled lines, that is, identical lines of equal characteristic impedances.

It was pointed out earlier that the c and π modes reduce to the even and odd modes, respectively, for symmetric coupled lines. The propagation constants for these modes are given by

$$\gamma_{e,o} = \gamma_{c,\pi} = \left[\left(Y_0 \pm Y_m\right)\left(Z_0 \pm Z_m\right)\right]^{1/2} \tag{8.27}$$

where

$$Y_0 = Y_1 \text{ or } Y_2 \qquad Z_0 = Z_1 \text{ or } Z_2$$

In terms of line constants, the characteristics of even and odd modes can be obtained from (8.23) to (8.25) by substituting $L_1 = L_2 = L_o$ and $C_1 = C_2 = C_o$. The expressions are given as

$$\beta_{e,o} = \omega\left[L_oC_o - L_mC_m \pm \left(L_mC_o - L_oC_m\right)\right]^{1/2} \tag{8.28}$$

$$Z_{0e} = \frac{\omega}{\beta_e}\left(L_o + L_m\right) = \frac{\beta_e}{\omega}\left(\frac{1}{C_o - C_m}\right) \qquad Y_{0e} = \frac{1}{Z_{0e}} \tag{8.29}$$

$$Z_{0o} = \frac{\omega}{\beta_o}\left(L_o - L_m\right) = \frac{\beta_o}{\omega}\left(\frac{1}{C_o + C_m}\right) \qquad Y_{0o} = \frac{1}{Z_{0o}} \tag{8.30}$$

where $\beta_{e,o}$ are the phase constants of lossless coupled lines given by $\gamma_{e,o} = j\beta_{e,o}$. The lines are characterized by inductance per unit length L_o and capacitance per unit length C_o. The mutual inductance is L_m and the mutual capacitance is C_m.

Alternatively, the propagation constants may be written in terms of the phase constants of the lines and the coefficients of inductive and capacitive couplings k_L and k_C. If we define [12]

$$k_L = L_m/L_o \tag{8.31}$$

$$k_C = C_m/C_o \tag{8.32}$$

and

$$\beta_o = \omega\sqrt{L_o C_o} \tag{8.33}$$

we can write (8.28) as

$$\beta_{e,o} = \beta_{eff}\sqrt{1 \pm \delta} \tag{8.34}$$

where effective propagation constant β_{eff} is given by

$$\beta_{eff} = \beta_o\left(1 - k_L k_C\right)^{1/2} \tag{8.35}$$

and

$$\delta = \frac{k_L - k_C}{1 - k_L k_C} \tag{8.36}$$

In (8.34), positive and negative signs correspond to the even and odd modes, respectively.

For coupled lines propagating TEM modes, coupled mode parameters are normally expressed in terms of even- and odd-mode capacitances C_e^a, C_o^a for the air dielectric ($\varepsilon_r = 1$) structure and those with dielectric substrate $C_e(\varepsilon_r)$, $C_o(\varepsilon_r)$. These are related to self- and mutual inductances and capacitances through the equations

$$L_o = \frac{\mu_0\varepsilon_0}{2}\left\{\frac{1}{C_o^a} + \frac{1}{C_e^a}\right\} \tag{8.37}$$

$$L_m = \frac{\mu_0\varepsilon_0}{2}\left\{\frac{1}{C_e^a} - \frac{1}{C_o^a}\right\} \tag{8.38}$$

$$C_o = \frac{1}{2}\left[C_o(\varepsilon_r) + C_e(\varepsilon_r)\right] \tag{8.39}$$

and

$$C_m = \frac{1}{2}\left[C_o(\varepsilon_r) - C_e(\varepsilon_r)\right] \tag{8.40}$$

The coupling coefficients k_L and k_C are defined by

$$k_L = \frac{L_m}{L_o} = \frac{C_o^a - C_e^a}{C_o^a + C_e^a} \tag{8.41}$$

and

$$k_C = \frac{C_m}{C_o} = \frac{C_o(\varepsilon_r) - C_e(\varepsilon_r)}{C_o(\varepsilon_r) + C_e(\varepsilon_r)} \tag{8.42}$$

The effective propagation constant, β_{eff}, can be expressed as

$$\beta_{eff} = \frac{\omega}{c}\sqrt{\varepsilon_{re}}\sqrt{\frac{1 - k_L k_C}{1 - k_L^2}} \tag{8.43}$$

where

$$\varepsilon_{re} = \frac{C_o(\varepsilon_r) + C_e(\varepsilon_r)}{C_o^a + C_e^a} \tag{8.44}$$

and impedances can be written as

$$Z_{0e} = \frac{\omega}{\beta_e}\frac{\mu_0\varepsilon_0}{C_e^a} \tag{8.45}$$

$$Z_{0o} = \frac{\omega}{\beta_o}\frac{\mu_0\varepsilon_0}{C_o^a} \tag{8.46}$$

with

$$\beta_{e,o} = \omega\sqrt{\mu_0\varepsilon_0}\sqrt{\frac{C_{e,o}(\varepsilon_r)}{C_{e,o}^a}} \tag{8.47}$$

The methods for evaluating the even- and odd-mode capacitances will be described in Section 8.3 and closed-form expressions will be presented in Section 8.5.

8.3 Characteristics of Coupled Microstrip Lines

The methods of analysis discussed in the previous section are quite general. They may be applied to coupled lines in a homogeneous medium such as coupled striplines or coupled lines in an inhomogeneous medium such as coupled microstrip lines. Whereas coupled striplines are nondispersive in nature, coupled microstrip lines exhibit dispersive characteristics at higher frequencies. Quite often, coupled microstrip lines are used at frequencies where quasi-static analysis holds good and dispersion effects are negligible. Nevertheless, fullwave analysis helps in determining the frequency range of validity of quasi-static analysis. Both the quasi-static analysis as well as fullwave analysis for coupled microstrip lines with equal impedances are described in this section. The geometry of coupled microstrip lines is shown in Figure 8.3(a), and the field distributions for even and odd modes are given in Figure 8.3(b).

8.3.1 Quasi-Static Analysis

Almost all the methods described in Chapter 1 for the quasi-static analysis of a microstrip have also been employed to calculate even- and odd-mode capacitances of coupled microstrip lines. The conformal transformation method does not yield a simple closed-form solution in this case [13]. Green's function technique has been described by Bryant and Weiss [14,15]. The variational method in the space domain has been used by Krage and Haddad [12] and Bergandt and Pregla [16] to determine the upper bound on capacitances for the coupled line configuration enclosed in a box. The variational method in FTD has been described in [17].

Variational Method in Space Domain [12, 16]

In this method scalar potential functions, which are solutions of Laplace's equation, are expanded in a Fourier series. The Fourier coefficients are determined from the continuity conditions of potential functions and the stationary property of the stored electric energy with respect to Fourier coefficients. Once the potential functions for even and odd modes are known, these can be used to determine the capacitances for these modes.

For the purpose of analysis, the coupled microstrip configuration can be divided into four separate regions as shown in Figure 8.3(a).

Potentials are assumed to be $\phi = V_1$ and $\phi = V_2$ on the left and right strips, respectively. The outer conducting walls are at $\phi = 0$ potential. The field configuration in each of the four regions is obtained from a solution of Laplace's equation

$$\nabla^2 \phi_i = 0 \qquad i = 1, 2, 3, 4 \tag{8.48}$$

The potentials ϕ_i that satisfy (8.48) and the boundary conditions on the enclosure may be written in terms of Fourier expansions as

$$\phi_1 = \sum_{m=1}^{\infty} A_m \sinh\left(\frac{m\pi y}{H}\right)\sin\left(\frac{m\pi x}{2L}\right) \tag{8.49}$$

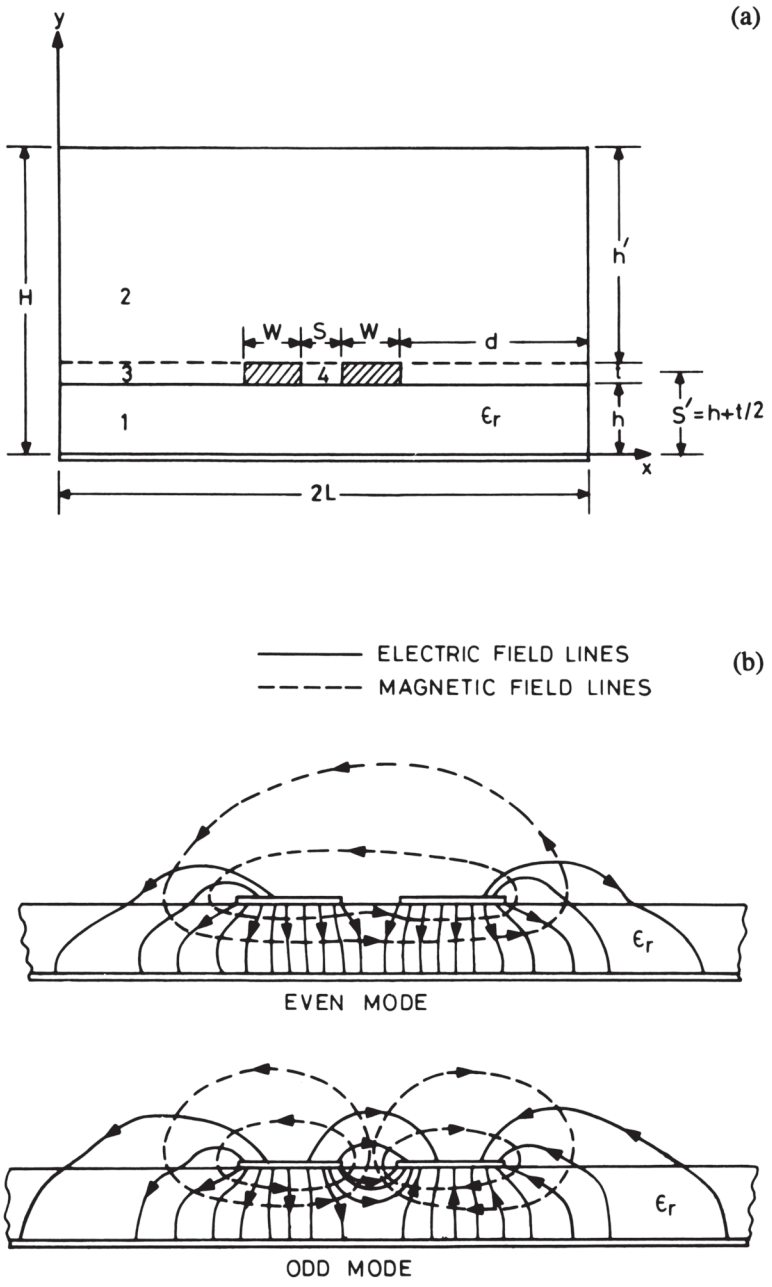

Figure 8.3 (a) Symmetric coupled microstrip lines in an enclosure and (b) even- and odd-mode field configurations in coupled microstrip lines.

$$\phi_2 = \sum_{m=1}^{\infty} B_m \sinh\frac{m\pi(H-y)}{H}\sin\left(\frac{m\pi x}{2L}\right) \tag{8.50}$$

$$\phi_3 = \sum_{m=1}^{\infty} \left\{ \left[C_m \sinh \frac{m\pi(Y - S')}{d} + D_m \cosh \frac{m\pi(Y - S')}{d} \right] \cdot \sin \frac{m\pi x}{d} + V_1 \frac{x}{d} \right\} \tag{8.51}$$

$$\phi_4 = \sum_{m=1}^{\infty} \left\{ \left[E_m \sinh \frac{m\pi(Y - S')}{S} + F_m \cosh \frac{m\pi(Y - S')}{S} \right] \cdot \sin \frac{m\pi(x - d - W)}{S} + V_1 + (V_2 - V_1)(x - d - W)/S \right\} \tag{8.52}$$

where $S' = h + t/2$ and $d = (2L - 2W - S)/2$. For the even mode $V_1 = V_2$, and $V_1 = -V_2$ for the odd mode.

The Fourier coefficients A_m, B_m, . . . , F_m are determined from the continuity of potentials at the boundaries and the stationary property of the stored electric energy with respect to Fourier coefficients. The stored energy in region i is given by

$$W_i = \frac{\varepsilon_i}{2} \iint \left[(E_{xi})^2 + (E_{yi})^2 \right] \quad dx\, dy \tag{8.53}$$

where

$$E_{xi} = -\frac{\partial \phi_i}{\partial x} \qquad E_{yi} = -\frac{\partial \phi_i}{\partial y}$$

The total capacitance of the structure may then be obtained from

$$C = \frac{2}{V^2}(W_1 + W_2 + W_3 + W_4) \tag{8.54}$$

where $V(= |V_1| = |V_2|)$ is the potential of a strip. The value of C is twice the even- or odd-mode capacitance of a single strip to ground.

Evaluation of Fourier Coefficients

The stored energy W_i can be evaluated in terms of the coefficients A_m, B_m, C_m, D_m, E_m, and F_m. The continuity of potential at $y = h$ and $y = h + t$ helps in eliminating A_m and B_m. Therefore, W_i can be written in terms of C_m, D_m, E_m, and F_m.

The stationary property of the energy W_i with respect to Fourier coefficients C_m, D_m, E_m, and F_m gives

$$\frac{\partial W_i}{\partial C_m} = 0 \qquad \frac{\partial W_i}{\partial D_m} = 0 \qquad \frac{\partial W_i}{\partial E_m} = 0 \qquad \frac{\partial W_i}{\partial F_m} = 0 \tag{8.55}$$

for $m = 1, 2, 3, \ldots, \infty$ and $i = 1, 2, 3,4$.

Equation (8.55) generates four sets of equations. Each set contains an infinite number of simultaneous, linear, inhomogeneous equations. These equations can be solved with a computer to determine the Fourier coefficients.

For an exact computation the series in (8.49) to (8.52) should be infinite. However, in practice only a finite number of terms M are used. Detailed convergence considerations indicate that [16] convergence using a finite number of terms is faster for larger values of ε_r, large W/H and small S/H. Moreover, convergence is faster for even-mode capacitance compared to odd-mode capacitance. It has also been observed that $M = 23$ gives a reasonable compromise between accuracy and computation time [16].

Variational Method in the Spectral Domain [17]

This method is similar to the variational method in the spectral domain described for a single microstrip in Chapter 1.

In this method the capacitance is calculated from a variational expression in terms of charge distribution. Evaluation is carried out in the Fourier transform domain, and the capacitance may be written as

$$\frac{\varepsilon_o}{C} = \frac{1}{\pi}\int_0^\infty G(\alpha)\tilde{\rho}^2(\alpha)\,d\alpha \tag{8.56}$$

For coupled lines (8.56) becomes

$$\frac{\varepsilon_o}{C_e} = \frac{1}{\pi}\int_0^\infty G(\alpha)\tilde{\rho}_e^2(\alpha)\,d\alpha \tag{8.57}$$

and

$$\frac{\varepsilon_o}{C_o} = \frac{1}{\pi}\int_0^\infty G(\alpha)\tilde{\rho}_o^2(\alpha)\,d\alpha \tag{8.58}$$

where

$$G(\alpha) = \frac{1}{\alpha\left[\varepsilon_r \coth(\alpha h) + \coth(\alpha h')\right]} \tag{8.59}$$

$\tilde{\rho}_e$ and $\tilde{\rho}_o$ are the Fourier transforms of charge density functions for the even and odd mode, respectively. One may use the following expressions for charge density distribution:

$$\tilde{\rho}_e(\alpha) = J_0(\alpha W/2)\cos\{\alpha(W+S)/2\}$$
$$\tilde{\rho}_o(\alpha) = jJ_0(\alpha W/2)\sin\{\alpha(W+S)/2\}$$

Discussion of Results

Figure 8.4 shows the variation of even- and odd-mode impedances with strip width W/h and gap spacing S/h for $\varepsilon_r = 9.6$ [18]. It has been assumed that the strip thick-

ness t is zero and the enclosure recedes to infinity. The effect of gap spacing and strip width on effective dielectric constants ε_{re}^{e} and ε_{re}^{o} is shown in Figure 8.5. It maybe observed from these figures that impedances decrease and effective dielectric constants increase with an increase in strip width. For a given value of S/h and W/h, the even-mode impedance and effective dielectric constant are higher than odd-mode values. Even- and odd-mode characteristics show opposite variations with an increase in S/h such that, for S/h tending to infinity, the even- and the odd-mode characteristics approach each other and are equal to single microstrip values.

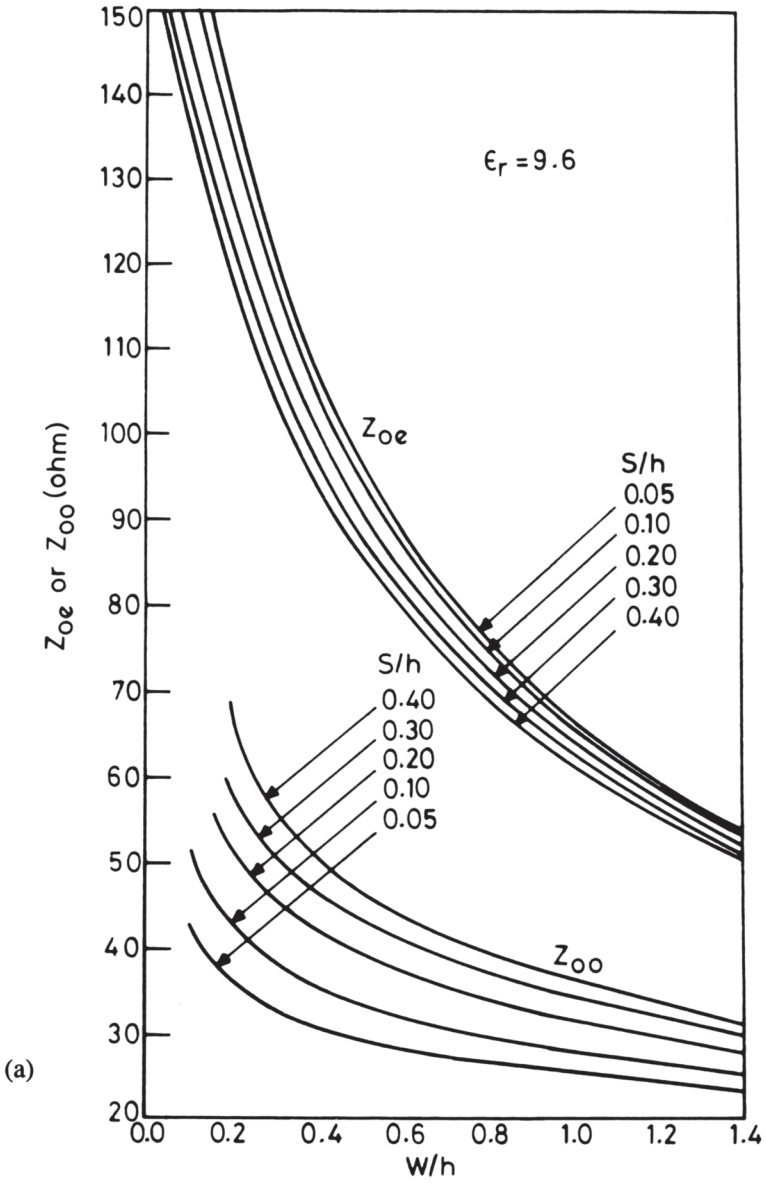

Figure 8.4 Even- and odd-mode characteristic impedances for coupled microstrip lines: (a) ε_r = 9.6, S/h = 0.05 to 0.4, W/h = 0.1 to 1.4; (b) ε_r = 9.6, S/h = 0.6 to 5.0, W/h = 0.04 to 1.4; and (c) ε_r = 9.6, S/h = 0.05 to 2.0, W/h = 1.0 to 5.0 (from [18], © 1972 Van Nostrand Reinhold. Reprinted with permission.).

For the special case of $H = 2h$ and $L = \infty$ the characteristics of coupled microstrip lines can be obtained in a simple closed-form expression by using the method of conformal transformation. In this case coupled microstrip lines behave like coupled striplines with the effective dielectric constant given by $(\varepsilon_r + 1)/2$. The even- and odd-mode impedances are obtained [19] as

$$Z_{0o} = \frac{30\pi}{\sqrt{(\varepsilon_r + 1)/2}} \frac{K(k_o')}{K(k_o)} \tag{8.60}$$

$$Z_{0e} = \frac{30\pi}{\sqrt{(\varepsilon_r + 1)/2}} \frac{K(k_e')}{K(k_e)} \tag{8.61}$$

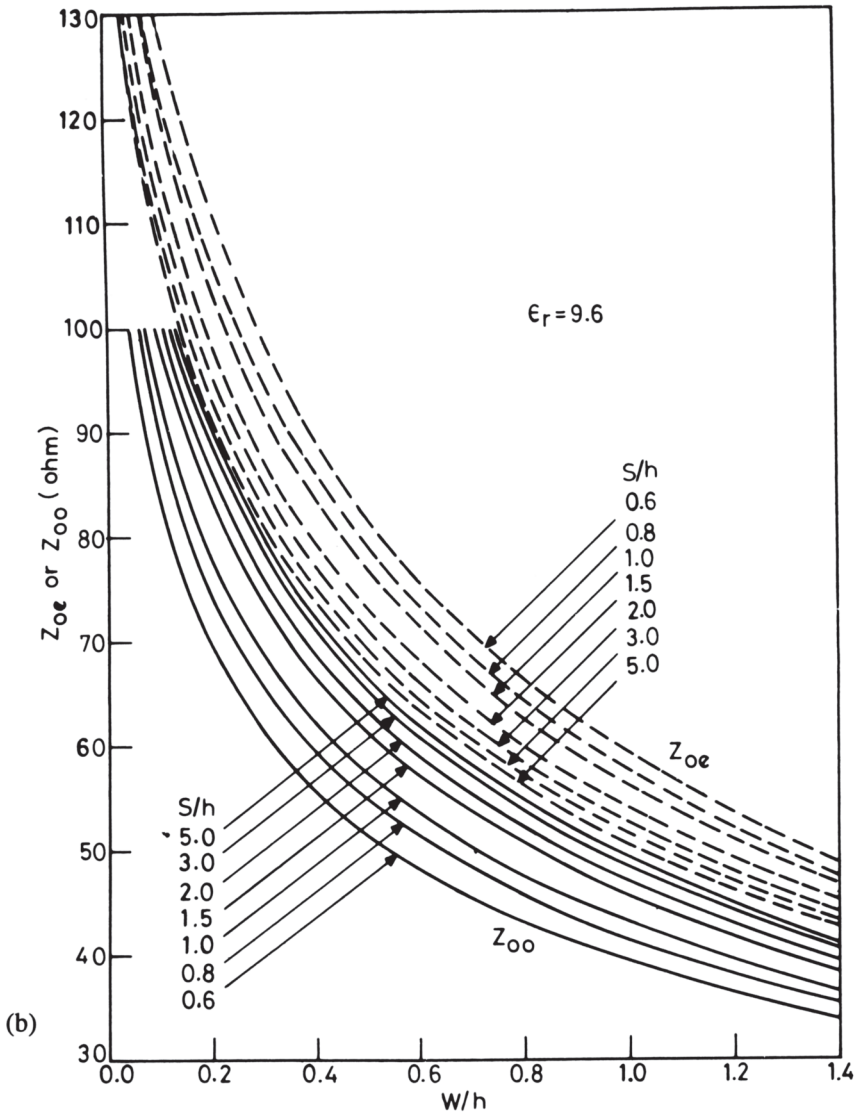

Figure 8.4 (continued).

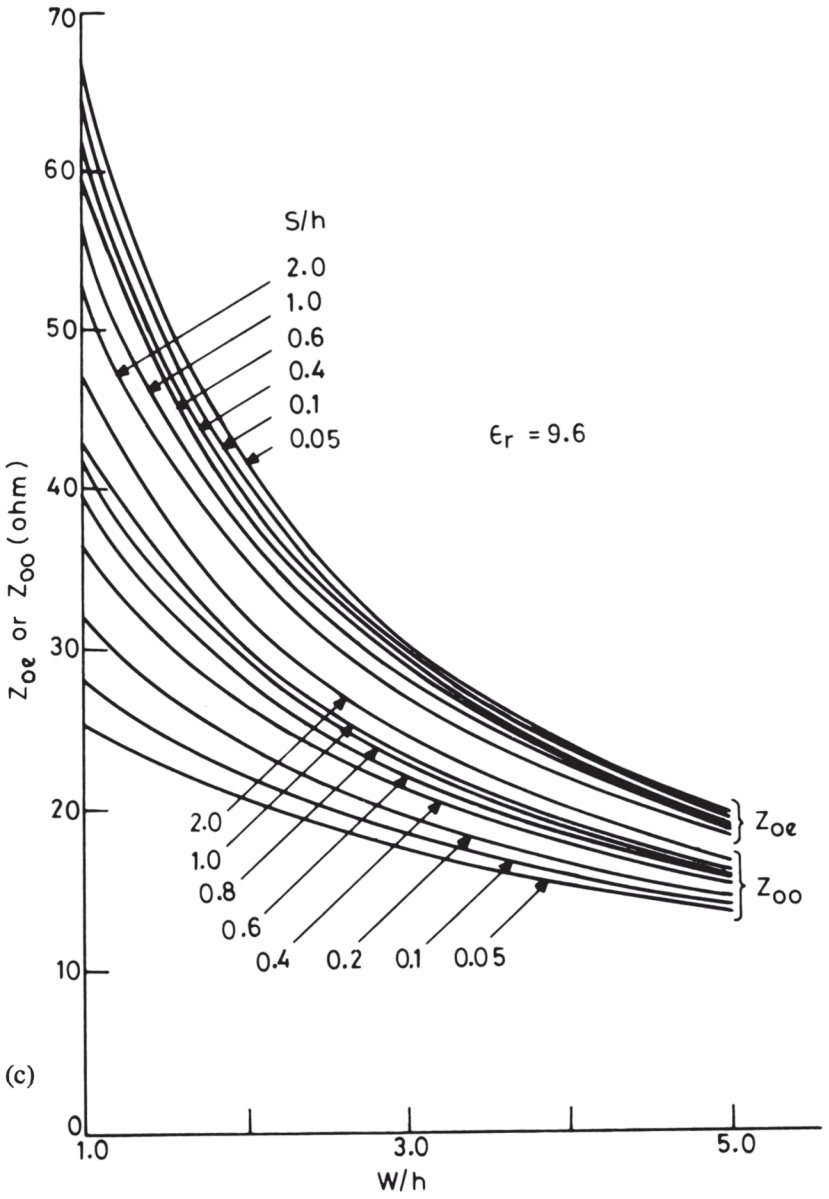

Figure 8.4 (continued).

where $K(k_e)$ and $K(k_e')$ are the elliptic function and its complement with

$$k_e = \tanh\left(\frac{\pi}{4}\frac{W}{h}\right)\tanh\left[\frac{\pi}{4}\left(\frac{W+S}{h}\right)\right] \qquad k_e'^2 = 1 - k_e^2 \tag{8.62a}$$

$$k_o = \tanh\left(\frac{\pi}{4}\frac{W}{h}\right)\coth\left[\frac{\pi}{4}\left(\frac{W+S}{h}\right)\right] \qquad k_o'^2 = 1 - k_o^2 \tag{8.62b}$$

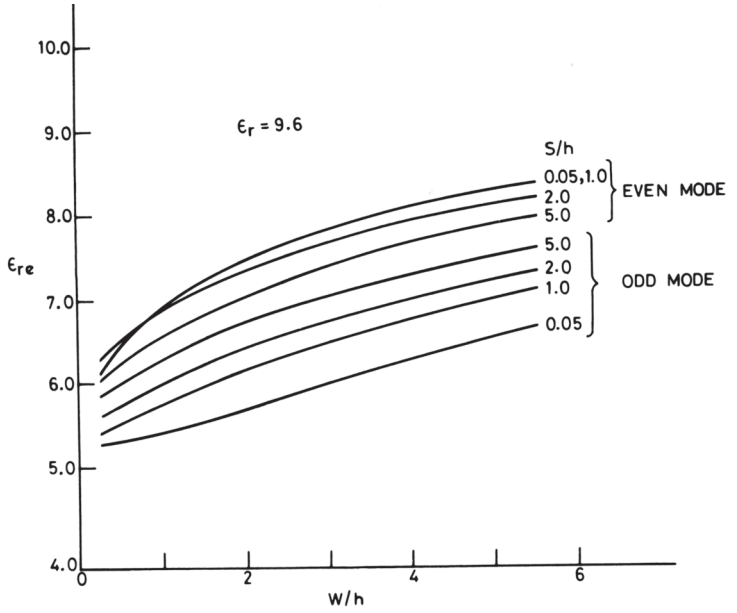

Figure 8.5 Even- and odd-mode effective dielectric constants for coupled microstrip lines (ε_r = 9.6, S/h = 0.05 to 5.0, W/h = 0.2 to 5.5) (from [18], © 1972 Van Nostrand Reinhold. Reprinted with permission.).

8.3.2 Fullwave Analysis

It was pointed out in Chapter 2 that quasi-static analysis for microstrip holds for wavelengths greater than the transverse dimensions of the line. At higher frequencies, the line shows a dispersive nature and a fullwave analysis is needed. The analytical technique used for fullwave analysis of single microstrip, slotline, and coplanar lines can also be applied to the coupled line configuration. Krage and Haddad [20] have used the same field-matching technique for both single microstrip and coupled microstrip configurations. The spectral domain technique has been used in references [21–36] for the fullwave analysis of coupled microstrip lines. Its application by various authors to the same configuration differs only in the choice of basis functions for expressing current density (for microstrip lines) and electric field (for slotline). The rate of convergence of the resultant series depends upon the choice of basis functions.

In this section Galerkin's method in the spectral domain is employed to analyze both symmetric and asymmetric coupled microstrip lines.

Symmetric Coupled Microstrip Lines

The current basis functions for the symmetric coupled microstrips may be obtained from a translation of the corresponding basis functions for the single microstrip line (see (2.27)). These functions may be either of sinusoidal type [23, 27] or of Chebyshev type [28, 29] with proper edge singularity. Sinusoidal type basis functions and their Fourier transforms were described earlier in connection with the fullwave analysis of coplanar strips in Section 7.2.3. The Chebyshev polynomials

are found to be efficient especially for tightly coupled lines [30]. The current distribution on the strips in terms of these basis functions is described (see Figure 8.9 for the co-ordinate system) [28] as

$$J_z(x) = \sum_{m=1}^{\infty} a_m J_{zm}(x) \tag{8.63}$$

$$J_x(x) = \sum_{n=0}^{\infty} b_n J_{xn}(x) \tag{8.64}$$

where

$$J_{zm}(x) = \begin{cases} \dfrac{T_{m-1}(2x'/W)}{\sqrt{1-(2x'/W)^2}} & m = 1,2,3\ldots \text{for} |S/2| \le x \le |S/2+W| \\ 0 & \text{elsewhere} \end{cases} \tag{8.65a}$$

$$J_{xn}(x) = \begin{cases} U_n(2x'/W)\sqrt{1-(2x'/W)^2} & n = 0,1,2,\ldots \text{for} |S/2| \le x \le |S/2+W| \\ 0 & \text{elsewhere} \end{cases} \tag{8.65b}$$

where $T_n(x)$ and $U_n(x)$ are Chebyshev polynomials of the first and second kind, respectively.

Here, $x' = x + x_o$ for the left strip and $x' = x - x_o$ for the right strip with $x_o = (W + S)/2$. Fourier transforms of the Chebyshev polynomials, (8.65), can be obtained by using the identities [29]

$$\int_{-1}^{1} \frac{\cos(\alpha x) T_n(x)}{\sqrt{1-x^2}} dx = \pi J_n(\alpha) \text{Re}\{j^n\} \tag{8.66a}$$

$$\int_{-1}^{1} \frac{\sin(\alpha x) T_n(x)}{\sqrt{1-x^2}} dx = \pi J_n(\alpha) \text{Im}\{j^n\} \tag{8.66b}$$

$$\int_{-1}^{1} \sqrt{1-x^2} \cos(\alpha x) U_n(x) dx = \frac{\pi(n+1)}{\alpha} J_{n+1}(\alpha) \text{Re}\{j^n\} \tag{8.66c}$$

$$\int_{-1}^{1} \sqrt{1-x^2} \sin(\alpha x) U_n(x) dx = \frac{\pi(n+1)}{\alpha} J_{n+1}(\alpha) \text{Im}\{j^n\} \tag{8.66d}$$

where $j = \sqrt{-1}$. Other details of this method are similar to those discussed for a single microstrip in Chapter 2.

The characteristic impedances for the even and odd modes defined on power-current basis agree well with experimental results and may be obtained from the relation

$$Z_o = 2\frac{\iint P_z \, dx\, dy}{|I_z|^2 + |I_x|^2} \qquad I_z = \sum_m a_m \int_{S/2}^{(W+S)/2} J_{zm}\, dx \quad I_x = \sum_n b_n \int_{S/2}^{(W+S)/2} J_{xn}\, dx \tag{8.67}$$

where P_z is the z-component of the Poynting vector and the integral is evaluated over the cross section of a coupled microstrip configuration.

The numerical results obtained in [29] are shown in Figures 8.6 and 8.7. Figure 8.6 shows the propagation constants for the even and odd modes as a function of separation between the strips. It is observed that for small values of S/W, $\beta_e > \beta_{iso}$

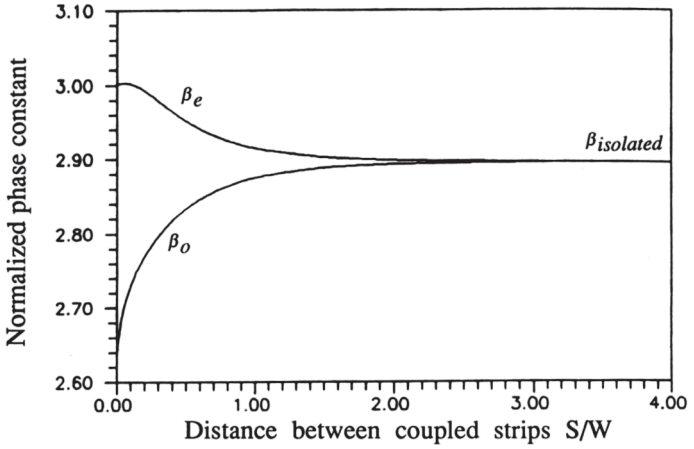

Figure 8.6 Dependence of phase constants of coupled microstrip lines on the spacing ($\varepsilon_r = 9.8$, $h/\lambda_o = 0.0212$, $W/h = 4.72$) (from [29], © 1992 IEEE. Reprinted with permission.).

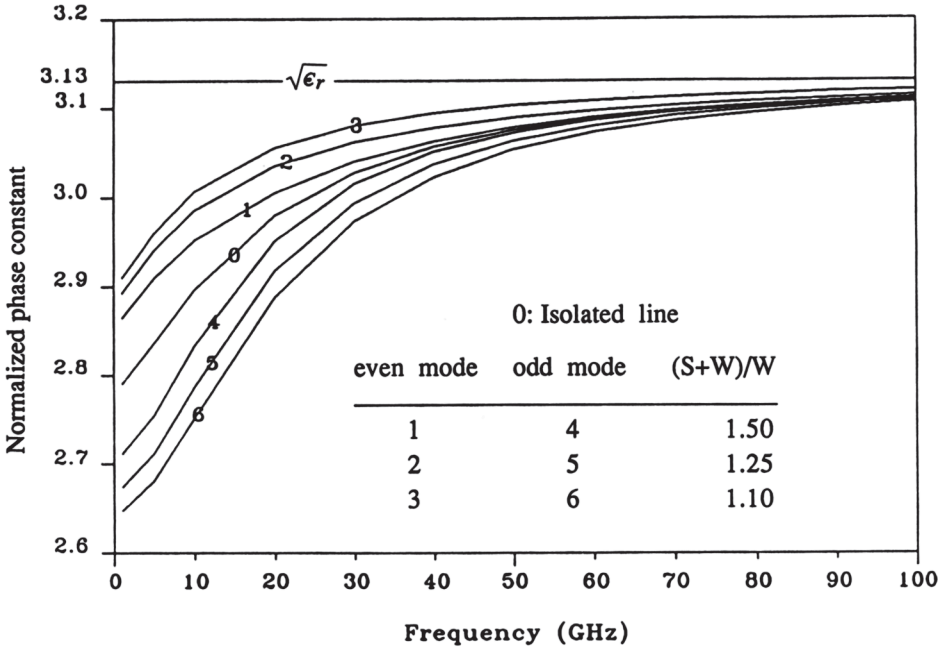

Figure 8.7 Effect of dispersion on even- and odd-mode phase constants of coupled microstrip lines ($\varepsilon_r = 9.8$, $h/W = 0.2115$, $W = 0.635$ mm) (from [29], © 1992 IEEE. Reprinted with permission.).

> β_o; where β_e, β_{iso}, and β_0 are the phase constants corresponding to even-mode, isolated microstrip and odd-mode, respectively. When S → 0 the strips contact on inside edges, and phase constant for the even mode approaches the phase constant of an isolated strip with twice the width. For large separation between the strips (S/W > 4) the phase constants of the even and odd modes converge to the phase constant of an isolated strip. This feature of coupling can be used as a guideline in the layout of strips to avoid coupling between the neighboring strips. Dispersion behavior of β/k_o for the coupled modes is plotted in Figure 8.7. As in the case of isolated microstrip, the value of β/k_o increases with frequency for the modes of a coupled microstrip line, ultimately reaching $\sqrt{\varepsilon_r}$ for very high frequencies. The dispersion behavior of the characteristic impedance is shown in Figure 8.8.

Asymmetric Coupled Microstrip Lines

Galerkin's method in the spectral domain has also been applied to evaluate the characteristics of asymmetric coupled microstrip lines (see Figure 8.9). The total strip current is the sum of the current on each strip. Also, the current on the strips are not equal to each other because of the absence of symmetry. Therefore, we can write [35]

$$J_z(x) = \begin{cases} \sum_{m=1}^{M_1} a_{m1} J_{zm1}(x) & \text{for the left strip} \\ \sum_{m=1}^{M_2} a_{m2} J_{zm2}(x) & \text{for the right strip} \end{cases} \tag{8.68a}$$

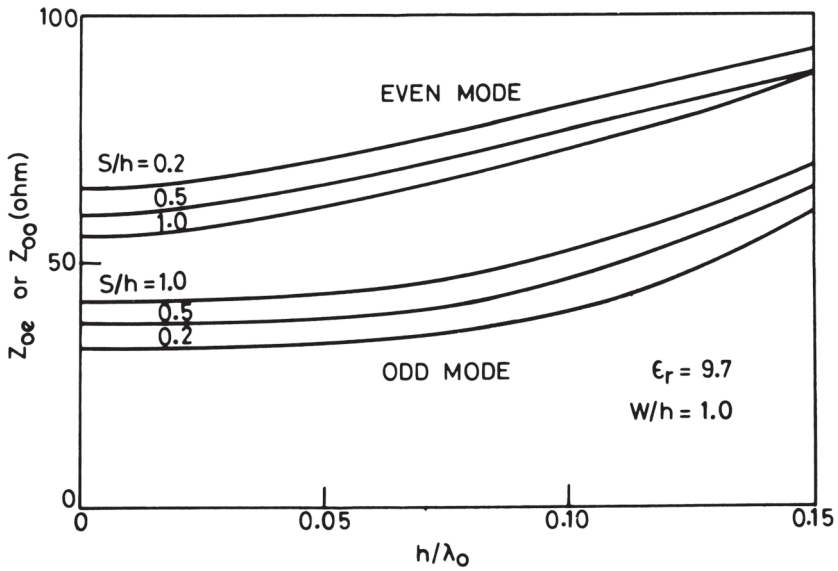

Figure 8.8 Effect of dispersion on even- and odd-mode impedances of coupled microstrip lines (from [23], © 1972 S. Hirzel Verlag. Reprinted with permission.).

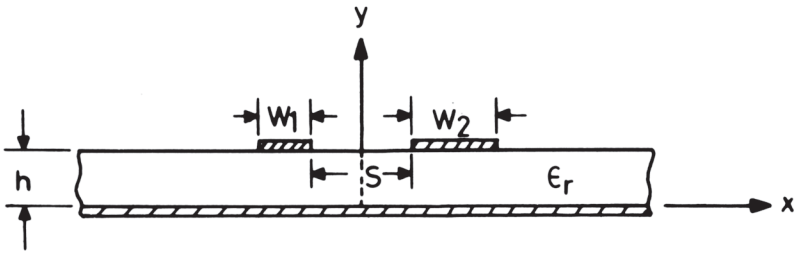

Figure 8.9 Coupled microstrip lines with unequal impedances (asymmetric lines).

$$J_x(x) = \begin{cases} \sum_{n=0}^{N_1} b_{n1} J_{xn1}(x) & \text{for the left strip} \\ \sum_{n=0}^{N_2} b_{n2} J_{xn2}(x) & \text{for the right strip} \end{cases} \tag{8.68b}$$

Here, subscripts 1 and 2 define the strips. The basis functions can be obtained by generalizing the basis functions of (8.65) for different strip widths. For the coordinate system shown in Figure 8.9, the basis functions can be expressed as [35]

$$J_{zmi}(x) = \begin{cases} \dfrac{T_{m-1}\left(2x_i'/W_i\right)}{\sqrt{1-\left(2x_i'/W_i\right)^2}} & i = 1, 2 \text{ and } m = 1, 2, 3\ldots \text{ over the strips} \\ 0 & \text{outside the strips} \end{cases} \tag{8.69a}$$

$$J_{xnj}(x) = \begin{cases} U_n(2x_j'/W_j)\sqrt{1-(2x_j'/W_j)^2} & j = 1, 2 \text{ and } n = 0, 1, 2, 3\ldots \text{ over the strips} \\ 0 & \text{outside the strips} \end{cases} \tag{8.69b}$$

where $x' = x + x_{o1}$ for the left strip and $x' = x - x_{o2}$ for the right strip, with $x_{oi} = (W_i + S)/2$.

The characteristic impedance for the two strips may be defined on a voltage-current basis. This is given below

$$Z_0^{(1)} = \frac{V^{(1)}}{I^{(1)}} = \frac{\int_o^h E_y\left(-(W_1+S)/2, y\right) dy}{\sum_m a_{m1} \int_{-(W_1+S/2)}^{-S/2} J_{zm1}(x')\, dx'} \tag{8.70}$$

$$Z_o^{(2)} = \frac{V^{(2)}}{I^{(2)}} = \frac{\int_o^h E_y\left((W_2+S)/2, y\right) dy}{\sum_m a_{m2} \int_{S/2}^{(W_2+S/2)} J_{zm2}(x')\, dx'} \tag{8.71}$$

The analysis of asymmetric coupled lines is described in terms of c and π modes defined in Section 8.2.

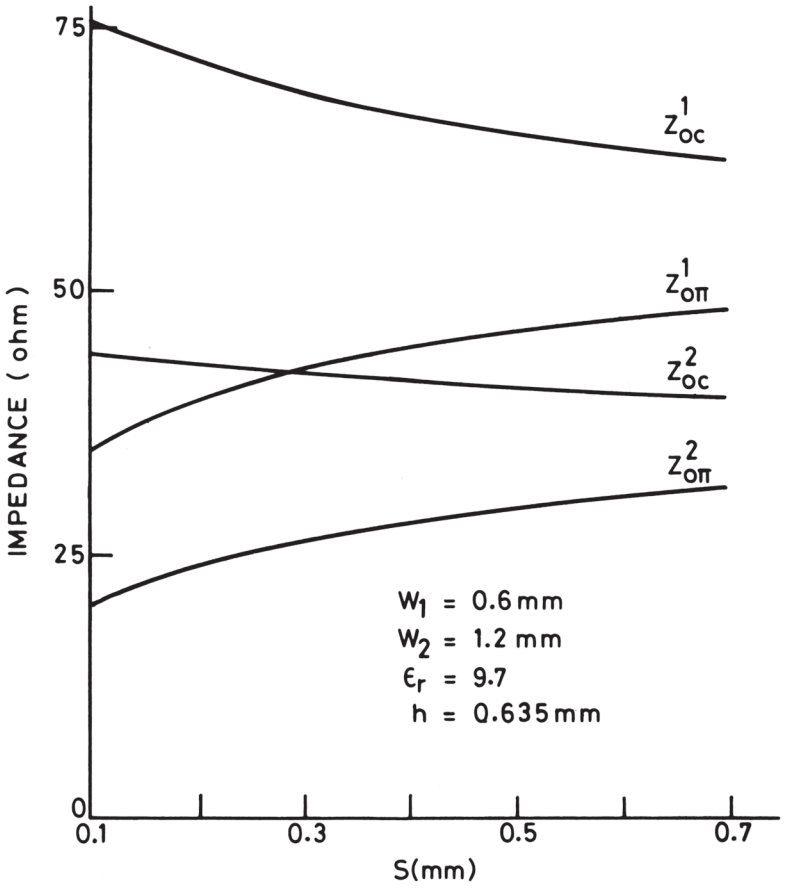

Figure 8.10 Variation of characteristic impedances of asymmetric coupled microstrip lines with gap spacing *S* (from [25], © 1977 Microwave Exhibitions & Publishers. Reprinted with permission.).

Figure 8.10 shows the characteristic impedances for the case of asymmetric coupled microstrip lines [25]. Note that the two lines have different impedances for the *c* and π modes. The narrow line has a higher impedance than the wider line. Moreover, for larger spacing the *c*- and π-mode impedances for the two lines approach their respective single line impedances. The effect of dispersion on the effective dielectric constant for the two modes is shown in Figure 8.11. It may be observed from this figure that the effective dielectric constants of the *c* and π modes increase with the increase in strip width of line 2. Also, the measured values show good agreement with calculated results.

The characteristic impedance of asymmetric coupled microstrip lines may also be defined in terms of power and current. This definition in its most general form is [28]

$$Z_{\ell m} = \frac{\text{Power associated with the } \ell \text{ for mode m } (= P_{\ell m})}{((\text{Normalized current on line } \ell \text{ for mode } m)^2 = I^2_{\ell m})} \tag{8.72}$$

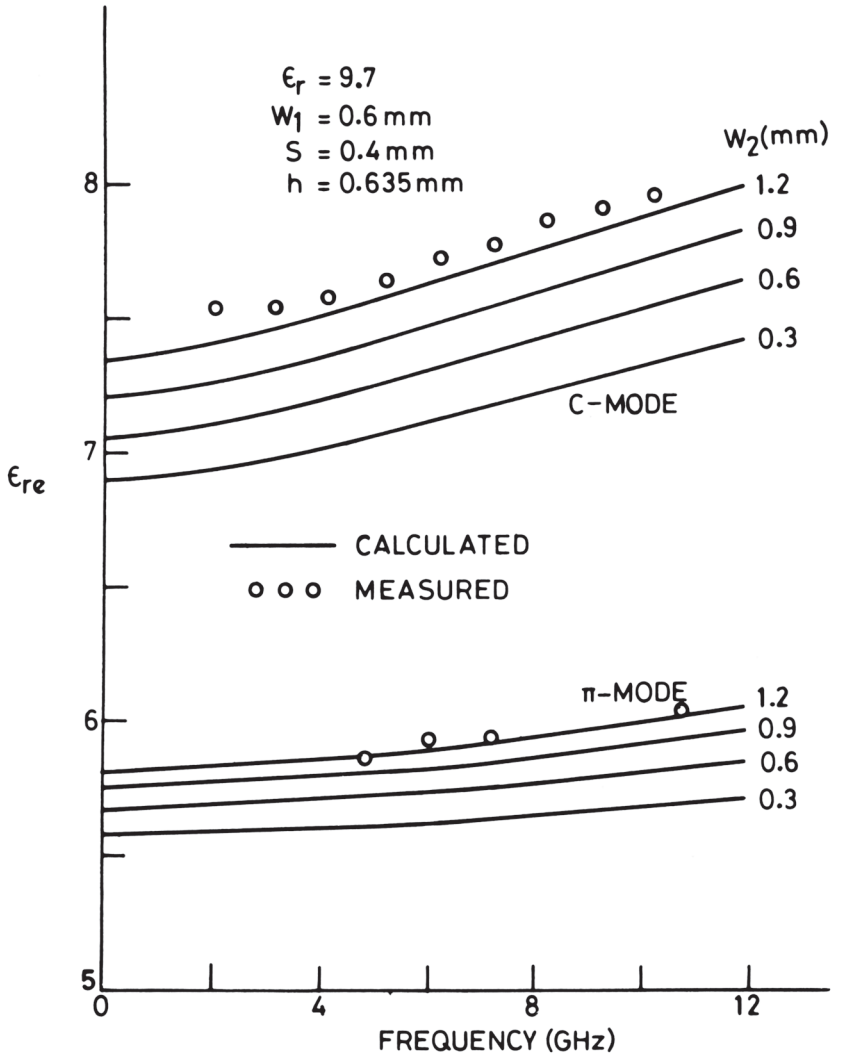

Figure 8.11 Effect of dispersion on the effective dielectric constants of asymmetric coupled microstrip lines (from [25], © 1977 Microwave Exhibitions & Publishers. Reprinted with permission.).

In (8.72), $P_{\ell m}$ is calculated by integrating the z-component of the Poynting vector over the cross section of the coupled microstrip line configuration when the current distribution on line ℓ corresponds to the solution for currents when $\beta = \beta_m$ and all the other line currents are zero.

Fullwave analysis of coupled microstrip lines has been extended to configurations with more than two strips, symmetric as well as asymmetric [27, 32–35]. The basis functions for the analysis can be based on symmetry considerations for the symmetric cases [27] and in a general form for the asymmetric cases [28]. The number of basis functions required increases with the increase in the number of strips, asymmetry, and the tightness of coupling.

Fullwave analysis is useful for calculating very accurately the effect of dispersion on the even- and odd-mode phase velocities and characteristic impedances.

However, sufficient accuracy compatible with fabrication tolerances and measurement errors can also be achieved in the limited range of parameters by using suitable dispersion models. These models have the advantage of saving computational time. Dispersion models for coupled microstrip lines are described in the following subsection.

8.3.3 Dispersion Models

It has been observed [37] that the LSE-mode model for the dispersion in a single microstrip line can be used for coupled microstrip lines also. For its application to coupled microstrip lines, Z_{0m} in (1.72) and (1.73) should represent even- and odd-mode impedances of the total parallel-coupled configuration rather than that of a single line of the coupled pair. Relations (1.71) and (1.73) modified for a coupled microstrip line are rewritten below

$$\varepsilon_{re}^{e,o}(f) = \varepsilon_r - \frac{\varepsilon_r - \varepsilon_{re}^{e,o}(0)}{1 + G(f/f_p)^2} \tag{8.73}$$

where

$$f_p = \frac{Z_{0m}}{2\mu_0 h} \tag{8.74}$$

$$G \approx 0.6 + 0.009\, Z_{0m} \tag{8.75}$$

For the even mode, the total mode impedance is half that of a single line of the coupled pair since the two strips are at the same potential and the total current is twice that of a single strip. Therefore, the effect of dispersion on ε_{re} for the even mode can be computed by substituting $Z_{0e}/2$ for Z_{0m} in (8.74) and (8.75). In the case of the odd mode, the two strips are at opposite potentials, and the voltage between the strips is twice that of a single strip to ground. Thus Z_{0m} should be replaced by 2 Z_{0o} for the odd mode. Consequently, (8.74) and (8.75) for constants f_p and G may be written for the two modes as follows:

$$f_p = \begin{cases} \dfrac{Z_{0e}}{4\mu_0 h} & \text{even mode} \\ \dfrac{Z_{0o}}{\mu_0 h} & \text{odd mode} \end{cases} \tag{8.76}$$

$$G = \begin{cases} 0.6 + 0.0045\, Z_{0e} & \text{even mode} \\ 0.6 + 0.018\, Z_{0o} & \text{odd mode} \end{cases} \tag{8.77}$$

The odd mode is less dispersive compared to the even mode. For example, the increase in the effective dielectric constant is about 12 percent for the odd mode and about 19 percent for the even mode at a frequency of 30 GHz for 50-Ω coupled microstrip lines on 0.64-mm alumina substrate. Dispersion at other frequencies can be obtained from Figure 8.12.

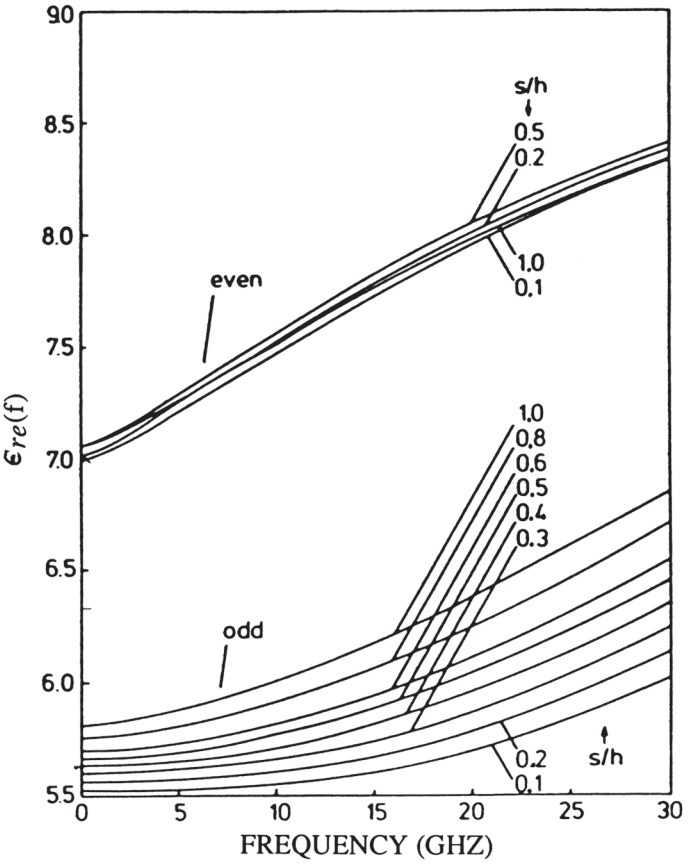

Figure 8.12 Effect of dispersion in ε_{re} for symmetric coupled microstrip lines ($\varepsilon_r = 9.7$, $h = 0.64$ mm, $W/h = 1$) (from [39], © 1984 IEEE. Reprinted with permission.).

Getsinger's dispersion model [37] gives relatively accurate results for alumina substrate for which it has been adjusted. However, it has been found to give inaccurate values for extreme values of gap width [38]. Kirschning and Jansen have reported closed-form expressions that model the dispersion in coupled microstrip lines with better accuracy and larger range of parameters [39]. These expressions have been obtained by curve-fitting the numerical results of the spectral-domain hybrid-mode approach. The range of validity is specified to be [39]

$$0.1 \le u \le 10 \quad 0.1 \le g \le 10 \quad 1 \le \varepsilon_r \le 18 \quad f_n \le 25 \tag{8.78}$$

for an error of not more than 1.4 percent. In (8.78), u (= W/h) denotes the normalized strip width and g (= S/h) is the normalized gap width. The normalized frequency f_n is defined in (8.80).

To account for a more complicated form of frequency dependence Kirschning and Jansen have modified (8.73). The modified expression is given as

$$\varepsilon_{re}^{e,o}(f_n) = \varepsilon_r - \frac{\varepsilon_r - \varepsilon_{re}^{e,o}(0)}{1 + F_{e,o}(f_n)} \tag{8.79}$$

Here, $\varepsilon_{re}^{e,o}(0)$ denotes the static value of the effective dielectric constant for the even and odd modes. Accurate expressions for these are given in Section 8.5. The variable f_n denotes the normalized frequency and is defined as

$$f_n = f\,(\text{GHz}) \cdot h\,(\text{mm}) \tag{8.80}$$

Equation (8.80) implies that frequency f is in gigahertz and the substrate thickness h is in millimeters.

The factor $F_{e,o}(f_n)$ accounts for the dispersion of effective dielectric constant in (8.79). The expression for $F_e(f_n)$ is given as

$$F_e(f_n) = P_1 P_2 \left[(P_3 P_4 + 0.1844 P_7) f_n \right]^{1.5763} \tag{8.81}$$

with

$$P_1 = 0.27488 + \left(0.6315 + \frac{0.525}{(1 + 0.0157 f_n)^{20}} \right) u - 0.065683 e^{-8.7513u}$$

$$P_2 = 0.33622 \left(1 - e^{-0.03442 \varepsilon_r} \right)$$

$$P_3 = 0.0363 e^{-4.6u} \left[1 - \exp\left(-(f_n / 38.7)^{4.97} \right) \right]$$

$$P_4 = 1 + 2.751 \left[1 - \exp\left(-(\varepsilon_r / 15.916)^8 \right) \right]$$

$$P_5 = 0.746 + 0.334 \exp\left(-3.3 (\varepsilon_r / 15)^3 \right)$$

$$P_6 = P_5 \exp\left(-(f_n / 18)^{0.368} \right)$$

$$P_7 = 1 + 4.069 P_6 \cdot g^{0.479} \exp\left(-1.347 g^{0.595} - 0.17 g^{2.5} \right)$$

For the odd-mode effective dielectric constant, the effect of dispersion is described by

$$F_o(f_n) = P_1 P_2 \left[(P_3 P_4 + 0.1844) P_{15} f_n \right]^{1.5763} \tag{8.82}$$

with

$$P_8 = 0.7168 \left(1 + \frac{1.076}{1 + 0.0576 (\varepsilon_r - 1)} \right)$$

$$P_9 = P_8 - 0.7913 \left[1 - \exp\left(-(f_n / 20)^{1.424} \right) \right] \tan^{-1}\left(2.481 (\varepsilon_r / 8)^{0.946} \right)$$

$$P_{10} = 0.242 (\varepsilon_r - 1)^{0.55}$$

$$P_{11} = 0.6366 \left(e^{-0.3401 f_n} - 1 \right) \tan^{-1}\left[1.263 (u/3)^{1.629} \right]$$

$$P_{12} = P_9 + \frac{1 - P_9}{1 + 1.183 u^{1.376}}$$

$$P_{13} = \frac{1.695 P_{10}}{0.414 + 1.605 P_{10}}$$

$$P_{14} = 0.8928 + 0.1072 \left[1 - \exp\left(-0.42 (f_n / 20)^{3.215} \right) \right]$$

$$P_{15} = \left| 1 - \frac{0.8928 (1 + P_{11}) P_{12} \exp\left(-P_{13} g^{1.092} \right)}{P_{14}} \right|$$

The upper frequency limit for (8.81) and (8.82) is $f_n = 25$, that is, 25 GHz for a substrate thickness of 1 mm and higher for thinner substrates.

Dispersion in the characteristic impedance has also been modeled with a maximum error of less than 2.5 percent over the range of parameters specified in (8.78) and $f_n \leq 20$ [39]. It is observed that the impedances increase with frequency, and the rate of increase for the odd mode is very small for frequencies up to 30 GHz for microstrip lines on alumina substrate.

8.4 Measurements on Coupled Microstrip Lines

Symmetrical coupled microstrip lines are characterized by even- and odd-mode impedances and propagation constants. Knowledge of these characteristics is essential for designing directional couplers and edge-coupled resonators. Under ordinary conditions, both of the modes are excited and it is difficult to determine the odd- and even-mode parameters from the measured data. One way to measure these characteristics is to selectively excite one mode and measure its characteristics. The selective excitation of modes and measurements becomes easier with the use of a microwave network analyzer. Measurement techniques for impedances and phase constants are described in the following sections.

8.4.1 Impedance Measurements

The setup for measuring even- and odd-mode impedances is illustrated in Figure 8.13 [40]. As shown, the signal from the source is divided equally into the two transmission lines. The path length of one of these lines is adjustable so that the relative phase of the waves propagating in them can be controlled for selectively exciting the even or odd mode. The amplitude ratio of the waves is unity. The relative phase and amplitude can be measured using a harmonic frequency converter and a phase-gain indicator (two subunits of the network analyzer system).

The coupled microstrip section is now introduced between the transmission test unit and harmonic frequency converter. The mode of excitation can be selected by controlling the phase. The phase indicator should read 0° for even-mode excitation and 180° for odd-mode excitation.

The characteristic impedance can be determined from the VSWR measurement.

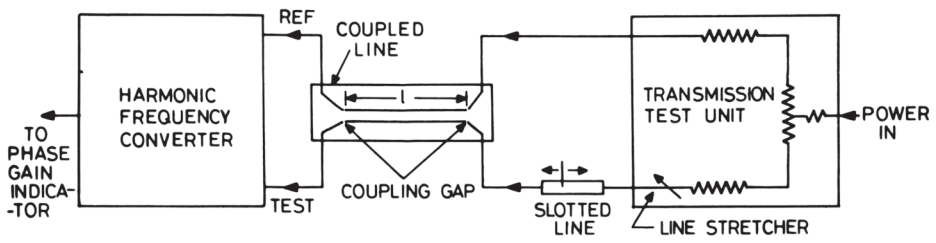

Figure 8.13 Test setup for measuring even- and odd-mode impedances of coupled lines.

To measure VSWR, a slotted line should be inserted to one arm between the transmission test unit and the coupled lines. A compensating air line length should be inserted in the other arm. The measurements should preferably be carried out at a frequency where the coupling length is approximately $\lambda_m/4$, because at this wavelength the effect of the even- or odd-mode impedance on VSWR is at a maximum. At the same time, the effect of any discontinuity capacitance is minimum.

Even- and odd-mode impedances can be obtained from the relations

$$Z_{0e} = Z_0\sqrt{\text{VSWR}_e} \quad Z_{0o} = Z_0/\sqrt{\text{VSWR}_0} \tag{8.83}$$

since Z_{0e} is greater than Z_0 and Z_{0o} is less than Z_0. VSWR_e and VSWR_o are the VSWR values for even- and odd-mode excitations, respectively.

8.4.2 Phase Constant Measurements

The phase constants for the two modes can be determined by measuring the resonance frequencies corresponding to these modes. Loading effects on the resonator due to the transmission test unit and the harmonic frequency converter can be minimized by introducing coupling gaps between them and the coupled lines, as shown in Figure 8.14. The coupled pair will act as a lightly loaded single resonator and will exhibit two resonant frequencies. The odd-mode resonance frequency will be higher than the even-mode resonance frequency. While calculating guide wavelength from resonance frequency, the effect of gap capacitance should be taken into account. The guide wavelength for a half-wave coupled section is given by

$$\lambda = 2\left(\ell + 2\Delta\ell_g\right) \tag{8.84}$$

where ℓ is the length of resonant line and $\Delta\ell_g$ is the equivalent line length associated with the gap capacitance C_g, which is given approximately by

$$\Delta\ell_g = f\lambda_m C_g Z_o \tag{8.85}$$

and f is the resonance frequency for the half-wave resonator.

Even- and odd-mode resonances may also be obtained by proper terminations at the two ends of a coupled line section [41]. If a coupled line section is $(2n + 1)\lambda/4$ long and the two ends are connected in parallel, an even-mode resona-

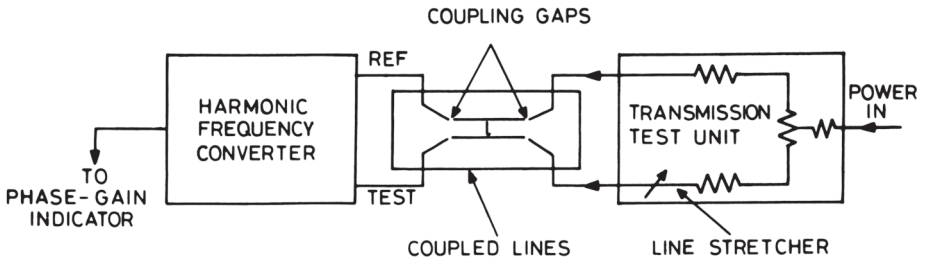

Figure 8.14 Setup for measuring phase velocities in coupled lines.

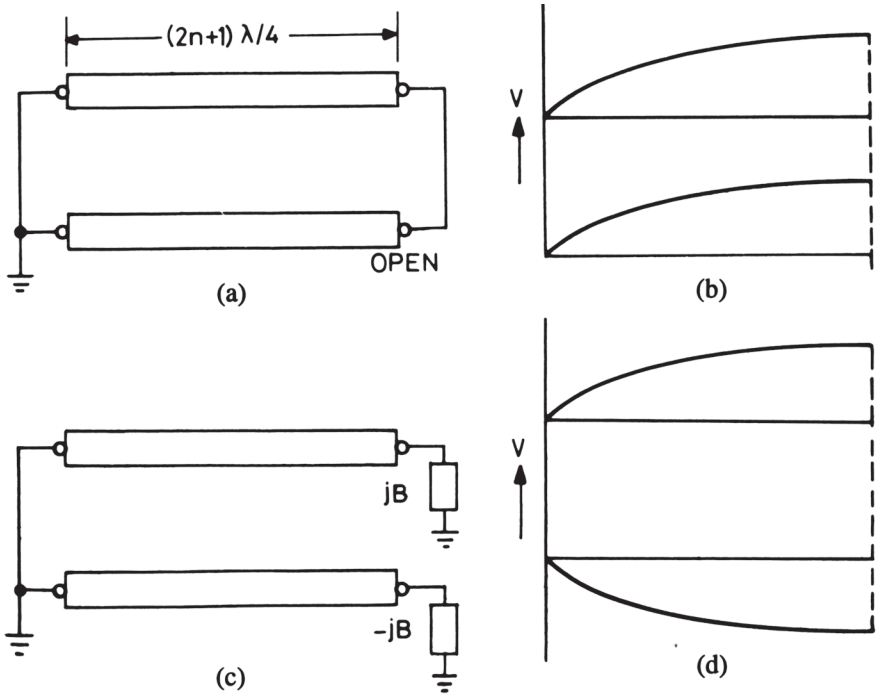

Figure 8.15 Voltage distribution for even- and odd-mode excitations: (a) configuration for enforcing the even mode, (b) voltage distribution for the even mode, (c) configuration for enforcing the odd mode, and (d) voltage distribution for the odd mode.

tor is obtained when one end is open and the other is grounded. This situation is shown in Figure 8.15(a).

Voltage distribution on the two lines (for the case $n = 0$) is shown in Figure 8.15(b). Since the two lines are connected in parallel at both ends, the voltages on these two lines are in phase everywhere. This structure behaves as an even-mode resonator for any excitation, and the network analyzer setup is not needed for exciting the even mode. A similar arrangement for an odd-mode resonator is shown in Figure 8.15(c). At one end of the coupled section, the two lines are connected in parallel and shorted to ground. This end becomes a voltage node. At the other end the two lines are loaded by two susceptances of opposite sign, and thus the antiphase nature of the voltage waveform on two lines is ensured.

Even- and odd-mode parameters can now be evaluated by measuring resonance frequency, Q-factor, and input VSWR for two types of resonators [41].

Excitation of these structures is carried out by a gap-coupled microstrip feedline placed close to the coupled line configuration.

8.5 Design Considerations for Coupled Microstrip Lines

Coupled microstrip structures are characterized by the characteristic impedances (or admittances) and phase velocities for the two modes. The analysis of coupled

microstrip lines for these characteristics can be carried out by using one of the methods outlined in Sections 8.2 and 8.3. Although the analysis can be carried out to determine the characteristics for a given set of coupled line parameters, it does not provide simple design equations for the direct synthesis of coupled line circuits. For purposes of synthesis, one prepares either a table or a graph for a number of sets of coupled line parameters and uses these tables, for example, to obtain the desired information. This procedure is time consuming and may also involve some sacrifice in accuracy. However, to avoid these disadvantages, one can write synthesis design equations instead. These equations may be derived from the results of analysis. In order to save computation time the analysis results may also be written in the form of closed-form equations.

Closed-form approximate expressions can be used to initiate the analysis or synthesis procedure. These can also be used as final results whenever the demand on specifications of the circuit is not very tight. Closed-form approximate expressions for the capacitances of symmetric coupled microstrip lines are derived in the following section.

8.5.1 Design Equations

Design equations for coupled lines should relate mode impedances and effective dielectric constants to the coupled line geometry; that is, strip width W, spacing S between the strips, dielectric thickness h, and dielectric constant ε_r. One may write design equations for these characteristics directly in terms of the parameters of coupled lines. Alternatively, static capacitances for the coupled line geometry may be used as an intermediate step. It is seen that the latter approach yields simpler design equations. Therefore, mode characteristics will be described in terms of static capacitances. Even- and odd-mode capacitances for the symmetric coupled lines are obtained first.

Even-Mode Capacitance [42]

As shown in Figure 8.16(a) the even-mode capacitance C_e can be divided into three capacitances; that is,

$$C_e = C_p + C_f + C_f' \tag{8.86}$$

C_p denotes the parallel plate capacitance between the strip and the ground plane. C_f is the fringe capacitance at the outer edge of the strip; it is the fringe capacitance of a single microstrip line and can be evaluated from the capacitance of the microstrip line and the value of C_p. The term C_f' accounts for the modification of fringe capacitance C_f of a single line due to the presence of another line. Expressions for C_p, C_f, and C_f' are given below

$$C_p = \varepsilon_0 \varepsilon_r W/h \tag{8.87}$$

$$2C_f = \sqrt{\varepsilon_{re}}/\left(cZ_{0m}\right) - \varepsilon_0 \varepsilon_r W/h \tag{8.88a}$$

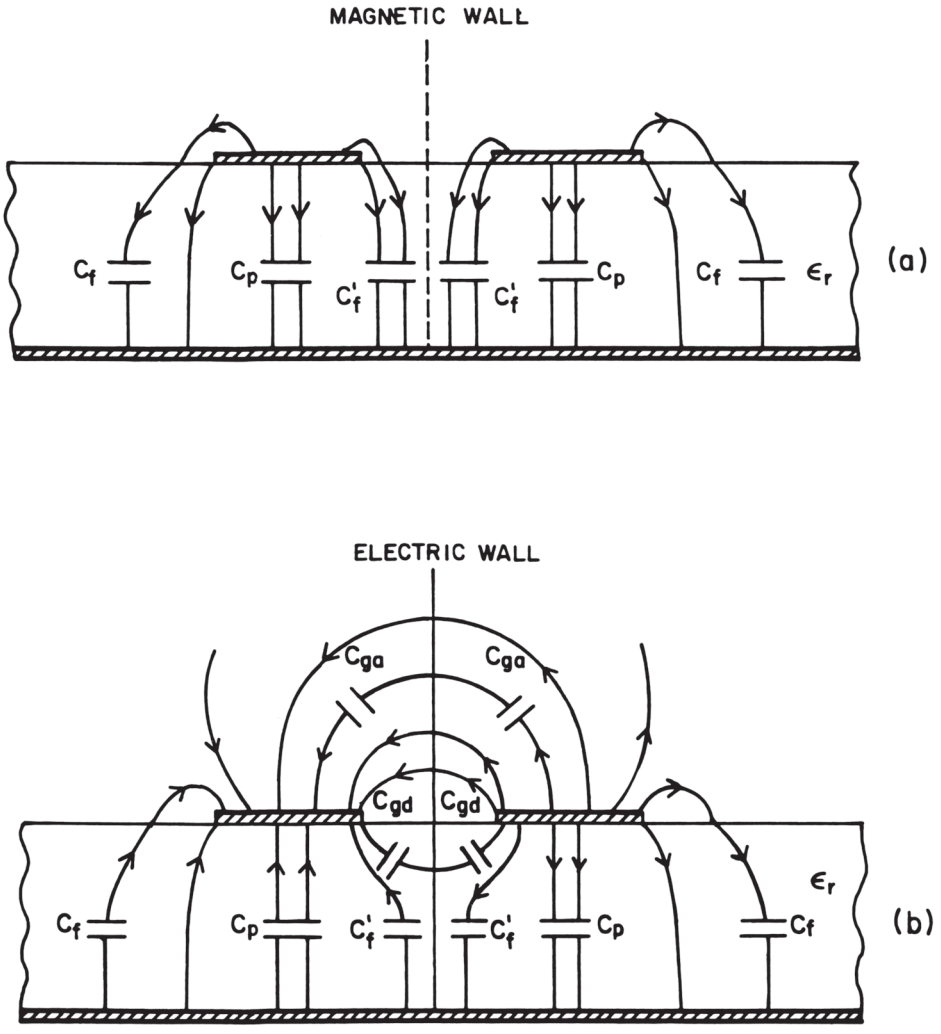

Figure 8.16 Analysis of coupled microstrip lines in terms of capacitances: (a) even mode capacitance and (b) odd-mode capacitance.

and

$$C'_f = \frac{C_f}{1 + A(h/S)\tanh(10S/h)}\left(\frac{\varepsilon_r}{\varepsilon_{re}}\right)^{1/4} \tag{8.88b}$$

where

$$A = \exp\left[-0.1\exp(2.33 - 1.5W/h)\right]$$

The capacitances obtained by using the above design equations were compared with those obtained from [39]. The values are found to be accurate to within 3 percent over the following range of parameters

$$0.1 \le W/h \le 10 \qquad 0.1 \le S/h \le 5 \qquad 1 \le \varepsilon_r \le 18$$

Odd-Mode Capacitance [43]

The odd-mode capacitance C_o can be decomposed into five constituents C_f, C_p, C'_f, C_{gd} and C_{ga} as shown in Figure 8.16(b); that is,

$$C_o = C_p + C_f + C'_f + C_{gd} + C_{ga} \tag{8.89}$$

Expressions for C_p, C_f, and C'_f are the same as those given earlier in the case of even mode. The capacitance C_{gd} may be calculated from the corresponding coupled stripline geometry with the spacing between the ground planes given by $2h$. The value of C_{gd} is obtained from the relation

$$C_{ga} = 0.5\left(C_{os} - C_{es}\right) \tag{8.90}$$

where C_{os} and C_{es} are the odd- and even-mode capacitances of the corresponding coupled striplines.

The capacitance C_{ga} describes the gap capacitance in air. Its value can be obtained from the capacitance of the corresponding coplanar strips with air as dielectric and the fringe capacitances. Bedair has suggested the following expression for C_{ga} [43]:

$$C_{ga} = C_{cps} - (C_f - C_{fs}) - (C_f - C_{fs}) \tag{8.91a}$$

with

$$C'_{fs} + C'_{fs} = 0.5C_{os} - C_p - C_{gd} \tag{8.91b}$$

where C_{cps} is the capacitance of CPS in the half space. From (7.64) one obtains

$$C_{cps} = \varepsilon_o/2\frac{K(k')}{K(k)} \qquad k = \frac{S}{S+2W} \tag{8.92}$$

A direct substitution of (8.90) and (8.91) in (8.89) yields the following simple expression for C_o:

$$C_o = 0.5C_{os} + C_{cps} \tag{8.93}$$

Equation (8.93) has a very simple interpretation. According to this the lower-half portion of the coupled microstrip line is modeled as a coupled stripline and the upper-half portion as a CPS. The capacitance C_{os} is calculated from

$$C_{os} = 4\varepsilon_o\,\varepsilon_r\frac{K\left(k_o\right)}{K\left(k'_o\right)} \tag{8.94}$$

The modulus k_o has been defined in (8.62b).

The capacitances obtained by using the above design equations are accurate to within 3 percent, compared with the values obtained from [39], over the range of parameters

$$0.1 \le W/h \le 10 \qquad 0.1 \le S/h \le 4 \qquad 2 \le \varepsilon_r \le 18$$

More accurate values of capacitances can be obtained from the closed-form expressions for static impedances and effective dielectric constants given next.

Effective Static Dielectric Constants

Effective dielectric constants ε_{re}^{e} and ε_{re}^{o} for even and odd modes, respectively, can be obtained from C_e and C_o by using the relations

$$\varepsilon_{re}^{e} = C_e/C_e^{a} \tag{8.95a}$$

and

$$\varepsilon_{re}^{o} = C_o/C_o^{a} \tag{8.95b}$$

Accurate closed-form expressions for the effective dielectric constants are available [39]. These are reproduced here as

$$\varepsilon_{re}^{o}(0) = \frac{\varepsilon_r + 1}{2} + \frac{\varepsilon_r - 1}{2}\left(1 + \frac{10}{v}\right)^{-a_e b_e} \tag{8.96}$$

with

$$v = \frac{u\left(20 + g^2\right)}{10 + g^2} + ge^{-g}$$

$$a_e = 1 + \frac{1}{49}\ell n\left[\frac{v^4 + (v/52)^2}{v^4 + 0.432}\right] + \frac{1}{18.7}\ell n\left[1 + \left(\frac{v}{18.1}\right)^3\right]$$

$$b_e = 0.564\left(\frac{\varepsilon_r - 0.9}{\varepsilon_r + 3}\right)^{0.053}$$

The error in ε_{re}^{e} is within 0.7 percent over the range of parameters

$$0.1 \le u(= W/h) \le 10 \quad 0.1 \le g(= S/h) \le 10 \quad 1 \le \varepsilon_r \le 18 \tag{8.97}$$

$$\varepsilon_{re}^{o}(0) = \varepsilon_{re}(0) + \left\{0.5\left(\varepsilon_r + 1\right) - \varepsilon_{re}(0) + a_o\right\}e^{-c_o\left(g^{d_o}\right)} \tag{8.98}$$

with

$$a_o = 0.7287\left(\varepsilon_{re}(0) - 0.5\left(\varepsilon_r + 1\right)\right)\left(1 - e^{-0.179u}\right)$$

$$b_o = \frac{0.747\varepsilon_r}{0.15 + \varepsilon_r}$$

$$c_o = b_o - \left(b_o - 0.207\right)e^{-0.414u}$$

$$d_o = 0.593 + 0.694e^{-0.562u}$$

where $\varepsilon_{re}(0)$ is the static effective dielectric constant of a single microstrip of width W as discussed in Chapters 1 and 2. The error in $\varepsilon^{o}_{re}(0)$ is stated to be on the order of 0.5 percent.

Characteristic Impedances

Characteristic impedances Z_{0e} and Z_{0o} can be obtained from the expressions for capacitances and (8.45) to (8.47). One obtains

$$Z_{0e} = \left(c\sqrt{C^{a}_{e}C_{e}}\right)^{-1} \tag{8.99a}$$

$$Z_{0o} = \left(c\sqrt{C^{a}_{o}C_{o}}\right)^{-1} \tag{8.99b}$$

where C^{a}_{e} and C^{a}_{o} are even- and odd-mode capacitances for the coupled microstrip line configuration with air as dielectric.

Accurate closed-form expressions for the static characteristic impedance for the even and odd modes have been obtained by Kirschning and Jansen [39]. These are accurate to within 0.6 percent over the range of parameters specified in (8.97) and are given as

$$Z_{0e} = Z_0 \frac{\sqrt{\varepsilon_{re}(0)/\varepsilon^{e}_{re}(0)}}{1 - Q_4\sqrt{\varepsilon_{re}(0)}\cdot Z_0/377} \tag{8.100}$$

with

$$\begin{aligned}
Q_1 &= 0.8695u^{0.194}\\
Q_2 &= 1 + 0.7519g + 0.189g^{2.31}\\
Q_3 &= 0.1975 + \left[16.6 + \left(\frac{8.4}{g}\right)^{6}\right]^{-0.387} + \frac{1}{241}\ell n\left[\frac{g^{10}}{1 + (g/3.4)^{10}}\right]\\
Q_4 &= \frac{2Q_1}{Q_2}\cdot\frac{1}{u^{Q_3}e^{-g} + \left(2 - e^{-g}\right)u^{-Q_3}}
\end{aligned} \tag{8.101}$$

$$Z_{0o} = Z_0 \frac{\sqrt{\varepsilon_{re}(0)/\varepsilon^{o}_{re}(0)}}{1 - Q_{10}\sqrt{\varepsilon_{re}(0)}\cdot Z_0/377}$$

with

$$Q_5 = 1.794 + 1.14\ell n\left[1 + \frac{0.638}{g + 0.517g^{2.43}}\right]$$

$$Q_6 = 0.2305 + \frac{1}{281.3}\ell n\left[\frac{g^{10}}{1 + (g/5.8)^{10}}\right] + \frac{1}{5.1}\ell n\left(1 + 0.598g^{1.154}\right)$$

$$Q_7 = \frac{10 + 190g^2}{1 + 82.3g^3}$$

$$Q_8 = e^{-[6.5+0.95\ell n(g)+(g/0.15)^5]}$$

$$Q_9 = \ell n(Q_7)(Q_8 + 1/16.5)$$

$$Q_{10} = Q_4 - \frac{Q_5}{Q_2}\exp\left[\frac{Q_6 \ell n(u)}{u^{Q_9}}\right]$$

In (8.100) and (8.101), $\varepsilon_{re}(0)$ is the static effective dielectric constant, Z_0 is the static characteristic impedance for a microstrip line of width W, and $\varepsilon_{re}^{e,o}(0)$ represents the static effective dielectric constant for a coupled microstrip line.

Closed-form expressions for characteristic impedances and effective dielectric constants, as given above, may also be used to obtain accurate values of capacitances for the even and odd modes. The relationship between these quantities is obtained from (8.95) and (8.99) and is given as

$$C_{e,o} = \frac{1}{c}\frac{\sqrt{\varepsilon_{re}^{e,o}(0)}}{Z_{0(e,o)}} \tag{8.102a}$$

$$C_{e,o}^{a} = \frac{1}{c}\frac{1}{Z_{0(e,o)}\sqrt{\varepsilon_{re}^{e,o}(0)}} \tag{8.102b}$$

Design equations for the analysis and synthesis of coupled microstrip lines have been reported by Akhtarzad et al. [44] also. But their results indicate an error on the order of 10 percent. Nomograms for the design of coupled lines have been reported in [45, 46]. A scaling procedure is also available [47, 48] for determining even- and odd-mode impedances, which requires for its usage the accurate design values for any other dielectric. Empirical formulas for the capacitance of multiple-coupled lines have been reported by Dalby [49].

Abbosh has employed conformal mapping and empirical adjustments to obtain the following expressions for even- and odd-mode capacitances of symmetrical coupled microstrip lines [82].

$$C_e = 2\varepsilon_0\left(\varepsilon_r \frac{K(k_1)}{K'(k_1)} + \frac{K(k_2)}{K'(k_2)}\right) \qquad C_o = 2\varepsilon_0\left(\varepsilon_r \frac{K(k_3)}{K'(k_3)} + \frac{K(k_4)}{K'(k_4)}\right) \tag{8.103}$$

where

$$k_1 = \tanh\left(\frac{\pi}{4}\frac{W}{h}\right)\tanh\left(\frac{\pi}{4}\left(\frac{W}{h} + \frac{S}{h}\right)\right), \qquad k_2 = \tanh\left(\frac{\pi}{4}\frac{W/h}{1 + \pi W/h}\right)\tanh\left(\frac{\pi}{4}\frac{W/h + S/h}{1 + \pi W/h}\right)$$

$$k_3 = \tanh\left(\frac{\pi}{4}\frac{W}{h}\right)\coth\left(\frac{\pi}{4}\left(\frac{W}{h} + \frac{S}{h}\right)\right), \qquad k_4 = \frac{W/h}{W/h + S/h} \tag{8.104}$$

The even- and odd-mode characteristic impedances may be calculated from these capacitances according to (8.99). The characteristic impedances obtained from (8.103) and (8.100) were compared with the values obtained from full-wave electromagnetic simulators [82]. In spite of its simplicity, the accuracy of (8.103) is claimed to be better than that of (8.100). The maximum error in impedance is found to be about 5 percent for a narrow spacing of $S/h = 0.0001$. Relatively, the accuracy is better for odd-mode impedance for narrow gap width and higher substrate dielectric constant. The even-mode impedance values are more accurate for wider strips.

Asymmetric coupled microstrip lines

Asymmetric coupled microstrip lines have been studied extensively [9, 10, 25, 28, 36, 50–56] because they provide design flexibility in addition to their impedance transformation property. Analysis of asymmetric coupled lines was described in Section 8.2.2. Mode characteristics were obtained in terms of primary parameters of the lines: self-capacitances C_1 and C_2, self-inductances L_1 and L_2, as well as mutual capacitance C_m and mutual inductance L_m. Expressions for self- and mutual capacitances have been derived in [52]. The inductances L_1, L_2, and L_m can be obtained from the self- and mutual capacitances, C_1^a, C_2^a, and C_m^a, of the corresponding geometry with air as dielectric. The relationship between the capacitance matrix $[C^a]$ and the inductance matrix $[\mathbf{L}]$ of the coupled lines is

$$[\mathbf{L}] = \mu_o \varepsilon_o [\mathbf{C}^a]^{-1} \tag{8.105}$$

where

$$[\mathbf{L}] = \begin{bmatrix} L_1 & L_m \\ L_m & L_2 \end{bmatrix} \quad \text{and} \quad [\mathbf{C}^a] = \begin{bmatrix} C_1^a & C_m^a \\ C_m^a & C_2^a \end{bmatrix} \tag{8.106}$$

From (8.105) and (8.106) one obtains

$$L_1 = \mu_o \varepsilon_o \frac{C_2^a}{\Delta C} \qquad L_2 = \mu_o \varepsilon_o \frac{C_1^a}{\Delta C} \qquad L_m = \mu_o \varepsilon_o \frac{C_m^a}{\Delta C} \tag{8.107}$$

where

$$\Delta C = C_1^a C_2^a - (C_m^a)^2$$

Capacitances for the asymmetric coupled shielded microstrip lines have been obtained in [53]. Characteristic impedance values for the shielded and open configurations are found to be in agreement with available published data.

The capacitance expressions discussed above are valid for coupled microstrip lines with zero strip thickness. In actual practice, the metal strips have finite thickness, and the coupled lines are enclosed in a metallic box for purposes of handling, for example. In addition, the effect of fabrication tolerances and the finite amount of losses should also be considered while designing a coupled line circuit. These effects are considered next.

Effect of Strip Thickness

When the strip conductors are of finite thickness t, C_e can be evaluated using (8.87) for C_p and modifying C_f, (8.88a) to include the effect of strip thickness. In this case C_f becomes [42]

$$C_f(t) = 0.5\left\{\frac{\sqrt{\varepsilon_{re}(t)}}{cZ_{0m}(t)} - \varepsilon_o\varepsilon_r\frac{W}{h}\right\} \tag{8.108}$$

where $\varepsilon_{re}(t)$ and $Z_{0m}(t)$ are the characteristics of microstrip with finite thickness t and are given by (2.124) to (2.127). The increase in the value of C_o due to finite thickness t is given by $C_f(t)$, (8.108), and another term representing gap capacitance evaluated from

$$C_{gt} = 2\varepsilon_o t/S \tag{8.109}$$

Due to the increase in even- and odd-mode capacitances with finite strip thickness, the even- and odd-mode impedances are expected to decrease. The amount of the decrease in impedance can be evaluated. It is seen that the percentage of increase in C_o^a or C_e^a with thickness is more than that in C_o or C_e. Therefore, effective dielectric constants $\varepsilon_{re}^e(t)$ and $\varepsilon_{re}^o(t)$ should decrease with thickness. The percentage decrease in $\varepsilon_{re}^o(t)$ is found to be more than that in $\varepsilon_{re}^e(t)$ because of an additional gap capacitance C_g, with air as dielectric. These observations are verified by exact numerical results available in [16, 57]. The percentage increase in C_o is found to be twice that of C_e. The effect of strip thickness on the modal characteristics could be considerable for coupled lines with $t/S = 0.1$ and $t/W = 0.1$ [58].

Effect of Enclosure

When coupled microstrip lines are enclosed in a metallic box the electric field lines in air terminate prematurely at the walls of the box. This will give rise to an increase in the mode capacitances resulting in a decrease in the mode impedances and effective dielectric constants. The percentage decrease in odd-mode values (with the size of the enclosure) should be less than that for the even mode because a few lines for the odd mode terminate on the walls of the enclosure. Figure 8.17(a, b), obtained from exact numerical evaluation, shows this trend [15]. Coupled microstrip lines with a top cover have been modeled by Bedair [53, 59].

8.5.2 Losses [60]

The coupled microstrip lines also has two types of losses: ohmic and dielectric. The even- and odd-mode attenuation constants due to ohmic losses in coupled microstrip lines can be determined using Wheeler's incremental inductance formula. Its application to the coupled line configuration (Figure 8.18) gives for the odd-mode attenuation constant (due to strips only)

$$\alpha_{co} = \frac{8.688R_s}{240\pi Z_{0o}}\frac{\delta\left(\sqrt{\varepsilon_{re}^o}Z_{0o}\right)}{\delta n}\ \text{(dB/unit length)} \tag{8.110}$$

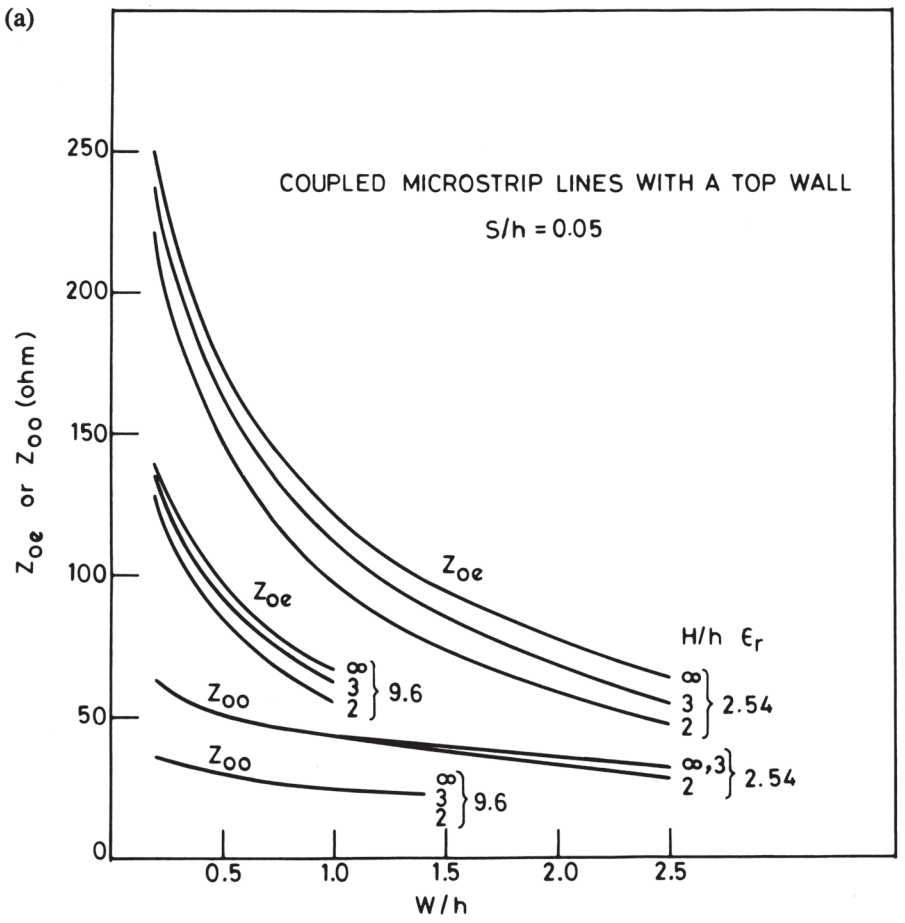

Figure 8.17 (a) Variation of characteristic impedances of coupled microstrip lines with shield: height ratio *H/h* and (b) variation of phase velocities in coupled microstrip lines with shield: height ratio *H/h*.

where

$$\frac{\delta\left(\sqrt{\varepsilon_{re}^{o}}Z_{0o}\right)}{\delta n}=\frac{2}{h}\left\{\left(1-\frac{S}{2h}\right)\frac{\partial\left(\sqrt{\varepsilon_{re}^{o}}Z_{0o}\right)}{\partial(S/h)}-\left(1+\frac{t}{2h}\right)\frac{\partial\left(\sqrt{\varepsilon_{re}^{o}}Z_{0o}\right)}{\partial(t/h)}\right.$$
$$\left.-\left(1+\frac{W}{2h}\right)\frac{\partial\left(\sqrt{\varepsilon_{re}^{o}}Z_{0o}\right)}{\partial\left(W/h\right)}\right\} \tag{8.111}$$

Similarly, the even-mode attenuation constant is given by

$$\alpha_{ce}=\frac{8.686R_s}{240\pi Z_{0e}}\frac{\delta\left(\sqrt{\varepsilon_{re}^{e}}Z_{0e}\right)}{\delta n}\ \text{(dB/unit length)} \tag{8.112}$$

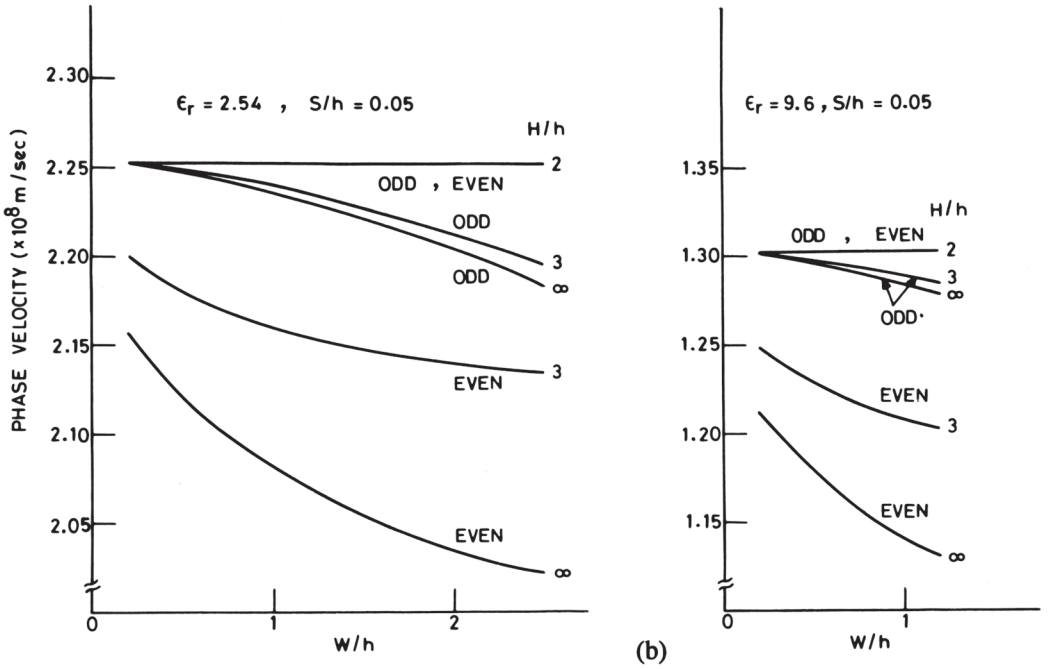

Figure 8.17 (continued)

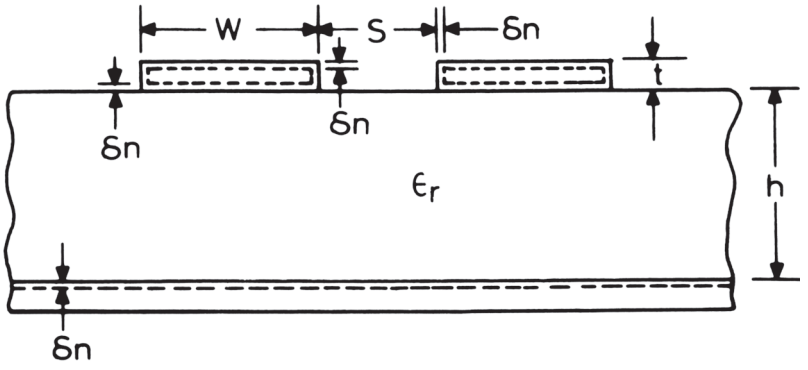

Figure 8.18 Coupled microstrip lines configuration for the calculation of ohmic losses.

where

$$\frac{\delta(\sqrt{\varepsilon_{re}^{e}}Z_{0e})}{\delta n}=\frac{2}{h}\left\{\left(1-\frac{S}{2h}\right)\frac{(\partial\sqrt{\varepsilon_{re}^{e}}Z_{0e})}{\partial(S/h)}-\left(1+\frac{t}{2h}\right)\frac{(\partial\sqrt{\varepsilon_{re}^{e}}Z_{0e})}{\partial(t/h)}-\left(1+\frac{W}{2h}\right)\frac{(\partial\sqrt{\varepsilon_{re}^{e}}Z_{0e})}{\partial(W/h)}\right\} \tag{8.113}$$

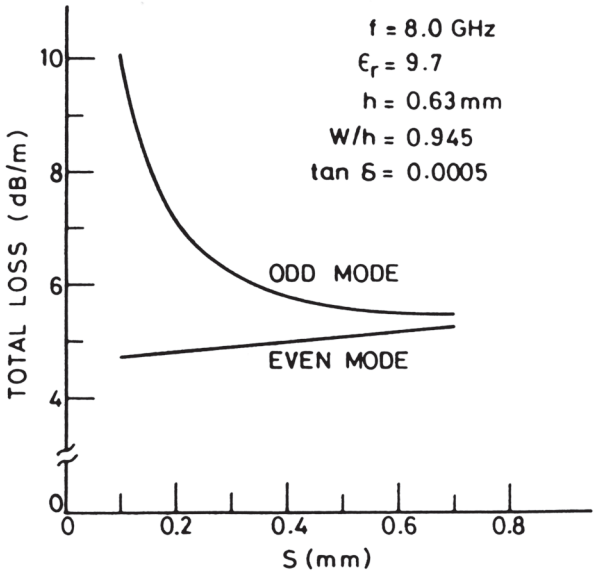

Figure 8.19 Even- and odd-mode losses in coupled microstriplines (from [42], © 1979 IEEE. Reprinted with permission.).

In the above relations R_s is the sheet resistivity of metallization. It is observed that the odd-mode attenuation constant is always higher than the even-mode value. Also, it is more sensitive to changes in the spacing S between the lines than is α_{ce}. This is borne out by the plot of even- and odd-mode losses in Figure 8.19.

The attenuation due to dielectric loss α_d is given by [60]

$$\alpha_{do} = 27.3 \frac{\varepsilon_r}{\sqrt{\varepsilon_r^o}} \frac{\varepsilon_r^o - 1}{\varepsilon_r - 1} \frac{\tan\delta}{\lambda_0} \quad \text{(dB/unit length)} \tag{8.114}$$

$$\alpha_{de} = 27.3 \frac{\varepsilon_r}{\sqrt{\varepsilon_r^e}} \frac{\varepsilon_r^e - 1}{\varepsilon_r - 1} \frac{\tan\delta}{\lambda_0} \quad \text{(dB/unit length)} \tag{8.115}$$

where tan δ is the loss tangent of the dielectric substrate.

The total attenuation constants α_o and α_e for odd and even modes are given by

$$\alpha_o = \alpha_{co} + \alpha_{do} \tag{8.116}$$

and

$$\alpha_e = \alpha_{ce} + \alpha_{de} \tag{8.117}$$

The resultant even- and odd-mode impedances of lossy coupled lines are complex and may be obtained from the relations

$$Z_{0o}(\text{Lossy}) = Z_{0o}\left\{1 - j\frac{\alpha_{co}}{\beta_o} + j\frac{\alpha_{do}}{\beta_o}\right\} \tag{8.118}$$

$$Z_{0e}(\text{Lossy}) = Z_{0e}\left\{1 - j\frac{\alpha_{ce}}{\beta_e} + j\frac{\alpha_{de}}{\beta_e}\right\} \tag{8.119}$$

The relations for impedances are useful for studying the effect of line losses on circuit performance, for example, directivity of a directional coupler.

Like in a microstrip line, slotline, and coplanar lines, leaky modes have also been found to exist in coupled microstrip lines. Excitation of these modes gives rise to an additional loss. Effects of metal thickness and finite substrate width on leaky waves in coupled microstrip lines is discussed in [61].

8.5.3 Effect of Fabrication Tolerances [62]

The sensitivity analysis described earlier for other lines can also be applied to coupled transmission lines to account for the effect of tolerances. Since coupled lines are characterized by even- and odd-mode impedances and phase velocities, the effect of tolerances on coupled lines can be represented in terms of the effect on these characteristics.

The maximum change in the value of impedances may be written as

$$\left|\frac{\Delta Z_{0x}}{Z_{0x}}\right|_{\max} = \left|\frac{\Delta W}{W} S_W^{Z_{0x}}\right| + \left|\frac{\Delta S}{S} S_S^{Z_{0x}}\right| + \left|\frac{\Delta h}{h} S_h^{Z_{0x}}\right| + \left|\frac{\Delta \varepsilon_r}{\varepsilon_r} S_{\varepsilon_r}^{Z_{0x}}\right| \tag{8.120}$$

where x designates the mode, even or odd. Similarly the maximum change in the effective dielectric constants is given by

$$\left|\frac{\Delta \varepsilon_{re}^x}{\varepsilon_{re}^x}\right|_{\max} = \left|\frac{\Delta W}{W} S_W^{\varepsilon_{re}^x}\right| + \left|\frac{\Delta S}{S} S_S^{\varepsilon_{re}^x}\right| + \left|\frac{\Delta h}{h} S_h^{\varepsilon_{re}^x}\right| + \left|\frac{\Delta \varepsilon_r}{\varepsilon_r} S_{\varepsilon_r}^{\varepsilon_{re}^x}\right| \tag{8.121}$$

The above relations can be utilized to determine the change in coupled line characteristics like VSWR performance and change in coupling constant. Alternatively, for a given set of values of ΔZ_{0x} and $\Delta \varepsilon_{re}^x$ the trade-off between tolerances can be determined; that is, tolerance on one parameter may be increased or decreased at the cost of tolerances in other parameters.

The effects of tolerances on VSWR performance and coupling constant are described below.

VSWR performance of coupled microstrip lines

The VSWR performance of coupled microstrip lines may be obtained from

$$\text{VSWR} = \left[1 - \frac{|\Delta Z_0|_{\max}}{Z_0}\right]^{-1} \tag{8.122}$$

where the change in coupler impedance Z_0 $(= \sqrt{Z_{0e}\, Z_{0o}})$ represented by $|\Delta Z_0|_{\max}$ is obtained from

$$\frac{|\Delta Z_{0\max}|}{Z_{0|}} = \left|\frac{\Delta Z_{0o}}{Z_{0o}} S_{Z_{0o}}^{Z_o}\right| + \left|\frac{\Delta Z_{0e}}{Z_{0e}} S_{Z_{0e}}^{Z_0}\right| \tag{8.123}$$

Since $Z_0 = \sqrt{Z_{0e}\, Z_{0o}}$

$$S_{Z_{0e}}^{Z_0} = S_{Z_{0o}}^{Z_0} = 0.5 \tag{8.124}$$

and (8.123) becomes

$$\frac{|\Delta Z_{0\max}|}{Z_0} = 0.5\left[\left|\frac{\Delta Z_{0o}}{Z_{0o}}\right| + \left|\frac{\Delta Z_{0e}}{Z_{0e}}\right|\right] \tag{8.125}$$

where

$$\left|\frac{\Delta Z_{0e}}{Z_{0e}}\right| = \left|\frac{\Delta W}{W} S_W^{Z_{0e}}\right| + \left|\frac{\Delta S}{S} S_S^{Z_{0e}}\right| + \left|\frac{\Delta \varepsilon_r}{\varepsilon_r} S_{\varepsilon_r}^{Z_{0e}}\right| + \left|\frac{\Delta h}{h} S_h^{Z_{0e}}\right| \tag{8.126}$$

and a similar relation holds for ΔZ_{0o}.

Change in the Coupling Constant C

The coupling constant C is defined by

$$C = \frac{Z_{0e} - Z_{0o}}{Z_{0e} + Z_{0o}} \tag{8.127}$$

Since the coupling constant is a function of W, h, S, and ε_r, one can write

$$\frac{|\Delta C|_{\max}}{C} = \left|\frac{\Delta W}{W} S_W^C\right| + \left|\frac{\Delta h}{h} S_h^C\right| + \left|\frac{\Delta \varepsilon_r}{\varepsilon_r} S_{\varepsilon_r}^C\right| + \left|\frac{\Delta S}{S} S_S^C\right| \tag{8.128}$$

Using equations (8.125) and (8.128) the effect of tolerances on the coupled microstrip characterstics can be estimated. It is shown in Figure 8.20 for the VSWR performance and the change in the coupling constant for $\varepsilon_r = 9.7$ [42]. It may be observed from this figure that the effect of tolerances increases with the increase in the coupling constant. Further analysis shows that the dielectric thickness h and the gap width S are the most critical parameters affecting the coupling constant [62]. Also, VSWR is mainly controlled by variations in h and ε_r.

8.5.4 Coupled Microstrip Lines with Dielectric Overlays

The analysis of coupled microstrip lines reported in Section 8.3 shows that the effective dielectric constants for even and odd modes of coupled microstrip lines are not equal. The even-mode effective dielectric constant is higher than its odd-mode counterpart value. This is because of the relatively higher density of the electric field lines in air for the odd mode. On alumina substrate, this difference is normally less than 12 percent. Although different even- and odd-mode phase velocities produce only a small perturbation on the coupler impedance $Z = \sqrt{Z_{0e}\, Z_{0o}}$ and the

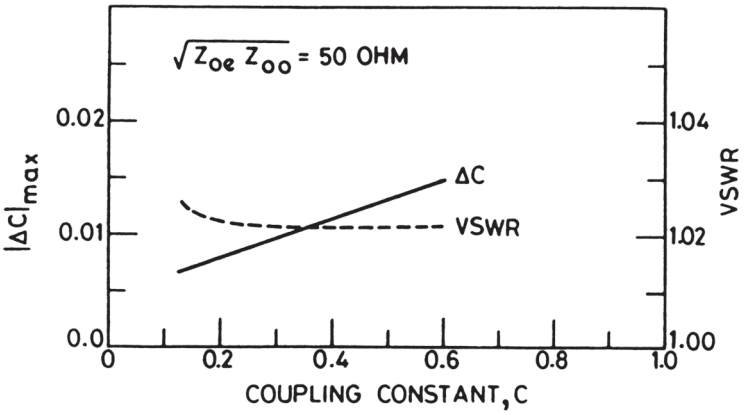

Figure 8.20 Effect of tolerances on coupling constant and VSWR performance of coupled microstrip lines ($\varepsilon_r = 9.7 \pm 0.25$, $h = 0.63 \pm 0.025$ mm, $\Delta W = \pm 0.0025$ mm, $\Delta S \pm 0.0025$ mm) (from [42], © 1979 IEEE. Reprinted with permission.).

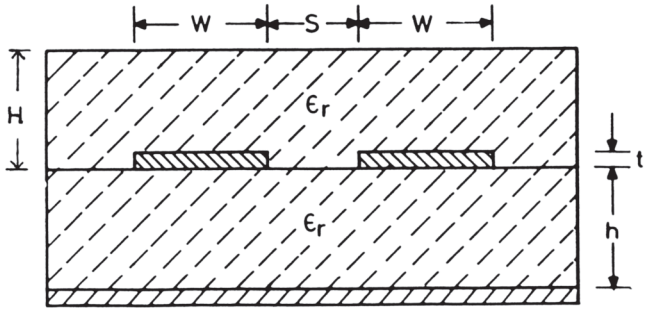

Figure 8.21 Coupled microstrip lines with a dielectric overlay to equalize even- and odd-mode phase velocities.

midband voltage coupling coefficient C (Equation 8.127) in most practical cases, the change in directivity of the coupler is significant. From infinite directivity for an ideal coupler, the directivity of a mircostrip 10-dB coupler on alumina substrate with $v_{odd}/v_{even} = 1.125$ decreases to about 12.5 dB. The deterioration in directivity is higher for loose coupling [63].

If a dielectric slab having dielectric constant equal to that of the substrate is placed over the coupled lines (see Figure 8.21), the odd-mode effective dielectric constant will increase more than that of the even mode. The increase in ε_{re}^{o} will be higher for thick overlay slabs. With the right amount of overlay thickness the effective dielectric constants for the two modes can be made equal. The use of a dielectric overlay not only improves the velocity ratio, but it also tightens the midband coupling compared to coupled microstrip lines without dielectric overlays. One would also expect a decrease in coupler impedance Z_0 because of the increased effective dielectric constants for the two modes.

The change in the amount of coupling and impedance due to the overlay can be determined analytically if the equalized value of phase velocity is known. For coupled lines without overlay we know that the coupler impedance Z_0 is given by

$$Z_0 = \sqrt{Z_{0o} Z_{0e}} \tag{8.129}$$

with

$$Z_{0o} = Z_{0o}^{a} / \sqrt{\varepsilon_{re}^{o}} \tag{8.130}$$

and

$$Z_{0e} = Z_{0e}^{a} / \sqrt{\varepsilon_{re}^{e}} \tag{8.131}$$

Now, with the dielectric overlay in place, let the effective dielectric constant for both modes be ε_{re}^{c} (where c stands for coupled lines). Then, the new values of impedances are given by

$$Z'_{0o} = Z_{0o}^{a} / \sqrt{\varepsilon_{re}^{c}} = Z_{0o} \sqrt{\varepsilon_{re}^{o} / \varepsilon_{re}^{c}} \tag{8.132}$$

$$Z'_{0e} = Z_{0e}^{a} / \sqrt{\varepsilon_{re}^{c}} = Z_{0e} \sqrt{\varepsilon_{re}^{e} / \varepsilon_{re}^{c}} \tag{8.133}$$

Therefore,

$$Z'_0 = \sqrt{Z'_{0o} Z'_{0e}} = Z_0 \left(\sqrt{\varepsilon_{re}^{o} \varepsilon_{re}^{e}} / (\varepsilon_{re}^{c}) \right)^{1/2} \tag{8.134}$$

The change in coupling can be estimated as follows. The voltage coupling coefficient with overlay is

$$C' = \frac{Z'_{0e} - Z'_{0o}}{Z'_{0e} + Z'_{0o}} \tag{8.135}$$

or

$$C' = \frac{Z_{0e} - Z_{0o} g}{Z_{0e} + Z_{0o} g} \tag{8.136}$$

where $g = \sqrt{\varepsilon_{re}^{o} / \varepsilon_{re}^{e}}$. Substituting the value of Z_{0e}/Z_{0o} from (8.127) gives

$$C' = \frac{(1 + C) - (1 - C) g}{(1 + C) + (1 - C) g} \tag{8.137}$$

It shows that the new coupling C' depends on the ratio of ε_{re}^{e} and ε_{re}^{o} and the coupling of the uncompensated coupler. It does not depend on the final value of ε_{re}^{c} nor on Z'_0.

Coupled microstrip lines with a dielectric overlay have been analyzed comprehensively [64–69]. Characteristic impedance and wavelength ratio λ_0/λ_g have been determined as a function of the overlay thickness H, gap S, and frequency. Results for $S/h = 0.4$, $W/h = 1$, and $\varepsilon_r = 10$ as a function of H/h are plotted in Figure 8.22.

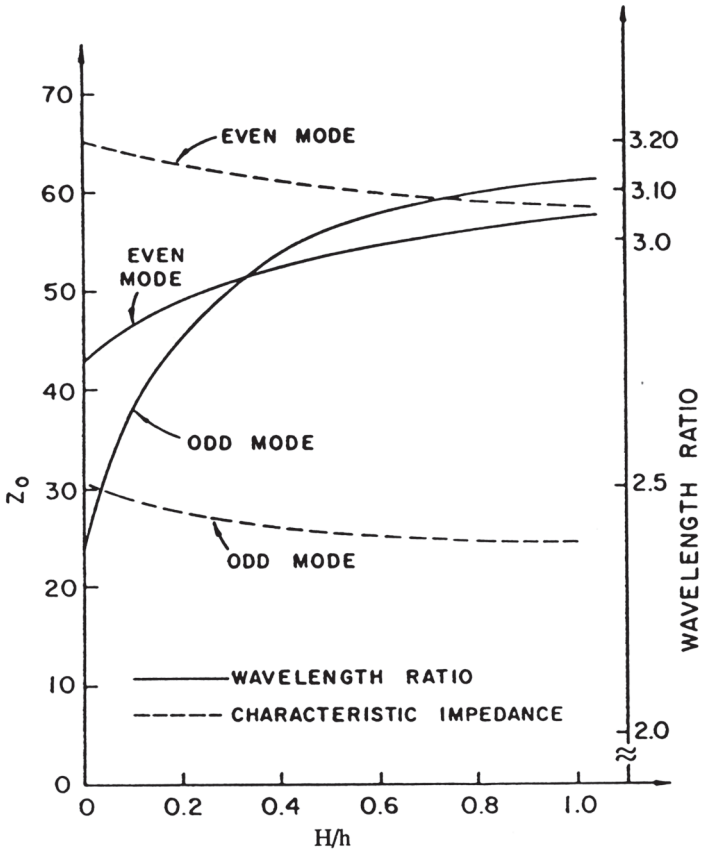

Figure 8.22 Characteristic impedance Z_0 and wavelength ratio λ_0/λ_g for the coupled microstrip lines with an overlay ($\varepsilon_r = 10$, $W/h = 1$, $S/h = 0.4$, $2\pi h/\lambda_0 = 0.1$) (from [68]).

It is observed that a crossing of even- and odd-mode wavelength ratios occurs at a relatively small overlay thickness. Klein and Chang have reported an improvement in isolation from 25 dB to 60 dB in a 10-dB coupler with an overlay [69].

Directivity Improvement Techniques

If the coupled microstrip line with dielectric overlay is backed by a ground plane such that $H/h = 1$, the geometry will look like a coupled strip line geometry and the even- and odd-mode phase velocities will be equal.

Improvement in the directivity of a microstrip line directional coupler may also be obtained by loading the coupler with a lumped reactance. The loading of the coupler in the middle with a suitable lumped capacitance C across the coupled lines [see Figure 8.23(a)] has been reported by Dydyk [83]. In-phase and out-of-phase excitation of the symmetrical coupler shows that the capacitor does not affect the even-mode characteristics. Odd-mode characteristics, however, are affected because of the presence of capacitor 2C across the coupled lines (using symmetry). The design equations for the compensated coupler are given by [83]

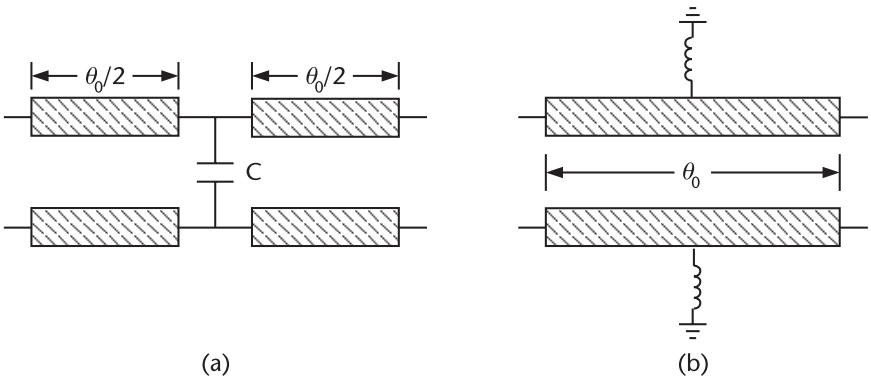

Figure 8.23 (a) Capacitive compensation for improved directivity of an edge coupled microstrip line directional coupler (after [83], © 1999 IEEE. Reprinted with permission). (b) Inductive compensation for improved directivity of an edge coupled microstrip line directional coupler (after [84], © 2010 IEEE. Reprinted with permission).

$$2\omega C = \frac{1 - \tan^2(\theta_o/2)}{Z_{0oi}} \qquad Z_{0oa} = Z_{0oi}\cot(\theta_o/2) \tag{8.138}$$

where θ_o is the actual odd-mode electrical length of the coupler, Z_{0oi} is the ideal odd-mode impedance, and Z_{0oa} is the actual odd-mode impedance. Another compensation technique in the form of shunt inductance loading at the middle of the coupler (Figure 8.23(b)) has been suggested, especially for loose directional couplers [84]. A maximum directivity of 56 dB has been reported [84].

8.5.5 Effect of Dielectric Anisotropy

It has been assumed in the analysis presented in Section 8.3 and in the design equations given in this section that the dielectric substrate is isotropic. However, substrates such as sapphire and Epsilam-10[1] are anisotropic. This anisotropy can be used to advantage in the design of coupled microstrip lines as shown by Szentkuti [70]. The transformation from anisotropic to the isotropic case can be carried out in the same manner as has been done for the single microstrip (discussed in Section 2.4.4). The relative difference between the odd- and even-mode phase velocities is plotted in Figure 8.24 for four types of substrates. It may be observed from here that the difference in phase velocities decreases with the increase in ratio $\varepsilon_r^x/\varepsilon_r^y$, where ε_r^x and ε_r^y are the x and y components, respectively, of the anisotropic dielectric constant.

8.6 Slot-Coupled Microstrip Lines

The edge coupled microstrip lines discussed in Section 8.3 are useful coupled line geometry for realizing couplers with loose coupling. For tight coupling (3 to 6 dB)

[1]Trademark of Rogers, Inc.

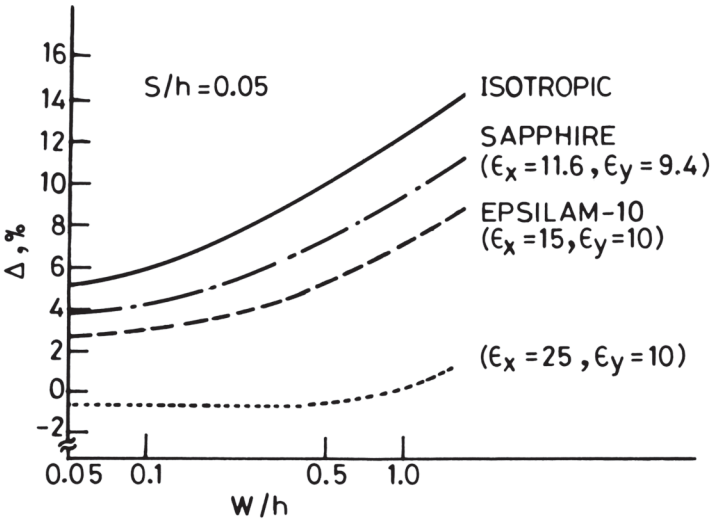

Figure 8.24 Relative difference between odd- and even-mode phase velocities for anisotropic substrates (from [70] © 1976 IEE (U.K.). Reprinted with permission.).

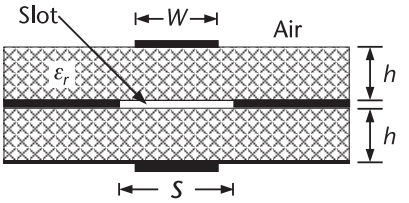

Figure 8.25 Cross-section of slot-coupled microstrip lines.

one may employ these lines in Lange coupler or tandem coupler configurations. The wire crossovers required for this purpose are not convenient from a manufacturing point of view. Broadside coupled microstrip lines, on the other hand, are more suitable for tight, as well as loose, couplers. Tanaka et al. introduced broadside coupled microstrip line geometry [85]. The cross-section of this geometry is shown in Figure 8.25. It consists of two microstrip lines that couple through a slot in the common ground plane. This geometry can support two modes, even- and odd-modes. The electric field configuration for these modes is shown in Figure 8.26. The even-mode field distribution is such that the electric field is confined between the strip and slot edges, as shown in (Figure 8.26(a)), with no field in the parallel slot region. Therefore, the slot may be covered by a magnetic wall (MW) for the purpose of approximate analysis [86]. It may be noted that the presence of a coupling slot does not affect the odd-mode field distribution (Figure 8.26(b)) and is similar to that of the mode in a microstrip line. Therefore, the slot may be closed by an electric wall (EW) for analysis purposes, and one may use microstrip line design formulas for the odd-mode.

Conformal mapping analysis is most suitable for arrival at the closed-form design equations. However, the analysis is accurate under a quasi-static limit. We pre-

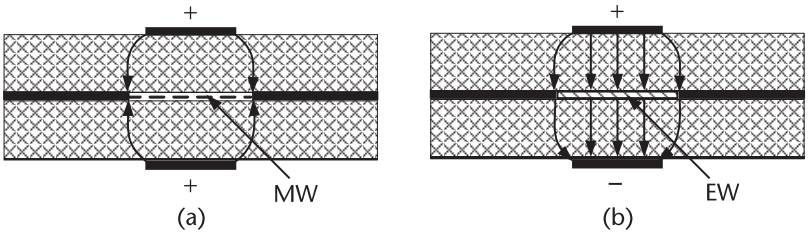

Figure 8.26 Electric field distribution for the coupled line modes in slot-coupled microstrip lines. (a) Even-mode field distribution, and (b) odd-mode field distribution (after [86], © 1991 IEEE. Reprinted with permission).

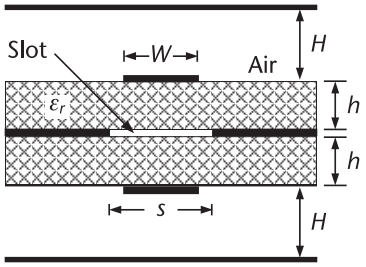

Figure 8.27 Shielded coupled line geometry for conformal mapping analysis.

sent this analysis next. The assumptions for conformal mapping analysis include: (1) the common ground plane is infinitely wide; (2) the strips are infinitely thin; and (3) a magnetic wall may be placed at the air-dielectric interface of microstrip lines. The last assumption is found to be valid for narrow slots and also leads to a fairly accurate design for wide slots [86].

Conformal mapping analysis

For simplicity in conformal mapping analysis, we shield the coupled line geometry from top and bottom, as shown in Figure 8.27. The design for the unshielded line is retrieved for a value of *H/h*, which increases as substrate dielectric constant decreases. The even-mode characteristics are sensitive to this ratio. The line capacitance for even- and odd-modes is determined by applying a number of mappings in sequence, so that the given transmission line is transformed into a parallel plate line with homogeneous dielectric. Also, only one-half of the geometry needs to be considered, due to the symmetry of the line midway through the slot.
The line capacitance for the even-mode may be expressed as

$$C_e = C_{1e} + C_{2e} \tag{8.139}$$

where the geometries for determining C_{1e} and C_{2e} are shown in Figure 8.28(a). The final expressions for these capacitances are obtained as [86]

$$C_{1e} = 2\varepsilon_0 \frac{K(k_1)}{K'(k_1)} \quad \text{and} \quad C_{2e} = 2\varepsilon_0\varepsilon_r \frac{K(k_2)}{K'(k_2)} \tag{8.140}$$

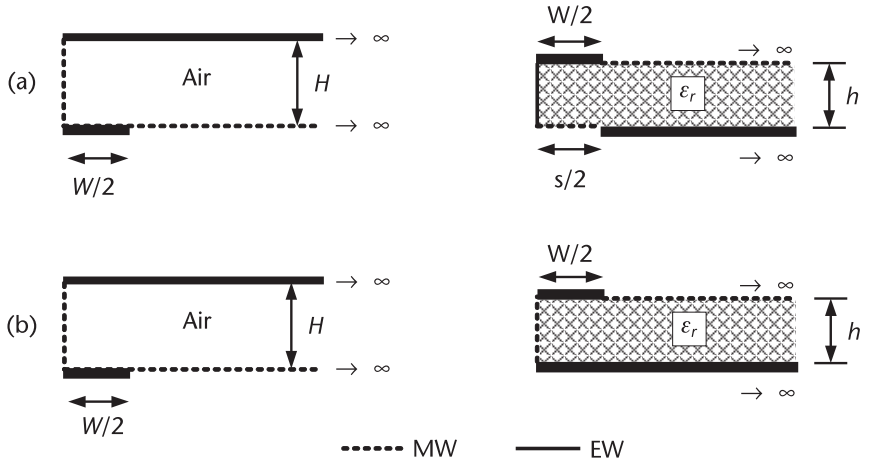

Figure 8.28 Decomposition of line geometry for determining the capacitances C_1 and C_2 (a) Decomposition for even-mode (after [86], © 1991 IEEE. Reprinted with permission) and (b) decomposition for odd-mode (After [86]).

where

$$k_1 = \tanh\left(\frac{\pi}{4}\frac{W}{H}\right) \quad \text{and} \quad k_2 = \frac{\cosh\left(\pi W/(4h)\right)}{\sqrt{\sinh^2\left(\pi S/(4h)\right) + \cosh^2\left(\pi W/(4h)\right)}} \tag{8.141}$$

Here $K(k)$ is the complete elliptic integral of the first kind and $K'(k) = K(k')$, $k' = \sqrt{1-k^2}$. A simple and accurate expression for the ratio is given in (7.12).

The line capacitance for the odd-mode C_o is decomposed similar to that for the even-mode, (8.139), with the geometries for determining C_{1o} and C_{2o} shown in Figure 8.28(b). These capacitances are obtained as [86]

$$C_{1o} = C_{1e} = 2\varepsilon_0 \frac{K(k_1)}{K'(k_1)} \quad \text{and} \quad C_{2o} = 2\varepsilon_0\varepsilon_r \frac{K(k_3)}{K'(k_3)} \tag{8.142}$$

where

$$k_3 = \tanh\left(\pi W/(4h)\right) \tag{8.143}$$

It may be noted that the odd-mode capacitance is independent of the slot width S.

The relative effective dielectric constants and characteristic impedances for the coupled line modes are obtained from line capacitances as

$$\varepsilon_{re}^{e,o} = \frac{C_{e,o}(\varepsilon_r)}{C_{e,o}(\varepsilon_r = 1)} \quad \text{and} \quad Z_{0(e,o)} = \frac{60\pi}{\sqrt{\varepsilon_{re}^{e,o}}} \frac{1}{C_{e,o}(\varepsilon_r = 1)} \tag{8.144}$$

The coupled mode characteristics for any set of coupled line parameters may be computed from (8.144). These are plotted in Figure 8.29 for $\varepsilon_r = 4$, $H/h = 15$. It may be observed that the even-mode characteristics approach odd-mode characteristics as the slot width S approaches zero.

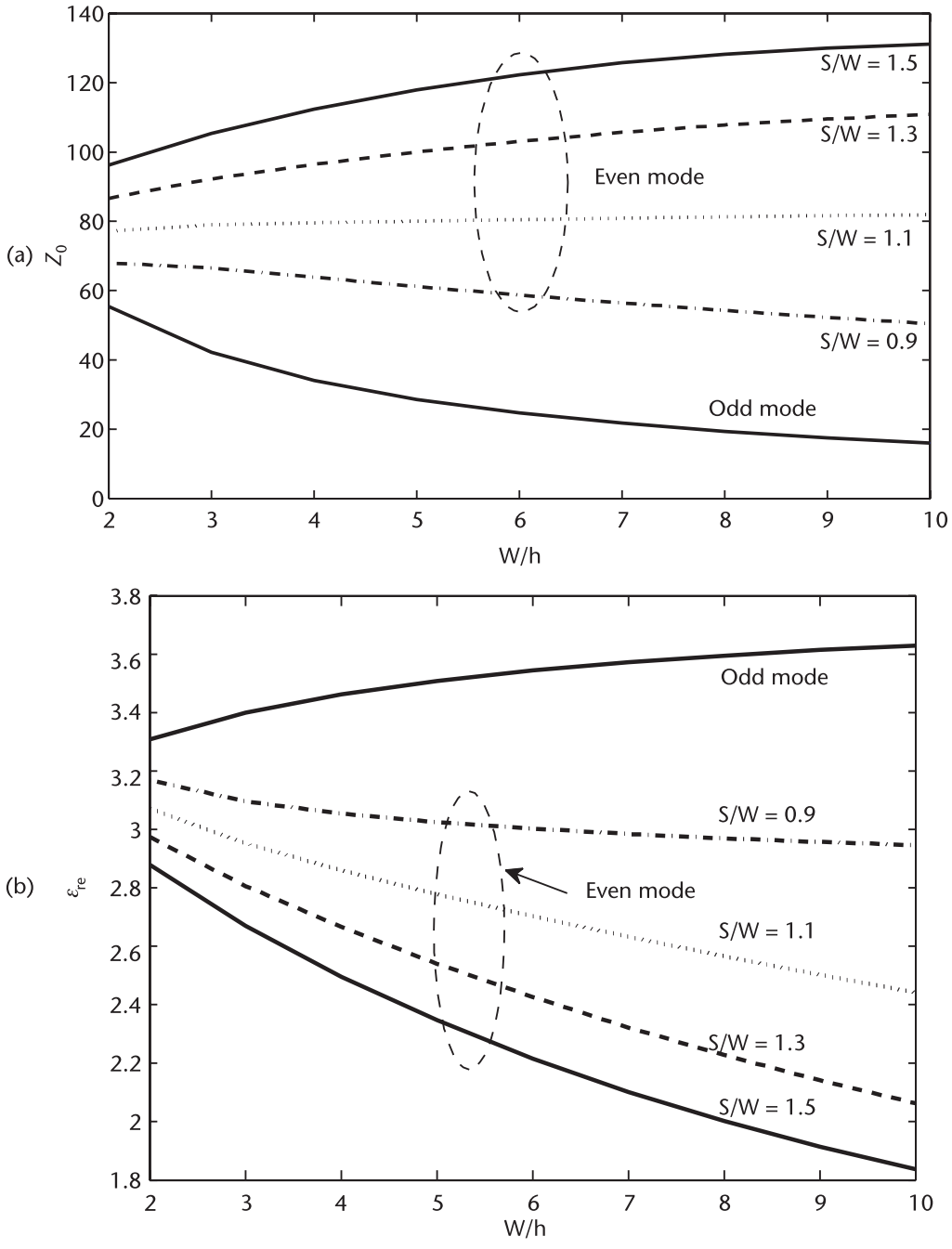

Figure 8.29 (a) Variation of characteristic impedance for slot-coupled microstrip lines, $\varepsilon_r = 4$, $H = 15h$. (b) Variation of relative effective dielectric constant for slot-coupled microstrip lines, $\varepsilon_r = 4$, $H = 15h$.

Full-wave analysis of the slot-coupled microstrip line geometry has been reported based on spectral domain approach [86]. The unknown electric field across the slot and the longitudinal current along the strips are expanded in basis functions. The characteristic impedance of the modes is determined according to power-current definition, unlike the voltage-current definition employed in quasi-static analysis. The characteristic impedance values for 1 GHz are compared with values obtained from conformal mapping method (CMM) [86]. The maximum difference is found to be about 5 percent for the even-mode and about 1 percent for the odd-mode [86]. Therefore, the design of slot-coupled microstrip lines under quasi-static limit may be carried out using CMM.

Applications of this coupled microstrip line configuration in the design of coupled line directional couplers and ultrawide band balun is described in Chapter 5. Circuit applications of coupled microstrip lines, such as broadband directional couplers, coupled line filters, dc blocks, and baluns, are discussed in [87].

8.7 Coupled Multiconductor Microstrip Lines

Two strip coupled microstrip lines are used in many circuits. The performance of these circuits can be improved by using multistrip/multiconductor microstrip lines. These lines also find applications in VLSI interconnections and antennas [27, 31–34, 71–76]. Analysis of these lines is briefly summarized next.

Very large scale integrated (VLSI) chips require millions of closely spaced interconnection lines that integrate the components on a chip. Multilayer interconnections in two or more planes play the most significant role in determining the size, power consumption, and clock frequency. In particular, capacitances, inductances, cross talk, and propagation delays associated with the interconnections in high-density environments on a chip or wafer have become the major factors in the evolution of very high speed integrated circuit technology. Capacitances and inductances associated with interconnections on the same plane are discussed next. For other characteristics such as propagation delays, cross talk, and failure analysis the reader may refer to [75].

The schematic diagram of a few interconnection lines on the same plane is shown in Figure 8.30. For the switching speeds commonly encountered in VLSI circuits the system or lines shown in Figure 8.30 can be characterized by a capacitance matrix [**C**] and an inductance matrix [**L**]. The inductance matrix can be obtained from the capacitance matrix as in (8.105). The diagonal elements of the capacitance matrix C_{ii} are called self-capacitances and represent the capacitance between the strip conductors and the ground. The off-diagonal elements are called coupling (interconnection) capacitances or mutual capacitances.

The capacitance for a single microstrip line was determined in Chapter 1 using various techniques. Some of these techniques were extended to coupled microstrip lines in Section 8.2. The same techniques can also be used to determine the capacitance matrix of multiconductor microstrip lines. The most commonly used methods are the integral equation method of Section 1.2.3, the variational method in

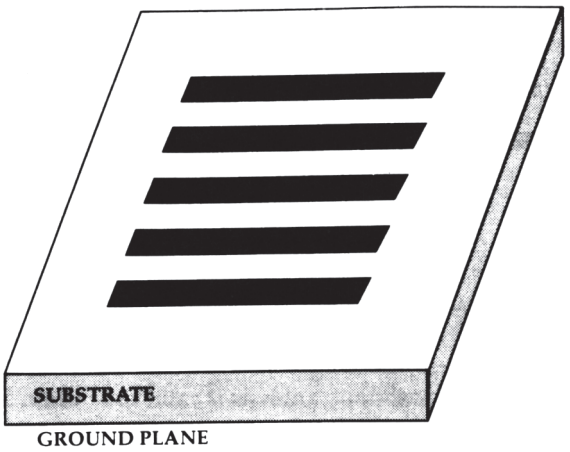

Figure 8.30 Schematic of a few interconnections printed as microstrip lines.

FTD of Section 1.2.4, the congruent transformation technique [8], and the network analog method [77].

Multiconductor transmission lines, including coupled microstrip lines, are discussed comprehensively in [88].

The various capacitances for three coupled microstrip lines are shown in Figure 8.31. For the symmetric layout the even- and odd-mode approach can be used to reduce the computational effort. The even mode corresponds to the situation when all the strips are at the same potential, say $+V_o$. In the odd-mode case, one of the strips is at the potential $-V_o$, and the rest are at $+V_o$. The capacitances (per unit length) shown in Figure 8.31 are related to the even- and odd-mode capacitances (per unit length) defined above by the set of equations [75]

$$C_1^e = C_{11} \qquad C_2^e = C_{22} \qquad C_3^e = C_{33} \tag{8.145}$$

$$C_1^o = C_{11} + 2C_{12} + 2C_{13} \tag{8. 146a}$$

$$C_2^o = C_{22} + 2C_{12} + 2C_{23} \tag{8. 146b}$$

$$C_3^o = C_{33} + 2C_{13} + 2C_{23} \tag{8. 146c}$$

The dependence of the self- and mutual capacitances on the strip width W is shown in Figure 8.32 for single-level three-strip interconnections on GaAs substrate [75]. T is the strip thickness in this figure. It is observed from Figure 8.32(a) that the self-capacitances increase almost linearly with strip width W. The capacitance C_{22} for the middle strip is lower than C_{11} or C_{33} because of the shielding effect of outer strips. The mutual capacitances C_{12} and C_{23} between the nearest neighbors is higher than between the next-to-nearest neighbor C_{13} (see Figure 8.32(b)). The inductance values can be obtained from the capacitance values and (8.105). Mutual inductances are plotted in Figure 8.33 as a function of strip width W.

Design equations for the even- and odd-mode capacitances and inductances (per unit length) for the multiconductor microstrip lines are available in [49]. The

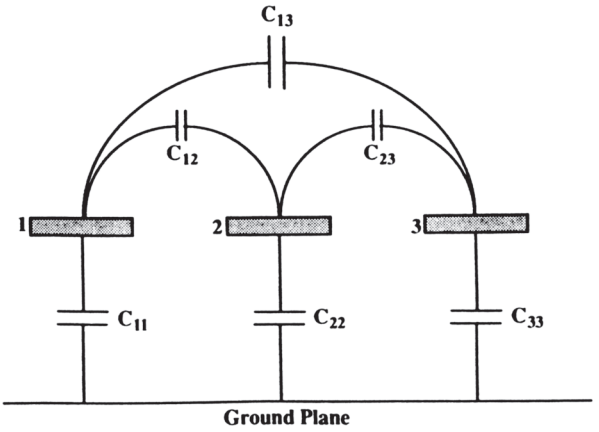

Figure 8.31 Various capacitances between three coupled microstrip lines (from [75], © 1994 John Wiley. Reprinted with permission.).

open-end capacitance may be added to these capacitance values to obtain the overall capacitance for a given line length L.

For digital circuits the quasi-static analysis is valid only when switching speeds are on the order of one nanosecond. When the rise time of the switching pulse reduces to tens of picoseconds, a fullwave analysis of the multiconductor microstrip lines becomes necessary [27].

8.8 Discontinuities in Coupled Microstrip Lines

Sections of coupled microstrip lines are used extensively for the design of directional couplers, filters, and other components. Although characteristics of uniformly coupled microstrip lines have been studied extensively, characterization of discontinuities and junctions in coupled lines is not readily available. An open end is perhaps the only coupled microstrip line discontinuity described in detail [78]. A closed form expression is also available for open-end discontinuity. In this section we describe an approach that can be used to analyze discontinuities in coupled microstrip lines with a considerable savings in computation time. It is called the *network model* of coupled microstrip lines. This model makes use of the planar waveguide model of microstrip line discussed in Chapter 1.

8.8.1 Network Model [79]

A network model for coupled microstrip lines has been developed. The model consists of two parallel plate waveguide sections that are coupled to each other through a lumped-element network. The coupled line section and its planar lumped model are shown in Figure 8.34. The parallel plate sections, also called planar segments, model the electric fields underneath the strips and the fringing fields at the outer edges e_1. The lumped-element network represents the electromagnetic coupling between the strips. The coupling due to the electric field across the gap is modeled by

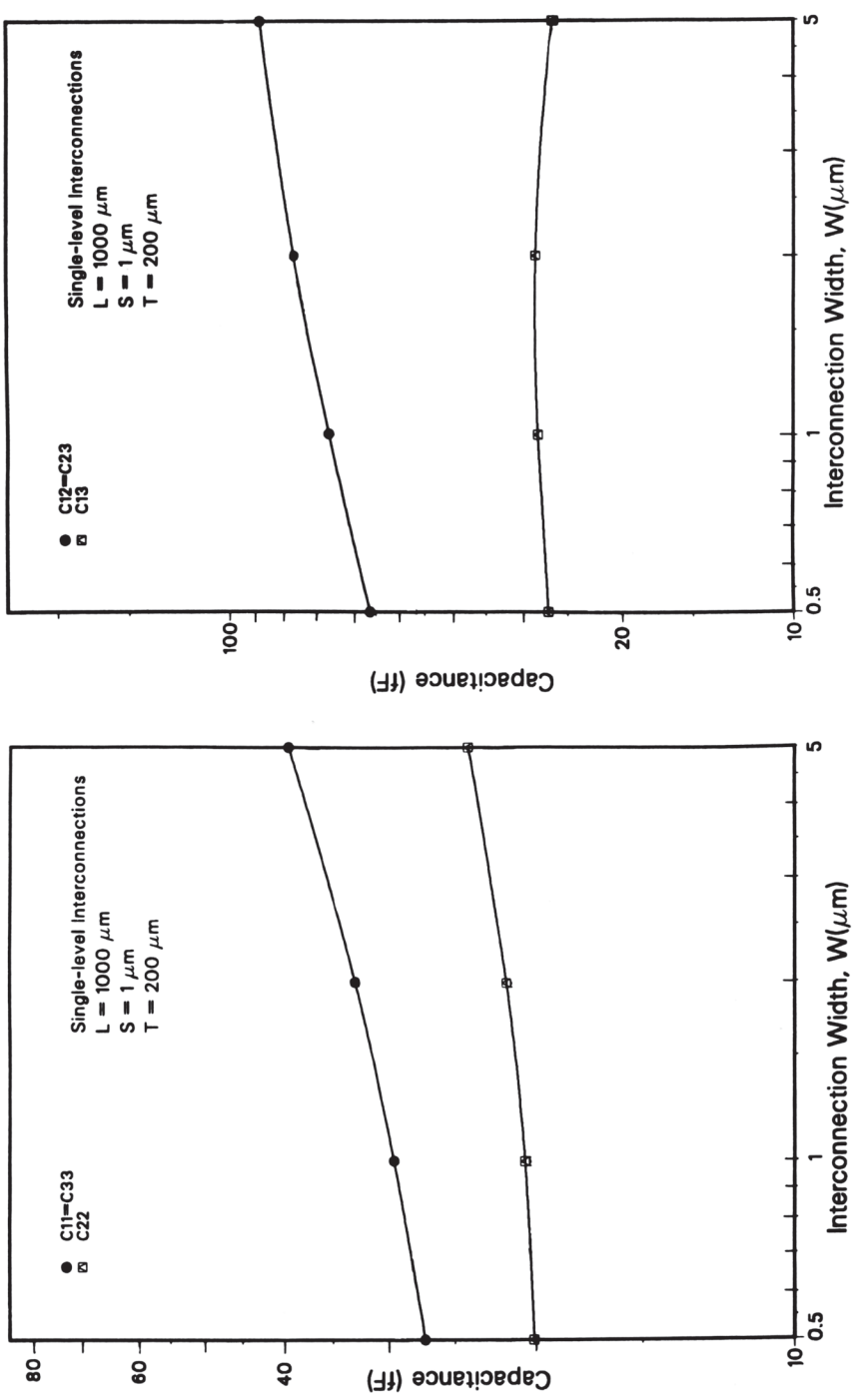

Figure 8.32 (a) Variation of the self-capacitances with the strip width W for three strip interconnections on GaAs and (b) variation of the mutual-capacitances with the strip width W for three strip interconnections on GaAs (from [75], © 1994 John Wiley. Reprinted with permission.).

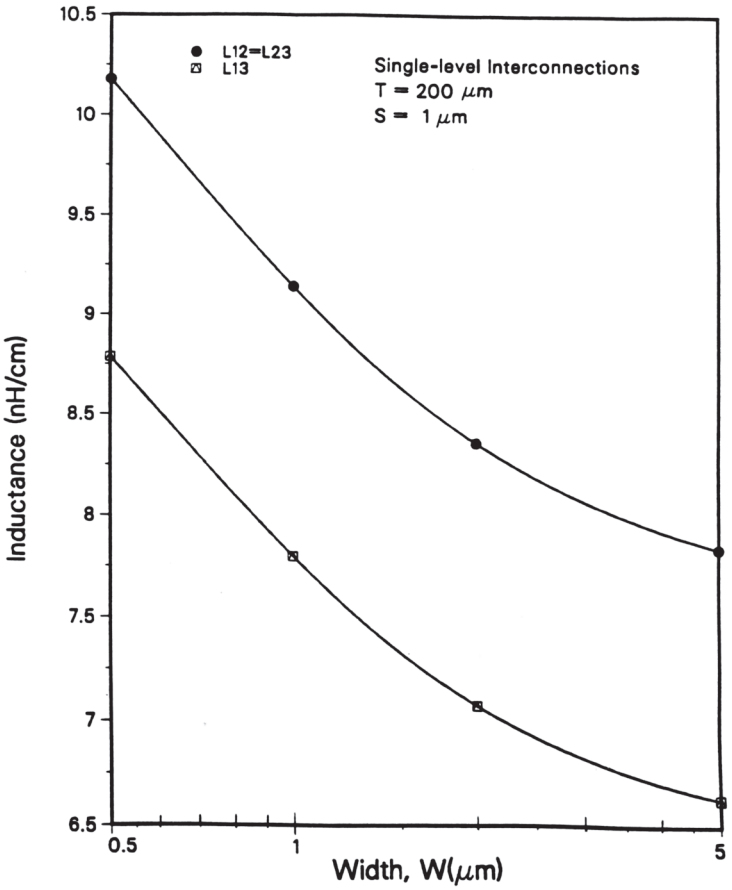

Figure 8.33 Variation of the mutual-inductances with the strip width W for three strip interconnections on GaAs (from [75], © 1994 John Wiley. Reprinted with permission.).

a capacitive network, and the magnetic field coupling is represented by an inductive network. Some details of the parallel plate section and the lumped network are given next.

The parallel plate waveguide model for the microstrip line has been described in Chapter 1. In the present context, the parallel plate waveguide accounts for the fringing fields only at the outer edges. So their effective widths $W_e(f)$ are chosen to account for outward extension at outer edges only. Keeping this in mind we write

$$W_e(f) = W + \frac{W_{em}(f) - W}{2} = \frac{W_{em}(f) + W}{2} \tag{8.147}$$

where W is the physical width of the strip and W_{em} is the width of an equivalent parallel plate waveguide for a single microstrip line. The value of W_{em} can be obtained from (1.84b) and is repeated here:

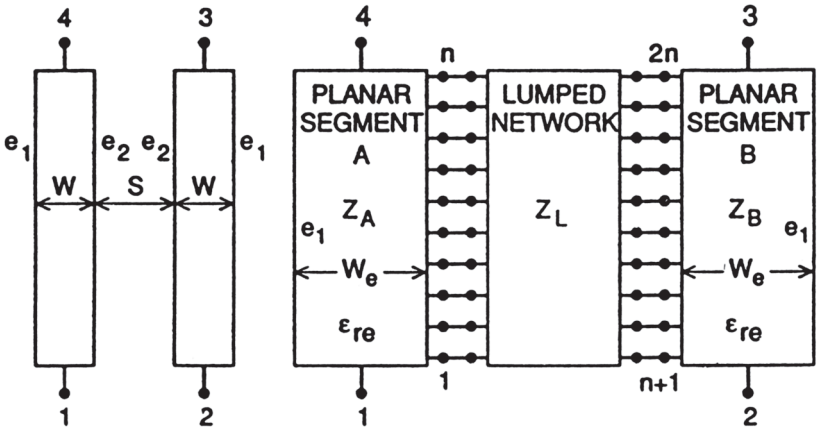

Figure 8.34 A section of coupled microstrip lines and its planar-lumped model (from [79], © 1992 IEEE. Reprinted with permission.).

$$W_{\text{em}}(f) = \frac{120\pi h}{Z_{0\text{m}}(f)\sqrt{\varepsilon_{\text{re}}(f)}} \tag{8.148}$$

Lengths of these sections are equal to the physical length of the coupled line section. The parallel plate waveguide sections in Figure 8.34 are connected through a multiport network. To implement this connection a number of ports are introduced on the inner edge of each of the parallel plate sections. Multiport impedance matrices for the waveguide sections are derived from the two-dimensional Green's function for the rectangular geometry [80].

Capacitive Network

The capacitive network represents the electric field coupling between the parallel plate waveguide sections. Electric field coupling is very similar to the gap coupling between microstrip lines described in Section 3.4.2. A π-network model of the resultant capacitive network was discussed there. The capacitive network for a coupled line section of length $\Delta\ell$ is shown in Figure 8.35(a). Here capacitance C_{f} accounts for the fringe electric field between the inner edge of the strip and the ground plane. The value of C_{f} is obtained by subtracting the parallel plate capacitance from the even-mode capacitance of the coupled microstrip lines. One obtains

$$C_f = \left(C_e - \frac{\varepsilon_o \varepsilon_{re} W_e}{h}\right)\Delta\ell \tag{8.149}$$

The capacitance C_{g} represents the electric field across the gap. It is defined as

$$C_{\text{g}} = \frac{C_{\text{o}} - C_{\text{e}}}{2}\Delta\ell \tag{8.150}$$

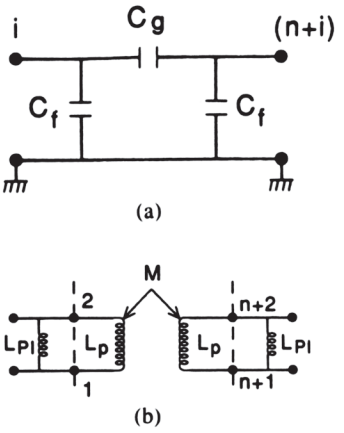

Figure 8.35 Coupling networks between coupled lines: (a) capacitive network representation of coupling between coupled lines section of length $\Delta\ell$ and (b) inductive network representation of coupling between coupled lines section of length $\Delta\ell$ (from [79], © 1992 IEEE. Reprinted with permission.).

where C_o and C_e are the odd- and even-mode capacitances per unit length of the coupled line (Section 8.5.1). The π-network shown in Figure 8.35(a) has the admittance matrix

$$[\mathbf{Y}_C] = j\omega \begin{bmatrix} C_f + C_g & -C_g \\ -C_g & C_f + C_g \end{bmatrix} \equiv j\omega[\mathbf{C}_G] \tag{8.151}$$

When the lumped network of Figure 8.28 has n ports on each side, the complete $\mathbf{Y}_c$-matrix will be $2n \times 2n$ with four $n \times n$ submatrices. Each of these submatrices is diagonal in nature.

Inductive Network

The magnetic field between the strips is modeled by the self- and mutual inductances. Let us consider Figure 8.34 in which two adjacent ports of the planar waveguide network A (say 1 and 2) face the corresponding ports (n + 1) and (n + 2) of the planar waveguide network B. The inductive coupling network between these ports may be drawn as shown in Figure 8.35(b). Values of L_p and M are obtained from an analysis of the coupled line section with air as dielectric, as described by (8.106). The inductance per unit length of the parallel plate section is denoted by L_{pl} and is given by

$$L_{pl} = \frac{\mu_o h}{W_e} \tag{8.152}$$

The admittance matrix associated with the inductive coupling network is tridiagonal in nature. It is given by

$$[\mathbf{Y}_L] = \frac{-j}{\omega\left(L_p^2 - M^2\right)}[\mathbf{L}_G] \tag{8.153}$$

The details of matrix $[L_g]$ can be found in [79]. The admittance matrix of the gap network is then obtained as

$$[Y_G] = [Y_C] + [Y_L] = j\omega[C_G] - \frac{j}{\omega(L_p^2 - M^2)}[L_G] \tag{8.154}$$

Multiport admittance matrices of the planar waveguide sections are now combined with the admittance matrix of the gap network to obtain the characteristics of the coupled line section. The network model described above has been found to correctly predict the coupling coefficient S_{21} and the higher order mode cutoff frequencies. It has been used to analyze a coupled microstrip section with chamfered right-angled bends discontinuity to single microstrip lines (see Figure 8.36). Calculated S_{21} parameter for this circuit is found to agree with measured values. The network model can be applied to various types of discontinuities in coupled microstrip lines.

8.8.2 Open-End Discontinuity

Similar to the open end in a microstrip line, the open end in coupled microstrip lines is capacitive in nature and can be characterized in the form of an additional line length $\Delta\ell_{o,e}$ for each mode. Closed-form expressions for $\Delta\ell_{o,e}$ have been reported [39, 81]. These are given as

$$\Delta\ell_e = \Delta\ell_{oc}(u,\varepsilon_r) + \left\{\Delta\ell_{oc}(2u,\varepsilon_r) - \Delta\ell_{oc}(u,\varepsilon_r) + 0.0198h \cdot g^{R_1}\right\} \cdot \exp(-0.328g^{2.244}) \tag{8.155a}$$

$$\Delta\ell_o = \Delta\ell_{oc}(u,\varepsilon_r)(1 - e^{-R_4}) + hR_3 \cdot e^{-R_4} \tag{8.155b}$$

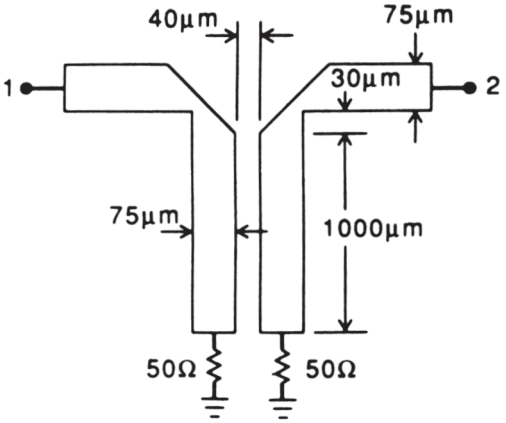

Figure 8.36 A coupled microstrip section with chamfered bends (from [79], © 1992 IEEE. Reprinted with permission).

with

$$R_1 = 1.187\left\{1 - \exp(-0.069u^{2.1})\right\}$$

$$R_2 = 0.343 \cdot u^{0.6187} + \frac{0.45\varepsilon_r}{1+\varepsilon_r} u^{\{1.357+1.65/(1+0.7\varepsilon_r)\}}$$

$$R_3 = 0.2974(1 - \varepsilon^{-R_2})$$

$$R_4 = \left(0.271 + 0.0281\varepsilon_r\right) \cdot g^{\{1.167\varepsilon_r/(0.66+\varepsilon_r)\}} + \frac{1.025\varepsilon_r}{0.687+\varepsilon_r} \cdot g^{\{0.958\varepsilon_r/(0.706\varepsilon_r)\}}$$

$$u = W/h \text{ and } g = S/h$$

The quantities $\Delta\ell_{oc}(u, \varepsilon_r)$ and $\Delta\ell_{oc}(2u, \varepsilon_r)$ represent open-end extension values for a single line with widths W and $2W$, respectively. The range of applicability of (8.155) is again defined by (8.97), and the associated accuracy is about 5 percent. It is found that line length extension $\Delta\ell_e$ decreases asymptotically to $\Delta\ell_{oc}(u, \varepsilon_r)$ as the spacing S/h is increased.

References

[1] Ozaki, H., and J. Ishii, "Synthesis of a Class of Stripline Filters," *IRE Trans.*, Vol. CT-5, 1958, pp. l04–109.

[2] Louisell, W. H., *Coupled Mode and Parametric Electronics*, New York: John Wiley, 1960.

[3] Isaacs, J. C., and N. A. Strakhov, "Crosstalk in Uniformly Coupled Lossy Transmission Lines," *Bell System Tech. J.*, Vol. 52, 1975, pp. 101–115.

[4] Sato R., and E. G. Cristal, "Simplified Analysis of Coupled Transmission-Line Network," *IEEE Trans.*, Vol. MTT-18, 1970, pp. 122–131.

[5] Hazony, D., *Elements of Network Synthesis*, New York: Reinhold, 1963, Ch. 15.

[6] Chang, F. Y., "Transient Analysis of Lossless Coupled Transmission Lines in a Non-Homogeneous Dielectric Medium," *IEEE Trans.*, Vol. MTT-18, 1970, pp. 616–626.

[7] Richards, P. I., "Resistor Transmission Line Circuits," *Proc. IRE*, Vol. 56, 1948, pp. 217–220.

[8] Chao, C. L., "On the Analysis of Inhomogeneous Asymmetrical Coupled Transmission Lines,"*18th Mid-West Symp. Circuits and Systems*, Montreal, 1975, pp. 568–572.

[9] Tripathi, V. K., "Asymmetric Coupled Transmission Lines in an Inhomogeneous Medium," *IEEE Trans.*, Vol. MTT-23, 1975, pp. 734–739.

[10] Tripathi, V. K., "Properties and Applications of Asymmetric Coupled Line Structures in an Inhomogeneous Medium," *Proc. 5th European Microwave Conf.*, Hamburg, 975, pp. 278–282.

[11] Costamagna, E., and U. Maltese R, "Linee Accoppiate Asimmetriche in Dieletbico non Omogeneo, *Alta Freq.*, Vol. 40, 1971, pp. 757–741. (in Italian)

[12] Krage M. K., and G. I. Haddad, "Characteristics of Coupled Microstrip Transmission Lines-I: Coupled-Mode Formulation of Inhomogeneous Lines, II: Evaluation of Coupled-Line Parameters," *IEEE Trans.*, Vol. MTT-18, 1970, pp. 217–228.

[13] Pregla, R., "Calculation of the Distributed Capacitances and Phase Velocities in Coupled Microstrip Lines by Conformal Mapping Techniques," *AEU*, Vol. 26, 1972, pp. 470–474.

[14] Brymt, T. G., and J. A. Weiss, "Parameters of Microstrip Transmission Lines and of Coupled Pairs of Microstrip Unes," *IEEE Trans.*, Vol. MTT-16, 1968, pp. 1021–1027.

[15] Young. L., and H. Sobol (Eds.), *Advances in Microwaves*, Vol. 8, New York: Academic Press, 1974, pp. 295–520.

[16] Bergandt, H. G., and R. Pregla, "Calculation of Even- and Odd-Mode Capacitance Parameters for Coupled Microstrips," *Archiv. Elektr. Ubertr.*, Vol. 26, 1972, pp. 153–158.

[17] Kowalski, G., and R. Pregla, "Calculation of the Distributed Capacitances of Coupled Microstrips Using a Variational Integral," *Archiv. Elektr. Ubertr.*, Vol. 27, 1973, pp. 51–52.

[18] Gunston, M. A. R., *Microwave Transmission Line Impedance Data*, London: Van Nostrand Reinhold, 1972, Ch. 6.

[19] Gladwell, G. M. L., and S. Coen, "A Chebyshev Approximation Method for Microstrip Problems," *IEEE Trans.*, Vol. MTT-23, 1975, pp. 865–-870.

[20] Krage, M. K, and G. I. Haddad, "Frequency Dependent Characteristics of Microstrip Transmission Lines," *IEEE Trans.*, Vol. MTT-20, 1972, pp. 678–688.

[21] Knorr, J. B., et al., "Hybrid Mode Analysis of Planar Lines," *Proc. 8th Asilomar Conf.*, 1974.

[22] Knorr, J. B., and K. D. Kuchler, "Analysis of Coupled Slots and Coplanar Strips and Dielectric Substrate," *IEEE Trans.*, Vol. MTT-23, 1975, pp. 541–548.

[23] Kowalski, G., and R. Pregla, "Dispersion Characteristics of Single and Coupled Microstrips," *Archiv. Elektr. Ubertr.*, Vol. 26, 1972, pp. 276–280.

[24] Davies, J. B., and D. G. Corr, "Computer Analysis of the Fundamental and Higher Order Modes in Single and Coupled Microstrip," *Electron. Lett.*, Vol. 6, 1970, pp. 806–808; see errata, Vol. 7, 1971, p. 284. .

[25] Jansen, R. H., "Fast Accurate Hybrid Mode Computation of Nonsymmetrical Coupled Microstrip Characteristics," *Proc. 7th European Microwave Conf.*, Copenhagen, 1977, pp. 135–139.

[26] Jansen, R. H., "High-Speed Computation of Single and Coupled Microstrip Parameters Including Dispersion, High-Order Modes, Loss and Finite Strip Thickness," *IEEE Trans.*, Vol. MTT-26, 1978, pp. 75–82.

[27] Farr, E. G., et al., "A Frequency-Dependent Coupled-Mode Analysis of Multiconductor Microstrip Lines with Application to VLSI Interconnect Problems," *IEEE Trans.*, Vol. MTT-34, 1986, pp. 307–310.

[28] Tripathi, V. K, and H. Lee, "Spectral-Domain Computation of Characteristic Impedances and Multiport Parameters of Multiple Coupled Microstrip Lines," *IEEE Trans.*, Vol. MTT-37, 1989, pp. 215–221.

[29] Bagby, J. S., et al., "Entire-Domain Basis MOM Analysis of Coupled Microstrip Transmission Lines," *IEEE Trans.*, Vol. MTT-40, 1992, pp. 49–57.

[30] Tzuang, C. K. C., and J. T. Kuo, "Modal Current Distributions on Closely Coupled Microstrip Lines: A Comparative Study of the SDA Basis Functions," *Electron. Lett.*, Vol. 26, 1990, pp. 464–465.

[31] Mu, T. C., et al., "Characteristics of Multiconductor, Asymmetric Slow Wave Microstrip Transmission Lines," *IEEE Trans.*, Vol. MTT-34, 1986, pp. 767–772.

[32] Marx, K. D., "Propagation Modes, Equivalent Circuits and Characteristic Terminations for Multiconductor Transmission Lines with Inhomogeneous Dielectrics," *IEEE Trans.*, Vol. MTT-21, 1973, pp. 450–457.

[33] Tripathi, V. K, "On the Analysis of Symmetrical Three-Line Microstrip Circuits," *IEEE Trans.*, Vol. MTT-25, 1977, pp. 726–729.

[34] Janiczak, B. J., "Phase Constant Characteristic of Generalized Asymmetric Three-Coupled Microstrip Lines," *Proc. IEE*, *Part H*, Vol. 132, 1985, pp. 23–26.

[35] Qian, Y., and E. Yamashita, "Characterization of Picosecond Pulse Crosstalk Between Coupled Microstrip Lines with Arbitrary Conductor Width," *IEEE Trans.*, Vol. MTT-41, 1993, pp. 1011–1016.

[36] Kitazawa, T., and R. Mittra, "Analysis of Asymmetric Coupled Striplines," *IEEE Trans.*, Vol. MTT33, 1985, pp. 643–646.

[37] Getsinger, W. J., "Dispersion of Parallel-Coupled Microstrip," *IEEE Trans.*, Vol. MTT-21, 1973, pp. 144.-145.

[38] Hammerstad, E., and O. Jensen, "Accurate Models for Microstrip Computer-Aided Design," *IEEE MTT-S Digest*, 1980, pp. 407–409.

[39] Kirschning, M., and R. H. Jansen, "Accurate Wide-Range Design Equations for Parallel Coupled Microstrip Lines," *IEEE Trans.*, Vol. MTT-32, 1984, pp. 83–90; see also corrections, *IEEE Trans.*, Vol. MTT-33, 1985, p. 288.

[40] Napoli, L. S., and J. J. Hughes, "Characteristics of Coupled Microstrip Lines," *RCA Review*, Vol. 31, 1970, pp. 479–498.

[41] Rizzoli, V., "Resonance Measurement of Even and Odd Mode Propagation Constants in Coupled Microstrips," *Int. Microwave Symp. Digest*, 1975, pp. 106–108.

[42] Garg, R., and I. J. Bahl, "Characteristics of Coupled Microstrip Lines," *IEEE Trans.*, Vol. MTT-27, 1979, pp. 700–705; see also corrections, *IEEE Trans.*, Vol. MTT-28, 1980, p. 272.

[43] Bedair, S. S., "On the Odd-Mode Capacitance of the Coupled Microstriplines," *IEEE Trans.*, Vol. MTT-28, 1980, pp. 1225–1227.

[44] Akhtarzad, S., et al., "The Design of Coupled Microstrip Lines," *IEEE Trans.*, Vol. MTT-23, 1975, pp. 486–492.

[45] Shamanna, K. N., et al., "Parallel-Coupled Microstrip Line is Easy to Determine with Nomograms," *Electron. Design*, Vol. 11, May 24, 1976, pp. 78–81.

[46] Avdeyev, E. V., and V. I. Potapova, "Nomograms for Coupled Open Microstrip Lines," *Telecomm. Radio Eng.*, Part 2, Vol. 28, 1973, pp. 89–93.

[47] Shamasundara, S. D., and N. Singh, "Design of Coupled Microstrip Lines," *IEEE Trans.*, Vol. MTT-25, 1977, pp. 232–233.

[48] Shamasundara, S. D., et al., "Apply Standard Curves to Strange Substrates," *Microwaves*, Vol. 16, September 1977, pp. 116–117.

[49] Dalby, A. B., "Interdigital Microstrip Circuit Parameters Using Empirical Formulas and Simplified Model," *IEEE Trans.*, Vol. MTT-27, 1979, pp. 744–752.

[50] Tripathi, V. K., and C. L. Chang, "Quasi-TEM Parameters of Non-Symmetrical Coupled Microstrip Lines," *Int. J. Electron.*, Vol. 45, No. 2, 1978, pp. 215–223.

[51] Kal, S., et al., "Normal-Mode Parameters of Microstrip Coupled Lines of Unequal Width," *IEEE Trans.*, Vol. MTT-32, 1984, pp. 198–200.

[52] Bedair, S. S., "Characteristics of Some Asymmetrical Coupled Transmission Lines," *IEEE Trans.*, Vol. MTT-32, 1984, pp. 108–110. "'.

[53] Bedair, S. S., "Characteristics of Asymmetrical Coupled Shielded Microstrip Lines," Proc. IEE, Part H, Vol. 132, 1~85, pp. 342–343.

[54] Allen, J. L., "Non-Symmetrical Coupled Lines in an Inhomogeneous Dielectric Medium," *Int. J. Electron.*, Vol. 38, 1975, pp. 337–347.

[55] Llinner, I. J. P., "A Method for the Computation of the Characteristic Immitance Matrix of Multiconductor Striplines with Arbitrary Widths," *IEEE Trans.*, Vol. MTT-22, 1974, pp. 930–937.

[56] El-Deeb, N. A., et al., "Design Parameters of Inhomogeneous Asymmetrical Coupled Transmission Lines," *IEEE Trans.*, Vol. MTI-31, 1983, pp. 592–596.

[57] Kollipara, R.T., and V. K. Tripathi, "Dispersion Characteristics of Moderately Thick Microstrip Lines by the Spectral Domain Method," *IEEE Microwave Guided Wave Lett.*, Vol. 2, 1992, pp. 100–101.

[58] Jansen, R. H., "A Comprehensive CAD Approach to the Design of MMIC's up to MM-Wave Frequencies," *IEEE Trans.*, Vol. MTT-36, 1988, pp. 208–219.

[59] Bedair, S. S., and M. I. Sobhy, "Accurate Formulas for the Computer-Aided Design of Shielded Microstrip Circuits," *Proc. IEE, Part H*, Vol. 127, 1980, pp. 305–308.

[60] Rama Rao, B., "Effect of Loss and Frequency Dispersion on the Performance of Microstrip Directional Couplers and Coupled Line Filters," *IEEE Trans.*, Vol. MTT-22, 1974, pp. 747–750.

[61] Tien, C. C., et al., "Effects of Metal Thickness and Finite Substrate Width on Leaky Waves in Coupled Microstrip Lines," *IEEE MTT-S Digest*, 1992, pp. 499–502.

[62] Shamasundara, S. D., and K. C. Gupta, "Sensitivity Analysis of Coupled Microstrip Directional Couplers," *IEEE Trans.*, Vol. MTT-26, 1978, pp. 788–794.

[63] Buntschuh, C., "High Directivity Microstrip Couplers Using Dielectric Overlays," *IEEE G-MTT Symp. Digest*, 1975, pp. 125–127.

[64] Wolters, K. C., et al., "Analysis and Experimental Evaluation of Distributed Overlay Structures in Microwave Integrated Circuits," *IEEE G-MTT Symp. Digest*, 1968, pp. 123–130.

[65] Sheleg, B., and B. E. Spielman, "Broad-Band Directional Couplers using Microstrip with Dielectric Overlays," *IEEE Trans.*, Vol. MTT-22, 1974, pp. 1216–1220.

[66] Paolino, D. D., "MIC Overlay Coupler Design using Spectral Domain Techniques," *IEEE Trans.*, Vol. MTT-26, 1978, pp. 646–649.

[67] Atsuki, K., and E. Yamashita, "Three Methods for Equalizing the Even and Odd-Mode Phase Velocity of Coupled Strip Lines with an Inhomogeneous Medium," *Trans. IECE Japan*, Vol. 56–8, No. 7, 1972, pp. 424–426.

[68] Su, L., et al., "Design of an Overlay Directional Coupler by a Full-Wave Analysis," *IEEE Trans.*, Vol. MTT-31, 1983, pp. 1017–1022.

[69] Klein, J. L., and K. Chang, "Optimum Dielectric Overlay Thickness for Equal Even and Odd Mode Phase Velocities in Coupled Microstrip Circuits," *Electron. Utt.*, Vol. 26, 1990, pp. 274–276.

[70] Szentkuti, B. T., "Simple Analysis of Anisotropic Microstrip Lines by a Transform Method," *Electron. Leu.*, Vol. 12, 1976, pp. 672–673.

[71] Fukuoka, Y., et al., "Analysis of Multilayer Interconnection Lines for a High-Speed Digital Integrated Circuit," *IEEE Trans.*, Vol. MTT-33, 1985, pp. 527–552.

[72] Carin, L., and L. J. Webb, "Isolation Effects in Single- and Dual-Plane VLSI Interconnects," *IEEE Trans.*, Vol. MTT-38, 1990, pp. 396–404.

[73] Gilb, J. P. K., and C. A, Balanis, "Asymmetric, Multi-Conductor Low-Coupling Structures for High-Speed, High-Density Digital Interconnects," *IEEE Trans.*, Vol. MTT-89, 1991, pp. 2100–2106.

[74] Kiziloglu, K., et al., "Experimental Analysis of Transmission Line Parameter in High-Speed GaAs Digital Cirqaits Interconnects." *IEEE Trans.*, Vol. MTT-59, 1991, pp. 1361–1867.

[75] Goel, A. K., *High-Speed VLSI Interconnections: Modeling, Analysis and Simulation*, New York: John Wiley, 1994.

[76] Anandan, C. K., et al., "Broad-Band Gap Coupled Microstrip Antenna," *IEEE Trans.*, Vol. AP-38, 1990, pp. 1581–1586.

[77] Goel, A. K., and Y. R. Huang, "Parasitic Capacitances and Inductances for Multilevel Interconnections on GaAs-Based Integrated Circuits," *Electromag. Waves Appl.*, Vol. 5, 1991, pp. 477–502.

[78] Jansen, R. H., and N. H. L. Koster, "Accurate Results on the End Effect of Single and Coupled Microstrip lines for Use in Microwave Circuit Design," *Arch. Elektr. Ubertra*, Vol. 34, 1980, pp. 453–459.

[79] Sabban, A, and K. C. Gupta, "A Planar-Lumped Model for Coupled Microstrip Lines and Discontinuities," *IEEE Trans.*, Vol. MTT-40, 1992, pp. 245–252.

[80] Chadha, R., and K. C. Gupta, "Segmentation Method Using Impedance Matrices for Analysis of Planar Microwave Circuits," *IEEE Trans.*, Vol. MTT-29, 1981, pp. 71–74.

[81] Kirschning, M., et al., "Coupled Microstrip Parallel Gap Model for Improved Filter and Coupler Design," *Electron. Lett.*, Vol. 19, 1983, pp. 377–379.

[82] Abbosh, A. M., "Analytical Closed-Form Solutions for Different Configurations of Parallel Coupled Microstrip Lines," *IET Microw. Antennas Propag.*, Vol. 3, 2009, pp. 137–147.

[83] Dydyk, M., "Microstrip Directional Couplers with Ideal Performance via Single-Element Compensation," *IEEE Trans. Microwave Theory Tech.*, Vol. 47, 1999, pp. 956–964.

[84] Lee, S., and Y. Lee, "A Design Method for Microstrip Directional Couplers Loaded with Shunt Inductors for Directivity Enhancement," *IEEE Trans. Microwave Theory Tech.*, Vol. 58, 2010, pp. 994–1002.

[85] Tanaka, T., et al., "Slot-coupled Directional Couplers Between Double Sided Substrate Microstrip Lines and Their Applications," *IEEE Trans. Microwave Theory Tech.*, Vol. 36, 1986, pp. 1752–1757.

[86] Wong, M.-F., et al., "Analysis and Design of Slot-Coupled Directional Couplers Between Double-Sided Substrate Microstrip Lines," *IEEE Trans. Microwave Theory Tech.*, Vol. 29, 1991, pp. 2123–2129.

[87] Mongia, R., I. Bahl, and P. Bhartia, *RF and Microwave Coupled-Line Circuits*, Norwood, MA: Artech House, 1999.

[88] Paul, C. R., *Multiconductor Transmission Lines, Second Edition*, New Jersey: IEEE Press, 2008.

CHAPTER 9

Substrate Integrated Waveguide (SIW)

9.1 Introduction

The development of complex microwave and mm-wave circuits and systems requires integration of passive components, active devices, transmission lines, and antennas. In most cases, various components of a system are designed and manufactured separately, and different fabrication technologies are required to implement each component at the best.

A number of different fabrication technologies are available for the implementation of microwave and millimeter-wave components.

Printed planar technologies, such as those based on microstrip line and coplanar waveguide, represent the ideal choice for manufacturing a variety of passive components, interconnects, and antennas, operating in the microwave frequency range. These technologies lead to compact, low-profile, and light-weight components, which can be manufactured by adopting inexpensive fabrication processes. Nevertheless, printed components often exhibit significant losses, especially at mm-wave frequency; moreover, they are subject to radiation leakage and undesired coupling between adjacent elements, and exhibit limited power-handling capability.

Conversely, when losses are an issue and complete shielding is required, metallic waveguide technology appears to be the most suitable solution. Metallic waveguides guarantee very low losses and good quality factor, which are mandatory for highly-selective filters, and they permit to deal with high power levels. However, in contrast to planar technologies, metallic waveguides are heavy and bulky structures, and their fabrication is expensive and time consuming.

Furthermore, when multiple fabrication technologies are adopted for manufacturing different portions of a system, a final integration phase is required. The combination of components manufactured by using different technologies is a complicated task that requires the use of properly designed transitions. Transitions introduce additional losses and usually lead to narrower operation bandwidth and extra packaging costs.

To overcome these issues and bridge the technological gap between lossy planar technologies and bulky metallic waveguides, the substrate integrated waveguide (SIW) has been proposed. SIW technology allows for the implementation of classical rectangular waveguides in planar form: they are based on a dielectric substrate, where two ground planes replace the top and bottom sides of the waveguide, and

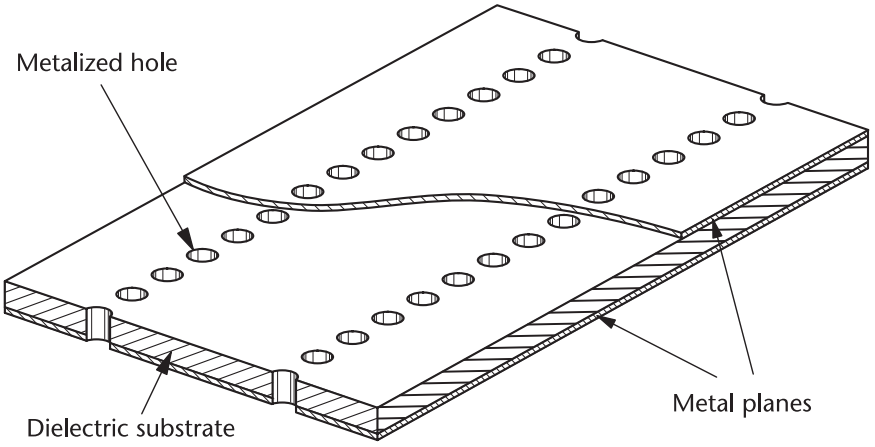

Figure 9.1 Substrate integrated waveguide configuration.

two rows of metalized cylindrical holes or slots electrically connect the two ground planes and emulate the metallic side walls of classical waveguides (Figure 9.1).

The first appearance of the SIW structure can be found in a Japanese patent in 1994 [1]. Subsequently, a structure similar to the SIW was proposed in [2] under the name of parallel-plate waveguide and in [3] as laminated waveguide. However, the fundamental development of SIW technology and components can be attributed to the seminal works of Ke Wu and his group at the École Polytechnique de Montréal, Canada, starting from 2001 [4–7].

SIW technology combines the advantages of planar technologies and classical metallic waveguides: SIW components are light and compact, they can be manufactured in planar form by adopting well established and cost-effective processing techniques (like printed circuit board or low temperature co-fired ceramic), and at the same time they exhibit high quality factor, high power-handling capability, and practically complete electromagnetic shielding. The most significant advantage of SIW technology is the possibility to integrate a complete system in a single substrate, including passive components, active elements, possibly chip-sets, and antennas. Since the complete system is fabricated in the same substrate by using the same technology, there is no need for transitions between different components and sub-circuits, thus reducing losses and parasitics. Moreover, SIW circuits can be easily connected to microstrip lines and coplanar waveguides, realized in the same substrate.

9.1.1 Geometry

The SIW structure is realized in a dielectric substrate, metalized at top and bottom. The top and bottom metal layers are electrically connected by two rows of closely-spaced metalized cylindrical holes (usually named metal vias or posts), which define the side walls of the waveguide (Figure 9.1). In some cases, the cylindrical holes can be replaced by metalized slots.

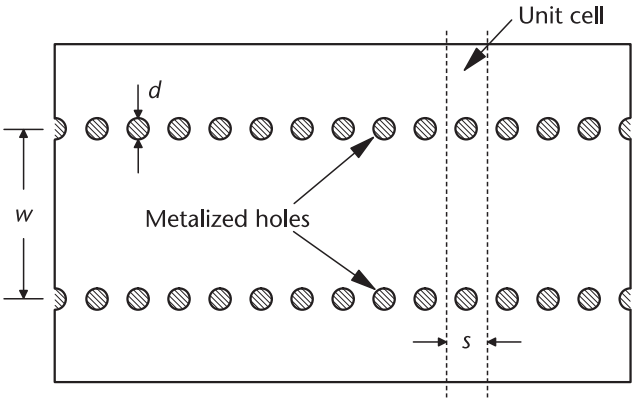

Figure 9.2 Geometry of a substrate integrated waveguide (top view).

Dielectric substrates, usually adopted for the microstrip and coplanar waveguide circuits, can be used for SIW structures. The thickness of the dielectric layer is typically small compared to the width of the waveguide, and may range from 0.2 to 1 mm. The relative dielectric constant ε_r is usually in the range from 2 to 10.

The geometry of the SIW is fully defined by three parameters: the diameter d of the holes, the width w of the waveguide, and the longitudinal spacing s between the holes (Figure 9.2). As the SIW structure resembles the rectangular waveguide, its width w is mainly related to the cutoff frequency of the fundamental SIW mode and therefore to the operation frequency band, as discussed below. The diameter d of the holes is typically a small fraction of w: a value $d < w/8$ is recommended to avoid possible band-gap effects, due to the periodic modulation of the waveguide width [6]. The longitudinal spacing s affects the confinement of the electromagnetic field, as it determines the gap-width $(s - d)$ between pairs of metal vias. The minimum value is $s = d$, which means no gap appears and the shielding is perfect. If the value of s increases, the gaps become larger and the field confinement degrades. A golden rule is $s < 2.5\ d$ [6], and $s = 2\ d$ is the typical choice.

The SIW transmission line is a periodic structure, and for modeling purposes it may be useful to identify its unit cell, which comprises a portion of double-grounded dielectric substrate with two metalized holes (Figure 9.2).

9.1.2 Operation Principle

The wave propagation in SIW structures is similar to the propagation in classical rectangular waveguides: the fundamental mode of the SIW resembles the TE_{10} mode of a rectangular waveguide (Figure 9.3). With this mode configuration, the surface current flows along the top and bottom metal planes of the SIW exactly like in a rectangular waveguide, and on the sides it can flow vertically along the metalized surface of the cylinders, being minimally perturbed by the gaps (provided that the gaps are small). For this reason, the electromagnetic field is confined inside the SIW and there is no radiation leakage.

This operation mechanism only applies to the TE_{n0} modes of the rectangular waveguide, where the surface current on the side walls flows in vertical direction.

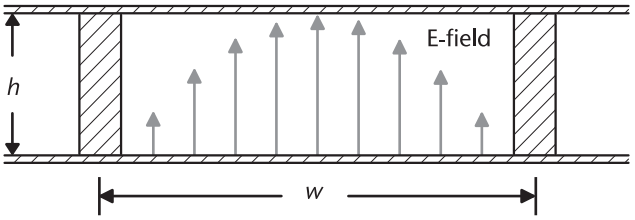

Figure 9.3 Electric field pattern of the fundamental SIW mode (front view).

For the other modes of the rectangular waveguide, namely TM modes and TE_{np} modes with $p \neq 0$, the surface current on the side walls has a longitudinal component, and consequently it would be strongly perturbed by the gaps. For this reason, these modes are not supported by the SIW structure. In conclusion, the only modes supported by SIW structures are those similar to the TE_{n0} modes of the rectangular waveguide.

Due to their geometry and their mode pattern, SIW components can be classified as H-plane waveguide structures [8]. The electric field is normal to the broad wall and its amplitude does not vary in the vertical direction. Moreover, the thickness h of the substrate plays no role in the characteristics of wave propagation, except for conductor losses.

9.2 Analysis Techniques of SIW

A variety of modeling techniques have been applied or specifically developed for the analysis of SIW structures, both in the case of straight interconnects and in the case of complex components. In the former case, the aim of the analysis is the calculation of the propagation and attenuation constants of the SIW modes versus frequency, as well as the determination of the modal field pattern of the fundamental mode and possibly of the next higher modes. In the latter case, the analysis should provide the frequency response of the SIW component, for instance in terms of the scattering matrix referred to the ports of the component, and also the radiation characteristics in the case of SIW antennas.

9.2.1 Equivalent Rectangular Waveguide

The easiest (but yet very effective and widely adopted) technique for modeling SIW structures exploits the similarity between SIW and rectangular waveguide. As the SIW modes exhibit the same dispersion characteristics as the modes of conventional rectangular waveguides [9], the SIW structure can be approximated by an equivalent rectangular waveguide with proper width. An analytical relation can be determined between the width of the equivalent rectangular waveguide and the geometrical dimensions of the SIW.

The first and most commonly used relation was proposed in [9]. The effective width w_{eff} of the equivalent rectangular waveguide can be obtained from the empirical equation

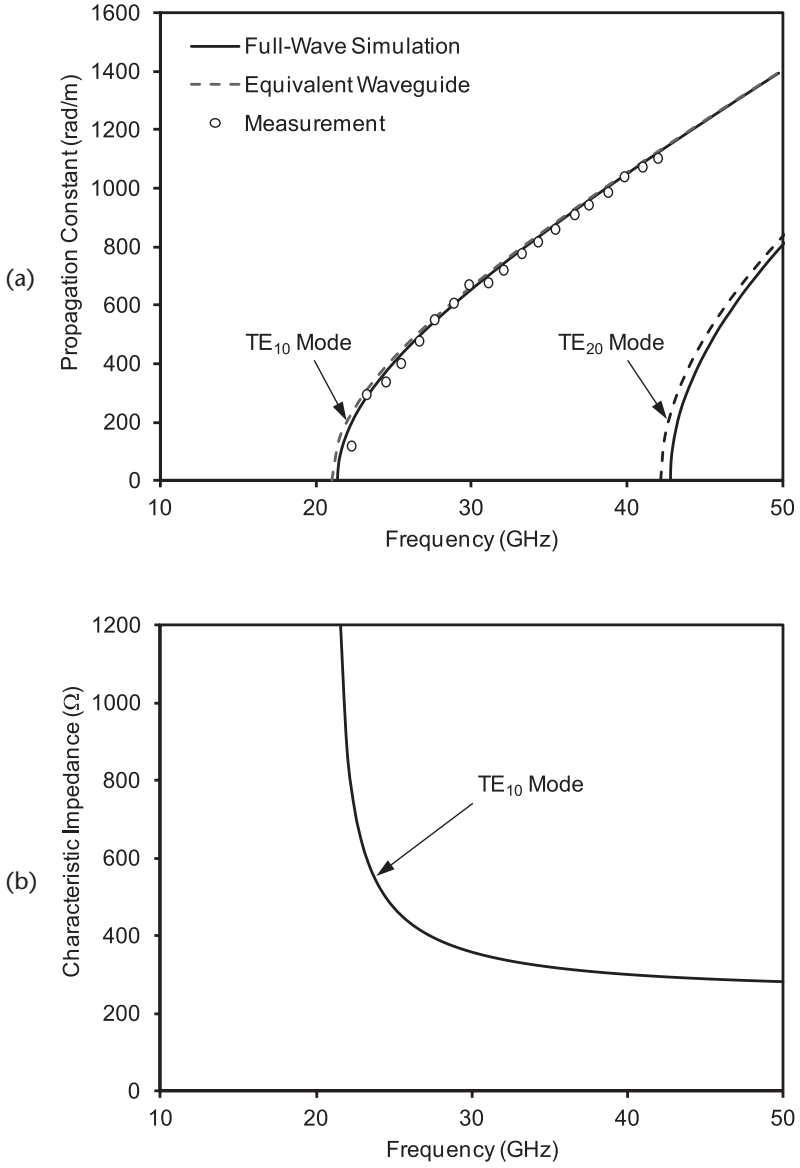

Figure 9.4 Dispersion curves of the SIW modes: (a) propagation constant of the first and second SIW modes (solid line: full-wave simulation, dashed line: equivalent waveguide model, dots: measurements from [9]); (b) characteristic impedance of the fundamental SIW mode, calculated by adopting the formulas of the wave impedance of the equivalent rectangular waveguide [8].

$$w_{\text{eff}} = w - \frac{d^2}{0.95s} \tag{9.1}$$

where dimensions w, d, and s are shown in Figure 9.2. Once the width of the equivalent waveguide is available, classical formulas for calculating the dispersion characteristics of rectangular waveguides can be used [8].

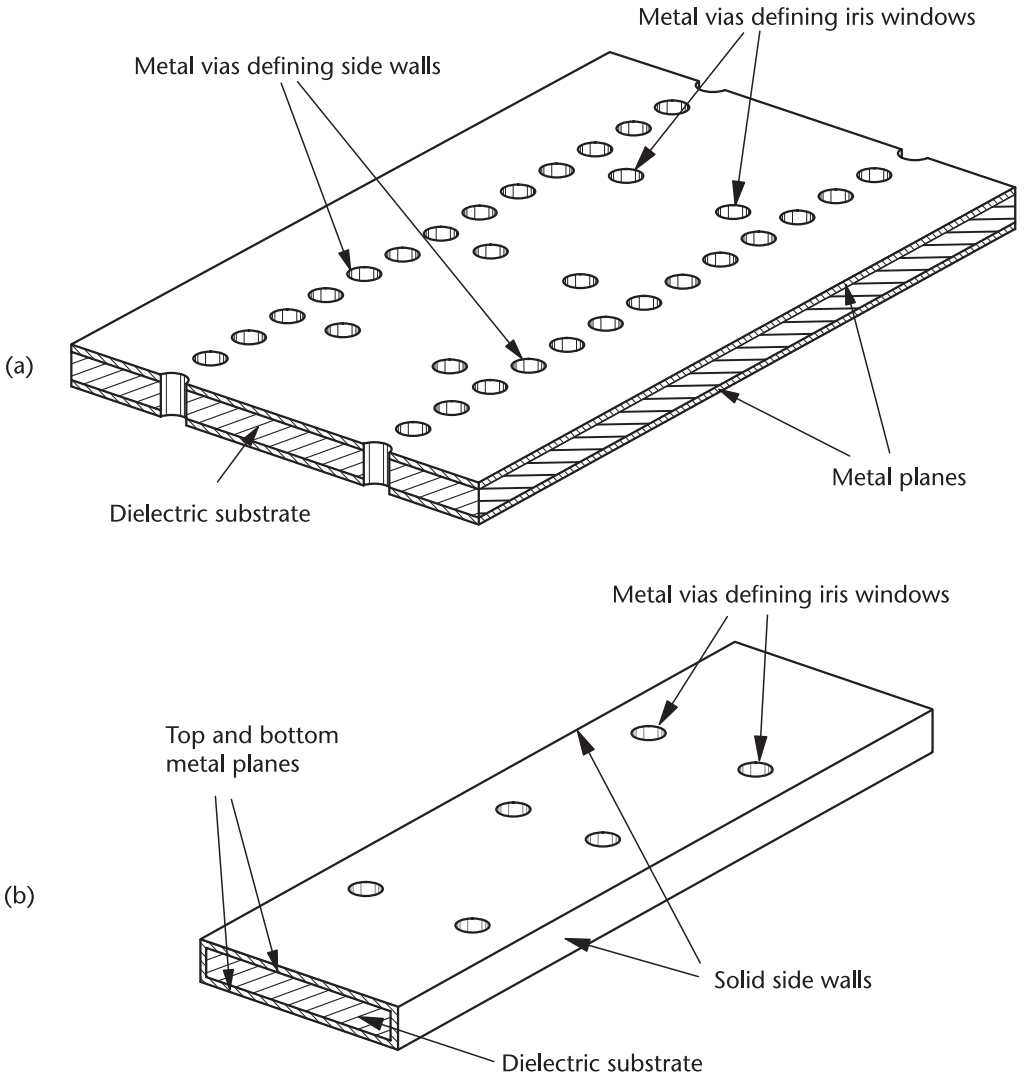

Figure 9.5 Modeling of SIW components based on the equivalent waveguide concept: (a) original SIW component; (b) simplified geometry.

Moreover, the effective width concept is very useful to define the characteristic impedance of SIW. In fact, SIW structures are not uniform along the propagation direction, and the electric and magnetic modal fields slightly change at different cross-sections. For this reason, a practical way to define the characteristic impedance of the SIW is the wave impedance of the equivalent rectangular waveguide, calculated as the ratio of the transverse components of the electric and magnetic fields [8].

Figure 9.4a shows the propagation constant of the first two modes of an SIW structure with dimensions $w = 5.25$ mm, $d = 0.8$ mm, $s = 1.5$ mm, and the dielectric constant of the substrate $\varepsilon_r = 2.2$. From equation (9.1), the effective width is $w_{eff} = 4.80$ mm. The results achieved by applying the equivalent waveguide concept

compare well with the full-wave analysis of the SIW and with measurements from [9]. In addition, Figure 9.4*b* shows the characteristic impedance of the fundamental mode of the same SIW structure, calculated by using analytical formulas for the equivalent rectangular waveguide [8].

Equation (9.1) is valid for $s < 4d$ and it has an accuracy within ±5% [9]. This precision is acceptable for many applications: it allows for a preliminary dimensioning of SIW interconnects and it simplifies the geometry of SIW components, as the rows of metal vias can be replaced by solid walls (Figure 9.5). The use of the equivalent waveguide is helpful in full-wave analysis, and it also allows to apply to SIW circuits the design concepts of classical waveguide components. In some cases the use of (9.1) may be critical, for instance in the case of selective filters and narrow-band components, where small inaccuracies in the cutoff frequency may lead to a significant shift of the frequency response.

Other formulas have been proposed to determine the equivalence between SIW and rectangular waveguide. A refinement of equation (9.1) was proposed in [6] to include the effect of d/w. The following equation was determined by empirical criteria:

$$w_{\text{eff}} = w - 1.08\frac{d^2}{s} + 0.1\frac{d^2}{w}\cdot \tag{9.2}$$

Equation (9.2) provides a more accurate determination of effective width of the equivalent rectangular waveguide, and its range of validity is defined by the conditions $s < 3d$ and $d < w/5$.

Another relation was derived in [10] by using a semi-analytical approach. The relation between w and the effective width w_{eff} is given by

$$w = \frac{2\,w_{\text{eff}}}{\pi}\cot^{-1}\left(\frac{\pi\,s}{4\,w_{\text{eff}}}\ln\frac{s}{2d}\right) \tag{9.3}$$

This equation is different from (9.1) and (9.2) in the derivation technique, because it is not obtained in an empirical way, but it is comparable in terms of accuracy. Anyway, equation (9.3) presents a substantial difference from the other relations concerning the range of values of w_{eff} it can provide. In fact, according to equation (9.1), the effective width w_{eff} is always smaller than w. Similarly, according to equation (9.2), $w_{\text{eff}} < w$ in all practical cases, being the condition $s < 10.8w$ always satisfied. According to equation (9.3), the width of the equivalent rectangular waveguide is larger than the width of the SIW when $s > 2d$, w and w_{eff} coincide when $s = 2d$, and $w_{\text{eff}} < w$ when $s < 2d$. This result should not surprise, because when the longitudinal spacing s is large, the electromagnetic field tends to be less confined inside the rows of metalized cylindrical holes, with a consequent increase in the effective width w_{eff} as well as in radiation losses.

9.2.2 Full-wave Modeling of SIW Interconnects

A more accurate characterization of SIW interconnects is based on the full-wave electromagnetic modeling. The full-wave analysis of straight SIW interconnects

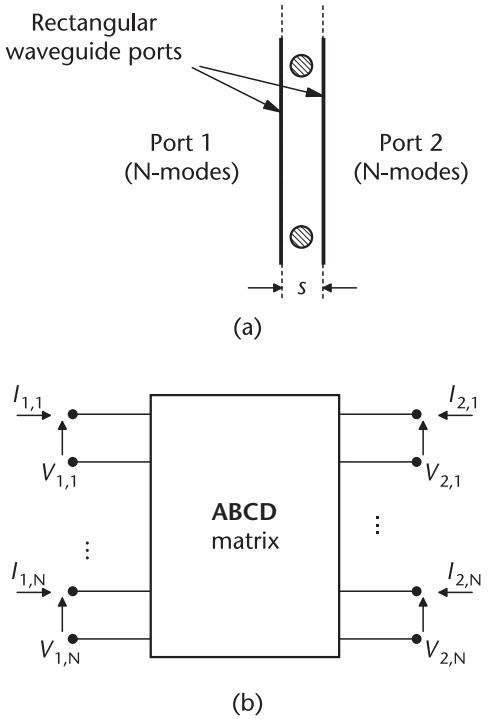

Figure 9.6 Topology of the SIW structure adopted in the formulation of the eigenvalue problem: (a) geometry of the unit cell; (b) definition of the **ABCD** matrix.

aims to determine the curves of propagation and attenuation constants versus frequency, and the field pattern of the SIW modes.

The modeling of SIW interconnects usually exploits the periodicity of the structure, which allows considering the unit cell of the periodic structure instead of a section of the waveguide (Figure 9.2). The analysis techniques based on the modeling of the unit cell take advantage of the Floquet-Bloch theorem and lead to a substantial reduction in the computational cost.

The analysis techniques adopted for the modeling of SIW interconnects can be divided in three major groups:

1. full-wave methods that lead to the formulation of a classical eigenvalue problem [9], [11-14];
2. integral equation techniques, that formulate the problem in terms of a transcendental equation [2];
3. analysis approaches based on the surface impedance concept [7], [15].

Analysis Methods Leading to an Eigenvalue Problem

An efficient technique for the determination of the dispersion diagram of SIW structures is based on the use of an electromagnetic solver, either commercial or in-house developed, able to characterize the unit cell as a two-port circuit [9]. Any full-wave simulation method can be adopted for this analysis. The ports of the circuit are defined at the long sides of the unit cell and are represented by rectangular

waveguide ports, which are broader than the SIW width (Figure 9.6a). A number N of rectangular waveguide modes are defined at each port: since the SIW is an H-plane structure, only TE_{n0} modes of the rectangular waveguide are considered at the ports.

The electromagnetic solver usually provides the generalized scattering or admittance matrix of the two-port circuit, which subsequently needs to be converted into the **ABCD** matrix [8]. The **ABCD** matrix relates the modal voltages and the inward modal currents of the rectangular waveguide modes at the ports of the circuit (Figure 9.6b) in the form

$$\begin{bmatrix} \mathbf{V}_1 \\ \mathbf{I}_1 \end{bmatrix} = \begin{bmatrix} \mathbf{A} & \mathbf{B} \\ \mathbf{C} & \mathbf{D} \end{bmatrix} \cdot \begin{bmatrix} \mathbf{V}_2 \\ -\mathbf{I}_2 \end{bmatrix} \tag{9.4}$$

where $\mathbf{V}_1$ and $\mathbf{V}_2$ are the column vectors of the modal voltages at port 1 and port 2, respectively, and similarly $\mathbf{I}_1$ and $\mathbf{I}_2$ are the column vectors of the inward modal currents at port 1 and port 2, respectively. The column vectors $\mathbf{V}_1$, $\mathbf{V}_2$, $\mathbf{I}_1$, and $\mathbf{I}_2$ have dimension N and the **ABCD** matrix has dimensions $2N \times 2N$.

Once the **ABCD** matrix of the two-port circuit is available, the Floquet-Bloch theorem is applied, and the periodicity of the electromagnetic field at the ports of the SIW structure is enforced by the matrix equation

$$\begin{bmatrix} \mathbf{V}_1 \\ \mathbf{I}_1 \end{bmatrix} = e^{\gamma s} \begin{bmatrix} \mathbf{V}_2 \\ -\mathbf{I}_2 \end{bmatrix} \tag{9.5}$$

where γ represents the complex propagation constant at a given frequency f and s is the length of the unit cell. The combination of equations (9.4) and (9.5) leads to the formulation of the eigenvalue matrix problem

$$\begin{bmatrix} \mathbf{A} & \mathbf{B} \\ \mathbf{C} & \mathbf{D} \end{bmatrix} \cdot \begin{bmatrix} \mathbf{V}_2 \\ -\mathbf{I}_2 \end{bmatrix} = e^{\gamma s} \begin{bmatrix} \mathbf{V}_2 \\ -\mathbf{I}_2 \end{bmatrix} \tag{9.6}$$

The calculation of the eigensolutions of (9.6) must be repeated frequency-by-frequency, and the eigenvalues of (9.6) yield the dispersion curves of the SIW modes. In particular, the i-th eigenvalue provides the complex propagation constant γ_i of the i-th SIW mode, and consequently:

$$\alpha_i = \mathrm{Re}\{\gamma_i\} \tag{9.7a}$$

$$\beta_i = \mathrm{Im}\{\gamma_i\} \tag{9.7b}$$

where α_i and β_i represent the attenuation constant and the propagation constant of the i-th SIW mode, respectively, calculated at the given frequency f.

The cutoff frequency f_c of the dominant SIW mode, defined as the frequency where $\alpha = \beta = 0$ in the lossless case or simply $\alpha = \beta$ otherwise, can be used to determine the effective width w_{eff} of the equivalent rectangular waveguide. This approach for calculating the width of the equivalent waveguide is usually more accurate compared to the one based on equations (9.1–9.3).

The eigenvectors obtained from (9.6) are the weight coefficients, which permit to express the SIW modal fields on the ports as a linear combination of the TE_{n0} modes of the rectangular waveguide. More specifically, the i-th eigenvector Λ_i allows to reconstruct the modal fields of the i-th SIW mode on the port section:

$$\mathbf{e}_i^{\mathrm{SIW}} = \sum_{n=1}^{N} \Lambda_{i,n}\ \mathbf{e}_n^{\mathrm{RW}} \tag{9.8}$$

where $\mathbf{e}_i^{\mathrm{SIW}}$ is the i-th electric modal vector of the SIW, $\mathbf{E}_n^{\mathrm{RW}}$ is the n-th electric modal vector of rectangular waveguide, and $\Lambda_{i,n}$ is the n-th element of the i-th eigenvector.

It is important to observe that the SIW structure is not homogeneous along the propagation direction, and therefore the modal field pattern is not preserved at any cross-section, as it happens, for instance, in a rectangular waveguide. The electric modal field calculated by equation (9.8) represents the SIW modal field on the port section. A different choice of the unit cell (Figure 9.2) would lead to different modal fields.

Another simple method for the determination of the mode spectrum of SIW structures, belonging to the class of methods leading to an eigenvalue problem, is the numerical multimode calibration technique [11], which is inspired by the procedure adopted for the experimental characterization of multimodal transmission lines. This approach can be applied in conjunction with general purpose electromagnetic solvers, and it allows to simultaneously determine the complex propagation constants of several SIW modes.

In the numerical multimode calibration technique, two SIW structures with different lengths are numerically simulated under multimode excitation. The generalized scattering or admittance matrices provided by the electromagnetic analysis of the two structures are subsequently converted into generalized transfer matrices, namely $\mathbf{T}^1$ and $\mathbf{T}^2$, which relate the amplitudes of the incident and reflected waves at port 1 to the amplitudes of the incident and reflected waves at port 2.

Each of the two structures comprises three blocks, namely one SIW section and two port transitions. The port transition may connect, for instance, the SIW to a rectangular waveguide (Figure 9.7(a)). The three blocks are characterized by their respective generalized transfer matrix, and N modes are considered both at the rectangular waveguide ports and in the SIW section. Matrices $\mathbf{T}_x$ and $\mathbf{T}_y$ refer to the first and second port transitions, respectively, whereas matrix $\mathbf{T}_{\mathrm{SIW}}$ refers to the SIW section (Figure 9.7(b)). Matrices $\mathbf{T}^1$ and $\mathbf{T}^2$ can be expressed as follows

$$\mathbf{T}^1 = \mathbf{T}_x\ \mathbf{T}_{\mathrm{SIW}}^1\ \mathbf{T}_y \tag{9.9a}$$

$$\mathbf{T}^2 = \mathbf{T}_x\ \mathbf{T}_{\mathrm{SIW}}^2\ \mathbf{T}_y \tag{9.9b}$$

where the superscripts 1 and 2 denote the first and second structure, respectively. The port transitions denoted by matrices $\mathbf{T}_x$ and $\mathbf{T}_y$ are identical for both structures. Matrices $\mathbf{T}_{\mathrm{SIW}}^1$ and $\mathbf{T}_{\mathrm{SIW}}^2$ are diagonal, as they represent the generalized transfer matrices of straight waveguides, and they can be expressed as

$$\mathbf{T}_{\mathrm{SIW}}^1 = \mathrm{diag}[e^{\gamma_1 \ell_1}\ \ldots\ e^{\gamma_N \ell_1}, e^{-\gamma_1 \ell_1}\ \ldots\ e^{-\gamma_N \ell_1}] \tag{9.10a}$$

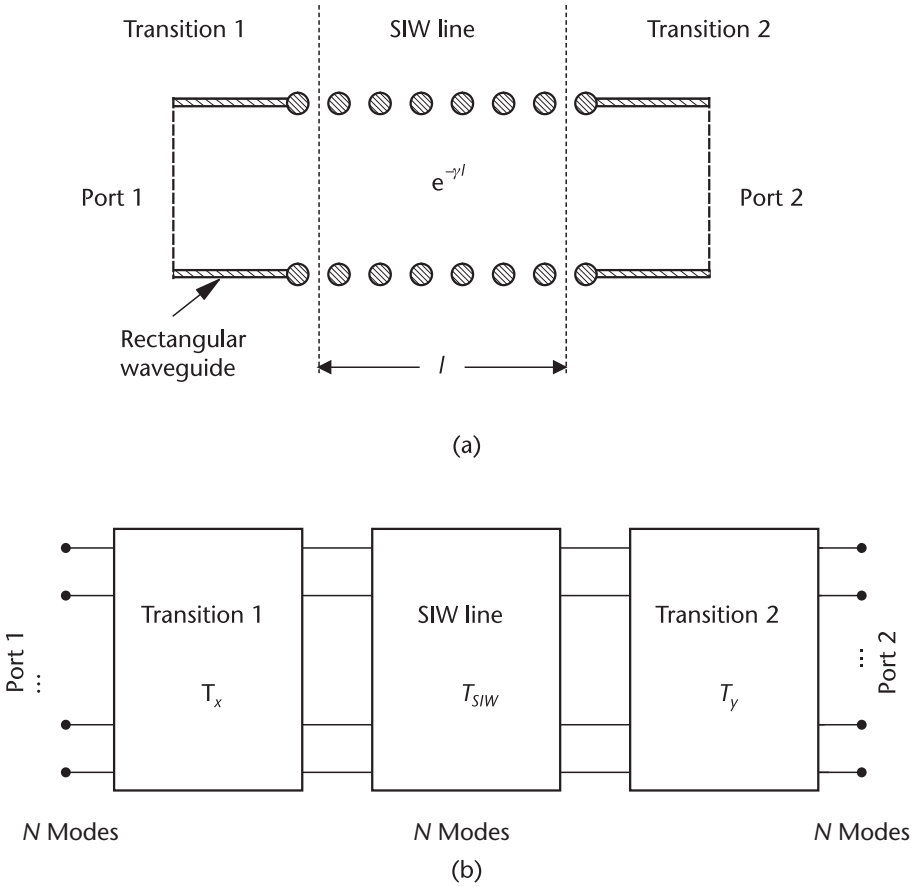

Figure 9.7 SIW structure adopted in the numerical multimode calibration technique: (a) geometry of the SIW structure; (b) block diagram of the structure.

$$\mathbf{T}^2_{\mathrm{SIW}} = diag[e^{\gamma_1 \ell_2} \ \ldots \ e^{\gamma_N \ell_2}, \ e^{-\gamma_1 \ell_2} \ \ldots \ e^{-\gamma_N \ell_2}] \tag{9.10b}$$

In (9.10), γ_i represents the complex propagation constant of the i-th SIW mode (with $i = 1, \ldots, N$), and ℓ_1 and ℓ_2 are the lengths of the SIW section in the first and second structure, respectively.

By cascading the matrices defined in (9.9) and (9.10), the following eigenvalue matrix equation is derived

$$\mathbf{T}^{12} \ \mathbf{T}_x = \mathbf{T}_x \ \mathbf{T}^{12}_{\mathrm{SIW}} \tag{9.11}$$

where

$$\mathbf{T}^{12} = \mathbf{T}^1 \ (\mathbf{T}^2)^{-1} \tag{9.12a}$$

$$\mathbf{T}^{12}_{\mathrm{SIW}} = \mathbf{T}^1_{\mathrm{SIW}} \ (\mathbf{T}^2_{\mathrm{SIW}})^{-1} \tag{9.12b}$$

As $\mathbf{T}^{12}_{\mathrm{SIW}}$ is a diagonal matrix, the eigenvalues of $\mathbf{T}^{12}$ coincide with the elements of the diagonal of $\mathbf{T}^{12}_{\mathrm{SIW}}$. Therefore

$$e^{\gamma_i \Delta \ell} = \lambda_i \tag{9.13}$$

where λ_i represents the i-th eigenvalue of T^{12} and $\Delta\ell = \ell_1 - \ell_2$. Equation (9.13) allows to determine the complex propagation constants of N pairs of modes, each pair related to two modes propagating in opposite directions.

By repeating this procedure frequency-by-frequency, the dispersion characteristics of the SIW structure are obtained. In particular, the attenuation and propagation constants are calculated by applying (9.7) to the values of γ_i resulting from (9.13).

Other numerical techniques, specifically developed for the modeling of SIW structures, allow to obtain the eigenvalue matrix equation directly from the formulation of the electromagnetic problem, and not from the post-processing of a matrix describing the response of the circuit.

The application of finite-difference techniques allows for great flexibility both in the geometry of the structure and in the substrate material, which can be lossy and anisotropic. The finite-difference frequency-domain (FDFD) method was applied in [12] to the modeling of the unit cell of an SIW structure to calculate the propagation constants and the modal field vectors. In this formulation, the value of frequency is set and the propagation constants are determined through the solution of the eigenvalue problem. Absorbing Boundary Conditions (ABC) or Perfectly Matched Layers (PML) are adopted at the sides of the waveguide, to impose the radiation boundary condition that permits to account for radiation leakage. The formulation of the FDFD problem results into the generalized eigenvalue problem

$$\mathbf{A}\mathbf{x} = \gamma \mathbf{B}\mathbf{x} \tag{9.14}$$

where γ is the complex propagation constant and $\mathbf{x}$ is the vector of the electric and magnetic field components. This method yields directly the propagation constants of the SIW modes at a given frequency.

A different FDFD approach for the calculation of the dispersion curve is possible, where the propagation constant β is set and the aim of the calculation is the determination of the corresponding complex frequency. This approach was proposed in [13], and leads to the following standard eigenvalue problem

$$\mathbf{A}\mathbf{x} = j\omega' \mathbf{x} \tag{9.15}$$

where ω' is the complex angular frequency and $\mathbf{x}$ is the vector of the electric and magnetic field components. The eigenvalues of matrix $\mathbf{A}$ allow to determine the eigenfrequencies f_i and the corresponding attenuation constant α_i for the given value of β

$$f_i = \frac{\mathrm{Re}\{j\omega_i'\}}{2\pi} \tag{9.16}$$

$$\alpha_i = \frac{\mathrm{Im}\{j\omega_i'\}}{v_g} \tag{9.17}$$

where v_g is the group velocity and is defined as

$$v_g = \frac{d\omega}{d\beta} \tag{9.18}$$

The method of lines (MoL) was also applied to the determination of the propagation characteristics of SIW interconnects through the direct formulation of an eigenvalue problem [14]. In the application of MoL, the structure is handled analytically in one direction and there is a segmentation in the other direction. ABC are considered on the lateral sides of the SIW, thus accounting for radiation effects. The formulation of the MoL yields a matrix eigenvalue equation in the form (9.14), where γ is related to the complex propagation constant and $\mathbf{x}$ is related to the electric field components, as detailed in [14].

Integral equation techniques

The modeling of SIW interconnects based on the formulation of an integral equation and its solution by the Method of Moments (MoM) was originally proposed in [2]. The MoM modeling is particularly efficient in the case of SIW interconnects, due to the simple geometry of the structure, the homogeneous dielectric medium, and the vertically independent field configuration. Compared to finite-element and finite-difference methods, the integral equation technique leads to a significant improvement in computational efficiency.

As both the structure geometry and the field amplitude are uniform along the *y*-direction (Figure 9.8), the solution of the problem can be formulated in terms of a two-dimensional analysis. Moreover, due to the periodicity of the structure, the single unit cell of the SIW is considered, with proper periodic boundary conditions (Figure 9.8). Symmetries can be exploited if the calculation of only a particular class of modes is required: namely, a perfect magnetic wall on the symmetry plane

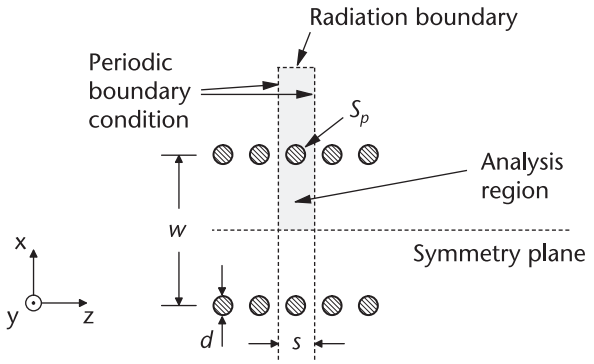

Figure 9.8 Geometry of the SIW structure used in the analysis by the integral equation technique (from [2], © 1998 IEEE. Reprinted with permission).

is considered to calculate the fundamental and the odd modes, whereas a perfect electric wall on the symmetry plane is considered to calculate the even modes.

Consequently, the generic structure considered in the analysis consists of one cylindrical post located in a rectangular domain, with periodic boundaries on two sides, the symmetry boundary condition on another side, and the radiation boundary on the fourth side, as shown in Figure 9.8. The unknown quantity of the integral equation is the electric current density $\mathbf{J}_p$ flowing in the y direction along the surface of the metal post. The electric field generated by the electric current density $\mathbf{J}_p$ is expressed as a Green's integral, through the dyadic Green's function $\underline{\mathbf{G}}$. By imposing the electric wall condition on the surface of the metal post, the resulting integral equation is expressed in the form

$$\int_{S_p} \underline{\mathbf{G}}(\mathbf{r},\mathbf{r}') \cdot \mathbf{J}_p(\mathbf{r}') \; dS' = 0 \tag{9.19}$$

where S_p represents the boundary of the metal post. In (9.19) the Green's function is expanded in terms of TE_z modes, propagating in the $\pm x$ direction, with the wavenumber k_{zn} defined according to the Floquet theorem

$$k_{zn} = k_z + \frac{2\pi n}{s} \tag{9.20}$$

where k_z is the complex wavenumber in the z-direction and n is an integer number. In the solution of the integral equation by the MoM, the unknown electric current $\mathbf{J}_p$ is approximated as the linear combination of basis functions $\mathbf{J}_{pj}$, e.g. piece-wise linear functions defined on S_p. The application of the MoM in the Galerkin form leads to

$$\det[\mathbf{Z}] = 0 \tag{9.21}$$

where the entries of matrix $\mathbf{Z}$ are given by

$$Z_{ij} = \int_{S_{pj}} \int_{S_{pi}} \mathbf{J}_{pi}(\mathbf{r}) \cdot \underline{\mathbf{G}}(\mathbf{r},\mathbf{r}') \cdot \mathbf{J}_{pj}(\mathbf{r}') \, dS' \, dS \tag{9.22}$$

The eigensolutions of (9.21) can be calculated numerically, frequency by frequency. The eigenvalues provide the complex values of wavenumbers k_{zi}, which allow for calculating the attenuation and propagation constants of the i-th SIW modes

$$\alpha_i = \mathrm{Im}\{k_{zi}\} \tag{9.23a}$$

$$\beta_i = \mathrm{Re}\{k_{zi}\} \tag{9.23b}$$

The i-th eigenvector is the coefficient vector of the electric current density $\mathbf{J}_{pi}$ of the i-th SIW mode on the surface S_p of the metal post. Subsequently, the electric modal vector of the i-th SIW mode can be computed through the Green's integral (9.19).

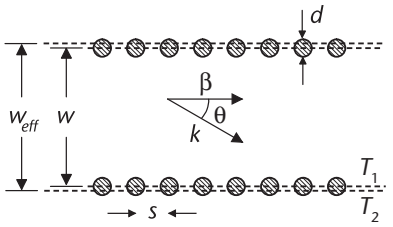

Figure 9.9 SIW geometry considered in the transverse resonance method (from [7], © 2006 IEEE. Reprinted with permission).

Analysis based on the surface impedance concept

An efficient but approximate analysis method for calculating the propagation characteristics of SIW structures is based on the surface impedance concept. In this approach, the rows of metalized cylindrical holes are represented as complex impedance walls, and the propagation and attenuation constants are obtained by the transverse resonance technique [7,15].

In classical rectangular waveguides, the fundamental TE_{10} mode can be represented as the superposition of two plane waves, propagating in symmetrical directions [8]. The same model can be applied to SIW structures, where the fundamental mode is expressed as the combination of two symmetrical plane waves propagating at an angle $\pm\theta$ with respect to the longitudinal direction (Figure 9.9). If k is the wavenumber at the operation frequency, its longitudinal component $\beta = k\cos(\theta)$ represents the propagation constant.

For lossless waveguides, the propagation constant at the cutoff frequency f_c is $\beta = 0$, and therefore at the cutoff the two waves propagate in opposite directions and the angle results $\theta = \pm 90°$. Conversely, in the case of lossy waveguides, the cutoff frequency is conventionally defined by the condition $\alpha = \beta$.

In the lossless case, at the cutoff frequency the two plane waves are incident perpendicularly on the periodic rows of metal cylinders. These waves are subject to a complex reflection coefficient S_{11}, which can be computed in different ways. A full-wave MoM analysis was proposed in [7] for the rigorous calculation of the reflection coefficient. A simplified model was used in [15], under the approximation of modeling the posts as thin wires, and in [16], where squared metal posts are considered.

The analysis algorithm starts by setting a tentative value f_c of the cutoff frequency. The value of the reflection coefficient calculated at f_c allows for computing the normalized impedance Z_L seen by the plane wave on the plane T_1, where the centers of the metal posts are located (Figure 9.9):

$$Z_L = \frac{1 + S_{11}}{1 - S_{11}} \tag{9.24}$$

The periodic row of metal cylinders can be approximated by a solid metal wall with surface impedance Z_S, located in the shifted plane T_2 (Figure 9.9). Consequently, the impedance Z_L can be transformed into a surface impedance $Z_S = R_S\,(1+j)$, referred to the shifted plane T_2. Both R_S and the separation Δw between planes T_1

and T_2 can be calculated by exploiting the relation between the two impedances Z_L and Z_S, which are linked by the equation

$$Z_L = r + jx = \frac{Z_S + j\tan(k_c\Delta w)}{1 + j\ Z_S \tan(k_c\Delta w)} = \frac{Z_S + jA}{1 + j\ Z_S A} \tag{9.25}$$

where r and x represent the real and imaginary part of Z_L, respectively, $k_c = 2\pi/\lambda_c$ is the complex wavenumber of the plane wave, λ_c is the cutoff wavelength, and A is given by

$$A = \tan(k_c\Delta w) \tag{9.26}$$

The real and imaginary part of equation (9.25) yield a system of two equations

$$\begin{cases} r = R_S[1 + A(r + x)] \\ R_S(rA - xA - 1) = A - x \end{cases}. \tag{9.27}$$

By obtaining R_S from the first equation of (9.27) and replacing it in the second equation, the following quadratic equation results

$$A^2(r + x) + A(1 - r^2 - x^2) + (r - x) = 0 \tag{9.28}$$

whose solution yields the value of A, which in turn permits to calculate the plane separation Δw by using (9.26). Subsequently, R_s can be computed by using the first equation of (9.27).

Since the distance between the two planes T_1 is given by w, the distance between the two planes T_2 corresponds to the effective width $w_{\text{eff}} = w + 2\Delta w$.

In the case of lossless structures, the resonance condition is

$$w_{\text{eff}} = \frac{\lambda_c}{2} \tag{9.29}$$

whereas in the case of lossy structures the transverse resonance condition must be imposed: the summation of the impedances seen looking into both sides of the SIW structure must be zero. It finally results [7]

$$w_{\text{eff}} = \frac{2}{k_c}\sqrt{\text{Re}\{\cot^{-1}[R_S(1 - j)]\}^2 - \text{Im}\{\cot^{-1}[R_S(1 - j)]\}^2} \tag{9.30}$$

This procedure is iterated, starting from the tentative value of the cutoff frequency f_c, until the condition on the effective width w_{eff} of the equivalent waveguide defined by (9.29) or by (9.30) is met.

The calculation of the complete dispersion diagram of the SIW structure is based on the same approach, simply varying the direction of propagation θ of the pair of plane waves [7].

9.2.3 Full-wave Modeling of SIW Components

The full-wave modeling of SIW components is a key point in the design and development of SIW technology. In fact, the availability of flexible and accurate electromagnetic simulators is particularly important to fully exploit the potential and the flexibility of the SIW technology. For this reason, besides the use of commercial full-wave electromagnetic solvers, ad-hoc numerical simulation tools have been developed for the characterization and design of SIW components, with the aim to calculate their scattering or admittance matrices.

Finite-difference time-domain method

A popular and flexible numerical technique applied to the full-wave modeling of SIW components is the finite-difference time-domain (FDTD) method [17]. The FDTD method allows the modeling of SIW components with arbitrary geometry and any kind of dielectric substrate (including anisotropic and inhomogeneous materials). Moreover, this modeling technique provides the broadband solution in a single-pass simulation, with any kind of source excitation, and input/output transitions can be easily included in the full-wave simulation.

In general, the FDTD technique exhibits a rather limited computational efficiency, due to long computing time and large memory requirements. These issues become even more critical in the modeling of waveguide components, when the aim of the calculation is the determination of the parameters of the circuit, for instance in terms of the scattering matrix. In this case, there is the problem to separate the incident wave from the reflected wave in the time domain. This problem is circumvented by adopting long input and output feeding sections, as discussed in [17], but this solution further increases the size of the analysis domain and, consequently, the time and memory requirements.

An innovative and efficient solution to overcome this limitation is based on the calibration technique, commonly adopted in practical circuit measurements [17]. Among the variety of numerical calibration methods proposed in the literature (including the short-open calibration and the thru-reflection-line calibration), the thru-line calibration technique is a very powerful and computationally efficient method, which was applied to the numerical modeling of SIW components and circuits in [17]. In the application of the thru-line calibration technique, the analysis domain is subdivided into different sections (e.g., input line, device under test, output line; (Figure 9.10(a)). The application of this technique requires the analysis of three different structures: the first analysis involves the characterization of the complete structure, consisting of the device under test connected to the input and output transitions (Figure 9.10(a)), with the aim to determine the transfer matrix $\mathbf{T}_D$, which is expressed in the form

$$\mathbf{T}_D = \mathbf{T}_X \mathbf{T}_{DUT} \mathbf{T}_Y \tag{9.31}$$

where $\mathbf{T}_{DUT}$ represents the transfer matrix of the device under test, and $\mathbf{T}_X$ and $\mathbf{T}_Y$ are the transfer matrices of the input and output transitions, respectively. The second analysis requires the modeling of the thru connect, consisting of the direct connection of the input and output transitions (Figure 9.10(b)), to determine the transfer matrix $\mathbf{T}_T$ defined as

$$\mathbf{T}_T = \mathbf{T}_X \mathbf{T}_Y \tag{9.32}$$

Finally, the third analysis considers the line connect, consisting of a straight SIW section with the same length of the device under test, and connected to the input and output transitions (Figure 9.10(c)). This analysis leads to the calculation of the transfer matrix $\mathbf{T}_L$

$$\mathbf{T}_L = \mathbf{T}_X \mathbf{T}_{SIW} \mathbf{T}_Y \tag{9.33}$$

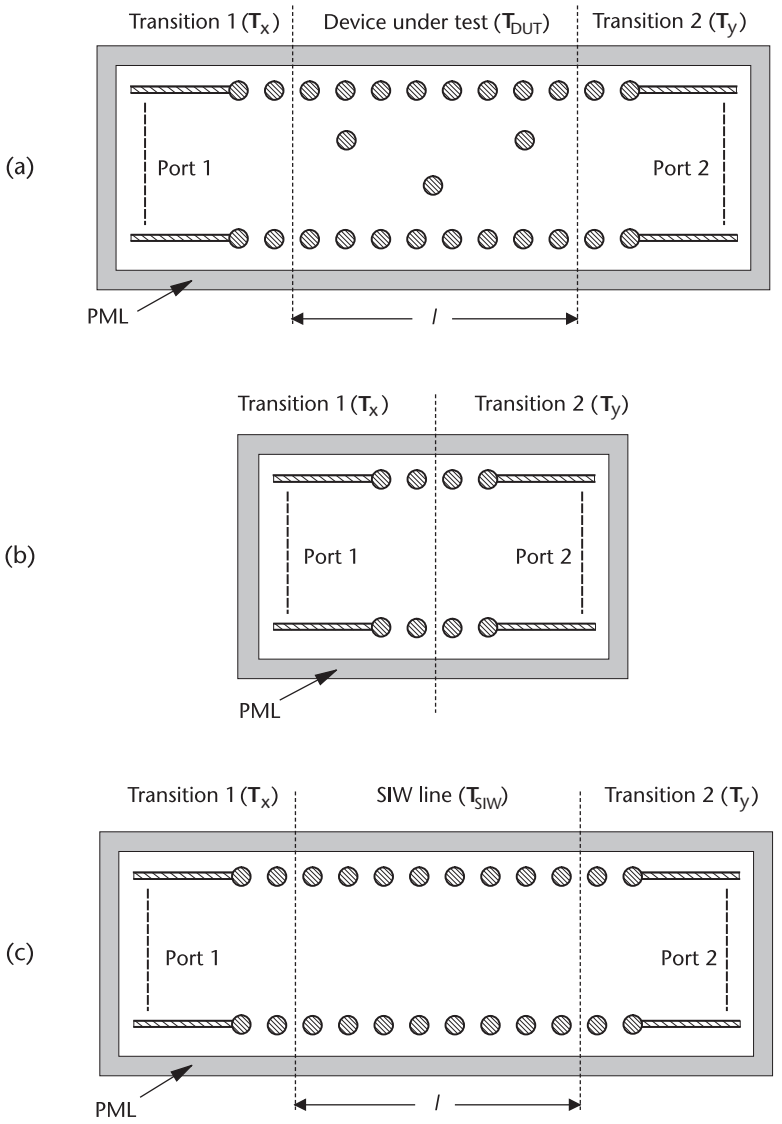

Figure 9.10 SIW geometries considered in the FDTD method with numerical thru-line calibration technique: (a) complete structure; (b) thru connect; (c) line connect.

where $\mathbf{T}_{SIW}$ represents the transfer matrix of the straight SIW section. The thru-line calibration technique requires the algebraic manipulation of the three matrices and the solution of eigenvalue problems, as detailed in [17]. It finally leads to the determination of the transmission matrix $\mathbf{T}_{DUT}$.

In these analyses, absorbing boundary conditions or a perfectly matched layer (PML) are defined around the SIW structure, to take into account possible radiation effects. Particular care should be exercised in the choice of the length of the input and output transitions: the transitions should be long enough, so that the field generated by the source exhibits the proper SIW mode structure at the interface between the transition and the device under test.

Method of Moments and Cylindrical Eigenfunction Expansion

The integral equation method is a particularly efficient technique for the modeling of SIW components, due to their intrinsic characteristics. In fact, the geometry of SIW components is usually quite simple (being only composed of metalized cylinders), the dielectric substrate is generally homogeneous, and the electromagnetic shielding, yet not perfect, is practically complete if the gaps between metal cylinders are sufficiently small. These features can be exploited in the application of the integral equation method, which can take advantage of the similarity with classical H-plane waveguide components. The integral equation method is more efficient than finite-difference or finite-element techniques, because it requires the definition of the problem unknowns only on the boundaries of the investigation domain, namely the contour of the metal cylinders.

An efficient implementation of the integral equation method for the modeling of SIW components was proposed in [18,19], where the classical integral equation solved by the method of moments is combined with the use of a cylindrical eigenfunction expansion. In this implementation, the electromagnetic field inside the structure is determined by the electric current densities $\mathbf{J}_s$ and the magnetic current densities $\mathbf{M}_s$ defined on the port segments (Figure 9.11). The current densities on the remaining portion of the external contour can be ignored, because the field is completely confined inside the SIW structure provided that the metal cylinders are closely spaced. The field scattered by the metal cylinders (both the posts defining the side walls of the SIW structure and possible internal posts) is expressed in terms of a summation of cylindrical functions. The total electric field inside the SIW component has only the z component and it can be expressed as

$$E^z(\mathbf{r}) = E^z_{\mathrm{PORT}} + \sum_{n=1}^{N} \sum_{m=-M}^{+M} a_{m,n} H_m^{(2)}(\beta_s\ \rho_n)\ e^{jm\phi_n} \tag{9.34}$$

where N is the overall number of the metal cylinders (including side walls and internal posts), $H_m^{(2)}$ is the m-th order Hankel function of the second kind, ρ_n and ϕ_n are the local polar coordinates of the n-th metal cylinder (with the origin located at the center of the cylinder), β_s is the phase constant in the dielectric substrate, and $a_{m,n}$ represents an unknown coefficient (related to the amplitude of the m-th order Hankel function of the n-th metal cylinder).

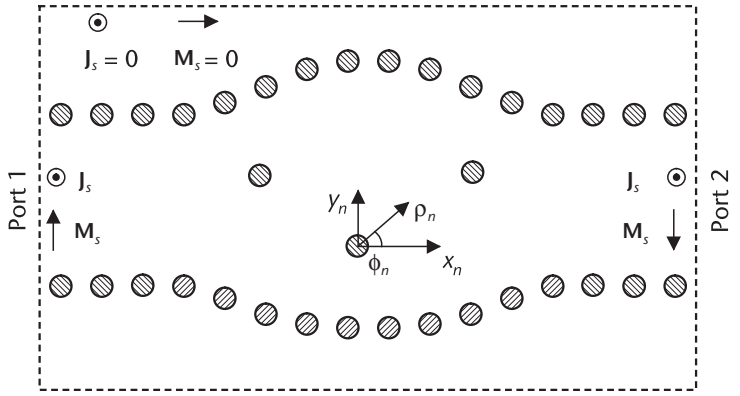

Figure 9.11 SIW geometries considered in the hybrid method of moments and cylindrical eigenfunction expansion (from [18], © 2008 IEEE. Reprinted with permission).

E^{Z}_{PORT} represents the total electric field generated by the unknown electric current density $\mathbf{J}_s$ and magnetic current density $\mathbf{M}_s$ defined on the port segments. In order to determine E^{Z}_{PORT}, each waveguide port is divided into a number of segments (named sub-ports), and $\mathbf{J}_s$ and $\mathbf{M}_s$ are assumed constant in each sub-port. The electric fields generated by $\mathbf{J}_s$ and $\mathbf{M}_s$ on each sub-port are given by

$$E^{z}_{J} = -\frac{\omega\mu_s I_J}{4}\int_0^L H_0^{(2)}(\beta_s\,\rho'_n)\,dl' \tag{9.35a}$$

$$E^{z}_{M} = \frac{j\beta_s I_M}{4}\int_0^L \sin(\phi')H_1^{(2)}(\beta_s\,\rho'_n)\,dl' \tag{9.35b}$$

where E^{z}_{J} and E^{z}_{M} represents the electric field generated by I_J and I_M current densities on the sub-port, respectively, ρ'_n is the local coordinate calculated from the considered sub-port, L is the length of the sub-port and μ_s is the magnetic permeability of the dielectric substrate. Consequently, E^{z}_{PORT} can be computed by summing the contributions of all sub-ports.

The integral equation is obtained by enforcing the proper boundary conditions, which are of two types. The first type of condition is imposed on the contour of the metal posts, where the electric wall condition (or, alternatively, the Leontovic condition in the case of finite metal conductivity) is set. The second condition is imposed on the port segments, where the condition is $E^z = I_{\mathrm{M}}$, i.e., the z-component of the electric field is equal to the transverse component of the magnetic current density at the center of each sub-port.

Finally, the solution of the integral equation by the method of moments (MoM) leads to the determination of the impedance matrix $\boldsymbol{Z}$ of the SIW component [19].

Boundary Integral-Resonant Mode Expansion (BI-RME) method

The BI-RME method is a hybrid integral equation/modal technique, originally developed for classical waveguide components [20] and subsequently applied for the modeling of SIW structures [21].

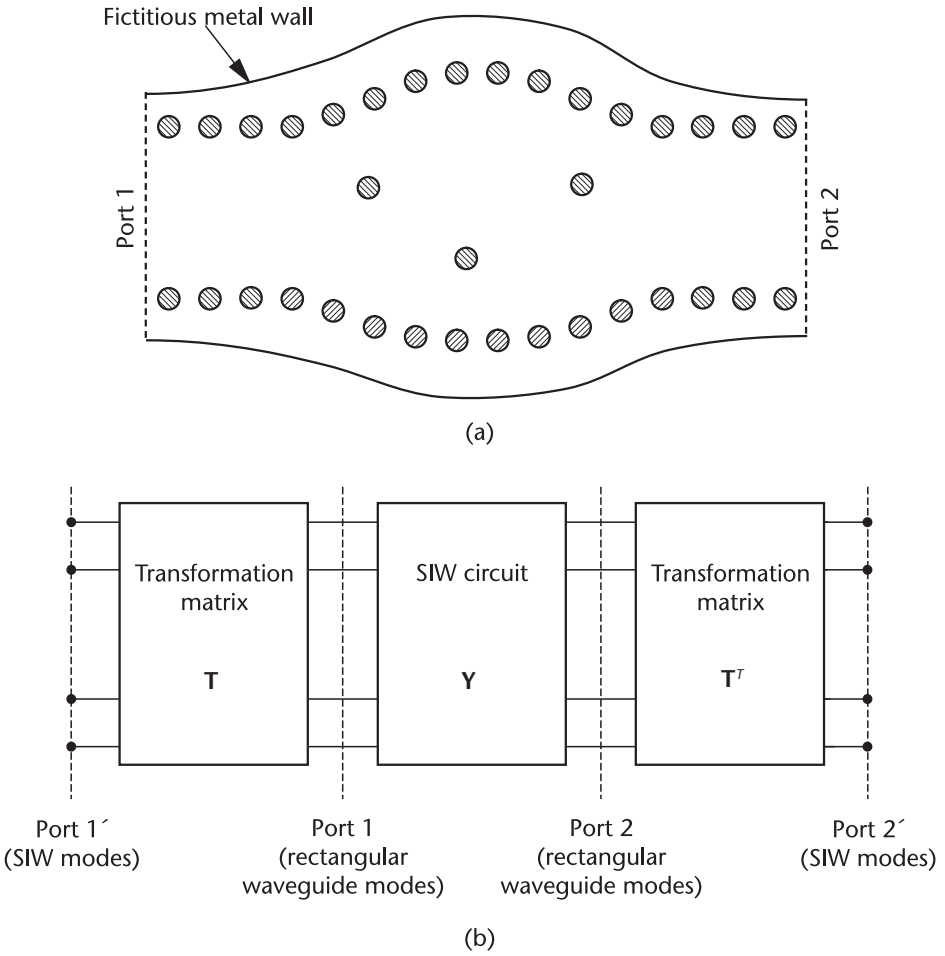

Figure 9.12 SIW circuit considered in the BI-RME method: (a) geometry of the circuit, with exterior metal walls; (b) transformation required to map the rectangular waveguide modes into SIW modes (from [21], © 2008 IEEE. Reprinted with permission).

The BI-RME method permits the direct determination of the wideband frequency response of SIW components: this feature depends on the particular form of the generalized admittance matrix Y calculated by the BI-RME method, which is expressed in the form of a pole expansion in the frequency domain.

In the lossless case, the SIW component is composed of ideal dielectric material and perfect conductor, and the radiation loss is negligible: consequently, in the application of the BI-RME method, the structure is supposed to be completely shielded by an external fictitious metal wall defined around the actual SIW component (Figure 9.12(a)). In addition, the input and output ports of the circuit are defined as rectangular waveguide modes: as an example, two physical ports, with N rectangular waveguide modes defined on each port, are considered in this case (Figure 9.12(a)). Under these hypotheses, the $\mathbf{Y}$ matrix relating $2N$ modal currents and voltages of the rectangular waveguide ports can be expressed as

$$\mathbf{Y}(\omega) = \frac{1}{j\omega}\mathbf{A} + j\omega\mathbf{B} + j\omega^3\mathbf{C}\left(\Omega^4 - \omega^2\Omega^2\right)^{-1}\mathbf{C}^{\mathrm{T}} \tag{9.36}$$

where $\omega=2\pi f$ is the angular frequency, **A** and **B** are $2N \times 2N$ matrices, related to the low-frequency behavior of the admittance matrix, **Ω** is a M-element diagonal matrix, whose entries are the resonance angular frequencies of the first M modes of the cavity obtained by short-circuiting the ports of the SIW circuit, and **C** is a $2N\times M$ matrix related to the coupling between the ports modes and the aforementioned resonant cavity modes. The calculation of matrices **A**, **B**, **C** and Ω by the BI-RME method is detailed in [20]. Matrices **A**, **B**, **C** and Ω are frequency independent matrices and, therefore, the expression of the **Y** matrix in (9.36) exhibits an explicit dependency on the angular frequency ω. Consequently, once these matrices are known, this representation of the **Y** matrix allows to calculate the frequency response of the circuit at any frequency of interest in a negligible time, with no need of frequency-by-frequency full-wave analyses. For this reason, the BI-RME method is a very efficient technique for modeling and design of complex SIW structures.

The expression of the **Y** matrix determined in (9.36), however, relates modal currents and voltages of the rectangular waveguide ports, whereas the relation between modal voltages and currents of the SIW modes is actually required.

The generalized admittance matrix **Y′** relating $2P$ modal voltages and currents of the SIW modes can be obtained from **Y** matrix by a port mode transformation (Figure 9.12(b)). This transformation is based on the technique described in Sec. 9.2.2, where the P modal vectors of each SIW port are expressed as a linear combination of the N modal vectors of the embedding rectangular waveguide, as in formula (9.8). To perform this change, the transformation matrix **T** needs to be defined [22]: in the case of a two-port circuit, the block diagonal matrix **T** is defined as

$$\mathbf{T} = \left(\begin{array}{ccc|ccc} \Lambda_{1,1} & \cdots & \Lambda_{1,N} & 0 & \cdots & 0 \\ \vdots & \ddots & \vdots & \vdots & \ddots & \vdots \\ \Lambda_{P,1} & \cdots & \Lambda_{P,N} & 0 & \cdots & 0 \\ \hline 0 & \cdots & 0 & \Lambda_{1,1} & \cdots & \Lambda_{1,N} \\ \vdots & \ddots & \vdots & \vdots & \ddots & \vdots \\ 0 & \cdots & 0 & \Lambda_{P,1} & \cdots & \Lambda_{P,N} \end{array}\right) \tag{9.37}$$

where $\Lambda_{p,n}$ represents the p-th element of the n-th eigenvector of the **ABCD** matrix of the unit cell of the port SIW, as discussed in Sec. 9.2.2. The generalized admittance matrix **Y′** relating modal currents and voltages of the SIW modes can be obtained as

$$\mathbf{Y}' = \mathbf{T}\,\mathbf{Y}\,\mathbf{T}^{\mathrm{T}} \tag{9.38}$$

where matrix **Y′** has dimensions $2P\times 2P$ and can be still expressed in the form of a pole expansion in the frequency domain (9.36), provided that matrices **A, B,** and **C** are replaced by the corresponding primed matrices:

$$\begin{aligned} \mathbf{A}' &= \mathbf{T}\,\mathbf{A}\,\mathbf{T}^{\mathrm{T}} \\ \mathbf{B}' &= \mathbf{T}\,\mathbf{B}\,\mathbf{T}^{\mathrm{T}} \\ \mathbf{C}' &= \mathbf{T}\,\mathbf{C} \end{aligned} \tag{9.39}$$

whereas matrix Ω, which is not related to the port modes, remains unchanged.

If the conductor and dielectric losses in the SIW component are low but not negligible, formulation (9.36) of the admittance matrix can be modified to account for conductor and dielectric losses, by using a perturbation approach [21]. In this case, the dielectric substrate is characterized by a complex dielectric permittivity $\varepsilon = \varepsilon_0\varepsilon_r - j\sigma_d / \omega$, where ε_0 is the dielectric permittivity of vacuum, ε_r is the relative dielectric constant of the medium, σ_d is the conductivity of the dielectric material, and the conductor has a finite conductivity σ_c. The expression of the generalized admittance matrix **Y** results

$$\begin{aligned} \mathbf{Y}(\omega) = \frac{1}{j\omega}\mathbf{A} + \frac{\sigma_{\mathrm{d}}}{\varepsilon_0\varepsilon_{\mathrm{r}}}\mathbf{B} + j\omega\mathbf{B} + \omega^2\mathbf{C}\left(\mathbf{\Omega}^3\mathbf{Q} + j\omega\,\mathbf{\Omega}^2 - \omega^2\mathbf{\Omega}\mathbf{Q}\right)^{-1}\mathbf{C}^T \\ + j\omega^3\mathbf{C}\left(\mathbf{\Omega}^4 + j\omega\,\mathbf{\Omega}^3\mathbf{Q}^{-1} - \omega^2\mathbf{\Omega}^2\right)^{-1}\mathbf{C}^T \end{aligned} \tag{9.40}$$

where **Q** is an *M*-element diagonal matrix, whose entries are the quality factors of the cavity modes. The quality factor of cavity modes depends on both the conductivity σ_d of the dielectric substrate and the conductivity σ_c of the conductor [21]. Expression (9.40) of the generalized admittance matrix preserves all the advantages of (9.36): same as the lossless expression, it represents a mathematical model of the frequency response of the SIW component, and it permits its broadband modeling representation in one single full-wave calculation. Moreover, also in the lossy case, the transformation from the **Y** matrix relating modal currents and voltages of the rectangular waveguide ports to the **Y**′ matrix relating modal voltages and currents of the SIW modes can be performed with the technique discussed above, by adopting the transformation matrix **T** defined in (9.37).

Radiation loss can be accounted for by including in the full-wave analysis additional ports, located at the sides of the SIW circuits, which are subsequently connected to matched loads [21]. This solution permits to include radiation loss in a numerical method which is intrinsically developed for shielded components, without spoiling the representation of the admittance matrix based on the resonant cavity modes. A sufficient number of propagating modes need to be considered at each side port, to guarantee an accurate approximation of the radiation condition. As a consequence, this requirement prevents the use of the solution based on lateral matched ports in the modeling of the SIW unit cell: in fact, in this case, the width of the lateral ports is too small, and usually all modes are below cutoff in the frequency band of interest.

As an example, the BI-RME method is applied to the electromagnetic simulation of a band-pass SIW filter operating at 28 GHz, with two centered and two offset metal posts, first proposed in [5]. The geometry of the filter is shown in Figure 9.13(a), and its dimensions are: $w = 5.563$ mm, $d = 0.775$ mm, $s = 1.525$ mm, $o = 1.01$ mm, $s_1 = 4.71$ mm, $s_2 = 5.11$ mm; the dielectric substrate has a thickness

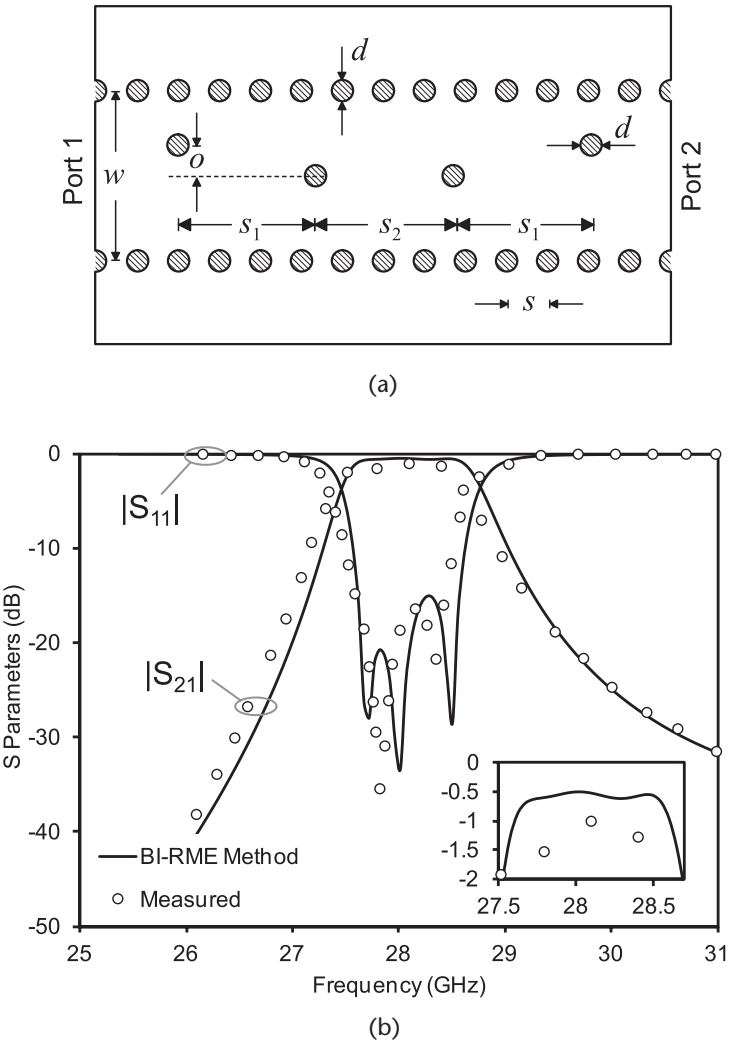

Figure 9.13 Band–pass SIW filter at 28 GHz, analyzed by the BI-RME method: (a) geometry of the SIW filter (w = 5.563 mm, d = 0.775 mm, s = 1.525 mm, o = 1.01 mm, s_1 = 4.71 mm, s_2 = 5.11 mm, h = 0.787 mm; ε_r = 2.2, tan δ = 0.002, $\sigma_c = 4\times10^7$s/m); (b) scattering parameters of the SIW filter, obtained by BI-RME simulations and by measurements. (from [21], © 2008 IEEE. Reprinted with permission).

h = 0.787 mm, a relative dielectric constant ε_r = 2.2 and dielectric conductivity σ_d = 0.0011 S/m (corresponding to a loss tangent tan δ = 0.002 at 28 GHz), and the metal conductivity is $\sigma_c = 4\times10^7$ S/m. The effect of surface roughness was not taken into account. In the BI-RME analysis of this filter, N = 20 rectangular waveguide modes are considered at each port, and M = 200 cavity modes are used in the **Y** matrix expression of (9.40). Since radiation losses are negligible in this structure, no side ports need to be defined. The BI-RME simulation results are shown in Figure 9.13(b) and compared with measured data from [5]. The inset of Figure 9.13(c) shows that the simulated insertion loss of this filter at 28 GHz is around 0.55 dB (0.15 dB due to dielectric loss and 0.4 dB to conductor loss), while the measured

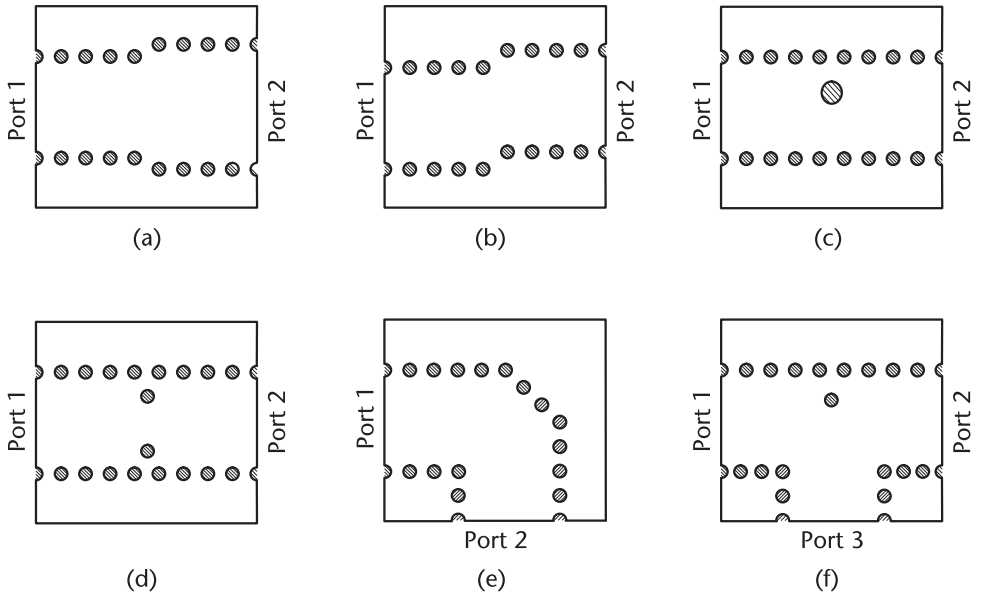

Figure 9.14 Examples of elementary SIW discontinuities, representing the building blocks for modeling SIW components: (a) step in width; (b) offset junction; (c) inductive post; (d) iris window; (e) mitered bend; (f) T–junction.

one is 1 dB: the difference is attributed to the effect of the transitions from the microstrip to the SIW structure, which are not included in the simulation. The insertion loss of this SIW filter is remarkably low, and comparable with the performance of microstrip circuits.

9.2.4 Equivalent Circuits Models of SIW Discontinuities

Besides the full-wave modeling of SIW components, the use of equivalent circuit models represents an efficient and powerful design tool [22]. The use of equivalent circuit models is especially important in the design of large SIW circuits, where the increased complexity leads to unduly long computing time even when using efficient electromagnetic simulation techniques. This approach is a traditional technique for the analysis and optimization of waveguide components, which dates back to the fundamental work of Nathan Marcuvitz [23] in the 1940's.

The basic idea is very simple: the modeling of complete and complex waveguide circuits is usually time consuming, due to the large size of the structure. The computational burden can be reduced by adopting a segmentation technique: the circuit is subdivided into elementary building blocks, which are analyzed separately and characterized by scattering or admittance matrices. Finally, the matrices calculated for all building blocks are combined, to determine the frequency response of the entire circuit. In large circuits some elementary building blocks may appear several times throughout the structure: in this case, each building block topology needs to be analyzed only once, thus providing an additional advantage. The segmentation technique becomes significantly more efficient if the matrices character-

izing the elementary building blocks are determined through equivalent circuits instead of full-wave analyses.

In the case of passive SIW components, the elementary building blocks can be a variety of simple SIW discontinuities, like iris windows, waveguide sections with inductive posts, or waveguide bends (Figure 9.14). The equivalent circuit models characterizing these elementary building blocks consist of the combination of inductors, capacitors, resistors, and ideal waveguide sections [22].

If accurate results are required, particular requirements are imposed on the features of the equivalent circuit models. First of all, equivalent circuit models are usually required to be multimodal: as closely spaced discontinuities interact also through the evanescent higher-order modes, the fundamental mode on the ports is not sufficient to describe this physical phenomenon. Therefore, these building blocks are characterized by generalized matrices, where a few modes (usually 3 to 10) are defined at each physical port, and consequently the equivalent circuit model is multimodal. In addition, the technique adopted for deriving the equivalent circuit model plays an essential role in the accuracy of the results: simple equivalent circuits like the ones proposed in [23] do not guarantee sufficient accuracy over a wide band, and are not recommended. Accurate models may be obtained from sets of full-wave analyses and subsequent fitting or processing of the results. As a final requirement, equivalent models need to be parametric: an analytical expression provides the value of each lumped element as a function of the geometrical dimensions of the building block. Parametric equivalent circuit models are particularly helpful, because they can be adopted for the design and optimization of SIW components, and not only for their analysis.

A particularly effective technique for deriving equivalent circuit models is based on the use of BI-RME method [22]. The BI-RME method provides the generalized admittance matrix **Y** of the building block in the form of a pole expansion in the frequency domain, as discussed in the previous section. In the lossless case [21], the *ij*-th entry of the **Y** matrix (9.36) is given by

$$Y_{ij}(\omega) = \frac{A_{ij}}{j\omega} + j\omega B_{ij} + j\omega^3 \sum_{m=1}^{M} \frac{C_{im}C_{jm}}{\omega_m^2(\omega_m^2 - \omega^2)} \tag{9.41}$$

where i and j refer to the port modes, and M is the number of resonances of the cavity obtained by short-circuiting the ports of the building block. The quantities A_{ij}, B_{ij}, C_{im}, and ω_m are frequency independent and are calculated very efficiently by the BI-RME method [20].

By extracting the term for $\omega \to \infty$ from the summation in (9.41), the expression of Y_{ij} is recast in the form

$$Y_{ij}(\omega) = \frac{1}{j\omega} A_{ij} + j\omega \left(B_{ij} - \sum_{m=1}^{M} \frac{C_{im}C_{jm}}{\omega_m^2} \right) + j\omega \sum_{m=1}^{M} \frac{C_{im}C_{jm}}{\omega_m^2 - \omega^2} \tag{9.42}$$

This expression can be easily identified as the parallel combination of an inductor, a capacitor, and M LC-series resonators (Figure 9.15(a)). The value of the lumped elements appearing in Figure 9.15(a) are directly obtained from expression (9.42) as

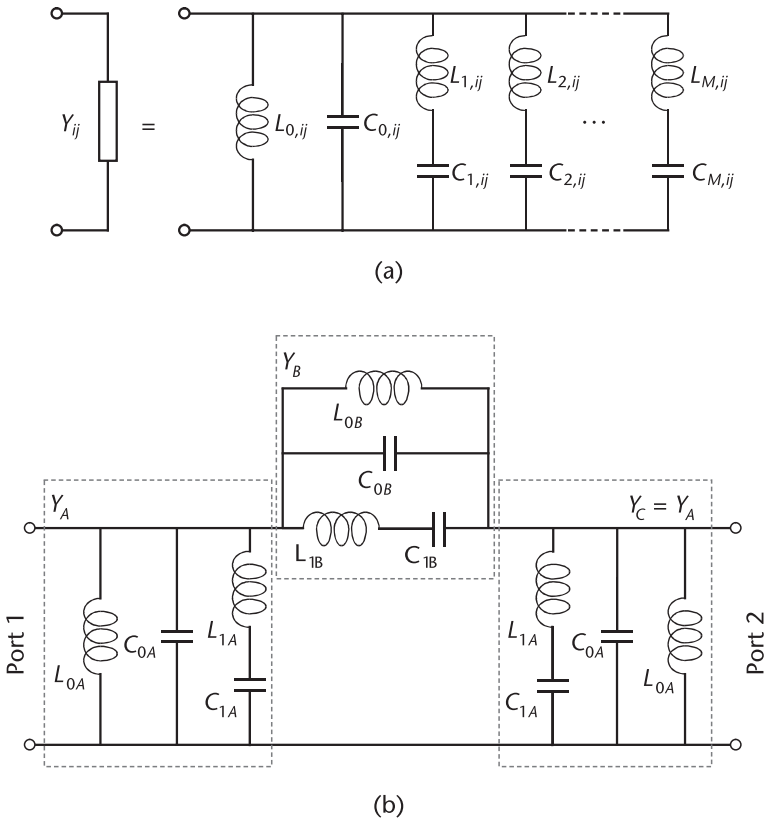

Figure 9.15 Equivalent lumped-element circuit model (from [22], © 2008 Wiley Periodicals, Inc. Reprinted with permission): (a) equivalent circuit of Y_{ij}; (b) simplified π-type equivalent circuit of a two-port elementary building block.

$$L_{0,ij} = \frac{1}{A_{ij}} \tag{9.43a}$$

$$C_{0,ij} = B_{ij} - \sum_{m=1}^{M} \frac{C_{im}C_{jm}}{\omega_m^2} \tag{9.43b}$$

$$L_{m,ij} = \frac{1}{C_{im}C_{jm}} \tag{9.43c}$$

$$C_{m,ij} = \frac{C_{im}C_{jm}}{\omega_m^2} \tag{9.43d}$$

As this equivalent circuit is directly derived from the full-wave modeling, the physical meaning of each lumped element can be identified. In particular, L_0 and C_0 are related to the low-frequency behavior of the frequency response, whereas the LC-series resonators are associated to the resonant modes of the cavity obtained by short-circuiting the ports of the building block [20, 22]. Consequently, the accuracy

of the model is strictly related to the number of LC-series resonators: including additional resonators in the equivalent circuit model increases its accuracy and extends its frequency range of validity.

The identification of the equivalent lumped-element circuit for the *ij*-th entry of the **Y** matrix allows, in turn, to directly derive the equivalent model of the building block. When adopting a π-type model, the resulting equivalent circuit is shown in Figure 9.15(b) in the case of a 2-port circuit, where $Y_A = Y_C = Y_{11}+Y_{12}$ and $Y_B = -Y_{12}$. In this schematic, the equivalent circuit is simplified by considering only one LC-series resonator. By using this procedure, the topology of the equivalent circuit and the values of the lumped elements can be directly obtained from the result of a full-wave analysis, thus avoiding any initial guess or fitting procedure. Of course, the procedure illustrated here in the case of two-port building blocks can be extended to an arbitrary number of ports.

This approach also allows to determine parametric equivalent circuit models, where the values of the lumped elements depend on the geometrical dimensions of the structure. Parametric models can be achieved by performing repeated full-wave analyses for different geometrical dimensions and by fitting through polynomials the value of the lumped elements [22].

The same approach can be applied in the derivation of equivalent circuit models of lossy building blocks, where both dielectric and conductor losses are considered [24]. The conductor has a finite metal conductivity σ_c and the dielectric medium is characterized by a complex dielectric permittivity $\varepsilon = \varepsilon_0\varepsilon_r - j\sigma_d / \omega$. The expression of the *ij*-th entry of the **Y** matrix, after extracting the term for $\omega \to \infty$ from the summation, results in

$$Y_{ij}(\omega) = \frac{1}{j\omega}A_{ij} + \frac{\sigma_d}{\varepsilon_0\varepsilon_r}B_{ij} + j\omega\left[B_{ij} - \sum_{m=1}^{M}\frac{C_{im}C_{jm}}{\omega_m^2}\right] + j\omega\sum_{m=1}^{M}\frac{C_{im}C_{jm}}{\omega_m^2 + j\omega\omega_m / Q_m - \omega^2} \quad (9.44)$$

where Q_m is the quality factor of the *m*-th resonant cavity mode [24].

Expression (9.44) of the **Y** matrix can be identified as the parallel combination of an inductor, a resistor, a capacitor, and *M* RLC-series resonators. The value of the lumped elements can be analytically obtained from expression (9.44) as

$$R_{0,ij} = \frac{\varepsilon_0\varepsilon_r}{\sigma_d B_{ij}} \quad (9.45a)$$

$$L_{0,ij} = \frac{1}{A_{ij}} \quad (9.45b)$$

$$C_{0,ij} = B_{ij} - \sum_{m=1}^{M}\frac{C_{im}\,C_{jm}}{\omega_m^2} \quad (9.45c)$$

$$R_{m,ij} = \frac{\omega_m}{Q_m\,C_{im}\,C_{jm}} \quad (9.45d)$$

$$L_{m,ij} = \frac{1}{C_{im}C_{jm}} \quad (9.45e)$$

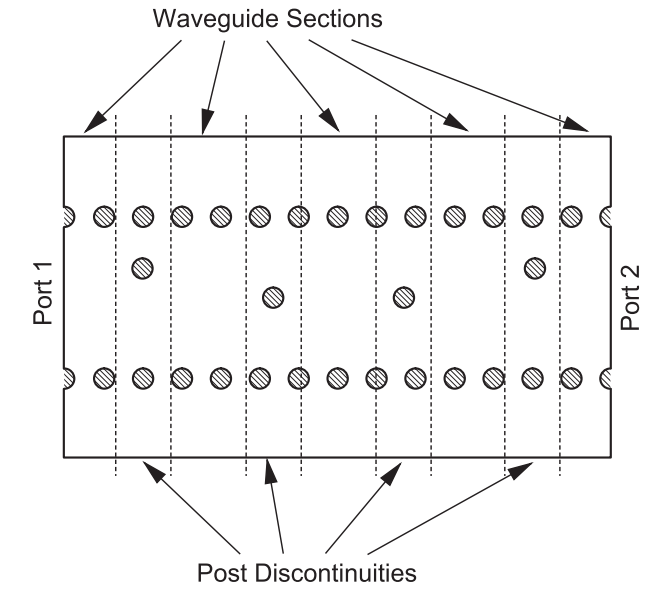

(a)

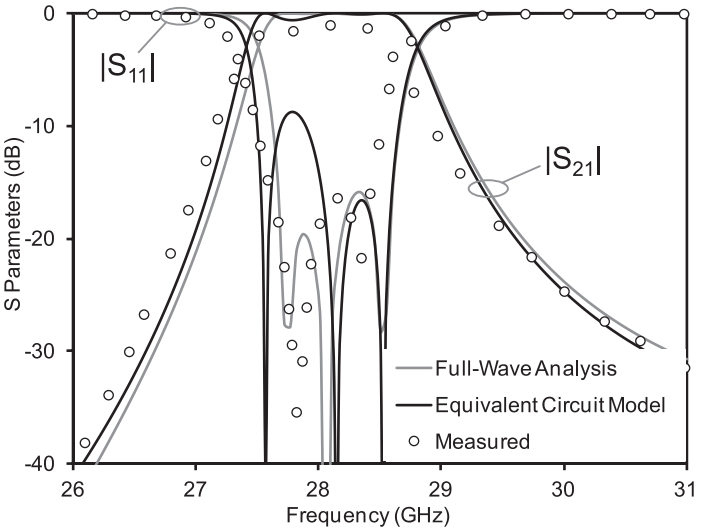

(b)

Figure 9.16 Modeling of a band-pass SIW filter at 28 GHz by segmentation technique and equivalent circuit models: (a) geometry of the filter and adopted segmentation (dimensions in Figure 9.13); (b) scattering parameters of the SIW filter, obtained by full–wave simulations, equivalent circuit model, and measurements (from [22], © 2008 Wiley Periodicals, Inc. Reprinted with permission).

$$C_{m,ij} = \frac{C_{im}C_{jm}}{\omega_m^2} \tag{9.45f}$$

The derivation of the complete model resembles the procedure followed in the lossless case, with the only addition of the resistors that account for losses [24].

The use of parametric equivalent circuit models allows for a very fast analysis and design of SIW circuits. Moreover, once the circuit models are available, the design of SIW circuits can be performed with no need of full-wave simulators, but only using a Spice-like circuit simulator. To better explain the use and features of equivalent circuit models, the analysis of the band-pass SIW filter shown in Figure 9.13(a) is reported as an example.

By adopting the segmentation technique, the circuit is subdivided into nine subcircuits: two centered-post discontinuities, two offset-post discontinuities, and five SIW sections (Figure 9.16(a)). Each discontinuity is modeled by a lumped-element equivalent circuit, with five modes per port and one LC series resonator. The value of each lumped element (inductance or capacitance) depends on the value o of the offset of the post, and it is expressed by a third-order polynomial function. The SIW sections are modeled by using the analytical frequency response of the corresponding equivalent rectangular waveguide, and also in this case five modes per port are considered. The frequency response of the filter, calculated by using the equivalent circuit models, is shown in Figure 9.16(b), and it compared well with the en-bloc analysis performed by the BI-RME method and with measurements results from [5].

9.3 Design Considerations

The design of SIW interconnects and components can be performed by using the analysis techniques described in Section 9.2, and following the same design rules adopted for the design of classical waveguide components.

In addition, the specific characteristics of SIW structures need to be accounted for: in fact, the different mechanisms of loss, the radiation leakage, and the possible band-gap effect due to the periodicity of the metal posts determine the efficiency of SIW circuits.

The preliminary step for the design of SIW components is the determination of the basic geometry of the SIW structure, namely the width w of the waveguide, the diameter d of the holes, and the longitudinal spacing s between the holes (Figure 9.2). The selection of w is related to the operation frequency band, as w basically determines the cutoff frequency of the fundamental mode of the SIW. The choice of d and s is related both to technological constraints (depending on the fabrication process) and to performance optimization (for instance, to loss minimization). The dielectric substrate has usually a relative dielectric constant ε_r is usually in the range from 2 to 10 and a thickness h = 0.2-1 mm. The choice of the dielectric substrate depends on a variety of factors: for instance, substrates with high dielectric constant are adopted with the aim to shrink the size of the component, while thick substrates are preferred to reduce conductor loss (as discussed in this Section).

9.3.1 Mechanisms of Loss

There are three major mechanisms of loss in SIW structures: conductor loss, dielectric loss, and radiation leakage [21]. Conductor and dielectric losses in SIW

structures exhibit similar characteristics as in (dielectric-filled) metallic rectangular waveguides. Conversely, radiation leakage does not exist in classical waveguides, because they are completely shielded, and it appears in SIW structures because of the gaps between the metalized holes.

If all kinds of losses are reasonably small, the attenuation constant α_{TOT} for the fundamental mode of an SIW interconnect is the summation of the three contributions of loss:

$$\alpha_{TOT} = \alpha_C + \alpha_D + \alpha_R \tag{9.46}$$

where α_C represents the attenuation constant due to conductor loss, α_D is the attenuation constant due to dielectric loss, and α_R denotes the attenuation constant due to radiation leakage.

Conductor loss is due to the finite conductivity σ_c of the metal walls, including the top and bottom metal planes as well as the vertical vias. Due to the similarity of the field propagation in SIW and rectangular waveguide, the attenuation constant α_C for the fundamental mode of an SIW can be calculated quite accurately by using the analytical formula [8] valid for the equivalent rectangular waveguide with width w_{eff}

$$\alpha_C = \frac{\sqrt{\pi f \varepsilon_0 \varepsilon_r}}{h\sqrt{\sigma_c}} \frac{1 + 2\left(f_c/f\right)^2 h/w_{eff}}{\sqrt{1-\left(f_c/f\right)^2}} \tag{9.47}$$

where σ_c is the metal conductivity, ε_0 is the free space permittivity, ε_r is the relative dielectric constant of the dielectric substrate, and f_c is the cutoff frequency of the SIW structure.

Conductor loss is affected by the substrate thickness h: for a given transmitted power, increasing the dielectric thickness reduces the amplitude of the electric current density flowing in the top and bottom metal layers, thus reducing the power dissipated by Joule effect. It results that attenuation constant α_C is practically proportional to the inverse of the substrate thickness h. Therefore, increasing the thickness is an effective way to reduce the conductor loss in SIW structures. The maximum thickness is determined either by $w_{eff}/2$ (in order to preserve the maximum bandwidth of the single-mode regime) or by practical technological reasons. Conversely, the variation in the diameter of the metal vias and in their longitudinal spacing produces minor effects [25].

Dielectric loss is attributed to the loss tangent tan δ of the dielectric substrate. Also in the case of α_D, the similarity of the field propagation in SIW and rectangular waveguide allows for using the analytical formula of classical rectangular waveguides [25] to calculate the attenuation constant α_D for the fundamental mode of an SIW structure

$$\alpha_D = \frac{\pi f \sqrt{\varepsilon_r}}{c\sqrt{1-\left(f_c/f\right)^2}} \tan\delta \tag{9.48}$$

where c is the speed of light in vacuum, and f_c is the cutoff frequency of the SIW structure. The use of formula (9.48) guarantees a reasonable accuracy in the calcu-

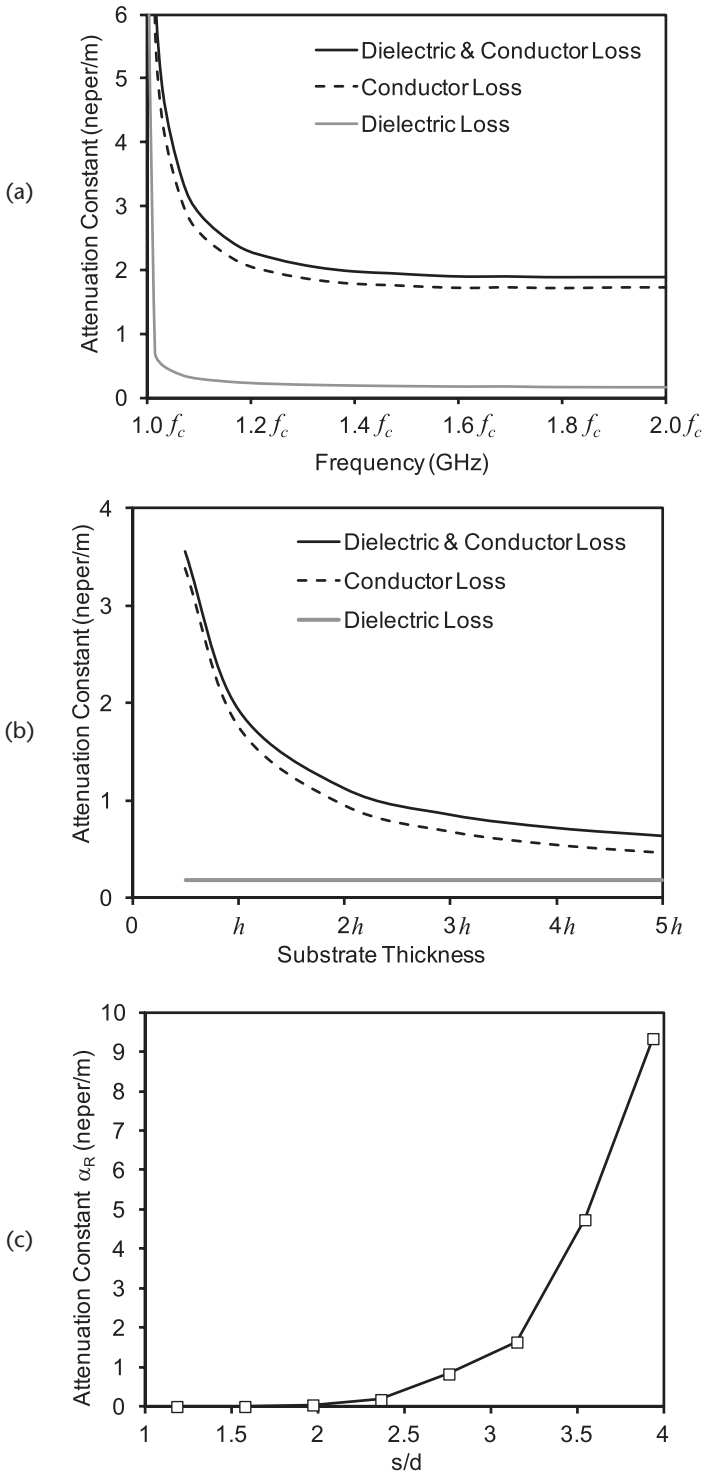

Figure 9.17 Attenuation constant in a substrate integrated waveguide: (a) attenuation constant versus frequency; (b) attenuation constant versus substrate thickness at f = 1.5 f_c; (c) attenuation constant due to radiation leakage versus *s/d* ratio at *f* = 1.5 f_c. (from [21], © 2008 IEEE. Reprinted with permission).

lation of α_D. The attenuation constant α_D is practically unaffected by the geometrical dimensions of the SIW structure [25].

For most dielectric substrates, dielectric loss is the major contribution of loss when operating at mm-waves. This depends on two main factors: the intrinsic properties of the materials and the dependence on frequency of α_C and α_D. Typical substrates adopted for SIW structures have tan δ between 10^{-3} and 10^{-4}, and they are laminated with copper having a conductivity σ_c around $5 \cdot 10^7$ S/m. Concerning the frequency dependence, the attenuation constant α_D due to dielectric loss is practically proportional to the frequency f, whereas the attenuation constant α_C due to conductor loss is proportional to the $f^{1/2}$, and therefore its contribution becomes less significant when operating at higher frequency.

Radiation leakage is caused by the gaps between the metal vias, which spoil the shielding of SIW structures. The effect of radiation leakage can be minimized by closely spacing the metal vias: the leakage is negligible if the ratio between the longitudinal spacing and the via diameter is $s/d < 2.5$, and a practical design rule is $s/d = 2$.

An SIW interconnect with the following geometrical dimensions is considered as an example: $w = 3.97$ mm, $d = 0.635$ mm, $s = 1.016$ mm; the substrate thickness $h = 0.254$ mm, relative dielectric constant $\varepsilon_r = 9.9$ and tan $\delta = 0.0002$, and metal conductivity $\sigma_c = 5 \cdot 10^7$ S/m. The corresponding cutoff frequency of the SIW interconnect is $f_c = 13.58$ GHz.

Figure 9.17(a) shows the frequency behavior of the attenuation constant $\alpha_C + \alpha_D$, due to conductor and dielectric losses. In addition, the values of α_C and α_D versus frequency are reported separately. In all three cases, the attenuation is very large near the cutoff frequency of the SIW, and tends to become constant in the central portion of the single-mode frequency band. These plots are obtained by a full-wave simulation [24]. In this SIW structure, the attenuation constant α_R due to radiation leakage is negligible if compared to the contribution of conductor and dielectric loss.

The same SIW structure is adopted to investigate the effect of the substrate thickness h on losses, which is shown in Figure 9.17(b). The effect is significant on α_C, which can be drastically reduced by increasing h. Conversely, α_D does not practically change when modifying h: therefore, the geometrical dimensions do not permit to decrease dielectric losses, being the only solution the use of a dielectric material with smaller loss angle.

The radiation leakage is finally considered, where the longitudinal spacing s is modified, being all other dimensions kept at their nominal values. Figure 9.17(c) shows that the attenuation constant α_R due to radiation is practically negligible for small values of the ratio s/d, and tends to increase when s/d is larger than 2.

In general, losses in SIW structures are higher than in hollow rectangular waveguides operating at the same frequency. Dielectric losses play an important role, as they are present in SIW structures and not in classical hollow metallic waveguides. Moreover, conductor losses in SIW are larger than in classical waveguides, because α_C is proportional to the inverse of the thickness of the structure, and SIW are typically much thinner than metallic rectangular waveguides.

A comparison with planar transmission lines (e.g., microstrip line and coplanar waveguide) is not straightforward, for a number of reasons. The attenuation

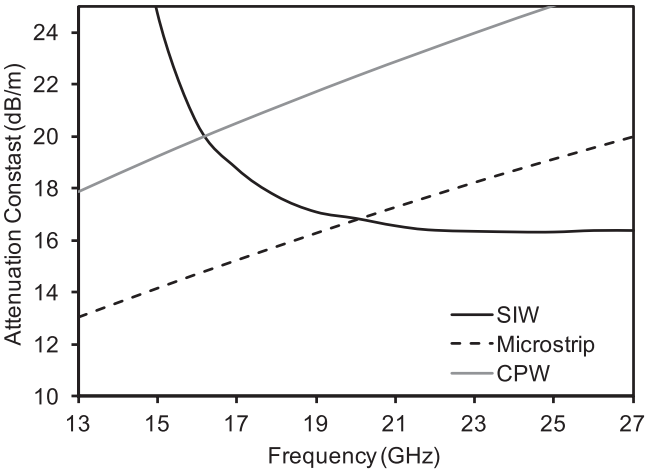

Figure 9.18 Comparison of the attenuation constant in SIW interconnect, microstrip line, and coplanar waveguide (from [24], © 2008 IEEE. Reprinted with permission).

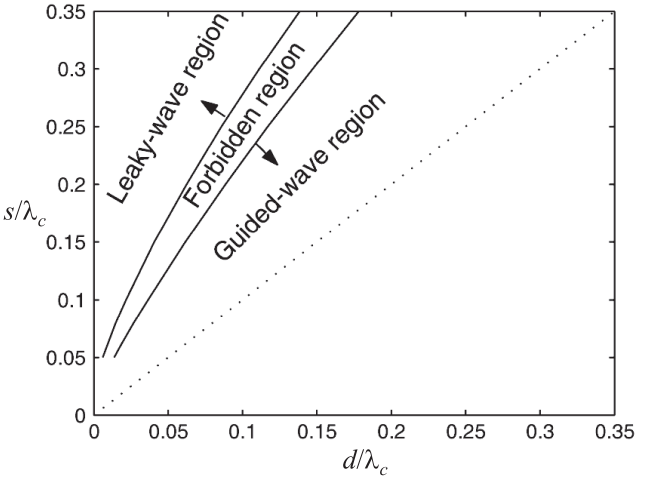

Figure 9.19 Guided wave region and leaky-wave region in SIW structures (from [7], © 2006 IEEE. Reprinted with permission).

constant in SIW structures changes with frequency as in classical waveguides: it assumes a very large value near the cutoff frequency and it tends to become flat in the center of the single-mode frequency band (Figure 9.18). Conversely, the attenuation constant of microstrip lines and coplanar waveguides is monotonically increasing with frequency. Moreover, in SIW structures the substrate thickness can be increased with the aim to reduce the conductor loss. The same increase of the substrate thickness could have undesired and detrimental effects in the case of microstrip lines: also in this case, in fact, the conductor loss would be reduced, but the structure becomes more subject to radiation leakage, especially in the presence of bends or discontinuities.

A comparison of losses in different planar waveguides and transmission lines has been performed. In this comparison, an SIW structure, a microstrip and a coplanar waveguide are designed on the same dielectric substrate (substrate thickness $h = 0.254$ mm, relative dielectric constant $\varepsilon_r = 9.9$, $\tan\delta = 0.0002$, $\sigma_c = 5 \cdot 10^7$ S/m). The dimensions of the SIW structure are w = 3.97 mm, $d = 0.635$ mm, $s = 1.016$ mm, and microstrip line and coplanar waveguide are dimensioned to exhibit a characteristic impedance of 50 Ω: the width of the microstrip is 0.24 mm, the conductor width of the coplanar waveguide is 0.24 mm and its gaps are 0.1 mm.

The results are shown in Figure 9.18, which reports the attenuation constant of the three planar interconnects, in the single-mode operation band of the SIW. They show that, with this dielectric substrate, the SIW structure exhibits better performance in terms of losses in the upper part of the operation frequency band.

9.3.2 Guided–wave and Leaky-wave Regions of Operation

As already stated, the electromagnetic performance of SIW structures strongly depends on the diameter d of the metalized holes, their longitudinal spacing s, and the width w of the waveguide (Figure 9.2). In particular, if the longitudinal spacing s becomes large, the electromagnetic field is not confined anymore inside the waveguide and the SIW tends to radiate. This radiation effect can be considered either as a power leakage (if the structure is intended as a transmission line), or as a contribution to radiation (if the structure is designed to be a leaky-wave antenna).

When the SIW structure is used as a transmission line, the geometry of the SIW is optimized for radiation loss minimization. Since the SIW structure is subject to intrinsic sources of loss (namely dielectric and conductor losses), radiation leakage α_R can be considered acceptable if it does not exceed the other types of loss [7]. With the typical values of dielectric and conductor loss in SIW structures, the attenuation due to radiation leakage can be considered acceptable up to a maximum value of 10^{-4} neper/rad. This condition on the radiation leakage defines a set of constraints for the geometrical parameters of SIW structures: in particular, dimensions d and s must be properly selected in order to meet these constraints, thus defining the guided-wave region in the d-s plane (Figure 9.19).

Conversely, when the SIW structure is intended to be a leaky-wave antenna, the radiation leakage should largely exceed the contribution due to conductor and dielectric losses: if the radiation leakage per unit length (or per wavelength) is too small, the size of the antenna becomes excessively large. For standard characteristics of dielectric substrates, a minimum value of attenuation due to radiation leakage can be set as 10^{-3} neper/rad [7]. In this case, the geometrical constraints determine the leaky-wave region in the d-s plane (Figure 9.19).

There is an additional region (denoted as the forbidden region in Figure 9.19), where radiation losses are too high for using the SIW as a transmission line and too low for designing a leaky-wave antenna. This region and the corresponding combinations of d and s should be avoided.

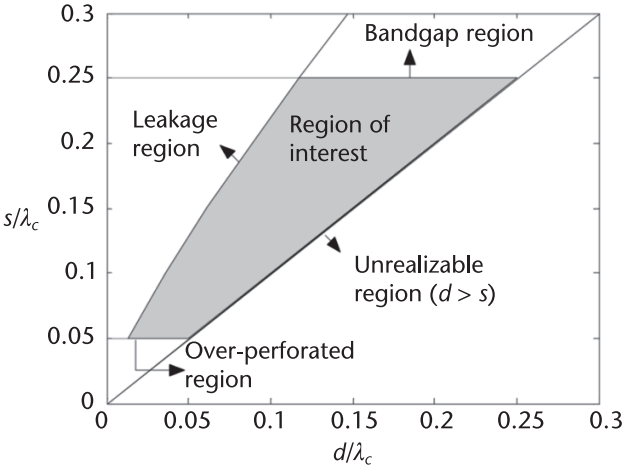

Figure 9.20 Region of interest for the design of SIW structures in the *d*–*s* plane (from [7], © 2006 IEEE. Reprinted with permission).

9.3.3 Band-gap Effects in SIW Structures

SIW is a periodic structure and consequently it is subject to band-gap effects. The presence of a band-gap spoils the performance of the SIW structure, both in the case of guided waves and in the case of leaky-wave operation.

As discussed in [7], the first band-gap appears at

$$\beta s = \pi \tag{9.49}$$

where β is the propagation constant of the SIW. This equation can be used to determine the longitudinal spacing *s* required to locate the band-gap at the upper limit of the single-mode bandwidth. As the single-mode bandwidth ranges from f_c to 2 f_c, the propagation constant at 2 f_c is

$$\beta = \sqrt{k_0^2 - k_c^2} = \sqrt{4k_c^2 - k_c^2} = \sqrt{3}k_c = \frac{2\sqrt{3}\pi}{\lambda_c} \tag{9.50}$$

where k_c and λ_c represent the cutoff wave-number and the cutoff wavelength of the fundamental SIW mode, respectively. Combining (9.49) and (9.50) results in

$$\frac{s}{\lambda_c} = \frac{1}{2\sqrt{3}} \tag{9.51}$$

Under this condition, the first band-gap is centered at the cutoff frequency $2f_c$ of the second mode of the SIW. In this way, since the band-gap has a finite bandwidth, the single-mode bandwidth of the SIW is partially reduced [7]. This effect can be completely avoided by adopting a condition more restrictive than (9.51), for example $s/\lambda_c < 0.25$. As $\lambda_c \cong 2w$, this condition can be reformulated as $s < w/2$.

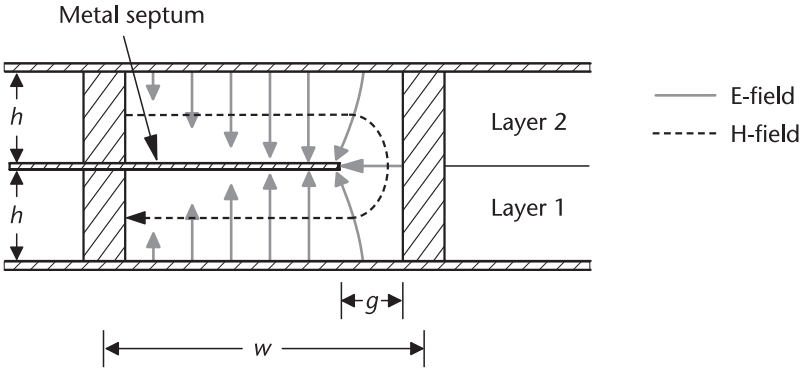

Figure 9.21 Substrate integrated folded waveguide configuration and field pattern (front view).

9.3.4 SIW Design Rules

The results achieved in the previous sections allow to derive a set of design rules for choosing the geometrical dimensions of SIW structures [7]. These rules permit to identify a region in the *d*-*s* plane, where the SIW operates as a transmission line with minimum radiation leakage and no band-gap.

The first condition depends on a physical reason: the diameter d of the metalized cylindrical holes cannot exceed their longitudinal spacing s (otherwise the metal cylinders would intersect), and therefore $s > d$. The second condition is needed to avoid any band-gap in the single-mode frequency band of the waveguide, and can be expressed as $s/\lambda_c < 0.25$. Furthermore, to minimize radiation leakage the gap size should be small, and therefore the ratio between the spacing s and the post diameter d is limited by the condition $s/d < 2$. Finally, a last condition is defined to avoid over-perforated substrates: by setting $s > \lambda_c/20$, the number of metalized cylindrical holes should not exceed 20 per wavelength.

To summarize, the four conditions

$$s > d \tag{9.52a}$$

$$s/\lambda_c < 0.25 \tag{9.52b}$$

$$s/d < 2 \tag{9.52c}$$

$$s > \lambda_c/20 \tag{9.52d}$$

define a region in the *d*-*s* plane (marked in gray in Figure 9.20), which should be selected for the design of SIW structures.

9.4 Other SIW Configurations

SIW structures exhibit two major limitations when compared to traditional planar transmission lines: their bandwidth is narrower and their size is larger.

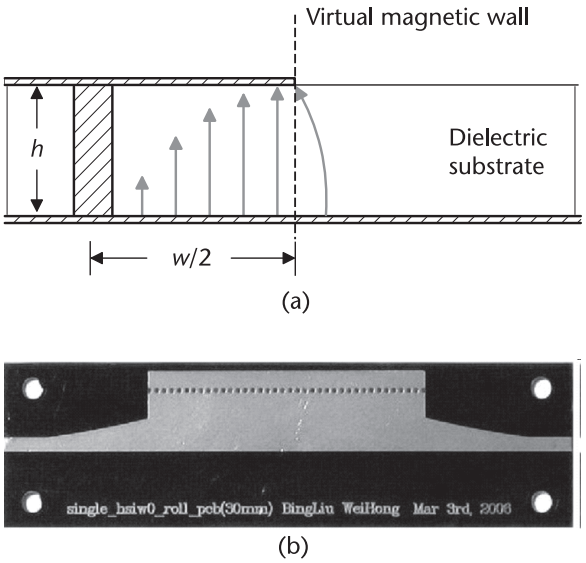

Figure 9.22 Half–mode substrate integrated waveguide: (a) configuration and electric field pattern (front view); (b) photograph of a prototype, with transitions to microstrip lines (from [30], © 2006 IEEE. Reprinted with permission).

The operation bandwidth of the SIW is limited to about one octave and corresponds to the single-mode bandwidth of the waveguide, i.e. an SIW structure can be used from the cutoff frequency f_c of the fundamental mode to the cutoff frequency 2 f_c of the first upper mode. This represents a limitation in comparison to microstrip lines or coplanar waveguides, where the fundamental mode has no cutoff and the transmission lines can typically be used from DC to some tens of GHz.

In turn, the cutoff frequency f_c determines the width of the SIW, as in any rectangular waveguide [8]. Therefore, the size of the SIW is determined by the operation frequency. The width of an SIW is usually larger than the width of a microstrip line. To make a fair comparison, anyway, the width of an SIW should be compared with the minimum distance between two adjacent microstrip lines to avoid cross coupling: in this case, the difference in size appears much less significant. Conversely, compared to hollow rectangular waveguides, SIW structures benefit from the size reduction due to the dielectric loading, which makes them more compact by the factor $\sqrt{\varepsilon_r}$.

Several SIW configurations have been developed to overcome these limitations in bandwidth and compactness, as discussed in this Section.

9.4.1 Substrate Integrated Folded Waveguide (SIFW)

The substrate integrated folded waveguide (SIFW) is based on the concept of the folded waveguide, originally proposed in [26], and it allows for reducing the waveguide width by using a dual-layer substrate.

The SIFW is basically an SIW folded around a metal septum (Figure 9.21). The propagation characteristics of the SIFW mainly depend on the waveguide width w,

the substrate thickness h, and gap width g. As the SIFW is not an H-plane component, its mode pattern and propagation characteristics also depend on the substrate thickness. This structure exhibits the same propagation characteristics as the SIW, provided the geometrical dimensions are carefully selected [27].

Compared to an SIW implemented in the same substrate, the SIFW leads to a reduction in width of a factor ranging from 2 to 3. The reduction factor depends on the geometrical dimensions. As shown in [27], for 2 $g/w = h/w$ the width reduces to a half of that of a conventional SIW, and for $h/w = 0.4$ and $g/w = 0.05$ (very small gap) the width reduces to one third. In the former case, where the gap width is comparable with the substrate thickness, the width reduction is only due to the folding of the waveguide. In the latter case, where the gap width is extremely small, the electric field near the gap becomes very large and this effect determines a capacitive loading, which leads to a further reduction of the waveguide width.

The SIFW exhibits larger non-radiative losses than the corresponding SIW, due to the large amplitude of the electric field in the gap region. Consequently, the loss increase is small for broad gaps and becomes more significant if the gap width is very small. The radiation loss from SIFW should be less from the left sidewall because the magnetic field in the upper and lower halves is expected to be equal and opposite (Figure 9.21). However, the magnetic field near the right sidewall becomes vertical and the corresponding longitudinal current on the sidewall is likely to excite vertical slots between the cylinders. This concept has been verified in relation to a slotline suspended in rectangular waveguide [28].

A prototype of SIFW operating in X band was proposed and demonstrated in [27]. A dielectric substrate with ε_r=2.2 and thickness h=1.515 mm was adopted; the geometrical dimensions $w = 7.75$ mm and $g = 0.9$ mm provide a reduction of a factor two with respect to a conventional SIW with the same cutoff frequency (whose width should be $w = 15.5$ mm).

Besides the compactness, SIFW structures present some favorable features: in particular, they are easy to fabricate as they do not require internal vias and they preserve the complete electrical shielding as the unfolded SIW. Approximate formulas for the design of SIFW were proposed in [29].

9.4.2 Half-Mode Substrate Integrated Waveguide (HMSIW)

The half-mode substrate integrated waveguide (HMSIW) is obtained by removing a half of the SIW, cutting along the symmetry plane in the propagation direction (Figure 9.22(a)) [30].

The HMSIW is based on the approximation that the symmetry plane of the SIW is a virtual magnetic wall for the fundamental mode: if a half of the waveguide is removed, the open side of the waveguide is nearly equivalent to a magnetic wall, due to the high ratio of width to height. For this reason, when cutting away half of the waveguide, the field distribution of the fundamental mode remains practically unchanged, while the width of the waveguide is reduce to a half.

The width of the HMSIW can be simply calculated as half of the width of the standard SIW structure. Nevertheless, a more accurate design should take into account the effect of fringing fields, which slightly modify the effective width of the

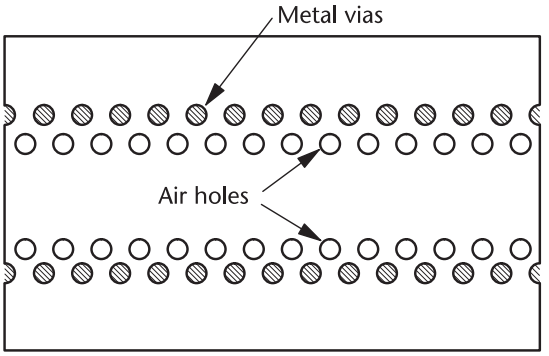

Figure 9.23 Substrate integrated slab waveguide configuration (top view).

waveguide and consequently change its cutoff frequency. This effect can be taken into accounted by reducing the width by a correcting terms Δw, which is expressed by empirical formulas. A rigorous discussion of the propagation properties of HMSIW structures is provided in [31].

The HMSIW was proposed for the first time in [30], where the design and the experimental characterization of a prototype operating in Ku band is reported (Figure 9.22(b)).

The major advantage of the HMSIW is its limited complexity: it permits to reduce to approximately a half the size of the SIW and the fabrication complexity is maintained at the same level as for the conventional SIW. Losses in HMSIW are comparable to those in conventional SIW, except in a small frequency band just above the cutoff, where the open side of the HMSIW behaves like a slot with uniform field distribution and radiation loss is very significant [31].

A combination of the SIFW and HMSIW techniques was also proposed [32], resulting in the folded half-mode substrate integrated waveguide (FHMSIW), which leads to a further size reduction.

9.4.3 Substrate Integrated Slab Waveguide (SISW)

The substrate integrated slab waveguide (SISW) represents the implementation in SIW technology of the dielectric slab loaded rectangular waveguide, originally proposed in [33]. This modified SIW configuration permits a significant enhancement in the single-mode bandwidth.

In the SISW, the dielectric substrate is periodically perforated with air holes, located in the lateral portions of the waveguide (Figure 9.23). This process allows to reduce the effective dielectric constant ε_{eff} in the side portions of the waveguide, which results as a weighted average of the dielectric permittivity of the substrate and of the air. In the central portion of the waveguide, where there are no air holes, the value of the dielectric constant remains unchanged at ε_r. The fundamental mode of the SISW (that resembles the TE_{10} mode of the rectangular waveguide) has the electric field more concentrated in the central portion of the waveguide, and consequently it practically experiences the original dielectric constant ε_r and its cutoff frequency is scarcely affected by the presence of the air holes. Conversely, in the second (TE_{20}-like) mode of the SISW, the electric field is more concentrated in the

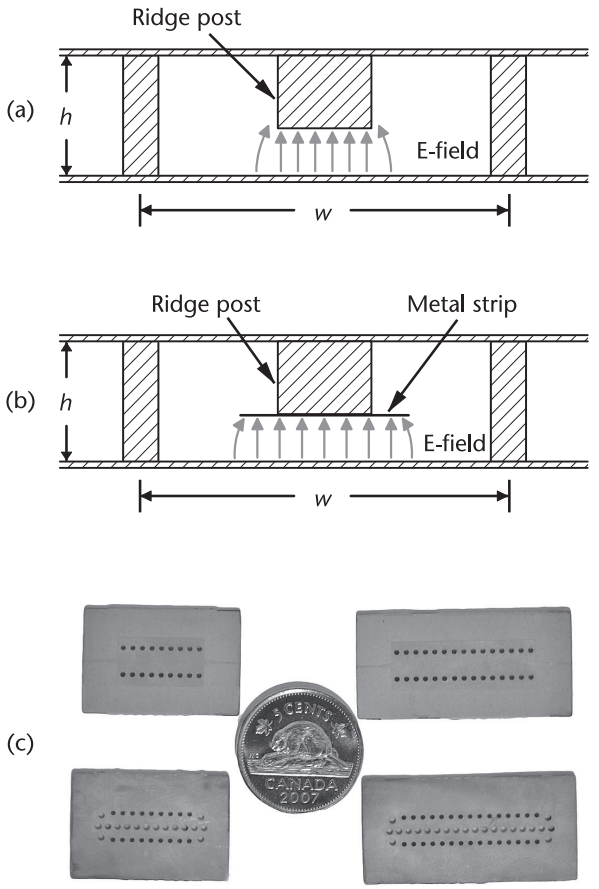

Figure 9.24 Substrate integrated ridge waveguide configurations: (a) structure without metal strip (front view); (b) structure with metal strip (front view); (c) photograph of two SIRW prototypes with different length (from [38]).

side portions of the waveguide, and therefore it is subject to the effective dielectric constant ε_{eff}, which is lower than ε_r. As a consequence, the cutoff frequency of the second mode increases.

The SISW was firstly proposed in [34], where a prototype covering the X and Ku bands was implemented. With a proper location and dimensioning of the air holes and the use of a dielectric substrate with ε_r=10.2, a waveguide with single-mode band from 7.5 GHz to 18 GHz was realized.

The amount of bandwidth enhancement in the SISW mainly depends on the dielectric material of the substrate: the use of materials with high dielectric constant ε_r leads to a larger contrast between the dielectric constant ε_r experienced by the fundamental mode and the effective constant ε_{eff} undergone by the second mode. The higher the contrast, the more significant the bandwidth increase. Moreover, the bandwidth enhancement can be improved by tightly packing the air holes, because this permits to lower the effective dielectric constant in the lateral portions of the

waveguide, thus further increasing the cutoff frequency of the second mode. The minimum distance between air holes is limited by technological constraints.

The major advantages of the SISW are the simple geometry and the single layer configuration, which allow an easy and cost effective implementation.

9.4.4 Substrate Integrated Ridge Waveguide (SIRW)

The substrate integrated ridge waveguide represents the SIW counterpart of the ridge rectangular waveguide described in [35]. In the ridge waveguide, by adding a ridge in the middle of the broad wall of a rectangular waveguide, the cutoff frequency of the fundamental mode is shifted to lower frequency, whereas the second mode is practically unperturbed. This effect determines a broader single-mode bandwidth. In addition, since the cutoff frequency of the fundamental mode in the ridge waveguide is lower than in the standard waveguide with the same width, the compactness of the waveguide is improved.

The first version of the ridge waveguide in SIW technology was reported in [36-37]: in this case, the ridge is realized by a row of metal posts with partial height, located in the middle of the broad wall of the SIW (Figure 9.24(a)). A prototype covering the frequency band from 4.9 GHz to 13.39 GHz was fabricated and measured, based on a double layer substrate. Subsequently, it was shown that the structure proposed in [36-37] suffers from band-gap issues, that arise when using ridge posts with large diameter [38]. This is a serious limitation, since the best performance in terms of broad operation bandwidth can be achieved with large diameter of the ridge posts.

The second version of the ridge SIW was then proposed in [38]. In this structure, the issue of the band-gap is overcome by adding a metal strip, that connects the bottom of the ridge posts (Figure 9.24(b)). This ridge SIW configuration does not exhibit any band-gap, even for a large diameter of the ridge posts.

The single-mode bandwidth of ridge SIW can be maximized by properly selecting the dimensions of the ridge posts. The use of long ridge posts permit to obtain large bandwidth, as they minimize the gap between the post and the ground plane and therefore they create a large capacitance. In SIW implementation, using long ridge posts (and consequently small gaps) implies adopting a very thin dielectric layer: therefore, the limit is usually imposed by technological constraints. The diameter of the ridge posts also plays an important role: increasing the diameter of the ridge posts allows increasing the single-mode bandwidth, even though an optimum value exists and using larger diameters does not provide any further improvement [38].

A ridge SIW based on this configuration was designed and fabricated in [38] (Figure 9.24(c)), covering the frequency band 6.8-25.0 GHz (which is almost three times broader than the single-mode bandwidth of a standard SIW). Furthermore, the width of this ridge SIW structure is 40% smaller than a conventional SIW with the same cutoff frequency.

Losses in ridge SIW are slightly larger than in standard SIW, due to increased conductor losses. This is mainly attributed to the mode pattern, where the electric field is strongly concentrated under the metal strip. For the same reason, the frequency behavior of the attenuation constant is rather odd: it is similar to a classical

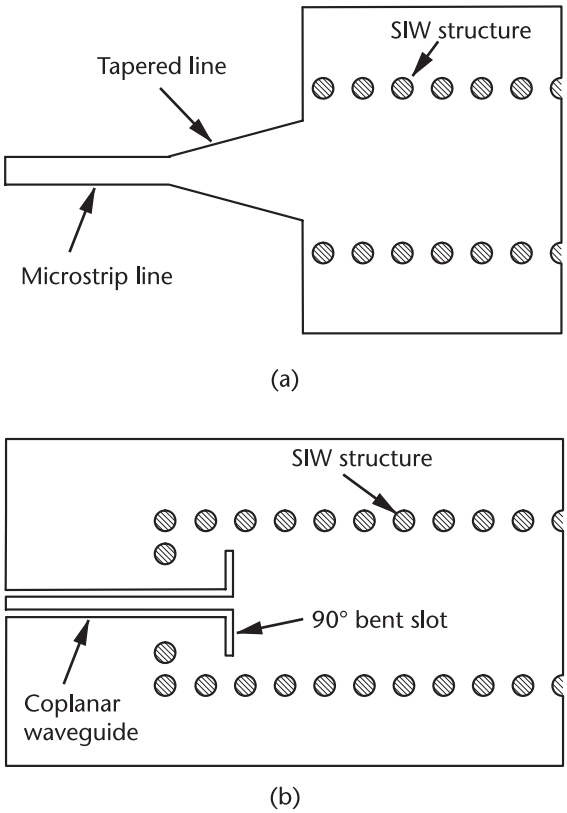

Figure 9.25 Different types of transitions: (a) tapered microstrip–to–SIW transition; (b) coplanar waveguide–to–SIW transition with 90° bend slot.

waveguide at low frequency, with high loss near the cutoff, and it resembles the typical behavior of a microstrip line at higher frequencies, where the attenuation constant monotonically increases with frequency [38].

The configuration of the ridge SIW is slightly more complicated than classical SIW, due to the presence of partial height metal posts. Its fabrication requires the use of two dielectric layers and may become difficult when using PCB technology, whereas the use of LTCC technology appears more suitable.

The major advantage of the ridge SIW is represented by its extremely broad operation bandwidth, which provides unique peculiarities and application potential in the scenario of SIW technology. In addition, the ridge SIW combines the wide bandwidth with a very compact size.

A further improvement can be achieved by combining the concepts of the ridge SIW and of the SISW: by adding air holes in the lateral portions of the ridge SIW, the cutoff frequency of the second mode can be increased, thus obtaining an even larger single-mode bandwidth. A ridge SISW covering the single-mode frequency band 7.1-30.7 GHz was designed and fabricated in [38].

9.5 Transitions Between SIW and Planar Transmission Lines

As widely discussed in previous sections, SIW technology permits to integrate classical rectangular waveguides in planar form in a dielectric substrate, by adopting the manufacturing techniques traditionally used for microstrip-lines and coplanar-waveguide circuits. Consequently, since these three transmission lines share the same physical medium and the same fabrication process, they can be realized simultaneously on the same dielectric substrate. This feature opens interesting perspectives for hybrid circuits and systems, but at the same time it poses the problem of implementing proper transitions between SIW structures and microstrip/CPW transmission lines.
The use of such transitions is also required for the experimental characterization of SIW prototypes by means of a vector network analyzer, which typically needs to be connected to a 50-Ω planar transmission line: for this reason, prototypes of SIW components usually require transitions to input/output microstrip lines or CPW lines.

Therefore, the design of transitions between SIW structures and planar transmission lines represents a key element in the development of SIW components. A significant effort has been devoted to the design of a variety of different transition topologies, which need to be broadband, possibly planar, and easy to fabricate.

9.5.1 Microstrip-to-SIW Transitions

The geometry of the transitions between microstrip lines and SIW structures is usually quite simple, because of the similarity between the modal fields in the two structures.

A compact, single layer transition between microstrip line and SIW is obtained by connecting the conductor of the microstrip to the top wall of the SIW through a tapered microstrip section (Figure 9.25(a)), and the ground plane of the microstrip to the bottom wall of the SIW [4]. The taper of the microstrip line allows to reduce the discontinuity effects and to guarantee a good matching. Long linear tapers, usually up to half wavelength, are required to achieve broadband input matching.

The tapered microstrip transition is the most commonly adopted microstrip-to-SIW transition for several reasons: its geometry is very simple and easy to fabricate, its dimensions are compact and the insertion loss is quite low. The design of this transition usually requires full-wave simulations, to determine the length of the taper and its width. Analytical equations, derived from curve fitting, have been proposed in [39] to evaluate the optimum dimensions of the taper, with no need of full-wave simulations. By adopting these tapered transitions, it is generally possible to obtain an input reflection coefficient lower than -20 dB over the full standard single-mode bandwidth of the SIW (conventionally defined as the frequency range from 1.25 f_0 to 1.9 f_0).

If the substrate thickness of the microstrip line differs from the thickness of the SIW structure, the connection of the microstrip to the top wall of the SIW can be performed through a via hole [40]. This solution is mainly applicable in the case of LTCC technology.

9.5.2 CPW-to-SIW Transitions

In several cases, coplanar waveguides are preferred to microstrip lines, especially when they need to be integrated on the same substrate with SIW structures. In fact, thick substrates are used to reduce conductor loss in SIW structures, and this prevents the use of microstrip lines on the same substrate, because they may be subject to large radiation leakage. Conversely, CPW is compatible with thick substrates, as its electrical parameters can be optimized practically with any substrate thickness.

Different transition topologies have been proposed to connect coplanar waveguides to SIW structures. The most common solution is based on a coplanar waveguide with a 90° bend of each slot inside the SIW structure (Figure 9.25(b)) [41]. A stub can be added in the CPW line with the aim to better match the transition. In some cases, the angle of the bent slots can be optimized to improve the matching as well as the bandwidth performance [42]. The major issue of this transition topology is related to spurious radiation: this transition is similar to a center-fed slot antenna, which radiates both in the substrate (thus exciting the SIW mode) and outside the SIW structure (thus determining undesired radiation loss).

A modified version of this transition was proposed in [43] for an electrically thick high-permittivity substrate. The main feature of this transition is the presence of an SIW cavity around the 90° bent slots. This transition permits to achieve wideband performance: measurements demonstrated 40% bandwidth with 15 dB return loss or better and 0.5 dB insertion loss for a single transition in the 50 GHz frequency range.

An alternative topology of CPW-to-SIW transition, specifically developed for grounded CPW, makes use of a current probe [44]: the current vertically flowing through the probe generates a magnetic field, which matches with the magnetic field of the fundamental mode of the SIW structure.

In general, the performance of CPW-to-SIW transitions in terms of bandwidth is significantly inferior to microstrip-to-SIW transitions. Typical values of achievable relative bandwidth are in the order of 20% to 30%. The performance is better in the case of conductor-backed CPW, where transitions with an input reflection coefficient lower than -20 dB are able to cover the full standard single-mode bandwidth of the SIW [42].

9.6 SIW Components and Antennas

SIW technology allows implementation of a variety of components and antennas, with characteristics very similar to the corresponding planar components and antennas in classical metallic waveguide technology. This similarity has fostered the rapid growth of several passive and active components in SIW technology, as the same configurations and design rules developed for classical waveguide components have been applied to the implementation of SIW components.

Besides the compact size, low weight and low cost, SIW implementation exhibits a number of special features. The most important feature of SIW components is the design flexibility, which mainly depends on the possibility to arbitrarily define the shape of the components: in fact, the post walls as well as the internal metal cylinders can be freely located, thus offering large flexibility to the designer. Moreover,

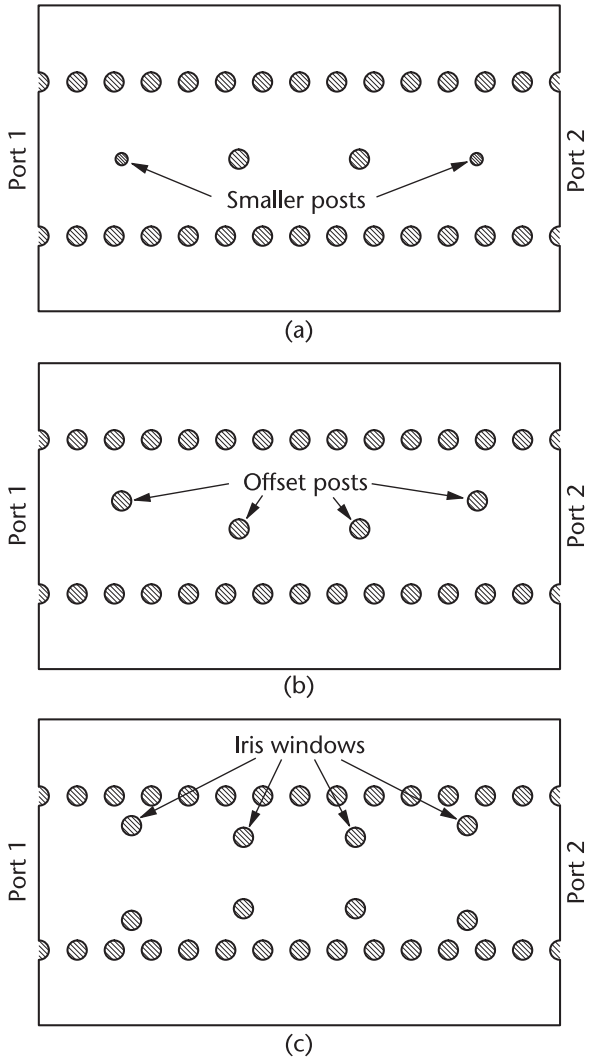

Figure 9.26 Inline SIW filter topologies: (a) centered post inline filter; (b) offset post inline filter; (c) filter with iris windows.

the possibility to stack several dielectric substrates and obtain multilayer circuits permits to realize compact components and to integrate multiple functions in minimum space. Finally, the easy integration of SIW structures with planar transmission lines allows to combine various technologies in the same substrate: for the same reason, the integration of active devices is less problematic in SIW components than in classical metallic waveguides.

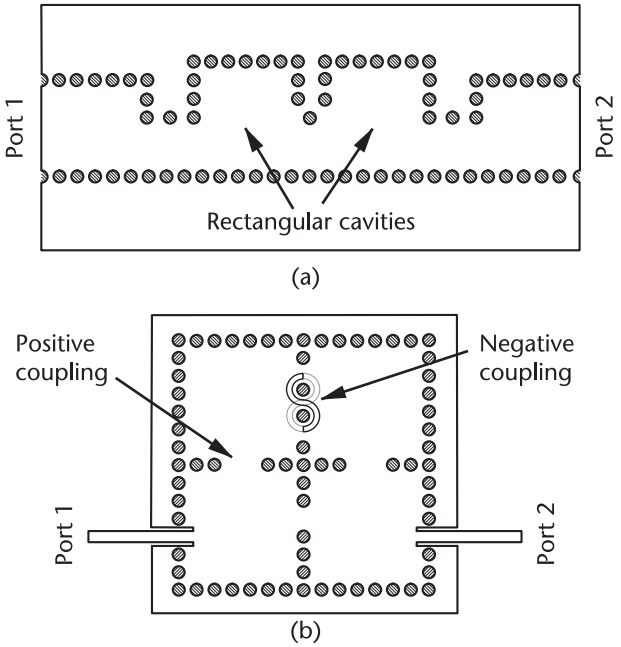

Figure 9.27 SIW filters based on resonant cavities: (a) rectangular cavity SIW filter; (b) SIW filter with rectangular cavities, featuring positive and negative cross–coupling.

9.6.1 Passive Components

The first and most common passive components implemented in SIW technology have been the filters, with several topologies proposed and demonstrated along the years. SIW filters represent a good compromise between classical metallic waveguide filters and printed microstrip filters: SIW filters are definitely better than microstrip filters in terms of performance, especially in the mm-wave frequency range, where the microstrip is too lossy to design high Q components. Compared to waveguide filters, SIW filters are much lighter, more compact and by far less expensive, even though they cannot achieve extremely high selectivity.

SIW Filters

Simple SIW filters are based on inline configurations: they consist of a straight SIW section (defined by two rows of metal cylinders) and some additional isolated metal cylinders located inside the SIW, which are used to defined the filter cavities. In the simple configuration, called the inductive post SIW filter, the cavities are defined by single metal posts, either centered or offset with respect to the vertical symmetry plane of the SIW structure (Figures 9.26(a) and 9.26(b)) [5]. The longitudinal spacing of such metal cylinders is in the order of half guided wavelength. In centered post SIW filters, all internal cylinders have different diameters, and the first and last metal cylinders usually have a very small diameter (Figure 9.26(a)): the small diameter is required to achieve good input matching, but it poses serious technological issues (especially in the mm-wave frequency range) and it tends to increase

conductor loss (as large electric current density flows along the surface of the thin metal cylinder). For this reason a different topology is typically preferred, where the internal metal posts defining the filter cavities are properly offset from the symmetry plane of the SIW structure (Figure 9.26(b)). In this filter configuration, the diameter of the internal metal cylinders is usually kept constant, and in most cases it is identical to the diameter of the metal cylinders used to define the side walls of the SIW.

Another class of inline SIW filters is represented by the SIW filters with iris windows, where the filter cavities are defined by pairs of symmetrically located metal cylinders (Figure 9.26(c)) [45]. As in classical iris filters in metallic waveguide technology, the filter design requires the determination of the cavity lengths and of the width of the iris windows. Typically the inner cavities have higher quality factor (and therefore the corresponding iris windows are more closed) and the external cavities have lower quality factor (and consequently the external iris windows are more open).

A more flexible SIW filter configuration is based on properly shaped resonant cavities: SIW cavities with various sizes and shapes are connected by an opening or a short evanescent waveguide section (Figure 9.27(a)). Both rectangular [46] and circular cavities [47] have been adopted to implement SIW filters. Besides the increased design flexibility, cavity filters often allow to locate transmission zeros out of the pass-band, thus improving the filter selectivity.

A significant enhancement in filter performance can be achieved by exploiting the cross-coupling between adjacent cavities (Figure 9.27(b)), with the use of positive and negative coupling structures [48], [49]. Both positive and negative coupling structures are needed to generate transmission zeros at finite frequencies in the frequency response of the filter, thus achieving higher selectivity and designing elliptic and quasi-elliptic filters. Positive coupling can be simply obtained by an iris window connecting two SIW cavities [48]. Negative coupling is more difficult to obtained in SIW technology, and it can be realized by an iris window and two balanced slots with a pair a metal cylinders [49] (Figure 9.27(b)).

The filter dimensions can be reduced by the use of dual-mode cavities, where each nearly-square or nearly-circular cavity supports two almost degenerate resonant modes [50]. Dual mode SIW filters permit to achieve higher filter selectivity in a very compact size. In dual-mode cavity filters, the frequency response exhibits a number of poles which is twice as large as the number of resonant cavities. The use of oversized SIW cavities has also been proposed [51], with the advantage to improve the stop-band performance by inserting transmission zeros (related to the interaction of higher order cavity modes).

Another possible technique aiming at reducing the overall filter dimensions is based on multi-layer configurations, where the SIW cavities are stacked in different dielectric layers and are connected by openings in the common metal plane [52]. This filter configuration is particularly suitable for LTCC implementation [53–54].

One of the major limitations of SIW filters is related to losses: in fact, losses determine the maximum value of the quality factor of the filter cavities, and this value poses a limit to the filter selectivity. In most cases, particularly at high frequency, the main contribution to losses is due to the dielectric substrate, and therefore it depends on the tan δ of the dielectric material. In this case, the maximum achiev-

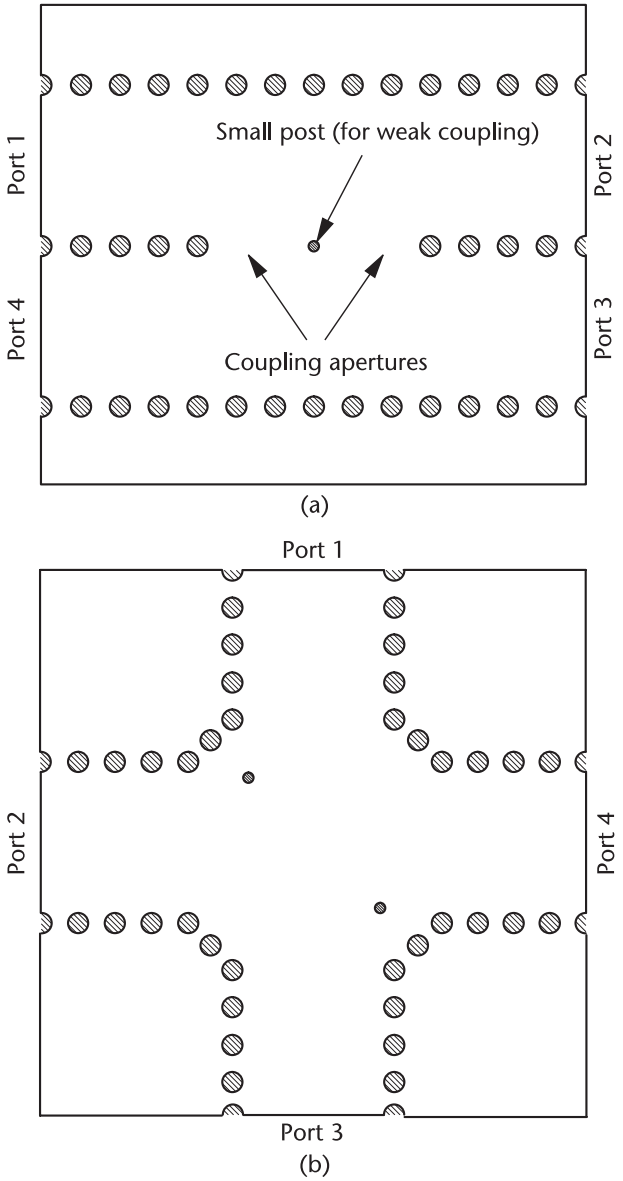

Figure 9.28 Directional couplers in SIW technology: (a) coupler consisting of two adjacent SIW structures with an opening in the common wall; (b) cruciform shape SIW coupler.

able quality factor of the filter cavities is $Q = 1/\tan\delta$ [55]: in practical cases, the achievable quality factor of SIW cavities is in the order of $Q = 500$.

A design technique particularly suitable to overcome this limitation in SIW filters is based on the predistortion concept [56]: by properly dimensioning the filter cavities and couplings, the use of predistortion permits to realize a filter response with in-band flatness equivalent to a filter with higher quality factor. As an example [56], although the adopted dielectric material allows for obtaining SIW resonators

with a quality factor Q = 500, the use of predistortion permits to realize a filter response with in-band flatness equivalent to a filter with Q = 2000, not achievable otherwise with the adopted material in SIW technology. Nevertheless, this improvement in the filter selectivity is obtained at the cost of degrading the input matching of the filter.

SIW filters have been implemented from the low microwave range (starting from few GHz), up to the mm-wave frequency band, at 60 GHz [45] and 180 GHz [57], by using various fabrication technologies. At very low frequencies, the use of SIW filters becomes unpractical due to the large size. Conversely, the implementation of SIW filters at high frequencies requires a special care in the substrate selection, as the issue of dielectric loss tends to spoil the filter performance.

Tunable filters represent a special class of SIW filtering structures, where the frequency response and the pass-band can be modified electronically. Different tuning solutions have been proposed and experimentally verified in SIW technology: PIN diodes mounted on top of SIW cavities were used in [58] for tuning the pass-band of a two-pole filter from 1.55 GHz to 2.00 GHz, and RF MEMS switches were adopted in [59] to achieve a tuning range from 1.2 GHz to 1.6 GHz in the pass-band of a two-pole filter.

SIW Directional Couplers

Another important class of passive components widely developed in SIW technology are directional couplers.

The traditional waveguide coupler, consisting of two adjacent waveguides with an opening in the common wall, can be implemented in single-layer SIW technology, simply by removing some metal cylinders in the common wall between two parallel SIW structures (Figure 9.28(a)) [60]. By properly selecting the width of the opening, the coupling strength can be optimized at the desired value (e.g., –3 dB, –6 dB, or –10 dB). Weak coupling is obtained by placing a thin metal cylinder in the center of the aperture [60]. This coupler topology is compact and easy to fabricate, thanks to the single-layer geometry. It allows for achieving relatively broadband performance (with relative bandwidth in the order of 25%).

A very compact 3-dB directional coupler was proposed in [61], based on a cruciform shape in single-layer SIW technology: it consists of the cross-over of two SIW structures, with two additional metal cylinders located inside the square junction (Figure 9.28(b)). This hybrid coupler topology is simple and compact, and it was able to reach 18% bandwidth.

An alternative configuration of SIW coupler is based on a dual-layer structure [62]: this coupler consists of two parallel waveguides, located one on top of the other, with two oblique parallel resonant slots in their common broad wall. The coupling strength can be varied from –3 dB to –6 dB, depending on the position, length, and angle of the coupling slots. A bandwidth of 16% was experimentally verified [62].

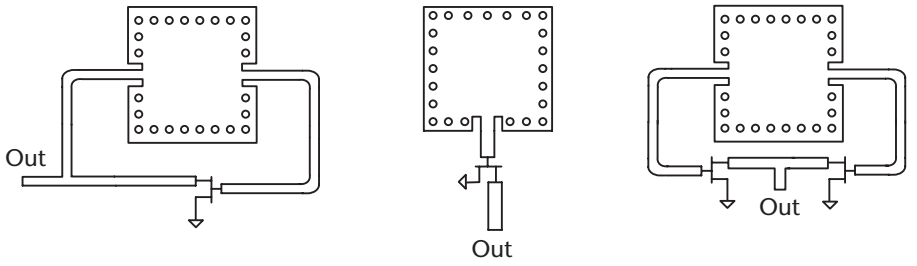

Figure 9.29 Oscillator circuits in SIW technology: (a) feedback oscillator, (b) reflection oscillator, (c) push-push reflection oscillator (from [76].)

SIW Diplexers and Multiplexers

Planar SIW diplexers and multiplexers represent a class of SIW components similar to filters: they consist of a power divider cascaded with two (or more) planar filters and find application as channel separators in microwave communication systems. Planar SIW diplexers operating at 5 GHz [63] and at 25 GHz [50] have been fabricated and tested. In these structures, the filter selectivity and the isolation between the channels represent figures of merit of the component.

Among the passive components, several more structures have been implemented in SIW technology, including power dividers [64], phase shifters [65], circulators [66], baluns [67], magic-T [68], and six-port circuits [69].

9.6.2 Active Circuits

The design flexibility of SIW technology offers several possibilities for the implementation of active circuits, such as oscillators, mixers, and amplifiers. In particular, the development of SIW active components takes advantage of the possibility to mount active devices directly on top of the SIW structures, with no need of complex and lossy interconnections, as it usually happens in the case of classical metallic waveguides: in fact, the interconnection of active devices with SIW structures is typically based on simple and compact microstrip-to-SIW or CPW-to-SIW transitions. In few cases, the active devices are mounted directly inside the dielectric substrate: even thought this solution appears more suitable to the full system integration and better preserves the complete shielding of the SIW structures, it is often avoided, mainly because of technological and repeatability issues.

SIW Oscillators

The development of oscillators is particularly suited to SIW technology, thanks to the possibility to realize resonant cavities with relatively high quality factor. Two major SIW oscillator topologies have been implemented: the former is the feedback oscillator, composed of an amplifier circuit and an SIW cavity located in the feedback loop of the amplifier, which acts as a frequency selector (Figure 9.29(a)); the

latter topology is the reflection oscillator, consisting of a cavity resonator connected to the gate of a transistor and presenting a negative resistance (Figure 9.29(b)).

A feedback oscillator operating at 12 GHz was firstly demonstrated in [70], with output power of 0 dBm and phase noise of –105 dBc/Hz at 1 MHz offset from the carrier. A reflection type oscillator operating in the X band was proposed in [71]: in this circuit, a transistor is connected to an SIW cavity. Moreover, a varactor diode mounted on top of the cavity allows for frequency tunability of the resonant cavity and, consequently, of the oscillation frequency: the resulting frequency tuning range is 460 MHz, with output power from 6.5 to 10 dBm and phase noise of 88 dBc/Hz at 100-kHz offset. Another reflection type oscillator at 35 GHz based on a Gunn diode was presented in [72]: it is based on an SIW cavity, with the active device is integrated at the edge of the cavity by removing a via hole and placing the diode in the substrate. The measured output power was 15.7 dBm, the phase noise was –91.2 dBc/Hz at a frequency offset of 100 KHz from the carrier, and the DC to RF efficiency of the oscillator resulted 0.74%. Similar reflection type oscillators were proposed in [73], where a Gunn diode is located near the center of the SIW cavity, and in [74], where frequency tuning capability was added by integrating a varactor diode together with a Gunn diode inside the SIW cavity.

A different oscillator topology, based on the push-push oscillator concept (Figure 9.29(c)), was proposed in [75]. This push-push oscillator, operating at 29.5 GHz, is based on the combination of two reflection type oscillators, which share the same SIW cavity with fundamental resonance at 14.75 GHz. The output of the two reflection type oscillators are connected using a Wilkinson power combiner, in such a way that the two oscillators are synchronized in frequency and oscillate out-of phase: consequently, the signals at the fundamental frequency are canceled at the output and the components at the second harmonic at 29.5 GHz are summed together.

SIW Mixers

Different mixer topologies are available in SIW technology. An SIW mixer can be implemented by combining an SIW 3-dB hybrid coupler and the active device. This SIW mixer topology was firstly proposed in [77]: it is single-balanced mixer, based on two diodes connected back-to-back and an SIW hybrid coupler, which is able to cover the entire X band with a measured conversion loss of 6.8 dB. An alternative millimeter-wave mixer operating in the frequency range 34–40 GHz was reported in [78], which integrates a single balanced mixer MMIC and a folded SIW filter. The dimension of this circuit is quite compact, only 3×3 cm^2 including an IF output amplifier. Measurements exhibited a conversion gain of 4 dB. A mixed technology mixer, based on the hybrid integration of SIW structures and conventional microstrip lines, was developed in [79] as a part of a 24 GHz automotive radar.

The combination in a single compact component of oscillator and mixer functionalities is obtained by the self-oscillating mixer [80], [81], where one single transistor is used both to generate the oscillation and to perform the mixing. These circuits are designed by properly biasing and loading the oscillator circuit, in order to achieve maximum conversion gain. The first SIW self-oscillating mixer was pre-

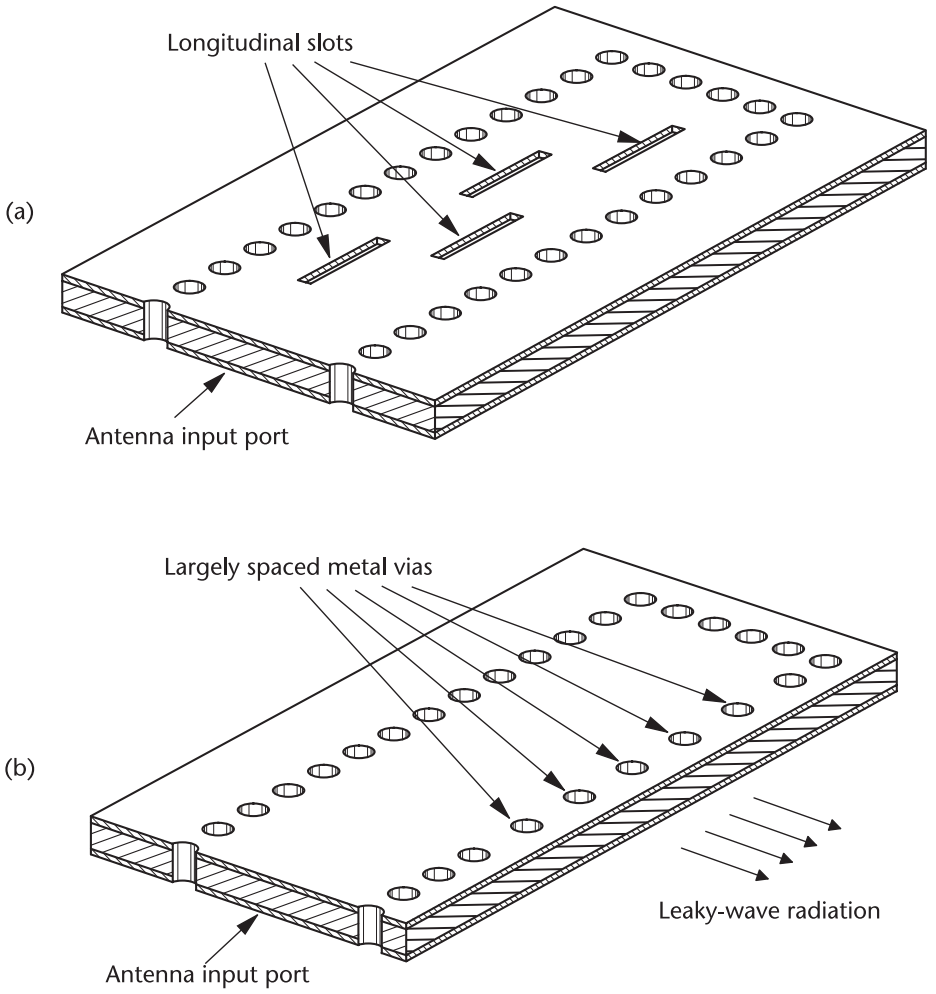

Figure 9.30 Different types of SIW antennas: (a) SIW slot array antenna; (b) SIW leaky-wave antenna.

sented in [80]: it was based on a feedback oscillator, with a FET amplifier circuit connected to a rectangular SIW cavity. The fundamental oscillation frequency was 14.3 GHz, but the structure was designed as a sub-harmonic mixer: in this way, the second harmonic of the oscillator was mixed with an RF signal at 30.4 GHz, to produce an intermediate frequency at 1.7 GHz with a measured conversion loss of 8.6 dB.

SIW Amplifiers

Another active SIW component is the amplifier, which has anyway received quite limited attention. The first example of an SIW amplifier, proposed in [82], was operating in the X band and was based on two SIW-to-microstrip transitions, with a single transistor amplifier mounted on the microstrip line. In the SIW-to-microstrip transitions, printed interdigital capacitors were adopted both as DC blocks and to

improve the impedance matching. Measurements demonstrated a gain of 10 dB with less than 2 dB of ripple.

A different configuration was proposed in [83] for a power amplifier operating in the frequency range 3.7–4.2 GHz: the combination of a low-impedance microstrip line and a short-circuited SIW structure were adopted to suppress the second and third harmonics in the power amplifier, thus improving its efficiency.

The combination of half-mode SIW power dividers and amplifiers was exploited in [84] to demonstrate a Ka-band amplifier based on spatial power combining. The structure is based on a two way SIW to HMSIW power divider: in each of the HMSIW branches there are four SIW-to-microstrip transitions, thus permitting to connect eight amplifiers and effectively resulting in an 8-way power divider. This amplifier features a small-signal gain of 19.5 dB and a saturated output power of 30.6 dBm. The measured power combining efficiency of the amplifier was 72%.

9.6.3 Antennas

Radiation from SIW structures can be obtained essentially in two main ways: the first technique, named the SIW slot array antenna, consists in etching slots in the top metal surface of the SIW structure (Figure 9.30(a)); in the second technique, named the SIW leaky-wave antenna, radiation is obtained by increasing the longitudinal spacing s of the side-wall metal cylinders (Figure 9.30(b)).

Slotted SIW Antennas

SIW slot array antennas look very similar to classical slotted-waveguide antennas, where a number of longitudinal resonant slots are etched in the broad wall of the waveguide (Figure 9.30(a)). The longitudinal spacing of the slots is usually half guided-wavelength and the slots are alternatively positioned, slightly offset from the vertical symmetry plane: this topology permits to feed the radiating slots with the proper amplitude and phase for broadside radiation at the desired operation frequency [85]. SIW slot arrays can be designed by adopting the method developed by Elliot [86], taking care to include the effects of internal high-order mode coupling: in fact, this coupling mechanism cannot be ignored in SIW structures, since the substrate thickness is usually much smaller than the SIW width. Circular polarization is obtained by alternate rotation of slots by +45°/–45° [87].

While most of SIW slot antennas have been designed and fabricated in the microwave frequency range (e.g., at 10 GHz in [85] and at 24 GHz in [79]), a single slot SIW antenna operating at 94 GHz was demonstrated in [88] and a double slot antenna operating at 60 GHz was reported in [89]. Compared to the corresponding antennas in classical waveguide technology, SIW slot arrays exhibit significant advantages in terms of reduced weight and cost. Conversely, gain and antenna efficiency in SIW slot arrays are worse than in classical slotted waveguide arrays, especially due to dielectric loss.

SIW based array feed networks

In most cases, an array antenna consists of several rows of slots (i.e., slotted SIW structures), located next to each other, and fed by a power divider, realized either in microstrip line [85] or in SIW technology [79]. This solution permits to obtain similar directivity in the two principal planes of the radiation pattern.

Several feeding networks have been proposed and implemented to achieve scanned-beam or multiple-beam SIW slot array antennas: by properly selecting the input port, these feeding networks allow to modify the amplitude and phase of each row of slots, thus scanning the direction of maximum radiation. An attractive solution used to generate multi-beam antennas is the Rotman lens, which features a simple design and compact size [90]: a Rotman lens with seven input ports and nine outputs was implemented at 28.5 GHz to scan the beam to seven different directions. A Blass matrix based on SIW technology, operating at 16 GHz, was proposed in [91]: this feeding network consists of a double-layer structure, with a matrix of 4 × 16 cross couplers. Compared with the conventional waveguide implementation, the Blass matrix in SIW technology features several advantages, including lower cost, easier fabrication and low profile. The SIW implementation of the Butler matrix was proposed in [92–93]: this matrix comprises 90° hybrid couplers, cross couplers, phase shifters and power splitters, and is based on a standard single-layer printed circuit board process, which is particularly cost effective and suitable for mass production. The Nolen matrix was also proposed in SIW technology: it is a special case of the Blass matrix, where the termination loads are suppressed. A 4×4 Nolen matrix beam-forming network operating at 12.5 GHz was proposed in [94].

Leaky-Wave SIW Antennas

Leaky-wave SIW antennas are straight SIW structures, with increased longitudinal spacing in one row of side-wall metal cylinders and located near the edge of the dielectric substrate (Figure 9.30(b)) [95]. These antennas exploit the radiation leakage due to the sufficiently large gaps between the side-wall metal cylinders. The radiation leakage increases if the gaps are large, and this permits to reduce the overall length of the leaky-wave antenna at the cost of large beamwidth. Nonetheless, large gaps may lead to band-gap effects, which prevent the propagation of the electromagnetic field inside the SIW and reduce the operation bandwidth of the antenna. In leaky-wave SIW antennas, the direction of maximum radiation depends on the propagation constant of the waveguide mode, and the radiation pattern can be computed from the value of the electromagnetic field at the edge of the SIW structure. One of the major issues in the design of leaky-wave SIW antennas is related to the field reflection at the interface between dielectric and air: a maximum value of allowed dielectric permittivity can be calculated, which prevents total internal reflection at the dielectric/air interface [95].

A leaky-wave SIW antenna based on the second (quasi TE_{20}) mode of the SIW structure was proposed in [96]: this antenna topology features a particular feed system to excite the second SIW mode and provides better performance compared

to the classical leaky-wave antenna based on the fundamental mode of the SIW structure.

Other SIW Antenna Topologies

Besides the two major SIW antenna categories (namely, the slotted waveguide array and the leaky-wave antenna), other antenna configurations have been proposed for implementation in SIW technology.

The dual V-type linearly tapered slot antenna [97] represents a modified version of the Vivaldi antenna. Due to its multimode SIW feeding network, this structure is able to generate both the sum and difference beams, and for this reason it is particularly suitable for monopulse antenna applications.

Several topologies of cavity-backed SIW antennas have been also developed [98-100]. The structure proposed in [98] is very simple: it consists of an SIW cavity, fed by a coplanar waveguide etched on one side of the substrate, with a rectangular slot located on the opposite side. A more compact solution was proposed in [99], where the rectangular slot is replaced by a meander line. A Ku-band SIW cavity-backed antenna array was developed in [100]: this antenna consists of a 2×2 array of metal patches, backed by SIW cavities. The structure was implemented by adopting a double layer PCB fabrication process, with the metal patches fed by a microstrip feeding line in the top layer, and SIW cavities in the bottom layer. This solution guarantees a relatively high aperture efficiency of 70% over a reasonably wide bandwidth (9%), and a front-to-back ratio of 20 dB.

Active SIW cavity backed antennas were also developed, by integrating a transistor oscillator in a cavity-backed antenna. The first implementation [101] was based on the simple structure proposed in [98], where the gate of the transistor is connected to the input coplanar waveguide of the antenna. In this configurations, the role of the SIW cavity is twofold: it is used as a feedback by the transistor, with a beneficial effect on the phase noise of the oscillator, and simultaneously it permits to improve the slot antenna performance, by suppressing the excitation of surface waves. A more compact version of active SIW cavity backed antenna was proposed in [102], where the entire circuitry is located on top of the SIW cavity, thus permitting the implementation of two dimensional arrays.

An H-plane sectoral horn antenna in SIW technology was proposed in [103]. The flares of the horn are realized by using metal vias, and a dielectric loading, integrated in the same substrate, allows high gain and narrow beam-widths in both the E- and H-plane.

The concept of the Yagi-Uda antenna has been exploited to develop SIW antennas. The first version [104] consists of a truncated SIW structure, with an additional row of metal cylinders axially aligned in front of the aperture to act as the directors of a Yagi-Uda antenna. A prototype operating at 60 GHz was demonstrated, with a gain of 12 dB. Another version was proposed in [105] and consists of a stacked multilayer array, resulting in a very small footprint of the entire geometry.

Finally, frequency selective surfaces (FSS) and polarizers have been developed [106–108], based on the characteristics of SIW technology: they are components strictly related to antennas, both for the operation principle and for their applications. These structures consist of a planar periodic array of SIW cavities, connected

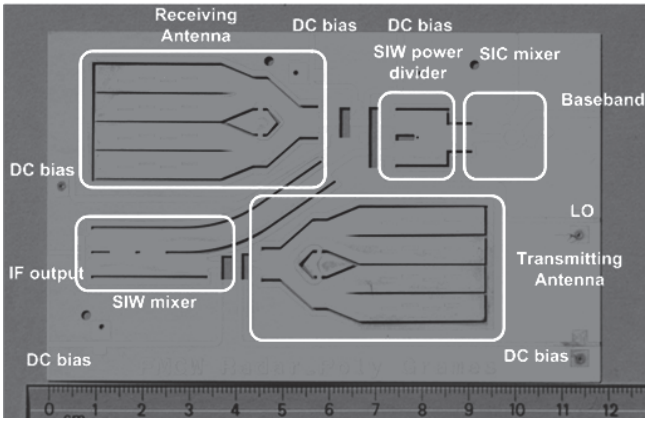

(a)

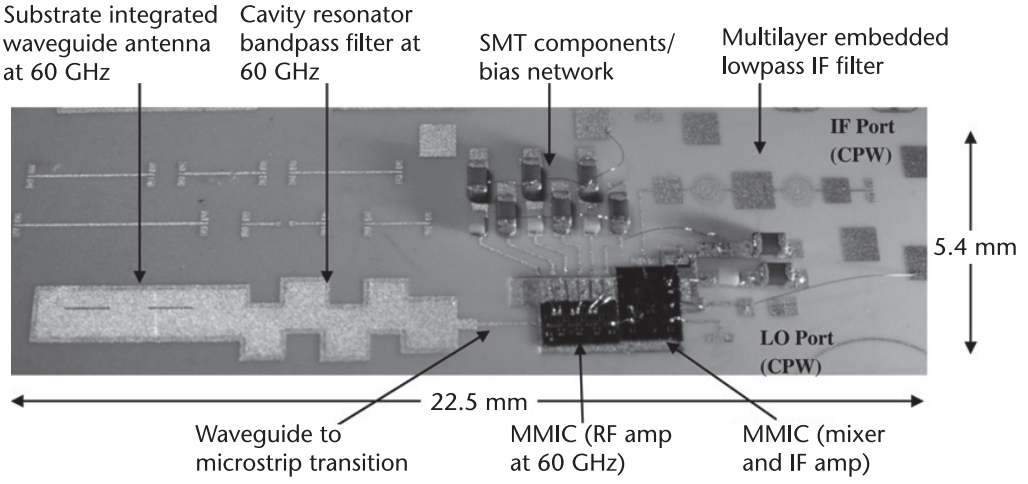

(b)

Figure 9.31 Examples of System-on-Substrate integration: (a) 24–GHz FMCW radar front-end (from [79], © 2008 IEEE. Reprinted with permission); (b) 60–GHz multi-chip module receiver (from [110], © The Institution of Engineering and Technology 2007. Reprinted with permission).

to the exterior through properly designed coupling slots. The FSS selectivity depends both on the coupling slots and on the resonant mode of the SIW cavity.

9.6.4 System-on-Substrate (SoS)

The previous sections highlighted the possibility to apply SIW technology to the development of a variety of passive and active components, as well as of antennas and arrays. They also discussed the option to easily interconnect SIW components to microstrip and CPW circuits, realized on the same dielectric substrate. These possibilities open interesting perspectives for the implementation of complete systems on a single substrate: in this way, the concept of the System-in-Package (SiP),

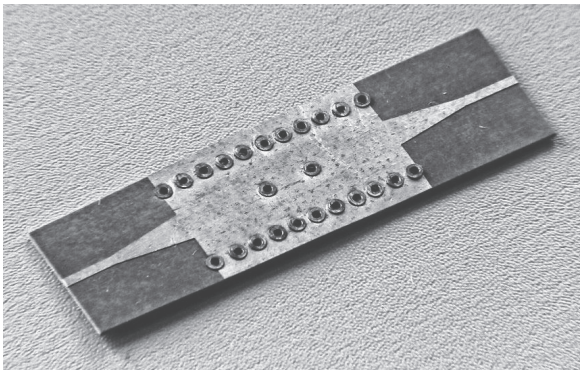

Figure 9.32 Early version of SIW filter, with the metal vias implemented by using metal rivets.

widely adopted in the design of RF and microwave circuits, can be extended and gradually replaced by the paradigm of the System-on-Substrate (SoS) [109].

There are two major methodologies for the deployment and integration of SoS. A flexible and compact approach consists in the development of all components and antennas on one single substrate, by combining SIW and microstrip or CPW technologies (Figure 9.31(a)). This approach permits to exploit the advantages of SIW as well as of other planar technologies that can be efficiently integrated in the same substrate. The complete front-end of a 24 GHz frequency-modulation continuous-wave (FMCW) radar based on SoS approach was presented in [79]. The circuit (shown in Figure 9.31(a)) integrates on the same substrate several building blocks, including up-converters, down-converters, power dividers, as well as one receiving and one transmitting 16-element slotted-wave antenna array. The complete radar was fabricated on a RT/Duroid 6002 dielectric substrate with a dielectric constant of 2.94 and a thickness of 0.508 mm. The fabrication process was similar to standard hybrid MICs fabrication process, commonly used in the case of microstrip circuits. First, the sidewalls of the SIW were realized by laser cutting, and subsequently the metallization of cut-through sidewalls was made by sputtering a thin copper layer on them followed by electroplating. Finally, standard photolithography process was used to define the microstrip pattern.

The other methodology for the deployment of SoS is based on the use of multi-chip modules, which are mounted on SIW circuits. In this case, the active portion of the circuit or even the complete front-end are integrated in the chipset, whereas some specific components, like selective filters, low-loss interconnects, and directive antennas, are implemented off-chip in SIW technology (Figure 9.31(b)). This methodology allows a simplification of the design, while exploiting the features of SIW technology for those components which cannot be efficiently integrated in a chipset. A 60 GHz receiver based on multi-chip modules in GaAs technology was proposed in [110]. The receiver chain (shown in Figure 9.31(b)) integrates a slotted waveguide antenna connected to a cavity filter, followed by an SIW-to-microstrip transition and two MMICs (a three-stage low-noise amplifier and a 90° balanced diode mixer with IF amplifier), fabricated in pHEMT technology.

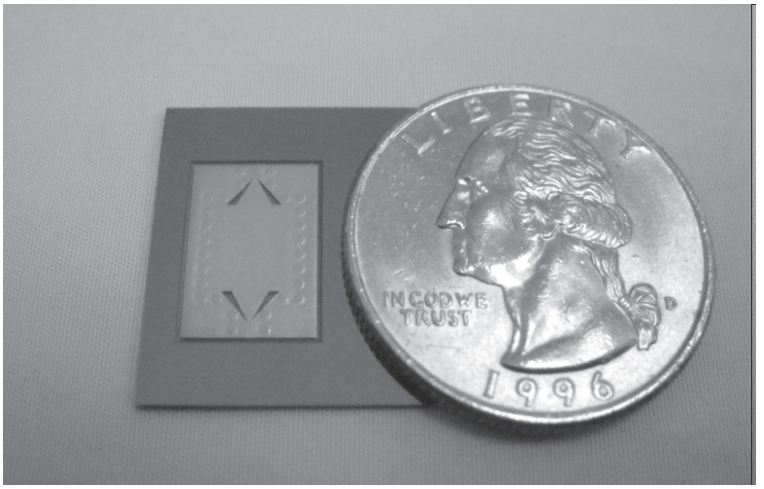

Figure 9.33 Silicon-based SIW interconnect (from [111], © The Institution of Engineering and Technology 2011. Reprinted with permission).

The SoS concept represents the ideal platform for developing cost-effective, easy-to-fabricate and high-performance mm-wave systems. In fact, in the implementation of SoS there is no need of complex transitions between components fabricated by different technologies (e.g., metallic rectangular waveguide and microstrip technology), thus generally achieving lower losses and broader bandwidth. This improvement is particularly significant when operating at mm-wave frequencies. Moreover, SIW circuits and systems are completely shielded: this feature prevents radiation leakage and spurious undesired coupling between adjacent systems. In addition, this approach avoids the need of packaging, thus reducing the overall system cost and development effort.

9.7 Fabrication Technologies and Materials

The large majority of SIW components and circuits have been developed in the frequency range from 3 GHz to 30 GHz, with some examples up to 60 or 90 GHz and very limited implementations above 100 GHz. At low frequencies (below 3 GHz), the size of the SIW structures becomes large, as it is related to the operation wavelength. Moreover, in this frequency range where typical losses are relatively low, the advantage of SIW over microstrip line and CPW circuits is less significant. At high frequencies, fabrication tolerances become prohibitively strict and losses spoil the performance of the circuits; therefore, special care in the selection of the materials and sophisticate fabrication technologies are required.

9.7.1 Fabrication by PCB and LTCC Technologies

The most common fabrication technology used for implementing SIW structures has been the printed circuit board (PCB) technique, which is also widely adopted

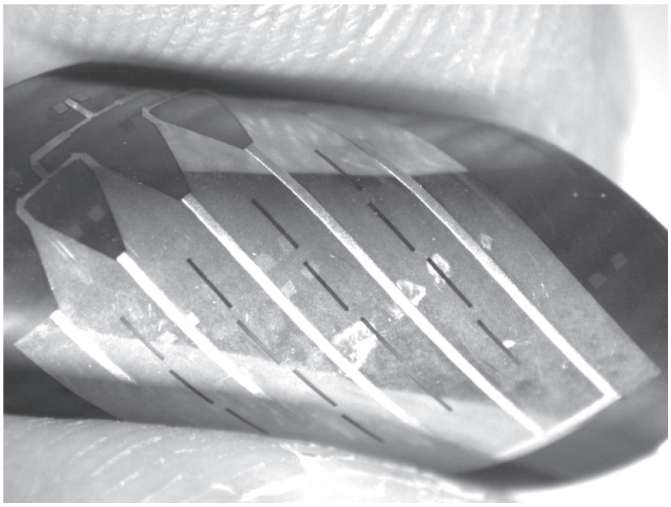

(a)

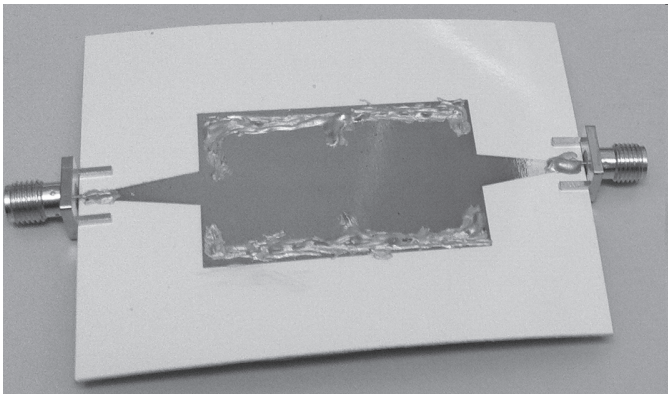

(b)

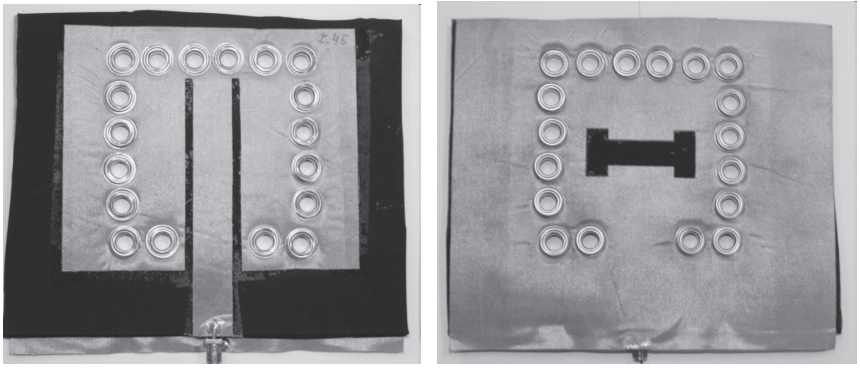

(c)

Figure 9.34 Novel materials for the realization of SIW components: (a) slotted SIW antenna on a flexible substrate (from [112], © 2009 IEEE. Reprinted with permission); (b) inkjet-printed paper-based SIW filter [113]; (c) cavity-backed antenna on textile (from [114]).

for manufacturing microstrip line and CPW circuits. Plastic and ceramic dielectric substrates typically used for microstrip circuits can be adopted also for the development of SIW components. In the early versions of SIW components, the holes were perforated by a drilling machine and the metal vias were implemented by using metal rivets (Figure 9.32). More recently, the metalized holes have been usually obtained either by micro-drilling or laser cutting, and their metallization is subsequently performed by metal plating or by filling the holes by a conductive paste.

PCB fabrication is a conventional and widely proven manufacturing process, often available in small companies and research laboratories. It exhibits several advantages, including low costs and good design flexibility. In addition, it allows to implement both SIW and standard printed circuits on the same substrate, thus permitting the integration of the complete systems according to the SoS approach [109].

Besides PCB fabrication, low-temperature co-fired ceramic (LTCC) technology is particularly suitable for the implementation of SIW components and antennas. The possibility of using several layers represents an interesting opportunity to reduce the footprint of SIW components, for instance by stacking or folding the cavities of SIW filters [53–54].

9.7.2 Integration of SIW on Silicon

Micro-machined, silicon-based SIW structures were developed for application in the mm-wave frequency range [111]. In these structures, benzocyclobutene (BCB) polymer filled into a deep etched silicon cavity is used as a dielectric substrate, and the via structures are realized with metal-coated silicon columns. This fabrication technique is particularly interesting for the potential integration of the SIW structures with silicon-based circuits or RF MEMS devices. Straight SIW interconnects with CPW-to-SIW transitions were demonstrated (Figure 9.33), with insertion loss of 1.4 dB in the frequency range from 25 to 40 GHz.

9.7.3 Use of Novel Substrate Materials

The use of novel materials and technologies has been investigated for the implementation of low-cost and flexible SIW structures. In particular, the use of a flexible plastic substrate was proposed [112] for the implementation of an SIW-based slot array antenna operating at 79 GHz (Figure 9.34(a)). The prototypes were fabricated in a polyimide flex foil using a PCB fabrication process. The manufacturing steps needed to form the metal vias are based on ion track technology: as the first step, Kapton foils are treated by irradiation with heavy ions and subsequent by wet etching. The ions determine tracks in the material, and these tracks are selectively etched to create pores. In the final step, the surface of the foil is irradiated and etched, and the pores perforate the whole thickness of the foil. As shown in Figure 9.34(b), the flexibility of this substrate opens interesting perspectives for its applications in the development of conformal circuits and antennas such as wearable antennas.

Recent studies have demonstrated the possibility of using the photographic paper for microwave circuit applications, where conductive strips are realized by

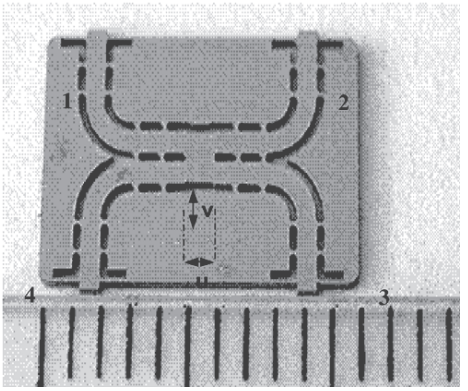

Figure 9.35 W–band hybrid coupler in SIW technology, based on metalized slots (from [115], © 2006 IEEE. Reprinted with permission).

ink-jet printing [113], through the use of silver micro-particles in suspension in the ink. The use of paper allows low fabrication costs of microwave circuits, and the proposed manufacturing technology is fully eco-friendly in the entire life cycle of the circuit, both during the manufacturing of the components (as it avoids the use of acids typically adopted in chemical etching) and at the time of disposal, at the end of the life time of the device (since paper is rapidly bio-degradable). SIW interconnects and components based on inkjet-printed paper substrates was demonstrated in [113], in the frequency range around 5 GHz: the example of an SIW filter on paper is shown in Figure 9.34(a). In the fabrication of SIW structures, the via holes were perforated by a laser and were filled by thin wires and sealed by conductive epoxy, to prevent possible radiation leakage. While losses are still an issue for SIW components on papers, significant improvements of the electromagnetic properties of paper substrates are expected in the next few years and the use of paper for microwave applications may become popular.

Another unconventional material, which is receiving attention for microwave applications and specifically for SIW implementation, is represented by textile fabrics. The implementation of SIW antennas entirely fabricated from textile materials was firstly proposed in [114], for application in wearable systems. The structure, shown in Figure 9.34(c), consists of a cavity-backed slot antenna operating in the 2.45 GHz industrial, scientific and medical band, for short range communication between rescue workers. The SIW textile antenna was assembled by gluing two conductive fabrics onto the textile substrate by means of adhesive sheets. The structure was perforated to implement the via holes and, finally, eyelets were fixed in the holes. This solution permits to preserve the flexibility of the substrate. A prototype of the antenna was demonstrate in [114]: good performance was obtained in terms of input matching and radiation pattern. Moreover, measurements performed on the antenna after bending and integration into clothing indicate high robustness against deformation and low influence of the human body on antenna performance, making the design well-suited for on-body use.

9.7.4 Solutions for High Frequency Operation of SIW

The use of SIW structures at high frequency has to face several issues, related to the increased impact of losses, to manufacturing inaccuracies, and technological constraints.

To partially overcome these limitations, a modified topology of SIW metal vias can be adopted. As widely discussed in this Chapter, SIW structures are usually based on two rows of cylindrical metal vias, which define the side walls of the waveguide (Figure 9.1). When operating at high frequency, however, the high-quality realization of metalized via holes and their small longitudinal spacing are difficult to accomplish using existing precision machining processes. To improve the quality of SIW structures at frequency higher than 60 GHz, the rows of cylindrical metal vias can be replaced by metalized slots that are easier to implement. An example is reported in [115], where a W-band hybrid coupler and a multiport circuit have been implemented in SIW technology, based on metal slots instead of cylinders

Sophisticate technologies have also been applied to overcome the technological issues. At frequencies higher than 100 GHz, SIW components have been fabricated by using photo image-able thick-film technology [57], which guarantees excellent dimension tolerance and low dielectric loss. The fabrication is based on the following steps: at the beginning, a uniform metal layer is printed on an alumina substrate to define the bottom wall of the SIW structure. Subsequently, a dielectric layer with 10-μm thickness is printed on the metallic bottom, and a photo-imaging process is adopted to define the SIW sidewalls. This step is repeated until the required substrate thickness is achieved. As a last step, a metal layer is deposited to form the upper wall of the SIW structure. SIW filters operating at 180 GHz were fabricated by using this technology and experimentally verified in [57].

References

[1] Shigeki, F., "Waveguide line," (in Japanese) *Japan Patent* 06-53 711, Feb. 25, 1994.

[2] Hirokawa, J., and M. Ando, "Single-Layer Feed Waveguide Consisting of Posts for Plane TEM Wave Excitation in Parallel Plates," *IEEE Tran. Ant. Propagat.*, Vol. 46, No. 5, 1998, pp. 625–630.

[3] Hiroshi, U., T. Takeshi, and M. Fujii, "Development of a 'Laminated Waveguide,'" *IEEE Trans. Microwave Theory Tech.*, Vol. 46, No. 12, 1998, pp. 2438–2443.

[4] Deslandes, D., and K. Wu, "Integrated Microstrip and Rectangular Waveguide in Planar Form," *IEEE Microwave Wireless Comp. Lett.*, Vol. 11, No. 2, 2001, pp. 68–70.

[5] Deslandes, D., and K. Wu, "Single-Substrate Integration Technique of Planar Circuits and Waveguide Filters," *IEEE Trans. Microwave Theory Tech.*, Vol. 51, No. 2, 2003, pp. 593–596.

[6] Xu, F., and K. Wu, "Guided-Wave and Leakage Characteristics of Substrate Integrated Waveguide," *IEEE Trans. Microwave Theory Tech.*, Vol. 53, No. 1, 2005, pp. 66–73.

[7] Deslandes, D., and K. Wu, "Accurate Modeling, Wave Mechanisms, and Design Considerations of a Substrate Integrated Waveguide," *IEEE Trans. Microwave Theory Tech.*, Vol. 54, No. 6, 2006, pp. 2516–2526.

[8] Collin, R. E., *Field Theory of Guided Waves*, Wiley-IEEE Press, 1991.

[9] Cassivi, Y., et al., "Dispersion Characteristics of Substrate Integrated Rectangular Waveguide," *IEEE Microwave Wireless Comp. Lett.*, Vol. 12, No. 9, 2002, pp. 333–335.

[10] Che, W., et al., "Analytical Equivalence Between Substrate-Integrated Waveguide and Rectangular Waveguide," *IET Microwave Ant. Propagat.*, Vol. 2, No. 1, 2008, pp. 35–41.

[11] Xu, F., and K. Wu, "Numerical Multimode Calibration Technique for Extraction of Complex Propagation Constants of Substrate Integrated Waveguide," *IEEE MTT-S International Microwave Symposium Digest (IMS 2004)*, Fort Worth, TX, June 5–12, 2004, pp. 1229–1232.

[12] Xu, F., et al., "Finite-Difference Frequency-Domain Algorithm for Modeling Guided-Wave Properties of Substrate Integrated Waveguide," *IEEE Trans. Microwave Theory Tech.*, Vol. 51, No. 11, 2003, pp. 2221–2227.

[13] Xu, F., K. Wu, and W. Hong, "Equivalent Resonant Cavity Model of Arbitrary Periodic Guided-Wave Structures and Its Application to Finite-Difference Frequency-Domain Algorithm," *IEEE Trans. Microwave Theory Tech.*, Vol. 55, No. 4, 2007, pp. 697–702.

[14] Yan, L., et al., "Investigations on the Propagation Characteristics of the Substrate Integrated Waveguide Based on the Method of Lines," *IEE Proc. Microwaves, Ant. Propagat.*, Vol. 152, No. 1, 2005, pp. 35–42.

[15] Bray, J. R., and L. Roy, "Resonant Frequencies of Post-Wall Waveguide Cavities," *IEE Proc. Microwaves, Ant. Propagat.*, Vol. 150, No. 10, 2003, pp. 365–368.

[16] Zeid, A., and H. Baudrand, "Electromagnetic Scattering by Metallic Holes and its Applications in Microwave Circuit Design," *IEEE Trans. Microwave Theory Tech.*, Vol. 50, No. 4, 2002, pp. 1198–1206.

[17] Xu, F., K. Wu, and W. Hong, "Domain Decomposition FDTD Algorithm Combined with Numerical TL Calibration Technique and its Application in Parameter Extraction of Substrate Integrated Circuits," *IEEE Trans. Microwave Theory Tech.*, Vol. 54, No. 1, 2006, pp. 329–338.

[18] Wu, X. H., and A. A. Kishk, "Hybrid of Method of Moments and Cylindrical Eigenfunction Expansion to Study Substrate Integrated Waveguide Circuits," *IEEE Trans. Microwave Theory Tech.*, Vol. 56, No. 10, 2008, pp. 2270–2276.

[19] Wu, X. H., and A. A. Kishk, *Analysis and Design of Substrate Integrated Waveguide Using Hybrid Method—Synthesis Lectures on Antennas*, Morgan & Claypool Publishers, 2010.

[20] Conciauro, G., M. Guglielmi, and R. Sorrentino, *Advanced Modal Analysis*, Wiley, New York, 2000.

[21] Bozzi, M., L. Perregrini and K. Wu, "Modeling of Conductor, Dielectric and Radiation Losses in Substrate Integrated Waveguide by the Boundary Integral-Resonant Mode Expansion Method," *IEEE Trans. Microwave Theory Tech.*, Vol. 56, No. 12, 2008, pp. 3153–3161.

[22] Bozzi, M., L. Perregrini, and K. Wu, "A Novel Technique for the Direct Determination of Multi-mode Equivalent Circuit Models for Substrate Integrated Waveguide Discontinuities," *International J. RF and Microwave Computer-Aided Engineering*, Vol. 19, No. 4, 2009, pp. 423–433.

[23] Marcuvitz, N., *Waveguide Handbook*, McGraw-Hill Book Company Inc., New York, 1951.

[24] Bozzi, M., L. Perregrini, and K. Wu, "Modeling of Losses in Substrate Integrated Waveguide by Boundary Integral-Resonant Mode Expansion Method," *IEEE MTT-S International Microwave Symposium Digest (IMS 2008)*, Atlanta, GA, June 10–15, 2008, pp. 515–518.

[25] Bozzi, M., et al., "On the Losses in Substrate Integrated Waveguides and Cavities," *International J. Microwave and Wireless Technologies*, Vol. 1, No. 5, 2009, pp. 395–401.

[26] Chen, G. L., T. L. Owen, and J. H. Whealton, "Theoretical Study of the Folded Waveguide," *IEEE Trans. Plasma Science*, Vol. 16, No. 2, 1988, pp. 305–311.

[27] Grigoropoulos, N., B. S. Izquierdo, and P. R. Young, "Substrate Integrated Folded Waveguides (SIFW) and Filters," *IEEE Microwave Wireless Comp. Lett.*, Vol. 15, No. 12, 2005, pp. 829–831.

[28] Satyamurthy, Y., and R. Garg, "Excitation of Untilted Edge Slots by a Suspended Slotline," *Electron. Lett.*, Vol. 29, No. 17, 1993, pp. 1553–1554.

[29] Che, W., et al., "Analysis and Experiments of Compact Folded Substrate Integrated Waveguide," *IEEE Trans. Microwave Theory Tech.*, Vol. 56, No. 1, 2008, pp. 88–93.

[30] Hong, W., et al., "Half Mode Substrate Integrated Waveguide: A New Guided Wave Structure for Microwave and Millimeter Wave Application," *Proc. Joint 31st International Conference on Infrared Millimeter Waves and 14th International Conference on Terahertz Electronics*, Shanghai, China, Sept. 18–22, 2006, p. 219.

[31] Lai, Q., et al., "Characterization of the Propagation Properties of the Half-Mode Substrate Integrated Waveguide", *IEEE Trans. Microwave Theory Tech.*, Vol. 57, No. 8, 2009, pp. 1996–2004.

[32] Zhai, G. H., et al., "Folded Half Mode Substrate Integrated Waveguide 3 dB Coupler," *IEEE Microwave Wireless Comp. Lett.*, Vol. 18, No. 8, 2008, pp. 512–514.

[33] Vartanian, P. H., and A. L. Helgesson, "Propagation in Dielectric Slab Loaded Rectangular Waveguide," *IEEE Trans. Microwave Theory Tech.*, Vol. 6, No. 2, 1958, pp. 215–222.

[34] Bozzi, M., et al., "Efficient Analysis and Experimental Verification of Substrate Integrated Slab Waveguides for Wideband Microwave Applications," *International J. RF and Microwave Computer-Aided Engineering*, Vol. 15, No. 3, 2005, pp. 296–306.

[35] Cohn, S. B., "Properties of Ridge Waveguide," *Proc. IRE*, Vol. 35, No. 8, 1947, pp. 783–788.

[36] Che, W., et al., "Propagation and Band Broadening Effect of Planar Integrated Ridged Waveguide in Multilayer Dielectric Substrates," *IEEE MTT-S International Microwave Symposium Digest (IMS 2008)*, Atlanta, GA, June 10–15, 2008, pp. 217–220.

[37] Che, W., et al., "Investigations on Propagation and the Band Broadening Effect of Ridged Rectangular Waveguide Integrated in a Multilayer Dielectric Substrate," *IET Microwaves, Ant. Propagat.*, Vol. 4, No. 6, 2010, pp. 674–684.

[38] Bozzi, M., S. A. Winkler, and K. Wu, "Broadband and Compact Ridge Substrate Integrated Waveguides," *IET Microwave Ant. Propagat.*, Vol. 4, No. 11, 2010, pp. 1965–1973.

[39] Deslandes, D., "Design Equations for Tapered Microstrip-to-Substrate Integrated Waveguide Transitions," *IEEE MTT-S International Microwave Symposium Digest (IMS 2010)*, Anaheim, CA, May 23–28, 2010, pp. 704–707.

[40] Huang, T.-Y., T.-M. Shen, and R.-B. Wu, "Design and Modeling of Microstrip Line to Substrate Integrated Waveguide Transitions." in *Passive Microwave Components and Antennas*, pp. 225–246, V. Zhurbenko (editor), In Tech, 2010.

[41] Deslandes, D., and K. Wu, "Integrated Transition of Coplanar to Rectangular Waveguides," *IEEE MTT-S International Microwave Symposium Digest (IMS 2001)*, Baltimore, MD, June 5–10, 2001, pp. 619–622.

[42] Chen, X.-P., and K. Wu, "Low-Loss Ultra-Wideband Transition Between Conductor-Backed Coplanar Waveguide and Substrate Integrated Waveguide," *IEEE MTT-S International Microwave Symposium Digest (IMS 2009)*, Boston, MA, June 7–12, 2009, pp. 349–352.

[43] Patrovsky, A., M. Daigle, and K. Wu, "Millimeter-Wave Wideband Transition from CPW to Substrate Integrated Waveguide on Electrically Thick High-Permittivity Substrates," *37th European Microwave Conference 2007*, Munich, Germany, Oct. 8–12, 2007, pp. 138–141.

[44] Deslandes, D., and K. Wu, "Analysis and Design of Current Probe Transition from Grounded Coplanar to Substrate Integrated Rectangular Waveguides," *IEEE Trans. Microwave Theory Tech.*, Vol. 53, No. 8, 2005, pp. 2487–2494.

[45] Choi, S. T., et al., "A V-Band Planar Narrow Bandpass Filter using a New Type Integrated Waveguide Transition," *IEEE Microwave Wireless Comp. Lett.*, Vol. 14, No. 12, 2004, pp. 545–547.

[46] Chen, X., et al., "Substrate Integrated Waveguide (SIW) Linear Phase Filter," *IEEE Microwave Wireless Comp. Lett.*, Vol. 15, No. 11, 2005, pp. 787–789.

[47] Tang, H. J., et al., "Optimal Design of Compact Millimetre-Wave SIW Circular Cavity Filters," *Electron. Lett.*, Vol. 41, No. 19, 2005, pp. 1068–1069.

[48] Chen, X.-P., K. Wu, and Z.-L. Li, "Dual-Band and Triple-Band Substrate Integrated Waveguide Filters With Chebyshev and Quasi-Elliptic Responses," *IEEE Trans. Microwave Theory Tech.*, Vol. 55, No. 12, 2007, pp. 2569–2578.

[49] Chen, X.-P., and K. Wu, "Substrate Integrated Waveguide Cross-Coupled Filter With Negative Coupling Structure," *IEEE Trans. Microwave Theory Tech.*, Vol. 56, No. 1, 2008, pp. 142–149.

[50] Tang, H. J., et al., "Development of Millimeter-Wave Planar Diplexers Based on Complementary Characters of Dual-Mode Substrate Integrated Waveguide Filters With Circular and Elliptic Cavities," *IEEE Trans. Microwave Theory Tech.*, Vol. 55, No. 4, 2007, pp. 776–782.

[51] Chen, X.-P., K. Wu, and D. Drolet, "Substrate Integrated Waveguide Filter With Improved Stopband Performance for Satellite Ground Terminal," *IEEE Trans. Microwave Theory Tech.*, Vol. 57, No. 3, 2009, pp. 674–683.

[52] Hao, Z. C., et al., "Multilayered Substrate Integrated Waveguide (MSIW) Elliptic Filter," *IEEE Microwave Wireless Comp. Lett.*, Vol. 15, No. 2, 2005, pp. 95–97.

[53] Chen, B.-J., T.-M. Shen, and R.-B. Wu, "Dual-Band Vertically Stacked Laminated Waveguide Filter Design in LTCC Technology," *IEEE Trans. Microwave Theory Tech.*, Vol. 57, No. 6, 2009, pp. 1554–1562.

[54] Chien, H.-Y., *et al.*, "Miniaturized Bandpass Filters With Double-Folded Substrate Integrated Waveguide Resonators in LTCC," *IEEE Trans. Microwave Theory Tech.*, Vol. 57, No. 7, 2009, pp. 1774–1782.

[55] Kurokawa, K., *An Introduction to the Theory of Microwave Circuits*, Academic Press, New York, 1969.

[56] Mira, F., J. Mateu, and M. Bozzi, "Substrate Integrated Waveguide Predistorted Filter at 20 GHz," *IET Microwave Ant. Propagat.*, Vol. 5, No. 8, 2011, pp. 928–933.

[57] Stephens, D., P. R. Young, and I. D. Robertson, "Millimeter-Wave Substrate Integrated Waveguides and Filters in Photoimageable Thick-Film Technology," *IEEE Trans. Microwave Theory Tech.*, Vol. 53, No. 12, 2005, pp. 3832–3838.

[58] Armendariz, M., V. Sekar, and K. Entesari, "Tunable SIW bandpass filters with PIN diodes," *40th European Microwave Conference 2010*, Paris, France, Sept. 26–Oct. 1, 2010, pp. 830–833.

[59] Sekar, V., M. Armendariz, and K. Entesari, "A 1.2–1.6–GHz Substrate-Integrated-Waveguide RF MEMS Tunable Filter," *IEEE Trans. Microwave Theory Tech.*, Vol. 59, No. 4, 2011, pp. 866–876.

[60] Hao, Z. C., et al., "Single-layer substrate integrated waveguide directional couplers," *IEE Proc. Microwaves Ant. Propagat.*, Vol. 153, No. 5, 2006, pp. 426–431.

[61] Djerafi, T., and K. Wu, "Super-Compact Substrate Integrated Waveguide Cruciform Directional Coupler," *IEEE Microwave Wireless Comp. Lett.*, Vol. 17, No. 11, 2007, pp. 757–759.

[62] Ali, A., *et al.*, "Wideband Two-Layer SIW Coupler: Design and Experiment," *Electron. Lett.*, Vol. 45, No. 13, 2009, pp. 687–689.

[63] Hao, Z. C., et al., "Planar Diplexer for Microwave Integrated Circuits," *IEE Proc. Microwaves, Ant. Propagat.*, Vol. 152, No. 6, 2005, pp. 455–459.

[64] Song, K., Y. Fan, Y. Zhang, "Eight-Way Substrate Integrated Waveguide Power Divider With Low Insertion Loss," *IEEE Trans. Microwave Theory Tech.*, Vol. 56, No. 6, 2008, pp. 1473–1477.

[65] Cheng, Y. J., W. Hong, and K. Wu, "Broadband Self-Compensating Phase Shifter Combining Delay Line and Equal-Length Unequal-Width Phaser," *IEEE Trans. Microwave Theory Tech.*, Vol. 58, No. 1, 2010, pp. 203–210.

[66] D'Orazio, W., and K. Wu, "Substrate-Integrated-Waveguide Circulators Suitable for Millimeter-Wave Integration," *IEEE Trans. Microwave Theory Tech.*, Vol. 54, No. 10, 2006, pp. 3675–3680.

[67] Zhang, Z.-Y., and K. Wu, "A Broadband Substrate Integrated Waveguide (SIW) Planar Balun," *IEEE Microwave Wireless Comp. Lett.*, Vol. 17, No. 12, 2007, pp. 843–845.

[68] He, F. F., *et al.*, "A Planar Magic-T Using Substrate Integrated Circuits Concept," *IEEE Microwave Wireless Comp. Lett.*, Vol. 18, No. 6, 2008, pp. 386–388.

[69] Xu, X., R. G. Bosisio, and Ke Wu, "A New Six-Port Junction Based on Substrate Integrated Waveguide Technology," *IEEE Trans. Microwave Theory Tech.*, Vol. 53, No. 7, 2005, pp. 2267–2273.

[70] Cassivi, Y, and K. Wu, "Low Cost Microwave Oscillator Using Substrate Integrated Waveguide Cavity," *IEEE Microwave Wireless Comp. Lett.*, Vol. 13, No. 2, 2003, pp. 48–50.

[71] He, F. F., et al., "A Low Phase-Noise VCO Using an Electronically Tunable Substrate Integrated Waveguide Resonator," *IEEE Trans. Microwave Theory Tech.*, Vol. 58, No. 12, 2010, pp. 3452–3458.

[72] Zhong, C., et al., "Ka-Band Substrate Integrated Waveguide Gunn Oscillator," *IEEE Microwave Wireless Comp. Lett.*, Vol. 18, No. 7, 2008, pp. 461–463.

[73] Zhong, C., et al.,, "Parallel Type Substrate Integrated Waveguide Gunn Oscillator," *Microwave Optical Tech. Lett.*, Vol. 50, No. 10, 2008, pp. 2525–2527.

[74] Cao, Z., X. Tang, and K. Qian, "Ka-Band Substrate Integrated Waveguide Voltage-Controlled Gunn Oscillator," *Microwave Optical Tech. Lett.*, Vol. 52, No. 6, 2010, pp. 1232–1235.

[75] Georgiadis, A., et al., "Push-Push Oscillator Design Based on a Substrate Integrated Waveguide (SIW) Resonator," *39th European Microwave Conference 2009*, Rome, Italy, Sept. 29–Oct. 1, 2009, pp.1231–1234.

[76] Bozzi, M., A. Georgiadis, and K. Wu, "Review of Substrate Integrated Waveguide (SIW) Circuits and Antennas," *IET Microwave Ant. Propagat.*, Vol. 5, No. 8, 2011, pp. 909–920.

[77] Chen, J.-X., et al., "Development of a Low Cost Microwave Mixer Using a Broad-Band Substrate Integrated Waveguide (SIW) Coupler," *IEEE Microwave Wireless Comp. Lett.*, Vol. 16, No. 2, 2006, pp. 84–86.

[78] Chen, J.-X., et al., "A Compact Millimeter-Wave Mixer Module," *Proc. Asia-Pacific Microwave Conference 2005*, Suzhou, China, December 4–7, 2005, pp. 3446–3448.

[79] Li, Z., and K. Wu, "24–GHz Frequency-Modulation Continuous-Wave Radar Front-End System-on-Substrate," *IEEE Trans. Microwave Theory Tech.*, Vol. 56, No. 2, 2008, pp. 278–285.

[80] Xu, J., and K. Wu, "A Subharmonic Self-Oscillating Mixer Using Substrate Integrated Waveguide Cavity for Millimeter-Wave Application," *IEEE MTT-S International Microwave Symposium Digest (IMS 2005)*, Long Beach, CA, June 12–17, 2005, pp. 2019–2022.

[81] Zhang, Z.-Y., K. Wu, and N. Yang, "A Millimeter-Wave Sub-Harmonic Self-Oscillating Mixer Using Dual-Mode Substrate Integrated Waveguide Cavity," *IEEE Trans. Microwave Theory Tech.*, Vol. 58, No. 5, 2010, pp. 1151–1158.

[82] Abdolhamidi, M., and M. Shahabadi, "X-Band Substrate Integrated Waveguide Amplifier," *IEEE Microwave Wireless Comp. Lett.*, Vol. 18, No. 12, 2008, pp. 815–817.

[83] He, F. F., et al., "Suppression of Second and Third Harmonics Using λ/4 Low-Impedance Substrate Integrated Waveguide Bias Line in Power Amplifier," *IEEE Microwave Wireless Comp. Lett.*, Vol. 18, No. 7, 2008, pp. 479–481.

[84] Jin, H., et al., "A Novel Spatial Power Combiner Amplifier Based on SIW and HMSIW," *IEICE Trans. Electron.*, Vol. E92–C, No. 8, 2009, pp. 1098–1101.

[85] Yan, L., et al. "Simulation and Experiment on SIW Slot Array Antennas," *IEEE Microwave Wireless Comp. Lett.*, Vol. 14, No. 9, 2004, pp. 446–448.

[86] Elliott, R. S., "An Improved Design Procedure for Small Arrays of Shunt Slots," *IEEE Trans. Antennas Propagat.*, Vol. 31, No. 1, 1983, pp. 48–53.

[87] Chen, P., et al., "A Substrate Integrated Waveguide Circular Polarized Slot Radiator and Its Linear Array," *IEEE Antennas Wireless Propagat. Lett.*, Vol. 8, No. 1, 2009, pp. 120–123.

[88] Stephens, D., P. R. Young, and I. D. Robertson, "W-band substrate integrated waveguide slot antenna," *Electron. Lett.*, Vol. 41, No. 4, 2005, pp. 165–167.

[89] Samanta, K. K., D. Stephens, and I. D. Robertson, "60 GHz Multi-Chip-Module Receiver with Substrate Integrated Waveguide Antenna and Filter," *Electron. Lett.*, Vol. 42, No. 12, 2006, pp. 701–702.

[90] Cheng, Y. J., et al., "Substrate Integrated Waveguide (SIW) Rotman Lens and Its Ka-Band Multibeam Array Antenna Applications," *IEEE Trans. Antennas Propagat.*, Vol. 56, No. 8, 2008, pp. 2504–2513.

[91] Chen, P., et al., "A Double Layer Substrate Integrated Waveguide Blass Matrix for Beamforming Applications," *IEEE Microwave Wireless Comp. Lett.*, Vol. 19, No. 6, 2009, pp. 374–376.

[92] Chen, P., et al., "A Multibeam Antenna Based on Substrate Integrated Waveguide Technology for MIMO Wireless Communications," *IEEE Trans. Antennas Propagat.*, Vol. 57, No. 6, 2009, pp. 1813–1821.

[93] Chen, C.-J., and T.-H. Chu, "Design of a 60–GHz Substrate Integrated Waveguide Butler Matrix—A Systematic Approach," *IEEE Trans. Microwave Theory Tech.*, Vol. 58, No. 7, 2010, pp. 1724–1733.

[94] Djerafi, T., N. J. G. Fonseca, and K. Wu, "Planar Ku-Band 4×4 Nolen Matrix in SIW Technology," *IEEE Trans. Microwave Theory Tech.*, Vol. 58, No. 2, 2010, pp. 259–266.

[95] Deslandes, D., and K. Wu, "Substrate Integrated Waveguide Leaky-Wave Antenna: Concept and Design Considerations," *Proc. Asia-Pacific Microwave Conference 2005*, Suzhou, China, December 4–7, 2005, pp. 346–349.

[96] Xu, F., K. Wu, and X. Zhang, "Periodic Leaky-Wave Antenna for Millimeter Wave Applications Based on Substrate Integrated Waveguide," *IEEE Trans. Antennas Propagat.*, Vol. 58, No. 2, 2010, pp. 340–347.

[97] Cheng, Y. J. , W. Hong, and K. Wu, "Design of a Monopulse Antenna Using a Dual V-Type Linearly Tapered Slot Antenna (DVLTSA)," *IEEE Transact. Antennas Propagat.*, Vol. 56, No. 9, 2008, pp. 2903–2909.

[98] Luo, G. Q., et al., "Planar Slot Antenna Backed by Substrate Integrated Waveguide Cavity," *IEEE Antennas Wireless Propagat. Lett.*, Vol. 7, No. 1, 2008, pp. 236–239.

[99] Bohorquez, J. C., et al., "Planar Substrate Integrated Waveguide Cavity-Backed Antenna," *IEEE Antennas Wireless Propagat. Lett.*, Vol. 8, No. 1, 2009, pp. 1139–1142.

[100] Awida, M. H., and A. E. Fathy, "Substrate-Integrated Waveguide Ku-Band Cavity-Backed 2×2 Microstrip Patch Array Antenna," *IEEE Antennas Wireless Propagat. Lett.*, Vol. 8, No. 1, 2009, pp. 1054–1056.

[101] Giuppi, F., et al., "Tunable SIW Cavity Backed Active Antenna Oscillator," *Electron. Lett.*, Vol. 46, No. 15, 2010, pp. 1053–1055.

[102] Giuppi, F., et al., "A Compact, Single-Layer Substrate Integrated Waveguide (SIW) Cavity-Backed Active Antenna Oscillator," *IEEE Antennas Wireless Propagat. Lett.*, Vol. 11, No. 1, 2012, pp. 431–433.

[103] Wang, H., et al., "Dielectric Loaded Substrate Integrated Waveguide (SIW)—Plane Horn Antennas," *IEEE Trans. Antennas Propagat.*, Vol. 58, No. 3, 2010, pp. 640–647.

[104] Wu, X.Y., and P. S. Hall, "Substrate Integrated Waveguide Yagi-Uda Antenna," *Electron. Lett.*, Vol. 46, No. 23, 2010, pp. 1541–1542.

[105] Kramer, O., T. Djerafi, and K. Wu, "Very Small Footprint 60 GHz Stacked Yagi Antenna Array," *IEEE Trans. Antennas Propagat.*, Vol. 59, No. 9, 2011, pp. 3204–3210.

[106] Luo, G. Q., et al. "Theory and Experiment of Novel Frequency Selective Surface Based on Substrate Integrated Waveguide Technology," *IEEE Trans. Microwave Theory Tech.*, Vol. 53, No. 12, 2005, pp. 4035–4043.

[107] Luo, G. Q., et al. "Design and Experimental Verification of Compact Frequency-Selective Surface With Quasi-Elliptic Bandpass Response," *IEEE Trans. Microwave Theory Tech.*, Vol. 55, No. 12, 2007, pp. 2481–2487.

[108] Winkler, S. A., et al, "Polarization Rotating Frequency Selective Surface Based on Substrate Integrated Waveguide Technology," *IEEE Trans. Antennas Propagat.*, Vol. 58, No. 4, 2010, pp. 1202–1213.

[109] Wu, K., "Towards System-on-Substrate Approach for Future Millimeter-Wave and Photonic Wireless Applications," *Proc. Asia-Pacific Microwave Conference 2006*, Yokohama, Japan, Dec. 12–15, 2006, pp. 1895–1900.

[110] Samanta, K. K., D. Stephens, and I. D. Robertson, "Design and Performance of a 60–GHz Multi-Chip Module Receiver Employing Substrate Integrated Waveguides," *IET Microwaves, Antennas Propagat.*, Vol. 1, No. 5, 2007, pp. 961–967.

[111] Hyeon, I.-J., et al., "Fully Micromachined, Silicon-Compatible Substrate Integrated Waveguide for Millimetre-Wave Applications," *Electron. Lett.*, Vol. 47, No. 5, 2011, pp. 328–330.

[112] Cheng, S., H. Yousef, and H. Kratz, "79 GHz Slot Antennas Based on Substrate Integrated Waveguides (SIW) in a Flexible Printed Circuit Board," *IEEE Trans. Antennas Propagat.*, Vol. 57, No. 1, 2009, pp. 64–71.

[113] Moro, R., et al., "Novel Inkjet-Printed Substrate Integrated Waveguide (SIW) Structures on Low-Cost Materials for Wearable Applications," *42nd European Microwave Conference 2012*, Amsterdam, The Netherlands, Oct. 28–Nov. 2, 2012.

[114] Moro, R., et al., "Wearable Textile Antenna in Substrate Integrated Waveguide Technology," *IET Electron. Lett.*, Vol. 48, No. 16, 2012, pp. 985–987.

[115] E. Moldovan, R.G. Bosisio and K. Wu, "W-Band Multiport Substrate-Integrated Waveguide Circuits," *IEEE Trans. Microwave Theory Tech.*, Vol. 54, No. 2, 2006, pp. 625–632.

About the Authors

Inder J. Bahl received his Ph.D. in electrical engineering in 1975. Dr. Bahl has over forty years of experience working in the microwave field. From 1969 to 1981, Dr. Bahl researched artificial dielectrics, parametric amplifiers, pin diode phase shifters, microwave and millimeter wave integrated circuits, printed antennas, phased array antennas, millimeter wave antennas, and medical and industrial applications of microwaves. He joined the ITT Gallium Arsenide Technology Center in 1981, and worked on microwave and millimeter wave GaAs ICs. At Cobham (formerly ITT GTC/Tyco Electronics), he continued working on GaAs ICs as a Distinguished Fellow of Technology until he retired in 2010. His interests include device modeling; high efficiency high power amplifiers (HPAs); broadband HPAs; high power limiter/LNAs and switches; compact, low-loss, and broadband multibit phase shifters, switches, and attenuators; 3-D MMICs; and development of MMIC products for commercial and military applications. He has been directly responsible for the design of over 400 MMICs, including low noise amplifiers, driver amplifiers, broadband amplifiers, power amplifiers (high power, high efficiency and broadband), dc and ac coupled transimpedance and limiting amplifiers, multibit phase shifters, narrow and broadband SPDT switches, redundant switches, programmable attenuators, balanced mixers, quadrature downconverters, upconverters, transmit chip, receive chip, and transmit/receive chips. He has developed modules consisting of MMICs for PAR and ECM applications.

Dr. Bahl is the author/co-author of over 160 research papers. He has authored and co-authored 14 books and holds 16 patents. He is an IEEE Fellow and a member of the Electromagnetic Academy. He is the editor of the *Int. Journal of RF and Microwave Computer-Aided Engineering*.

Ramesh Garg was born in Hissar, India, on October 18, 1945. He received an M.Sc. Hons. in physics from Panjab University, Chandigarh, India, in 1968, and a Ph.D. from the Indian Institute of Technology (IIT), Kanpur, in 1975. From 1975 to 1981, he was with the Advanced Centre for Electronic Systems (ACES), IIT Kanpur, as a research engineer, working on transmission lines for microwave integrated circuits and computer-aided design.

Since 1981, Professor Garg has been with the IIT Kharagpur (India), first as an assistant professor with the Radar and Communication Centre and now as a professor with the Department of Electronics and Electrical Communication Engineering. He was a visiting assistant professor at the University of Houston in Texas from 1985 to 1987, and a research associate at the University of Ottawa in Canada in 1994. His research interests have primarily been in the areas of leaky wave antennas, printed

lines, printed antennas, computer-aided-design, and computational techniques. He has published more than 50 papers in reference journals. He is a co-author/author of the books *Computer Aided Design of Microwave Circuits*, *Microstrip Antenna Design Handbook*, and *Analytical and Computational Techniques in Electromagnetics* (Artech House).

Professor Garg was a recipient of the 1987 IIT Kharagpur Silver Jubilee Research Award. He was chairman of the IEEE Kharagpur Section in 1991. He is a Fellow of IEEE and IETE (India).

Maurizio Bozzi was born in Voghera, Italy, on June 1, 1971. He received an M.Sc. in electronic engineering and a Ph.D. in electronics and computer science from the University of Pavia, Italy, in 1996 and 2000, respectively.

In 2002, he joined the Department of Electronics of the University of Pavia as an assistant professor. Since 2005, he has been an adjunct professor at the University of Pavia, where he currently teaches two courses, Antennas and Numerical Techniques for Electromagnetics. He has held research positions with various European and American universities, including the Technische Universitaet Darmstadt, Germany, the Universitat de Valencia, Spain, and the École Polytechnique de Montréal, QC, Canada. His main research activities concern the development of numerical methods for the electromagnetic modeling and design of microwave and mm-wave components (frequency selective surfaces, reflect arrays, electromagnetic bandgap structures, substrate integrated waveguides, waveguide components, and microwave printed and integrated circuits). He authored the chapter "Periodic Structures" in the *Wiley Encyclopedia of RF and Microwave Engineering* (2005) and co-edited the book *Periodic Structures* (2006). He was the guest editor of the special issue on "RF/Microwave Communication Subsystems for Emerging Wireless Technologies" in *IET Microwaves, Antennas & Propagation* (June 2011). He has authored more than 65 journal papers and more than 160 conference papers.

Professor Bozzi is a senior member of the Institute of Electrical and Electronics Engineers (IEEE), a member of the Education Committee of IEEE MTT-S, and a founding member of the Topical Group MAGEO (Microwaves in Agriculture, Environment, and Earth Observation) of the European Microwave Association (EuMA). He was the general chair of the IEEE MTT-S International Microwave Workshop Series on Millimeter Wave Integration Technologies in 2011. He was the leader of the focus area on "Substrate Integrated Waveguide (SIW) Technology" in the framework of the COST Action IC0803 "RF/Microwave Communication Subsystems for Emerging Wireless Technologies."

Professor Bozzi was the recipient of the Best Young Scientist Paper Award at the XXVII General Assembly of the International Union of Radio Science (URSI) in 2002, of an URSI Young Scientist Award, and of the MECSA Prize for the best paper presented by a young researcher at the Italian Conference on Electromagnetics (XIII RINEM) in 2000. He was also the co-recipient of the EUCAP 2010 Best Student Paper Award and the ACES 2010 2nd Best Student Paper Award.

Index

D